ULTRA-HIGH FREQUENCY INDUCTION ENERGY EFFECTS ON REFRACTORY OXIDES AS APPLIED TO

PROCESSING AND IMMOBILIZATION OF RADIOACTIVE WASTE

A Dissertation

Presented in Partial Fulfillment of the Requirements for the

Degree of Doctorate of Philosophy

with a

Major in Mechanical Engineering

in the

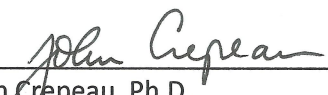College of Graduate Studies

University of Idaho

by

Jay A. Roach

May 2014

Major Professor: John Crepeau, Ph.D.

Authorization to Submit Dissertation

This dissertation of Jay A. Roach, submitted for the degree of Doctorate of Philosophy with a major in Mechanical Engineering and titled "Ultra-High Frequency Induction Energy Effects on Refractory Oxides as Applied to Processing and Immobilization of Radioactive Waste," has been reviewed in final form. Permission, as indicated by the signatures and dates below, is now granted to submit final copies to the College of Graduate Studies for approval.

Major Professor:	_John Crepeau_	Date:	9 May 2014
	John Crepeau, Ph.D.		
Committee Members:	_Daniel Cordon_	Date:	9 May, 2014
	Daniel Cordon, Ph.D.		
	Syyed Ali Siahpush	Date:	9th/May/2014
	Ali Siahpush, Ph.D.		
	(signature)	Date:	9th May 2014
	Vivek Utgikar, Ph.D.		
Department Administrator:	_John Crepeau_	Date:	9 May 2014
	John Crepeau, Ph.D.		
Discipline's College Dean:	_____	Date:	_____
	Larry Stauffer, Ph.D.		

Final Approval and Acceptance

Dean of the College Of Graduate Studies:	_____	Date:	_____
	Jie Chen, Ph.D.		

ABSTRACT

The application of ultra-high frequency induction melting of refractory oxides (e.g., borosilicate glass [BSG]) has been extensively investigated to determine the feasibility of developing and implementing an innovative inductively heated draining technique that is reliable and predictable. The primary purpose is for immobilizing highly radioactive waste streams resulting from reprocessing of spent nuclear fuel. This work has included development and validation of a numerical model, using ANSYS® MultiPhysics software, as well as numerous proof-of-concept and pilot-scale experimental tests.

The model is a steady state axially-symmetric geometry for a cylindrical water-cooled crucible that includes two separate induction energy sources operating at different frequencies. It accounts for the induction energy interactions, thermal conduction, convection, and radiation effects, as well as hydrodynamic phenomenon due to buoyancy effects. The material property models incorporated into the numerical model include temperature dependence up to 2,000^{o}C of key parameters including density, specific heat, thermal conductivity, and electrical conductivity, which can vary by several orders of magnitude within the temperature variations seen. The model has been experimentally validated, and shown to provide excellent representation of steady state temperature distributions, convection cell configurations, and flow field velocities for molten low conductivity materials. Thus, it provides the capability to conduct parametric studies to understand operational sensitivities and geometry effects that determine the performance of the inductively heated draining device, including scale-up effects.

Complementary experimental work has also been conducted to test the model predictions, and iteratively used to improve the model accuracy. However, the primary focus of the experimental efforts was to demonstrate the feasibility of the inductively heated draining technique for application to immobilization of radioactive waste in a BSG. Proof-of-concept experiments were conducted demonstrating the ability to induce sufficient energy into a miniaturized geometry such that melting will occur using an ultra-high frequency (i.e. 30 megahertz [MHz] range as compared to normal operations in the 250 kilohertz [kHz] to 2 MHz range). Exhaustive pilot-scale experiments were also conducted to evaluate the operation of the various inductively heated drain devices that were designed and implemented into large diameter (i.e. 300 and 400 mm) cold crucible induction melter systems.

ACKNOWLEDGEMENT

DEDICATION

I would like to extend a very special "thank you" to Prof. Dmitry B. Lopukh. Dmitry is the Department Chair at the St. Petersburg State Electrotechnical University under whose guidance my research was conducted. He was my mentor for this work and has become my very close friend through our many collaborative projects related to Cold Crucible Induction Melting. I could not have completed this work without his support, knowledge, professionalism, and friendship.

TABLE OF CONTENTS

LIST OF FIGURES

LIST OF TABLES

CHAPTER 1.   BACKGROUND

The objective of this research is to investigate the behavior and controllability of ultra-high frequency induction energy effects on refractory oxides, and specifically borosilicate glass (BSG). These efforts are related to developing an innovative approach to processing and immobilizing the challenging high level radioactive waste (HLW) (i.e., waste that specifically results from dissolution/reprocessing of spent nuclear fuel) inventories, although other potential high-temperature applications may benefit as well.

Specifically, the focus is on testing and validation of an inductively heated draining technique that could complement the primary immobilization technology. The approach envisioned is based on the same electromagnetic concepts as the cold crucible induction melter (CCIM) technology, which is discussed in more detail later, and could be integrated into a CCIM platform for a robust waste immobilization capability.

Several countries, including France, Russia, South Korea, and India, have active programs ongoing that are focused on the use of CCIM systems for immobilizing radioactive waste in a glass matrix. These programs are in various stages of development and implementation, and have different missions. Both France and Russia have actually implemented versions of CCIMs for vitrifying different types of radioactive waste. South Korea and India are in technology validation stages for their applications. However, these programs are each focused on a specific goal of processing their respective HLW inventories, and none of these efforts have in the past, or recently, investigated the type of integrated inductively heated drain CCIM system that is the focus of this research. If such efforts are ongoing, they have not been published or otherwise made publicly available.

In Russia, the SIA Radon facility has been operating a CCIM for immobilization of low and intermediate level radioactive inorganic wastes, primarily from medical sources, since the late 1990s [1]. This was the first CCIM system implemented in the world for processing radioactive waste. SIA Radon collaborated with researchers at the St. Petersburg State Electrotechnical University (ETU-LETI) to validate their initial design. The current system is a 550 mm diameter crucible that uses a 1.76 MHz, 160 kW high frequency generator. Other sizes and shapes (e.g., oval) have been used in the past. Radon processes a BSG at nominal temperatures of $1,150^{o}$C to $1,300^{o}$C. Glass is drained from the Radon CCIM system using a water-cooled tube that extends from the bottom of the crucible up into the zone of highest temperature within the melt pool volume (i.e., approximately 200 mm). The system includes a water-cooled conical plug that is lifted up from the top, providing

an opening for the molten glass to drain out, as desired. This design is effective for the feed chemistry and process implemented at Radon; however, it would not be an acceptable approach in the US for immobilizing HLW due to the concentrations of metals in the feed that can settle to the bottom of the melter, leading to electrical short circuiting and dramatically decreased melter life. The SIA Radon CCIM system does not use any mechanical stirring or bubbling for processing the waste. In the last decade, the US DOE has worked with SIA Radon extensively to test the CCIM technology performance on several HLW simulants using their CCIM test platforms [2, 3].

In France, high level radioactive waste (HLW) (i.e., waste resulting from dissolution and reprocessing of spent nuclear fuel) has been vitrified using induction melters for several decades. Until recently, however, the French have only used hot-wall induction melters. In this process, a metal container is loaded with a mixture of HLW and glass forming chemicals. The container is then heated with an induction coil (i.e., electromagnetically) such that the material is melted and the radionuclides in the waste are immobilized in the resulting glass matrix. Recently, a research and development organization within AREVA (formerly called Cogema), in collaboration with the Commissariat à l'énergie atomique et aux énergies alternatives (CEA), completed a near 25 year research and development program that resulted in a CCIM system that was retrofitted into the La Hague vitrification facility in France, with hot operations beginning in 2010 [4]. In this system, BSG is processed at nominally 1,200^{o}C, similar to the Russian CCIM application, although the waste being processed is significantly different. The AREVA CCIM system is a 650 mm diameter system, that uses a 275 kHz, 300 kW generator. This was the first CCIM platform in the world that was installed in a hot cell facility for processing HLW. In the La Hague CCIM system, glass is drained through an opening in the bottom of the crucible that has a double, water-cooled, slide gate valve system. AREVA has installed a water-cooled mechanical stirrer, as well as three bubbler tubes, to ensure homogeneity in the melt pool and to avoid build-up of skull or other materials on the bottom of the melter, particularly near the drain opening. Reliable operation of the drain is highly reliant on these supporting functions, as well as the properties of the melt. As a result, there are key constraints on viscosity and liquidus temperature (T_L), which is the temperature at which crystalline phases begin to form in the glass melt. These constraints lead to very low average waste loadings (i.e., 20 wt%) and thus, overall processing inefficiencies. If the glass was processed at higher temperatures, the waste loading could be increased; however, the draining system is not designed to have prolonged contact with materials above the current operating temperature.

In South Korea, investigation of the CCIM technology for vitrification of low and intermediate level radioactive, combustible waste resulting from nuclear power plant operations began in the late 1990's and was deployed at the Ulchin Vitrification Facility in 2008 [5]. The Nuclear Environment Technology Institute (NETEC) is the organization within the Korean Hydro & Nuclear Power Co., Ltd., that has responsibility for radioactive waste management in South Korea. NETEC has collaborated with CEA to develop a specialized CCIM system for their waste processing application. The NETEC CCIM processes a BSG at nominally 1,250^{o}C. Again, this is very similar to the French and Russian processing parameters, although a different BSG composition is used for their application. The NETEC CCIM is a 550 mm diameter system that uses a 275 kHz, 300 kW generator, similar to the AREVA system. A key difference is that NETEC has eliminated the mechanical stirrer, and instead incorporated twelve bubblers that maintain melt homogeneity, as well as a vigorous stirring condition within the melt (i.e., no cold cap is formed). During processing the melt pool surface functions as an incinerator as the combustible waste is fed into the crucible and oxidized, leaving the residual radioactive metals in the glass matrix. The draining process is similar to the AREVA design, and is appropriate for this unique application.

Finally, an example of more recent interest in the CCIM technology in the international community has emerged in India, with a research and development program being implemented around 2000. Similar to France, India has extensive experience in hot-wall induction melting for immobilization of HLW. Additionally, India has implemented conventional electrode-type joule-heated ceramic lined melters (JHCMs) for immobilizing their HLW. However, they are experiencing the same limitations on waste loading, throughput, and operational temperatures as the US related to these conventional melter designs [6]. As a result, researchers at the Bhabba Atomic Research Centre (BARC) have developed an engineering scale prototype of a full-scale CCIM system that will eventually vitrify HLW in India [7]. The BARC CCIM processes a specialized barium BSG (i.e., due to use of a thorium-based fuel cycle) composition at nominally 1,250^{o}C. The BARC CCIM is a 500 mm diameter system that uses a 250 kHz, 350 kW generator. In the BARC CCIM system, glass is drained through a water-cooled tube that extends 200 mm up from the bottom of the crucible, which is also water-cooled. A water-cooled plug is lifted when draining is desired, similar to the Radon draining system design.

This is not intended to be an exhaustive list of every country in the international community that either currently, or in the past, has expressed an interest or investigated the CCIM technology for

radioactive waste processing applications. However, these examples appear to represent the primary areas of CCIM research, development, and overall expertise currently existing worldwide.

1.1.   Motivation for Research

In the United States (US), the baseline technology for immobilization of the HLW resulting from reprocessing of spent nuclear fuel is vitrification in a BSG matrix using conventional JHCMs. This is a mature and well understood technology that has been implemented not only in the US, but throughout the world. Nevertheless, it has several limitations and the US continues to invest tens of millions of dollars annually to push the limits of the technology in an attempt to meet the technical and schedule challenges associated with HLW disposition.

The CCIM technology has been identified in numerous studies [8 – 10] as a potential alternative to the JHCM technology. It has also been identified by the US Department of Energy (DOE) Office of Nuclear Energy program as a potential technology for immobilizing some of the waste streams projected to be generated by advanced fuel cycles [11]. The CCIM has been demonstrated as a viable technology by the international community and, as previously discussed, was implemented at the La Hague Vitrification Facility in France for immobilization of their HLW in 2010. Interest in the CCIM technology has grown in the US due to the increasingly challenging waste chemistries that are projected to be processed in the DOE vitrification facilities, such as the planned Waste Treatment and Immobilization Plant (WTP) at the Hanford Site. Over the past decade or more, US and foreign researchers (e.g., France, Russia, and South Korea) have been collaboratively investigating the use of CCIM technologies for processing of some of these more challenging US waste streams.

The CCIM technology offers several benefits over conventional JHCMs. These include:

- Ability to operate at higher temperatures (i.e., mitigation of limitations of materials of construction),

- Greater process flexibility (e.g. insensitive to thermal cycling, ability to process refractory-corrosive chemistries, etc.),

- Greater specific throughput due to energy deposition physics (i.e., volumetric direct joule-heating), and

- Higher waste loadings due to the ability operate at higher temperatures.

The beneficial characteristics related to higher operational temperatures, mitigation of limitations related to materials of construction, greater process flexibility, and the energy deposition physics lend this technology to being adapted to an inductively heated draining concept (i.e., a miniaturized version of a CCIM). Such an approach could potentially eliminate the processing constraints associated with the conventional draining techniques used, including those discussed above.

Some of these advantages, such as higher operating temperatures and greater process flexibility, are obvious due to the basic operational physics and construction configuration of the CCIM technology (see Figure 1-1**)**. Others have only been demonstrated empirically or anecdotally, and the actual physics and mechanisms that produce these characteristics, while understood, can be challenging to accurately predict and control. As a result, over the last 15 years or so, modelling efforts for CCIM systems processing refractory oxides, such as BSG, have increased significantly. Nevertheless, due to the complex interdependencies of the many variables of

Figure 1-1. Schematic of typical CCIM. [56]
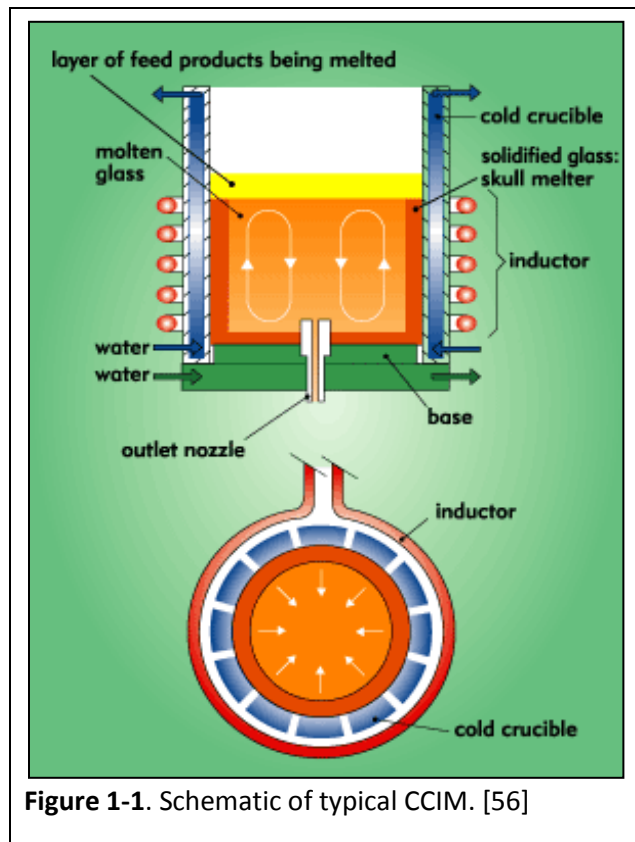
the systems, including temperature-dependent material properties, dynamic coupling conditions (i.e., temperature variations, melt pool height changes, electromagnetic coupling/transparency of components, etc.), chemical behavior of the melt, etc., the analytical results reported from the various models are generally specific to a given configuration, and/or provide only qualitative results in the context of application to other systems.

As mentioned, the benefits of the CCIM technology, in general, cannot be fully realized due to the limitations associated with the typical glass draining systems used in both JHCM and CCIM systems. Conventional drain designs (i.e., resistance heated tubes, inductively heated tubes, water cooled slide valves, water-cooled plus/tube systems, etc.) generally require direct contact of the molten product with the mechanical components of the draining mechanism, and/or they result in cooled

zones in the melter bottom that are susceptible to precipitates and crystalline phase (i.e., spinel) accumulation. Finally, these designs are all sensitive to the viscosity of the glass, which is highly temperature dependent. The chemistry of the glass also plays a major role in the melt viscosity, especially for those situations in which there are conditions that are amenable to crystalline phase formation upon cooling (e.g.,. waste streams high in iron, chromium, or aluminum). For this reason, significant limitations are placed on the glass properties, specifically the T_L previously mentioned, such that it is generally required to be a minimum of 100^oC below the operating melt temperature (T_m). For example, the typical operating condition for a conventional JHCM is $1,150^oC$ to $1,200^oC$, thus requiring the T_L to be a maximum of $1,050^oC$.

Induction melting has been investigated since the late 1930's and some of the earliest patents in the US were developed from efforts conducted by the US Bureau of Mines related to metal refining and purification. These systems operated in the 10 to 100 kilohertz(kHz) range, depending on size and material properties. Similarly, the CCIM system developed by the French for vitrification of their HLW operates in the 250 to 300 kHz range [12]. However, because there is an inverse relationship between the geometry (i.e. diameter of a cylindrical crucible) and the frequency for providing optimal energy deposition in a material of a given electrical conductivity, an inductively heated system that is designed to operate effectively for a 25 to 40 mm diameter system (typical drain diameter range) for processing BSG and other similar refractory materials theoretically requires a frequency in the 25 to 30 megahertz (MHz) range. However, very little is known regarding the coupling behavior, heat transfer characteristics, and overall controllability of systems operating in this frequency range. Additionally, the coupling effects of the ultra-high frequency field with the melter environment (i.e. physical infrastructure, geometry effects, sensors, control signal interference, etc.) are not well understood. Finally, the overall behavior of an actual miniaturized CCIM system operating at an ultra-high frequency versus the theoretically predicted behavior (or that extrapolated from empirical data) is not known and has not been evaluated. The proposed research will investigate these phenomena to allow a determination to be made regarding the feasibility for implementation of such a system in an actual processing facility.

To effectively address this challenge, extensive experimentation and testing is required. This is expensive and schedule intensive, requiring significant time, manpower, energy consumption, and materials consumption. Therefore, a model was developed that allows parametric and scoping studies to be cost-effectively performed that helped optimize the use of experimental and testing

resources, thus providing more focused testing and germane results. Extensive modeling of CCIM systems has been conducted by several groups. Their work has been primarily focused in two areas: metal refining and HLW vitrification. These efforts will be discussed in more detail in the literature review section. Nonetheless, development of a model for this effort was necessary to provide a representative and available tool for investigating the application of a dual frequency CCIM system, which none of these models offers. Other limitations of those models were also identified, which are discussed in more detail below.

1.2. Past Work and Literature Review Related to Modelling

The concept of using cold wall induction melters, with no ceramic refractory, for melting materials has been known and practiced for several decades. In fact, induction-based levitation melting for ultra-pure materials was proposed by Muck and patented as early as 1923 [13]. The earliest identified patent for an actual CCIM system was granted in 1931 to the Siemens und Halske Company [14] and many dozens of variants of this original idea have also been patented. This early work was focused almost exclusively on processing and refining of ultra-pure metals and single crystal metals for specialty applications. As such, it revolved primarily around processing materials with relatively low electrical resistivities, when compared to refractory materials such as BSGs. As a result, the systems investigated are generally operating at much lower frequencies, typically in the hundreds of hertz to tens of kilohertz range, depending on the geometry of the system and material properties. While these investigations, both experimental and numerical modeling, have continued to the present, in recent years an increase in the experimental and modeling efforts associated with operation of CCIMs for processing of refractory oxides has occurred. Additional details of some of the relative accomplishments of these two areas of focus are discussed below.

Extensive experimental work, as well as numerical modeling, has been conducted for evaluation of CCIM processing of metals and some refractory oxides. This work has included more conventional cold crucible induction systems, as well as levitation melting techniques. Induction processing of metals, including ferromagnetic, paramagnetic, and diamagnetic types, induces significant Lorentz forces in the material and these forces are large enough to overcome the body forces (i.e. gravity). If the induction system is configured properly, full levitation of the melt can be achieved.

Significant bodies of work have been developed in empirical design of CCIMs in general [15 – 18], as well as in numerical model development of CCIM processes for metal melts, also known as "skull

melting" [19 - 30]. Bojarevics, Pericieious, Harding, and Wickins [31 - 36] represent the most recognized and authoritative work in this area. Additionally, Umbrashko, Baake, Nacke, and Jakovics [37, 38] have conducted some very similar modeling, and amassed an equally impressive body of work.

Figure 1-2 shows results from the modeling efforts for an aluminum melt that was completed by Bojarevics, et al. Similarly, Figure 1-3 illustrates results from the Umbrashko, et al., modeling efforts. Both results show the pronounced effects of Lorentz forces when melting metals, which have no impact for the materials of interest to this research. However, these efforts have laid a strong foundation for modeling of CCIM processes, in general.
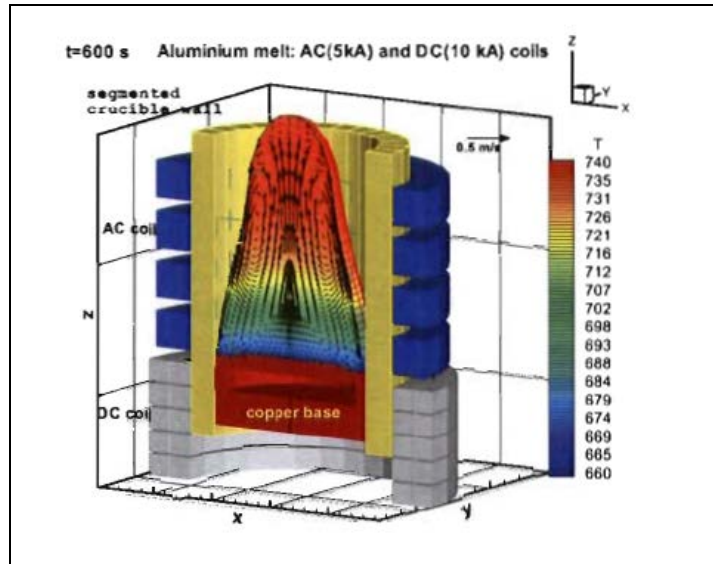
Figure 1-2. CCIM modeling results for aluminum melting conducted by Bojarevics, et al. [32]

While the numerical methods developed and validated are applicable, and in some instances, the same modeling software, ANSYS® [39] is used, the specific process parameters modeled and tested experimentally are significantly different from those of interest for this work (i.e., melting refractory materials). Additionally, none of these efforts incorporate dual frequency systems, which is a focus of this research.
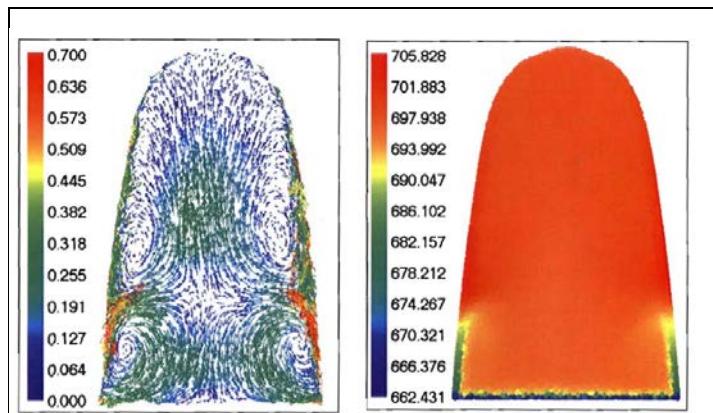
Figure 1-3. CCIM modeling results for aluminum melting conducted by Umbrashko, et al. [36]

Another important body of work, which has had growing interest over the past decade, and is more related to the research conducted in this effort, includes modeling and experimental testing of CCIM systems for specific application to processing of refractory oxides, including BSGs. Outside of

Russian researchers, the majority of this work has been conducted by French researchers, although both India [40] and Korea [41] have also constructed test platforms and conducted modelling and testing. The Koreans have also been involved in modeling and experimental work related to CCIM processing of corium (a 78/22 weight ratio mixture of UO_2 and ZrO_2, which results when the core of a nuclear reactor experiences a meltdown) [42]. This work is mentioned because, while not related to their ongoing glass processing experimental work, it has laid a foundation for further modeling by Korean researchers for additional CCIM applications.

Within Russia, the St. Petersburg State Electrotechnical University "LETI" (ETU-LETI) represents the authority on experimental work and modeling of CCIM processes for a wide variety of applications, including processing of metals, specialty glasses, corium, refractory oxides and glasses. The author has collaborated closely with ETU-LETI since 2001, which has included not only the research reported herein, but other CCIM related investigations. Thus, the Russian work in this area is not cited. However, in some instances these same ETU-LETI researchers have collaborated with other international researchers, such as Naacke, et al., from the Institute of Electrothermal Processes at the University of Hannover [43, 44]. Naacke, et al., have also conducted modeling and experimental work related to CCIM processing of refractory oxides, including yttrium-barium-copper oxides and zirconium oxides [45 – 48]. However, all of this work was performed for single frequency systems operating in the 350 kHz to 400 kHz range, which is well out of the scope and focus of the present research efforts.

Limited publications are available on modeling of CCIM systems for processing refractory materials such as BSG or other glass and glass-ceramic compositions. The earliest work conducted by Schiff, et al., in 1996, included a mathematical model of a cylindrical crucible with water-cooled walls and bottom that inductively heated a glass melt [49]. The model determined the thermal convection characteristics of the glass. The axially symmetric 2D model included electromagnetic, hydrodynamic, and thermal effects; however, it neglected the effect of the water-cooling at the boundaries, which can have significant impact on the magnetic field intensity and power level in the melt. In their model, an analytical solution of the Bessel equation was used to obtain the magnetic field intensity in the melt.

In 2003, Hawkes developed a mathematical model for a specific CCIM system at the Idaho National Laboratory, for which this author led the design and construction, that used FIDAP® [50] software to simulate the glass melting process. The model was later enhanced to include subsidence effects [51,
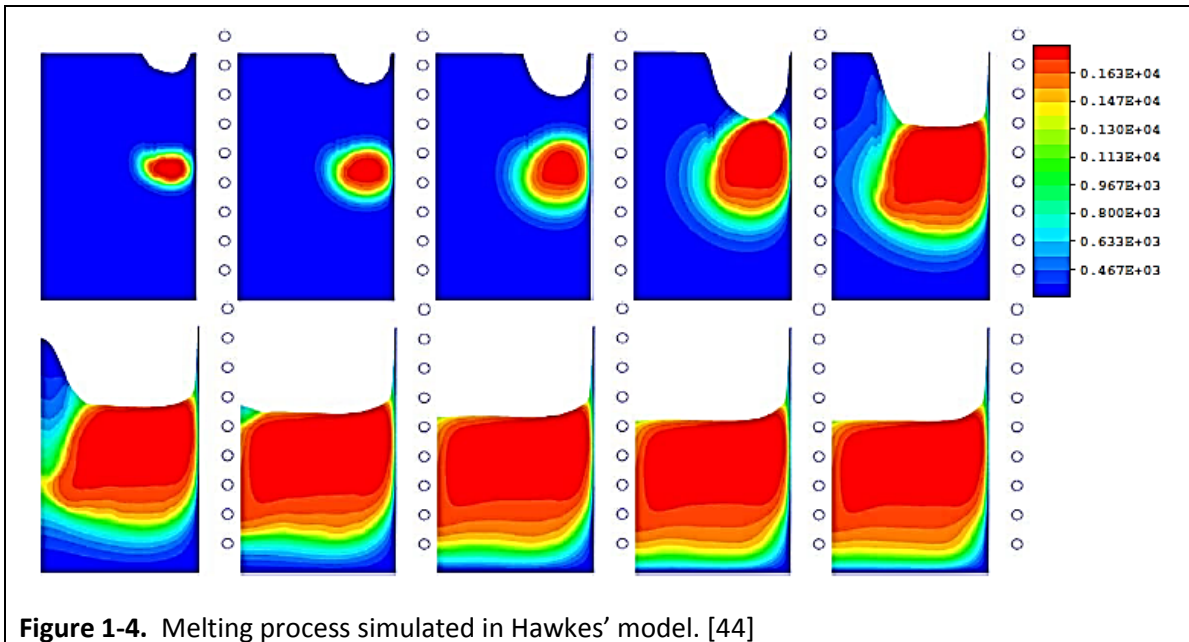
Figure 1-4. Melting process simulated in Hawkes' model. [44]

52]. This model evaluated the electromagnetic vector potential to obtain the results, similar to the approach used in the model developed as part of the work reported in this dissertation. A proportional power controller was used in Hawkes' model to set a fixed level of power in the melt at 60 kW. This was determined by the actual power level of the generator used in the system. However, in practice, this level was never achieved because, at much lower levels, the BSG would overheat, reaching temperatures near 2,000°C, begin to vigorously boil, and generate vapors containing some of the semi-volatile constituents of the glass. This affected the chemistry of the melt, and thus its material properties, which is unacceptable. Additionally, when boiling occurs, the axial symmetry assumption is no longer valid. Thus, the resulting temperature profile, shown in Figure 1-4, may not be representative, especially for the maximum temperature value.

French researchers have developed the most authoritative body of work related to modeling and experimental efforts for CCIM processing of BSGs [53 – 59]. Their work is most closely aligned with the work conducted as part of this research effort, particularly the model development efforts. Accordingly, a more detailed discussion of these efforts and results will be provided.

The French government has been sponsoring development of induction melter systems for implementation in treatment facilities for immobilization of HLW for the past 35 years or so, with focus on CCIMs during the past 25 years. The early systems, some of which are still in operation in both France and the United Kingdom (e.g. Sellafield Plant) were hot wall induction melters. The

induction field is designed to couple with the metal container and then the waste and glass mixture is heated and melted via conduction from the container.

During the late 1980's to early 1990's they began investigating the CCIM technology, which at the time was being developed and implemented in Russia for processing of low and intermediate level radioactive waste. The French; however, wanted to develop the CCIM technology for implementation into a hot cell environment and embarked on an aggressive design and experimental program. Many papers have been published, referenced above, that describe the French vitrification systems and development history, but they provide very few details on the design of their CCIM system because this information is considered proprietary and is protected from disclosure. Similarly, many papers on their modeling results have been published, particularly in the last 5 years, which was coincidentally, around the time that the initial reports on the collaborative efforts with the Russians to develop a model were being presented. However, based on the complexity and comprehensiveness of the French CCIM models, it is clear that these efforts have been ongoing for quite some time.

The French researchers have developed both two dimensional (2D) and three dimensional (3D) models [53 – 59] that predict the behavior of many parameters for their CCIM systems. For example, 3D electrical models are available that allow investigation of the energy efficiency for different configurations of the cooling sectors that constitute the structure of the crucible. This model can be used to optimize the sector configuration such that the energy deposition (i.e. volumetric power density) in the glass can be maximized. Figure 1-5 demonstrates how the power density in the glass is almost three times higher for a crucible design that does not have an upper flange that electrically connects the crucible sections (e.g. processing of radioactive waste requires a

Figure 1-5. Electromagnetic model of CCIM systems demonstrates effect of crucible cooling tube designs by Jacoutot, et al. [53]
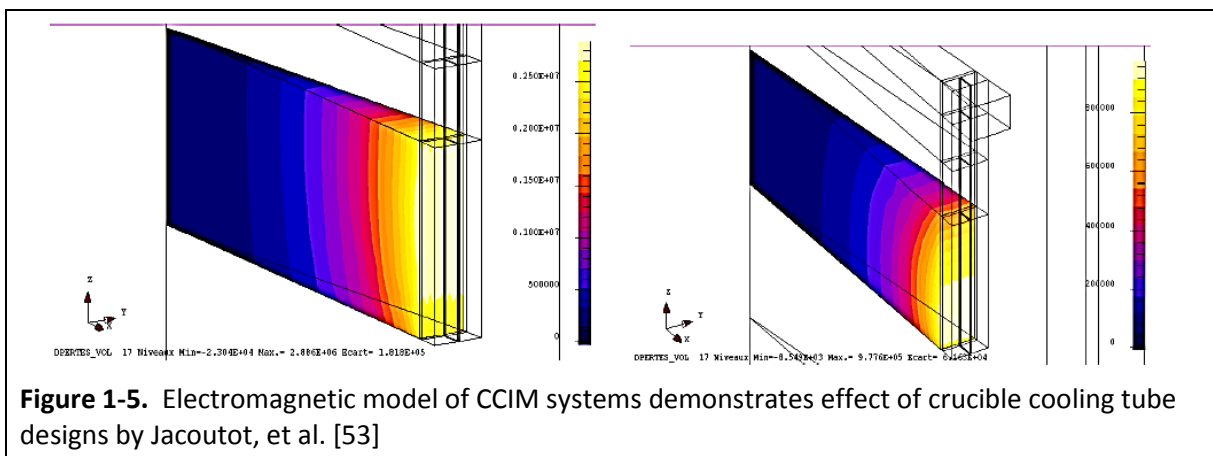
crucible cover lid that necessitates a flanged design and thus short circuits the crucible sections along the top).

Additionally, 2D and 3D models that couple the electromagnetic effects with the thermal and hydrodynamic effects have been developed. In one of these models, two commercial software packages are coupled to solve the governing Maxwell, Navier-Stokes, and energy equations.

FLUX® software [60] is used to solve the inductance equations and the results are then coupled to the FLUENT® software [61], which solves the Navier-Stokes and thermal equations. This coupling requires interfacing meshes from a finite element and finite volume based protocols; however, these adaptive meshing approaches are well known. Results of this coupled model have been reported in multiple papers authored by the French researchers, with interesting results. Figure 1-6 provides direct comparison of the temperature distributions obtained from two separate instances using the 3D coupled model developed by the French researchers. The distributions appear to be similar, but not identical. Closer examination of some of the model assumptions, as well as the results and conclusions drawn, provide for some interesting observations that can be made.

The model developed as part of this research effort, although only a 2D axially-symmetric model, has many similarities with that developed by the French researchers. The basic equations are the same (i.e. simplified Maxwell equations, Navier-Stokes equations, and energy and momentum equations). The modeling simplifications are due to key assumptions, which are also similar between the two models, such as neglecting of the Lorentz forces, neglecting displacement currents in Ampere's law, assuming

Figure 1-6. Comparison of temperature distributions in different 3D model outputs developed by French researchers. [53, 57]
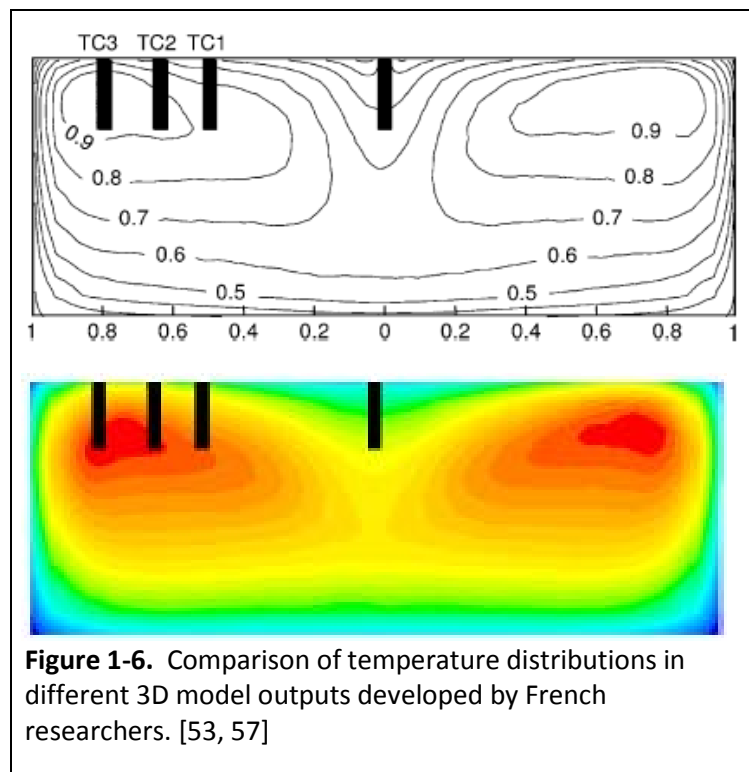
laminar flow, and assuming incompressible Newtonian fluid. The material properties are modeled

as temperature-dependent variables, for the most part, although this is discussed in more detail below.

So, in large part, the French model is similar to that developed in this work; however, there are some key and important differences. It is these differences that may also have led to increased inconsistencies between model results and experimental data. For example, the glass is assumed to have a constant emissivity of 0.9. This was shown not to be the case during the experimental work conducted as part of this research. In fact, the emissivity is not constant, and the 0.9 value is quite high. This is discussed in more detail later in this dissertation. Also, the authors indicated that the primary convergence criteria used to couple their model was based on the root mean square difference between temperature values. The model developed for this research was based on convergence of the pressure values at the nodes. Both of these factors may have led to some of the inconsistencies mentioned earlier. For example, the French researchers concluded that the thermocouples resulted in an overall lower temperature in the glass melt. Refer to Figure 1-7. The three graphs show that their 2D modeling consistently indicates higher temperatures than measured, except for the locations least affected by the lower emissivity and in areas with slow velocity fields, such that the hydrodynamic effects are less, and thus the convergence approach may have less impact. Figure 1-8 shows yet additional data from the 3D model, which indicates these same inconsistencies. The depth of these thermocouples is not given; however, the discrepancies appear to be greatest in areas of higher thermal gradients (refer back to Figure 1-6).

Another key area of difference in the two models is related to the temperature-dependent material property models used. Significant effort was put into development of the model for this research to ensure that the material properties were representative up to 2,000^{o}C. These results will be presented in more detail later. This effort was taken because many of the material properties exhibit significant change with temperature, and internal temperatures in a non-stirred bath of molten glass with a surface temperature of 1,250^{o}C, for example, are known to reach up to 1,600^{o}C or 1,700^{o}C. Thus, this is why it is of utmost importance to have representative material property data. However, as can be seen in Figure 1-9, the material properties, on average, are only modeled to about 1,525^{o}C. Also, note that actual measurements are only available up to about 1,325^{o}C. The lack of glass property data for higher temperatures was also found to be an issue when developing the material models used for the ANSYS® model developed as part of this research.
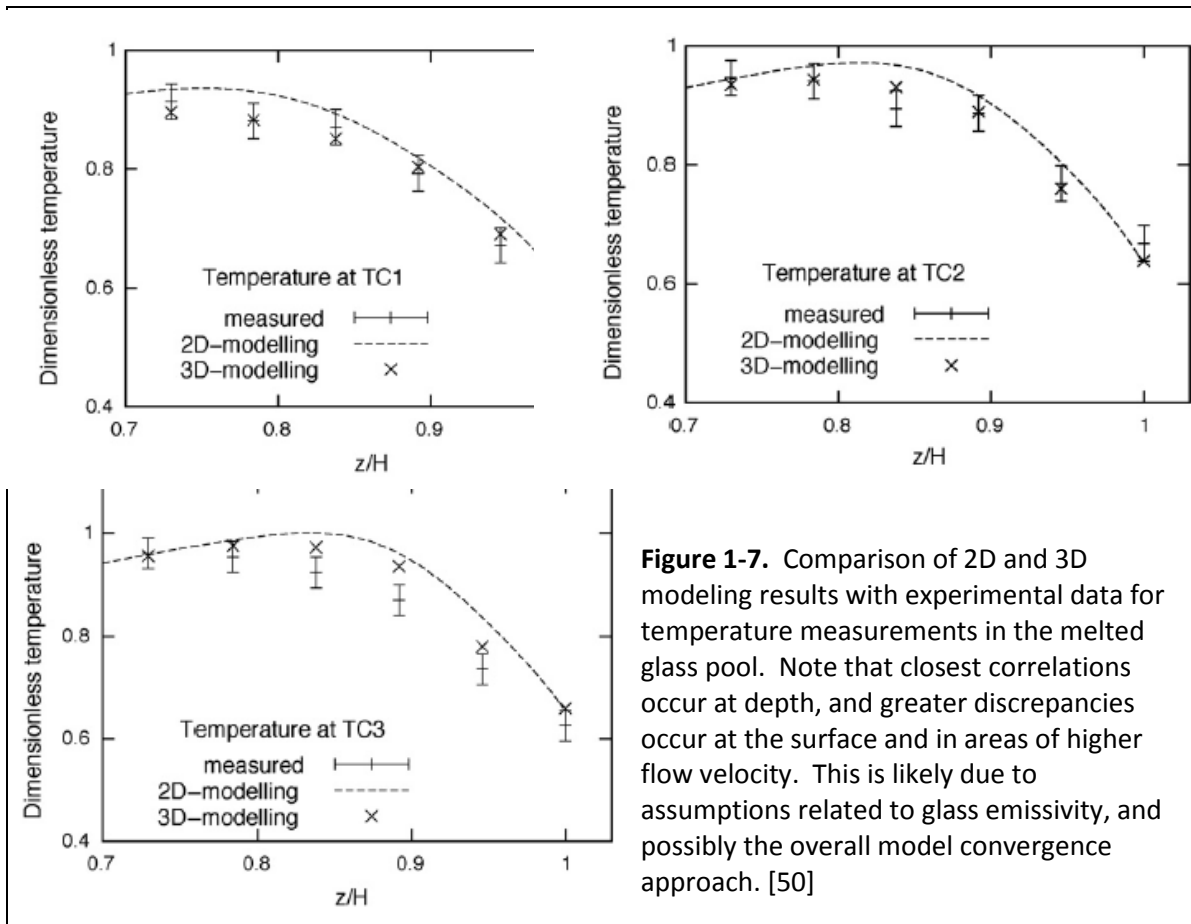
Figure 1-7. Comparison of 2D and 3D modeling results with experimental data for temperature measurements in the melted glass pool. Note that closest correlations occur at depth, and greater discrepancies occur at the surface and in areas of higher flow velocity. This is likely due to assumptions related to glass emissivity, and possibly the overall model convergence approach. [50]
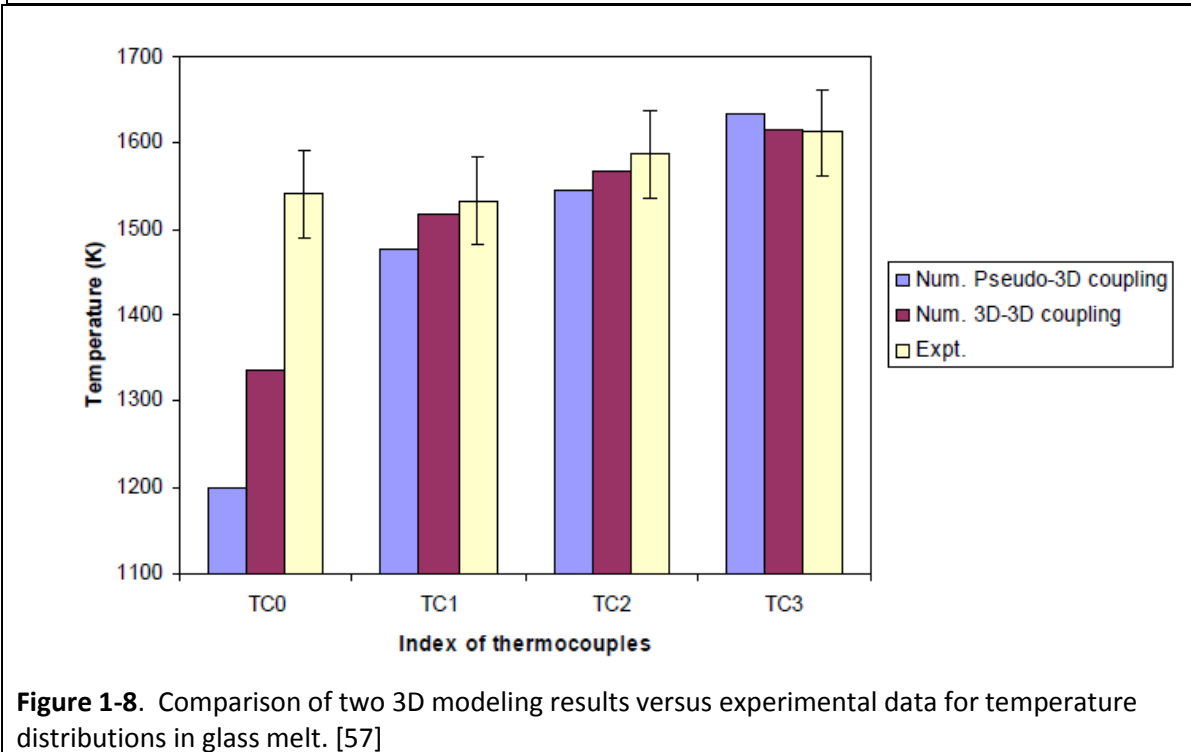
Figure 1-8. Comparison of two 3D modeling results versus experimental data for temperature distributions in glass melt. [57]

Figure 1-9. Material property models used by French researchers. [54]

Figure 1-10. 3D model of a fully developed glass melt produced by French researchers. [57]
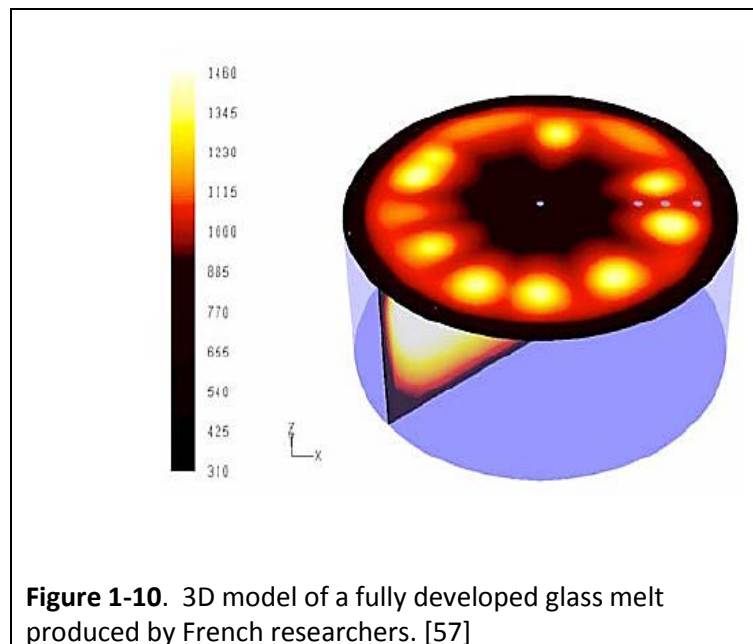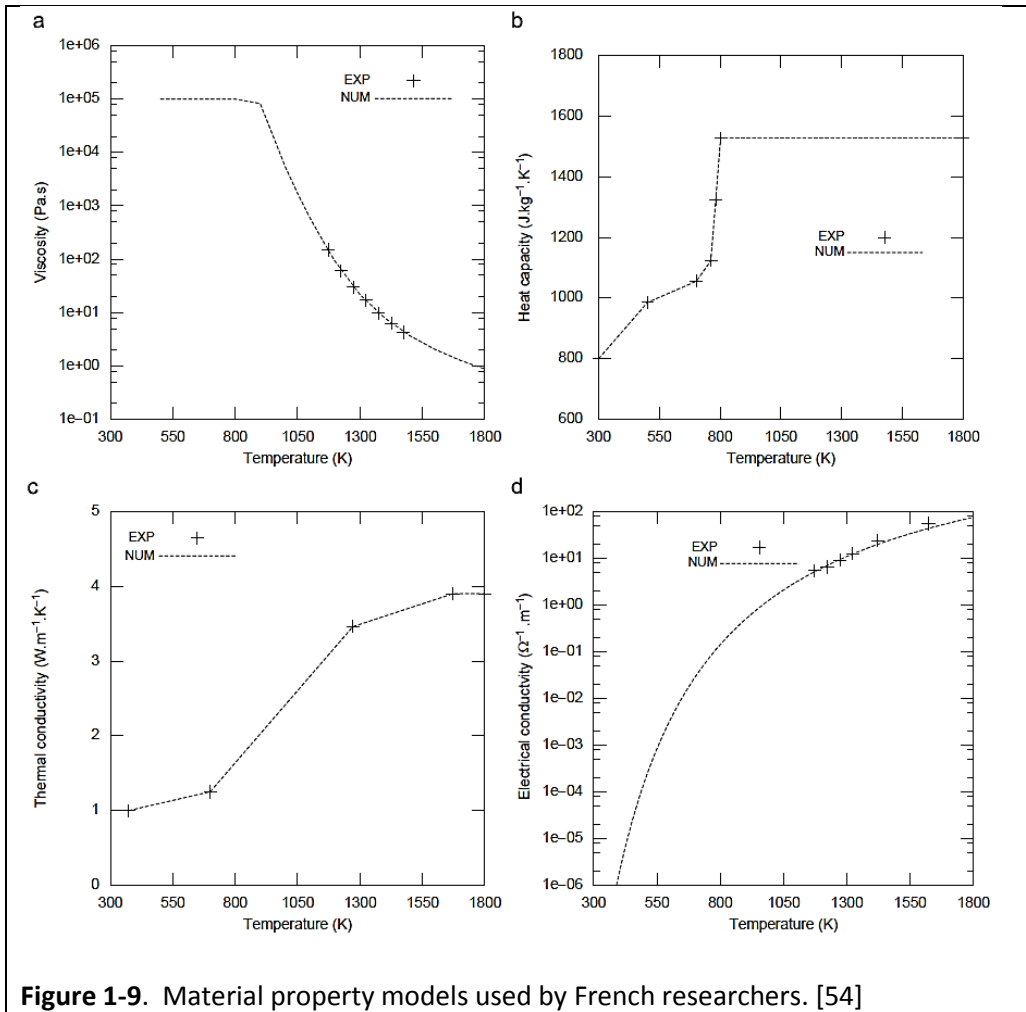
In summary, the French researchers have developed a very complex and sophisticated 3D model that offers more capabilities than the model developed as part of this research. See Figure 1-10. However, the French model also has some limitations (e.g., material property models) that have been mitigated, to some extent, in the model developed. Additionally, regardless of the overall functionality of the French model, it is not in the public domain, and thus not available to support this research work. Specifically, the model developed as part of this research served more as a tool to support the experimental work and focus the testing efforts and resources. It was not intended to represent an addition to the state-of-the-art in algorithms or innovative protocol for modeling coupled physics for high frequency electromagnetic systems. Instead, the approach was to take the best tool available, in this case it was the ANSYS® MultiPhysics software, and adapt it to the needs of the research.

Finally, regarding prior work, not a single reference could be located that described any experimental or analytical work that had been performed related to modeling, design, or testing of a draining mechanism such as envisioned in this research effort. The smallest cold crucibles described, which are cited in the references provided, are between 10 cm and 15 cm in diameter. Similarly, the CCIM system with the highest frequency that could be found in references was work conducted by the Russian collaborators, which was in the 5 MHz range. Limited test results were available. These bodies of work represent systems that are an order of magnitude different in geometry and frequency from the scope of this research effort.

1.3.   Objectives and Scope of Research

The primary objective of this research work is to investigate the behavior of ultra-high frequency energy effects on refractory oxide materials, and particularly when coupled with a CCIM technology platform. The purpose of these efforts is to evaluate the feasibility of applying the induction heating principles of the CCIM technology on a miniature scale to provide an innovative draining concept. If successful, the combined systems would provide a robust integrated dual-frequency CCIM technology that can be demonstrated for immobilization of radioactive waste into glass and ceramic matrices. Specifically, the inductively heated drain system would function as a non-mechanical valve for processing (i.e. draining/casting) very high temperature molten glass or ceramic materials.

The scope of the research included investigating the ability to use the electromagnetic principles of a CCIM, and the temperature-dependent coupling characteristics of the induction field with a

refractory material, on a much smaller scale, such that a draining system can be devised that does not require any direct contact of the high temperature molten product with the materials of construction. The challenge associated with this endeavor lies in the fact that virtually no research has been conducted on induction melting systems at this small scale, or using the required ultra-high frequencies. The work discussed herein was conducted on the premise of application in a CCIM system. This platform was selected because the design of a CCIM is intended to minimize electrical losses from the induction field of the primary heating coil, and is thus amenable to introduction of a second high frequency induction system integrated into the assembly to function as a draining technology. The final concept, which was defined after several design iterations, is shown in Figure 1-11, although this was not the final optimized configuration, which is described in Chapter 11.

The work included both modeling and extensive experimental investigation. The model, once validated, was used to evaluate the effects of design changes and how they impact the performance of the system. Parameters such as the number of turns and geometry (i.e. placement) of those turns, geometry of the outlet (i.e. throat shape, diameter, length), and scale-up effects. These mathematical results were used to focus the experimental designs and efforts. This was necessary because the experimental runs themselves are complex, time consuming, and expensive. Each major experiment typically requires one full day of preparation of the equipment, one full day of experiment, and half a day to dismantle the set-up, with at least four experimenters operating the equipment and performing data collection.

Figure 1-11. Model of CCIM system with an ultra-high frequency inductively heated drain system integrated into the assembly.
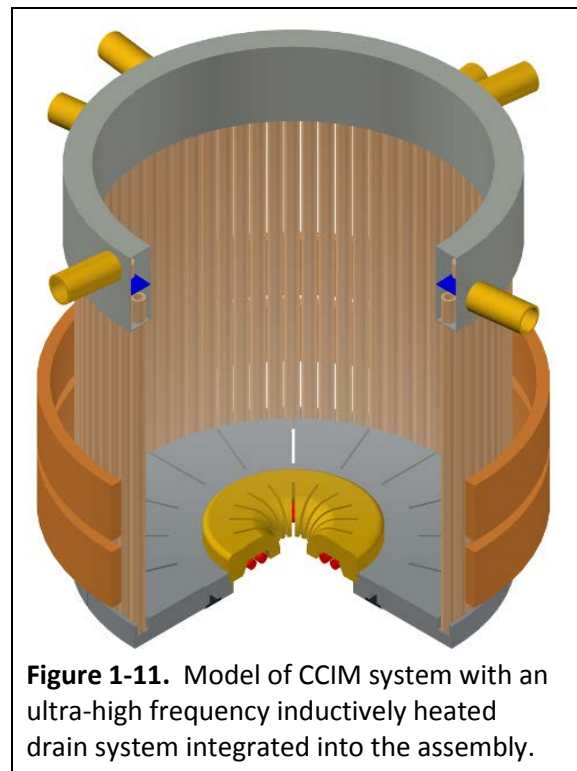
The model was developed in a methodical manner, beginning with a simplified model and systematically increasing the complexity until it became more and more representative of the actual experimental conditions. Once the model was developed and functioning, significant experimental work was conducted specifically for the purpose of validating the model. The initial efforts only

investigated a conventional CCIM with a single induction energy source. The baseline system was a 30 cm diameter stainless steel water-cooled crucible using a 60 kW power supply oscillating at 1.76 MHz with a comprehensive high-accuracy calorimetry system. This configuration was used to develop the boundary conditions for the model (i.e. heat fluxes at walls, bottom, and free surface), and to provide a platform for model validation. Significant efforts were also made by the collaborators to develop electrical sensors to measure key parameters, such as current and voltage on the inductor at various operating conditions. Although this work was outside the scope of the research defined in this dissertation, the data developed were used to better define the electrical parameters used in the models. The primary method of model validation was direct comparison of temperature distributions within the melt volume at a specific operating condition using a BSG.

The material properties of refractory oxide materials, such as BSG, are highly temperature dependent. The intent of the research work is to demonstrate the ability to process materials at very high temperatures (i.e. up to 2,000^{o}C). Unfortunately, comprehensive material property data for glasses through the expected range of temperatures are not available. Accordingly, significant efforts were put into developing these data. Various methods were employed, including compositional comparisons with published data for other glasses, extrapolation, experimental measurements, and consultation with glass chemists from other National Laboratories.

After the initial validation of a representative model, sensitivity studies were conducted on the model to investigate the overall impacts of the uncertainties associated with the temperature-dependence of the material properties. The thermal conductivity, specific heat, density, and electrical resistivity were the key properties evaluated. Additionally, separate experiments were specifically designed and conducted to evaluate the surface emissivity of the glass being used for the integrated experimental runs. This was necessary because discrepancies between the experimental results and model data indicated that the assumptions and values being used were most likely in error. Since virtually no data are published on glass emissivity for this temperature range, experiments were conducted to determine this property more completely for incorporation into the model.

Once the basic single frequency, 1.76 MHz CCIM model was validated, a second independent model was developed using the same model platform for an ultra-high frequency system operating at nominally 27 MHz. This model was used to investigate some of the key geometry parameters of the

drain configuration. These results were used to design the proof of principle experiments that were conducted.

The final, step in the model development involved integration of the 1.76 MHz model with the 27 MHz model. Once this model was validated to provide representativeness and convergence, it was then used as the primary tool for developing the inductively heated drain design, including evaluation of the effects of key geometry parameters, as mentioned above. The model was also used to investigate scale-up effects for systems up to one meter in diameter. A CCIM system with a 407 mm diameter crucible was designed using this model. It was then constructed and successfully operated. The specifics and importance of this activity are discussed in more detail later in this dissertation.

The experimental work conducted was extensive because several objectives had to be accomplished. These included not only testing and validation of the overall high-frequency inductively heated draining system, but also model validation and enhancement, as well as material property data development and validation. In general, the experimental work and model development efforts were accomplished in an iterative and complementary approach.

The initial phase of experimental work was focused on model validation and enhancement. These tests were conducted using a baseline CCIM configuration, which was determined by the available equipment. Namely, a 60 kW, 1.76 MHz high frequency generator with a 300 mm diameter CCIM system constructed of non-magnetic stainless steel. The system was instrumented with thermocouples and a thermocouple deployment system for measuring temperature distribution within the melt volume, as well as, rotameters, precision flow meters, and thermistors for measuring cooling water flow and temperatures to determine heat fluxes for the various boundaries of the system.

The next phase of testing was focused on validating proof-of-principle for the drain concept. These experiments specifically investigated the ability of a 27 MHz induction field to effectively couple with a molten BSG in a very small geometry. The tests also demonstrated the ability of the melt front to propagate both upward and downward.

Based on modeling results, an integrated CCIM test platform was designed, built, and tested that included the ultra-high frequency induction heating capability. This platform was used to evaluate the performance of the inductively heated draining system and to enhance the design for

controllability, predictability, and reliability. Because the model was limited in its direct application to actual experimental conditions, some design parameters could only be evaluated experimentally to determine their effects. For example, geometry features such as the number of isolation slits in the drain throat and body could not be modeled because it is a 2D axially symmetrical model. Estimates of the energy flux could be changed to predict behavior, but these had to be evaluated experimentally. Direct measurement of this parameter is not practical within the confines of this research, especially such measurements in a high temperature (e.g. 1,400^{o}C melt and 27 MHz field). The energy deposition characteristics in the drain throat area also have significant impact on the melt conditions, and thus the pouring characteristics. For this reason, pressure variation methods were investigated to control the pour rate and to affect timely and controllable stoppage.

The final experimental efforts included in this research were design, construction, and testing of a large integrated test platform. The purpose of this work was to further validate the representativeness and utility of the integrated model, specifically for validation of scale-up effects. A 407 mm diameter integrated CCIM was successfully operated using the same 60 kW, 1.76 MHz generator. The crucible configuration, including the materials of construction, geometry, and other key parameters were optimized using the validated model.

The work conducted as part of this research effort was done so in close collaboration with ETU-LETI, and specifically, Professor Dmitry Lopukh, Professor Boris Polevodov, Dr. Alexander Martynov, Sergei Chepluk, and Anton Vavilov. All of the testing performed to support this research was conducted at the laboratory in ETU-LETI. The ETU-LETI researchers were working to develop methods to indirectly determine the melt conditions using electrical parameters such that the power level and frequency could be automatically adjusted to optimize the various stages of processing. This led to development of innovative sensors and a comprehensive data acquisition system for obtaining high accuracy calorimetry and other data. Several additional experiments beyond those reported here were conducted as part of this collaborative research. However, the author participated in every experiment discussed in the body of this dissertation, analyzed the data from all experiments, and directed the test plans and objectives that were germane to this work.

CHAPTER 2.   BASE MODEL DEVELOPMENT

This section will describe the overall model development approach, as well as the steps taken to validate its representativeness and to establish an understanding of the uncertainty introduced by the assumptions. Additionally, the application of the model to design optimization and system behavior prediction will be discussed. In support of validating both input parameters (e.g., boundary conditions) and representativeness of the model results, several experiments were run using different CCIM configurations. The data obtained that were germane to development and validation of the model are discussed in this chapter. The actual experimental setups and overall results are described in subsequent chapters.

2.1. Modeling Approach

The commercial finite element modeling software ANSYS® MultiPhysics [39] was selected to develop a model that could be used to investigate the coupled thermal and hydrodynamic processes associated with melting of materials using induction energy, with specific focus on a BSG composition. This software was selected because it has well-developed protocol , algorithms, and, element types for application to high frequency induction systems. Additionally, this software has the ability to couple the thermal, hydrodynamic, and electrical phenomenon to provide a model that can deliver representative results in a standard 32-bit or 64-bit desktop computer platform.

The initial model was very simplified, only incorporating a single frequency induction system, fixed heat loss boundary conditions, estimated electrical parameters, and fixed-value average material properties. Over the course of this research effort, the model has been significantly enhanced. It is constructed of three calculation steps simulating melt initiation, melt pool steady state, and achieving glass draining conditions using a second, ultra-high frequency induction system. Significant efforts were focused on developing and validating the temperature-dependent material properties, and these have been incorporated into the model also.

The characteristics of the melting process in a CCIM and the resulting condition of the melt volume is a function of multiple fields and effects that are coupled to produce a quasi-steady state condition. These include electromagnetic, temperature, and hydrodynamic (i.e. convection flow that occurs due to buoyancy) effects, as well as temperature-dependent material properties such as thermal conductivity, electrical resistivity, specific heat, viscosity, and density. These effects are inextricably coupled and interdependent. For example, the temperature field depends on the

behaviour of the energy deposition due to the electromagnetic field. However, the characteristics
of the electromagnetic field are dependent on the electrical conductivity of the material, and the
electrical conductivity is dependent on the temperature of the material. The electrical conductivity
can vary by several orders of magnitude within the melt volume, as can the viscosity, due to their
strong temperature dependence. This results in active velocity fields due to the resulting buoyancy
effects, thus making convergence challenging in a complex model.

The ANSYS model that has been developed conducts analyses using three calculation blocks, which
are:

- Electromagnetic calculation block for single and dual frequency heating
- Thermal calculation block for conductivity, convection, and radiation
- Hydrodynamic calculation block for buoyancy driven flow.

The electromagnetic block is first executed to establish an initial temperature distribution. This
result becomes the input to the thermal and hydrodynamic calculation blocks. These calculation
blocks incorporate the effects of the temperature-dependent material properties in the energy and
momentum equations, creating buoyancy driven velocity fields. This is an iterative calculation that
proceeds until the pre-defined convergence criteria for the various parameters are satisfied. At
steady state, melt movement stabilizes, forming convection cells within the melt volume. The
theoretical basis of these calculations is discussed below.

2.1.1.Electromagnetic Calculation Block

The electromagnetic calculation block is based on Maxwell's equations for a quasi-static condition,
which allows displacement currents in the busses and melt to be neglected. This can be defined
with the following equations and simplifying assumptions, described by Rudnev [62], as follows:

$$\nabla \times \mathbf{H} = \mathbf{J} + \frac{\partial \mathbf{D}}{\partial t} \qquad \text{(from Ampere's law)} \tag{2 – 1}$$

$$\nabla \times \mathbf{E} = - \frac{\partial \mathbf{B}}{\partial t} \qquad \text{(from Faraday's law)} \tag{2 – 2}$$

$$\nabla \cdot \mathbf{B} = 0 \qquad \text{(from Gauss'law)} \tag{2 – 3}$$

$$\nabla \cdot \mathbf{D} = \rho_{charge} \qquad \text{(from Gauss' law)} \tag{2 – 4}$$

where:

H is magnetic field intensity vector

J is total conduction current density vector (includes source and induced currents)

D is electric flux density, or displacement current density

E is electric field intensity vector

B is magnetic flux density vector

ρ_{charge} is electric charge density.

For most practical applications where the current frequencies are less than 10 MHz, the induced conduction current density, **J,** is much greater than the displacement current density, $\partial \mathbf{D}/\partial t$, so the last term on the right side of equation 2-1 can be neglected. Additionally, this is a valid assumption for systems in which the magnetic field effects are weak (i.e. low magnetic permeability) [59].

The Maxwell equations are combined with the appropriate constitutive relationships as follows:

$$\mathbf{B} = \mu_r \mu_0 \mathbf{H} \qquad\qquad (2-5)$$

$$\mathbf{J} = \sigma \mathbf{E} \qquad (\text{Ohm's law}) \qquad\qquad (2-6)$$

where μ_r and σ denote, respectively, the relative magnetic permeability and electrical conductivity of the material. The constant $\mu_0 = 4\pi \times 10^{-7}$ H/m, is the magnetic permeability of free space, or vacuum. For refractory oxides, such as the BSG used for this research, the magnetic permeability is assumed to be approximately equivalent to free space, thus $\mu_r = 1$. Also, since the magnetic flux density, **B,** satisfies a zero divergence condition (equation 2-3), it can be expressed in terms of a vector potential **A** as:

$$\mathbf{B} = \nabla \times \mathbf{A} \qquad\qquad (2-7)$$

An important convergence factor is based on defining the magnetic vector potential being equal to zero at the calculation boundary. Thus the following Dirichlet condition is set:

$$\mathbf{A} = 0 \quad (\text{at the calculation boundary}) \qquad\qquad (2-8)$$

After other simplifying assumptions (i.e. negligible hysteresis and magnetic saturation, steady state harmonic current), and application of some vector algebra, the following can be derived:

$$\mathbf{J} = -\sigma \frac{\partial \mathbf{A}}{\partial t} + \mathbf{J}_s \qquad\qquad (2-9)$$

$$\frac{1}{\mu_r\mu_0}\left(\frac{\partial^2 \mathbf{A}}{\partial r^2} + \frac{1}{r}\frac{\partial \mathbf{A}}{\partial r} + \frac{\partial^2 \mathbf{A}}{\partial z^2} - \frac{\mathbf{A}}{r^2}\right) = -\mathbf{J_s} + j\omega_r\sigma\mathbf{A} \qquad (2-10)$$

where $\mathbf{J_s}$ is the source current density in the induction coil and ω_r is the frequency in radians per second.

Equation 2-10 is the primary equation that is solved for an axially symmetric cylindrical system.

Determining the electromagnetic field is accomplished using different approaches. For the melt initiation process, and single frequency heating of the melt pool, after removal of the starter ring, a constant voltage is defined for the large inductor. Depending on which process is being modelled, this values changes. As the coupling of the field with the melt increases, the current density changes and this determines an overall power in the melt. The analysis block is iterated in time steps until the calculation results converge to the defined value, which is specific to the system being used. The voltage levels defined as input (i.e. initial conditions) to the modelling used for this work were determined experimentally for the specific test configuration, at a nominal operating temperature, which was the basis for the numerical model. The primary purpose for developing this model was to be able to investigate the application of an induction energy draining device in CCIMs. Accordingly, the electromagnetic calculation block accommodates defining two separate frequencies and coupling the effects using superposition. This final calculation is accomplished by setting an initial current density and voltage on the large inductor, as well as initial current density and a maximum power level limit for the small inductor that drives the draining process.

 2.1.2. Thermal and Hydrodynamic Calculation Blocks

The thermal calculation block is based on convergence of the energy equation with the internal heat sources resulting from electromagnetic field dissipation. This is defined as follows [57]:

$$Q = \frac{\partial(\rho c_P T)}{\partial t} + \nabla \cdot (\rho c_P T\mathbf{V}) + \nabla(-k\nabla T) \qquad \text{(from Fourier's law)} \qquad (2-11)$$

where:

       Q is heat source density induced by eddy currents

       ρ is density of the material

       c_P is specific heat of the material

       T is temperature

k is thermal conductivity of the material

V is velocity vector

Note that in the energy equation, the viscous dissipation terms, and thus viscous heating, of the full equation can be neglected because this effect is minimal as compared to the joule-heating effects of the induction energy [58]. This assumption is valid because the Brinkman number, defined by the following equation [63], satisfies the following condition for the flow regime within the glass melt:

$$\mathrm{Br} = \frac{\mu_{\mathrm{ref}} V_{\mathrm{ref}}^2}{k_{\mathrm{ref}}(T - T_{\mathrm{ref}})} \ll 1 \qquad (2 - 12)$$

where:

μ_{ref} is the dynamic viscosity at a reference temperature

V_{ref} is average velocity for the reference condition

k_{ref} is the thermal conductivity at the reference condition

$T - T_{\mathrm{ref}}$ is the difference from the reference temperature

Thus, the energy equation is simplified to:

$$Q = \frac{\partial(\rho c_P T)}{\partial t} + \nabla(-k\nabla T) \qquad (2 - 13)$$

This result is then coupled with the hydrodynamic effects resulting from convergence of the momentum equations. That is:

$$\frac{D\rho}{Dt} + \rho\nabla \cdot \mathbf{V} = \frac{\partial\rho}{\partial t} + \frac{1}{r}\frac{\partial(\rho r u_r)}{\partial r} + \frac{1}{r}\frac{\partial(\rho u_\theta)}{\partial \theta} + \frac{\partial(\rho u_z)}{\partial z} = 0 \qquad \text{(continuity equation)} \qquad (2 - 14)$$

$$\rho\frac{D\mathbf{V}}{Dt} = -\nabla P + \rho\mathbf{g} + \mu\nabla^2\mathbf{V} \qquad \text{(Navier} - \text{Stokes equation)} \qquad (2 - 15)$$

where:

V is velocity in all dimensions (u_r, u_θ, u_z)

P is pressure

g is body forces

μ is dynamic viscosity of material

The Navier-Stokes equation, which represents conservation of momentum, is expanded in cylindrical coordinates as follows [51]:

r – momentum   (2 – 16)

$$\rho\left(\frac{\partial u_r}{\partial t} + u_r\frac{\partial u_r}{\partial r} + \frac{u_\theta}{r}\frac{\partial u_r}{\partial\theta} - \frac{u_\theta^2}{r} + u_z\frac{\partial u_r}{\partial z}\right) = -\frac{\partial p}{\partial r} - \left[\frac{1}{r}\frac{\partial}{\partial r}(r\tau_{rr}) + \frac{1}{r}\frac{\partial\tau_{r\theta}}{\partial\theta} - \frac{\tau_{\theta\theta}}{r} + \frac{\partial\tau_{rz}}{\partial z}\right] + F_r$$

θ – momentum   (2 – 17)

$$\rho\left(\frac{\partial u_\theta}{\partial t} + u_r\frac{\partial u_\theta}{\partial r} + \frac{u_\theta}{r}\frac{\partial u_\theta}{\partial\theta} + \frac{u_r u_\theta}{r} + u_z\frac{\partial u_\theta}{\partial z}\right) = -\frac{1}{r}\frac{\partial p}{\partial r} - \left[\frac{1}{r^2}\frac{\partial}{\partial r}(r^2\tau_{r\theta}) + \frac{1}{r}\frac{\partial\tau_{\theta\theta}}{\partial\theta} + \frac{\partial\tau_{\theta z}}{\partial z}\right] + F_\theta$$

z – momentum   (2 – 18)

$$\rho\left(\frac{\partial u_z}{\partial t} + u_r\frac{\partial u_z}{\partial r} + \frac{u_\theta}{r}\frac{\partial u_z}{\partial\theta} + u_z\frac{\partial u_z}{\partial z}\right) = -\frac{\partial p}{\partial z} - \left[\frac{1}{r}\frac{\partial\tau_{\theta z}}{\partial\theta} + \frac{1}{r}\frac{\partial\tau_{\theta z}}{\partial\theta} + \frac{\partial\tau_{zz}}{\partial z}\right] + F_z$$

where the shear stresses are defined by the following constitutive equations:

$$\tau_{rr} = -\mu\left[2\frac{\partial u_r}{\partial r} - \frac{2}{3}(\nabla\cdot\mathbf{V})\right] \tag{2 – 19}$$

$$\tau_{\theta\theta} = -\mu\left[2\left(\frac{1}{r}\frac{\partial u_{\theta r}}{\partial\theta} + \frac{u_r}{r}\right) - \frac{2}{3}(\nabla\cdot\mathbf{V})\right] \tag{2 – 20}$$

$$\tau_{zz} = -\mu\left[2\frac{\partial u_z}{\partial z} - \frac{2}{3}(\nabla\cdot\mathbf{V})\right] \tag{2 – 21}$$

$$\tau_{r\theta} = \tau_{\theta r} = -\mu\left[r\frac{\partial}{\partial r}\left(\frac{u_\theta}{r}\right) + \frac{1}{r}\frac{\partial u_r}{\partial\theta}\right] \tag{2 – 22}$$

$$\tau_{rz} = \tau_{zr} = -\mu\left[\frac{\partial u_z}{\partial r} + \frac{\partial u_r}{\partial z}\right] \tag{2 – 23}$$

$$\tau_{\theta z} = \tau_{z\theta} = -\mu\left[\frac{\partial u_\theta}{\partial z} + \frac{1}{r}\frac{\partial u_z}{\partial\theta}\right] \tag{2 – 24}$$

These are simplified significantly when the axially symmetric assumption is implemented.

The Boussinesq approximation states that, for buoyancy driven flows, density differences are sufficiently small and can be neglected, except where they appear in terms multiplied by gravity in the momentum equations [63]. However, these applications are generally applied to much less

viscous flow regimes (e.g. warm and cold water, air flow, etc.). For the molten glass used in this research, both the density and viscosity are dependent on temperature. The density changes by about 10% within the temperature range of interest in this model (i.e. 700°C to 1,500°C), and the viscosity can change by orders of magnitude, dramatically altering the velocity field. For this reason, the Boussinesq approximation is not incorporated into the model.

For induction melting of certain materials, such as metals, Lorentz forces are a dominant factor in the overall hydrodynamic characteristics. Lorentz forces are defined by [57]:

$$\mathbf{F} = \rho_{charge}[\mathbf{E} + (\mathbf{V} \times \mathbf{B})] \qquad\qquad (2-25)$$

where **F** is the total force (electric and magnetic) produced.

However, for refractory oxide materials, such as the BSG used in this research, the hydrodynamic flow regime is dominated by buoyancy effects, and Lorentz forces can be neglected [56], although they may produce some minor effects on velocity and temperature distribution within the melt. This is readily verified experimentally (see Figure 2-1.) since the melt does not undergo any uplifting or pulling away from the crucible walls, as seen in induction melting of metals. Thus, the only forces included in the Navier-Stokes equation for this model are gravity forces, and specifically do not include Lorentz force effects.

Additionally, since the CCIM system has been modelled as an axially symmetric geometry, the momentum terms and shear stresses in the θ-direction are ignored. This also results in normal velocity components to the axis being assumed to equal zero. The no slip condition is also assumed, thus vertical and tangential velocity components at the wall and bottom are assumed to equal zero. Finally, a further simplification is the assumption that normal velocity components to the melt pool surface are equal to zero. This is valid in a system
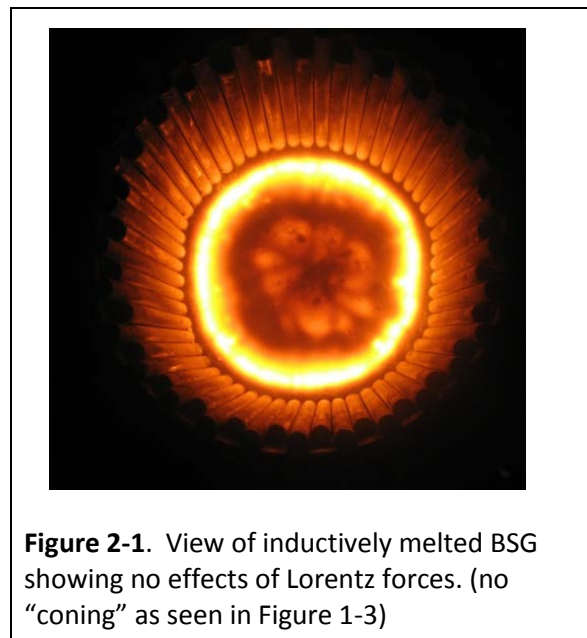
Figure 2-1. View of inductively melted BSG showing no effects of Lorentz forces. (no "coning" as seen in Figure 1-3)

that does not incorporate stirring or bubbling. These assumptions significantly simplify the model and accelerate convergence; however, they do introduce errors in the results as compared to

experimental values. For example, the actual system does not exhibit a purely axially symmetric behaviour, although it is close and this is a reasonable approximation.

As previously indicated, the material property parameters are defined as functions of temperature. Convergence is based on achieving a steady state condition for both velocity and temperature fields. Thus, the thermal calculation block is coupled with the hydrodynamic block. Steady state for these coupled calculations is based on convergence of the nodal pressure values. The resulting nodal temperatures are then checked to ensure agreement, within a much tighter tolerance. This approach, while more challenging to achieve convergence, provides more representative results as compared to models that rely solely on convergence of temperature values.

2.1.3.Boundary and Initial Conditions

During the early stages of developing the model a simplistic approach was taken in defining the boundary conditions, especially for the thermal conditions. Specifically, the basic CCIM test platform (i.e. no secondary inductor or draining system) was instrumented with calorimetry capabilities to measure specific heat losses from the bottom, sides, and top of the melt pool. The calorimetry system has been progressively improved to provide for comprehensive capabilities to determine a complete energy balance on the CCIM test platform. Figure 2-2 provides a schematic of the calorimetry and data acquisition system currently installed.
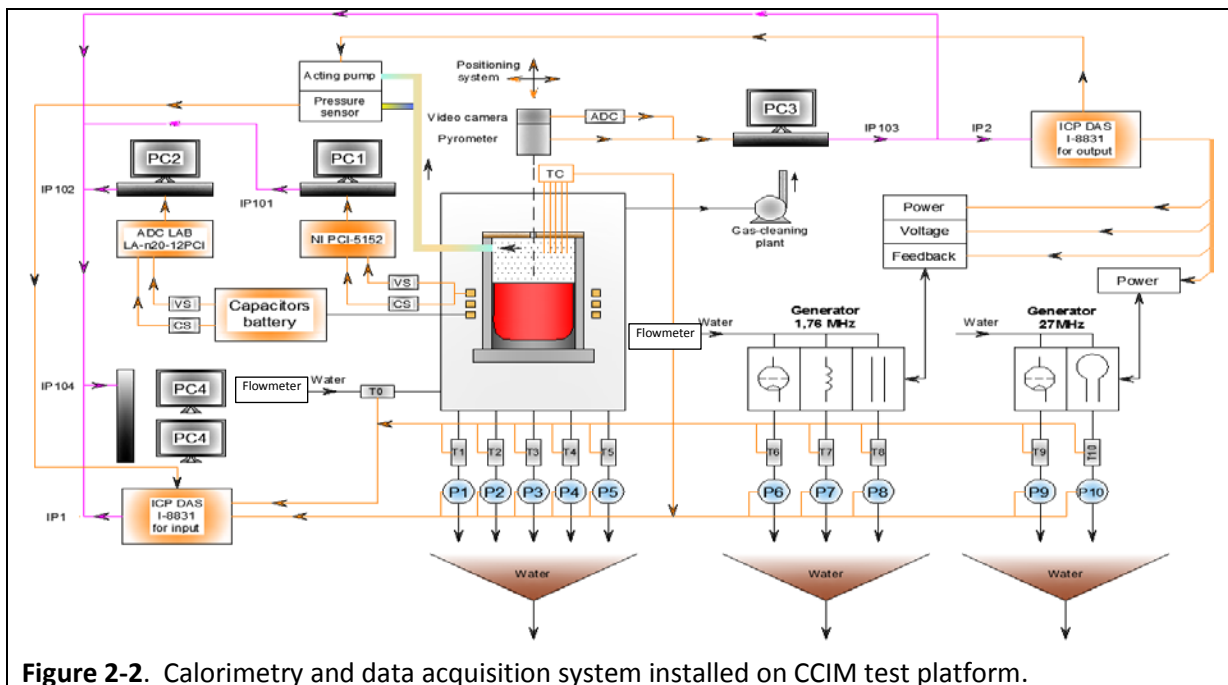
Figure 2-2. Calorimetry and data acquisition system installed on CCIM test platform.

This system served as the geometry basis for the model, with the addition of the inductively heated draining system. Figure2-3 shows a schematic of the geometry that defined the initial model.

The initial CCIM test set up did not allow for isolating the radiation heat sources on the crucible wall above the melt from the convection heat sources, so these are combined into a single heat flux boundary condition. In addition, the eddy current induced heat in the stainless steel crucible tubes was not isolated either. A special platform configuration was designed and testing conducted, which is discussed later, that determined these electrical losses. This is important to be able to understand and model the effects of less or more conductive crucible materials (i.e. copper versus stainless steel). Additionally, the process of experimental development of the emissivity characteristics of the molten BSG surface provided a means to determine the radiation energy contribution to the crucible wall.

Figure 2-3. Schematic of original concept for a CCIM with drain device integrated.

Despite their overall limitations, these initial values were very useful in determining that the model was converging and providing expected results. The initial values used were based on operating the existing CCIM with an approximate maximum surface temperature of 1,200^{o}C. The bottom of the initial CCIM test platform was constructed of ceramic brick and was not water-cooled. The enhanced design included a water cooled bottom integrated with a water cooled drain flange, which resulted in different boundary conditions. The initial boundary conditions were as shown in Table 2-1.

Table 2-1. Boundary conditions for initial modelling.

Surface	Thermal Flux Value (W/cm^2)
Crucible Side	16
Crucible Bottom	1
Melt Pool Top	7
Drain Side	27
Drain Bottom	1

Eventually, a radiation heat transfer boundary condition was set for the melt pool surface and bottom opening of the drain, which is discussed in more detail later. Additionally, for modelling purposes, the thermal flux from the top surface of the drain geometry is assumed to be zero.

Several tests were conducted to refine the thermal boundary conditions being used in the model. This was necessary because these values were only valid for one operating regime (i.e. surface maximum temperature of 1,200^{o}C). The first test was conducted using a 300 mm diameter stainless steel crucible with a 3-turn inductor. The physical characteristics of the model, which were based on this geometry, were as shown in Table 2-2.

Table 2-2. System geometry for initial test.

Feature	Dimension
Internal diameter of crucible	300 mm
Height of melt volume in cold crucible	200 mm
Internal diameter of inductor	320 mm
Height of inductor	200 mm
Number of turns on inductor coil	3

Note that for all modelling and experimental work, the frequency of the primary generator is 1.76 MHz.

The first stage of model development was focused on achieving a steady-state for the melt. Integration of the secondary ultra-high frequency, as well as the melt initiation capabilities came later.

BSG is not conductive at low temperatures and will not couple with the electromagnetic field below approximately 800°C (i.e. σ = 1.24e-4 ohm-m). In an actual CCIM system, an initiator (i.e. metal, graphite, etc.) is placed in the start-up frit and the induction field couples with this material initially. As it heats up, the energy is conducted into the surrounding glass, forming small molten pools that then begin to preferentially couple with the induction field, assuming the generator is "tuned" properly (i.e. oscillating at a frequency that will couple effectively with the molten glass - Note: this is discussed in more detail later). A couple of options exist to "force" the model to couple with the glass and obtain steady state when it does not include a melt initiation step: 1) an initial temperature and inductor current density can be set that will ensure melting, or 2) a fixed power density can be set in the glass volume. The original approach used the first option because the inductor current during operation is a known and measurable quantity.

Initially, the approach used was to set the entire melt volume at 800°C. The initial value for the current density is dependent on whether a 2-turn or 3-turn inductor is used.

To ensure that this would not impact the results, a comparison was made between a uniform starting temperature and a simulated temperature gradient, as
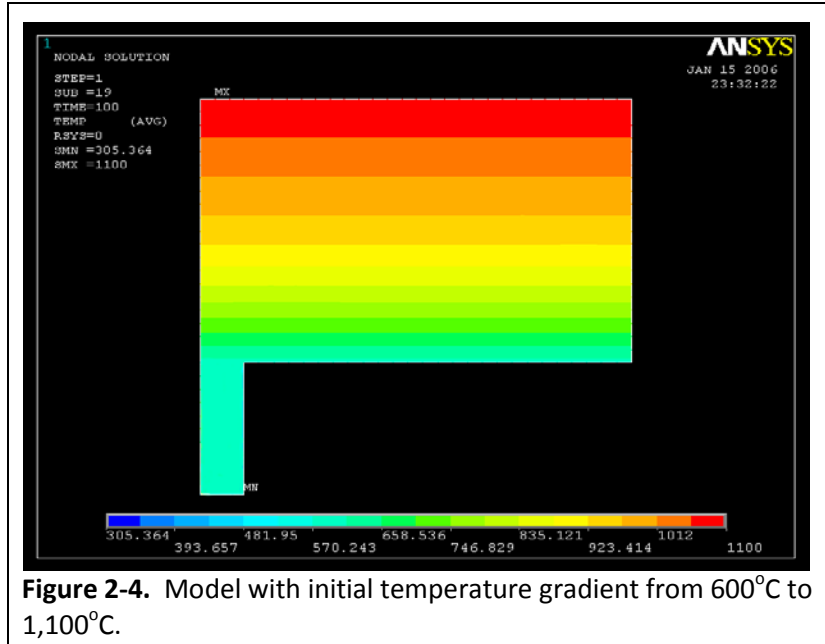
Figure 2-4. Model with initial temperature gradient from 600°C to 1,100°C.

illustrated in Figure 2-4. This initial condition was shown to have no impact on the steady state temperature distribution, although it did require more time to converge, as expected. This investigation was important because it demonstrated that starting with a predefined temperature distribution, such as in the case of the melt initiation model, has no impact on the steady state result, all other parameters being the same. Another important result of this effort, which is discussed later, was that it demonstrated the feasibility of initiating a melt in the drain body at a lower temperature above the drain throat than originally thought.

Another comparison for the starting condition was conducted for two different starting conditions. The first had an initial constant glass temperature of 20°C and the second had an initial constant glass temperature of 1,000°C. This investigation showed that virtually no difference in the steady state condition exists. These results are shown in Figures 2-5 and 2-6.

As previously discussed, the initial thermal boundary conditions were fixed specific heat flux values based on experimental data. Multiple experiments were conducted and calorimetry data were collected for a variety of operating modes. Test platforms with 2-turn and 3-turn inductor coils were tested, with varying melt temperatures and melt depth. Table 2-3 gives an example of some of these test results. Several more data were collected during each test; however, they are consistent with Table 2-3.
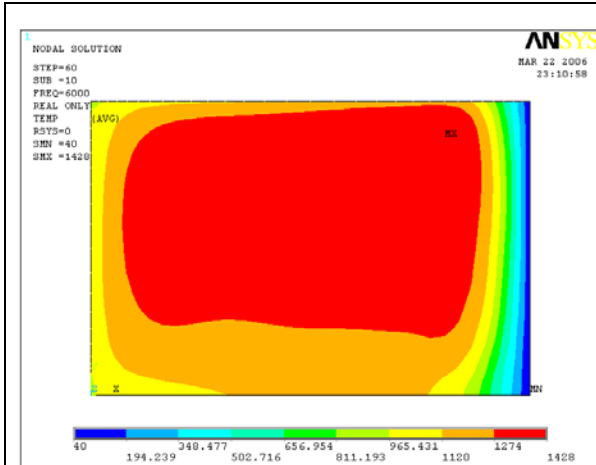
Figure 2-5. Temperature distribution for 20°C starting temperature.
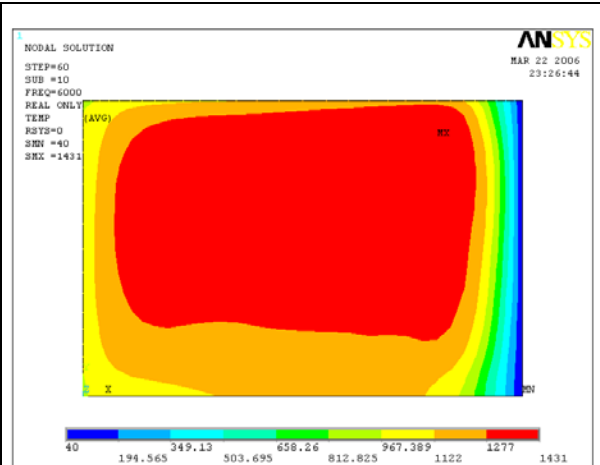
Figure 2-6. Temperature distribution for 1,000°C starting temperature.

Table 2-3. Experimental results of measured heat losses from crucible side at various conditions.

Mode No.	Melt depth, cm	T_{melt}, °C	Power in melt, kW	Specific thermal flux, W/cm²
1 2-turn inductor	10.5	1,350	16.3	**16.5.**
2 2-turn inductor	9.0	1,150	11.4	**13.4**
3 2-turn inductor	9.0	1,000	8.51	**10.0**
4 2-turn inductor	3.0	1,410	-	**32.4**
5 2-turn inductor	3.0	1,450	-	**34.4**
6 2-turn inductor	3.0	1,300	-	**25.6**
7 (3-turn inductor)	15.0	1,050	20.7	**13.9**
8 (3-turn inductor)	15.0	1,027	19.5	**13.4**
9 (3-turn inductor)	15.5	1,010	21.1	**13.9**
10 (3-turn inductor)	15.0	965	17.6	**11.39**

These results were used to establish a linear relationship for the bulk heat transfer coefficient at the crucible wall, as a function of temperature, which is used in the enhanced model. It is referred to as a "bulk" heat transfer coefficient because it accounts for contributions from conduction, convection, radiation, and eddy current heat sources. The melt pool height was taken into account to determine the specific heat flux, which was then converted to a value for α(T) based on the following equation:

$$q = \alpha(T)A(T_{melt} - T_{env}) \hspace{4cm} (2-24)$$

where A is the surface area and T_{env} is the temperature of the surrounding environment. The resulting relationship is shown in Figure 2-7.

A different approach was used to determine the appropriate heat transfer coefficient for the ceramic bottom because it was not water cooled. Instead, thermocouples were placed on the bottom of the crucible located on the centerline axis and 10 cm out from the axis (See Figure 2-8.).

Figure 2-7. Heat transfer coefficient from sides of crucible.

After a melt pool had been established, thermocouples were lowered into the melt directly above the thermocouples at a distance of 5 mm. The temperatures and distances were used to calculate the average glass conductivity in this region. This was then used to determine an average heat transfer coefficient in the ceramic. The conductivity values of the glass could not be used directly without first determining the temperature profile in the bottom region. This resulted in an average heat transfer coefficient of

Figure 2-8. Placement of thermocouples in melter bottom to determine heat flux.

approximately 500 W/m^2-K for the ceramic-bottom melter. As reference, Figures 2-9 and 2-10 show the 2-turn and 3-turn CCIM test platforms. All other parameters are the same for each test system (i.e. crucible dimensions, power supply, etc.).

The ceramic bottom was used for the majority of the experimental work; however, as the design of the drain advanced, so did the crucible bottom design. The configuration of the integrated drain and bottom has evolved into an all-metallic water-cooled design. Thus, for modeling purposes, the heat transfer coefficient is determined for each configuration using calorimetry, similar to the process used for the crucible side wall. Cooling requirements for specific drain and bottom configurations have been determined using the ANSYS® MultiPhysics software, with electromagnetic and thermal effects coupled.

Figure 2-9. Two-turn CCIM test platform.

The hydrodynamic block calculation is the most difficult to couple and reach steady state. For that reason, a significant amount of model functionality was confirmed using only the electromagnetic and thermal

Figure 2-10. Three-turn CCIM test platform.

calculation blocks. The complexity of the model has been systematically increased. For example, the initial model did not account for the temperature dependence of all of the material properties (i.e. electrical conductivity), but used fixed average values to simplify initial calculations and ensure functionality of the model. The next version accounted for the temperature-dependence of the material properties. Once this was demonstrated to function properly, the hydrodynamic effects were coupled with the thermal calculation block. Finally, the electromagnetic block was modified to include the dual frequency capability, and the geometry of the model was enhanced to include the induction drain device.

2.2. Glass Material Properties Definition

Knowledge of the behavior of the material properties as a function of temperature is crucial to developing a representative numerical model. Unfortunately, very little data are available for glass behavior through a range of temperatures. And, almost no data are available for material properties at temperatures above 1,200°C, except for some limited viscosity and electrical conductivity data.

2.2.1.Validating Glass Composition for Correlating Available Material Properties Data

The material properties used in the model were based on a known glass composition that is referred to as "SRL-411" [64]. Farnsworth [65] identifies key material properties for the SRL-411 glass composition at various temperatures up to 1,200°C. See Table 2-4. The data for this glass composition was used because it was all that could be found that actually had documented material properties, including thermal conductivity, specific heat, and density through a range of temperature values.

Table 2-4. Material properties for SRL-411 glass.

Temperature °C	Density kg/m³	Specific Heat J/kg-K	Thermal Conductivity W/m-K
22	2,610	920	1.05
100	2,603	1,000	1.11
200	2,598	1,100	1.16
300	2,590	1,180	1.16
400	2,575	1,270	1.22
500	2,555	1,910	1.63
600	2,531	1,820	1.17
700	2,501	1,520	1.05
800	2,458	1,500	1.20
900	2,405	1,610	1.48
1,000	2,352	1,730	1.83
1,100	2,321	1,880	2.23
1,200	2,310	2,020	2.62

Unfortunately, no glass frit was available with the exact composition of SRL-411 glass. However, a very similar start-up frit was available, with a designation of AC18647H, which had been developed for the Defense Waste Processing Facility (DWPF). The DWPF is a vitrification plant located at the Savannah River Site that immobilizes radioactive wastes in a BSG matrix using JHCM technology. The composition of the AC18647H [66] frit is not identical to SRL-411, so some analysis had to be

completed to determine if the material property values for SRL-411 would be representative. A common method to make this evaluation is to compare "families" of similarly behaving oxides in the compositions. The comparison is not exact because the oxides in the compositions are not reported in the same manner. Table 2-5 shows the composition of the SRL-411 and AC18647H glasses. Table 2-6 makes a comparison between the glasses on the similar oxide family basis.

Table 2-5. Compositions of SRL-411 and AC18647H glasses.

SRL-411		AC18647H	
Oxide	Weight %	Oxide	Weight %
Al_2O_3	12.0	Al_2O_3	6.5
B_2O_3	8.3	B_2O_3	7.7
CaO	5.2	CaO	1.3
Cr_2O_3	-	Cr_2O_3	0.1
Fe_2O_3	8.0	Fe_2O_3	10.8
K_2O	(reported with Na_2O)	K_2O	-
Li_2O	9.4 (Li_2O+ TiO_2+CuO)	Li_2O	4.8
MgO		MgO	-
MnO_2	3.2 (MnO_2+ NiO)	MnO	1.40
Na_2O	9.4 (Na_2O+ K_2O)	Na_2O	11.8
NiO	(reported with MnO_2)	NiO	0.2
SiO_2	44.5	SiO_2	55.5
TiO_2	(reported with LiO_2	TiO_2	0.22
TOTAL	100.0	TOTAL	100.0

Table 2-6. Comparison of weight percentage of families of oxides for SRL-411 and AC18647H.

SRL-411		AC18647H	
Oxide Family	Weight %	Oxide Family	Weight %
Glass forming oxides (SiO_2, Al_2O_3, B_2O_3)	64.5	Glass forming oxides (SiO_2, Al_2O_3, B_2O_3)	69.9
Alkali metal oxides (K_2O, Li_2O, Na_2O)	17.8	Alkali metal oxides (K_2O, Li_2O, Na_2O)	16.6
Iron and similar oxides (Fe_2O_3, Cr_2O_3, MnO, TiO_2, NiO)	12.2	Iron and similar oxides (Fe_2O_3, Cr_2O_3, MnO, TiO_2, NiO)	12.2
Glass modifier oxides (MgO, CaO)	5.2	Glass modifier oxides (MgO, CaO)	1.3
TOTAL	100.0	TOTAL	100.0

These oxides can be grouped in several categories, including glass formers, alkali metals, iron oxides and those with similar properties, and modifying oxides, and then compared. Because of the

groupings that were provided in [64] for the SRL-411 composition, assumptions were made regarding weight percentages of some of the individual oxides. Typically, these values were taken as a ratio of the component weight percentage that they are combined with based on the ratio of the AC18647H glass. However, the SRL-411 property data does not include two key properties: viscosity and electrical conductivity.

Significant work has been accomplished by researchers at the Pacific Northwest National Laboratory to investigate the effects of composition and temperature on the electrical conductivity and viscosity of many glass compositions [67]. In this document, one of the glass compositions studied, referred to as CVS3-6, has very similar weight percentages in the oxide families, defined above, as both the SRL-411 and AC18647H. The CVS3-6 composition, on an oxide family basis, is compared to the AC18647H composition in Table2- 7.

Table 2-7. Comparison of CVS3-6 composition to AC18647H.

AC18647H		CVS3-6	
Oxide Family	**Weight %**	**Oxide Family**	**Weight %**
Glass forming oxides (SiO_2, Al_2O_3, B_2O_3)	69.9	Glass forming oxides (SiO_2, Al_2O_3, B_2O_3, P_2O_5)	65.7
Alkali metal oxides (K_2O, Li_2O, Na_2O)	16.6	Alkali metal oxides (K_2O, Li_2O, Na_2O)	18.2
Iron and similar oxides (Fe_2O_3, Cr_2O_3, MnO, TiO_2, NiO)	12.2	Iron and similar oxides (Fe_2O_3, Zr_2O_3, Cr_2O_3, NiO, Nd_2O_3)	12.2
Glass modifier oxides (MgO, CaO)	1.3	Glass modifier oxides (MgO, CaO)	3.9
TOTAL	**100.0**	**TOTAL**	**100.0**

This work also included diagrams that provided a tool to evaluate compositions that were close to the baseline compositions. As an example, Figure 2-11 provides one of those graphs showing the effects of various components on electrical conductivity as they vary in weight per cent from the baseline. The diagram shown was developed specifically for the glasses in the CVS3-6 family, as identified in the document. Evaluation of these specific components for the AC18647H glass composition provided strong confidence that the behaviour of the CVS3-6 glass would be representative of this glass. Unfortunately, the report did not include any data to help provide better validation.

Another body of work conducted extensive viscosity and electrical resistivity measurements on another DWPF frit formulation that was also very similar in composition to the CVS3-6 frit, as well as

the frit being used in this research [68]. Data from this composition were used to help validate the material property information used to develop the models.

Figure 2-11. Component effects on electrical conductivity at melting temperature. [67]
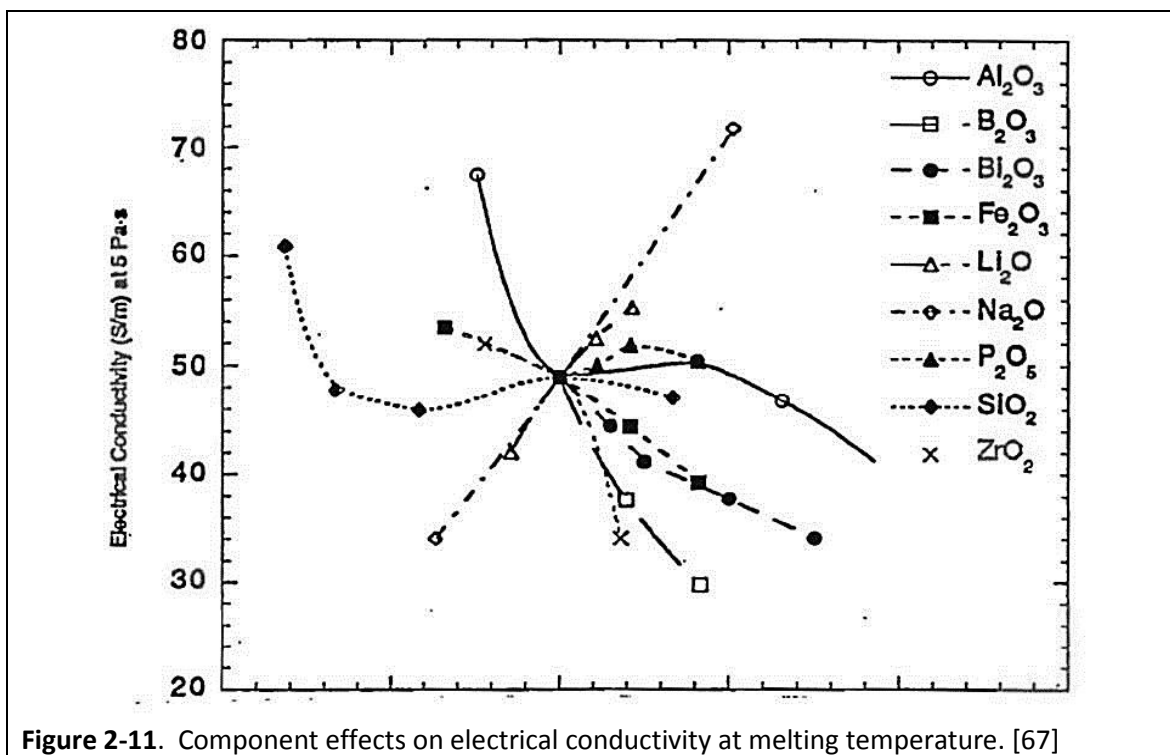
2.2.2.Determining Electrical Resistivity and Viscosity

The electrical resistivity and viscosity data were fit to Volgel-Tamman-Fulcher (VTF) equations, and then converted to exponential form.   The curve fits were performed using MathCad and correlations factors of 0.98713 and 0.99293 for electrical resistivity and viscosity, respectively were achieved. The resulting equations are as follows:

$$\rho_e(T) = e^{\left(-0.91956 + \frac{1739.58}{T - 375.613}\right)} \qquad \text{(electrical resistivity, ohm} - \text{m)} \qquad (2-27)$$

$$\mu(T) = e^{\left(-5.28918 + \frac{5831.1139}{T} - 280.1372\right)} \qquad \text{(viscosity, Pa} - \text{s)} \qquad (2-28)$$

The results are shown in Figures 2-12 and 2-13.

2.2.3.Determining Specific Heat, Thermal Conductivity and Density

Extrapolation of the other properties obtained from [65] for specific heat, thermal conductivity, density, and was more of a challenge to determine reasonable values. As previously stated, none of

the data were for temperatures above 1,200°C. Assumptions were made about the material properties, primarily that they would all be asymptotic to some value rather than expanding to infinity, or experiencing anomalies in the temperature range between 1,200°C and 2,000°C. It is important to note that several of the properties exhibit "elbows" as the glass is going the transition from solid to liquid. The SRL-411 data were curve fit using various techniques and the results are shown in Figures 2-14 through 2-16.

The equations developed were as follows:

$$\rho(T) = 4.84436\left[e^{(-6.75765\times10^{-3})T}\right] + 2294.35 \qquad \text{(density)} \qquad (2-29)$$

$$c_P(T) = (-7.5\times10^{-4})T^2 + 3.095T - 615.5 \qquad \text{(specific heat)} \qquad (2-30)$$

$$k(T) = (-1.25\times10^{-6})T^2 + (6.685\times10^{-3})T - 3.6065 \qquad \text{(thermal conductivity)} \qquad (2-31)$$

Figure 2-12. Curve fit for electrical resistivity data.
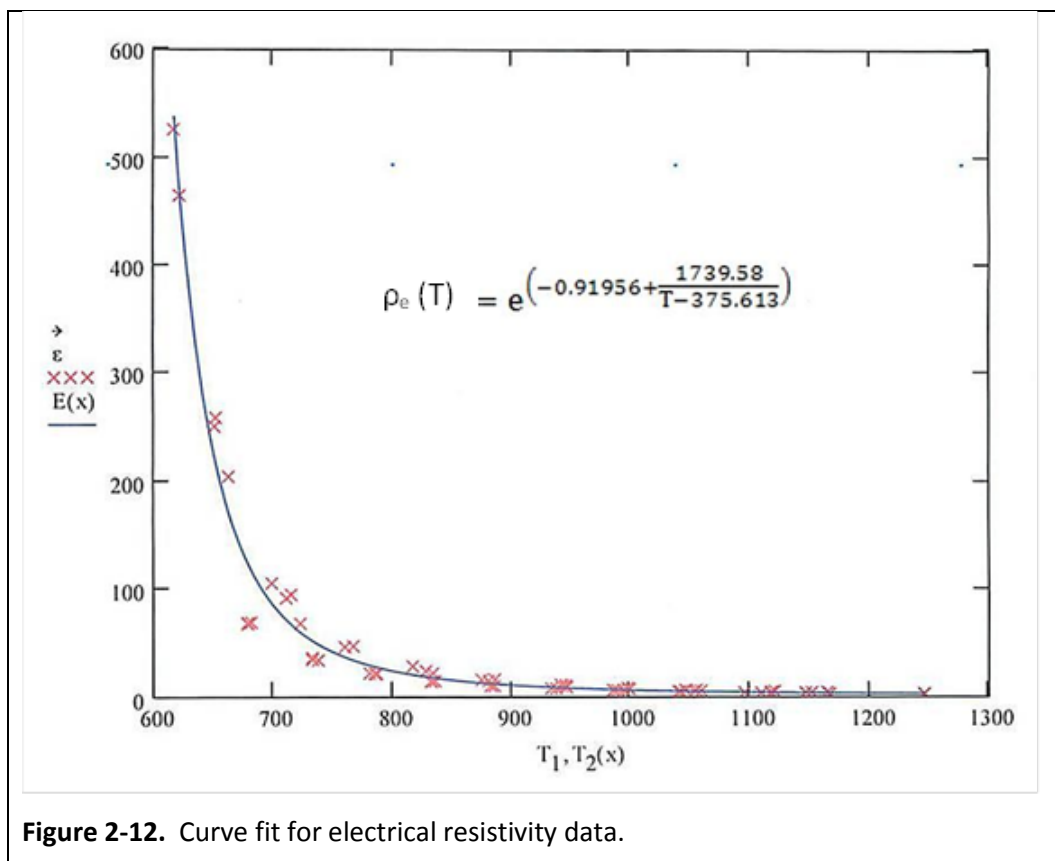
Relative to thermal conductivity, extensive bodies of work have been developed in researching methods to accurately measure this property. What has been discovered is that the effective thermal conductivity is actually a combination of conduction and radiation heat transfer effects.

Tarakanov, et al [69] noted that thermal conductivity increases by a factor of 1.5 to 2.0 for temperature changes from ambient to $300^{\circ}C - 400^{\circ}C$, above which the changes are comparatively small. Additionally, radiative conductivity effects below temperatures of $400^{\circ}C$ to $500^{\circ}C$ are negligible, but increase dramatically with temperature above this region, to the point of dominating the overall heat transfer process at very high temperatures.

$$\mu(T) = e^{\left(-5.28918 + \frac{5831.1139}{T} - 280.1372\right)}$$

Figure 2-13. Curve fit for viscosity data.

The equation of the curve is:

$$C_p(T) = (-7.5 \times 10^{-4})*T^2 + 3.095*T - 615.5$$

Figure 2-14. Curve fit for specific heat data.

Figure -2-15. Curve fit for density data.

The equation of the curve is:

$$\rho(T) = (4.84436 \times 10^4) \cdot e^{(-6.75765 \times 10^{\wedge}-3) \cdot T} + 2294.35$$

Figure 2-16. Curve fit for thermal conductivity data.

The equation of the curve is:

$$k(T) = (-1.25 \times 10^{-6}) \cdot T^2 + (6.685 \times 10^{-3}) \cdot T - 3.6065$$
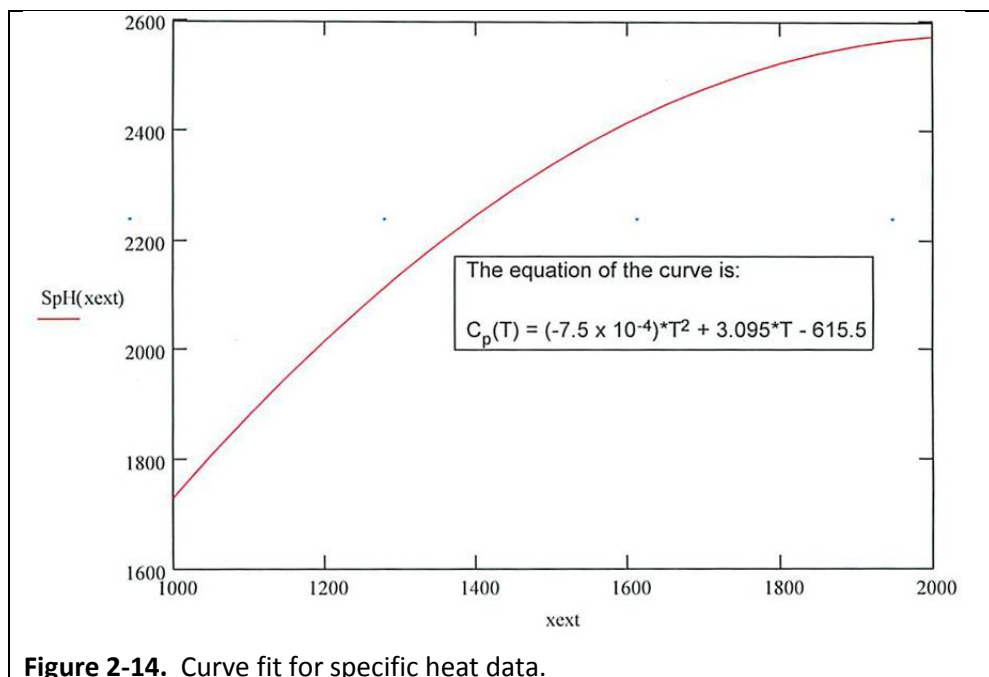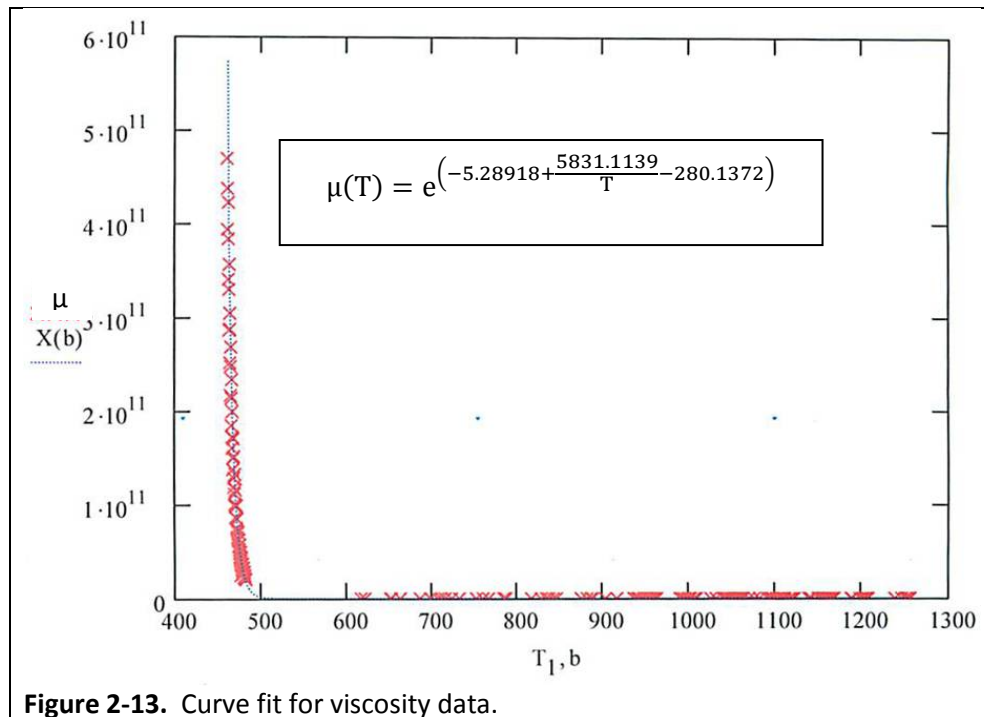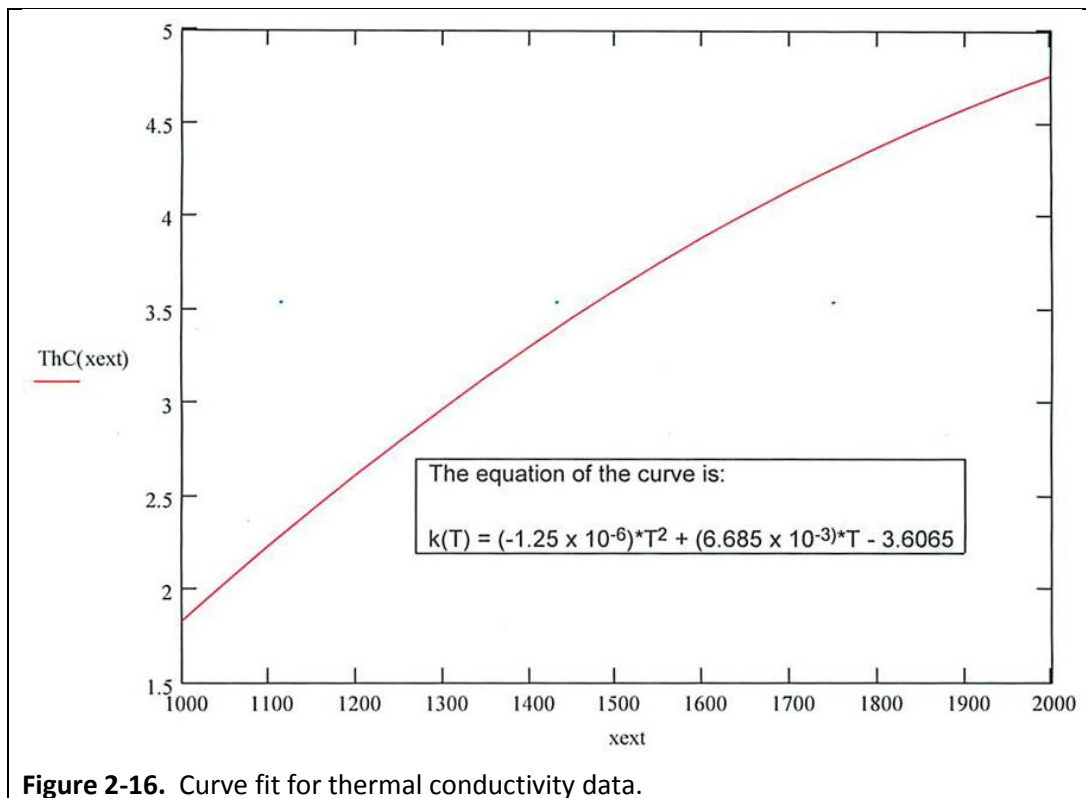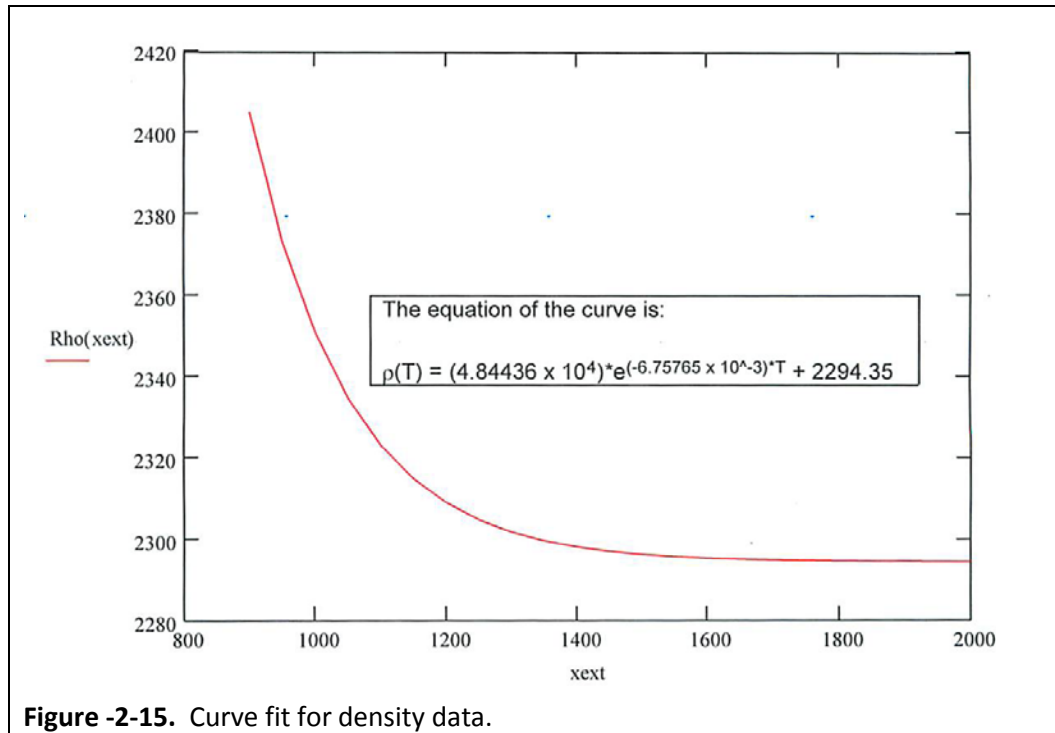
Details of the development of the material property models shown above are in Appendix A.

2.2.4.Determining the Emissivity

The final material property that required determination was the emissivity. In the early stages of modelling a fixed value 0f 0.5 was assumed; however, this required investigation because the power losses to the crucible walls from the model were not consistent with the experimental data. Additionally, sensitivity analyses conducted for the model indicated that changes in the emissivity value have significant effect on the steady state temperature distribution. This is discussed in more detail later.

An experiment was set up and conducted that used a two-color optical pyrometer (Siemens Ardocell PZ Profibus 7MC3060-PZ40) to make radial temperature measurements along two paths for three different steady state modes. The same measurement paths were used for each mode. The objective was to make measurements at different average surface temperatures. This was primarily defined by pyrometer measurements, but also visually. Figure 2-17 shows a comparison of the melt surfaces for the three steady state modes established at 856°C, 996°C, and $1,145^{o}$C, respectively.

Figure 2-17. Comparison of three different steady state modes established for emissivity determination. Notice the obvious difference in average surface temperature (see Table 2-8).

Steady state in the CCIM is determined by establishing a steady condition of the active power supplied to the inductor. This is determined primarily by calorimetry data from the generator anode. Additionally, comparison was made with the direct measurement of the inductor current and voltage using sensors that were developed specifically for this work. Reliable, high accuracy sensors that can operate in high frequency fields (i.e. 2 MHZ range) are not commercially available.

Figure 2-18 shows the measured electrical signals, as well as various calorimetric data that demonstrate the established steady state mode. The numbered arrows indicate the steady state

modes reached during this experiment. In this graph, P_{cc1} is the power in the crucible walls, P_{a1} is the power on the generator anode, P_{at} is the power on the inductor.

Figure 2-18. Steady state modes established for emissivity determination.
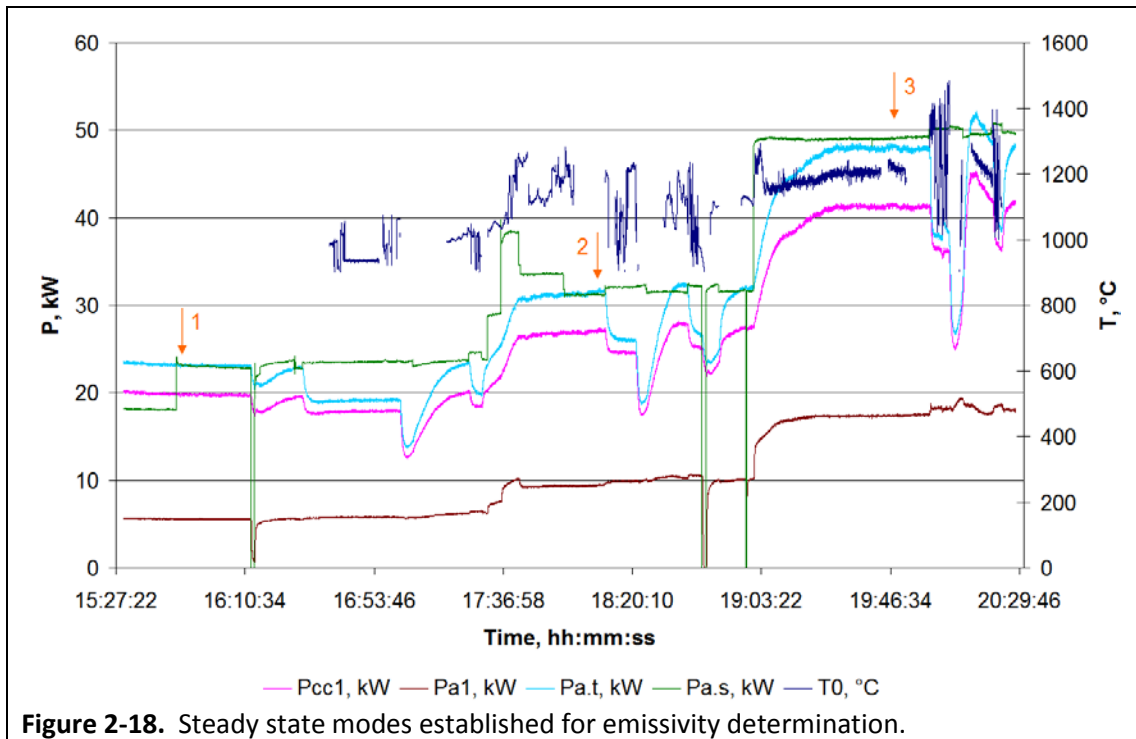
All of these are determined with calorimetry. P_{as} is the power on the inductor indicated by the high frequency sensors. Comparison of P_{at} and P_{as} provides an indication of the response time (i.e. time constant) of the melt condition to the power supplied by the generator, as well as response to changes, such as removal of the melter cover lid.

For each steady state mode, temperature measurements were taken along two paths across the surface of the melt from the wall to the centerline. Figures 2-19 through 2-21 show the temperature data collected, as well as a sixth order polynomial curve that was determined for each set. These polynomial equations were then integrated and used to determine average emissivity values for each steady state mode. Note that temperature values reported in Figures 2-19 through 2-21 are in Kelvin.

The curve fit for the first steady state mode data set is the following sixth order polynomial:

$$T(x) = \frac{1}{0.2} \int_{0}^{0.2} [1.171 \times 10^3 + (5.497 \times 10^3)x - (4.154 \times 10^5)x^2 + (1.017 \times 10^7)x^3 - (1.078 \times 10^8)x^4$$

$$+ (5.162 \times 10^8)x^5 - (9.146 \times 10^8)x^6]\, dx \quad (x \text{ is radial location on surface}) \qquad (2-32)$$
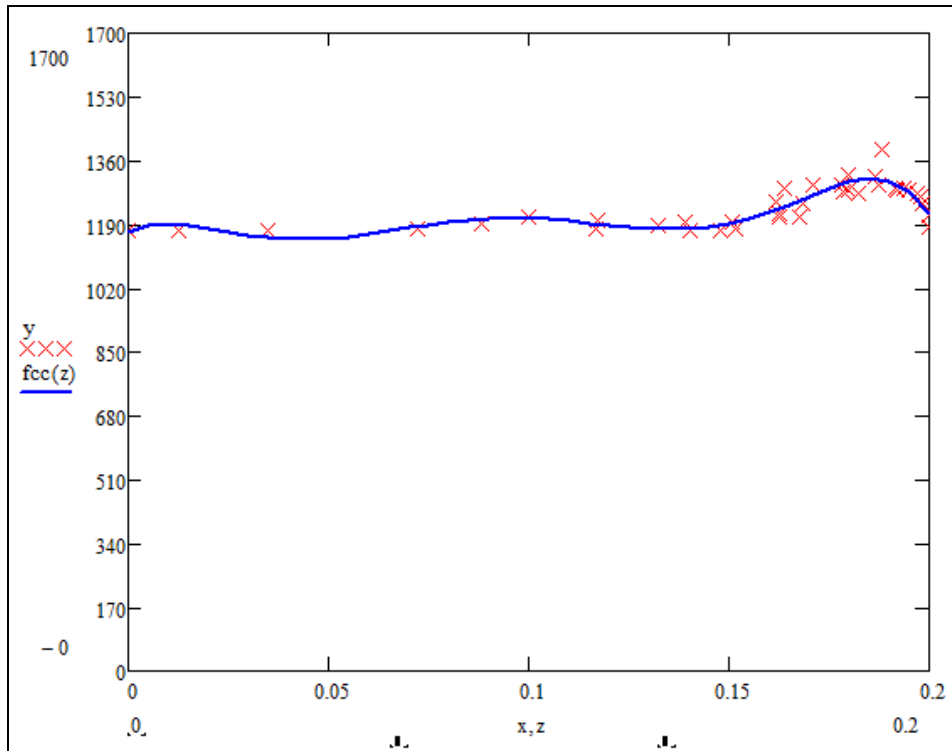
Figure 2-19. Temperature measurements and corresponding curve fit for first steady state mode.
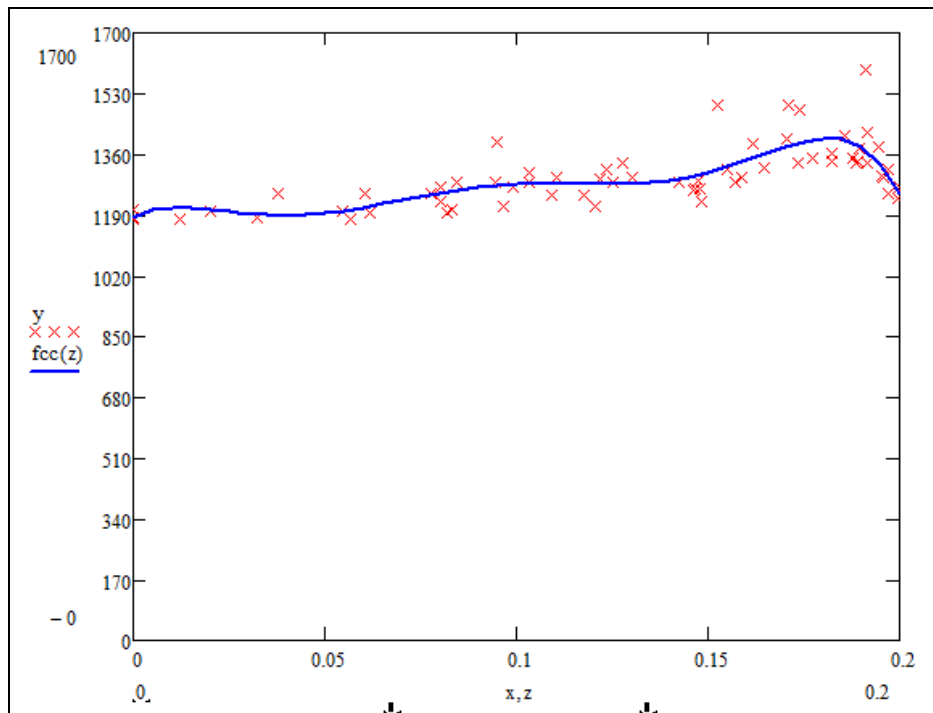
Figure 2-20. Temperature measurements and corresponding curve fit for second steady state mode.

The curve fit for the second steady state mode data set is the following sixth order polynomial:

$$T(x) = \frac{1}{0.2} \int_0^{0.2} [1.183 \times 10^3 + (5.756 \times 10^3)x - (3.830 \times 10^5)x^2 + (9.307 \times 10^6)x^3 - (9.870 \times 10^7)x^4$$

$$+ (4.765 \times 10^8)x^5 - (8.560 \times 10^8)x^6] \, dx \qquad (2-33)$$

The curve fit for the third steady state mode data set is the following sixth order polynomial:

$$T(x) = \frac{1}{0.2} \int_0^{0.2} [1.317 \times 10^3 + (3.286 \times 10^3)x - (1.761 \times 10^5)x^2 + (3.802 \times 10^6)x^3 - (3.872 \times 10^7)x^4$$

$$+ (1.921 \times 10^8)x^5 - (3.651 \times 10^8)x^6] \, dx \qquad (2-34)$$

Figure 2-21. Temperature measurements and corresponding curve fit for third steady state mode.
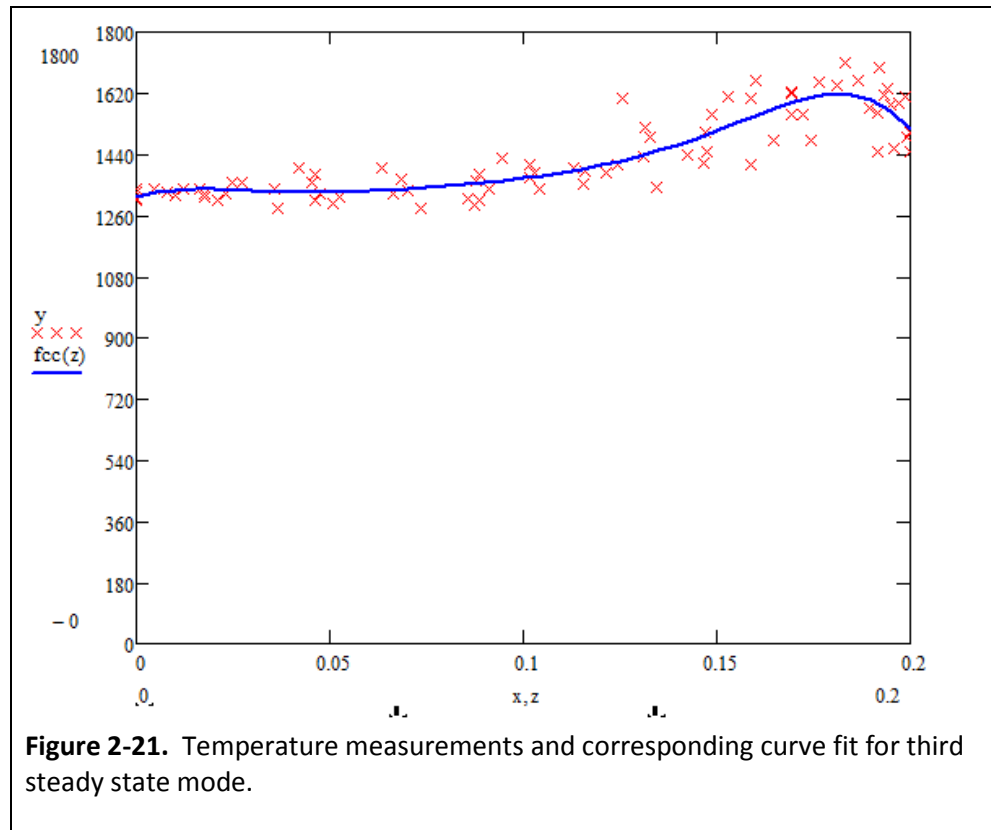
Using these data, the emissivity can then be calculated using the Stefan-Boltzmann law and the assumption of behavior as a gray body (i.e. not sensitive to frequency spectral effects in the temperature range of interest). This is defined by the following equation:

$$\varepsilon = \frac{P_{\text{rad.int}}}{\sigma \frac{1}{0.2} \left(\int_0^{0.2} T(r) \, dr \right)^4 S} \qquad (2-35)$$

where:

P$_{rad.int}$ is the total power emitted by radiation from the melt surface

σ is 5.6704 X 10^{-8}, Stefan-Boltzmann constant

S is Area of the melt pool surface

An alternate approach is to raise each temperature to the fourth power then integrate rather than take the overall result of the integration and raise it to the fourth power as in Eq 34. This approach is represented as follows:

$$\varepsilon = \frac{P_{rad.int}}{\sigma \frac{1}{0.2}\left(\int_0^{0.2} T(x)^4 dx\right) S} \qquad (2-36)$$

Yet another approach is to divide the surface area into concentric circular areas and use an average temperature. An infrared imager was used to collect the data for this approach, which is accomplished using the following equation

$$\varepsilon = \frac{P_{rad}}{\sigma \sum_1^i (T_i^4 - T_0^4) S_i} \qquad (2-37)$$

where:

T_1 is the average temperature in each circular surface area or ring

$S_i = \pi(R_i^2 - R_{i-1}^2)$, which is the surface area of ring i.

The total emitted power, P$_{rad}$, is determined by calorimetry data from the crucible walls, P$_{cc1,rad}$, and the melter cover lid, P$_{cov1,rad}$. The data used to determine the P$_{rad}$ value for emissivity determinations are provided in Figure 2-22.

The test times indicated by the numbered arrows in Figure 2-22 indicate when the cover was removed and additional glass frit was added to the melter. The frit was added to provide a temporary thermal shield from the radiation heat from the surface. Removal of the lid also eliminated reflection of the radiant heat emitted to the lid back onto the crucible walls. These combined effects allowed determination of the power provided to the crucible walls solely from radiation heat transfer.
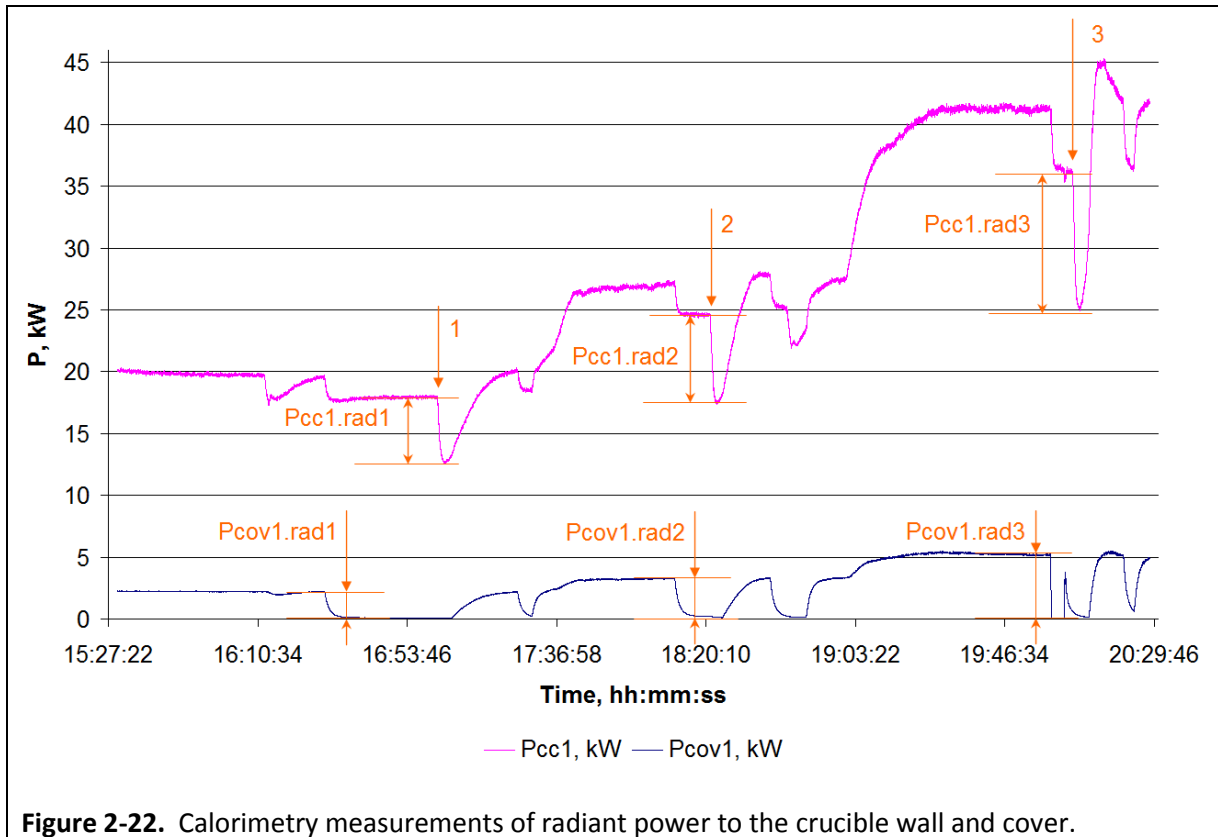
Figure 2-22. Calorimetry measurements of radiant power to the crucible wall and cover.

The two measured values, Pcov.rad and Pcc1. rad, were then summed for the total radiated power from the melt surface. For the three steady state modes, the emitted power was 9.05 kW, 12.7 kW, and 21.1 kW, respectively. For comparative analysis, an infrared imager was used to capture a thermal image of the melt surface for the first steady state mode. This data, shown in Figure 2-23, was used with equation 2-31 to develop an integrated emissivity value using an alternative approach. The approach was applied twice, once with 10 surface area rings, and another with 500 surface area rings. Figure 2-24 shows an image from the view camera used to collect temperature data with the Siemens three-color pyrometer. Table 2-8 gives the results from the various approaches for calculating the temperature dependent emissivity.

Table 2-8. Comparison of various methods for calculating emissivity.

Mode No.	Average temperature, °C	Calculation with Eq 2-35	Calculation with Eq 2-37, j=500	Calculation with Eq 2-36	Calculation with Eq 2-37, J=10
1	856	0.5064[*]	0.4804[*]	0.4859[*]	0.7000[*]
2	996	0.5539	0.4997	0.5421	0.5400
3	1,145	0.5473	0.4607	0.5212	0.4700

Note that for the first mode, these values (marked with [*]) have a higher level of uncertainty because the average temperature is at the lowest end of the operating range for the pyrometer used, which is only valid, per manufacturer specifications at a minimum of 930°C. Therefore, these data will be neglected. Accordingly, the emissivity for the first steady state mode was based on the data from the infrared imager data. This data indicated an average surface temperature, T_{avg}, of 856°C. This was substituted into the following equation:

$$\varepsilon = \frac{P_{rad}}{\sigma\left(T_{avg}^4 - T_0^4\right)S} \qquad\qquad (2-38)$$
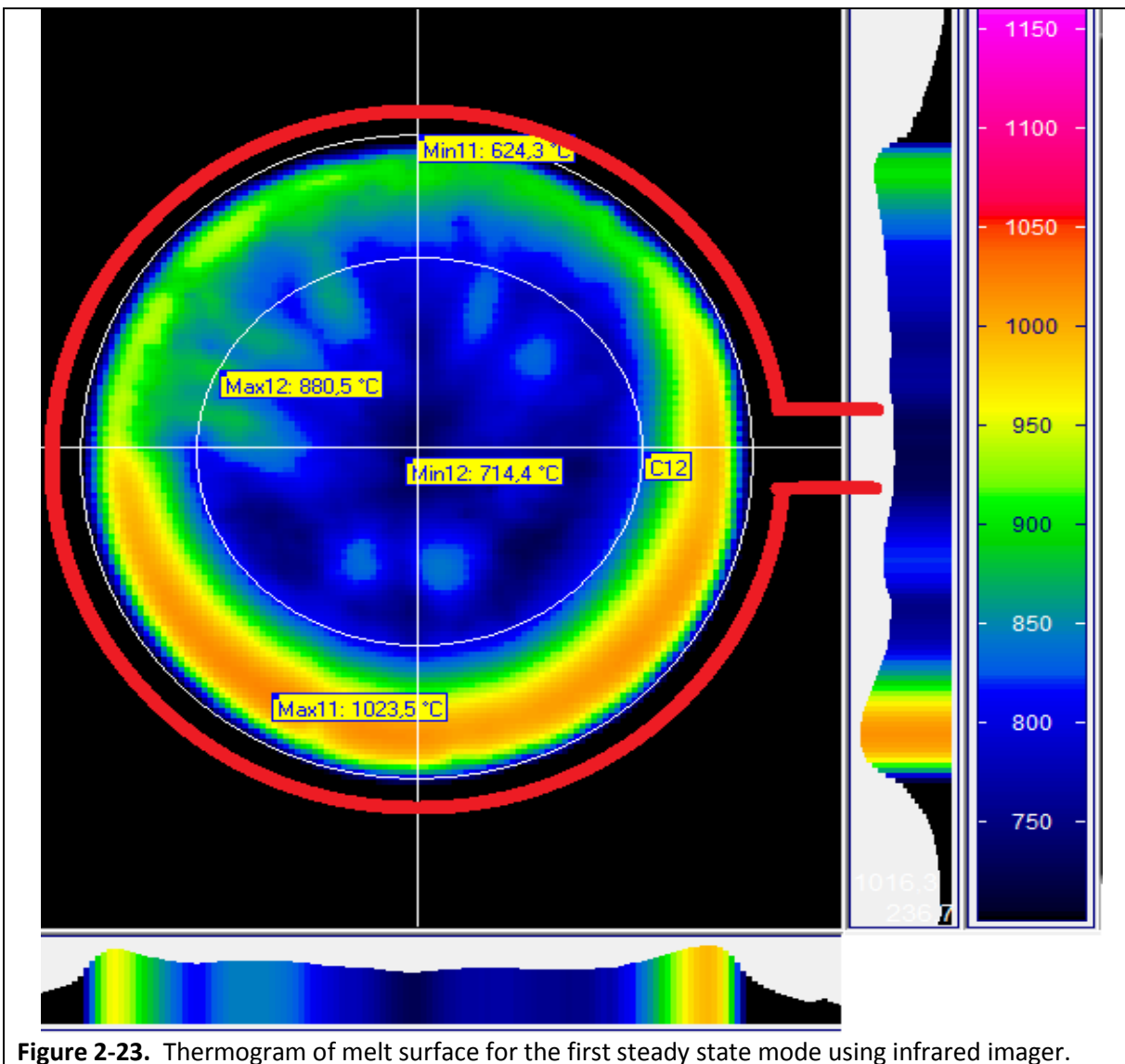
Figure 2-23. Thermogram of melt surface for the first steady state mode using infrared imager.
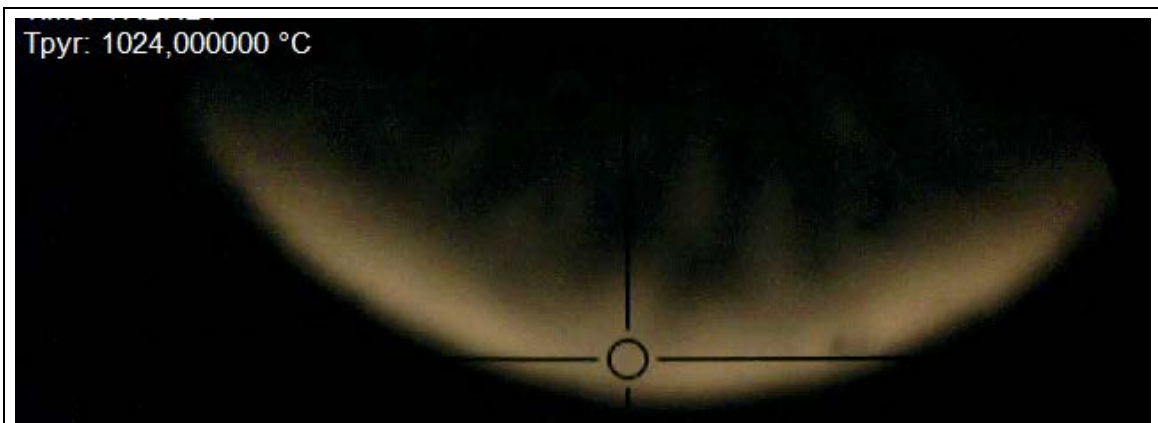
Figure 2-24. Image of melt surface as seen from the pyrometer camera with crosshair target.

This calculation results in an emissivity value of 0.635, at 856°C, which is considered more accurate, and is consistent with the trend that the emissivity is higher at lower temperatures. This may be because, at lower temperatures, the melt viscosity is higher, making the surface smoother.
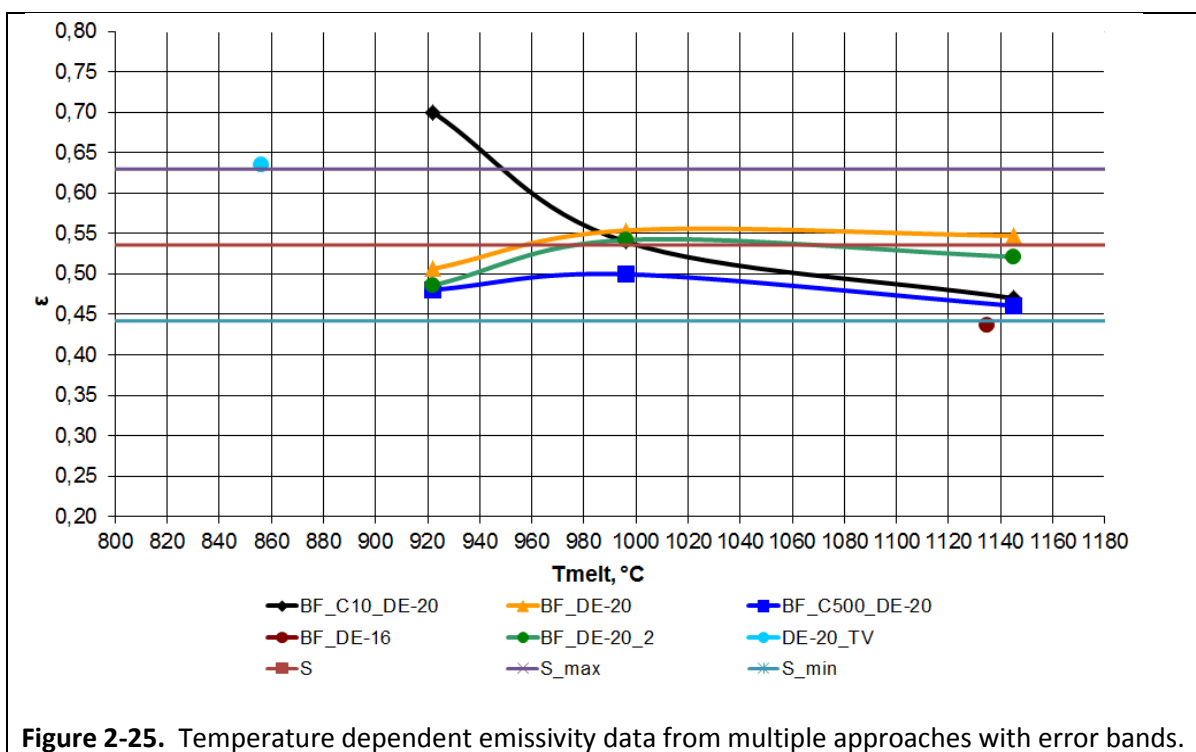
Figure 2-25. Temperature dependent emissivity data from multiple approaches with error bands.

Due to the increased surface tension effects, the effective surface area from which to emit energy may be less. However, this is just an assumption and no efforts were made to verify this. The cumulative results of the calculations resulted in the data presented in Figure 2-25.

Error bands are included because the measurement errors from calorimetry, pyrometry, polynomial approximation, and measurement position sum to between 15% and 20%. Taking this into account, the data from the infrared imager for all modes, and the results from equation 2-35, for the second and third modes, were assumed to be most representative. These data, when combined, result in the temperature dependent emissivity relationship presented in Figure 2-26, which was incorporated into the model.
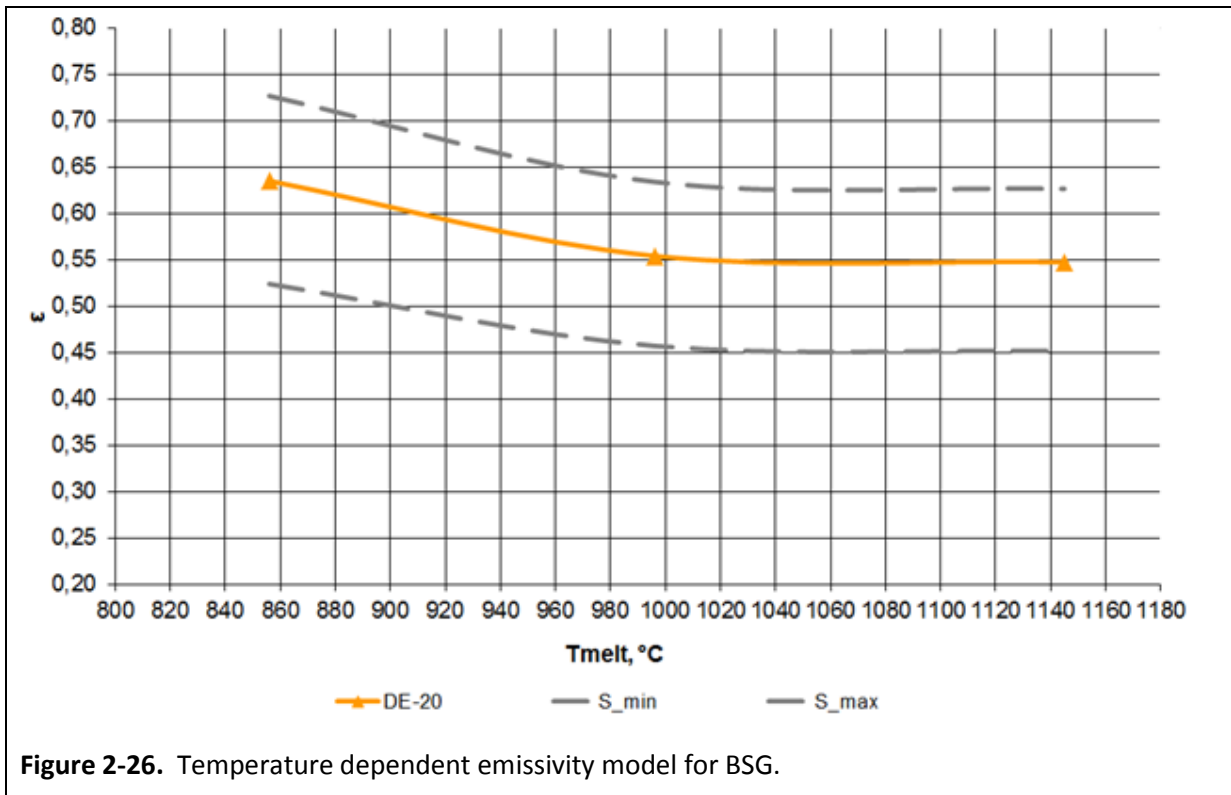
Figure 2-26. Temperature dependent emissivity model for BSG.

2.2.5. Inductor Electrical Efficiency

Another key parameter needed to correlate modeling with equipment/sensor readings and experimental results is the electrical efficiency of the generator, and more specifically of the

inductor. In other words, this parameter will help determine how much of the energy applied to the inductor is available to the melt. The electrical losses in the various components of the system that are within the influenced area of the induction field must be known to determine this. As a starting point, the electrical efficiency of the inductor, η_e, for this specific system can be determined by the following equation:

$$\eta_e = \frac{P_2}{P_2 + (P_{ind.e} + P_{cc.e} + P_{cov.e} + P_{bot.e})} \times 100\%$$ (2 − 39)

where:

P$_2$ is total electrical power on the inductor, kW

P$_{ind.e}$ is electrical losses in the inductor, kW

P$_{cc.e}$ is electrical losses in the cold crucible, kW

P$_{cov.e}$ is electrical losses in the crucible cover, kW

P$_{bot.e}$ is electrical losses in the crucible bottom, kW.

However, when compared to the cold crucible, the electrical losses in the other components will be very small. Accordingly, as a first estimation, the electrical efficiency can be calculated using the following simplified equation:

$$\eta_e = \frac{P_2}{P_2 + P_{cc.e}} \times 100\%$$ (2 − 40)

The technique used to determine P$_{cc.e}$ was to install a separate water-cooled section in the crucible assembly that was geometrically similar to the other sections in the crucible. The tube was electrically and thermally isolated from the other sections. See Figure 2-27.

Figure 2-27. Separate water-cooled section to determine inductor electrical efficiency.
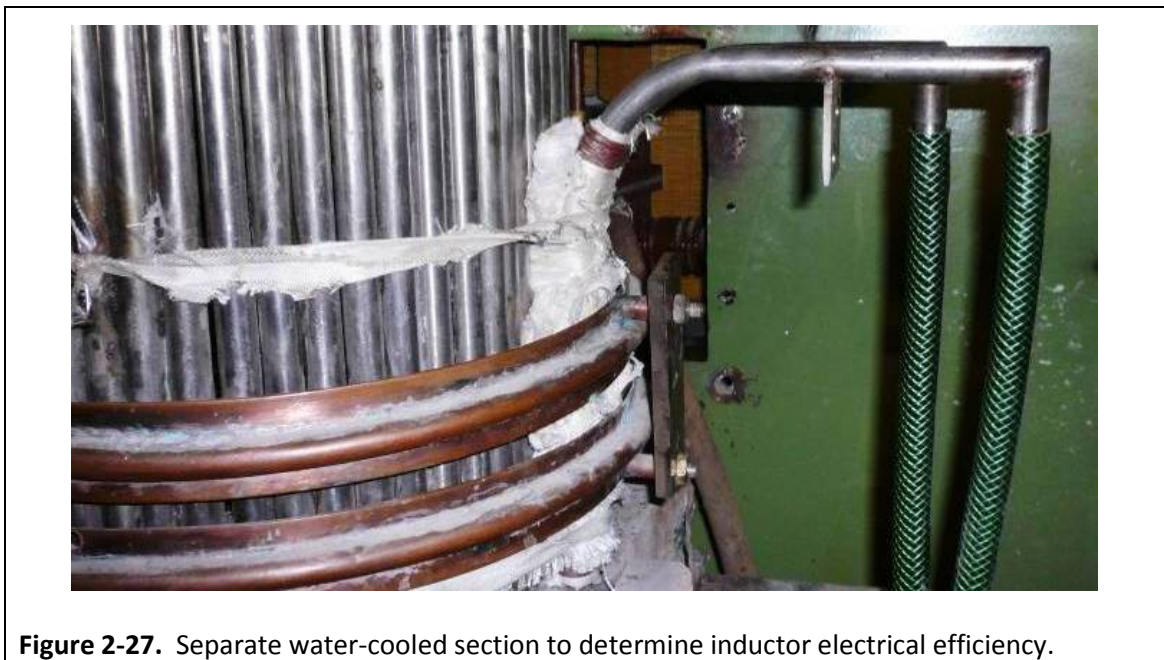
Calorimetry was taken during an experiment to determine the power losses in the individual section. This value was then multiplied by the number of sections in the crucible assembly to

determine the total electrical losses in the crucible, $P_{cc.e}$. The test setup used a two-turn 100 mm high inductor on a 300 mm diameter stainless steel crucible. Table 2-9 shows the data obtained for several operational conditions. Figures 2-28 and 2-29 compare the inductor electrical efficiency to thermal losses of the system and generator operational parameters, respectively, at several operational modes.

Subsequently, the electrical losses in the bottom, $P_{bot.e}$, and cover lid, $P_{cov.e}$, were estimated to improve the accuracy for determining the inductor electrical efficiency. This was accomplished by powering on the generator with no melt in the crucible, such that no heat sources influence the calorimetry data. Measurements indicated that the cover absorbed about 430 watts and the bottom absorbed about 450 watts, for this specific test configuration.

Table 2-9. Melting parameters and electrical efficiency for two-turn inductor.

Time, hh:mm	$P_{cc\,e}$, kW	P_{cc}, kW	U_{cb}, kV	U_a, kV	I_a, A	I_g, A	P_2, kW	η_e, %
12:57	8.56	31.66	2.62	7.63	5.41	1.24	23.10	72.96
13:02	8.71	32.18	2.61	7.63	5.42	1.24	23.47	72.92
13:10	7.91	27.96	2.27	6.68	4.72	1.09	20.04	71.68
13:27	7.46	23.68	2.15	6.27	4.22	1.05	16.22	68.49
13:43	7.19	20.23	2.02	5.89	3.70	1.01	13.04	64.42
13:47	6.43	19.29	2.04	5.84	3.62	1.03	12.85	66.62
13:55	6.81	15.39	1.90	5.68	2.67	0.97	8.57	55.69
14:03	8.03	17.64	2.56	7.05	4.26	1.30	9.61	54.48
14:06	8.41	19.44	2.36	6.64	4.17	1.20	11.03	56.74

(P_{cc} is total thermal and electrical loss in crucible, U_{cb} is voltage on capacitor bank, U_a is anode voltage, I_a is anode current, I_g is grid current)

These values can now be included in equation 2-39 as constants to result in the following equation for determining η_e:

$$\eta_e = \frac{P_2}{P_2 + (P_{ind\,e} + P_{cc\,e} + 0.43 + 0.45)} \times 100\% \qquad (2-41)$$

A second test was then conducted using a three-turn, 200 mm high inductor, in the 300 mm diameter stainless steel crucible. Figure 2-30 compares the inductor efficiency to the melt parameters during the second test with the three-turn inductor coil.
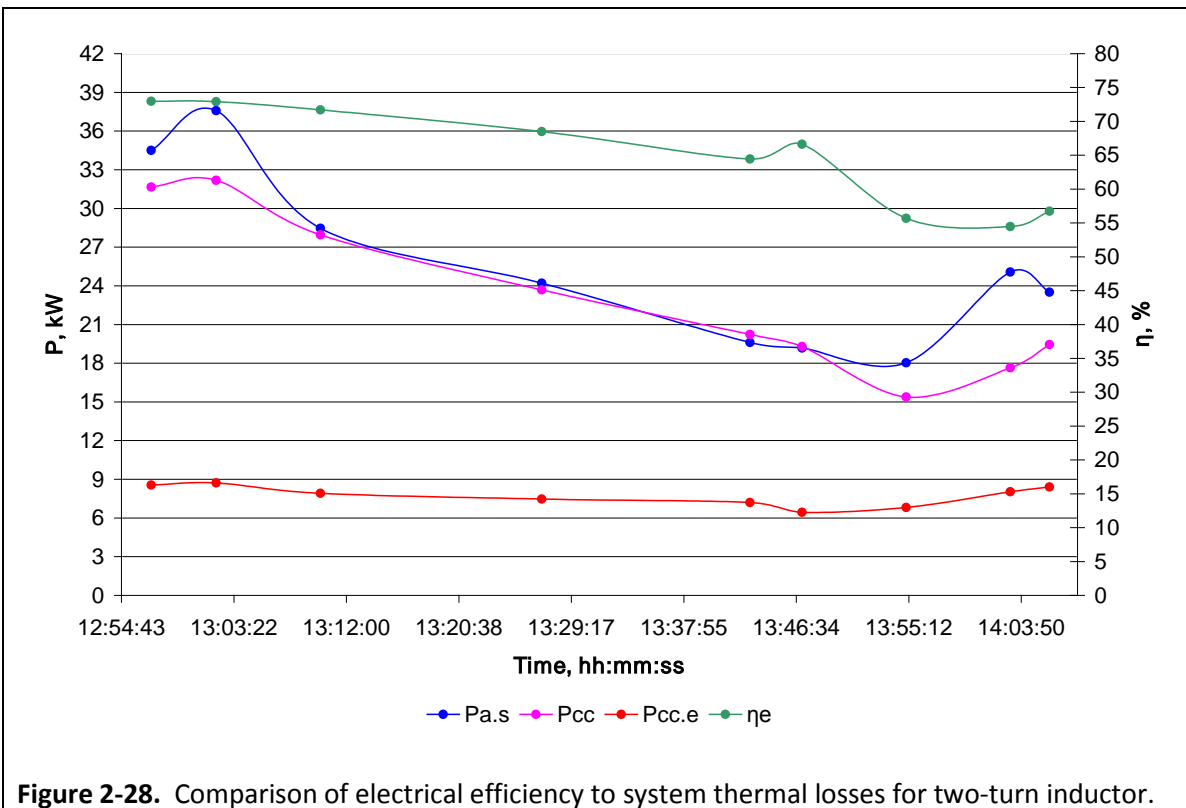
Figure 2-28. Comparison of electrical efficiency to system thermal losses for two-turn inductor.

($P_{a.s}$ is total power determined by sensors, P_{cc} is total thermal and electrical loss in crucible, $P_{cc.e}$ is electrical loss in crucible)
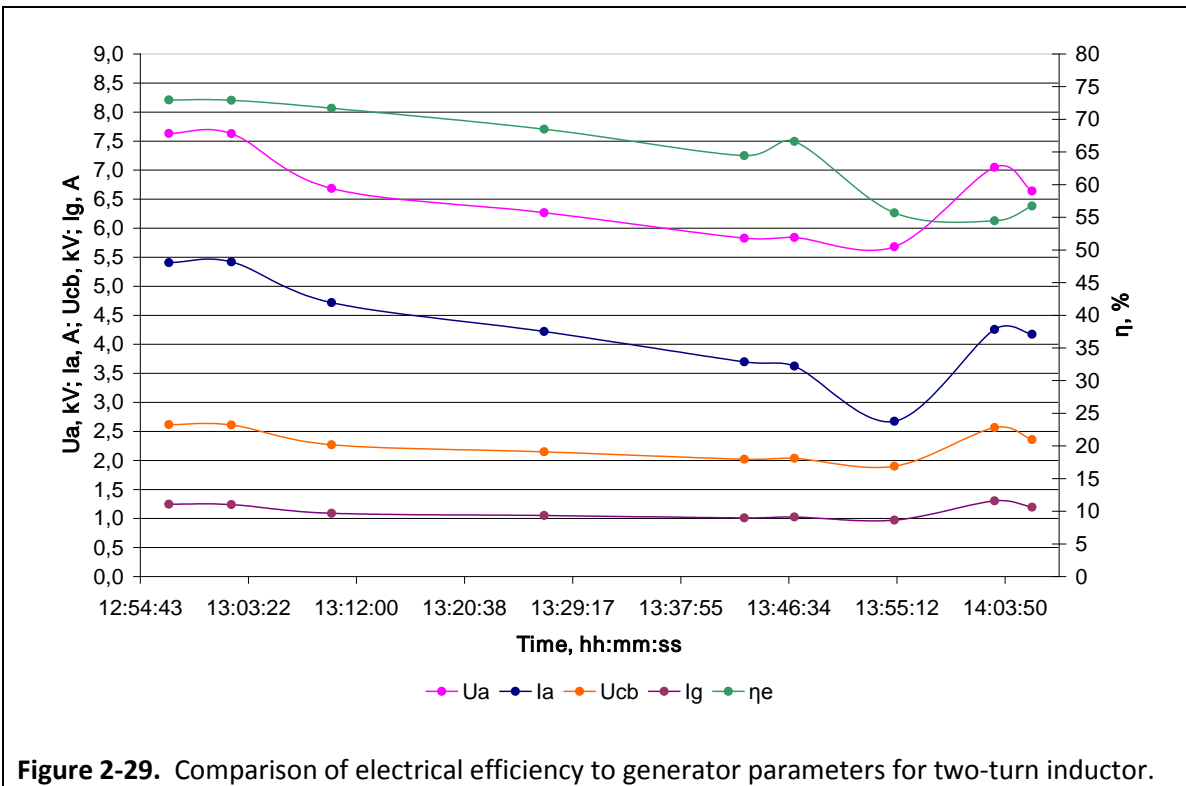
Figure 2-29. Comparison of electrical efficiency to generator parameters for two-turn inductor.

(U_a is anode voltage, I_a is anode current, U_{cb} is capacitor bank voltage,)
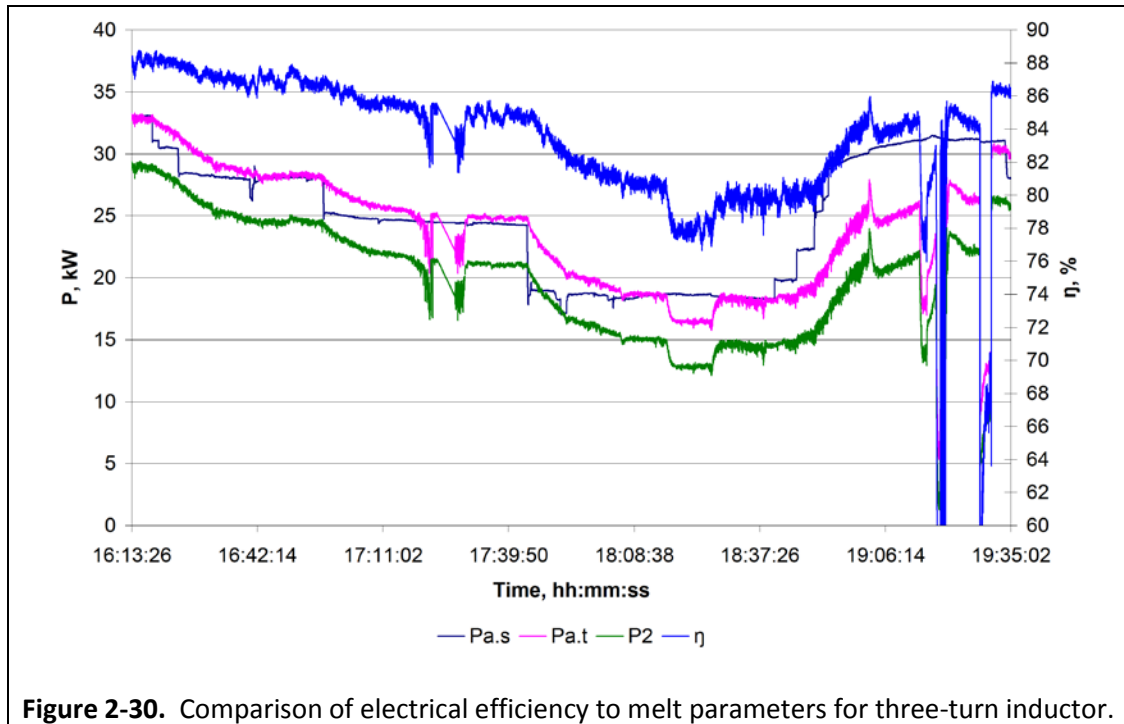
Figure 2-30. Comparison of electrical efficiency to melt parameters for three-turn inductor.
($P_{a.s}$ is total power determined by sensors, $P_{a.t}$ is total power determined by calorimetry, P_2 is total electrical power on inductor)

Table 2-10 provides a summary of heat balance data and efficiencies for several operational modes. Notes that define the variables and other factors in determining the results are included after the table.

Table 2-10. Heat balance data and inductor efficiencies for several modes with three-turn inductor.

Mode #	T_{surf}, °C	T_{melt}, °C	$P_{a.t}$, kW	$P_{a.s}$, kW	P_{cc}, kW	$P_{cc.e}$, kW	P_{cov}, kW	$P_{cov.e}$, kW	P_{bot}, kW	$P_{bot.e}$, kW	$P_{ind.e}$, kW	P_e, kW
1	1,450	1,741	32.8	32.9	25.08	3.04	2.83	0.43	0.5	0.45	0.30	28.88
2	1,193	1,605	28.4	28.3	21.27	2.85	2.37	0.43	0.5	0.45	0.26	24.67
3	1,165	1,583	24.5	24.4	18.22	2.9	2.04	0.43	0.3	0.45	0.24	20.74
4	1,089	1,376	18.2	18.4	12.51	2.8	1.52	0.43	0.3	0.45	0.20	14.52
5*	1,052	-	25.8	31.1	18.75	3.04	2.67	0.43	0.4	0.45	0.21	21.90
6**	1,138	-	26.4	31.1	17.63	3.11	4.07	0.43	0.4	0.45	0.22	22.41

Table 2-10. Heat balance data and inductor efficiencies for several modes with three-turn inductor. (continued)

Mode #	T_{surf}, °C	T_{melt}, °C	η_e, %	$P_{rad.cc}$, kW	$P_{rad.cov}$, kW	$P_{int.rad}$, kW	P_{side}, kW	$P_{0\,side}$, W/cm^2	$P_{0\,bot}$, W/cm^2	$P_{0\,cov}$, W/cm^2	$P_{0\,rad}$, W/cm^2
1	1,450	1,741	87.25	5.43	2.83	8.26	19.65	10.25	0.75	4.01	11.69
2	1,193	1,605	86.08	4.54	2.37	6.91	16.73	8.72	0.64	3.35	9.78
3	1,165	1,583	83.76	3.91	2.04	5.95	14.31	7.46	0.48	2.89	8.42
4	1,089	1,376	78.91	2.91	1.52	4.43	9.60	5.00	0.35	2.15	6.27
5*	1,052	-	84.13	5.12	2.67	7.79	13.63	7.11	0.50	3.78	11.02
6**	1,138	-	84.18	7.80	4.07	11.87	9.83	5.12	0.50	5.76	16.80

NOTES:

1. For calculations, total melt pool height is the sum of melt depth plus bottom skull, and for all modes is equal to 220 mm. The actual melt depth is 175 mm.

2. Electrical losses in the cover and the bottom are assumed constants at 430 W and 450 W, respectively.

3. The view factor for radiation heat flux from the melt pool surface onto the crucible cover is 0.343, and onto the interior crucible walls is 0.657.

4. Total heat losses are used to determine specific heat fluxes in the components of the system.

5. *is mode prior to addition of frit on melt pool surface, **is mode immediately after addition of frit. During this time of the experiment, one of the cooling water flowmeters appeared to not be operating properly, so these data are suspect and thus shown in red.

6. T_{surf} is the melt pool surface temperature determined using a spectral pyrometer located at the same position for each mode.

7. Bottom and cover areas are based on 300 mm exposed diameter, or 706.5 cm^2.

8. Crucible wall interior area is based on 220 mm total melt pool height, or 1918.2 cm^2.

9. $P_{rad.cc}$ is radiation on crucible walls.

10. $P_{rad.cov}$ is radiation on the cover.

11. $P_{int.rad}$ is radiation from the melt surface (crucible walls plus cover).

12. $P_{0\,rad}$ is specific heat flux from the melt pool surface.

13. $P_{0\,bot}$ is specific heat flux from the melt to the crucible bottom.

14. $P_{0\,side}$ is specific heat flux from the melt to the crucible walls.

15. T_{melt} is melt temperature measured by an immersed thermocouple, 38 mm deep at 75 mm from the inside wall.

These measurements provided data that were important in determining power requirements, and thus the limits of the capabilities of the existing equipment. Additionally, the results were used in the model for boundary conditions and constraints in various analyses and optimization studies.

CHAPTER 3.   MODEL VALIDATION

Once the base model was developed, efforts were made to validate the model. This was critical to the research because the model was used to conduct many parametric studies, the results of which were directly used for geometry details and experimental designs. The validation process involved three primary areas: sensitivity studies of the model parameters, sensitivity studies of the material properties, and direct comparison of modeling results with experimental results.

The base model is considered the single frequency model for steady state modes. The full, integrated model eventually included a start-up module and a dual frequency module, to simulate the casting process. These stages are transient and not readily validated. However, results were used to predict behaviors in the actual system.

3.1. Model Parameter Studies

In the model developed, steady state is achieved when there is no longer any change in the non-stationary condition within the melt. The basis of the calculation is simultaneous solution of the hydrodynamic and energy equations. The energy equation includes an internal energy source, which is a function of how the induction energy is coupling with the glass melt. Because the electrical conductivity is temperature dependent, the internal heat source must be iteratively recalculated after an appropriate number of time steps. Thus, the accuracy of the model results is dependent on three parameters:

- Overall time of calculation (heating) to ensure steady state is reached,
- Length of time step increment for simultaneous solution of energy and hydrodynamic equations,
- Length of time step increment to recalculate the internal heat sources.

Two criteria are used to determine that the solution has converged for the stationary conditions:

- Convergence of each iteration,
- Maintaining a thermal power balance.

Evaluation of convergence in ANSYS® is determined by the following approach:

$$\frac{\text{Results}_{n+1} - \text{Results}_n}{\text{Results}_{n+1}}$$

$$(3-1)$$

An example of a convergence evaluation from ANSYS® is given in the following excerpt:

Convergence Monitor

Iter	VY	VX	VZ	PRES	TEMP
1	3.511E-05	1.196E-05	0.000E+00	3.031E-06	3.552E-04
2	1.728E-04	1.908E-05	0.000E+00	7.052E-04	7.405E-05
3	7.588E-05	2.380E-05	0.000E+00	3.021E-04	1.878E-05
4	5.948E-05	1.742E-05	0.000E+00	8.015E-05	6.717E-06
5	4.703E-05	1.637E-05	0.000E+00	1.418E-05	3.679E-06
6	4.288E-05	1.436E-05	0.000E+00	1.682E-04	2.911E-06
7	3.945E-05	1.329E-05	0.000E+00	3.520E-05	2.447E-06
8	3.693E-05	1.231E-05	0.000E+00	1.027E-05	2.147E-06
9	3.481E-05	1.152E-05	0.000E+00	4.519E-06	1.925E-06
10	3.282E-05	1.081E-05	0.000E+00	3.444E-06	1.750E-06

```
*** LOAD STEP   10      SUBSTEP   10  COMPLETED.
*** CUM ITER =  1000  TIME STEP NUMBER =   100
*** TIME =  10000.0       TIME INC =  100.000
```

Velocity convergence in this example is approximately 3.3×10^{-5}, temperature convergence is about 1.8×10^{-6}, and pressure convergence is about 3.4×10^{-6}.

The power balance of applied heat sources is compared to the heat losses from conduction and radiation. It is determined as follows:

$$PB = \frac{P_{loss} - P_{el}}{P_{loss}} \times 100\ \% \qquad\qquad (3-2)$$

where

$P_{loss} = P_t + P_r$

P_t = negative heat transfer to wall faces

P_r = negative radiation heat transfer from melt surface

P_{el} = total applied energy as volumetric heat sources in the fluid elements.

This analysis was conducted on a total time duration of 10,000 seconds, which, as discussed below, was found to be inadequate. The model was developed to allow maximum flexibility in its application. One feature is the use of a variable (mm) to control the coarseness or fineness of the grid. It functions as a multiplier on the number of divisions in a given length that the default setting of the software provides. To evaluate the effect of the calculation time, a base case using a fine grid (mm = 4) was established with a time step-interval of 100 seconds, and a heat source recalculation

interval of 1000 seconds, with a total calculation time of 30,000 seconds. Deviations from the base case results are calculated in the following manner:

$$D = \frac{T - T_{base}}{T_{base}} \times 100 \%$$

$$(3-3)$$

Model solution results are given in Tables 3-1 and 3-2.

Table 3-1. Effect of total heating time on temperature, convergence, and power balance.

No.	Value	T_{max}		Pressure convergence	Velocity convergence	Power balance %
	Metric	°C	Deviation %			
1	30,000	1413	-	1.08e-06	2.4e-06	- 0.0285
2	20,000	1412	- 0.043	3.4e-06	1.33e-05	- 0.16
3	10,000	1414	0.071	1.26e-05	3.4e-04	- 0.794
4	5,000	1433	1.39	8.68e-03	4.62e-03	16.0

Table 3-2. Effect of total heating time on velocity components and flow function.

No.	Value	Vy				Vx				ψ			
		Vy, (+)		Vy, (-)		Vx, (+)		Vx, (-)		ψ (+)		ψ (-)	
	Metric Time	mm/s	Deviation %	mm/s	Deviation %	mm/s	Deviation %	mm/s	Deviation %	10^{-3} m²/s	Deviation , %	10^{-3} m²/s	Deviation %
1	30,000	0.470	-	-6.086	-	0.821	-	-1.58	-	1.692	-	-2.728	-
2	20,000	0.471	0.21	-6.015	1.17	0.808	-1.6	-1.57	-0.64	1.697	0.3	-2.722	0.09
3	10,000	0.467	-0.64	-4.02	-33.4	0.654	-25.5	-1.302	-21.35	1.758	3.84	-2.450	-11.3
4	5,000	0.509	-7.66	-8.73	43.5	0.308	-66.5	-3.92	40.3	1.878	9.99	-2.009	-35.7

The calculation time was varied between 5,000 and 30,000 seconds. The following definitions are applicable for the data in Tables 3-1 and 3-2, as well as other tables below that present data related to the sensitivity analysis:

- **T_{max}** – maximum temperature.
- **Vx(+), Vx(-)** – maximum value of velocity in positive and negative *x*-axis directions.
- **Vy(+), Vy(-)** – maximum value of velocity in positive and negative *y*-axis directions.
- **Deviation %** - deviation from base value.
- **Ψ** - glass melt flow function (positive is counterclockwise)

Analysis of Tables 3-1 and 3-2 indicates that, while melt temperature convergence can be reached at a process duration of 10,000 *s*, the velocity and flow function deviations are unacceptably high. This

is because the time step used in these calculations was 100 seconds, providing only 100 iterations, which is not adequate.

The number of iterations can be increased directly by reducing the time step, or indirectly by increasing the overall calculation time. In this case the process calculation time was increased to 30,000 *s*. The difference in velocity fields between 30,000 second and 20,000 second process times is only about 2 %. Thus, an overall process calculation time of 20,000 seconds is sufficient to provide accurate results. Similarly, acceptable results can also be obtained using a process duration time of 10,000 seconds and decreasing the time step interval.

However, even with a high number of iterations, if the process calculation time is too short, uncertain results can be obtained. For example, the model was run with a 4,000 second process calculation with 20 second time steps, resulting in 200 iterations. Figure 3-1 and Figure 3-2 show the patterns of temperature and velocity fields for these conditions. As can be seen in these figures, the center of the

Figure 3-1. Temperature field for 4,000 second process time and 20 second time steps.
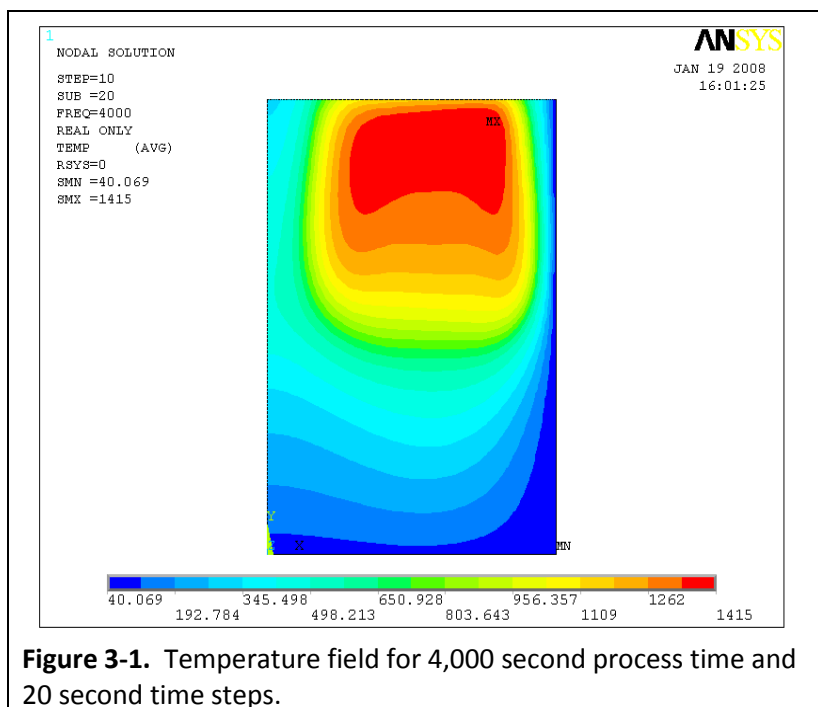
glass melt is not heated, and, as a result, the velocity fields are not representative. This is indicative of the fact that the calculation time was too short. To ensure that the model parameters were optimal for accurate results, as well as minimum processing time, the time step increment effect was also evaluated. Using a base case of 10,000 second process calculation time with a 1000 second interval for heat source recalculation, the time step-interval was varied between 10 seconds and 100 seconds, with a fine mesh (i.e., mm = 4). The calculation results are reported in Table 3-3 and Table 3-4.

As can be seen, high accuracy is achieved when the time step interval is at 25 seconds, which correlates to 400 iterations for this case. However, when the time step-interval is increased to 100

seconds (i.e., 100 iterations), then deviations from the base case of up to 33 % are seen, which is unacceptable.

The time interval for recalculation of the internal heat source was also evaluated. The model was run using 1000 *s*, 250 *s*, and 100 *s* time intervals. The calculation results are given in Tables 3-5 and 3-6. As can be seen from the data reported in Tables 3-5 and 3-6, the 1,000 second recalculation interval for the internal energy sources (i.e., 10-fold recalculation relative to overall process time) is adequate to achieve temperature deviations of less than 1% and velocity deviations of less than 5%from the base case, which is acceptable.

Table 3-3. Effect of time-step interval on temperature, convergence, and power balance.

No.	Value — Metric / Time	T_{max} °C	T_{max} Deviation %	Pressure convergence	Velocity convergence	Power balance %
1	10	1,417	-	9.012e-07	1.79e-06	0.394
2	25	1,414	-0.218	3.8e-07	1.22e-06	0.062
3	100	1,414	-0.218	1.26e-05	3.4e-04	-0.794

Table 3-4. Effect of time step interval on velocity components and flow function.

No.	Value — Metric / Time	Vy Vy, (+) mm/s	Vy, (+) Deviation %	Vy, (-) mm/s	Vy, (-) Deviation %	Vx, (+) mm/s	Vx, (+) Deviation %	Vx, (-) mm/s	Vx, (-) Deviation %	ψ (+) 10^{-3} m²/s	ψ (+) Deviation %	ψ (-) 10^{-3} m²/s	ψ (-) Deviation %
1	10	0.465	-	-6.00	-	0.834	-	-1.579	-	1.681	-	2.672	-
2	25	0.47	1.05	-6.08	1.33	0.833	0.12	-1.573	0.38	1.683	0.12	2.71	2.2
3	100	0.467	0.43	-4.02	33.0	0.654	-21.0	-1.302	-17.0	1.758	4.3	2.45	8.3

Table 3-5. Effect of internal heat source re-calculation interval on temperature, convergence, and power balance.

No.	Value — Metric / Time	T_{max} °C	T_{max} Deviation %	Pressure convergence	Velocity convergence	Power balance %
1	100	1,422	-	7.05e-06	1.57e-05	1.6
2	250	1,422	0	7.05e-06	1.57e-05	1.6
3	1,000	1,420	0.566	1.26e-06	4.49e-06	1.05

Table 3-6. Effect of heat source re-calculation interval on velocity components and flow function.

No.	Value	Vy				Vx				ψ			
		Vy, (+)		Vy, (-)		Vx, (+)		Vx, (-)		ψ (+)		ψ (-)	
	Metric Time	mm/s	Deviation %	mm/s	Deviation %	mm/s	Deviation %	mm/s	Deviation %	10^{-3} m²/s	Deviation %	10^{-3} m²/s	Deviation %
1	100	0.493	-	-5.811	-	0.849	-	-1.57	-	1.653	-	-2.615	-
2	250	0.459	-6.8	-5.863	0.89	0.846	0.35	-1.57	0	1.655	0.12	-2.618	0.11
3	1,000	0.47	-4.87	-6.08	3.77	0.888	3.4	-1.57	0	1.683	2.2	-2.709	3.6

Figure 3-2. Axial (left) and radial velocity (right) fields for 4,000 sec process time and 20 sec time steps.
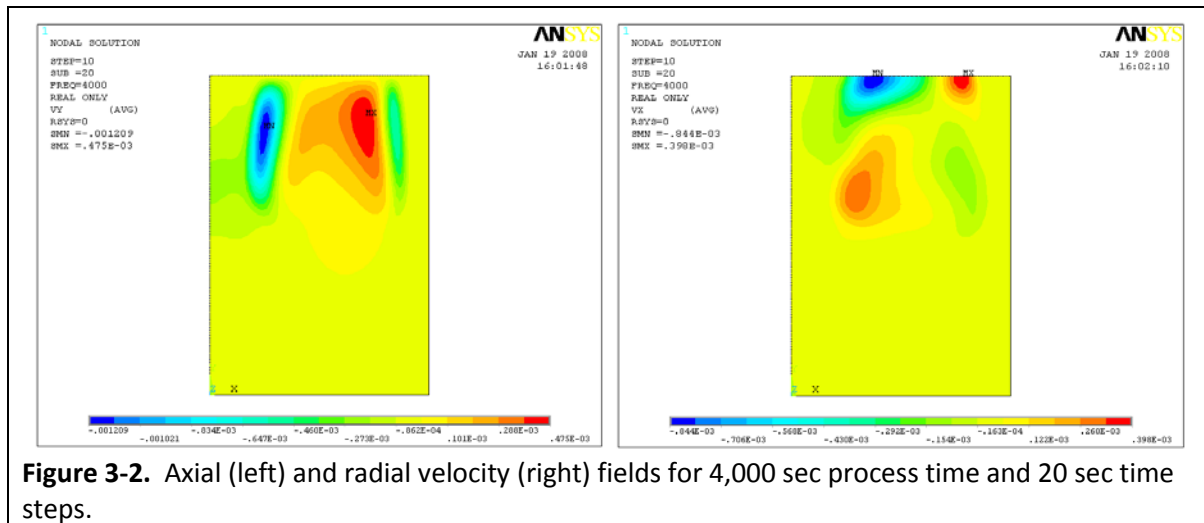
The next model parameter investigated was the effect of grid fineness to determine an optimum (i.e., acceptable results in minimum time). As previously mentioned, the model was developed with a grid impact variable, mm. The number of nodes along each line of the mesh geometry is multiplied by this factor. Thus, a coarse grid results from mm = 0.5., whereas a fine grid results from mm = 4. Figure 3-3 shows the primary areas of the model, the melt volume, the inductor, and the "shield" area. Figure 4 shows the mesh generated at mm = 1. The shield area is used in electromagnetic modeling to set the extent of the field effects. Results of the model were compared for several values of mm. The resulting number of nodes for each is given in Table 3-7.

Table 3-7. Number of mesh nodes for grid impact factors evaluated.

mm	Melt	Inductor	Shield	Total
0.5	600	30	1,062	1,692
1	2,400	60	4,171	6,631
2	9,600	240	15,615	25,455
4	38,400	960	57,814	97,174
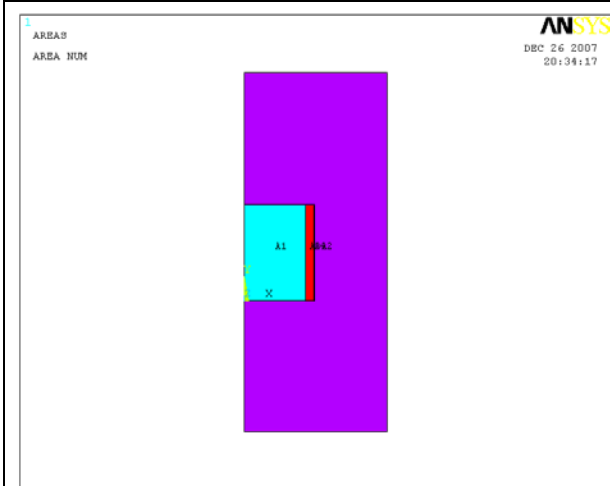
Figure 3-3. Primary design areas of the model.
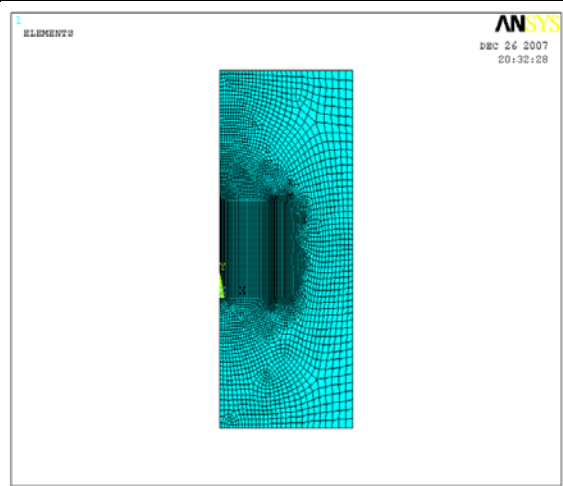
Figure 3.4. Example mesh at mm = 1
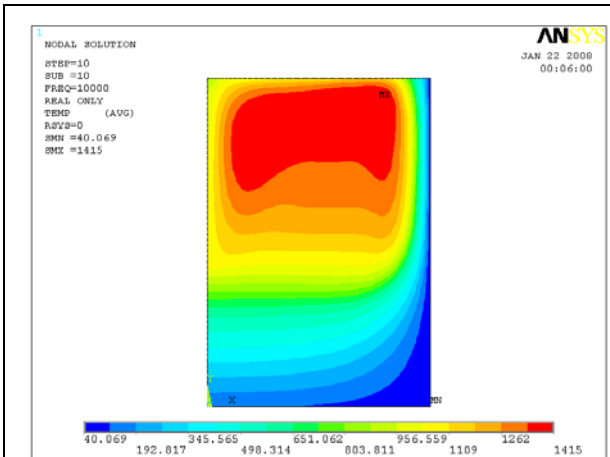
Figure 3-5a. Temperature field.
mm = 1; parameters: 10,000, 1000, 100
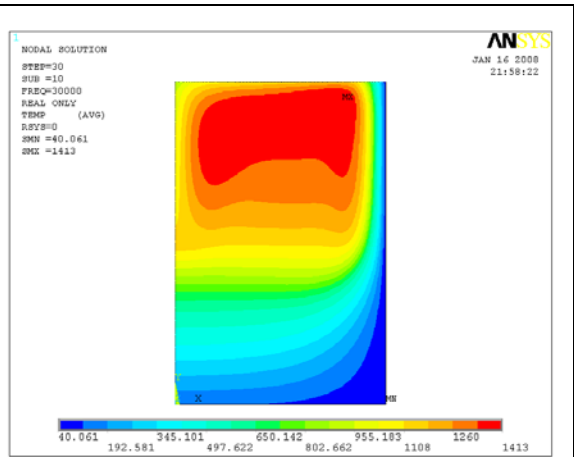
Figure 3-5b. Temperature field.
mm = 4; parameters: 30,000, 1000, 100
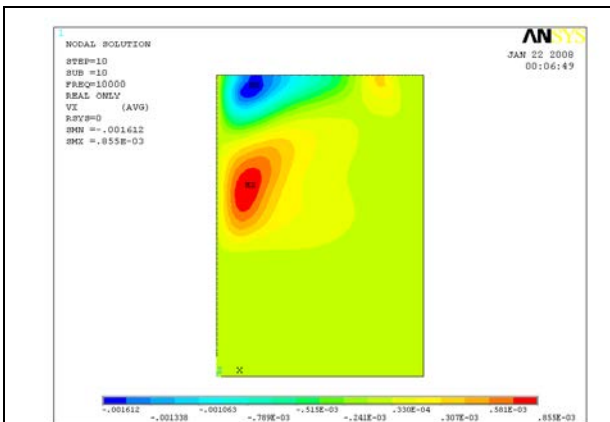
Figure 3-6a. Horizontal velocity field.
mm = 1; parameters: 10,000, 1000, 100
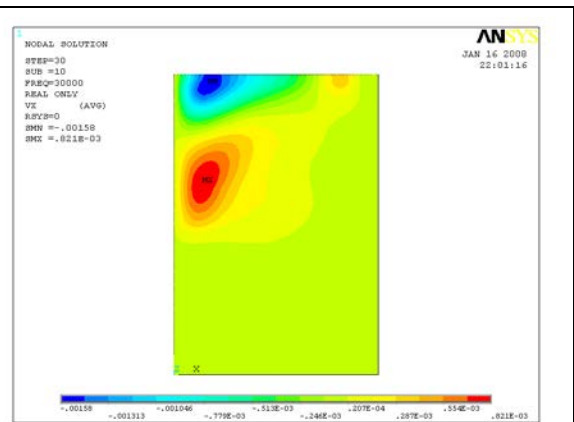
Figure 3-6b. Horizontal velocity field.
mm = 4; parameters: 30,000, 1000, 100

Figure 3-7a. Vertical velocity field.
mm = 1; parameters: 10,000, 1000, 100

Figure 3-7b. Vertical velocity field.
mm = 4; parameters: 30,000, 1000, 100

Figure 3-8a. Flow function (ψ) field.
mm = 1; parameters: 10,000, 1000, 100

Figure 3-8b. Flow function (ψ) field.
mm = 4; parameters: 30,000, 1000, 100
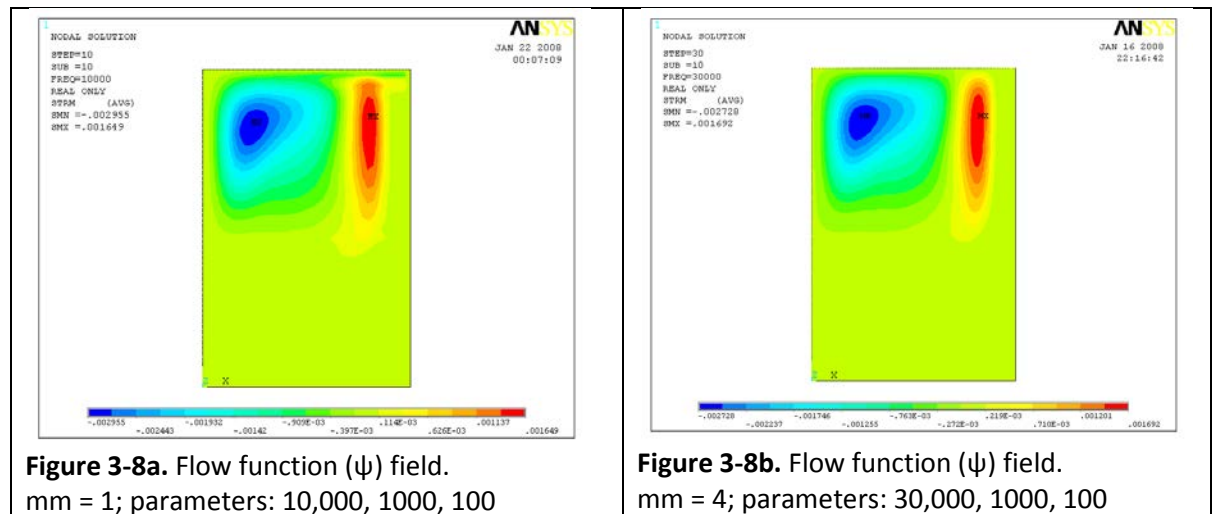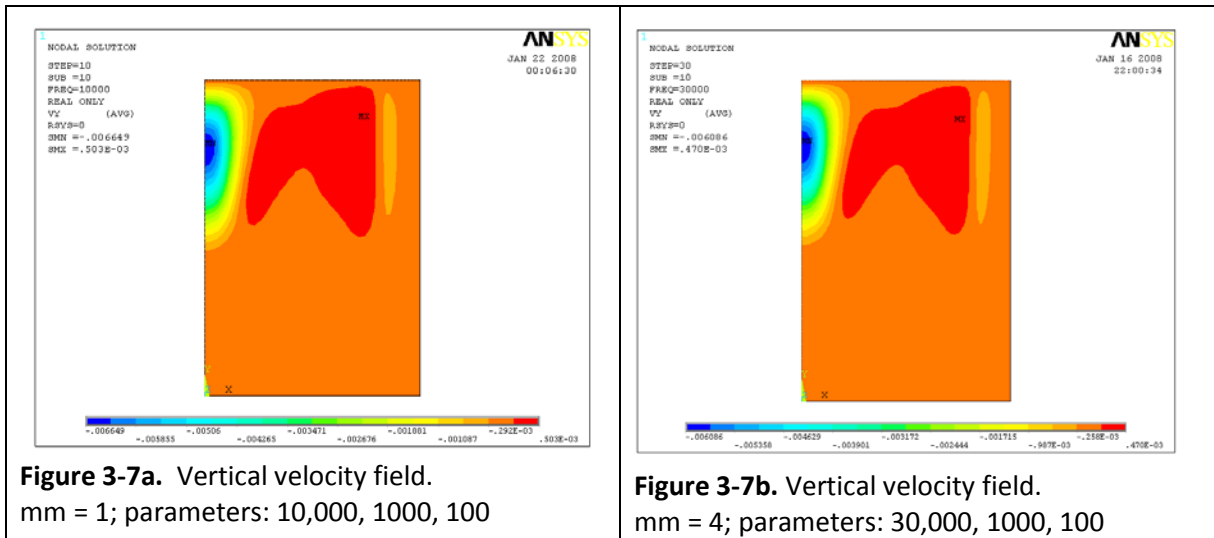
The resulting field distributions are approximately similar for the various grids considered. The results for two versions are shown in Figure 3-5a/b through Figure 3-8a/b for comparison (recall Figure 3-1 for 4,000 second process time). In each case, the left side of the figure corresponds to mm = 1, process duration of 10,000 seconds, heat source recalculation interval of 1000 seconds, and a time step-interval of 100 seconds. The right side corresponds to mm = 4, process duration of 30,000 seconds, heat source recalculation interval of 1000 seconds, and a time step-interval of 100 seconds. The results of calculations conducted for mm = 4, 2, 1, and 0.5 are shown in Table 3-8 and Table 3-9. The model for mm = 4 used a total process duration of 30,000 seconds, while the remaining calculations were performed for a process duration of 10,000 seconds. All other iteration parameters were the same.

Table 3-8. Effect of grid fineness (number of nodes) on temperature, convergence, and power balance.

No.	Value Metric mm	T_max °C	T_max Deviation %	Pressure convergence	Velocity convergence	Power balance %	Process sec
1	4	1,413	-	1.08e-06	2.4e-06	-0.0885	30,000
2	2	1,417	0.283	2.08e-06	2.38e-05	0.68	10,000
3	1	1,415	0.141	3.44e-06	3.2e-05	5.39	10,000
4	0.5	1,367	-3.25	3.44e-06	2.7e-05	32.3	10,000

Table 3-9. Effect of grid fineness (number of nodes) on velocity components and flow function.

No.	Value Metric mm	Vy, (+) mm/s	Vy, (+) Deviation %	Vy, (-) mm/s	Vy, (-) Deviation %	Vx, (+) mm/s	Vx, (+) Deviation %	Vx, (-) mm/s	Vx, (-) Deviation %	ψ (+) 10^{-3} m²/s	ψ (+) Deviation %	ψ (-) 10^{-3} m²/s	ψ (-) Deviation %
1	4	0.47	-	-6.086	-	0.821	-	-1.58	-	1.692	-	-2.728	-
2	2	0.475	1.15	-6.109	7.02	0.816	-0.61	-1.57	-0.633	1.689	0.177	-2.739	0.4
3	1	0.503	6.56	-6.60	8.45	0.855	4.2	-1.612	-6.8	1.649	-2.6	-2.955	7.681
4	0.5	0.768	38.8	-8.39	37.8	0.816	-0.613	-1.581	0.063	1.627	-4.3	-3.134	12.95

Obviously, a finer calculation grid will provide the highest accuracy; however, this then requires a much larger number of iterations to achieve the result, and thus much more processing time. Based on these results, it appears that mm = 2 is a good compromise on process time and accuracy. The data in Table 3-10 and Table 3-11 illustrate the comparative results on convergence and deviation from the base case, demonstrating the quality of the results at mm = 2. For each case, the time step is 100 seconds, and the internal heat source recalculation time is 1,000 seconds. The results are compared to 30,000 second process time with mm = 4, which was demonstrated as the base case.

Table 3-10. Effect of process duration at mm = 2 on temperature, velocity, and power balance.

No.	Value Metric Time	T_max °C	T_max Deviation %	Pressure convergence	Velocity convergence	Power balance %
1	10,000	1,417	0.283	2.08e-06	2.38e-05	0.68
2	5,000	1,404	0.986	5.529e-06	6.77e-03	1.15
3	30,000	1,413	-	1.08e-06	2.4e-06	-0.0885

The results shown in Tables3-10 and 3-11 demonstrate that at mm = 2, a process duration of 10,000 seconds and a time step-interval of 100 seconds, and a heat source recalculation interval of 1000 seconds provides results that give inaccuracies for melt temperature of only 0.283 %, and for melt velocity of only 6.1 %. Thus, most future calculations were conducted using these values for the base

model. However, later ANSYS® versions were on 64-bit platforms and many of the prior calculation time limitations were eliminated, allowing much finer meshes to be used, when needed.

Table 3-11. Effect of process duration at mm = 2 on velocity components and flow function.

No.	Value	Vy				Vx				ψ			
		Vy, (+)		Vy, (-)		Vx, (+)		Vx, (-)		ψ (+)		ψ (-)	
	Metric Time	mm/s	Deviation %	mm/s	Deviation %	mm/s	Deviation %	mm/s	Deviation %	10^{-3} m^2/s	Deviation %	10^{-3} m^2/s	Deviation %
1	10,000	0.475	1.06	-6.109	3.7	0.816	0.61	-15.7	0.63	1.689	0.177	-2.733	0.5
2	5,000	0.549	16.8	-1.368	23.4	0.453	81.3	-0.909	76.8	2.024	31.4	-2.367	27.4
3	30,000 (mm=4)	0.470	-	-6.086	-	0.821	-	-1.58	-	1.692	-	-2.728	-

The final model parameter investigated for its effect on the calculation results was the "shield" area. As mentioned earlier, when conducting electromagnetic field calculations using finite-element approaches, the mesh must be extended to an area for which the vector potential boundary condition to be set to zero. If the border of the shield is located too closely to the inductor, this is a bad assumption, and result in poor calculation accuracy. To ensure that the selected shield geometry, calculations were made and results compared for three cases. The shield areas considered are shown in Figure 3-9a/b/c. The model has been developed with variables that can be changed to readily investigate and compare results. These variables are: Re = screen radius and Ze = screen height. The inductor geometry, which is fixed, is defined as follows: R1n = external radius of inductor, and Z1 = inductor height. For this evaluation, the various ratios investigated included: Re/R1n = 2 and Ze/Z1 = 4; Re/R1n = 3 and Ze/Z1 = 6; and Re/R1n = 1.33; Ze/Z1 = 2.67. In the figure, the "a" geometry (far left) represents the base case, while the "b" and "c" cases represent shield areas that are 1.5 times larger and smaller, respectively, than the base case.

The calculation results are presented in Table 3-12 and Table 3-13. Row #1 in those tables refers to the base case, while rows #2 and #3 refer to the "b" and "c" cases shown in Figure 3-9, respectively.

Figure 3-9a. Shield geometry.
Re = 0.35m
Ze = 0.82m

Figure 3-9b. Shield geometry.
Re = 0.516
Ze = 1.54m

Figure 3-9c. Shield geometry.
Re = 0.23m
Ze = 0.59m
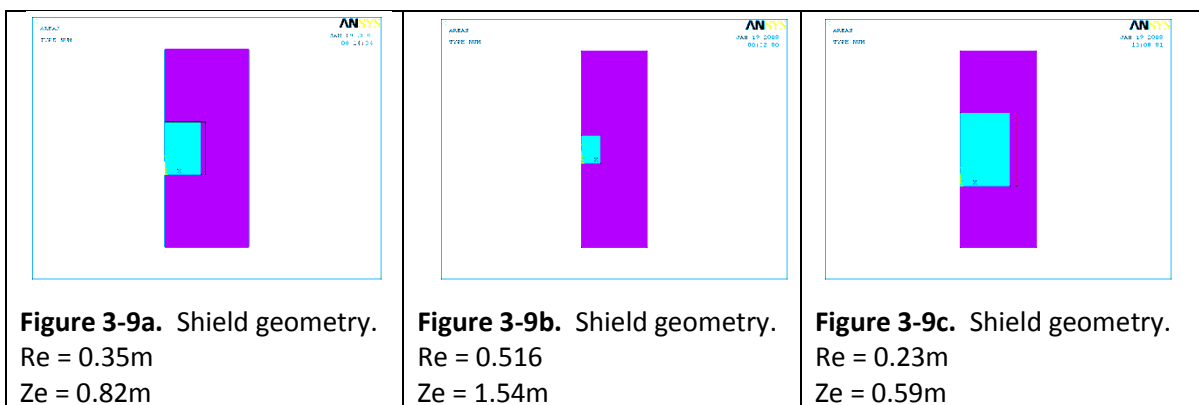
It follows from Tables 3-12 and 3-13 that the effect of the shield area on the calculation results is not significant for the ratios selected. This is primarily due to the method in which the electromagnetic calculation block is designed in that it simulates the electrical conditions at the steady state, stationary condition. That is to say, that during the calculation process, the distribution of heat sources is determined and normalized such that the total power in all of the elements equals the pre-set power level. However, for calculations in which the inductor voltage is set, any decrease in the shield dimensions would have more significant effect on the results.

Table 3-12. Effect of shield area on maximum temperature velocity, and power balance.

No.	R_e/R_{1n} Z_e/Z_1	T_{max} °C	Deviation %	Pressure convergence	Velocity convergence	Power balance %
1	2 / 4	1,417	-	2.08e-06	2.38e-05	0.68
2	3 / 6	1,418	0.0706	1.39e-06	1.973e-05	0.57
3	1.33 / 2.67	1,414	0.212	2.7e-06	2.699e-05	0.83

Table 3-13. Effect of shield area on velocity components and flow function.

Value	Vy				Vx				ψ			
	Vy, (+)		Vy, (-)		Vx, (+)		Vx, (-)		ψ (+)		ψ (-)	
Metric / Case	mm/s	Deviation %	mm/s	Deviation %	mm/s	Deviation %	mm/s	Deviation %	10^3 m^2/s	Deviation %	10^3 m^2/s	Deviation %
1	0.475	-	-6.109	-	0.816	-	-1.370	-	1.689	-	-2.733	-
2	0.467	-1.7	-6.067	-0.68	0.812	-0.49	-1.568	-0.127	1.673	-0.95	-2.70	1.2
3	0.497	3.5	-6.22	1.8	0.829	1.6	-1.524	0.89	1.753	3.7	-2.83	3.5

3.2. Material Property Sensitivity

Once the model parameters were defined that would provide consistent, reliable, and accurate results, with good convergence, the sensitivity of the calculation results to the material properties was investigated. This was important because of the uncertainty in these values, especially at temperatures above 1,200°C. The thermal conductivity, density, specific heat, viscosity, and electrical resistivity were all evaluated. All of the temperature dependent values were varied by ±20%. The electrical resistivity was additionally varied by ± one order of magnitude.

This was accomplished within the ANSYS® code by defining variables that were multiplied by the temperature-dependent model values. All calculations were performed using a process duration

time of 10,000 seconds, a time step interval of 100 seconds, with the internal heat source recalculated each 1,000 seconds, and the grid impact factor set at mm = 2.

3.2.1.Thermal Conductivity

The first property investigated was the thermal conductivity, using a "kc" parameter in the model. Table 3-14 provides comparative results for the values investigated. As can be seen from the data, under-estimation of the thermal conductivity has a greater impact on the results, particularly for the vertical velocity components; however, the effect on the temperature field is minimal. This is expected because, for example, as the thermal conductivity is decreased, the temperature increases and thus the density decreases, producing greater buoyancy forces, resulting in increased Vy. The important observation is that, in general, a 20% change in the thermal conductivity has minimum (i.e. less than 10% for key characteristics) impact on the overall results.

Table 3-14. Comparison of effects of ±20% for thermal conductivity.

Parameter	kc=1.2	Deviation %	kc=1.1	Deviation %	Base kc=1	kc=0.9	Deviation %	kc=0.8	Deviation %
T,°C	1,379	-2.68	1,396	-1.4	**1,417**	1,444	1.9	1,470	5.7
Vx (+) mm/s	0.829	1.59	0.828	1.5	**0.816**	0.788	-3.4	0.791	-3.06
Vx(-) mm/s	-1.561	0.57	-1.568	0.13	**-1.56**	-1.559	-0.7	-1.537	-2.1
Vy (+) mm/s	0.491	3.36	0.482	1.5	**0.475**	0.449	-5.5	0.444	-6.5
Vy (-) mm/s	-5.653	-7.47	-5.894	-3.5	**-6.11**	-6.356	6.9	-6.661	9.02

3.2.2.Specific Heat

The effect of a ±20% change in the specific heat was also evaluated. This was accomplished by introducing the variable "kh" in the model code. These results are shown in Table 3-15. While the variation in specific heat does not change the temperature by much at all, it has significant impact on the velocity field, especially vertical components. This is due to the combined effects of the slight change in temperature, which leads to a change in density, coupled with the effect of that impact on the convection terms in the momentum equation.

However, once again, the overall impact for the temperature distribution is not significant. Also, in the extrapolated range, the predicted specific heat only varies by a total of about 30%, so a 20% error in this range is unlikely. Also note that at ±10%, the total effect results in changes of 8.5% or less for all key parameters.

Table 3-15. Comparison of effects of ±20% for specific heat.

Parameter	kh=1.2	Deviation %	kh=1.1	Deviation %	Base kh=1	kh=0.9	Deviation %	kh=0.8	Deviation %
T,ºC	1408	0.63	1411	-0.21	**1417**	1422	0.35	1429	0.85
Vx (+) mm/s	0.768	-5.8	0.789	-2.1	**0.816**	0.840	2.9	0.873	7.0
Vx(-) mm/s	-1.461	-6.9	-1.513	-3.6	**-1.57**	-1.634	4.1	-1.703	8.5
Vy (+) mm/s	0.404	-14.9	0.437	-8.0	**0.475**	0.521	9.7	0.572	20.4
Vy (-) mm/s	-5.60	-8.03	-5.862	-4.1	**-6.11**	-6.416	5.0	-6.735	10.2

3.2.3.Density

The next property evaluated was the density. Similar to the other properties, a "kd" variable was introduced into the model code as a multiplier. The results of this investigation are provided in Table 3-16.

From these data, similar results can be seen as those for changes in specific heat. Small changes are seen in the temperature; however, more significant effects are observed in velocity components, particularly vertical positive velocities. This is primarily due to the changes in the buoyancy forces again. Although, it should be pointed out that in the extrapolated temperature range, thermal conductivity is almost linear at 2,300 W/m-K, so 20% variations from the predicted values are highly unlikely.

Table 3-16. Comparison of effects of ±20% for density.

Parameter	kd=1.2	Deviation %	kd=1.1	Deviation %	Base kd=1	kd=0.9	Deviation %	kd=0.8	Deviation %
T,ºC	1,397	-1.4	1,405	-0.84	**1,417**	1,430	0.92	1,446	2.0
Vx (+) mm/s	0.852	4.4	0.835	2.3	**0.816**	0.786	-3.7	0.765	-6.2
Vx(-) mm/s	-1.624	3.4	-1.602	2.0	**-1.57**	-1.529	-2.6	-1.471	-6.9
Vy (+) mm/s	0.416	-12.4	0.443	-6.7	**0.475**	0.507	6.7	0.531	11.8
Vy (-) mm/s	-6.223	1.8	-6.204	1.5	**-6.11**	-6.008	-1.7	-5.878	-12.6

3.2.4.Viscosity

The viscosity was also evaluated for ±20% changes. This was accomplished by introduction of the variable "kv" in the ANSYS® code. The results of this investigation are given in Table 3-17.

Table 3-17. Comparison of effects of ±20% for viscosity.

Parameter	kv= 1.2	Deviation %	kv= 1.1	Deviation %	Base kv=1	kv= 0.9	Deviation %	kv= 0.8	Deviation %
T °C	1,431	0.99	1,425	0.564	**1,417**	1,409	-0.56	1,402	-1.05
Vx (+) mm/s	0.726	-11.0	0.767	-6.004	**0.816**	0.872	6.8	0.934	14.5
Vx(-) mm/s	-1.401	-10.8	-1.48	-5.7	**-1.57**	-1.673	6.5	-1.793	14.2
Vy (+) mm/s	0.456	-4.0	0.466	-1.9	**0.475**	0.483	1.6	0.490	3.1
Vy (-) mm/s	-5.456	-10.7	-5.759	-5.7	**-6.11**	-6.516	6.6	-6.978	14.2

These data indicate that, once again, the changes have little impact on temperature, but do have significant effects (i.e. over 14% in some cases) to the velocities. With the temperature range seen in the melt volume, the viscosity can actually vary by two orders of magnitude; however, between 75% and 80% of the melt volume, at steady state, is typically in a temperature range in which the viscosity varies by less than an order of magnitude. In addition, within the extrapolated temperature range, the viscosity slope is virtually flat at about a value of 2 Pa-s. Therefore, investigation of a ±20% range was deemed acceptable.

3.2.5. Electrical Resistivity

Another material property evaluated was the electrical resistivity. This property was investigated for both ±20% and ± one order of magnitude. This is because within approximately 75% to 80% of the melt volume, the temperature range can result in 3 to 4 orders of magnitude difference for the electrical resistivity. However, in the extrapolated temperature range, the behavior is much flatter and varies between about 3 ohm-cm and 2 ohm-cm. As before, this is accomplished by introduction of a variable, "kr" in the model.

The effects of a ±20% change are given in Table 3-18. These results indicate that an increase in the electrical resistivity results an almost 5% difference in the vertical velocity component, while the impact from a decrease in resistivity is almost negligible. For all cases, the temperature changes are insignificant. Overall, these effects for the higher end of the temperature scale are inconsequential.

Next, the impacts to the model results were investigated for order of magnitude changes for the electrical resistivity. This work revealed some interesting results, and also demonstrated the importance of selecting the appropriate oscillation frequency of the generator for efficient operation. Table 3-19 provides the results for the various parameters of interest.

Table 3-18. Comparison of effects of ±20% for electrical resistivity.

Parameter	kv=1.2	Deviation %	kv=1.1	Deviation %	Base kv=1	kv=0.9	Deviation %	kv=0.8	Deviation %
T,ºC	1422	0.35	1419	0.14	**1417**	1413	-0.28	1,409	-0.56
Vx (+) mm/s	0.809	-0.86	0.812	-0.49	**0.816**	0.822	0.73	0.829	1.6
Vx(-) mm/s	-1.564	-0.38	-1.567	-0.19	**-1.57**	-1.575	0.31	-1.581	0.7
Vy (+) mm/s	0.467	-2.3	0.47	-1.05	**0.475**	0.481	1.26	0.488	2.7
Vy (-) mm/s	-6.004	-4.7	-6.072	-0.62	**-6.11**	-6.158	0.78	-6.218	1.7

Table 3-19. Comparison of effects of order-of-magnitude changes for electrical resistivity.

Description	kr = 10	Deviation %	Base kr = 1	kr = 0.1	Deviation %
$T_{melt\,max}$ ºC	1,430	+0.92	**1,417**	1,278	-9.81
Vx(+) mm/s	0.793	-2.82	**0.816**	1.005	+23.16
Vx(-) mm/s	-1.538	-2.04	**-1.57**	-1.455	-7.33
Vy(+) mm/s	0.445	-6.32	**0.475**	0.695	+46.32
Vy(-) mm/s	-5.866	-3.99	**-6.11**	-6.629	+8.49
ψ(+) m^2/s	0.001723	+2.01	**0.001689**	0.001105	-34.58
ψ(-) m^2/s	0.002509	-8.20	**0.002733**	0.004825	+76.55
Volume specific power sources W/m^3	$0.552 \cdot 10^7$	-2.13	**$0.564 \cdot 10^7$**	$1.13 \cdot 10^7$	+100.35

As can be seen from these data, an order of magnitude increase in the electrical resistivity has a small effect on the results, primarily in flow velocities. However, an order of magnitude decrease has significant impacts. This is because a decrease in the electrical resistivity effectively decreases the volume of the melt in which the energy is deposited. This is referred to as the skin depth or skin effect [16], which is described in more detail later. However, from [16], the current density through the melt volume can be estimated as:

$$\mathbf{J_y} = \mathbf{J_0} e^{-y/\delta} e^{jy/\delta} \qquad (3-4)$$

where:

$\mathbf{J_y}$ is current density at distance y from the surface

$\mathbf{J}_0$ is current density at the melt surface (inside crucible wall)

y is distance from surface toward the center

δ is penetration depth.

Thus, at the depth where δ is equal to y, the current density equals $e^{-1}\mathbf{J_0}$, which equals about $0.37\mathbf{J_0}$. The power density at that same location will be then a function of e^{-2}. Additionally, the penetration depth can be defined as:

$$\delta \cong 5030 \sqrt{\frac{\rho_e}{\mu_r \omega}} \qquad\qquad (3-5)$$

where:

ρ_e = 1/σ , which is electrical resistivity (recall σ = electrical conductivity) in ohm-m

μ_r is relative magnetic permeability (which is equal to unity for this glass)

ω is frequency of oscillation in Hertz (Note that in the derivation this is originally the radian frequency, but is converted to the actual cycles per second for ease of use, hence the numeric term preceding the radical.)

The net effect is that, for the case of the model which uses a fixed power source, the volume specific power density is approximately doubled. This causes an overheating condition near the surface, increasing the buoyancy effects, and thus significantly increasing the absolute value of the velocity components and the overall flow function field. Figures 3-10a/b/c through 3-14a/b/c graphically depict the contrasting modeling results from the order of magnitude changes in the electrical resistivity for several key parameters.

While the maximum temperature from this effect is reduced by almost 140°C, the volume of melt in the higher temperature range (i.e. above $1,150^\circ$C) is dramatically increased. The flow function (ψ) serves as a measure of the overall intensity of the hydrodynamic processes. This field is increased by over 76%, in spite of the fact that the viscosity is increased significantly due to the much lower temperature. This is an interesting phenomenon and must be considered when pairing the current

frequency of a generator with a material to be processed. For example, as an exercise, the current

frequency effects were examined to validate the impact.
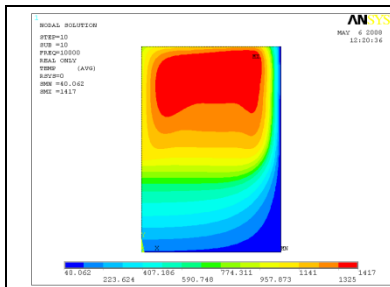
Figure 3-10a. Temperature field for base case.
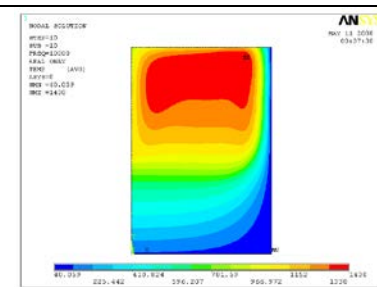
Figure 3-10b. Temperature field for kr = 10.
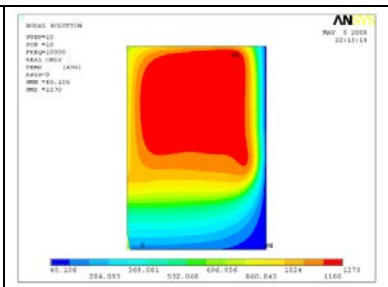
Figure 3-10c. Temperature field for kr = 0.1.
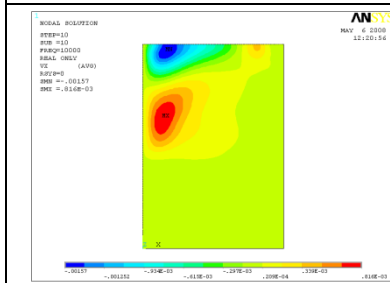
Figure 3-11a. Vx velocity field for base case.
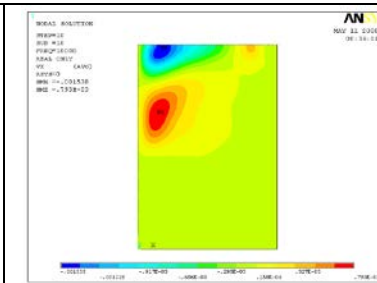
Figure 3-11b. Vx velocity field for kr = 10.
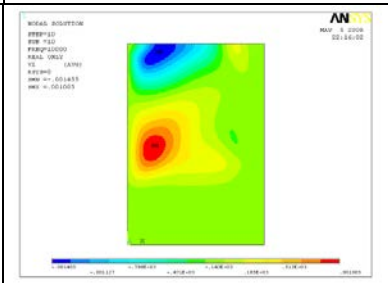
Figure 3-11c. Vx velocity field for kr = 0.1.
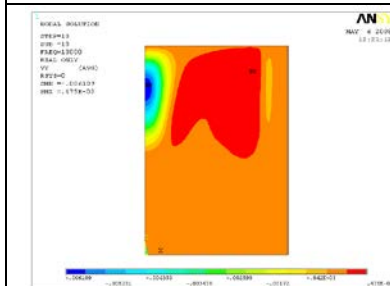
Figure 3-12a. Vy velocity field for base case.
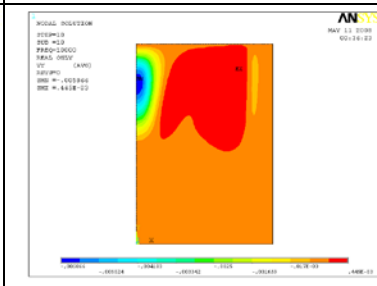
Figure 3-12b. Vy velocity field for kr = 10.
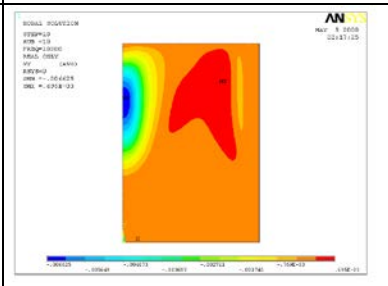
Figure 3-12c. Vy velocity field for kr = 0.1.
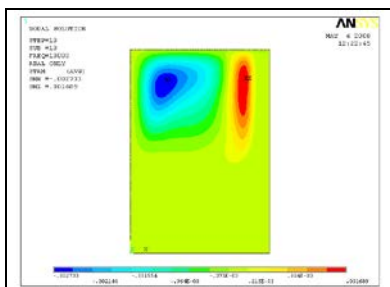
Figure 3-13a. Flow function ψ for base case.
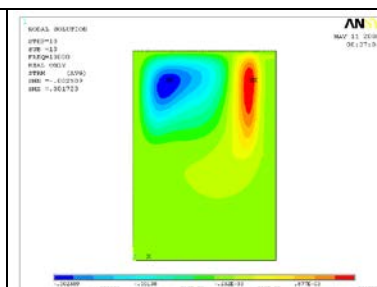
Figure 3-13b. Flow function ψ for kr = 10.
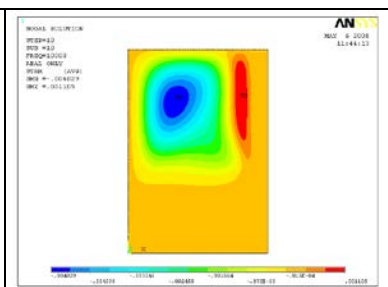
Figure 3-13c. Flow function ψ for kr = 0.1.
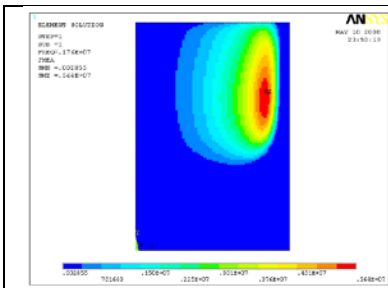
Figure 3-14a. Power sources for base case	**Figure 3-14b.** Power sources for kr = 10	**Figure 3-14c.** Power sources for kr =0.1
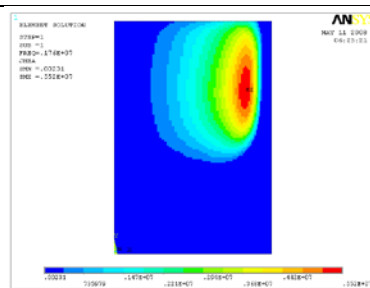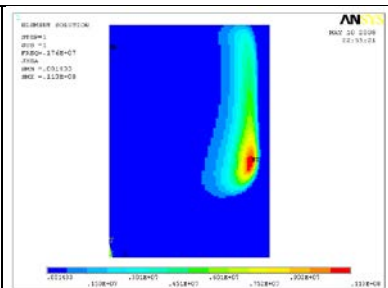
For this research, all of the experimental efforts, and thus the modeling, are conducted using a 1.76 MHz primary high frequency power generator. From equation 3 - 5, decreasing the electrical resistivity, ρ_e, by an order of magnitude should have the same effect as increasing the frequency, ω, by an order of magnitude. Figures 3-15a/b through 3-19a/b clearly demonstrate that the results are virtually identical for these two cases, thus providing an indirect validation of the model.
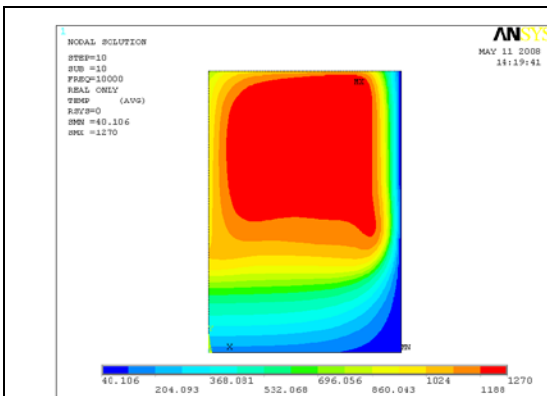
Figure 3-15a. Temperature field for ω = 17.6MHz.	**Figure 3-15b**. Temperature field for kr = 0.1.
Figure 3-16a. Vx velocity field for ω = 17.6MHz.	**Figure 3-16b.** Vx velocity field for kr = 0.1.
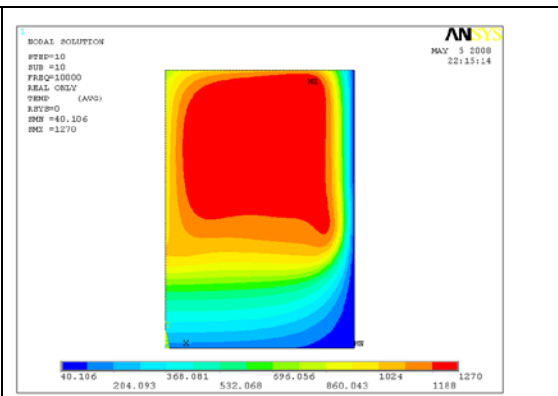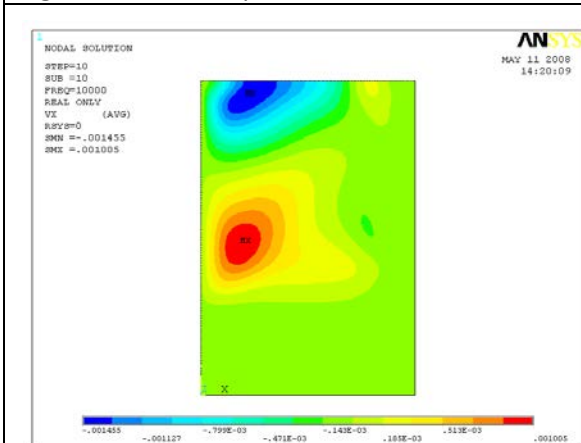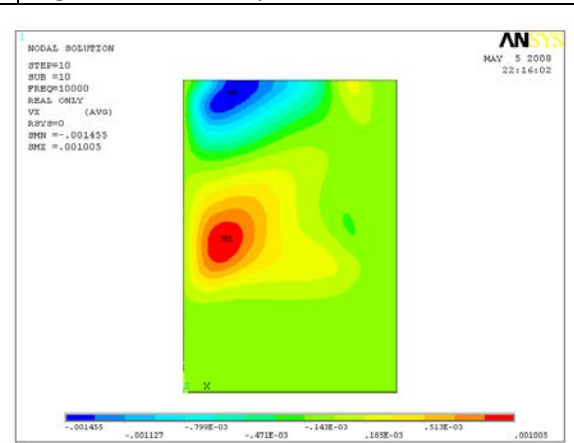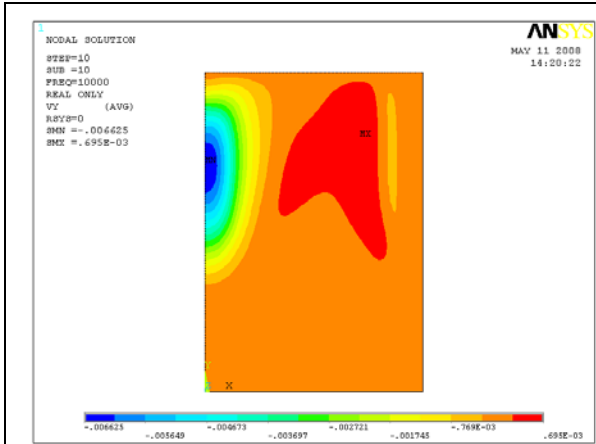
Figure 3-17a. Vy velocity field for ω = 17.6MHz.
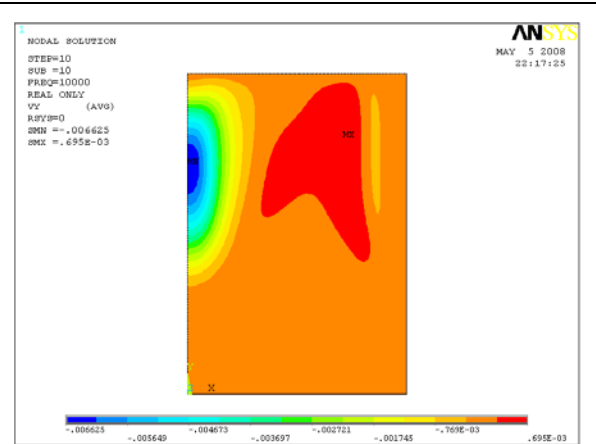
Figure 3-17b. Vy velocity field for kr = 0.1.
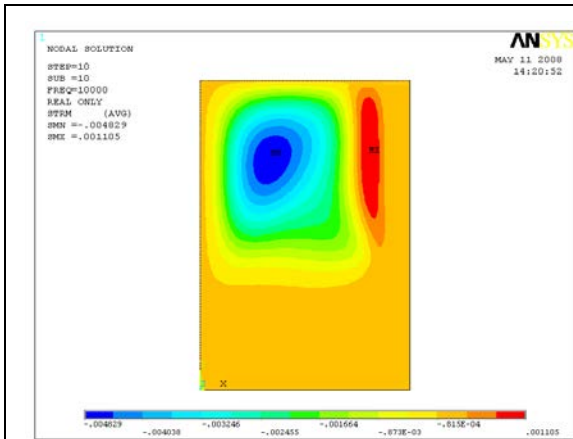
Figure 3-18a. Flow function field for ω = 17.6MHz.
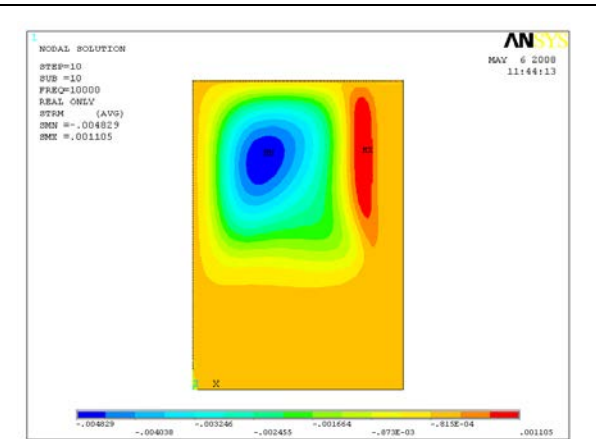
Figure 3-18b. Flow function field for kr = 0.1.
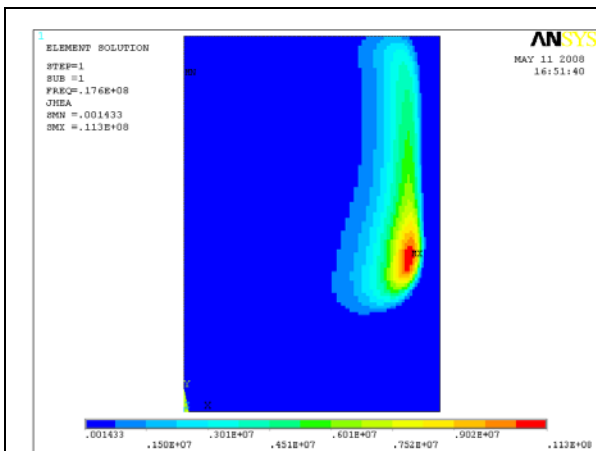
Figure 3-19a. Specific power for ω = 17.6MHz.
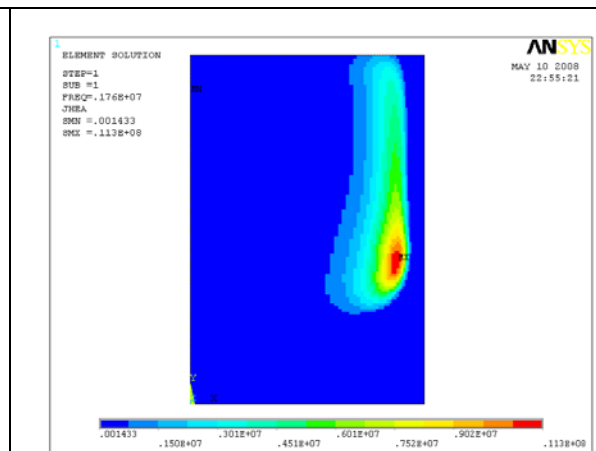
Figure 3-19b. Specific power for kr = 0.1.

3.2.6.Emissivity

The final material property investigated was the emissivity. Initially, the base value accepted for use in the model was a constant of 0.5. However, since some key differences were observed in the measured temperatures near the melt surface versus the model results, this property was investigated. Emissivity values of 0.2 and 0.3 were evaluated to determine the extent of impact to the steady state condition. Lower emissivity values were selected for multiple reasons. First, the model does not provide for reflected radiation back onto the melt surface from the crucible walls, which extend above the melt surface. This heat reflected back onto the surface may have a similar effect as a lower overall emissivity. Second, the temperatures just below or at the surface of the melt, at all locations, routinely measure higher than the model predicts. This is also indicative of a potentially lower effective emissivity. Figures 3-20 through 3-22 compare the results of these investigations. As expected, as the emissivity is reduced the maximum temperature increases, as does the temperature profile near the surface of the glass melt. While the temperature increase is concentrated primarily near the surface (i.e., maximum temperature on the surface increased by over $60^{\circ}C$ – see Figures 3-23 and 3-24), an overall temperature increase, although smaller, is also seen throughout the melt to about mid-depth. This is not consistent with the experimental data. Therefore, significant effort was focused on determining a more accurate, and temperature dependent emissivity value for this glass and melter configuration. This was discussed in detail in Section 2.1.4 (refer back to Figure 2-26). The summary result is that at low surface temperatures around $850^{\circ}C$ to emissivity peaks at about .635 +/- 20%, linearly decreasing to about 0.55 at $1,000^{\circ}C$, and maintaining that value through higher temperatures.

Figure 3-20. Temperature distribution for ε = 0.5.

Figure 3-21. Temperature distribution for ε = 0.3.

Figure 3-22. Temperature distribution for ε = 0.2.

Figure 3-23. Temperature distribution along melt surface for ε = 0.3.

Figure 3-24. Temperature distribution along melt surface for ε = 0.2.
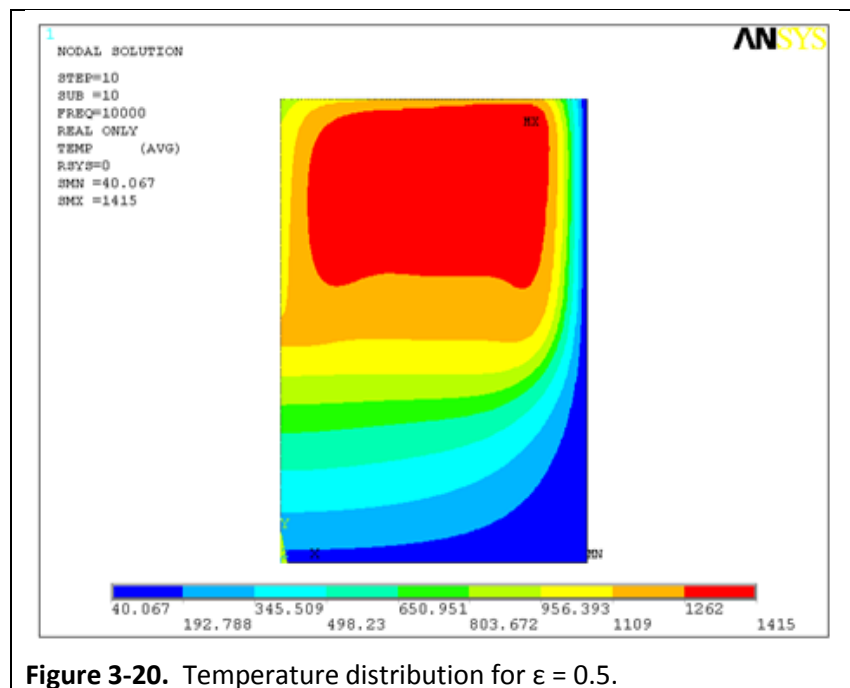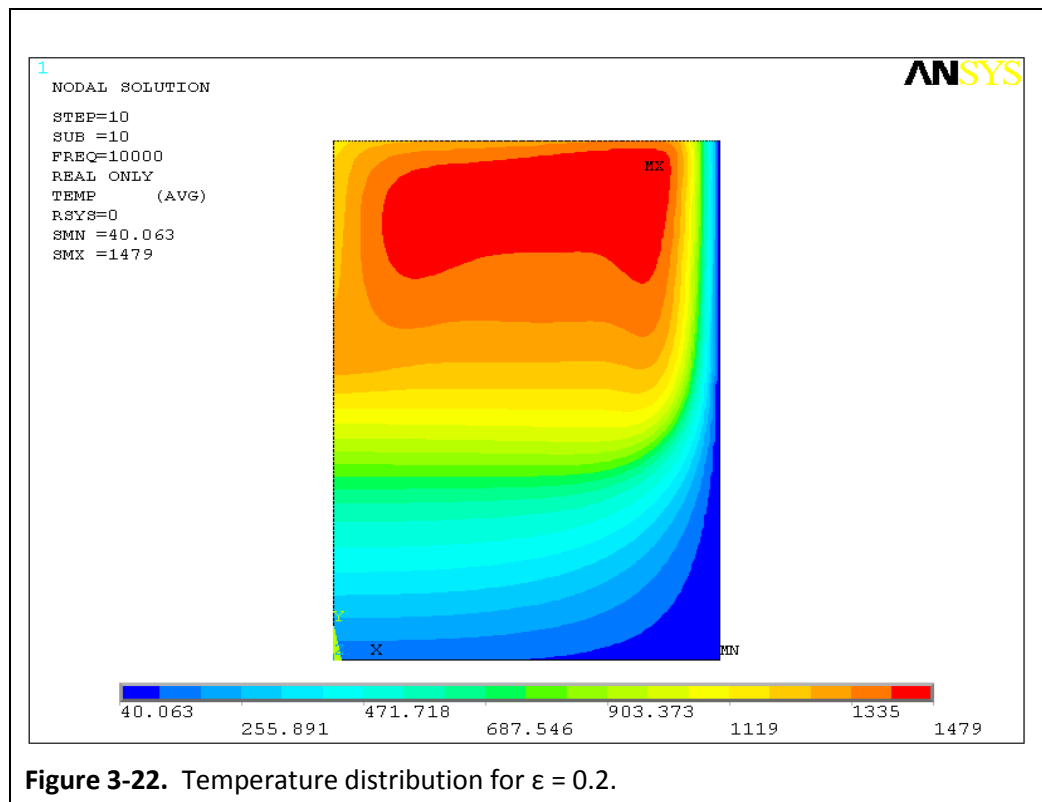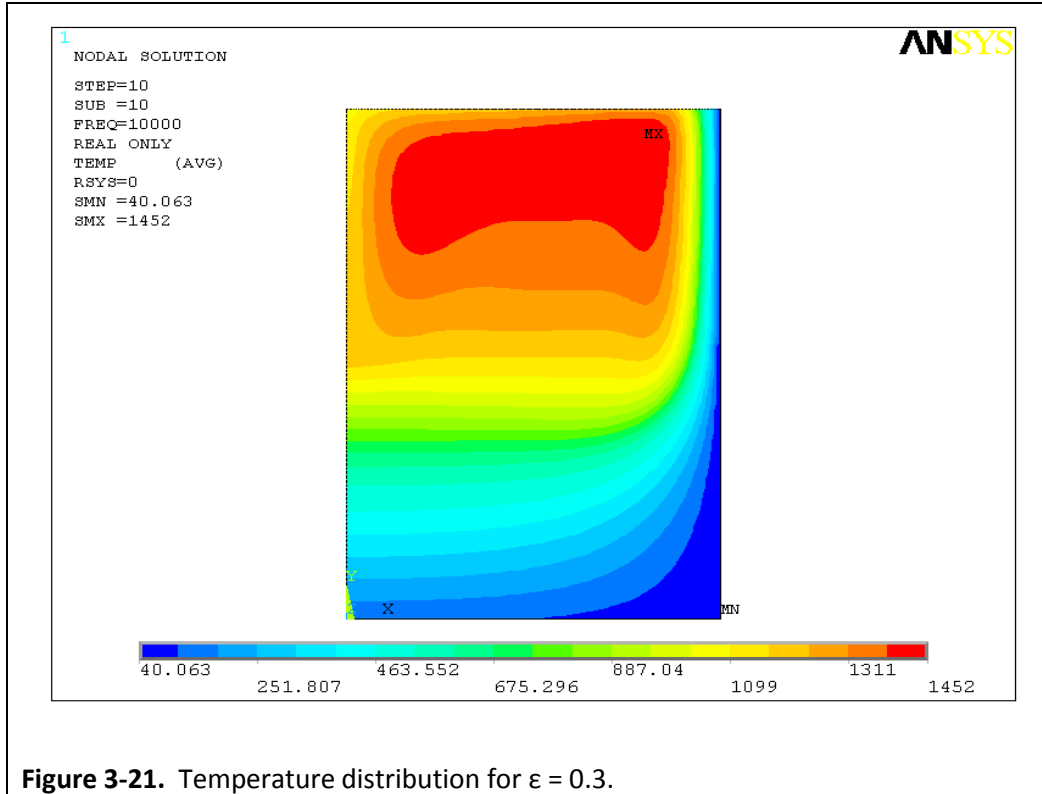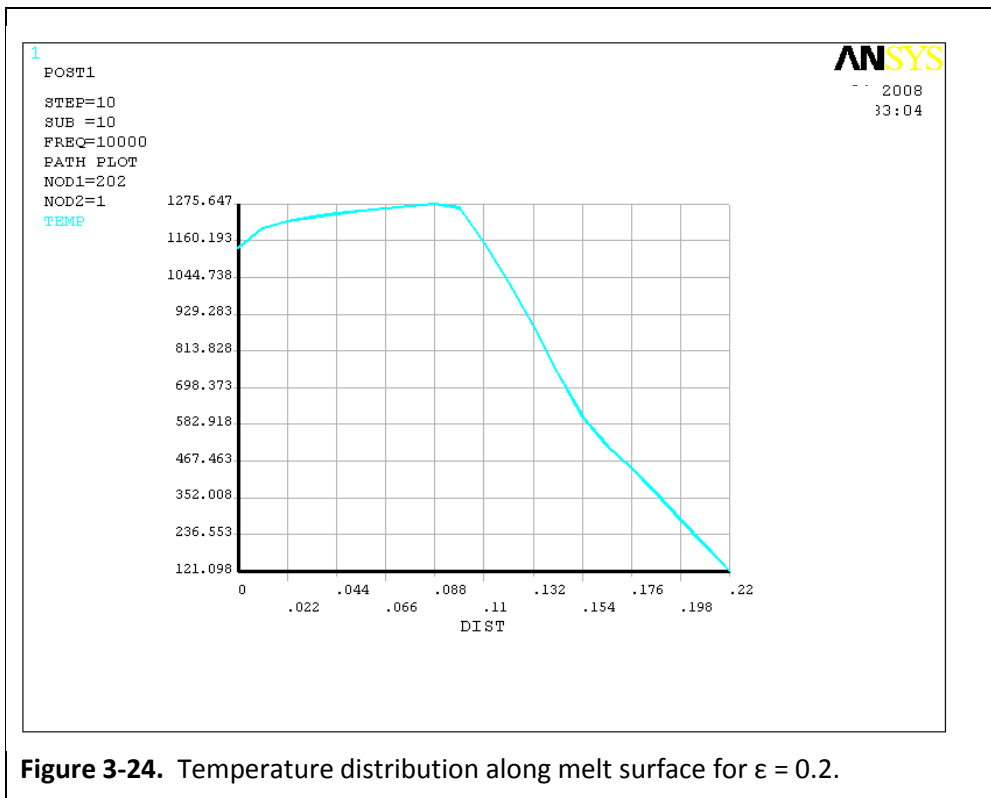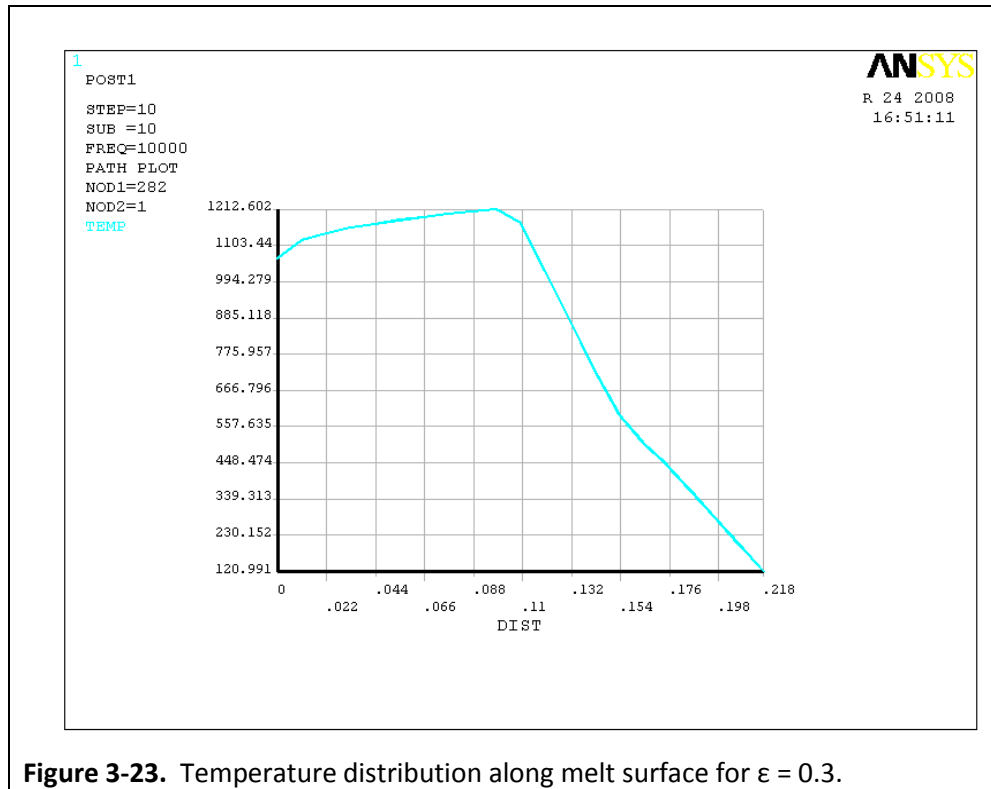
3.3. Comparison of Model Calculations to Experimental Results

The effort put forth to conduct analysis of the various model parameters, as well as the sensitivity studies on the material property values, resulted in a high confidence level that the assumptions made regarding the glass composition and associated material properties, including the extrapolation methods, were appropriate. However, because the model was going to be used as a tool to help guide the designs and focus the experimental work, strong validation of its representativeness was necessary.

The final step in validating the model was to make direct comparisons between the model results and experimental measurements. The easiest, and most direct, approach to accomplish this is to measure the temperature distribution within the melt. See Figure 3-25 (same as Figure 2-9, but repeated here for convenience).

Several experimental runs were completed on different configurations and then modeled to compare the results. Melter systems with two-turn and three-turn inductors, with different melt levels, and different maximum surface temperatures were investigated. Initially, only systems with
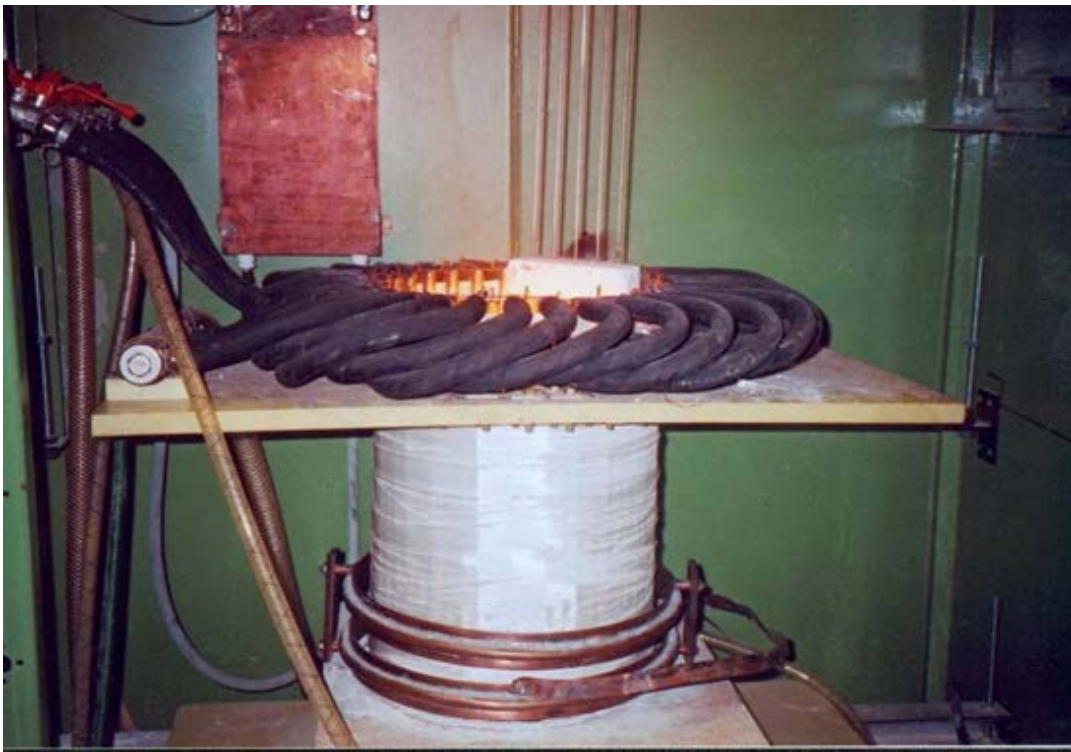
Figure 3-25. Example two-turn inductor CCIM system for measuring temperature profile.

ceramic bottoms were evaluated for model
validation. However, eventually CCIM platforms
with water-cooled metallic bottoms were also
tested. These tests allowed iterative
improvement of the boundary conditions and
material properties used in the model. As
indicated earlier, the systems did not include
the drain device. The results, which
demonstrated that the model provides very
representative steady state data, are discussed
below. As previously mentioned, more details
of the experimental setups and results are
discussed in later chapters.

The first tests were conducted using a two-turn
inductor with a nominal melt depth of 10 cm
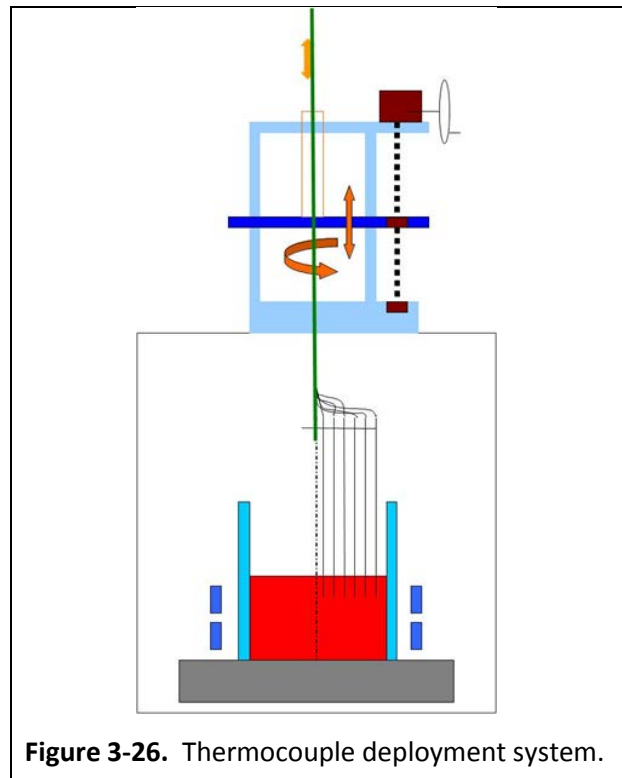
Figure 3-26. Thermocouple deployment system.

(shown in Figure 3-25.) An array of Type K thermocouples was assembled in a mechanism that could
be lowered and raised into the melt pool. The thermocouples were arranged in a radial line from
near the center of the melt pool to near the crucible wall. Figure 3-26 gives a schematic of the
thermocouple deployment system. For the initial test, four thermocouples were used, but this was
later increased to five, then seven, and eventually eight.

During the first test using the two-turn inductor system, temperature measurements were made at
various depths for three different melt modes. These were defined by the maximum melt surface
temperature. This temperature was measured at the point on the melt surface that was found to be
the highest. The measurements were made by first measuring the temperature, then slightly
stirring the surface at that point to remove any cold cap that may have formed and measuring the
temperature again. The temperatures for three modes were 1,350^{o}C (no cold cap existed at this
high temperature), 1,150^{o}C/1,280^{o}C, and 1,000^{o}C/1,280^{o}C. The melt pool height for each mode was
105 mm, 90 mm, and 90 mm, respectively. The actual temperature measurements for the third
mode, 1,000^{o}C/1,280^{o}C, are given in Table 3-20. All temperatures above 1,100^{o}C are shown in red.
These data show good agreement with the model results for a similar configuration, as shown in
Figure 3-27. Another strong indicator of the representativeness of the model for this particular

configuration is demonstrated by the results of the first mode, which was at a very high surface temperature of 1,350^{o}C. For this condition, the model predicted a hot spot would dip down to the bottom of the melt pool and directly contact the ceramic base. This is shown in Figure 3-28. After these experiments were completed the glass ingot was removed from the crucible once it cooled. The photographs in **Figure 3-30** clearly show an area on the ingot that is not glassy, but is a crystalline material. The glass in this location, had interacted with the ceramic base, as the model had predicted, and had to be broken away. Tests of similar configuration that are conducted at lower maximum temperatures do not experience this phenomenon.

Table 3-20. Temperature data from two-turn inductor CCIM at 1,000^{o}C surface temperature.

Depth in Melt, cm	Radial distance from center axis, cm			
	3	**6.1**	**8.6**	**11.0**
0.2	763	777	826	973
1.2	973	1,068	1,155	1,349
2.2	1,128	1,217	1,295	1,410
3.2	1,245	1,278	1,335	1,352
4.2	1,292	1,292	1,326	1,332
5.2	1,295	1,278	1,295	1,284
6.2	1,242	1,223	1,228	1,237
6.9	1,169	1,163	1,169	1,169
8.2	1,102	1,099	1,094	1,089
9.2	1,042	1,029	1,011	930
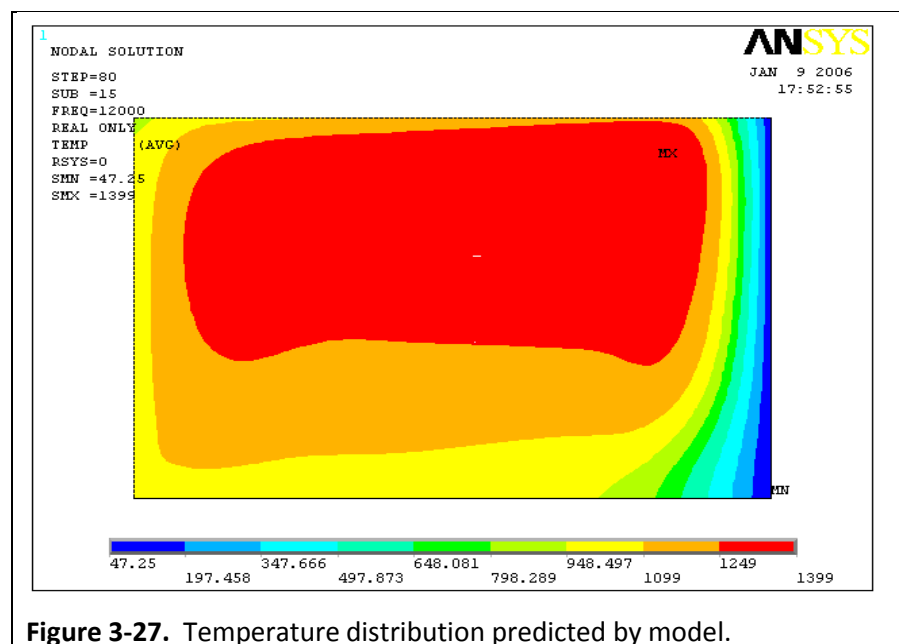
Figure 3-27. Temperature distribution predicted by model.
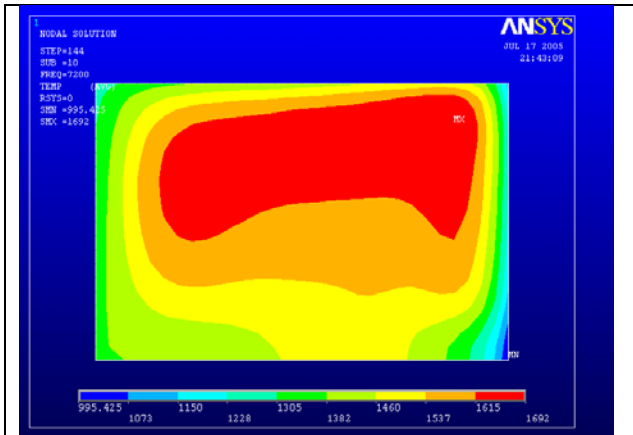
Figure 3-28. Model prediction of hot spot at bottom.

Figure 3-29. Crystalline phase resulting from interaction with ceramic base.

The next test configuration included a three-turn inductor CCIM system with an eight thermocouple (Type K) array for temperature measurements. Tests were conducted for various maximum surface temperatures and melt pool heights. The basic test configuration is depicted in Figure 3-30. Figure 3-31 shows the thermocouples being lowered into the melt.

Similar to the results for the two-turn system, comparison of the experimental measurements with the model predictions were very good. Table 3-21 gives the temperature measurement data for a test that had a melt pool height of 15 cm and a maximum surface temperature of 1,100^{o}C. Figure 3-32 shows the temperature distribution results from the ANSYS® model. The CCIM configuration and conditions were similar to

Figure 3-30. Three-turn inductor test configuration with eight thermocouple array.

the experimental set-up. These results are also in good agreement with the model, for the data points obtained. During the test, the thermocouples located at 3.1 cm and 9.8 cm from the center axis failed. The one located at 3.1 cm failed immediately, but the cause was uncertain since this is not a particularly hot zone in the melt pool (see 8.1 cm and 9.8 cm radial locations).

Table 3-21. Temperature data from three-turn inductor CCIM at 1,100°C surface temperature.

Depth, cm	Radius, cm						
	1.9	**3.1**	**4.8**	**6.4**	**8.1**	**9.8**	**10.6**
0	649	-	685	744	768	817	916
2	993	-	1,045	1,071	1,177	1,150	1,288
4	1,070	-	1,124	1,205	1,346	1,367	1,407
6	1,123	-	1,150	1,177	1,218	-	1,246
8	1,123	-	1,150	1,177	1,177	-	1,150
10	1,057	-	1,031	1,070	1,044	-	1,031
12	948	-	935	967	948	-	866
14	842	-	817	799	817	-	690
14.7	805	-	781	781	762	-	661
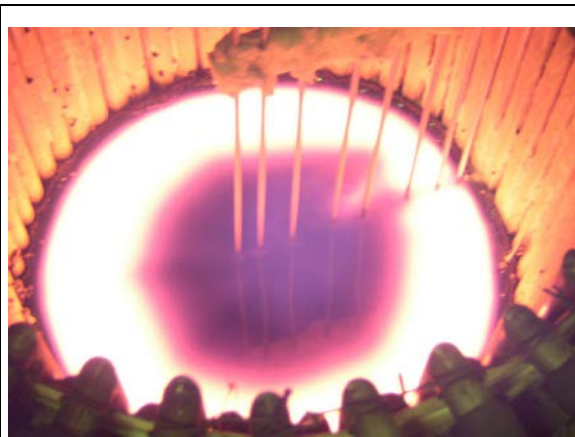
Figure 3-31. Lowering of eight thermocouple array into melt.
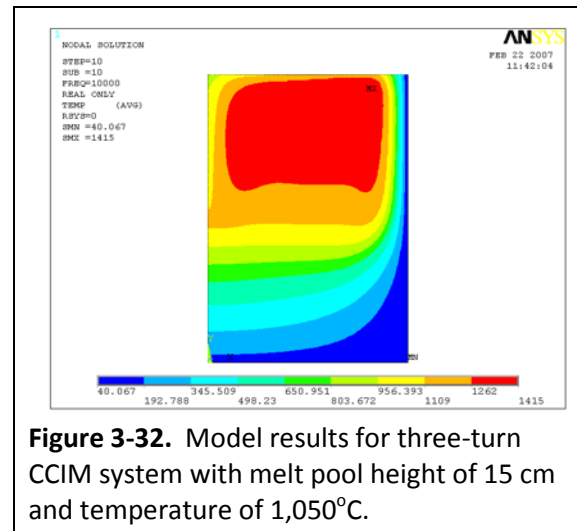
Figure 3-32. Model results for three-turn CCIM system with melt pool height of 15 cm and temperature of 1,050°C.

The Type K thermocouples, which are nickel-chromium/nickel-aluminum junctions in titanium sheathing, became unreliable. For subsequent testing, Type S thermocouples were used. They were platinum/platinum-rhodium junctions specially made in quartz sheathing. These thermocouples proved to be more reliable, but also failed during tests.

The deployment system for the Type S thermocouples was improved so that the thermocouples were securely held in a known and fixed position. The design of the Type S quartz thermocouples is shown in Figure 3-33. The improved deployment system is shown in Figure 3-34. Several modes were operated and temperature data collected. The details for one of those modes are included here. This mode operated at a surface temperature of 1,200°C and a melt pool height of 18 cm, which was different from the other two modes previously reported. The temperature data collected during this test is reported in Table 3-22.

For data comparison, the model was configured as closely to the experiment as possible. Several runs were made with varying power levels until the same nominal maximum surface temperature was achieved.

Table 3-22. Temperature measurements taken during experiment (CCIM Test #5).

Depth, cm	Temperature, °C							
	Number of thermocouple							
	1	2	3	4	5	6	7	8
0	878.8	906.6	938.2	928.29	921.1	850.6	926.5	1,000.6
1	1,042.8	1,165.7	1,260.4	1,135.6	1,139.2	1,178.0	1,263.5	1,313.2
2	1,188.5	1,328.8	1,318.2	1,311.4	1,264.3	1,340.5	1,362.1	1,440.9
3	1,253.4	1,261.6	1,383.9	1,314.9	1,387.4	1,360.0	1,389.8	1,451.5
4	1,280.0	1,322.5	1,367.3	1,335.6	1,381.6	1,390.2	1,421.0	1,426.6
5	1,326.7	1,347.4	1,355.0	1,346.8	1,393.0	1,400.0	1,414.6	1,386.6
6	1,337.2	1,312.8	1,343.3	1,365.9	1,353.6	1,401.8	1,409.9	1,386.4
7	1,324.7	1,335.0	1,329.8	1,331.9	1,356.8	1,379.7	1,372.7	1,357.0
8	1,322.0	1,325.6	1,322.2	1,331.3	1,335.7	1,348.9	1,349.1	1,321.7
9	1,275.0	1,299.1	1,281.1	1,298.9	1,293.5	1,288.9	1,309.3	1,282.7
10	1,237.0	1,240.6	1,237.4	1,241.4	1,234.0	1,235.1	1,239.9	1,248.2
11	1,177.1	1,176.9	1,165.6	1,176.7	1,172.4	1,174.3	1,180.2	1,186.5
12	1,097.0	1,108.8	1,098.0	1,105.2	1,106.5	1,106.0	1,118.1	1,107.5
13	1,040.6	1,052.8	1,042.2	1,045.6	1,045.1	1,043.3	1,046.5	1,011.7
14	987.2	995.0	984.9	995.0	986.3	987.1	980.6	918.7
15	925.1	928.9	921.2	925.7	915.1	904.4	876.9	772.6
15.5	915.9	917.1	908.6	912.0	905.2	890.6	859.9	773.1
16	879.0	879.0	881.2	871.7	863.4	836.6	788.7	722.7
16.5	853.4	854.4	853.2	848.5	836.8	802.8	747.3	701.5
17.5	801.0	800.4	801.4	789.3	770.9	727.0	682.3	694.0
18	750.2	751.2	752.9	745.6	736.8	708.4	674.3	689.72

Note: Values in blue text are likely not valid (i.e., lower than actual) due to heat losses in the quartz tubes.

Figure 3-33. Type S thermocouple in quartz sheath.

Figure 3-34. Thermocouple deployment system.
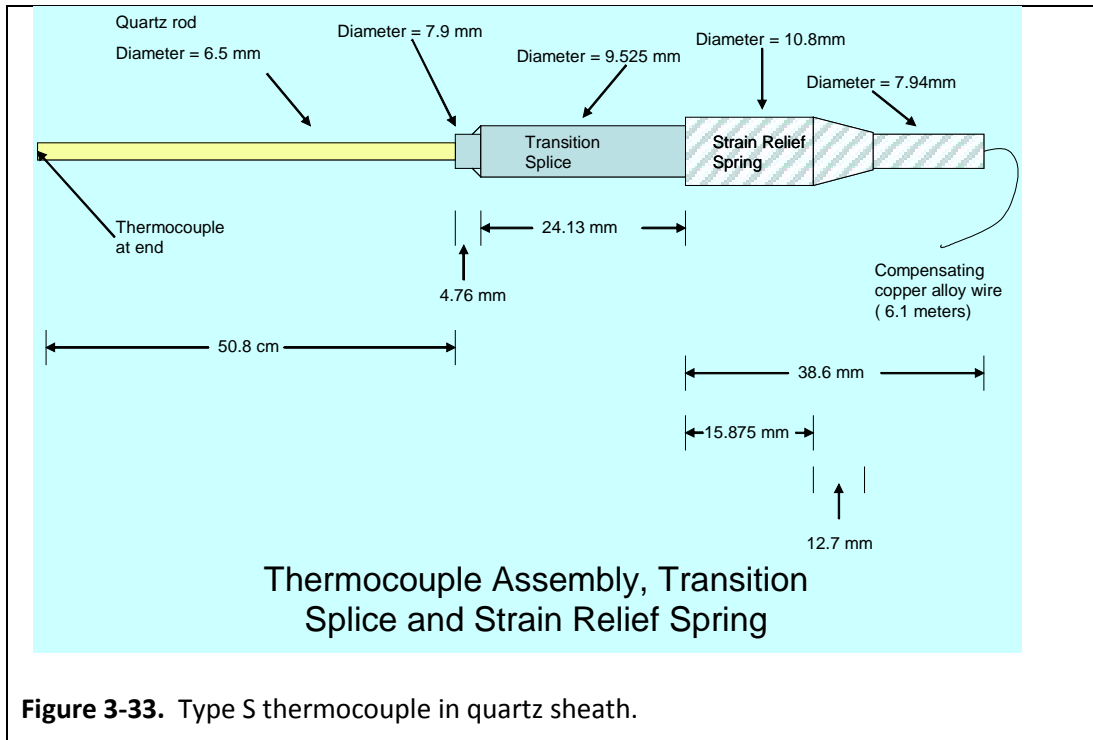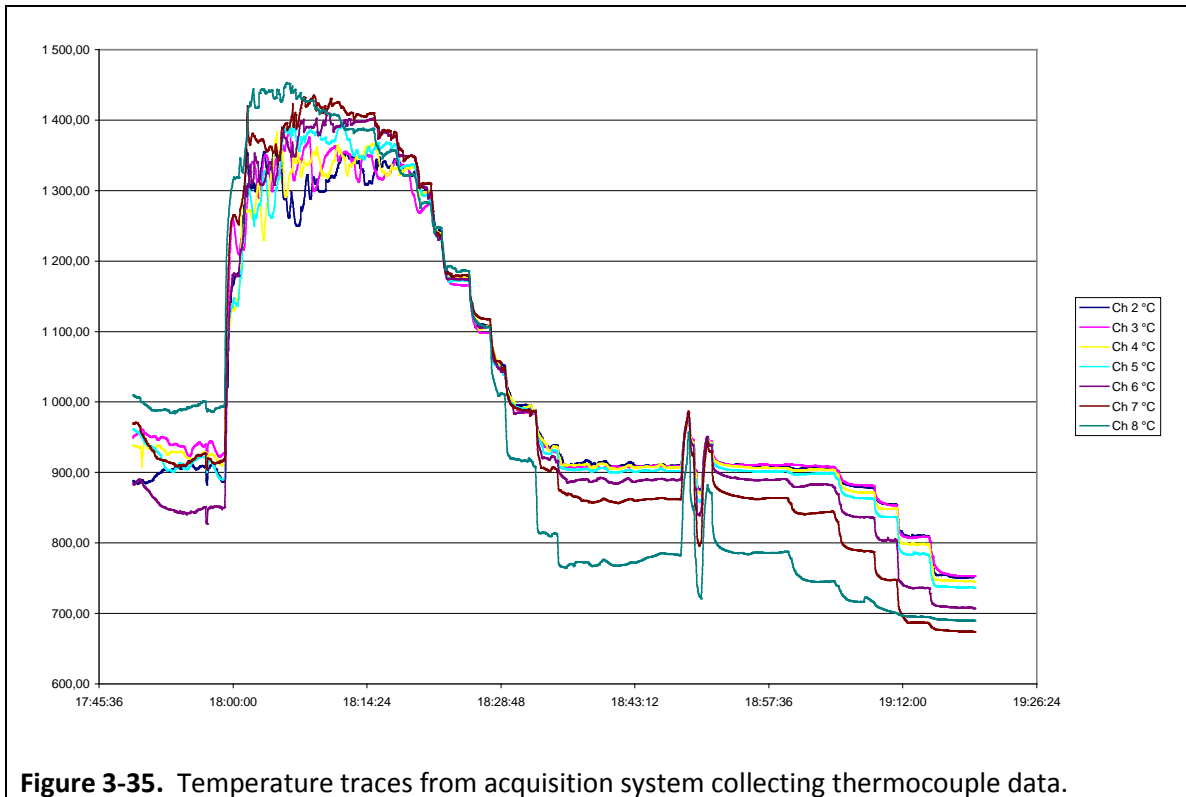
Figure 3-35. Temperature traces from acquisition system collecting thermocouple data.

Once the model results were verified, they were compared on a point by point basis with the thermocouple data from Table 3-26. (Note that the temperature data taken on the surface are measuring low, most likely due to the shielding effect of the quartz sheath. The thermocouple junction was inside the quartz a small amount, so at this measurement, the junction was not actually in contact with the melt. The low readings were validated with a calibrated pyrometer.)

An automated data acquisition system was installed that collected the thermocouple data continuously. This is why the temperature data in the table is reported to so many significant digits. The signal traces are shown in Figure 3-35. The results for the data comparison for several of the thermocouple positions are given in Figures 3-36 through 3-40. These results show excellent correlation and demonstrate that the model provides very representative data for the actual system.

Some key observations were drawn, not only from the data depicted in Figures 3-36 through 3-40, but also from the data collected in several additional test runs and modes (see Appendix C). First, the greatest deviations between experimental data and model results occur along the centerline and surface. The centerline variances are most likely due to the axially-symmetric assumption of the model. However, these deviations impact a small percentage of the total melt volume, and thus

minimally impact the model results elsewhere. The surface variances may be due to inadequate effective emissivity values in the model, which were shown to be partially temperature-dependent. This is why the investigation discussed in Section 2.1.4 was conducted.
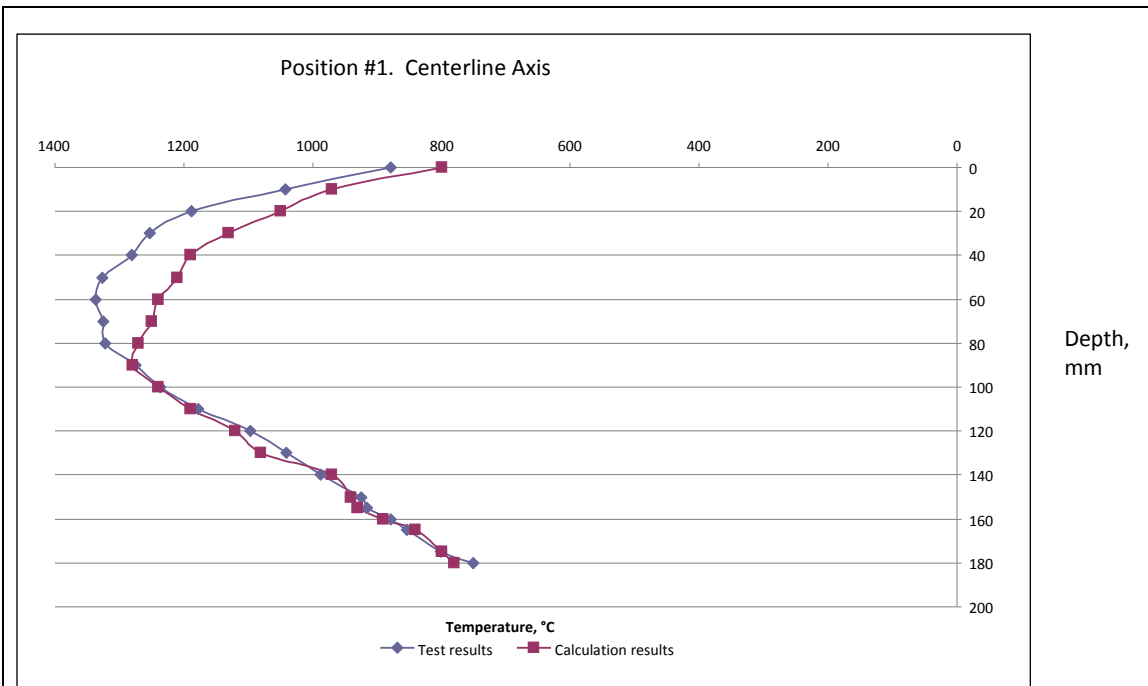
Figure 3-36. Comparison of temperature data along centerline.
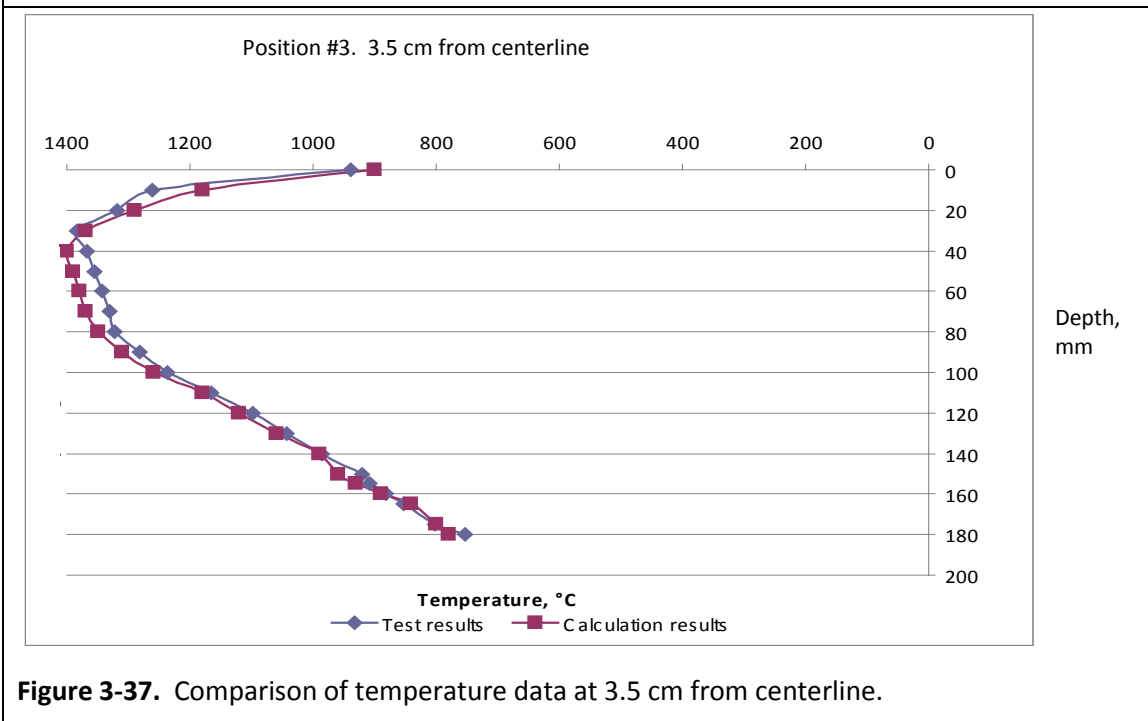
Figure 3-37. Comparison of temperature data at 3.5 cm from centerline.

Figure 3-38. Comparison of temperature data at 7.0 cm from centerline.

Figure 3-39. Comparison of temperature data at 10.5 cm from centerline.

Figure 3-40. Comparison of temperature data at 12.25 cm from centerline.
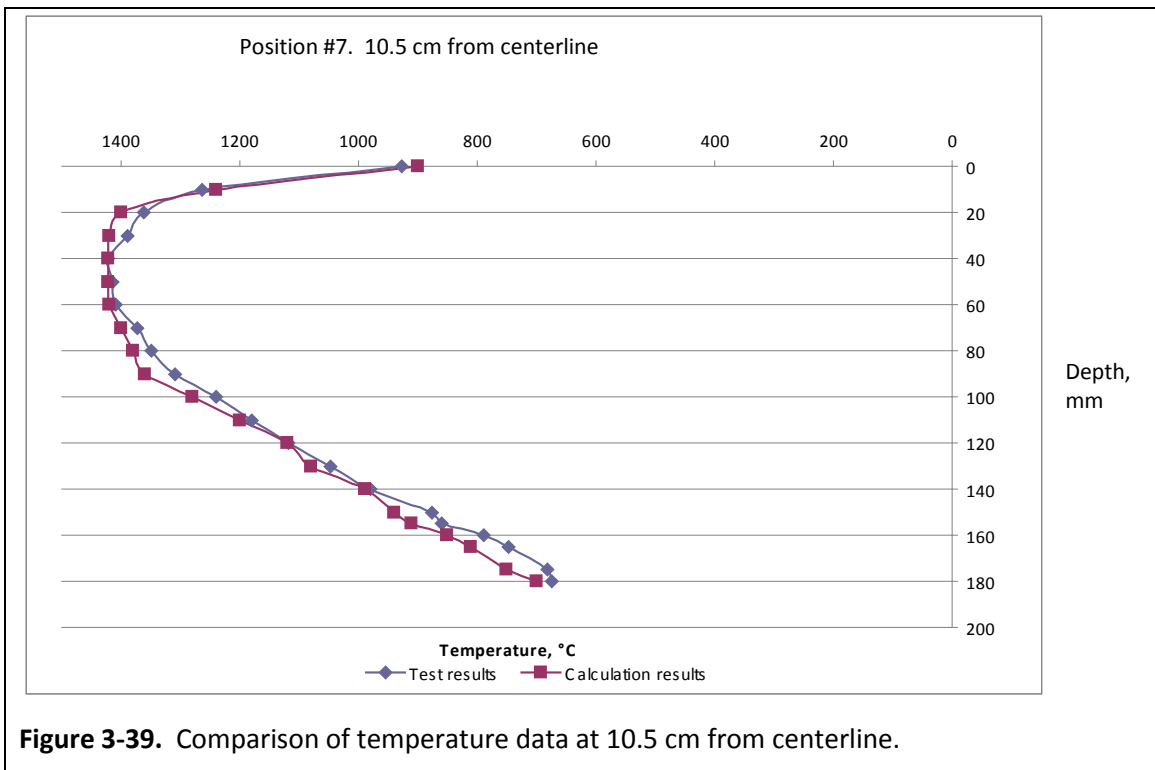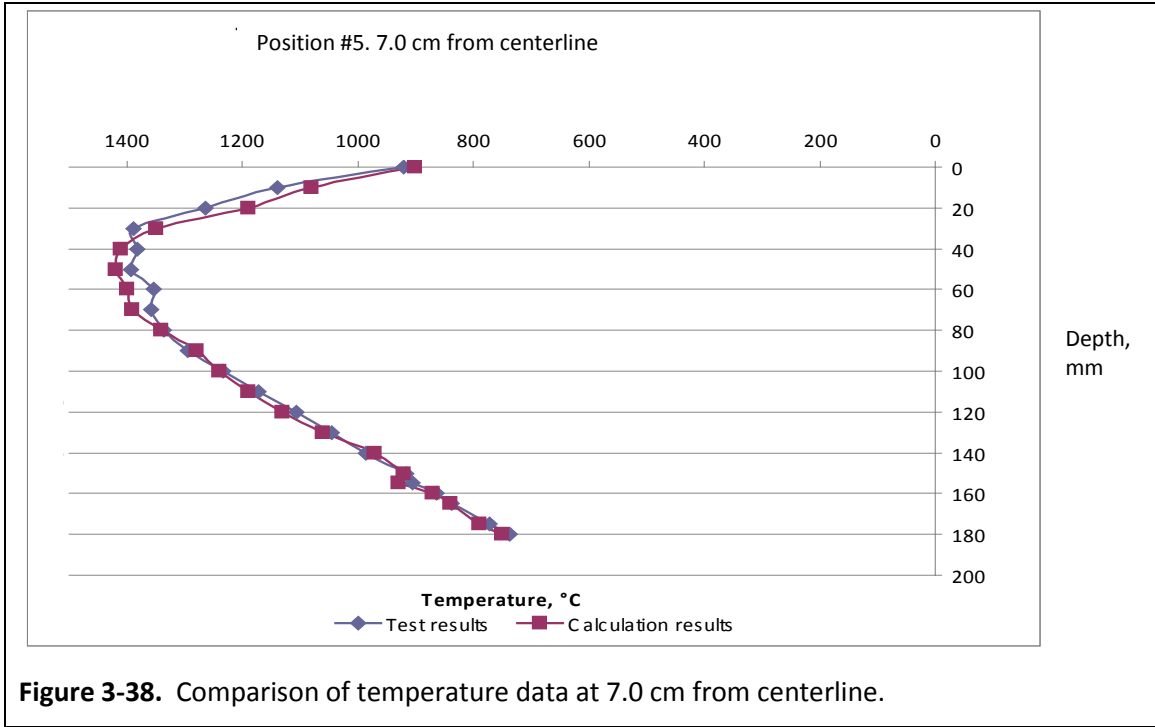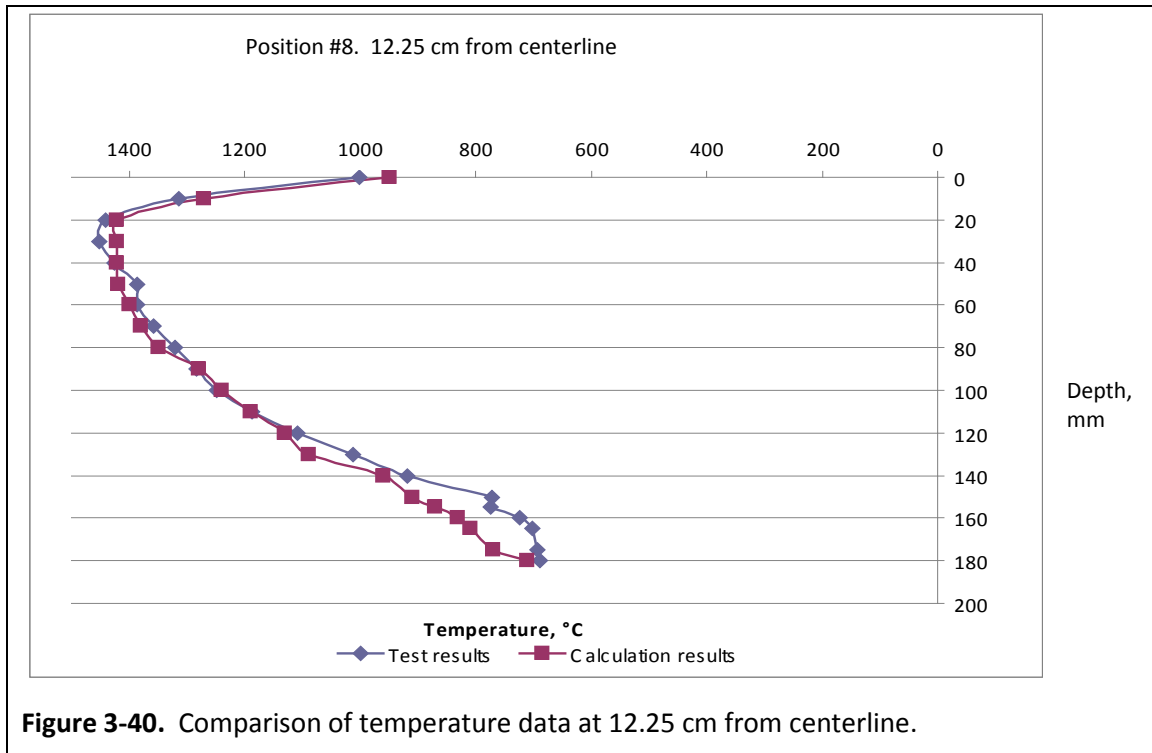
3.4. Investigation of Crystallization Effects in the Melt

Crystallization of the melt in areas where interaction occurred with the ceramic bottom was observed in some of the tests. It was unclear how this may impact the overall model results, so this was investigated.

This is an important characteristic to understand because, as mentioned above, crystallization was observed at the bottom in some of the tests and this could potentially change the melt characteristics since the thermal conductivity, electrical resistivity, and viscosity of the glass changes as these crystalline phases form. However, because these changes occur near the bottom where the glass temperatures are below 700°C, the viscosity and electrical resistivity changes will have little to no impact.

Accordingly, the model was used to investigate the impacts to the velocities, temperature distribution, and maximum temperatures when this crystallization occurs. This was accomplished by adding a multiplying factor, kc, to the baseline temperature dependent thermal conductivity values for temperatures below 700°C. The results are presented in Figures 3-41 through Figure 3-43.

As can be seen from these figures, the maximum temperature does not change appreciably; however, the volume of melt at the highest temperatures (i.e., above $1,100^{o}$C) is reduced and this results in a larger volume of cooled glass in the bottom of the melter, which will make draining the melt much more difficult. This was shown experimentally in the first CCIM test conducted, which is discussed later in this dissertation.

Figure 3-44 compares the temperature results for each case along the centerline axis. It is interesting to note that the primary deviations from the base case, kc = 1.0, occur at depths beginning at about 10 cm. Referring back to Figure 3-36, this is the same region that the model results match the experimental values almost exactly. These data were collected during the first mode of a test and, thus, not much crystallization had occurred yet. This also serves to provide more confidence in the validity of the model. Table 3-23 summarizes the deviations of key parameters from the base case.

When taken together, all of the results of model in comparison to experimental data provide strong correlation and thus strong confidence in the model. Based on these findings, the model can be effectively applied to investigation of the melter and draining systems.
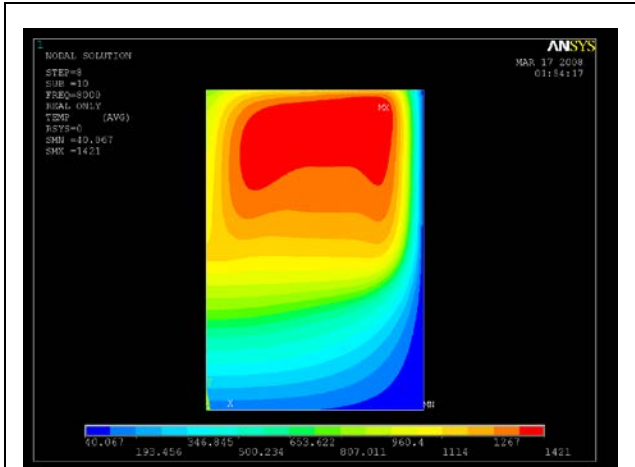
Figure 3-41. Temperature distribution and maximum at kc = 1.0.
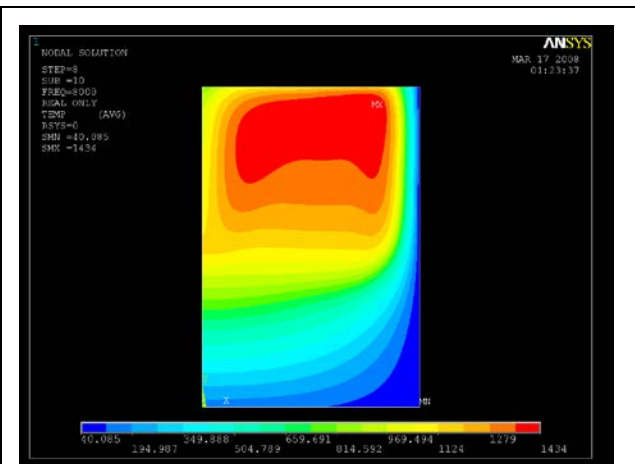
Figure 3-42. Temperature distribution and maximum at kc = 1.2.
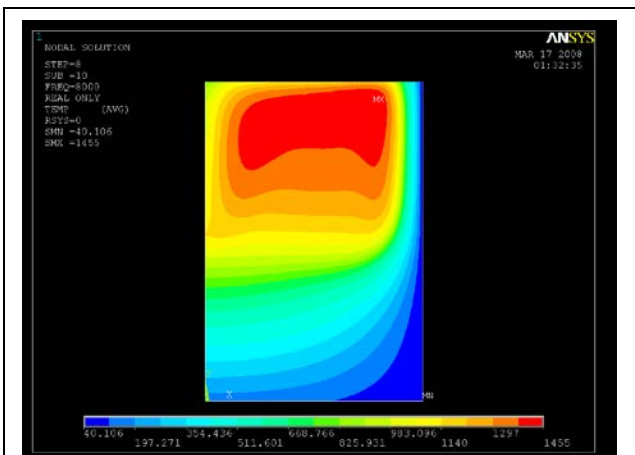
Figure 3-43. Temperature distribution and maximum at kc = 1.5.

Figure 3-44. Comparison of temperatures along centerline for various kc values.
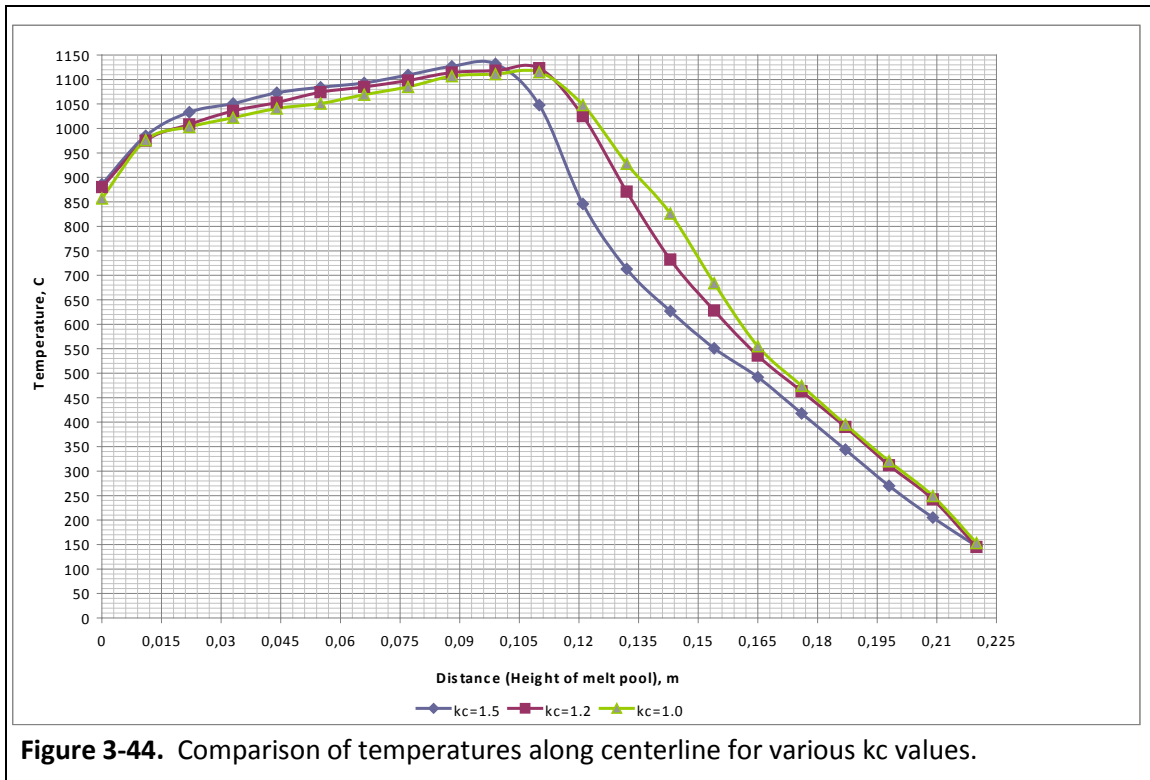
Table 3-23. Deviations of key parameters for variations in kc from base case.

Parameter (maximum)	Base kc=1	kc=1.2	Deviation %	kc=1.5	Deviation %
Tº, C	1,417	1,430	0.917	1,450	2.3
Vx (+), mm/s	0.816	0.827	1.35	0.868	6.4
Vx (-), mm/s	-1.57	-1.56	-0.64	-1.532	-2.4
Vy (+), mm/s	0.475	0.467	-1.7	0.443	-6.7
Vy (-), mm/s	-6.11	-5.974	-2.2	5.718	-6.4

3.5. Validation of the Electromagnetic Calculation Block

The final check of the model was focused on the validity of the high frequency electromagnetic calculation block. Specifically, because there were plans to enhance the model to include the ability to investigate the melt initiation process, the initial conditions for the electromagnetic calculation had to be modified. In the original approach, a constant power level was set in the melt volume and the calculations were nested and integrated until the convergence criteria were met. However, for investigation of the melt initiation process this is not an appropriate approach. For this second case, an inductor voltage value must be met. In ANSYS®, this requires defining an external circuit that includes primarily a voltage source and inductor. Development of this portion of the model required

significant input from the ETU-LETI faculty. (Note that for investigation of steady state melt conditions, the previous approach is still used.)

The focus to validate the approach was to re-evaluate the model parameters that could specifically impact the electromagnetic calculation results. The allowable coarseness of the mesh was first investigated. For example, the skin depth in the copper inductor (electrical resistivity $\rho_e = 2 \times 10^{-8}$) is several orders of magnitude smaller than that of the glass melt (electrical resistivity at 1,400^{o}C, $\rho_e = 2.18 \times 10^{-2}$). This leads to the conclusion that the grid within the melt volume can be much more coarse than that in the copper inductor. An initial grid was defined as shown in Figure 3-45, and subsequent grid impact factors of mm = 2 and mm = 4 were also evaluated to determine the effect on the calculation results. Additionally, the dimensions of the calculation area were investigated. Recall that in ANSYS®, electro-magnetic field calculations are bounded by an area that simulates infinity. Within the software, this is accomplished through the use of a specially designed element called

Figure 3-45. Mesh for electromagnetic model at mm = 1.

INFIN110. Figure 3-46 shows the separate calculation areas that correlate to the varying grid coarseness. For the calculation area, a base case of 20 cm radius by 30 cm height was used, then doubled in both dimensions to evaluate the effects on the results. For the variations in both mesh fineness and calculation area, deviations from the base case of less than 1% were observed, so these parameters were taken as acceptable.

Once the configuration was demonstrated to be acceptable, the next step was to compare the calculation results of the ANSYS® model with those of another electromagnetic calculation software called Maxwell 2D/3D. This software is recognized as an industry standard and the results were assumed to represent the benchmark by which the ANSYS® results could be evaluated for accuracy. The calculation results were also compared to another calculation method referred to as the method of total flux (MTF). These comparative analyses were conducted by ETU-LETI.

A simple case was used that can be solved analytically due to the non-temperature dependence of the solution, thus the results are known. This included calculating several key electrical parameters for a 4 cm radius by 10 cm tall non-magnetic austenitic stainless steel (i.e. $\mu_r \approx$ 1.0) exposed to an induction field at a frequency of 2.5 kHz. The material has an electrical resistivity of 0.9 x 10^{-6} ohm-m. From equation 3-5, the
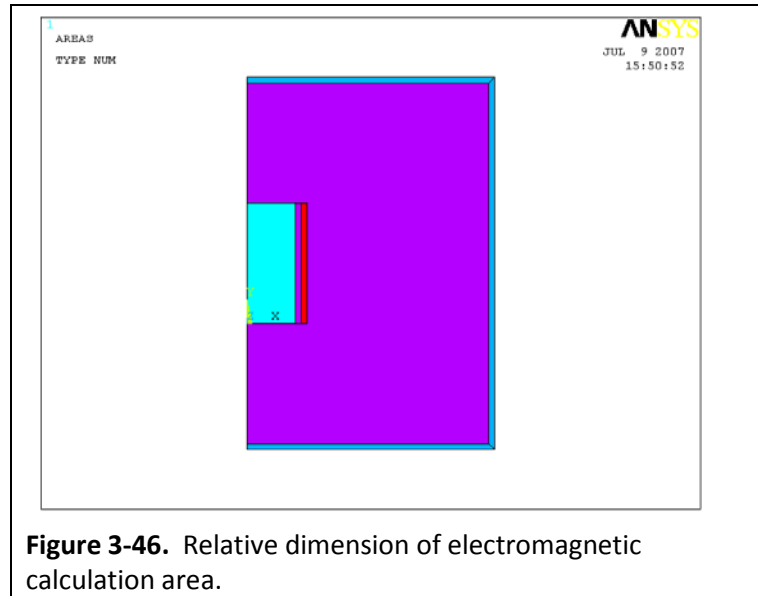
Figure 3-46. Relative dimension of electromagnetic calculation area.

skin depth is determined to be 0.0096 m, or about 1 cm. Figure 3-47 shows the resulting distribution of heat sources in the work piece. If this is investigated for the power density levels up to a value of e^2, which defines the skin depth, based on a 4 cm radius, one can visually observe from the image shown in Figure 3-48 that this is qualitatively demonstrated by the model results. This is based on the value of the power density being 0.234 x 10^9 W/m^3. When multiplied by e^{-2}, this results in a value of 0.316 x 10^8 W/m^3. This range of values for power density shows the skin depth,

which does agree with the expected value of about 1 cm.

Additionally, Table 3-24 provides direct comparison of the calculation results from Maxwell 2D/3D, ANSYS®, and MTF. These results demonstrate that, in general, the key parameters calculated by ANSYS® are within about 4% of the Maxwell 2D/3D results. This requires some explanation.
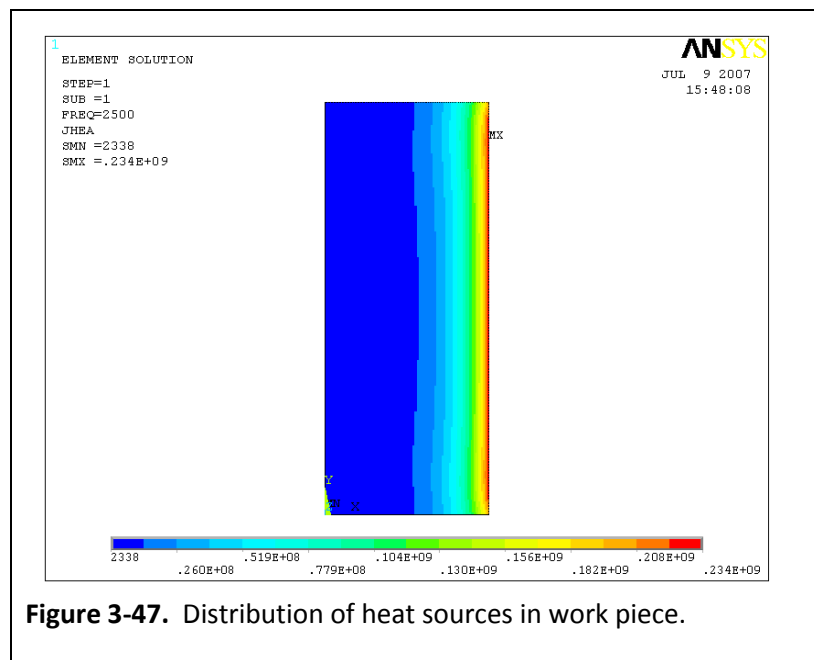
Figure 3-47. Distribution of heat sources in work piece.

Table 3-24. Comparison of electromagnetic calculation results for various approaches.

Variable	Maxwell® results	ANSYS® results	ANSYS® Inaccuracy, %	MTF results	MTF Inaccuracy, %
r_1	$0.3092 \cdot 10^{-4}$	$0.369 \cdot 10^{-4}$	19.3	$0.369 \cdot 10^{-4}$	19.3
r_2	$0.1443 \cdot 10^{-3}$	$0.1456 \cdot 10^{-3}$	0.9	$0.156 \cdot 10^{-3}$	8.1
r_i	$0.175 \cdot 10^{-3}$	$0.182 \cdot 10^{-3}$	4.2	$0.193 \cdot 10^{-3}$	10.1
z_i	$0.486 \cdot 10^{-3}$	$0.489 \cdot 10^{-3}$	0.49	$0.517 \cdot 10^{-3}$	6.2
η_i	0.824	0.789	3.1	0.809	1.8
$\cos\phi$	0.36	0.373	3.6	0.373	3.7

The key parameters that are used to evaluate the accuracy of the ANSYS® electromagnetic calculation results include the active resistance of the actual induction coil, the active resistance as a result of the induction into the work piece, the total active resistance of the induction system (inductor plus work piece), the total impedance of the induction system, the electrical efficiency of the induction system, and the phase shift angle of the current (relative to the surface) as it penetrates into the material. These are defined in the following analysis provided by ETU-LETI:

Figure 3-48. Approximate skin depth in work piece.

$$r_1 = \frac{\rho_{e,1}}{\delta} \cdot \frac{2\pi R_1}{ga_1} \cdot w^2 \qquad \text{(active resistance of induction coil)} \qquad (3-6)$$

where:

$\rho_{e,1}$ is resistance of inductor coil metal

δ is skin depth (as defined by equation $3-5$)

R_1 is radius of the induction coil

a_1 is height of the induction coil

g is ratio of metal to air in induction coil (i.e. defines width of metal and spacing of turns)

w is number of turns of the induction coil.

$$r_2 = \frac{P_2}{I_i^2} \qquad \text{(active resistance of the work piece)} \qquad (3-7)$$

where:

P_2 is the power induced in the work piece

I_i is the current on the induction coil (calculated by ANSYS®).

Thus,

$$r_i = r_1 + r_2 \qquad \text{(active resistance of the induction system)} \qquad (3-8)$$

Also,

$$z_i = \frac{U_i}{I_i} \qquad \text{(total impedance of the induction system)} \qquad (3-9)$$

where U_i = voltage applied to the induction coil as input in ANSYS®.

$$\eta_i = \frac{r_2}{r_i} \qquad \text{(efficiency of induction system)} \qquad (3-10)$$

$$\cos(\varphi) = \frac{r_i}{z_i} \qquad \text{(cosine of phase shift angle)} \qquad (3-11)$$

As seen in Table 3-24, the largest error reported is for the active resistance in the induction coil, r_1, which is 19.3 %. However, since the contribution of r_1 is an order of magnitude less than the total active resistance of the system, the effect of this inaccuracy is minimal, with the error of the total active resistance of the system being only 4.2%. This is an acceptable margin of error because when the mesh is refined to provide only a 1% error (i.e., at mm = 4) the calculation time is unacceptably long.

Thus, the defined model approach and parameters can be used for subsequent evaluations of melt initiation studies; however, the fixed power level approach must still be used for investigation of steady state melt conditions. This is because, for conditions in which the bulk of the glass does not actually couple with the induction field, near infinite values of power in the melt result in the calculations when the temperature dependent electrical resistivity values are used in conjunction with an input current or voltage.

This is illustrated in Figures 3-49 and 3-50. These resulted from running the model with a fixed input current density and a temperature dependent resistivity. Time step increments of 2 seconds and 10 seconds were used. In both cases, neither converged and provided erroneous solutions. Refer back to Figures 2-5 and 2-6 to see the results from the same model except that a fixed power level was applied rather than a fixed current density.

Figure 3-49. Two second time step with $\rho_e(T)$.

Figure 3-50. Ten second time step with $\rho_e(T)$.
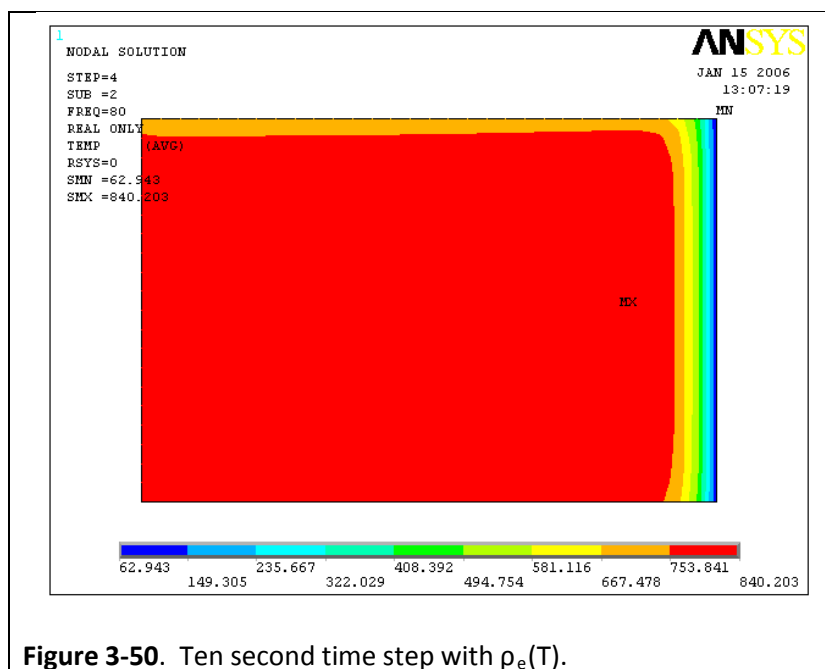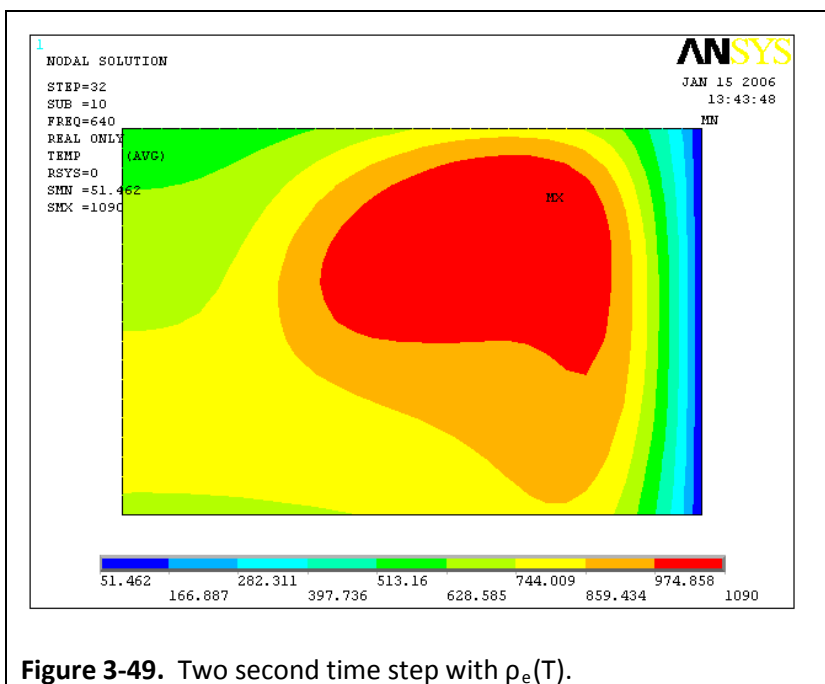
These results led to the use of a fixed power in the melt as an initial condition for the steady state model. The value used is dependent on the melter configuration and was determined experimentally using a precision calorimetry system, coupled with the electrical efficiency analysis.

In comparison, when a fixed power level is set as an initial condition, both the 2-second and 10-second time steps result in better convergence, with nearly identical results, which provides a basis for using the 10 second time step for scoping studies, providing faster convergence. These results are illustrated in Figures 3-51 and 3-52. The models were set at a power level, determined by a fixed current of 153 A in the drain inductor, and represent 15 minutes of operation.

Figure 3-51. Temperature distribution for 2 second time step.

Figure 3-52. Temperature distribution for 10 second time step**.**
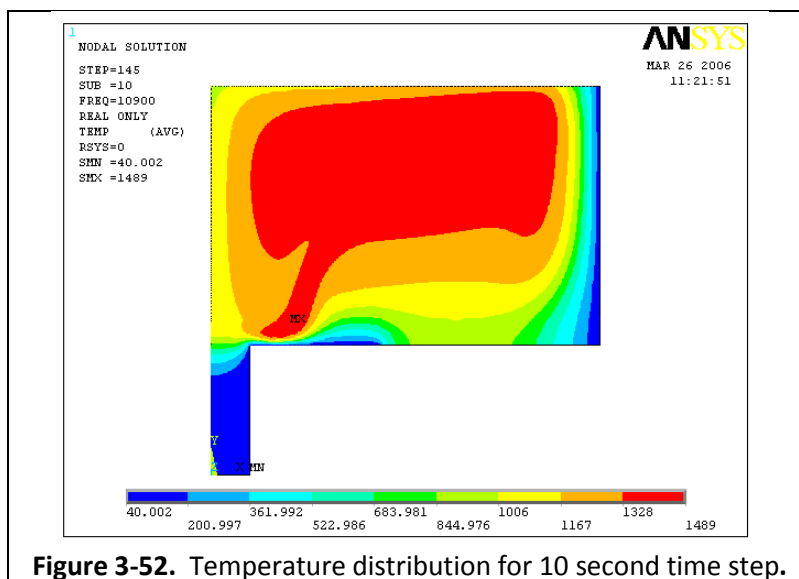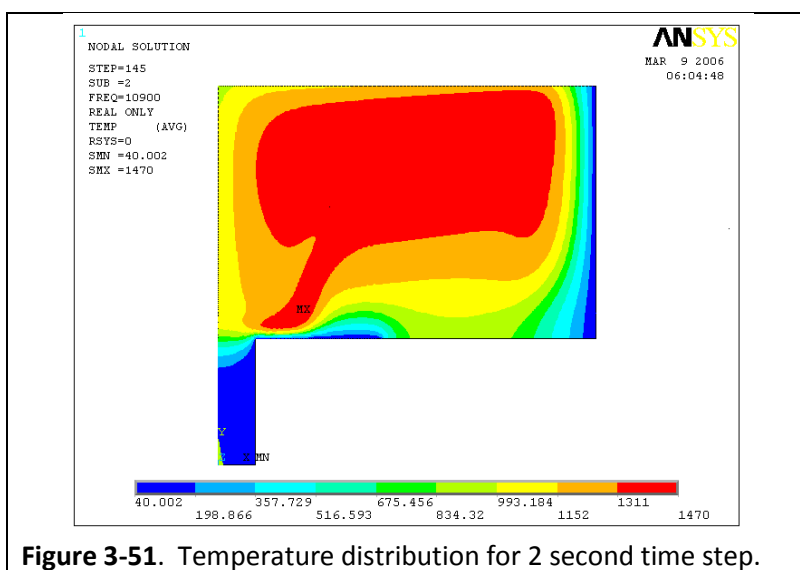
In general, the conclusion of the preceding investigations and analyses is that, for the intended application, the electromagnetic calculation block within the ANSYS® model will provide representative results for both the melt initiation process and steady state mode analysis. However, the errors maybe greater related to analysis of the 27 MHz frequency system. Recall that the displacement currents, $\partial \mathbf{D}/\partial t$, from equation 2-1 (Ampere's Law) are generally neglected. Although this is a low magnetic permeability system, the displacement currents are more pronounced for systems operating above 10 MHz and their effects are not quantified for the analyses conducted herein.

CHAPTER 4.   BASE MODEL APPLICATION

Throughout the course of this research, the model was applied to design and evaluation of the inductively heated draining system, as well as the CCIM system itself. The model was continually improved and enhanced in an iterative process between experimental measurements and the model results. The following discussion describes the application of the model only. The related experimental efforts and results are discussed in subsequent chapters.

4.1. Inductively Heated Drain System Parameters

Extensive analytical and experimental work has been conducted for evaluation of inductively heated systems. Prior to discussing the application of the model, it is necessary to understand the underlying theory that forms the basis for the physical design of a CCIM system. Venable and Kinn [16] present an excellent discussion of the analytical derivation of some of the key design parameters for effective inductive heating. This is summarized here to provide the necessary background.

4.1.1.Theory of Induction Heating

An electromotive force is produced in any conductive material that is subjected to a changing electromagnetic field (e.g. from an oscillating current source such as a high frequency generator). If a conductive path exists that allows the flow of current, the induced electromotive force produces a current along this path. Energy is thus produced in the form of heat due to the resistance of the path to the current flow.

To further explain the phenomenon of induction heating, two important laws must be mentioned: Ampere's law and Faraday's law. Recall equation 2-1:

$$\nabla \times \mathbf{H} = \mathbf{J} + \frac{\partial \mathbf{D}}{\partial t} \quad \text{(from Ampere's law)} \qquad\qquad (2-1)$$

If the displacement currents are assumed to be zero, and the equation is converted from SI units to CGS units, the more commonly used system, the equation becomes:

$$\nabla \times \mathbf{H} = 0.4\pi \mathbf{J} \qquad \text{(from Ampere's law)} \qquad\qquad (4-1)$$

where:

H is the magnetic intensity vector in oersteds

J is the total conduction current density vector in amperes per square centimeter.

Also, recall equations 2 - 2, 2 - 5, and 2 - 6:

$$\nabla \times \mathbf{E} = -\frac{\partial \mathbf{B}}{\partial t} \quad \text{(from Faraday's law)} \tag{2-2}$$

$$\mathbf{B} = \mu_r \mu_0 \mathbf{H} \tag{2-5}$$

$$\mathbf{J} = \sigma \mathbf{E} \quad \text{(Ohm's law)} \tag{2-6}$$

If these are also converted to CGS units and combined they yield the following:

$$\nabla \times \mathbf{E} = \mu \times 10^{-8} \frac{\partial \mathbf{H}}{\partial t} \quad \text{(from Faraday's law)} \tag{4-2}$$

where:

E is the electric field intensity vector in volts per centimeter (cm)

σ is $1/\rho_e$ in which ρ_e is expressed in microohm-cm

μ is the product $\mu_r \mu_0$ expressed as a numeric

For a conducting medium exposed to a harmonically changing magnetic field, an equation can be derived from equations $4-1$ and 4 - 2 describing the distribution of induced current in the medium. This is referred to as the eddy current equation and is represented by the LaPlacian:

$$\nabla^2 \mathbf{J} = j \frac{8\pi^2 \mu \omega}{\rho_e} \times 10^{-3} \mathbf{J} \tag{4-3}$$

In induction heating processes, the "skin effect" is a term used to describe the current density dissipation from the surface of the conducting medium to its interior. A simple example can be used to mathematically depict this effect. If a harmonically varying magnetic field is placed above a conducting plane, and the conditions defined by equations 4 - 1 and 4 - 2 are applied, the solution to the LaPlacian (equation 4 - 3) becomes equation 3 - 4, which was defined earlier as:

$$\mathbf{J}_y = \mathbf{J}_0 e^{-y/\delta} e^{jy/\delta} \tag{3-4}$$

In equation 3-4, the first exponential term represents the decrease in magnitude of the current density, J_y, as a function of the distance from the surface into the conducting medium, y. The second exponential term represents the phase shift between the current on the surface and the current at some depth, y.

Figure 4-1 illustrates the generalized current density decrease and phase shift that occurs at depth into the conductive medium. At the point where the exponential y/δ becomes unity, the current has fallen to e^{-1}, or about 0.37 of the surface current density. This value is referred to as the depth of penetration, "skin depth" or "skin effect", δ, of the current.

Integration of the curve yields the total current applied to the system. At the point represented by the skin depth, approximately 87% of the total available current is deposited in this volume.

Figure 4-1. Current density dissipation and current phase shift with penetration depth. [16]

Thus, the depth of penetration can be defined as:

$$\delta = 5.03 \sqrt{\frac{\rho_e}{\mu_r \omega}} \qquad (4-4)$$

where:

δ is depth of current penetration in cm

$\rho_e = 1/\sigma$, which is electrical resistivity in microohm-cm

μ_r is relative magnetic permeability (which is equal to unity for this glass)

ω is frequency of oscillation in cycles per second
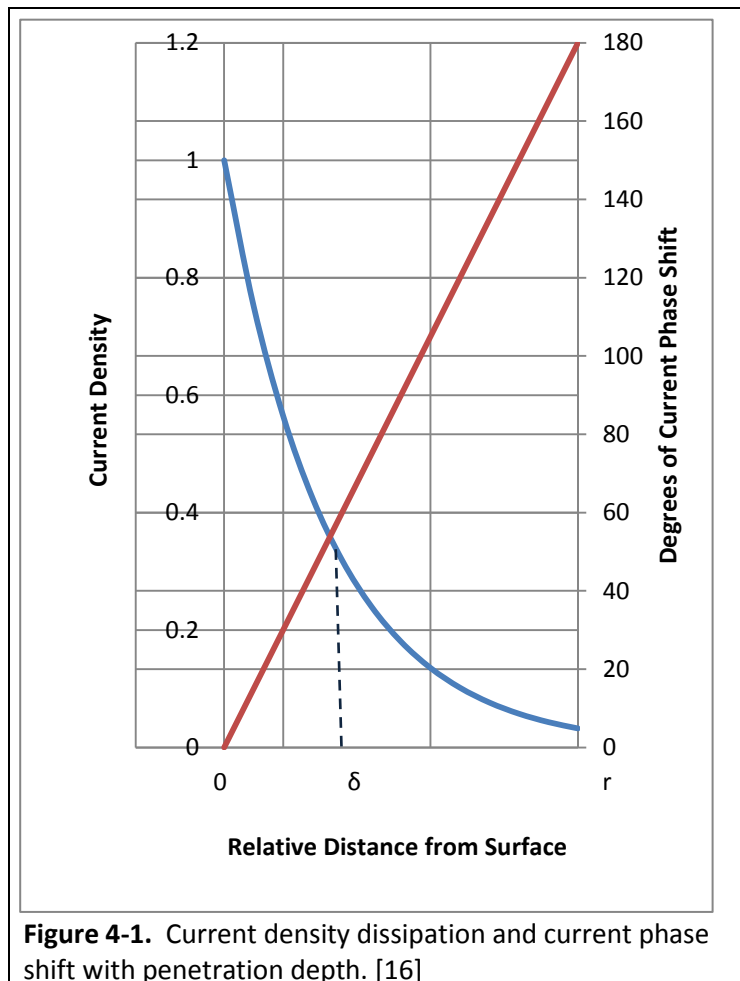
When this is converted from CGS to SI units it is the same as equation 3 - 5, given earlier. Figure 4-1 also illustrates the fact that at a depth not far beyond δ the current is 180 degrees out of phase with the surface current. However, because there is so little current at depths greater than δ, this has almost no effect. Thus, the depth of penetration is the depth to which the total induced current can flow uniformly and produce the same heating effect as that predicted by equations 4-3 and 3-4. Additionally, equation 4-4 defines the effective cross-section of a conductor of unit height carrying an alternating current with pronounced skin effect.

For heating a solid circular cylinder, such as the geometry of the CCIM system used for this research, Venable and Kinn [16] show that a differential equation that describes the current flux distribution within the cylinder is as follows:

$$\frac{d^2\mathbf{H}}{dr^2} + \frac{1}{r}\frac{d\mathbf{H}}{dr} - jm^2\mathbf{H} = 0 \qquad (4-5)$$

where:

$$m^2 = \frac{8\pi^2\mu\omega}{\rho} \times 10^{-3} \qquad (4-6)$$

As before, these are presented in CGS units. The solution of this equation defines the current around the cylinder at any radius, r. So, the power generated in any elementary cylinder of radius, r, is simply:

$$P = \frac{H^2 m^2 \rho M_1^2(mr)}{8\pi M_0^2(ma)} \qquad (4-7)$$

where:

       a is the maximum radius of the cylinder

       M_1 is a particular Bessel function of the argument mr

       M_0 is a particular Bessel function of the argument ma (where m is defined in equation 4-6)

Integration of equation 4-5 from r = 0 to r = a gives an equation for the total power generated in a cylinder of unit length, thus the total power per unit volume, as follows:

$$P_v = \frac{1}{2}H_0^2\mu\omega\mathbf{G}(ma) \times 10^{-7} \qquad (4-8)$$

where:

$$\mathbf{H_0} = \mathbf{H}\sqrt{2} = \text{peak magnetizing force in oersteds}$$

$$\mathbf{G}(\text{ma}) = \frac{1}{\text{ma}} \frac{\text{ber(ma)ber}'(\text{ma}) + \text{bei(ma)bei}'(\text{ma})}{\text{ber}^2(\text{ma}) + \text{bei}^2(\text{ma})} \qquad (4-9)$$

The product, ma, has an important relation to the depth of penetration, δ, and the diameter, d, of the cylinder, which is:

$$\text{ma} = \frac{d}{\delta\sqrt{2}} \qquad (4-10)$$

This allows the power per unit volume, P_v, to be expressed as a function of G(d/δ), as follows:

$$P_v = \frac{1}{2}\mathbf{H_0^2}\mu\omega\mathbf{G}\left(\frac{d}{\delta}\right) \times 10^{-7} \qquad (4-11)$$

Thus a maximum power occurs when G(d/δ) is a maximum since all other values in equation 4 - 11 are assumed constants. Figure 4-2 shows G(d/δ) as compared to the ratio d/δ. This illustrates that G(d/δ) is a maximum when d/δ is approximately equal to 3.5. With this known relationship, it can be combined with equation 4-4 to determine the three primary design variables for a cylindrical inductively heated system, namely diameter, frequency, and electrical resistivity.

While it will be shown that, for scale-up purposes, this relationship does not always
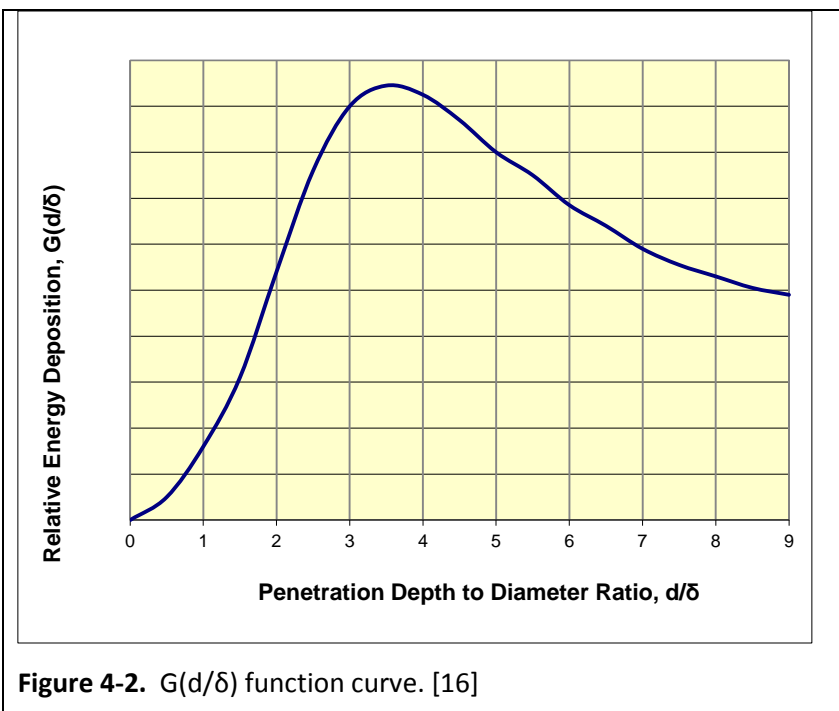
Figure 4-2. G(d/δ) function curve. [16]

produce the optimal operational parameters, it does provide a reasonable starting point for design of most systems below about 50 cm in diameter, and is particularly valid for very small systems in the 2 cm to 10 cm diameter range.

4.1.2. Initial Drain Design Concepts and Modelling – 27 MHz Heating Effects

This background provides the basis for the initial designs that were modelled and investigated to understand the overall feasibility of the concept, as well as to evaluate effects of certain parameters.

The first evaluation made was to determine the effect of a cooled draining system on the overall temperature characteristics (both distribution and maximum) of the molten volume. Figure 4-3 and Figure 4-4 show comparisons of model results for a CCIM without and with a drain assembly. No energy was applied to the drain inductor. Although the images appear to represent different conditions, closer inspection reveals that the temperature characteristics throughout the bulk of the molten volume are similar. The maximum temperature is less than 4% lower, although the temperature above the throat of the drain is significantly lower (i.e. 500°C), as expected. The contrast in the appearance of the profiles is due to the differences in the temperature color gradation in ANSYS®. This is primarily due to the broader temperature range in the melt volume.
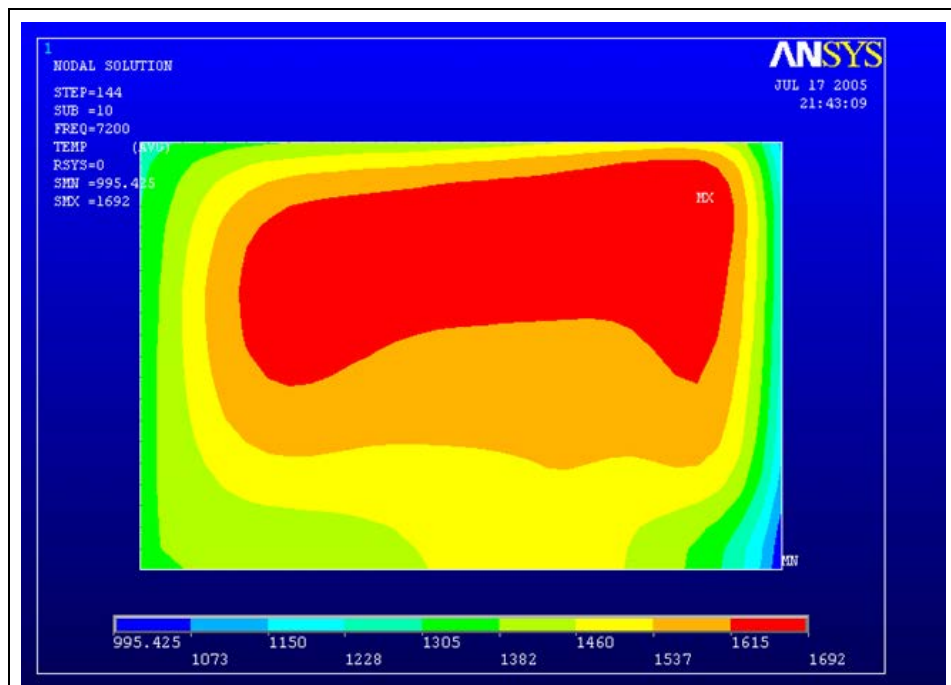
Figure 4-3. Temperature distribution without drain assembly.
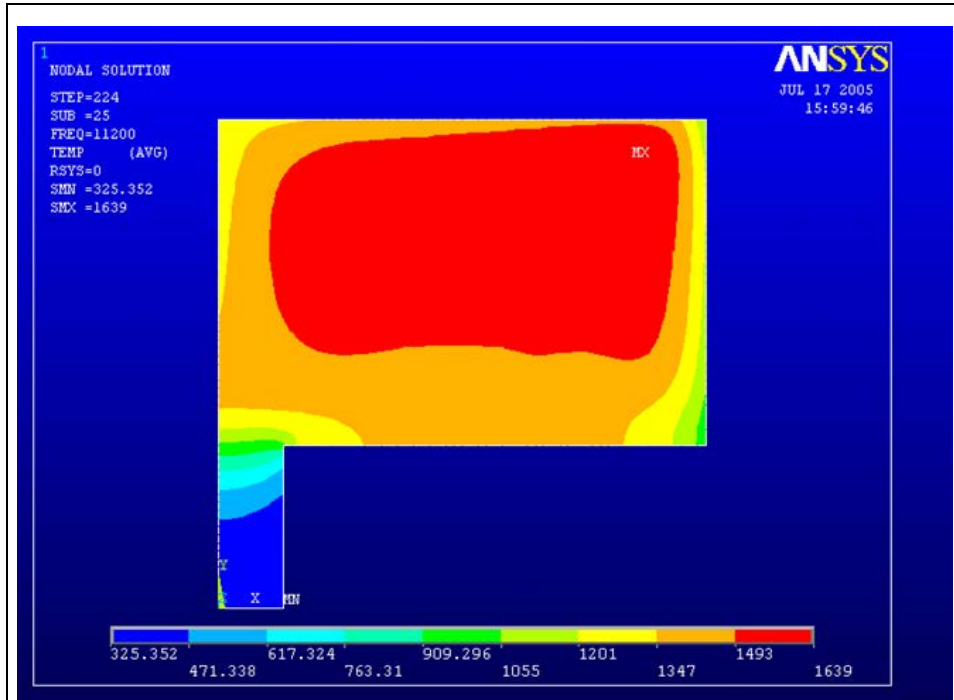
Figure 4-4. Temperature distribution in the drain volume.
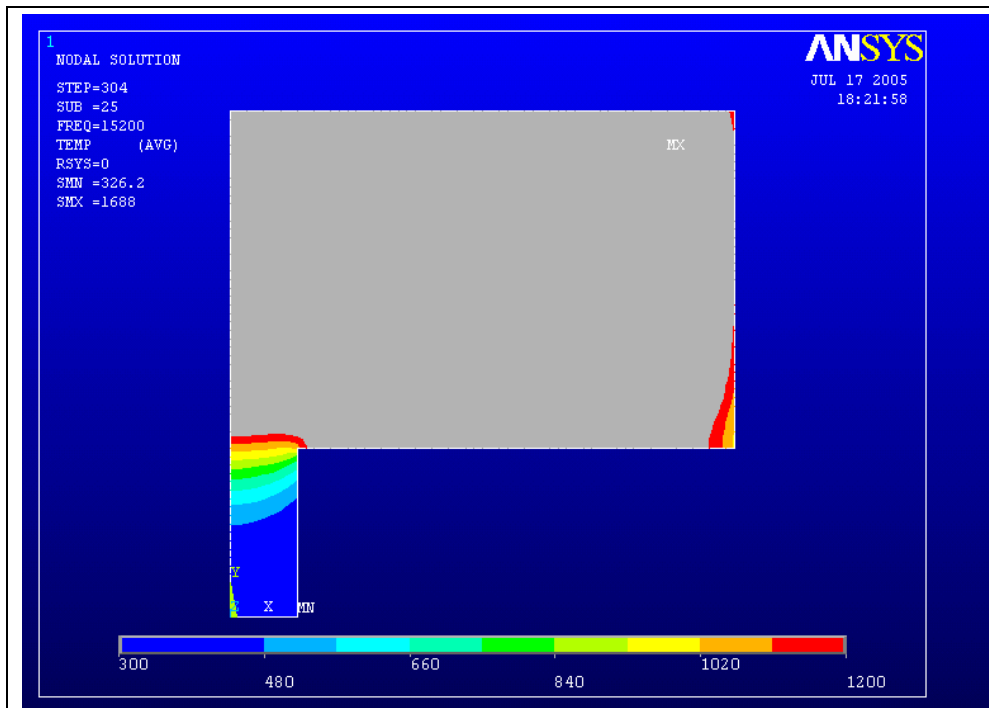
Figure 4-5. Temperature distribution in the drain volume.

Figure 4-5 provides better resolution of the temperature distribution within the drain. This is a steady state result and shows that at normal operating temperatures the open drain would never melt through and leak without added power. For these model runs, the primary frequency was 1.76 MHz, the drain inductor frequency, when used, was 27 MHz, the melt volume was 30 cm in diameter and 10 cm deep. The melter crucible was set at 45 cm height, the primary inductor was modelled with two turns on a 36 cm diameter, with the height of each turn at 4 cm and the distance set at 2.5 cm. The drain geometry was set at 3 cm in diameter and 5 cm deep. The initial model included only one turn on the drain inductor with a 6 cm diameter, height of each turn at 8 mm, located 1 cm from the bottom of the melter. Based on the results from investigation of a conical bottom geometry, discussed below, a second investigation was conducted using a two-turn drain inductor.

Because the glass used in this research has a very high electrical resistivity, ρ_e, the minimum temperature, and thus the maximum ρ_e, that would couple with the induction field and establish, propagate, and maintain a melt volume had to be determined. This was accomplished using the model and the same geometry and parameters used in the prior investigation. The drain inductor geometry effects were evaluated using both a single turn coil and two-turn coil.

The boundary and initial conditions (i.e. specific heat losses, power levels, etc.) were determined primarily from experimental values obtained using calorimetry. The heat loss from the side walls was set at 16 W/cm^2, the bottom surface heat loss was set at 1 W/ cm^2, and heat loss from the top was set at 7 W/ cm^2. Later models used more refined temperature-dependent boundary conditions for conduction and radiation heat transfer. This approach was used for initial investigations to keep these scoping studies simpler with quicker convergence.

The approach was to set the electrical resistivity at a constant value that correlates to a specific temperature. This will determine the minimum temperature that must be reached in the area above the drain throat to ensure that the electromagnetic field would couple with the glass sufficiently to propagate the melt into the drain body. Note that these evaluations were conducted using only the electrical and thermal calculation blocks since the primary area of interest is directly above the drain throat. Figures 4-6 through 4-10 illustrate the results for a single turn drain inductor with the electrical resistivity values set at those equal to 200°C, 373°C, 573°C, 673°C, and 773°C, respectively. These values were determined from the curve fit equation 2-27 presented in Section 2.1.4, which is repeated below:

$$\rho_e(T) = e^{\left(-0.91956 + \frac{1739.58}{T - 375.613}\right)} \qquad \text{(electrical resistivity)} \qquad (2-27)$$
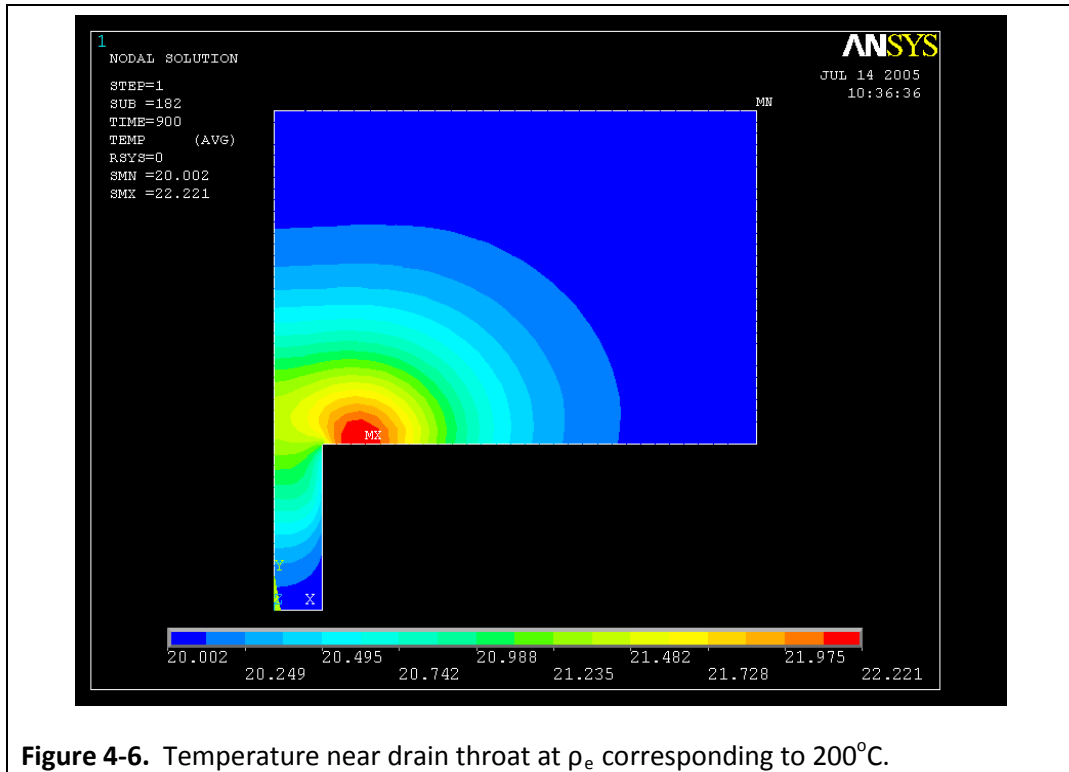
Figure 4-6. Temperature near drain throat at ρ_e corresponding to 200°C.
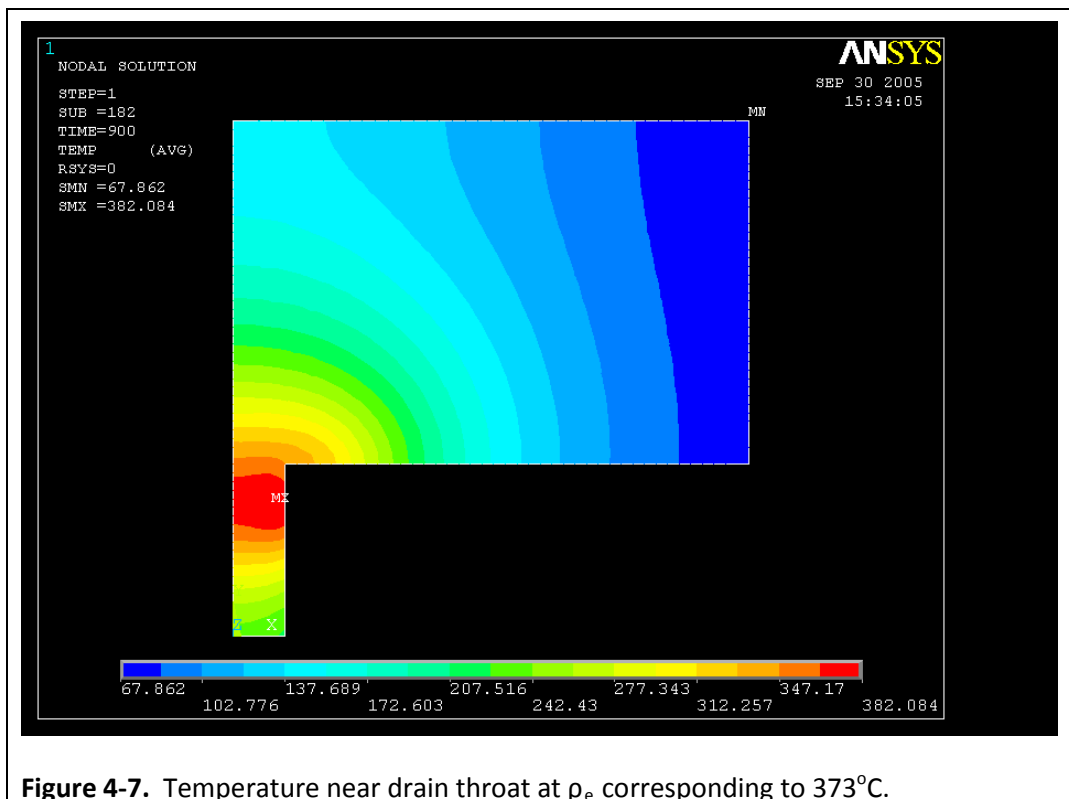
Figure 4-7. Temperature near drain throat at ρ_e corresponding to 373°C.
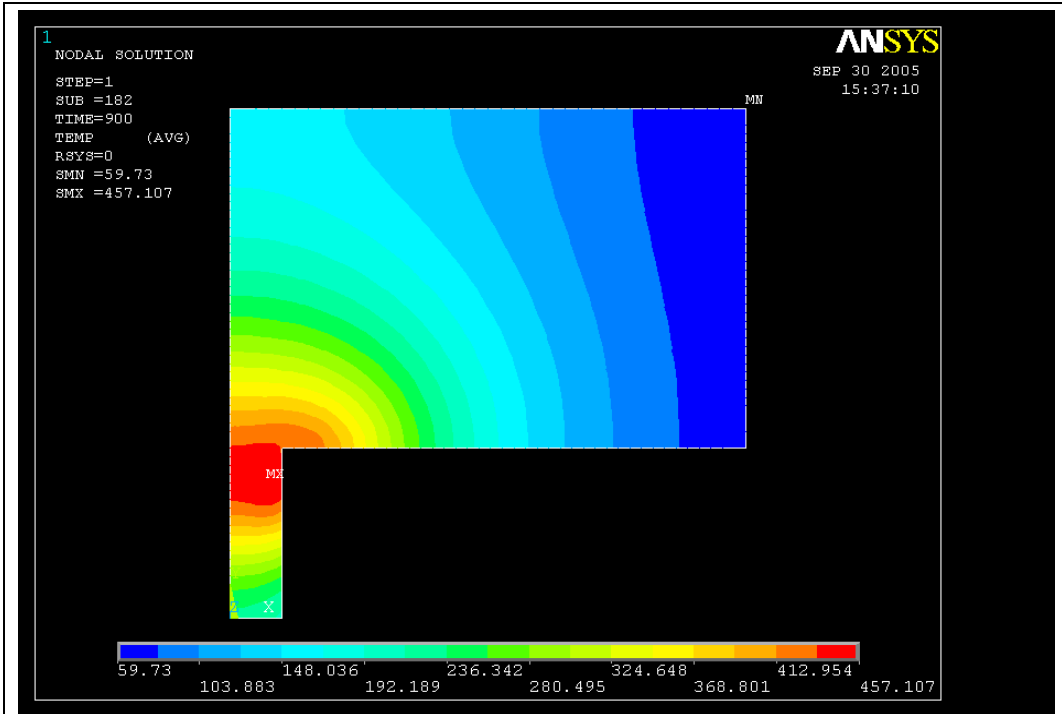
Figure 4-8. Temperature near drain throat at ρ_e corresponding to 573°C.
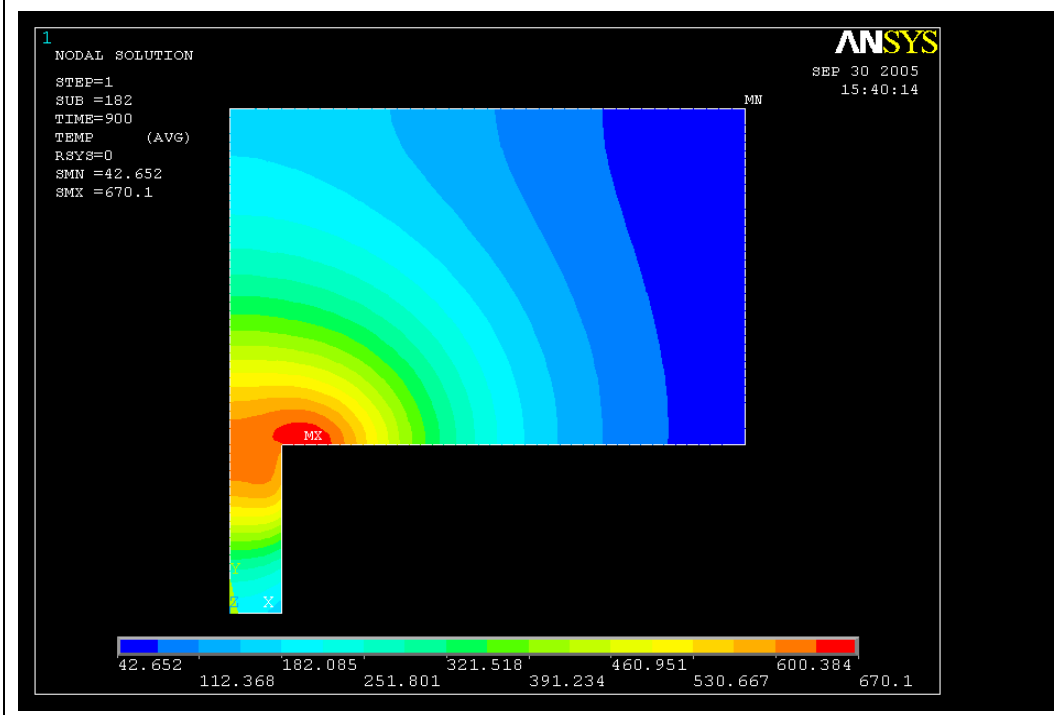
Figure 4-9. Temperature near drain throat at ρ_e corresponding to 673°C.

Figure 4-10. Temperature near drain throat at ρ_e corresponding to 773°C.
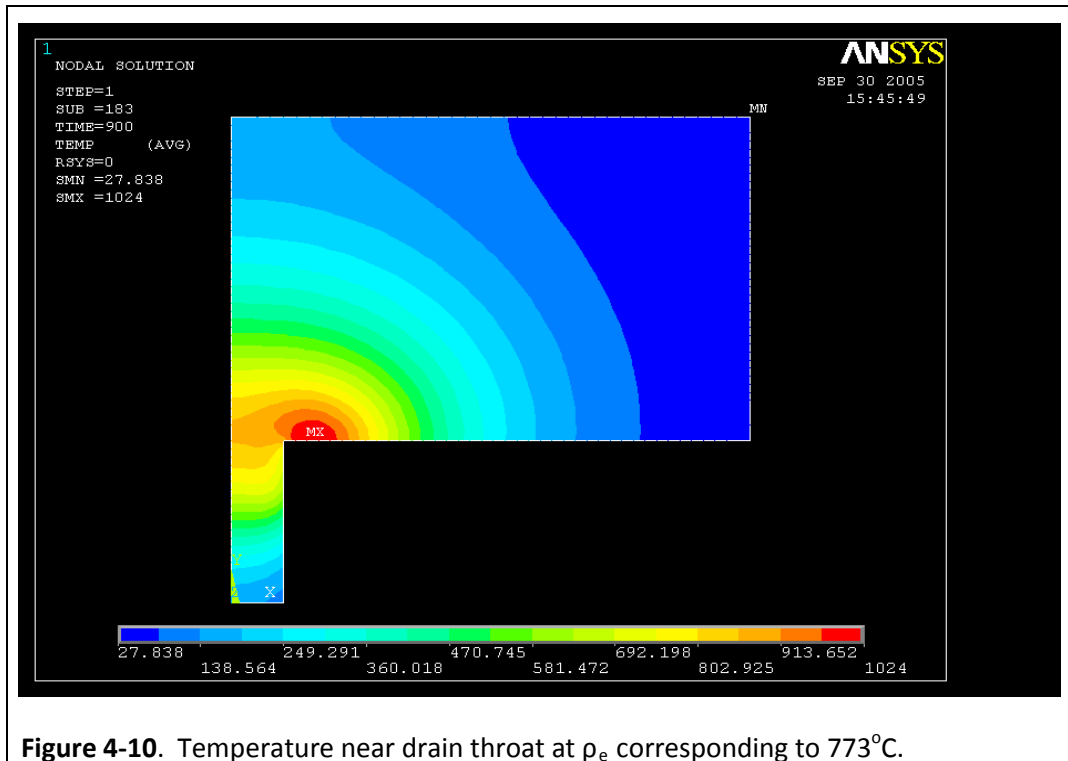
These figures clearly demonstrate that the glass temperature above the drain throat must be near773^{o}C to allow effective coupling of the electromagnetic field to the glass, such that a draining process can be initiated; however, the ceramic bottom is also being heated up significantly. This phenomenon was demonstrated experimentally in testing discussed earlier.

Similarly, an investigation was conducted to evaluate the effect of a two-turn drain inductor. These results are shown in Figures 4-11 through 4-16, correlating to the electrical resistivity value for 200°C, 373°C, 573°C, 673°C, 773°C, and 873°C. For this evaluation all model parameters were the same as the previous calculations; however, the drain inductor coil included a second turn that was spaced 4 mm from the upper turn, and the distance from the upper turn to the bottom of the crucible was increased to 20 mm. This was done because the prior modelling indicated that overheating of the bottom could occur, since this configuration is based on a non-cooled ceramic bottom (i.e. correlating to 1 W/cm^2). Later studies were conducted for water-cooled metallic bottom crucibles, which have different boundary conditions.

These results illustrate that, while the total power level was kept constant at 4 kW, the two-turn inductor provided much better heating within the drain body, yet producing similar temperature distribution results above the drain throat at about the same temperatures. While early testing
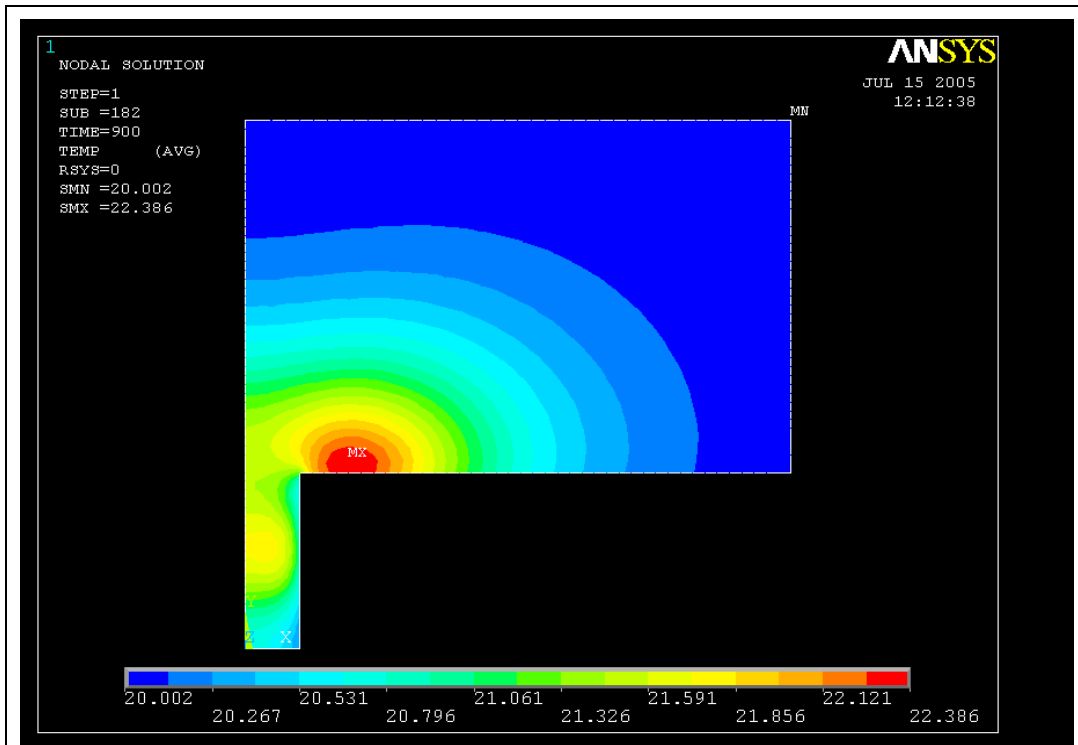
Figure 4-11. Temperature near drain throat at ρ_e corresponding to 200°C (two-turn coil)
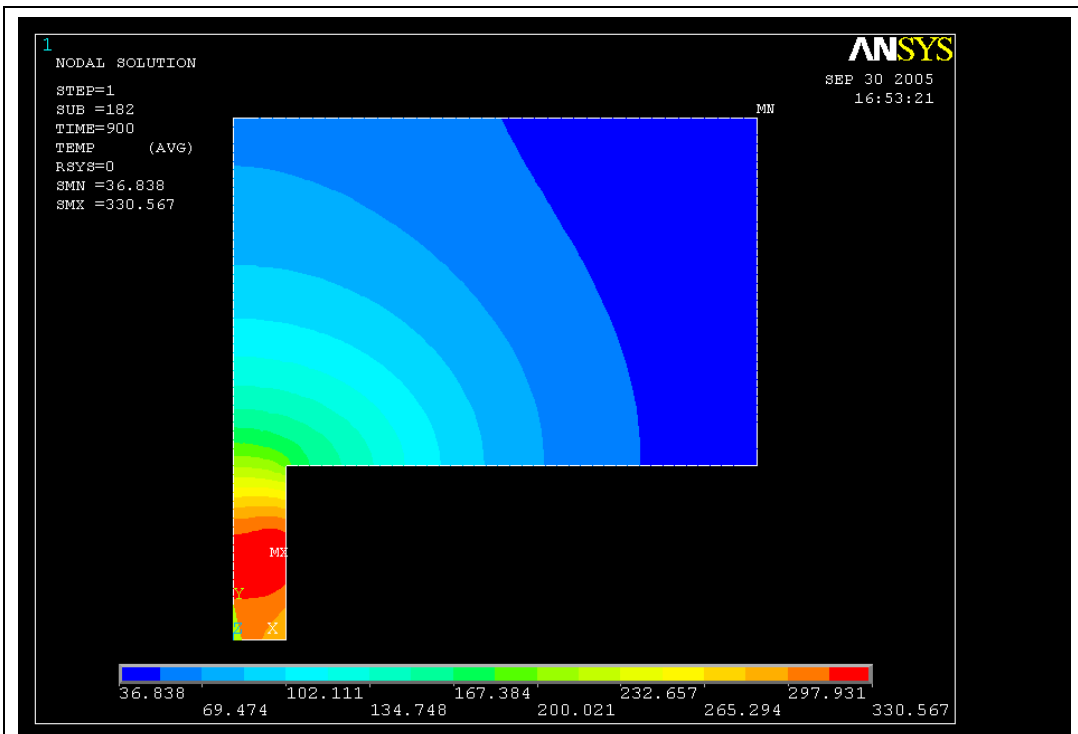
Figure 4-12. Temperature near drain throat at ρ_e corresponding to 373°C (two-turn coil)
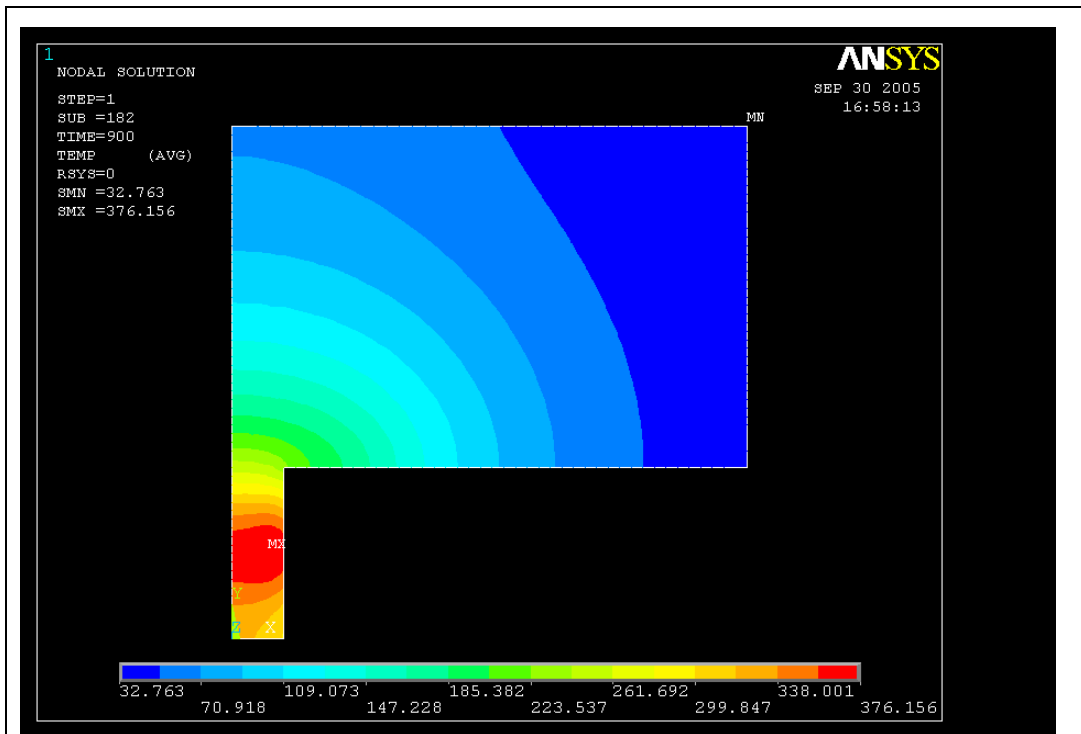
Figure 4-13. Temperature near drain throat at ρ_e corresponding to 573°C (two-turn coil)
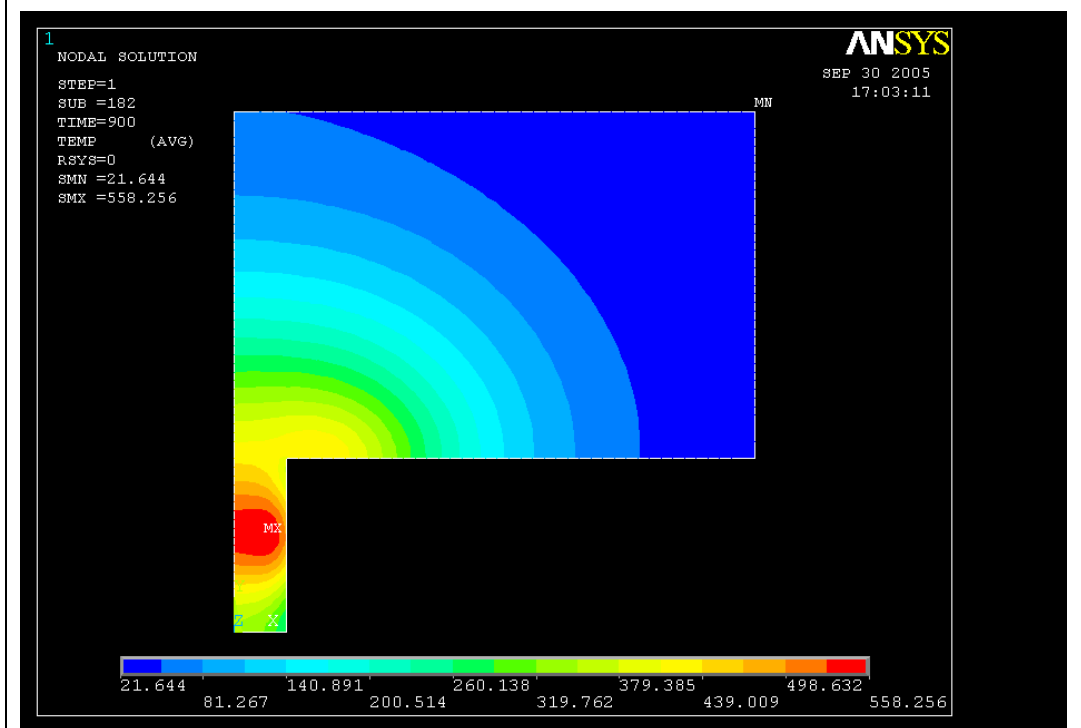
Figure 4-14. Temperature near drain throat at ρ_e corresponding to 673°C (two-turn coil)
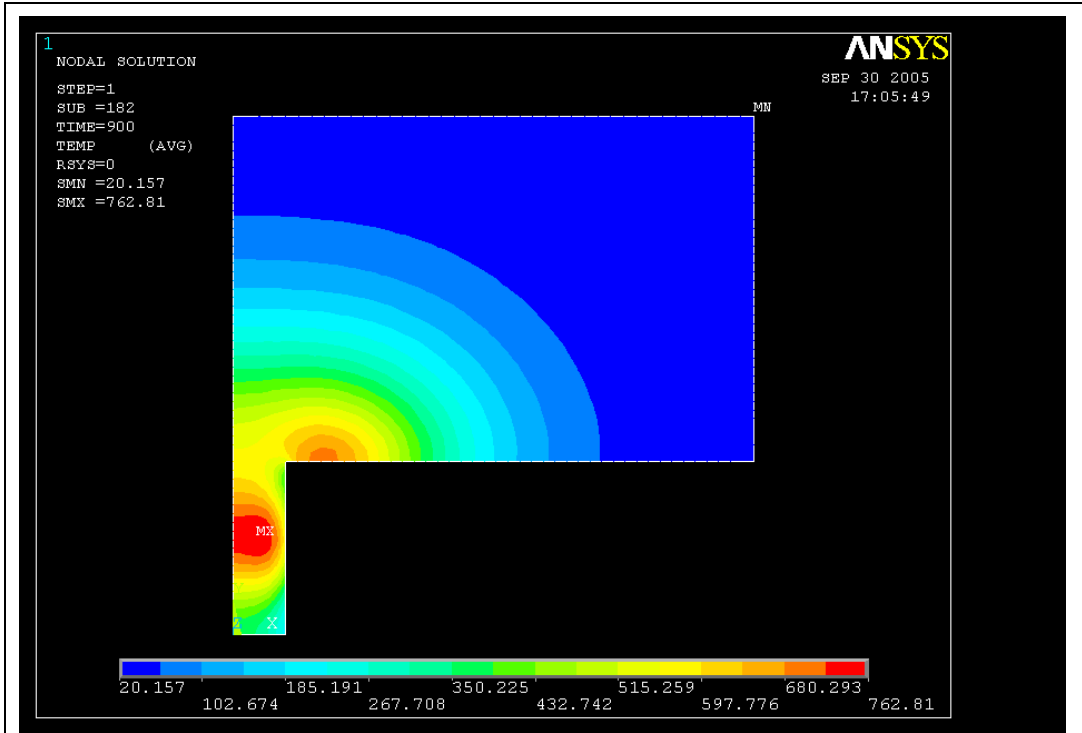
Figure 4-15. Temperature near drain throat at ρ_e corresponding to 773°C (two-turn coil)
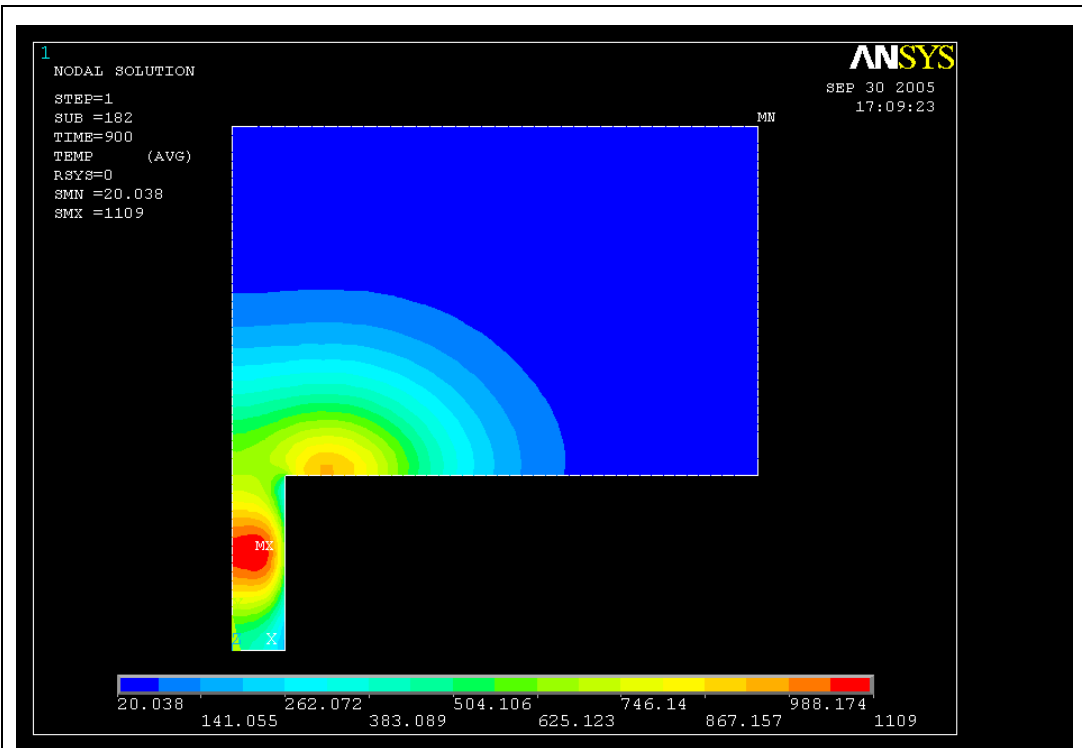
Figure 4-16. Temperature near drain throat at ρ_e corresponding to 873°C (two-turn coil)

used a single turn drain inductor, based on these results, later testing and the final proposed configuration uses a two-turn coil (planar), as well as the ability to be translated during different processes. As was indicated earlier, the modelling and experimental efforts were closely coupled in an iterative process. More discussion on these efforts is included in subsequent chapters.

 4.1.3.Initial Drain Design Concepts and Modelling – Conical Design

The next investigation conducted using the model was focused on the overall shape of an integrated CCIM system with an inductively heated draining device. This study was focused on the bottom configuration of the melter system. Specifically, the concept of a conically shaped crucible bottom with an integrated drain was investigated for feasibility. The evaluation was based on nominal geometry for a system of this size (i.e., 30 cm diameter). The boundary and initial conditions (i.e., specific heat losses, induction power levels, etc.) were based on experimental values determined using calorimetry. Heat losses from the side of the crucible were set at 14 W/cm^2 and the losses in the drain assembly were set at 30 W/cm^2. The nominal power in the drain was established at 4 kW. This value was determined mathematically based on the volume of glass in the drain body and the specific heat of the glass, which was later demonstrated to be insufficient.

This investigation was conducting using only the electrical and thermal blocks of the model for simplicity to specifically evaluate the effect of heat deposition on the configuration of the induction coil. Figures 4-17 through 4-20 illustrate the effects of the maximum temperature and its location due to the geometry of the induction coil, all other parameters being the same. Figure 4-17 illustrates a three-turn coil with all turns energized. Notice that the maximum temperature is at 1,476^{o}C and, as expected, is located in the center of the drain body.

In comparison, Figures 4-18 through 4-20 show the relative effects of a single turn energized. The top, middle, and bottom turn is individually energized in these figures, respectively.

While this model does not account for all of the temperature dependent properties, or the hydrodynamic effects, it does provide a qualitative evaluation of the induction coil geometry effects coupled with a conical bottom geometry. From this result, it is clear that the most effective induction coil design will include multiple turns and be located as close to the bottom of the crucible as possible. However, in either case, inadequate heating of the volume above the drain throat occurs to initiate coupling of the 1.76 MHz energy from the primary inductor for this configuration.

Nevertheless, the benefits of the location and use of multiple turns can be incorporated into a more conventional flat bottom design, which is easier to manufacture.

These features will have to be integrated with realistic geometry constraints such that an optimum configuration can be determined. As will be demonstrated later in this work, the optimal balance between drain geometry and inductor geometry resulted in a two-turn configuration. The iterative modelling and experimental process that resulted in this design is discussed in subsequent chapters.

The combined results of the model investigations, coupled with the initial analytical treatment, provided validation of the drain concept, in general, and helped identify key parameters required to develop an effective design. Based on these results, as well as the extensive effort expended in validation of the model, the model was then used to iteratively define and refine the drain geometry. These efforts are also described in detail in subsequent chapters.
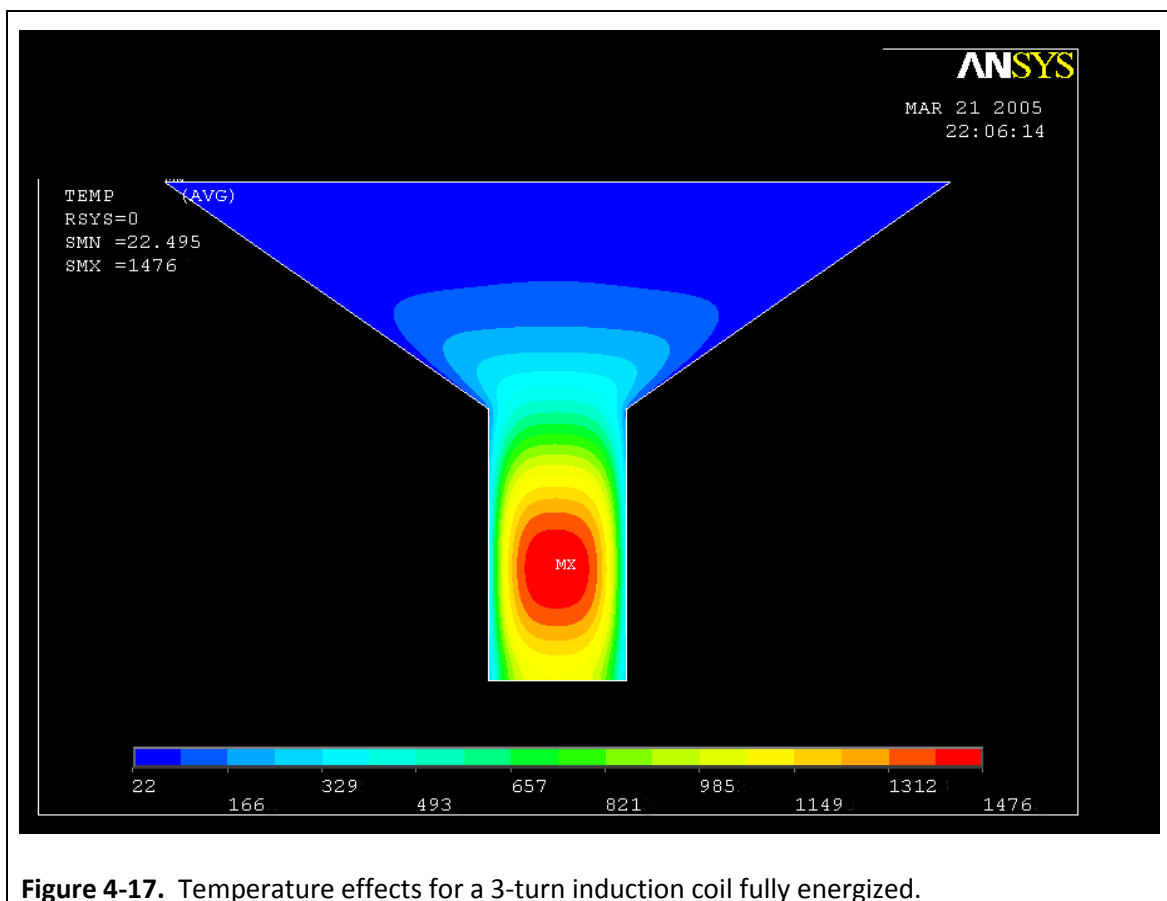
Figure 4-17. Temperature effects for a 3-turn induction coil fully energized.
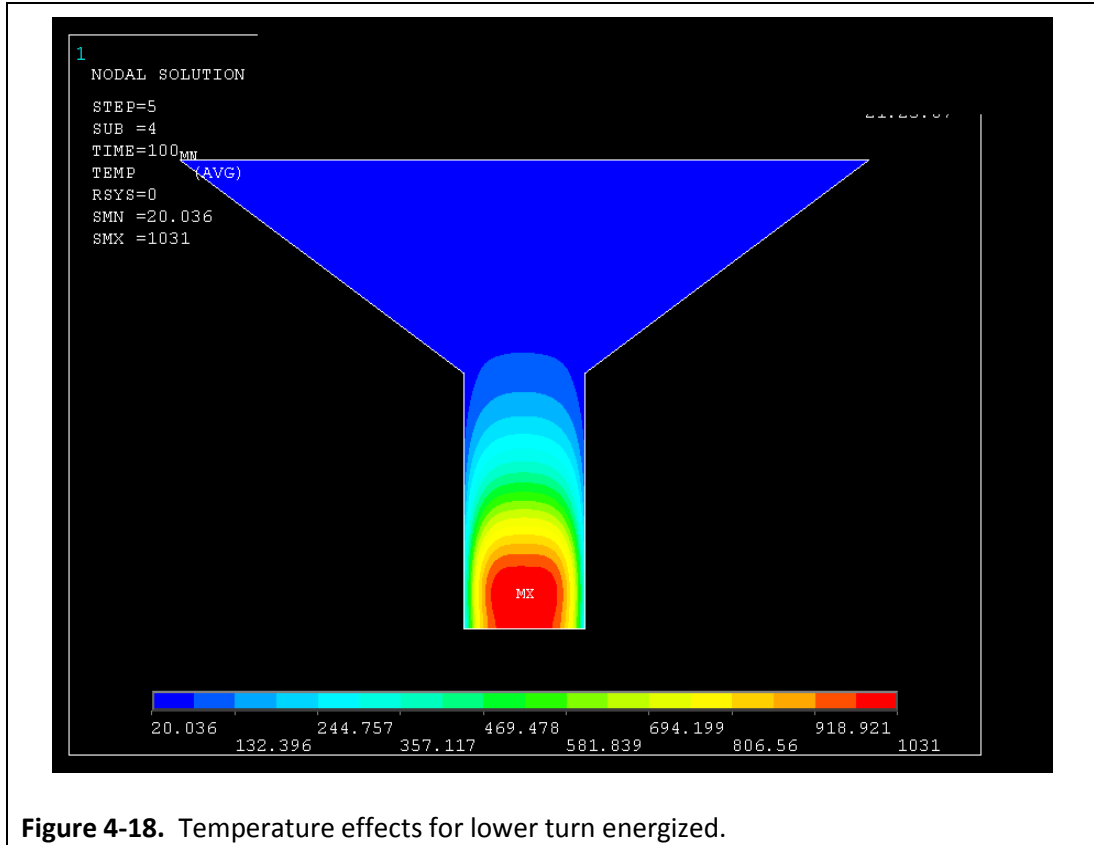
Figure 4-18. Temperature effects for lower turn energized.
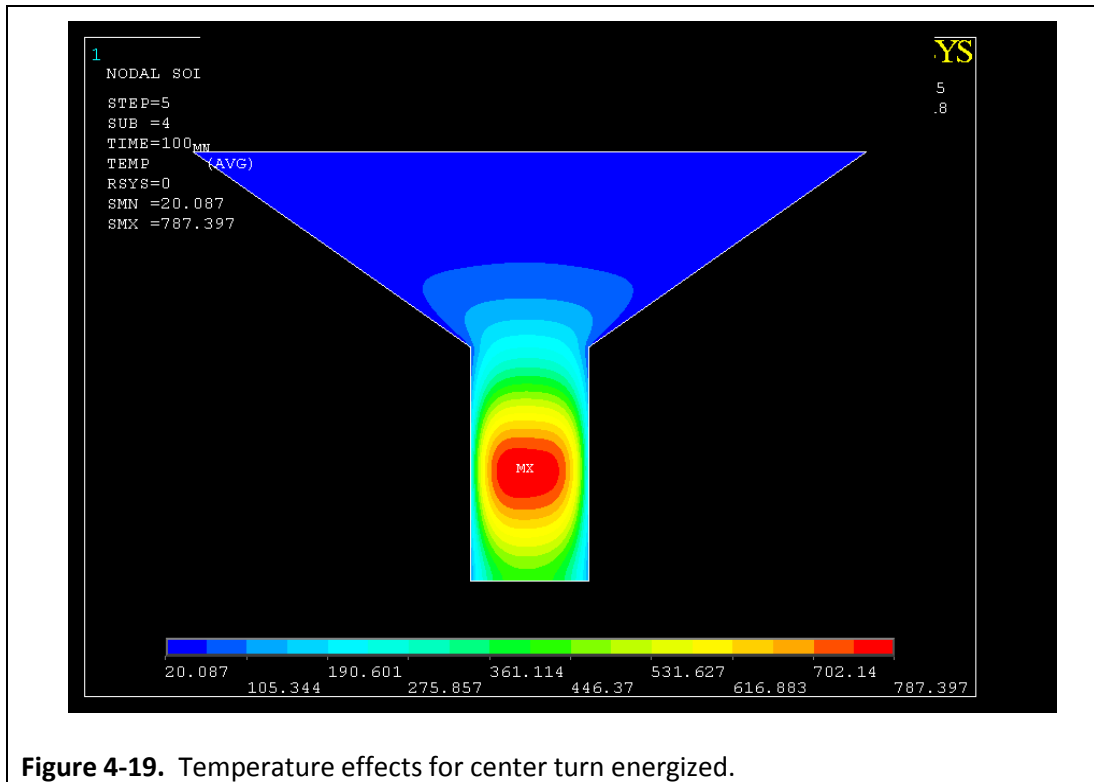
Figure 4-19. Temperature effects for center turn energized.

Figure 4-20. Temperature effects for upper turn energized.
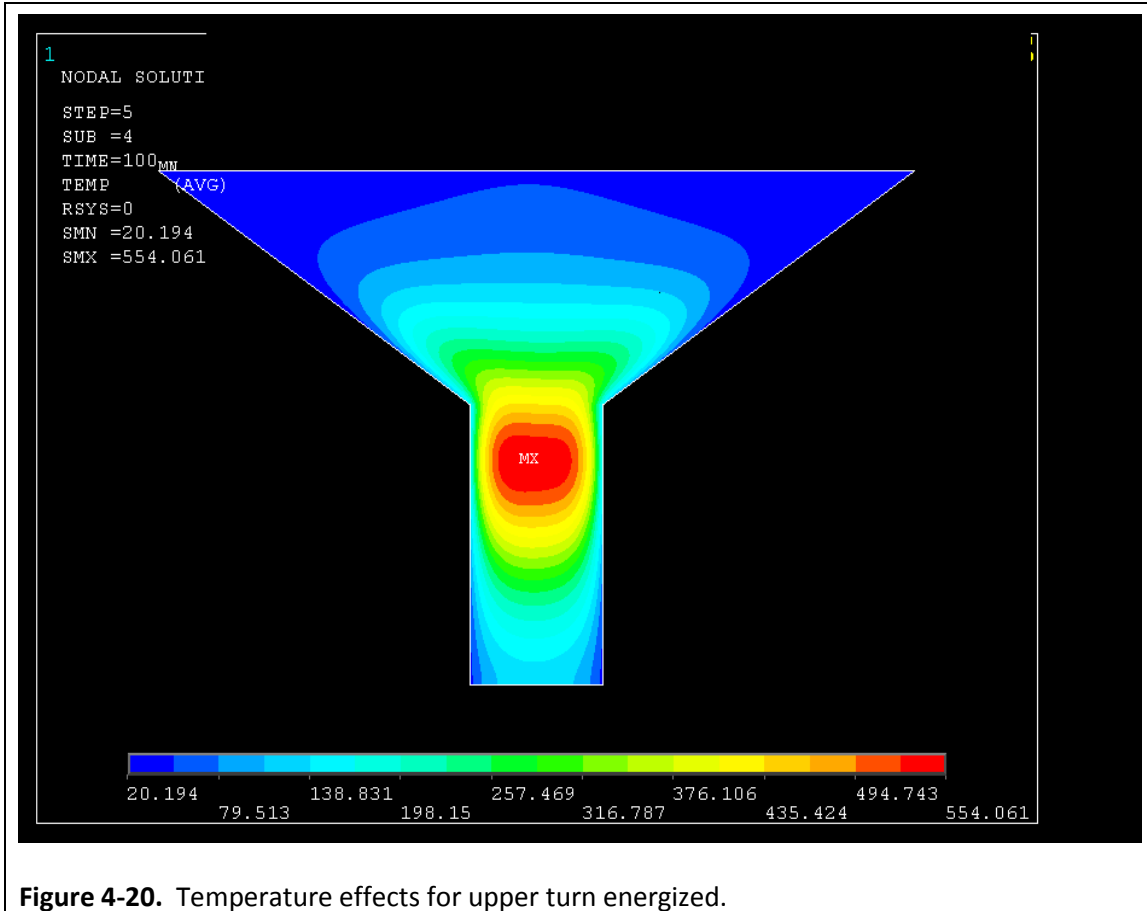
4.1.4. Initial Drain Design Concepts and Modelling – Heated Melt Pool Effects

The final scoping investigation conducted for the drain system parameters also used a simplified approach, only implementing the thermal and electrical calculation blocks. This effort was focused on understanding the effects on the temperature distribution above and within the drain body due to an idealized initial temperature distribution that roughly estimates the actual conditions. In this evaluation, the 1.76 MHz inductor is not energized, rather the temperature distribution simulates the effects of this process without the calculation complexity. Only the 27 MHz drain inductor is energized and the effects investigated. The temperature distribution approximation was obtained from experimental measurements. Figure 4-21 shows the initial condition for the temperature distribution in the molten glass volume. The results of this temperature distribution was compared to the base model in which the entire melt volume was assumed to be constant at 800°C (using a fixed value for electrical resistivity).

Figure 4-21. Initial temperature distribution used for evaluations.
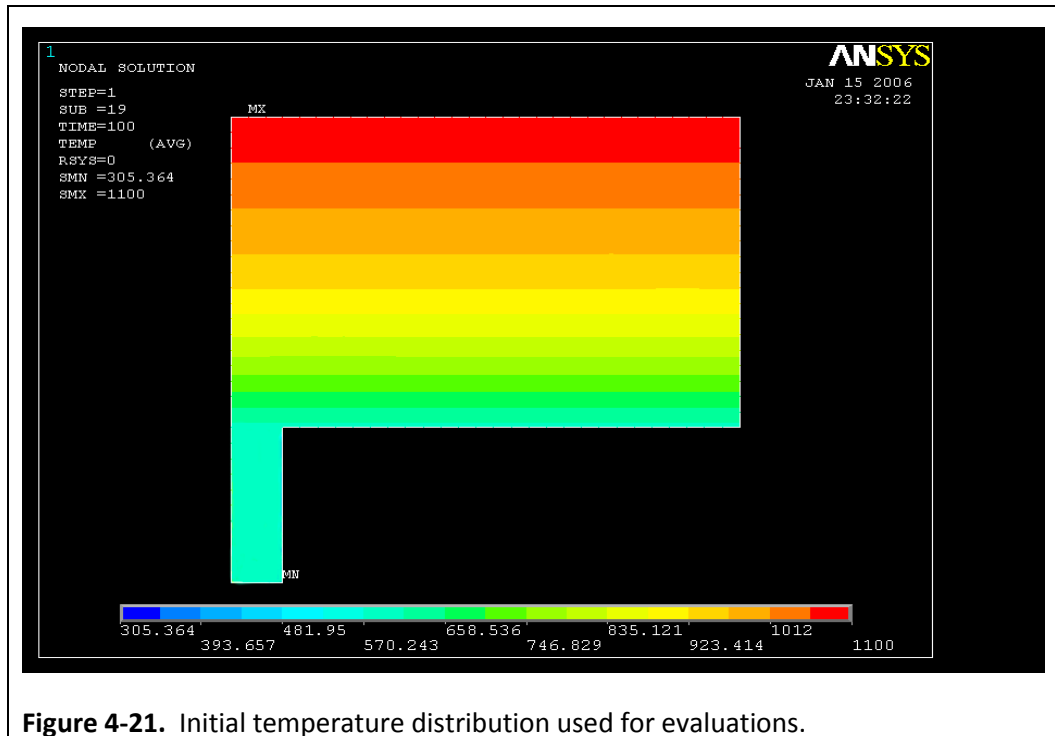
The following series of figures (Figures 4-22 through 4-26) show the comparison of the modeling results for the base case and the initial temperature distribution case.

As can be seen from these results, the system with the initial temperature distribution takes a little longer, but it eventually converges to the same steady state temperature distribution as the base case. (Note that for this investigation, the steady state is defined as the point at which the entire volume of glass within the drain is between 800°C and 900°C)

An important feature demonstrated by this analysis is that the draining process can be initiated with the 27 MHz induction energy at a lower temperature than originally shown. Observe that the temperature at the bottom in the second configuration is only about 600°C. This may also be an indication that operation of this draining approach will be easier to control, and more reliable than originally thought. This is primarily because the results indicate that it may not require such high temperatures near the bottom to initiate a draining. They also indicate that implementation of a water-cooled bottom into the design is likely feasible. Although, due to expediency, the initial testing was conducted on a melter system with a non-cooled refractory bottom However, these results are preliminary and experimental work in a test platform demonstrated otherwise.

Fixed temperature base case | Temperature distribution case
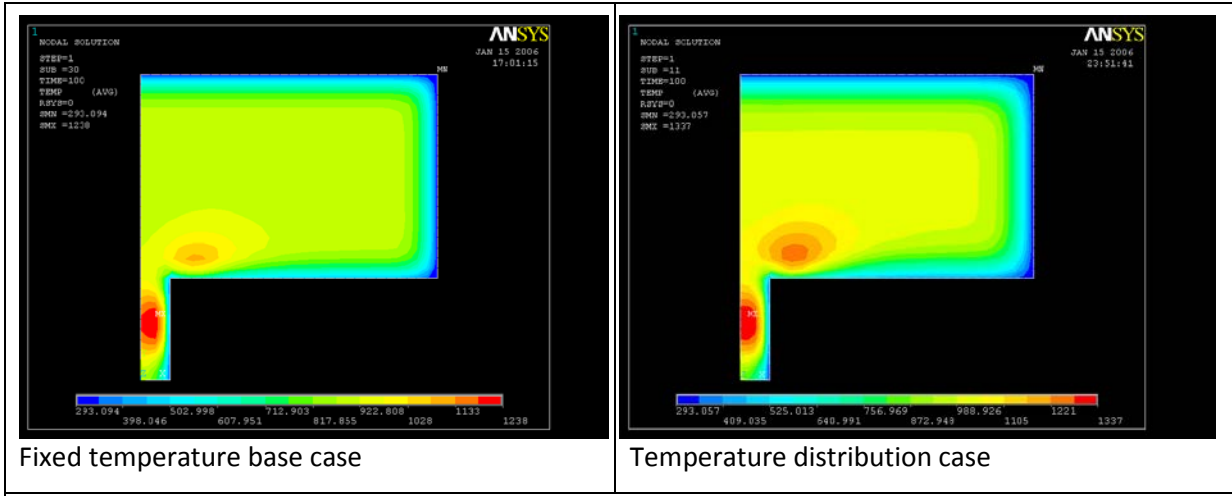
Figure 4-22. Comparison of temperature distributions after 100 seconds.

Fixed temperature base case | Temperature distribution case
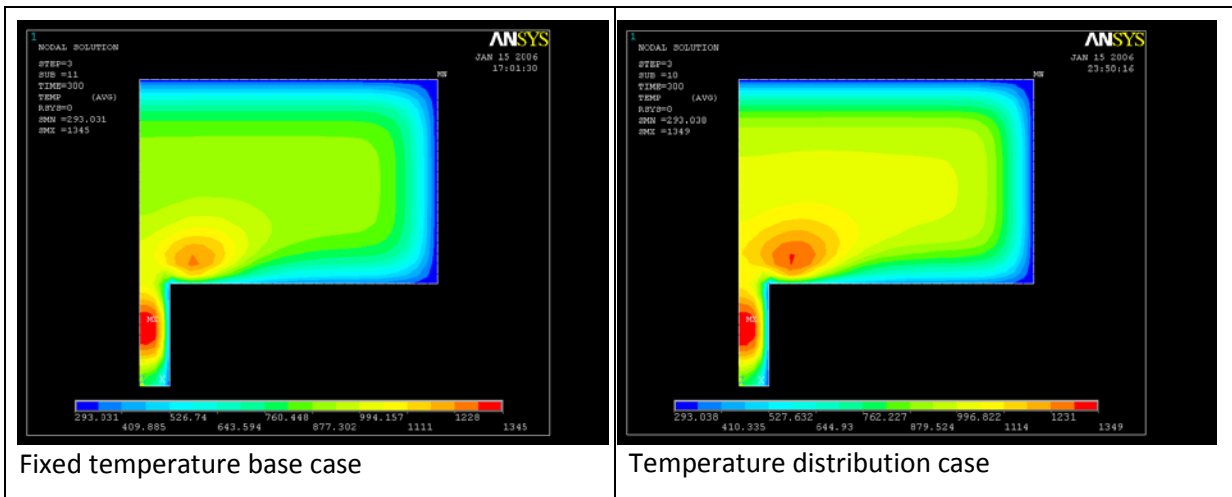
Figure 4-23. Comparison of temperature distributions after 300 seconds.

Fixed temperature base case | Temperature distribution case
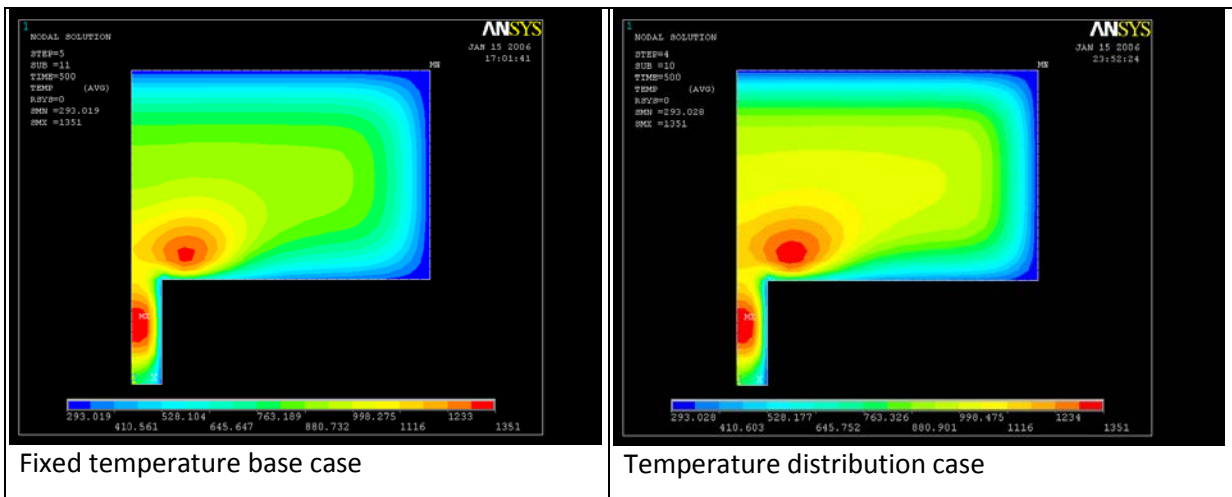
Figure 4-24. Comparison of temperature distributions after 500 seconds.

Fixed temperature base case	Temperature distribution case

Figure 4-25. Comparison of temperature distributions after 700 seconds.

Figure 4-26. Steady state temperature distribution after 800 seconds.
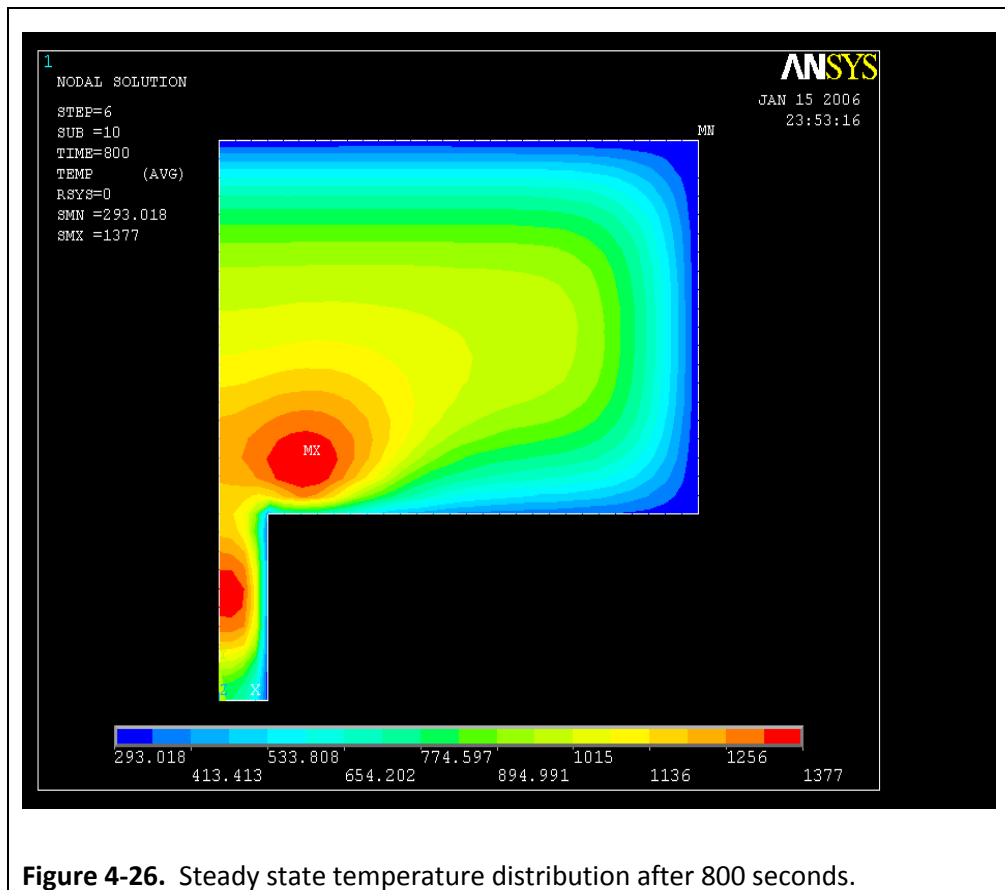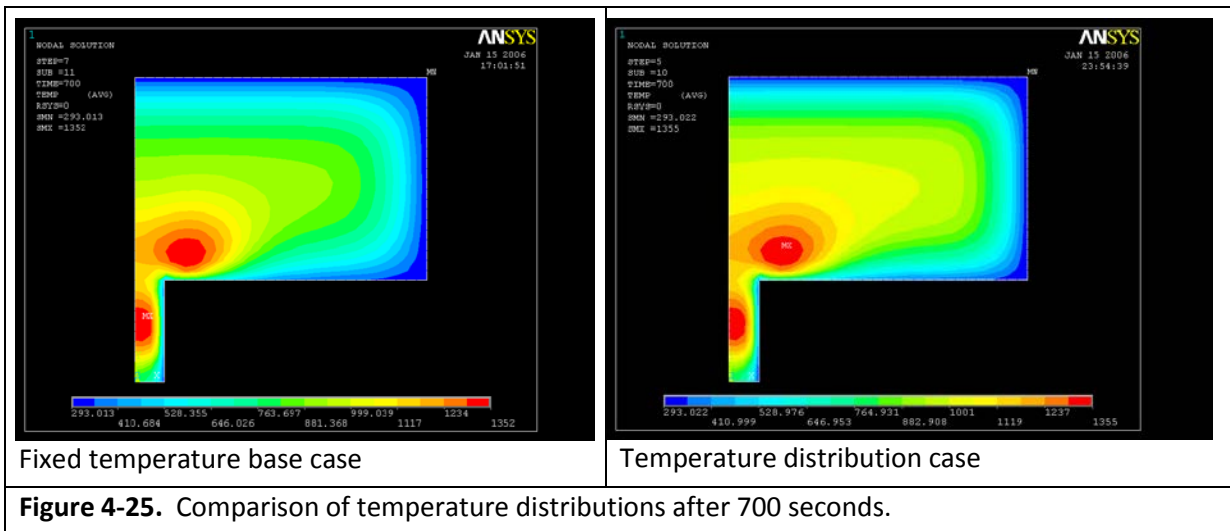
4.2. Drain System Geometry Optimization (Mathematical)

The evolution of the drain design proceeded through several iterations between mathematical modeling and experimental testing. This section discusses the mathematical investigations and

iterations of the design, based on application and enhancement of the validated model. Specifically, geometry changes and related boundary conditions, as appropriate were incorporated into the model; however, none of these changes required modifications to the basis of the calculations blocks, and thus the model results were still valid for these enhancements.

4.2.1.Effects of Water-Cooled Flange

The initial drain design included a water-cooled upper flange with a 15 cm diameter. An initial investigation of the drain geometry was to evaluate the effect of this cooled section on the overall temperature distribution, particularly near the bottom of the crucible, and within the drain body. The first evaluation was made using a fixed temperature of the melt volume of 800°C, and only the drain inductor was energized (i.e. 27 MHz inductor), using the thermal and electrical calculation blocks for simplicity (i.e., no hydrodynamic effects considered).

Figures 4-27 through 4-31 show the comparative modeling results of the base case (i.e. ceramic bottom with 1 W/cm^2 heat loss) with a variable heat loss coefficient along the bottom (i.e. 27 W/cm^2 along boundary of drain flange). These results show that, while additional time is required to achieve the same steady state condition as the base case, the volume within the drain is still heated adequately to initiate the draining process. This is an important observation because processing high temperature molten glass and ceramic products will require cooling of the drain assembly. While the exact configuration was not determined at this point in the work, this exercise clearly demonstrated the overall feasibility.

| Base case for constant heat loss along bottom | Variable heat loss along bottom |

Figure 4-27. Temperature after 100 seconds of calculation time.

| Base case for constant heat loss along bottom | Variable heat loss along bottom |

Figure 4-28. Temperature after 300 seconds of calculation time.

| Base case for constant heat loss along bottom | Variable heat loss along bottom |

Figure 4-29. Temperature after 500 seconds of calculation time

| Base case for constant heat loss along bottom | Variable heat loss along bottom |

Figure 4-30. Temperature after 700 seconds of calculation time.

Variable heat loss along bottom

Figure 4-31. Temperature after 900 seconds of calculation time.

Additional complexity to the model and analysis were subsequently implemented to better represent the actual melter/drain conditions, or at least closer to them. These are discussed as appropriate.

4.2.2. Effects of Thermal Gradient and Variable Boundary Conditions

The next investigation included increased complexity, and more closely approached the representative conditions within the melter volume. In this study, an initial condition with non-uniform temperature distribution (as illustrated in Figure 4-21, above) was coupled with the non-uniform heat loss coefficient along the bottom boundary. The functionality of the model to accurately represent this is important to being able to predict the glass melt condition in the area above the drain opening.

The results are shown in Figures 4-32 through 4-34. They indicate that, while even more time is required to achieve the desired steady state condition (i.e. 1,300 seconds versus 900 seconds), the important finding is that the system was still capable of increasing virtually the full volume within the drain body to temperatures above 800°C to 900°C. However, it is important to note that the overall electrical losses in the system, especially for the 27 MHz power source, are not fully accounted for in this analysis, as later testing demonstrated.
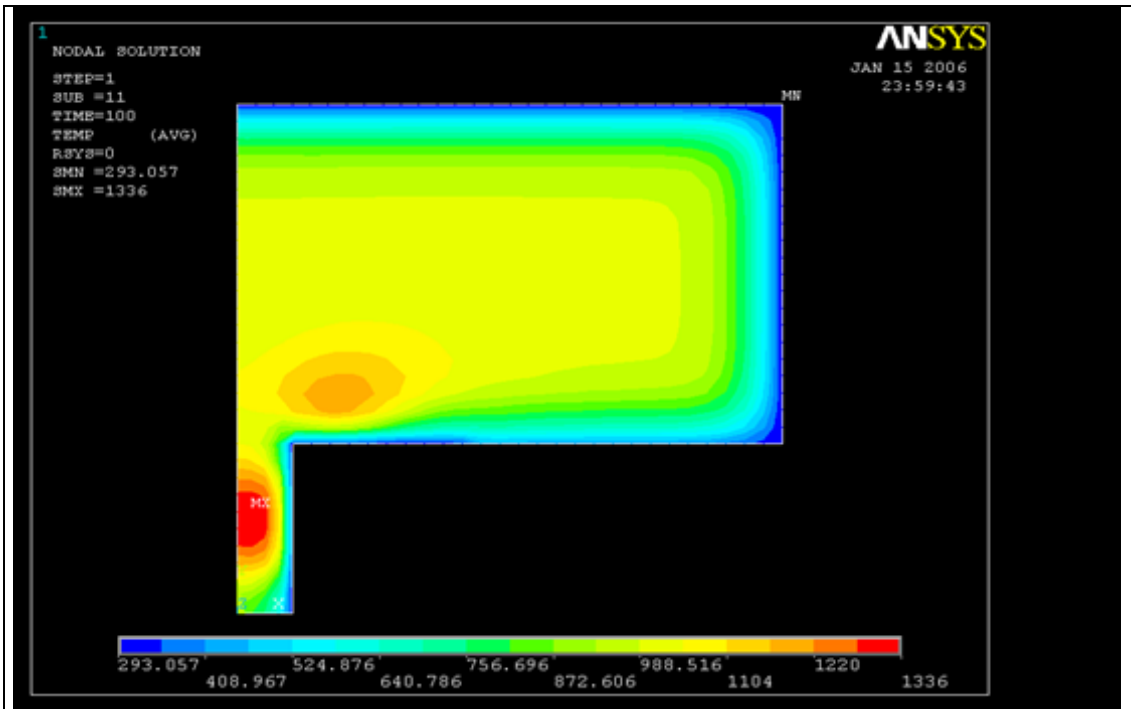
Figure 4-32. Thermal distribution after 100 seconds.
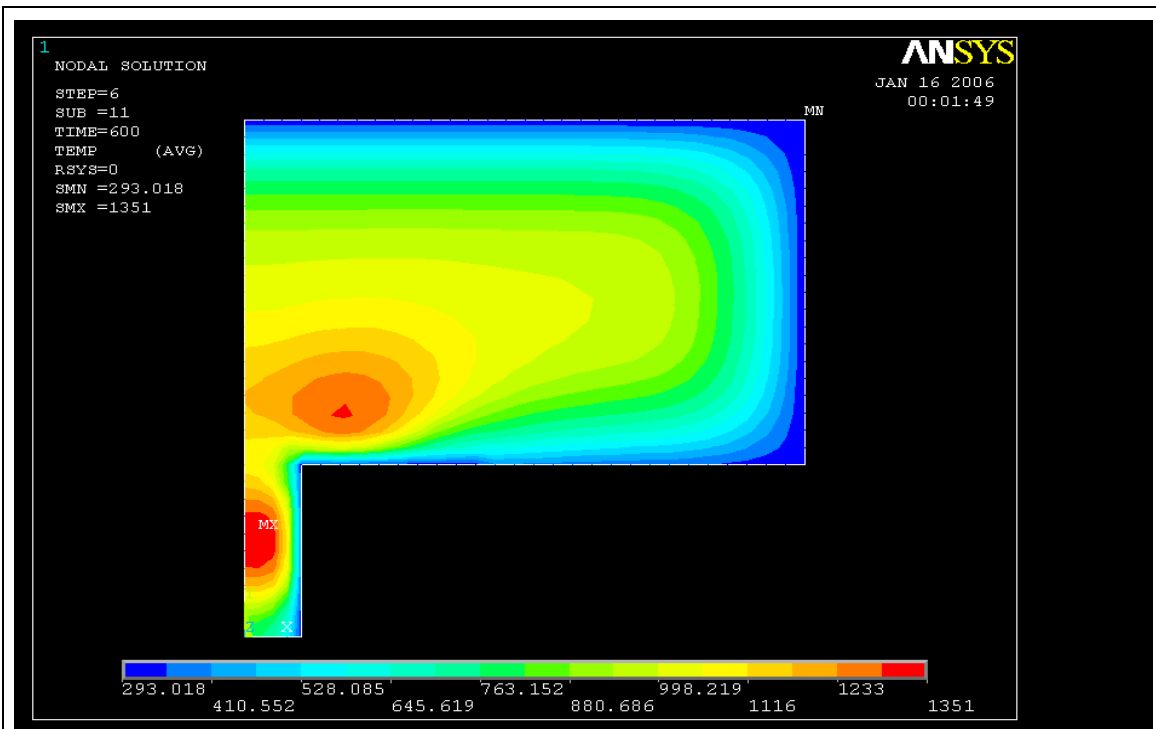
Figure 4-33. Thermal distribution after 600 seconds.
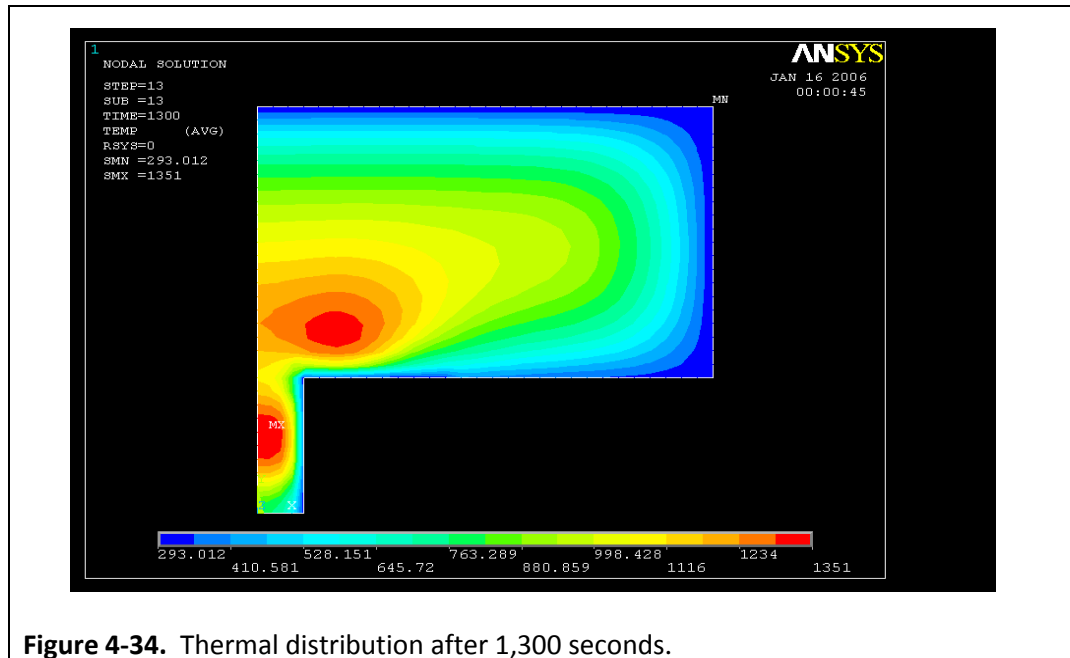
Figure 4-34. Thermal distribution after 1,300 seconds.

4.2.3.Basic Geometry Effects

The next investigations were focused on analysis of the effects of the drain geometry. This included the basic shape and size of the drain system, as well as the inductor geometry. These were all conducted using only the thermal and electrical calculation blocks. A fixed temperature of 800°C was used as the initial condition.

The first studies investigated the effects of changing the geometry of the drain from a right circular cylinder to conical shape. The base case is a 3 cm diameter by 5 cm long drain tube. Various configurations were considered including a 4 cm top diameter, a 5 cm top diameter, and a reduced bottom diameter of 2 cm. For all of these analyses, the drain length was held constant and a three-turn inductor was used. The primary purpose of these studies was to gain an understanding of the qualitative effects of the geometry changes. Figures 4-35 and 4-36 show the results for the 4 cm and 5 cm upper diameter drains, respectively.

These results demonstrate that the heating within the drain body is improved for the conical design, although additional power is required.

On the other hand, Figure 4-37 shows the results of reducing the bottom diameter to 2 cm. For this configuration, the glass within the drain body is not effectively heated using the same power level as for the other larger upper diameter designs.

Figure 4-35. 4 cm upper diameter after 700 seconds.

Figure 4-36. 5 cm upper diameter after 700 seconds.

Figure 4-37. 2 cm upper diameter after 700 seconds.
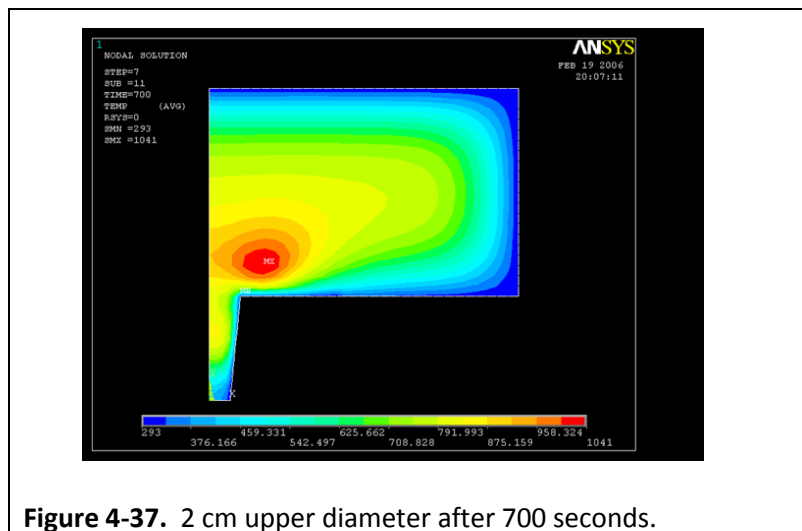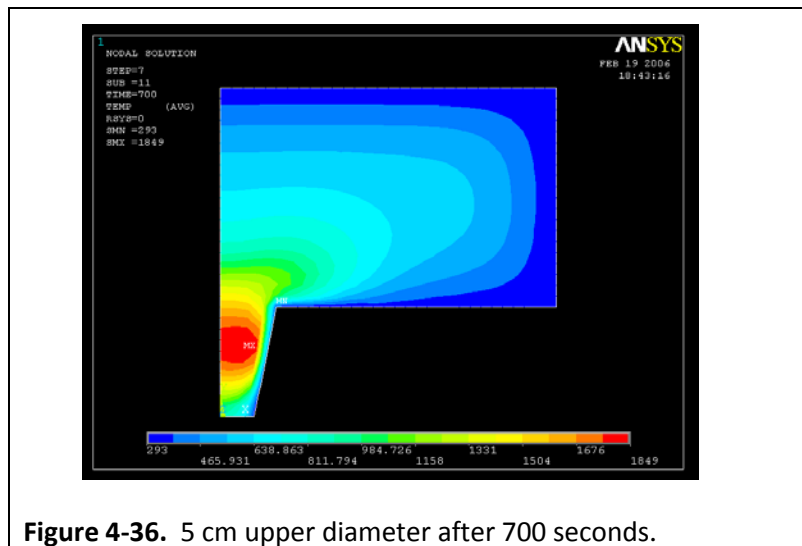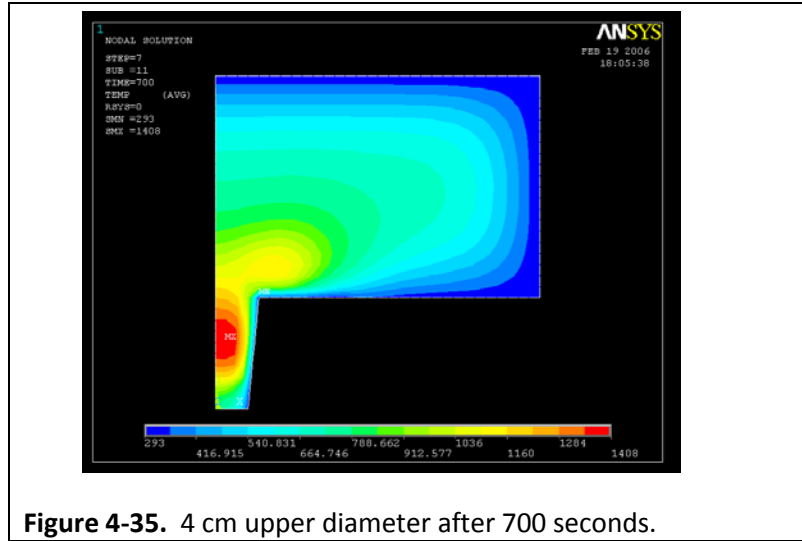
The general conclusion from these analyses is that the conical design provides an improved temperature distribution that is more amenable to initiating a draining process. However, the drain diameter should not be less that 3 cm diameter for the 27 MHz range induction system.

4.2.4. Effects of Fully Coupled Model (Hydrodynamic Effects with Dual Frequency)

The next step in the model application was to investigate the drain geometry with the fully coupled hydrodynamic, thermal, and electrical calculation blocks, using two induction sources (i.e. 1.76 MHz and 27 MHz), as well as the temperature dependent material properties. This feature is of significant importance and key to obtaining representative temperature distributions. Recall that earlier investigations used gradient temperature profiles as initial conditions. Figure 4-38 through Figure 4-40 demonstrates the dramatic effect of using a fixed value for electrical resistivity versus a temperature dependent property on the characteristics of the melt, including temperature and velocity profiles.

The initial dual frequency model application was an investigation of the conical drain geometry with a ceramic bottom crucible. Specifically, the drain had a 5 cm top diameter with a 3 cm bottom diameter and length of 5 cm, as in the previous model. The drain inductor was a single turn design with a 4 cm inside diameter with a 6 mm by 6 mm rectangular shape. These results are shown in Figures 4-41 and 4-42. Figure 4-41 shows the steady state temperature achieved by the 1.76 MHz

| ρ_e = constant (temperature is in Kelvin) | $\rho_e = \rho_e(T)$ (temperature is in Celsius) |

Figure 4-38. Temperature distributions.
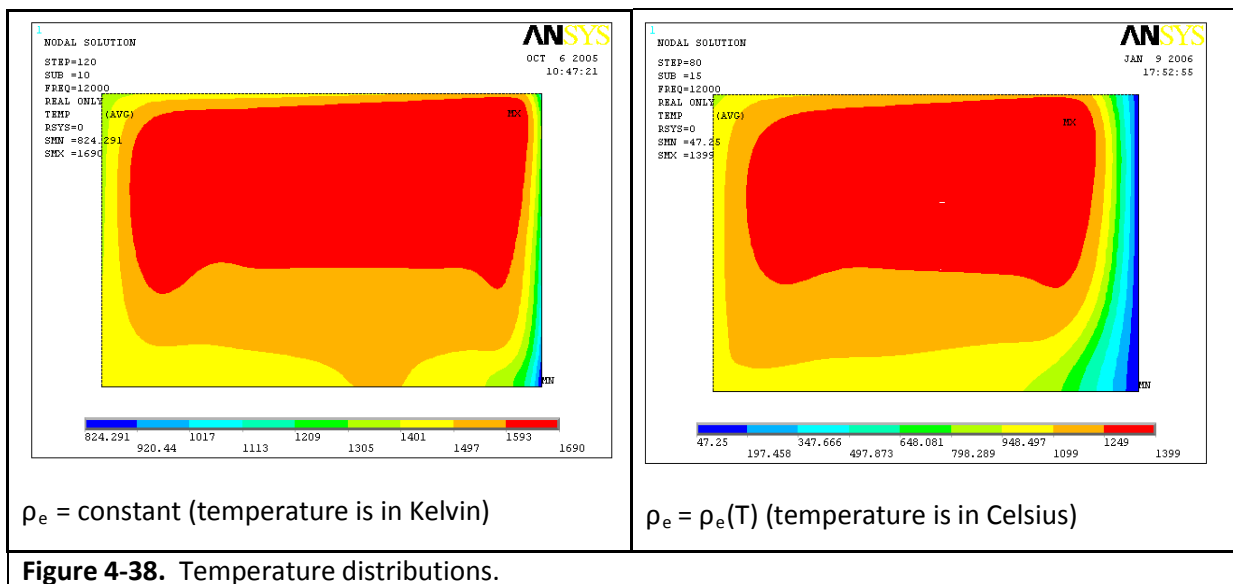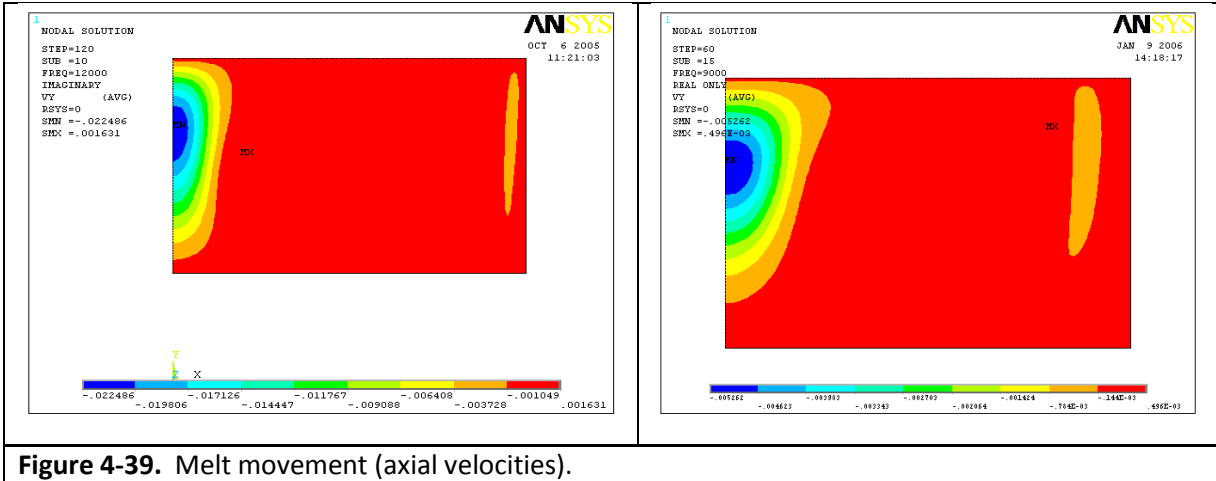
Figure 4-39. Melt movement (axial velocities).
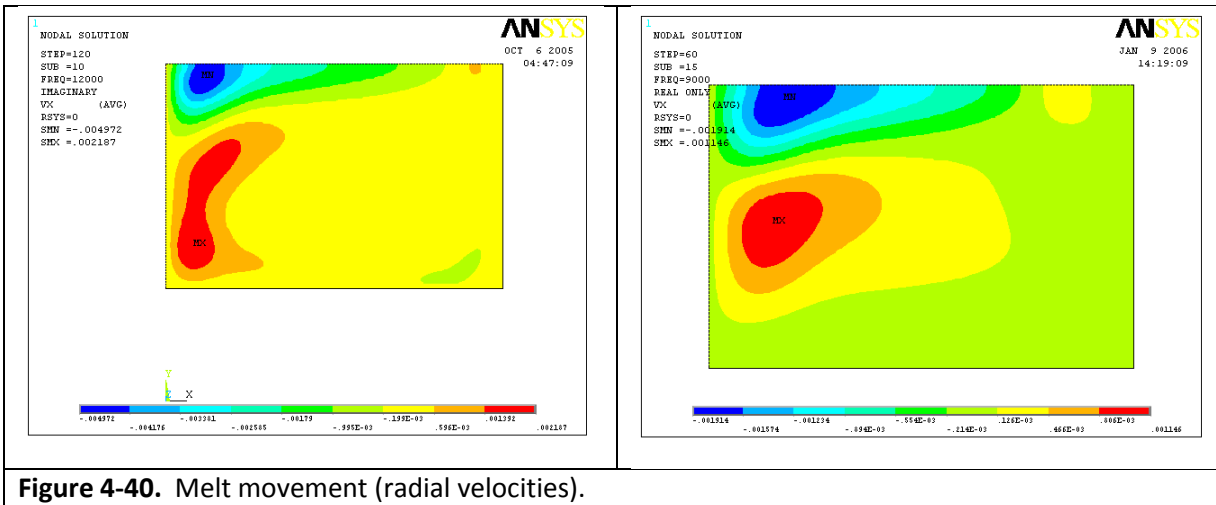
Figure 4-40. Melt movement (radial velocities).
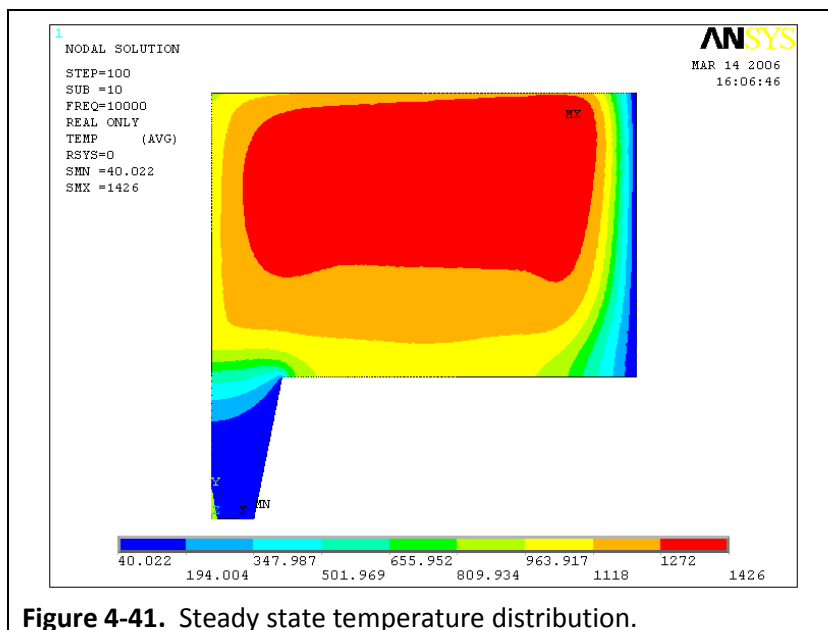
Figure 4-41. Steady state temperature distribution.

Figure 4-42. Temperature distribution due to drain inductor.

Figure 4-43. Steady state temperature distribution (cooled drain flange).

Figure 4-44. Temperature distribution due to drain inductor.
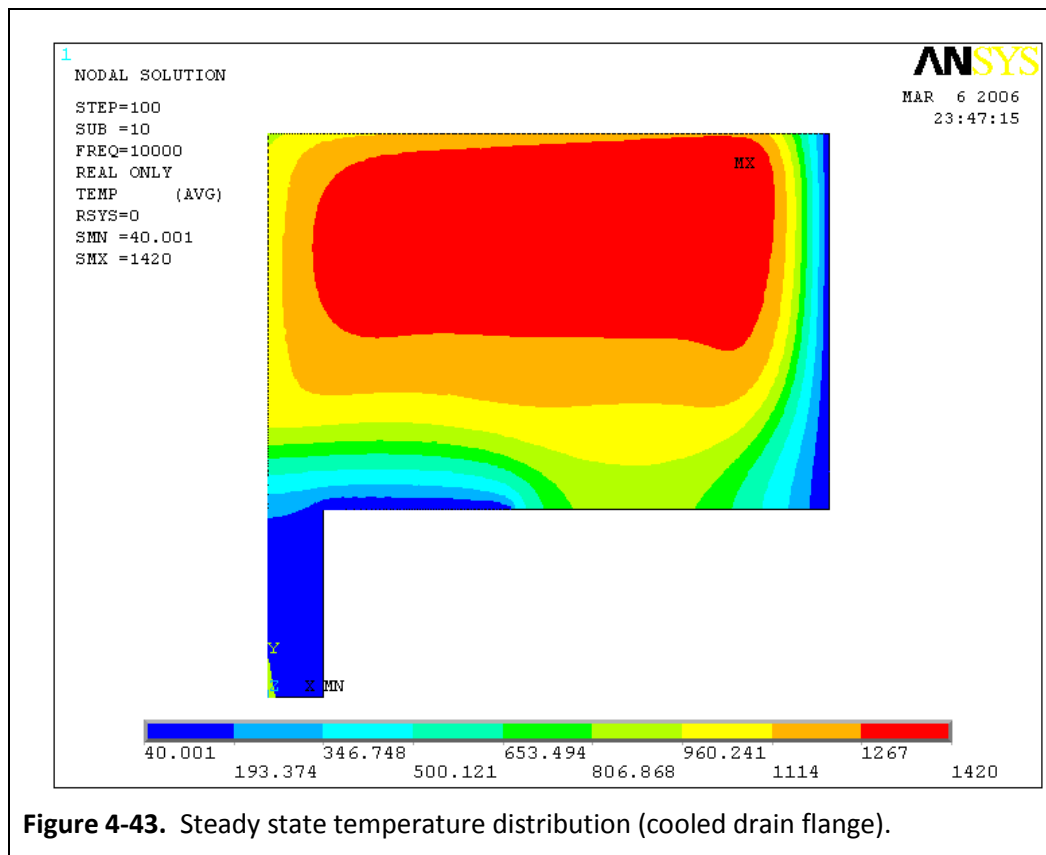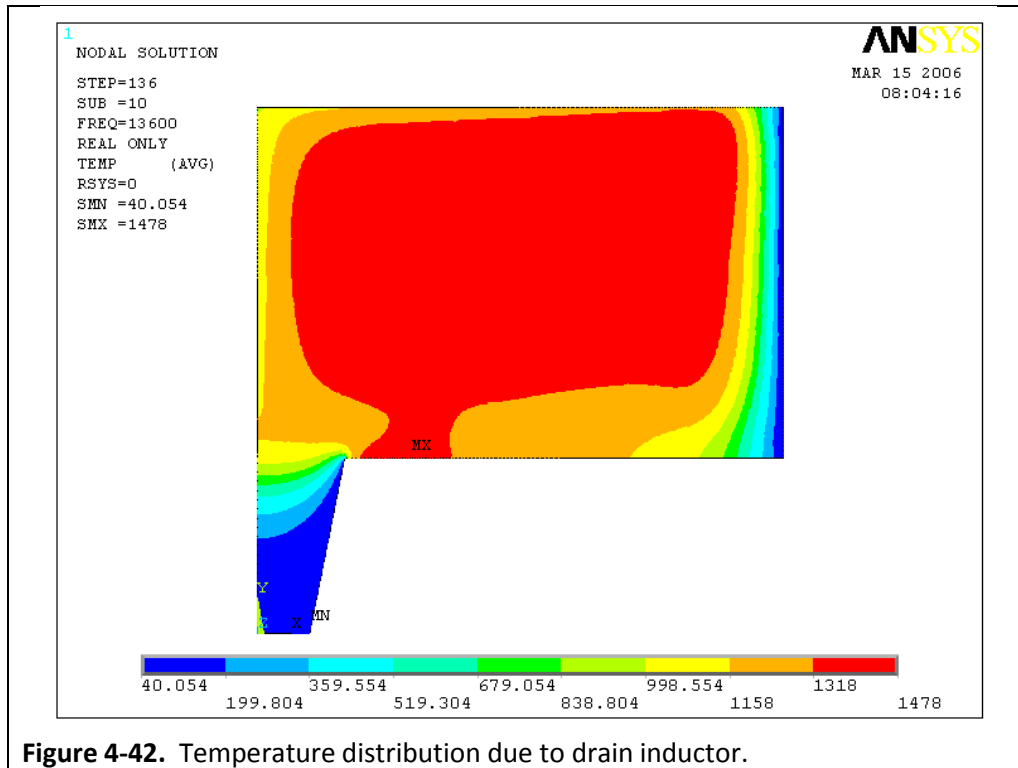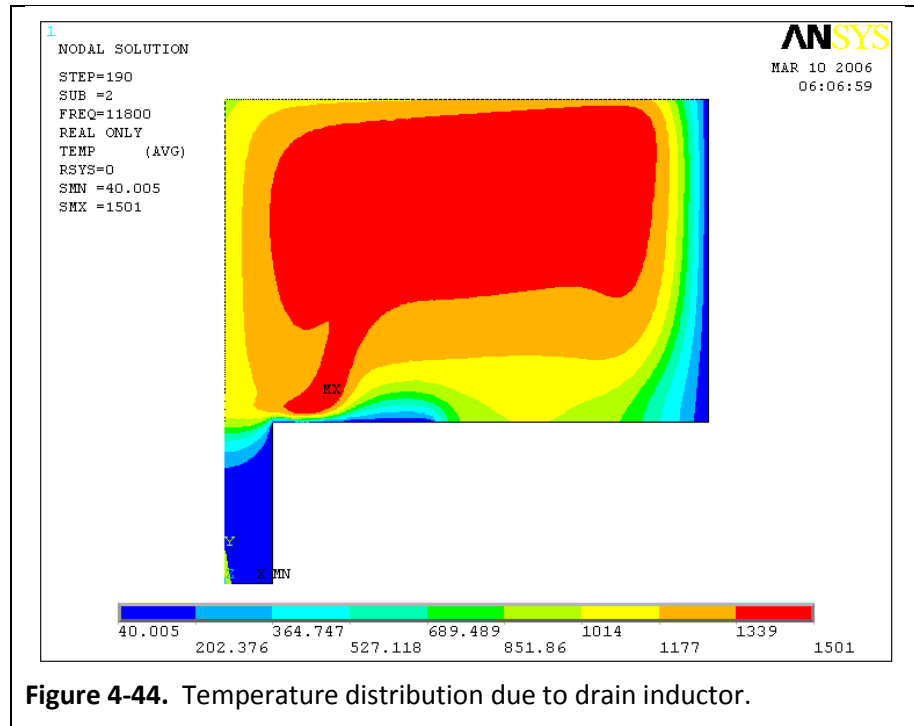
inductor alone. Figure 4-42 shows the resulting temperature distribution after the drain inductor (27 MHz) is energized. Compare these results to those in Figures 4-43 and 4-44 for a drain with a water-cooled flange.

The results show that, without a cooling flange on the drain, the ceramic bottom becomes overheated. This effect was demonstrated experimentally also, which was discussed above in relation to the model validation efforts.

Cooling Flange with Coupled Model

The subsequent investigation implemented the variable heat transfer coefficients along the bottom boundary to represent the water-cooled flange of the drain device, for investigating the ability to obtain conditions for casting. These results are provided in Figures 4-45 and 4-46.

This model run simulated 30 minutes of operation of the drain inductor at 153 A of current. Clearly, the glass volume within the drain body was not heated sufficiently to initiate a draining process. Accordingly, the drain inductor current was increased by 10% to 168 A (i.e. 6.8 kW) and the heating time was 60 minutes. This result is presented in Figure 4-45. These parameters did not produce sufficient heating to initiate the draining process either, so the drain inductor current was increased by an additional 10% to 184 A (i.e. 8.2 kW). This result is shown in Figure 4-46.

Figure 4-45. Temperature distribution using 168 A (6.8 kW) at one hour.

Figure 4-46. Temperature distribution using 184 A (8.2 kW) at one hour.
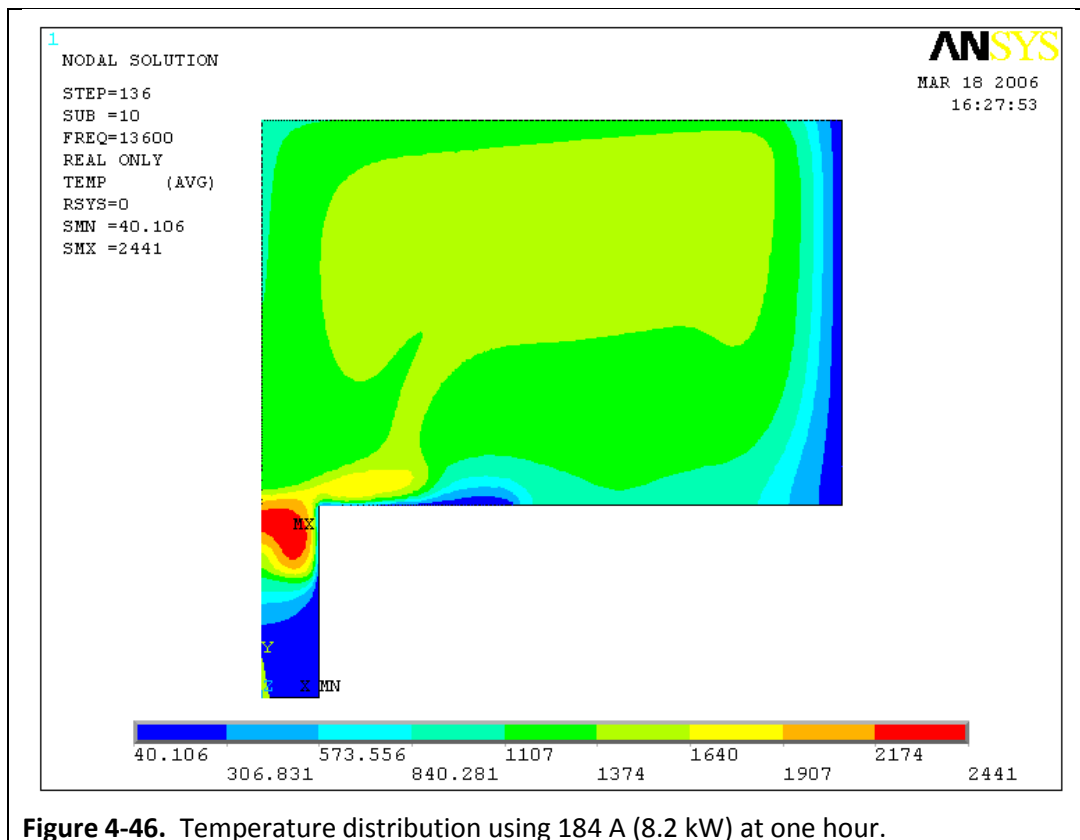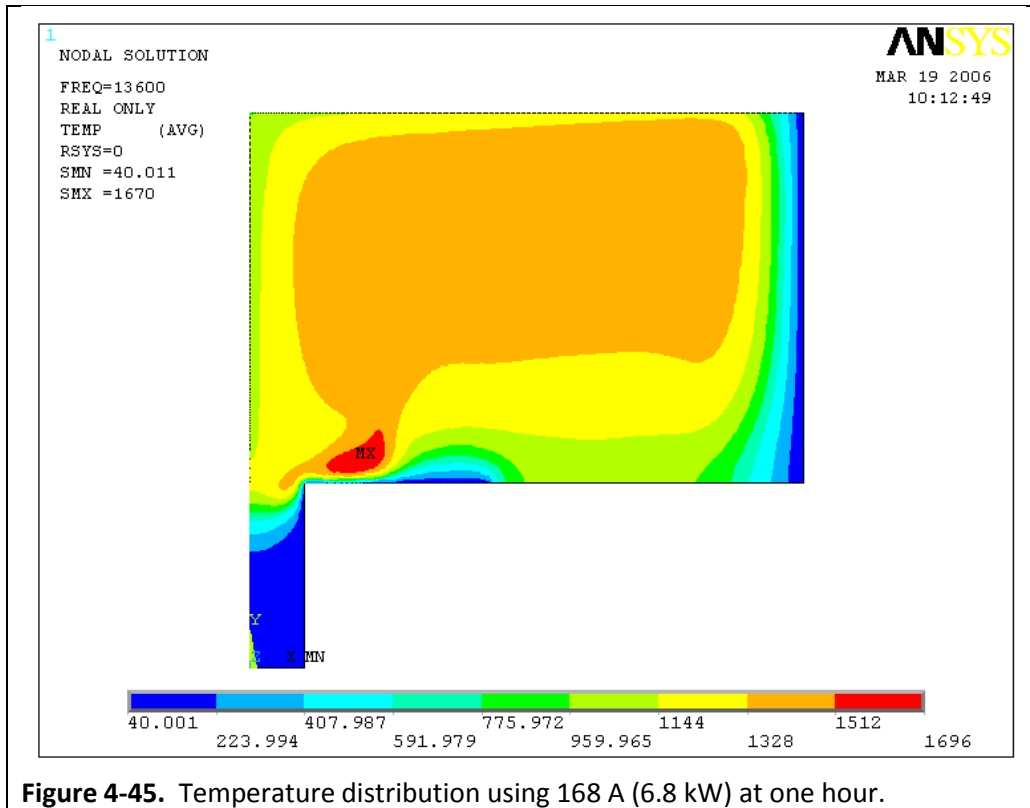
While these results were preliminary, and additional work was required at this stage to refine the temperature dependent material properties, several findings were apparent. First, the corner of the drain was absorbing a lot of energy and thus, it was not conducting into the drain body efficiently. Thus, the next investigations were for a drain geometry with a rounded transition. Second, the 27 MHz generator that was available was rated at 4.5 kW; accordingly it was modified to increase the capacity to 8 kW to provide adequate power to ensure that the draining process could be initiated. Additionally, recapping the prior drain geometry investigations, when the drain diameter was decreased the heating was efficient horizontally through the drain body, but was less effective in the longitudinal direction, as compared to the increased drain diameter. Also, the drain appears to be too long because the heat losses through the side of the drain wall are excessive due to the water cooling and the glass is cooled before it can extend to the open end. All of these results were incorporated into the next investigations.

The modifications to the 27 MHz generator to increase the total power to 8 kW resulted in necessitating a reduction in the current requirements to initiate melting due to limitations of some of the components. Thus, investigations of the minimal current that would result in effective heating of the glass within the drain body were conducted. The electrical calculation block of the model was enhanced to account for the gradual heating process, which changes the electrical conductance of the glass within the subtended area of the electromagnetic field of the 27 MHz inductor, and thus changes the actual power induced in the glass for each load step.

An additional enhancement of the model was to include a radiation heat transfer boundary condition on the end face of the drain. Prior calculations were simplified with a fixed heat loss value across the face. These combined changes result in much more accurate predictions of the melt temperature profile, and thus the melt velocity profiles.

For the rounded drain geometry, the first investigation was conducted using a two-turn inductor. The model geometry is shown in Figures 4-47 and 4-48. (Note the sections in the melt pool geometry. These are constructed to provide the capability to evaluate induced power in specific areas of the melt, which is demonstrated in later discussions.) Several power levels, as determined by the current set on the inductor, were investigated to determine the overall heating capability. These are illustrated in Figures 4-49 through 4-52. Based on these calculations, for this particular glass, with the two turn inductor, the minimum effective current is 160 A. This produces adequate heating without overheating in the main glass volume.
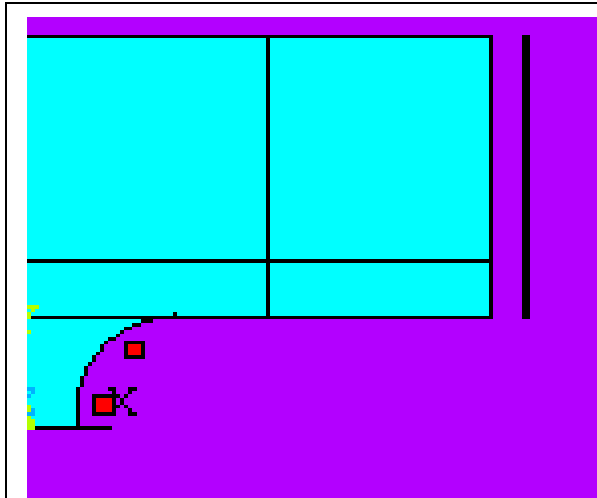
Figure 4-47. Model geometry for rounded drain with two-turn inductor**.**
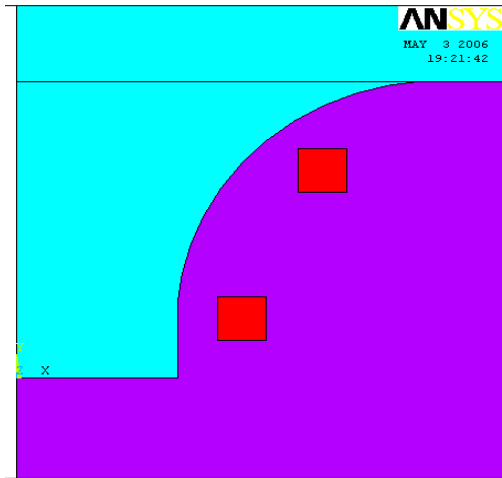
Figure 4-48. Detail of drain and coil geometry.
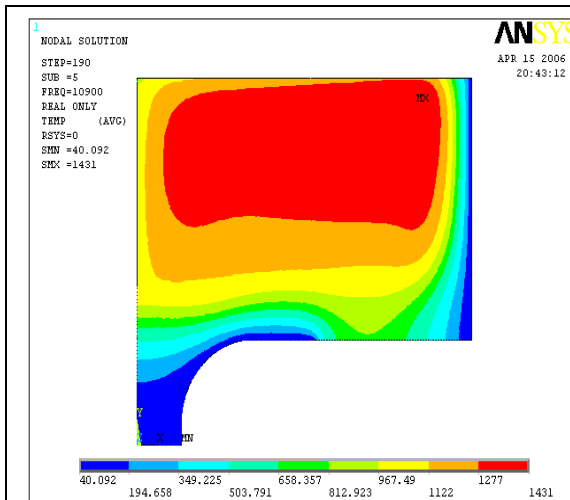
Figure 4-49. 27 MHz inductor at 120 A for 15 minutes simulated operation.
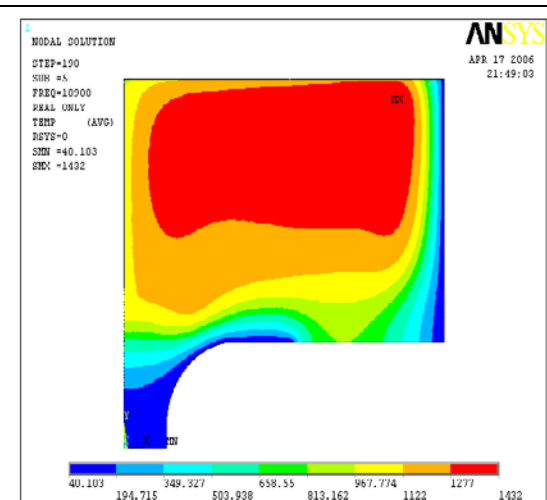
Figure 4-50. 27 MHz inductor at 140 A for 15 minutes simulated operation.

For the 120 A and 140 A current levels, the maximum temperature in the melt does not increase after 15 minutes, indicating that these power levels are too low. For the 160 A current level, good heating does occur. The melt temperature is increased by about 25°C after 15 minutes, indicating a significant change in the melt conditions. Additionally, a "tongue" of high temperature glass has formed and is migrating toward the drain. A current level of 180 A was also analyzed for a 15 minute simulated operation time. This produced excessive over heating for this specific chemistry, with the maximum temperature increased by over 300°C, to over $1,700^{o}$C, which is not an acceptable condition. In addition, the power level of the 180 A system, after 15 minutes was at 12.7 kW, which exceeds the capability of the actual generator available.
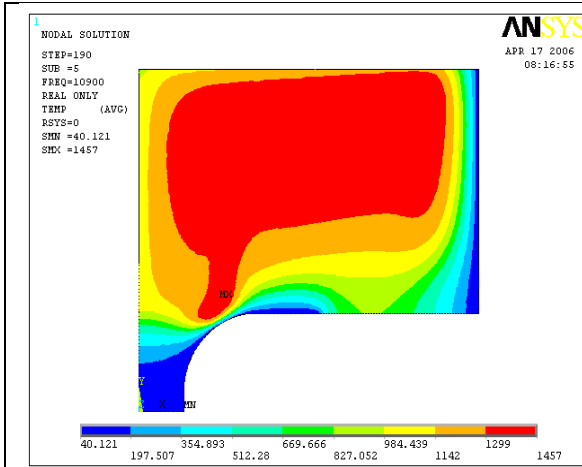
Figure 4-51. 27 MHz inductor at 160 A for 15 minutes simulated operation.
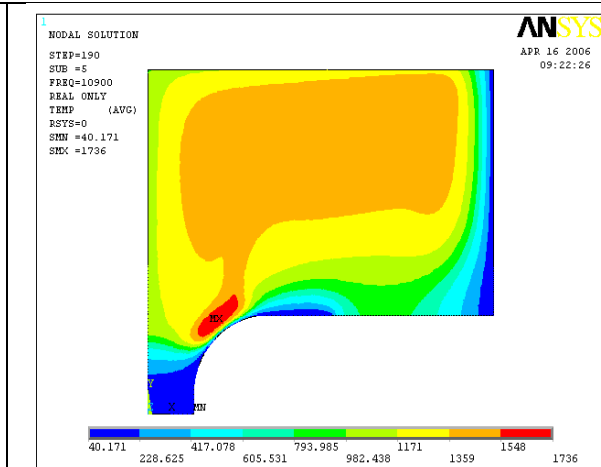
Figure 4-52. 27 MHz inductor at 180 A for 15 minutes simulated operation.

The 160 A system peaks at 7.2 kW, which is within the operating parameters of the modified generator. Thus, it was determined that the 160 A system is preferred and subsequent calculations to determine the ability to fully initiate a draining process were conducted using this configuration. The results are shown in Figures 4-53 through 4-56. Figure 4-54 illustrates how the tongue of high temperature molten glass is moving toward the drain body due to the radius transition geometry. This process continues until more of the glass volume within the drain body is at high temperature to support draining. However, as can be seen in the subsequent figures, the melt front will not transition to the bottom of the drain, even after 50 minutes of simulated operation.

The conclusion from these investigations was that the heat losses from the drain sides and bottom were overcoming the ability to conduct the heat into the glass in these areas; however, a melt line
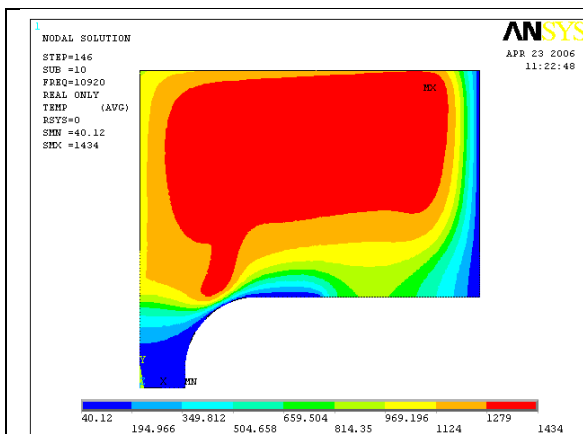
Figure 4-53. Temperature distribution after 15 minutes of operation.
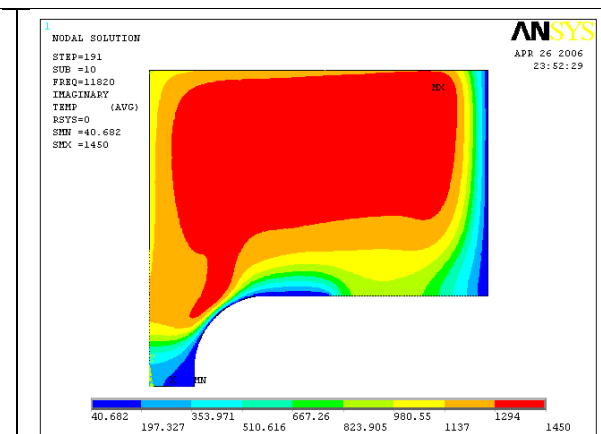
Figure 4-54. Temperature distribution after 30 minutes of operation.

Figure 4-55. Temperature distribution after 40 minutes of operation.

Figure 4-56. Temperature distribution after 50 minutes of operation.

Figure 4-57. Point within drain at which glass is at approximately 1,000^{o}C.
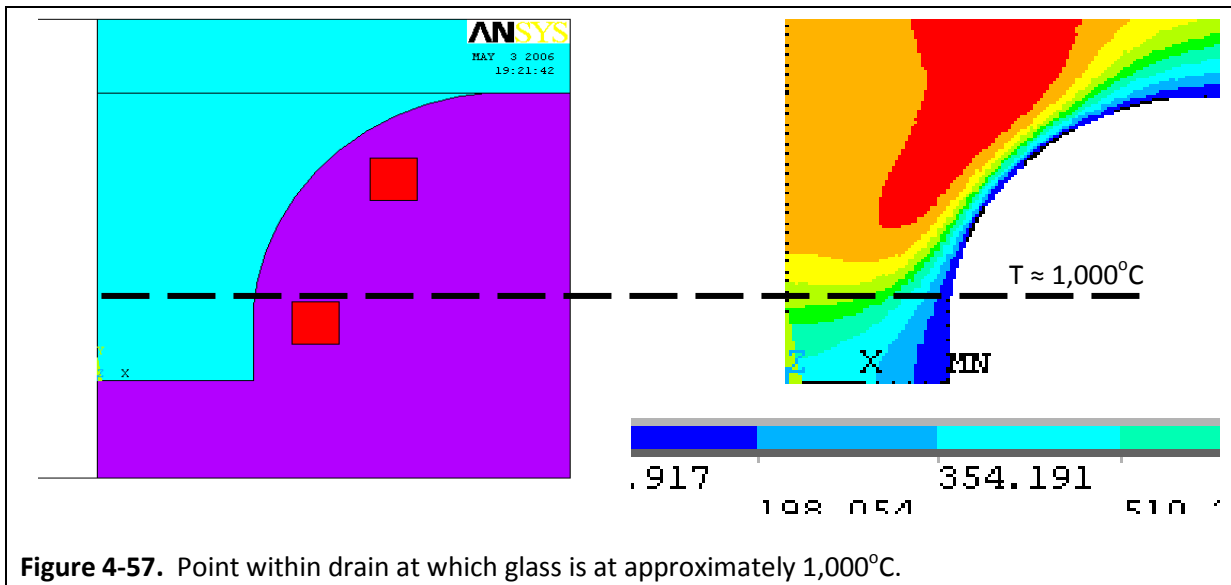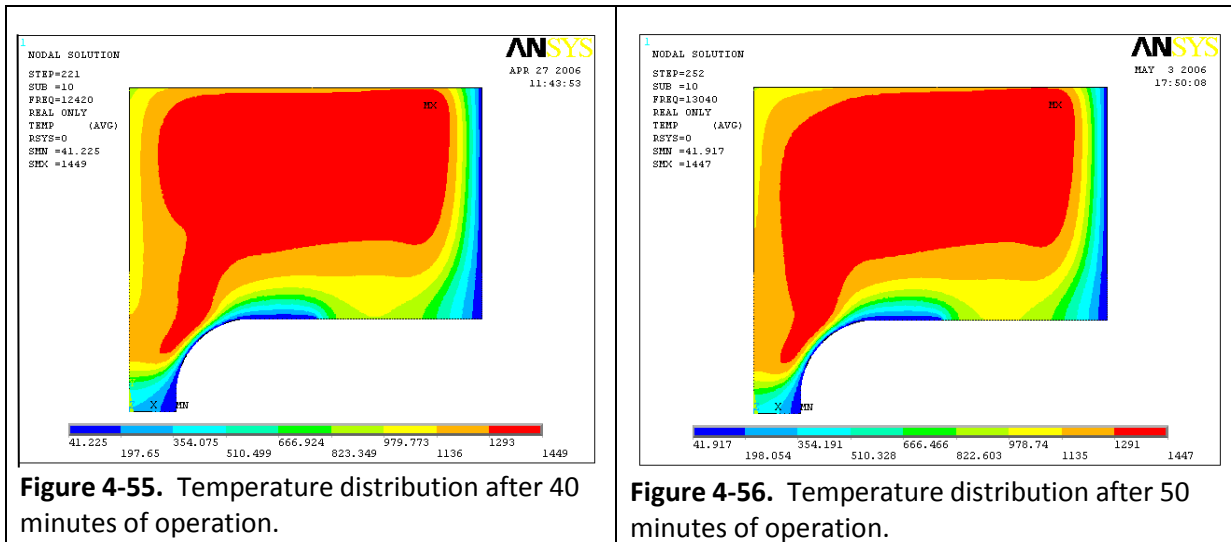
was clearly identified, as illustrated in Figure 4-57, and this eventually became a modified design basis (i.e. shorter drain body).

4.2.5. Additional Options Analysis and Design Optimization

Two options were investigated for feasibility related to the drain system configuration: 1) a single turn inductor design, and 2) a drain system design that allows the drain body to completely purge while maintaining a molten volume within the crucible to allow coupling of the electromagnetic field. This option was evaluated because initial analysis indicates that the drain will not be able to remove sufficient heat from the pour stream to stop the flow. It will only stop when the remaining

melt pool becomes very shallow and cools enough that it is too viscous to flow through the opening. If a method for controlling and stopping the casting process cannot be implemented, this approach will be required. It will ensure that sufficient melt remains for the 1.76 MHz field to couple with the melt pool such that frit can be added and a full melt pool re-established without re-installing the initiator. This would essentially enable semi-continuous processing.

Effect of Single Turn Inductor

While the two turn inductor offers some advantages regarding the electrical load on the 27 MHz generator, a single turn design has advantages related to simplicity in manufacturing and providing a better fit into a small space. Therefore, similar investigations were repeated for a one turn inductor with the same electrical limitations (i.e. 160 A and 8 kW) to determine the overall feasibility of the simpler design.

Figures 4-58 and 4-59 show the basic model geometry used for the single turn inductor system.
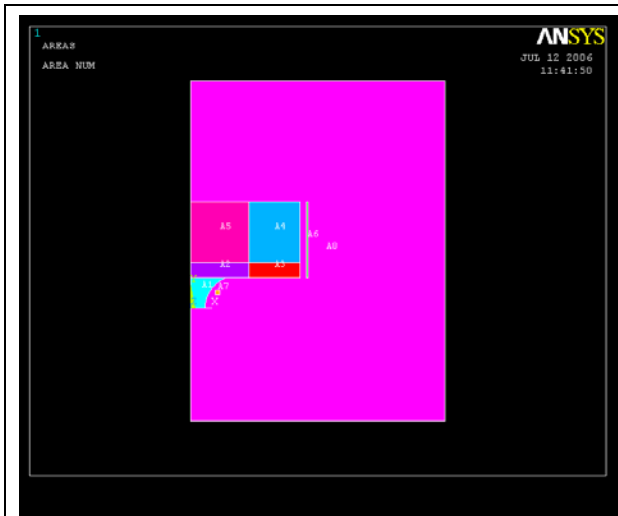
Figure 4-58. Single turn model geometry.   **Figure 4-59.** Detail of drain and coil geometry.

The modeling studies of the single turn coil were evaluated in detail to determine if this approach would be feasible. Figure 4-60 shows the temperature distribution prior to energizing the drain inductor. Figured 4-61 through 4-64 illustrate the heating process (temperature distribution) through 10, 20, 30, and 40 minutes respectively.
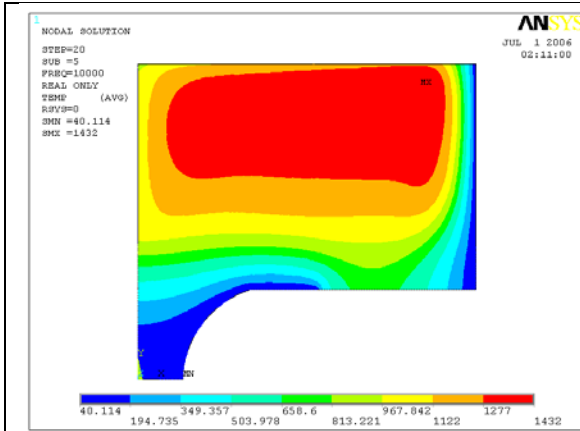
Figure 4-60. Steady state temperature distribution prior to energizing drain inductor.
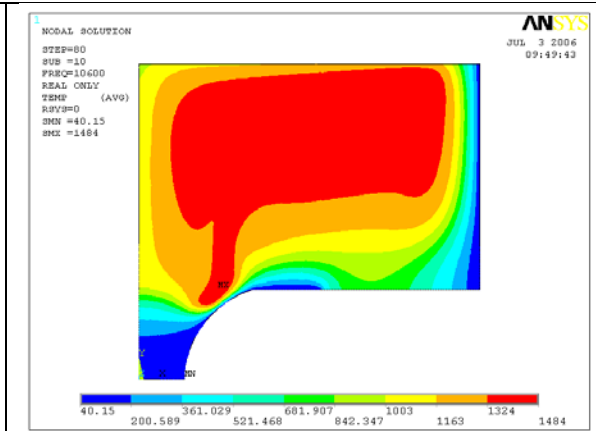
Figure 4-61. Temperature distribution after 10 minutes of operation of drain inductor.
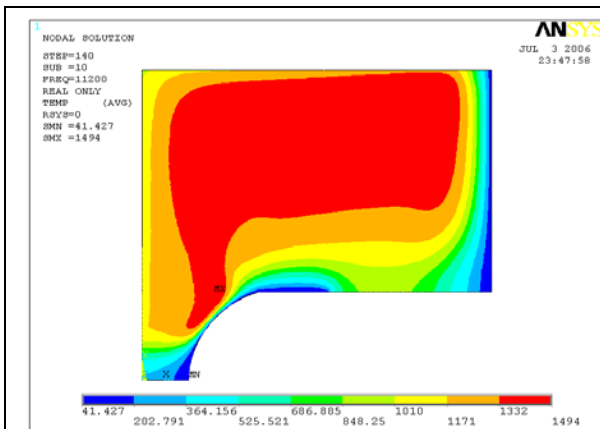
Figure 4-62. Temperature distribution after 20 minutes of operation of drain inductor
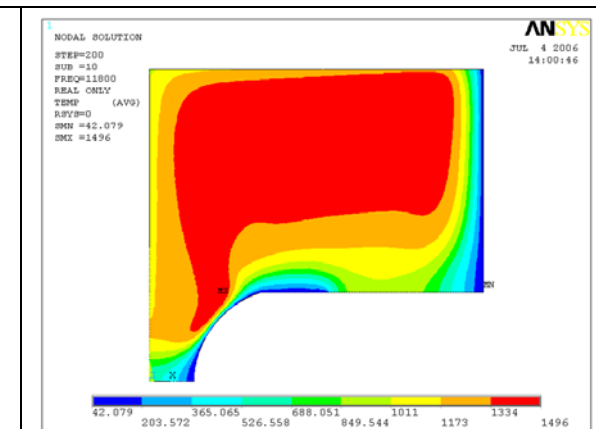
Figure 4-63. Temperature distribution after 30 minutes of operation of drain inductor
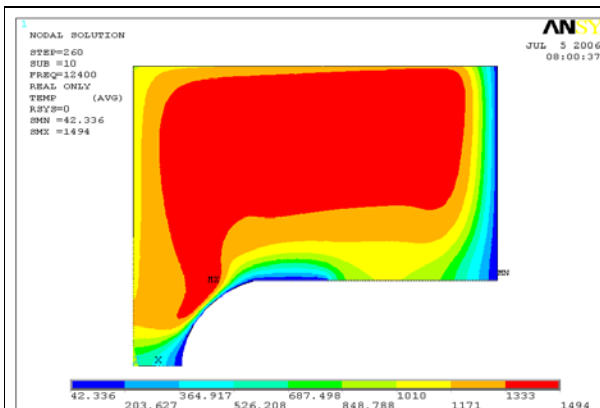
Figure 4-64. Temperature distribution after 40 minutes of operation of drain inductor.
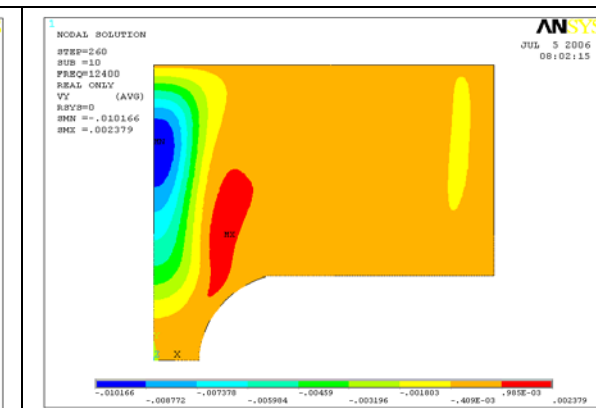
Figure 4-65. Axial velocity field at 40 minutes of operation of drain inductor.
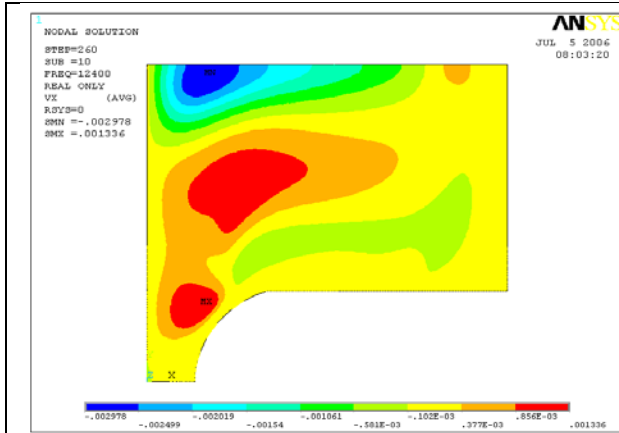
Figure 4-66. Radial velocity field at 40 minutes of operation of drain inductor.
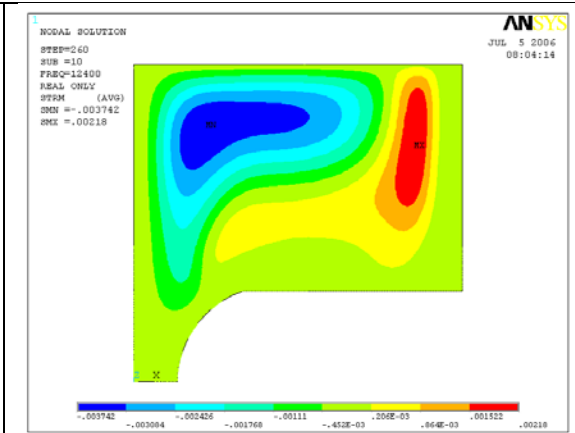
Figure 4-67. Stream function field at 40 minutes of operation of drain inductor.

Figure 4-65 and Figure 4-66 show the velocity component fields of the melt after 40 minutes of operation of the drain inductor. Similarly, Figure 4-67 illustrates the stream function. From these results the following conclusions can be made. First, operation of the drain inductor increases the maximum temperature of the main melt pool by 50°C to 60°C. This was also validated in the experimental work, which is discussed later in this dissertation. Second, while the single inductor does effectively heat up the upper portion of the drain volume, after 20 minutes, the melt front does not descend appreciably into the drain body. Additionally, a strong vertical melt flow forms over the top of the drain throat, indicating that, at steady state, a significant out flow of energy away from the drain is established. Thus, these results indicate that initiating an actual draining process is not likely with this configuration (i.e., combined drain device and inductor design).

Another option considered, which was also investigated experimentally, involved application of a drain geometry that would maintain a melt pool (referred to as a "bog") in the crucible and potentially completely evacuate the drain body after a draining event, thus eliminating the issue with melt through of the solid glass between subsequent draining events.

Actual drains were constructed and tested based on this concept; however, it is not ideal for the intended application. Retaining a dead volume in the bottom of a melter allows undesirable constituents in the melt to precipitate out and collect in this area over time. The primary negative effect is that, often, these are noble metals and other conductive materials that can eventually "short out" the melter by establishing a conductive path near the bottom. Other issues were observed related to the resulting skull insulating the melt from the induction field. Efforts will continue in parallel for identifying techniques to control the casting process.

The initial geometry investigated is illustrated in Figure 4-68. The specifics are given in Table 4-1.

Table 4-1. Model geometry for bog analysis.

Feature	Dimension, mm
Internal radius of crucible	150
Height of crucible	100
Internal radius of inductor	160
Depth of melt bog	45
Height of drain	45
Internal diameter of drain bottom	40
Height of drain inductor from bottom	20
Drain inductor cross-section	6 x 6
Distance between inductor and drain	5
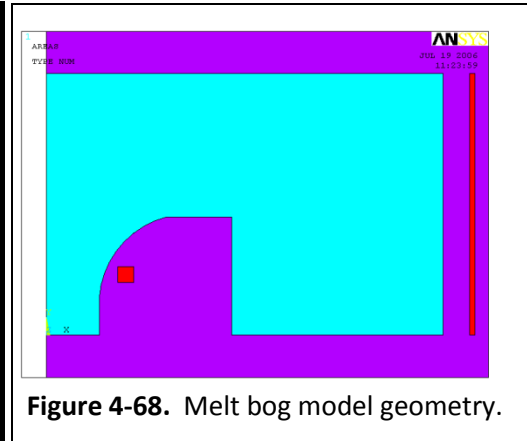
Figure 4-68. Melt bog model geometry.

As seen in Figure 4-69, at the beginning of the drain inductor operation, the energy deposition occurs in the glass that is at temperatures between 1,100°C and 1,200°C. Although this location is well above the drain throat, it is adequate to transition the melt front into the drain body, which is discussed below. The steady state temperature prior to energizing the drain inductor is shown in Figure 4-70. The condition after 10 minutes is shown in Figure 4-71. Comparison to the non-bog geometry shows that the glass temperature along the axis is much lower (refer to Figure 4-60). This results in differences in the characteristics of the heat up process and overall temperature distribution due to the drain inductor operation.
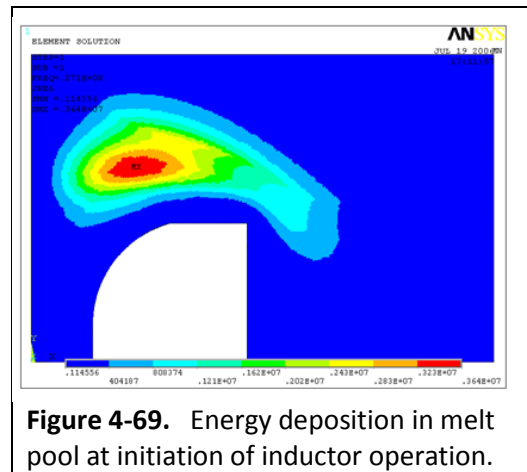
Figure 4-69. Energy deposition in melt pool at initiation of inductor operation.
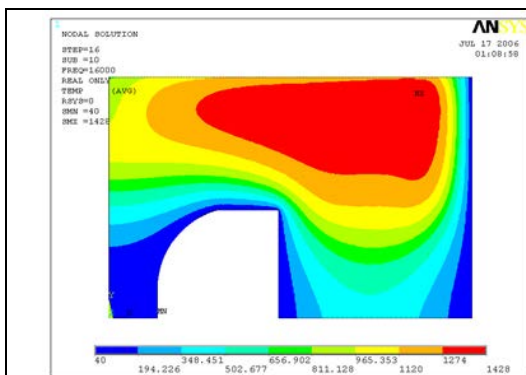
Figure 4-70. Temperature distribution prior to drain inductor operation.
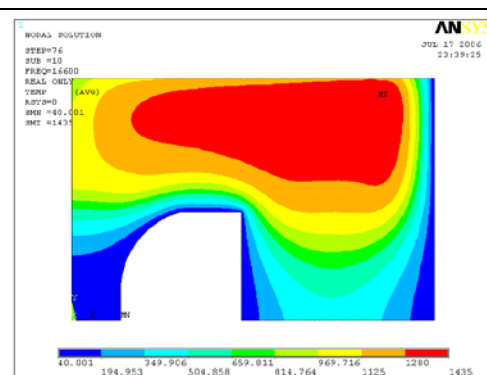
Figure 4-71. Temperature distribution after 10 minutes of operation of drain inductor.

After 10 minutes of operation of the drain inductor the melt pool is heated up much less, particularly along the axis and near the drain throat, as compared to the system without the melt bog (see Figure 4-61). On the other hand, due to the smaller volume of glass being heated by the primary 1.76 MHz inductor, the melt pool is heated much faster than the system without the melt bog. After 20 minutes of operation of the drain inductor at the same power level as other systems investigated (i.e. 8 kW), a molten tongue of high temperature glass progresses into the drain body similar to the other configurations. This is illustrated in Figures 4-72 and 4-73. However, significant over heating also occurs in this zone.
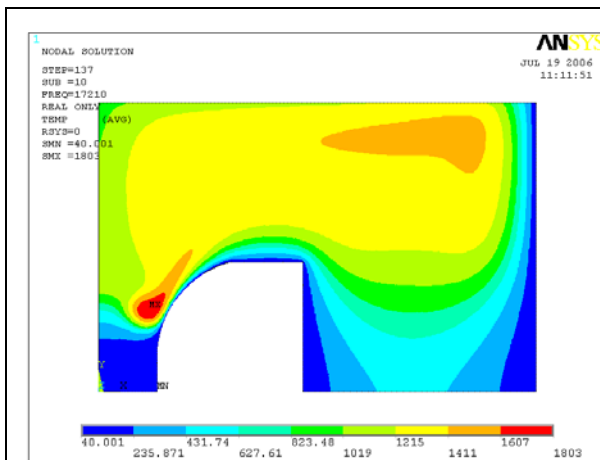
Figure 4-72. Temperature distribution after 20 minutes of drain inductor operation.
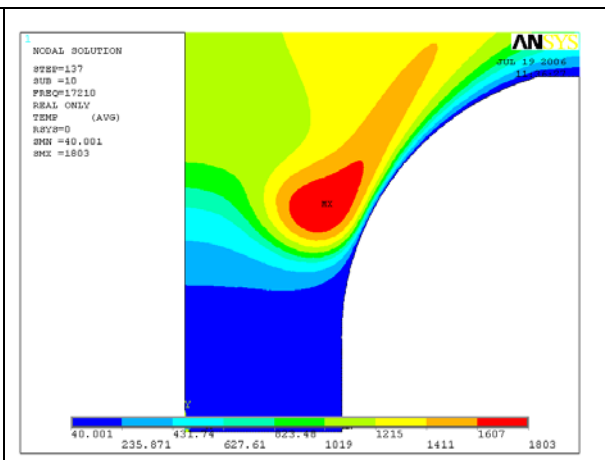
Figure 4-73. Temperature distribution detail in drain body.

This happens rapidly such that the high temperature glass has a tendency to move up faster than the heat can be conducted into the cooler glass in the lower area of the drain body. The result is that the high temperature front does not effectively conduct down into the drain body below the inductor. Once again, this illustrates the need to shorten the length of the drain tube.

Additionally, as the glass is drained from the crucible, the bog of hot glass remaining is a relatively small volume such that its specific power is dramatically increased, and the melt is quickly overheated. Thus during operation this must be controlled such that the power level of the 1.76 MHz generator is reduced sufficiently to mitigate this condition. Nevertheless, the geometry that includes the melt bog appeared to offer the potential to eliminate the difficulties associated with repeatedly melting through a solid glass plug in the drain, so this system was evaluated in more detail. As the design of the drain device progressed, this feature was completely eliminated. This is discussed in more detail in subsequent chapters.

Implementation of Geometry Improvements

Key features implemented in this model included the shortened drain geometry, as well as the radiation boundary condition along the drain opening. Additionally, the overall power in the inductor was limited to 4 kW to ensure that the glass in the drain was not over heated. While the 27 MHz generator had been modified to provide up to 8 kW, the efficiency of the actual generator required higher available power to apply 4 kW to the drain device.

Figure 4-74 illustrates the revised model and geometry with a steady state temperature distribution achieved with the 1.76 MHz generator prior to energizing the 27 MHz drain inductor. The model includes a single turn drain inductor because it was shown to be effective in prior investigations. This was analyzed using a fully coupled hydrodynamic model including electrical and thermal calculation blocks. The steady state condition was reached after 166.7 minutes of simulated time. This is very consistent with the experimental results, which are discussed in more detail in subsequent chapters.

Figures 4-75 through 4-77 demonstrate the effects of the heat up process due to the 27 MHz drain inductor. These figures clearly show that, with implementation of the geometry changes and model enhancements, the dual frequency heating system is capable of producing a high temperature tongue that descends into the drain body and fully heats the glass volume within the system to initiate the draining process within less than 45 minutes, once steady state is obtained.

These results demonstrate a basic drain and crucible geometry that will result in a successful draining process. This became the basis for much of the experimental efforts. However, many assumptions and simplifications are implemented into the model and mathematical analyses. This is especially true for a transient process such as glass casting. A continuous iterative process occurred over the span of this work to systematically improve the boundary conditions, operational parameters, and other parameters that could account for the results of the very complex processes involved. A major assumption is axial symmetry of the system; however, this is known to not be the actual condition. For example, the energy deposition is greater at the location in the crucible that is adjacent to the junction between the generator busses and the inductor. Seemingly insignificant geometry features, such as a sharp corner, if in the right location, will absorb energy and reduce the capacity and efficiency of the 27 MHz generator. These effects are learned by experience and subsequently accounted for in the actual component designs.

Figure 4-74. Steady state temperature distribution prior to energizing drain inductor.

Figure 4-75. Temperature distribution after 6.3 minutes of operating drain inductor.

Figure 4-76. Temperature distribution after 24.3 minutes of operating drain inductor.

Figure 4-77. Temperature distribution after 24.7 minutes of operating drain inductor.
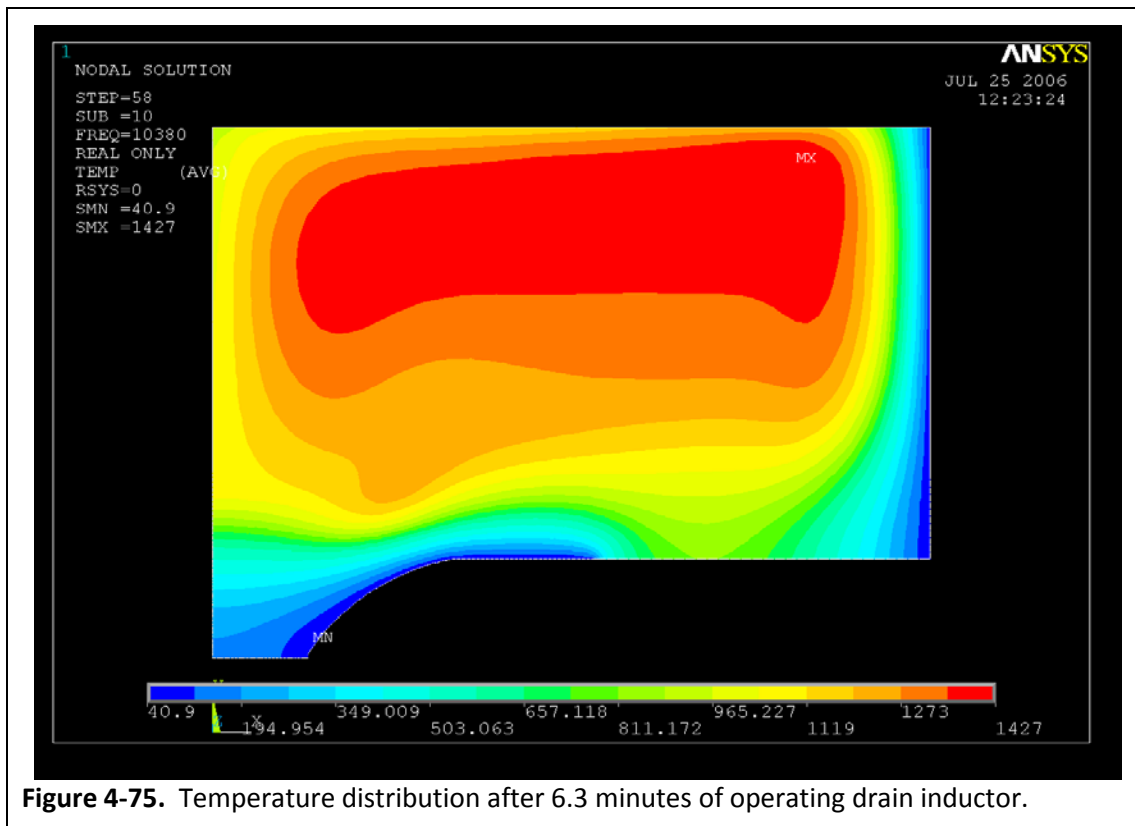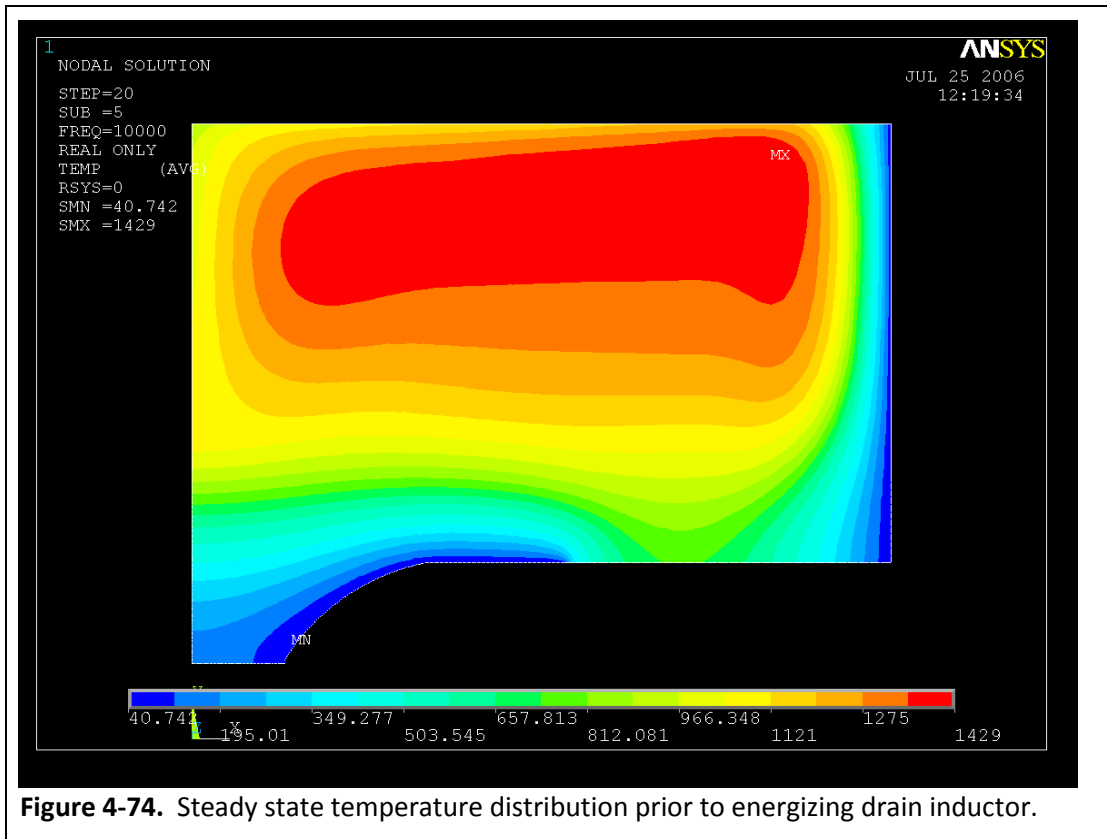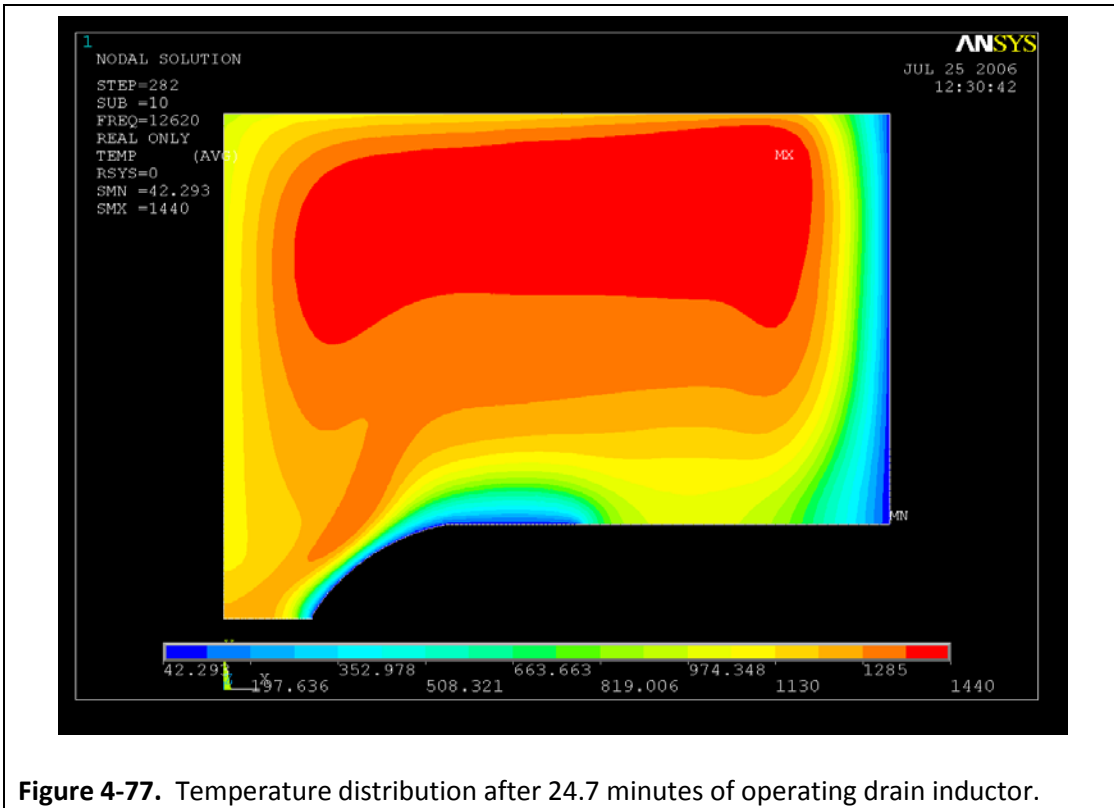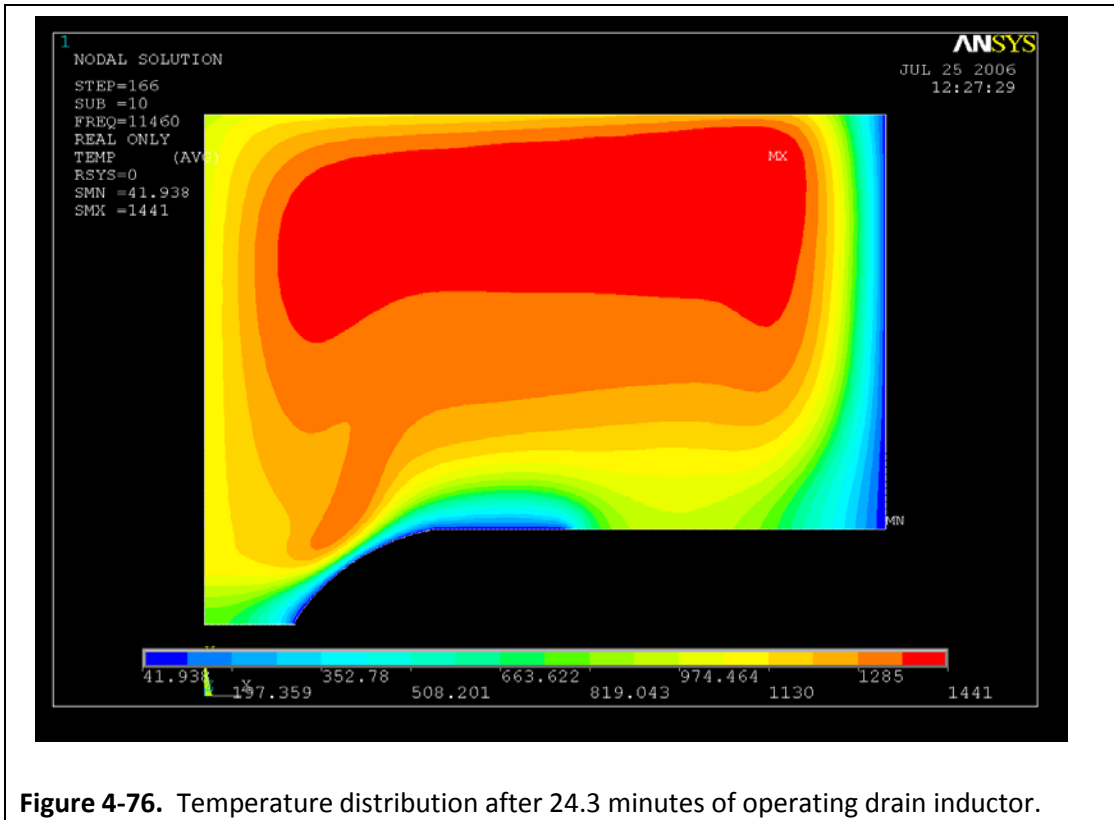
Drain Design for Melt Bog

As previously mentioned, the geometry that includes a melt bog provides some potential operational benefits, so this system was also analyzed further using some of the enhancements identified in earlier modeling analyses. Extensive analyses were conducted on the melt bog geometry parameters to help focus planned experimental efforts. A basic drain geometry that could be easily fabricated was envisioned, as illustrated in Figure 4-78 and Figure 4-79.
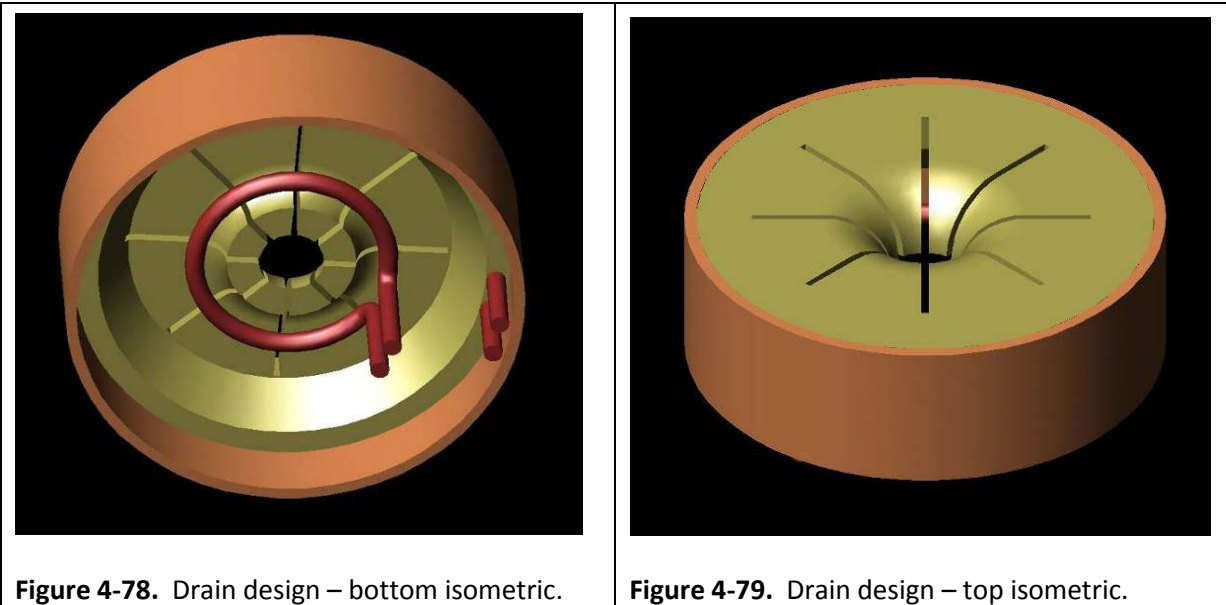
Figure 4-78. Drain design – bottom isometric.

Figure 4-79. Drain design – top isometric.

Prior to conducting extensive parametric and optimization studies, a simplified model of the geometry was analyzed for thermal distributions during operation. The calculations were intentionally conservative in that 6.5 kW of power was modeled to be focused in the vertical surfaces of the drain only (i.e., the outer lip and the drain body). Note that this is more than double the actual power induced in the drain (based on calorimetry data from testing). The actual energy deposition will include the horizontal surfaces, resulting in lower maximum temperatures than predicted by this conservative model. Boundary conditions for the cooling water channel were also conservative, but based on data from prior testing. All of the input energy was assumed to be removed via the cooling water channel only (i.e., no radiation heat losses). The resulting analysis indicated that the maximum temperature in the drain device would not exceed 584°C. The walls of the drain opening were set at 5 mm thick and this is recommended as a minimum, in spite of the conservative nature of the analysis, due to inevitable erosion over time of the high temperature

molten glass flowing past the edge of the bottom drain opening. The modeling results are shown in Figure 4-80.
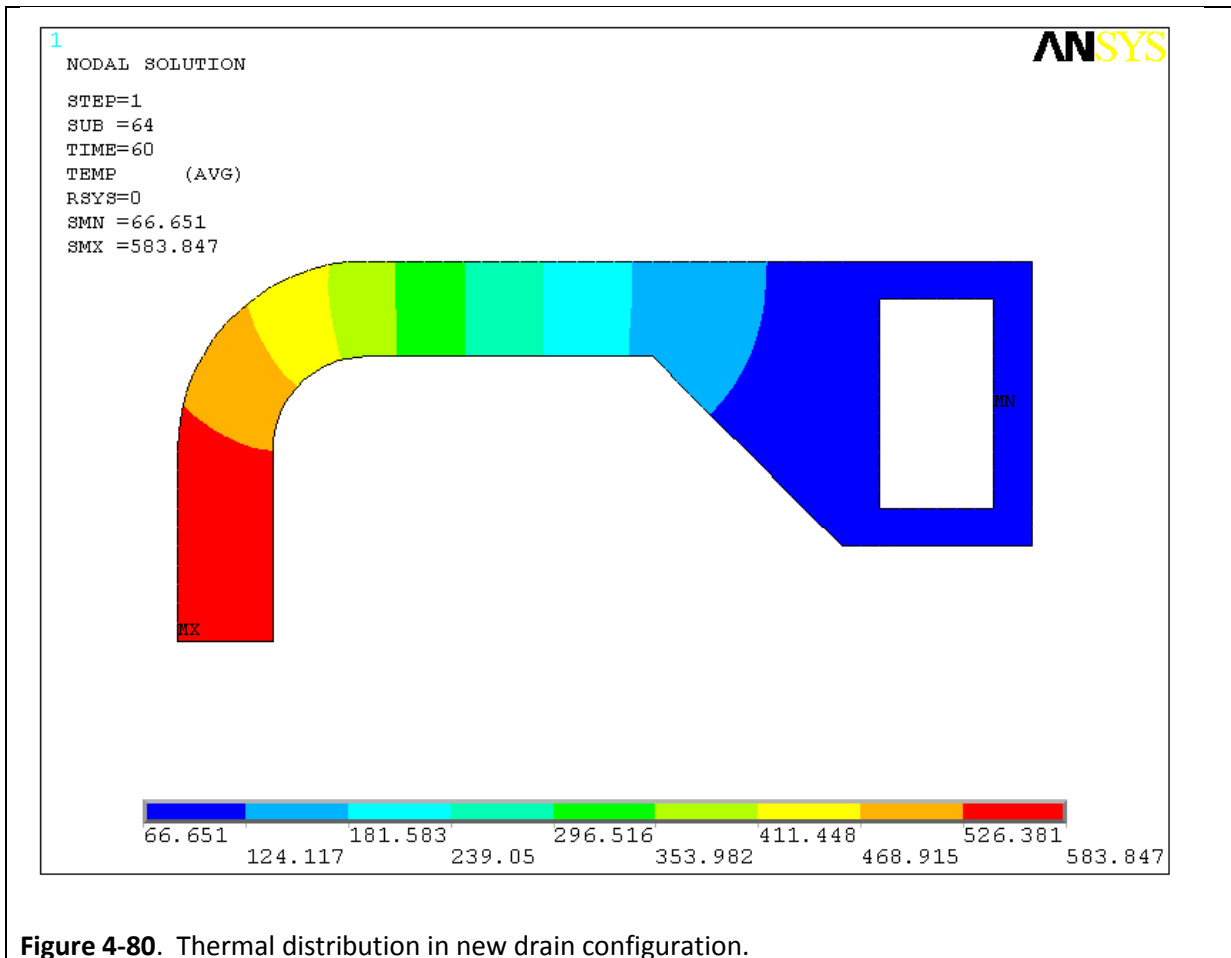
Figure 4-80. Thermal distribution in new drain configuration.

The drain geometry was designed such that it could accommodate either a single turn or two turn inductor. Additionally, the model used variable parameters for the inductor position, drain internal diameter, power induced into the melt, and current on the drain inductor, as shown in Table 4-2.

Table 4-2. Variable parameters for analysis of drain device with bog.

Parameter	Variable Parameter Value
Internal diameter of drain	40 mm, 30 mm, 25 mm, and 20 mm
Inductor location	5 mm, 10 mm, and 15 mm (with same diameter and with varying diameter to maintain minimum distance from drain body)
Maximum power induced in melt	4 kW, 6 kW
Drain inductor current	160 A, 175 A, 190 A, and 220 A

These variations and when they are used are described in more detail below.

A key feature of this modeling effort was related to the approach used for the electrical power calculations. For induction heating systems, ANSYS® provides for setting specific parameters, namely inductor current, inductor current density, or inductor voltage. However, as the glass is heated, its electrical resistivity decreases by several orders of magnitude, which results in infinite levels of power induced in the melt, from a model perspective. In reality, the vacuum tube generator used for the power sources in the experimental work (1.76 MHz and 27 MHz) are limited, of course, in the power level that can be delivered at a various stages of the melting process. Therefore, the model was modified to include specific limiting algorithms that represent the characteristics of the available power supplies. For example, the external characteristics of the generator (i.e. resulting R-L-C circuit characteristics due to coupling of the electromagnetic field to the melt) are expressed in the form of a dependent relationship between total voltage output and the generator power output. Because the generator has a fixed total internal impedance, this dependence is indirectly proportional, resulting in a total induced power limitation in the melt.

Sensors were developed that allowed determination of the external characteristics of the generators. This work, which was conducted by professors and graduate students at ETU-LETI, was not performed as part of this dissertation, but the results were leveraged to support the research.

Based on the data from the sensors, the approach taken in the model was to set a generator current, which is independent of the total impedance (i.e. internal plus induced). As the glass melts, the resistivity decreases and the total power in the glass increases. However, the maximum power is limited by the known characteristics of the generators. For the 27 MHz the maximum power level used was 4 kW, except for some specific instances, which are described in detail below.

For the analyses performed, long heating times were used to ensure that a condition that would allow draining of the glass was established. Based on earlier modeling efforts, as well as experimental results, the approach was to reach a minimum temperature of 900°C at the bottom of the drain. Similarly, earlier modeling (using the thermal and electrical calculation blocks only) demonstrated that the initial heating due to the drain inductor actually occurs due to the longitudinal electromagnetic field components, thus a primary focus of these analyses was to determine the power level induced into the melt that was sufficient to support the melt pool growth and thus draining. To evaluate this condition, the drain inductor was modeled in two different geometries: 1) with the inductor fixed in the middle position, and 2) with the inductor moving from the top to middle to bottom positions during the melting process to support the draining event. The

configurations for the moving inductor are shown in Figure 4-81. For the fixed middle position case, the inductor diameter is reduced to provide minimum distance from the drain, (see Figure 4-82).

| Top Inductor position | Middle inductor position | Bottom inductor position |

Figure 4-81. Inductor geometry for case of moving drain inductor with constant diameter.
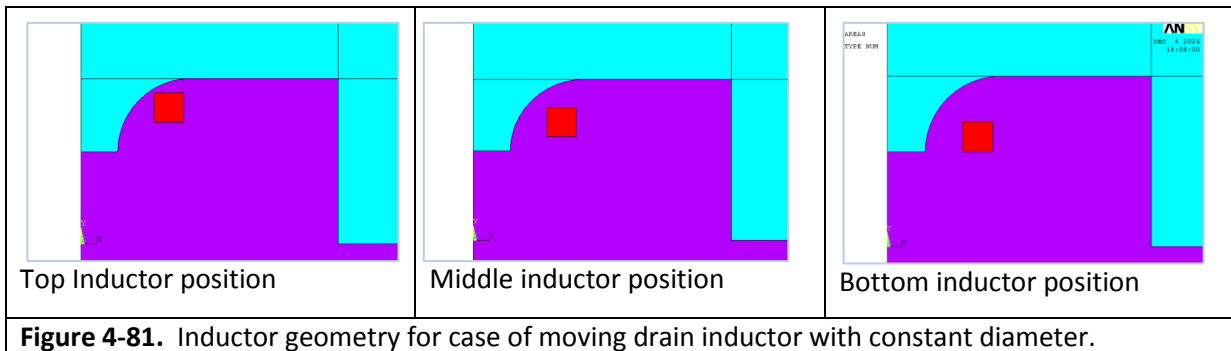
The geometric parameters for the full system used for this set of model analyses are provided in Table 4-3.

Table 4-3. System geometry used for analysis of drain device with melt bog.

Feature	Dimension, mm
Internal diameter of crucible	300
Melt height at perimeter	100
Melt height at drain	55
Internal diameter of bog	140
Drain height	20

Figure 4-82. Inductor geometry for fixed middle position of drain inductor with changing diameter to maintain minimum position from drain.
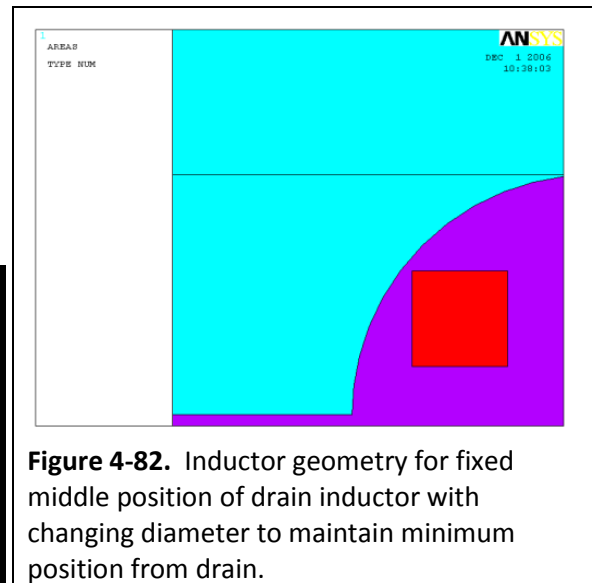
As previously discussed, the internal diameter of the drain was investigated at 40 mm, 30 mm, 25 mm, and 20 mm. The model geometry is shown in Figure 4-83.

The first investigation for this set of studies included the 40 mm diameter drain with the fixed middle position for the drain inductor (i.e. distance between the inductor and drain are minimum). The simulated operation time was 90 minutes. This configuration was selected because experimental work had been conducted with a very similar configuration. In that test, a successful draining event was achieved. This investigation would provide data to help validate the melt initiation step of the model analysis, or invalidate it, depending on the results. Fortunately, the modeling results did demonstrate that a drain event would be successful since the temperature achieved at the bottom of the drain, along the face of the opening, exceeds 900°C. This is

demonstrated in Figure 4-84. The initial power on the inductor was 3.24 kW and the maximum was maintained at 4 kW once achieved.

Figure 4-83. Model geometry for drain analyses (fixed middle inductor position shown).
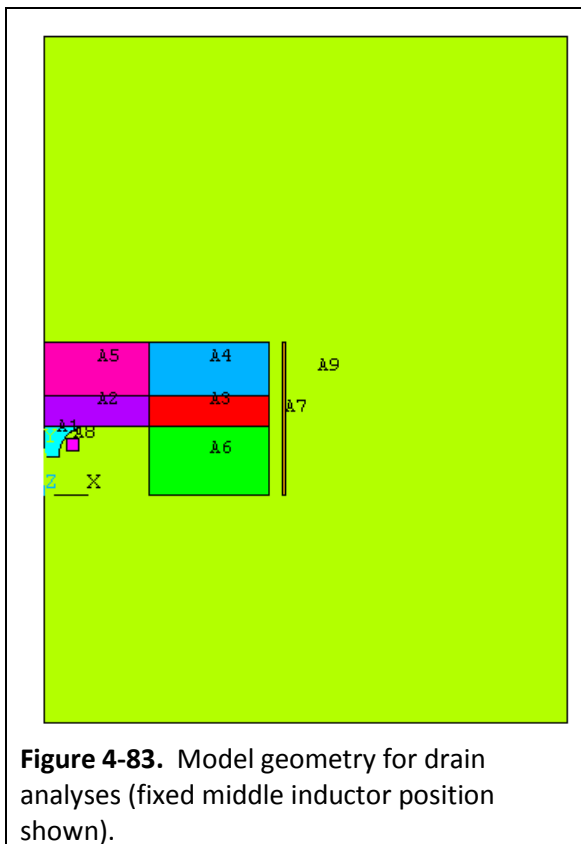
The next analysis was for a 30 mm drain internal diameter with the fixed middle position for the drain inductor. For this investigation, a steady state temperature distribution was achieved in the main melt using only the 1.76 MHz power supply, as shown in Figure 4-85. Subsequently, the 27 MHz inductor was energized and power maintained for 90 minutes at which time the resulting temperature distribution was evaluated. The end state temperature distribution is shown in Figure 4-86. As can be seen, the temperature at the bottom of the drain is near the target 900°C.

Figure 4-84. Temperature in 40 mm diameter drain at 90 minutes.

Figure 4-85. Steady state temperature distribution prior to operation of drain inductor for 30 mm diameter drain.

Figure 4-86. Temperature in 30 mm diameter drain at 90 minutes**.**
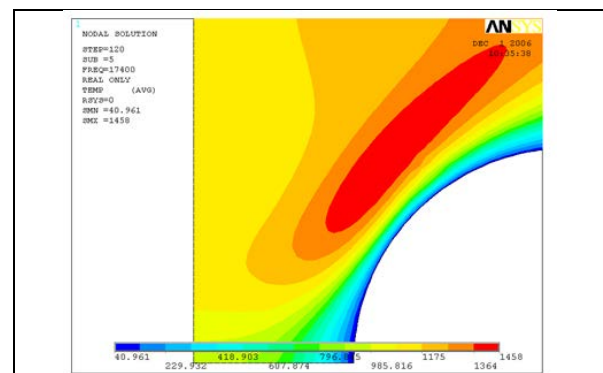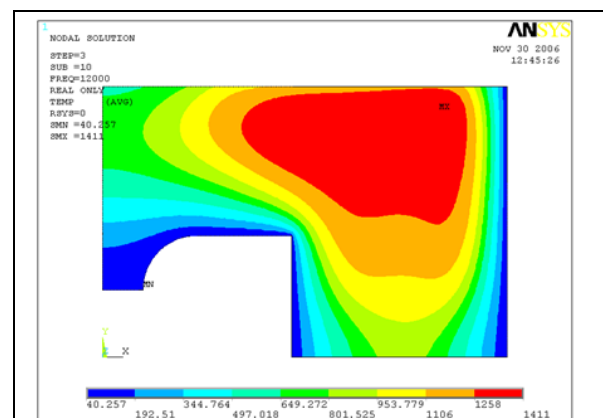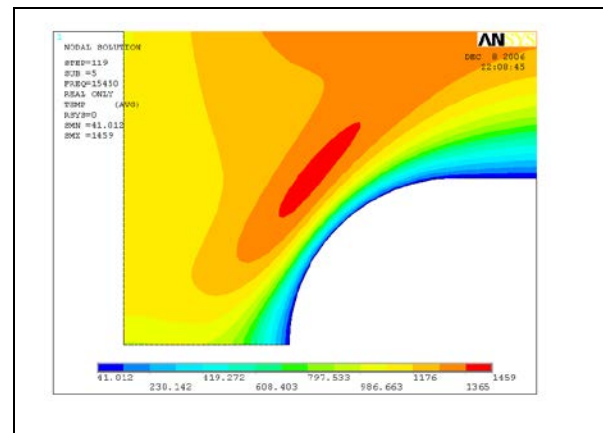
The next investigation analyzed the system for the configuration that includes a moving drain inductor. In this study, once the steady state temperature distribution was achieved, the drain inductor was energized with the initial position at the top location. The system was modeled for 30 minutes in this configuration with the maximum power level at 4 kW. The inductor was then translated to the middle and bottom positions and operated for 30 minutes in each position, again with a limiting power of 4 kW for each. The temperature distribution shown in Figure 4-87 resulted after the first step.

Figure 4-87. Temperature distribution after 30 minutes of operation with drain inductor in top position.
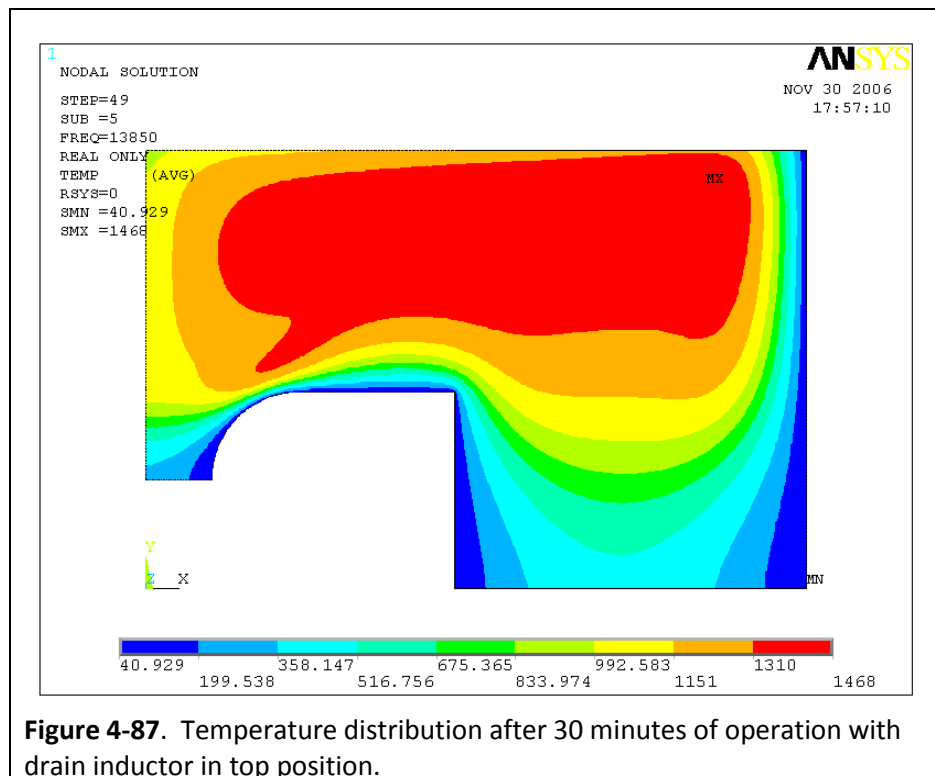
The initial power on the drain inductor is 2.45 kW. This increases to the 4 kW maximum during the 30 minute process. The figure indicates that a high temperature tongue has formed and is moving toward the drain throat.

As the inductor is moved to the middle position very little change is observed in the temperature distribution, including advancing of the high temperature zone into the drain body. Additionally, the power level on the drain inductor remains constant at 4 kW throughout the 30 minute operation time. See Figure 4-88. This is due to the fact that, as the inductor translates downward, the distance from the area of strongest coupling (to the longitudinal component of the electromagnetic field) is increased because the drain diameter decreases while the inductor diameter is constant.

However, it does maintain the distribution such that when the drain inductor is lowered to the bottom position, both the transverse and longitudinal components are able to couple to the high temperature zone. This resulted in more energy being absorbed and the melt front or tongue advanced into the drain body, as shown in Figure 4-89. Again, the power level is maintained at the 4 kW maximum during the entire 30 minute process time.
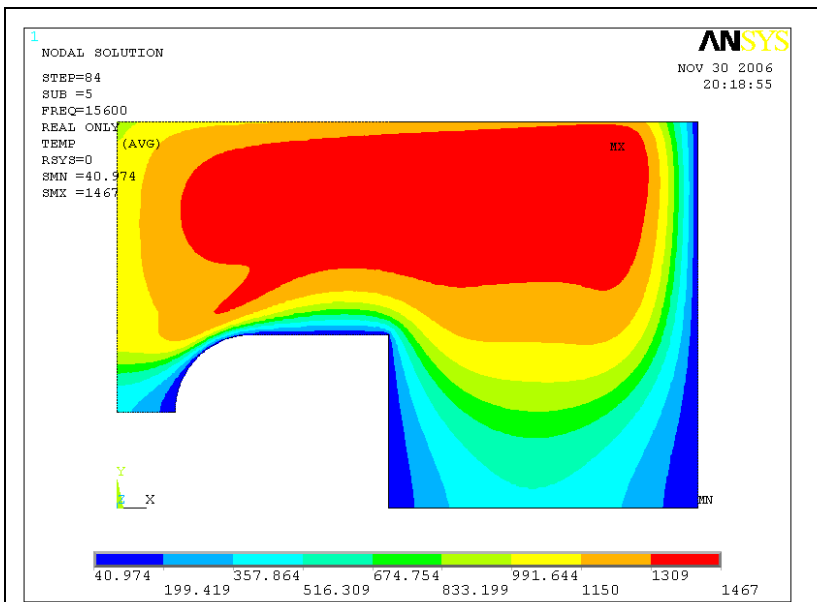
Figure 4-88. Temperature distribution after 30 minutes of operation with drain inductor in middle position.
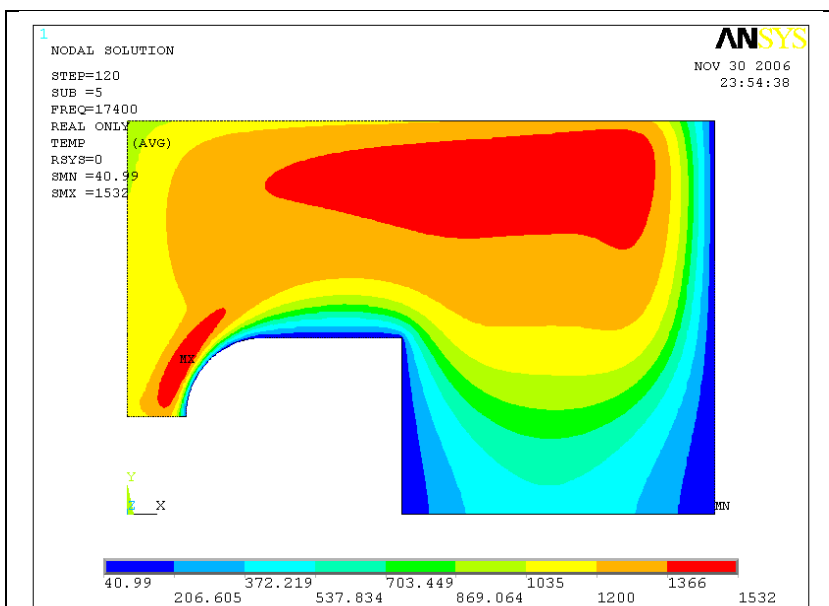
Figure 4-89. Temperature distribution after 30 minutes of operation with drain inductor in bottom position.

The temperature at the bottom of the drain has increased by about 300°C when compared to the fixed inductor system (refer back to Figure 4-86).

The next configuration analyzed was for the 25 mm diameter drain. For this investigation, only the fixed middle position inductor configuration was evaluated. All of the other model parameters were the same as the prior investigation. As before, an initial steady state temperature distribution was obtained using only the 1.76 MHz generator. This is shown in Figure 4-90. It is interesting to note that other than the physical drain geometry, all other model parameters are identical, yet the steady state temperature distributions between this case and the 30 mm diameter drain are not the same, which is an indication of the sensitivity of the behavior of the system to minor changes in the geometry.

Figure 4-90. Steady state temperature distribution prior to operating inductor for 25 mm diameter drain.
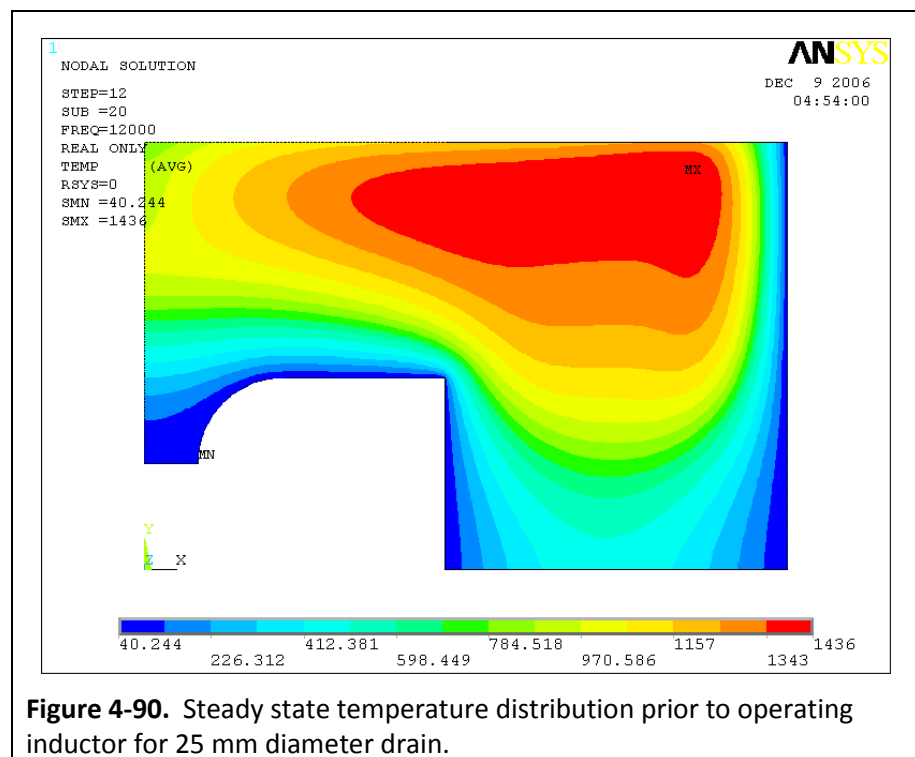
Once the steady state initial condition was achieved, the drain inductor was energized for 90 minutes, with an initial inductor power of 680 W and the maximum of 4 kW maintained once achieved. The results, shown in Figure 4-91, indicate that the temperature achieved at the bottom of the drain is approximately 100°C lower than the same investigation of the 30 mm diameter drain. This is a marginal condition for a draining event to be initiated, so the conclusion is that for this diameter drain, a moving inductor would be needed and that the improved heating conditions

produced by the translating inductor would ensure the viability of this geometry. (Note that the experimental system was modified to provide the ability to translate the drain inductor, such that this could be validated experimentally.)

Figure 4-91. Temperature distribution after 90 minutes of operation of drain inductor.
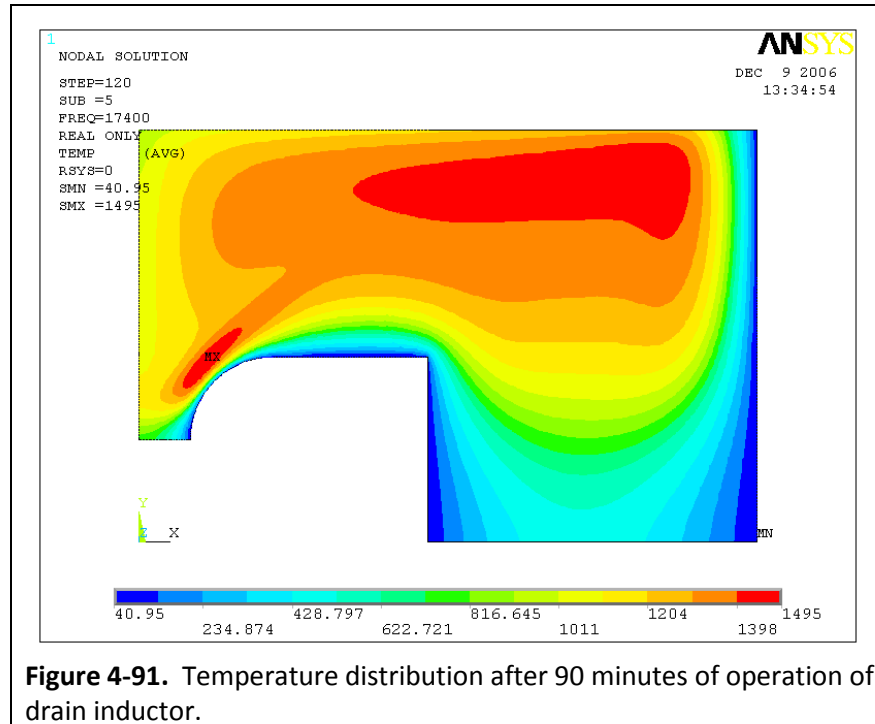
The next investigation was for the 20 mm diameter drain geometry. For this case, both the fixed and translating inductor systems were evaluated. Additional investigations were conducted for this diameter drain that included studies for systems that could achieve up to 6 kW maximum power on the drain inductor, as well as systems that could operate at higher inductor current levels, including 160 A, 175 A, 190 A, and 220 A (Note that all the prior investigations were conducted at 160 A inductor current.) This system was analyzed in great detail because the initial simplified modeling indicated that this diameter is a transition area at which the inductively heated drain system may not work. Additionally, the smallest feasible diameter is desired since it will provide the ability to maintain the most reliable control of the draining operations. Similar to the other analyses, an initial steady state temperature distribution was achieved. The distribution for this case was almost identical to that for the 25 mm diameter drain, as previously shown in Figure 4-90.

The first investigation for the 20 mm diameter drain was for the middle fixed position drain inductor. After 90 minutes of operation the melt front did not transition into the drain body. The

initial power level on the inductor was only 410 W, which was not adequate to support the draining process. This result is shown in Figure 4-92.

Figure 4-92. Temperature distribution after 90 minutes of operation for 20 mm diameter drain.
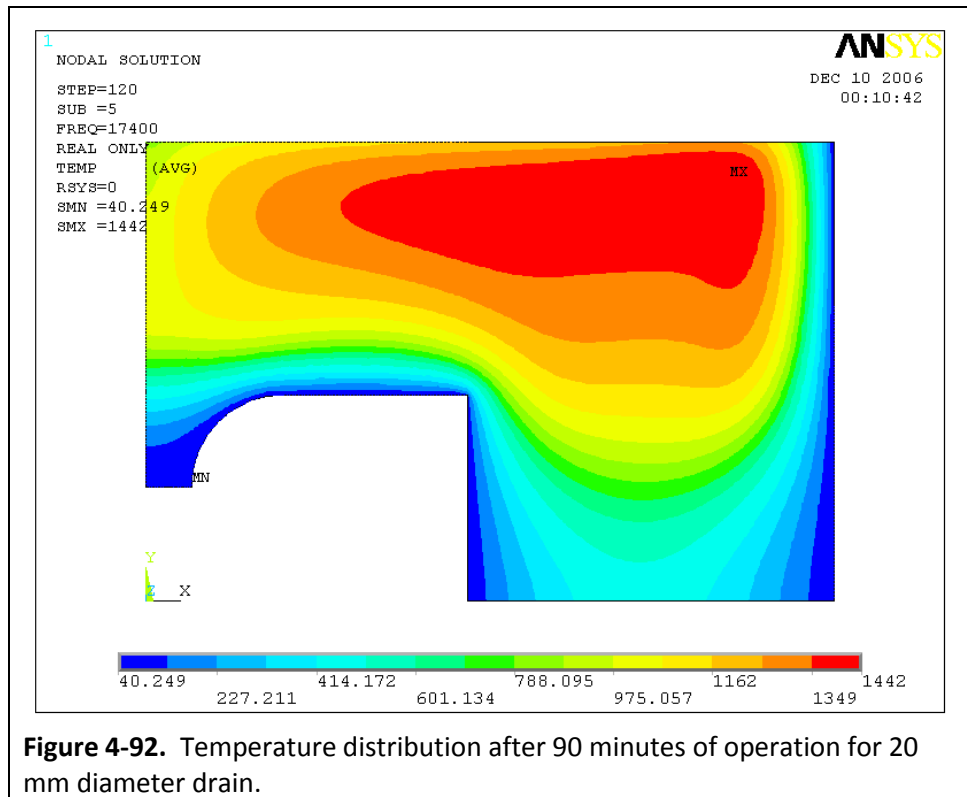
The next investigation of the 20 mm diameter drain was for the translating drain inductor. For the initial case with the moving inductor, a 4 kW power level was maintained. In a subsequent analysis this was increased to 6 kW. While prior tests only processed for 30 minutes at each location, for this study some stages required up to 60 minutes of processing time to achieve steady state. These are discussed in more detail, but it should be noted that the experimental results did not require this much time.

Once the initial steady state distribution was achieved, the drain inductor located at the top position was energized for 30 minutes. The initial power level on the inductor was 1.37 kW, with the maximum maintained at 4 kW. Figure 4-93 shows the results of this initial stage, which indicates that a melt tongue is beginning to form.

The inductor was then lowered to the middle position and operated for an additional 30 minutes. For this case, the initial power on the inductor was 4 kW and it was maintained throughout the

process time. The final temperature distribution for this inductor position is virtually unchanged from the top position, as illustrated in Figure 4-94.

Figure 4-93. Temperature distribution after 30 minutes of operation of inductor coil in top position.

Figure 4-94. Temperature distribution after 30 minutes of operation of inductor coil in middle position.
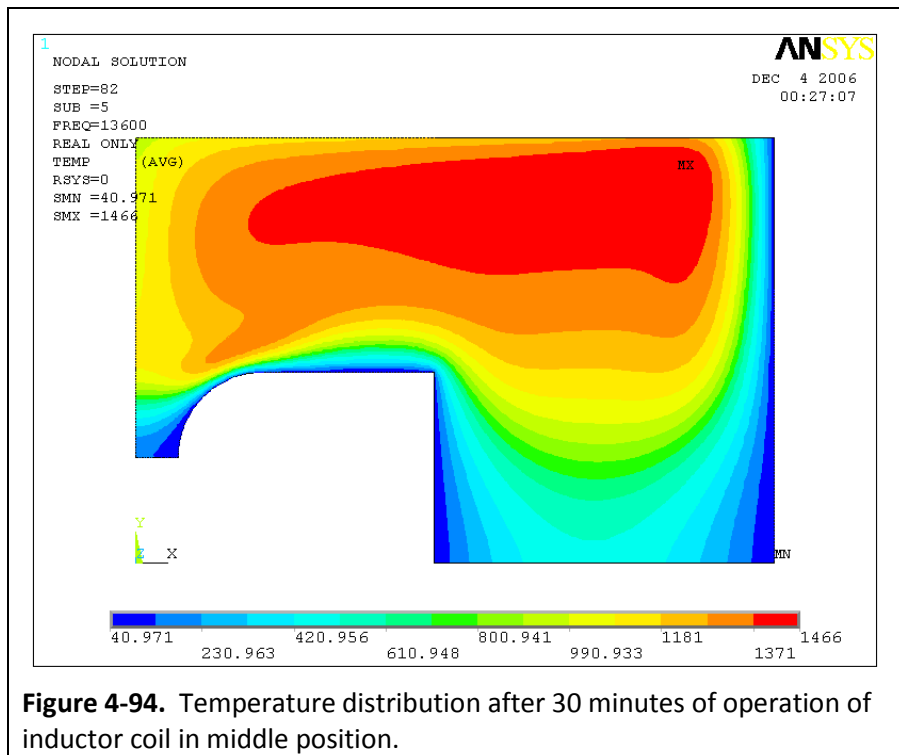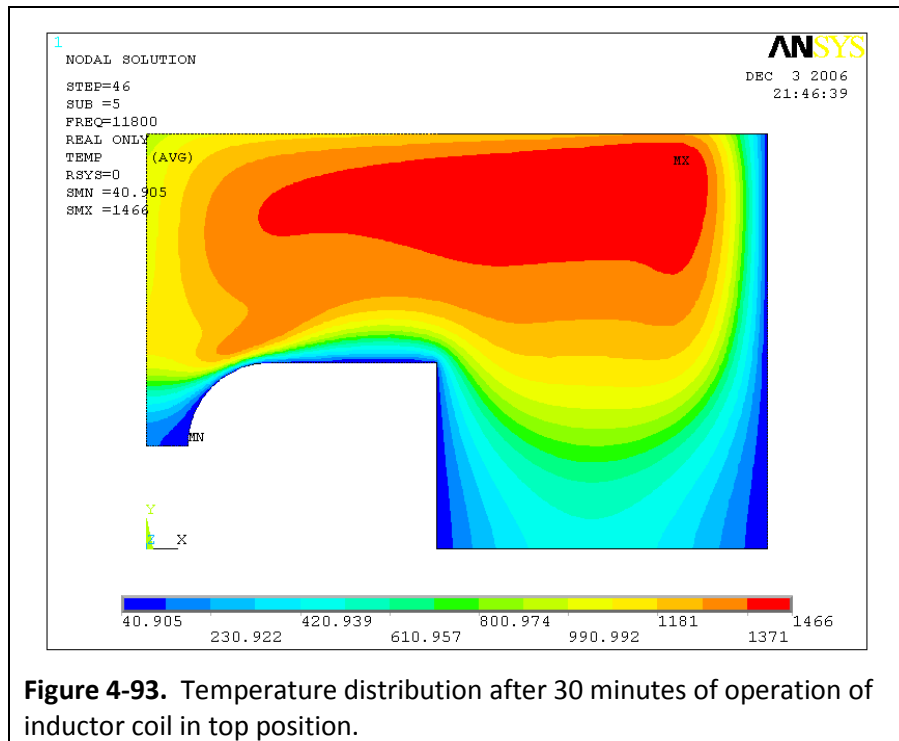
The drain inductor was then lowered to the bottom position and operated for 60 minutes. The initial power on the inductor was 4 kW; however, during the process time it dropped to 1.84 kW, indicating that the glass volume that is in the zone of influence of the drain inductor is actually cooling. This is illustrated in Figure 4-95.

Figure 4-95. Temperature distribution after 60 minutes of operation of the drain inductor at the bottom position.
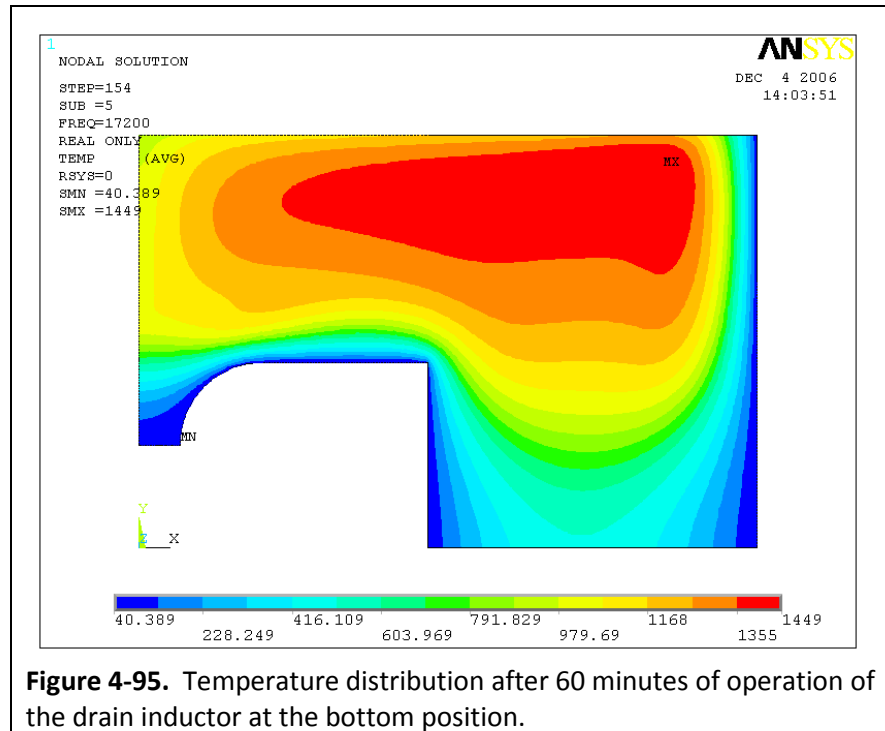
From this investigation, the conclusion was made that a 20 mm diameter drain will not function if the current in the inductor is limited to 160 A, and the total power is limited to 4 kW. For the available 27 MHz generator, increasing the total operational power to 6 kW is feasible; however, higher operating currents will be more problematic. Accordingly, the next investigation studied the characteristics for the translating drain inductor with a maximum allowable power level of 6 kW.

As in the previous analysis, the first step with the inductor in the top position performed as expected. The inductor was then lowered to the middle position and the maximum allowable power on the inductor was increased to 6 kW. For the 160 A inductor current, this resulted in an actual power level of 5.79 kW. While this indicates that the process was progressing and that the high temperature tongue was extending further into the drain throat, it also demonstrated that the magnetic coupling was not strong enough to reach the maximum 6 kW limit. This result is shown in Figure 4-96.

Figure 4-96. Temperature distribution after 60 minutes of operation of the drain inductor in the middle position. Maximum power not achieved.
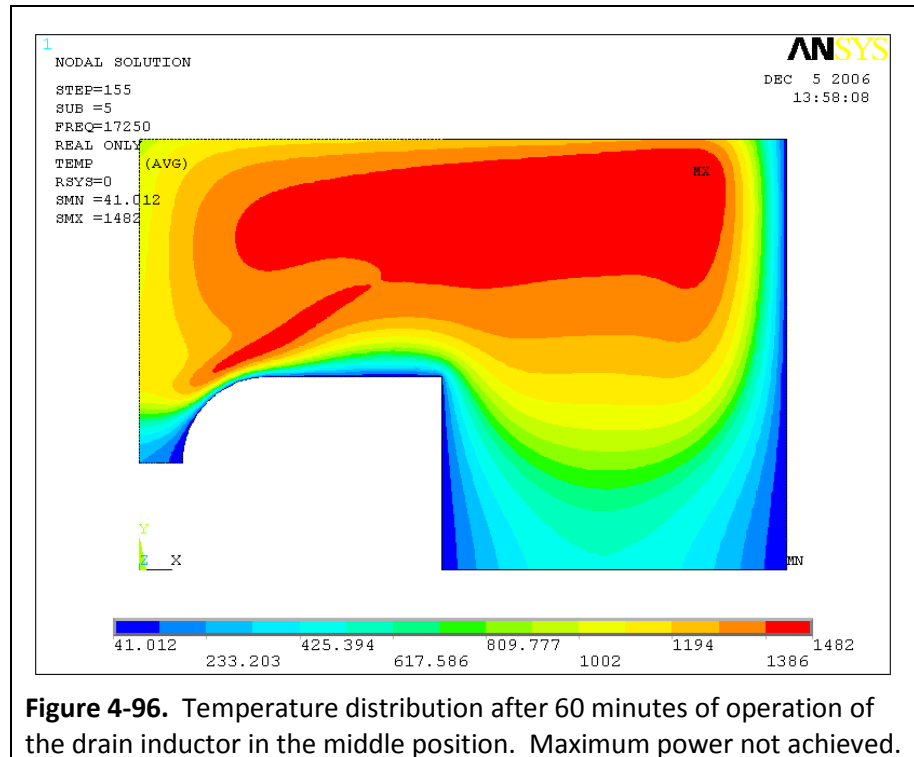
The drain inductor was then moved to the bottom position and the power in the melt began dropping, indicating again that the coupling was insufficient for the 20 mm diameter drain with 6 kW power available to initiate a draining event. Specific power levels induced into the glass by the drain inductor are shown in Table 4-4.

The important result from this analysis is that the intensity of the electromagnetic field is not sufficient to support the draining process. However, the only way to increase the electromagnetic field intensity is to either increase the inductor current or increase the coupling between the inductor and the melt. Since the temperature distribution is determined by the glass and the 1.76 MHz generator characteristics, and is thus fixed, the only approach to achieve a sustainable drain system for the 20 mm diameter configuration is to increase the maximum inductor current.

Table 4-4. Power level on inductor correlating to position and time.

Inductor Position	Process time (minutes)	Power level (kW)
Middle	60	5.79
Bottom	50	3.69
Bottom	100	3.22
Bottom	200	2.80
Bottom	300	2.60

Based on the previous results, analyses were conducted to evaluate the performance of a 20 mm diameter drain with higher current levels. The system was previously modeled with 160 A. In these analyses 175 A, 190 A, and 220 A systems were analyzed. While the available 27 MHz generator may be limited to 160 A, this is based on a larger induction coil diameter. Reduction of the drain inner diameter will also potentially reduce the outer diameter, and thus reduce the diameter of the inductor, which would allow a higher current for the vacuum tube generator.

The first high amperage drain inductor system was set at 220 A. This evaluation demonstrated that sufficient heating to initiate a draining event was reached within 60 minutes of simulated operation time. The initial power in the glass due to the drain inductor was 780 W, with the maximum power limited to 4 kW, which was achieved. These results are shown in Figure 4-97. This high current value was expected to establish an environment within the melt that would support draining; however, the primary purpose was to evaluate the temperature levels produced within the drain body. As can be seen, these temperatures are quite high and are likely unacceptable.

Figure 4-97. Temperature distribution at 220 A drain inductor current.
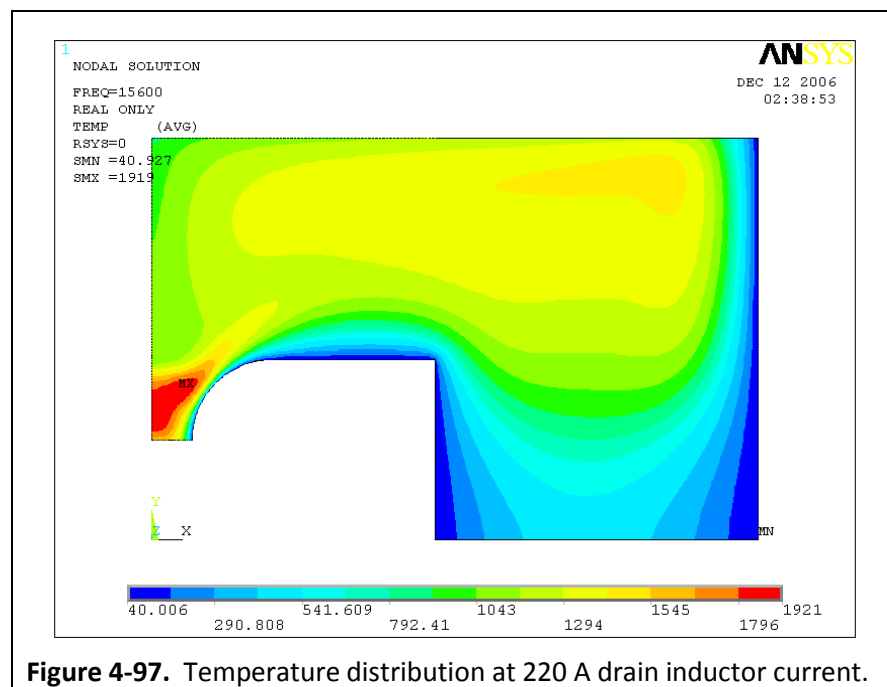
The next system evaluated used a 190 A inductor current. Similar to the 220 A system, the melt reached sufficient temperature to achieve a draining event within 60 minutes of operation. Additionally, the temperature distribution was almost identical to the 220 A system, likely due to the 4 kW total power limit, which was achieved. The initial power induced in the melt was 580 W. The resulting temperature distribution is illustrated in Figure 4-98.

The final system evaluated used a current of 175 A. In this analysis, the initial power induced in the melt was 490 W. After 60 minutes of simulated operation, the power in the melt had not reached the 4 kW limit, and was at 3.8 kW. This interim temperature distribution is shown in Figure 4-99. An additional 30 minutes at 175 A was modeled and the 4 kW maximum was reached, as well as a temperature distribution very similar to those achieved with the 190 A and 220 A systems.
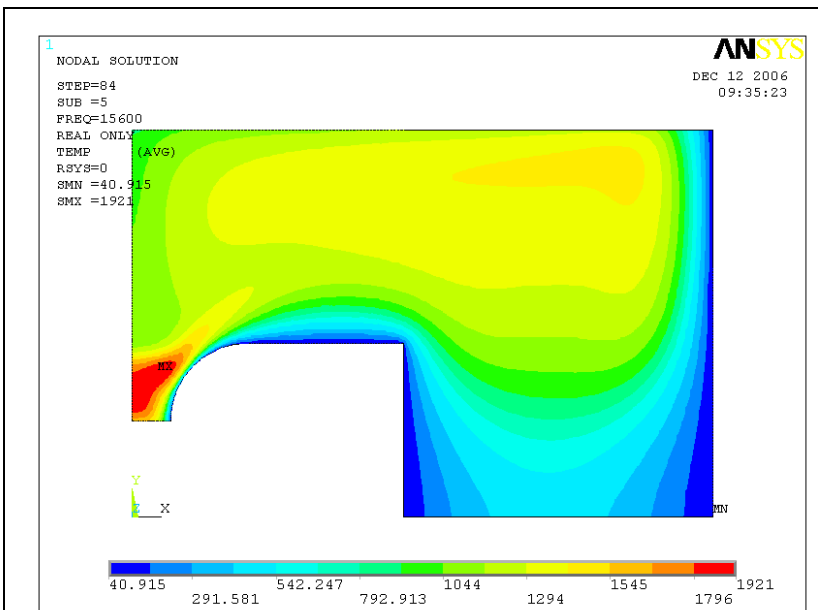
Figure 4-98. Temperature distribution at 190 A inductor current.
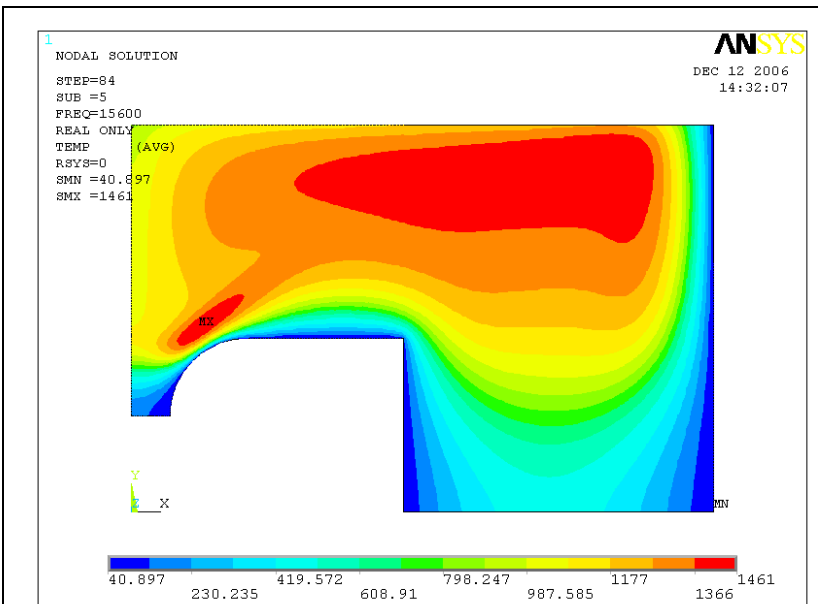
Figure 4-99. Temperature distribution at 175 A inductor current after 60 minutes of operation.

The final temperature distribution is shown in Figure 4-100. The conclusion from these analyses is that a draining event can be initiated with a 20 mm diameter drain at 175 A. This correlates to slightly less than 500 W of initial power induced in the melt by the drain inductor, which appears to be a key controlling parameter. For comparison, Table 4-5 shows the initial power levels for the various inductor amperage levels. Note that because the induction system is basically linear, the initial power in the melt is indirectly proportional to the square root of the inductor current.

Figure 4-100. Temperature distribution for 175 A inductor current after 90 minutes of operation.
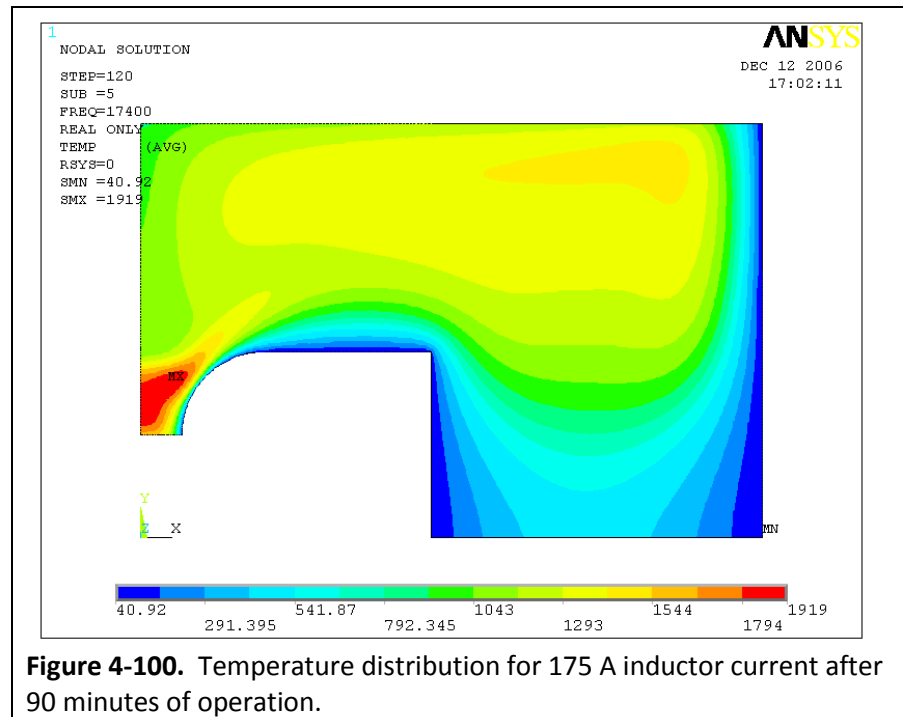
Table 4-5. Initial power levels induced in melt by drain inductor.

Drain inductor current (A)	220	190	175	160
Initial power in the melt (kW)	0.781	0.582	0.495	0.413

The overall conclusion is that, based on the characteristics of the available generator, a drain design with a 20 mm to 25 mm inside diameter is the appropriate geometry. This is the minimum diameter range that will be able to reliably produce the conditions within the drain body necessary to initiate a draining event. Although, if a higher power level generator was available, the modeling results indicate that even smaller drain diameters could be used if desired.

As indicated above, a key parameter that determines the ability to heat up the glass within the drain body to initiate a draining event is the initial power level induced in the melt. However, a second

important determining factor is the actual location of the energy deposition resulting from operation of the drain inductor. The following investigation was focused on developing a better understanding of the nature of the energy deposition for the various cases evaluated. In these studies, the configuration is for the drain inductor located in the middle position with minimum distance from the drain body, as previously defined. The profile shown is for the energy density, ranging from the maximum value to 10% of the maximum value, for the condition at the end of the operation time. The current on the drain inductor is 160 A for all cases, except as noted.

The first study was for the 40 mm diameter drain, which easily provides draining capability. The energy deposition profile, or the heat source, is shown in Figure 4-101. As can be seen, the energy source is concentrated closer to the drain throat than the center of the drain body.

The next study was for the 30 mm diameter drain. The final energy deposition profile is shown in Figure 4-102. While the basic location of the maximum value is near the same position as that for the 40 mm diameter drain, the volume of affected glass is much less, such that the 10% level does not extend as far down the drain body as that for the 40 mm diameter drain.

Figure 4-101. Heat source distribution for 40 mm diameter drain.

Figure 4-102. Heat source distribution for 30 mm diameter drain.
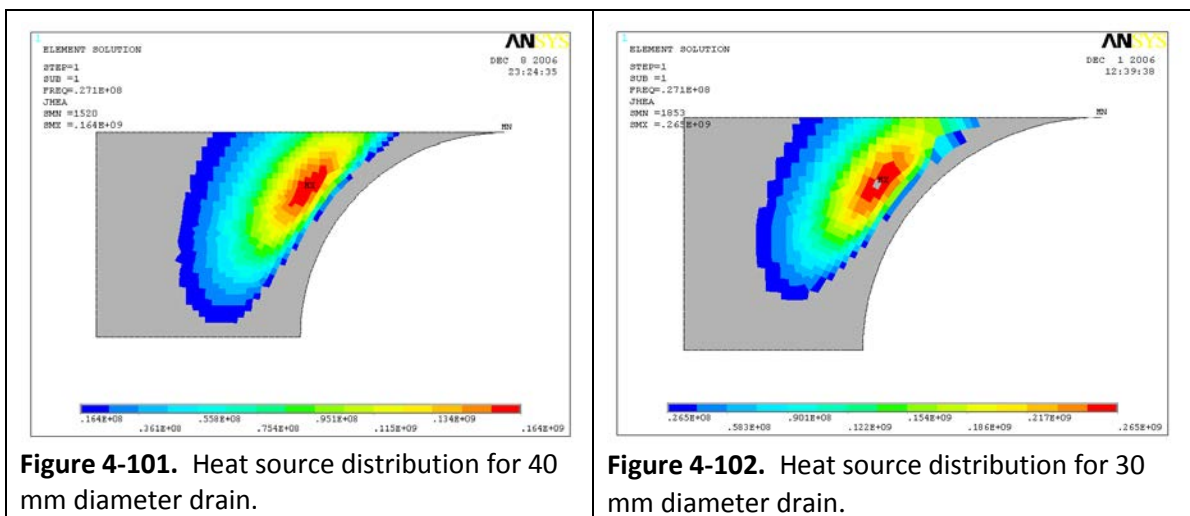
A 25 mm diameter drain was also investigated. As can be seen in Figure 4-103, the trend continues as the location of the maximum energy deposition is at approximately the same position as the other 40 mm and 30 mm diameter drains, while the 10% line continues to draw up higher into the drain body, thus impacting a smaller volume of glass within the drain.

Finally, the 20 mm diameter drain was investigated. Figure 4-104 shows the energy distribution for a 160 A drain inductor current. This clearly demonstrates why the system will not produce

conditions in the melt necessary to support a draining event. The location of the energy deposition is completely outside of the drain body, located well above it, and the 10% level shows that the energy is preferentially coupling with the main melt volume and not with the volume toward the drain.
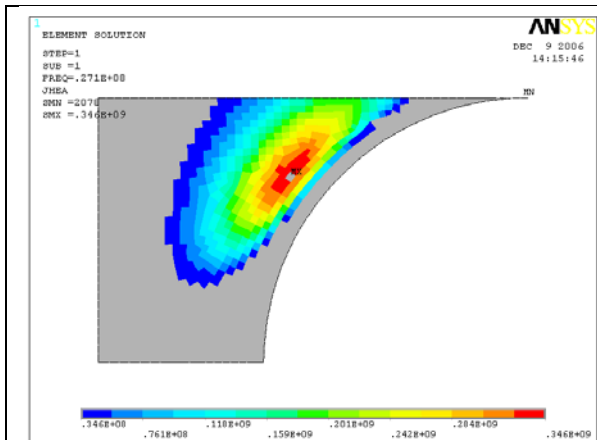
Figure 4-103. Heat source distribution for 25 mm diameter drain.
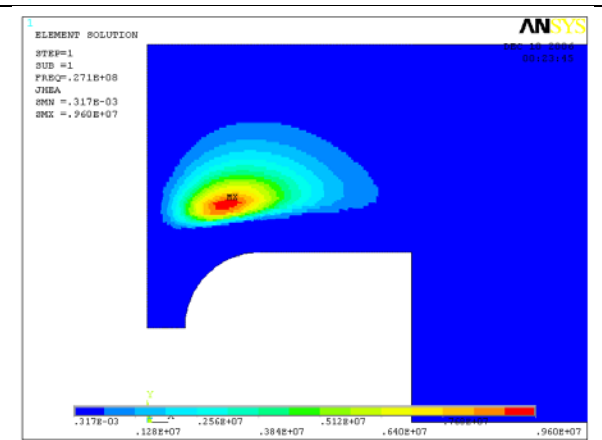
Figure 4-104. Heat source distribution for 20 mm diameter drain with 160 A inductor current.

A second evaluation for the 20 mm diameter drain was conducted using a 175 A drain inductor current. For this system, the energy deposition is dramatically different, and demonstrates that this produces the best energy density profile to initiate and maintain draining capability. Figure 4-105 illustrates this situation.

All of the preceding analyses investigating the energy deposition characteristics were conducted using a mesh refinement factor, mm, of 2 in the ANSYS® model. The results of these analyses will be key to optimizing and finalizing the drain geometry. To ensure that the results are accurate and representative, the analysis for the 20 mm diameter drain with a 175 A inductor current
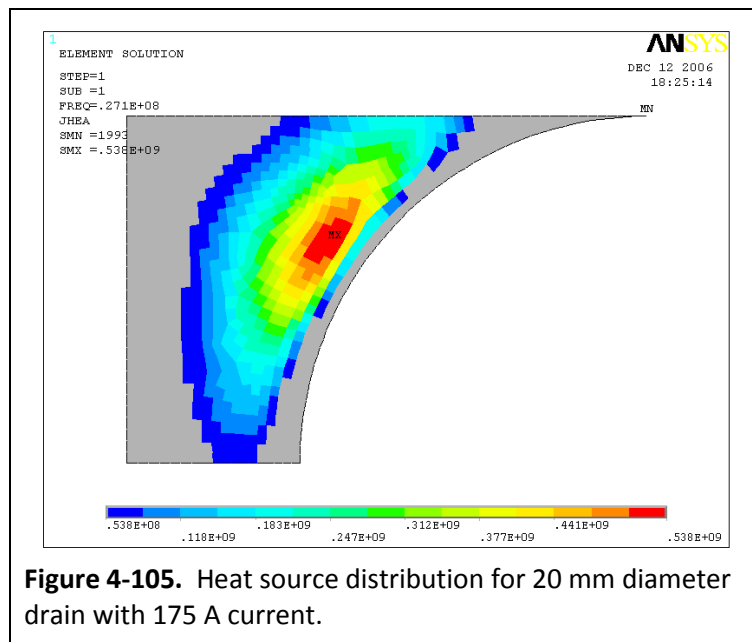
Figure 4-105. Heat source distribution for 20 mm diameter drain with 175 A current.

was repeated for mm = 4. This refines the mesh, nominally doubling the number of elements and increasing the number of nodes by approximately 125%. The results in Table 4-6 show that the results for mm = 2 are very accurate and this can be used confidently for subsequent analyses.

Table 4-6. Comparison of calculation results for coarse and fine meshes.

Parameter	mm = 2	mm = 4	Error
Maximum steady state melt temperature (without drain inductor) (^{o}C)	1,436	1,440	0.28%
Maximum melt temperature after 60 minutes of drain inductor operation (^{o}C)	1,921	1,946	1.28%
Maximum power within drain body after 60 minutes of drain inductor operation (kW)	2.331	2.363	1.35%

Some final comments on these results are warranted. The model software reports in much higher significant digits than are appropriate for the system due to key assumptions and estimations. For example, the data for the temperature dependent properties are based on glass compositions that are *near* the actual glass processed, but not the exact same glass. Additionally, most of the properties were estimated for temperatures above 1,200^{o}C. Also, the crucible and drain are designed to minimize the influence on the electromagnetic field, but there is still some attenuation and this is not specifically accounted for in the model. This means that actual power levels in the melt will likely be lower than the model calculations indicate, and thus power level requirements to produce the same results will be higher in the actual melter system. Finally, the chemical reactions and phase transitions (i.e. crystalline phase formation) within the melt volume, some of which are endothermic and others exothermic, are not accounted for in the model. However, based on the model validation efforts that were performed, it does provide fairly representative results and can be used as both a qualitative and semi-quantitative design tool for the inductively heated drain system.

CHAPTER 5.   START-UP MODEL DEVELOPMENT AND APPLICATION FOR MELT INITIATION

The model was enhanced to include the ability to investigate the melt initiation process. When processing a refractory oxide material, such as a BSG, in a CCIM system, the melt initiation, or start-up process, is achieved by introducing a conductive medium into the induction field within a mass of glass frit. As the induction field couples with the initiator, it is heated and the energy is transferred into the adjacent glass frit via thermal conduction. As the glass around the initiator begins to melt it becomes more conductive. This serves to electrically shield the ring from the induction field, which, due to the frequency of oscillation (i.e. selected to optimally couple with the molten glass) will preferentially be deposited into the glass resulting in growth of the molten pool until the entire volume in the CCIM is melted.

Various materials can be used to initiate the melt process in a CCIM. For example, the French CCIM system employs a sacrificial titanium ring [70] that is consumed during the start-up process. It represents such a small quantity of the total melt volume that the introduction of the titanium does not adversely affect the chemical composition of the glass. A similar approach is used by the Koreans [71] and the Russians in their industrial CCIM operations. These are closed systems due to the hazardous nature of the materials that are processed, and are thus inaccessible during operation. However, in the experiments conducted for this research the focus was primarily on the operational physics and parameters, and control of the process. The experimental set up involved an accessible crucible, which allowed retrieval and removal of the initiator ring. Thus, for the extensive experiments conducted as part of this

Figure 5-1. Graphite initiator ring during melt start-up.

research, a relatively large cross section (i.e. 4 cm square) graphite ring was used as the initiator. This was selected because it is readily available, inexpensive, and could be retrieved and reused multiple times. Figure 5-1 shows the graphite initiator ring glowing "red hot" within the crucible,

during the early stage of the melt initiation process. Figure 5-2 shows the ring immediately after removal. The gentleman in the photograph warming his hands is Professor Boris Polevodov. In spite of the heat from the melter in operation, the laboratory at ETU-LETI could get quite cold in the winter. (Note that this photograph was included as a tribute to Professor Polevodov who passed away during this research project.)

Figure 5-2. Graphite initiator ring immediately after removal from CCIM.

While the graphite ring was used for most of the testing, an alternate approach was investigated later as a result of operational experiences. This is discussed in a subsequent chapter.

5.1. Start-Up Model Development

The first efforts to enhance the ANSYS® MultiPhysics model developed for investigation of the CCIM process involved a simplified approach that was primarily focused on demonstrating the feasibility of modeling the process. The initial start-up model was not intended to be an integrated module with the full CCIM model, but rather a stand-alone code that provided the ability to refine the overall approach. The model was physically constructed according to the information in Table 5-1.

Table 5-1. Initial start-up model geometry.

Feature	Dimension, mm
Melt pool radius	150
Melt pool height	120
Inductor inside radius	180
Inductor external radius	185
Height of inductor	200
Ring internal radius	80
Ring external radius	120
Ring height	40

The geometry of the model is shown in Figure 5-3.

The oscillation frequency was set at 1.76MHz, as in previous models for the primary inductor current. The ring geometry was modeled in two different ways – as a solid 40 mm by 40 mm cross-section and as a hollow cross-section with a 10 cm thick wall. This was done because the electrical resistivity of graphite can range between 10^{-3} and 10^{-5} ohm-m. For this range of values (i.e. 100-fold) the penetration depth, δ, will vary by an order of magnitude since it is a function of the square root of the electrical resistivity (refer back to equation 3-5). See Table 5-2 for comparison of the skin depth for various common materials at 1.76 MHz. This means that, at 1.76 MHz, with an electrical resistivity of 10^{-5}, the penetration depth will only be about 1.2 mm.
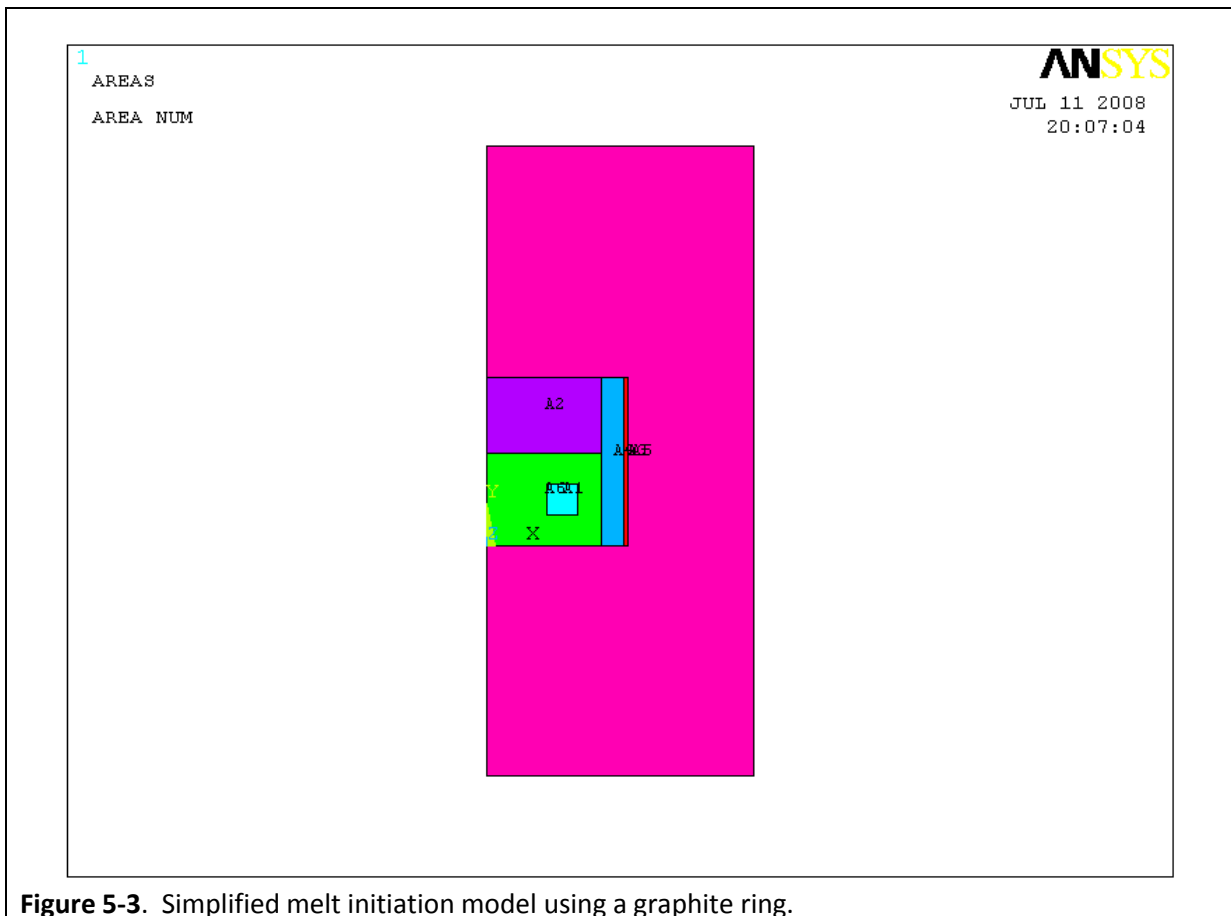
Figure 5-3. Simplified melt initiation model using a graphite ring.

Since all of the induction energy will be deposited in a shallow zone, the application of a hollow cross-section could be appropriately used to obtain accurate results while significantly reducing the calculation times of the model runs. Thus, the hollow cross-section was selected for graphite with electrical resistivity values between 10^{-4} and 10^{-5} ohm-m, while the solid graphite ring model was chosen for the electrical resistivity set at 10^{-3} (note that at this value, δ is nominally 12 mm, which is
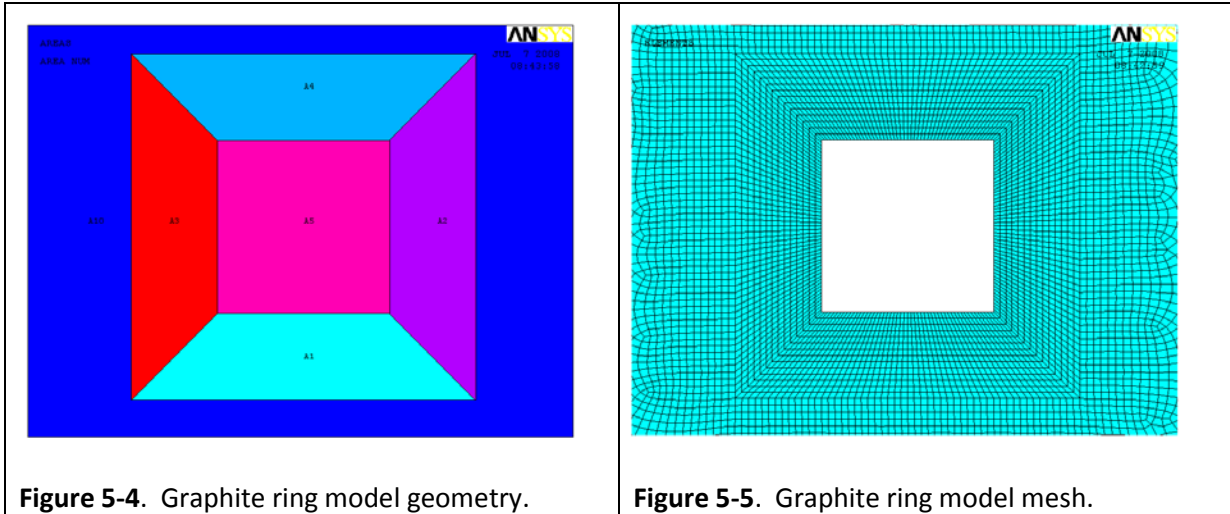
Figure 5-4. Graphite ring model geometry.

Figure 5-5. Graphite ring model mesh.

greater than the wall thickness of the hollow cross-section model). The ring model geometry and mesh are shown in Figures 5-4 and 5-5, respectively.

Table 5-2. Comparison of skin depth (δ) for common materials at 1.76 MHz.

Material	Copper	Nonmagnetic Steel	Graphite	Graphite	Glass at T>2,000°C	Glass at T=900°C
ρ, Ohm-m	2×10^{-8}	10^{-6}	10^{-4}	10^{-3}	10^{-2}	10^{-1}
δ, mm	5.36×10^{-2}	0.379	3.79	12.0	38.0	120.0

For the model using the graphite with electrical resistivity of 10^{-3} ohm-m, area A5 also includes a mesh.

This simplified model was executed by setting a fixed voltage of 5 kV on the two-turn inductor used in the model geometry. The first step was to determine the optimal mesh that would minimize the calculation time and memory needs, while providing representative results and reliable convergence. As in prior analyses, the mesh refinement variable, mm, was used to evaluate various levels of mesh "fineness", determined by setting mm equal to 1, 2, 3, and 4. This investigation was conducted for a graphite ring with electrical resistivity of 10^{-5} ohm-m. To determine the relative accuracy of the results, the total power was measured, which is the sum of the inductor power and the power in the graphite ring. This allows use of the ANSYS® post processor while not introducing any significant errors because the losses in the inductor are minimal as compared to those in the ring. The results of these analyses are shown in Table 5-3.

At mm = 3, the design area mesh includes approximately 160,000 elements. At mm = 4, the model would not converge. It is clear from the results that, while acceptable accuracy for the total power

can be achieved using mm = 2, the volume-specific power in the ring calculation error is

unacceptable. Thus, mm = 3 was selected for the actual analyses.

Table 5-3. Volume specific power in ring for various meshes using electrical resistivity of 10^{-5} ohm –m, and δ = 1.2 mm.

Parameter	mm = 1	mm =2	mm = 3
Nominal mesh size, mm	0.7	0.35	0.232
Number of steps within the penetration depth, δ	1.7	3.4	5.0
Nominal total power = Power in ring, P_{ring},+ power in inductor, P_{ind}, kW	3.28	3.27	3.27
Maximum volume specific power in ring, $P_{0\,ring}$, W/cm^3	490	724	832
Computational error for $P_{0\,ring}$, %	41	13	Assumed baseline value
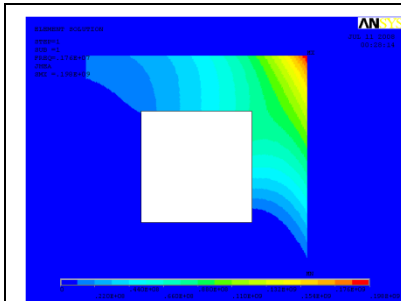
Figure 5-6. Distribution of heat sources within the ring.
$\rho_e = 10^{-3}$ Ohm-m;
$P_{ring}+P_{ind}$ = 23.68 kW
$P_{0\,ring}$ = 198 W/cm^3 maximum
mm = 1
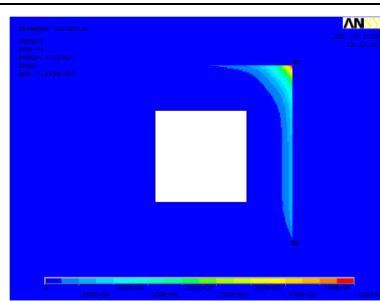
Figure 5-7. Distribution of heat sources within the ring.
$\rho_e = 10^{-4}$ Ohm-m;
$P_{ring}+P_{ind}$ = 9.01 kW; maximum
$P_{0\,ring}$ = 449 W/cm^3 maximum
mm = 1
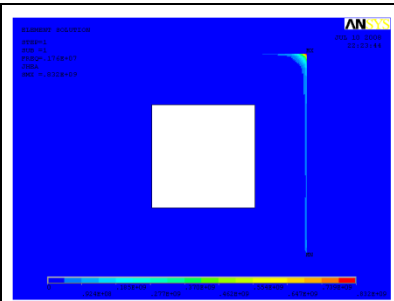
Figure 5-8. Distribution of heat sources within the ring.
$\rho_e = 10^{-5}$ Ohm-m;
$P_{ring}+P_{ind}$ = 3.27 kW
$P_{0\,ring}$ = 832 W/cm^3 maximum
mm = 1
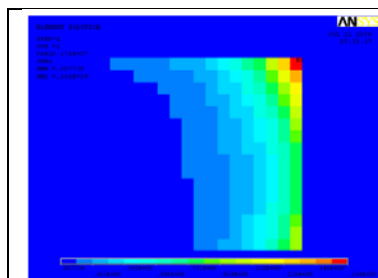
Figure 5-9. Distribution of heat sources within the ring.
mm = 1
$\rho = 10^{-3}$ Ohm-m
$P_{0\,ring}$ = 164 W/cm^3 maximum
$P_{ring}+P_{ind}$ = 30.35 kW
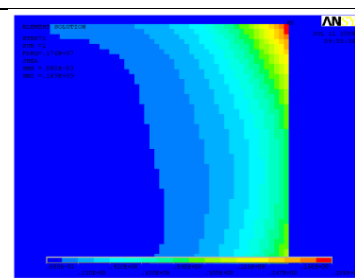
Figure 5-10. Distribution of heat sources within the ring.
mm = 3
$\rho = 10^{-3}$ Ohm-m
$P_{0\,ring}$ = 189 W/cm^3 maximum
$P_{ring}+P_{ind}$ = 30.91 kW

The first analyses investigated the effect of variable values for electrical resistivity. Specifically, values of 10^{-5}, 10^{-4}, and 10^{-3} were used. For the electrical resistivity of 10^{-3}, a solid graphite ring model was used since, as mentioned earlier, the value of δ for this resistivity, at 1.76 MHz, is 12 mm, which is greater than the wall thickness of the hollow model, introducing significant errors in the results. However, the initial investigations used the hollow model for simplicity and comparative evaluations. Figures 5-6 through 5-10, above, present comparative results for various values of δ and mm, as well as hollow versus solid ring models. Comparison of the results shown in Figures 5-6 and 5-9 illustrate the error introduced for the higher electrical resistivity value with the hollow model versus the solid model. Comparison of Figures 5-9 and 5-10 illustrates the errors introduced from using a mesh that is too coarse.

Table 5-4. Power in ring for various electrical resistivity values for 1.76MHz frequency and mm = 3.

Resistivity Ohm-m	10^{-3} Solid model	10^{-3} Hollow model	10^{-4} Hollow model	10^{-5} Hollow model
Penetration depth, mm	12	12	3.79	1.2
Nominal total power = Power in ring P_{ring}+ power in inductor P_{ind}, kW	30.91	23.68	8.84	3.27
Maximum volume-specific power in ring, $P_{0\,ring}$, W/cm^3	189	186	374	832

From Table 5-4, it can be seen that for the higher electrical resistivity values, the skin depth is much greater, which results in a near 20% error between the hollow and solid models for the total power, although the volume specific power is almost unchanged. This means that the difference in the power distribution is primarily observed in the deeper layers of the ring. These modeling results, and comparison with experimental data, indicate that the graphite that was used in the research ranges between 10^{-4} and 10^{-5} ohm-m. However, this initial model has limitations that will only support evaluation of the graphite with $\rho_e = 10^{-3}$ because a solid mesh is required to investigate the entire melt start-up process. This is because at a certain point in the process, once a significant melt pool has been established, the elements within the graphite ring volume are mathematically replaced, within the model, with elements for glass at the same temperature distribution. This simulates removal of the ring from the melt, although it does not account for the volume change. Nevertheless, it does provide the ability to investigate the characteristics and key parameters of the melt initiation process.

The following results are for investigation of a solid graphite ring with electrical resistivity of 10^{-3} through the melt initiation process. The purpose of this effort was to demonstrate the feasibility of modeling the process, which is why the model was simplified. However, this does introduce limitations that were eliminated in the later, more refined models. For example, the total power in the ring is an approximate value that is determined using the postprocessor capabilities of ANSYS® to investigate power levels along paths and in the area sections of the model. Additionally, the use of graphite with lower electrical resistivities will require a finer mesh in a solid ring model, which this model does not support. The solid ring model is necessary to couple the start-up model results with the second stage of heating to achieve steady state in the melt temperature distribution after removal of the ring. The initial model results illustrating the start-up process with a graphite ring are shown in Figure 5-11 through Figure 5-16.
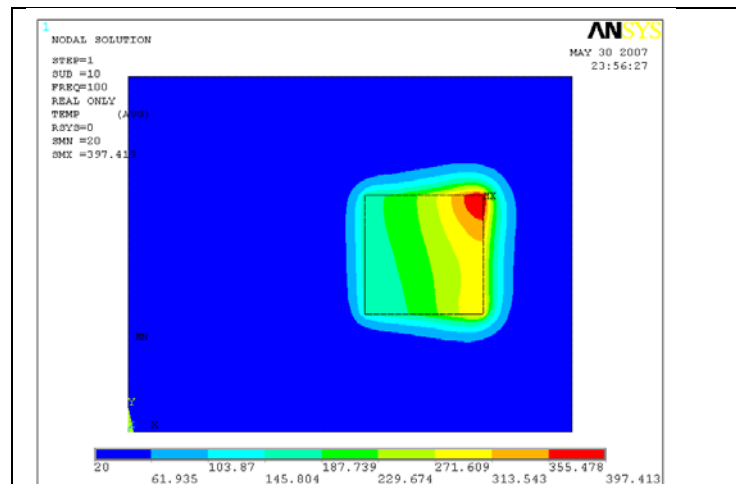
Figure 5-11. Temperature distribution after 100 seconds.
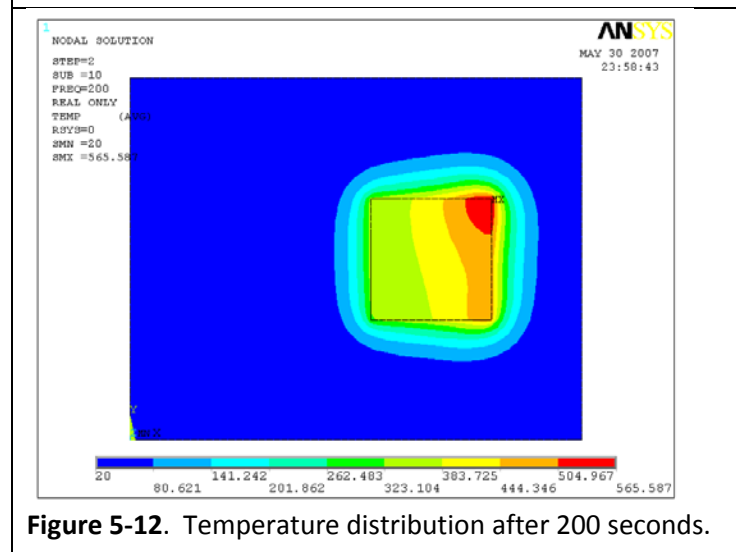
Figure 5-12. Temperature distribution after 200 seconds.

Figure 5-13. Temperature distribution after 1,800 seconds.

Figure 5-14. Temperature distribution after 2,700 seconds, just prior to removal of graphite ring.
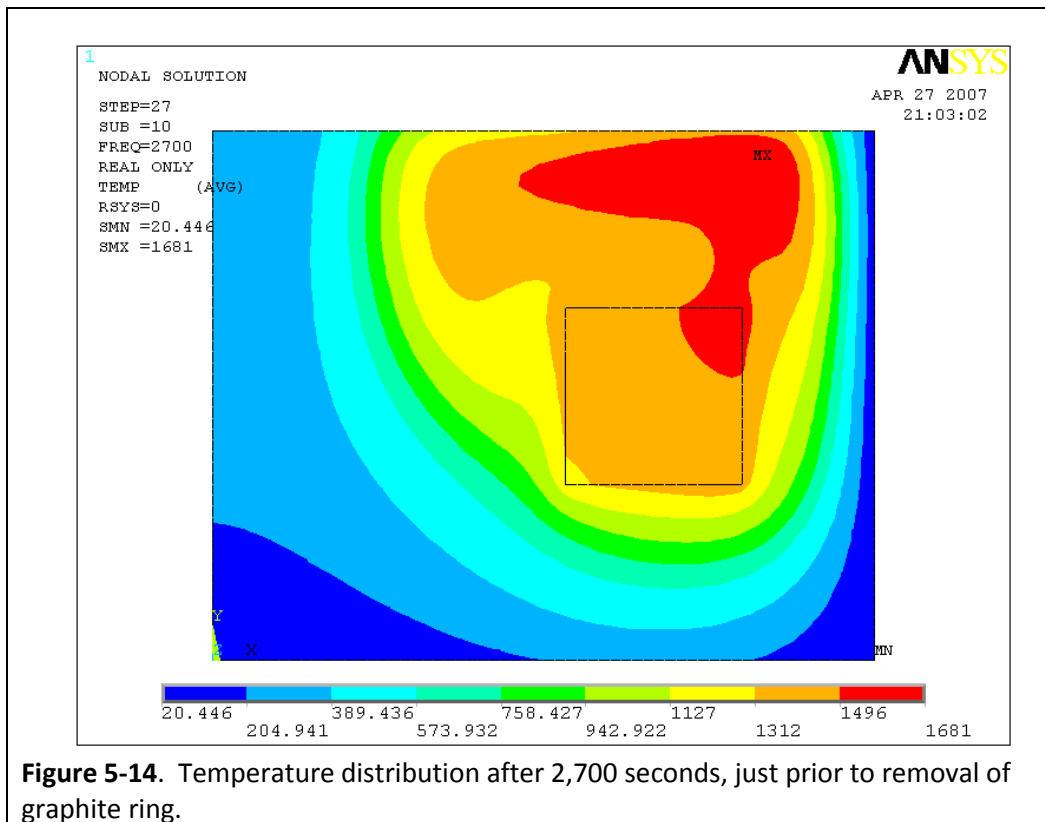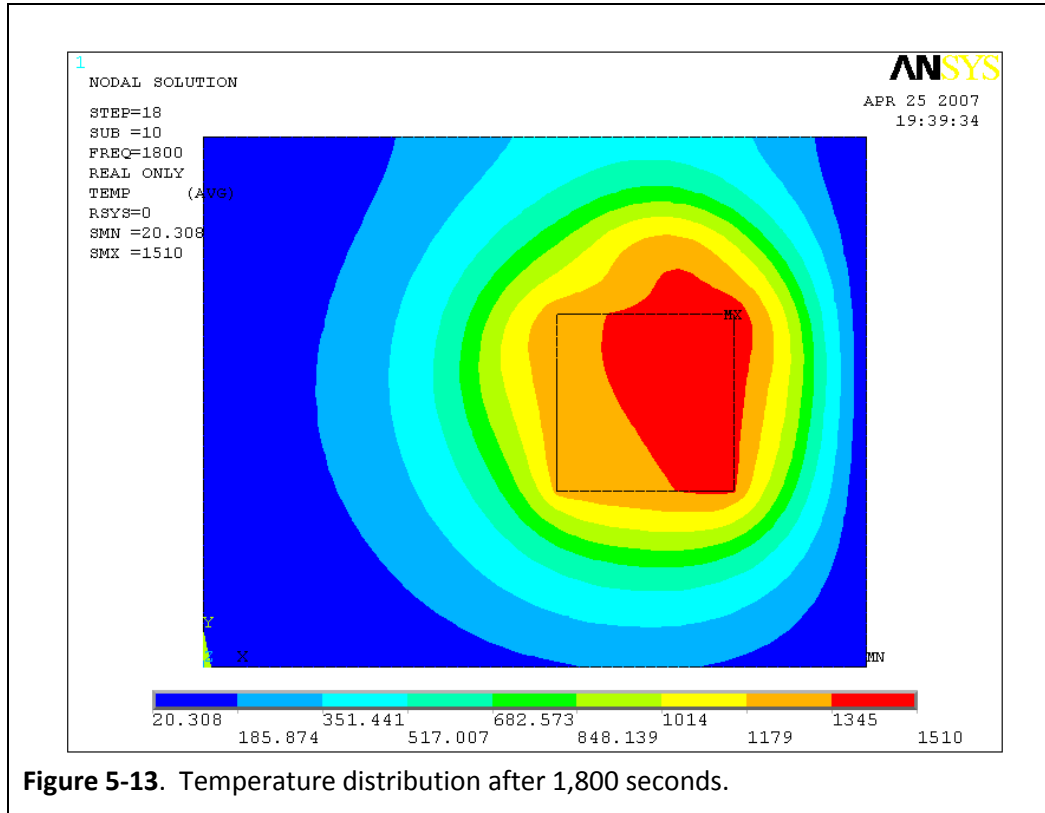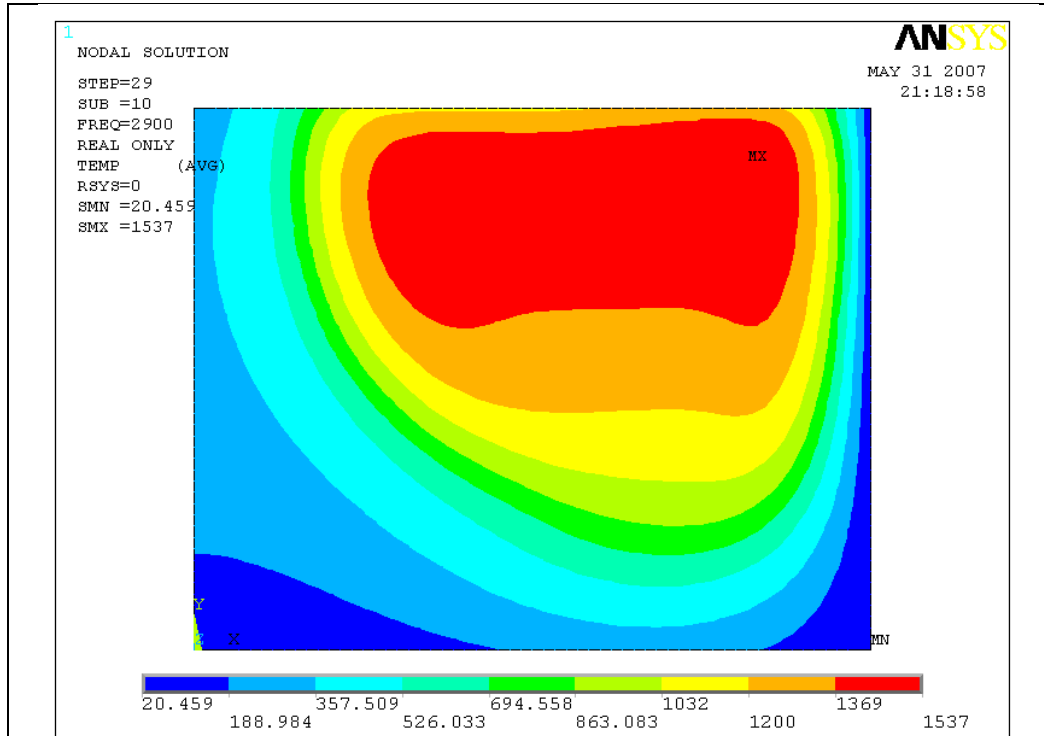
Figure 5-15. Temperature distribution after 2,900 seconds with ring removed.
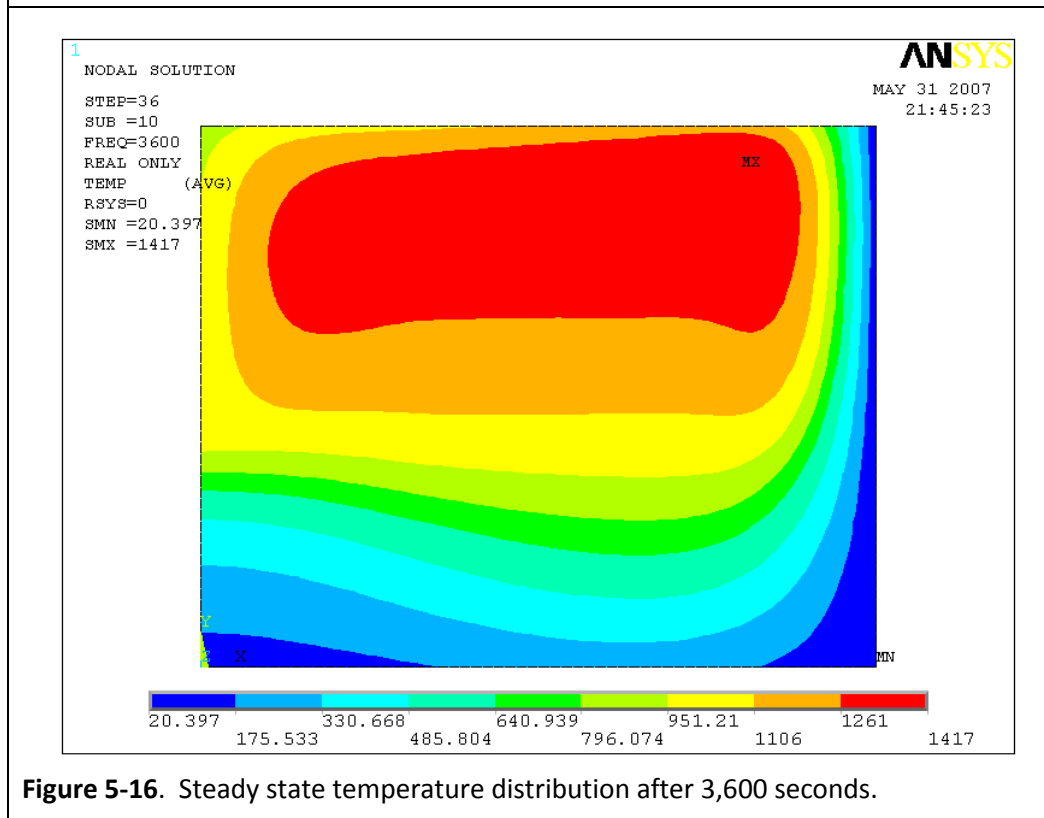
Figure 5-16. Steady state temperature distribution after 3,600 seconds.

As can be seen in the preceding figures, once the power induced in the ring exceeds the losses, its temperature increases to the point that it is hotter than the melting temperature of the glass. The glass then begins to melt and it preferentially couples with the induction field and the power into the glass increases, resulting in growth of the melt pool. Once the volume of molten glass around the ring completely covers it, this serves to shield the ring from the induction field and the energy is deposited almost entirely into the glass, accelerating growth of the melt pool. After removal of the ring, thermal balance is reached and the steady state temperature distribution is achieved.

This initial version of the start-up heating model block demonstrated the feasibility of the approach; however, additional investigation was necessary due to the increase in the volume specific power levels seen in the model upon removal of the ring (i.e., replacing the graphite ring element properties with those of glass at the same temperature distribution). This approach is illustrated in Figure 5-17 and Figure 5-18.

Investigation of this characteristic was accomplished on an improved model that incorporated the ability to investigate the effects of changes in the total impedance of the coupled system (i.e., the inductor, melt, and generator). Recall that the initial version used a fixed voltage on the inductor.

Figure 5-17. Volume specific power distribution with ring in place.

Figure 5-18. Volume specific power distribution with ring removed.
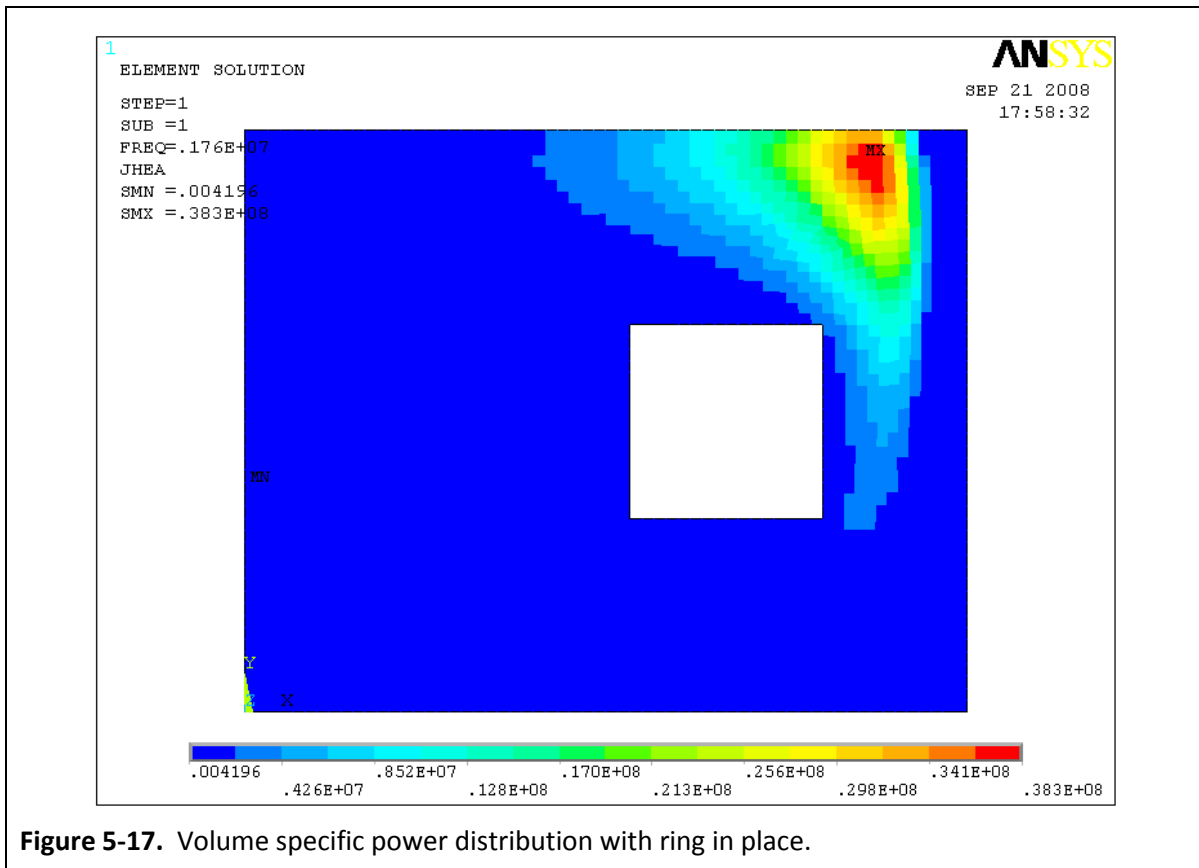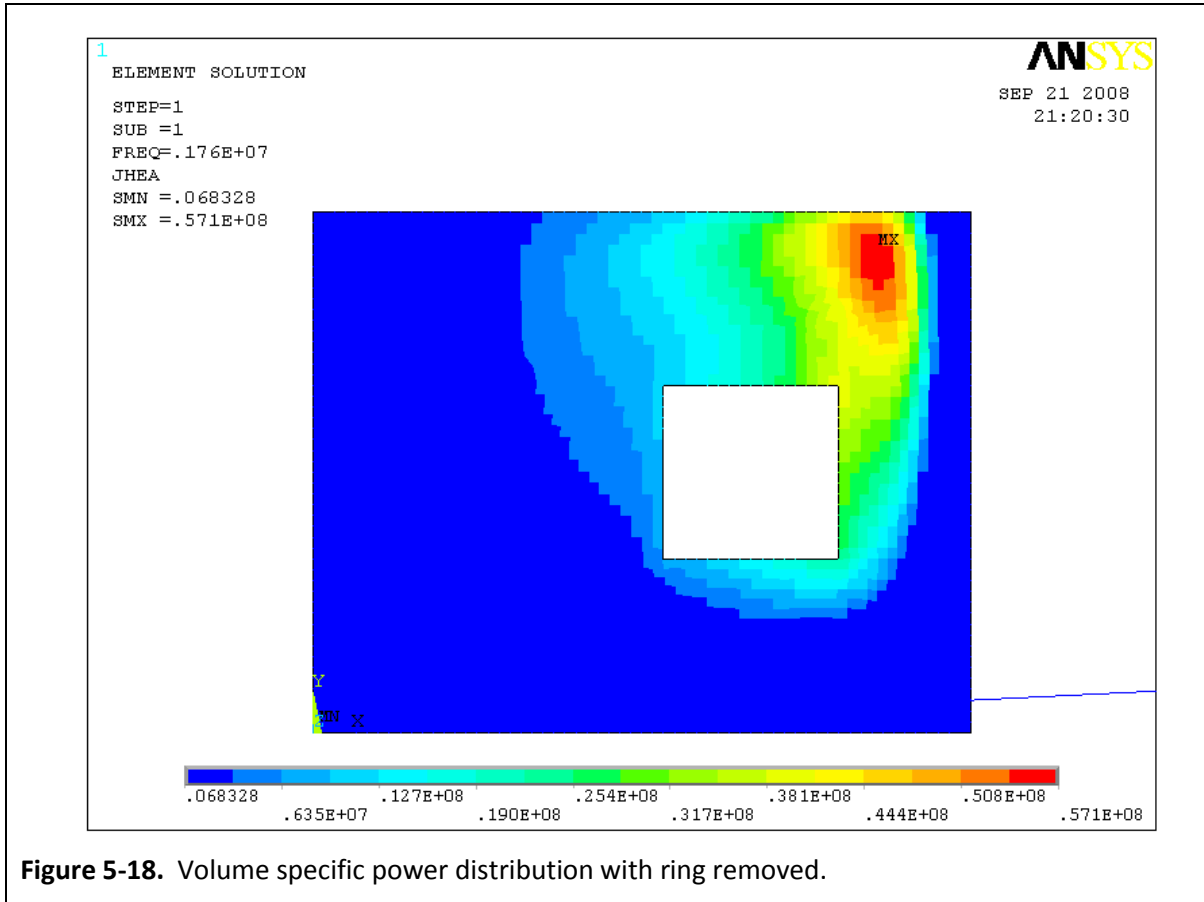
In the enhanced model, the inductor current is fixed such that a constant power of 11 kW is realized in the initiator ring. This is more representative of the actual operation of the system. The value of 11 kW was based on experimental measurements. The results demonstrated a similar phenomenon in which the volume specific power in the glass increased dramatically upon removal of the ring, nominally 2.5 times. The conclusion is that, while this is impossible to directly measure, similar changes do occur in the inductor current and voltage upon removal of the ring, as observed during experimental tests. This is most likely due to the influence of the "external" electrical circuit (i.e., the coupling of the initiator ring with the induction field versus the coupling of the glass melt with the induction field). To investigate this further, the model was modified to allow changing the impedance of the power source (Z_{int}) and its ratio to the inductor impedance (Z_{ind}), which is influenced by the coupled load active resistance. Models were run with $Z_{int} = Z_{ind}$ and $Z_{int} = 2Z_{ind}$. Additionally, the model allows changing the inductor voltage value (U_{ind}) to observe qualitative effects of the changes that can occur upon removal of the ring. The calculations were performed at mm = 2, and $\rho = 10^{-3}$ Ohm-m for the graphite ring. The Z_{ind} base value is set at 2.92 Ohm, which was

measured on the actual induction coil. Figure 5-19 through Figure 5-25 show the model results for various parameters after 2,800 seconds of calculation time, and then the ring is removed and the model is run for an additional 100 second time step. The figures are for $Z_{int} = 2Z_{ind} = 5.84$ Ohms. Results for $Z_{int} = 2.94$ Ohms are qualitatively similar.
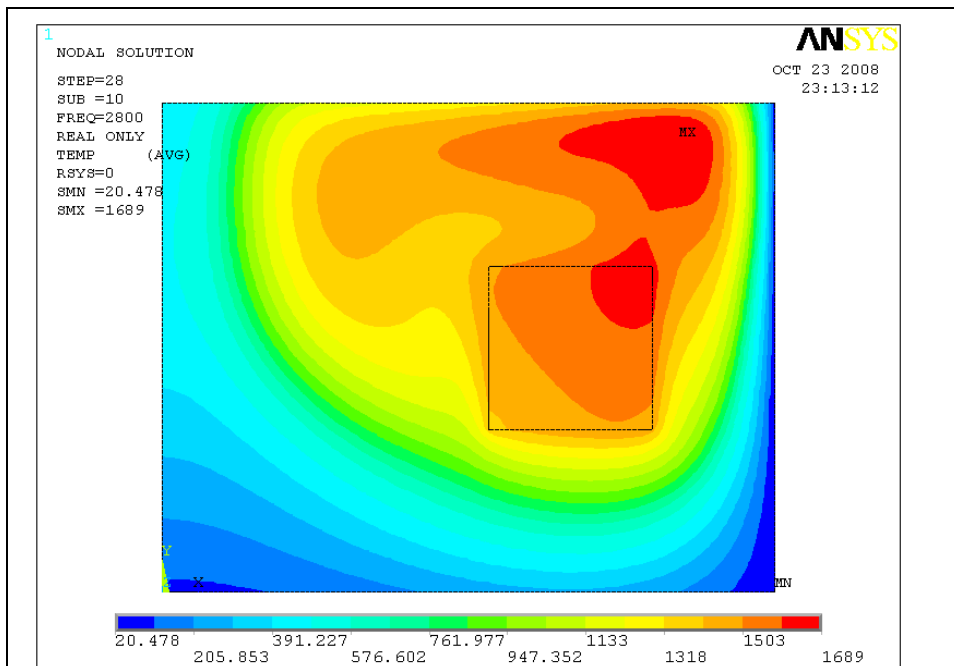
Figure 5-19. Temperature distribution in the melt and ring at 2,800 seconds.
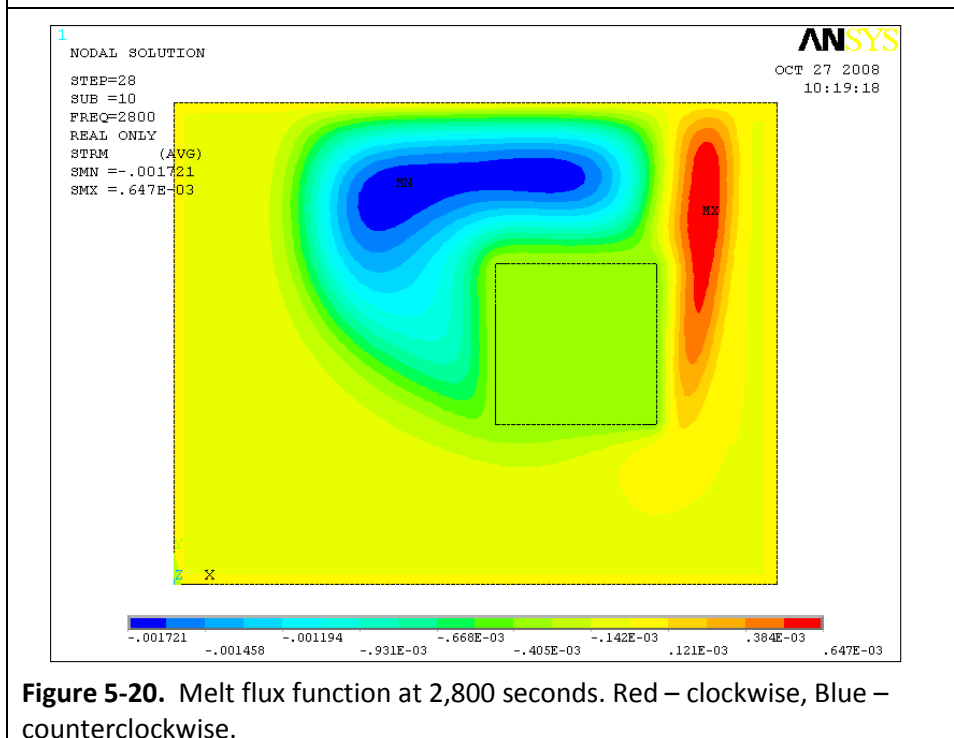
Figure 5-20. Melt flux function at 2,800 seconds. Red – clockwise, Blue – counterclockwise.
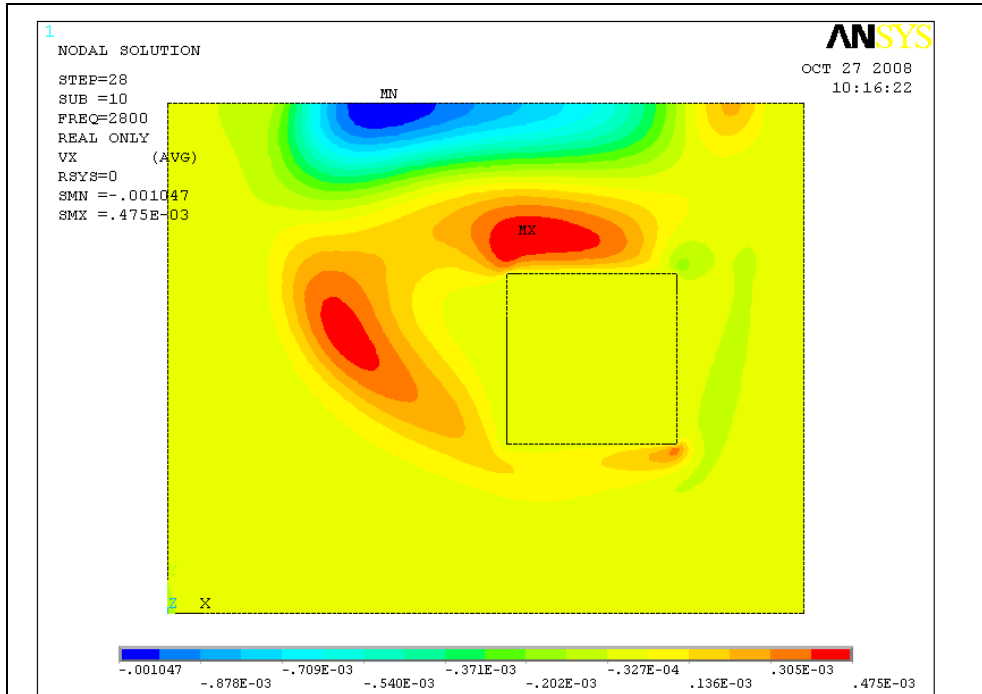
Figure 5-21. Horizontal velocity component.
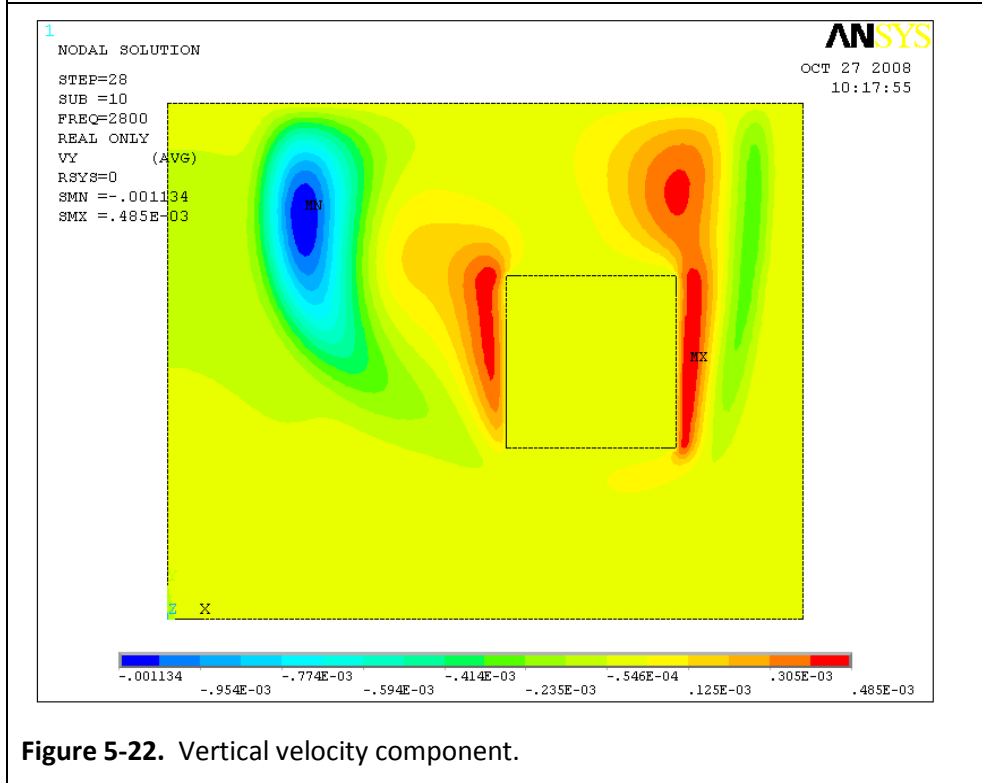
Figure 5-22. Vertical velocity component.

Figure 5-23. Power distribution in ring and melt at 2,800 seconds.

Figure 5-24. Temperature distribution in melt after removal of ring at 2,900 seconds.

Figure 5-25. Power distribution in melt after removal of ring at 2,900 seconds.
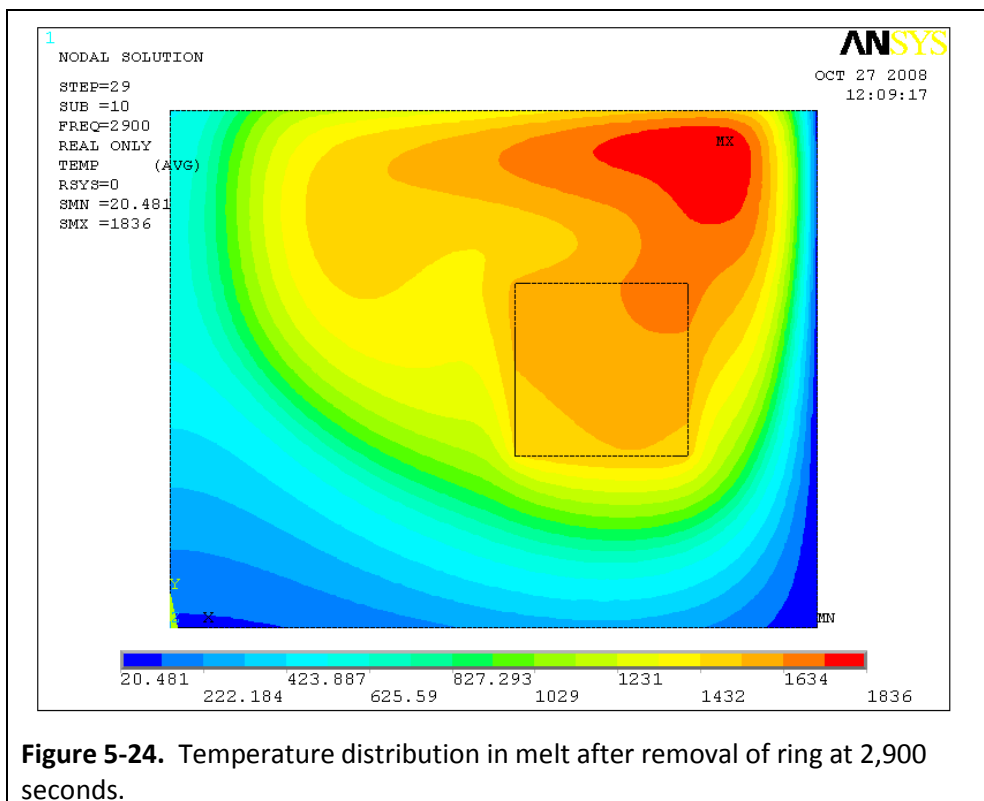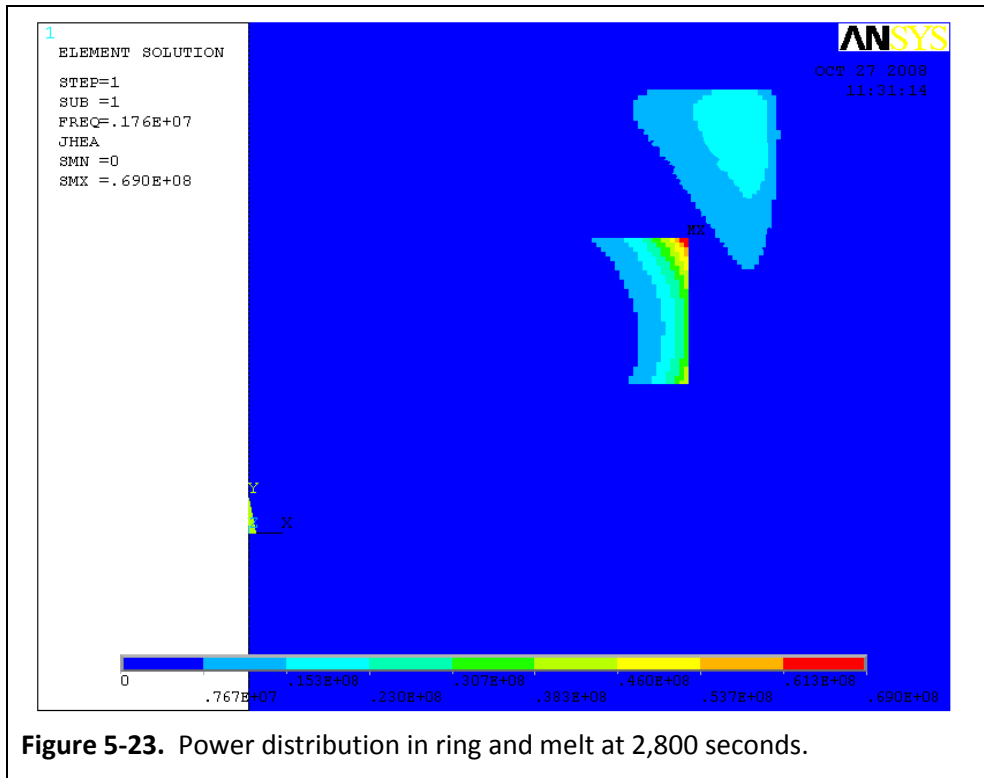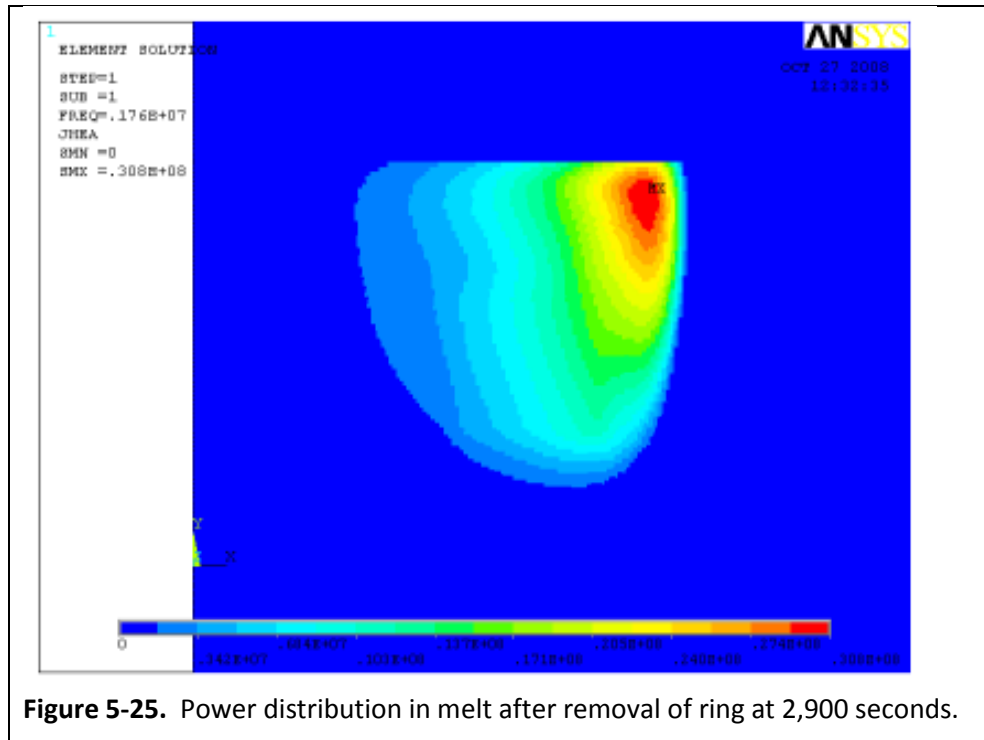
Tables 5-5 through 5-7 show summary comparative data of the modeling results.

Table 5-5. System Parameters: Z_{int} = Z_{ind} = 2.92 Ohm, U_{ind} = 2.5 kV, U_{gen} = 5.0 kV.

Condition	P_{sum}, kW	P_{glass}, kW	P_{ring}, kW	Z_{ind_h}, Ohm	R_{load}, Ohm	I_{ind}, A
With the ring	31.03	19.06	11.97	4.209	0.175	421
Without the ring	54.54	45.28	9.25	4.39	0.336	403

Table 5-6. System Parameters: Z_{int} = $2Z_{ind}$ = 5.84 Ohm, U_{ind} = 1.67 kV, U_{gen} = 5.0 kV.

Condition	P_{sum}, kW	P_{glass}, kW	P_{ring}, kW	Z_{ind_h}, Ohm	R_{load}, Ohm	I_{ind}, A
With the ring	6.37	4.0	2.37	6.66	0.18	178
Without the ring	11.2	9.3	1.9	6.84	0.337	173

Table 5-7. System Parameters: Z_{int} = $2Z_{ind}$ = 5.84 Ohm, U_{ind} = 3.75 kV.

Condition	P_{sum}, kW	P_{glass}, kW	P_{ring}, kW	Z_{ind_h}, Ohm	R_{load}, Ohm	I_{ind}, A
With the ring	31.7	19.9	11.84	6.66	0.18	399
Without the ring	56.18	46.68	9.49	6.84	0.337	388

For these tables, U_{gen} is voltage on the generator lamp anode; P_{sum} is power in the total coupled load (glass and initiator ring); P_{glass} is power in the glass; P_{ring} is power in the ring, or in glass when the ring is removed; Z_{ind_h} is full resistance of the inductor and coupled load based on parameters for the heated ring and melted glass; R_{load} is active resistance of the coupled load; I_{ind} is inductor current; and U_{ind} is inductor voltage.

Several observations can be drawn from these results. Because the internal resistance of the generator and the inductor resistance are electrically connected and constant, increasing Z_{int} by a factor of two reduces U_{ind} by a factor of 1.5. This is expected because the generator circuitry is very stable and the inductor power is only about 10% of the total power in the generator. Removal of the ring increases the active resistance of the coupled load, and thus U_{ind} decreases if Z_{int} is held constant (see Table 5-5 and Table 5-6). This results in a decrease in the inductor current and voltage, which is demonstrated qualitatively in the calculation results. On the other hand, to maintain the power level in the total volume upon removal of the ring, simulated by doubling the load resistance, the inductor voltage must be increased by 1.5 times (see Table 5-7). Thus, changing the Z_{int} value corresponds to changing the power setting of the generator and changing the Z_{ind} correlates to a change in the melt pool condition (i.e. removal of the ring). The Z_{int}/Z_{ind} ratio is thus very important during periods of dramatic change in the melt condition, and requires that the start-up model must take into account the internal resistance of the generator.

As previously mentioned, this initial model was simplified to allow evaluation of the overall feasibility of modeling the start-up process and to be able to investigate some of the key physical and model parameters. However, other phenomena exist in the actual conditions that are not captured in the model. These include the following:

1.   Once a significant melt pool has been established around the graphite ring, the density of the molten glass is greater than that of the graphite and it actually floats to the top (refer back to Figure 5-1).
2.   When the graphite ring reaches the surface, it interacts with the air and oxidation occurs, which releases gases, mass, and heat from the ring.
3.   At certain times during the process some areas of the graphite ring reach temperatures that result in ignition of the graphite, which releases additional heat into the melt.

Nevertheless, even with these limitations, after enhancement and refinement of the model to provide for evaluation of solid rings with lower electrical resistivity values, and the ability to take into account the changes in the generator internal impedance, the results are representative and provide an excellent tool for investigating and optimizing the start-up process. Recognizing the noted limitations, the start-up model was used to qualitatively evaluate the influence of the type of material used as an initiator, as well as the geometry. These investigations are discussed below.

5.2. Start-Up Model: Application to Evaluate Effects of Material of Initiator Ring

The influence of the material used for the initiator ring was first studied. Materials evaluated included graphite, silicon carbide, mild steel, and molybdenum. All rings used the same geometry with an inside radius of 180 mm, outside radius of 220 mm, and height of 40 mm. For these investigations, only the temperature-dependent electrical resistivity and density values were used. Average values were used for specific heat and thermal conductivity because these parameters do not have significant effects on the process being evaluated. Figure 5-26 and Figure 5-27 show the material properties incorporated into the model.
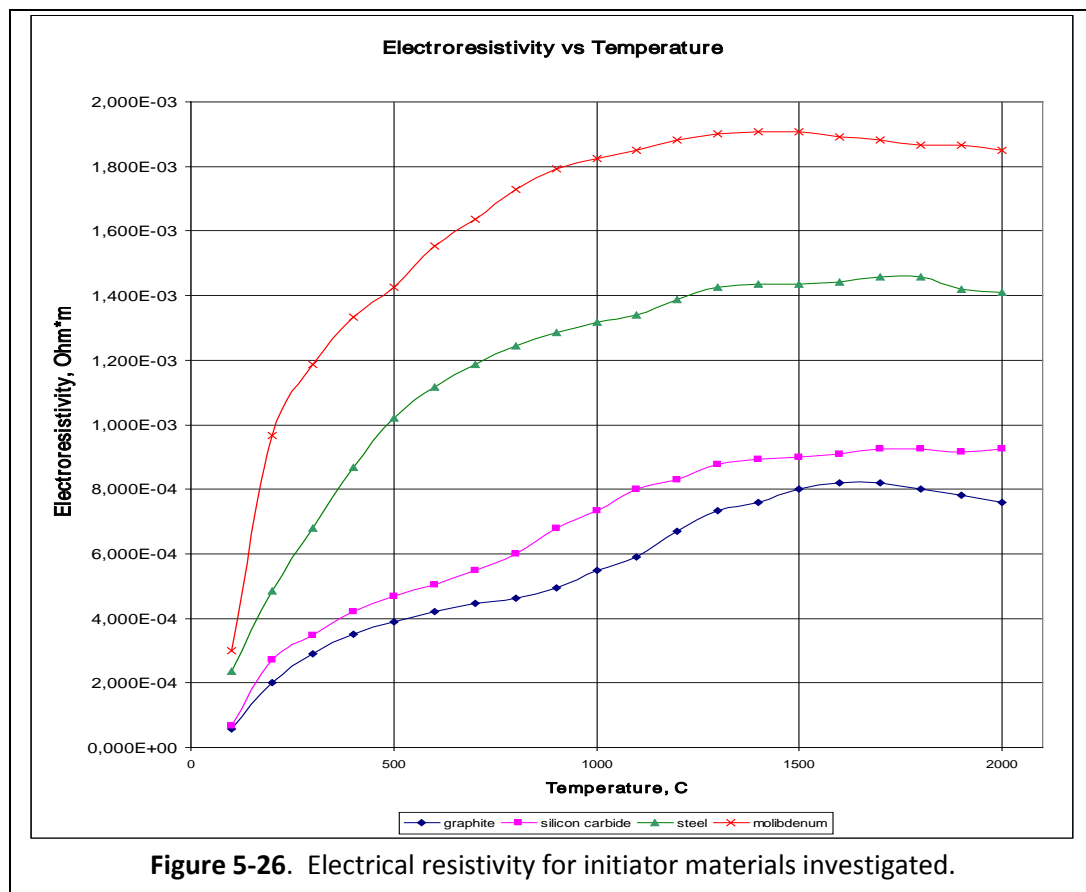
Figure 5-26. Electrical resistivity for initiator materials investigated.

Figure 5-27. Density for initiator materials investigated.
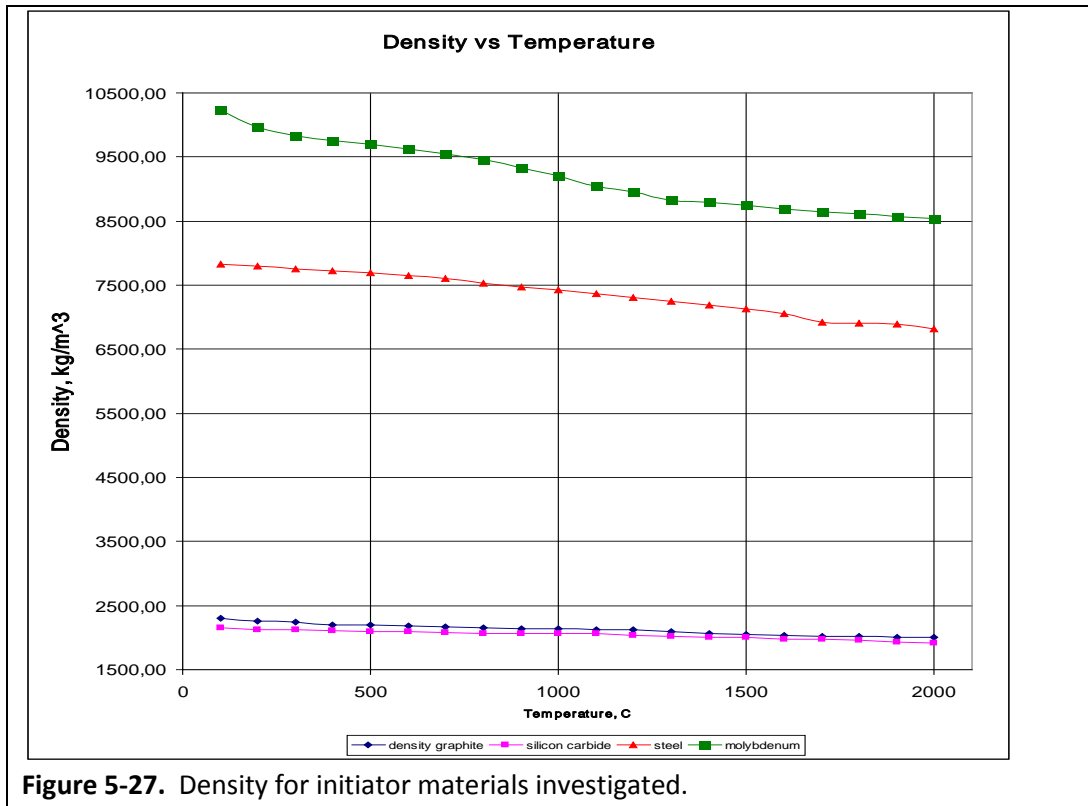
5.2.1.Initiator Ring in Crucible

These calculations were conducted using fixed voltage values on the inductor and for fixed times for comparison purposes. The voltage values used were based on experimental data. The basic model parameters for the calculations were as shown in Table 5-8.

Table 5-8. Parameters for start-up model analysis.

Parameter	Value
Internal diameter of the crucible	300 mm
Height of the melt pool	220 mm
Internal diameter of the inductor	340 mm
Number of inductor coils	2
Cross-section shape of the inductor coil	rectangular
Height of the inductor	220 mm
Oscillation frequency	1.76 MHz.
Voltage on the inductor during start-up	5 kV
Voltage on the inductor during melting	2.9 kV
Calculation time for start-up process	1,000 sec
Calculation time for the melting process	6,000 sec
Grid fineness factor	mm = 4

During the second stage, these parameters (i.e. 2.9 kV on the inductor) would result in severe over-heating of the glass if actually held for the full time. However, the model does not allow for adjustment of the voltage during the calculation run. Therefore, the criterion focused on is the time required to achieve temperatures near 1,000°C within the melt volume, which will ensure that the melting process would continue.

Figure 5-28 provides a comparison of the temperature fields within the ring and surrounding glass for each of the material types.

a) Graphite

b) Silicon Carbide

c) Steel

d) Molybdenum

Figure 5-28. Comparison of temperature distributions.
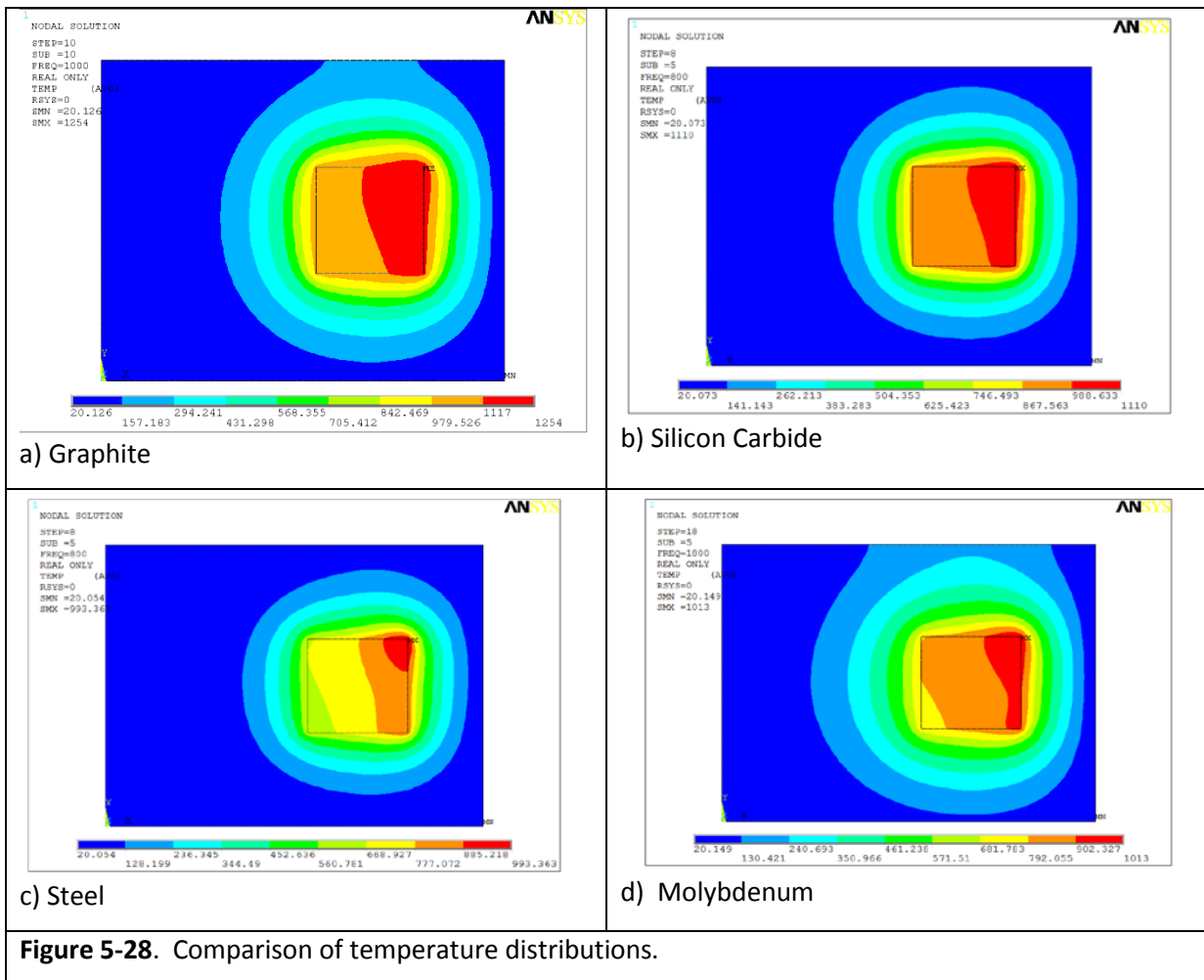
While the silicon carbide ring had a lower overall temperature compared to graphite after 1,000 seconds, the condition was sufficient to allow continued heat up and melt during the second stage. However, the steel and molybdenum did not produce conditions that would allow the melt to propagate, thus the calculation times had to be increased to 1,500 seconds and 2,000 seconds,

respectively, to achieve the desired conditions in the start-up stage. This was due to the fact that these materials have much higher densities and lower electrical resistivities.

Figure 5-29 provides comparative results for the power source distributions during the start-up process. While the distributions are similar, the maximum values decrease as the electrical resistivity does (i.e. from graphite to molybdenum). This correlates in less efficient induction heating and thus increased times to achieve start-up and a full melt pool.

a) Graphite

b) Silicon Carbide

c) Steel

d) Molybdenum
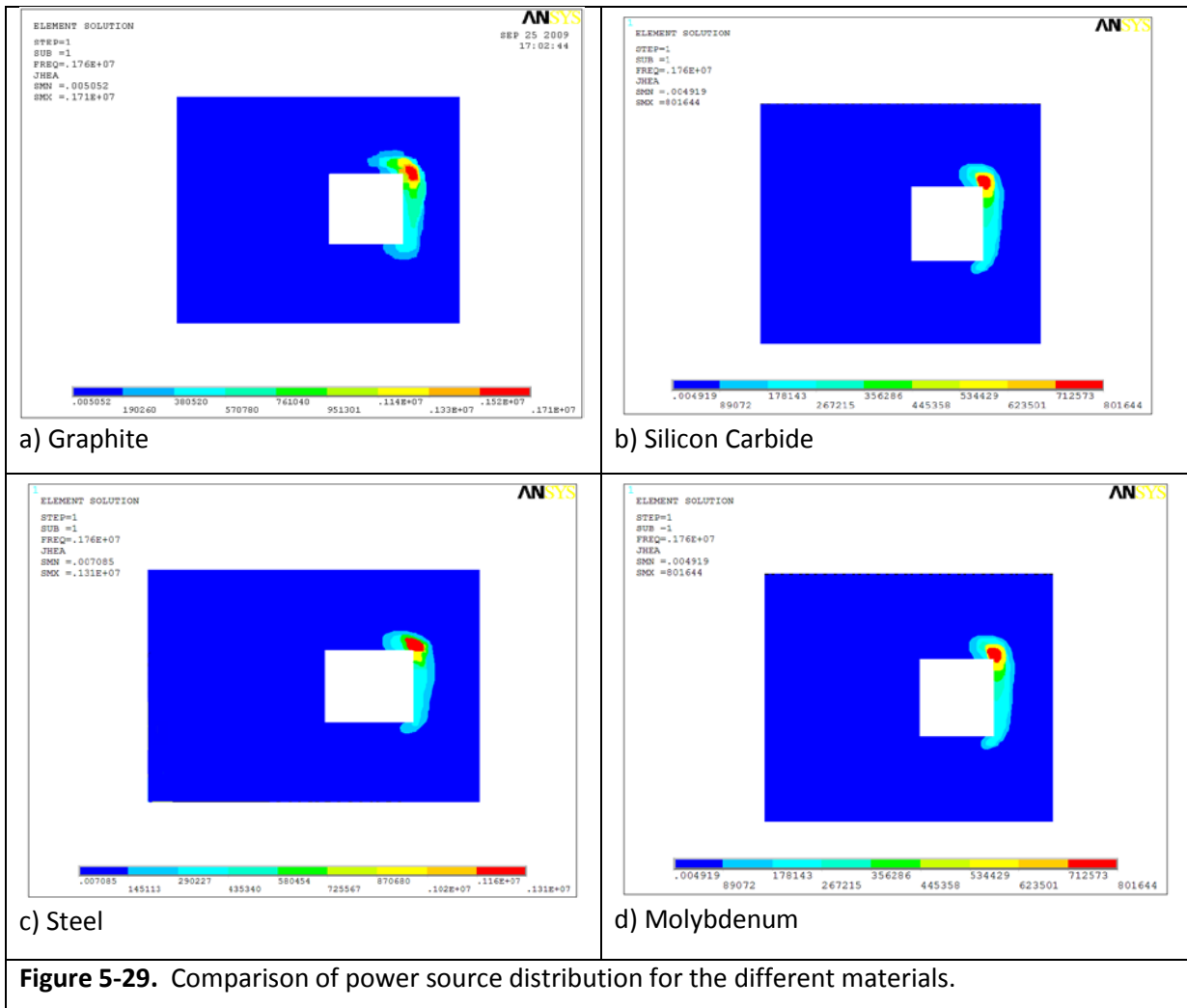
Figure 5-29. Comparison of power source distribution for the different materials.

The next parameter examined was the characteristics of the melt movement. Figure 5-30 and Figure 5-31 show the vertical and horizontal velocity components, respectively, for each of the materials. As can be seen, higher velocities are achieved in the graphite, for both directions. For the vertical component, a maximum velocity of 2.6 mm/sec is achieved, and the maximum horizontal velocity is 5.8 mm/sec (negative direction).   Note that negative velocities are based on standard

Cartesian coordinates. While the silicon carbide had a higher maximum horizontal velocity of 6.1 mm/sec, observation of the velocity distributions clearly show that the overall velocities are lower for the silicon carbide. This is due to the fact that the graphite produces higher temperatures, lowering the viscosity of the melt, and thus providing the ability for better mixing and more efficient start-up and melting.

a) Graphite

b) Silicon Carbide

c) Steel

d) Molybdenum

Figure 5-30. Comparison of vertical velocity components for the materials.
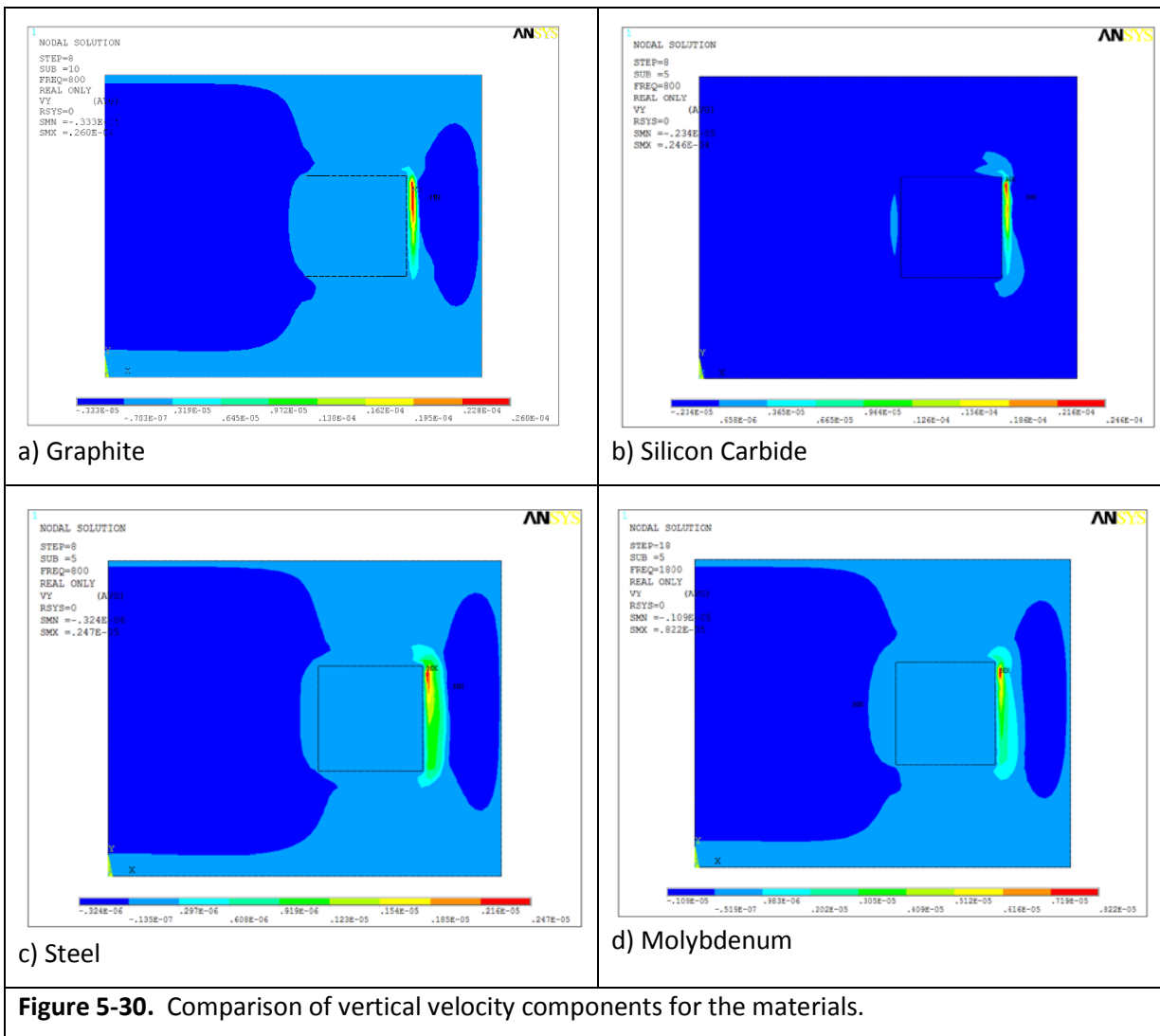
5.2.2. Initiator Ring Removed

The next series of calculations investigated the conditions of the system parameters after the ring is removed and the heating time is set at 6,000 seconds. For these calculations, the inductor voltage is decreased to 2.9 kV as the base case. However, this did not provide sufficient conditions to achieve the full melt pool for the steel and molybdenum materials. Thus, for these investigations, the

inductor voltage was increased to 3.2 kV and 3.4 kV, respectively. While use of other materials may be desirable in regards to their impact on the glass chemistry, from an overall efficiency perspective, materials such as steel and molybdenum are not desirable because the system requires longer start-up times and/or higher inductor voltages to reliably achieve a full melt.

a) Graphite

b) Silicon Carbide

c) Steel

d) Molybdenum

Figure 5-31. Comparison of horizontal velocity components for the materials.
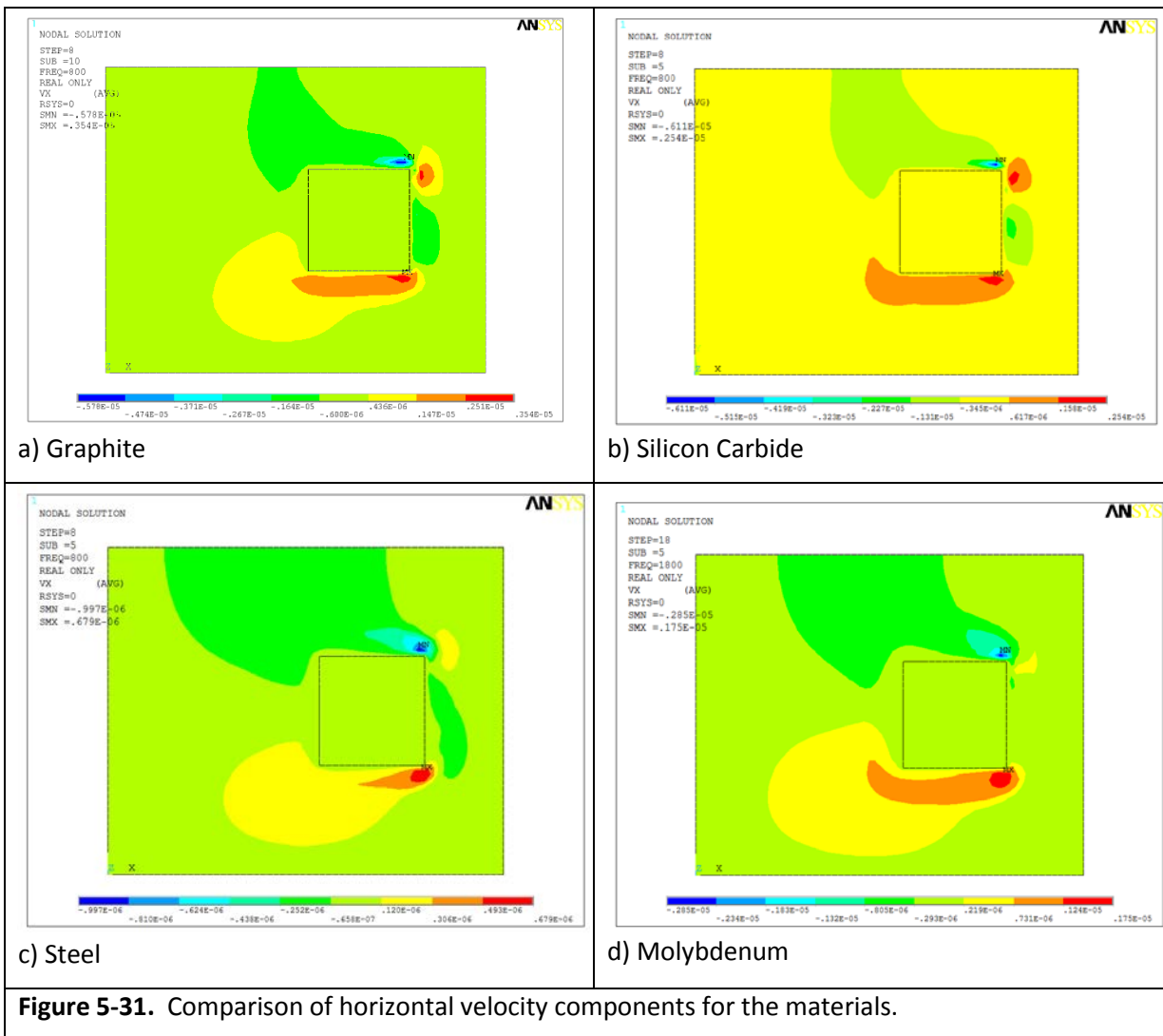
Both result in additional energy losses in the overall system. Figures 5-32 through 5-35 provide comparative results for the temperature distributions, power source distributions, vertical velocities, and horizontal velocities in the melt. Note that higher power sources are observed for steel and molybdenum due to use of increased inductor voltages, as compared to graphite and silicon carbide.

Figure 5-32. Comparison of temperature distributions for different materials.
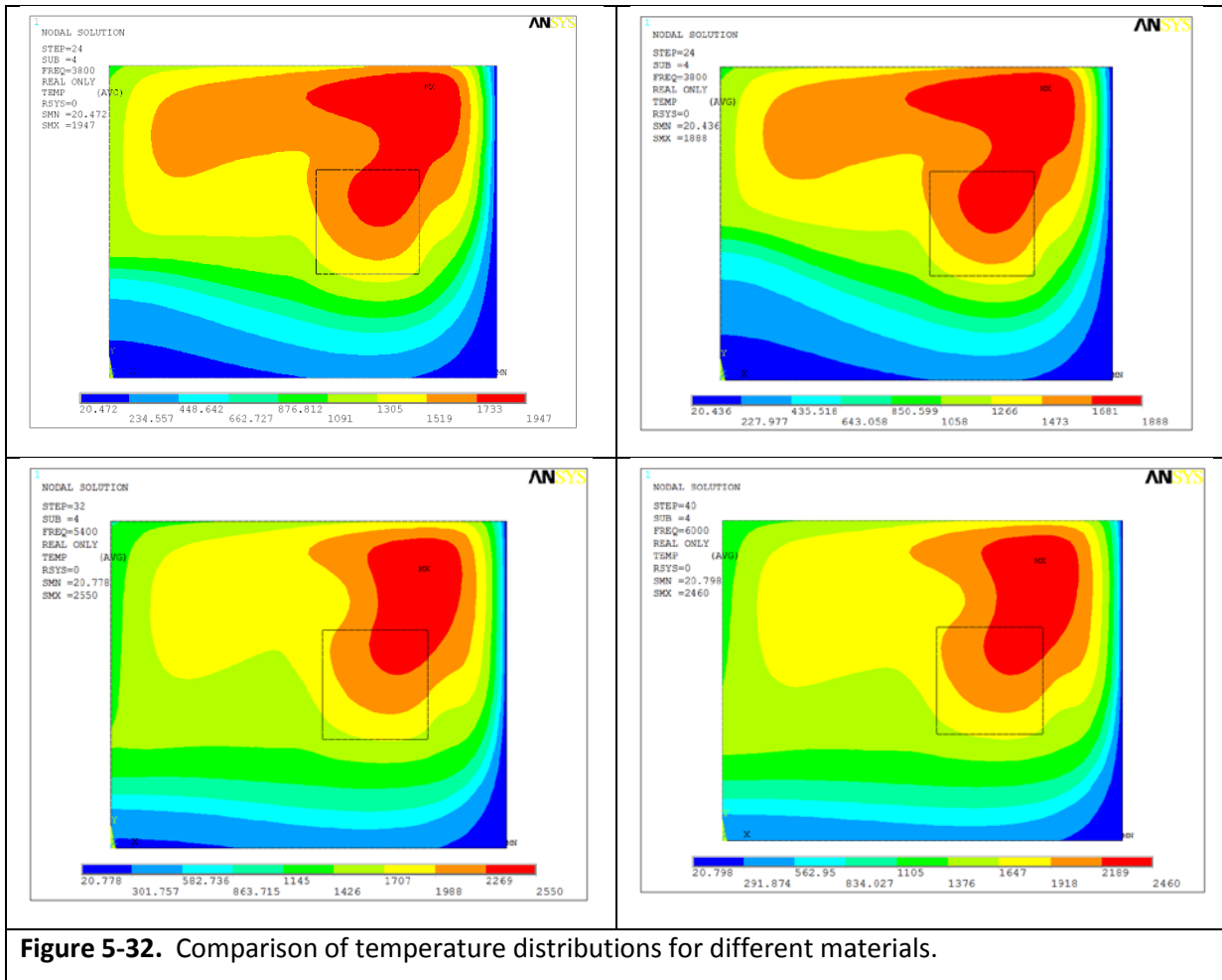
Note the similarity of temperature distributions for graphite and silicon carbide versus steel and molybdenum. Referring back to Figure 5-26 and 5-27, it is clear that the temperature dependence of the electrical resistivities and densities are similarly grouped, especially for density. Thus, the similarity of these temperature distributions is expected; however, the more important point is the relative maximum temperatures observed. These are qualitative, but provide a good representation of the differences observed in experimental results. They also point to the fact that for lower resistivity, higher density materials, much smaller cross-sections would be preferred due to the amount of energy absorbed and required to heat the ring such that the energy conducts sufficiently into the surrounding glass.

Another important observation is that, while the graphic depictions of the temperature distributions appear to demonstrate dramatically different results for graphite/silicon carbide versus steel/molybdenum, this is more a function of the color array used for the thermal bands.

a) Graphite b) Silicon Carbide

c) Steel d) Molybdenum

Figure 5-33. Comparison of power source distributions for different materials.
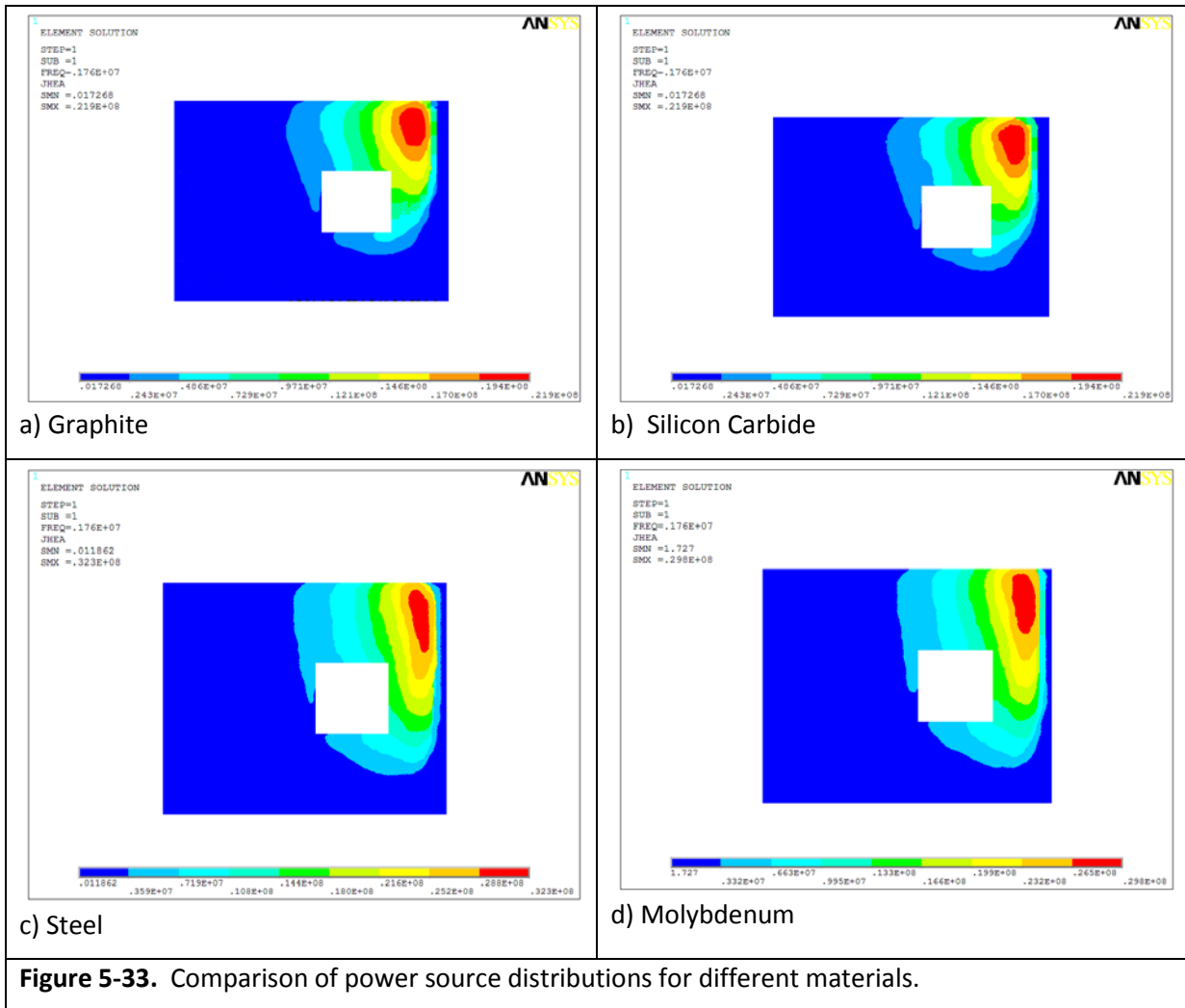
Investigation of the details of these distributions, at finer resolution, shows that they are similar. However, higher temperatures are produced in the steel/molybdenum systems.

Observation of the velocity component profiles shows very similar distributions and maximum values. This is because of two factors: 1) the velocities are buoyancy driven and the temperature-dependent density profile for the glass illustrates a flattening of the curve to an asymptotic value, such that the density changes have no effect above a certain temperature, and 2) the glass melt pool is at a quasi-steady state condition such that the convection cells are established and stable.

A summary of several system parameters from these model calculations are provided in Table 5-9. These are not necessarily quantitative data, but the results do provide excellent comparative performance results for the initiator rings constructed of various materials. An important point to keep in mind is that these results are specific to an induction system operating at 1.76 MHz.

Systems operating at lower frequencies would benefit from the use of materials of lower electrical resistivity, such as the titanium ring used in the French CCIM system [70], which operates at nominally 275 kHz. However, for this system, we can conclude from these data that use of the lower resistivity materials results in longer times and higher voltages required to achieve and maintain a melt pool. This directly correlates to an overall less efficient system. Thus, for the experimental efforts conducted as part of this body of work, selection of the graphite ring was the most efficient, from electrical efficiency, cost, and operability perspectives.

a) Graphite
b) Silicon Carbide
c) Steel
d) Molybdenum
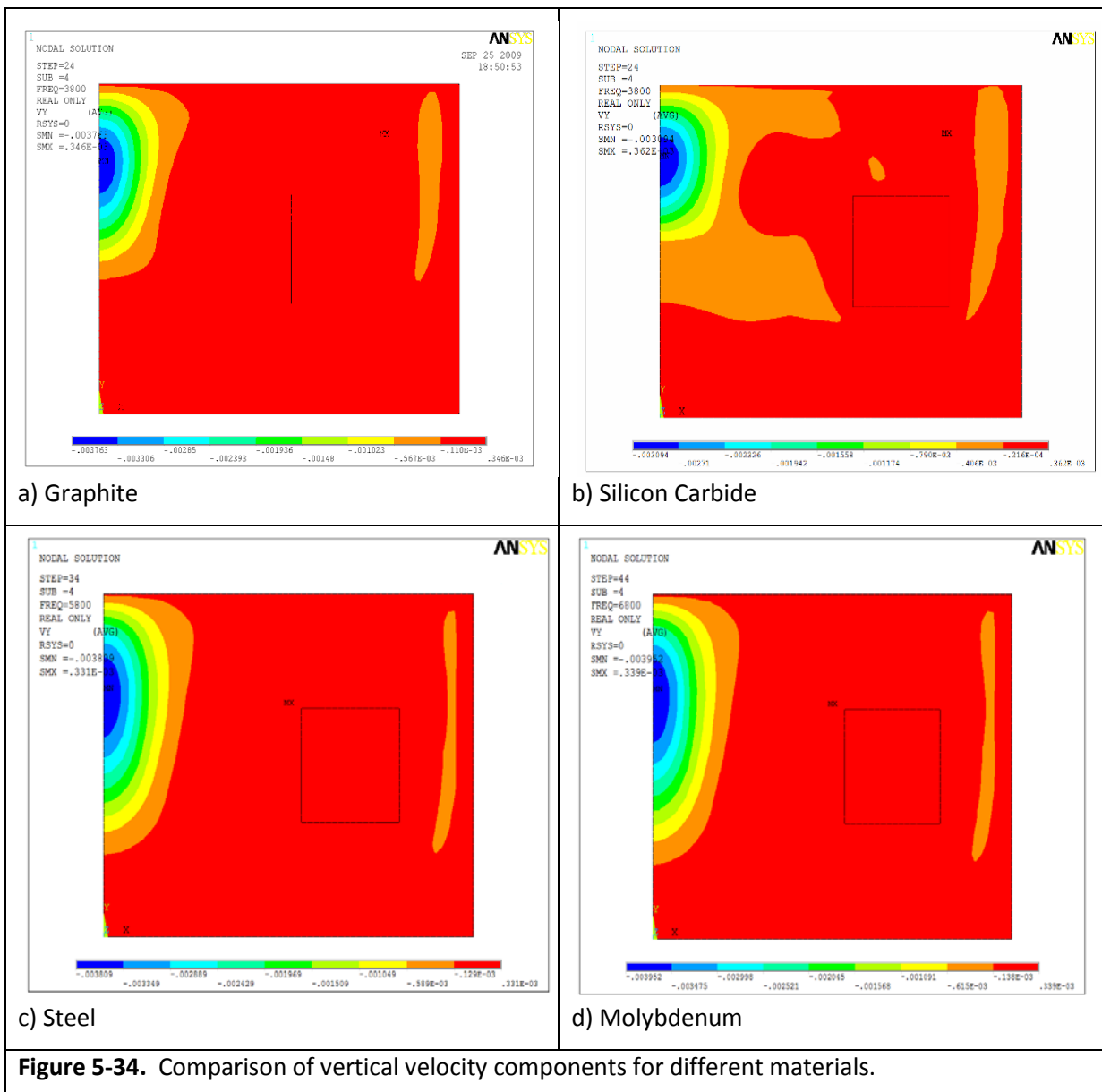
Figure 5-34. Comparison of vertical velocity components for different materials.
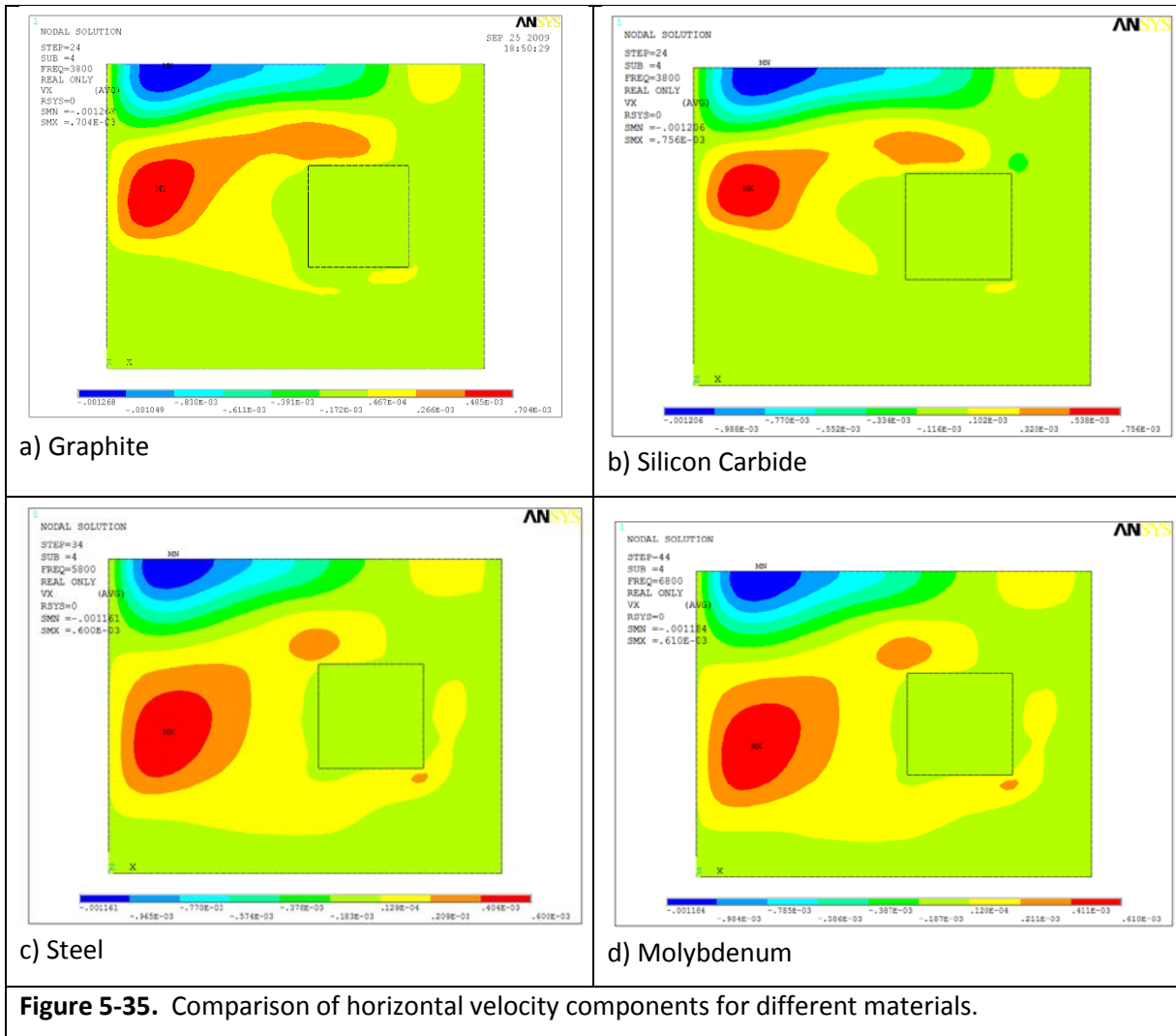
Figure 5-35. Comparison of horizontal velocity components for different materials.

Table 5-9. Summary results of process parameters for various initiator ring materials (at 1,000°C).

Parameter	Graphite	Silicon carbide	Steel	Molybdenum
Power supplied to the inductor, kW	34	33	38	41
Heat losses from crucible side, kW	11.98	11.24	13.53	13.09
Heat losses through crucible bottom, W	529	499	778	701
Total heat losses, kW	12.97	11.73	14.31	13.8
Average melt temperature on pool surface, °C	1,340	1,308	1,482	1,468
Specific heat flux from crucible side, W/cm^2	4.42	4.36	5.21	5.09
Specific heat flux from crucible bottom, W/cm^2	0.39	0.32	0.51	0.47
Power induced into material, kW	2.96	2.86	3.58	3.46
Start-up heating time, sec	1,000	1,000	1,500	2,000
Voltage on the inductor at starting heating, kV	5	5	5	5
Heating time during melting, sec	6,000	6,000	6,000	6,000
Voltage on the inductor during melting, kV	2.9	2.9	3.2	3.4

5.3. Investigation of Effects of Changing Parameters for the Initiator Ring

Based on the preceding results, use of the graphite initiator ring was determined to be appropriate. The ring geometry was then investigated to determine the effects on the start-up process.

5.3.1. Outer Diameter Changes (Inner Diameter Fixed)

Changes in the width were first evaluated. The base case is 40 mm wide by 40 mm high cross-section. The width was varied to include 55 and 25 mm widths. For each case, the center radius of the ring was held constant at 100 mm (i.e., +/- 15 mm on outside diameter). The total time of calculation and inductor voltage required to achieve the minimum conditions for melt casting, as determined for the base case, were used for all calculations. For each case, the temperature distribution in the melt pool, as well as velocity vectors, heat sources, and heat flux data are presented for comparison.

The initial conditions and geometry for the base case calculations were the same as those for the prior analysis, as shown in Table 5.8. Boundary conditions and material properties for model initiation were those determined in earlier efforts. These were then adjusted based on the model results. Some of the other model parameters and system conditions, which were used in the prior analyses for the various types of initiator ring materials, were investigated for these analyses and will be described in the following discussions. Graphite was used in all of the analyses because the preceding investigation showed that none of the alternate materials offered significant benefits.

The calculations are conducted in two stages: 1) the start-up process with the initiator ring in the crucible, and 2) melt pool formation with the initiator ring removed. To determine the minimum time to establish a condition that will ensure melt pool formation, calculations were made at 500 seconds, 1,000 seconds, and 2,000 seconds. These results are shown in Figure 5-36.

Figure 5-36. Temperature distribution after 2,000 (left), 1,000 (center), and 500 seconds (right).
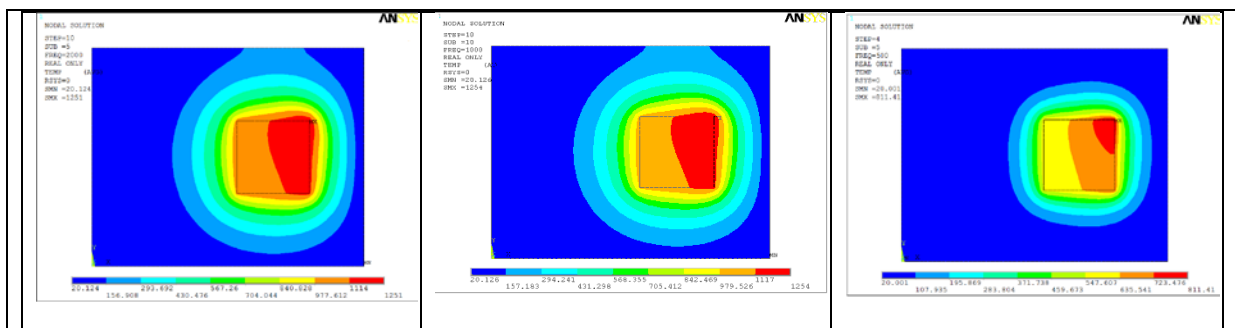
These results show that the temperature is virtually the same at 1,000 and 2,000 seconds. The temperature field after 500 seconds is not sufficient to form a melt pool upon removal of the initiator ring. Thus, 1,000 seconds was used for all calculations for the start-up process.

The next step was to determine the time required to form an adequate melt pool that would ensure that the melt is maintained. The results are shown in Figure 5-37.

Figure 5-37. Temperature distribution comparison after 6,000 seconds (after start-up).
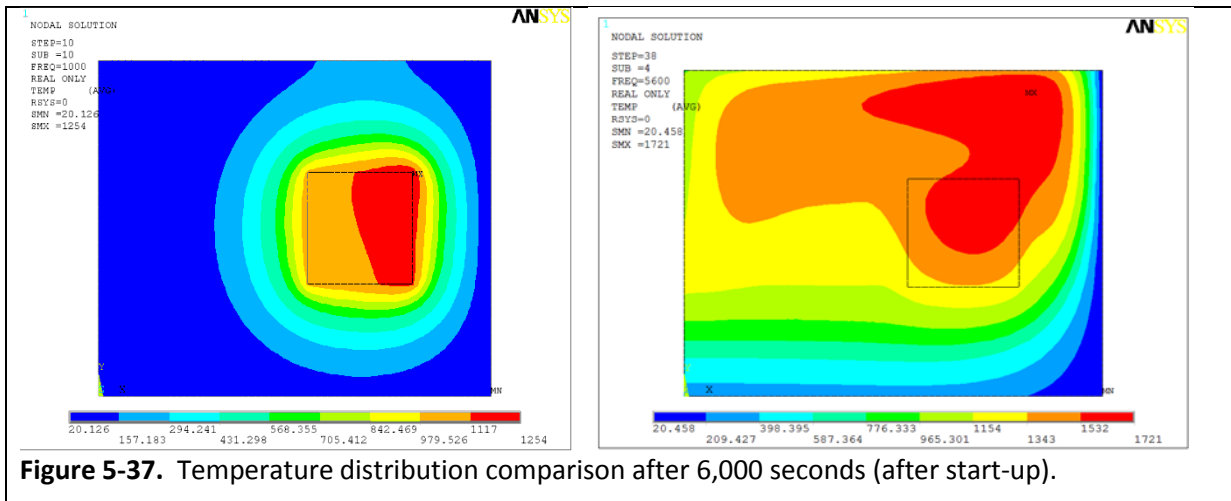
Note that the melt is over-heated in Figure 5-37 (right) due to the fact that the voltage is fixed and this model did not allow the ability to adjust the inductor voltage during the calculations. This was done to simplify the model, and thus accelerate the calculations since these were performed for comparative qualitative purposes only. Figures 5-38 through 5-40 provide results for the heat source distributions, horizontal and vertical velocity vectors. These figures demonstrate that the given configuration and calculation times result in a condition within the melter that ensures a full melt pool will form. Thus, this is the basis for comparison with other initiator geometries. Table 5-10 shows the values for key parameters obtained during the preceding analyses.

Table 5-10. Key parameters obtained from initial start-up model analysis.

Parameter	Value
Power supplied to the inductor	34 kW
Heat loss from crucible side wall	11.98 kW
Heat loss from the crucible bottom	529 W
Total heat loss from the crucible	12.97 kW
Average temperature on the melt pool surface	1,340°C
Heat flux to the crucible side	4.42 W/cm^2
Heat flux to a bottom	0.39 W/cm^2
Power released into the initiator ring	2.96 kW

A similar approach was used to ensure that the other geometries would result in a condition amenable to full melt pool formation.

The next investigation was of an initiator ring with width of 55 mm. As before, start-up times of 2,000, 1,000, and 500 seconds were evaluated. The results are shown in Figure 5-41.
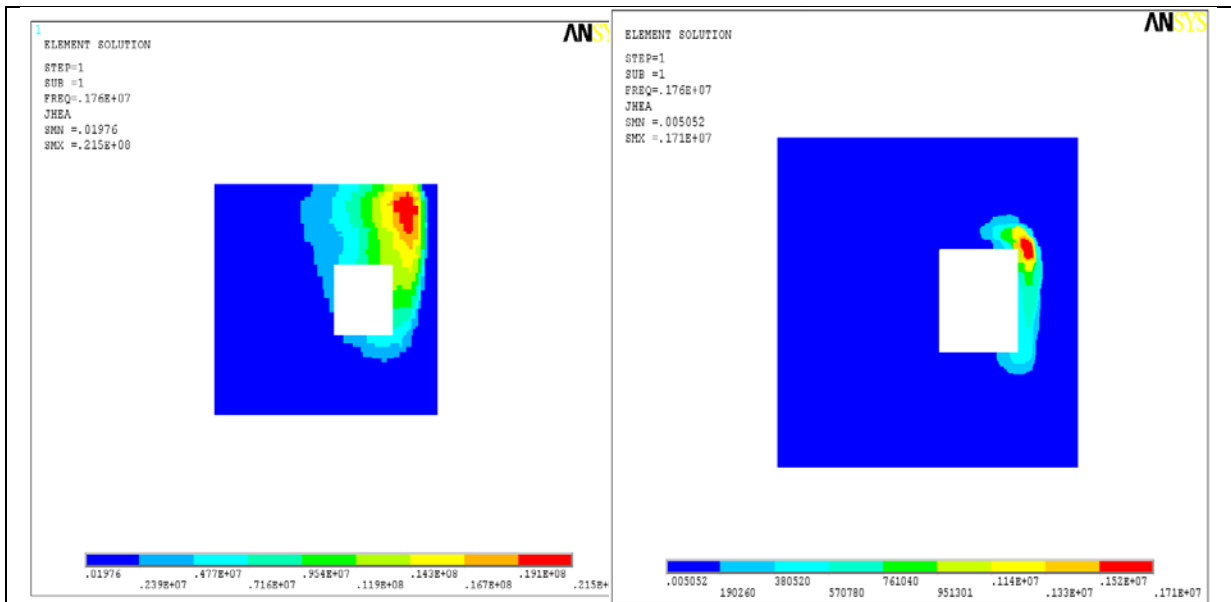
Figure 5-38. Heat source distributions at start-up and melt pool formation for the base case.
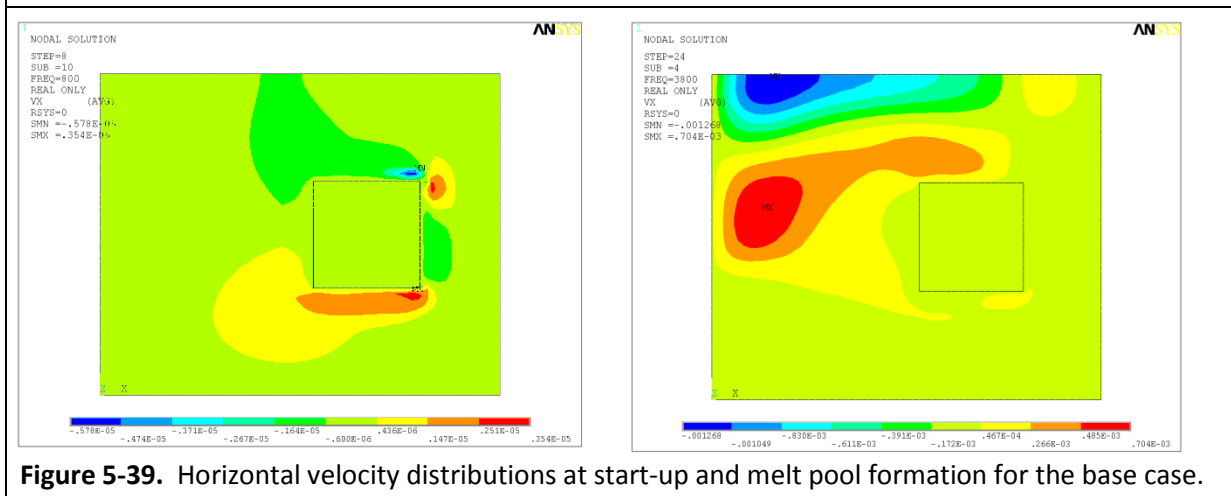
Figure 5-39. Horizontal velocity distributions at start-up and melt pool formation for the base case.

Although the melt heats up an additional 100°C between 1,000 seconds and 2,000 seconds, the condition after 1,000 seconds is sufficient to support formation of a melt pool. As a result, 1,000 seconds is used for subsequent calculations. As before, the 500 second melt start-up time is insufficient.
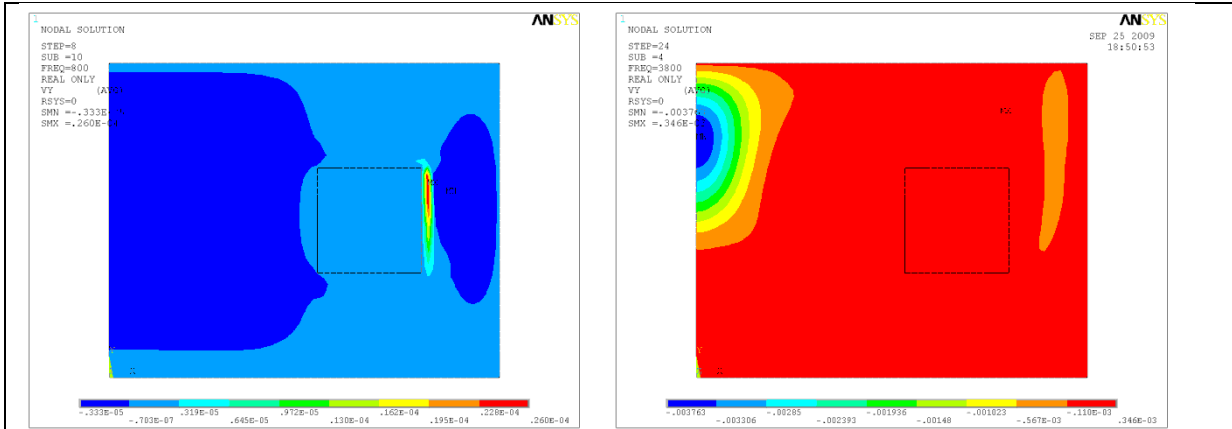
Figure 5-40. Vertical velocity distributions at start-up and melt pool formation for the base case.
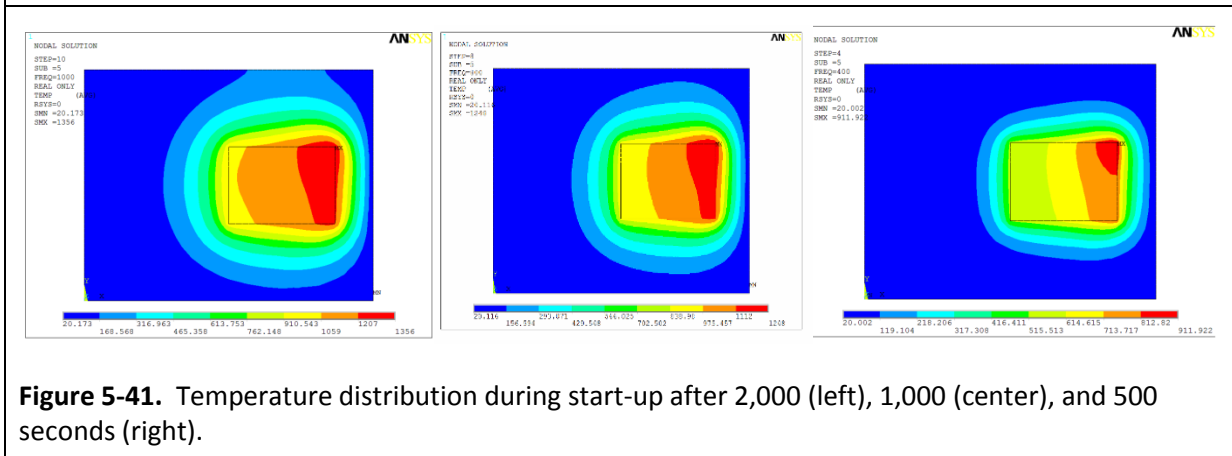
Figure 5-41. Temperature distribution during start-up after 2,000 (left), 1,000 (center), and 500 seconds (right).

Figure 5-42 through Figure 5-45 illustrate the temperature distributions, heat source distributions, horizontal velocity vector, and vertical velocity vectors for the 55 mm wide initiator ring. Recall that this geometry is based on a fixed inner diameter of 100 mm.
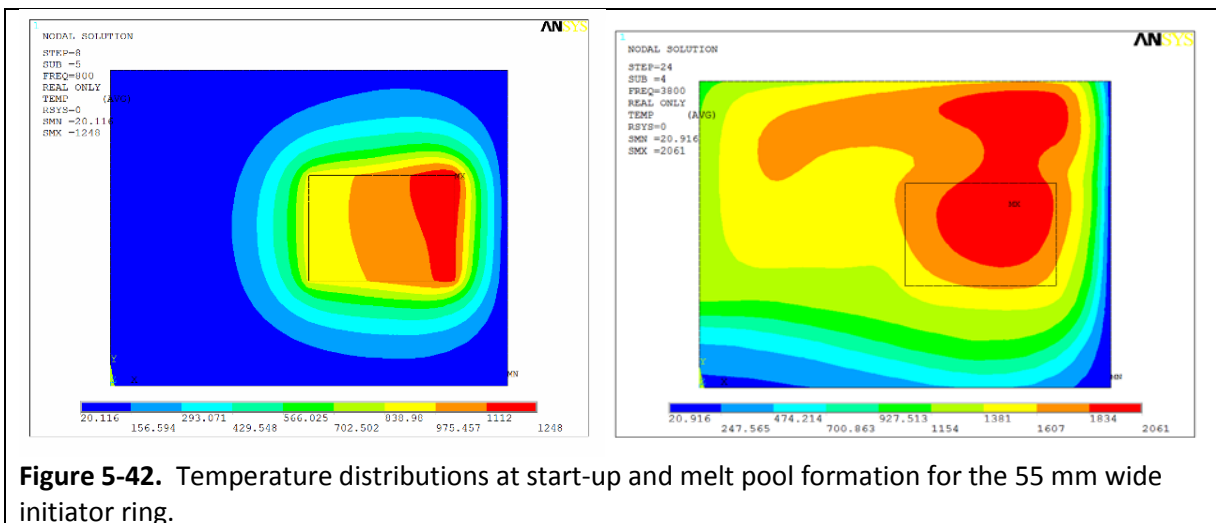
Figure 5-42. Temperature distributions at start-up and melt pool formation for the 55 mm wide initiator ring.
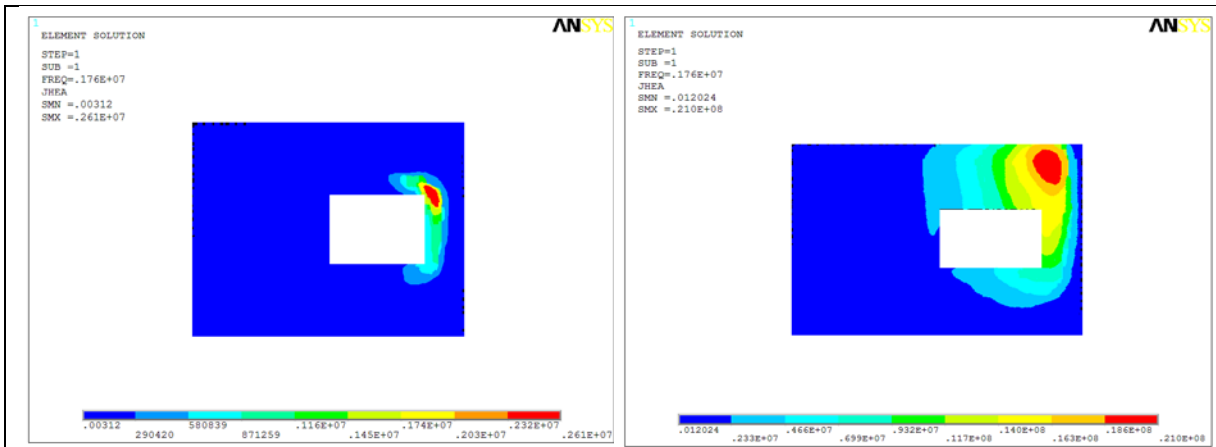
Figure 5-43. Heat source distributions at start-up and melt pool formation for the 55 mm wide initiator ring.
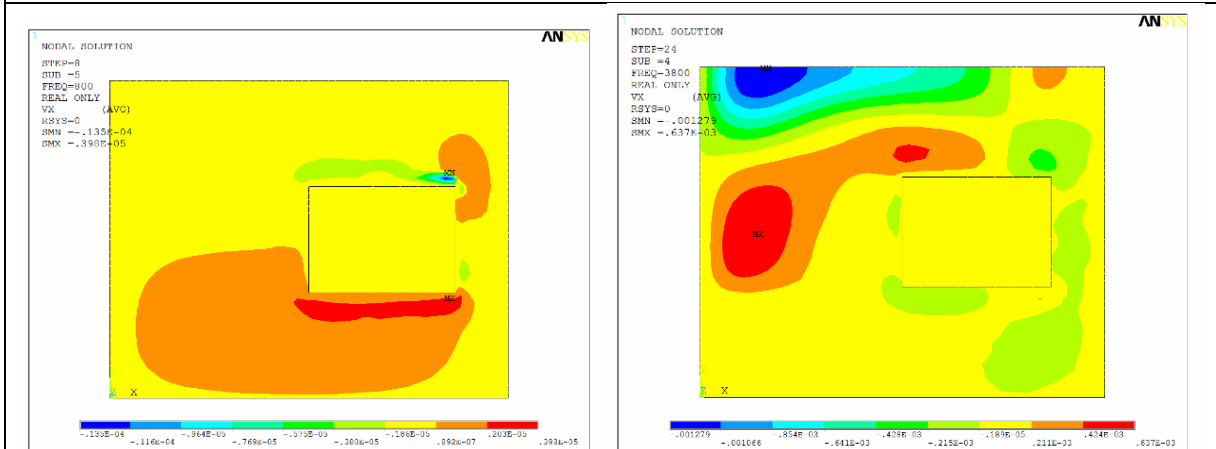
Figure 5-44. Horizontal velocity vector distributions at start-up and melt pool formation for the 55 mm wide initiator ring.
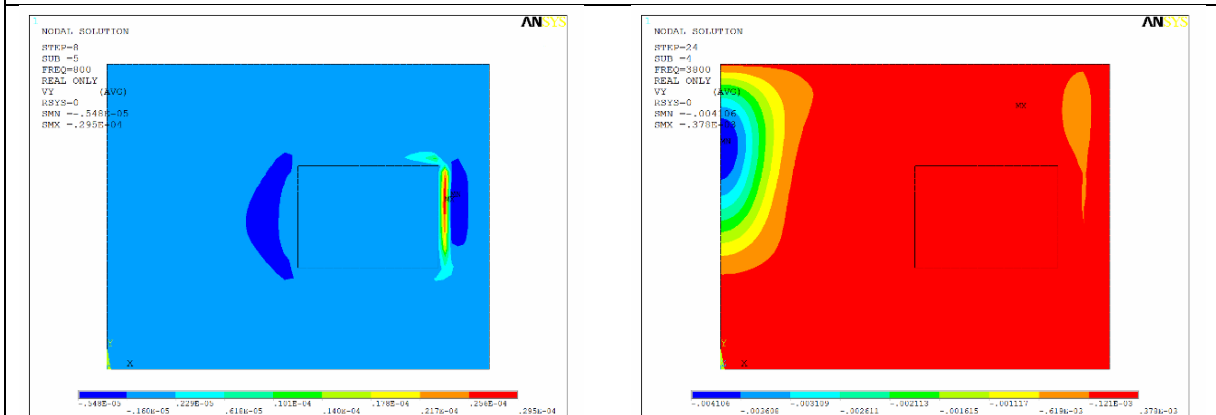
Figure 5-45. Vertical velocity vector distributions at start-up and melt pool formation for the 55 mm wide initiator ring.

In the preceding calculation the values obtained for key parameters are provided in Table 5-11.

Table 5-11. Key parameters obtained from start-up model analysis for 55 mm wide ring.

Parameter	Value
Power supplied to the inductor	35 kW
Heat loss from crucible side wall	12.84 kW
Heat loss from the crucible bottom	545 W
Total heat loss from the crucible	13.32 kW
Average temperature on the melt pool surface	1,389°C
Heat flux to the crucible side	4.56 W/cm^2
Heat flux to crucible bottom	0.41 W/cm^2
Power released into the initiator ring	3.13 kW

Finally, analysis was conducted on a ring with width of 25 mm. A similar approach was used as the previous calculations. The initial step was to determine the required start-up calculation time. As before, 2,000 seconds, 1,000 seconds, and 500 seconds were investigated. These results are shown in Figure 5-46.

As in the prior calculations for the base case, there is virtually no change between the 2,000 second result and the 1,000 second result. The 500 second time is not sufficient to ensure formation of a melt pool. Thus, 1,000 seconds was used for the start-up calculations for this case also. However, at 2.9 kV on the inductor, upon removal of the initiator ring (i.e., model restart) melt cooling was observed. Therefore, the inductor voltage was increased by about 10% to 3.2 kV for the 25 mm wide initiator ring case.
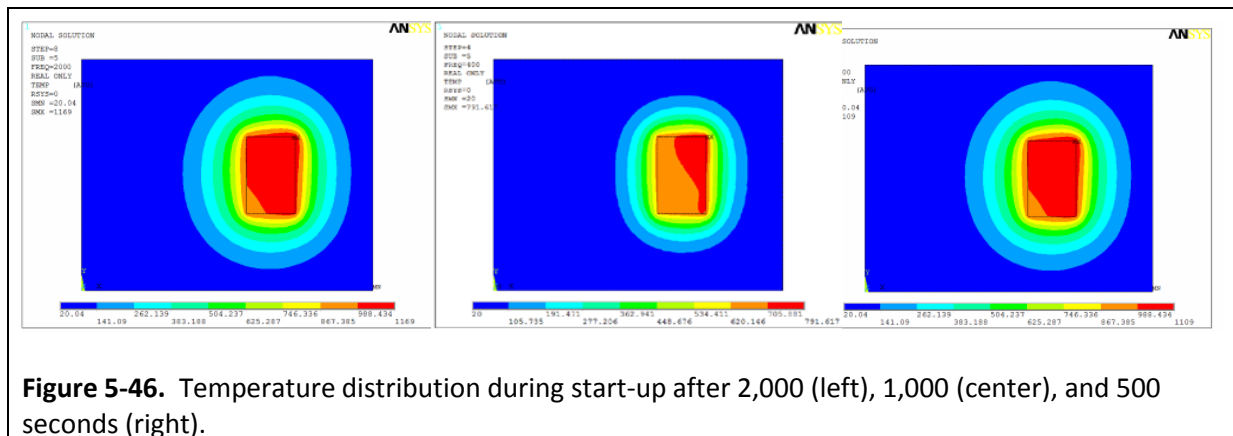
Figure 5-46. Temperature distribution during start-up after 2,000 (left), 1,000 (center), and 500 seconds (right).

The distributions of temperatures, heat sources, horizontal velocities and vertical velocities for the 25 mm wide initiator ring are shown in Figures 5-47 through 5-50.
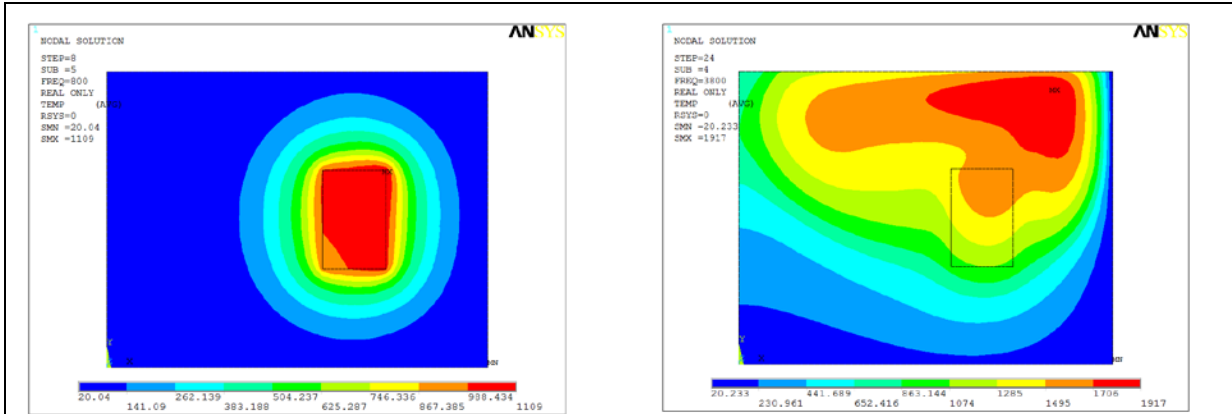
Figure 5-47. Temperature distributions at start-up and melt pool formulation for the 25 mm wide initiator ring.
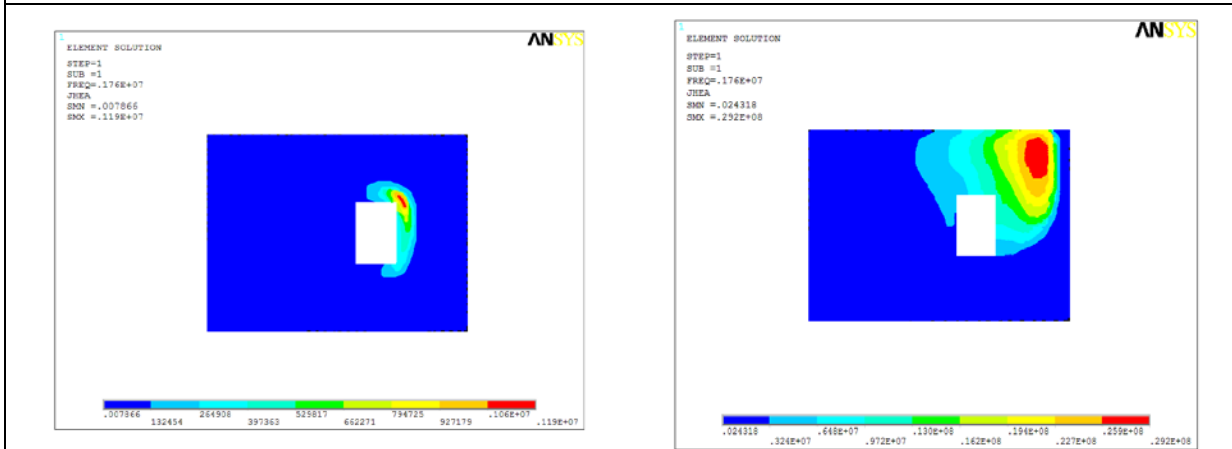
Figure 5-48. Heat source distributions at start-up and melt pool formulation for the 25 mm wide initiator ring.
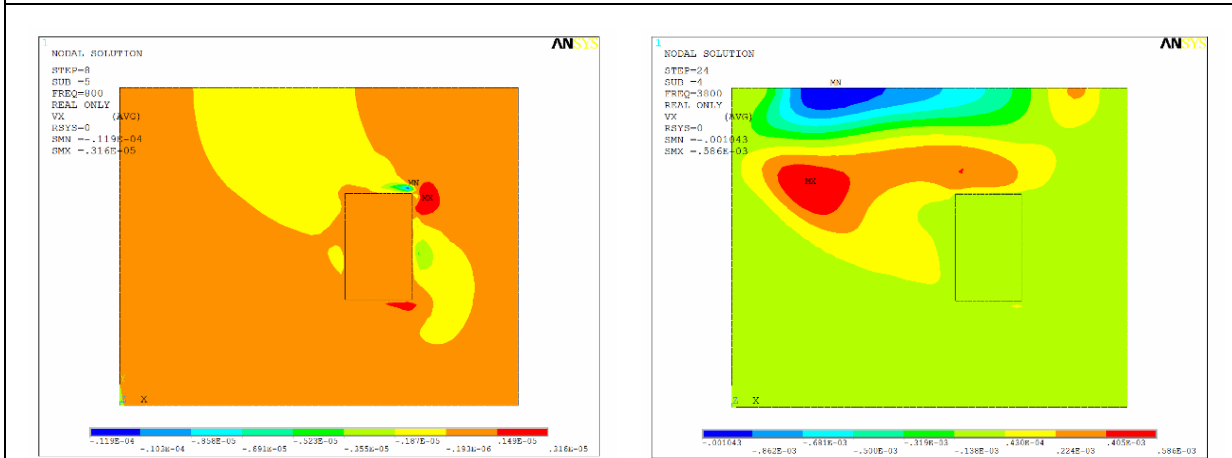
Figure 5-49. Horizontal velocity vectors at start-up and melt pool formulation for the 25 mm wide initiator ring.
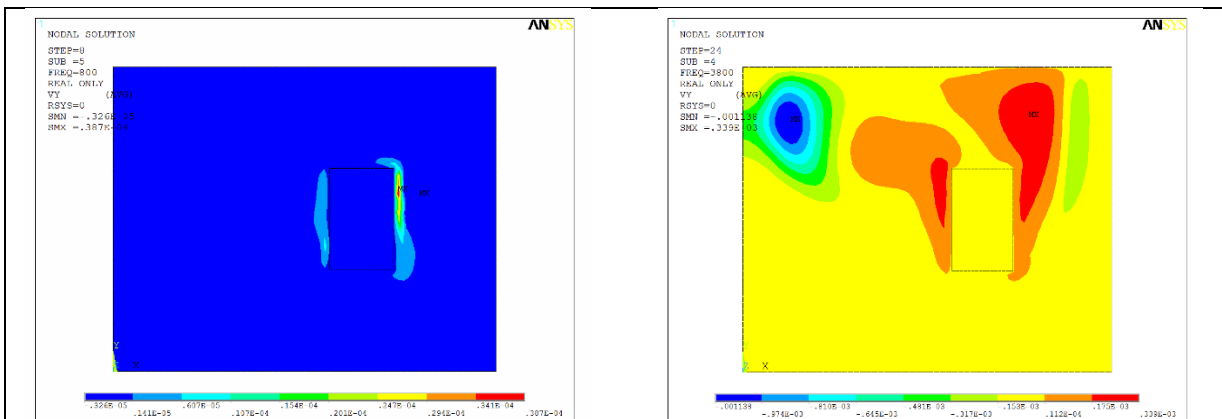
Figure 5-50. Horizontal velocity vectors at start-up and melt pool formulation for the 25 mm wide initiator ring.

In the preceding calculation the values obtained for key parameters are provided in Table 5-12.

Table 5-12. Key parameters obtained from start-up model analysis for 25 mm wide ring.

Parameter	Value
Power supplied to the inductor	39 kW
Heat loss from crucible side wall	14.8 kW
Heat loss from the crucible bottom	757 W
Total heat loss from the crucible	15.63 kW
Average temperature on the melt pool surface	1,336°C
Heat flux to the crucible side	5.21 W/cm^2
Heat flux to crucible bottom	0.68 W/cm^2
Power released into the initiator ring	3.86 kW
Voltage on the inductor during melting	3.2 kV

Figures 5-51 through 5-53, as well as Table 5-13, provide a comparison of the key parameters of the various configurations. The primary conclusion is that the 40 mm wide ring provides the most optimal condition for a CCIM operating at 1.76 MHz and processing this specific BSG composition.

Ring width of 40 mm	Ring width of 55 mm	Ring width of 25 mm
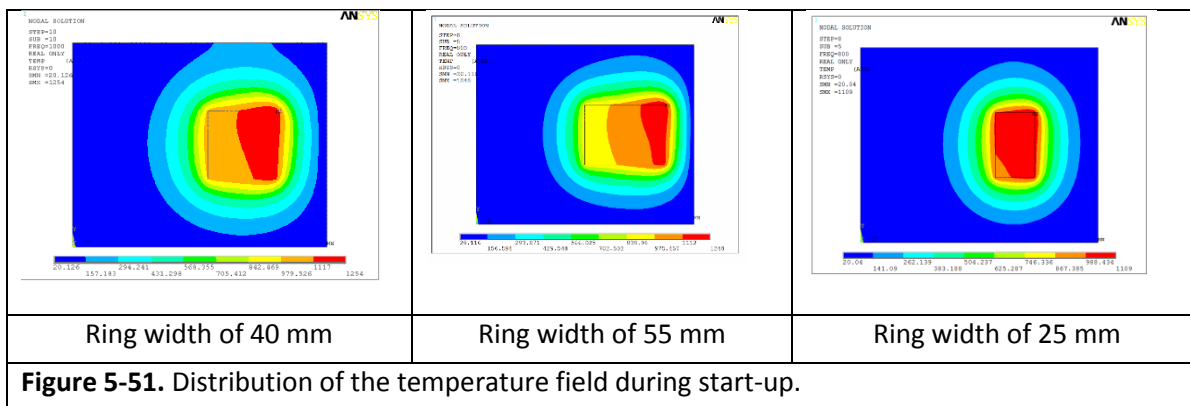
Figure 5-51. Distribution of the temperature field during start-up.

Ring width of 40 mm	Ring width of 55 mm	Ring width of 25 mm
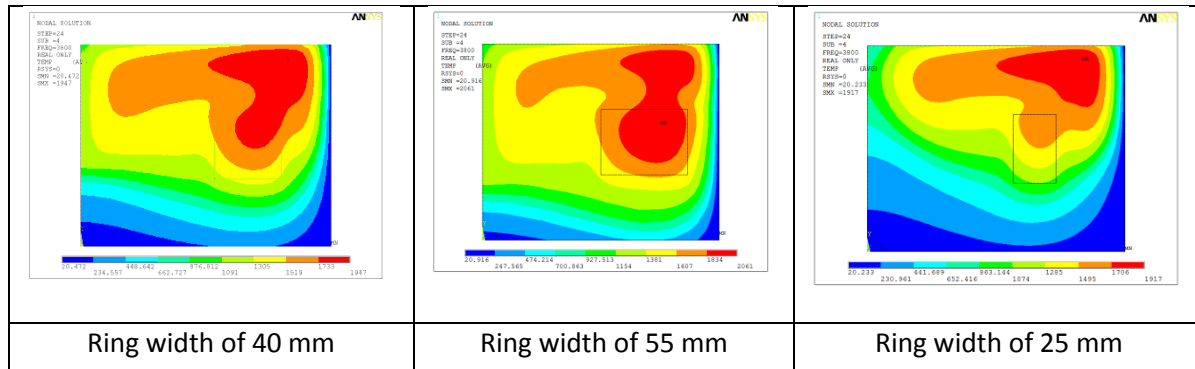
Figure 5-52. Distribution of the temperature field during melt pool formation.

Ring width of 40 mm	Ring width of 55 mm	Ring width of 25 mm
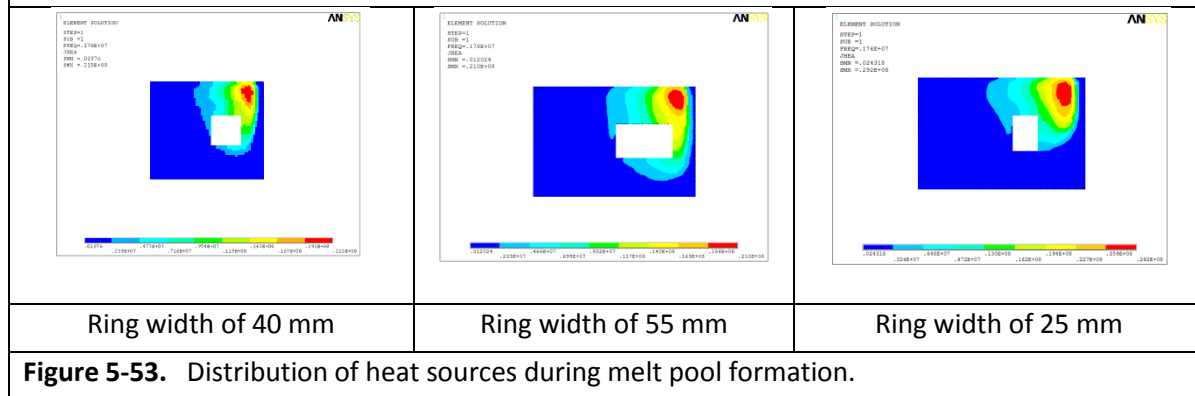
Figure 5-53. Distribution of heat sources during melt pool formation.

Table 5-13. Comparative results for various initiator ring widths.

No.	Description	Ring width, mm		
		25	40	55
1	Power supplied to the inductor, kW	39	34	35
2	Heat losses from the crucible side wall, kW	14.8	11.98	12.84
3	Heat losses from the crucible bottom, kW	0.76	0.53	0.55
4	Total heat from the crucible side and bottom, kW	15.63	12.97	13.32
5	Average temperature on the melt pool surface, °C	1,336	1,340	1,389
6	Specific heat flux from the crucible side wall, W/cm^2	5.21	4.42	4.56
7	Specific heat flux from the crucible bottom, W/cm^2	0.68	0.39	0.41
8	Power released into the ring, kW	3.86	2.96	3.13
9	Electrical power losses on the inductor, kW	1.347	1.012	1.103
10	Start-up heating time, sec	1,000	1,000	1,000
11	Voltage on the inductor during start-up, kV	5	5	5
12	Melt pool formation heating time, sec	6,000	6,000	6,000
13	Voltage on the inductor during melting, kV	3.2	2.9	2.9

5.3.2.Internal Diameter Changes

The next set of calculations conducted to evaluate geometry features for the initiator ring investigated the effect of changing the internal diameter (i.e., maintaining a constant outer diameter, resulting in an effectively thinner ring cross-section). For these calculations, a ring with an inner diameter of 105 mm (i.e., 15 mm wide ring) was investigated for comparison with the base case of 120 mm.   Because all previous calculations showed that 1,000 seconds for the start-up calculation time is sufficient, this was used as a starting point, with 500 seconds and 800 seconds also evaluated. The results are shown in Figure 5-54.

The temperature distributions are virtually identical for heating times of 1,000 seconds and 800 seconds, with maximum temperatures near 1,400^{o}C. Thus, 800 seconds can be used for this configuration. As before, the 500 seconds is not adequate to support melt pool formation.
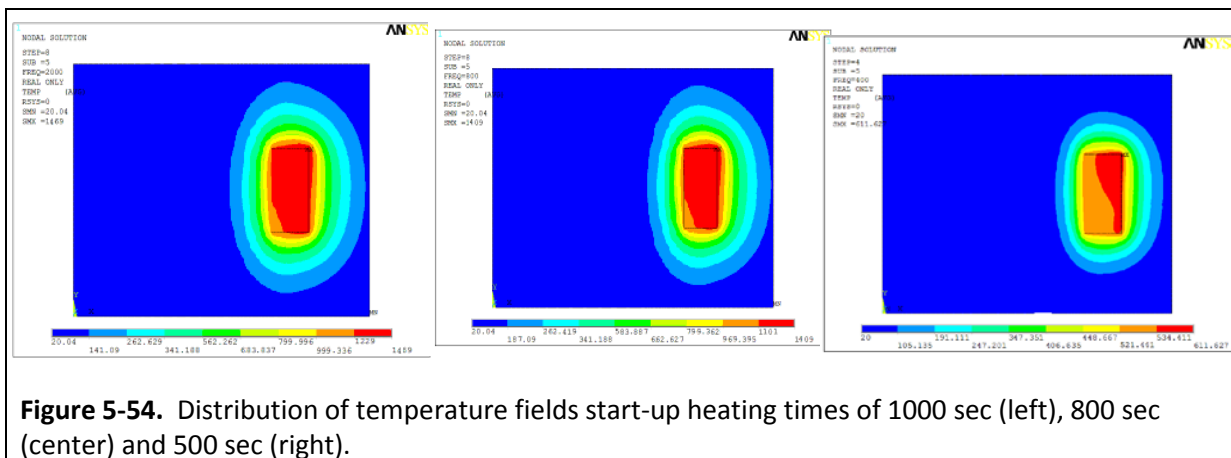
Figure 5-54. Distribution of temperature fields start-up heating times of 1000 sec (left), 800 sec (center) and 500 sec (right).

A similar situation occurred as with the narrow (i.e., 25 mm) initiator ring, in which cool down occurred after the initiator ring was removed and the model restarted. Thus, for this configuration, the inductor voltage was increased by ~10% to 3.2 kV. This power level ensured melt pool formation.

Figure 5-55 shows the temperature distributions for start-up and melt pool formation. Figure 5-56 through Figure 5-58 provide calculation results for the heat source distributions, horizontal velocity vectors, and vertical velocity vectors for the base case of 120 mm outside diameter, 30 mm thick initiator ring.
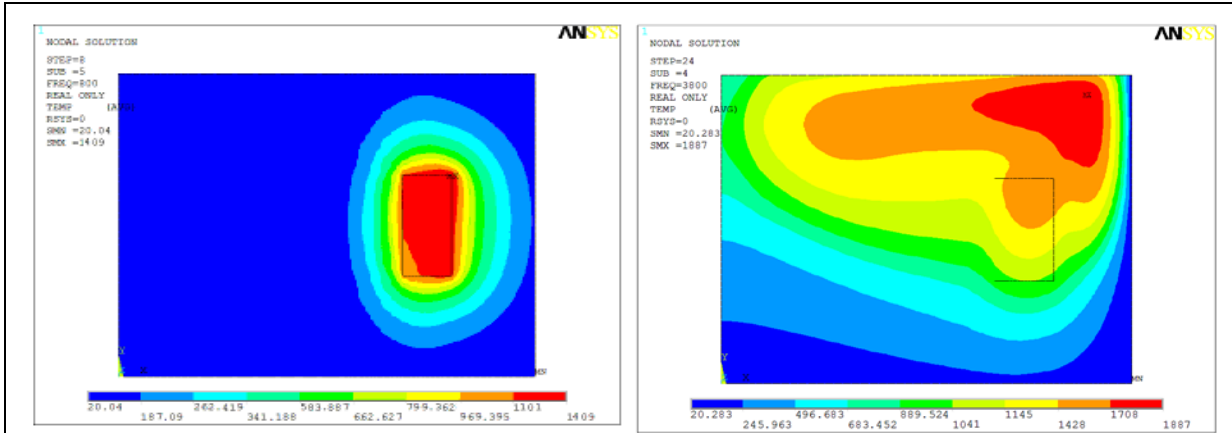
Figure 5-55. Temperature distributions for start-up heating and melt pool formation for the 15 mm wide initiator ring.
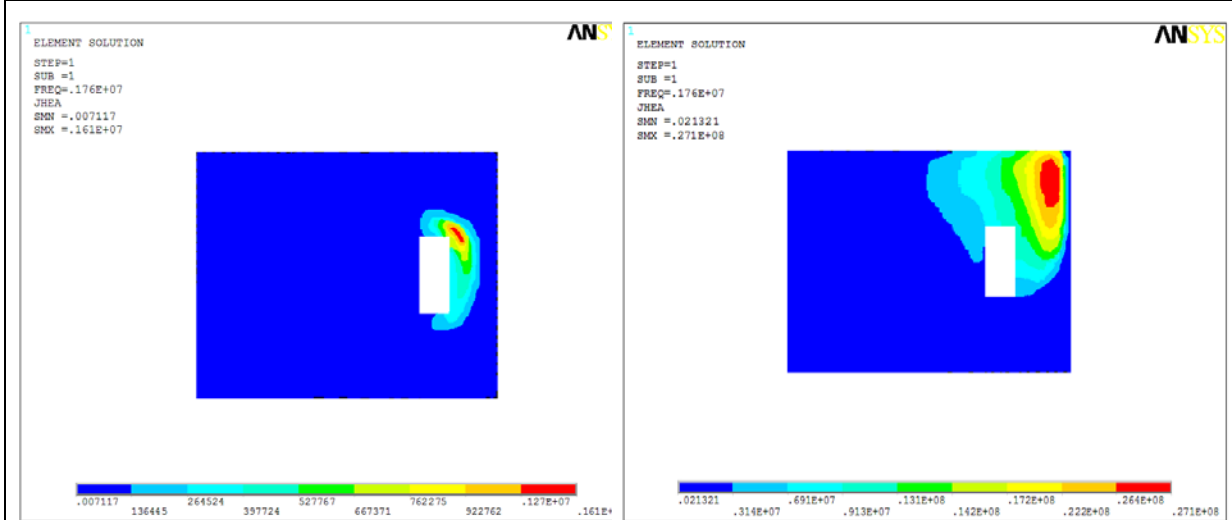
Figure 5-56. Heat source distributions for start-up and melting for the 15 mm wide ring.
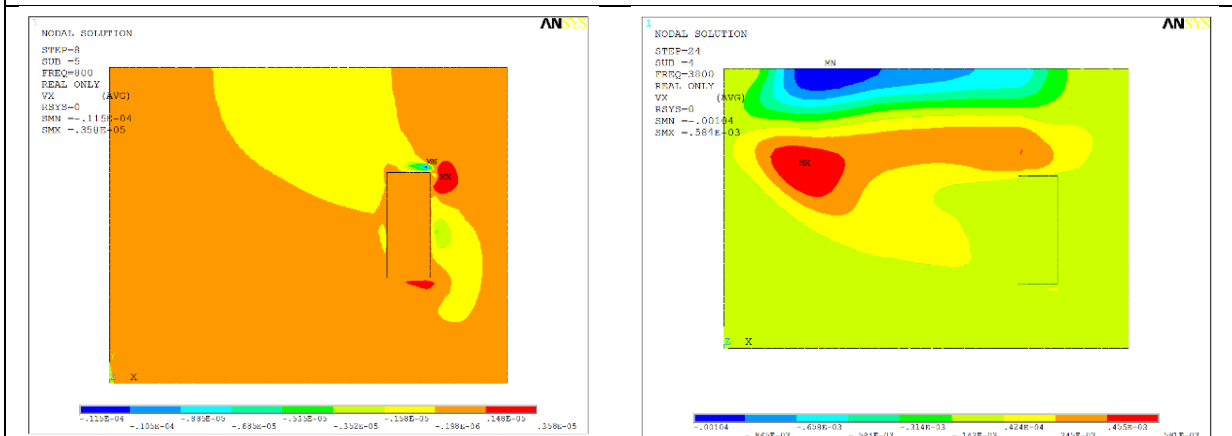
Figure 5-57. Horizontal velocity vectors for start-up and melting for the 15 mm wide ring.

Figure 5-58. Vertical velocity vectors for start-up and melting for the 15 mm wide ring.
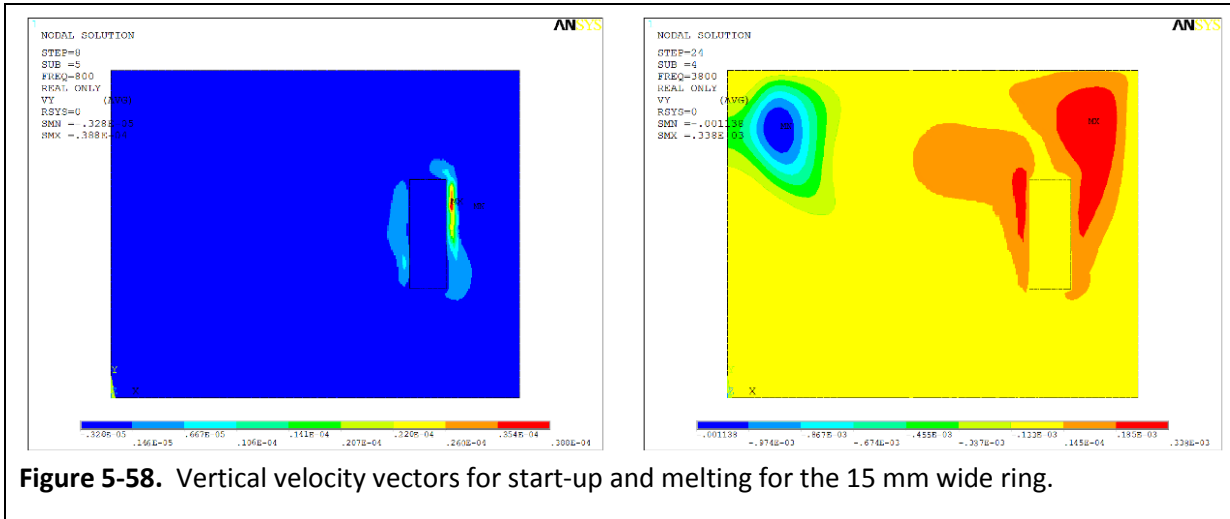
Figures 5-59 through 5-61, as well as Table 5-14, provide comparative results for the base case with the 105 mm inner diameter (i.e., 15 mm wide ring).

| Ring width of 40 mm | Ring width of 15 mm |
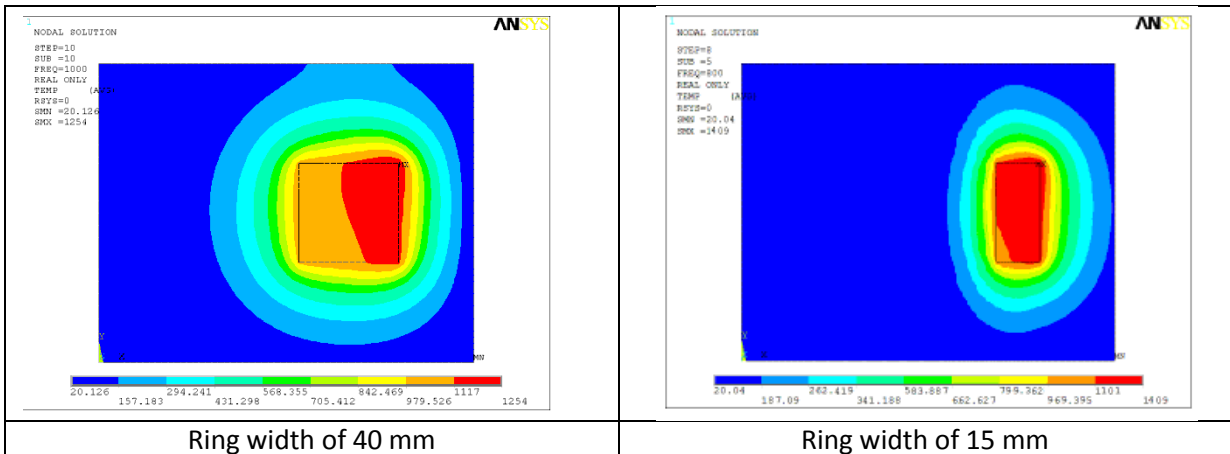
Figure 5-59. Comparison of temperature field during start-up.

| Ring width of 40 mm | Ring width of 15 mm |
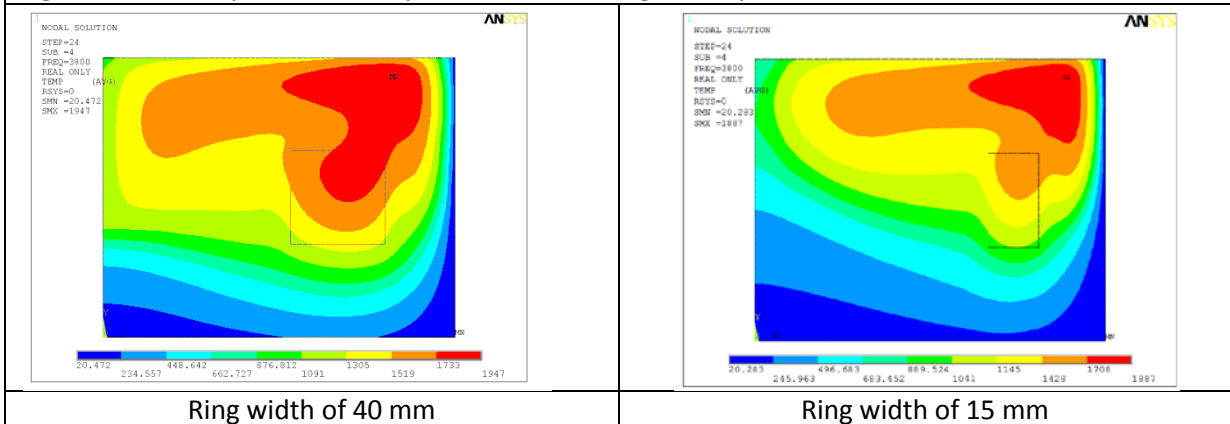
Figure 5-60. Comparison of temperature field during melt pool formation.

| Ring width of 40 mm | Ring width of 15 mm |

Figure 5-61. Comparison of heat sources during melt pool formation.
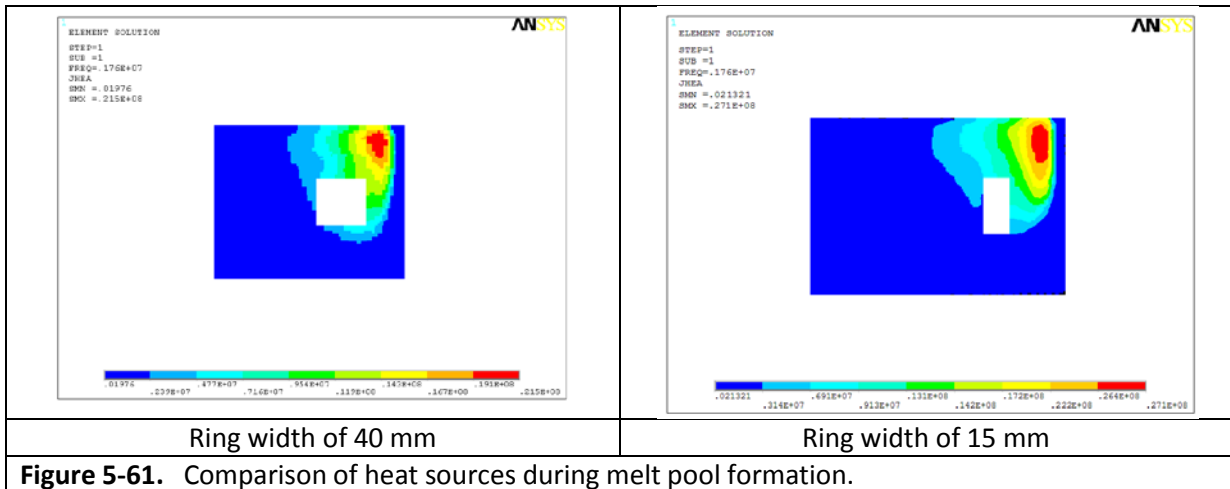
Thus, it can be observed that a thinner initiator ring may accelerate the start-up process; however, it requires more power. This is a trade-off that should be considered depending on the needs of a particular process.

Table 5-14. Comparative data for varying inner diameter initiator rings.

No	Description	Ring width, mm	
		40	15
1	Power supplied to the inductor, kW	34	39
2	Heat losses from pool side wall, kW	11.98	15.1
3	Power of heat losses from the pool bottom, kW	0.53	0.79
4	Power of heat losses from the pool side wall and its bottom, kW	12.97	15.97
5	Average temperature on the melt pool surface, °C	1,340	1,402
6	Specific heat flux from the pool side wall, W/cm^2	4.42	5.34
7	Specific heat flux from the pool bottom, W/cm^2	0.39	0.71
8	Power released into the ring, kW	2.96	4.05
9	Electrical power losses in the inductor, kW	1.012	1.445
10	Start-up heating time, sec	1,000	800
11	Voltage on the inductor during start-up, kV	5	5
12	Melt pool formation time, sec	6,000	6,000
13	Voltage on the inductor during melting, kV	2.9	3.2

5.3.3. Effect of Height Changes

The final investigation of the effects of ring geometry was focused on the height of the initiator ring. In this evaluation, the ring height was changed from the base case of 40 mm height to 50 mm and 60 mm. The same model parameters and initial conditions were used as in the prior investigations. Figure 5-62 shows the temperature distributions at start-up and melt pool formation stages. Figures

5-63 through 5-65 show the heat source distributions, horizontal velocity vectors, and vertical

velocity vectors for the two stages.
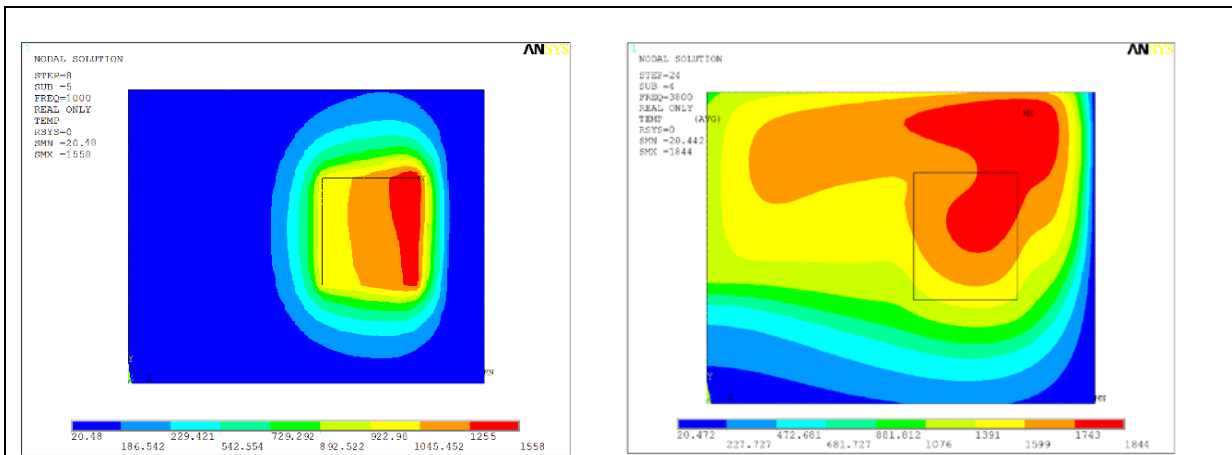
Figure 5-62. Temperature distributions for the 50 mm high initiator ring at start-up and melt pool formation stages.
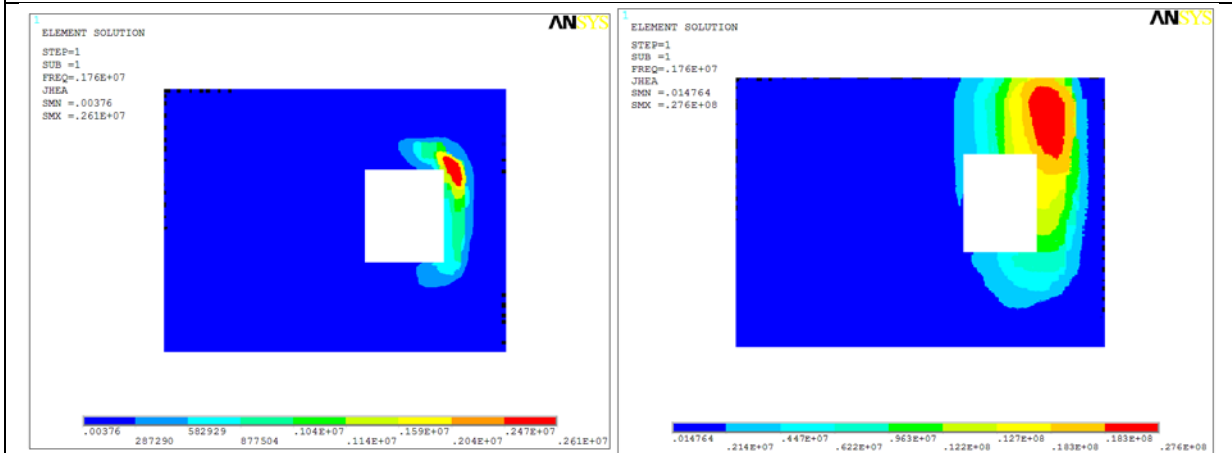
Figure 5-63. Heat source distributions for the start-up and melt pool formation stages for the 50 mm height initiator ring.
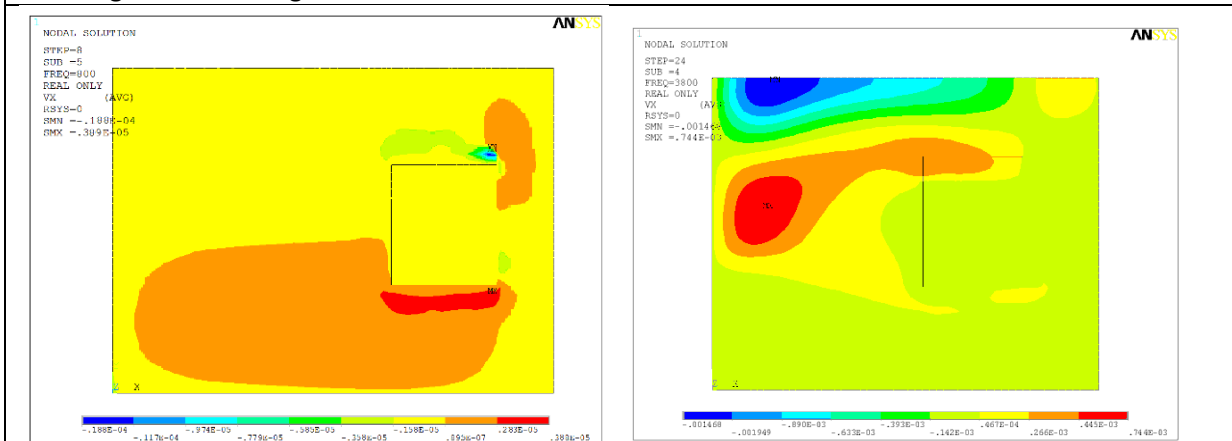
Figure 5-64. Horizontal velocity distributions at start-up and melt pool formation for the 50 mm high initiator ring.

Figure 5-65. . Vertical velocity distributions at start-up and melt pool formation for the 50 mm high initiator ring.
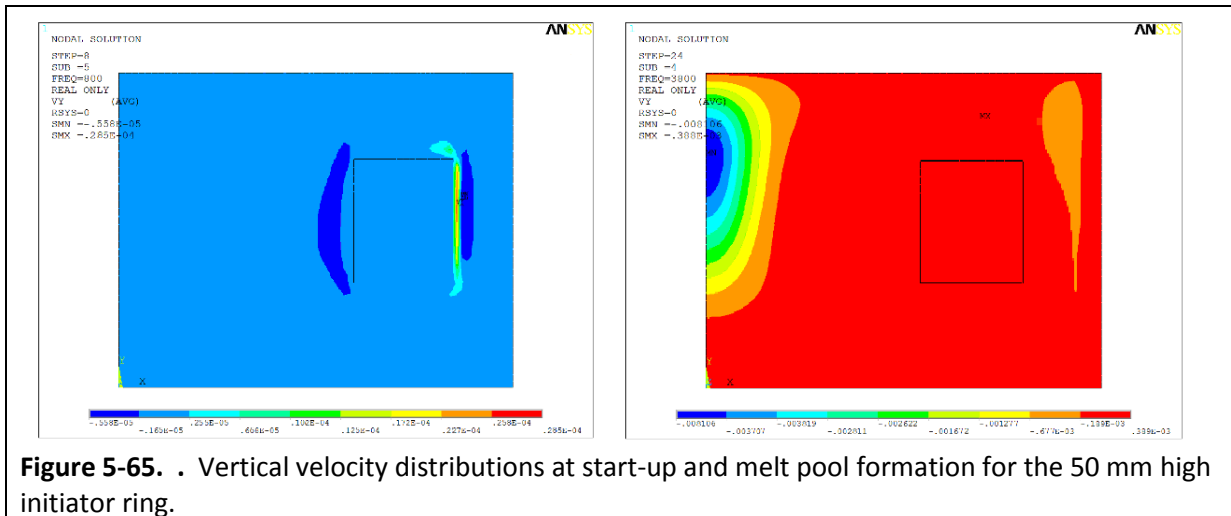
In the preceding calculation, values obtained for key parameters are provided in Table 5-15. All other model parameters were as previously defined in Table 5-8.

Table 5-15. Key parameters obtained from start-up model analysis for 50 mm high ring.

Parameter	Value
Power supplied to the inductor	36.5 kW
Heat loss from crucible side wall	12.14 kW
Heat loss from the crucible bottom	591 W
Total heat loss from the crucible	12.73 kW
Average temperature on the melt pool surface	1,309°C
Heat flux to the crucible side	4.57 W/cm^2
Heat flux to crucible bottom	0.46 W/cm^2
Power released into the initiator ring	3.37 kW

The next evaluation was for a ring height of 60 mm. As before, identical model parameters and initial conditions were used. Figure 5-66 shows the temperature distributions for the start-up and melt pool formation stages using the 60 mm height initiator ring.

Figure 5-66. Temperature distributions for 60 mm high ring at start-up and melt pool formation.
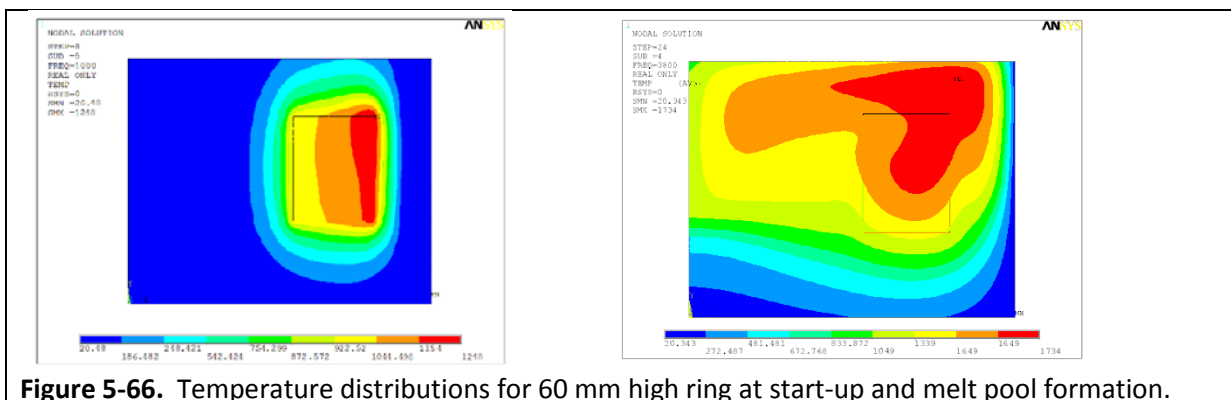
Figures 5-67 through 5-69 show the heat source distributions and the horizontal and vertical velocity

vectors for the start-up and melt pool formation stages for the 60 mm height initiator ring.
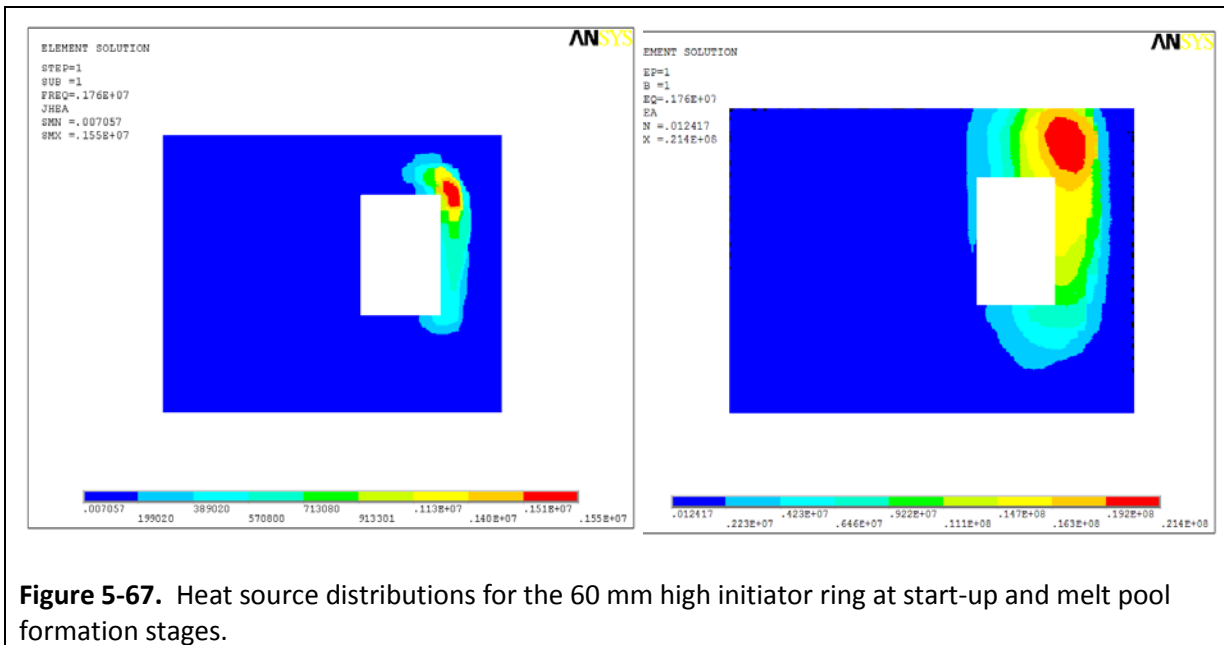
Figure 5-67. Heat source distributions for the 60 mm high initiator ring at start-up and melt pool formation stages.

In the preceding calculation values obtained for key parameters are provided in Table 5-16. All

other model parameters were as previously defined in Table 5-8.
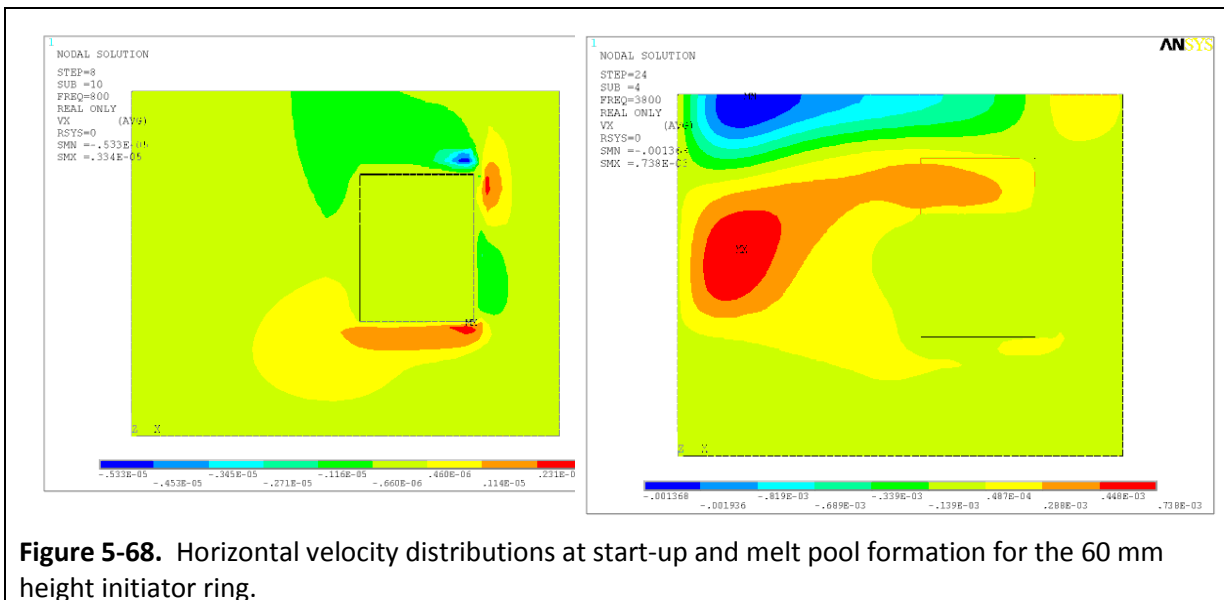
Figure 5-68. Horizontal velocity distributions at start-up and melt pool formation for the 60 mm height initiator ring.
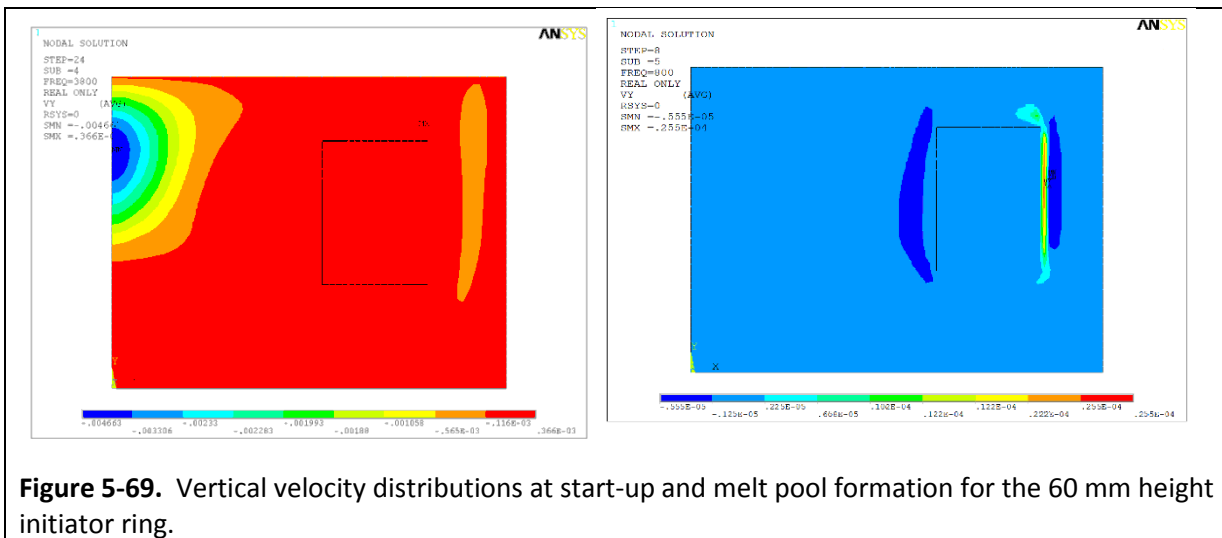
Figure 5-69. Vertical velocity distributions at start-up and melt pool formation for the 60 mm height initiator ring.

Table 5-16. Key parameters obtained from start-up model analysis for 60 mm high ring.

Parameter	Value
Power supplied to the inductor	37.35 kW
Heat loss from crucible side wall	13.37 kW
Heat loss from the crucible bottom	657 W
Total heat loss from the crucible	13.03 kW
Average temperature on the melt pool surface	1,296°C
Heat flux to the crucible side	4.99 W/cm^2
Heat flux to crucible bottom	0.63 W/cm^2
Power released into the initiator ring	3.86 kW

The following presents a comparison of the base case parameters to the two height variations investigated. The results for the temperature distributions at start-up and melt pool formation stages, as well as the heat source distribution at melt pool formation are presented in Figures 5-70 through 5-72. The results are summarized in Table 5-17.

Ring height of 40 mm	Ring height of 50 mm	Ring height of 60 mm
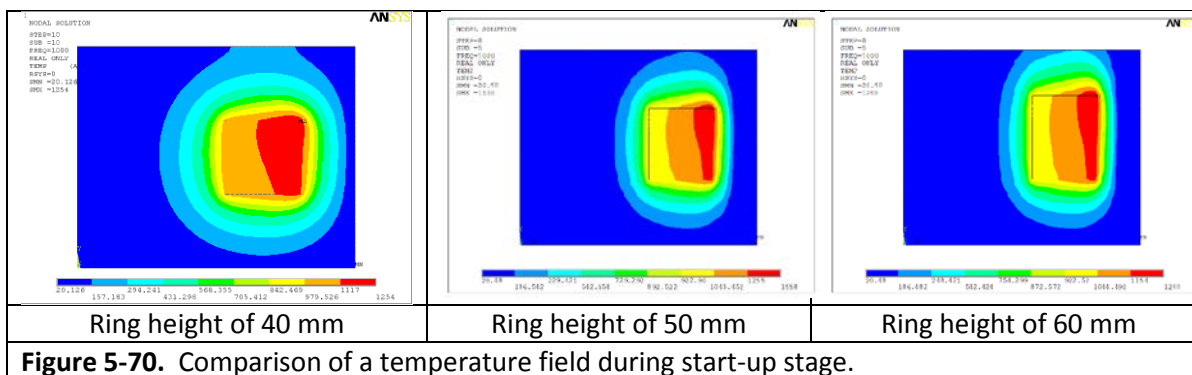
Figure 5-70. Comparison of a temperature field during start-up stage.

| Ring height of 40 mm | Ring height of 50 mm | Ring height of 60 mm |
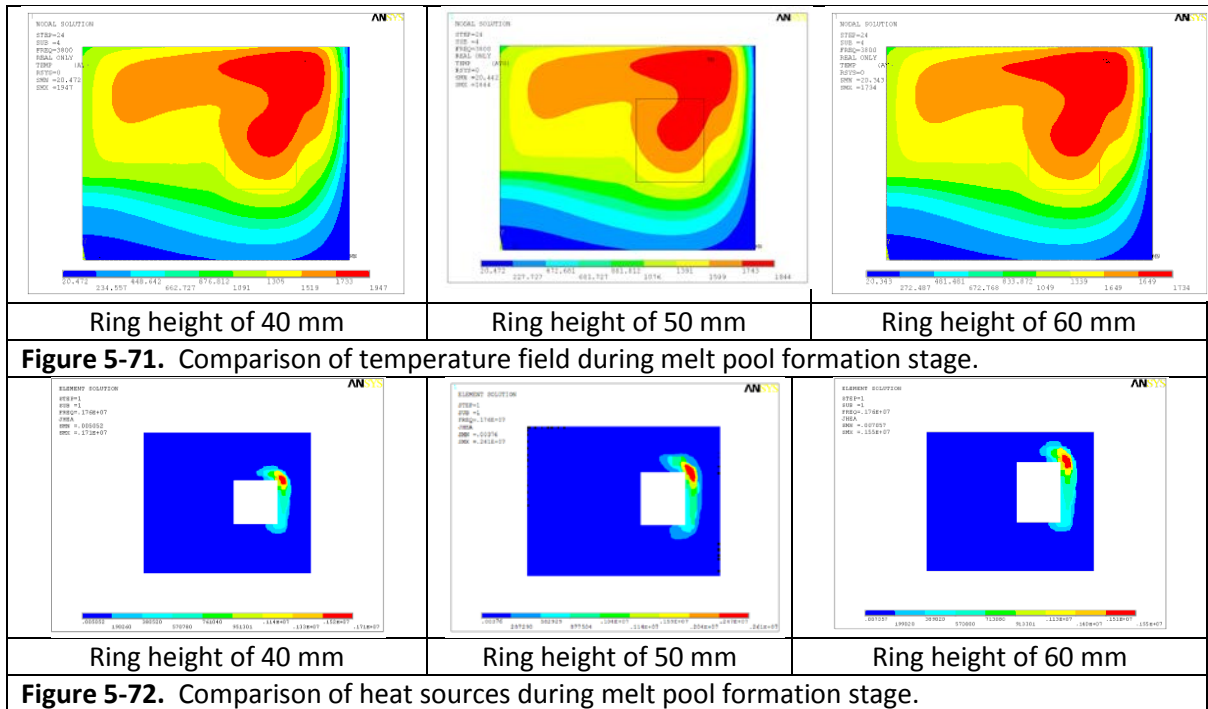
Figure 5-71. Comparison of temperature field during melt pool formation stage.

| Ring height of 40 mm | Ring height of 50 mm | Ring height of 60 mm |

Figure 5-72. Comparison of heat sources during melt pool formation stage.

As can be seen from these results, changing the height of the initiator ring does not appreciably impact the start-up process, or the ability to establish the conditions necessary to ensure melt pool formation. Thus, the decision to increase the ring height or not will be driven by other factors. For example, the ring used for most of the experimental work conducted was made of graphite.

Table 5-17. Comparison of key parameters for various initiator ring heights.

No.	Description	Ring height, mm		
		40	50	60
1	Power supplied to the inductor, kW	34	36.5	37.35
2	Power of heat losses from the crucible side wall, kW	11.98	12.14	12.37
3	Power of heat losses from crucible bottom, kW	0.53	0.59	0.66
4	Power of heat losses from crucible side and bottom, kW	12.97	12.73	13.03
5	Average temperature on the melt pool surface, °C	1,340	1,309	1,296
6	Specific heat flux from the crucible side wall, W/cm^2	4.42	4.57	4.99
7	Specific heat flux from the crucible bottom, W/cm^2	0.39	0.46	0.63
8	Power released into the ring, kW	2.96	3.37	3.86
9	Electrical power losses in the inductor, kW	1.012	1.254	1.398
10	Time of start-up, sec	1,000	1,000	1,000
11	Voltage on the inductor during start-up, kV	5	5	5
12	Time of heating during melt pool formation, sec	6,000	6,000	6,000
13	Voltage on the inductor during melt pool formation, kV	2.9	2.9	2.9
14	Maximum melt temperature, °C	1,947	1,844	1,734

Because the CCIM system used provided the capability to directly access the melt pool, the ring could be manually removed once a melt pool was completely established. However, for processing radioactive materials, this is not an option since those systems are closed for contamination control and worker protection. Most all of the radioactive waste streams that can be processed in a CCIM contain metal oxides that can be chemically reduced by the carbon in the graphite ring, causing them to separate and settle out of the molten pool. This is an undesirable situation for melter operation since it results in an electrical shorting of the energy induced into the melt causing an inefficient operation. Additionally, it can potentially result in bulk cooling of the melt and lead to loss of the melt pool. Nevertheless, for purposes of this work the decision was made to primarily use the 40 mm high ring, although other techniques were investigated. (Note that thinner rings were not evaluated because thinner sections of graphite become unstable and fracture after a few exposures to the high temperature glass melt.)

5.4. Integration of Start-Up Model with Base Model

The start-up model was integrated with the base ANSYS® MultiPhysics model once it was validated. This requires three separate stages, and thus a condition of quasi-steady state must be obtained. During the first stage, the initiator ring is in the model and the primary inductor (1.76 MHz) is energized. The melt pool height is at half of the full charge. Once the condition has been achieved that will ensure that the melt can be propagated upon removal of the ring (discussed earlier) this constitutes the first stage.

The second stage is actually subdivided into two separate steps. First, the elements that constitute the ring are changed to different elements with the properties of the glass at the same temperatures. This is an obvious simplification, as is the fact that the glass volume does not reduce during melting, as it does with the actual material in experiments. However, these simplifications do not affect the steady state conditions, only the time required to achieve the same volume with a full melt.

Second, the power level on the primary inductor is reset at a pre-defined level to achieve the desired maximum temperature in the melt. This is generally a combination of modeling results and empirical data from the experimental efforts. Additionally, new glass volume elements are added to the model to constitute the full charge in the crucible. Then the model calculations are restarted,

with only the primary inductor energized, and run until a steady-state temperature condition in the melt is achieved.

The final stage involves a restart using the model data obtained from the prior stages with the drain inductor (27 MHz) energized. The model is run for sufficient time to obtain a temperature on the open face of the drain body to support casting. The basic structure of this integrated model is shown in Figure 5-73. Note that the glass volume is divided into two separate areas to avoid a large matrix containing zero values during the start-up stage. The algorithm to write to the data matrices provides for rigid adherence to the separate design areas.

First Stage – melt start-up with initiator ring in place, primary inductor only energized.	**Second Stage** – initiator ring removed and replaced with glass, additional glass volume added, primary inductor only energized, steady state achieved.	**Third Stage** – drain inductor and primary inductor energized until temperature in drain opening achieved to support casting.

Figure 5-73. Graphical depiction of integrated model stages.

The actual model geometry is shown below in Figure 5-74.

First Stage	**Second Stage**	**Third Stage**
Primary inductor only energized	Primary inductor only energized	Primary and secondary inductor energized

Figure 5-74. Model geometry for three stages of integrated model that includes start-up and casting.
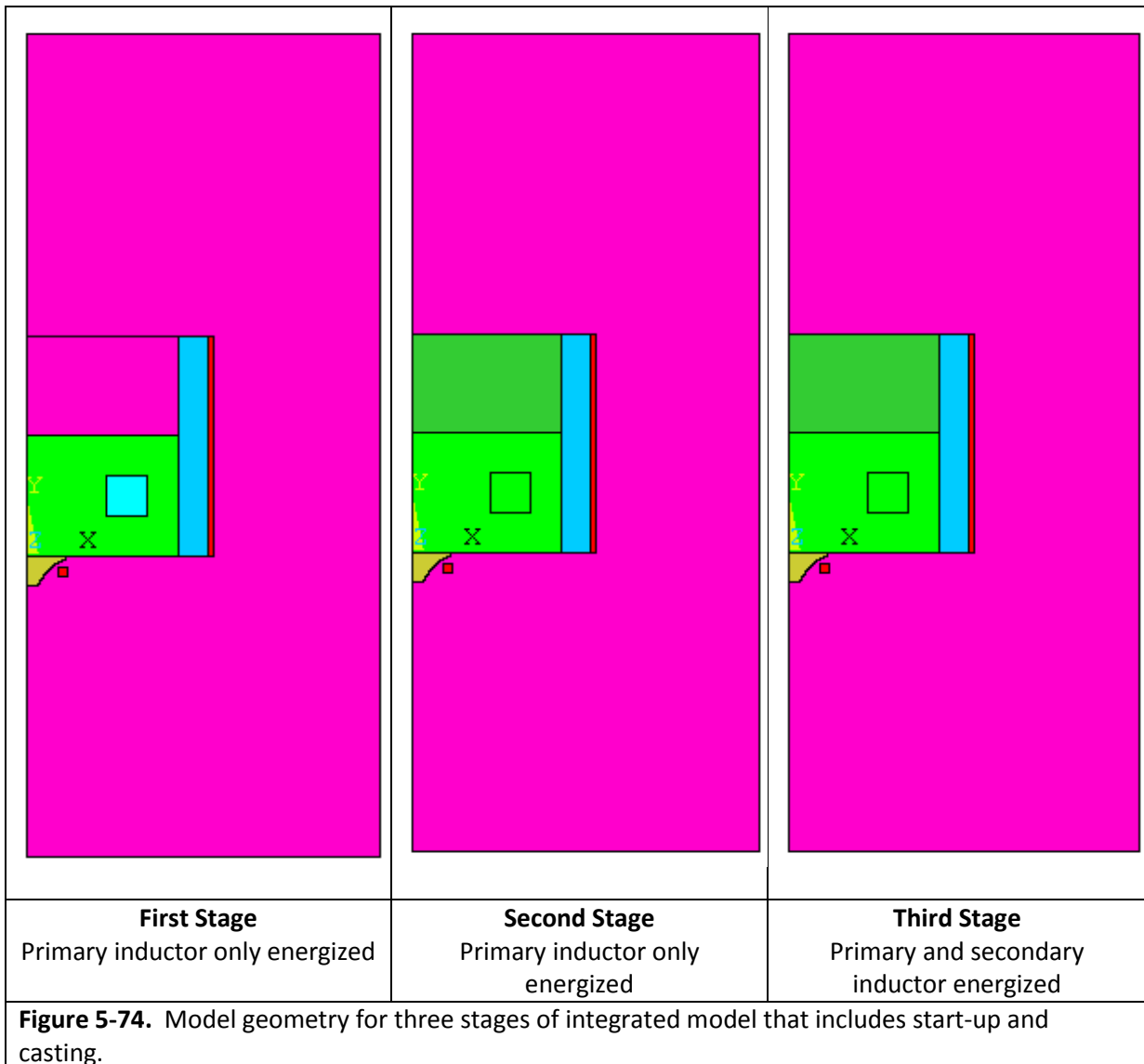
Key model parameters are as follows:

- First Stage: Inductor voltage is 5 kV and calculation time is 1,000 seconds.

- Second Stage: Inductor voltage is 3 kV and the calculation time is 6,000 seconds

- Third Stage: Inductor voltage is 2.5 kV and the calculation time is 5,000 seconds.

The final logic diagram for the model is depicted below in Figure 5-75. Figures 5-76 through 5-78 show the temperature distributions and the heat sources for the three stages of the model calculations. Figures 5-79 through 5-81 illustrate the horizontal (left) and vertical (right) velocity component distributions for the three stages.

Figure 5-75. Logic diagram of integrated model.
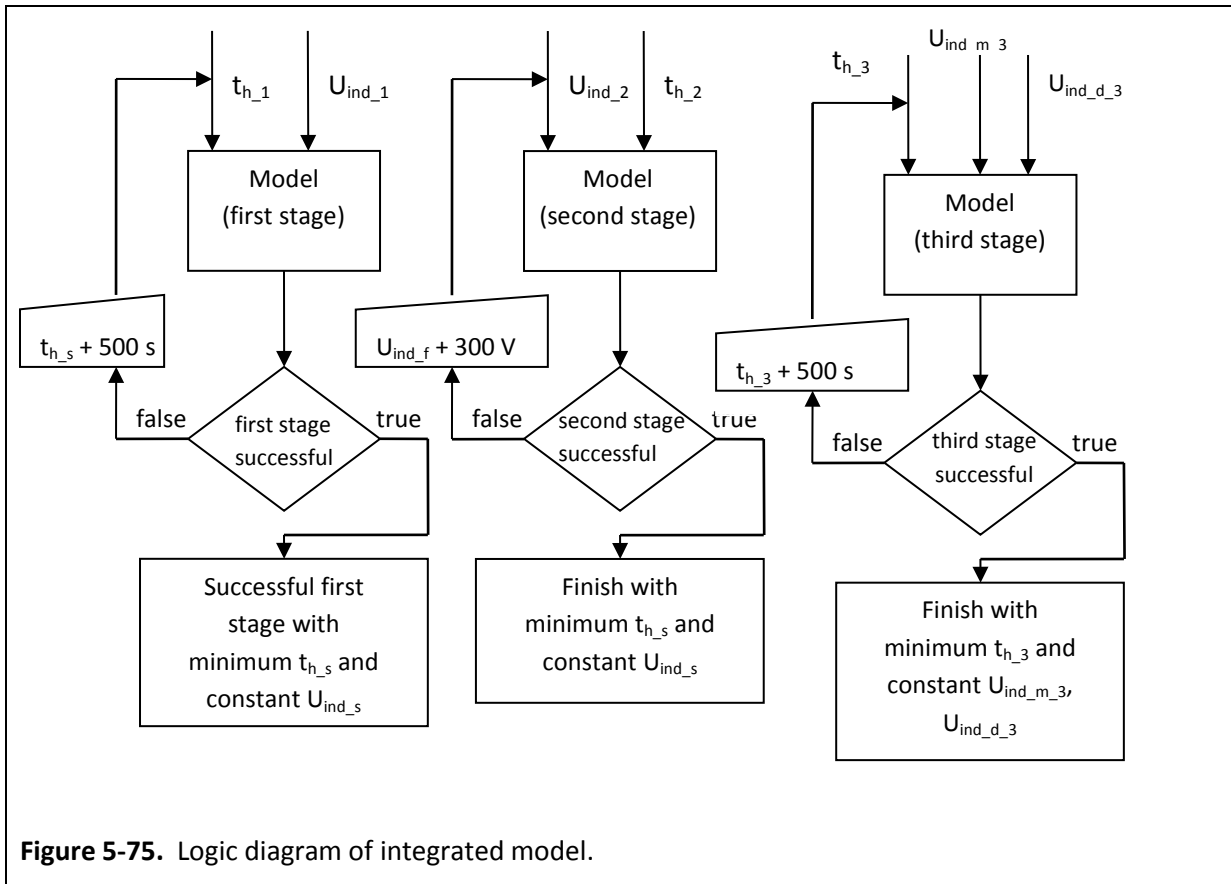
The model parameters used for these calculations were the same as previous calculations for the base case of a nominal 300 mm diameter melter, as defined in the prior analyses for the start-up model evaluation efforts. These results demonstrate a successful process from start-up through casting, which has also been demonstrated experimentally in the test platform that the model was based upon.

This represented the final stage of model development completed during the research reported in this dissertation. The model was demonstrated to be a very effective tool for conducting parametric analysis and helping to determine the focus and overall design for experiments and the test plans. This integrated model provides a very good representation of the actual physical processes involved in melt initiation, achieving a steady-state in the melt, and subsequent energizing of the drain inductor to allow the high temperature melt to propagate into the drain body, providing for bottom casting.
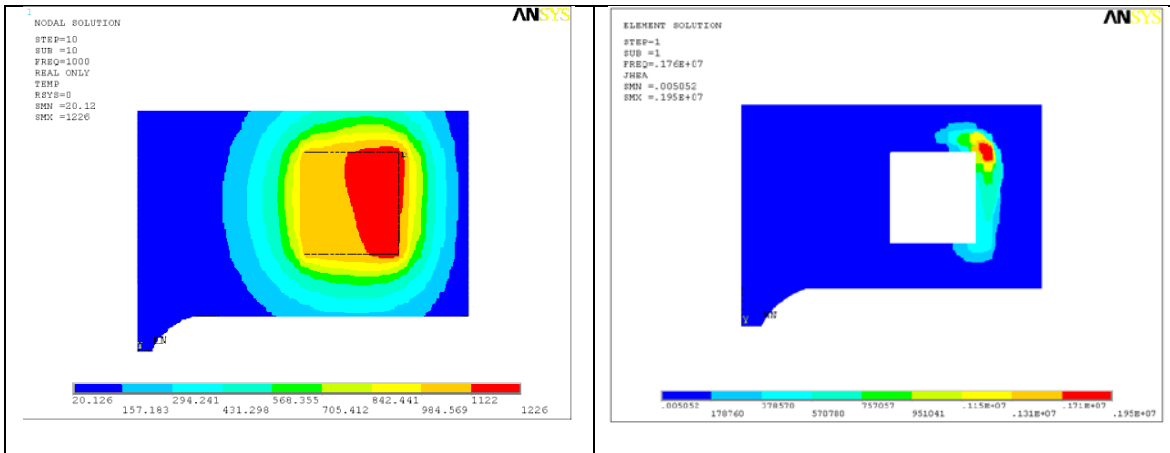
Figure 5-76. Temperature distribution and heat source distribution for the first stage.
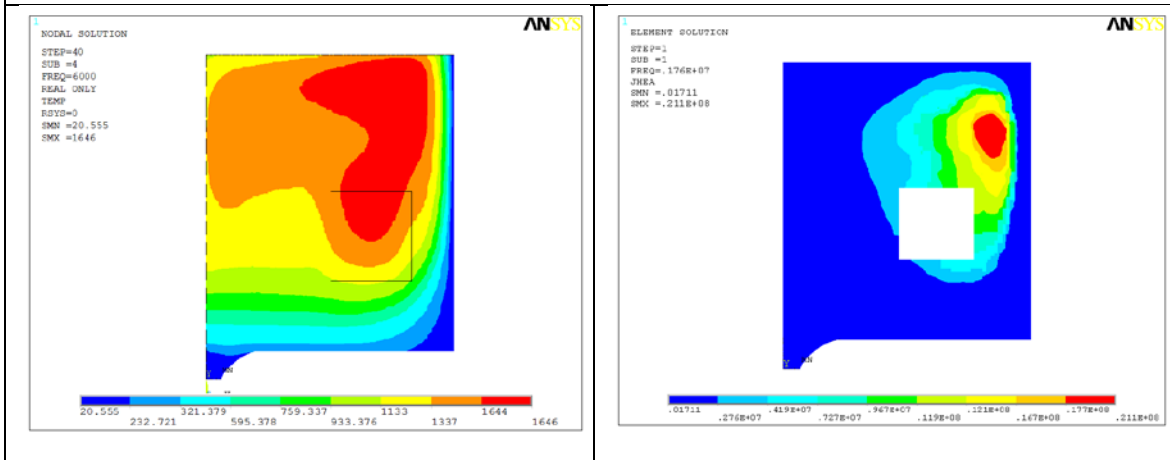
Figure 5-77. Temperature distribution and heat source distribution for the second stage.
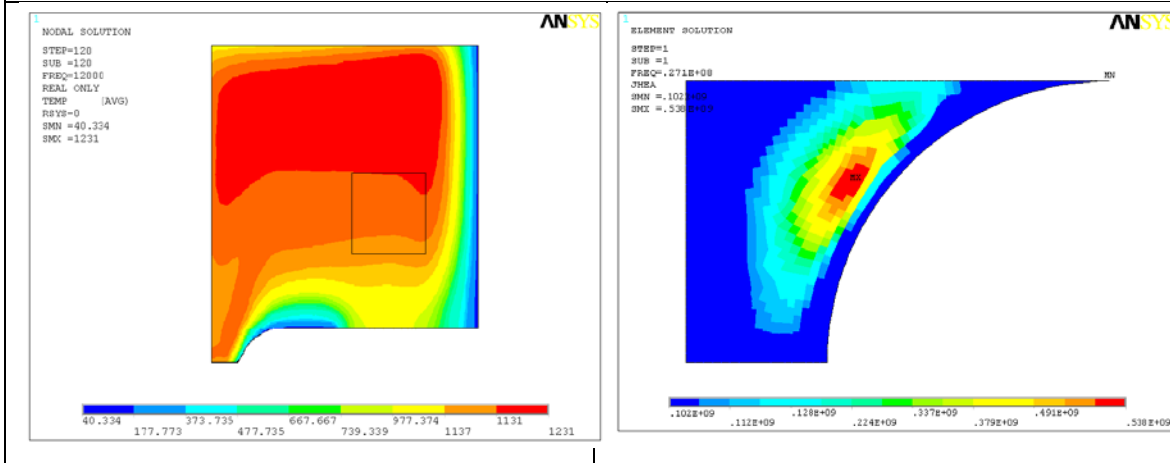
Figure 5-78. Temperature distribution and heat source distribution for the third stage.
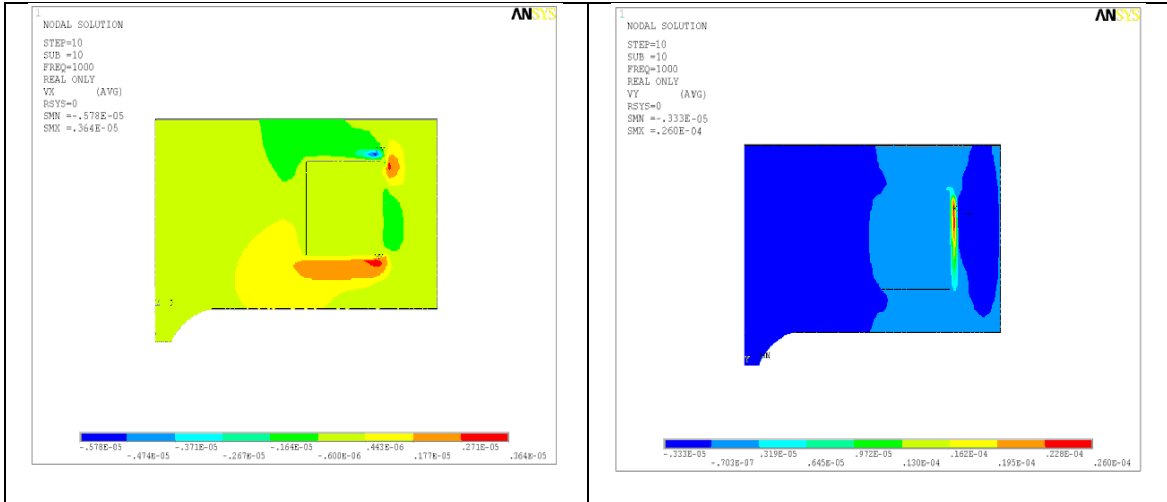
Figure 5-79. Horizontal (left) and vertical (right) velocity component distributions for the first stage.
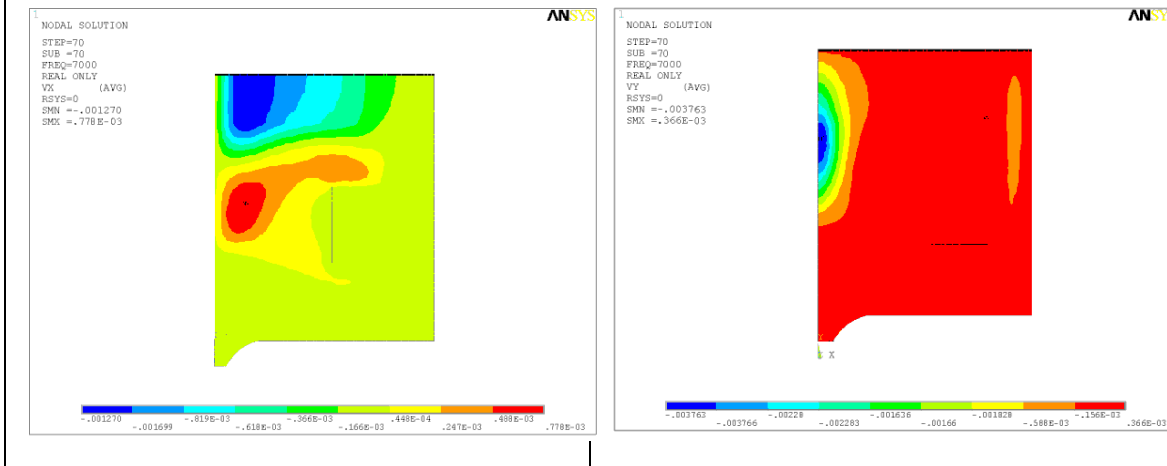
Figure 5-80. Horizontal (left) and vertical (right) velocity component distributions for the second stage.
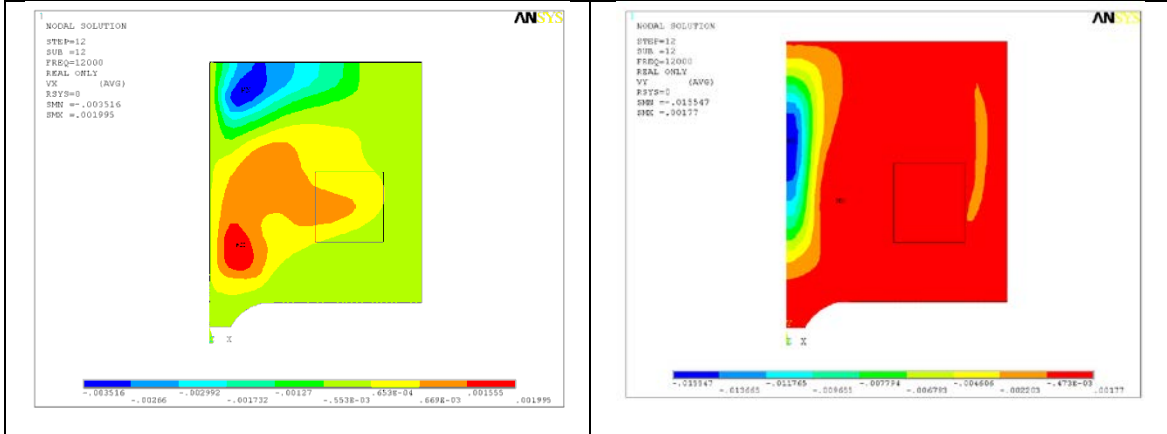
Figure 5-81. Horizontal (left) and vertical (right) velocity component distributions for the third stage.

CHAPTER 6.   SCALE-UP DESIGN INVESTIGATIONS

One of the primary benefits of having a validated model is to conduct parametric studies related to scale-up of the CCIM platform. This is important because it is often too costly and time consuming to iteratively build and test large scale systems to determine overall operability and reliability. In this investigation, a nominal 400 mm diameter system was evaluated for feasibility using the available high frequency power supplies, specifically the 60 kW, 1.76 MHz generator and the 8 kW, 27 MHz generator. From induction heating theory, it is known that the increase in diameter at a fixed frequency of 1.76 MHz will decrease the skin depth, thus increasing the diameter-to-skin depth ratio. This introduces uncertainties that require evaluation prior to constructing the system.

6.1. General Heating Conditions

The investigation was carried out in two stages: 1) steady state conditions were analyzed for a single frequency system (i.e., 1.76 MHz), then 2) steady state conditions were analyzed for a dual frequency system (i.e., 1.76 MHz on the primary inductor and 27 MHz on the drain inductor). The model parameters for these calculations are shown in Table 6-1.

6.1.1.Heating Conditions Comparison for Scale-Up

The boundary conditions were the same as used in previous calculations, as refined by improved calorimetry and modeling results. The analyses were conducted for the base case of 300 mm diameter and compared to the 400 mm diameter system. These investigations were focused on the primary parameters that impact the melt pool conditions, including temperature distribution, heat sources, melt convection velocities, power losses from the crucible and melt surfaces, and the average power in the melt. The power level used for the 400 mm system was selected such that the maximum temperature achieved in the melt is similar to that of the 300 mm system, or about 1,400^{o}C. This resulted in the use of 27 kW power into the melt. Figure 6-1 provides a comparison of the steady state temperature distribution for the 300 mm and 400 mm diameter systems.

From Figure 6-1, the overall effect of lower temperatures, especially in the lower layers of the melt pool are observed. The primary effect being a significant increase of the solid skull layer along the bottom from between 2mm and 4 mm to between 5 mm and 7 mm, which is not amenable for bottom glass casting. Table 6-2 provides data obtained for this analysis.

Table 6-1. Key model parameters for initial scale-up studies.
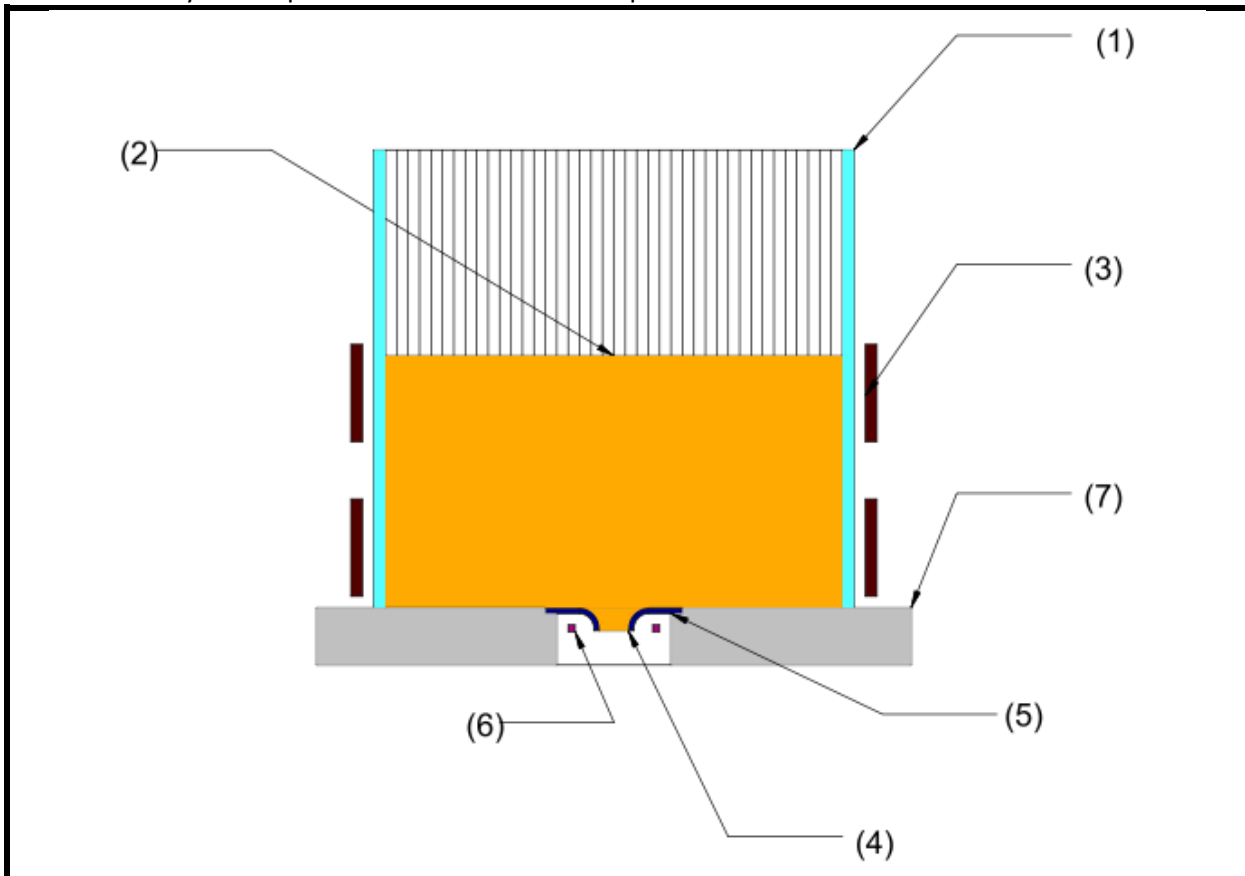
Parameter	Value
Cold crucible internal diameter (1)	400 mm
Melt pool height (2)	220 mm
Primary inductor internal diameter (3)	440 mm
Number of primary inductor turns	2
Cross-section of the inductor coils	rectangular
Primary inductor height	220 mm
Primary inductor current frequency	1.76 MHz
Drain internal diameter (4)	25 mm
Drain flange diameter (5)	120 mm
Small inductor internal diameter (6)	68 mm
Small inductor number of turns	1
Small inductor height	6 mm
Small inductor coil cross-section	rectangular
Small inductor current frequency	27 MHz
Cold crucible bottom material (7)	ceramic
Small inductor current	165 A

Crucible diameter of 300 mm, pool height of 200 mm	Crucible diameter of 400 mm, pool height of 220 mm

Figure 6-1. Steady state temperature distribution in the melt without the drain.
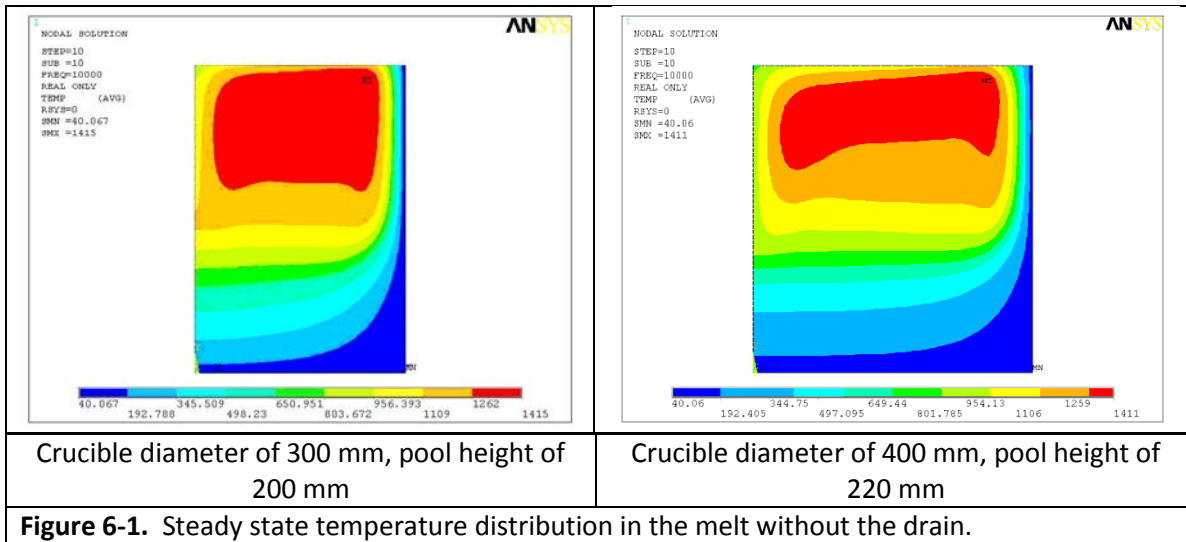
Table 6-2. Parameters from initial scale-up analysis for 400 mm diameter CCIM.

Parameter	Value
Power supplied to the melt	37 kW
Power of heat losses from the crucible side wall	13.44 kW
Power of heat losses from the crucible bottom	597 W
Total power of heat losses from the crucible side wall and bottom	14.37 kW
Heat flux to the crucible side wall	4.86 W/cm^2
Heat flux to the crucible bottom	0.48 W/cm^2

Note that the heat losses through the bottom are reduced from previous results due to the overall lower temperatures in this zone in the crucible. Figure 6-2 shows the distribution of heat sources in the 400 mm diameter system.

Figure 6-2. Heat source distribution in the 400 mm diameter system.
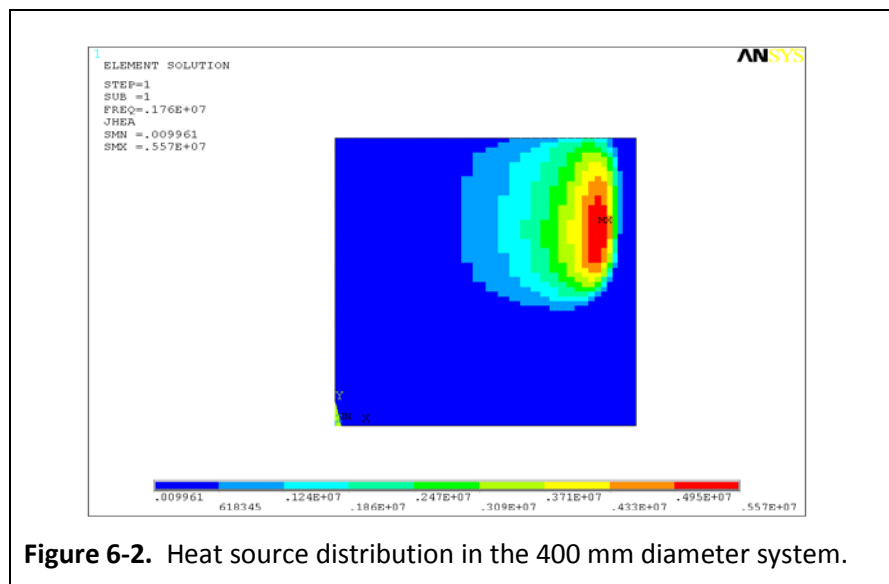
Figures 6-3 and 6-4 show the vertical and horizontal velocity vectors for the 400 mm diameter system.
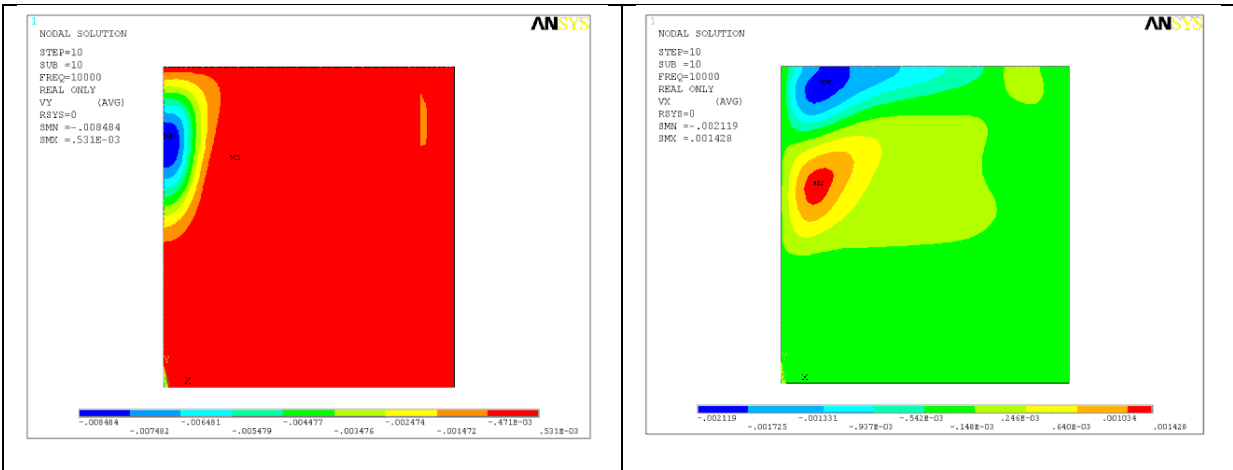
| **Figure 6-3.** Vertical velocity distribution. | **Figure 6-4.** Horizontal velocity distribution. |

Figures 6-5 through 6-8 show heat loss and temperature distributions along the side wall and bottom surfaces.
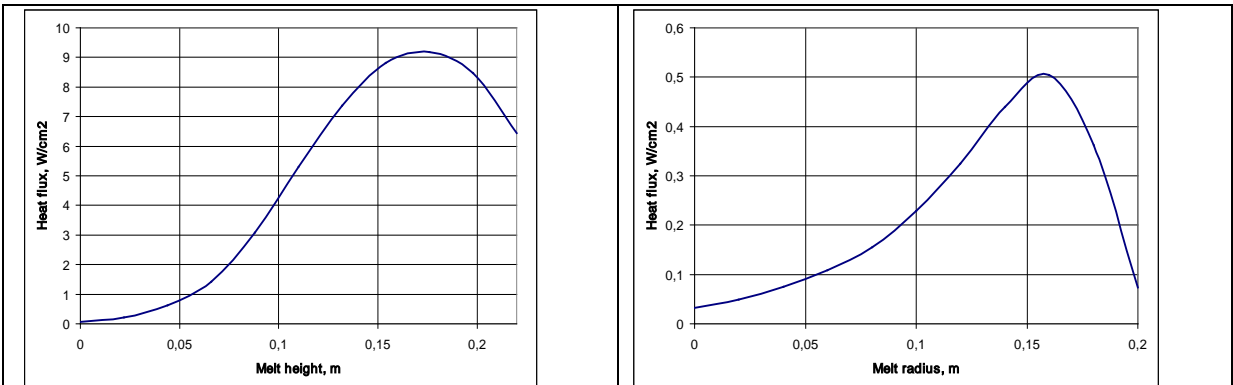
| **Figure 6-5.** Heat loss along sidewall. | **Figure 6-6.** Heat loss along bottom surface. |

| **Figure 6-7.** Temperature along sidewall. | **Figure 6-8.** Temperature along bottom. |
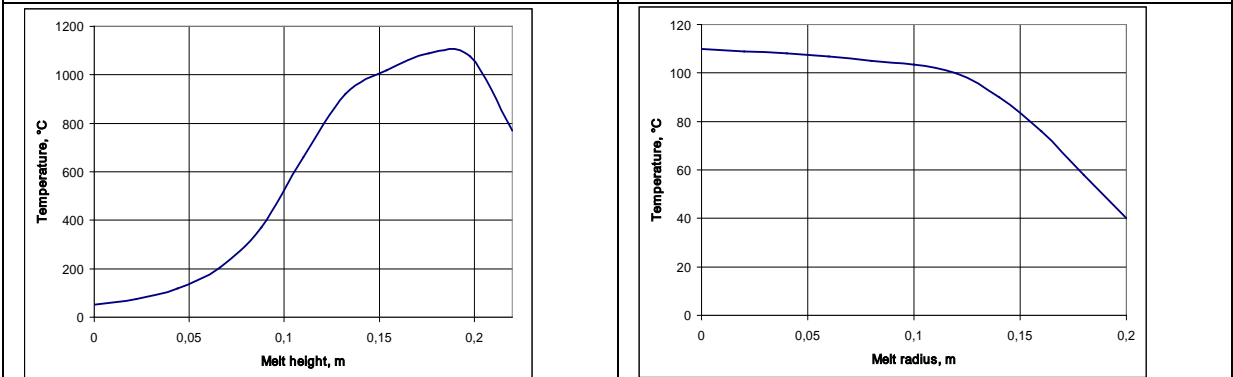
These diagrams are presented for comparison purposes with the results for the system that includes the drain device and the 27 MHz generator heating effects. As before, the power level was selected such that a maximum melt temperature of approximately 1,400°C was obtained. This resulted in the power level in the melt of 37 kW.

6.1.2. Effects of Drain and Dual Frequency Heating

Figure 6-9 shows the steady state temperature distributions for the 400 mm diameter system with no drain and single frequency heating versus with the drain and dual frequency heating.

The heat source distribution, and vertical and horizontal velocity profiles for the dual frequency system are shown in Figures 6-10 through 6-12.

| Single frequency (1.76 MHz) heating, no drain | Dual frequency heating with the drain |
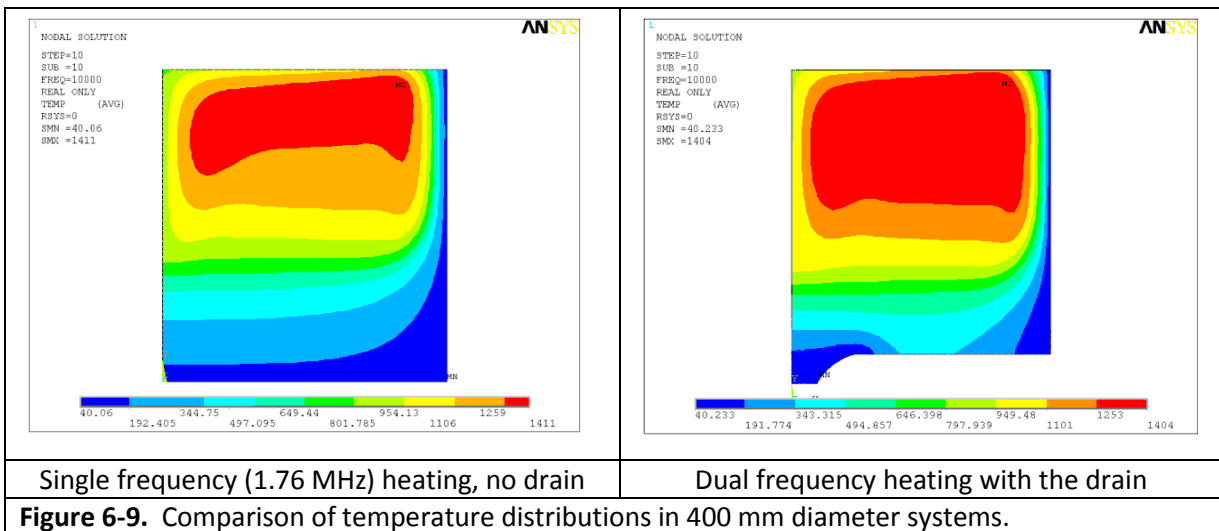
Figure 6-9. Comparison of temperature distributions in 400 mm diameter systems.
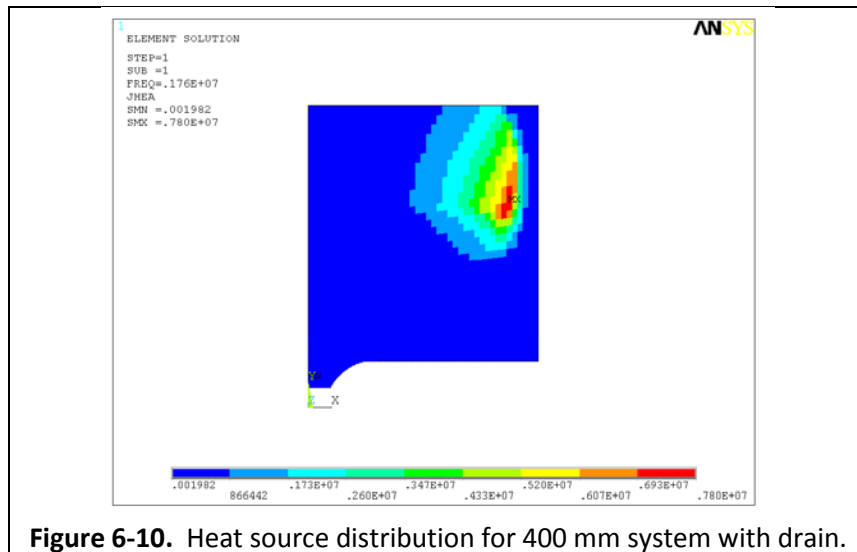
Figure 6-10. Heat source distribution for 400 mm system with drain.
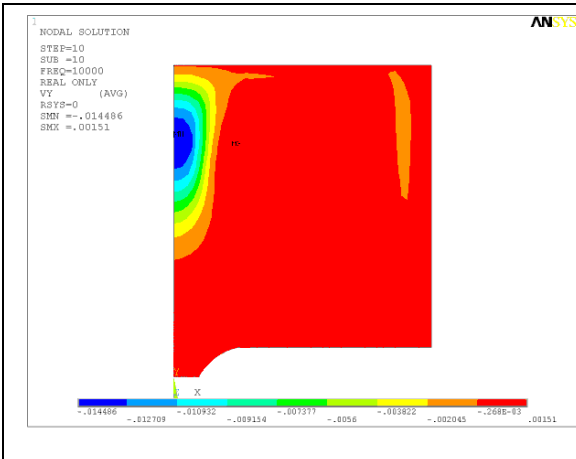
Figure 6-11. Vertical velocity profile for 400 mm dual frequency system with drain.
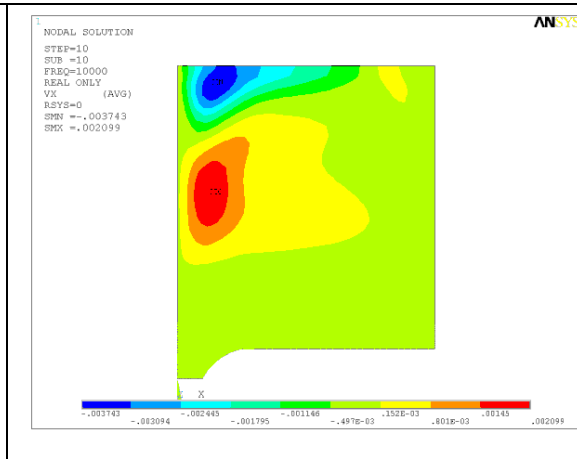
Figure 6-12. Horizontal velocity profile for 400 mm dual frequency system with drain.
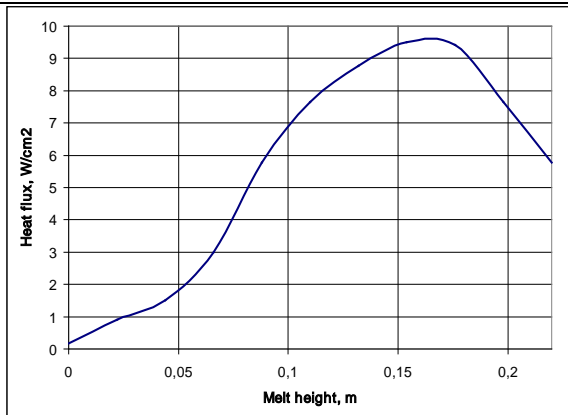
Figure 6-13. Heat loss along sidewall.
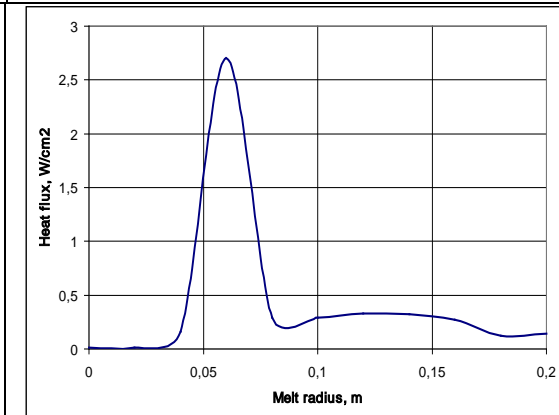
Figure 6-14. Heat loss along bottom surface.
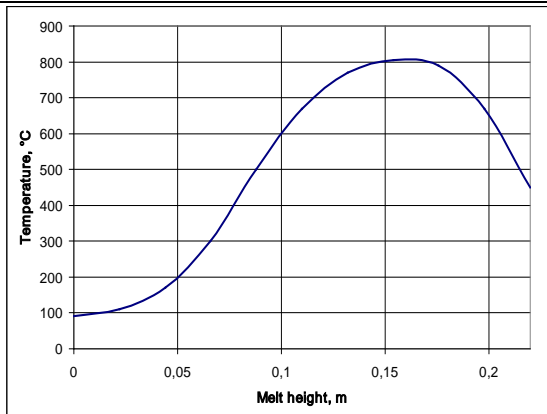
Figure 6-15. Temperature along sidewall.
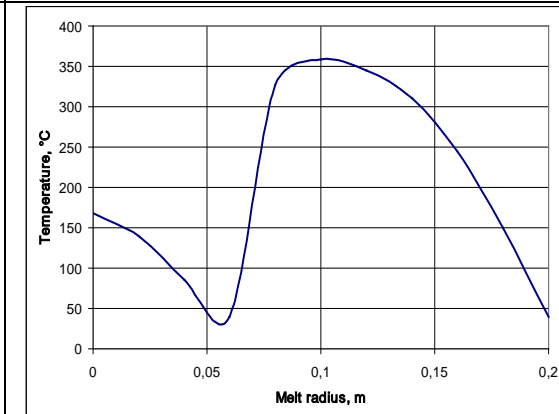
Figure 6-16. Temperature along bottom.

Figures 6-13 through 6-16 show heat loss and temperature distributions along the side wall and bottom surfaces.

The preceding figures illustrate some significant differences in the results due to the presence of the drain and the 27 MHz induction field. For example, the heat loss and temperature distributions along the side wall and bottom are much more complex for the system with the drain, as expected. Also, the velocities are much greater in the system with the drain due to the added energy from the 27 MHz generator. The general conclusions regarding comparison of the 400 mm diameter dual frequency system versus the 300 mm diameter system are as follows:

- While the 400 mm diameter system provides a larger melt pool volume and surface areas, thus increasing the productivity, the bottom skull is much thicker, which will likely not support bottom melt casting. Additional investigations are required to resolve this issue.

- Because the melt temperature distribution is generally more homogeneous, the specific heat flux to the side wall is decreased, making the system more efficient.

- The average melt velocities due to convection are increased, which helps reduce the hot spot in the melt and results in a more thermally homogeneous melt.

Although mentioned above, a key finding is that using the same generator power in the 300 mm diameter system provides a condition that allows for bottom casting; however, this is not the case for the 400 mm diameter system. This result was used to justify investment in modification of the 27 MHz generator such that it could provide up to 10 kW of power to be able to induce enough energy into the glass near the drain throat to allow casting. (Note that later calculations were conducted for the generator with 7 kW power for a 407 mm diameter CCIM and this was demonstrated to be inefficient to ensure conditions for bottom casting. This is discussed in more detail below.)

6.2. Application of Model to Investigate Configuration Changes to Improve Conditions for Bottom Casting

In addition to the need to increase the power and current capacity of the 27 MHz generator, which enables the melt casting process, several other factors can influence favorable conditions for bottom casting, especially in support of larger CCIM systems. One specific geometry variable to be considered is a different configuration for the primary inductor in which a horizontal turn is included below the bottom of the crucible.

6.2.1.Comparison of Heating Conditions for a Bottom Coil

The first investigation provides a comparison of a system with a conventional two-turn coil to a two-diameter three turn coil that includes one horizontal bottom coil. Only the 1.76 MHz power source is applied for initial comparison. The model parameters used for this and subsequent analyses are given in Table 6-3.

Additionally, due to the complexity of the induced electromagnetic field, the mesh refinement factor was set at mm = 6. This requires significantly longer processing times for each model, consequently the analyses were limited to specific configuration changes that, based on experience from actual testing, were considered to have the greatest impact on the steady state melt condition. Figure 6-17 shows the model geometries and Figures 6-18 through 6-21 compare the results.

This inductor geometry clearly improves the overall behavior of the melt relative to ensuring the ability to achieve bottom casting. These results were then compared to a similar system with a bottom turn with outside diameter of 407 mm. Again, this only includes a single frequency power source of 1.76 MHz. Figure 6-22 shows the model configurations used for the analyses. Figures 6-23 through 6-26, above, provide comparative results for the same parameters as the previous investigation for the two bottom coil configurations.

These results indicate that this change did not produce any significant differences in the melt characteristics. In general, a two-diameter inductor with the bottom coil having a 407 mm outer diameter is expected to be easier to fabricate, and be represented by the model results a little better, from an energy deposition perspective. This is because the model does not account for the losses associated with a significant change of diameter for the inductor turn (i.e., transition buss losses).

A final scoping analysis was performed for the single frequency application to investigate the effects of the drain upper diameter on the temperature distribution for the bottom coil configuration. For the previous two investigations, the drain length was set at 20 mm, with a 16 mm curve radius. This drain geometry is 10 mm long with an 8 mm radius, significantly reducing the upper cooled diameter on the bottom. This also provides the ability to reduce the diameter of the drain inductor coil, if desired. Figure 6-27 shows the geometries for the models evaluated. Figures 6-28 through 6-31 illustrate the comparative results for the long drain and short drain systems.

Table 6-3. Parameters for analysis of 400 mm CCIM with bottom coil.
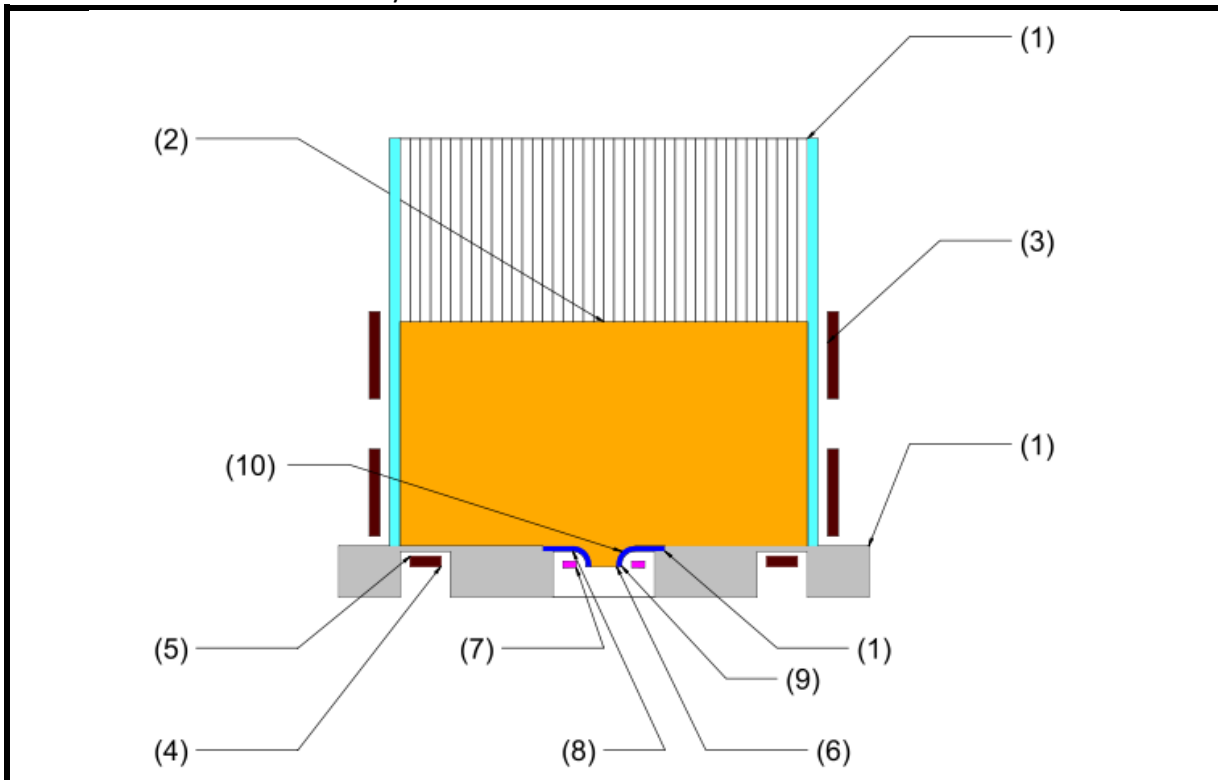
Parameter	Value
Melt pool radius (1)	203.5 mm (based on actual crucible)
Melt pool height (2)	200 mm
Internal radius of primary inductor side coils (3)	227.8 mm
Thickness of primary inductor side coils	2 mm
Height of the primary inductor side coils	85 mm (each turn), total 200 mm
Distance between primary inductor side coils	30 mm
External radius of the bottom coil (4)	203.5 mm and 153.5 mm
Internal radius of the bottom coil	153.5 mm and 103.5 mm
Distance from the melt pool to top of bottom coil (5)	10 mm
Thickness of the bottom coil	2 mm
Drain radius at bottom face (6)	13 mm
Internal radius of drain inductor (7)	27.5 mm, 22.5 mm, and 17.5 mm
External radius of drain inductor	45 mm, 41 mm, and 36 mm
Distance from drain inductor to melt pool bottom (8)	h_2 = 5 mm, 10 mm, 14 mm, and 20 mm
Distance from the drain inductor to melt in drain (9)	h_3 = 5 mm and 15 mm
Height of drain inductor (7)	6 mm
Height of drain body (6)	20 mm and 10 mm
Radius of curvature of drain body (10)	16 mm and 8 mm
Heat flux through the bottom of the crucible	0.64 W/cm^2
Heat flux through the crucible side wall	8.72 W/cm^2
Power on primary inductor power	37 kW
Power on drain inductor power	7 kW
Integrated emissivity value of the glass surface	0.5

The final analysis investigated the effects of the additional 27 MHz power source coupled with the bottom coil to determine their influence on the conditions to provide for bottom casting. This investigation compares the steady state melt conditions between a system with and without a bottom turn on the primary inductor coil. The external diameter of the bottom coil is set at 307 mm for this initial analyses for comparison to the single frequency calculations presented earlier. This initial configuration was selected because it was also thought that better heating may result with the bottom turn of the primary inductor located closer to the 27 MHz drain inductor. This would concentrate the power sources in the melt volume that is closest to the drain opening.

Figure 6-32 shows the model geometries for these comparative analyses. Figures 6-33 through 6-36 show the temperature distributions, velocity vectors, horizontal velocity distributions, and vertical velocity distributions.
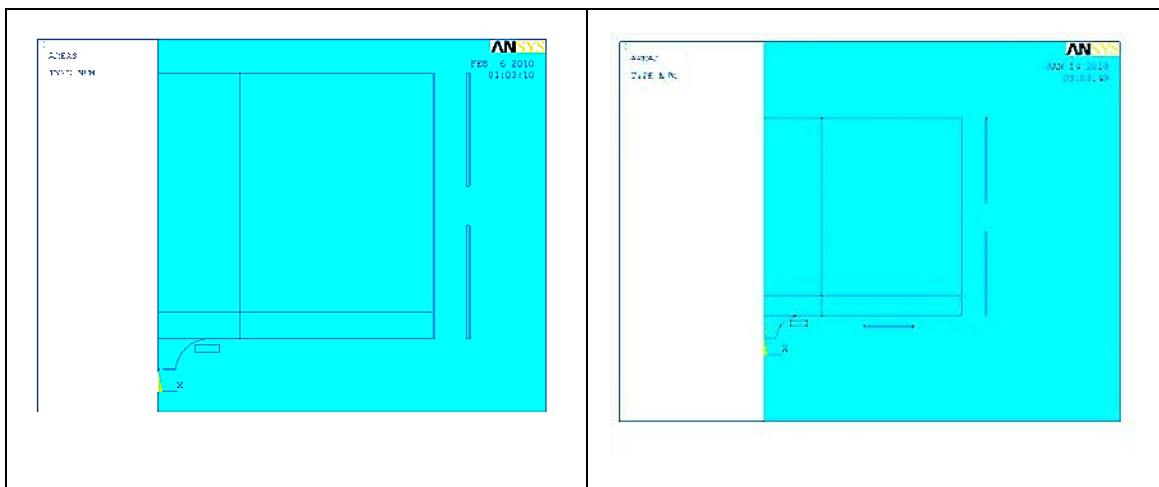
Figure 6-17. Model geometries used for analysis. (drain inductor is 27.5 mm ID, 45 mm OD)
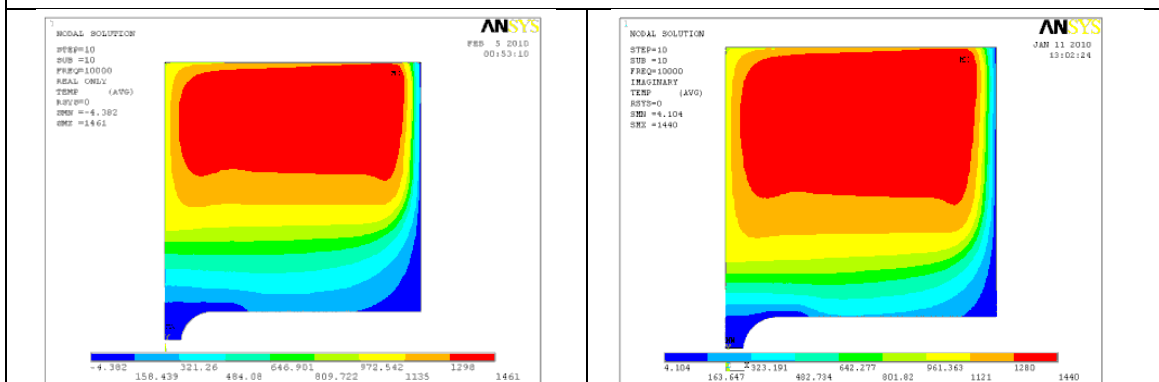
Figure 6-18. Comparison of temperature distributions in melt.
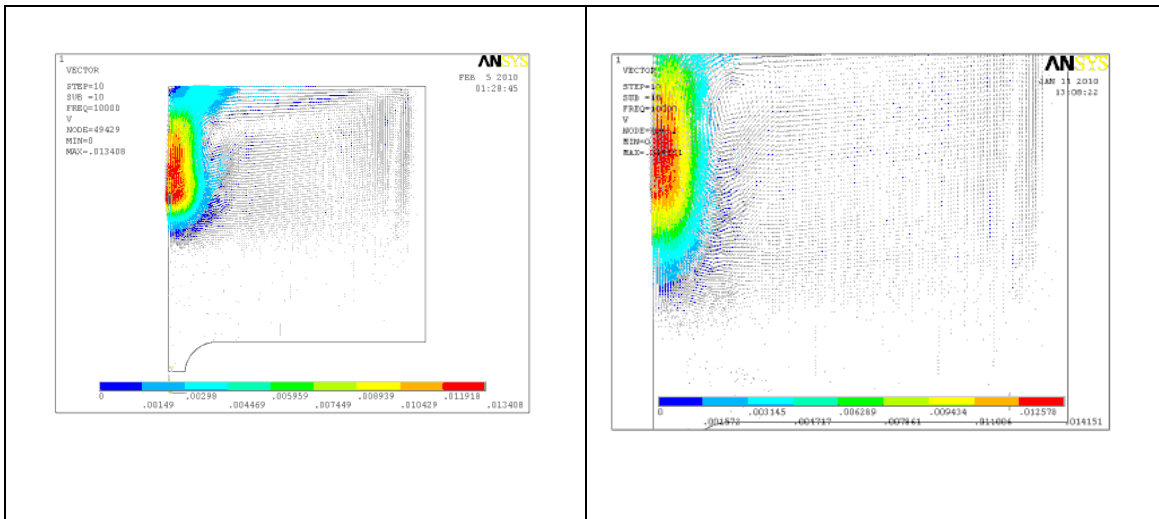
Figure 6-19. Comparison of velocity vector distributions.
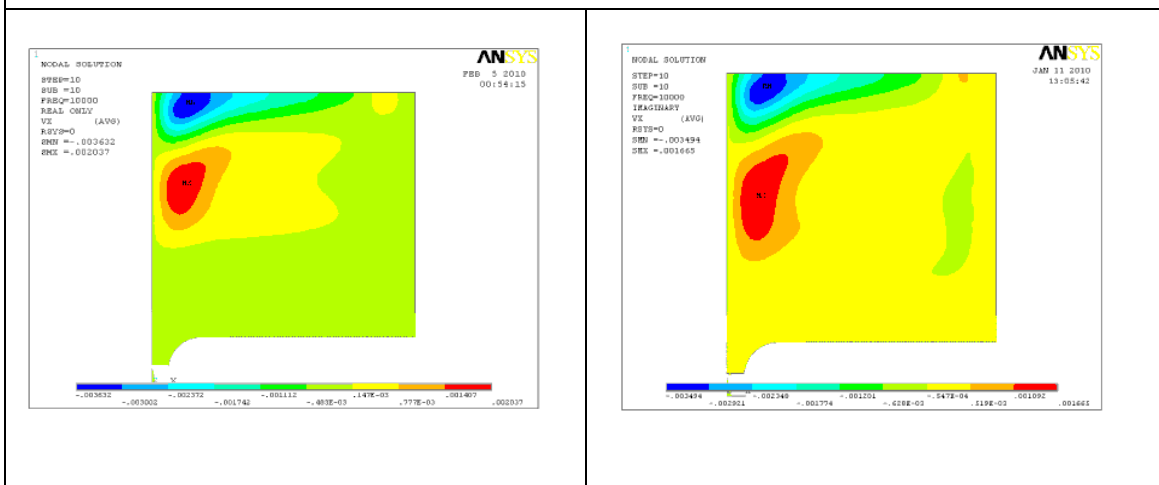
Figure 6-20. Comparison of horizontal velocity component.
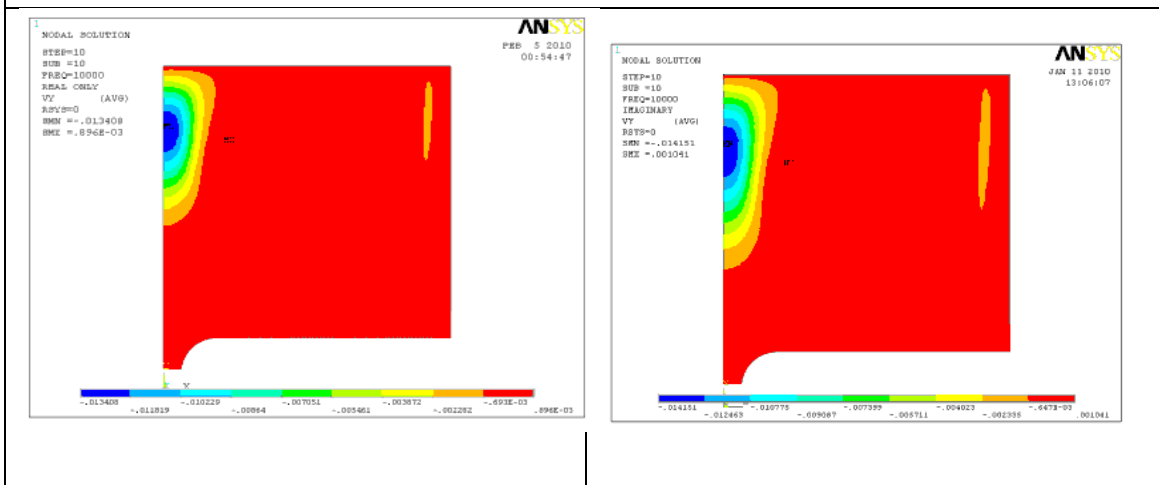
Figure 6-21. Comparison of vertical velocity component.
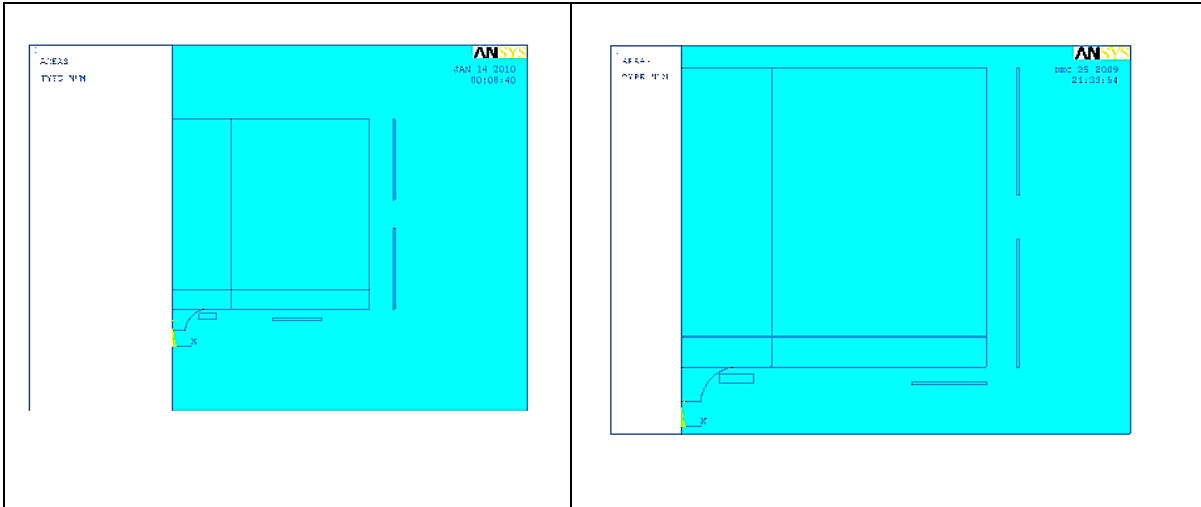
Figure 6-22. Model geometries for bottom inductor coil of 307 mm (left) and 407 mm (right).
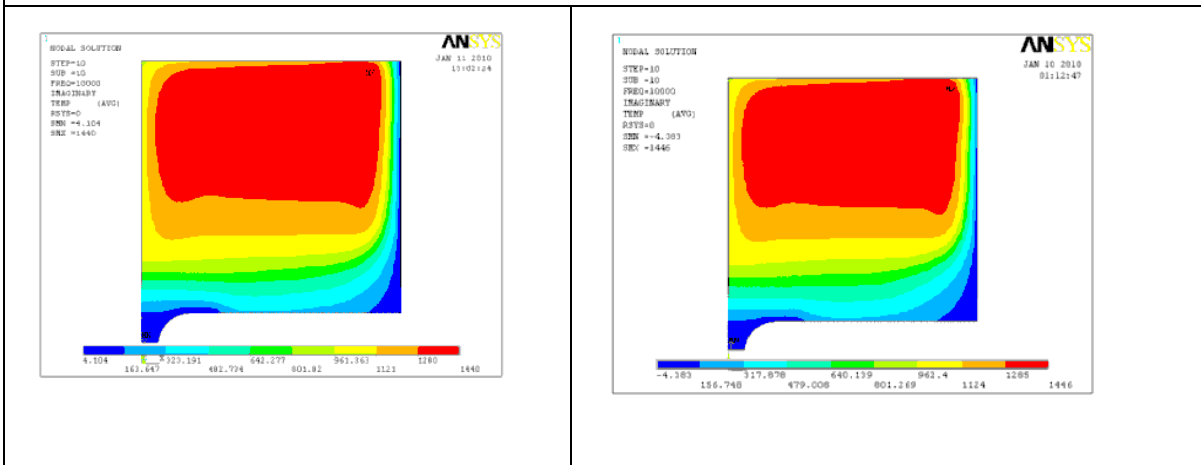
Figure 6-23. Comparison of temperature distributions.
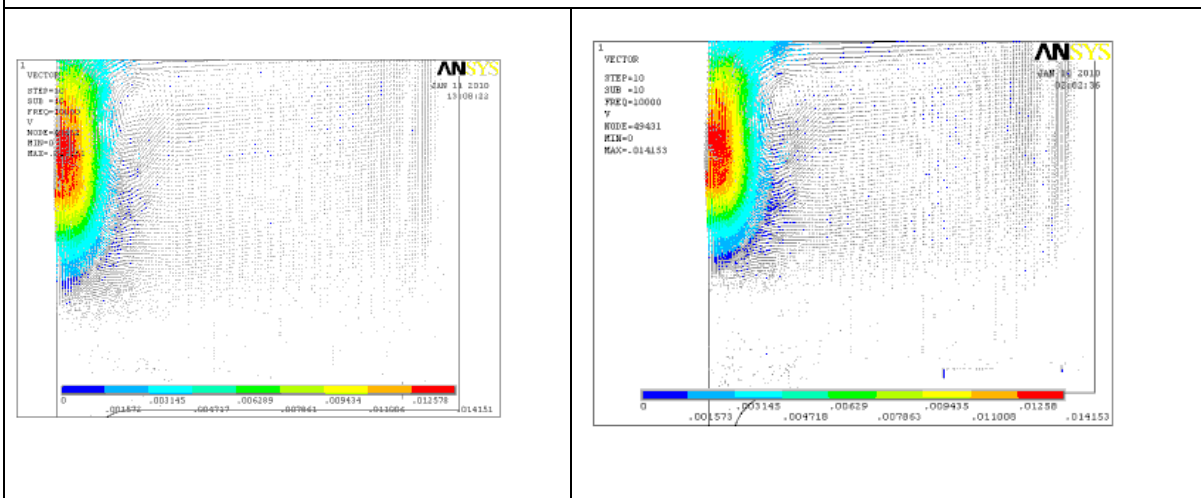
Figure 6-24. Comparison of velocity vector distributions.
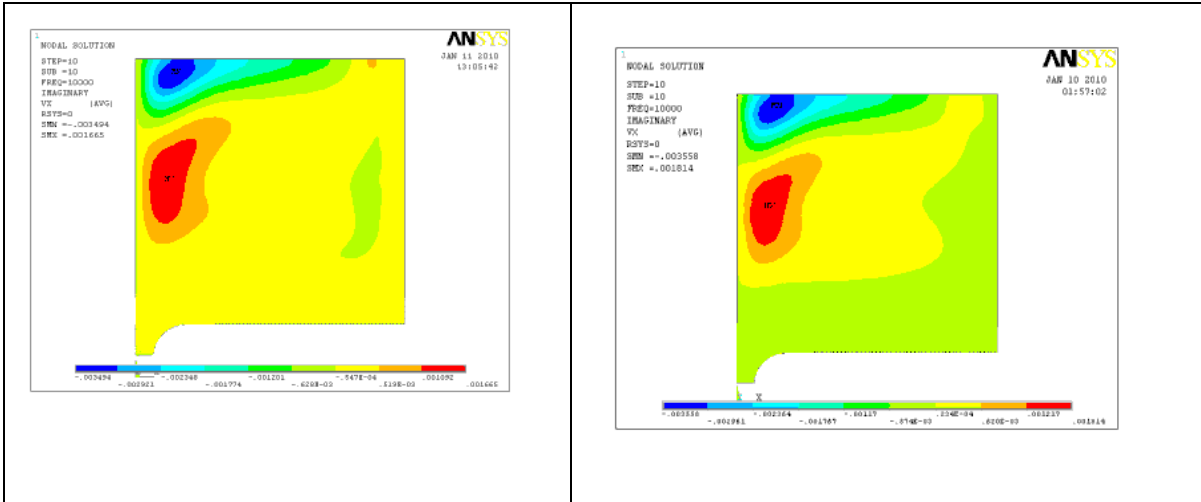
Figure 6-25. Comparison of horizontal velocity components**.**
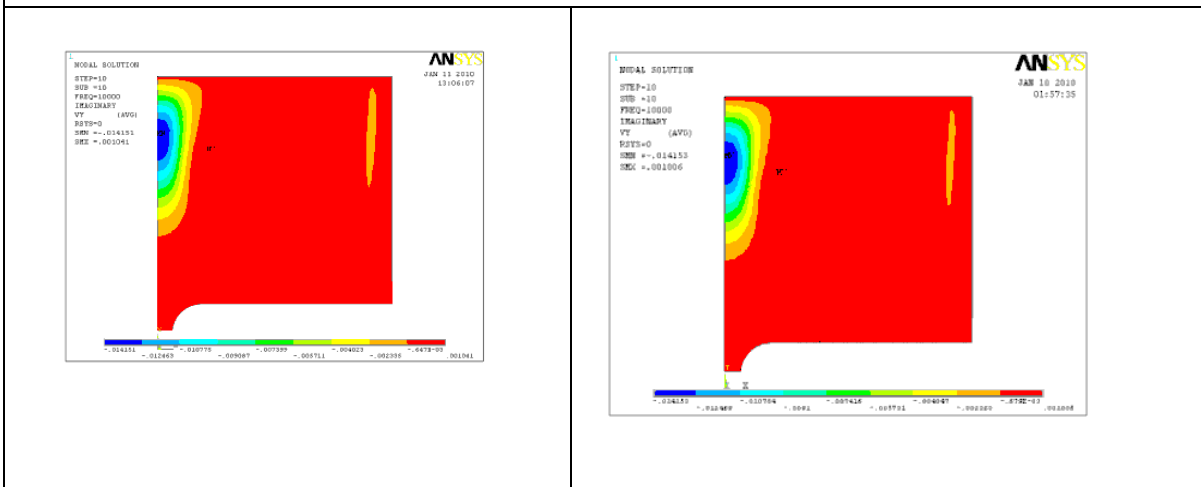
Figure 6-26. Comparison of vertical velocity components.
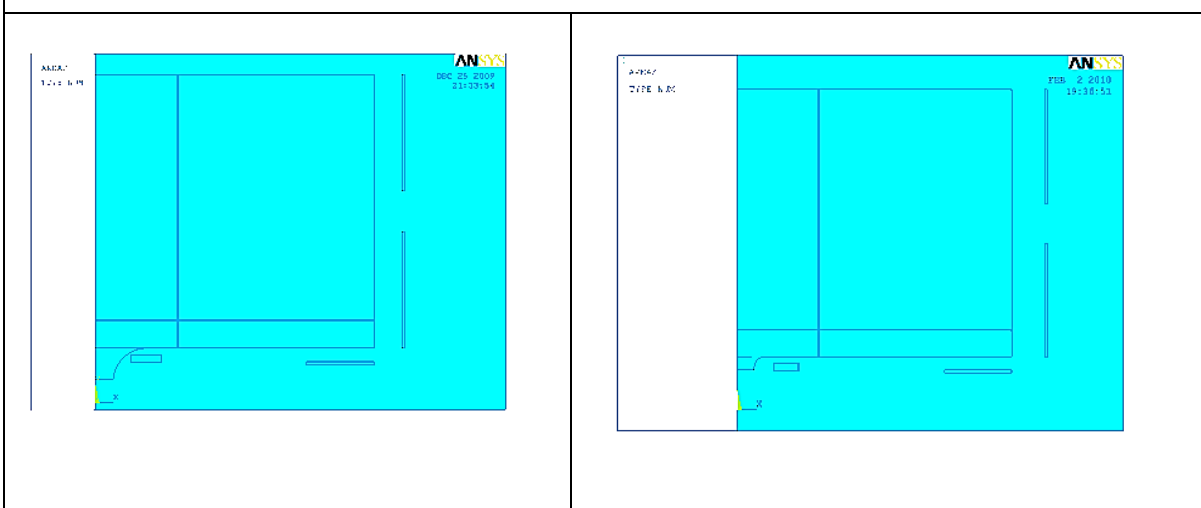
Figure 6-27. Model geometries for the systems with long drain (left) and short drain (right).
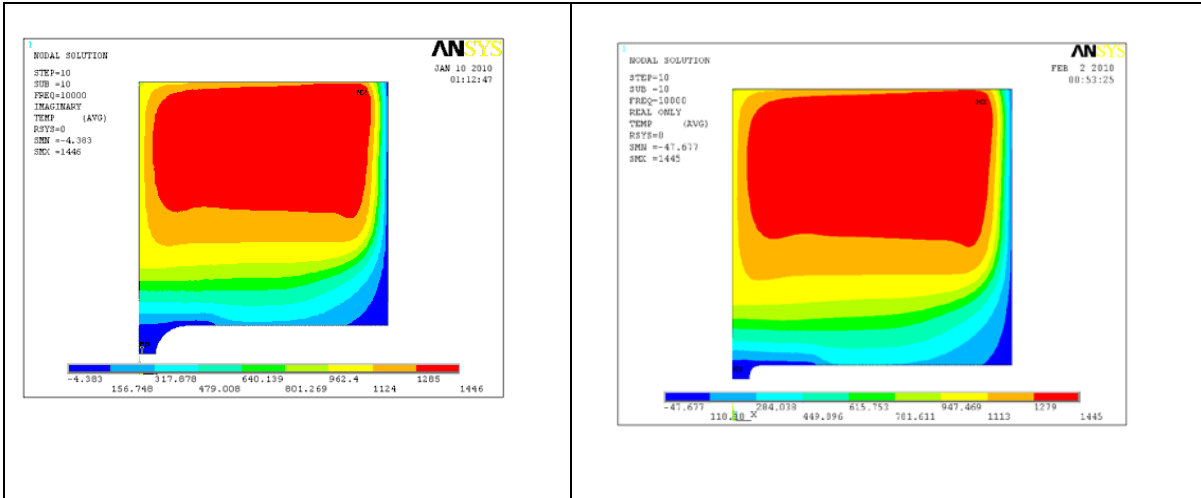
Figure 6-28. Comparison of temperature distributions.
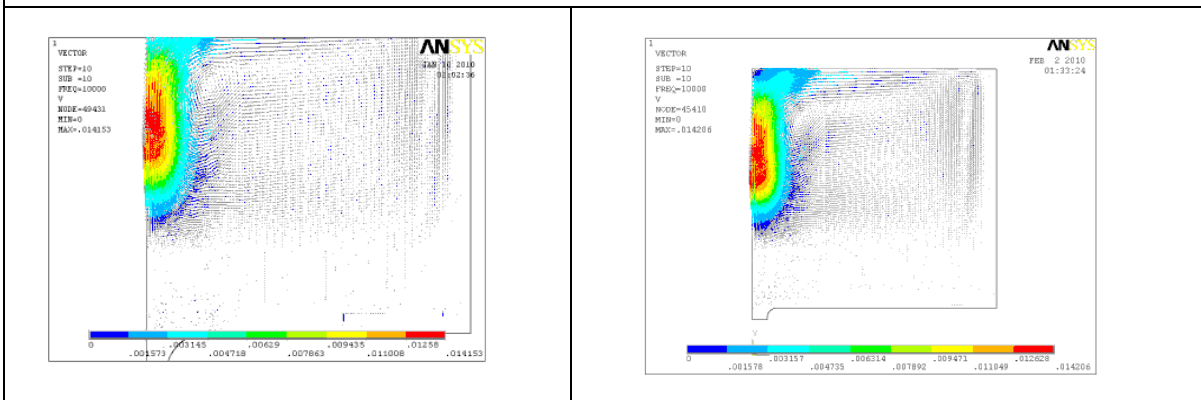
Figure 6-29. Comparison of velocity vectors.
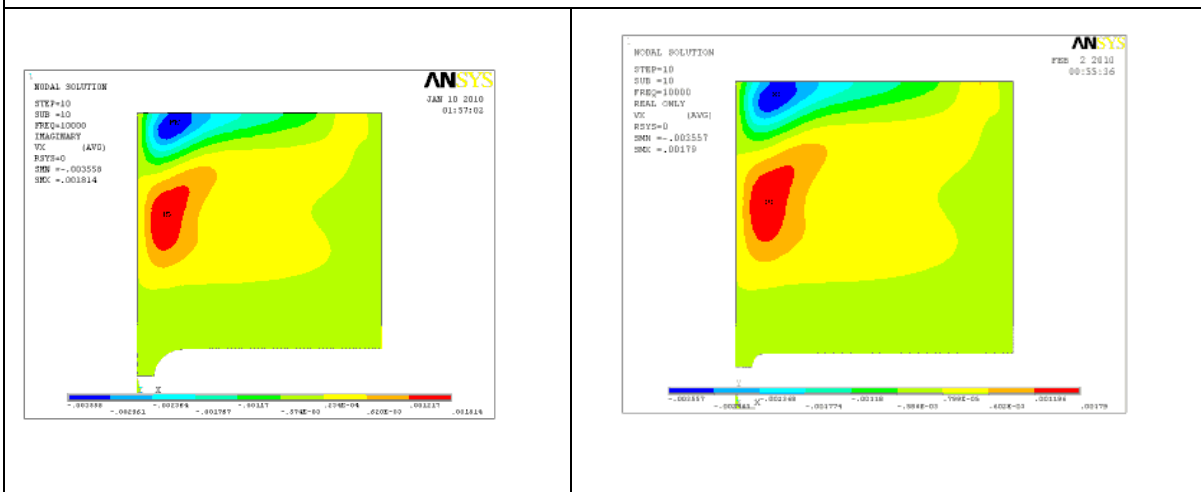
Figure 6-30. Comparison of horizontal velocity components.
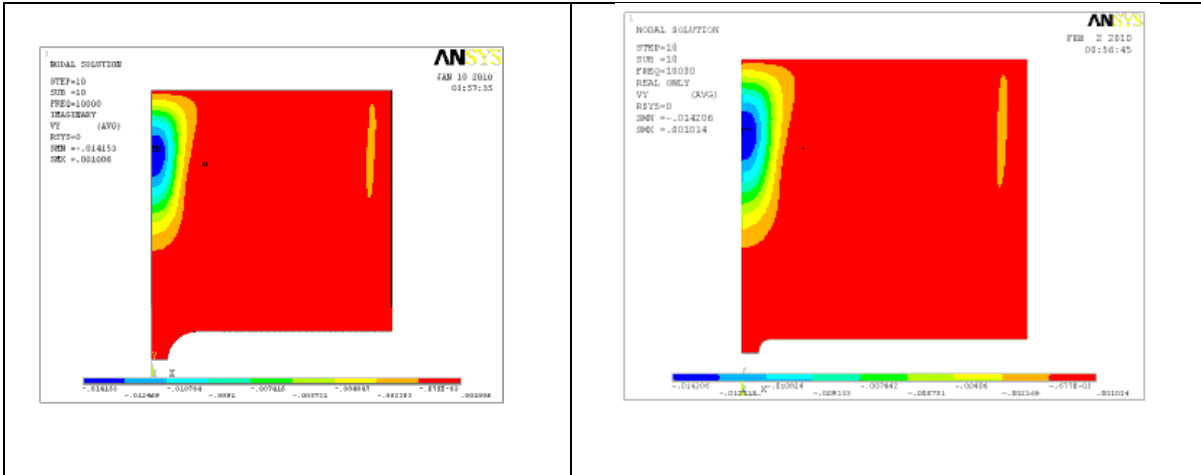
Figure 6-31. Comparison of vertical velocity components.
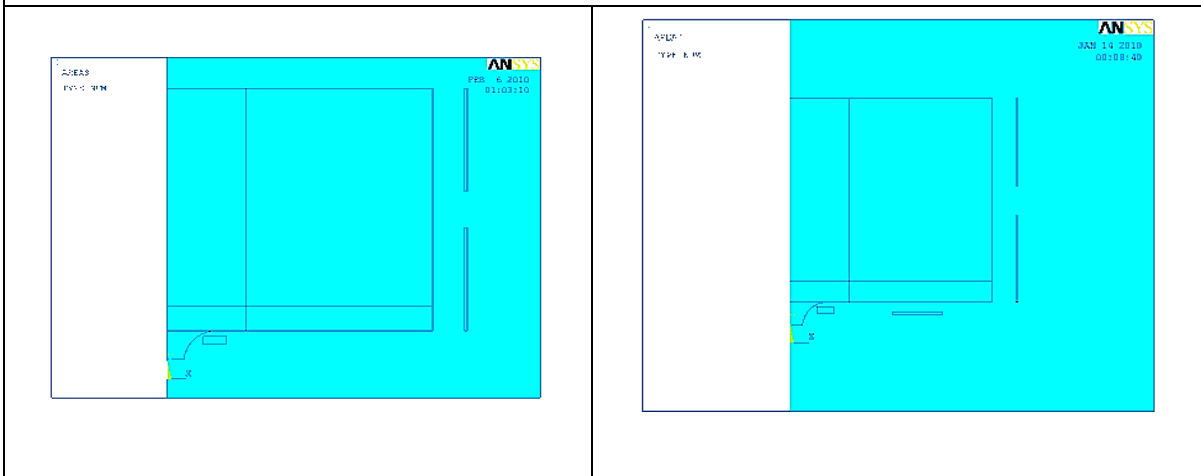
Figure 6-32. Model geometries used analysis without (left) and with (right) a bottom coil.
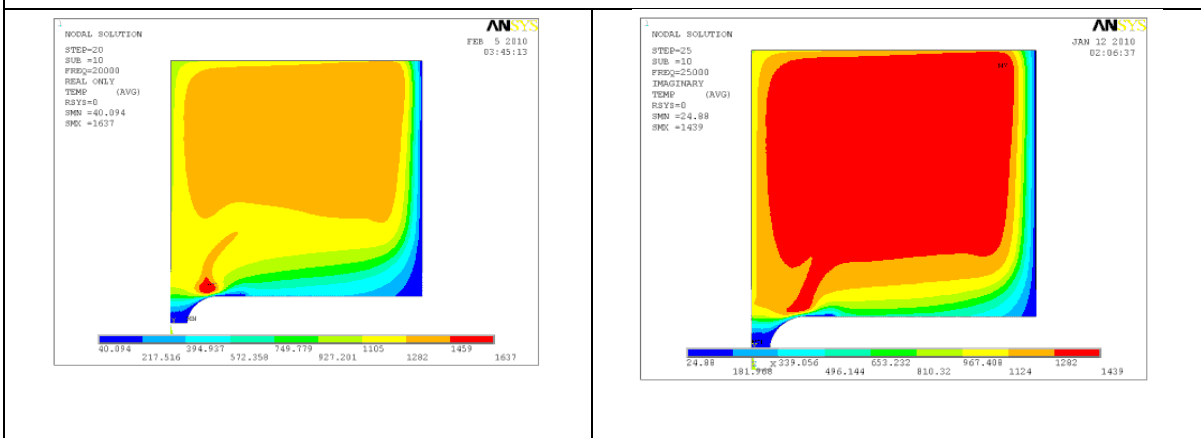
Figure 6-33. Comparison of temperature distributions in melt.
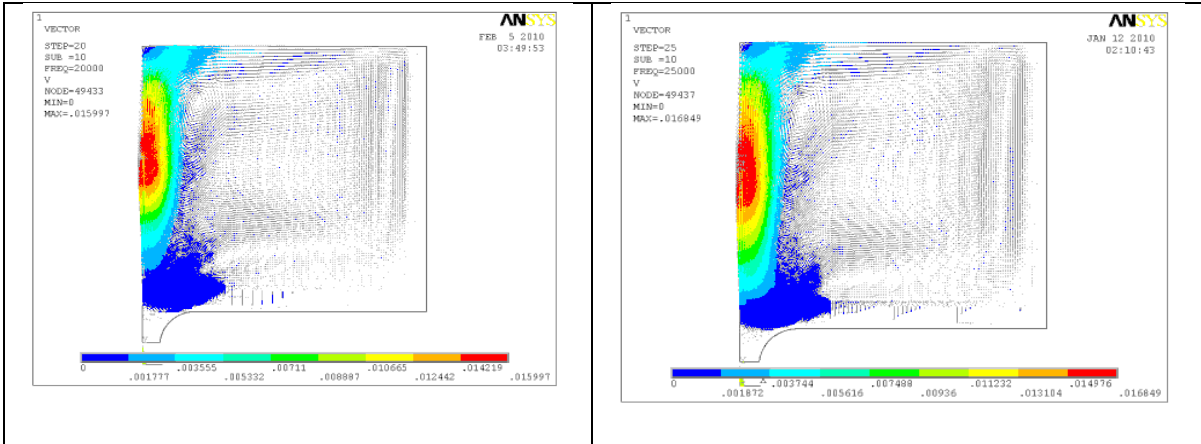
Figure 6-34. Comparison of velocity vector distributions.
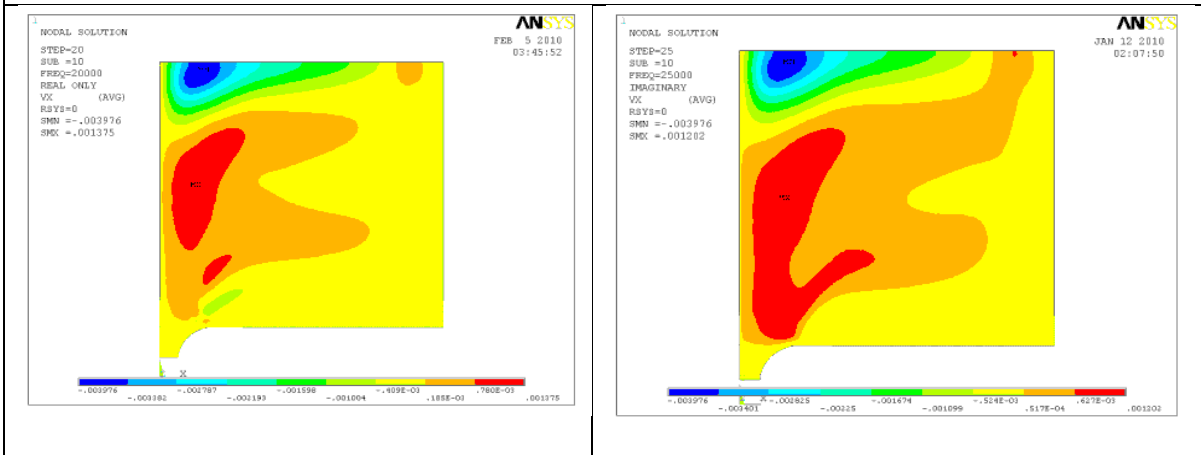
Figure 6-35. Comparison of horizontal velocity distributions.
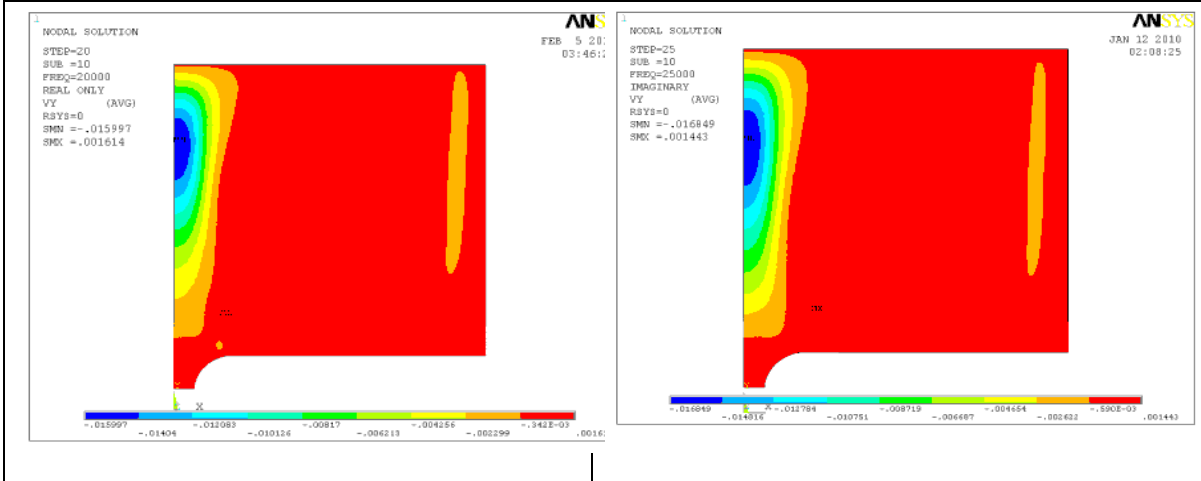
Figure 6-36. Comparison of vertical velocity distributions.

As can be seen in the preceding figures, the bottom coil clearly improves the melt condition for bottom casting; however, the melt "tongue" does not extend completely into the drain body.

6.2.2.Effects of Location and Geometry of Bottom Inductor Coil

The next investigation evaluated the effect of moving the bottom coil out (i.e. 407 mm diameter versus 307 mm diameter) for the dual frequency system. Figure 6-37 shows the model geometries used. Figures 6-38 through 6-41 compare the same parameters as the previous analysis.

These figures show that moving the bottom coil outward had little effect on the steady state melt conditions. The glass temperature within the drain body is still not sufficient to allow bottom casting; however, the conditions are slightly improved, which is counter-intuitive.
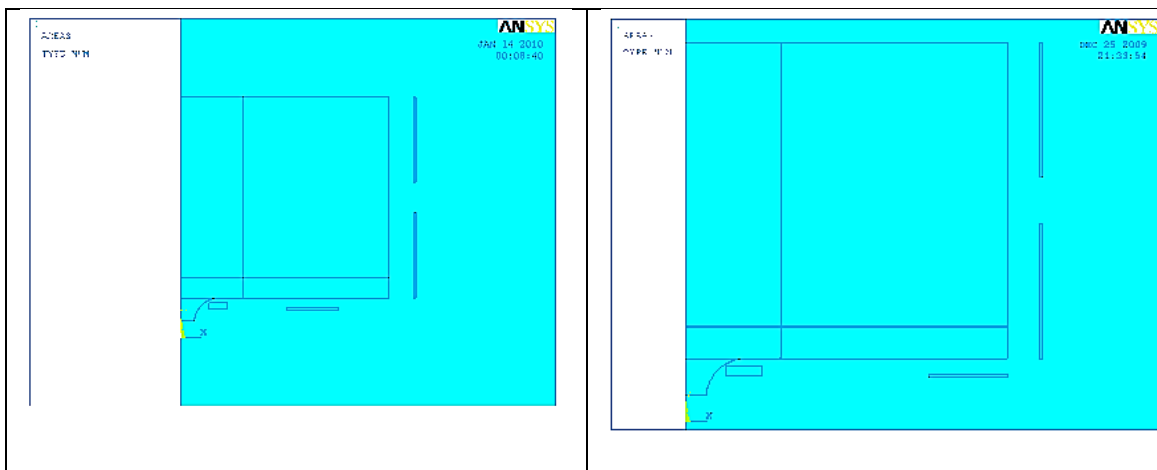
Figure 6-37. Model geometries with 307 mm (left) and 407 mm (right) diameters used for the analyses.
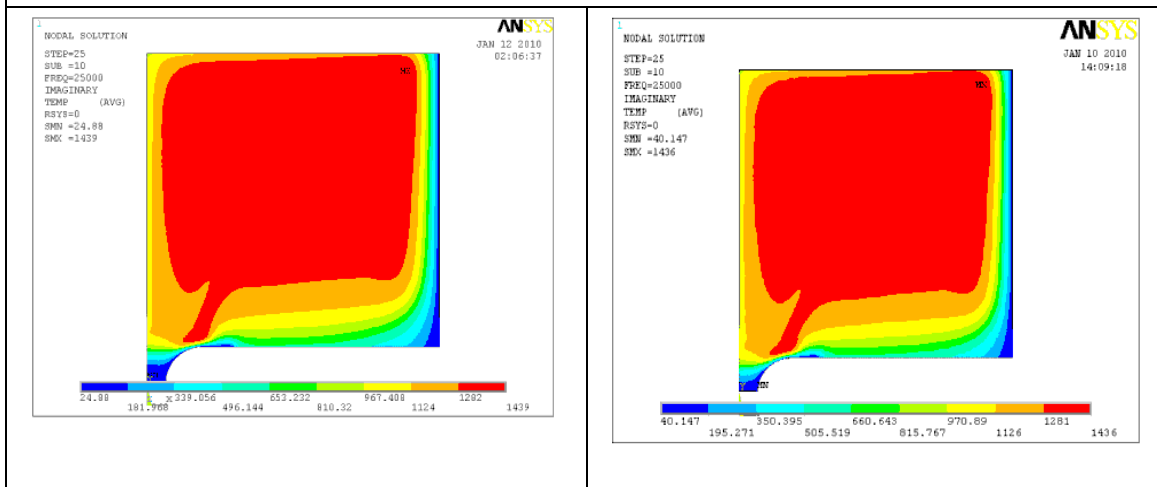
Figure 6-38. Comparison of temperature distributions in melt.
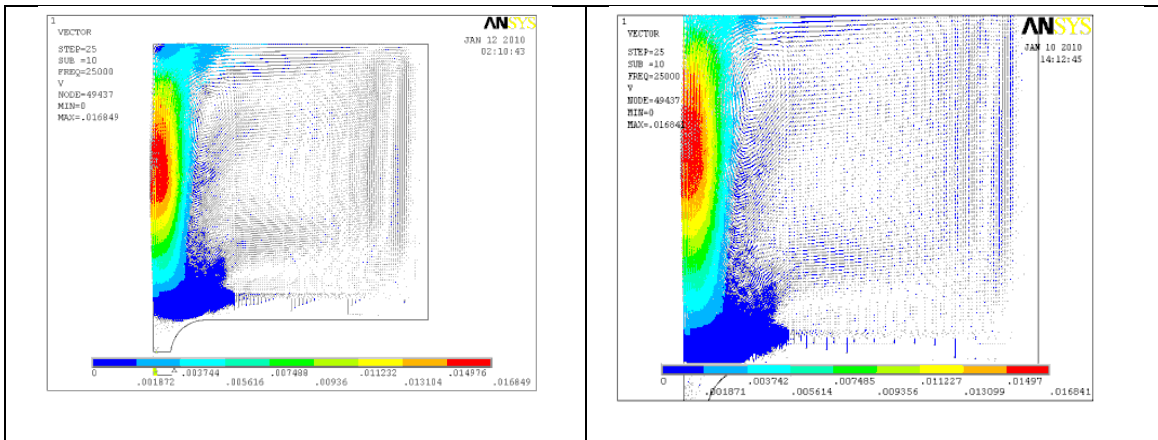
Figure 6-39. Comparison of velocity vector distributions.
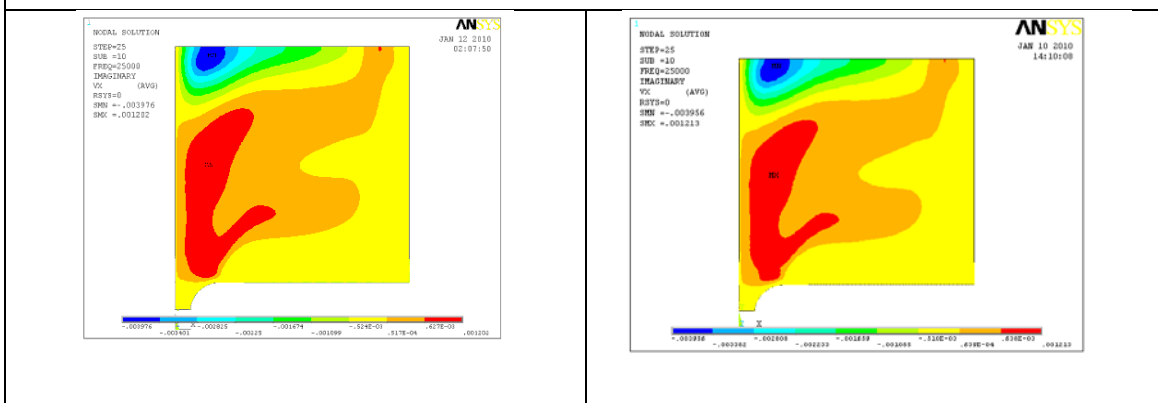
Figure 6-40. Comparison of horizontal velocity distributions.
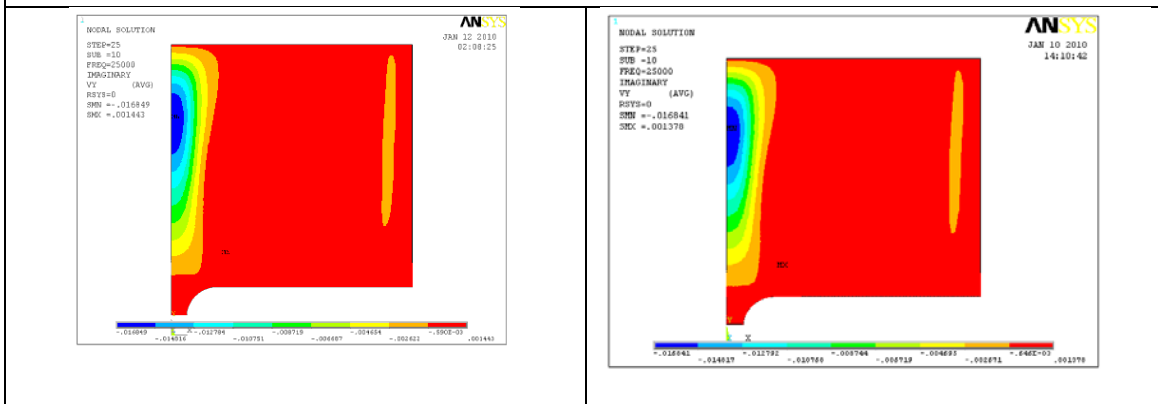
Figure 6-41. Comparison of vertical velocity distributions.

6.2.3. Effect of Drain Height

The next analysis investigated the effects of reducing the drain height from 20 mm to 10 mm, which also reduced the transition radius, as discussed in earlier evaluations. The model geometries used for these analyses are shown in Figure 6-42. Figures 6-43 through 6-46 illustrate the comparative

results of the same parameters shown in the previous calculations. Note that the drain inductor coil

is in the same position relative to the centerline axis of the crucible.
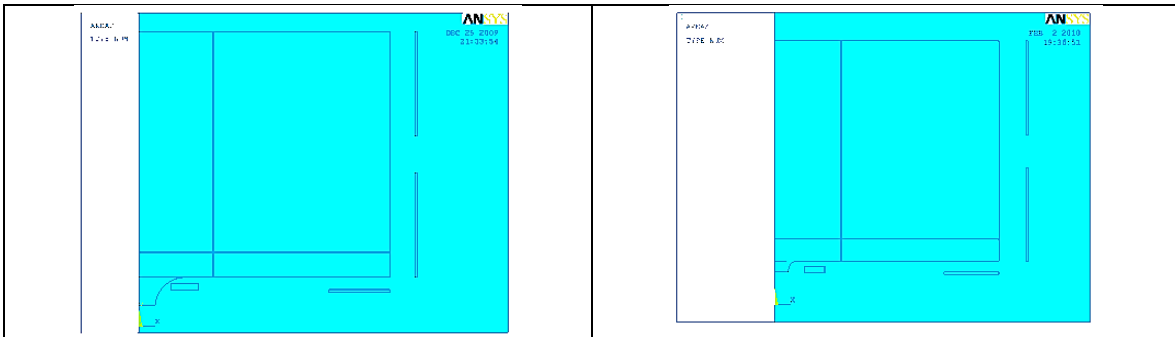
Figure 6-42. Model geometries with long (left) and short (right) used for analysis.
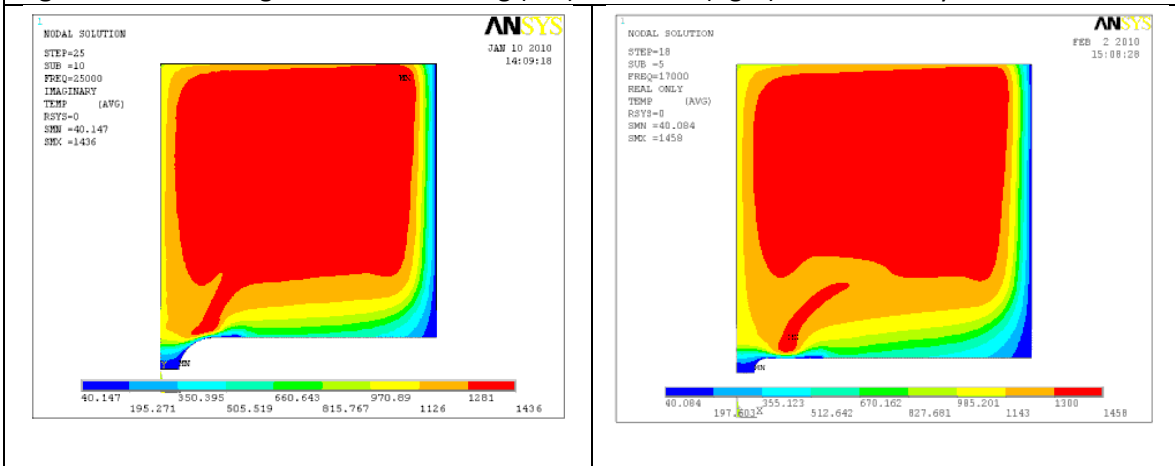
Figure 6-43. Comparison of temperature distributions in melt.
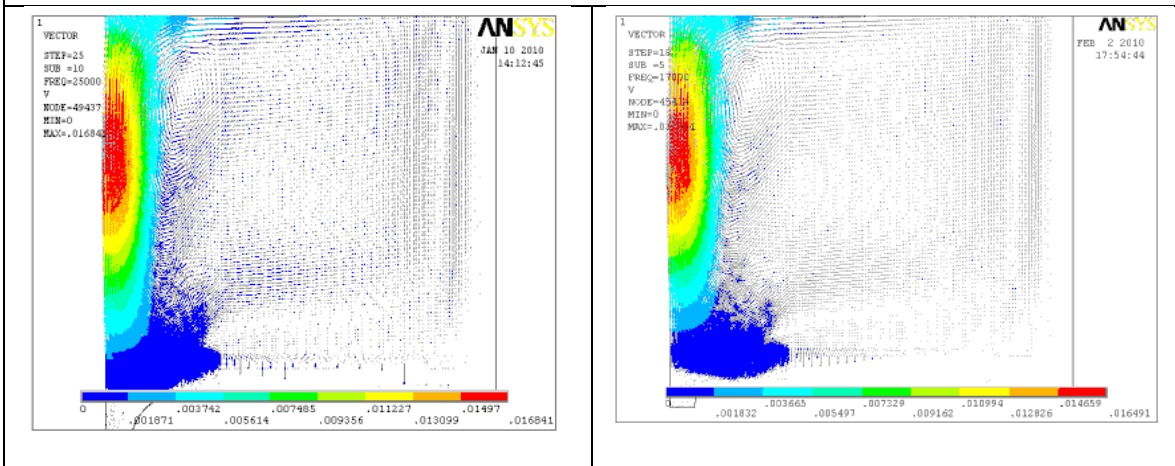
Figure 6-44. Comparison of velocity vectors.
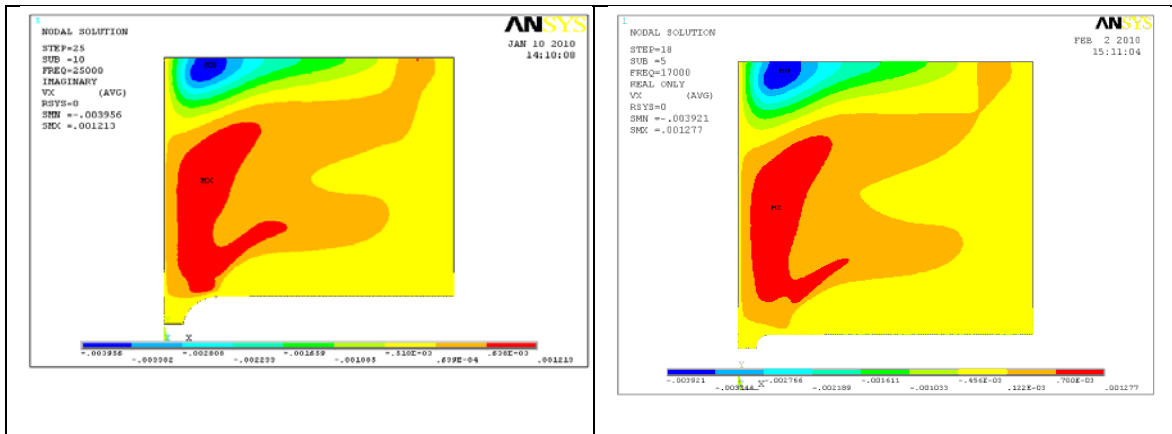
Figure 6-45. Comparison of horizontal velocity distributions.
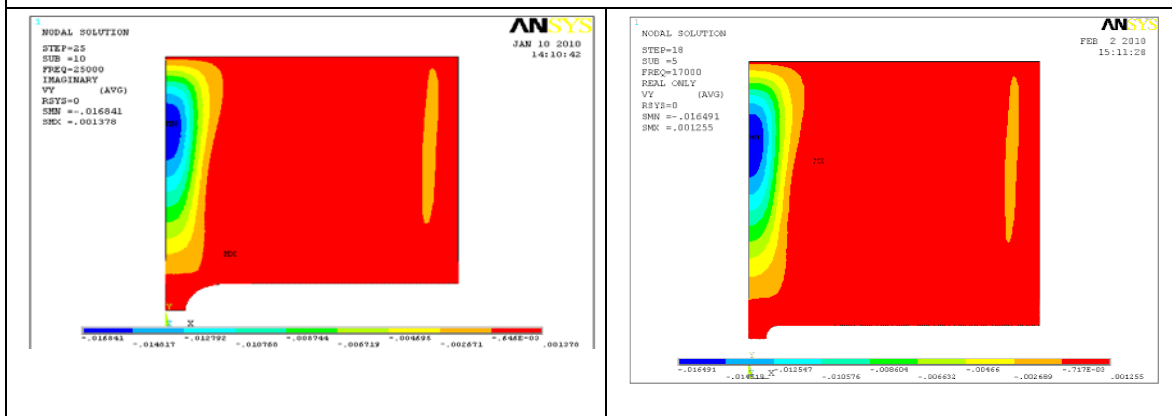
Figure 6-46. Comparison of vertical velocity distributions.

These analyses showed that for both drain geometries, the glass within the drain body did not reach temperatures that would promote casting. The smaller drain geometry did result in overall higher temperatures in the bottom glass layers; however, the zone of high temperature is too far away to conduct into the drain throat. For the larger diameter/height drain, the melt tongue approaches the drain throat but does not proceed into the drain body.

6.2.4.Effect of Translating Drain Inductor

The next analyses investigated the effect of moving the small inductor down to help coax the molten pool into the drain body. The geometry for the model is the same as that used in the prior analysis for the larger drain.

In this investigation, after a sufficient temperature is reached in the zone above the drain throat (12,500 seconds) the inductor is moved downward 10 mm to observe the effects. The following

series of images in Figure 6-47 show the temperature distribution beginning at 10,000 seconds through 25,000 seconds.

This analysis shows that, even with the displacement of the drain inductor, the melt will not move into the drain body. The temperature of the glass is sufficient to allow coupling; however, the power limitations from the 27 MHz generator of 7 kW, coupled with the drain geometry will not allow the melt to propagate down into the drain far enough to support casting. Recall that this power limitation was mentioned earlier. Figure 6-48 provides a graph of the power level on the drain inductor through the heating process, which clearly illustrates this situation.

Figure 6-47. Temperature distribution dynamics due to two-frequency heating and displacement of drain inductor 10 mm downward.

10,000 seconds

11,000 seconds

12,000 seconds

13,000 seconds (drain inductor moved 10 mm down at 12,500 seconds)
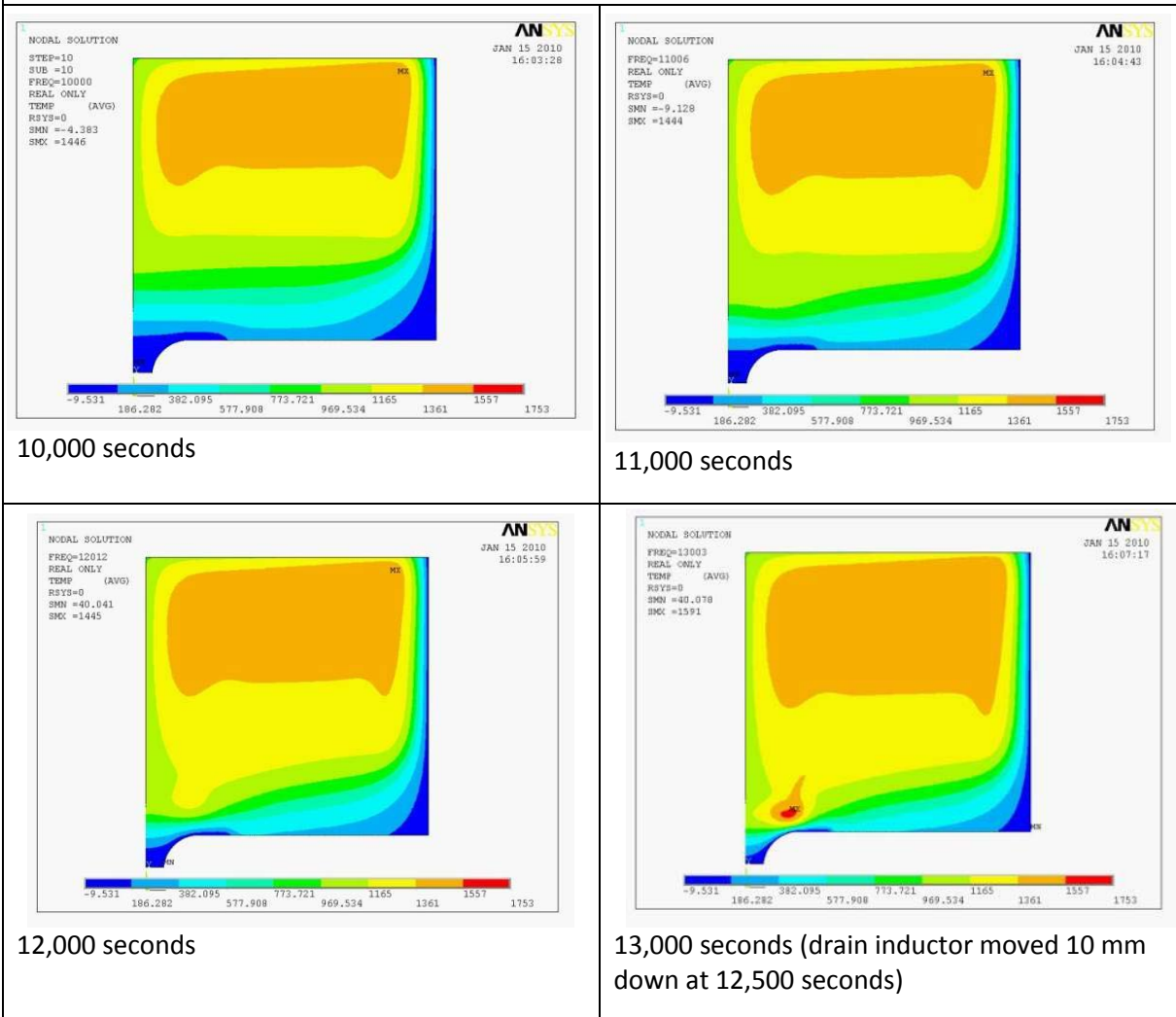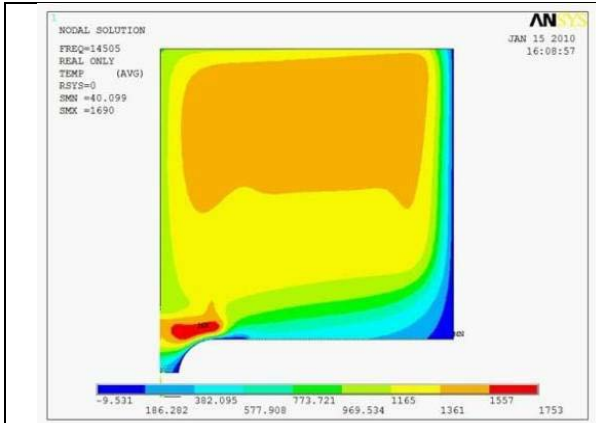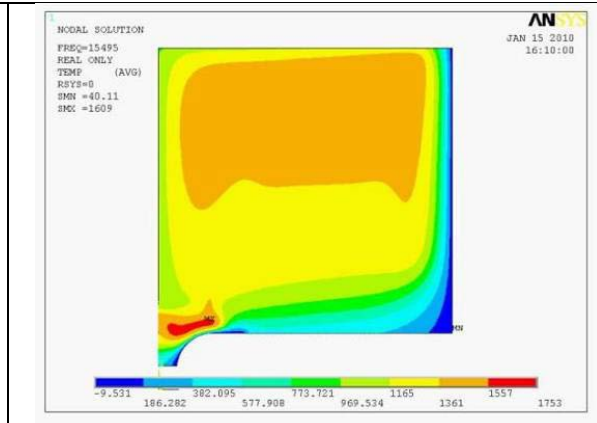
14,000 seconds

15,000 seconds
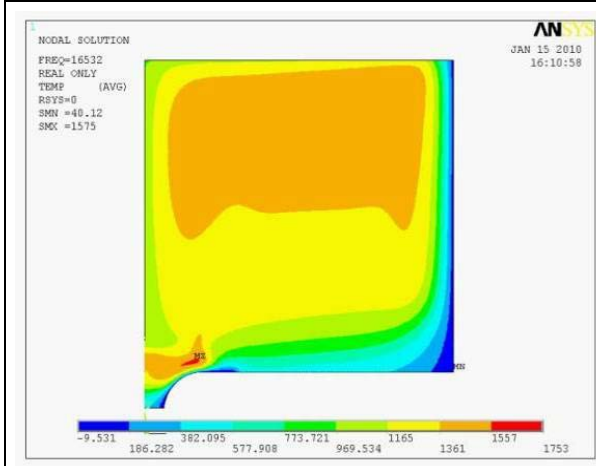
16,000 seconds
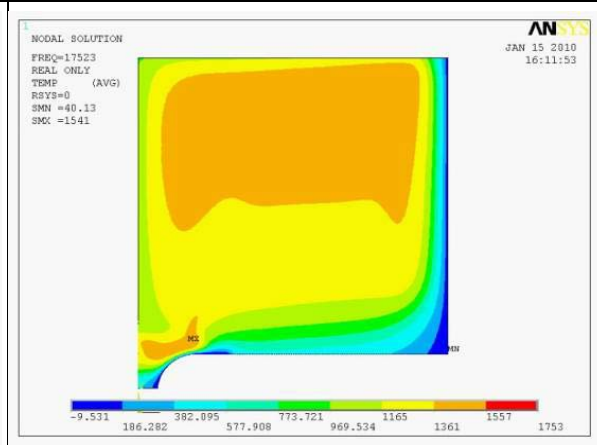
17,000 seconds
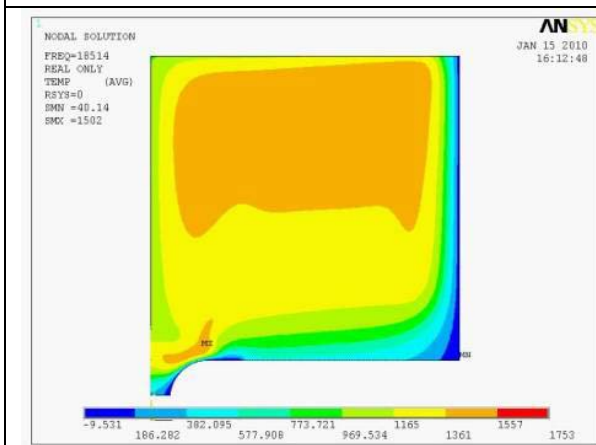
18,000 seconds

19,000 seconds

20,000 seconds

21,000 seconds

22,000 seconds

23,000 seconds

24,000 seconds

25,000 seconds

Figure 6-47. Temperature distribution dynamics due to two-frequency heating and displacement of drain inductor 10 mm downward.
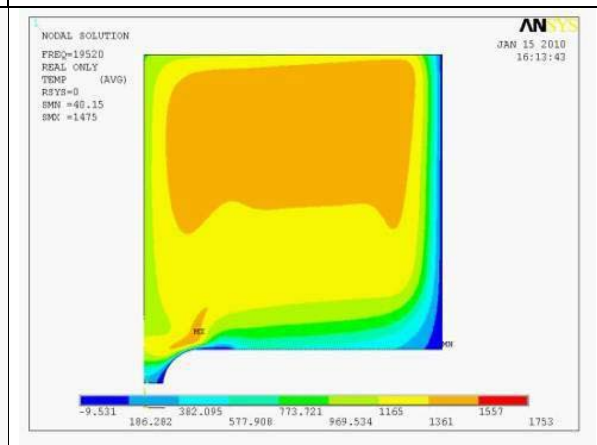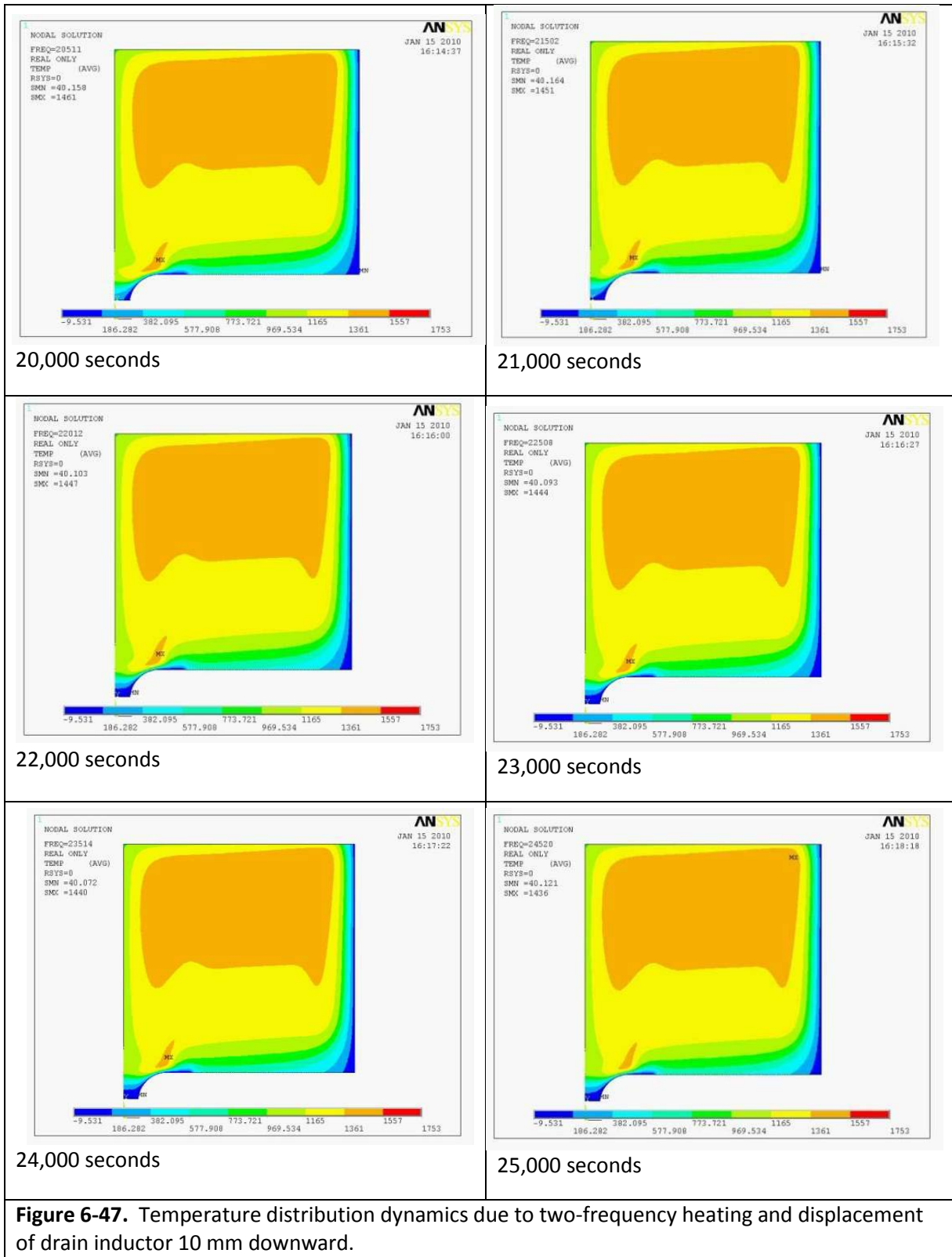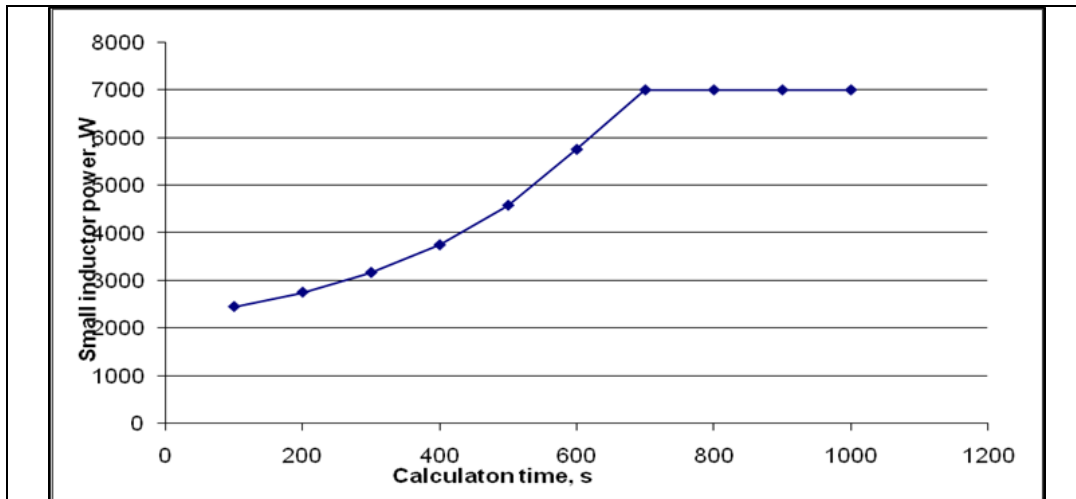
Figure 6-48. Power level in drain inductor with time as glass is heated.

From Figure 6-48, we observe that the maximum available power of the high frequency generator is reached after about 700 seconds of operation, which correlates to about 14,000 seconds in Figure 6-47. This is because the primary inductor is energized first until the temperature distribution is sufficient to provide coupling with the induction field from the drain generator. This indicates that additional power is required; however, prior to investing in that upgrade, it is more expedient to investigate the combined effects of revised drain geometry with drain inductor geometry.

As a supplemental investigation to the previous one performed, a more detailed and comprehensive analysis of the effects of moving the drain inductor to different positions was completed to evaluate if the power limitations could be overcome. Specifically, a steady state was achieved after 2,500 seconds of operation of the small inductor with the location (h_2) 5 mm below the crucible bottom. This is shown in Figure 6-49. Then the inductor was moved down 5 mm and held for 7,500 seconds, Figure 6-50. The inductor was then moved down again, such that the bottom face of the coil was parallel with the drain face, Figure 6-51. The inductor was then moved down again such that the top face of the coil was parallel with the drain face, Figure 6-52. This was then held for an additional 2,000 seconds to observe if the high temperature would proceed further into the drain body, Figure 6-53.

For each movement of the inductor, the starting condition was reset mathematically (i.e., within the model) such that it was the same as shown in Figure 6-49.
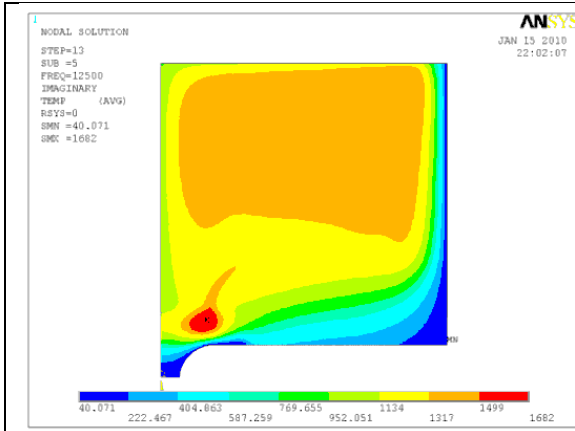
Figure 6-49. Heating with the small inductor in starting position. h_2 = 5 mm, Heating time of 2,500 sec., T_{end} = 100 – 130°C
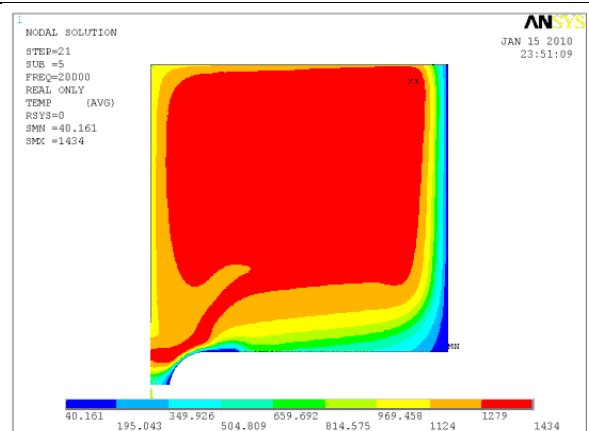
Figure 6-50. The small inductor is moved down 10 mm. h_2 = 10 mm, Heating time of 7,500 seconds, T_{end} = 510 – 550°C.
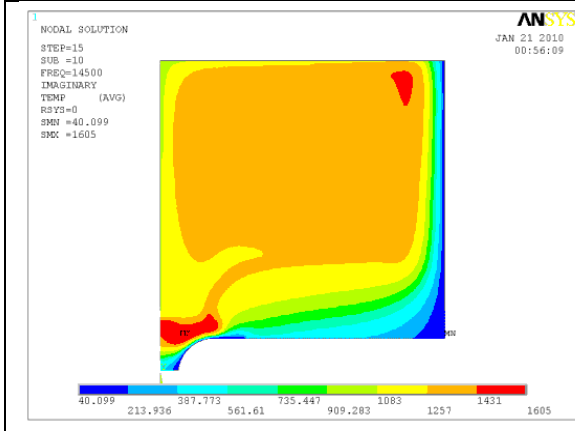
Figure 6-51. Small inductor moved downward such that bottom face is parallel with the drain face, T_{end} = 400 – 430°C
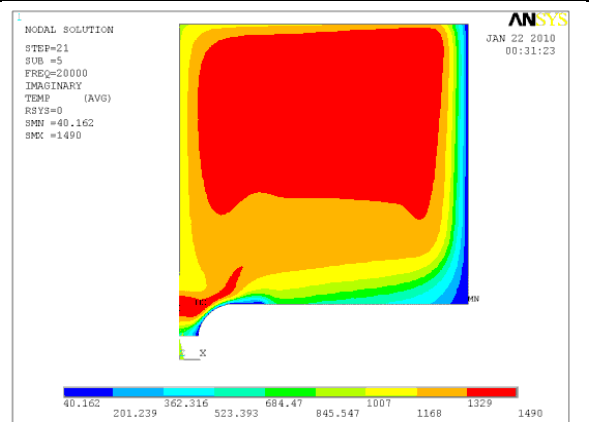
Figure 6-52. Small inductor moved downward such that top face is parallel with the drain face, T_{end} = 660 – 700°C
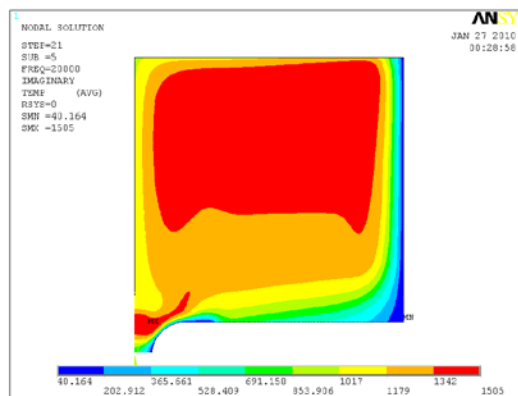
Figure 6-53. Small inductor moved downward such that top face is parallel with the drain face. T_{end} = 730°C (maximum) after 2,000 seconds.

From these calculations, one can observe that, while moving the inductor down after a steady state condition has been reached in the main melt pool using the two-frequency heating does improve the temperature conditions within the drain body, it is still not clear whether or not this will ensure that casting is possible. A maximum temperature of only 730°C was reached. Although this is above the melting point of the BSG used for the testing and modeling work, it may not support sustained bottom casting.

As was observed in Figure 6-47, the high temperature zone in the bottom layer is outside of the drain throat area, indicating that a smaller diameter drain inductor coil may be more effective at heating the zone above the drain throat. This will require use of the smaller diameter drain body.

 6.2.5.Effects of Drain Inductor Geometry

The next investigation analyzed the effects of various drain inductor geometries coupled with the smaller diameter/height drain geometry. The model parameters used for these calculations were as presented in Table 6-3, with the drain inductor diameter being varied as indicated.

Figure 6-54 shows the comparative geometries used for these calculations. Figures 6-55 through 6-58 compare the results for various parameters including temperature distributions, velocity vectors, horizontal velocity components, and vertical velocity components.

Figure 6-54. Model geometries used for calculations. Inductor internal diameters of 22.5 mm (left) and 17.5 mm (right).
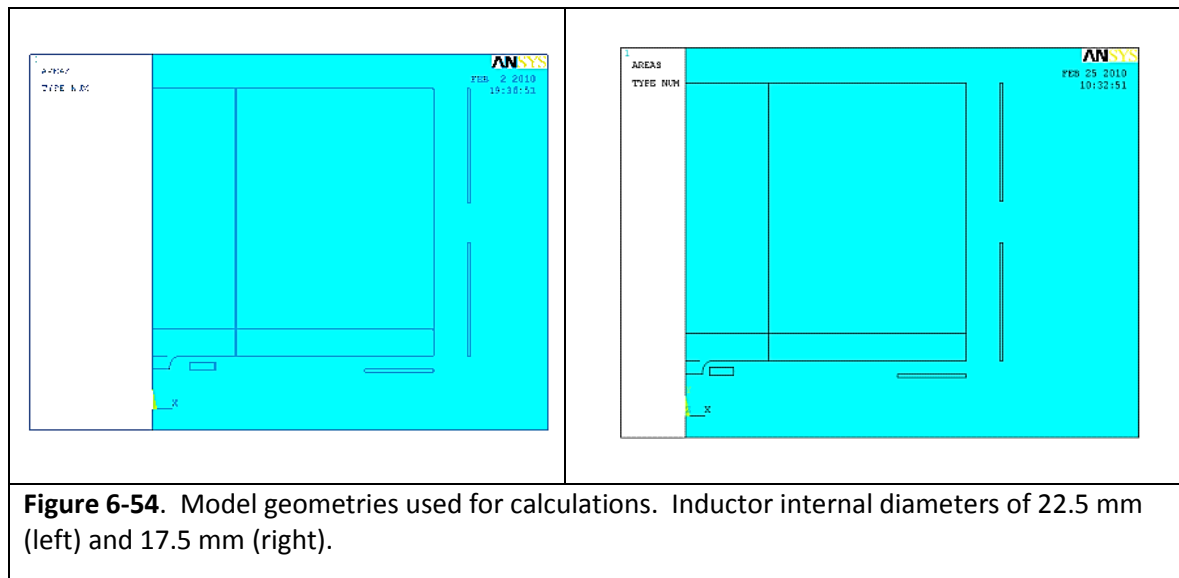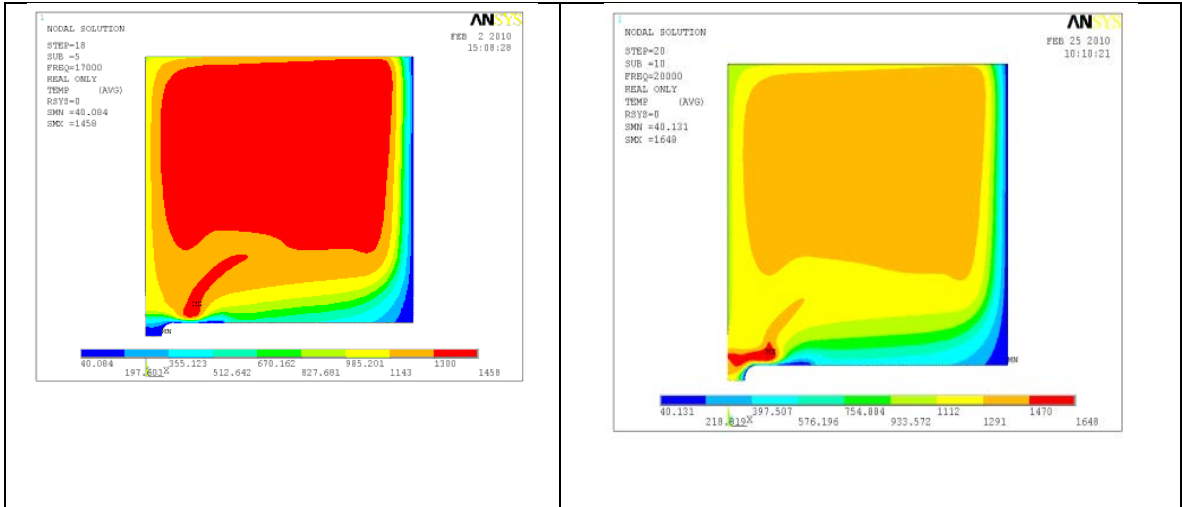
Figure 6-55. Comparison of temperature distributions in melt.
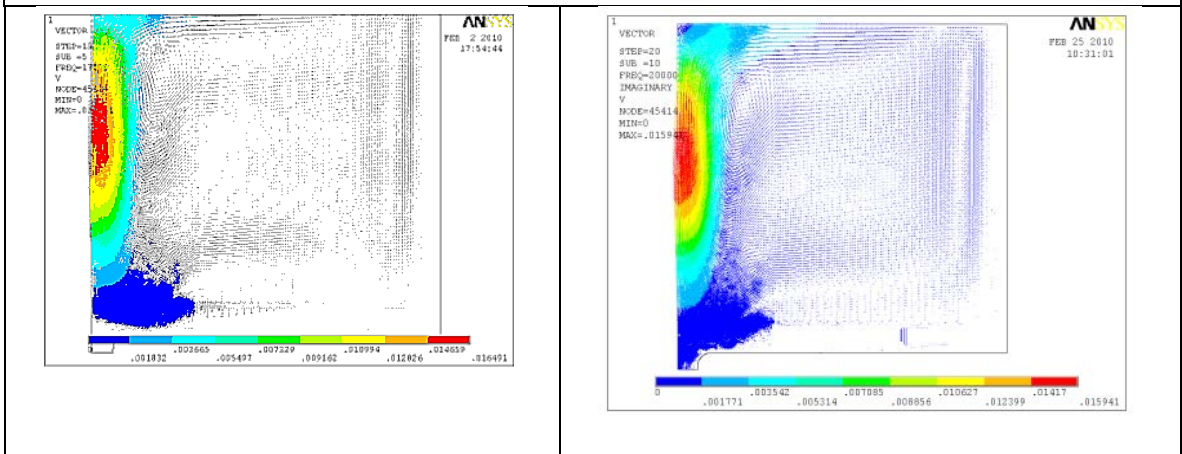
Figure 6-56. Comparison of velocity vector distributions in melt.
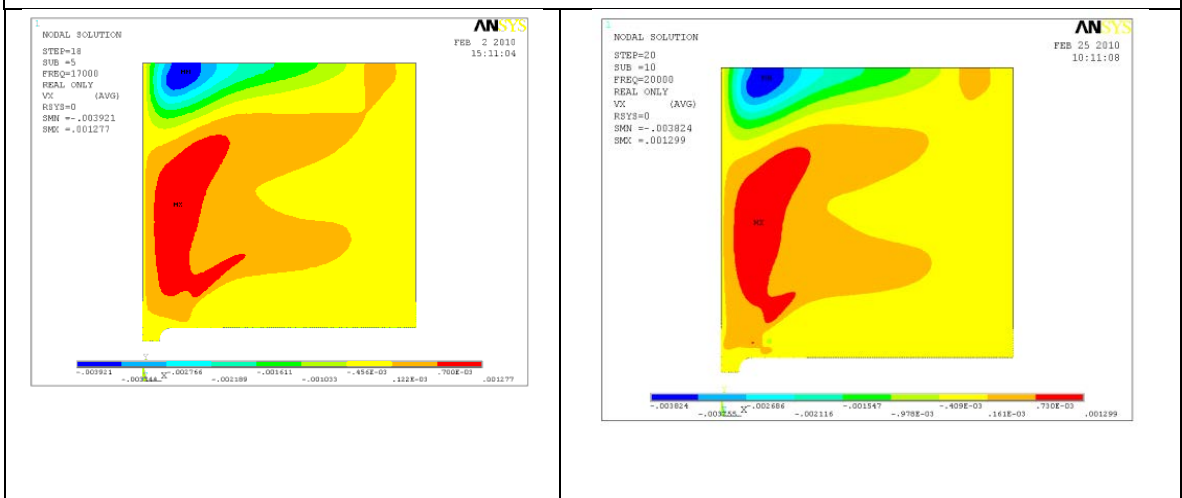
Figure 6-57. Comparison of horizontal velocity component distributions.
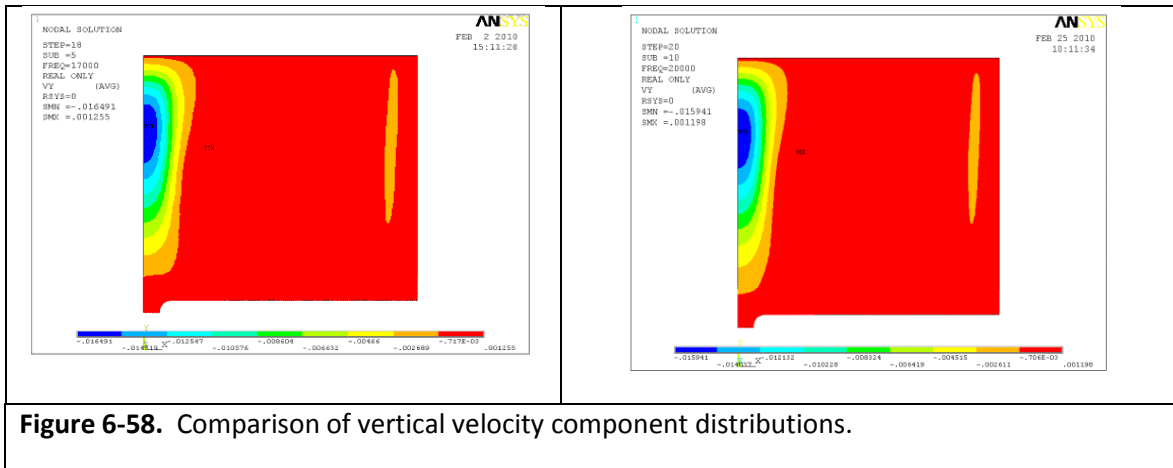
Figure 6-58. Comparison of vertical velocity component distributions.

These figures show that for the reduced diameter and height of the drain inductor, significant improvement is achieved in the melt pool zone above and within the drain body. A maximum temperature of 1,230^{o}C is achieved. The time required to achieve glass casting conditions is 2,000 seconds, with 1,270 seconds required for achieving the quasi-steady state conditions, and then an additional 730 seconds to reach the glass casting temperature within the drain body. See Figure 6-59.

This configuration provides conditions necessary for glass casting; however, from experimental work we know that when the inductor is this close to the drain body, arcing across and thus shorting of the high frequency generator can occur due to condensation from the cooling water in the drain and inductor coil. If this geometry is used, a water heater will have to be implemented into the system design to avoid the condensation.
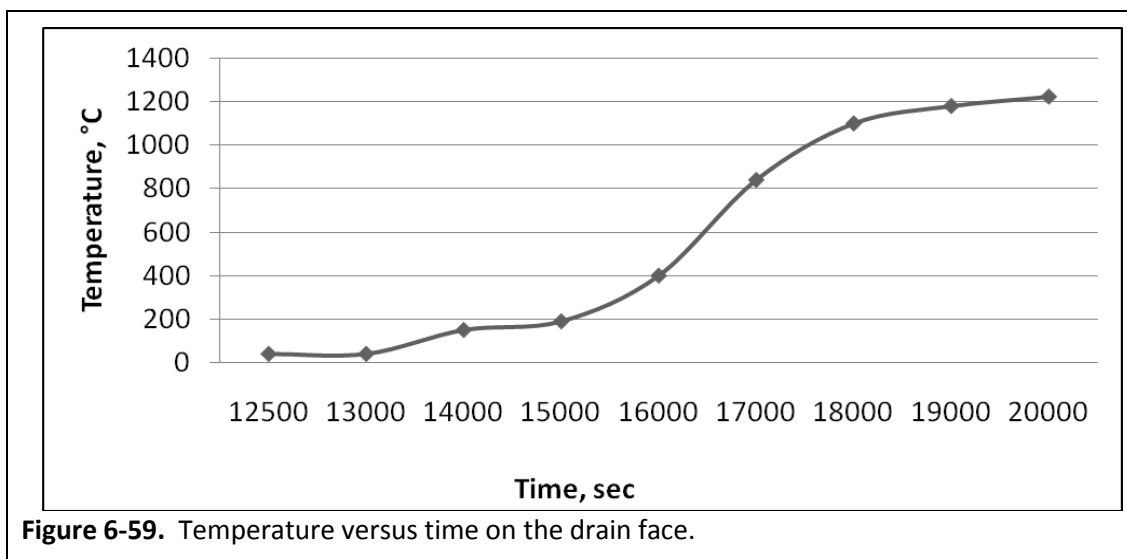
Figure 6-59. Temperature versus time on the drain face.

Thus, two additional configurations were evaluated that moved the coil away from the drain and crucible structures. The first investigation is a comparison of the results for the small diameter coil located at 5 mm and 10 mm from the crucible bottom. The geometries used are shown in Figure 6-60. The results for various parameters are shown in Figures 6-61 through 6-64.
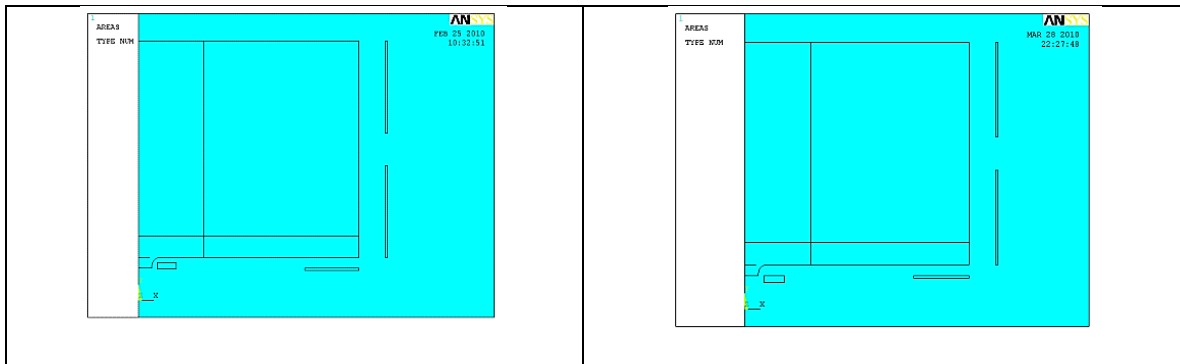
Figure 6-60. Model geometries used in the calculations. Small inductor at 5 mm (left) and 10 mm (right) from bottom of crucible.
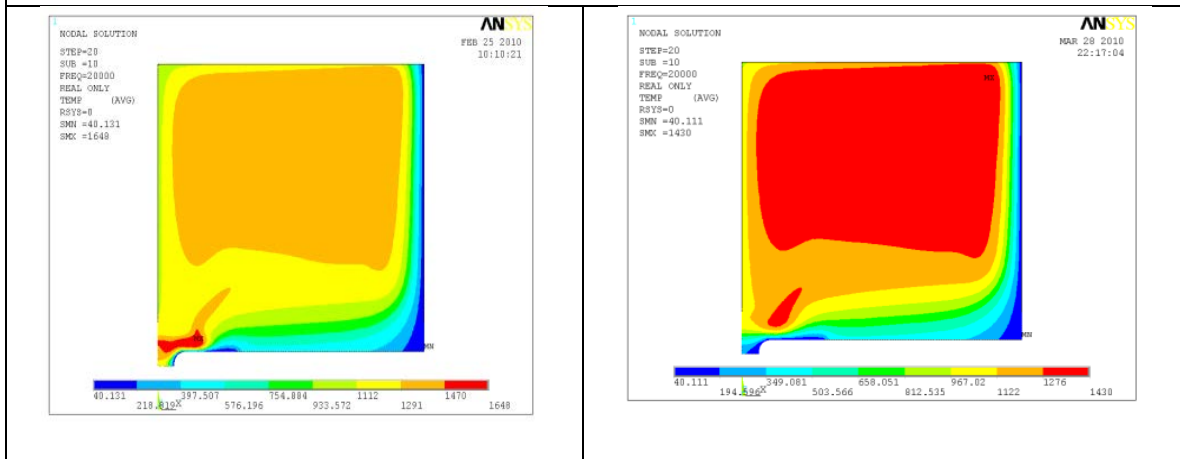
Figure 6-61. Comparison of temperature distributions in melt.
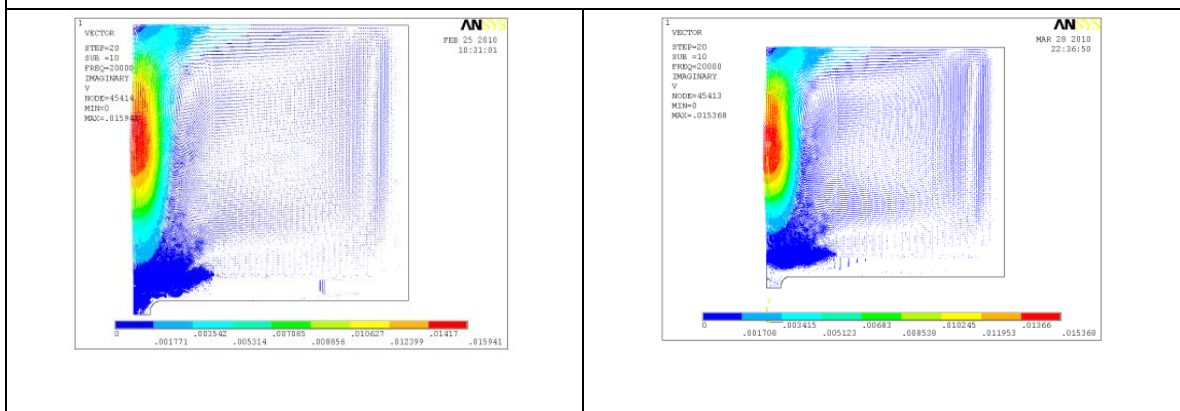
Figure 6-62. Comparison of velocity vector distributions in melt.
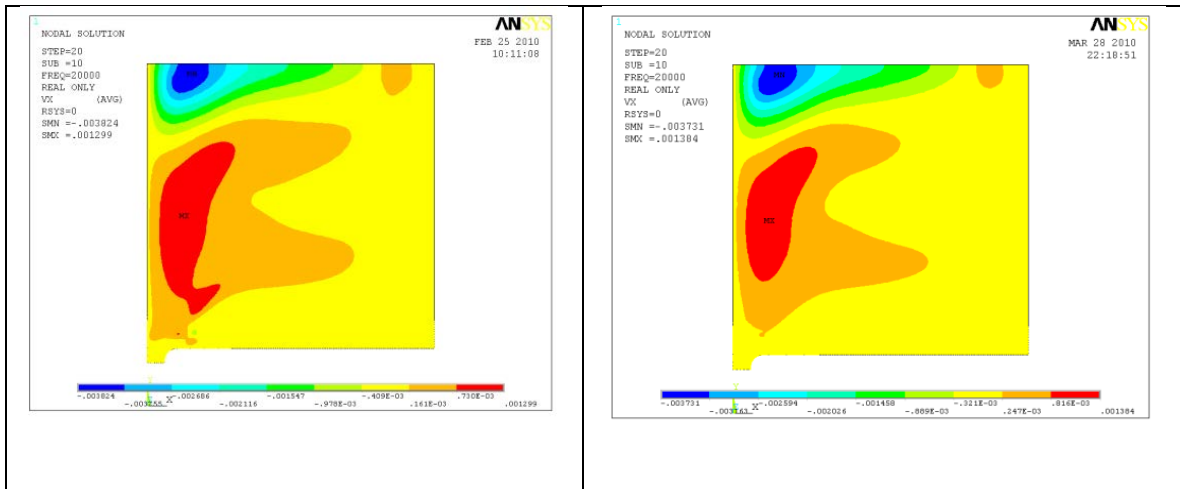
Figure 6-63. Comparison of horizontal velocity component distributions in melt.
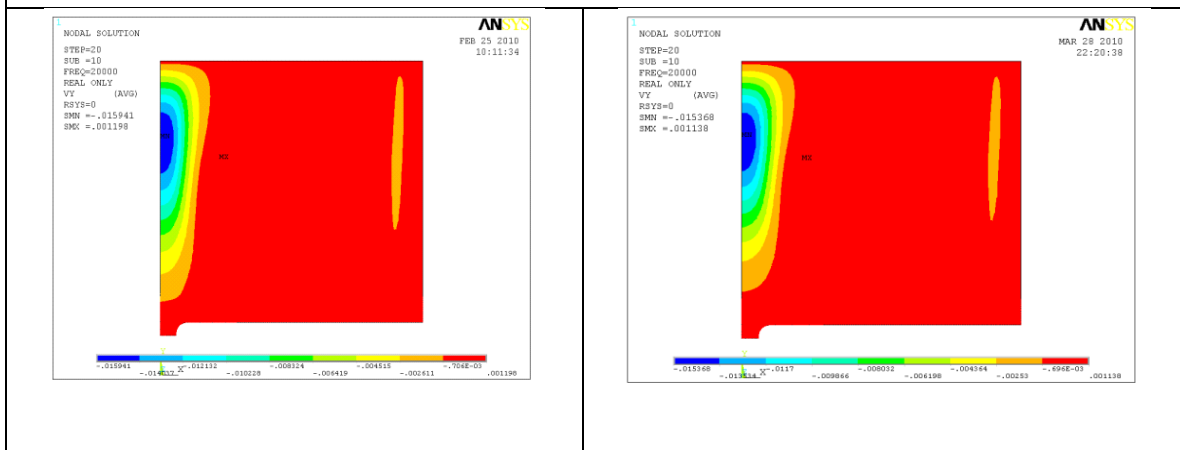
Figure 6-64. Comparison of vertical velocity component distributions in melt.

The results show that movement of the inductor down by 5 mm results in worse temperature conditions and will not support bottom casting.

A final comparison was made for the case in which the inductor is moved 5 mm down from the base case and 5 mm out (h_3 = 10 mm) from the centerline axis. This is compared to the same base case as the prior analysis.

The model geometries used in the calculations are shown in Figure 6-65. The results for various parameters are shown in Figures 6-66 through 6-69.
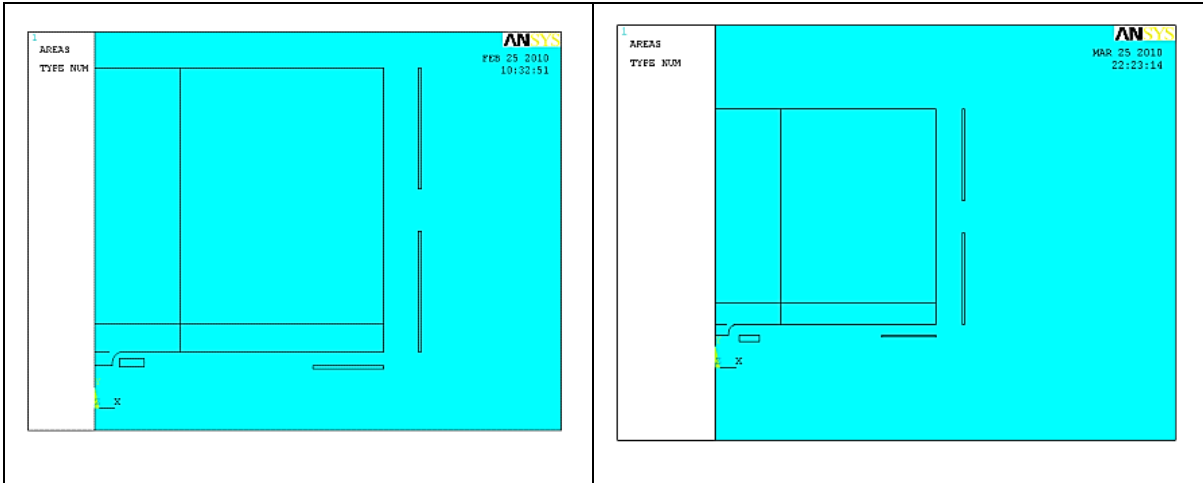
Figure 6-65. Model geometries used in calculations. Small inductor at 5 mm horizontal and vertical placements (left) and 10 mm horizontal and vertical placements.
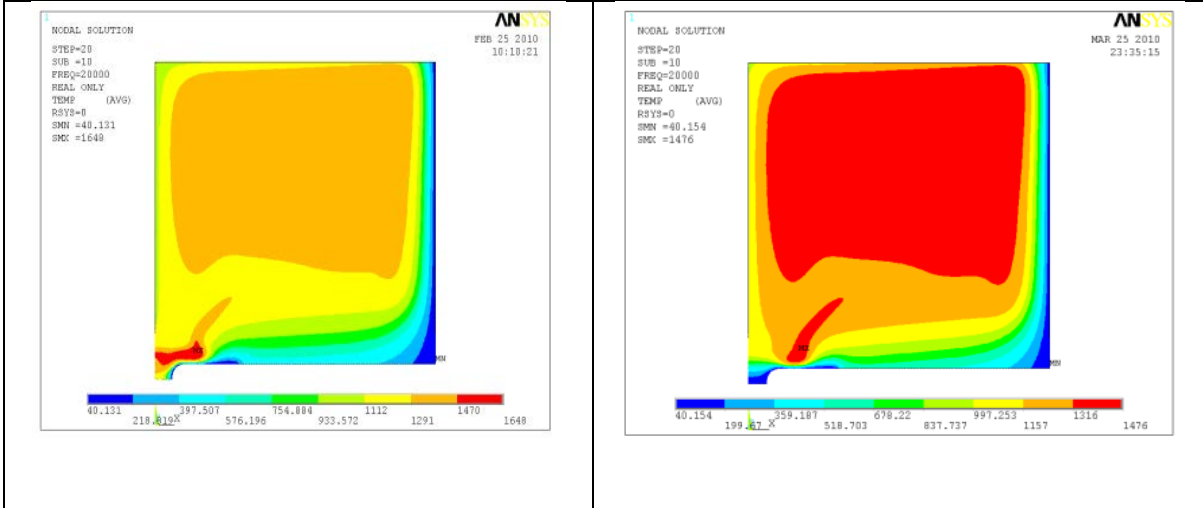
Figure 6-66. Comparison of temperature distributions in melt.
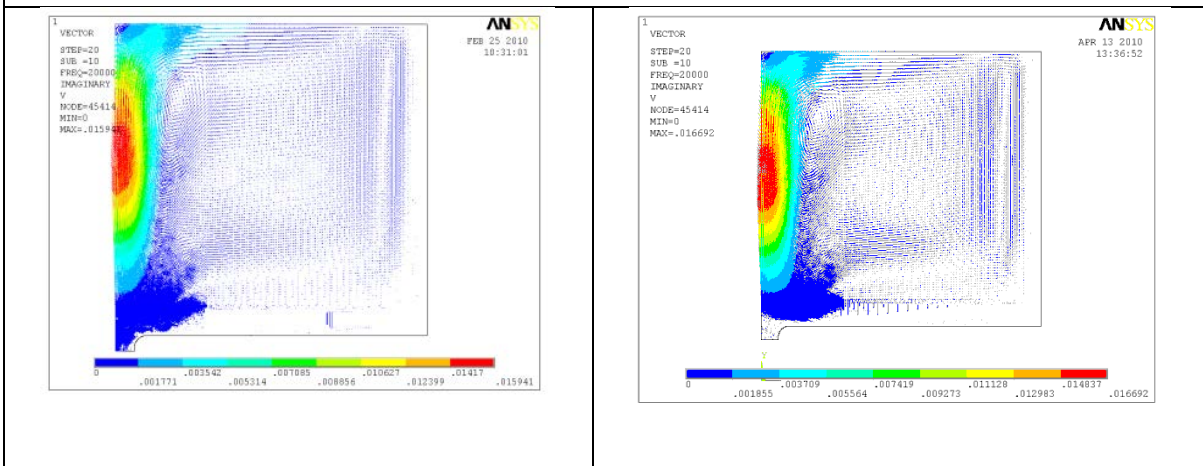
Figure 6-67. Comparison of velocity vectors in melt.
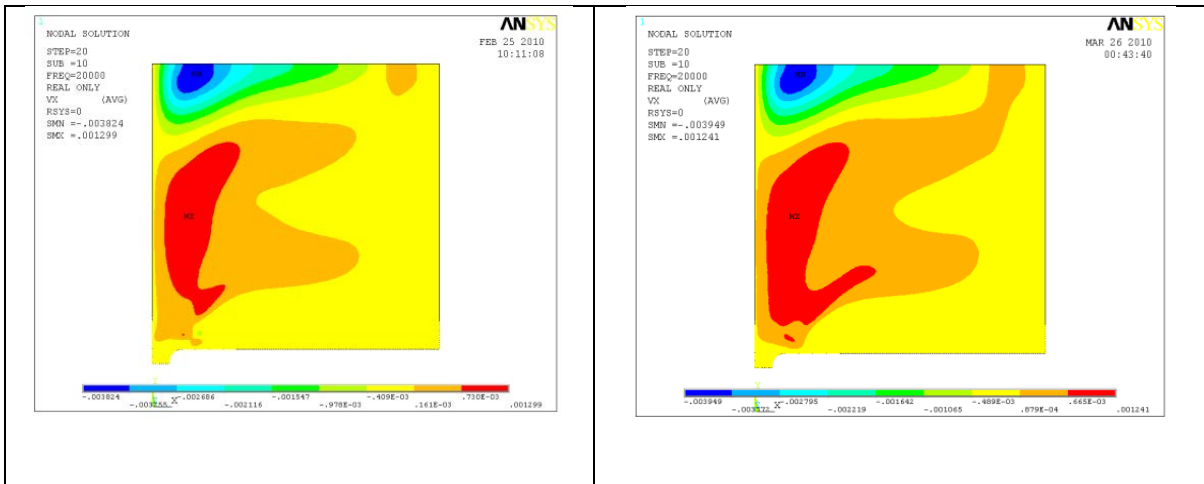
Figure 6-68. Comparison of horizontal velocity components in melt.
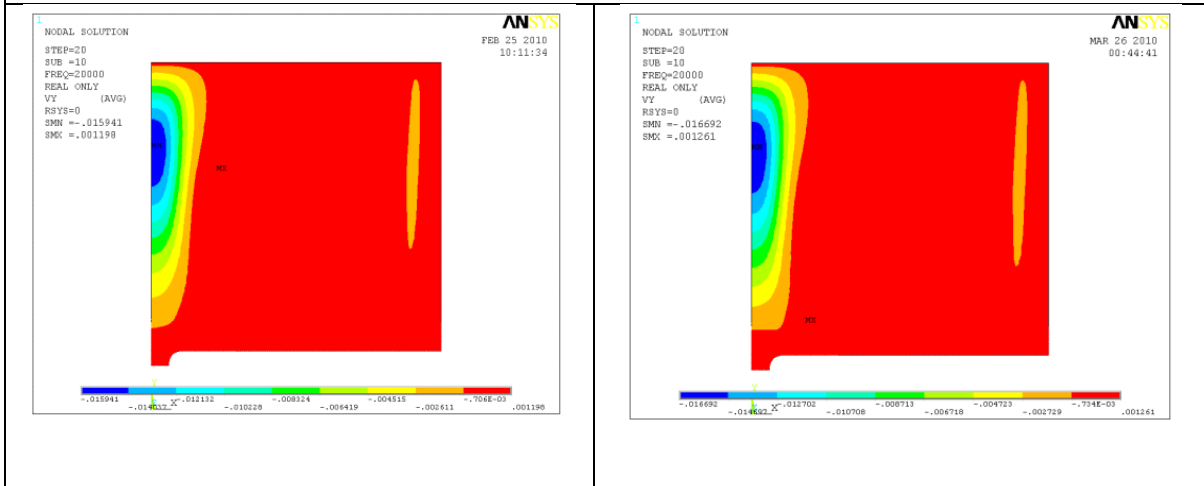
Figure 6-69. Comparison of vertical velocity components in melt.

Based on the results of the preceding analyses, the best configuration for the drain geometry is the smaller diameter and radius, as well as a reduced diameter for the inductor coil, with placement parallel with the bottom of the drain. These results were used to implement design changes and enhancements for the drain and high frequency inductor systems.

6.3. Investigation of Crucible Bottom and Drain Geometry Boundary Conditions

The purpose of this investigation was to determine the impact of the boundary condition used for the interface between the drain and the glass, as well as the bottom of the crucible. Initially, for simplification, a fixed heat flux of 30 W/cm^2 was used for the drain surfaces. This value was based on limited experimental measurements for the 27 MHz induction heating system at 1,200°C.

However, during the heat-up process, the heat flux is much lower and this can change the melt conditions in the vicinity of the drain. This was observed in experiments where the steady state temperature conditions are achieved faster than predicted by the model. This is believed to be due to the temperature dependent energy losses that are not specifically accounted for in the model using fixed heat loss boundary conditions. Thus, to investigate this, comparative calculations were conducted for a fixed boundary condition and a temperature-dependent boundary condition that is behaving as a radiation heat transfer phenomenon. The calculation time was fixed at 10,000 seconds. The model parameters used for this analysis were generally the same as presented in Table 6-3.

The model geometry is shown in Figure 6-70. Comparative results for various parameters are provided in Figure 6-71 through Figure 6-76. In each case, the radiation heat transfer boundary condition is presented on the right side of the figures.

Figure 6-70. Model geometry used in the calculations. Note that the drain inductor is not energized in this analysis.
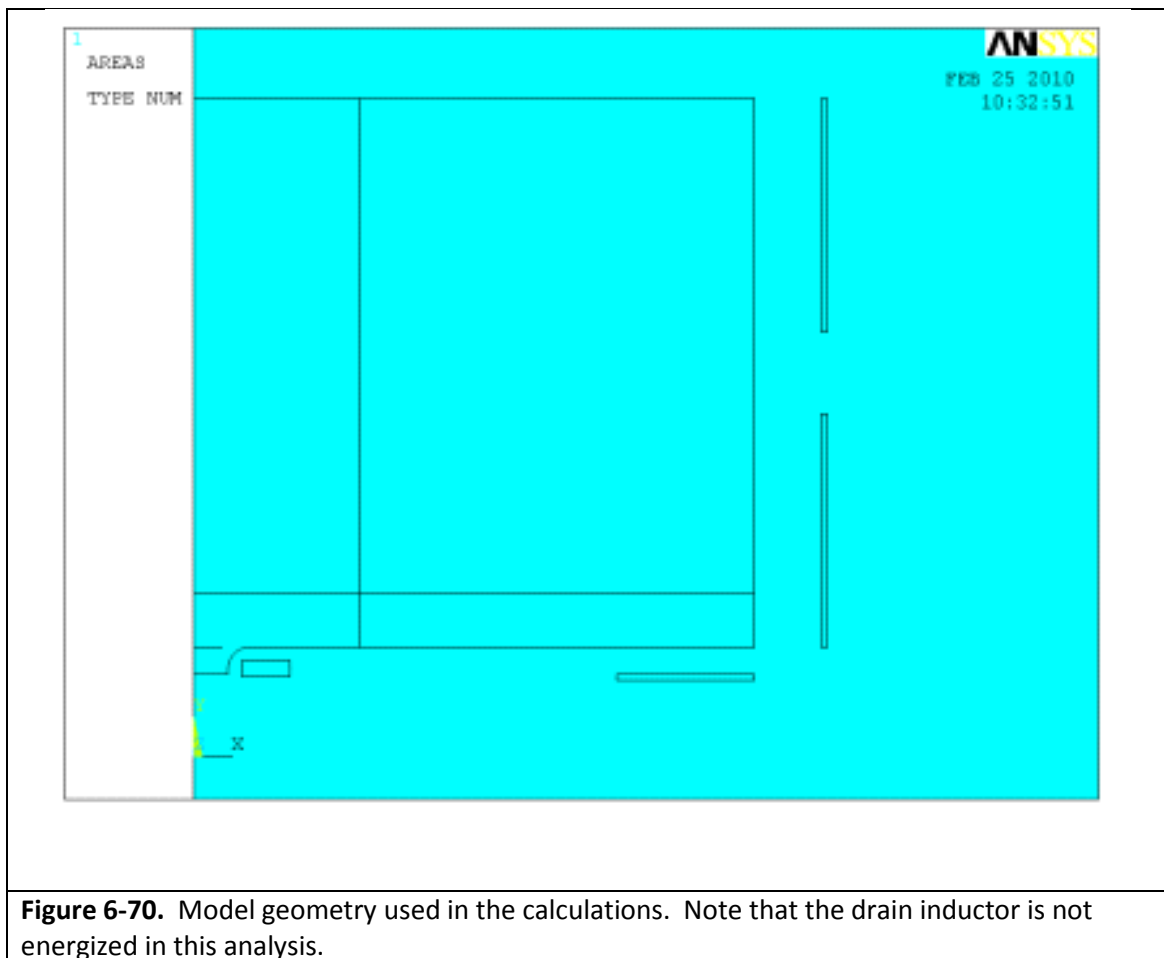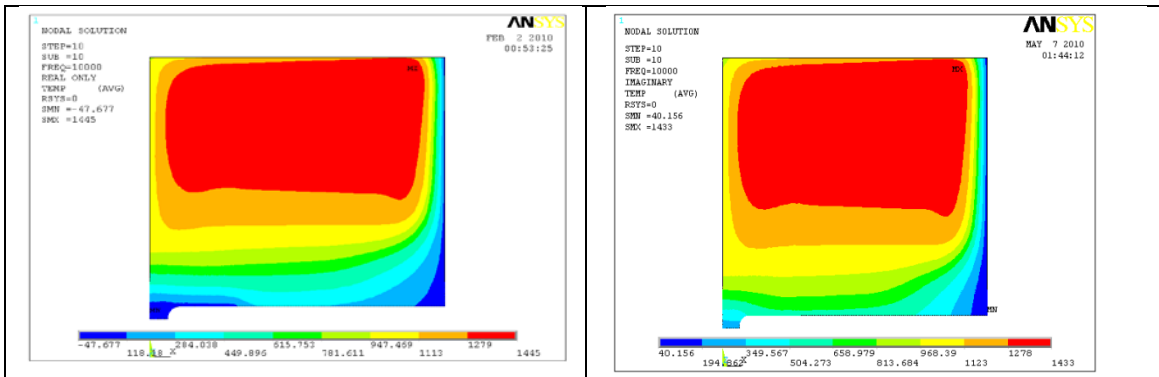
Figure 6-71. Comparison of temperature distributions in the melt.
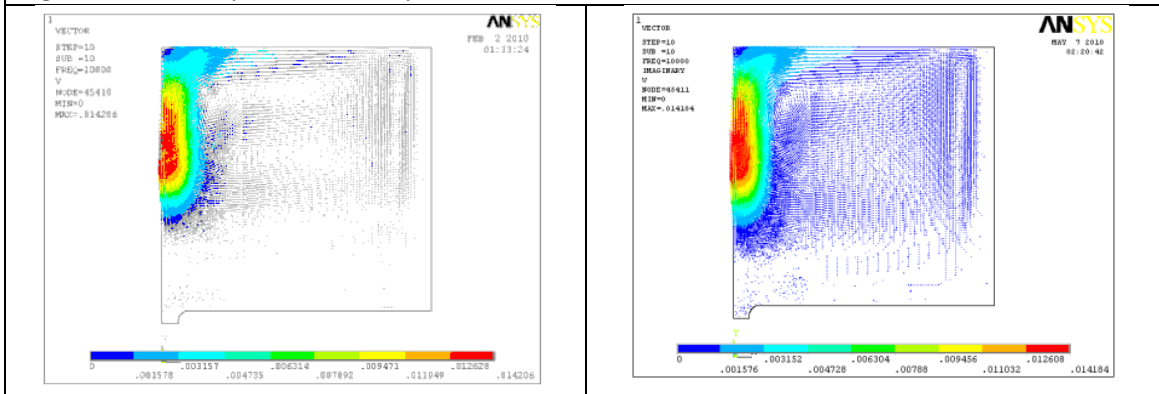
Figure 6-72. Comparison of velocity vector distributions in the melt.
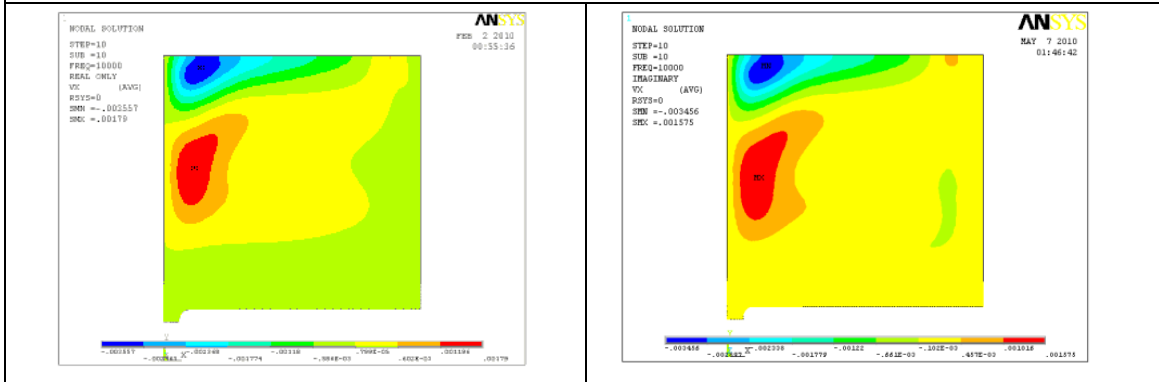
Figure 6-73. Comparison of horizontal velocity component distributions.
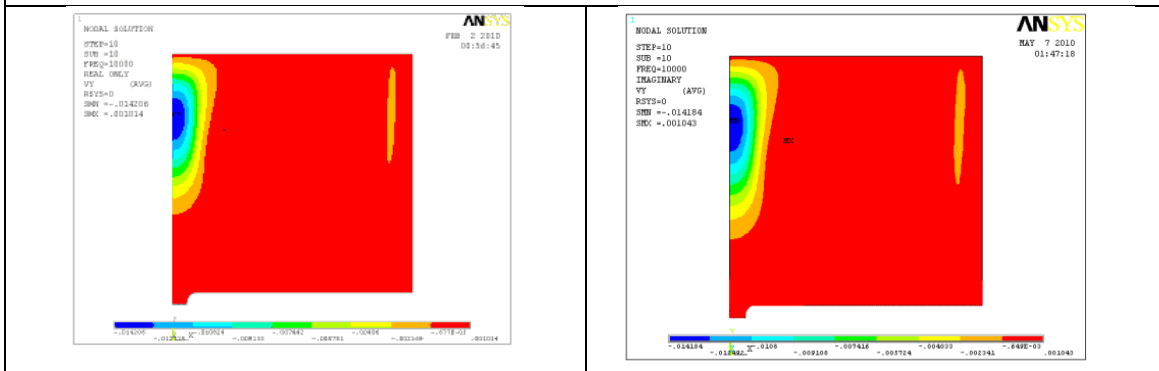
Figure 6-74. Comparison of vertical velocity component distributions.

These results show that, for the given calculation time, using the radiation type boundary condition results in higher temperatures near the lower layers and in the drain vicinity. In fact, the temperature within the drain throat is 250°C to 300°C higher. A closer look at these temperature distributions is provided in Figures 6-75 and 6-76.

| **Figure 6-75.** Distribution of temperatures in the melt between 40 and 350°C. | **Figure 6-76.** Distribution of temperatures in the melt between 350 and 650°C. |
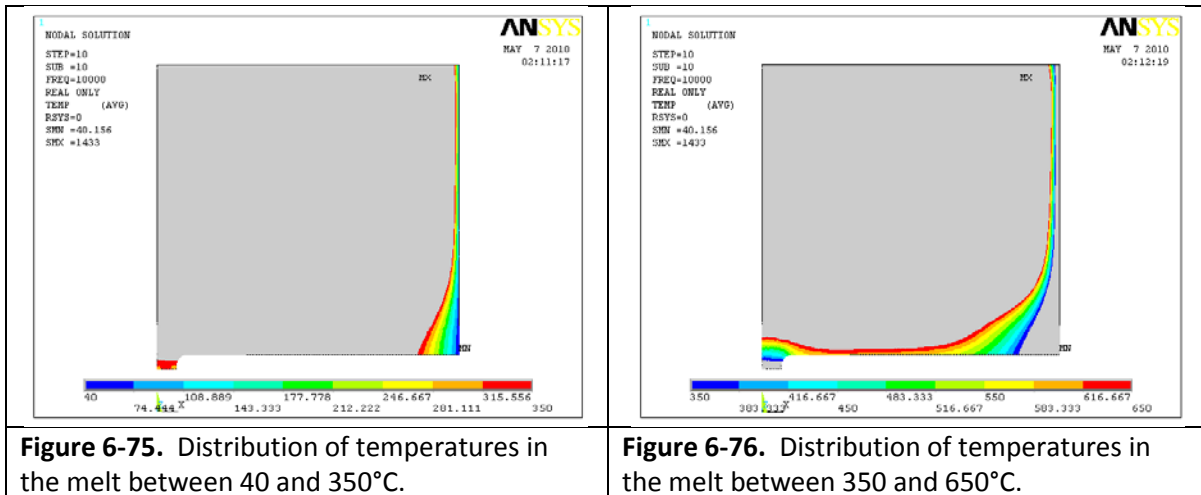
Recall from Figure 6-59, that significantly more time was required to reach these temperatures within the drain body. Thus, while use of this boundary condition does not change the steady state results, it is more representative of the actual conditions, and significantly reduces the calculation time, which is strong justification to implement it into the model.

6.4. Investigation of Oscillation Frequency Effects Associated with Industrial Scale CCIM Systems

All of the modeling studies conducted thus far have been on CCIM systems in the 300 mm to 400 mm diameter range. The 300 mm diameter system is considered the baseline since the initial model validation efforts were conducted using a CCIM system of this scale. The initial scale-up analyses were focused on a nominal 400 mm diameter system because this size was believed to be the largest system that, if optimized, could be powered by the available 60 kW generator with an oscillation frequency of 1.76 MHz.

However, there is an interest to be able to scale up to much larger CCIM platforms. The largest system in commercial operation for radioactive waste glass processing is the 650 mm unit installed in the La Hague Plant in France. Similarly, there is a 450 mm diameter in operation at the SIA Radon Production Association in Russia. However, US applications would likely require systems in the range of 900 mm to 1,000 mm in diameter. Systems this large have never been built and operated,

and no publications are available related to modeling of systems in this size range, nor are there any available for the systems in France or Russia.

While there are some theoretical optimal relationships between operational parameters, material properties, and geometry of induction melting systems (recall Figure 4-1 and Equation 4-10), as discussed earlier, operational experience has shown that these relationships may not scale up. For example, Russian researchers have shown [18] that optimal operational relationships for the "ma" factor from equation 4-10 is actually a range, nominally between 3 and 5, rather than a point value, and is determined by other characteristics, including glass properties and geometry effects.

Having a model that has been validated to be representative of CCIM systems provides the ability to investigate scale-up parameters and how to optimize the system. The first analysis conducted was a scoping study related to the effect of the frequency on the overall melt conditions, with particular interest in the temperature profile near the bottom layers. The initial investigation was for a nominal 1 m diameter CCIM system operating at 66 kHz. This frequency was selected because it represents a "ma" ratio of approximately 3 for the BSG material properties that are modeled.

The model parameters used for the analysis are given in Table 6-4. Note that the heat loss boundary conditions were determined experimentally using the 300 mm diameter CCIM system. The basic model geometry used for the following analyses is shown in Figure 6-77.

6.4.1.Induction Heating in a Large Scale Melter
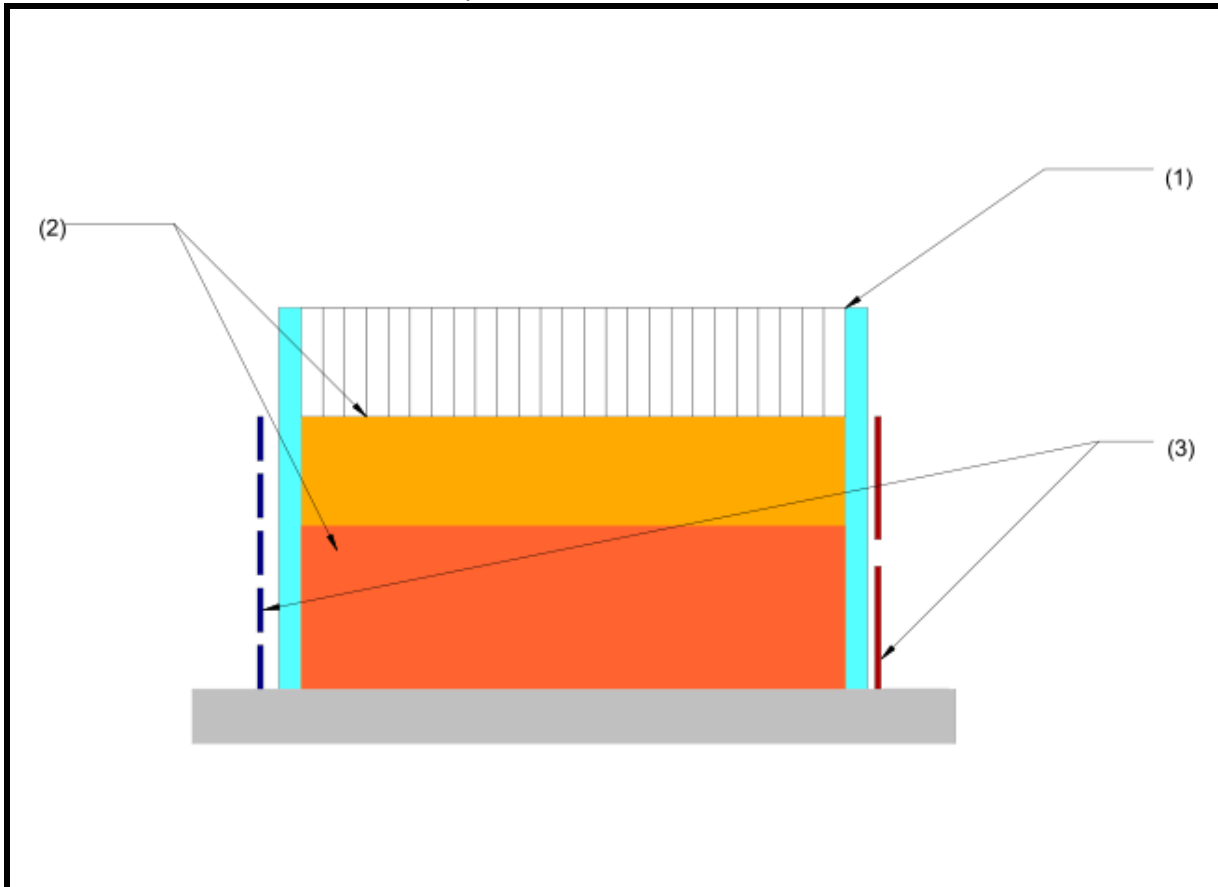
The primary purpose of this initial evaluation was to investigate the overall melt conditions for key parameters. These included temperature distribution, heat sources, melt velocities, thermal losses, and average power in the melt.

The power in the melt was selected such that the maximum temperature in the melt was similar to other investigations, namely 1,400^{o}C. Based on the estimated power losses, above, the power in the melt was set at 231 kW. However, this proved to be much more power that necessary. The actual power level set in the melt was around 130 kW, which resulted in a maximum temperature of 1,427^{o}C. Recall, the temperature in the 300 mm diameter baseline CCIM was at 1,426^{o}C. Figure 6-78 shows the results for the temperature distribution.

Several observations can be made from these initial results. First, the skull thickness is much larger on the sides and the bottom for this configuration. Although the increase along the side walls may

not be an issue, the increase at the bottom will make bottom casting even more difficult. If we assume that the skull is represented by the glass layers below 800°C, Figures 6-79 and 6-80 show the skull layer in gray. Thus the aspect ratio (i.e., melt pool height to diameter ratio) does not appear appropriate for the larger diameter systems.

Table 6-4. Parameters for initial analysis of 1,000 mm CCIM.

Parameter	Value
Cold crucible internal diameter (1)	1,000 mm
Melt pool height (2)	500 mm, 300 mm
Inductor internal diameter (3)	1,140 mm, 1,040 mm
Number of inductor coils (3)	5, 2
Inductor coil form	rectangular
Inductor individual coil height	80 mm, 225 mm
Total inductor height	500 mm, 300 mm
Average heat flux from side wall	5.14 W/cm^2 (146.8 kW total)
Average heat flux from bottom	0.44 W/cm^2 (3.45 kW total)
Average heat flux from melt pool surface	18.7 W/cm^2 (80.7 kW total)
Integrated emissivity	0.5
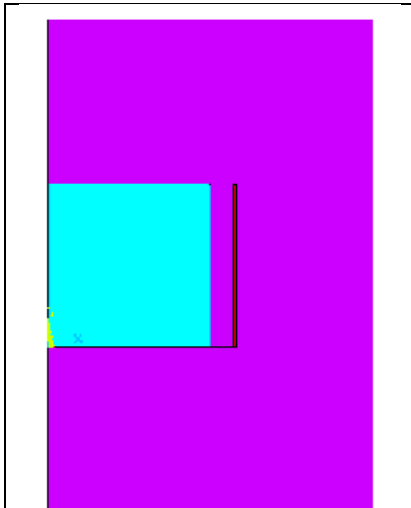
Figure 6-77. Model geometry for analysis of frequency effects on large scale CCIMs
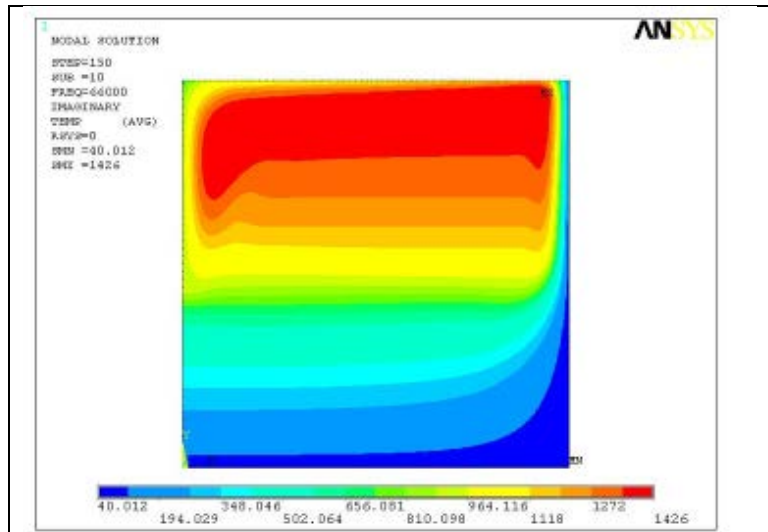
Figure 6-78. Temperature distribution for 1 m diameter CCIM at 66 kHz frequency.
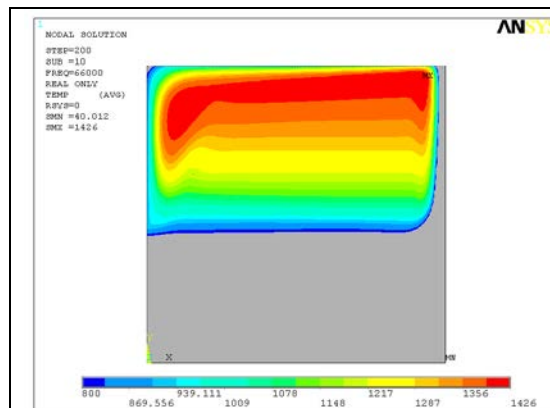
Figure 6-79. Skull layer in 1 m diameter CCIM at 66 kHz frequency (i.e. temperature >800°C).
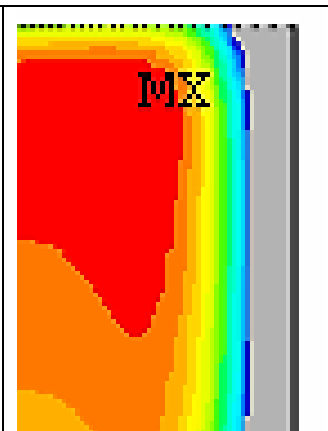
Figure 6-80. Blow-up of side wall skull layer.

As a comparison, for the 300 mm diameter unit at nominally the same temperature, the side wall skull is only 2 to 4 mm thick, while the 1 m diameter system has a skull thickness at 10 to 13 mm. The skull on the bottom layer is around 220 mm thick. Scale-up of the system obviously results in lower heat losses (i.e., thicker skull layers) so the system can be more energy efficient; however, the bottom layer conditions must be improved to support casting.

Several key parameters were investigated, including heat source distributions, horizontal and vertical velocity components, and the flow function (i.e., convection cells due to buoyancy effects).

Figure 6-81 shows the heat source distribution in the melt. When compared to the 300 mm diameter system, the effects of the lower frequency can be observed in the larger volume that the heat sources are distributed within.

Figure 6-81. Heat source distribution in the melt for 1 m diameter CCIM at 66 kHz frequency.
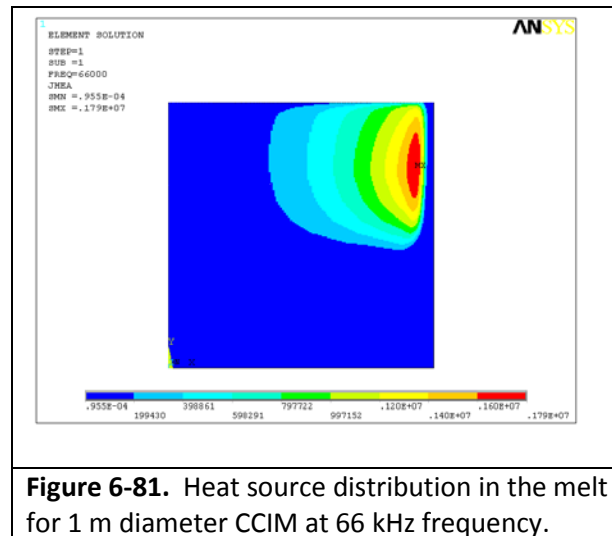
Figures 6-82 and 6-83 show the vertical and horizontal velocity components. These figures show that maximum absolute velocities of 2.5 mm/second are achieved. By comparison, the baseline 300 mm unit showed maximum velocities of around 0.7 mm/second.

Figure 6-82. Vertical velocity component in 1 m diameter CCIM at 66 kHz frequency.

Figure 6-83. Horizontal velocity component in 1 m diameter CCIM at 66 kHz frequency.
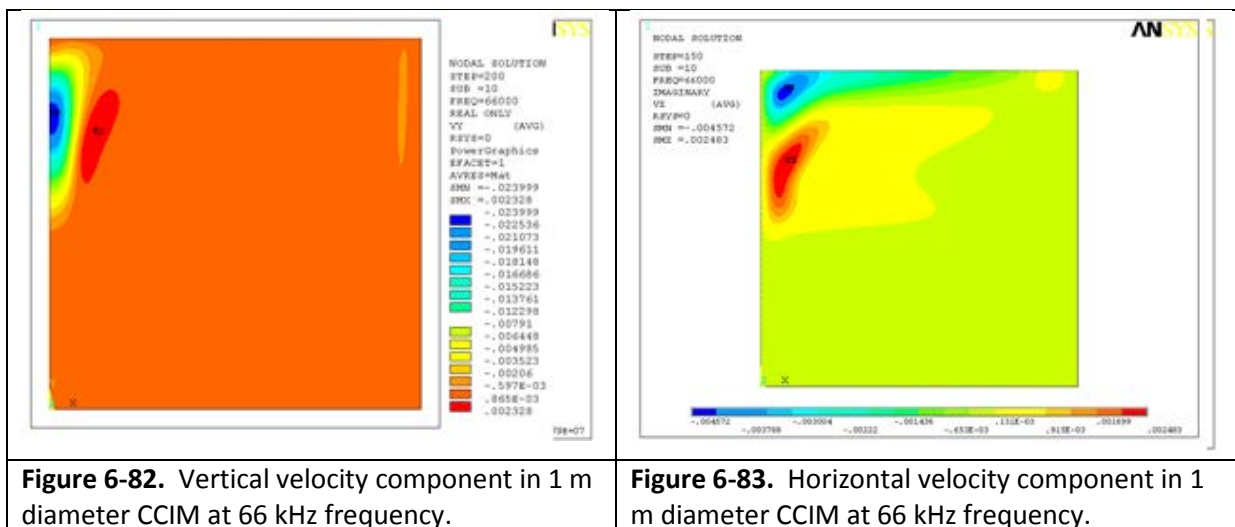
Figure 6-84 shows the velocity vector distribution in the melt. Two distinct convection cells are established due to the buoyancy forces resulting from density differences as a function of temperature.

Figure 6-84. Convection cells in melt volume.
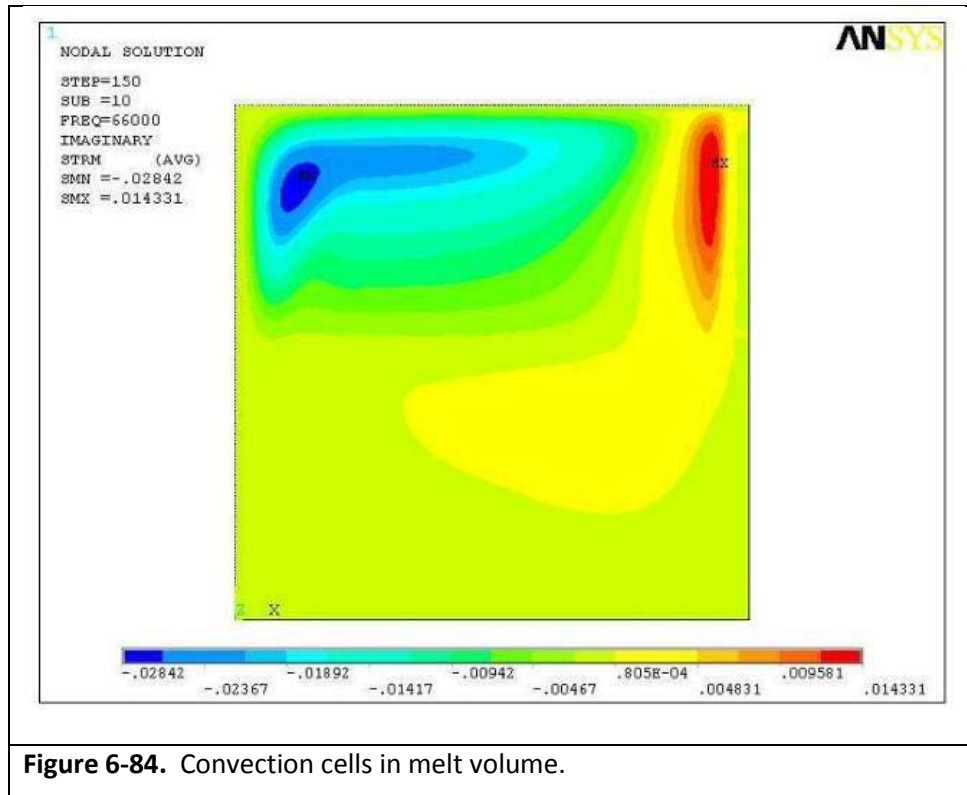
As previously mentioned, the heat losses in the 1 m diameter are much lower than in the 300 mm diameter when operated at 66 kHz. This is primarily due to the increased skin depth at this lower frequency, which reduces the skin effect at the side walls. The calculation results of these losses and heat fluxes are given in Table 6-5.

Table 6-5. Key calculation results for 1,000 mm diameter CCIM at 66 kHz frequency.

Sidewall surface area	1.57 m^2	Sidewall thermal losses	61.78 kW	Average heat flux through sidewall	3.82 W/cm^2
Melt pool bottom and top surface area	0.785 m^2	Bottom thermal losses	1.61 kW	Average heat flux through bottom	0.205 W/cm^2
Total power in the melt	130 kW	Melt pool top radiation losses	65.82 kW	Average heat flux from top surface	8.39 W/cm^2

Based on the results from this initial evaluation, additional analyses are needed. Key factors have already been shown to have significant influence on the melt conditions, including frequency, melt pool height to diameter ratio, and the inductor coil configuration (i.e., use of bottom coils). These factors and their influences are investigated in the following analyses.

6.4.2.Frequency Effects for Large Scale Melter

The next investigation compared the melt conditions for various frequencies. The frequencies selected represented the observed range of optimal "ma" relationships (i.e. 3 to 5) from past experiences. As previously discussed, for the glass properties used in the model, and the experimental work, a CCIM with a 1,000 mm diameter would require a generator with an oscillating frequency of 66 kHz for optimum operation, based on the theoretical approach. However, this was also demonstrated to be dependent on other factors such as the melt pool depth. For this investigation frequencies of 66 kHz, 250 kHz, and 660 kHz were evaluated. In all cases, all other operational and geometrical parameters were the same. The results are shown in Figure 6-85.

| 66 kHz | 250 kHz | 660 kHz |

Figure 6-85. Comparison of temperature distributions in a 1 m diameter CCIM at various frequencies.
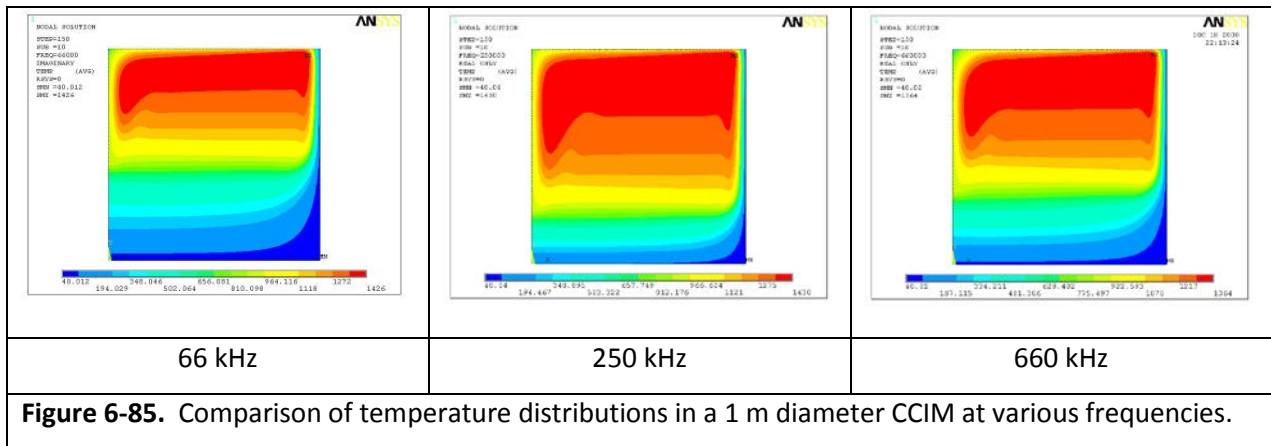
As can be seen, a frequency of 250 kHz provides much better temperature distribution within the melt than the predicted 66 kHz. Interestingly, the French CCIM system, which is 650 mm in diameter, is operated at a nominal 275 kHz for processing a similar BSG composition.

Figure 6-86 shows a comparison of the heat source distribution in the melt volume for the three frequencies. An interesting contrast to note is that, for induction heating of solid materials, as the heat source distribution is contracted (i.e., the depth of penetration of the induction energy is reduced) the volume of highest temperature is reduced. However, in this case, the high temperature volume increases, when comparing the behavior of the 66 kHz system to that of the 250 kHz and 660 kHz systems. Although, there is a cooling effect that occurs between 250 kHz and 660 kHz indicating that an optimum frequency is likely in that range.

| 66 kHz | 250 kHz | 660 kHz |

Figure 6-86. Distribution of heat sources in the melt for various frequencies**.**
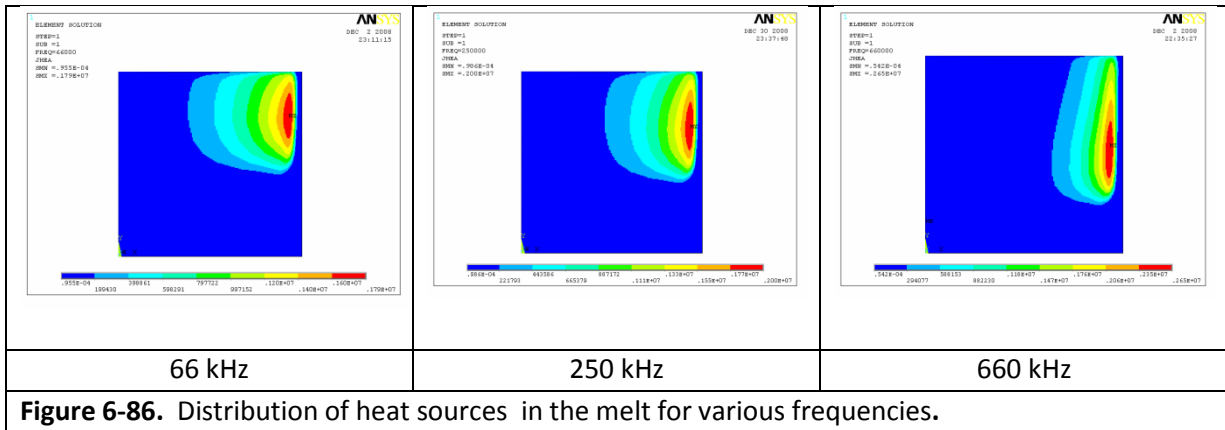
Figures 6-87 and 6-88 illustrate the vertical and horizontal velocity components. As expected, because the power in the melt is increased at the lower frequencies (i.e., from 130 kW to 175 kW), so are the vertical velocities. A comparison of these data are provided in Table 6-6.

| 66 kHz | 250 kHz | 660 kHz |

Figure 6-87. Vertical velocity component distributions for various frequencies.

| 66 kHz | 250 kHz | 660 kHz |

Figure 6-88. Horizontal velocity component distributions for various frequencies.
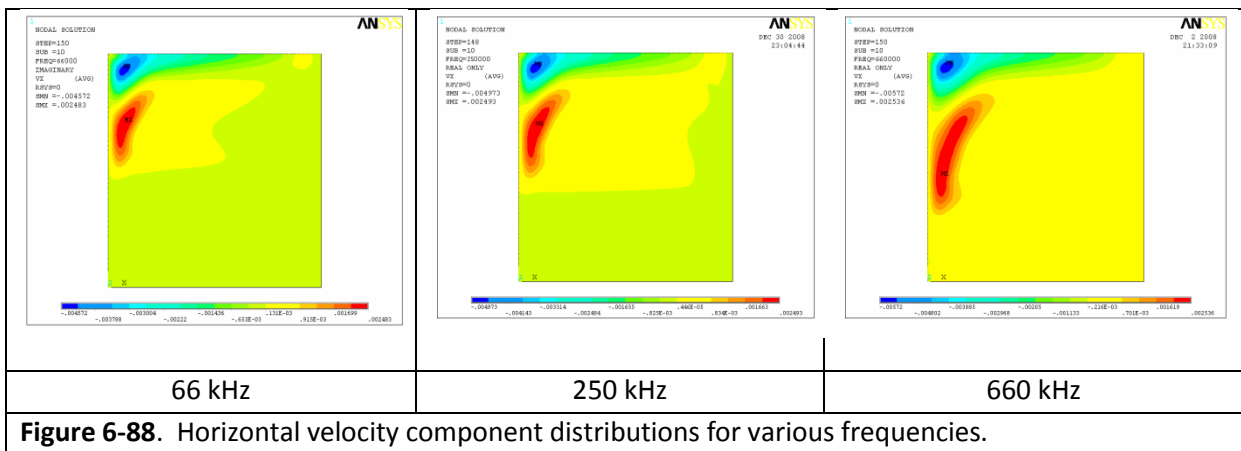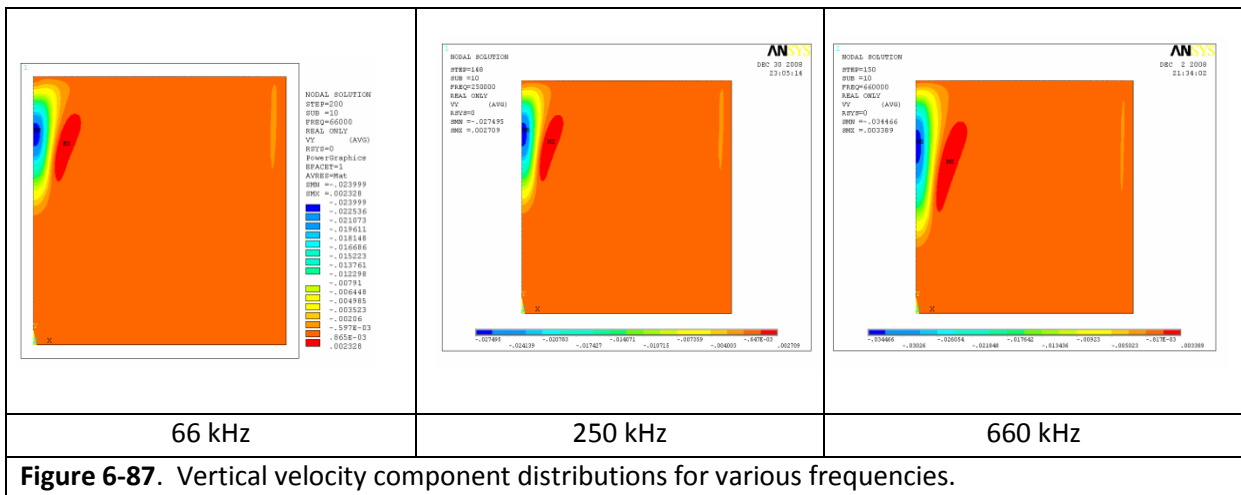
Table 6-6. Comparison of velocities for various frequencies.

Current frequency	66 kHz	250 kHz	660 kHz
Vertical velocity, mm/sec	2.33	2.71	3.39
Horizontal velocity, mm/sec	2.48	2.49	2.54

6.4.3. Effects of Melt Pool Height Aspect Ratio to Diameter in Large Scale Melter

The next scoping investigation made a comparison of the steady state conditions for a 1,000 mm diameter CCIM system with a melt pool height of 500 mm and 300 mm using the 250 kHz frequency evaluated in the prior analysis. For this configuration, the inductor was modeled with only two turns, and for each case the inductor was the same height as the melt pool. Other specific model parameters were the same as presented in Table 6-4.

A comparison of the temperature distributions for the two geometries is provided in Figures 6-89 and 6-90.
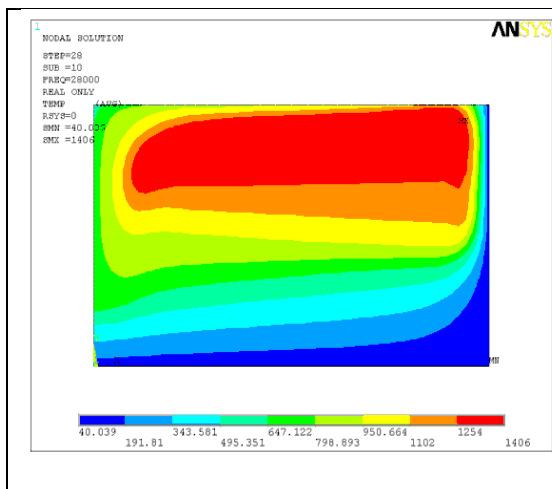
Figure 6-89. Temperature distribution for melt pool height of 300 mm.	**Figure 6-90.** Temperature distribution for melt pool height of 500 mm.
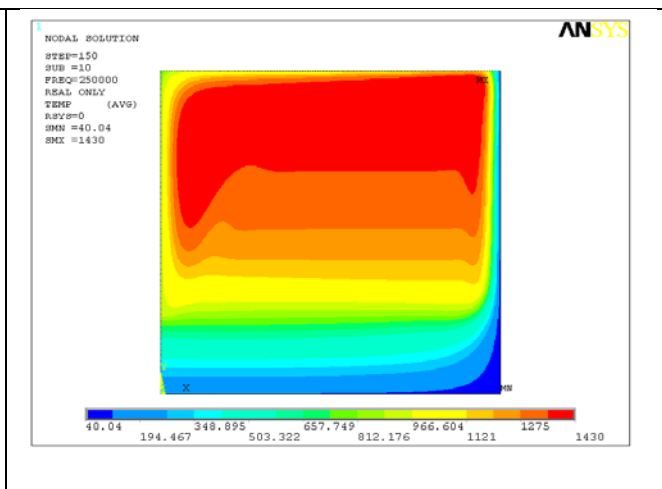
For the 500 mm melt pool depth, the power level used in the model was 175 kW. This provided the nominal maximum temperature of 1,400°C. However, for the 300 mm melt pool depth, only 130 kW was required to produce the same nominal maximum temperature. Additionally, the 300 mm deep melt pool provided higher temperatures near the bottom along the central axis. This is an important observation since the bottom drain is located along this axis, and having higher temperatures nearer to the drain throat will support the bottom casting process. The parameters shown in Table 6-7 were observed from the modeling results for the 300 mm melt pool depth.

Table 6-7. Parameters observed from analysis of 1,000 mm CCIM with 300 mm melt pool.

Parameter	Value
Power supplied to the inductor	130 kW
Total heat losses through the crucible side wall	33.85 kW
Total heat losses from the crucible bottom	1.2 kW
Total heat radiation loss from melt surface	55.42 kW
Heat flux through the crucible sidewall	3.74 W/cm^2
Heat flux through the crucible bottom	0.15 W/cm^2

Diagrams of the surface distributions of heat fluxes and temperatures for the 300 mm melt pool depth are shown in Figures 6-91 through 6-94.
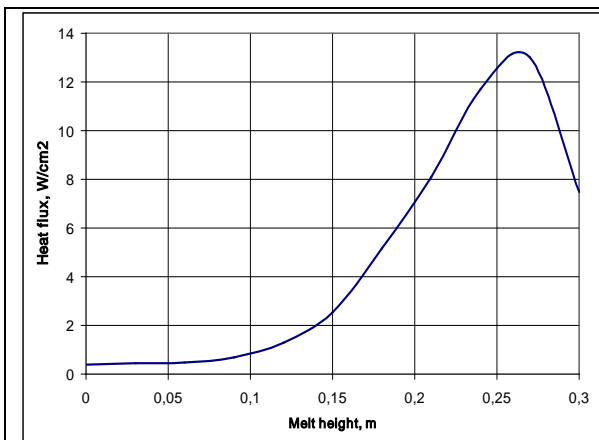
Figure 6-91. Heat flux distribution through side wall for 300 mm melt pool depth.
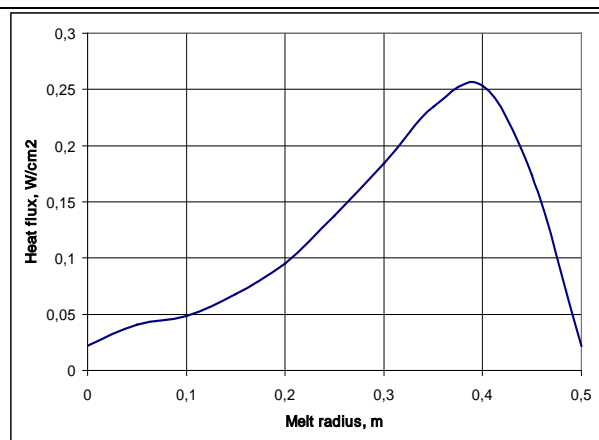
Figure 6-92. Heat flux distribution through bottom for 300 mm melt pool depth.
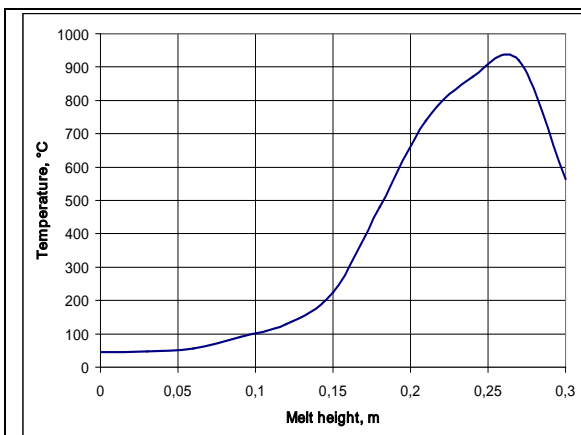
Figure 6-93. Temperature distribution along sidewall for 300 mm melt pool depth.
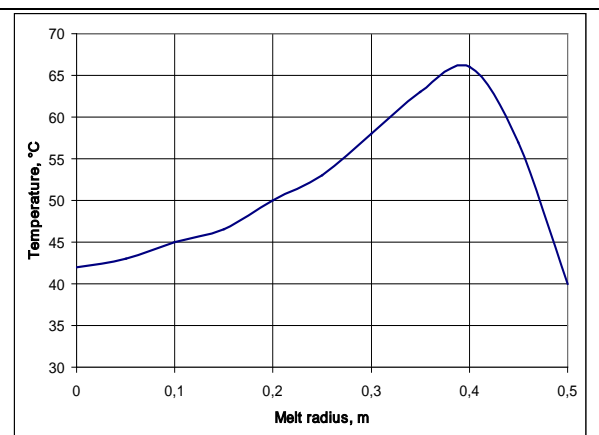
Figure 6-94. Temperature distribution along bottom for 300 mm melt pool depth.

One interesting observation from the analysis is that while horizontal absolute velocities are similar for both configurations, the vertical absolute velocities are much greater (i.e., approximately 4x) in the 500 mm deep melt pool.

 6.4.4.Combined Effects of Diameter, Frequency and Aspect Ratio in Large Scale Melters

The results of these two scoping studies warranted a more comprehensive investigation of the interaction of several key parameters, specifically the frequency, melt pool diameter, and melt pool depth. The following series of calculations investigate various combinations of 500 mm, 300 mm, and 200 mm melt pool heights, using frequencies of 1.76 MHz (the same as the generator in the ETU-LETI laboratory), 66 kHz, 300 kHz, and 660 kHz. Note that these models did not include the drain geometry, for simplicity. In all cases, the inductor height is the same as the melt pool height and the target maximum melt temperature was 1,450^{o}C. Power levels and calculation times were adjusted to achieve this temperature. Based on observations from experimental work and modeling analysis, the heat flux from the crucible side wall was assumed to be 8.72 W/cm^2. The other basic model parameters were as defined in Table 6-4.

The basic model geometry is shown in Figure 6-95. Note that the inductor appears to be modeled as a single turn, but is mathematically considered a two-turn inductor coil.

Figure 6-95. Basic model geometry for frequency and melt pool height variation studies.
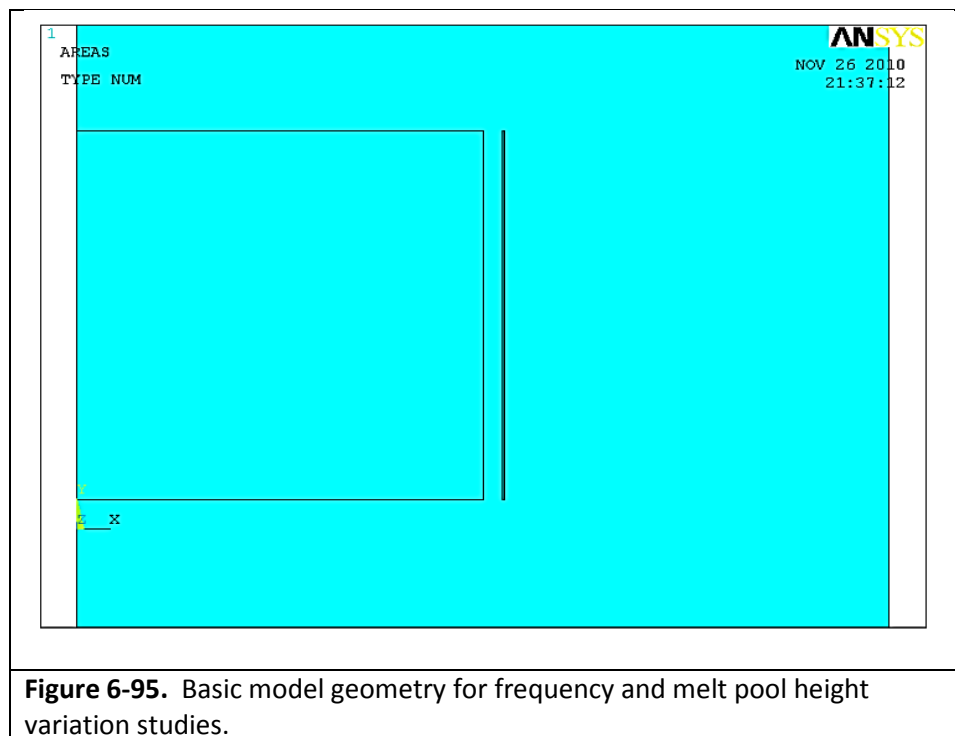
The first two calculations were for the extremes in frequency, namely 1.76 MHz and 66 kHz. The input parameters included the maximum power level of 230 kW and calculation time of 10,000 seconds. The results showed that the power level was much too high (i.e., the maximum temperature in the melt was approximately 1,600°C) and that a steady state condition was not reached, based on the thermal distributions. Thus, for the subsequent calculations the power level was reduced to 130 kW and the calculation time was increased to 25,000 seconds. For these calculations, frequencies of 300 kHz and 660 kHz were used.

These results show that using these parameters the target maximum temperature of 1,450°C is achieved, as well as the expected steady state temperature distribution. However, in both cases, the lower portion of the melt is at temperatures below 500°C, thus it is basically solid and not amenable to bottom casting. One possible solution is to reduce the height of the melt pool. The results for the four frequencies are compared in Figures 6-96 through 6-100.

1.76 MHz; 10,000 sec; 230 kW	66 kHz; 10,000 sec; 230 kW	660 kHz; 25,000 sec; 130 kW	300 kHz; 25,000 sec; 130 kW
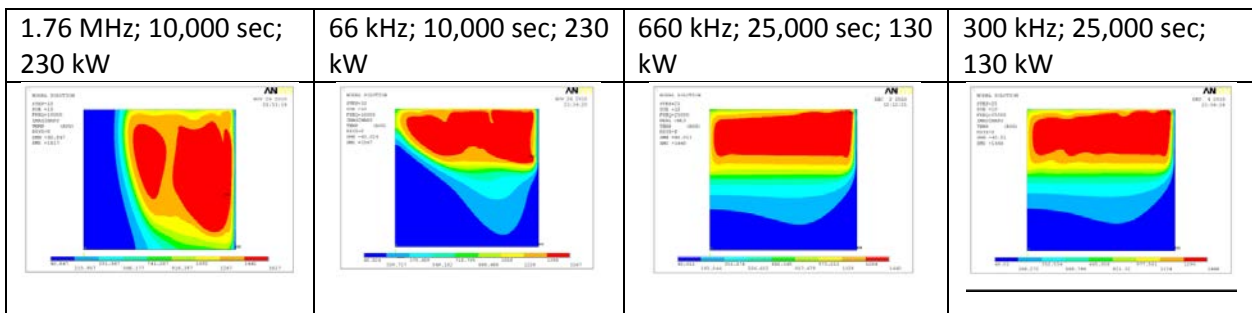
Figure 6-96. Comparison of temperature distributions.
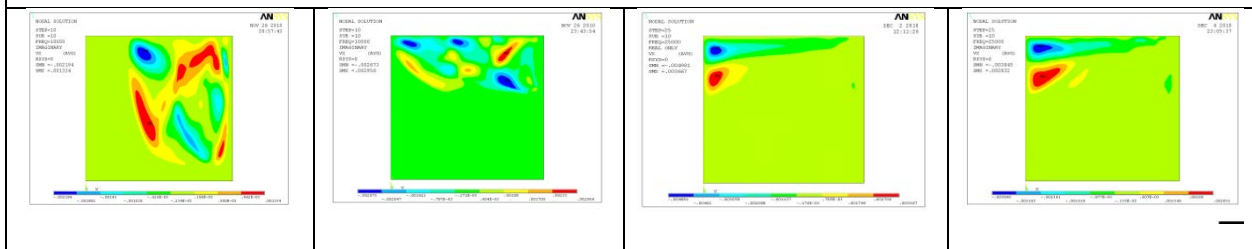
Figure 6-97. Comparison of horizontal velocity component distributions.
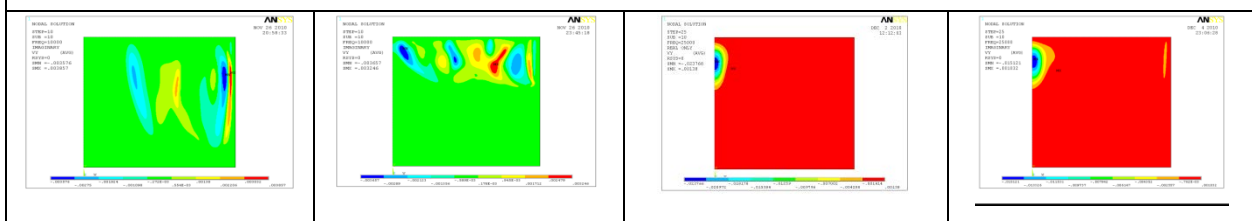
Figure 6-98. Comparison of vertical velocity component distributions.

1.76 MHz; 10,000 sec; 230 kW	66 kHz; 10,000 sec; 230 kW	660 kHz; 25,000 sec; 130 kW	300 kHz; 25,000 sec; 130 kW
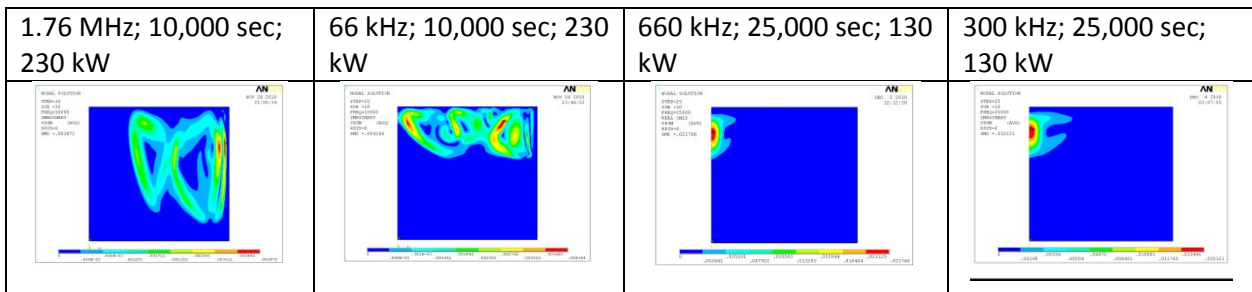
Figure 6-99. Comparison of total velocity component distributions.
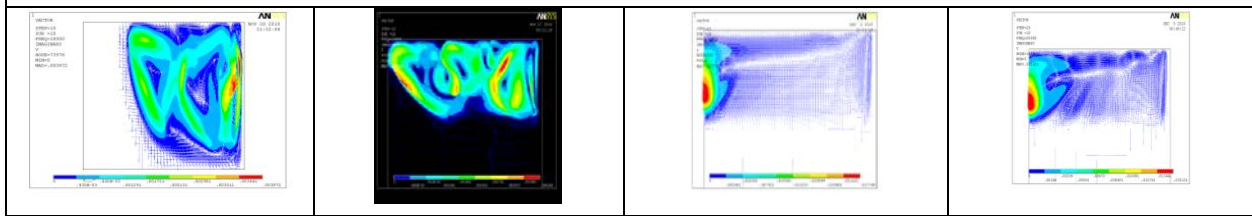
Figure 6-100. Comparison of velocity vector distributions.

The next series of calculations compared different melt pool heights for different frequencies. Specifically, systems with a frequency of 300 kHz were analyzed for 500 mm and 300 mm melt pool heights. For comparison, systems with a frequency of 660 kHz were analyzed for 300 mm and 200 mm melt pool heights. In each case, the inductor height was equal to the melt pool height. All of the parameters were the same as those used in the prior series of calculations, with the exception of the pool height. The geometries used for each model are show in Figure 6-101.

500 mm height 300 kHz 25,000 seconds 130 kW	300 mm height 300 kHz 25,000 seconds 130 kW	300 mm height 660 kHz 25,000 seconds 130 kW	200 mm height 660 kHz 25,000 seconds 130 kW
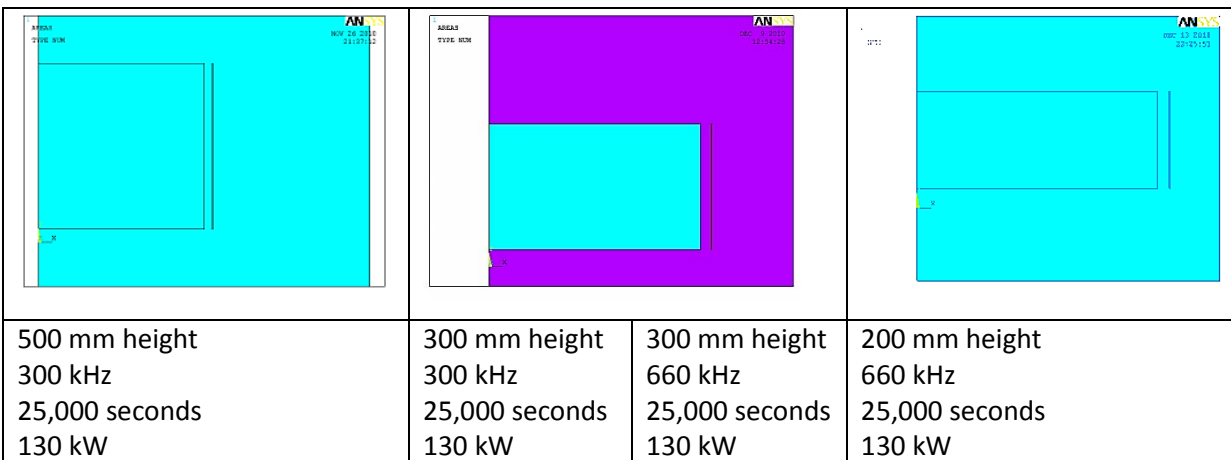
Figure 6-101. Model geometries used for analyses.

Several observations and conclusions can be made for these calculations. First, reducing the melt pool height definitely improves the temperature profiles near the bottom of the melt pool. It is also clear that certain combinations of frequencies with melt pool heights (and diameters) will result in

optimum conditions. For the 300 mm melt pool depths, increased velocities can be observed for the 660 kHz frequency versus the 300 kHz system. Closer observation also shows that the maximum temperature is further from the side wall for the 300 kHz system. These two results are primarily due to the decreased skin effect for the lower frequency system (i.e., great skin depth).

Another observation is that, as the melt pool height is reduced, the maximum temperature in the melt increases. For example, for the 500 mm height, the maximum temperature is 1,446^{o}C. However, for the 300 mm and 200 mm heights, the maximum temperatures are 1,476^{o}C and 1,562^{o}C, respectively. This is an indication that the required power level decreases with melt pool height, increasing the overall efficiency of the system.

Assuming that the skull is represented by glass volumes below 800°C, a comparison of the bottom skull layer thicknesses shows that for the 200 mm melt pool height (660 kHz) the skull is 15 mm thick. For the 300 mm melt pool height (300 kHz and 660 kHz) the skull is approximately 100 mm thick. Finally, the bottom skull thickness for the 500 mm deep melt pool is 260 mm. Thus the lower melt pool height results in conditions much more favorable for bottom casting. In general, for this BSG, a CCIM system with diameter of 1,000 mm will be optimal for bottom casting with a melt pool height of between 200 mm and 250 mm, and a frequency of between 300 kHz and 600 kHz. Note that very little difference results for the 300 mm melt pool height at 300 kHz and 660 kHz, although observation of the animations of the temperature distributions and velocity profiles shows that the system is more stable at 660 kHz. Figures 6-102 through 6-105 show the comparative results of the various systems.

500 mm height 300 kHz 25,000 seconds 130 kW	300 mm height 300 kHz 25,000 seconds 130 kW	300 mm height 660 kHz 25,000 seconds 130 kW	200 mm height 660 kHz 25,000 seconds 130 kW

Figure 6-102. Comparison of temperature distributions for the various systems.

500 mm height 300 kHz 25,000 seconds 130 kW	300 mm height 300 kHz 25,000 seconds 130 kW	300 mm height 660 kHz 25,000 seconds 130 kW	200 mm height 660 kHz 25,000 seconds 130 kW

Figure 6-103. Comparison of horizontal velocity component distributions for the various systems.
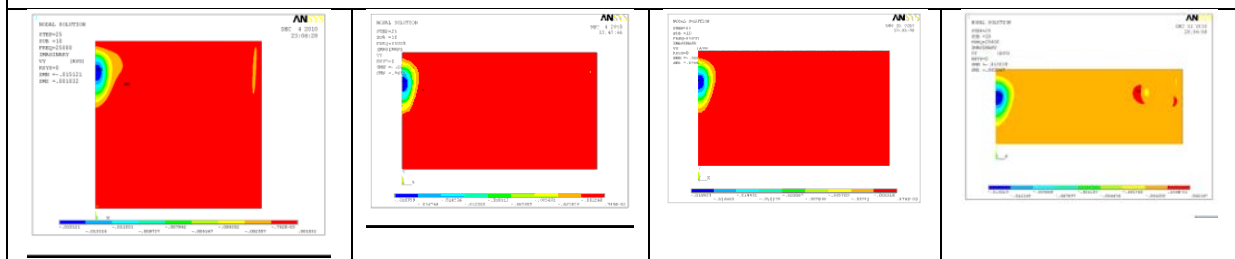
Figure 6-104. Comparison of vertical velocity component distributions for the various systems.
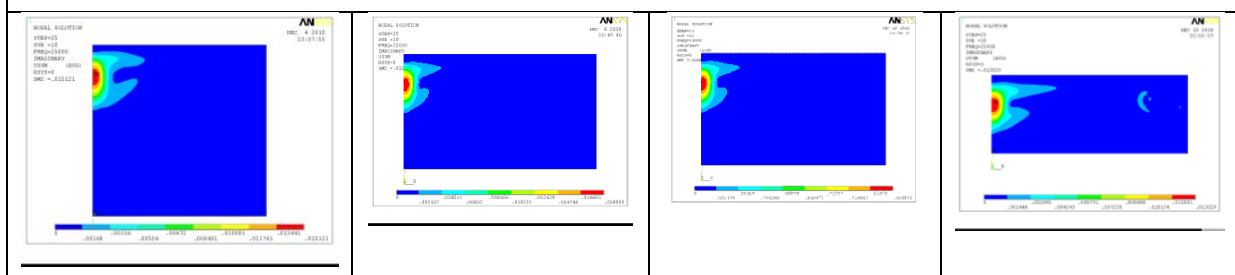
Figure 6-105. Comparison of total velocity distributions for the various systems.

One final application of the model for evaluating scale-up and the relationships between diameter, frequency, and melt pool height was completed. In this series of calculations the melt conditions are compared for several melt pool diameters (i.e., 400 mm, 700 mm, and 1 m), several melt pool heights (i.e., 500 mm, 300 mm, and 200 mm), as well as several frequencies (i.e., 66 kHz, 300 kHz, and 660 kHz). Additionally, the power levels were adjusted to provide nominally the same maximum temperature (within 10°C) in the melt, with the target temperature set at 1,470^{o}C. Thus, in the model, variables were defined as shown in Table 6-8.

Table 6-8. Model variables for scale up analysis of various CCIM sizes.

Parameter	Values
Melt pool diameter, D2	400 mm, 700 mm, and 1,000 mm
Melt pool height, A2	200 mm, 300 mm, and 500 mm
Power in the melt, P2	33 kW, 70 kW, and 120 kW

For the smaller diameter system, steady state temperature distributions can be achieved in 10,000 seconds of calculation. However, for the larger diameter systems 25,000 seconds is required. This is the only calculation parameter that is change between the various systems. All other boundary conditions are the same, including the mesh fineness factor mm = 6.

The first series of calculations was for systems with a melt pool height of 200 mm with a current frequency of 66 kHz. The results for the temperature distributions and velocity profiles are shown in Figure 6-106 and Figure 6-107, respectively.

Table 6-9 provides a summary of the calculation results. Note that the bottom skull thickness, h_{sk}, was determined by measuring the glass thickness from the bottom up to the 675°C isotherm. A higher temperature were used as comparisons in earlier calculations (i.e., 800°C); however, testing has demonstrated that the induction field will couple with the glass at this lower temperature.

400 mm diameter	700 mm diameter	1,000 mm diameter

Figure 6-106. Comparison of temperature profiles for various diameters. 200 mm melt pool height at 66 kHz frequency.

400 mm diameter	700 mm diameter	1,000 mm diameter

Figure 6-107. Comparison of temperature profiles for various diameters. 200 mm melt pool height at 66 kHz frequency.
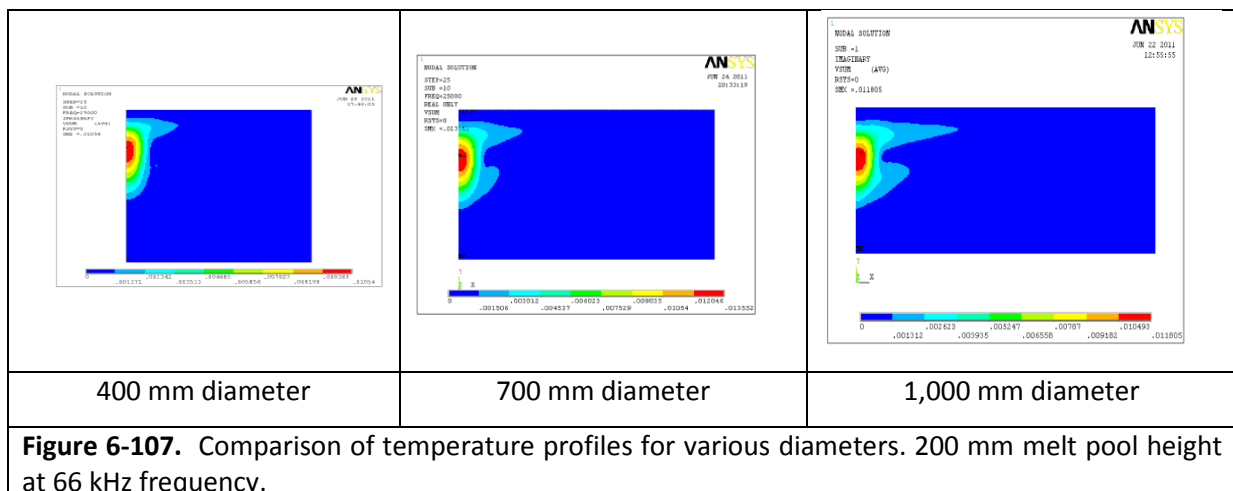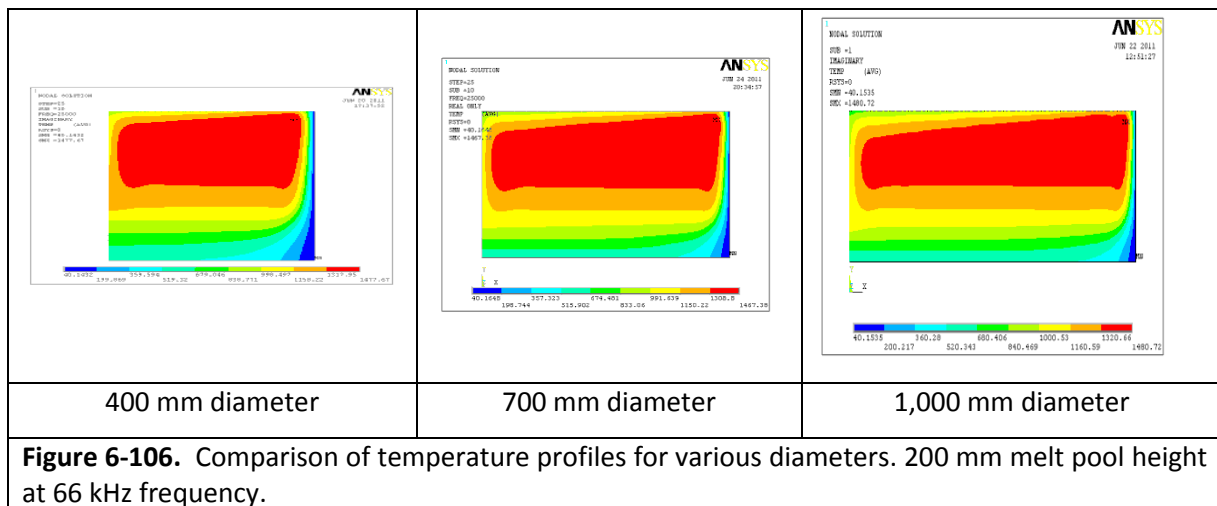
Table 6-9. Calculation results for melt pool height of 200 mm, current frequency of 66 kHz.

P_2/D_2	33 kW/400 mm	70 kW/700 mm	120 kW/1,000 mm
T_{max}, °C	1477	1467	1480
T_{s-axis}, °C	838	674	680
V_{max} (mm/sec)	11.5	13.5	11.8
h_{sk} (mm)	20.3	25.2	28.2

Note that: T_{max} is the maximum temperature in the melt volume, T_{s-axis} is the melt pool surface temperature at the centerline axis, V_{max} is the maximum melt movement velocity, and h_{sk} is the thickness of the bottom skull at the centerline axis. These are the same definitions for similar tables presented below.

Figure 6-108 illustrates the dependence of the melt pool velocity on the diameter. As can be seen in this figure, the maximum velocity is highest for the 700 mm diameter melt pool; however the bottom skull thickness is much greater. In fact, the relationship of the skull thickness, h_{sk}, to the melt pool diameter is virtually a linear relationship, as illustrated in Figure 6-109.

The next series of calculations investigated the behavior of the same geometry systems (i.e., 200 mm melt pool height; 400 mm, 700 mm, and 1,000 mm diameters). The results for the steady state temperature distributions are shown in Figure 6-110.
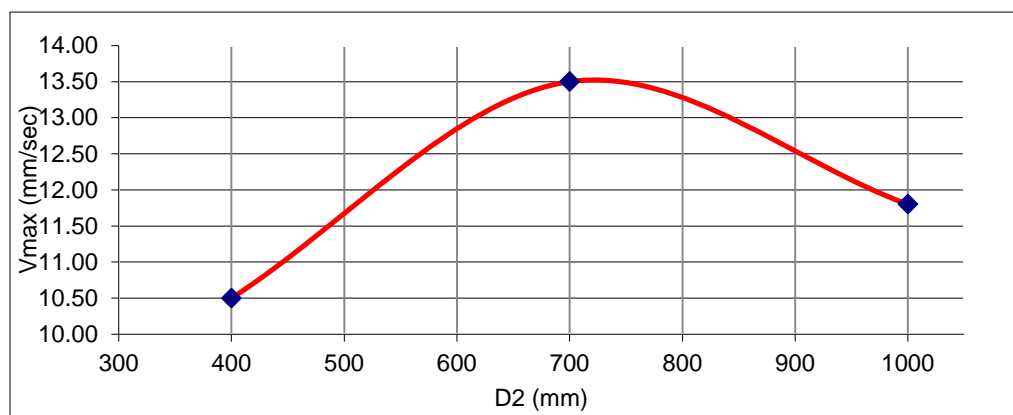
Figure 6-108. Maximum velocity dependence on diameter at 66 kHz frequency.
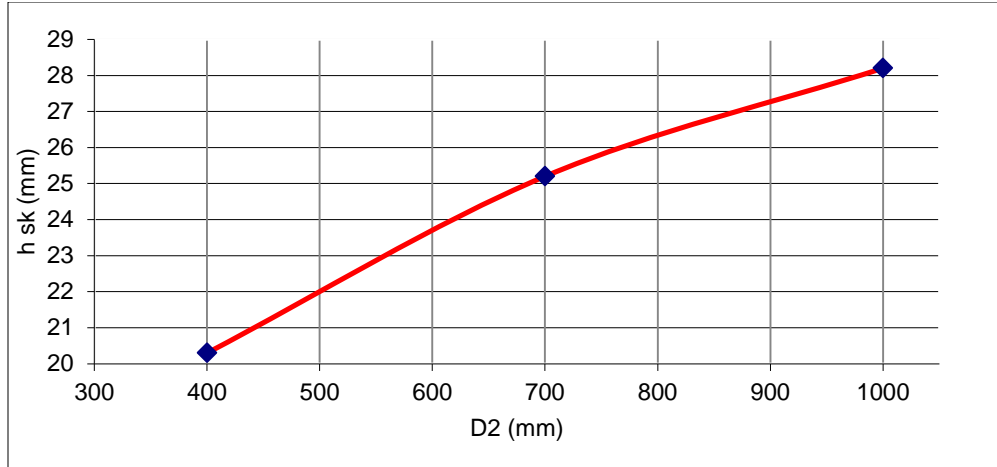
Figure 6-109. Bottom skull thickness dependence on diameter at 66 kHz frequency.

| 400 mm diameter | 700 mm diameter | 1,000 mm diameter |

Figure 6-110. Comparison of temperature profiles for various diameters. 200 mm melt pool height at 300 kHz frequency.
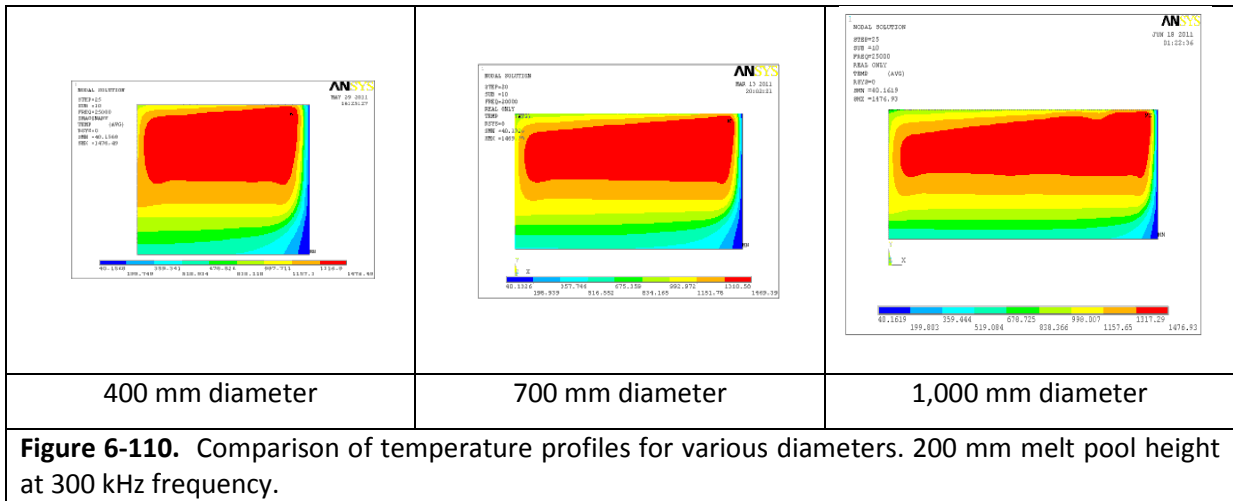
Figure 6-111 shows a comparison of the velocity profiles for the various diameters.

| 400 mm diameter | 700 mm diameter | 1,000 mm diameter |

Figure 6-111. Comparison of velocity profiles for various diameters. 200 mm melt pool height at 300 kHz frequency.
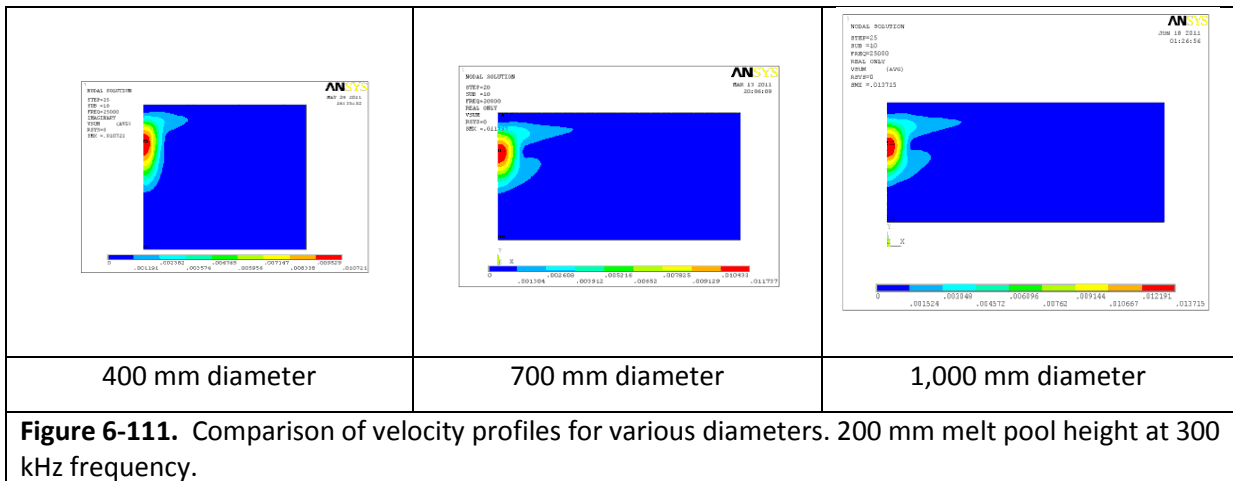
Table 6-10 provides a summary of the key parameters from these calculations.

Table 6-10. Calculation results for melt pool height of 200 mm, current frequency of 300 kHz.

P_2/D_2	33 kW/400 mm	70 kW/700 mm	120 kW/1,000 mm
$T_{max,}$ °C	1,476	1,469	1,476
$T_{s-axis,}$ °C	838	675	678
V_{max} (mm/sec)	10.3	11.7	13.7
h_{sk} (mm)	15.2	21.8	30.3

Dependencies of the maximum velocity and bottom skull thickness for the 300 kHz systems are presented in Figures 6-112 and 6-113, respectively.
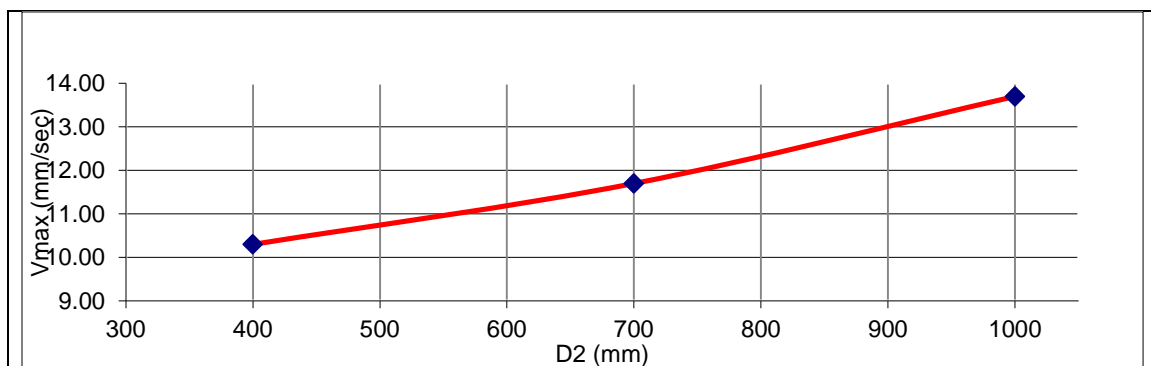
Figure 6-112. Maximum velocity dependence on diameter at 300 kHz frequency.
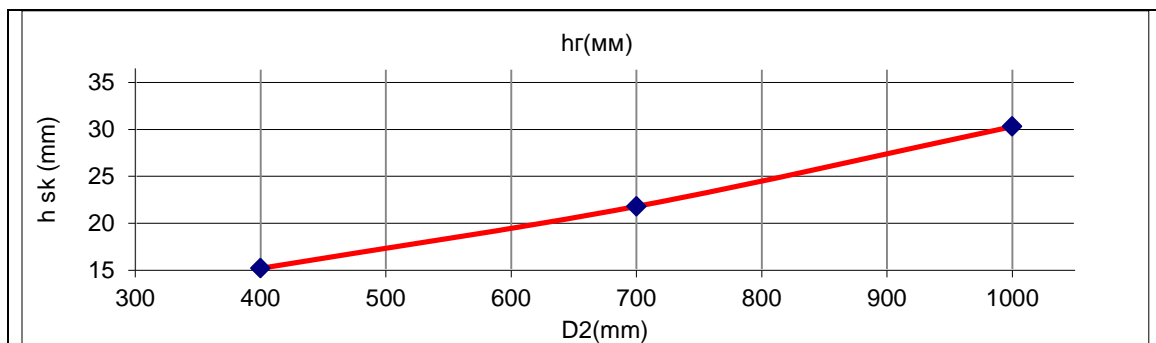
Figure 6-113. Bottom skull thickness dependence on diameter at 300 kHz.

From these figures one can observe that at a melt pool height of 200 mm and current frequency of 300 kHz, the maximum velocity and bottom skull thickness both increase significantly with diameter. This is likely because the higher velocities provide increased convective heat transfer effects at this quasi liquid/solid boundary. As can be seen, both relationships are basically linear with diameter.

The next series of calculations was performed for the same geometry systems at 660 kHz. The temperature and velocity profile comparisons are provided in Figures 6-114 and 6-115.

| 400 mm diameter | 700 mm diameter | 1,000 mm diameter |

Figure 6-114. Temperature profiles for various diameters. 200 mm melt pool height at 660 kHz.

| 400 mm diameter | 700 mm diameter | 1,000 mm diameter |

Figure 6-115. Velocity profiles for various diameters. 200 mm melt pool height at 660 kHz.
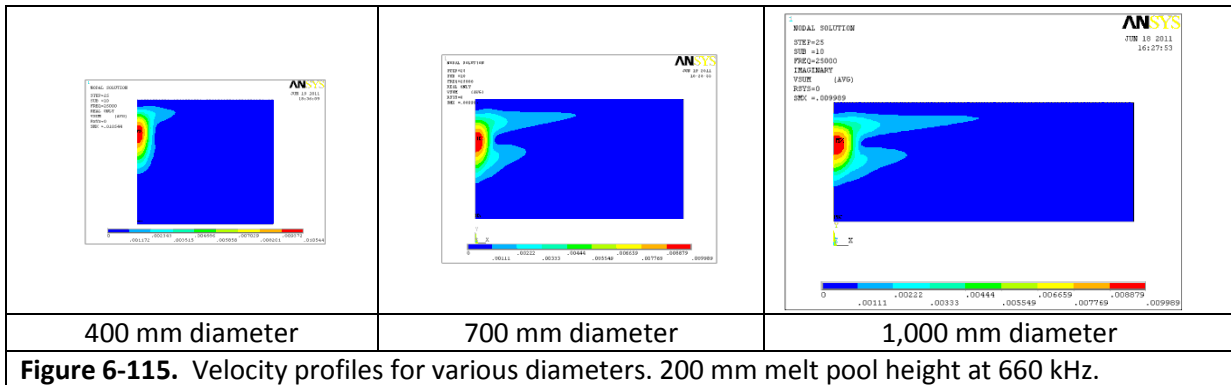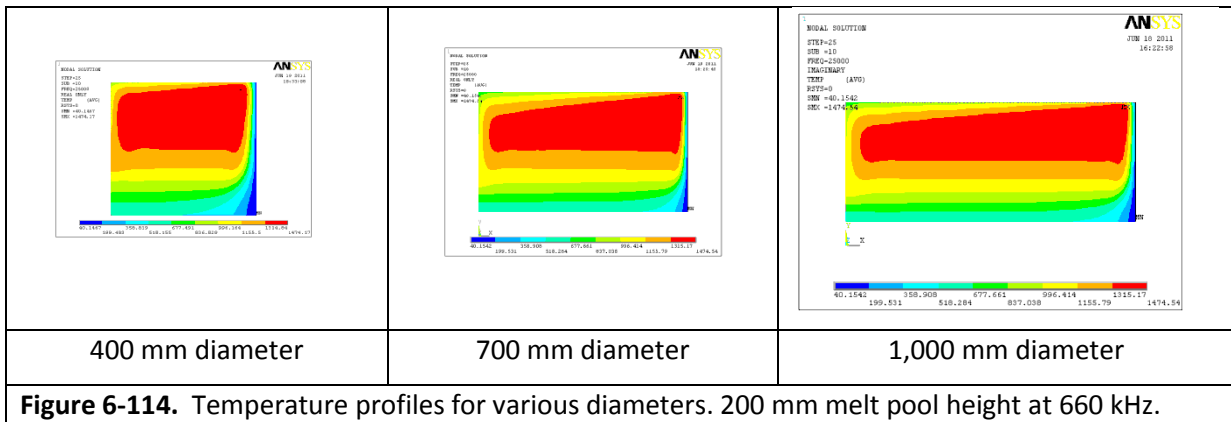
A summary of the results for key parameters is provided in Table 6-11.

Table 6-11. Calculation results for melt pool height of 200 mm, current frequency of 660 kHz.

P_2/ D_2	33 kW/400 mm	70 kW/700 mm	120 kW/1,000 mm
$T_{max,}$ ^oC	1,474	1,474	1,474
T_{s-axis}, ^oC	836	677	677
V_{max} (mm/sec)	10.5	9.90	9.90
h_{sk} (mm)	19.6	29.3	28.5

Figures 6-116 and 6-117 illustrate the dependencies of the velocity and bottom skull thickness on diameter, respectively.

Figure 6-116. Maximum velocity dependence on diameter.

Figure 6-117. Bottom skull thickness dependence on diameter.
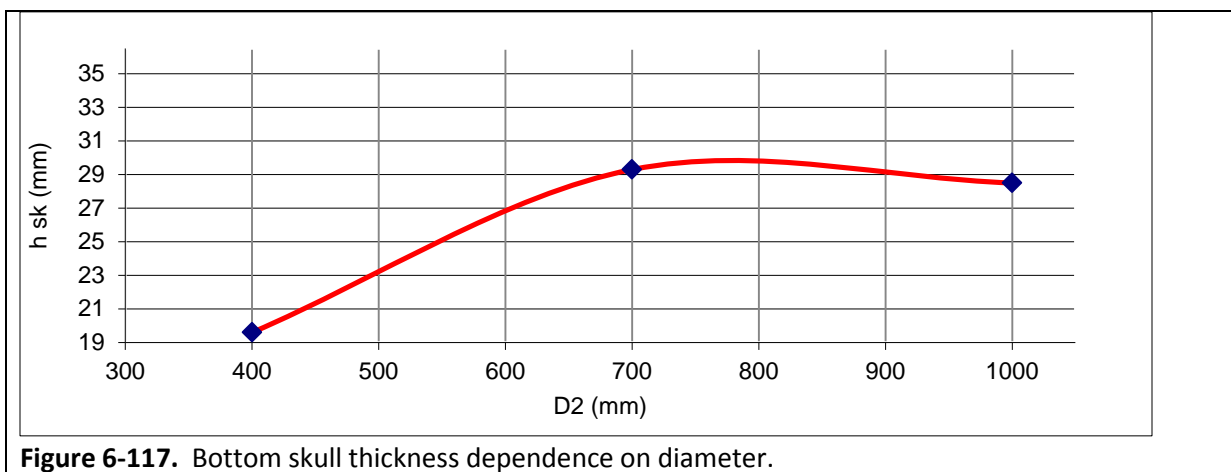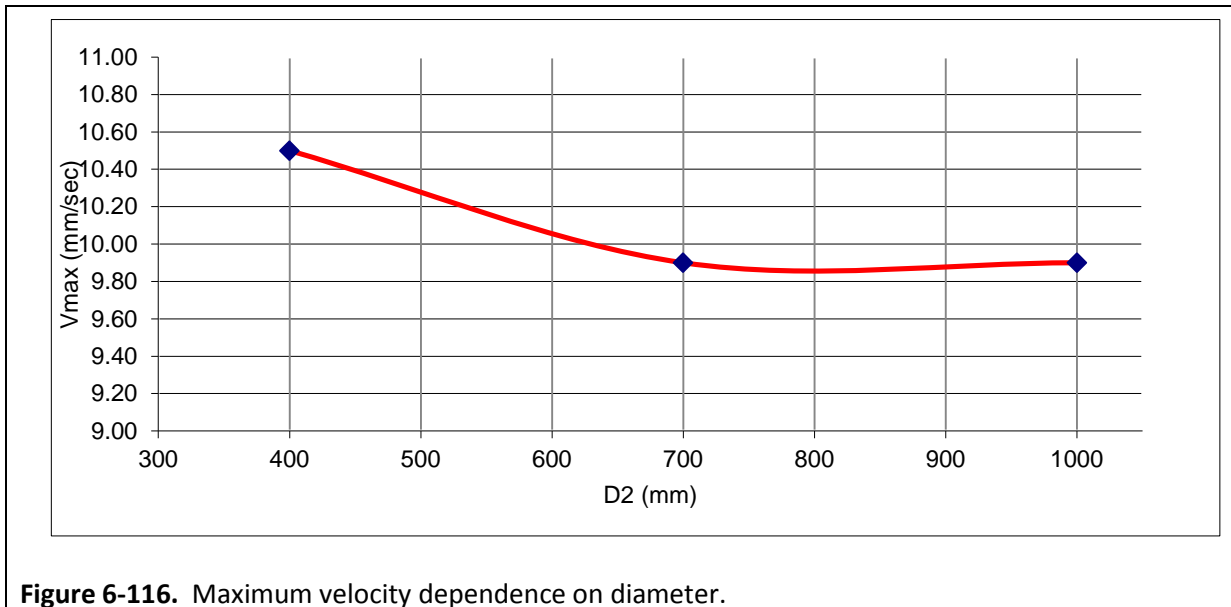
Further comparisons of the preceding results are presented below. Table 6-12 provides a summary of the effect of the diameter and frequency on the maximum velocity in the melt. From these data, and other results presented below, conclusions can be drawn regarding optimum combinations of diameter, frequency, and melt pool height.

Table 6-12. Comparison of V_{max} (mm\sec) for various frequencies and diameters.

Diameter (D2)	Frequency		
	66 KHz	300 kHz	660 kHz
400 mm	10.5	10.3	10.5
700 mm	13.5	11.7	9.9
1,000 mm	11.8	13.7	9.9

Figures 6-118 through 6-120 present this data for each diameter separately.

Figure 6-118. Maximum velocity dependence on frequency for 400 mm diameter melt pool.

Figure 6-119. Maximum velocity dependence on frequency for 700 mm diameter melt pool.

Figure 6-120. Maximum velocity dependence on frequency for 1,000 mm diameter melt pool.
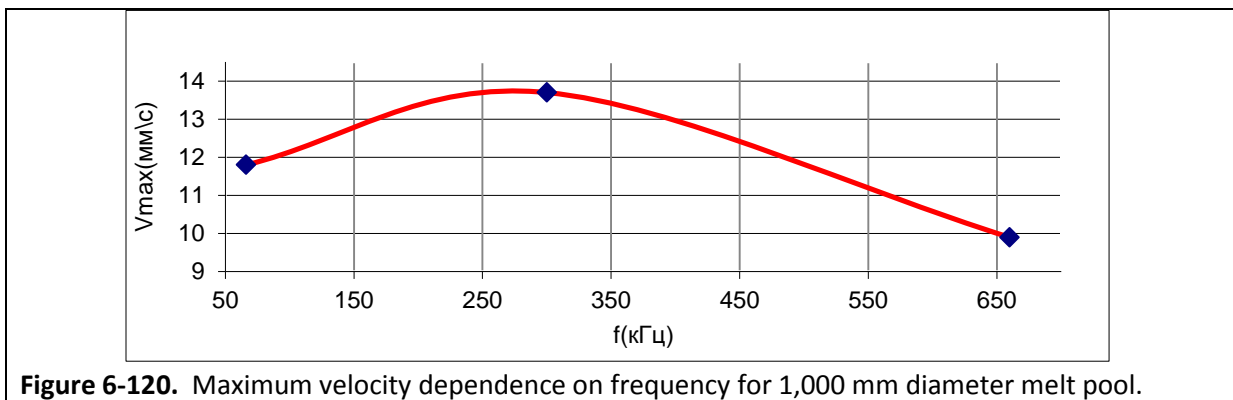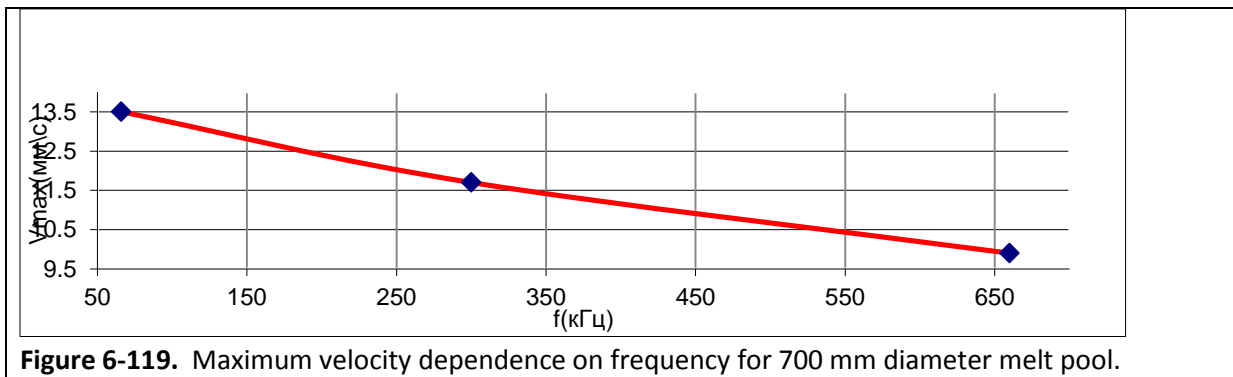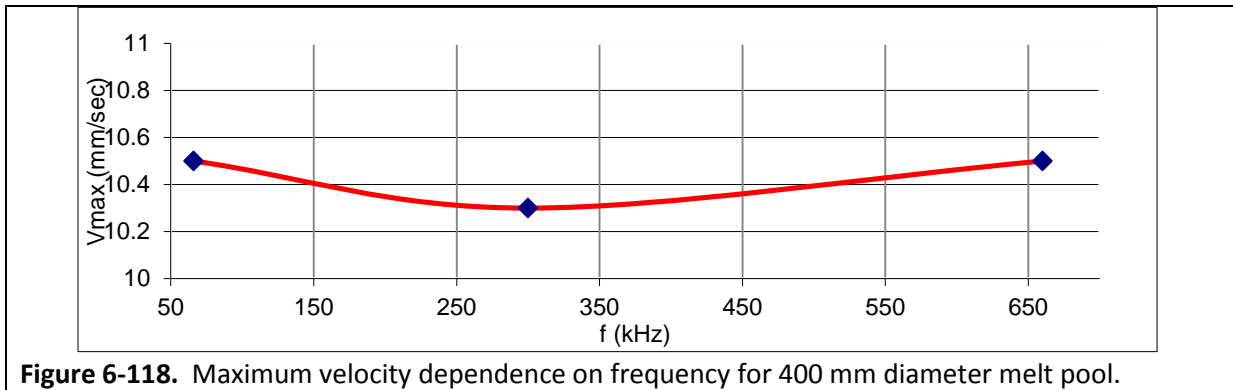
Table 6-13 compares the bottom skull thicknesses for various diameters and frequencies.

Table 6-13. Comparison of h_{sk} (mm) for various frequencies and diameters.

Diameter (D2)	Frequency		
	66 KHz	300 kHz	660 kHz
400 mm	20.3	15.9	19.6
700 mm	25.2	21.8	29.3
1,000 mm	28.2	30.3	28.5

Figures 6-121 through 6-123 present the skull thickness data for each diameter separately.

Figure 6-121. Dependence of bottom skull thickness on frequency for 400 mm diameter.

Figure 6-122. Dependence of bottom skull thickness on frequency for 700 mm diameter.

Figure 6-123. Dependence of bottom skull thickness on frequency for 1,000 mm diameter.
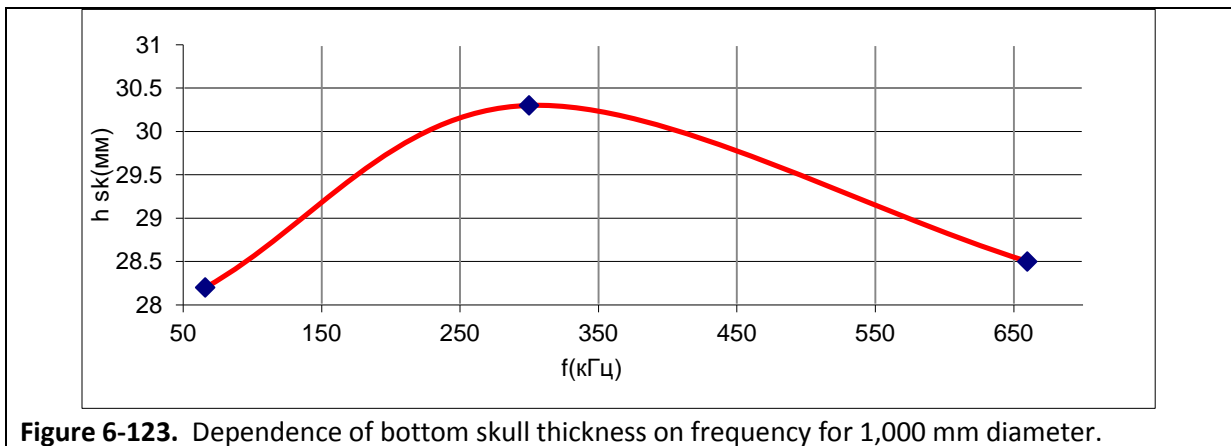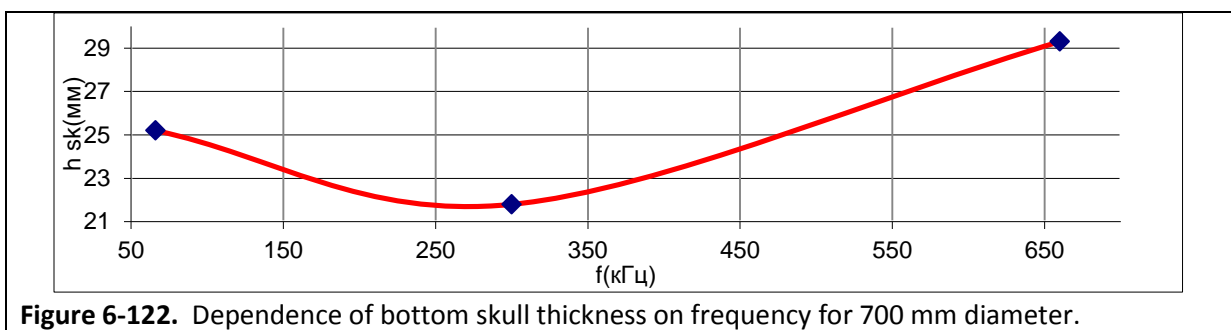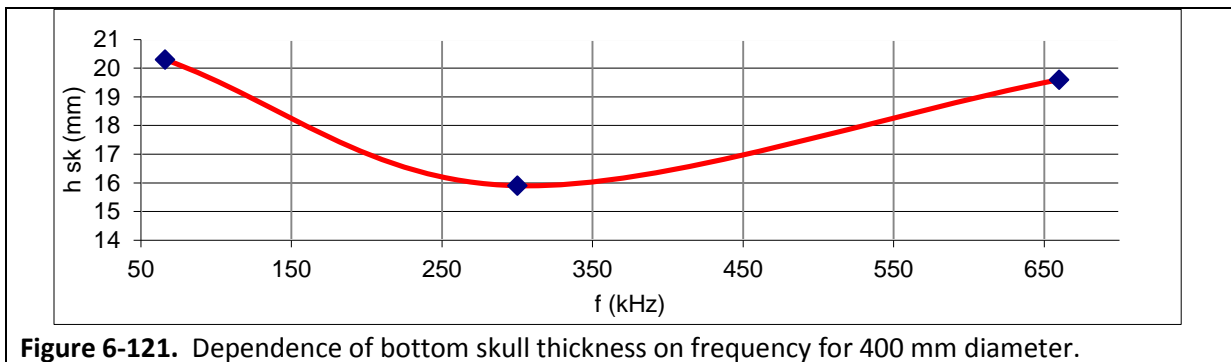
The final series of calculations performed to better understand the relationship between diameter, frequency, and melt pool height involved investigation of a 1.0 m diameter melt pool with varying melt pool heights for a fixed frequency of 300 kHz. All parameters were the same as previous calculations except for the power level for the 0.5 m melt pool height, for which it was increased to 130 kW from 120 kW. The temperature distributions are shown in Figure 6-124.

| 200 mm height | 300 mm height | 500 mm height |

Figure 6-124. Comparison of temperature distributions for various melt pool heights in 1,000 mm diameter melter at 300 kHz.
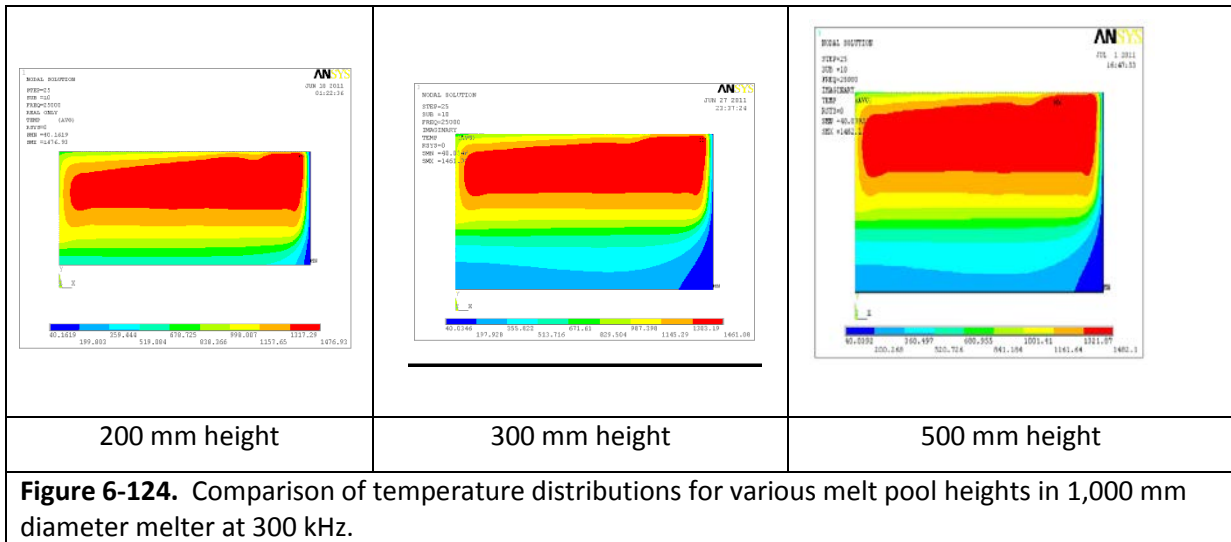
Similarly, Figure 6-125 provides a comparison of the total melt velocity profiles for the various melt pool heights.

| 200 mm height | 300 mm height | 500 mm height |

Figure 6-125. Comparison of velocity profiles for various melt pool heights in 1,000 mm diameter melter at 300 kHz.
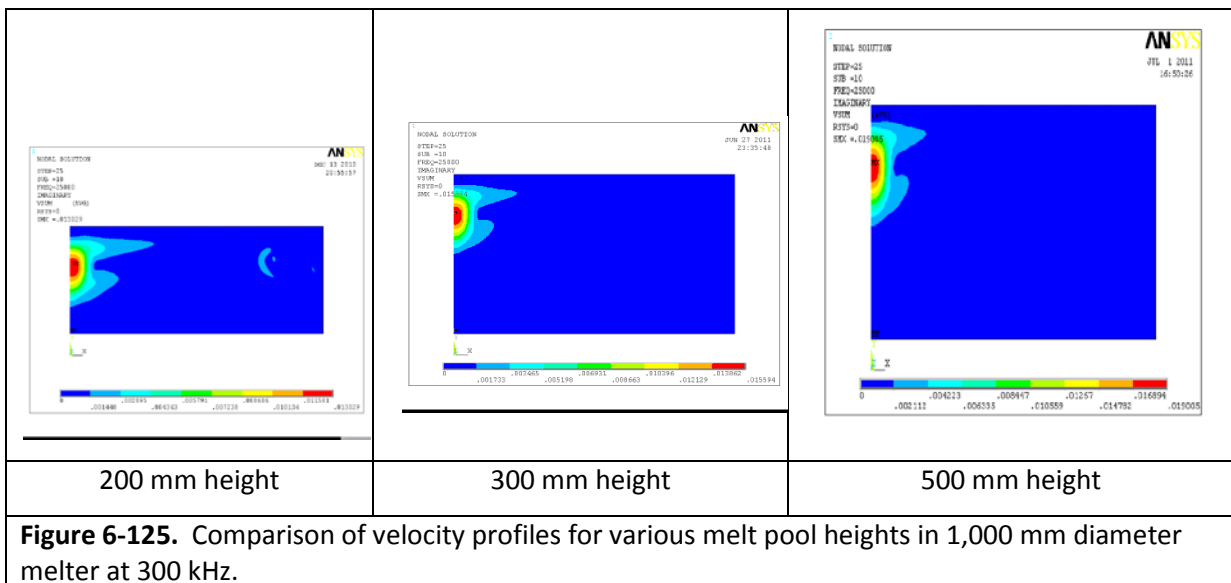
Table 6-14 provides a summary of the preceding results for several key parameters.

Table 6-14. Calculation results for melt pool diameter of 1,000 mm, current frequency of 300 kHz.

Melt pool height	200 mm	300 mm	500 mm
T_{max}, $^{\circ}C$	1,476	1,461	1,482
$T_{s\text{-}axis}$, $^{\circ}C$	678	671	680
V_{max} (mm/sec)	13.7	15.6	19.0
h_{sk} (mm)	30.3	56.0	78.1

Figure 6-126 presents the summary data from Table 6-14 in a graphical format for the dependence of the maximum velocity on the melt pool height for a melt diameter of 1,000 mm at 300 kHz. Similarly, Figure 6-127 shows the dependence of the bottom skull thickness on the melt pool height. Again, this is for a melter of 1,000 mm diameter at 300 kHz current frequency.

Thus, from these figures one can observe that for this configuration, although the velocity is increased at greater melt pool height, the bottom skull thickness increases dramatically, impeding bottom casting.

Based on the combined results of the preceding analyses, several key conclusions can be made related to an optimal configuration for this particular BSG. For a glass with the properties of the BSG
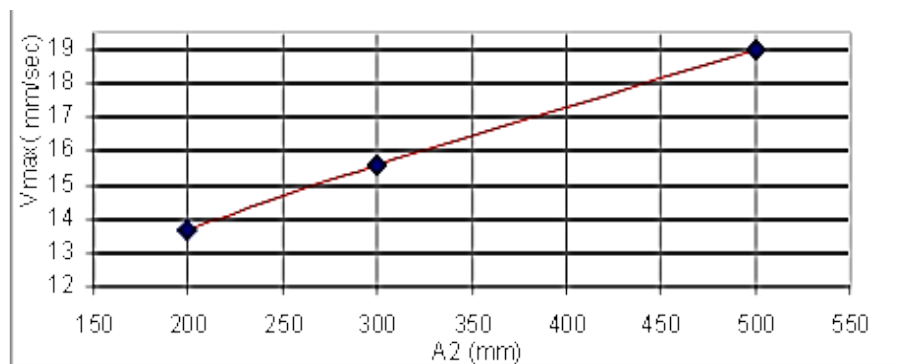
Figure 6-126. Maximum velocity dependence on melt pool height.
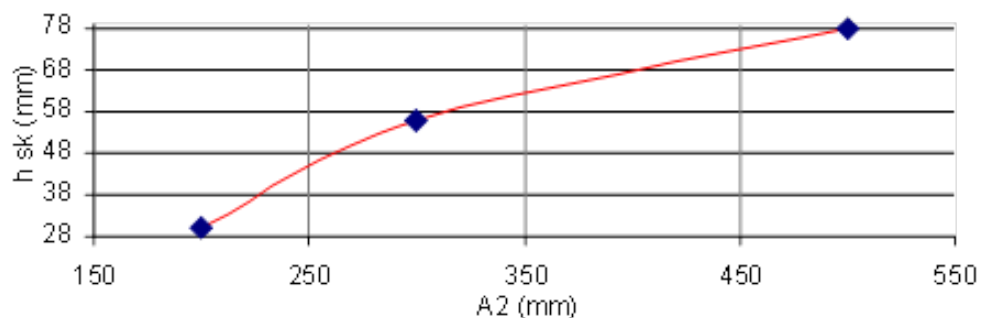
Figure 6-127. Bottom skull thickness dependence on melt pool height.

being used in the model and experimental work for this effort, the parameters defined in Table 6-15 are expected to provide an optimal system design for scale-up of a CCIM system that includes induction casting capabilities.

Table 6-15. Optimal parameters for scale-up of a CCIM with induction casting.

Parameter	Optimal Range
Cold crucible diameter	700 mm to 1,000 mm
Melt pool height	200 mm to 300 mm
Current frequency	300 kHz to 500 kHz

These parameters will provide the best conditions for bottom casting, while reducing the skin effect and thus providing more homogeneous temperature distributions. Finally, these parameters also provide more efficient energy use, and thus more reliable operation of the generator.

The preceding results are very significant because they can be directly applied to design of large diameter, industrial scale CCIM systems. This research illustrates the important relationships between diameter, frequency, and melt pool height for designing a large scale optimized CCIM system for processing of refractory oxides, such as BSG, as well as other formulations such as iron phosphate glasses and alumino-silicate glass ceramics. If similar studies have been conducted, they have not been published and thus were not available for reference or comparison.

CHAPTER 7.CCIM TESTING FOR MODEL VALIDATION AND DEFINITION OF PARAMETERS

Five initial tests were conducted to help validate the model, as well as to refine boundary conditions and other model parameters. These tests were performed in a 300 mm diameter CCIM platform without any draining device integrated into it. The crucible walls are constructed of stainless steel, 16 mm outside diameter tubing with 1.5 mm wall thickness, and the bottom is constructed of a low-carbon alumino-silicate refractory brick, referred to as chamotte. The stainless steel was selected because the potential application for the technology is for processing chemically corrosive slurries. The reason that a chamotte bottom was selected, over a water-cooled bottom, was to be able to keep the bottom as hot as possible to support the goal of initiating inductively heated bottom draining. The primary purpose of these tests was to compare the characteristics in the melt volume, especially near the bottom center of the crucible, to investigate the effects of changes in coil geometry (i.e.. two-turn versus three-turn), the melt pool depth, and the effect of a lid on the melter. This last investigation was performed for two reasons: 1) to obtain full calorimetry on the CCIM system to establish an energy/power balance (which provided data for determining the initial melt surface boundary conditions); and 2) although much of the testing requires access to the melter for temperature measurements, adding frit, etc., in practice, the melter will generally be covered. This will impact the overall thermal distribution, and thus the melt characteristics. In addition, these tests were used to take melt temperature measurements using the thermocouple array assembly described earlier, for eventual comparison to modeling results. The initial thermocouple array assembly included only five Type K thermocouples, but this was later expanded and enhanced to include eight Type K. and eventually Type S thermocouples. During the test, the generator was switched off for a few seconds to eliminate the coupling of the thermocouple components with the induction field and skewing the measurement. This approach was very effective. The tests are described below.

7.1. CCIM Test #1

CCIM Test #1 was conducted using a three turn inductor. A maximum temperature of 1,200^{o}C was maintained after steady state was achieved. This was determined by a traditional approach of dipping a thermocouple just below the surface skin in the brightest hot spot on the surface. Data logged during the test for various parameters are in Appendix C. Figure 7-1 shows the test set-up. The calorimetry data collected during the test are shown in Table 7-1.

Table 7-1. Calorimetry data from CCIM Test #1 for 1,200°C, with a three-turn inductor.

Component	Power, kW	Power in the melt, kW	Specific thermal flux to crucible side, W/cm²
Crucible	19.6		13.9*
Crucible lid	0.86	20.5	-
Inductor	0.28	-	-

Note: * includes radiation losses from melt onto side walls of crucible.

Figure 7-1. Test setup for CCIM Test #1.

Figure 7-2. Melt pool surface at steady state for CCIM Test #1

Figure 7-2 shows the melt pool surface during the CCIM Test #1 at steady state. Note the "under-heating" of the center of the melt

Figure 7-3 shows the glass ingot removed from the crucible after cooling. The left side is the full

Figure 7-3a. Full ingot from CCIM Test #1.

Figure 7.3b. Cross-section of ingot from CCIM Test #1.

ingot and the right side shows the cross-section. There is a thick crystalline phase in the center at the bottom that will clearly present challenges for bottom casting. Subsequent research and testing led to design changes to improve this condition. These are discussed as applicable.

7.2. CCIM Test #2

From the results of CCIM Test #1, the design for CCIM Test #2 included two primary changes: 1) a two-turn inductor versus a three-turn, and 2) multiple steady state modes including 1,350^{o}C, 1,150^{o}C, and 1,000^{o}C maximum surface temperatures (note that no surface film exists at 1,350^{o}C). Additionally, an apparatus was installed that allowed obtaining temperature profile measurements through the melt volume. Much of the details of these experimental results were described in Chapter 2 and will only be discussed briefly, as appropriate. The set-up for CCIM Test #2 is shown in Figure 7-4 (same as Figure 2-9, but repeated here for convenience). This figure shows the system after steady state has been achieved for the first mode of 1,350^{o}C. Figure 7-5 shows the inside of the CCIM as the thermocouple array is being lowered into the melt.
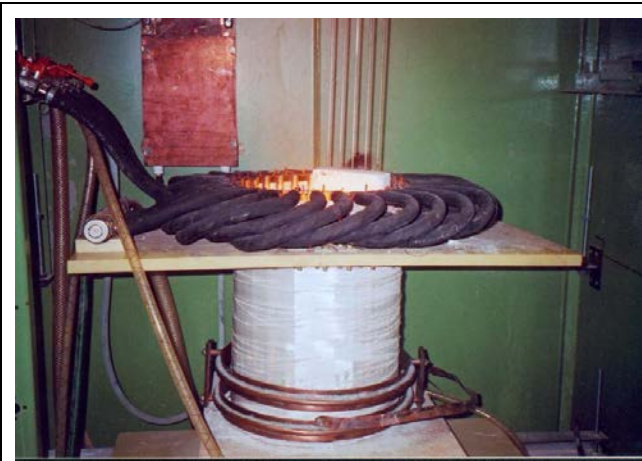
Figure 7-4. CCIM Test #2 Set-up – 300 mm diameter with two-turn inductor.
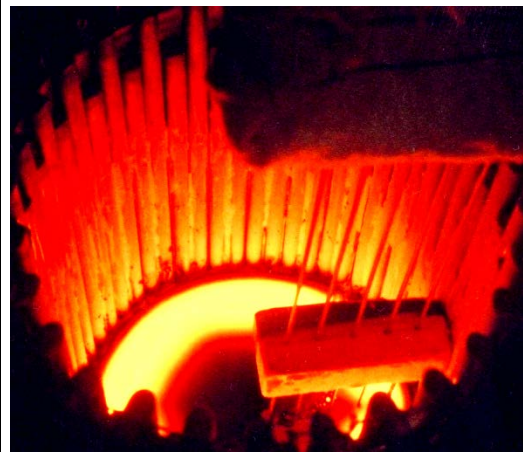
Figure 7-5. Temperature distribution measurement during CCIM Test #2.

Temperature profile data from this experiment were reported earlier in Table 3-20. This was the first experiment in which the temperature profile data were collected. Temperature profile measurements were repeated in several subsequent experiments such that adequate data could be used for comparison with the modeling results for validation, as well as to improve the approach to provide better temperature profile data. Other key data obtained during CCIM Test #2 are given in

Appendix C. Table 7-2 provides the calorimetry data collected for the various modes established during the test.

Table 7-2. Calorimetry data resulting from CCIM Test #2.

Mode No.	Component	a_2, cm	T_{melt}, ^{o}C	Power, kW	Power in melt, kW	Thermal flux to crucible, W/cm^2
1	Crucible	10.5	1,350	15.51	16.28	16.46[***]
	Crucible lid			0.77		-
	Inductor			0.35	-	-
2	Crucible	9.0	1,150[*] 1,280[**]	11.08	11.39	13.44[***]
	Crucible lid			0.31		-
	Inductor			0.28	-	-
3	Crucible	9.0	1,000[*] 1,180[**]	8.24	8.51	10.04[***]
	Crucible lid			0.27		-
	Inductor			0.21	-	-

Notes: * Melt surface maximum temperature measurement.
          ** Melt maximum temperature measurement under glass cold film.
          *** Includes conduction and radiation heat transfer

Figure 7-6 (previously provided as Figure 3-30, but repeated here for convenience) shows the ingot removed from CCIM Test #2. This shows a thick glass-ceramic layer near the bottom. During disassembly, the glass had to be chipped away from the chamotte bottom. This was due to interaction between the glass melt and the ceramic brick. This situation was later predicted by the ANSYS model.

Glass-ceramic crystalline material

Figure 7-6. Ingot from CCIM Test #2 two-turn inductor.
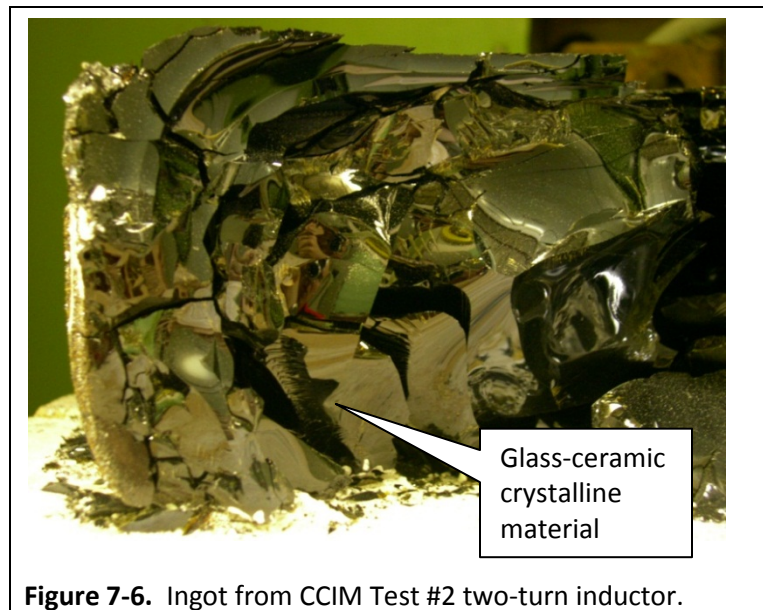
Based on these results, a decision was made to conduct more comprehensive experiments in the three-turn inductor CCIM system.

Varying temperature modes and melt depths were investigated to determine their impacts on the operational parameters and the temperature distribution. Additional calorimetry data were also obtained during these tests. The test details and results are described in the following discussions.

7.3. CCIM Test #3

CCIM Test #3 was accomplished using the same 300 mm diameter stainless steel crucible with a three-turn inductor as used in CCIM Test #1. For this test, a lower nominal maximum temperature (i.e.. on the surface) was used to collect temperature profile data. The thermocouple array was expanded to include eight thermocouples for this test and the depth change increments were reduced to 1 cm, resulting in more data points. Figure 7-7 shows the thermocouple array being deployed during the test.
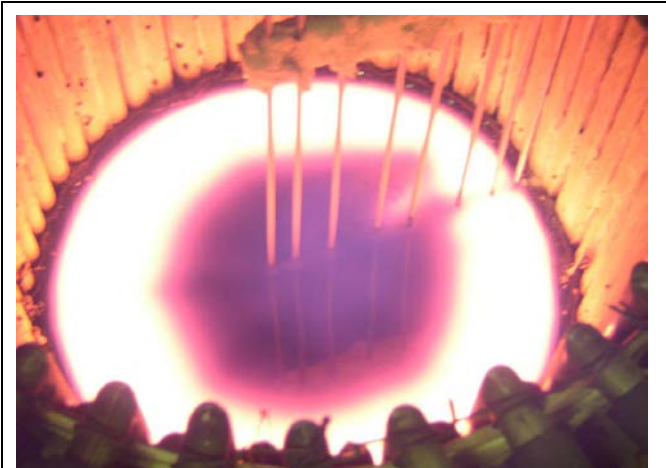
Figure 7-7. CCIM Test #3 Thermocouple Array

These measurements resulted in additional temperature profile data, as well as other key operational parameters. These are reported in Appendix C. Also, the heat flux into the chamotte bottom was estimated through a power balance (since it is not water-cooled for more direct measurement). This approach was improved in later experiments for more precise determination of the heat flux into the chamotte bottom.

The calorimetry data was obtained during CCIM Test #3 for steady state modes of 1,010^{o}C and 1,080^{o}C at a nominal melt pool depth of 155 mm. The results of these measurements are shown in Table 7-3.

Table 7-3. Calorimetry data resulting from CCIM Test #3, melt pool depth at 155 mm.

Time, hr:min	T_{melt}, ^{o}C	U_{ind}, kV	P_{ind}, kW	P_{cc}, kW	P_{lid}, kW	P_{bot}, kW	P_{tot}, kW	$P_{0\,side}$, W/cm^2
19:10	1,010	2.4	0.229	18.92	1.39	0.553	21.092	13.9
19:30	1,080	2.5	0.256	22.70	1.43	0.553	24.922	16.5

($P_{0\,side}$ is specific thermal flux from melt to crucible side including losses by radiation from the melt to the crucible side. T_{melt} is maximum surface temperature, U_{ind} is voltage on the inductor, P_{ind} is electrical losses in the inductor, P_{cc} is power into the cold crucible, P_{lid} is power into the lid, P_{bot} is power into the bottom, and P_{tot} is total power)

The glass ingot resulting from CCIM Test #3 is shown in Figure 7-8. Notice the thick bottom skull resulting from the lower temperature modes.

Figure 7-8a. Full ingot from CCIM Test #3.   **b**. Cross-section of ingot from CCIM Test #3.
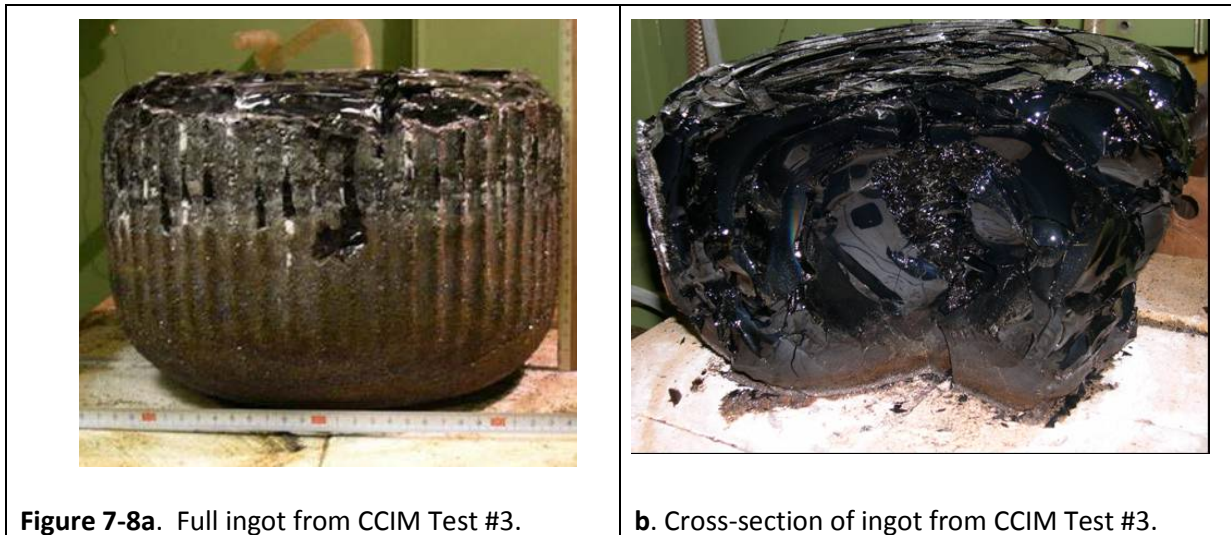
7.4. CCIM Test #4.

The three-turn inductor CCIM system was also used for CCIM Test #4. It had the same configuration as the previous test. The purpose of this test was to determine the effects of higher operating temperatures on the bottom skull thickness. This was achieved in two ways. First, a higher temperature mode was established for conducting one of the calorimetry tests, specifically 1,300^{o}C. Calorimetry was also taken at 1,027^{o}C and 965°C, including temperature profile measurements. The calorimetry data are discussed below. Other key data collected during the test are reported in Appendix C.

Table 7-4 shows a summary of the calorimetry data collected for the three modes identified above. These results continue to add to the data already collected for determining optimal operational conditions to ensure the feasibility of inductively heated bottom casting, as the efforts transition to modeling, design, and testing of integrated systems.

Table 7-4. Calorimetry data from CCIM Test #4, melt pool depth of 150 mm.

Time, hr:min	f, MHz	T_{melt}, ^{o}C	U_{ind}, kV	P_{ind}, kW	P_{cc}, kW	P_{lid}, kW	P_{bot}, kW	P_{tot}, kW	$P_{0\,side}$, W/cm^2
17:17	1.75	1,300	2.78	0.138	17.9	1.36	0.371	19.77	13.6
17:30	1.74	1,027	2.24	0.119	17.7	1.26	0.371	19.45	13.4
17:48	1.74	965	2.18	0.112	15.92	1.214	0.371	17.62	11.3

Figure 7-9 shows the test set-up during collection of the calorimetry data. The cover design shown was later improved for more accurate measurement.

Figure 7-9. Initial CCIM lid used for calorimetry data collection.

Figure 7-10 shows the thermocouples being deployed for temperature distribution measurements. This was for the lowest mode (i.e., 965°C). Note how viscous the melt surface appears.
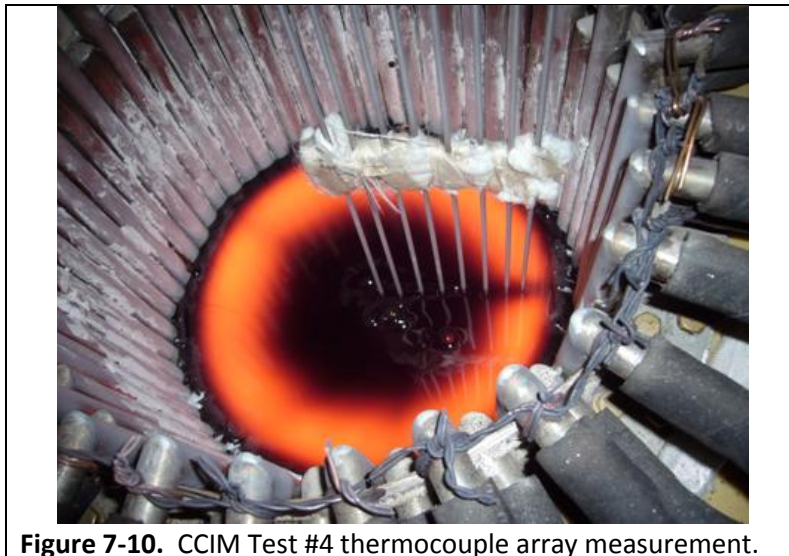
Figure 7-10. CCIM Test #4 thermocouple array measurement.

However, due to the sustained higher temperature operating modes and longer calorimetry times, the melt was able to obtain more homogeneous, higher temperature distributions. This resulted in a much thinner bottom skull, as can be seen in Figure 7-11.

Figure 7-11 a. Full ingot from CCIM Test #4.   **b.** Cross-section of ingot from CCIM Test #4.
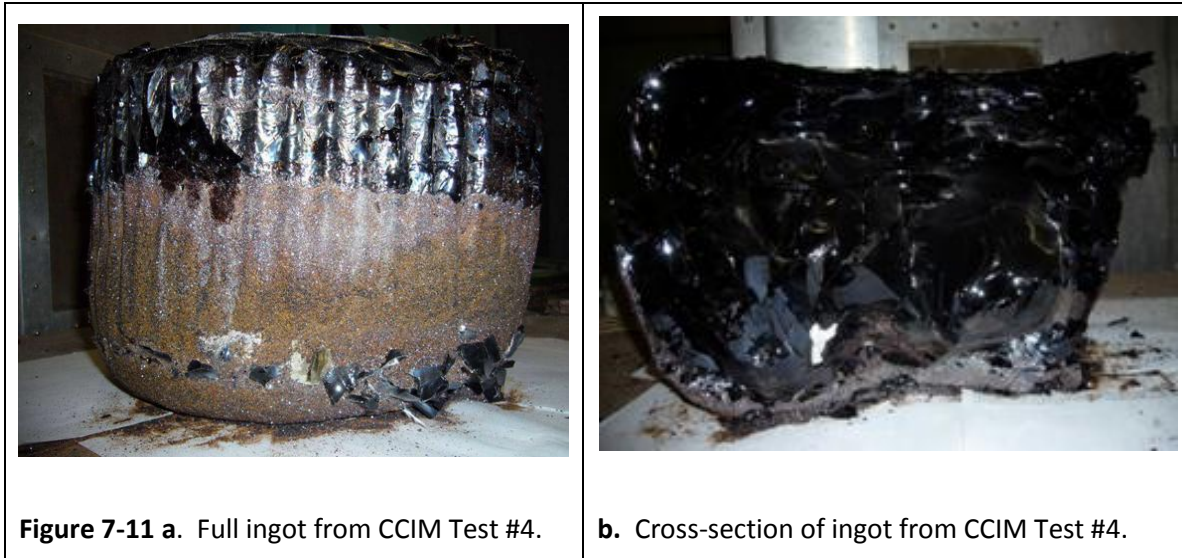
Table 7-5 provides a comparison of results from three different tests in the same CCIM configuration (i.e., three-turn inductor) at four different operational modes. The results are very consistent. Minor differences are likely due to slight variations in the melt pool height and overall measurement errors. This provides high confidence for implementation into the model as boundary conditions.

Table 7-5. Comparison of key calorimetry data from various tests.

Test	f, MHz	a_2, mm	T_{melt}, ^{o}C	U_{ind}, kV	P_{tot}, kW	$P_{0\,side}$, W/cm^2
#4	1.74	150	965	2.18	17.62	11.3
#3	1.95	155	1,010	2.11	21.09	13.9
#4	1.74	150	1,027	2.24	19.45	13.4
#1	1.87	150	1,050	2.37	20.73	13.86

7.5. CCIM Test #5

CCIM Test #5 was also conducted using the 300 mm stainless steel crucible, with a three-turn inductor. The test had several objectives: 1) to develop additional temperature distribution data, 2) to improve the understanding of the bottom thermal flux boundary condition, and 3) to further characterize the conditions of the bottom layer for a deeper melt volume (i.e.. 180 mm depth) to understand the limits for inductive bottom casting. During this test three steady state modes of 1,200^{o}C, 1,190^{o}C, and 1,150^{o}C were established and data taken.

For this test, specially made quartz sheathed platinum-platinum/rhodium thermocouples were used so they would last longer than the Type K thermocouples in the higher temperatures. These assemblies did perform better, although they failed eventually. However, this experiment did provide the most comprehensive temperature distribution data of all the tests. The thermocouple assembly is shown in Figure 7-12. The thermocouples are approximately 18.6 mm apart, with the inner most aligned with the central axis of the crucible.

Figure 7-12. CCIM Test #5 Pt-Pt/Rh thermocouple array.

Thermocouples were also installed at two locations along the bottom for the purpose of determining more accurate values of the heat flux to the chamotte brick. These were Type K (i.e.. nickel-chromium/nickel-aluminum junction) because the temperatures along the bottom are well within the operational range for these thermocouples. The thermocouples were installed such that one junction was on the crucible axis and one was approximately 100 mm from the central axis. This is shown in Figure 7-13 (the left side was previously shown in Figure 2-8, but is repeated here for convenience).

Figure 7-13. CCIM Test #5 thermocouple placement on the bottom surface.

The calorimetry data collected during CCIM Test #5 are provided in Table 7-6. The temperature distribution and other key data obtained during CCIM Test #5 are provided in Appendix C.

Table 7-6. Calorimetry data from CCIM Test #5. melt pool depth of 180 mm.

Mode	U_a, kV	I_a, A	I_g, A	U_{cont}. kV	T_{melt}, °C	P_{cc}, kW	P_{lid}, kW	P_{ind}, kW	P_{bus}, kW	P_{bot}, kW	$P_{a\ ind}$, kW
1	7.02	3.61	0.97	2.40	1,200	21.9	0.702	0.307	0.153	0.665	23.6
2	7.15	3.55	1.01	2.45	1,190	21.4	0.679	0.293	0.135	0.695	23.0
3	6.36	3.12	0.90	2.15	1,150	18.1	0.590	0.251	0.160	0.735	19.6

Note: U_{cont} is voltage on the capacitor bank (i.e., referred to as the "contour").

The temperature data collected from the bottom two thermocouples, in conjunction with the temperature data from thermocouples #1 and #5 in the array assembly (i.e., located directly above the thermocouples on the bottom) were used to determine the heat flux through the bottom.

Table 7-7 shows the actual measurements of the respective thermocouples for each of the steady state modes established.

Table 7-7. CCIM Test #5 temperature measurements for bottom heat flux determination.

Mode #	$T_{tc\ bot\ 1}$, °C	$T_{tc1-5cm}$, °C	$T_{tc1-10cm}$, °C	$T_{tc\ bot\ 2}$, °C	$T_{tc5-5cm}$, °C	$T_{tc5-10cm}$, °C
1	352.1	736.3	1,251	529.4	753.7	1,240
2	347.8	712.8	1,160	472.8	733.4	1,156
3	349.9	737.4	1,137	467.7	845.5	1,080

Note: $T_{tc\ bot\ 1}$ is the thermocouple located on the bottom at the axis.
$T_{tc1-5cm}$ and $T_{tc1-10cm}$ is the #1 thermocouple (i.e., on the axis) located at 5 cm and 10 cm above the bottom, respectively.
$T_{tc\ bot\ 2}$ is the thermocouple located on the bottom at a radial distance of 10 cm from the axis.
$T_{tc2-5cm}$ and $T_{tc2-10cm}$ is the #5 thermocouple (i.e., near 10 cm from the axis) located at 5 cm and 10 cm above the bottom, respectively.

Table 7-8 and Table 7-9 demonstrate the calculated heat flux and resulting "effective" coefficient of thermal conductivity in the two zones for the given modes. While this value was determined using Fourier's Law, it is referred to as λ since it actually includes conductivity, radiation, and convection effects.

If one assumes that the conditions for the axial location in Table 7-9 are representative of a radial area from the center out to 7.5 cm and the conditions for the peripheral location in Table 7-8 are

representative of a radial area between 7.5 cm and 15 cm, these constitute areas equal to 176.6 cm^2 and 529.9 cm^2, respectively. (Note, this was the approach used to determine the λ values.)

Table 7-8. CCIM Test #5 calculation of effective thermal conductivity coefficient for chamotte bottom near periphery.

Mode #	$T_{tc1\text{-}5cm}$ - $T_{tc\,bot\,1}$	$(T_{tc1\text{-}5cm} + T_{tc\,bot\,1})/2$	$\lambda_{mid1\,0\text{-}5cm}$. W/m-K	$P_{0\,bot1\text{-}5cm}$. W/m^2
1	384.2	544.2	1.4	10,760
2	365.0	530.3	1.5	10,950
3	387.5	543.7	1.4	10,850

Table 7-9. CCIM Test #5 calculation of thermal conductivity coefficient for chamotte bottom near center axis.

Mode #	$T_{tc5\text{-}5cm}$ - $T_{tc\,bot\,2}$	$(T_{tc5\text{-}5cm} + T_{tc\,bot\,2})/2$	$\lambda_{mid2\,0\text{-}5cm}$. W/m-K	$P_{0\,bot5\text{-}5cm}$. W/m^2
1	224.3	641.5	1.2	5,383
2	260.5	603.1	1.25	6,514
3	377.8	656.6	1.2	9,068

The specific heat fluxes through these two areas (Table 7-9) were determined using these values and the following equations:

$$P_{0\,bot\,1-5cm} = \frac{\lambda_{mid\,1\,0-5cm}(T_{tc1-5cm} - T_{tc\,bot\,1})}{0.05} \qquad (7-1)$$

and

$$P_{0\,bot\,2-5cm} = \frac{\lambda_{mid\,2\,0-5cm}(T_{tc5-5cm} - T_{tc\,bot\,2})}{0.05} \qquad (7-2)$$

These were then used to determine the total heat loss through the bottom. Thus, for the various modes the following results are obtained:

Mode 1: P_{bot} = 1.076 x 529.9 + 0.5883 x 176.6 = 665 W

Mode 2: P_{bot} = 1.095 x 529.9 + 0.6514 x 176.6 = 695 W

Mode 3: P_{bot} = 1.085 x 529.9 + 0.9068 x 176.6 = 735 W

These results provided useful data for defining boundary conditions in the ANSYS® model development and validation efforts.

CHAPTER 8.   INDUCTIVELY HEATED DRAIN SYSTEM DESIGN AND PROOF-OF-PRINCIPLE TESTING

As previously stated, the modeling and experimental efforts were conducted in an iterative approach, the results of each being used to enhance and advance the progress of the other. The work was focused in two main areas, development of the inductively-heated draining system, and scale-up studies. This chapter focuses on the design and testing of the inductively heated drain system.

8.1. Inductively Heated Drain System Preliminary Design

Prior to having a validated model to use for design optimization, the basic parameters had to be determined as a starting point for experimental work. Based on the material properties defined earlier, we know that at 1,200°C, the resistivity, ρ_e, is approximately 0.04 ohm-m. This also correlates to a temperature for this glass composition that provides an acceptable viscosity (~3 Pa-s) for casting. Using this information, some key geometry can be evaluated. If the oscillation frequency, ω, is assumed to be nominally 30 MHz, then using equation 3-5, we can obtain:

$$\delta = 503 \sqrt{\frac{0.04}{30,000,000}} = 0.0184\ m = 1.84\ cm \tag{8-1}$$

(Note that the frequency was assumed at 30 MHz based on the potential equipment that was available to conduct the testing, which was a nominal 27 MHz, 4 kW generator. Modification of this equipment was necessary to support the planned experiments, and the effects of these circuitry changes on the oscillation frequency were not known. However, as the experimental work proceeded, the actual oscillation frequency for the drain generator was shown to range between 27 MHz and 28 MHz.)

As previously discussed in Ch. 4, the optimum ratio between the diameter and skin depth is actually a range, depending on other factors of the system, such as scale or aspect ratio (i.e., melt pool depth to diameter). For intermediate sized systems that have been investigated in the past, a range for "ma" has generally been accepted as 3 to 5. However, due to the very small diameter of this system, as well as unknown operational characteristics, estimates of potential drain diameters were initially determined using a broader range of 2 to 7 for "ma". Using this range for "ma", a range for the diameter can be estimated using the following equation:

$$d_{drain} = (2 \ldots 7) \times 1.84\sqrt{2} = 5.2 \text{ to } 18.2 \text{ cm} \tag{8-2}$$

For obvious reasons, the diameter of the drain outlet will be at the lower end of this range due to the rate at which the molten glass would discharge from a large diameter opening, and the resulting amount of glass required to conduct the experiments. Additionally, the temperature at discharge is likely to be higher than 1,200°C, due to the frozen glass plug that will be located in the opening that will require melting through. Thus, the δ is expected to be smaller, and accordingly the range of optimal diameter. However, due to the limitations of the available equipment, the experimental setup does not represent an optimal geometry (i.e., a higher frequency would be more ideal). This was demonstrated in the various experimental results, and thus engineering aids to the draining process were identified and tested. These results are presented in more detail later.

Figure 8-1. Diagram of power losses from the drain system.
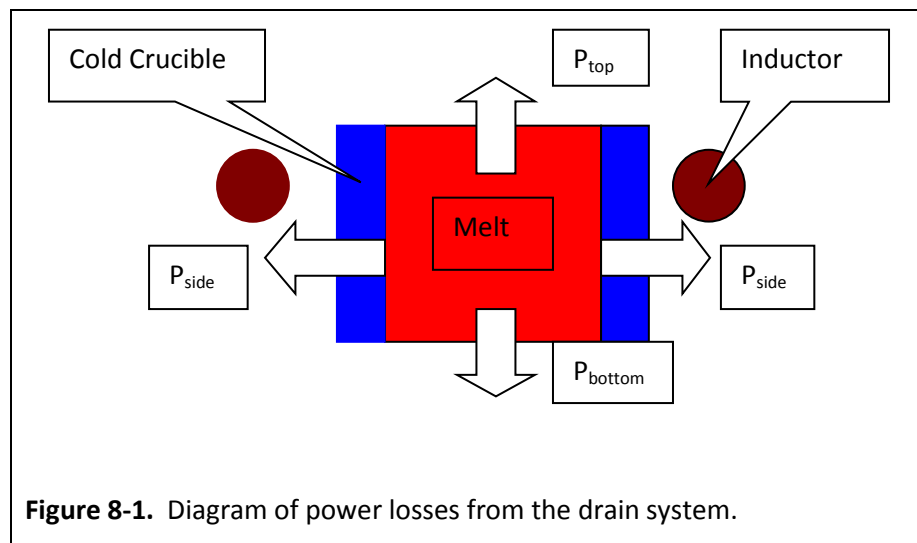
Based on known geometries and experience with other molten glass draining systems (e.g., the CCIM at the Idaho National Laboratory), for the initial calculations and testing, diameters of 3 cm and 4 cm were selected. These diameters were then used to evaluate various drain geometry options. Referring to Figure 8-1., the equation for the heat losses from the drain system was defined as:

$$P_{melt} = P_{side} \times A_{side} + P_{top} \times A_{top} + P_{bottom} \times A_{bottom} \qquad (8-3)$$

where,

$$A_{side} = \pi \times d_{drain} \times h_{drain} \qquad (8-4)$$

$$A_{top} = A_{bottom} = \pi \times \frac{d_{drain}^2}{4} \qquad (8-5)$$

From related experimental tests in a 300 mm diameter crucible with a frequency of 1.76 MHz, at 1,200°C on the melt pool surface, the heat flux through the walls was determined using calorimetry to be approximately 14 W/cm^2. However, for this higher frequency and much more pronounced skin effect, the specific heat loss is expected to be higher through the drain tube wall. Therefore, the specific heat flux was estimated at 30 W/cm^2. For radiation heat losses from the bottom and top open surfaces, the emissivity was estimated to be 0.5, based on initial limited calorimetry data. These relationships were used to determine the overall power requirements to determine potential initial geometry. The dependencies for a range of drain heights are shown in Table 8-1.

Table 8-1. Dependencies of power requirements on drain diameter and height.

h_{drain}, cm	3	4	5	6	8	10
P_{melt}, W d_{drain} = 3 cm	990	1,273	1,556	1,838	2,404	2,967
P_{melt}, W d_{drain} = 4 cm	1,384	1,761	2,138	2,515	3,268	4,022

Based on these results, as well as ease of fabrication for the proof of principle testing, the initial drain geometry assumed was a 4 cm diameter drain with a height of 4 cm to 5 cm. This correlates to the power requirement for the drain generator being as much as 2,100 W. However, inefficiencies are known in the generator, as well as the inductor. If these are assumed to be 0.85 and 0.8, respectively, based on prior measurements, then the necessary power for melt casting is:

$$P_{gen} = \frac{2100}{0.85 \times 0.80} = \sim 3100 \text{ W} \tag{8-6}$$

The available generator is rated at 4 kW, which leaves very little reserve power, requiring the equipment to continuously operate above 75%. This contributes to its unreliability, especially for the initial conditions and at such a high frequency, so for this reason, the generator was modified in stages to be able to provide ~7 kW, and eventually up to ~10 kW. Experimental work would later show that even higher power than this is required for certain applications.

8.2. Proof of Principle Testing

The initial experiments conducted were proof-of-principle tests. These tests had several objectives: 1) to demonstrate the ability of a 4 cm diameter, 27 MHz CCIM to melt a refractory BSG composition and achieve a steady-state from various initial conditions; 2) to test the capabilities of the modified 27 MHz generator and to determine optimal operating parameters, 3) to determine boundary

conditions for the high frequency drain system, and 4) to determine the best CCIM configuration to facilitate the draining process.

8.2.1. Feasibility Tests

The initial testing was performed to demonstrate the operational feasibility of a "miniature" CCIM system. These are described below.

8.2.1.1. Drain Test #1

The first test conducted (Drain Test #1) was on a simple CCIM geometry that simulated a nominal 4 cm diameter by 5 cm (i.e., from bottom of inductor to top open surface) high drain system. The crucible was constructed of eleven 6 mm diameter copper tubes. A two-turn inductor was used, constructed of 6 mm diameter copper tubing with an inside diameter of 60 mm and a height of 20 mm. The test assembly, during and after the melt test, is shown in Figure 8-2.

Figure 8-2. Proof-of-principle testing of inductively heated drain concept
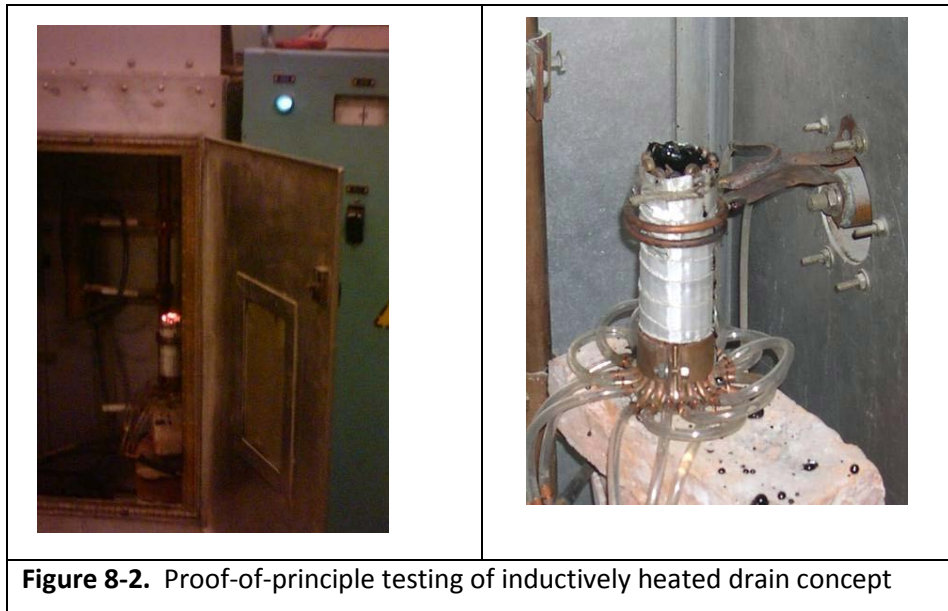
The bottom of this small CCIM was sealed with an alumina silicate ceramic putty (i.e., near the cooling sleeve) and then filled with glass frit. A few small graphite pieces were added into the frit in the volume within the inductor coils to initiate the melting process. The test was conducted using the BSG composition identified earlier. During Drain Test #1, two separate charges were loaded into the drain assembly and different steady state modes achieved, as measured by the surface temperature of 1,200^{o}C and 1,310^{o}C. In both cases, the melted zone extended about 20 mm above the top coil of the inductor, indicating that a stable melt convection pattern was established.

However, virtually no melt extended below the inductor, indicating that the bottom of the drain tube will likely need to be coincident with the bottom coil of the inductor. The total melt depth was about 37 mm, and the generator stabilized at about 28 MHz oscillation frequency. The BSG melting did not require much power in this configuration, nominally only 3.5 kW to 5 kW total. However, it is important to note that the specific thermal flux from the crucible sides was approximately double that seen in larger CCIMs operating at 1.76 MHz. For 1,200^{o}C it was 23.7

Figure 8-3. Ingot of BSG from Drain Test #1.

W/cm^2 and for 1,310^{o}C, 30.1 W/cm^2 was measured. This was important data for determining the initial boundary conditions used in the modeling efforts. Figure 8-3 shows the ingot removed from the crucible resulting from this test.

8.2.1.2. Drain Test #2

An additional test, Drain Test #2, was conducted using a zirconium dioxide (ZrO_2) composition. This material melts at approximately 2,700^{o}C, thus it should push the limits of the generator power capacity to test its operability at this higher level resulting from the modifications made. The test also provided the opportunity to investigate the optimal operating parameters (i.e., efficiency of the generator). During this test, three modes were established using the same charge. These modes were as follows:

- The first mode corresponds to the minimum temperature for which a stable mode is achieved, and below which spontaneous melt crystallization occurs.

- The second mode corresponds to conditions that represent the greatest power provided to the induction system (i.e., the coil, circuits, and melt) by the generator.

- The third mode is characterized by an increased lamp grid current, which corresponds to a significant increase in the generator efficiency while maintaining a relatively high power.

This results in reduced losses in the generator lamp anode as well as lower power consumption in the rectifier and anode transformer.

The Drain Test #2 results are summarized in Table 8-2.

Table 8-2. Operational parameters for Drain Test #2 Using ZrO_2.

Mode	I_a, A	I_g, mA	P_{cruc}, kW	P_{ind}, kW	Comments
1	1.62	360	4.83	2.31	Minimum stable mode
2	2.0	340	5.53	3.66	Maximum power mode
3	2.0	420	5.06	1.44	Maximum power mode with high lamp grid current

(I_a is current on the generator anode, I_g is current on the generator grid, P_{cruc} is power loss in the crucible, P_{ind} is active power on the inductor)

The results demonstrate that the modified generator is capable of reliably providing up to 9 kW (total from the system – determined by $P_{cruc} + P_{ind}$). They also demonstrate the ability to establish much more efficient operational parameters that can maintain a stable melt, while reducing the power losses. The ingot resulting from this test is shown in Figure 8-4.

8.2.1.3. Feasibility Testing Results

The overall results of the combined testing are that the concept is feasible and the available equipment appears to be adequate to support the research. The design for integration into a CCIM platform,

Figure 8-4. ZrO_2 ingot resulting from Drain Test #2.

however, required significant modification from the configuration used in the proof-of-principle testing. This will be discussed in more detail in subsequent sections.

8.2.2. Operational Characteristics Tests

The next four tests were conducted to help understand the effects of certain parameters, including the inductor height and the melt pool height, on the behavior of the system. The primary focus of this research is to develop a glass draining system that is free of mechanical components. Accordingly, the characteristics of the melt behavior in the bottom region above the drain and within the drain must be well understood. The following tests were performed to obtain this data.

8.2.2.1. Drain Test #3 and #4

Drain Test #3 and Drain Test #4 were conducted using the same 40 mm diameter drain with two-turn inductors of different heights (H_{ind}), and different melt pool depths (a_2). The top of each inductor was nominally located at the same relative position for the tests. The steady state temperature for each was approximately the same, although not exactly, due to the performance characteristics of the different configurations. The varying parameters also impacted the active power (P_{ind}) on the inductor. The results of Drain Test #3 and #4 are summarized in Table 8-3.

Table 8-3. Conditions and results for Drain Test #3 and #4.

Drain Test	H_{ind}, mm	T_{melt}, ^{o}C	a_2, mm	P_{ind}, kW
#3	14	1,300	25	1.2
#4	35	1,250	60	2.5

During these tests the melt pool extended below the bottom of the inductor approximately 11 mm and 25 mm for test #3 and #4, respectively. Analysis of these initial results does not allow definitively determining the geometry of the inductor, although general conclusions can be made that the taller inductor results in longer melt initiation times, and generally less efficient operation. Additionally, since the higher inductor produces a weaker external electromagnetic field, it will likely not provide good heating in the lower layers of a large crucible when integrated into a large scale CCIM system. However, the melt pool extended further below the coil with the high inductor.

Subsequently, two additional tests, Drain Test #5 and #6 were conducted. The objective of these tests was to compare the melt formation characteristics for various inductor positions.

8.2.2.2. Drain Test #5

The testing concept for Drain Test #5 is shown in Figure 8-5.
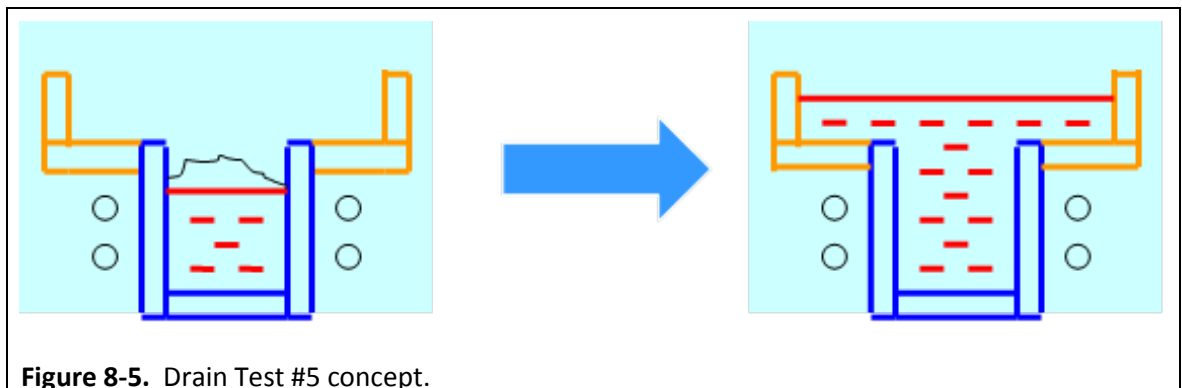
Figure 8-5. Drain Test #5 concept.

The blue sections represent the crucible and the orange sections represent a ceramic container constructed onto the crucible. The purpose of this test was to observe the behavior of extending the melt above the inductor into a colder melt pool zone.

For Drain Test #5, the inductor included two turns at 60 mm inside diameter with a 20 mm height. The crucible was 40 mm diameter, constructed of eleven 6 mm diameter copper tubes with a nominal height of 150 mm. The ceramic container was constructed of 10 mm thick plates. It was nominally 120 mm square with 40 mm high side walls. The distance from the top coil of the inductor to the bottom of the ceramic container averaged about 3 mm. See Figure 8-6.

During this test, after melt initiation was completed (note that small pieces of flexible graphite gasket material was used as the initiator) and a steady melt pool was formed within the inductor volume in the crucible, glass frit was measured and added to determine if the melt pool could propagate above the inductor coil due to thermal conduction. The experiment demonstrated that this was feasible, as indicated in Figure 8-7. Excellent heating was observed in the upper region into the ceramic container volume as evidenced by the heated "ring" visible in Figure 8-7. This also indicates that, for this

Figure 8-6. Drain Test #5 set-up.

configuration, good coupling is occurring in both the transverse (i.e., above the inductor) and longitudinal (i.e., within the inductor) directions of the electromagnetic field. The temperature near the bottom of the ceramic container was measured, using a pyrometer, at about 700°C.

At multiple points during the test, the generator was powered off and the melt allowed to cool to determine if the generator would be able to couple with the glass at a lower temperature. For each case, a full melt pool was able to be re-established. During one of these power-off conditions, the melt pool depth was measured, indicating that the maximum depth of 24 mm occurred at the center axis of the melt pool. This indicates that the hottest area in the melt pool volume was actually above the inductor in the ceramic container. After the final power-off condition, full voltage

was applied and the melt pool temperature quickly rose to about 1,400°C. Shortly after, the ceramic container was breached (i.e., due to dissolution) and the test had to be terminated. Table 8-4 gives the test conditions and generator modes observed during Drain Test #5.

Table 8-4. Conditions and generator modes observed during Drain Test #5.

hh:mm	I_g, mA	I_a, A	Note
16:00			Melt initiation in the upper zone of the cold crucible.
16:23	320	1.27	The melt pool propagates up to the crucible end-face.
16:28	300	1.30	High temperature melt pool volume is growing.
16:35	310	1.29	Upper zone of the melt pool has a visible heated "ring". Temperature of the bottom part of the ceramic container is about 700°C.
16:37	340	1.20	The melt pool depth is 24 mm in the cold crucible center. The melt is at the inductor top coil level. Generator is powered-off for 1 minute.
16:45	320	1.25	The ceramic sides have heated up. Generator is powered-off for 1 minute.
17:05	365	1.10	Generator powered off.
17:12	240	1.50	Maximum melt temperature on the surface is 1,050°C.
17:18	300	1.50	Maximum melt temperature on the surface is 1,400°C. Full voltage applied to the rectifier. Breakthrough occurred in the ceramic container after 40 seconds. Test was stopped.

(Note: I_g and I_a are the grid and the generating lamp anode currents, respectively.)
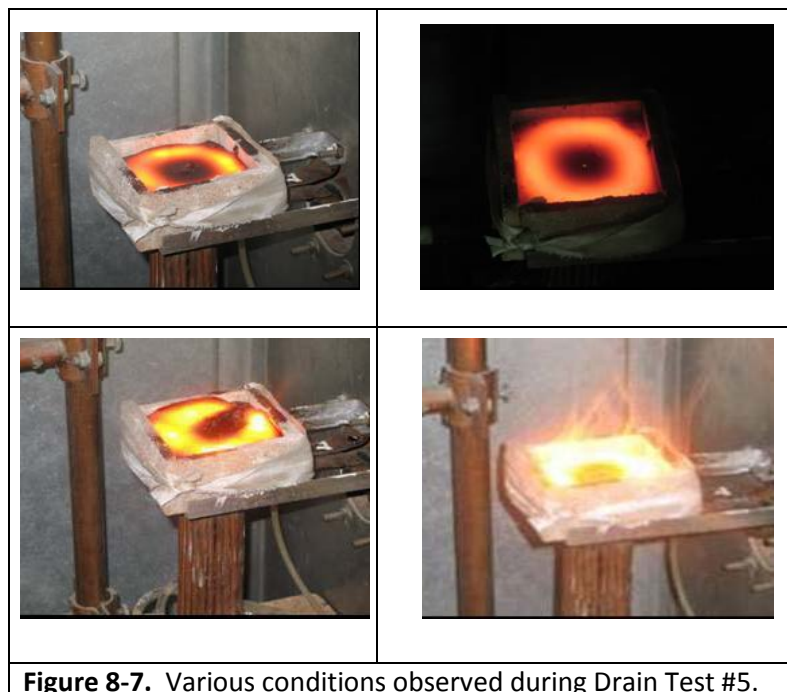
Figure 8-7. Various conditions observed during Drain Test #5.

After the final power-off condition, full voltage was applied and the melt pool temperature quickly rose to about 1,400°C. Shortly after, the ceramic container was breached (i.e., due to dissolution) and the test had to be terminated.

The key observations from Drain Test #5 are as follows:

- The melt pool was successfully propagated from within the inductor volume to a zone above the inductor.
- Glass heating was observed in the longitudinal (within the inductor) and transverse (above the inductor) zones of the electromagnetic field. The best heating actually occurred in the transverse field within the ceramic container. Apparently the glass is cooler, and thus more dense and viscous, such that the buoyancy effects are not present to move the melt upward. Heating occurs by overheating of the melt pool above the inductor such that heat transfer occurs through conduction into the lower zone of the melt pool.
- To minimize overheating of the ceramic, as well as to better balance the heating from the transverse and longitudinal fields, the inductor should be lowered to provide more clearance from the ceramic bottom (i.e., average 10 mm clearance).

8.2.2.3. Drain Test #6

Drain Test #6 used the same equipment and experimental set-up as Drain Test #5 except that the inductor was moved down such that it averaged about 10 mm clearance from the ceramic container. Also, the ceramic plates used to form the upper container were 15 mm thick versus 10 mm used in the prior test. The primary objective of this test was to demonstrate the ability to extend the melt pool from above the crucible down into the body of the drain. See Figure 8-8.

Figure 8-8. Drain Test #6 concept.
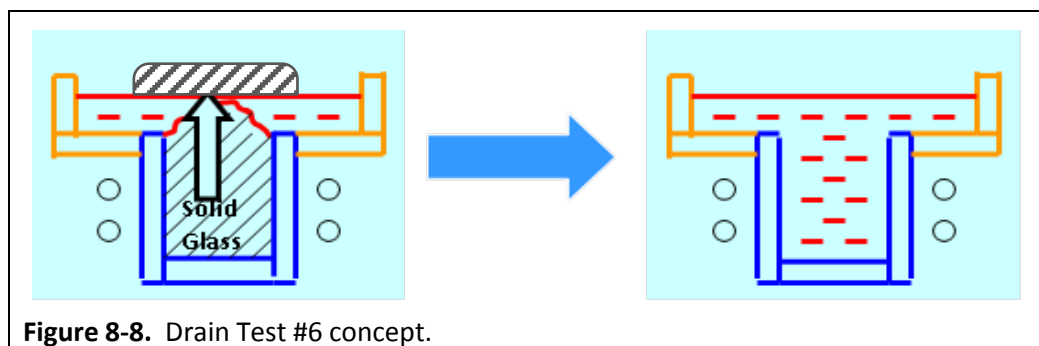
Another important objective of the test was to observe the behavior with extended periods of zero power (i.e., allowing the glass to cool more) and to further investigate the melting conditions. This will provide additional data in determining the process power parameters, and support further investigation of the drain design and operation. The test set-up, during the experiment, is shown in Figure 8-9.

The test was accomplished by first initiating a melt in the upper zone by operating the generator at about half power. As the glass was heated within the inductor it rose up due to buoyancy effects, allowing the glass in the crucible (i.e., within the inductor volume) to cool. This effect was expected due to the transverse heating observed in the previous test. At this point, frit was added and the power level increased to grow the melt pool volume in the ceramic

Figure 8-9. Drain Test #6 configuration.

container. The progression is shown in Figure 8-10. From these images, as well as the data presented in Table 8-5, the melt is being heated primarily due to the longitudinal electromagnetic field for this configuration. The melt depth in the ceramic container grew to 31 mm and was 90 mm along the center axis into the crucible body. At this point, the melt had propagated below the bottom of the inductor coil by about 20 mm. See Figure 8-11.

During the second stage of the test, the generator was switched off for increasing lengths of time such that the condition shown in Figure 8-8 could be established. For the time periods of one and two minutes, the thermal condition of the melt pool returned to the previous state within three and five minutes, respectively. However, after a zero-power condition for three minutes, the glass within the drain body (recall that it is water cooled) was at a low enough temperature such that electromagnetic coupling was not possible. This was the desired condition for this stage of the test, as shown in Figure 8-8. Upon resuming power and then increasing the mode, the melt volume in the ceramic container was observed to heat up to about 1,260°C, although after an extended time at a high power level. During this process, frit was continually added to observe the melt behavior.

Table 8-5. Conditions and generator modes for Drain Test #6.

Time, hr:min	Ig, mA	Ia, A	P_{ind}, kW	T_{melt}, °C	a_{2c}/a_{2up}, cm/cm	Note
9:55	290	0.6				Melt initiation.
10:05	310	1.3				Melt pool moves downward.
10:10	390	1		1500	48	The melt is level with upper face of drain.
10:28	310	1.5	1.63	1500	67	The melt pool in the ceramic container has diameter of ~66 mm.
10:55	320	1.5	1.58	1430	82/29	Frit added and growth of upper melt pool.
11:02	300	1.6		1400		Generator switched to full power.
11:10	310	1.3	2.12	1400	90/31	Power mode increased.
11:17	300	1.5				Zero power for 1 minute.
11:22	300	1.5			90	Power resumed at previous mode.
11:25	400	0.9				Zero power for 2 minutes.
11:37	300	1.5			90	Power resumed at previous mode.
11:40	400	0.85				Zero power for 3 minutes. Power is resumed and the top melt pool is more appreciably heated (i.e., transverse field).
11:50	390	1.1		1260	36	Increase of power mode.
12:00					41	Growth of melt pool depth in ceramic container is observed. Test is ended.
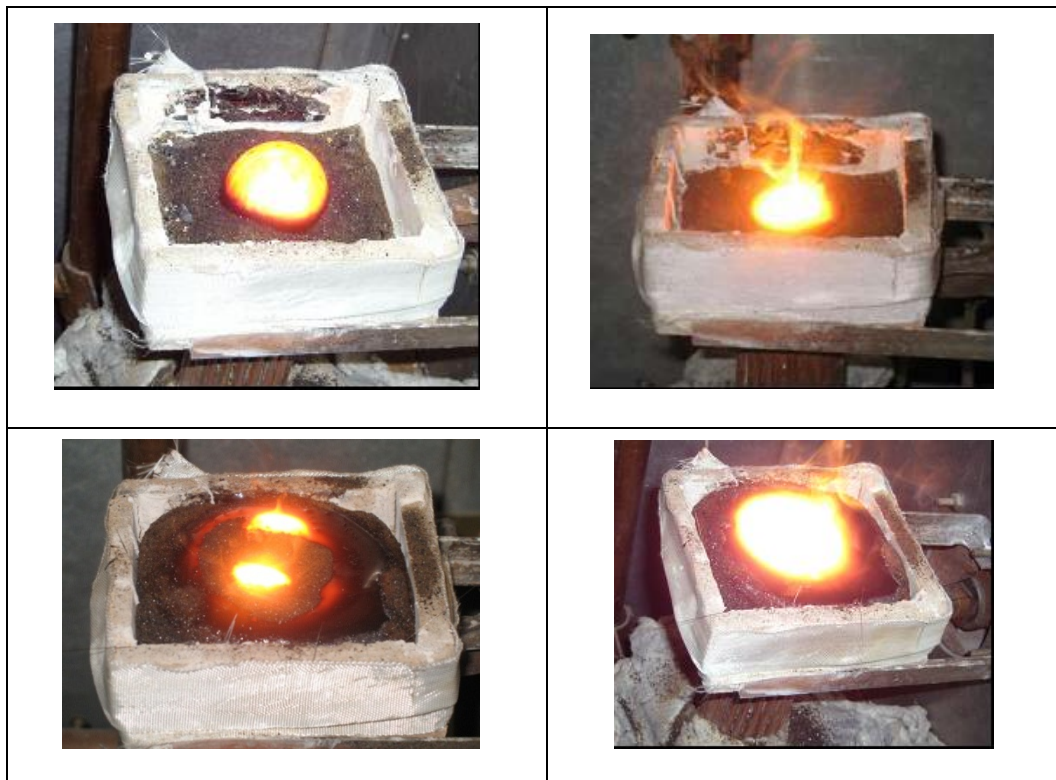
Figure 8-10. Phases of the upper glass melt pool during the first stage of Drain Test #6.

Figure 8-11. Bright spot below inductor showing melt pool level.

Figure 8-12 shows the surface temperature and generator modes observed during the test.

Figure 8-12. Maximum surface temperature and generator modes during Drain Test #6.
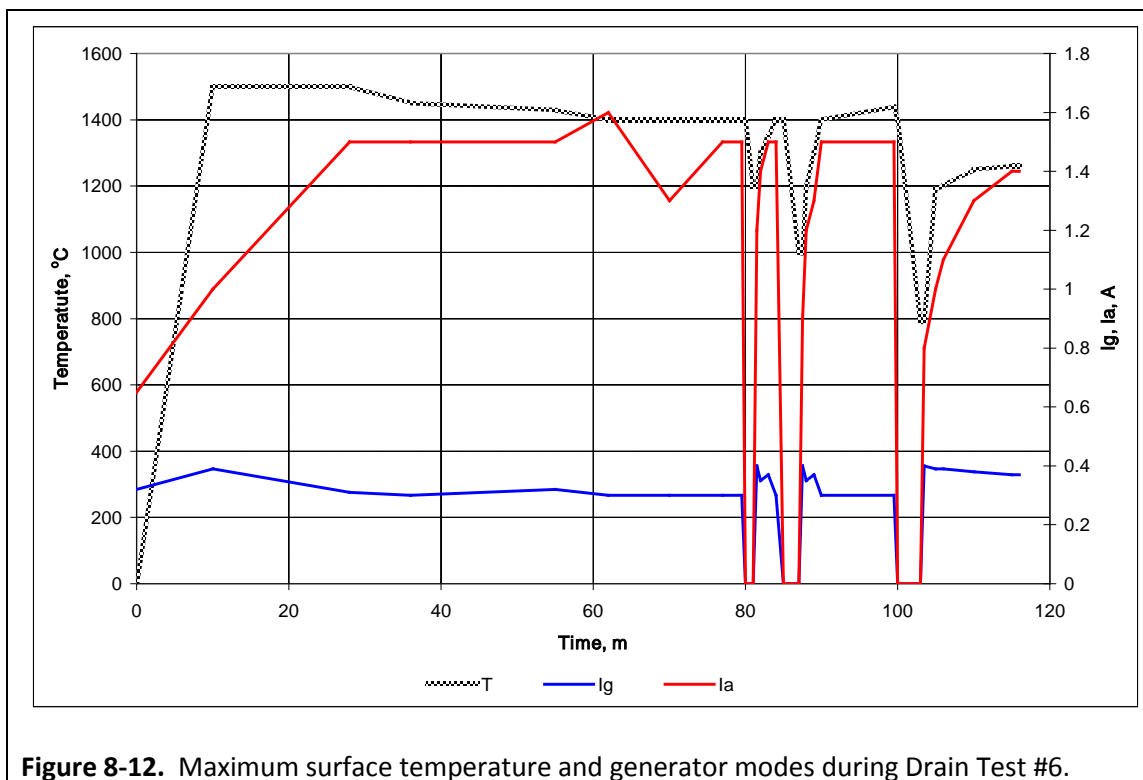
The melt pool depth in the ceramic container grew to about 41 mm, although a cool zone could be observed in the center of the melt pool. Nevertheless, the growth of the melt pool in this upper portion indicates that heating had begun again within the drain body (i.e., longitudinal field heating) and the melt pool was moving from above, down into the drain. Unfortunately, the test had to be terminated due to significant heating of the ceramic and concerns that a breach could occur. The progression of the melt pool growth in the ceramic container is shown in Figure 8-13 (upper right to lower left). The over-heating and near breach of the ceramic container are shown in Figure 8-14.
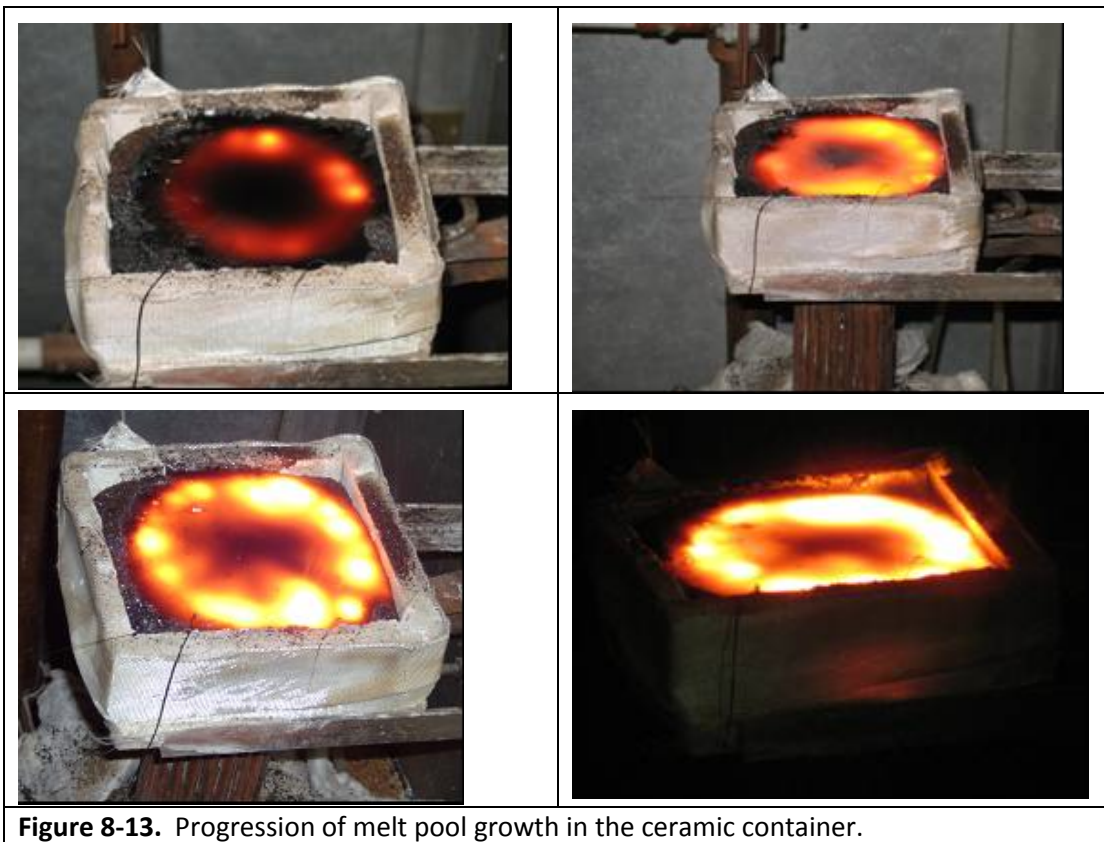
Figure 8-13. Progression of melt pool growth in the ceramic container.
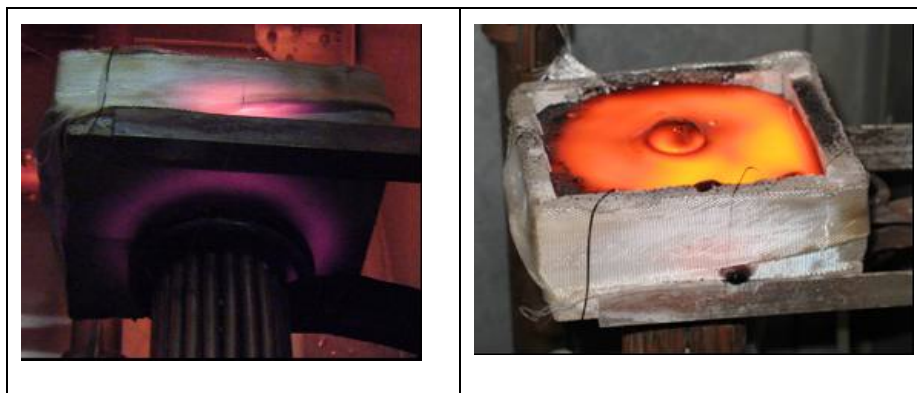
Figure 8-14. Over-heating and potential failure of the ceramic container.

The key observations from Drain Test #6 are as follows:

- The position of the inductor has a significant influence on the heating characteristics near the bottom, and specifically for the conditions of heating by the longitudinal or transverse components of the electromagnetic field. Increasing the distance of the inductor from the bottom of the ceramic container by approximately 8 mm resulted in increased longitudinal heating versus transverse heating, which provided much better melting conditions within the inductor, and thus within the drain body itself.

- The effects of the cooling rates and glass temperatures (i.e., zero power time periods) near the bottom zone of the melt pool above the drain opening and within the drain were observed. The heating effects of the transverse versus longitudinal components of the electromagnetic field were apparent.

- The ability of the transverse field to heat the glass above the drain such that the melt pool depth began to extend downward toward the drain opening was demonstrated. This provides further evidence that this drain concept is feasible.

8.3. Further Design Investigations Based on Test Results

After the preceding tests were completed, further investigations were made of the design for the drain device, as well as its implementation into an integrated system.

8.3.1. Analysis of the Glass Casting Process – Terminating the Draining Process

The following simple analysis was conducted to help determine 1) the ability to stop the casting process using the cooling capability of the drain device, and 2) the minimum height required for the drain body. A power balance was established for this analysis, which is shown in Figure 8-15.

Figure 8-15. Power balance for analysis.
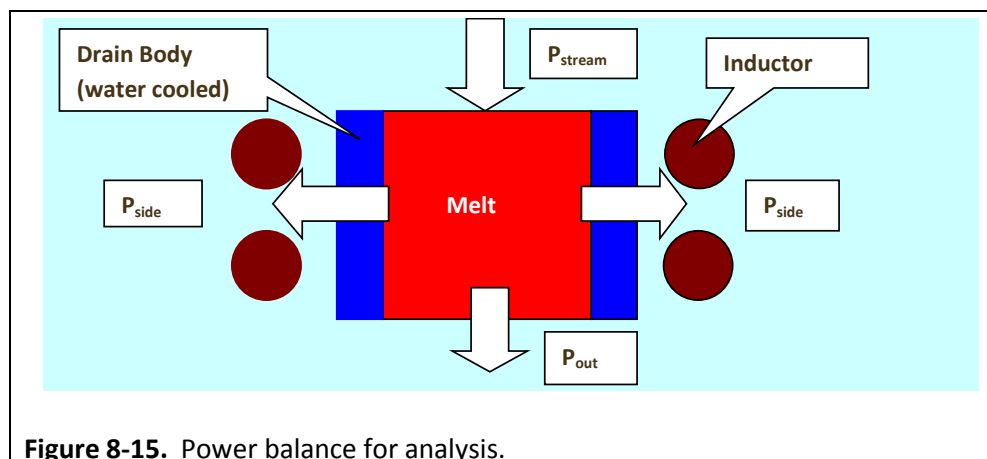
The total power into the system is represented by the power (i.e., heat energy) of the melt flwing into the drain body, P_{stream}. Part of this heat is removed through the sides of the drain body due to the water cooling, P_{side}, and the remainder flows out with the cooled glass, P_{out}. The energy balance is thus:

$$P_{stream} = P_{side} + P_{out} \qquad\qquad (8-7)$$

where, $P_{stream} > P_{out}$, always.

For the glass used for all of the testing conducted, the solidus temperature is about $450^{o}C$. Thus, with the goal to be able to stop the glass flow by the cooling effect of the drain device, the glass must be cooled to this temperature. To accomplish this, the following simplified equation would provide a conservative design if satisfied:

$$P_{stream} = P_{side} \qquad\qquad (8-8)$$

The follow parameters will be assumed:

- Melt temperature at the drain inlet, $T_{stream} = 1,200^{o}C$
- Specific heat, C_p, at $1,200^{o}C = 2,000$ J/kg-K
- Density, ρ, at $1,200^{o}C = 2,300$ kg/m^3
- Specific heat flux through the drain side wall, $P_{0\,side} = 40$ W/cm^2 (note that this is conservative.)
- $P_{out} = 0$ (no glass flow out, and neglect power associated with glass at $450^{o}C$).

Thus,

$$P_{stream} = C_p \times T_{stream} \times M_{cast} \qquad\qquad (8-9)$$

where, M_{cast} is the mass of glass cast per second.

Similarly, for this glass at $1,200^{o}C$, with a pour stream diameter of about 5 mm to 6 mm, the mass flow rate is approximately 0.008 kg/s. Accordingly, $P_{stream} = {\sim}18,700$ W. Additionally,

$$P_{side} = P_{0\,side} \times \pi d_{drain} \times h_{drain} \qquad\qquad (8-10)$$

where, d_{drain} = inside diameter of the drain, and h_{drain} = the height of the drain.

Using these assumptions and relationships, the data in Table 8-6 shows the heat removal capacity, P_{side}, for a variety of drain diameters and heights.

Table 8-6. P_{side} for various values of d_{drain} and h_{drain}. (heat removal capacity, P_{side}, in W)

d_{drain}, cm	h_{drain}, cm			
	5	10	20	40
1	628	1,256	2,512	5,024
2	1,256	2,512	5,024	10,048
3	1,885	3,770	7,540	15,080
4	2,512	5,024	10,048	20,096

These results indicate that casting cannot be stopped simply by the cooling capacity of the drain unless it is a very long drain (i.e., about 40 cm long). For this geometry, based on the initial testing, the casting process could never be initiated with this drain geometry. Thus, some other method will be required to stop the melt casting process once it is initiated. This will be investigated later.

8.3.2. Initial Design Concept for an Integrated System

Based on the results of the prior analysis and testing, an initial design for an "integrated system" was developed. The term "integrated system" refers to a CCIM system with an inductively heated drain device integrated into the design. The system, as envisioned, is shown in Figure 8-16.
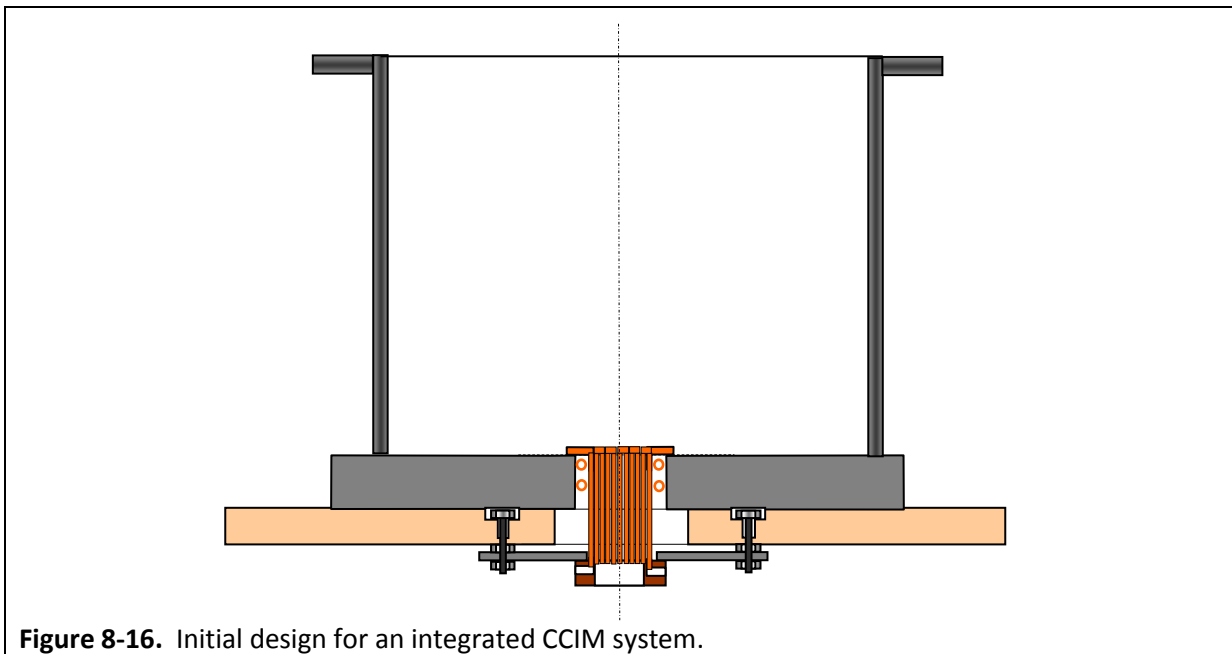
Figure 8-16. Initial design for an integrated CCIM system.

The drain device, which is actually a miniature CCIM system, is constructed of 6 mm diameter copper tubes, with a single tube being the supply and return for each double-section. At the top,

the tubes are bent 90° to provide a mounting lip, and to protect the ceramic bottom from the molten glass in this area, as well as to help cool it from heating that occurs from the electromagnetic field. This configuration, shown in Figure 8-17, was the second version of the drain device built and tested.

Figure 8-17. Second version of the drain device.

8.3.3. Drain Design Testing and Configuration Improvements

Prior to integrating a drain system into a melter platform, a few additional tests were conducted to obtain additional operational parameters necessary for the initial integrated design. These are described below.

8.3.3.1. Drain Test #7

Drain Test #7 was conducted to investigate the behavior or the new drain design. Addition of the water-cooled flange will impact the characteristics of the melt pool in the region near this surface. The primary goal is to be able to provide more power into the melt to obtain better conditions for melt casting, without damaging the ceramic bottom. This will also provide additional information that can be implemented into the model as operational parameters. The concept for the experimental design is shown in Figure 8-18.

This test was conducted with a similar approach to the prior drain tests. The melt was initiated within the drain body (i.e., longitudinal electromagnetic field). The power was then increased and a melt pool was formed above the inductor within the ceramic-walled container. As the melt pools began to extend toward each other, the pool within the inductor volume began to cool, and the

melt pool depth above the inductor reduced to only about 30 mm deep. Additional power was added in an effort to better heat the melt pool within the drain body and to allow the upper and lower melt pools to join. This process was observed to begin; however, as in previous tests, the ceramic walls of the container began to fail and the test had to be terminated. The primary modes observed in the test are shown in Table 8-7.

Figure 8-18. Drain Test #7 design.
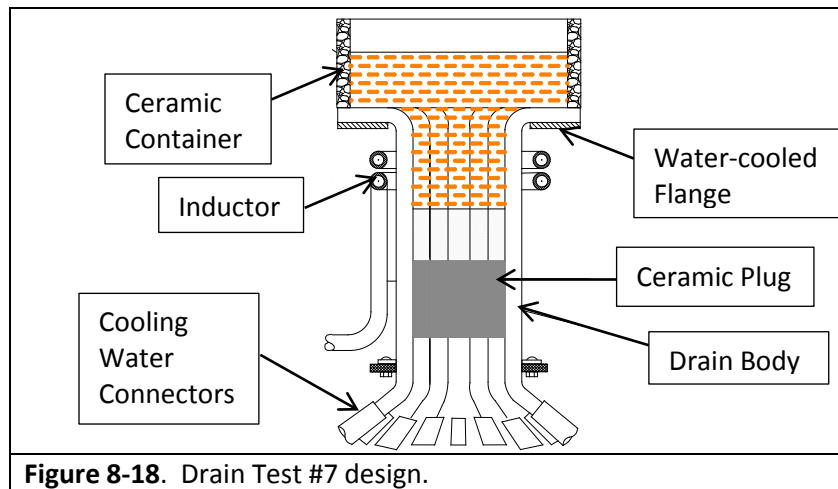
Figure 8-19 shows the experimental set-up during melt initiation (left) and with a full melt (right).

Figure 8-19. Drain Test #7 during start-up (left) and full melt (right) conditions.
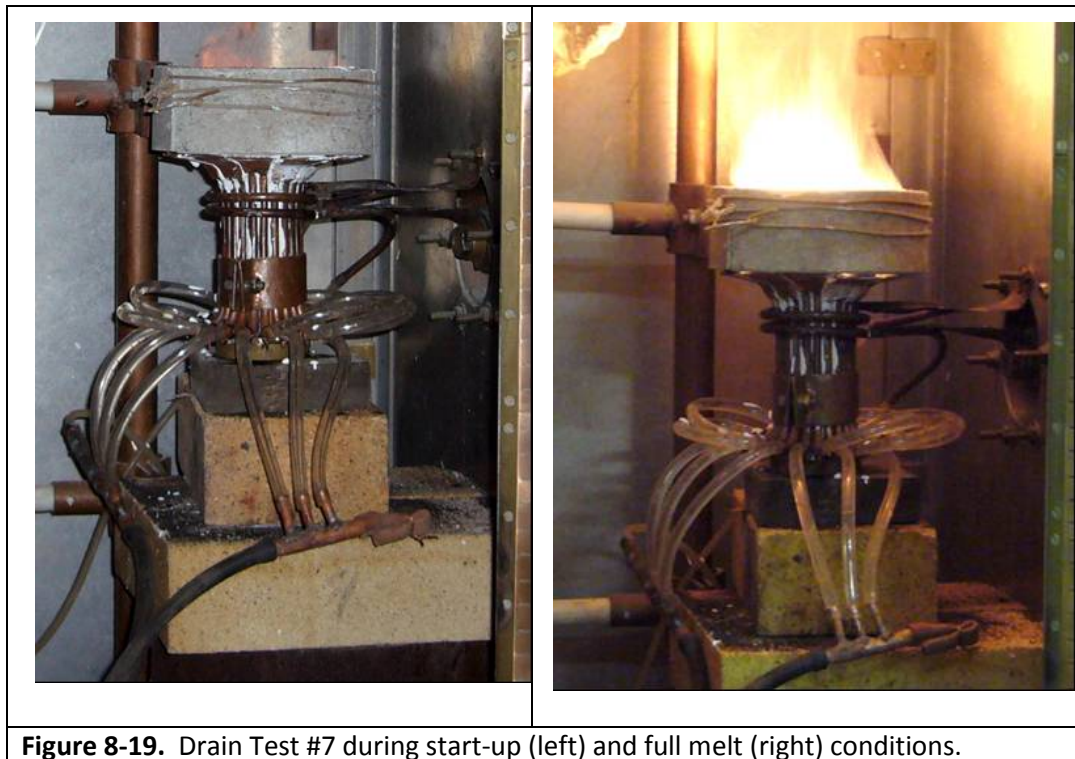
The ingot removed from the test system (see Figure 8-20) shows that the upper melt pool in the ceramic walled container and the drain body appeared to join, although closer investigation revealed that the upper and lower sections were actually bonded with a layer of sintered frit, and that the melt pools did not actually fully join.

Figure 8-20. Ingot from Drain Test #7.

Earlier modeling results indicated that about 6.8 kW would be required to allow this process to occur. However, due to the failure of the ceramic side wall during the test, a maximum power level of about 4.5 kW was achieved, thus sufficient power could not be applied and maintained to allow the melt pool to progress any further.

Key observations from Drain Test #7 were as follows:

- Implementation of the water-cooled flange had almost no impact on the overall melt conditions or the power characteristics. This is likely due to the fact that the energy that was used for heating and dissolution of the ceramic material is nominally equivalent to the power loss observed by the water-cooling of the flange.

- The use of a stationary inductor appears to limit the ability (i.e., requiring much more power) to join the melt pools within the inductor and in the zone above the drain body. The 27 MHz system will be modified to allow mechanical displacement of the inductor to observe the effects in future testing.

Table 8-7. Generator modes during Drain Test #7.

Mode	I_a, A	I_g,mA	Note
1	1.0	300	Melt initiation
2	1.2	300	Melt pool established within inductor.
3	1.4	280	Melt pool established in upper container, then begins to cool.
4	1.8	400	Power is increased and upper melt pool is beginning to grow and extend downward. Test terminated.

8.3.3.2. Drain Test #8

The prior test results led to questions regarding the performance of the 27 MHz generator. Specifically, the amount of current being supplied to the inductor was unclear. Recall that the modelling results indicated that approximately 160 A would be required to produce the conditions necessary to initiate melt casting.

In preparation for Drain Test #8, which was focused on investigating the effects of translation of the inductor during melting, a simple test was devised to determine the current on the inductor. The schematic of this preparatory test is shown in Figure 8-21.
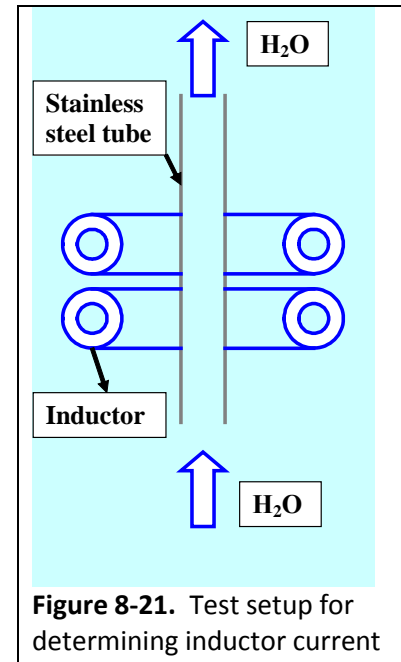
Figure 8-21. Test setup for determining inductor current

A two-turn inductor was used for the test. The water flowing through the stainless steel tube and the inductor was fed through high precision flow meters with high precision platinum thermistors on the input and output sides of each to measure water temperatures. This provided the needed accuracy of the calorimetry measurements to determine the operational parameters desired.

During the test, the generator was held at maximum operational modes when possible. These generator modes were recorded and the electrical losses in the stainless steel tube and inductor were determined. The data are presented in Table 8-8. This shows that, for the inductor configuration tested, the system cannot provide the required current to the inductor to enable casting, without additional modifications to the generator to provide even more power. However, the use of a one-turn inductor could provide nominally twice the current demonstrated during this test.

Table 8-8. Generator modes, calorimetry data, and derived parameters from pre-test.

Mode	I_a, A	I_g, A	$P_{e\text{-tube}}$, W	$P_{e\text{-ind}}$, W	I_{ind}, A	U_{ind}, V
1	0.5	0.315	108	261	-	-
2	0.5	0.315	111	414	101.5	5,278
3	0.6	0.35	137	566	112	5,824

(I_a is lamp anode current; I_g – grid current; $P_{e\text{-tube}}$ is electrical loss in the stainless steel tube; $P_{e\text{-ind}}$ is electrical loss in the inductor; I_{ind} is inductor current; U_{ind} is inductor voltage)

Based on these results, as well as those from prior tests, the drain configuration was redesigned for Drain Test #8, which was the last stand-alone drain test prior to integration into a CCIM platform. This design had a much shorter body (i.e., 50 mm), such that the melt could propagate through the drain volume. The outside diameter of the drain assembly was 160 mm.

Additionally, based on the results of the preparatory test, a one-turn inductor was used for this test, coupled with a mechanical assembly that provided the ability to translate the inductor up and down during various stages of heating. For purposes of the test, a copper sleeve was soldered to the top perimeter of the drain to serve as a container for the melt pool, in place of the ceramic that was failure prone in prior tests. Figures 8-22 through 8-24 show various views of the test assembly before and during the test.

The melt initiation process was started with the inductor at the lowest position (i.e., at the center of the drain body). Once a melt pool was initiated, the inductor was raised and the generator mode increased to allow propagation of the melt pool. During the test, the parameters shown in Table 8-9 were measured.

Table 8-9. Parameters measured during Drain Test #8.

Parameter	Values
Surface melt temperature (T_s)	1,700^{o}C
Lamp anode current (I_{anode})	2 A
Lamp grid current I_{grid})	0.38 A
Power in drain (calorimetry) (P_{drain})	4.3 kW

Figure 8-22. Top view of redesigned drain device used for Drain Test #8 – third version.
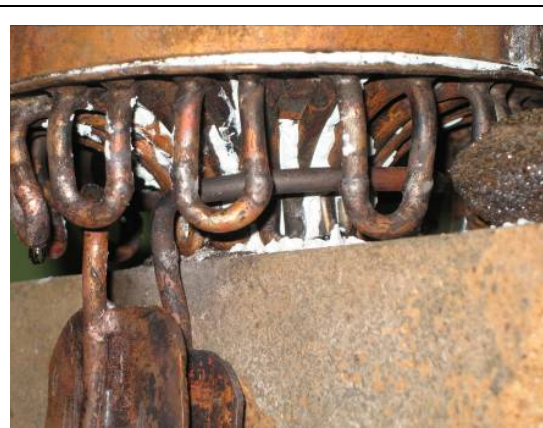
Figure 8-23. Side view of drain device used for Drain Test #8.

Figure 8-24. View of drain assembly during melt initiation for Drain Test #8.

Figure 8-25. View of maximum melt pool achieved during Drain Test #8.

Figure 8-26. View of ingot obtained during Drain Test #8.

The full melt pool achieved and resulting ingot from Drain Test #8 are shown in Figures 8-25 and 8-26. From these photographs, it is clear that the melt pool did not completely fill the copper container. This was likely due to the electrical "shorting" effect of the copper flange that was soldered to the perimeter.

While this test did not result in a casting condition, it did serve to demonstrate the functionality of the inductor translation system during operation of the 27 MHz generator. The system provides up to 30 mm of translation. The test also resulted in additional operational data for the 27 MHz generator and drain system to support subsequent integrated testing.

CHAPTER 9.INTEGRATED SYSTEM TESTING

CCIM Test #1 through CCIM Test #5 were instrumental in providing data to validate the model, as well as to improve the boundary conditions used. They also served to demonstrate that conditions can be obtained near the bottom layers of the melt pool that are amenable to casting using the concept for the inductively heated draining concept. Similarly, Drain Test #1 through Drain Test #8 demonstrated the feasibility of the inductively heated drain concept, and provided initial data for design and optimization.

Once the initial drain design and crucible configuration were determined, the drain assembly was integrated into a CCIM platform and a series of tests conducted to optimize the system such that reliable and controllable operation could be achieved. These integrated tests are described in detail below.

9.1.Integrated Test #1

Integrated Test #1 was conducted using the 300 mm diameter stainless steel crucible with a chamotte bottom. The *third version* of the drain device was used, as shown in Figure 9-1. Note that the plastic cooling lines were used for preliminary flow testing only and were replaced with copper connections prior to installation into the system. Only the primary feed and return lines were required for the configuration tested. The drain body was constructed of a series of 6 mm diameter copper tube that formed a cylinder of 40 mm inside diameter and 40 mm deep, with a perimeter ring of 25 mm height. This raises the drain opening up higher into the melt pool. The outside diameter was 160 mm. Figure 9-2 shows placement of the drain device during assembly of the integrated test platform. . The primary generator was the 60 kW, 1.76 MHz system with a two-turn inductor of 384 mm diameter and 100 mm height, intentionally lower than usual (i.e., 200 mm) to focus the energy nearer the bottom.
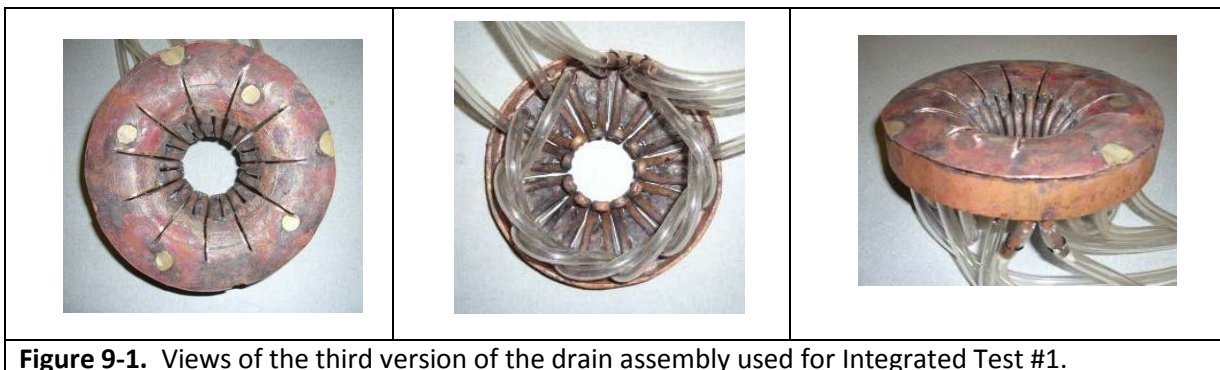
Figure 9-1. Views of the third version of the drain assembly used for Integrated Test #1.
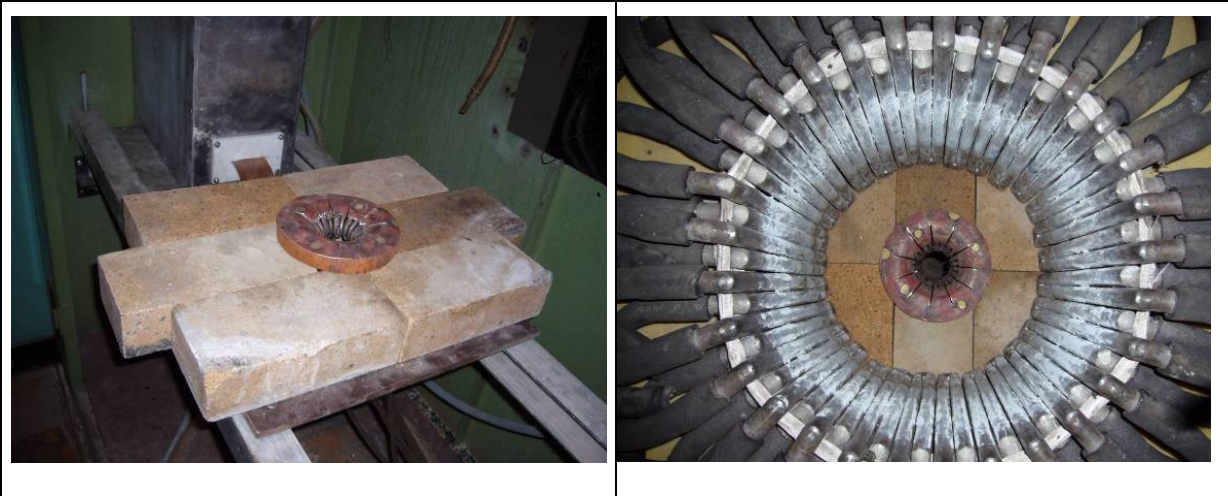
Figure 9-2. Placement of the drain during assembly of the test platform for Integrated Test #1.

The secondary generator was the 27 MHz system that had been modified to provide 8 kW. A single turn, 100 mm outside diameter inductor was used for the drain, with the initial position at 5 mm below the flange of the drain.

To retain the initial frit that is loaded into the crucible, a plug was made using the glass frit blended with a liquid glass adhesive. Figure 9-3 shows the drain device with the plug in place prior to testing. Figure 9-4 is an external view of the integrated test platform during the test.
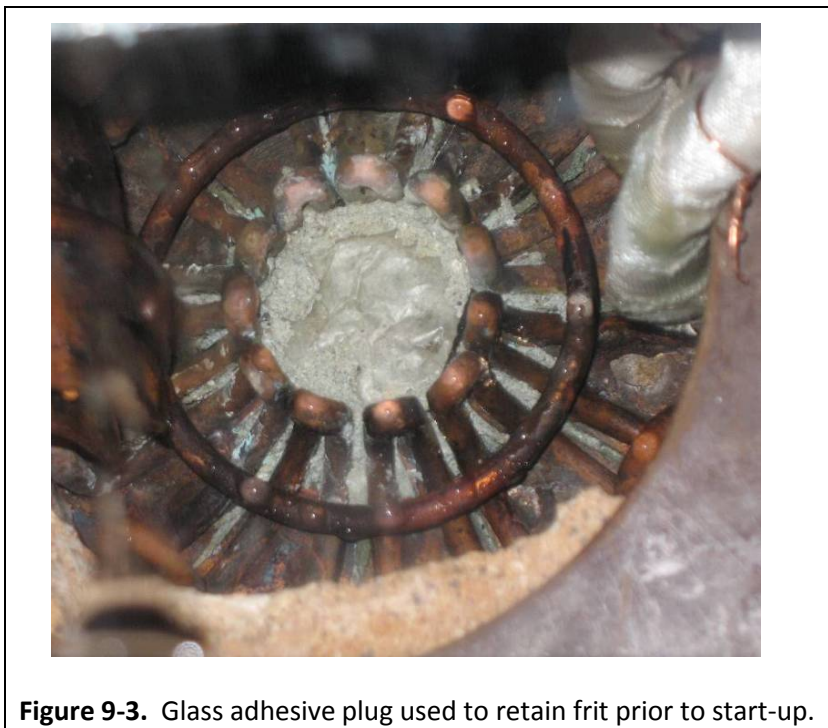
Figure 9-3. Glass adhesive plug used to retain frit prior to start-up.

Figure 9-4. Integrated Test #1 set-up.

During the first steady state mode achieved, the following parameters were observed:

Table 9-1. Parameters observed during Integrated Test #1 first steady state mode.

Parameter	Value
Lamp anode voltage for the 1.76 MHz generator, U_{a1}	6 kV
Lamp anode current for the 1.76 MHz generator, I_{a1}	3.45 A
Lamp grid current for the 1.76 MHz generator, I_{g1}	1.25 A
Melt pool depth, a_2	95 mm
Drain cooling water temperature, T_{drain}	17.1^oC
Maximum temperature on melt pool surface, T_{melt}	$1,210^oC$

The target maximum temperature was set at 1,200°C because this is representative of the operational temperature used in the JHCMs for immobilizing radioactive waste. This temperature helps control volatilization of certain constituents, especially cesium-137, into the off gas system. One objective of this research was to demonstrate the feasibility of this draining technique for implementation into various types of melter systems. Thus, if the technique was successful at this lower temperature, it would certainly be for higher operating temperatures (i.e., up to 1,350°C).

Once the steady state was achieved, the 27 MHz generator was powered on, energizing the drain coil. The power level was maintained between 60% and 70%. After about 13 minutes bubbles were observed on the surface of the melt pool in the center, as well as a marked increase in the lamp

anode current, which is the primary indicator of increased coupling. Approximately 5 minutes after this, the first draining was accomplished. Figure 9-5 and Figure 9-6 compare the melt pool surface as the glass within the drain body began to heat up and the bubbles occurred. Once the casting was initiated, the 27 MHz generator was powered off.
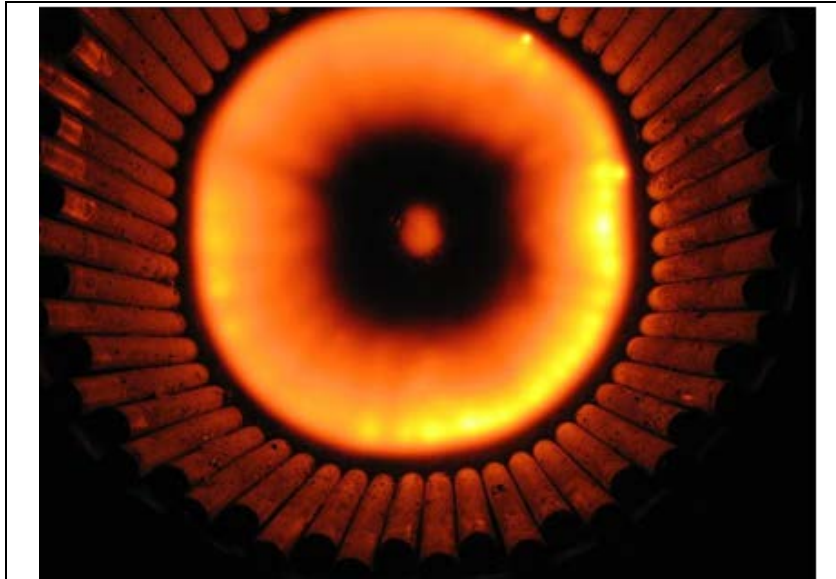
Figure 9-5. Melt pool surface at steady state mode, T_{max} = 1,210^{o}C
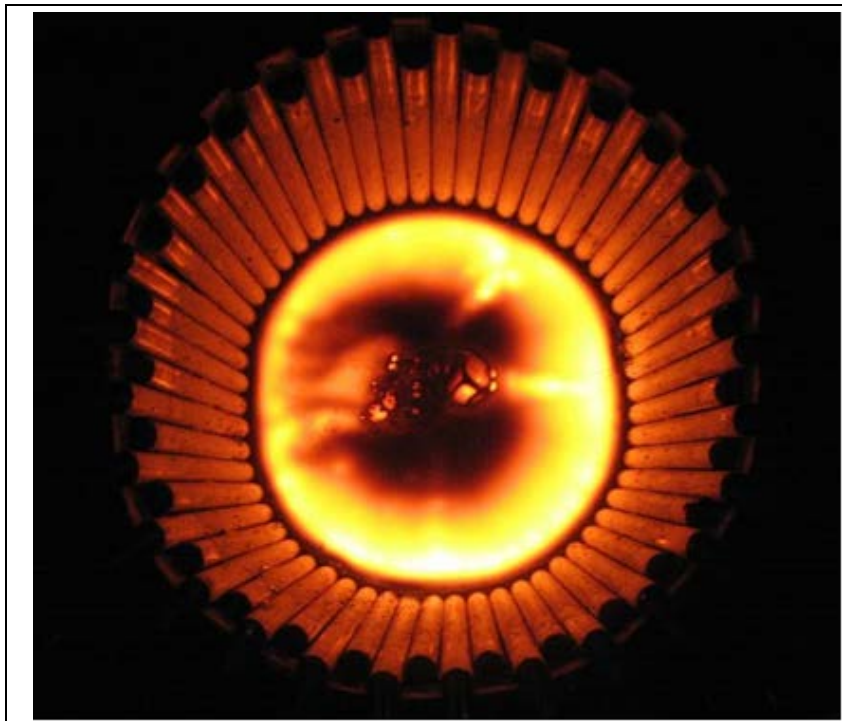
Figure 9-6. Bubbles observed in center of melt pool prior to casting.

As shown in previous analysis, the melt casting cannot be terminated from cooling of the drain body alone. This initial test was not equipped with any auxiliary systems to help stop the draining process, which is why the 25 mm lip was added to the drain device (refer back to Figure 9-1). This would result in a quantity of glass remaining in the crucible after the casting, with the intention that this volume would be sufficient to maintain coupling with the primary induction field and allow the process to be semi-continuous (i.e., frit could be added to the remaining melt pool to increase the volume such that additional castings could be completed). Near the end of the casting process the power level was increased on the 60 kW, 1.76 MHz generator in an attempt to overheat the melt such that the melt could be maintained and new frit added. However, the volume of remaining melt was insufficient to maintain coupling.

Accordingly, additional frit was added, along with the graphite ring, to initiate a new melt volume. A second steady state mode was readily achieved at 1,250°C. Once the steady state was achieved, the 27 MHz generator was powered on to initiate the melt casting process. During this second phase of the test, bubbles were observed after 23 minutes, and casting occurred at 27 minutes. Figure 9-7 shows a series of photographs taken during the second melt casting. The molten glass is poured into a stainless steel container filled with water. This produces a glass frit rather than a monolith, making it easier to re-use in subsequent tests.
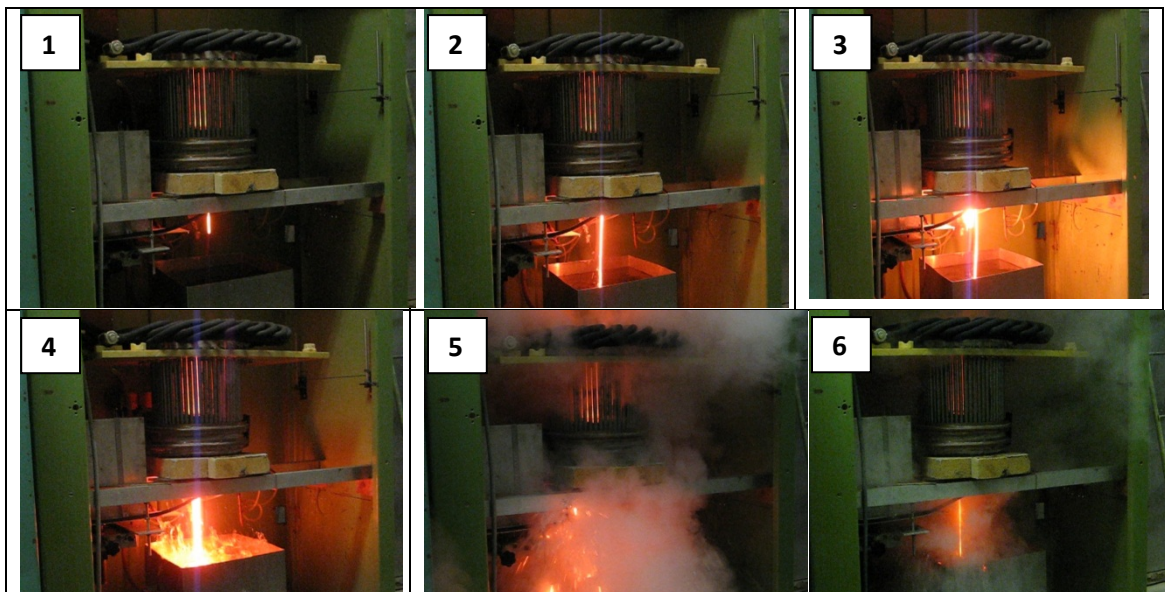
Figure 9-7. Second casting in an integrated system from initiation to end.

Initiation of the second casting required significantly more time than the initial casting, but this was intentional. The melt was exposed to the additional energy supplied by 27 MHz generator for an

extended period of time to allow for better heat transfer into the melt within the drain body. This resulted in less power being required from the 27 MHz generator to initiate the casting process, and provided another useful data point of process parameters, behavior, and eventual optimization. This was especially important since this was the first time that the integrated system with dual frequencies had been operated. Data obtained from this and subsequent tests were continually integrated into the model in an iterative process to ensure that it was representative. During the second steady state mode, the parameters observed are included in Table 9-2.

Table 9-2. Parameters observed during Integrated Test #1 second steady state mode.

Parameter	Value
Lamp anode voltage for the 1.76 MHz generator, U_{a1}	5.9 kV
Lamp anode current for the 1.76 MHz generator, I_{a1}	3.7 A
Lamp grid current for the 1.76 MHz generator, I_{g1}	1.3 A
Melt pool depth, a_2	120 mm
Drain cooling water temperature, T_{drain}	18.0^{o}C
Maximum temperature on melt pool surface, T_{melt}	1,250^{o}C

Table 9-3 gives the modes of the 27 MHz generator, as well as the temperature of the cooling water exiting the drain assembly, T_{drain}, during Integrated Test #1.

Table 9-3. Generator and drain conditions observed during Integrated Test #1.

t, min	I_{a27}, A	I_{g27}, A	T_{drain}, °C	Notes
1	1.0	0.3	23.9	27 MHz generator powered on
3	1.0	0.28	25.1	-
7	1.0	0.287	25.3	-
10	1.2	0.28	26.6	Generator mode increased
13	1.35	0.26	28.5	Bubbles observed in center of melt pool
18	1.7	0.3	28.8	First casting
Restart using graphite ring and additional frit				
1	1.2	0.36	20.8	27 MHz generator powered on
3	1.2	0.34	27.6	-
6	1.2	0.34	28.0	-
9	1.2	0.34	28.0	-
11	1.32	0.33	28.3	-
15	1.35	0.33	28.8	-
23	1.5	-	-	Bubbles observed in center of melt pool
26	1.3	-	-	Generator mode increased
27	1.5	-	-	Second casting

Note that, In Table 9-1, I_{a27} and I_{g27} are anode and grid current values for the 27 MHz generator.

Figure 9-8 shows the condition of the bottom opening of the drain after the first and second castings. Figure 9-9 shows a cross section of the ingot that remained in the crucible after the casting. Three phases are clearly present: 1) a black glassy phase (i.e., the volume that was actually fully melted), 2) a brownish matte phase (i.e., glass-ceramic crystalline phase), and 3) a brown porous phase (i.e., sintered frit). Loose frit is also visible. The condition of the ingot provides some explanation as to why the melt could not be maintained after casting. Only approximately half of the volume remaining in the crucible was in a condition to couple with the electromagnetic field.
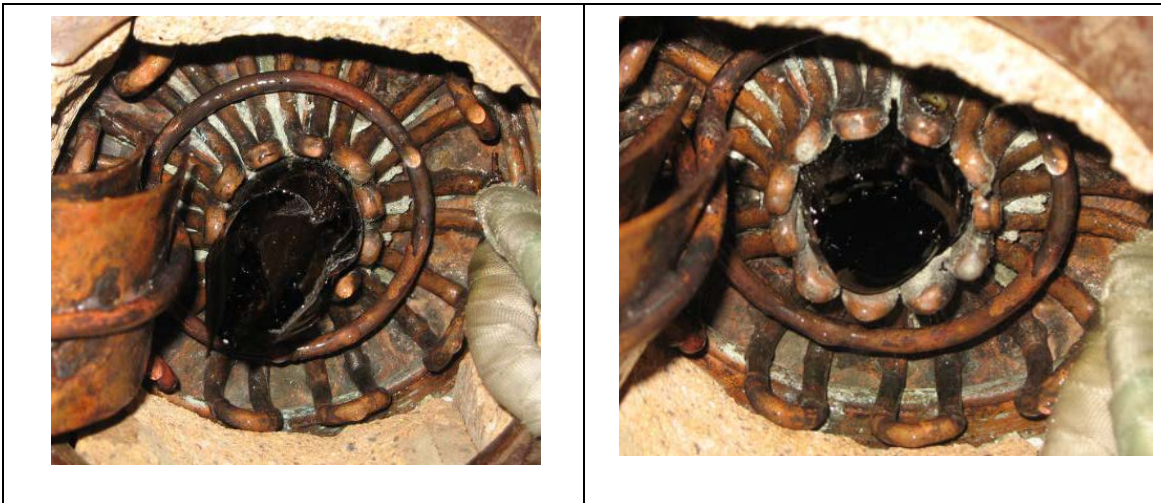
Figure 9-8. Drain conditions after first (left) and second (right) castings.

Figure 9-9. Ingot after disassembly showing three phases of glass product.

Key observations from Integrated Test #1 were as follows:

- The feasibility of a dual frequency induction melting integrated system for processing and casting refractory oxides was demonstrated and validated with multiple castings.
- Conditions of the skull and melt near the bottom have been better characterized and modifications to the drain design can be implemented to help mitigate the observed challenges.

9.2. Integrated Test #2

The basic equipment and configuration for Integrated Test #2 was the same as the previous test. Also as in the previous test, an auxiliary system for providing assistance in stopping the glass flow during casting was still not available.

Analysis of the ingot and operational parameters provided insight into the conditions after casting that led to the instability of the melt pool. This is best illustrated in Figure 9-10. As the glass drained, the top surface of the melt pool cooled, forming a skull. As the level dropped, this cooled, highly viscous layer approached the top of the drain opening but could not flow out. Heat was being removed from both the top and bottom from radiation and conductive heat losses (recall that the drain flange is water cooled, as well as the crucible sides. This layer of glass formed a non-conductive insulator, isolating the outer ring of glass from the center, and thus restricting the volume of melt that was available to couple with the electromagnetic field.

Accordingly, based on the results of Integrated Test #1, key modifications were made to the drain design. Specifically, the outside diameter was reduced from 160 mm to 140 mm, the inside diameter was decreased from 40 mm to 35 mm, and the height of the perimeter lip was increased from 25 mm to 45 mm. This increase also required translation of the inductor to maintain the 5 mm
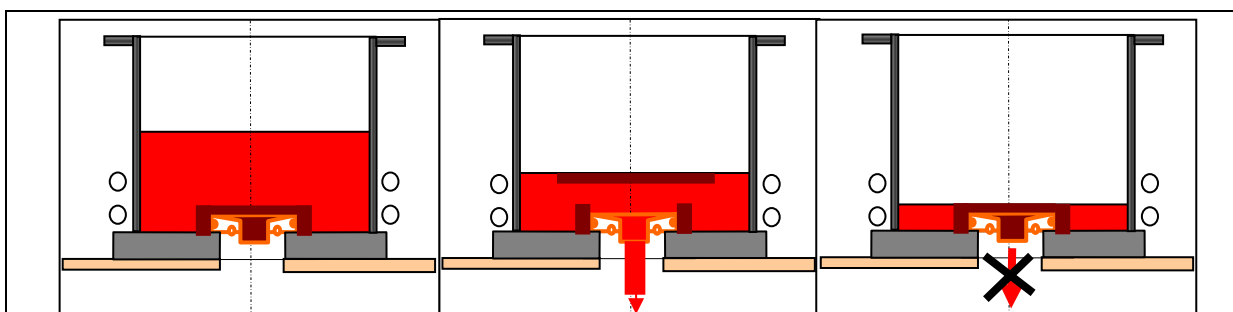
Figure 9-10. Illustration of casting effects from Integrated Test #1.

clearance from the bottom of the drain flange. These changes were made primarily to increase the volume of the melt pool after a casting such that frit can be added and the melt pool increased for additional castings without the need for an initiator ring. The resulting *fourth version* of the drain assembly is shown in Figure 9-11.
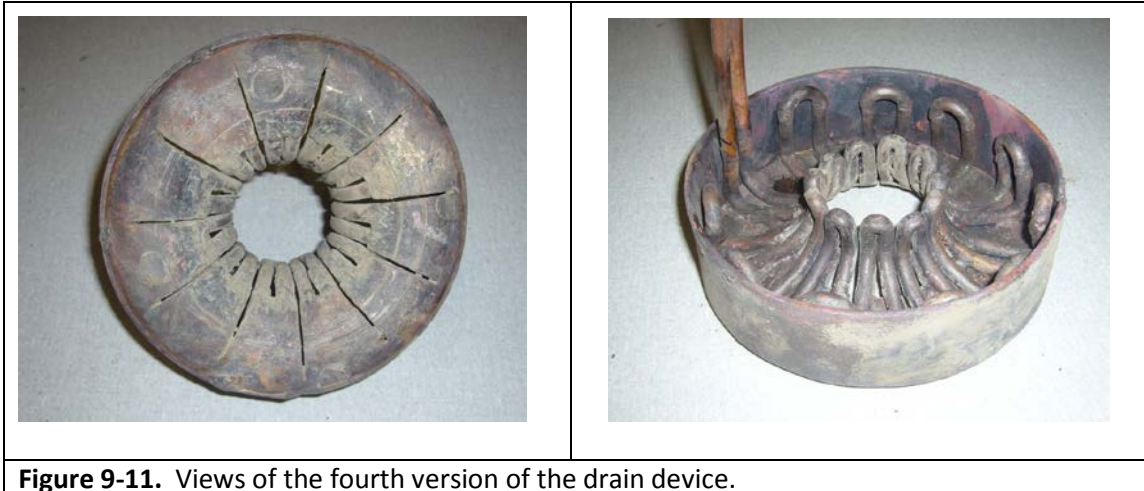
Figure 9-11. Views of the fourth version of the drain device.

During Integrated Test #2, three steady state modes were obtained and glass was cast at each mode. The modifications to the drain design were sufficient to allow multiple casts without requiring an initiator ring. Table 9-4 shows the key parameters for the 1.76 MHz generator, as well as the general melt conditions (i.e., depth and temperature). Table 9-5 shows data for the 27 MHz generator, as well as other key process data.

Table 9-4. 1.76 MHz generator modes and melt conditions during Integrated Test #2.

Time, hr:min	U_a, kV	I_a, A	I_g, A	U_{cont}, kV	Notes
16:42	6.0	3.65	1.3	1.9	a_2=90 mm. T_{melt}=1,250°C
18:40	5.64	3.45	1.2	1.84	a_2=110 mm. T_{melt}=1,450°C
20:12	5.59	3.26	1.05	1.84	a_2=90 mm. T_{melt}=1,100°C

(Ua is anode voltage on primary generator, Ia is anode current on primary generator, Ig is grid current on primary generator, Ucont is voltage on capacitor bank busses)

Table 9-5. 27 MHz generator modes and casting parameters during Integrated Test #2.

Casting	Casting duration, sec	Power duration, min	Cast mass, kg	I_{a27}, A	Rate, kg/h
1	-	21	8.6	1.3	-
2	56	22	12.2	1.0	784
3	60	16	11.9	1.0	714

The observed casting rates are too high for the target application. After the third casting, approximately 6.8 kg of glass remained in the crucible. The depth of the melt pool after each casting was approximately 30 mm. Upon disassembly of the melter, the glass thickness above the drain opening was 10 mm to 12 mm, the thickness over the drain flange was about 30 mm, and the depth in the perimeter ring ranged from 60 mm to 65 mm. The ingot looked very similar to that observed from Integrated Test #1. The bottom skull thickness thus ranged between 15 mm and 20 mm.

An interesting phenomenon occurred after the third casting. The frozen glass stream extending from the drain opening was hollow (see Figure 9-12), referred to as a "glass-cycle". This is believed to be due to the lower temperature of this final casting (i.e., only 1,100^{o}C). Such a condition would not be acceptable for the target applications. Similarly, a solid glass-cycle would also not be acceptable. Future enhancements to the draining system must be identified and implemented to eliminate this condition after casting.

Figure 9-12. View of drain bottom and hollow glass tube occurring after the third casting.
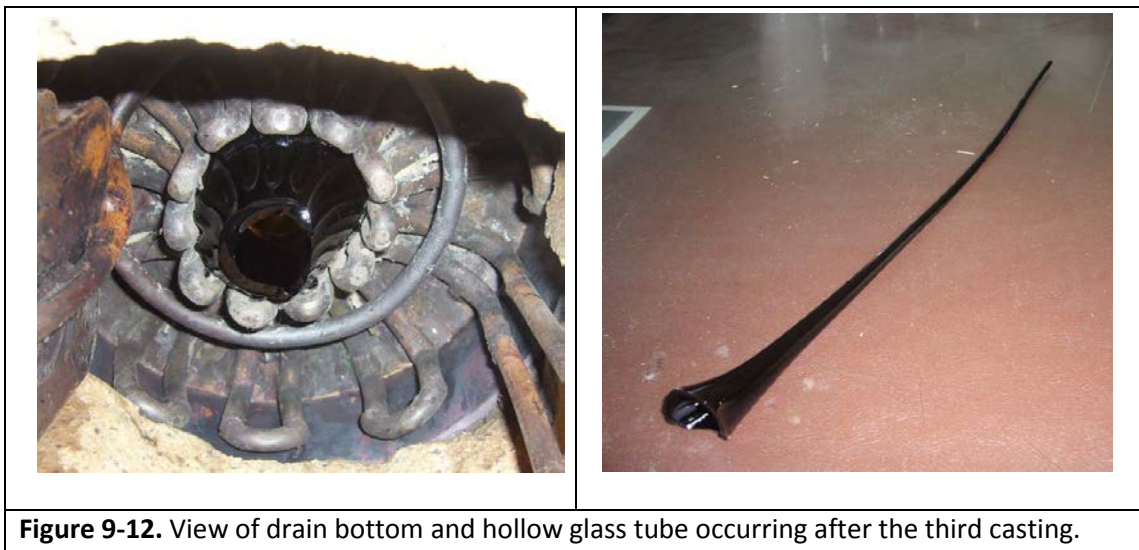
The key observations from Integrated Test #2 are as follows:

- A drain design that provides for maintaining at least 50 mm of melt after a casting cycle is sufficient to allow automatic restart (i.e., no initiator required) by adding frit, and thus a semi-continuous process.
- If a system requires flushing of the bottom melt volume to avoid build-up of crystalline phases, a different drain configuration and cast stoppage approach must be developed.
- A method of cast stoppage is needed to eliminate formation of glass-cycles after each casting.

9.3. Integrated Test #3

Based on the results of previous testing, the design of the drain was refined significantly. The body was constructed from a solid plate of copper approximately 24 mm thick. The configuration, which is described below, resulted from a series of analyses conducted using the ANSYS® model.

The use of a smaller drain diameter was desired due to the rate of glass pouring and difficulty in controlling it. Using the model, investigations showed that, if additional power is available from the 27 MHz generator (i.e., from 160 A to 175 A) casting can be accomplished in drain diameters ranging between 20 mm and 25 mm. Drains with 30 mm to 40 mm diameters were also investigated, and they readily achieve casting at the lower power levels. Based on these results, a *fifth version* of the drain device was designed. The key parameters are as follows:

- Inside diameter of the drain opening was 21.5 mm, with the ability to be increased.
- The drain was divided from the center radially into eight sections, each cut being approximately 50 mm long and I.0 to 1.5 mm wide.
- The lip around the perimeter was 45 mm high, formed by brazing a 21 mm high copper plate around the perimeter, which is the same as the previous design.
- A 10 mm by 10 mm channel was provided for cooling water flow.

Additionally, based on optimization studies from the model, the configuration of the inductor was redesigned to have a 60 mm inside diameter with two turns constructed of 6 mm diameter copper tubing spaced 4 mm apart. Figure 9-13 shows top and bottom views of the fifth version of the drain assembly. Figure 9-14 shows the installed drain assembly from the bottom, which also shows the placement of the new two-turn inductor. The new drain configuration allows implementation of the smaller diameter inductor. Additionally, it will significantly reduce the power losses because much less cooling capacity is provided with the new design. However, as previously discussed, the design concept had a conservative thermal analysis conducted using ANSYS® and was demonstrated to be sufficient for the conditions. Nevertheless, the new design will operate at much higher temperatures during heating and casting than the previous design.

For Integrated Test #3, a Type K thermocouple was installed on the ceramic bottom to measure the temperature of the glass in these lower zones. The junction was located in the center of the annulus

area formed between the drain perimeter and crucible wall.

Figure 9-13. Fifth version of drain device.
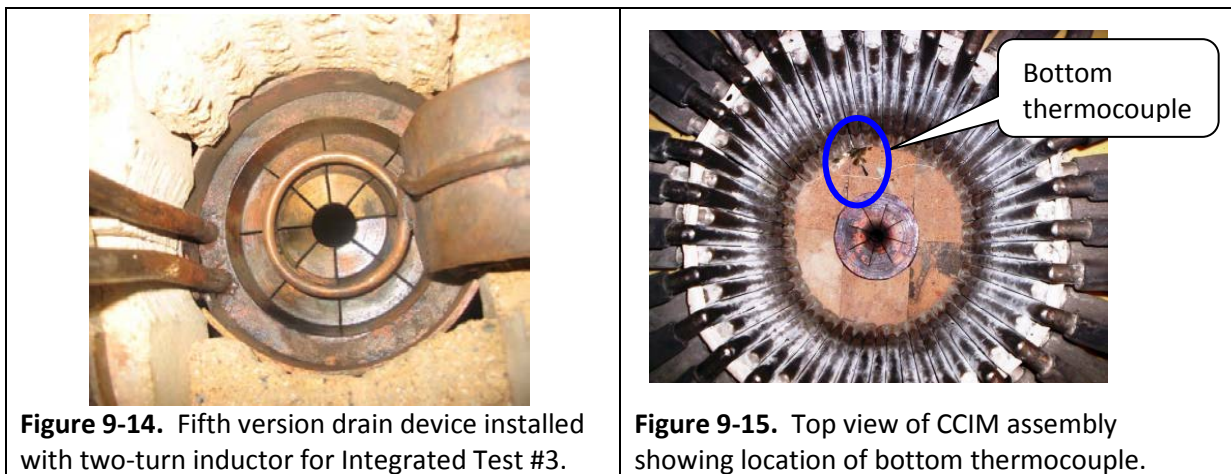
Figure 9-14. Fifth version drain device installed with two-turn inductor for Integrated Test #3.

Figure 9-15. Top view of CCIM assembly showing location of bottom thermocouple.

Figure 9-15 is a top view of the assembled CCIM system with the bottom thermocouple identified. Figure 9-16 shows the full assembly, including the open shielding cabinet. Note the electric motor (gray) and gear boxes (yellow) for translating the drain inductor up and down, as well as the improved water-cooled cover lid used for calorimetry (previously mentioned).

During this test the initial casting was successful. A steady state mode of 1,370°C was obtained after which the 27 MHz generator was powered and casting followed. However, due to the small diameter of the drain opening, a second casting could not be initiated electromagnetically.

Prior to casting, after the 27 MHz generator had been powered on for some time, the additional heat sources were easily observed with significant increase in the convection currents in the center

of the melt pool (see Figure 9-17). At the melt temperature of 1,470^{o}C, and approximately 2.2 kW
of energy deposition into the drain device, the cooling water temperature reached only 14.6^{o}C.

Figure 9-16. Integrated Test #3 setup showing system for inductor translation
and cover lid.
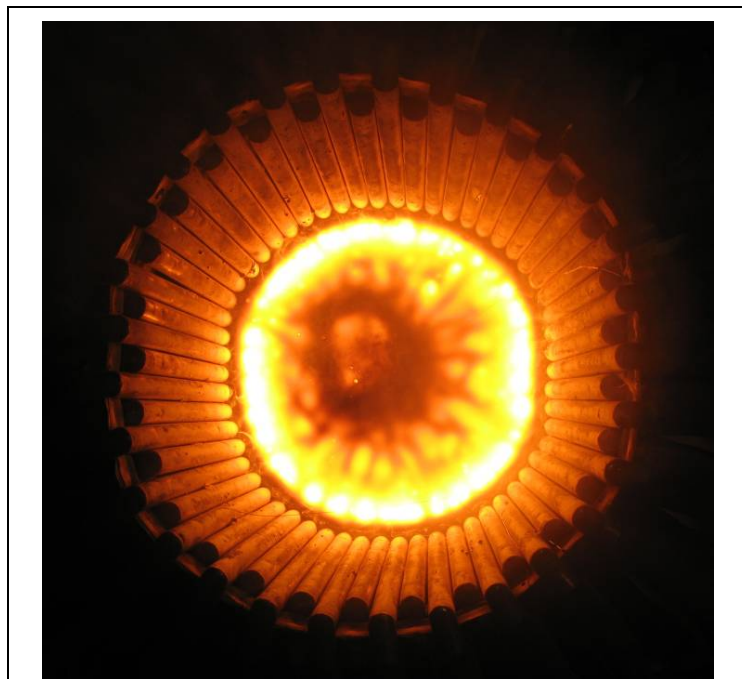
Figure 9-17. Melt pool with center convection currents due
to the 27 MHz generator.
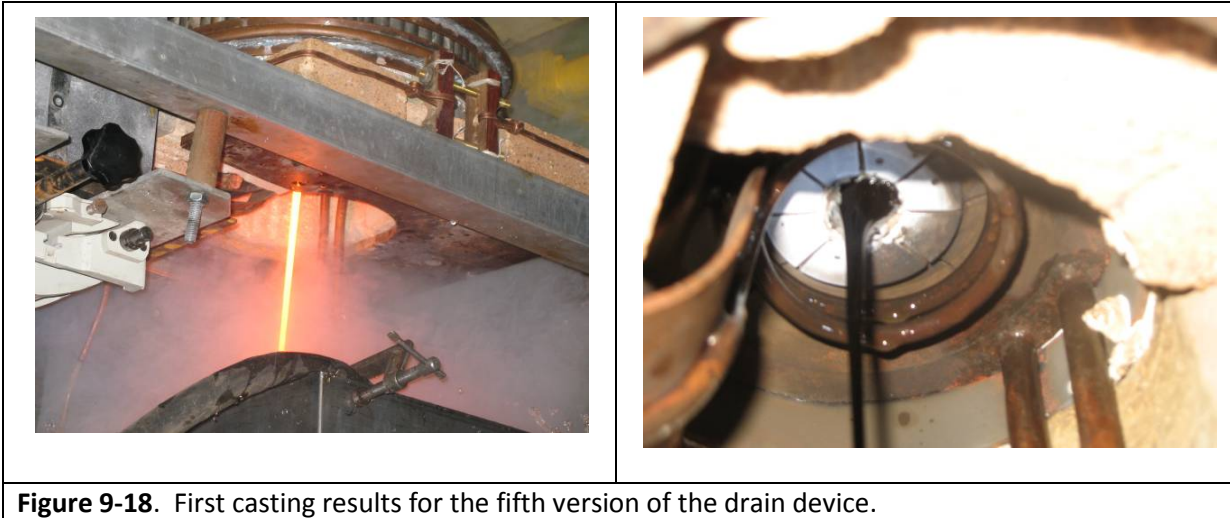
Figure 9-18. First casting results for the fifth version of the drain device.

During the test, overheating of the ceramic brick above the drain inductor busses was observed. Based on the generator parameters and calorimetry data from the drain device, an estimated 600 W of energy were absorbed into the chamotte. Figure 9-18 shows the first melt casting in the new drain design, as well as the resulting glass-cycle. The casting lasted about 100 seconds.

The white substance seen in the photograph on the right side in Figure 9-17 is primarily boron that volatilized out of the pour stream during casting. This was due to the high temperature of the melt pool (i.e., 1,470^{o}C). Also, note the condensation on the inductor coil. This is from both condensation due to the temperature of the cooling water (i.e., it cools the copper tube below the dew point) and the steam that is generated from pouring the molten glass into a water-filled container. This is problematic because it results in arcing between the coils due to the high frequency and voltage on the inductor. Shorting and arcing also occurred between the inductor and the drain device, as well as other components (see Figure 9-19). Figure 9-20 provides visual evidence that helps explain the challenge with controlling the arcing and shorting that were occurring due to the 27 MHz high frequency field. Improvements that resolved these issues were systematically implemented; however, the first step was to add additional shielding plates within the generator cabinet to provide a safer working environment.

After the initial casting, additional frit was added and a deep melt pool of 140 mm was established at a steady state temperature of 1,400^{o}C. As previously mentioned, the second casting was not successful using the 27 MHz generator alone and the glass skull in the drain body had to be punctured manually to help initiate the pour. Very little effort was required, indicating that the

| **Figure 9-19.** Arcing between thermocouple and CCIM enclosure. | **Figure 9-20.** 27 MHz field energizing a fluorescent bulb. (Dr. Alexander Martynov of ETU-LETI) |
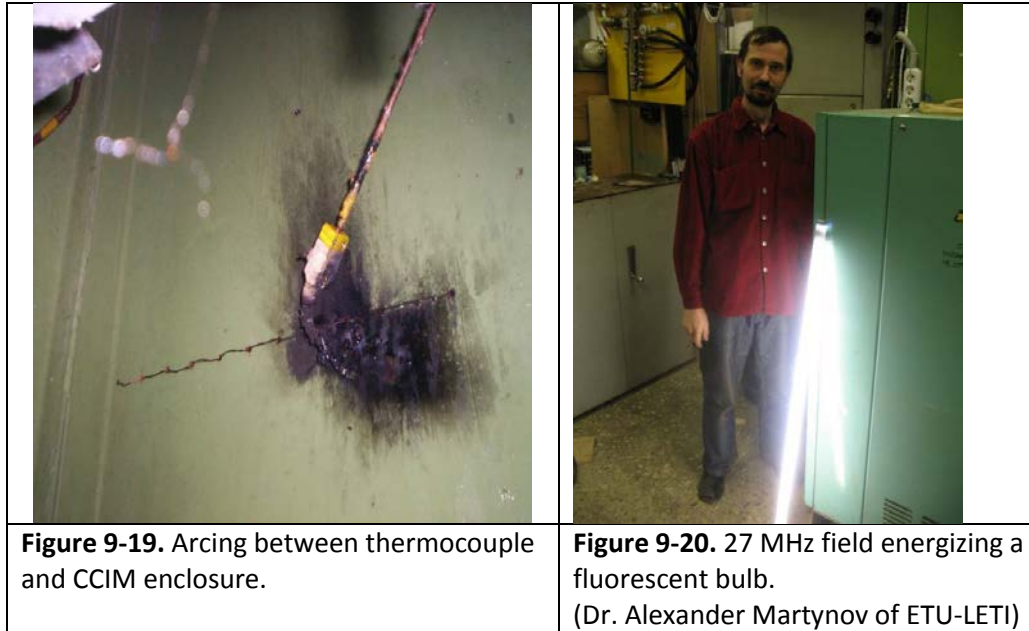
glass in the vicinity immediately above the drain opening was at sufficient temperature; however, the generator could not supply enough power to induce this melt to propagate into the small diameter drain body sufficiently. After the skull was broken in the drain opening, the 27 MHz generator was maintained at high power and casting was initiated when the power losses in the drain equaled about 2.3 kW. The second casting lasted about 140 seconds. During the two castings, the average glass flow rate was about 7.14 kg/min or 428.4 kg/hr. Details of the various melting stages, generator parameters, and conditions during Integrated Test #3 are provided in Table 9-6.

Upon disassembly of the crucible no indication of interaction between the melt and ceramic were observed, including the area in which the ceramic bottom was overheated. Additionally, no evidence of overheating or damage of the drain body was observed, indicating that the partial-cooling design of the new drain configuration is adequate to protect the device from damage, even at very high processing temperatures. However, glass melt had seeped between the refractory brick and the lip of the drain device. This occurred in the area above the drain inductor busses, indicating that, while there was no chemical interaction between the glass and ceramic brick, the glass was overheated significantly, reducing the viscosity to the point that the glass could flow through the small gap between the drain lip and chamotte brick. The gap can be easily removed during assembly using gaskets of appropriate material, or ceramic putty to seal the interface between the drain and bottom bricks.

Table 9-6. Melting stages and conditions during Integrated Test #3.

Time, hr:min	U$_a$, kV	I$_a$, A	I$_g$, A	U$_{ind}$, kV	f, MHz	I$_{g27}$, mA	I$_{a27}$, A	Comments
12:10	-	-	-	-	-	-	-	Generator is turned on.
12:41	10	4.1	1.8	6.01	1.87	-	-	Melting of frit and growth of melt pool.
12:49	10.1	4.76	1.63	3.73	1.84	-	-	Graphite initiator is removed.
13:06	8.48	5.0	1.22	2.85	1.83	-	-	Glass melt pool is formed.
13:20	8.03	4.94	1.14	2.7	-	-	-	T$_{drain}$ = 10.7^{o}C.
13:39	7.68	4.95	1.07	2.55	1.87	-	-	T$_{melt}$ = 1,163^{o}C, T$_{dr}$ = 12.6^{o}C.
14:08	7.7	4.96	1.09	2.58	1.88	-	-	T$_{melt}$ = 1,210^{o}C, T$_{dr}$ = 12.8^{o}C.
14:27	7.71	4.96	1.11	2.64	-	110	1.1	Small generator is turned on in a half-power operation mode. T$_{melt}$ = 1,370^{o}C, T$_{dr}$ = 14.1^{o}C.
15:02	7.63	4.97	1.22	2.67	1.88	300	1.5	T$_{dr}$ = 15.1^{o}C. Small generator is switched into a full-power mode
15:20	-	-	-	-	-	-	-	Arcing/damage to a grid controller in large generator. Additional feed-through capacitor is installed.
15:46	7.41	5.1	1.32	2.53	1.89	305	1.42	Test resumed - turn on generators.
16:15	8.33	5.86	1.6	3.17	-	305	1.61	T$_{melt}$ = 1,470^{o}C, T$_{drain}$ = 14.6^{o}C. Heating of chammote above busses of small inductor observed.
16:25	-	-	-	-	-	-	-	Start of melt casting.
16:27	9.42	5.17	1.06	3.73	-	-	-	Completion of casting. t$_c$ = 100 sec. Small generator is turned off. Frit added to increase melt pool.
16:36	8.95	6.8	1.08	2.92	-	-	-	T$_{melt}$ = 1,400^{o}C. Glass melt pool is formed. a$_2$ = 140 mm. Furnace calorimetry taken.
16:51	8	6.13	1.3	2.35	-	290	1.28	Small generator is turned on. T$_{drain}$ = 12.5^{o}C.
17:07	7.9	6.01	1.44	2.42	1.89	308	1.5	T$_{drain}$ = 15.1^{o}C.
17:26	7.82	5.83	1.32	3.17	-	350	1.6	T$_{drain}$ = 14.9^{o}C. Arcing/shorts between drain device and small inductor. Heating is stopped.

(U$_a$ is anode voltage in 1.76 MHz generator, kV; I$_a$ is anode current in 1.76 MHz generator, A; I$_g$ is grid current in 1.76 MHz generator, A; f is generator actual current frequency, MHz; U$_{ind}$ is large inductor voltage, kV; T$_{melt}$ is maximum temperature on the melt surface, ^{o}C; a$_2$ is height of glass melt pool, mm; T$_{drain}$ is temperature of water at outlet of drain device cooling system, ^{o}C; t$_c$ is duration of melt casting, sec; I$_{a27}$ is anode current in 27 MHz generator, A; I$_{g27}$ is grid current in 27 MHz generator, mA.)

However, the significant overheating of the glass was due to the high power level and long duration of operation of the 27 MHz generator during the attempt to induce the second casting. The drain design will require modification to correct this issue.

The glass layer over the drain was about 3 mm thick and a thin layer of unmelted frit remained between it and the upper drain surface. This is another indicator that the cooling is adequate for the drain device and the modeling was conservative for the design.

Key calorimetry data from Integrated Test #3 are provided in Table 9-7.

Table 9-7. Calorimetry data for Integrated Test #3.

Time, hr:min	T_{melt}, ^{o}C	a_2, mm	U_a, kV	I_a, A	I_g, A	U_{ind}, kV	P_{cc}, kW	P_{dr}, kW	P_{ind}, kW	P_{bus}, kW	P_Σ, kW
16:36	1,400	140	8.95	6.8	1.08	2.92	41.5	0.99	0.71	0.603	43.8

(P_{cc} is power in cold crucible; P_{dr} is power in drain; P_{ind} is power in inductor; P_{bus} is power in busses of generator; $P_\Sigma = P_{cc} + P_{dr} + P_{ind} + P_{bus}$.)

Key observations from Integrated Test #3 were as follows:

- The new design of the drain device is more efficient in general than the previous design; however, additional modifications and testing are needed to obtain reliability and optimization.

- Improved shielding and filtering is needed between the 27 MHz field and the other components, including data acquisition lines, of the system to avoid short circuits and arcing damage.

- Modifications to the 27 MHz inductor busses are needed (e.g., increased spacing from bottom, interchange positions of neutral and hot busses {hot currently on top, closest to bottom], transition to a coaxial feeder versus flat busses) to minimize overheating of ceramic bottom.

- A different type of ceramic brick material may be required that has lower concentrations of conductive impurities (i.e., carbon, iron, etc.)

- The drain opening of 21.5 mm is too small to support multiple castings, with current generator power capacity. The diameter should be increased as a first step for testing.

9.4. Integrated Test #4

Integrated Test #4 was conducted using the same equipment as the previous with the following modifications:

- The drain opening diameter was increased to 25 mm, constituting the *sixth version* of the drain.
- The chamotte brick installed above the 27 MHz inductor busses was half the thickness of the surrounding bricks, to increase the spacing between the busses and the bottom.
- A water-cooled container was used to receive the molten glass, rather than the container of water, to eliminate the steam and resulting arcing/shorting of the 27 MHz generator.

The modified drain assembly is shown in Figure 9-21.
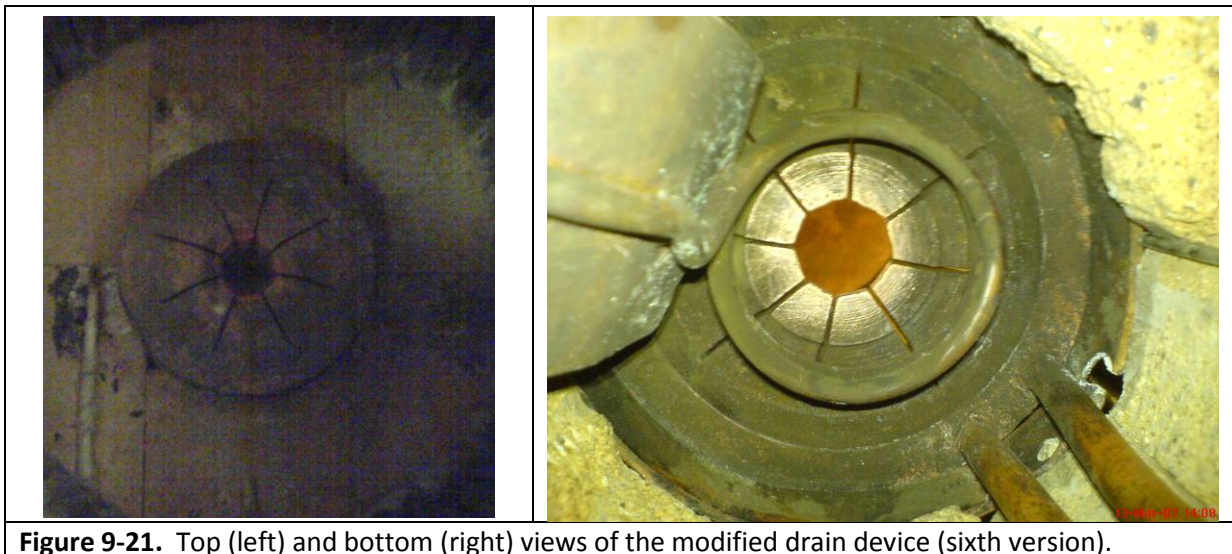
Figure 9-21. Top (left) and bottom (right) views of the modified drain device (sixth version).

The water-cooled container was constructed of 3 mm thick stainless steel. It was 470 mm high with an outside diameter of 320 mm and an inside diameter of 255 mm. The container is designed with an annulus volume that includes supply and return water connections for cooling. The dimensions of the water jacket was designed to ensure that the inside wall of the container would not exceed 500°C, based on inlet water temperature and flow rate.

The primary purpose of this container was to eliminate the steam and subsequent arcing/shorting, which did not allow maintaining power to the 27 MHz generator. As a result, to ensure a sustained casting process, the glass was being overheated, which leads to deleterious effects to the

composition of the glass, as well as the integrity of the crucible assembly. With the new container, coupled with the larger diameter drain device, casting should be able to reliably occur at lower temperatures. The 27 MHz generator power level may then be used to control the pour rate by addition of more or less power to effect the temperature, and thus the viscosity, of the molten glass.

| **Figure 9-22.** Water-cooled receipt container. | **Figure 9-23.** Thermocouples installed along bottom surfaces to measure thermal characteristics. |
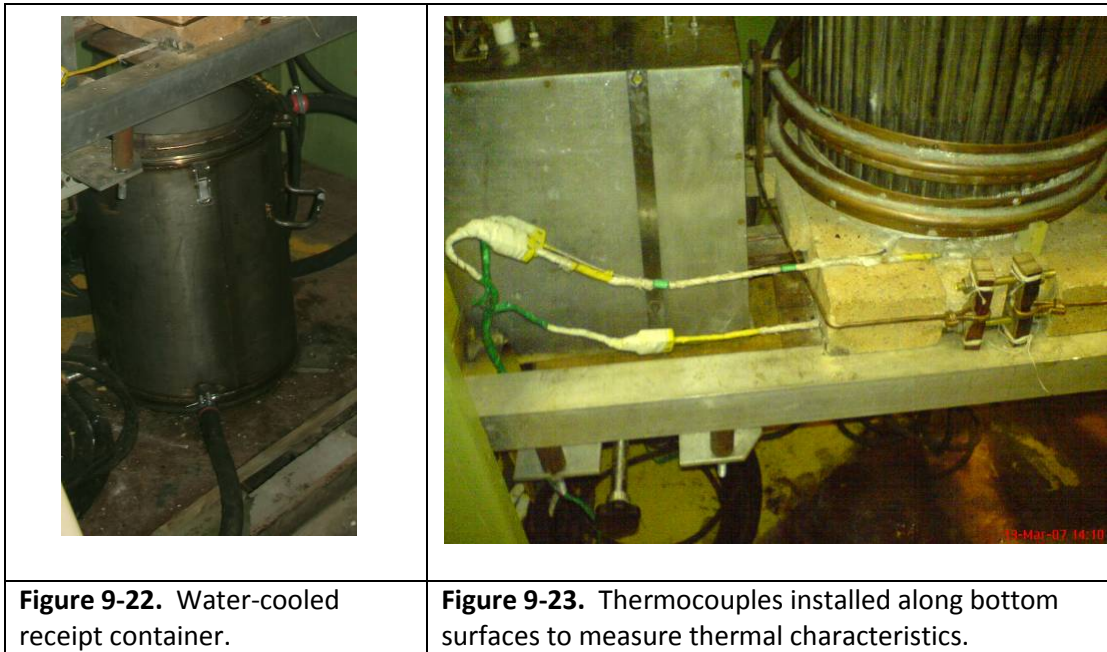
The water-cooled container is shown in Figure 9-22.

For Integrated Test #4, additional thermocouples were added to the bottom surfaces to determine the thermal characteristics during steady state and the casting process (See Figure 9-23). One was located on the ceramic brick above the inductor busses, one was located as before in the annulus area between the drain and the crucible wall, and one was located near the perimeter of the drain on the opposite side from the inductor busses. However, during start-up of the 27 MHz generator the first two thermocouples were destroyed due to the high frequency electromagnetic field. Unfortunately, due to an issue with the data acquisition during the test, the data from the remaining thermocouple was lost and no bottom temperature data were recorded during this test.

After the melt initiation process, a steady state temperature of $1,280^{o}$C was achieved and maintained. The temperature was intentionally lower than the previous test to avoid overheating of the glass such that the casting process could be better controlled. The temperature of the cooling water exiting the drain was 14.5^{o}C at this point. A melt pool depth of 130 mm was established. Recall that the inductor height is 100 mm. Additionally, it is located about 10 mm above the top

surface of the ceramic bottom, thus the melt pool was about 20 mm above the top coil of the inductor.

The 27 MHz generator was powered on to initiate the first melt casting process. Shortly thereafter, heating was observed on a corner of the chamotte brick adjacent to the inductor busses. Both generators were powered off and the heated corner was chamfered. The generators were powered back on and heating of the ceramic brick was eliminated by this modification. The testing was then resumed. However, the melt had cooled and there was concern that this process had allowed a thicker skull to form over the drain. The power for the 1.76 MHz generator was increased such that the glass melt temperature was at 1,450^{o}C. At this condition, the melt pool depth should have been greater than previously measured at 1,280^{o}C due to thermal expansion of the glass; however, it was 10 mm less. This confirmed that a thick skull had formed so the decision was made to conduct the first casting at the higher temperature of 1,450^{o}C. Due to this higher temperature, based on prior experience, the glass would be at a low viscosity and the flow rate too fast to allow any control with the power level of the generator so this investigation was eliminated for the first casting.

The first casting occurred after 57 minutes of operation of the 27 MHz generator. The cooling water in the drain was at 20.8^{o}C. The melt casting occurred independently with about 2 kW of power loss in the drain. The duration was 229 seconds. Figure 9-24 provides a comparison of the melt pool surface at the steady state mode without the drain inductor energized and after it has been powered on, just prior to casting. This is the desired effect of the second, high frequency inductor.

After the first casting was completed, the primary generator was powered on and frit was added to the crucible. A second melt pool was successfully obtained without requiring the initiator ring. A second steady state mode of 1,250^{o}C, with a melt pool depth of 135 mm, was obtained and maintained for a time, at which point the 27 MHz generator was powered on. Power levels were higher for this stage due to the skull that resulted from the first casting. Additionally, during the prior stage when the ceramic was being heated, glass had started seeping into a joint between two of the chamotte bricks located above the inductor busses. This glass became heated further during the second casting attempt and leaked through, dripping onto the inductor, creating short circuits and tripping the emergency stop switch on the 27 MHz generator. This led to overall difficulty in achieving the second casting. The glass leak is shown in Figure 9-25.
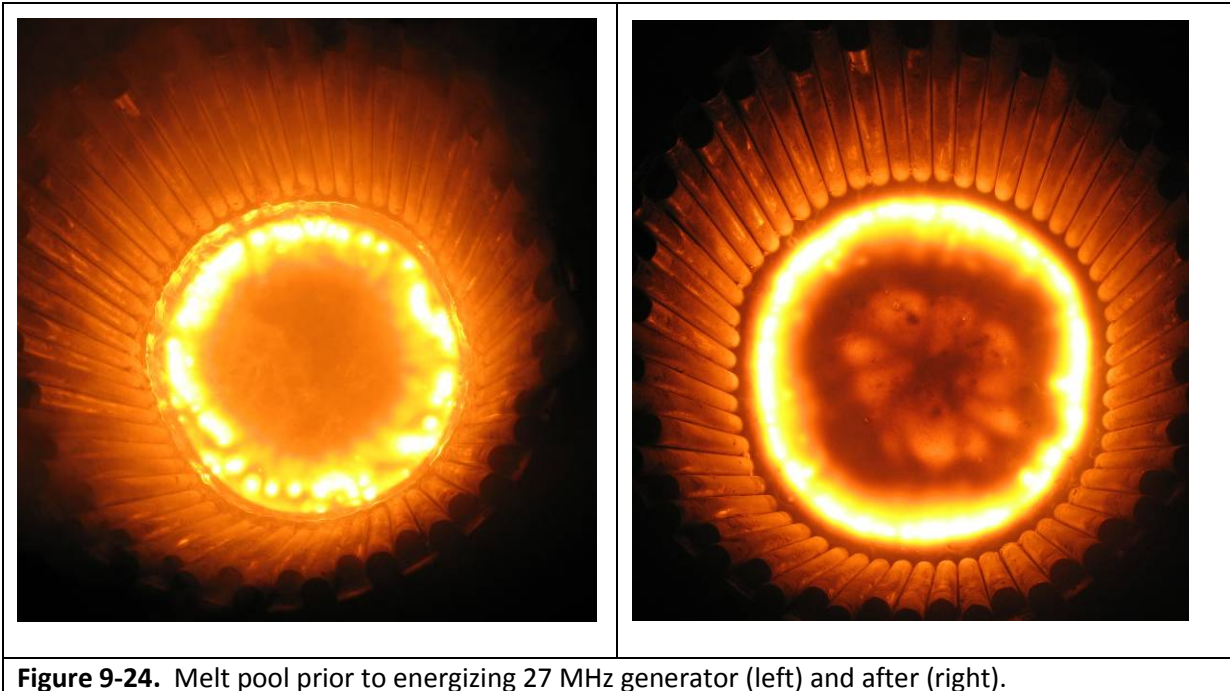
Figure 9-24. Melt pool prior to energizing 27 MHz generator (left) and after (right).

After 98 minutes at high power, the decision was made to manually puncture the skull to initiate the casting process. The force to remove the skull was minimal, once again demonstrating that the melt in the area above the drain opening was at high temperatures. With additional power from the generator, or a more efficient design that has lower losses, the melt front likely could have been propagated into the drain body completely. However, other geometry changes can also be implemented to improve the overall efficiency of the drain design.
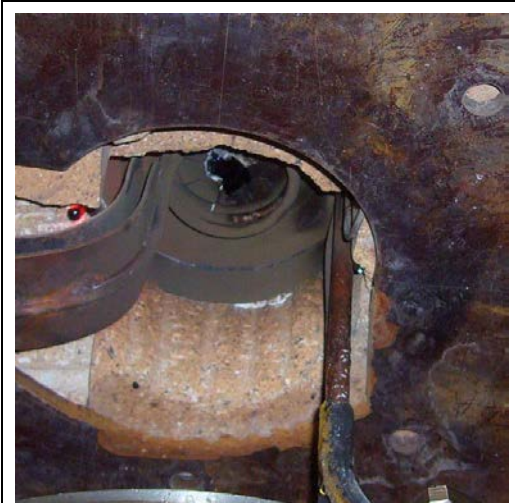
Figure 9-25. Melt leakage between the chamotte bricks.

Shortly after puncturing the skull, the glass began to flow out of the drain. The power loss in the drain device was about 2.2 kW at this time. For this casting, the melt pool depth was greater and the melt temperature lower. This resulted in a slightly thicker skull within the upper region of the drain body (i.e., effectively reducing the inside diameter of the drain) and higher viscosity. The result was a much longer duration for the casting of 330 seconds. With the steam generation issue mitigated, the 27 MHz was able to remain powered on. This provided an opportunity to observe the effects on the pour stream of increasing and decreasing the power level of the generator.

Noticeable changes in the stream diameter (i.e., mass flow rate) were seen, with the flow rate being directly proportional to the power level due to decreased viscosity. Figure 9-26 shows a comparison of the melt stream at a high power level on the 27 MHz generator and a lower level.

Figure 9-26. Comparison of pour stream diameter at high power (left) and low power (right) settings on 27 MHz generator.

These results were very encouraging because it indicates that, with the right combination of drain geometry, operational parameters, and applied energy or force, the flow rate can be controlled.

Recall that the steady state mode was at 1,250^{o}C prior to energizing the drain inductor. However, once it has been powered on for some time, the temperature of the melt pool generally increases by about 50°C or so, depending on the duration and power level of the 27 MHz generator. At the end of the second casting, the surface temperature of the melt pool was measured at 1,270^{o}C. It remained high due to the continuous operation of the 27 MHz generator during the casting process. During the second casting, the mass flow rate was measured at 4.54 kg/min or 272.4 kg/hr.

Operational parameters for the Integrated Test #4, including the various modes for the 1.76 MHz and 27 MHz generators, as well as key test stages, are provided in Table 9-8. The calorimetry data collected during the test are reported in Table 9-9.

Upon disassembly of the melter, the remaining ingot was determined to be approximately 65 mm deep. Above the drain opening, the thickness was about 20 mm. In spite of the ceramic bottom heating and the resulting leakage, no interaction between the glass and chamotte bricks was observed. A section of the ingot is shown during the disassembly process in Figure 9-27.

Table 9-8. Key generator modes and operational parameters during Integrated Test #4.

Time, hr:min	U_a, kV	I_a, A	I_g, A	U_{ind}, kV	f, MHz	I_{g27}, mA	I_{a27}, A	Comments
9:45	-	-	-	-	-	-	-	1.76 MHz generator powered on.
10:15	7.94	0.73	1.95	4.69	1.82	-	-	Melt initiation.
11:26	-	-	-	-	-	-	-	Graphite ring removed.
11:44	8.16	4.75	1.55	2.84	-	-	-	Formation of melt pool. Generator mode is decreased.
11:56	7.3	4.7	1.33	2.47	1.79	-	-	Generator mode is decreased.
12:05	6.83	4.61	1.26	2.37	-	-	-	T_{melt} = 1,200^{o}C. Generator mode is decreased.
12:10	6.68	4.5	1.24	2.34	-	-	-	Generator mode is decreased.
12:15	6.35	4.9	1.18	2.22	-	-	-	T_{melt} = 1,250^{o}C. a_2 = 130 mm. Cover lid in place.
12:20	6.36	4.4	1.27	2.27	1.73	-	-	System calorimetry taken.
13:25	6.68	4.5	1.35	2.41	1.74	-	-	T_{melt} = 1,035^{o}C. a_2 = 90 mm. Generator mode is increased.
13:50	6.66	3.9	1.29	2.35	-	-	-	T_{melt} = 1,280^{o}C. a_2 = 130 mm.
14:02	6.65	3.9	1.37	2.23	-	360	1.05	27 MHz generator powered on. T_{drain} = 14.5^{o}C.
14:11	6.6	3.9	1.41	2.1	-	365	1.3	Small generator frequency - 26.8 MHz. T_{drain} = 15.9^{o}C.
14:15	6.61	3.9	1.32	2.1	-	360	1.4	T_{drain} = 15.2^{o}C.
14:28	6.64	3.9	1.36	2.35	-	300	1.2	T_{drain} = 14.5^{o}C. Heating of brick above the busses observed.
15:28	8.21	4	1.83	2.92	1.75	310	1.3	Generators powered off. Brick corner chamfered. T_{drain} = 15.5^{o}C.
15:46	7.02	4.1	1.37	2.4	-	310	1.05	T_{melt} = 1,450^{o}C. a_2 = 120 mm.
16:25	7.35	4.8	1.2	2.52	1.79	300	1.6	Start of melt casting. T_{drain} = 20.8^{o}C at casting.
16:27	-	-	-	-	-	-	-	End of casting. t_c = 229 sec. 27 MHz generator powered off. Frit added and melt pool increased.
17:05	6.96	4.2	1.13	2.38	-	-	-	Conditions similar to those in previous casting.
17:08	6.79	4.1	1.1	2.32	-	307	1.2	27 MHz generator powered on. T_{drain} = 18.2^{o}C.
17:51	6.75	4.1	1.28	2.3	-	290	1.7	T_{drain} = 19.6^{o}C. Glass-cycle breaks off spontaneously.
18:46	6.85	4.0	1.22	2.38	-	300	1.65	Operator-initiated melt casting. T_{drain} = 22.1^{o}C at casting.
18:50	-	-	-	-	-	-	-	End of casting and test. t_c=330 sec.

(U_a is anode voltage in large generator, kV; I_a is anode current in large generator, A; I_g is grid current in large generator, A; f is large generator current frequency, MHz; U_{ind} is large inductor voltage, kV; T_{melt} is maximum temperature on the melt surface, ^{o}C; a_2 is height of glass melt pool, mm; T_{drain} is temperature of water at outlet of drain device cooling system, ^{o}C; t_c is duration of melt casting, sec; I_{a27} - anode current in small generator, A; I_{g27} is grid current in small generator, mA.)

An additional observation resulting from Integrated Test #4 was that the pour stream only contacts the upper portion of the drain internal diameter wall during casting. Due to surface tension and cooling, the pour stream necks down quickly, flowing freely through almost the entire drain body.

Table 9-9. Calorimetry data for Integrated Test #4.

Time, s	U_a, kV	I_a, A	I_g, A	U_{ind}, kV	P_{cc}, kW	P_{cov}, kW	P_{dr}, kW	P_{ind}, kW	P_{bus}, kW	P_Σ, kW
12:20	6.36	4.4	1.27	2.27	17.64	0.813	1.3	0.28	0.231	20.26

(P_{cc} is power in cold crucible; P_{dr} is power in drain device; P_{ind} is power in inductor; P_{bus} is power in buses of generator; P_{cov} is power in crucible's lid; $P_\Sigma = P_{cc} + P_{cov} + P_{dr} + P_{ind} + P_{bus}$.)

Figure 9-27. Remaining ingot from Integrated Test #4.

Figure 9-28. Pour stream configuration showing minimal contact with interior walls of drain opening.

This can be observed in Figure 9-28. Accordingly, the total height (i.e., thickness) of the drain device can be reduced, which will reduce power losses and make the system more efficient overall.

Key observations and conclusions from Integrated Test #4 are as follows:

- In its current configuration, the drain device cannot initiate subsequent castings after the skull has been deposited on the drain opening. To address these issues either the drain device must be modified such that it is more electrically efficient and/or the 27 MHz generator must be modified to provide additional power capacity.

- Several modifications to the drain device are needed to provide repeatable multiple castings without mechanical breaking of the skull. These include:

  o   Increasing the number of slits to improve the electromagnetic transparency,

- o Increasing the transition radius into the drain opening to bring the melt closer to the strongest energy sources from the induction field, and

- o Increasing the internal diameter of the drain to 30 mm.

- These changes should be implemented in stages so the individual effects of each modification can be observed to determine if all are necessary.

9.5. Integrated Test #5

Integrated Test #5 became a series of four tests that used all of the same equipment, configuration, and general parameters. These tests are referred to as Integrated Test #5a, #5b, #5c, and #5d. The first test was disrupted, but the second test was successful in achieving multiple, unassisted casting processes. As a result, a decision was made to conduct repeatability tests to ensure the reliability of the drain configuration, as well as to gather comparative data for a variety of operational modes. Because the objectives and parameters of these tests were so similar, they are reported here together as a series.

The tests used a 300 mm diameter stainless steel crucible. The primary and drain inductors were the same two-turn designs used in the previous test. The primary generator was the 60 kW, 1.76 MHz unit. The secondary generator, or drain generator, was the 27 MHz, 8 kW unit. The positions of the busses on the 27 MHz were switched such that the neutral bus was closest to the bottom of the crucible. Additionally, the cooling capacity of the cabinet was improved, allowing higher voltage on the oscillating tube. These modifications were expected to improve the overall efficiency of the generator, resulting in an increase in the available power by an estimated 10% to 15%. Finally, the chamotte bricks in the bottom were replaced with high-alumina bricks, which contain lower concentrations of impurities that can couple with the 27MHz field.

The significant equipment difference in the test configuration for this series of tests was the drain design. The sixth version included eight slits cut from the center to the periphery to provide some level of electromagnetic transparency. For this test, the number of slits was increased to 16. This is the *seventh version* of the drain device (see Figure 9-29).

Figure 9-29. Sixth version (left) versus seventh version (right) of drain device.
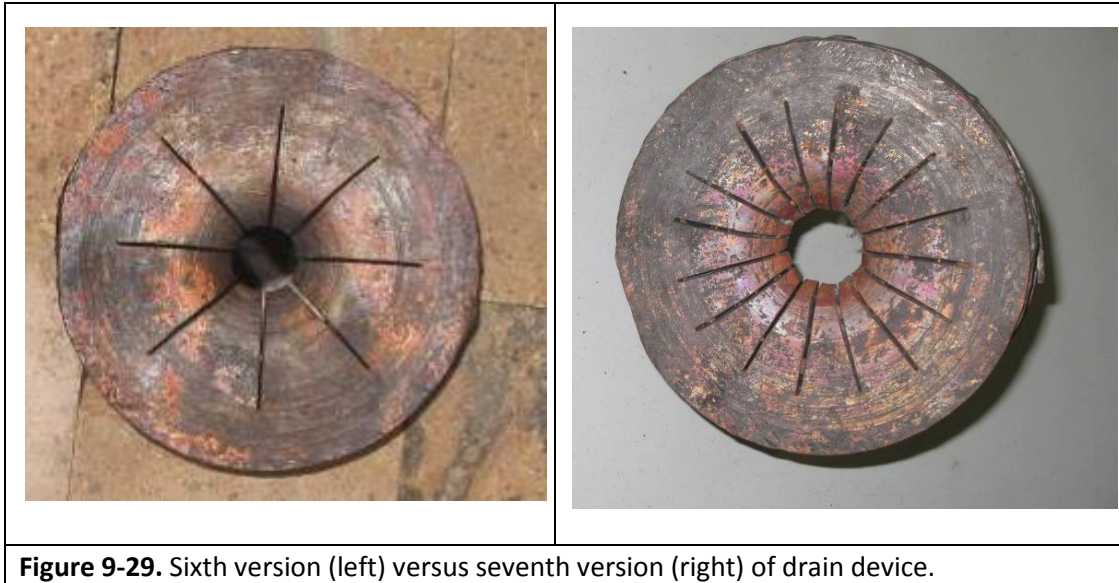
9.5.1. Integrated Test #5a

Integrated Test #5a was conducted with the objective of obtaining multiple castings without any operator assistance (i.e., by electromagnetic heating only). The melt was initiated and a steady state of 1,100^{o}C achieved. Calorimetry data were collected for this stage. The 27 MHz generator was then powered on and improved heating characteristics were observed as a result of the modifications to the generator. These are discussed in more detail later. Additionally, no heating of the new ceramic bricks occurred. However, the drain device cooling-water hoses used for this test were black. The pigment used to produce this color includes carbon and this factor, coupled with the increased efficiency of the generator, resulted in the hoses coupling with and being heated by the 27 MHz field. The test was halted, and the black hoses were removed and replaced with nonconductive hoses.

9.5.2. Integrated Test #5b

Integrated Test #5b was identical to #5a, with the exception of the installation of white hoses on the drain device. A steady state mode of 1,100^{o}C was obtained, with a melt pool depth of 140 mm, and calorimetry data were collected. After which, the 27 MHz generator was powered on in preparation for melt casting. The generator operated as expected and no undesirable heating conditions occurred. After 27 minutes, casting was initiated with the electromagnetic field. The casting duration was 97 seconds. Figure 9-30 shows the first casting using the seventh version of the drain. Note the white cooling-water hoses.
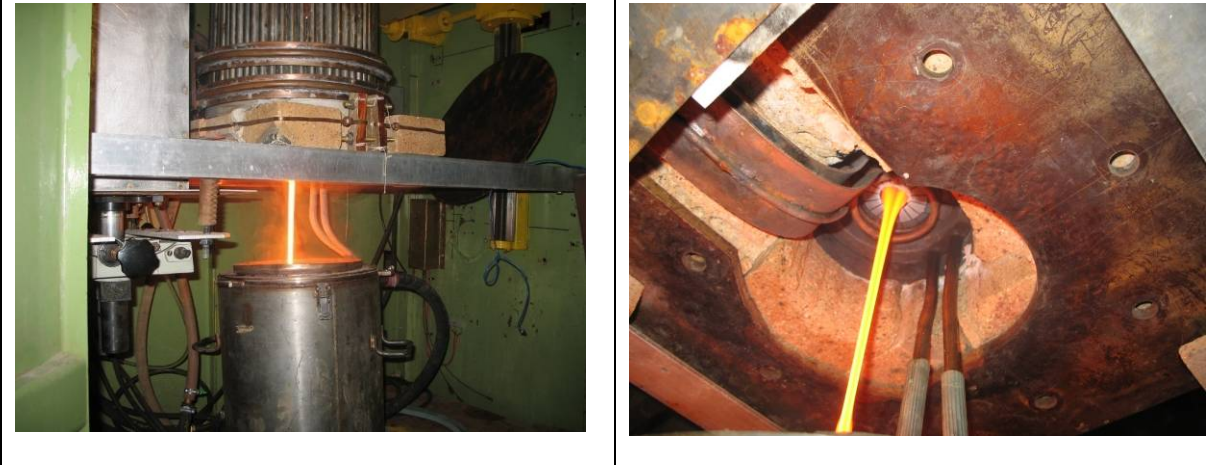
Figure 9-30. First casting using the seventh drain version near beginning (left) and end (right).

Many conditions of the system were the same in this test as in prior integrated tests, as well as subsequent tests, such as melt pool surface, pour stream, resulting glass skull and "glass-cycle". Accordingly photographs will only be shown for those instances in which something is different or unique to the specific test.

After the first casting was completed, frit was added, and the melt pool was re-established at 160 mm, with a steady state temperature of 1,400°C. Calorimetry data were collected for this mode. The 27 MHz generator was then powered on and, after only three minutes, casting began independently, with no operator assistance. This was the first time that multiple independent castings were achieved in a single melter run. The casting duration was 132 seconds, in spite of the higher temperature and lower melt pool depth, as compared to the first casting. This was due to a variety of opposing effects. First, during the first casting, a skull layer is formed in the upper portion of the drain opening, essentially reducing the flow diameter. Second, the higher temperature results in the melt pool maintaining a lower viscosity during the casting process, allowing more glass to be poured before it becomes too viscous to flow through the drain opening. These combined counter-acting effects present challenges in predicting the casting process characteristics, which is the primary reason that tests are repeated with changes in the key process variables (i.e., temperature and melt pool depth) to develop a better understanding of their effect on the casting process.

After the second casting was completed, frit was again added, and the melt pool was re-established at 140 mm, with a steady state temperature of 1,250°C. Full calorimetry was not collected during

this stage. The 27 MHz generator was powered on and, after about 5 minutes, the third casting was initiated independently. The casting duration was 170 seconds.

Table 9-10 provides data related to the three casting events during Integrated Test #5b. For comparison, refer back to the data for Integrated Test #2, Table 9-5, which used a drain with a 35 mm diameter (fourth version) as opposed to the 25 mm diameter used for this seventh version.

Table 9-10. Characteristics and conditions of the melt casting processes for Integrated Test #5b.

Casting #	a_{bot}, mm	Δa_2, mm	τ, min	T_{max}, $^\circ$C	t, sec	$P_{dr\,o}$, kW	$P_{dr\,max}$, kW	m_{glass}, kg	M_{cast}, kg/h
1		15	27	1,100	97	1.6	-	9.4	350
2	20	50	3	1,400	132	1.4	-	15.0	409
3		20	5	1,250	170	1.9	4.51	10.2	216

(a_{bot} is distance between large inductor and ceramic bottom, mm; Δa_2 is height of melt pool above large inductor, mm; τ is operation time of 27 MHz generator prior to casting, min; T_{max} is maximum temperature of melt pool surface, $^\circ$C; t is duration of melt casting, sec; $P_{dr\,o}$ is power in drain before the start of melt casting, kW; $P_{dr\,max}$ is maximum power in drain during casting, kW; m_{glass} is mass of glass melt poured, kg; M_{cast} is average rate of melt casting, kg/h)
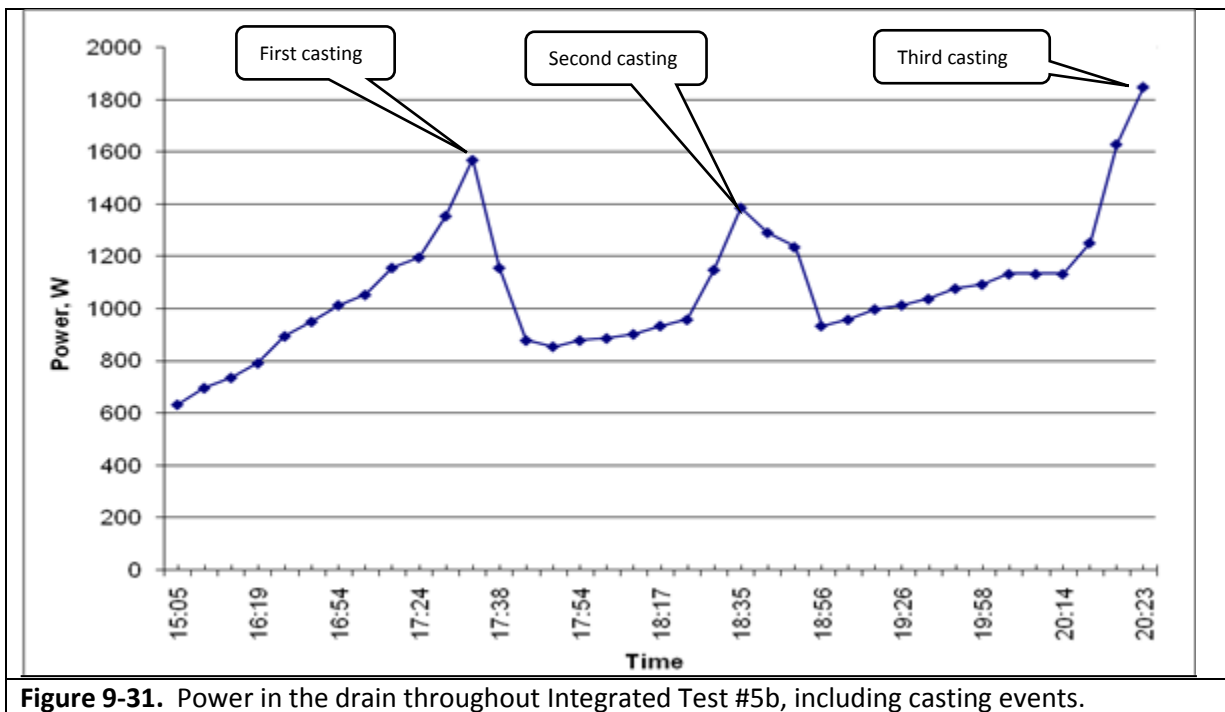
Figure 9-31. Power in the drain throughout Integrated Test #5b, including casting events.

Figure 9-31shows the power levels in the drain device, measured by calorimetry, throughout the entire Integrated Test #5b, including the moments castings were initiated.

During disassembly, the drain, ceramic bottom, and receipt container all performed as expected, with no indications of overheating or integrity issues.

Key observations from Integrated Test #5b were as follows:

- Multiple independent castings were achieved for the first time using the seventh version of the drain device.
- The casting characteristics were significantly improved over prior drain designs (i.e., casting rate and time required), indicating that the design concepts incorporated into this drain configuration will provide the basis for further optimization and improvements.
- The ability to have better control over the casting process (i.e., to control the pour rate, to include complete stoppage) will be necessary for optimizing the overall system.

9.5.3. Integrated Test #5c

Integrated Test #5c used the same equipment and configuration at #5b. Two separate steady state modes were established at $1,170^{\circ}$C and $1,150^{\circ}$C, with melt pool depths of 145 mm and 140 mm, respectively. Full calorimetry data were collected for both of these modes. After the calorimetry date were gathered for each steady state, the 27 MHz generator was powered on to initiate the casting process. For this test, two independent castings were successfully initiated after operation of the 27 MHz generator for 15 minutes and 6 minutes, respectively. Casting durations were 141 seconds and 158 seconds, respectively. No issues were discovered during disassembly. Table 9-11 presents data related to the two casting events during Integrated Test #5c.

Table 9-11. Characteristics and conditions of the melt casting processes for Integrated Test #5c.

Casting #	a_{bot}, mm	Δa_2, cm	τ, min	T_{max}, $^{\circ}$C	t, sec	$P_{dr\,o}$, kW	m_{glass}, kg	M_{cast}, kg/h
1	20	25	15	1,170	141	1.8	10.2	260
2		20	6	1,150	158	1.63	12.1	254

Figure 9-32 shows the power levels in the drain device, measured by calorimetry, throughout the entire Integrated Test #5c, including the moments castings were initiated. No new observations or conclusions resulted from this test other than another successful demonstration of the ability to independently initiate multiple melt castings with the seventh version of the drain device. Additional data were also collected for various operational modes.
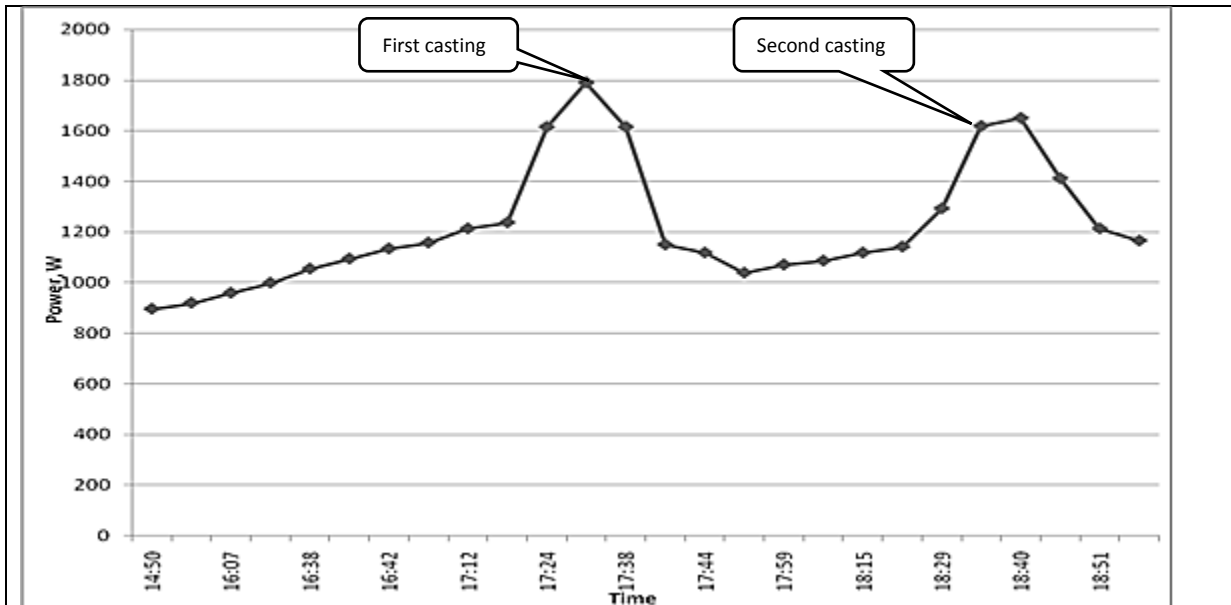
Figure 9-32. Power in the drain throughout Integrated Test #5c, including casting events.

9.5.4.   Integrated Test #5d

Integrated Test #5d used the same equipment and configuration as #5b and #5c. Two separate steady state modes were established at 1,200°C and 1,380°C, with melt pool depths of 135 mm and 140 mm, respectively. Full calorimetry data were not collected during this test. Once the steady state mode was established, the 27 MHz generator was powered on to initiate the casting process. For this test, two independent castings were successfully initiated after operation of the 27 MHz generator for 15 minutes and 5 minutes, respectively. This is very similar to the results from Integrated Test #5c. Casting durations were 141 seconds and 178 seconds, respectively. No issues were discovered during disassembly. Table 9-12 presents data related to the two casting events during Integrated Test #5d.

Table 9-12. Characteristics and conditions of the melt casting processes for Integrated Test #5d.

Casting #	a_{bot}, mm	Δa_2, cm	τ, min	T_{max}, °C	t, sec	$P_{dr\,o}$, kW	m_{glass}, kg	M_{cast}, kg/h
1	20	15	15	1,200	141	1.45	14.8	227
2		20	5	1,380	178	1.71	11.2	220

Figure 9-33 shows the power levels in the drain device, measured by calorimetry, throughout the entire Integrated Test #5d, including the moments castings were initiated.
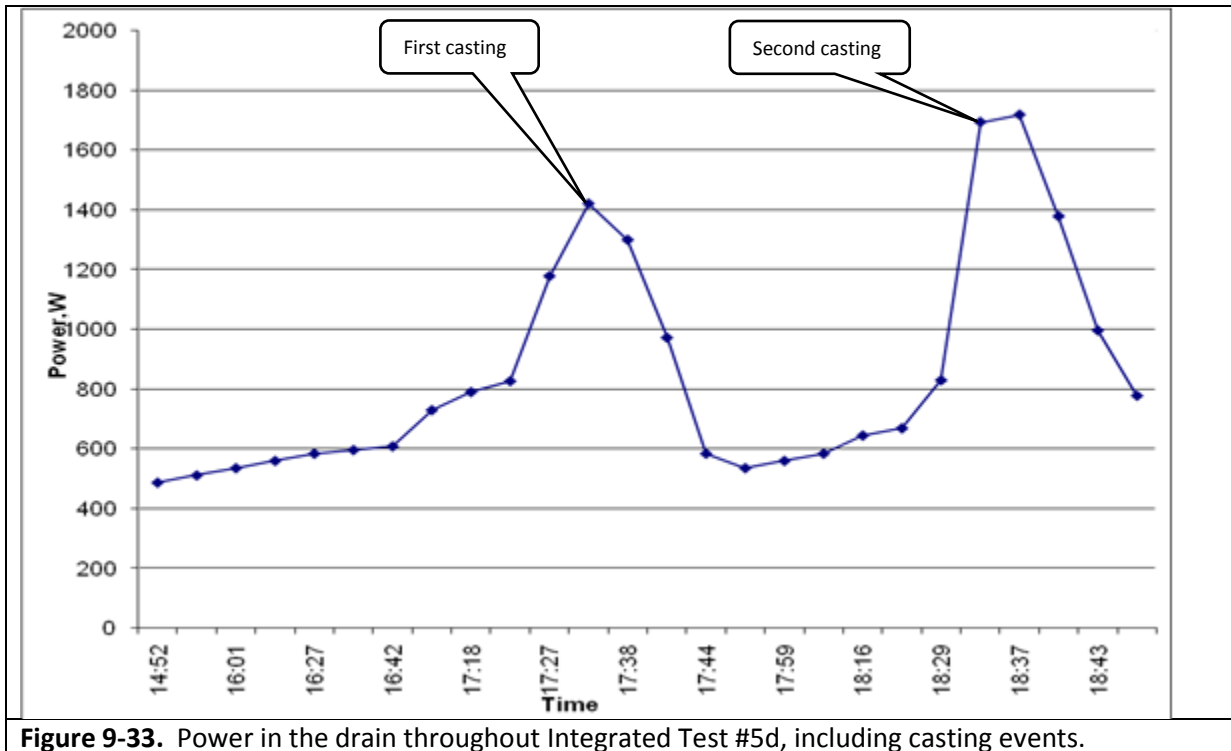
Figure 9-33. Power in the drain throughout Integrated Test #5d, including casting events.

Upon disassembly, no evidence of overheating or other damage to the ceramic bottom, drain device, receipt container, or any other key components was observed. Both generators functioned as expected, although arcing occurred at times between the coils of the drain inductor due to condensation on the copper tubes. This will be addressed in further design improvements.

Figure 9-34 shows the final disassembly of the CCIM after Integrated Test #5d, with no indications of damage or integrity issues for the drain device.
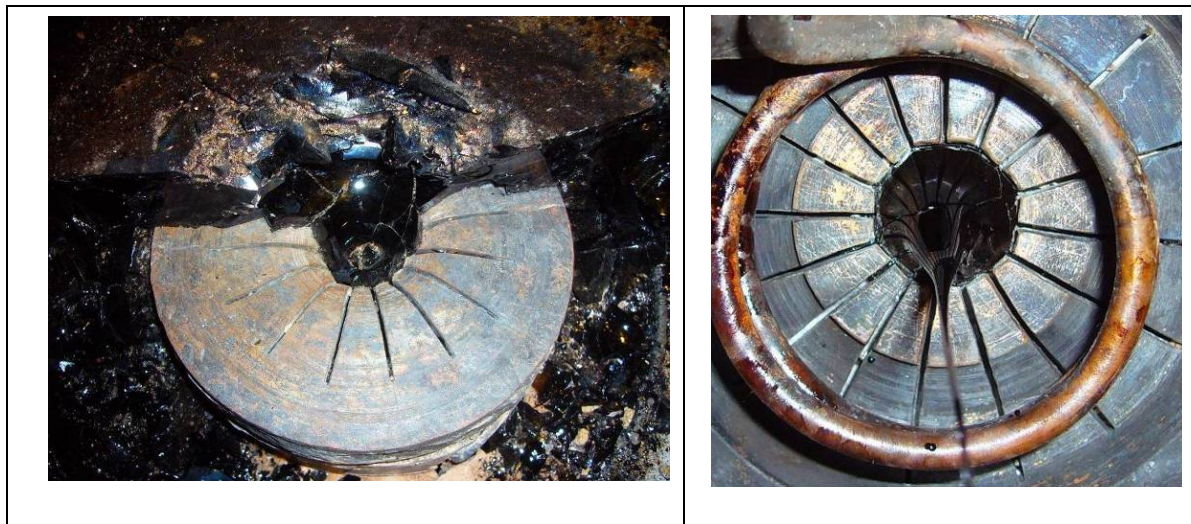
Figure 9-34. Top and bottom views of the drain device after multiple tests and casting processes.

9.6. Summary of Results

During the Integrated Test #5 series, seven independent castings were completed, four of which were follow-on castings after previous successful castings, during a single test. This was the first time that multiple independent castings were achieved. Key observations and conclusions from this series of tests are as follows:

- Increasing the number of slits from eight to 16 significantly improved the electromagnetic efficiency of the drain design. While improvements and optimization are still needed, this basic design will serve as the starting point for those efforts.

- In general, the casting process occurs too quickly to reliably have control of the mass flow rate during pouring. A method to control the mass flow, to include full stoppage, is needed for the likely applications of this technology.

- The configuration of the drain is such that it leaves a volume of molten glass of about 50 mm deep for restart purposes. This is not the most desirable situation since it allows build-up of crystalline phases, metals, and other undesirable materials in the melter. If a reliable method is implemented that effectively controls the mass flow and provide full stoppage, the drain configuration can be changed to eliminate this feature.

- The cooling system for the drain device is a once through system and the service water temperature is well below the dew point for the location of the test platform. This would likely be the case regardless of the location. The condensation on the inductor coils can cause arcing between the turns, as well as with other structural components near the 27 MHz source. A heated cooling-water supply will be required to eliminate this issue.

- This test series used a 100 mm high, two-turn primary inductor coil. Additional data are needed for a taller inductor design (i.e., three-turn) to investigate the operability of the drain along with the resulting, and different, characteristics of the lower layers of the melt that are expected. This is necessary because the higher inductor allows a larger volume of melt, which will improve the efficiency of the casting process and support the ultimate goal, which is to establish a continuous process (or at least semi-continuous).

Table 9-13 provides a direct comparison of several generator parameters, for both the primary and drain generators, as well as calorimetry data for the Integrated Test #5 series. It also includes, for comparison, similar data from Integrated Test #4 (sixth version of the drain device).

Table 9-13. Generator modes and calorimetry data comparison.

Integrated Test #	T_{melt}, °C	a_2, mm	U_a, kV	I_a, A	I_g, A	U_{ind}, kV	I_{a27}, A
4	1,450	130	6.36	4.4	1.27	2.27	1.6
5a	1,100	140	6.8	4.8	1.18	2.4	1.2
5b	1,100	135	7.0	5	1.15	2.51	1.1
5b	1,400	160	7.8	5.9	1.32	3.03	1.2
5c	1,170	145	7.4	4.6	1.12	2.89	1.3
5c	1,150	140	7.5	4.9	1.02	2.35	1.2
5d	1,200	135	6.5	6.05	0.98	2.41	-
5d	1,380	140	7.5	7.8	1.08	3.02	-

(U_a is anode voltage in large generator, kV; I_a is anode current in large generator, A; I_g is grid current in large generator, A; f is large generator current frequency, MHz; U_{ind} is large inductor voltage, kV; T_{melt} is maximum temperature on the melt surface, °C; a_2 is height of glass melt pool bath, mm; I_{a27} is anode current in generating tube of small generator, A.)

Table 9-13. Generator modes and calorimetry data comparison (continued).

Integrated Test #	I_{g27}, mA	P_{cc}, kW	P_{dr}, kW	P_{cov}, kW	P_{ind}, kW	P_{bus}, kW	P_{Σ}, kW
4	300	17.6	1.3	0.81	0.27	0.23	20.2
5a	290	21.2	1.5	1.92	0.39	0.89	25.5
5b	300	22.4	1.6	1.66	0.4	0.31	26.4
5b	310	27.2	1.9	3.58	0.51	0.3	33.5
5c	260	-	1.8	-	-	-	-
5c	290	-	1.63	-	-	-	-
5d	-	-	1.45	-	-	-	-
5d							

(I_{g27} is grid current in small generator, mA; P_{cc} is power in cold crucible; P_{dr} is power in drain device; P_{ind} is power in inductor; P_{bus} is power in buses of generator; P_{cov} is power in crucible lid; $P_{\Sigma} = P_{cc} + P_{cov} + P_{dr} + P_{ind} + P_{bus}$)

CHAPTER 10.   DRAIN DEVICE AND INTEGRATED SYSTEM IMPROVEMENTS

Several areas of improvement and overall design modification of the drain device and integrated system were identified as a result of the prior testing; however, the two areas that would have the greatest impact on the operation of the system are:

- The configuration of the drain device and crucible bottom to improve heating and pouring characteristics, and
- A method for controlling the mass flow rate during casting, to the point of full stoppage.

These areas were addressed and resulted in an overall improved system that provided the basic integrated design for final optimization. These investigations and results are discussed in detail in this chapter.

10.1.   Casting Control and Stoppage – Design Concepts

Due to the high frequency, and potentially very high temperatures (application dependent) a method for controlling the mass flow rate was sought that did not require any mechanical components near the drain inductor. This is also consistent with the objective of the electromagnetic draining concept, in general.

The concept that satisfied this constraint is the use of pressure differentials on the drain opening cross-section that can overcome the gravity force of the pour stream. In principle, this can be accomplished in three ways:

1. Pressure increase from below the drain exit,
2. Pressure decrease from above the drain entrance, or
3. A combination of both.

Each of these is discussed below in more detail.

10.1.1. Option 1

This option will require that the receipt container is sealed to the bottom of the crucible such that the applied pressure will induce an upward force on the drain exit. The receipt container will require modification to provide a port for applying the pressure within the container once the casting has been initiated. This concept is attractive because the gases in the container will be

heated as the melt is poured. Simultaneously, the volume of empty space will be decreasing, such that some portion of the force needed to stop the casting will be naturally supplied. A disadvantage is that it is likely that the dynamics of the process may be difficult to control and lead to bubbling as the melt pool becomes shallow (i.e., when the applied pressure is significantly greater than the hydrostatic pressure). This option is depicted in Figure 10-1, where P_a is the hydrostatic pressure of the melt pool and P_g is the back pressure of the gas.
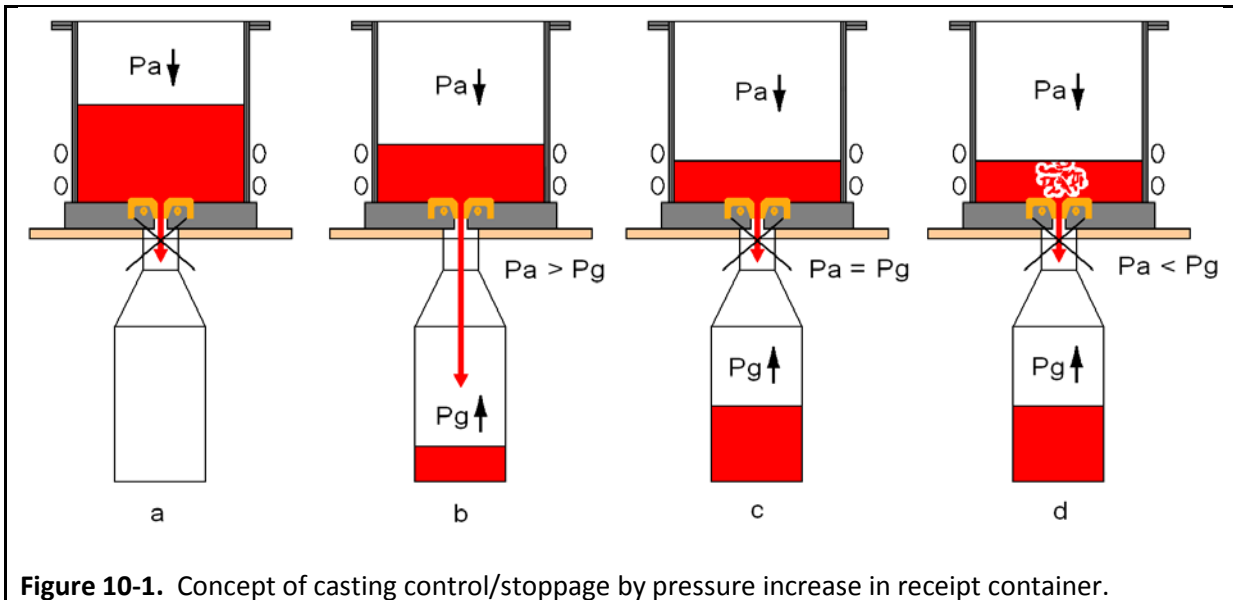
Figure 10-1. Concept of casting control/stoppage by pressure increase in receipt container.

Condition "a" represents the steady state condition prior to energizing the drain inductor. Condition "b' represents the control process once the casting has been initiated. Low to no pressure will be applied to allow the full casting to proceed. The pressure can be increased to slow the flow (i.e., mass flow rate control) which will continue as long as P_a is greater than P_g. Condition "c" represents full stoppage of the casting, which occurs when $P_a = P_g$. Finally, condition "d" represents the case in which the back pressure significantly exceeds the hydrostatic pressure and results in bubbling within the melt.

Note that this option does not require sealing the top of the crucible, although for most applications it would be. However, for the current test platform, sealing the crucible will require its complete redesign. Therefore, this option was the first method tested.

10.1.2. Option 2

This option will require that the crucible is sealed and integrated with an offgas duct such that the

applied vacuum (i.e., induced by an offgas suction fan or similar) will produce an upward force on the drain entrance. The crucible design will require modification to interface with a sealed lid such that an air-tight condition exists. The lid must also have a direct interface with the offgas system. This will allow an increase in the offgas suction to produce the force needed to control the glass mass flow rate. This option is depicted in Figure 10-2, where P_a is the hydrostatic pressure and P'_g is the vacuum induced by the offgas suction.

This concept is attractive because, for the target applications envisioned for the draining technology (i.e., processing radioactive materials), a sealed lid and offgas system will be required. Additionally, these systems are preferred to be operated in a slight vacuum for contamination control purposes. However, a potential disadvantage is that this method will introduce additional particulate and volatiles into the offgas system, which must then be removed and dispositioned. For the purposes of this research, however, the primary objective will be on demonstrating the overall feasibility of the concept.
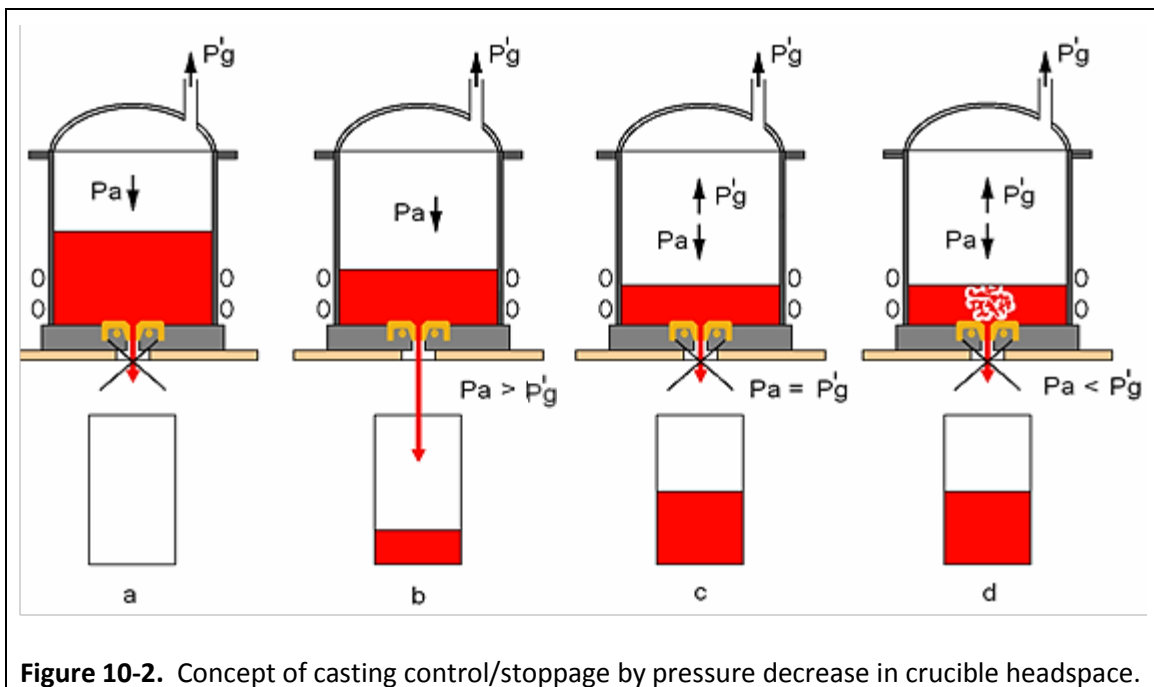
Figure 10-2. Concept of casting control/stoppage by pressure decrease in crucible headspace.

Condition "a" represents the steady state condition prior to energizing the drain inductor. Condition "b' represents the control process once the casting has been initiated. Low to no additional suction (i.e., some suction will always be present in the offgas system) will be applied to allow the full casting to proceed. The suction can be increased to slow the flow (i.e., mass flow rate control) which will continue as long as P_a is greater than P'_g. Condition "c" represents full stoppage of the

casting, which occurs when $P_a = P'_g$. Finally, condition "d" represents the case in which the vacuum induced by the suction significantly exceeds the hydrostatic pressure and results in bubbling within the melt. This situation will be easier to control with Option 2 because most lid interfaces are designed to allow some in leakage and/or have valve-controlled make-up air that can be used to balance the system to mitigate such issues.

10.1.3. Option 3

This option is a combination of both concepts, and would obviously be the most complex and expensive to implement. However, it would provide the greatest process control and optimization capability. Additionally, for the applications of the drain technology, both offgas lids and seals between the pour point and receipt container are common, making this option readily implementable. This concept is depicted in Figure 10-3.
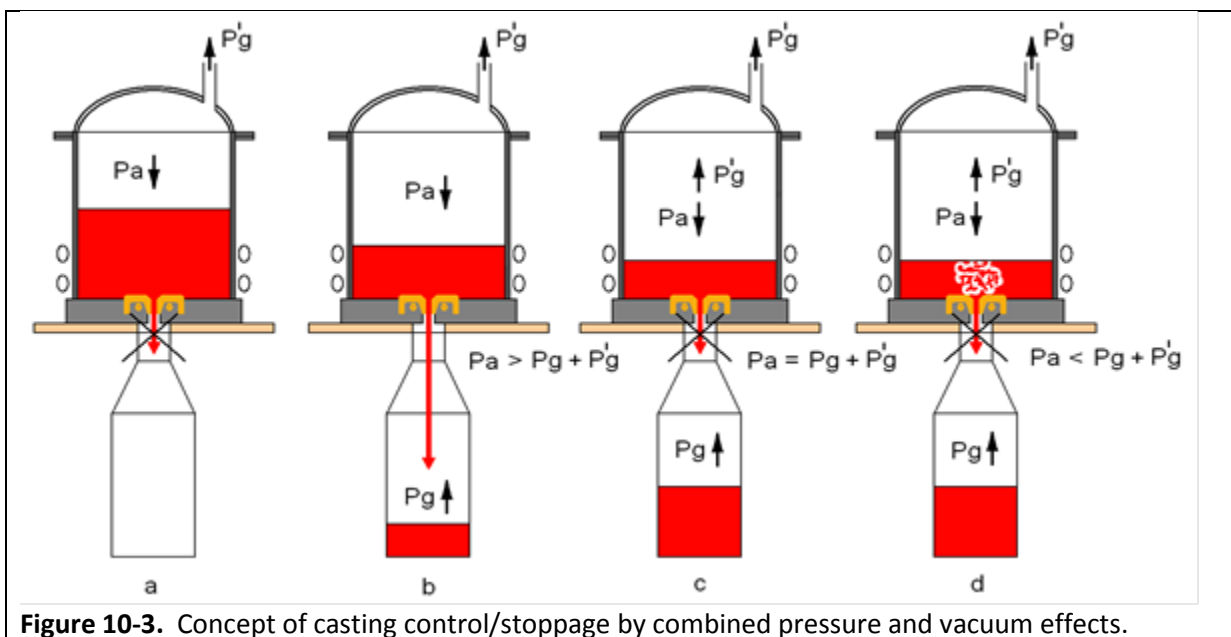
Figure 10-3. Concept of casting control/stoppage by combined pressure and vacuum effects.

Condition "a" represents the steady state condition prior to energizing the drain inductor. Condition "b' represents the control process once the casting has been initiated. Low to no additional suction (i.e., some suction will always be present in the offgas system) and low to no pressure in the container, P_g will be applied, allowing full casting to proceed. The suction and the pressure in the receipt container can be increased to slow the flow (i.e., mass flow rate control) which will continue as long as P_a is greater than P'_g and P_g combined. Condition "c" represents full stoppage of the casting, which occurs when $P_a = P'_g + P_g$. The combined effects would provide the ability to stop the

casting while minimizing impacts to the offgas or producing bubbling in the melt pool. Finally, condition "d" represents the case in which the vacuum induced by the suction combined with the pressure applied in the receipt container significantly exceed the hydrostatic pressure and results in bubbling within the melt. This undesirable condition would be easiest to control with this option.

10.2. Option 1 Feasibility Testing – Integrated Test #6

As previously mentioned, Option 1 was the first approach tested for feasibility, primarily because it was the most readily implemented. This feasibility test, Integrated Test #6, included two primary objectives:

- To observe the characteristics of the draining device for a system with a much higher primary inductor and melt pool, which also provides more casting time for the test, and

- To investigate the feasibility of controlling the mass flow rate during casting using pressure below the drain exit.

The equipment used for this test was mostly different from that used for the Integrated Test #5 series, other than the 1.76 MHz and 27 MHz generators, of course. The 300 mm diameter stainless steel crucible was used, but a three-turn 200 mm high inductor coil was installed versus the two-turn 100 mm high configuration used in the prior tests. The inductor was positioned 20 mm above the ceramic bottom. Additionally, the seventh version of the drain device was used.

The receipt container was also modified with a conical top section that interfaced with a ceramic sleeve/tube reducer. The small diameter end of the ceramic tube was sealed to the bottom of the drain device, inside of the inductor coil, using nonconductive ceramic putty. Similarly, the large diameter end of the ceramic tube was sealed to the top of the new conical section. This provided an air-tight seal for maintaining the pressure, and thus the force, needed to control the mass flow during casting, while also providing electrical isolation from the 27 MHz electromagnetic field. Figure 10-4 shows the primary test setup. The line from the air compressor is connected to the conical section just behind a view port, with the intention of providing a sweep across the glass to keep it clear during casting. Figure 10-5 is a photograph taken from underneath the crucible showing the transition area from the top of the conical section to the ceramic tube reducer to the bottom of the drain device.
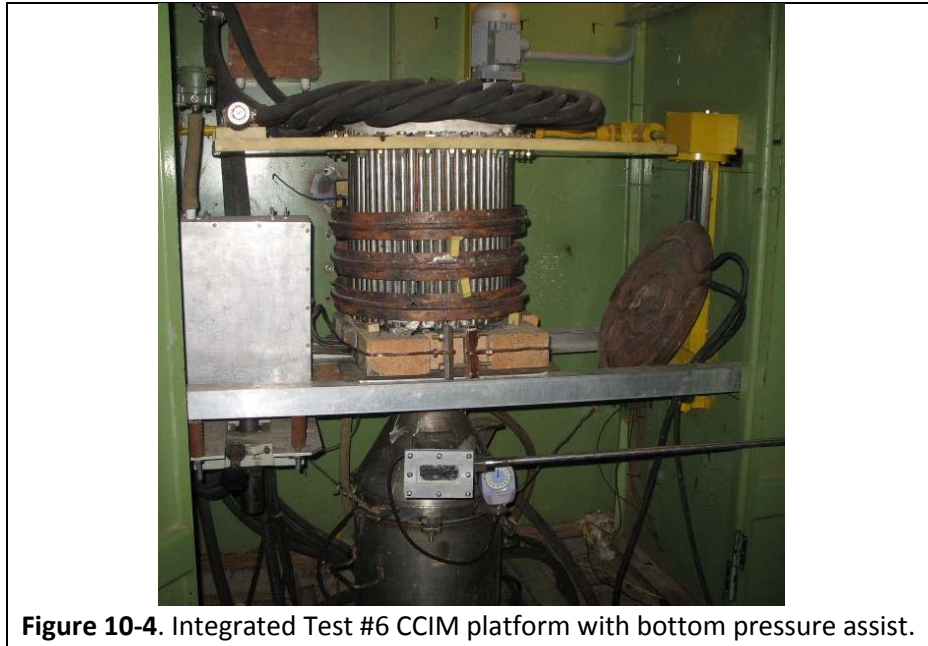
Figure 10-4. Integrated Test #6 CCIM platform with bottom pressure assist.

During Integrated Test #6, two steady state modes of 1,300^{o}C and 1,122^{o}C were achieved and maintained. Full calorimetry was taken for both steady state modes. After the first steady state mode was achieved, the 27 MHz generator was powered on. After 42 minutes, casting began independently. No external pressure was applied during this process.

After about one minute of casting, the valve was opened slowly and the pressure applied gradually. An immediate effect observed was that the pour stream was deviated and ran down the inside walls of the

Figure 10-5. Ceramic tube reducer connecting drain opening to receipt container in a leak-tight environment.

upper ceramic tube (see Figure 10-6). When the pressure reached about 20 mm Hg (0.39 psig) large bubbles began to emerge in the center of the melt pool (see Figure 10-7). The bubbling created downward forces in the melt as they rose, providing more momentum to the moving melt, and making it difficult to achieve a complete casting stoppage. Simultaneously, the pressure in the container continued to increase as the melt poured in and heated the existing gases in the container, as well as reduced the void volume. Manual control was erratic and generally not manageable. Eventually, after two minutes at a reduced pressure of about 15 mm Hg (0.29 psig) the casting stopped, although some bubbling was still observed. The effects of this can be seen in the

melt pool surface after the first casting, shown in Figure 10-8. The bubbling dissipated shortly thereafter and the casting was completely stopped.

After the first casting, a melt pool of about 70 mm deep remained. The initial full melt pool was about 210 mm deep, so about 2/3 of the melt volume was poured. Frit was added and a full melt pool of 210 mm was established at a steady state temperature of 1,122^{o}C. The 27 MHz generator was then powered on and after 15 minutes of operation melt casting began independently.

The second melt casting exhibited the same characteristics as the first casting. Namely, 1) melt casting initiated with no additional pressure, 2) pressure increased until bubbling of the melt occurs, 3) cooling of the melt in the drain body such that casting stops but sporadic bubbling occurs (likely through cracks or areas still soft due to high temperatures), and 4) casting stopped with no bubbling present.

Figure 10-6. Pour stream deviated due to pressure applied at drain exit.

Figure 10-7. Bubbling due to pressure in receipt container.

Figure 10-8. Melt pool after first showing effect of bubbling.
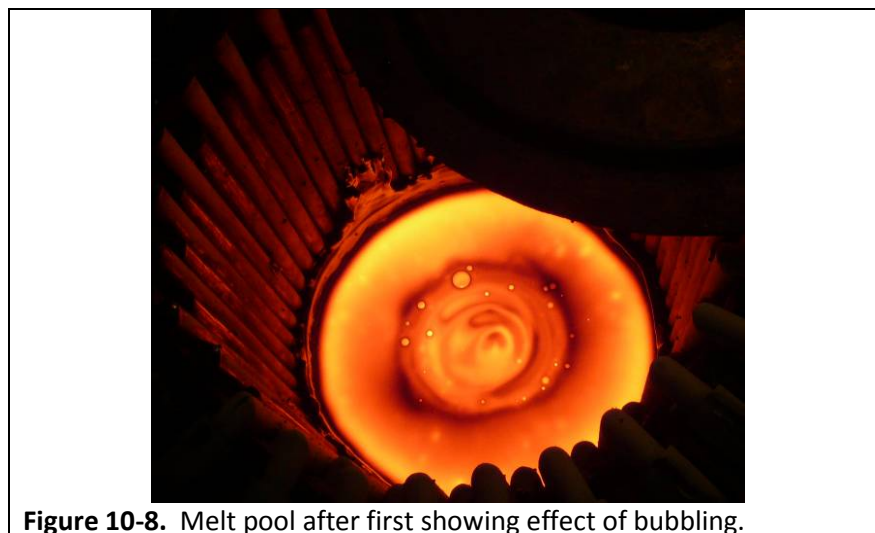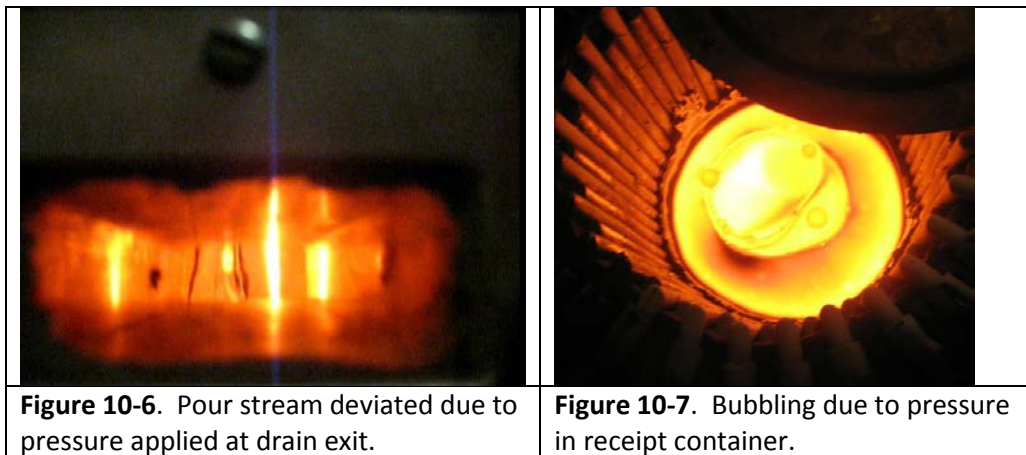
Key characteristics and conditions during the two castings are provided in Table 10-1.

Table 10-1. Key parameters during casting for Integrated Test #6.

Casting #	Δa_2 mm	τ, min	T_{max}, °C	t, sec	$P_{dr\,o}$, kW	m_{glass}, kg	M_{cast}, kg/h
1	20	42	1300	490	1.62	22.4	164
2	20	15	1122	480	1.71	19.8	149

(Δa_2 is a distance of melt pool above inductor, mm; τ is time of small generator operation prior to melt casting, min; T_{max} is maximum temperature of melt pool surface, °C; t is duration of melt casting, sec; $P_{dr\,o}$ is power in drain before the start of melt casting, kW; $P_{dr\,max}$ is maximum power in drain during casting, kW; m_{glass} is mass of glass melt poured, kg; M_{cast} is average rate of melt casting, kg/h)

Figure 10-9 presents data for the power in the drain throughout the Integrated Test #6 processes, including both castings.

Figure 10-9. Power in the drain throughout Integrated Test #6, including casting events.
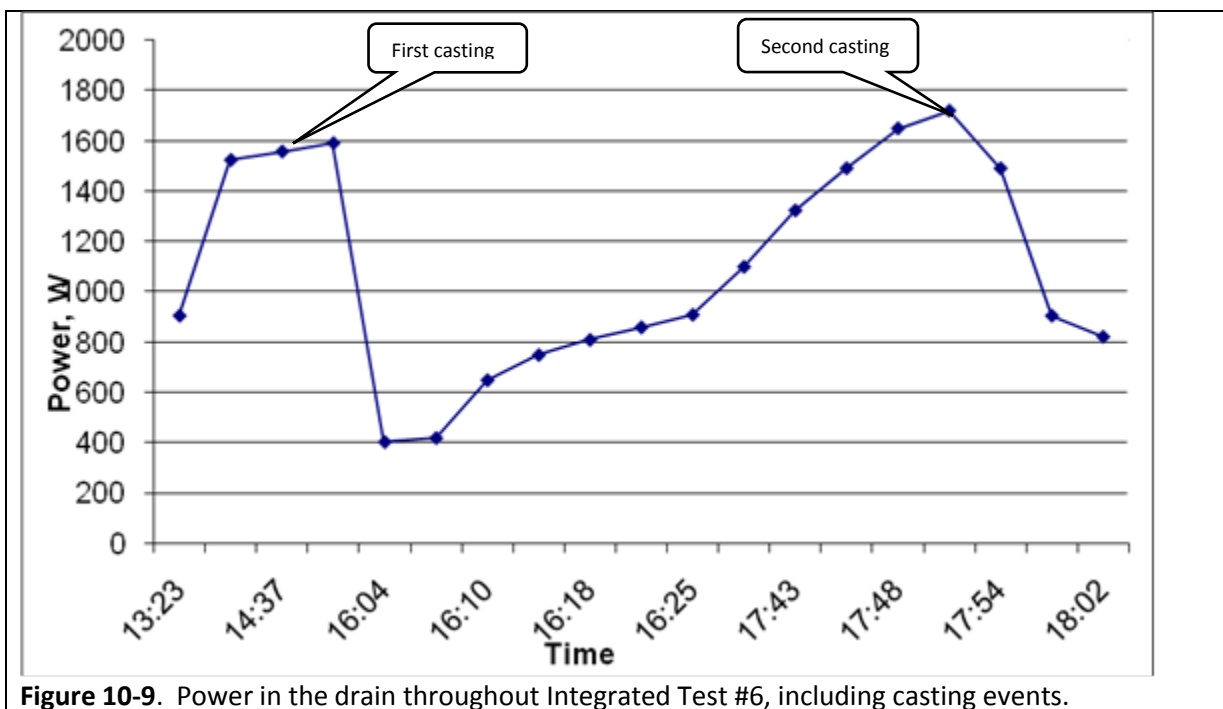
Upon disassembly, no damage to the drain body, crucible, or ceramic bottom were observed. This seventh version of the drain has now had nine separate casting events, five of which were follow-on during specific tests, with processing temperatures ranging from 1,100°C to 1,450°C.

As observed during the casting process, the applied pressure caused the pour stream to be diverted and flow onto the ceramic tube. Figure 10-10 shows the inside of the tube coated with glass.
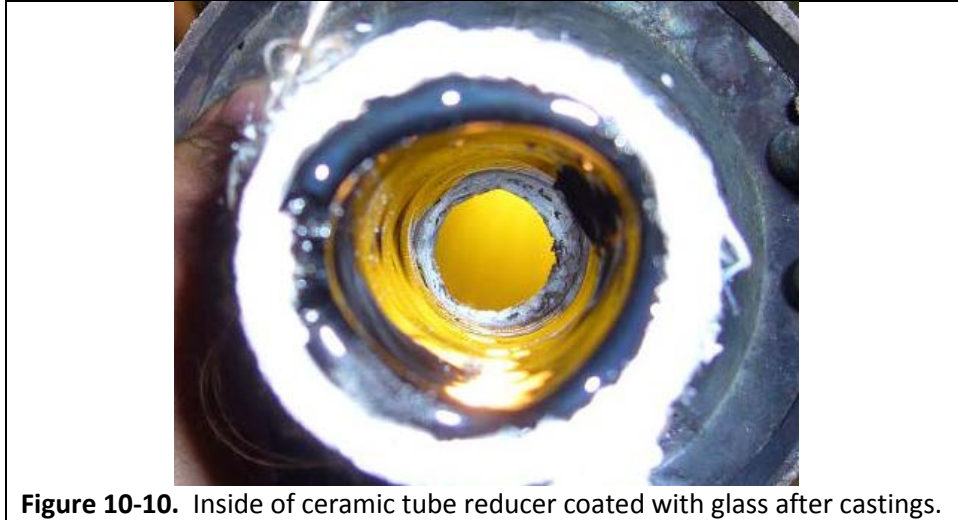
Figure 10-10. Inside of ceramic tube reducer coated with glass after castings.

Key observations from Integrated Test #6 were as follows:

- Repeated, independent castings were possible using the seventh version of the drain device in a CCIM system with a 200 mm high inductor and deeper melt pool.

- As predicted by the model, with the deeper bath, the skull layer near the bottom is thicker, so more time was required to initiate the casting after energizing the 27 MHz inductor. This was true for both the initial casting and subsequent castings.

- In spite of the greater hydrostatic pressure due to the increased melt pool depth, the mass flow rate was lower for this system. This is likely due to the overall lower temperature in the lower zones of the melt pool, which increased the viscosity. Note that mass flow rate measurements were taken prior to applying the pressure.

- In principle, a pressure applied to the exit face of the drain can be used to control the mass flow rate of the glass pour, to the point of full stoppage. However, the dynamic pressure environment makes controlling the process extremely difficult. Option 2, which applies a negative pressure (i.e., vacuum) on the entrance of the drain device will be evaluated.

10.3.   Option 2 Feasibility Testing – Integrated Test #7 Series

Implementation of Option 2 Pressure Assist System required significant modification to the crucible design. Specifically, it had to be able to provide a seal between the crucible wall and bottom, as well as between the crucible top and cover lid.

Additionally, based on the results of the prior testing, a drain design predicated on the concepts of the seventh version does not require being extended up into the melt pool like the other designs. This was demonstrated during the Integrated Test #6 that used a high inductor and melt pool, which is known to result in much lower temperatures in the lower zones of the melt, as well as thicker skull. This was also validated through the extensive modeling efforts.

10.3.1. Optimization of the Bottom and Drain Assembly Design

A new conceptual design for the bottom and drain assembly was developed to implement the Option 2 Pressure Assist System. The new design was intended to provide more stable positioning for the drain device, minimize the height of the drain device while maintaining structural integrity and cooling capacity, and to provide more positive sealing capability between the bottom and crucible side wall. In this concept, the bottom would be manufactured from a solid metal plate with cooling capacity located near the zone along the bottom that is known to become the hottest during operation. Figure 10-11 shows the assembly concept.
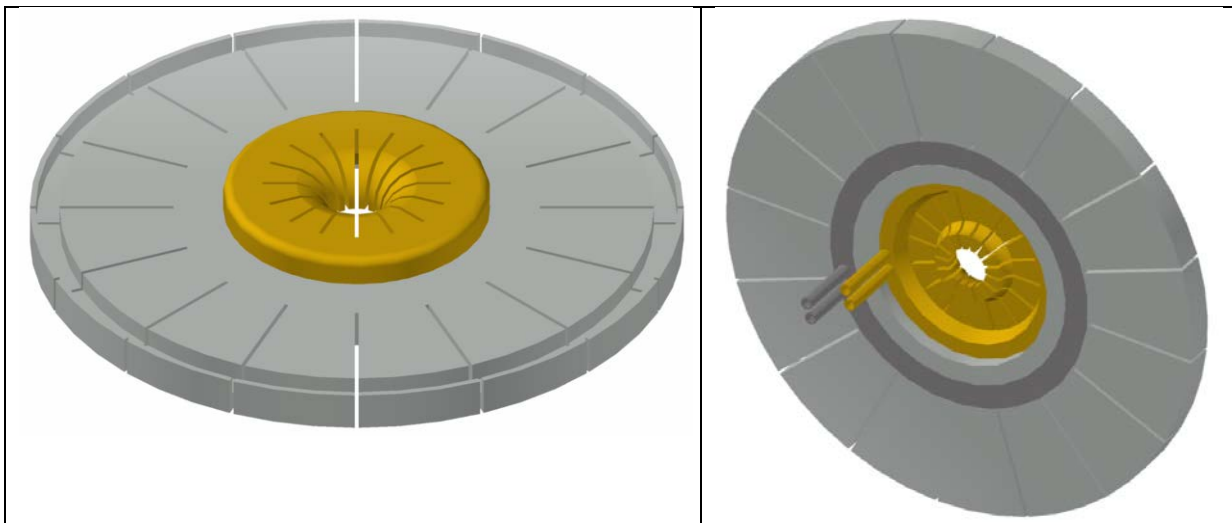
Figure 10-11. Top and bottom isometric views of the new metal bottom and drain assembly design.

For this design, the bottom is sized to accommodate a nominal 300 mm internal diameter crucible constructed using 12 mm diameter stainless steel tubes (i.e., the existing crucible). The bottom plate includes a 10 mm deep counter bore on the central axis that accommodates a 25 mm high by 135 mm outside diameter drain device. The opening in the drain device is 25 mm, and the length of the drain tube section is also 25 mm. This represents the *eighth version* of the drain device.

In principle, the bottom/drain assembly could be designed as a single plate of metal, as shown in Figure 10-12; however, the configuration above was selected because it offers greater flexibility for investigating modifications to the actual drain design and configuration, if necessary.

Figure 10-12. Single plate concept for new metal bottom and drain assembly design.
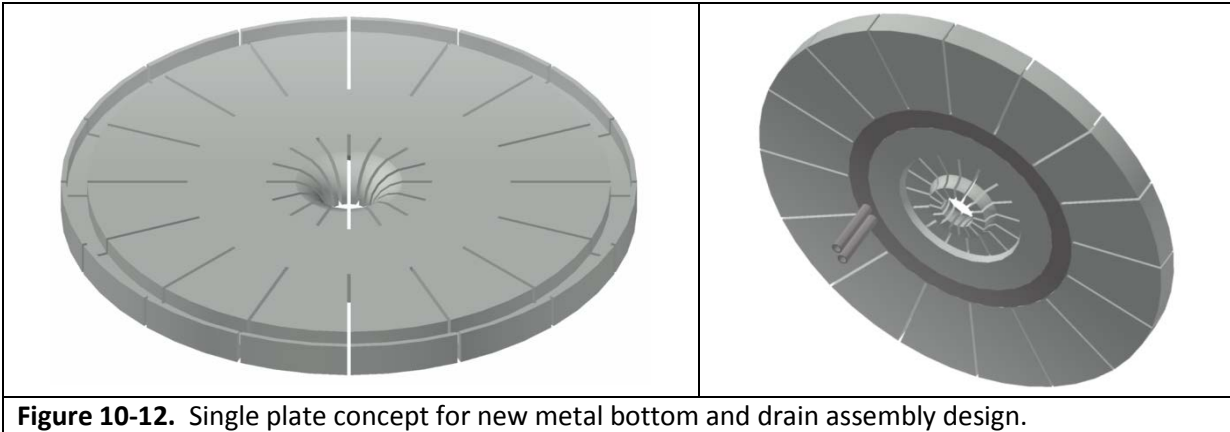
For example, the current drain inductor design is a two-turn cylindrical configuration (refer back to Figure 9-32). However, other configurations are planned to be investigated based on modeling results, and the drain device must be adapted to accommodate. Specifically, a planar two-turn inductor coil was implemented in subsequent tests. The eighth version of the drain is designed to accommodate this coil configuration. Figure 10-13 shows a conceptual drawing of an integrated system with the new drain and bottom configuration.

Figure 10-13. Conceptualized integrated CCIM system using new bottom and drain designs.
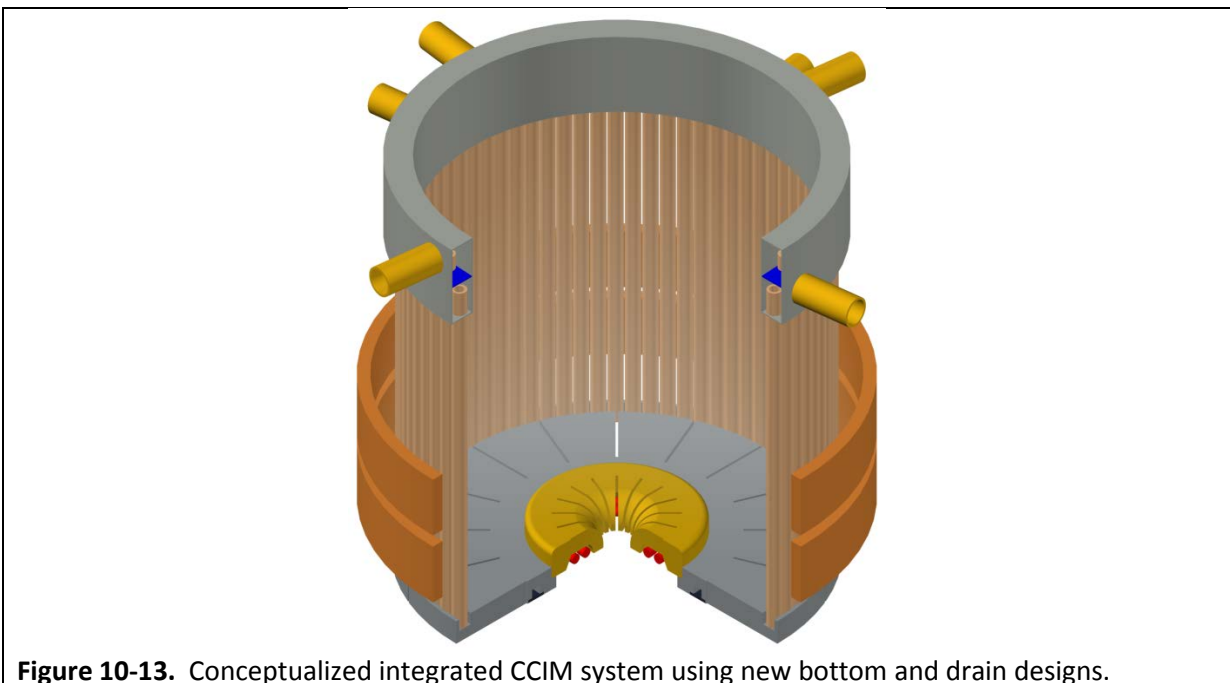
10.3.2. Integrated Test #7 Series– Investigation of New Bottom and Drain Designs

The new bottom design using a slitted solid plate had never been tested. Previously, the only bottom designs included ceramic bricks or a series of horizontal water-cooled tubes, similar to the crucible design. The ideal material of construction for the new design approach is copper, from an overall electrical/electromagnetic efficiency perspective. However, prior to making the investment for a large diameter CCIM constructed of copper, a smaller version for the existing 300 mm diameter stainless steel crucible was fabricated from aluminum and integrated into a CCIM platform for testing. Additionally, the mechanism for translating the inductor was modified to provide movement of the entire crucible. This would allow investigation of the effects of the distance of the inductor from the bottom of the crucible, in addition to the impacts of translation of the drain inductor, which had been investigated earlier. Since this bottom design had never been evaluated, a decision was made to conduct a series of two tests, Integrated Test #7a and #7b, to investigate its performance with a low height, two-turn inductor, as well as a higher three-turn inductor.

10.3.2.1.   Integrated Test #7a.

Integrated Test #7a used the CCIM platform with a two-turn, 100 mm high inductor. The drain inductor was modified to a two turn planar configuration with outside diameter of 80 mm and inside diameter of 65 mm. The primary objectives were 1) to obtain data on the performance of the new bottom design to determine how it would affect the characteristics of the lower zones of the melt pool, 2) to obtain data during the melt initiation process for input into the model, 3) to observe the effects of the inductor location on the bottom melt pool (i.e., due to translation of the crucible), 4) to test the eighth version of the drain and planar inductor performance, and 5) to validate operation of the new data acquisition system and components. Estimates were made for heat loss through the metal bottom plate, and the cooling system was designed based on modeling results, which indicated the areas of higher temperatures along the bottom where the cooling loop was located. The results showed that the design was conservative; however, this needed to be validated.

Integrated Test #7a, which used the aluminum bottom and copper drain, was configured as described in the previous section and depicted in Figure 10-11. The actual test setup is shown in Figure 10-14.

Significant improvements to the data acquisition system were implemented for this test, and all remaining tests, which included a LabVIEW® software [72] user interface for a network of sensors.

Additionally, a high temperature (i.e., up to 3,000^{o}C) Siemens ARDOCELL PZ 40 two-color pyrometer was incorporated into the data acquisition system. Figure 10-14 is a screen shot from the LabVIEW® interface for the pyrometer.

Figure 10-14. Exterior view (left) and bottom view showing drain (right) for Integrated Test #7.
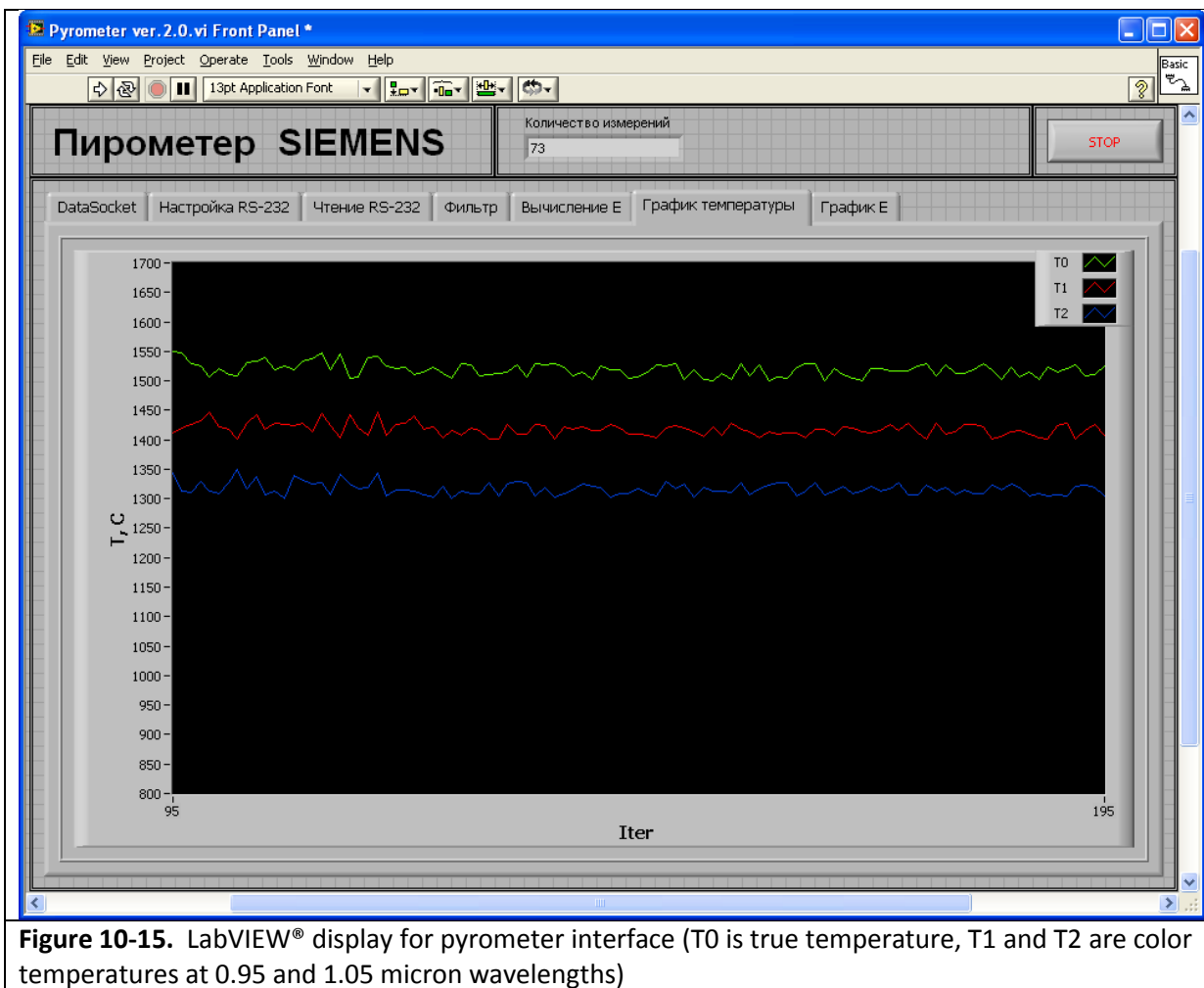
Figure 10-15. LabVIEW® display for pyrometer interface (T0 is true temperature, T1 and T2 are color temperatures at 0.95 and 1.05 micron wavelengths)

Figure 10-16. Siemens Pyrometer with Video Camera

Figure 10-17. Still shot of pyrometer video camera showing "cross-hairs: used to remotely position the pyrometer as desired.
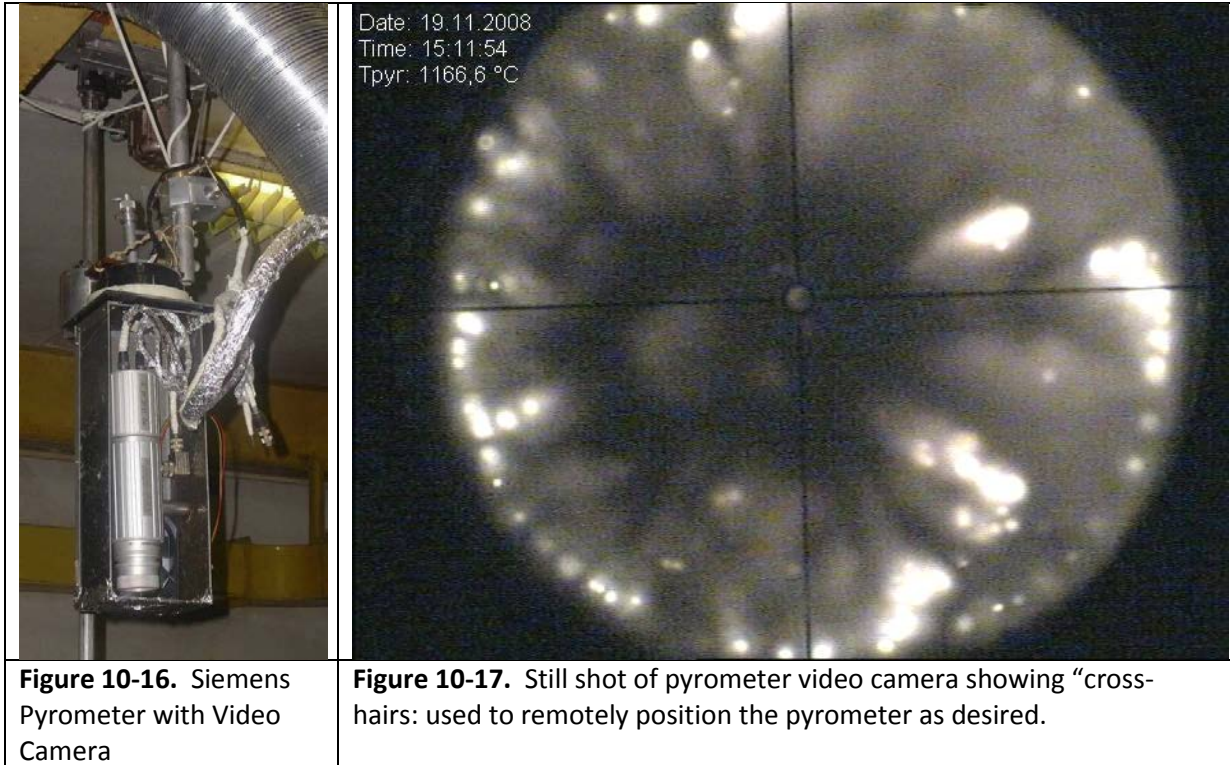
The new sensors and LabVIEW interface were designed and implemented by faculty and graduate students at ETU-LETI (hence the Russian language interface for portions). They were conducting research work on a methodology for automatic feedback control based on electrical parameters. In support of that work, the pyrometer was used to correlate the electrical parameters to physical conditions, with the ability to automatically digitally record many data points during the tests. The pyrometer was also used to support the work reported herein, which was to measure and determine the temperature-dependent emissivity value for the glass, as was discussed earlier. It also provided an excellent tool for measuring and recording the surface temperature at any location on the melt pool and at any time during a specific stage of the experiments.

Figure 10-16 shows the pyrometer assembly mounted above the CCIM, with an attached video camera that is centered on the measurement point of the pyrometer. The assembly is mounted on a motorized gimbal that allows movement to any desired location on the melt pool surface. A still shot from the pyrometer's video is shown in Figure 10-17.

During Integrated Test #7a, four steady state modes at different temperatures were achieved and maintained for calorimetry. Two castings were completed and the process parameters recorded, similar to previous tests. One of the test objectives was focused on collecting data from the melt

initiation process that could be used for modeling purposes. Data was desired for two full processes (i.e., initiator ring in, melt initiated, initiator ring removed). Accordingly, the pressure assist system for stopping the casting process was not necessary for the Integrated Test #7 series, and was not installed. Key electrical parameters and calorimetry data were obtained during the melt initiation process, specifically focused on comparison of conditions with the initiator ring in place versus removed. Finally, the effects on the system of the inductor location (i.e., vertical translation) were investigated. This was important because the impacts of the water-cooled bottom were unknown and the effects of the electromagnetic heating were yet to be quantified for various distances. Information was sought to determine the best location for the inductor that balanced effective heating of the lower zones of the melt pool with mitigating over-heating of the metal bottom plate.

Figure 10-18 provides example photographs of the various stages of Integrated Test #7a. The steady state mode shown is at 1,445^{o}C. The melt casting shown is for a steady state mode of 1,300^{o}C. This is why the pour stream has a large diameter and the flow is quite high, although it was not specifically measured during this test.

| a) melt initiation using graphite ring | b) full melt pool established | c) maximum steady state mode | d) melt casting |

Figure 10-18. Representative stages achieved during Integrated Test #7a.
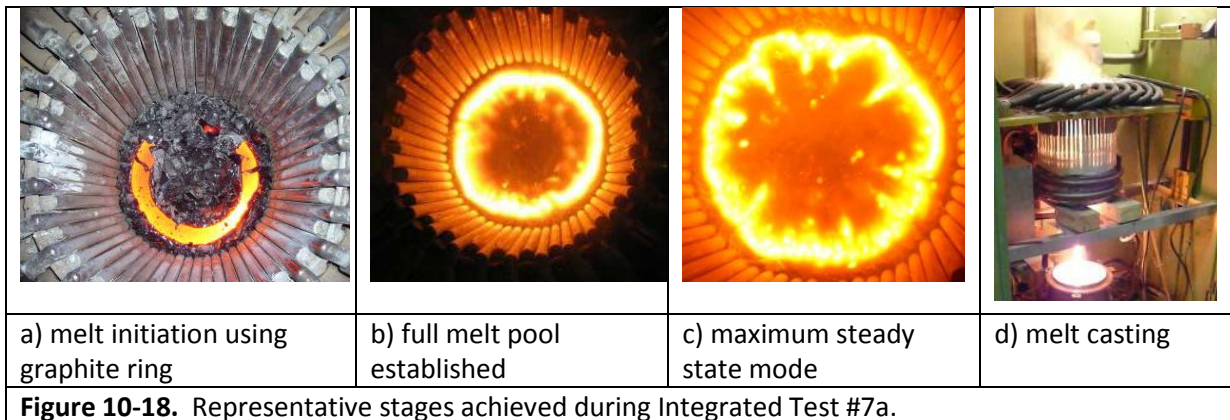
Melt Initiation Process: The parameters for the melt initiation process were collected for two complete cycles. The process data collected during these stages of the test are shown in Figure 10-19, in which the identified points represent the following actions or conditions:

1. first removal of graphite ring after melt initiation
2. ring placed back into the melt
3. second ring removal
4. charge added to crucible (note that this was in the form of glass pieces, not frit)
5. thermal loss increase from melt resulting from placing heated ring in the melt (i.e., still hot from first melt initiation).
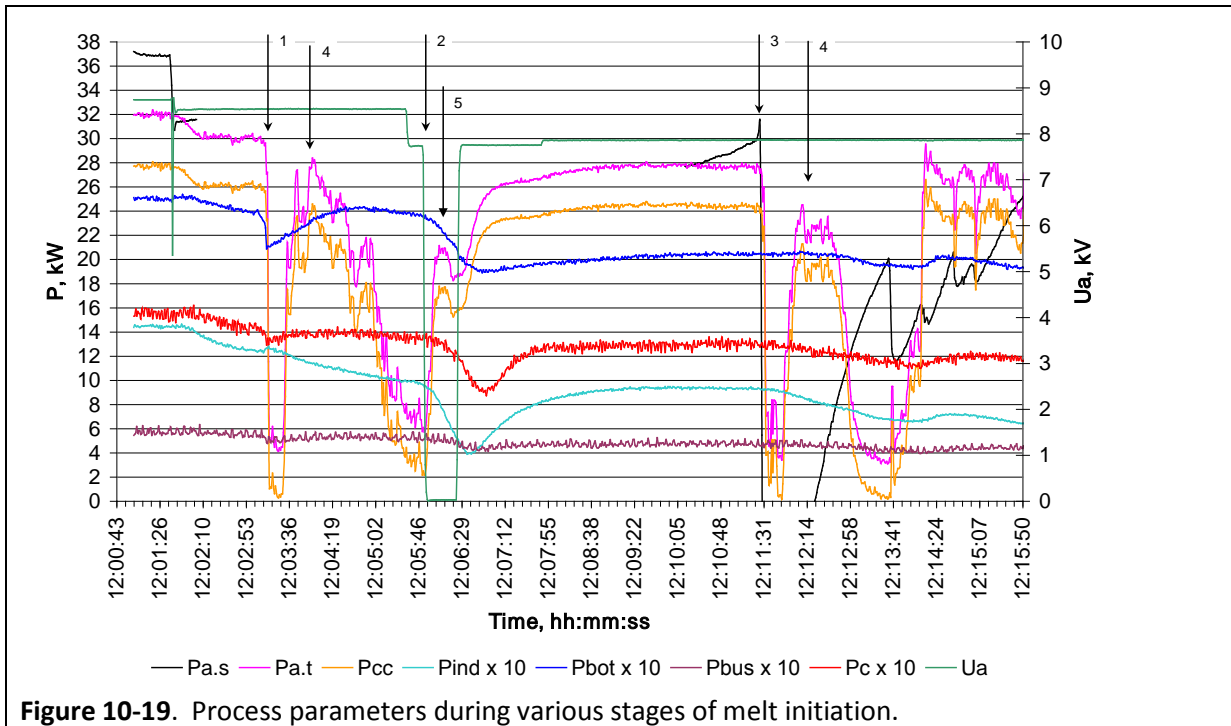
Figure 10-19. Process parameters during various stages of melt initiation.

(P_{cc} is total thermal and electric losses in the cold crucible; P_{ind} is electric losses in the inductor; P_{bot} is total thermal and electrical loss in the bottom and in the drain of the cold crucible; P_{bus} is electrical loss in generator buses; P_c is electrical loss in 1.76 MHz generator circuit)

After each removal of the ring, a distinct drop of about 1 kW in the thermal losses from the melt is observed, followed by rapid power release into the small volume melt pool that was present. Point 4 on Figure 10-18 is the time at which new charge was added to the melt pool, which began to absorb heat from the melt and a decrease in the thermal losses from the cold crucible are observed, again at approximately 1 kW. Then, the charge melts rather quickly and a melt pool is formed.

The first incident of adding charge included placing the heated graphite ring back into the melt. This resulted in an immediate increase in power losses from the crucible (point 2), even though the generator was powered off. Additionally, the small volume melt pool ring started to cool down, which began to occur after the power losses due to the heated graphite ring peaked (point 5). The 1.76 MHz generator was then energized, and the power in the melt began to progressively increase. At the time of 12:10 a steady-state condition was obtained. The second ring removal then occurred (point 3). Similar to the first ring removal, thermal losses in the cold crucible dropped sharply, and then began to grow. The second addition of charge began at point 4. Once the new charge was fully melted, a stationary melting mode was established.

Steady State Modes: Four different steady state modes at temperatures of 1,445^{o}C, 1,300^{o}C, 1,200^{o}C, and 1,050^{o}C were established and calorimetry data collected for each. Figure 10-20 shows the data collected for each of these conditions. The pyrometer data, T0 on the graph, is also shown for the first and third modes. The data traces appear erratic due to the convection forces creating movement. Data averaging and smoothing was implemented later to render this data easier to interpret. The arrows numbered 1 through 4 indicate the times that most closely represent the steady state modes. The Pa.s and Pa.t curves represent the total power based on the sensor readings and calorimetry, respectively. Thus, the lag during transition from one mode to the other of the Pa.t line is expected. This also presents challenges in understanding the true state of the melt pool without knowledge of either a response time constant to external inputs (i.e., power level from the generator), or a direct comparison with actual voltage and current readings of the system (i.e., the source of the deduced Pa.s curve). It is interesting to note that, for this glass in the current test platform (i.e., 300 mm diameter and 1.76 MHz nominal), at temperatures of 1,200^{o}C and below, a true steady state cannot be achieved. This is evidenced in the negative slope of the Pa.s curves during these times. The Pcov curve provides total power correlations due to radiation heat losses during the pyrometer readings (i.e., the cover lid had to be removed).
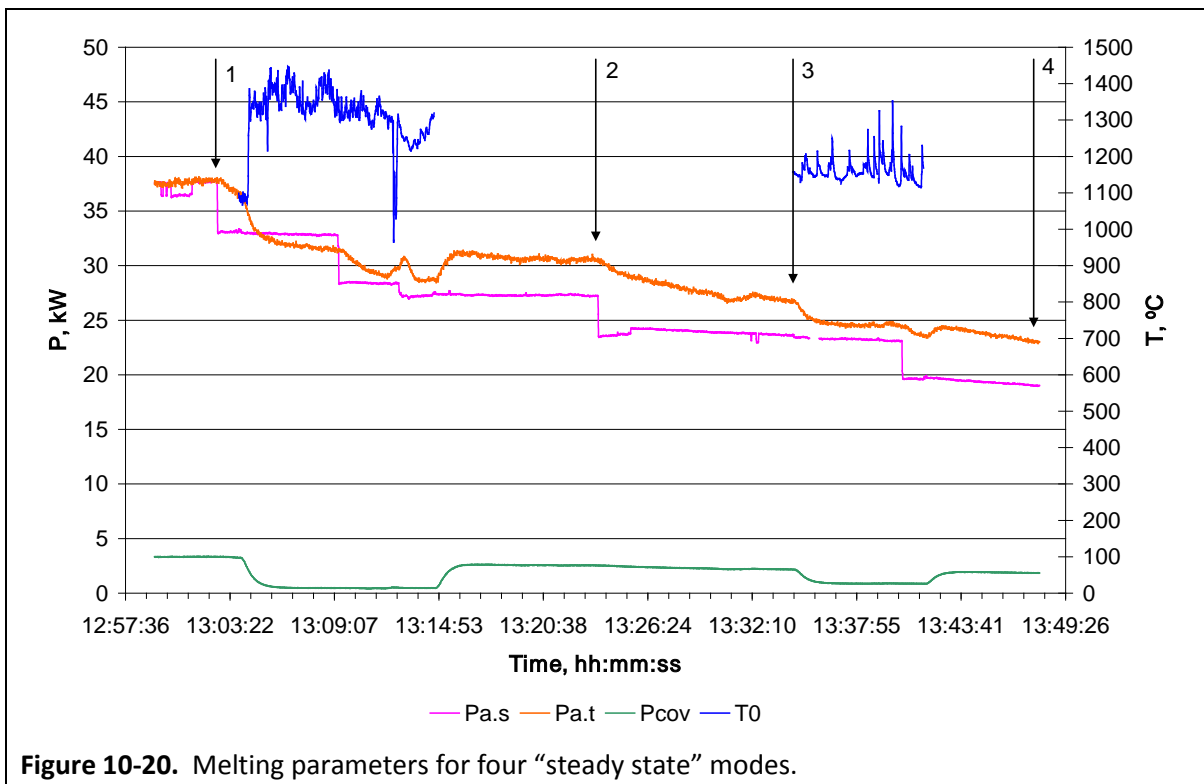
Figure 10-20. Melting parameters for four "steady state" modes.

Melt Casting: As part of the test objectives, melt casting was also performed to evaluate the performance of the eighth version of the drain, as well as the planar drain inductor. The melting parameters observed during the first casting are shown in Figure 10-21. After the 27 MHz generator was powered on (position 1.1 on the graph), an immediate increase in the power losses is observed. This was about 1.3 kW (i.e., 6.5 kW/5), which was due primarily to electrical losses in the metal bottom and drain device. Losses in the bottom increased by about 1.9 kW at which time the first casting was initiated (position 1.2). Near the end of the casting process, with the 27 MHz generator powered off, the losses in the bottom had decreased to about 0.56 kW (i.e., 2.8 kW ÷ 5) (position 1.3). Note that the bottom losses include both electrical from the generators, as well as thermal losses contributed by the heated bottom zone of the melt pool. At the time of casting, the anode and grid currents for the 27 MHz generator were 0.8 A and 0.196 A, respectively. The total power in the system, $P_{a.t}$, was 36 kW. Casting duration was 270 seconds.

The second casting required translation of the crucible upwards by 15 mm (i.e., bringing the primary inductor closer to the bottom of the crucible). The 27 MHz generator was powered on for 34 minutes with no casting initiated. Conditions were improving for melt casting, but this action would demonstrate the effect of translating the inductor. However, moving the crucible also moved the drain inductor away from the bottom of the drain device. As can be seen in Figure 10-22, this required operating the 27 MHz generator at much higher power levels, with the anode and grid currents being at 1.6 A and 0.9 A, respectively. At the time of casting, the thermal losses in the bottom were also higher than during the first casting, with the second casting reaching about 4.5 kW, or 0.9 kW more than required for the first casting. The casting duration was 81 seconds.

Table 10-2 provides a comparison of key parameters for the two castings performed during Integrated Test #7a. A key factor that contributed to the difficulties with the second casting was condensation on the inductor coil, which was leading to electrical shorting and resulting emergency stopping of the 27 MHz generator. A comparison of these test results with those using the ceramic bottom shows that the metal bottom has had very little impact on this parameter. For example, for the ceramic bottom, power losses between 2 kW and 4 kW were observed. Using the metal bottom

Table 10-2. Comparison of parameters during castings for Integrated Test #7a.

Casting #	$I_{a\,27}$, A	$P_{a.t}$, kW	P_{bot}, kW	t_{incl}, min	Casting time, s
1	0.8	36.0	3.8	24	270
2	1.6	39.5	4.2	76	81

t_{incl} is total time of operation of the 27 MHz generator
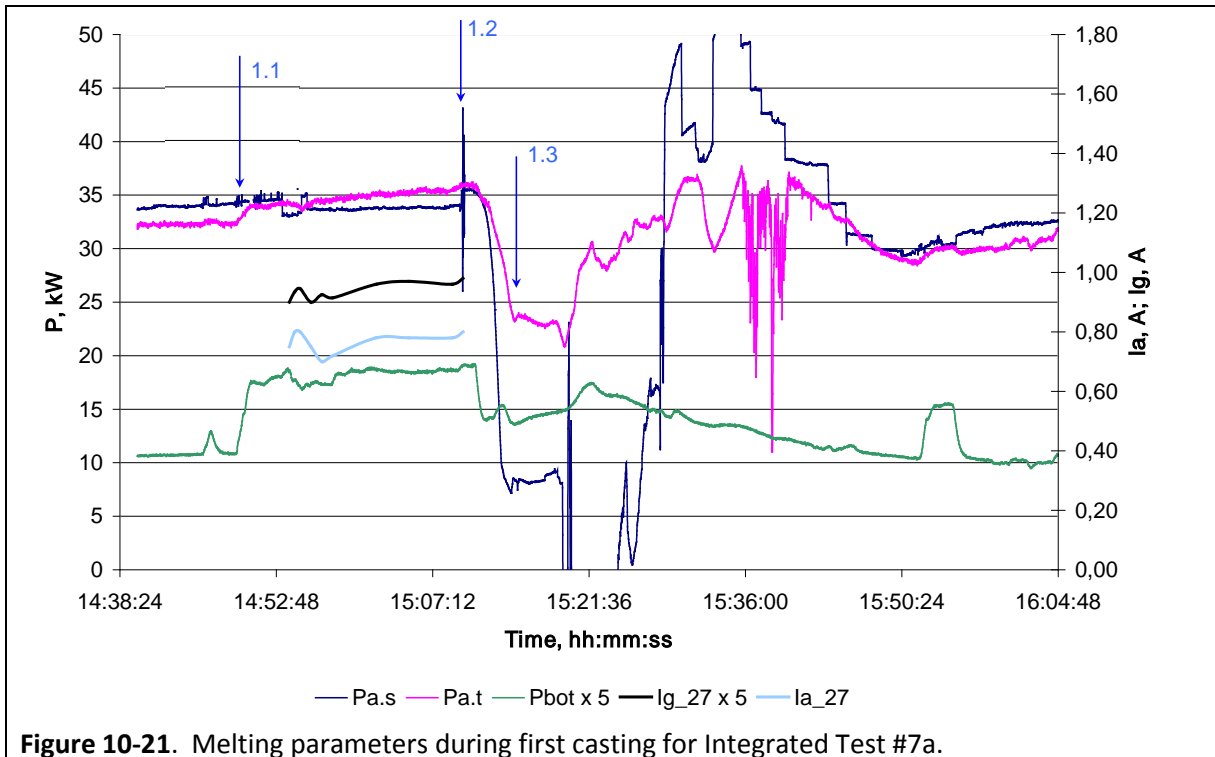
Figure 10-21. Melting parameters during first casting for Integrated Test #7a.

(Ig_27 is27 MHz generator lamp grid current; Ia_27 is 27 MHz generator lamp anode current; 1.1 is time at which 27 MHz generator powered on; 1.2 is time at which casting initiated; 1.3 is time at which casting slowed down/near stop)
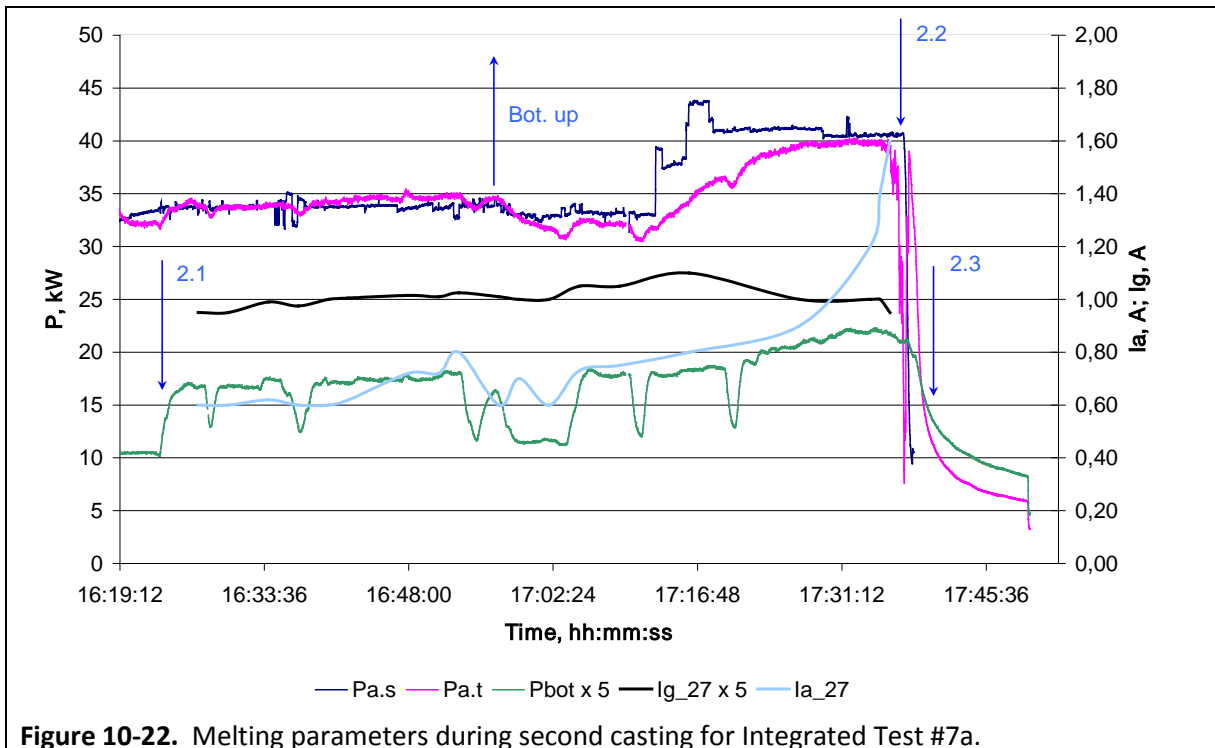
Figure 10-22. Melting parameters during second casting for Integrated Test #7a.

(Ig_27 is 27 MHz generator lamp grid current; Ia_27 is 27 MHz generator lamp anode current; 2.1 is time at which 27 MHz generator powered on; 2.2 is time at which casting initiated; 2.3 is time at which casting slowed down/near stop, Bot.up is time at which crucible was translated up 15 mm)

resulted in similar losses (i.e., 3.8 kW to 4.2 kW). Table 10-3 shows the various stages and operational parameters during the entire Integrated Test #7a.

Table 10-3. Stages and conditions of Integrated Test #7a.

Time, hr:min	Ia, A	Ig, A	Ucb, kV	Ua, kV	Notes
10:30	2.96	1.35	5.1	8	Start-up. Melt initiation with graphite ring.
11:19	-	-	-	-	Calibration of sensors
11:30	3.2	1.68	6	9.2	Melt pool established (ring floated to top)
12:11	3.59	1.48	5.52	8.5	Ring removal
12:15	8	0.91	4.2	8	Charge loading
12:28	5.51	1.47	3.78	8.3	Generator mode adjustment
12:35	-	-	-	-	Sensors recalibrated
13:02	5.42	1.24	2.61	7.63	The first steady state mode. a_2 = 96 mm. T_{melt} =1,445^{o}C.
13:23	4.59	1.12	2.28	6.72	The second steady state mode. T_{melt} = 1,300^{o}C.
13:34	4.12	1.07	2.16	6.27	The third steady state mode. T_{melt} = 1,200^{o}C
13:47	3.60	1.02	2.03	5.83	The fourth steady state mode. T_{melt} = 1,050^{o}C
13:48	-	-	-	-	T_{bot} = 48°C
13:49	2.64	0.97	2.48	5.5	Crucible raised 15 mm. T_{bot} = 45°C
13:57	-	-	-	-	Crucible lowered 20 mm.
14:09	-	-	-	-	T_{bot} = 41°C
14:00					First scanning of melt surface
14:46	5.2	1.23	3.33	7.3	T_{sec} = 7.7^{o}C. T_{melt} =1,300^{o}C
14:46	-	-	-	-	The 27 MHz generator powered on
15:10	-	-	-	-	The first casting
15:14	-	-	-	-	Casting finished, T_{bot} = 57°C, Casting time was 270 sec.
15:20	6.04	1.26	4.91	8.4	a_2 = 32 mm after casting, T_{sec} = 8.6^{o}C, T_{melt} = 1,340^{o}C.
15:33	5.79	1.36	3.96	8.5	Charge loading
15:43	5.6	1.19	3.59	8	a_2 =110 mm, T_{bot} = 39°C
15:51	4.76	1.08	3.17	7	T_{melt} = 1,280^{o}C
15:58	5.01	1.10	3.27	7.2	Stationary mode. T_{melt} = 1,370^{o}C
15:56	-	-	-	-	Second scanning of melt surface
16:11	-	-	-	-	T_{melt} = 1,300^{o}C. Charge loading. T_{bot} = 34°C
16:12	-	-	-	-	Third scanning of melt surface
16:23	-	-	-	-	The 27 MHz generator has been switched on. T_{melt} = 1,095^{o}C
16:57	4.63	1.08	3.27	7.3	The crucible raised 15 mm.
17.37	-	-	-	-	Second casting. T_{sec} = 8.9^{o}C
17:39	-	-	-	-	Casting finished. Casting time was 81sec.

(I_a is generating lamp anode current, A; I_g is generating lamp grid current, A; U_{cb} is voltage on the capacitor bank, kV; U_a is voltage on generating lamp anode, kV; a_2 is height of a melt pool, mm; T_{melt} is maximum temperature on pool surface, ^{o}C; T_{bot} is exit temperature of cooling water in bottom, ^{o}C; T_{sec} is exit temperature of cooling water in separate section, ^{o}C)

As can be seen, the time required to achieve casting ranged from 24 to 76 minutes, as compared to a range of 3 to 42 minutes for the ceramic bottom. However, this was primarily due to the condensation issues, which resulted in multiple interruptions in operation of the 27 MHz generator.

Key observations and conclusions: Integrated Test #7a provided the following observations and conclusions:

- Use of a water-cooled metal bottom versus ceramic has very little impact on losses, or on the characteristics and behavior of the melt, in general.
- Translation of the crucible to change the relative position of the inductor to the melt pool can be effective in producing the melt conditions desired.
- The eighth version of the drain operates satisfactorily, although additional improvements are needed. The slit lengths were increased to improve electromagnetic transparency near the coil.

10.3.2.2. Integrated Test #7b

The primary objective of Integrated Test #7b was to repeat the tasks from Integrated Test #7a using a CCIM system with a three-turn, 200 mm high inductor to collect operational data. The aluminum water-cooled bottom and eighth version of the drain were used as before, although no castings were conducted during this test. Additionally, thermocouples were added to obtain temperature data along the bottom surface near the edge of the drain (internal) and from the perimeter of the bottom plate near the inductor (external). These thermocouple locations are shown in Figure 10-23.

Modeling results indicate that for this configuration, a maximum temperature occurs in the melt pool approximately 75 mm from the inside crucible wall, and 38 mm deep. The CCIM platform used for Integrated Test #7b included a cover assembly with a Type C Tungsten/Rhenium thermocouple
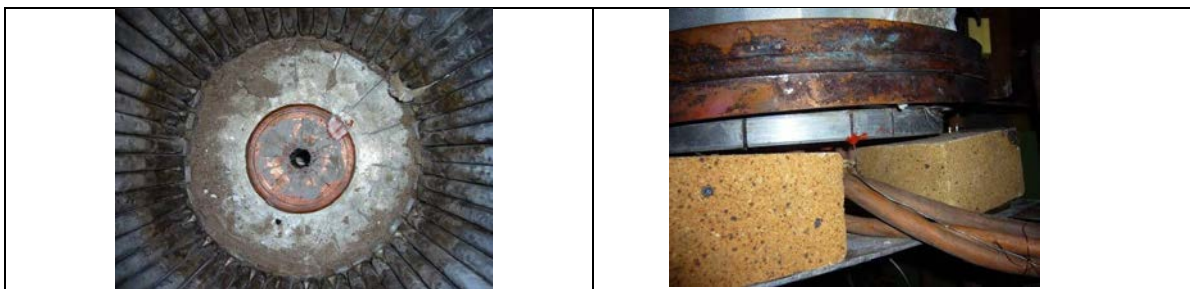
Figure 10-23. Thermocouples installed along interior (left) and exterior (right) surface of bottom.

with an alumina protective sheath. A Type C thermocouple is rated to 2,300°C; however, that is in an inert, vacuum, reducing environment. For this application, the thermocouple is expected to fail, but the sheath will increase its life to allow more data to be collected. The configuration of the cover/thermocouple assembly is shown in Figure 10-24.

Figure 10-24. Immersing thermocouple used for Integrated Test #7b.
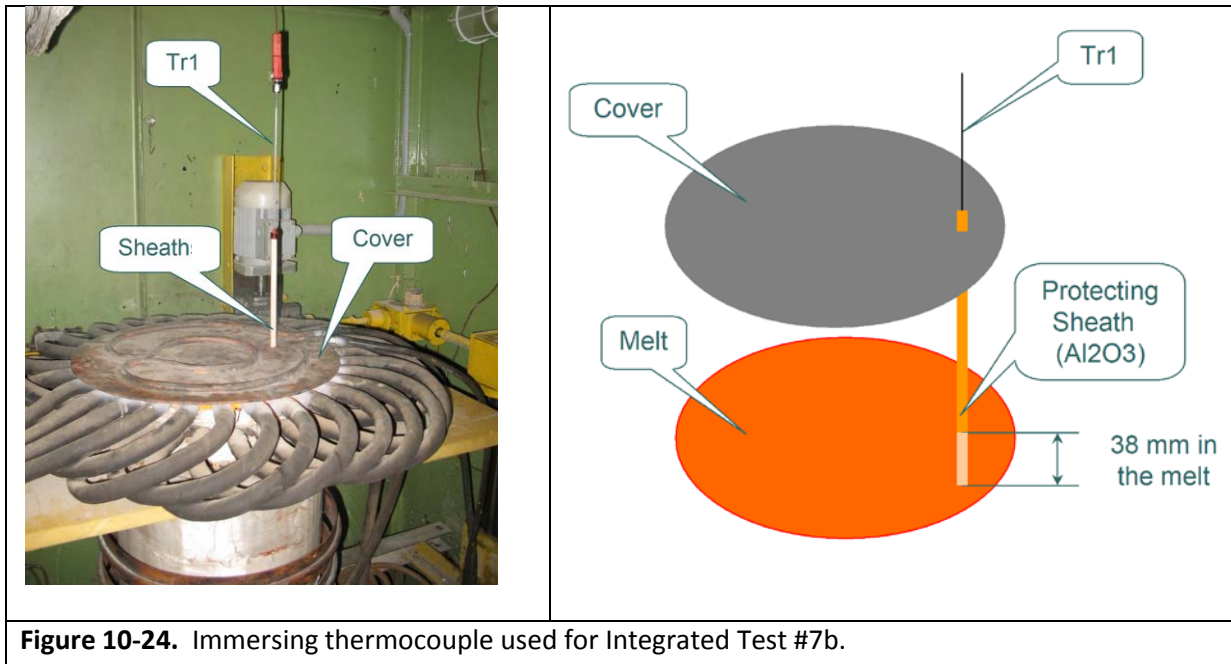
Figure 10-25 provides example photographs of the various stages of Integrated Test #7b. The steady state mode shown is at 1,450°C.

| a) melt initiation using graphite ring | b) maximum steady state mode of 1,450°C | c) melt pool at measurement with immersed thermocouple |

Figure 10-25. Representative stages achieved during Integrated Test #7a.
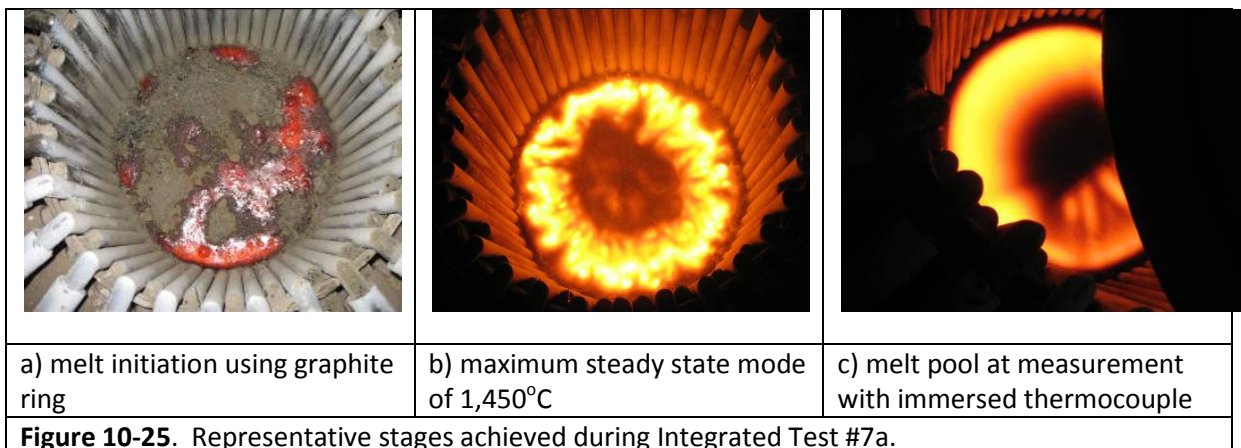
Melt Initiation Process: The parameters for the melt initiation process were obtained during Integrated Test #7b using the graphite ring as in previous tests. Initially, a well-used ring was placed in the crucible. However, the geometry of the ring had deteriorated due to oxidation processes

from multiple uses such that it was insufficient to successfully initiate a melt. A second, new ring was added and the start-up process continued. After the melt pool was established the rings were removed one at a time. Figure 10-26 shows key power loss parameters during the melt initiation process. The second ring was removed at the time indicated by location 1, and the first ring removed at location 2.

Analysis of the Pa.t graph in Figure 10-26 shows that upon removal of the second ring (point 1) the total active power fell by about 16 kW. If this is assumed to be the power that was in the ring, then at point 2, removal of the first ring, a drop of only about 2 kW is observed. This provides the explanation of why the first ring was unable to initiate a melt.

Steady State Modes: Four steady state modes were established at temperatures of 1,450°C, 1,293°C, 1,165°C, and 1,089°C. Power loss data for various elements during each steady state condition are presented in Figure 10-27. As observed during Integrated Test #7a, the modes that are much below 1,200°C do not actually represent steady state modes as there is a continuous decrease in the total active power during those stages.
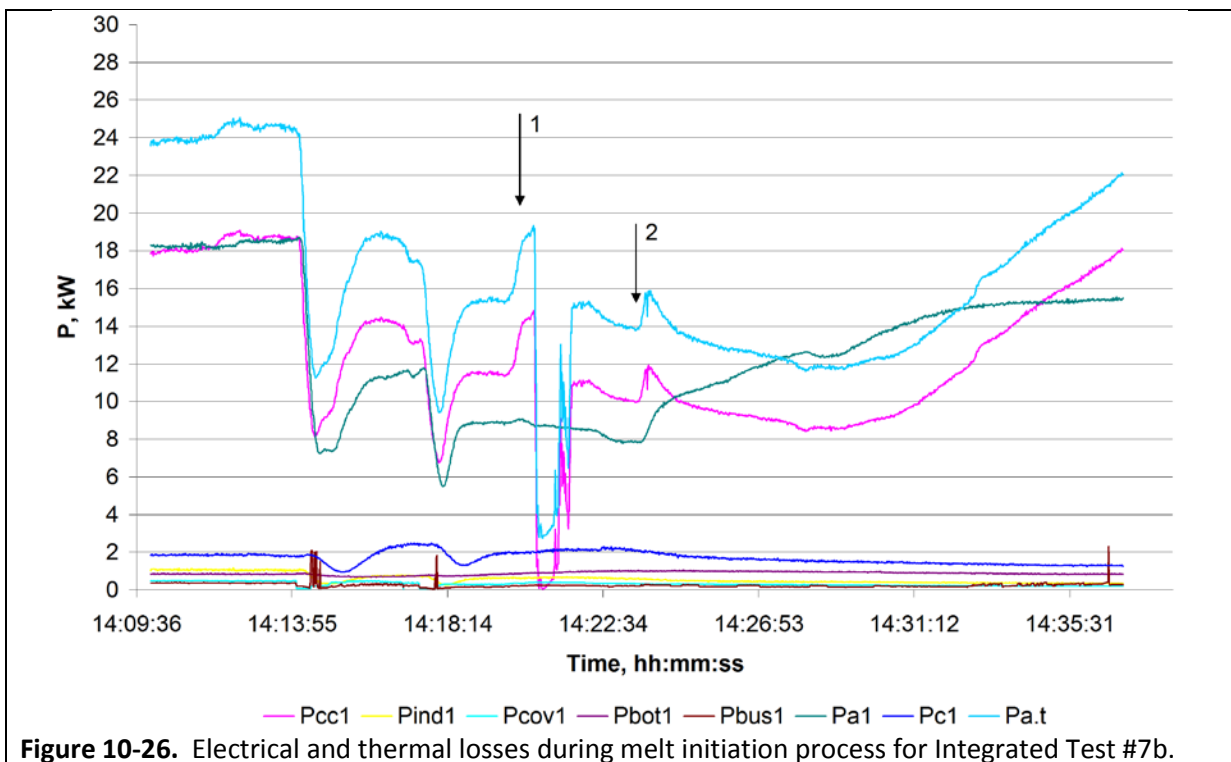
Figure 10-26. Electrical and thermal losses during melt initiation process for Integrated Test #7b.
(Pcc1 is electrical and heat losses in cold crucible, Pind1 is electrical losses in the inductor, Pcov1 is electric and heat losses in cover, Pbot1 is electrical and heat losses in bottom, Pbus1 is electrical losses in capacitor bank buses, Pa1 is heat losses in the generator lamp anode, Pc1 is electrical and heat losses in generator oscillatory circuits, Pa.t is total active power in the melt from calorimetry)
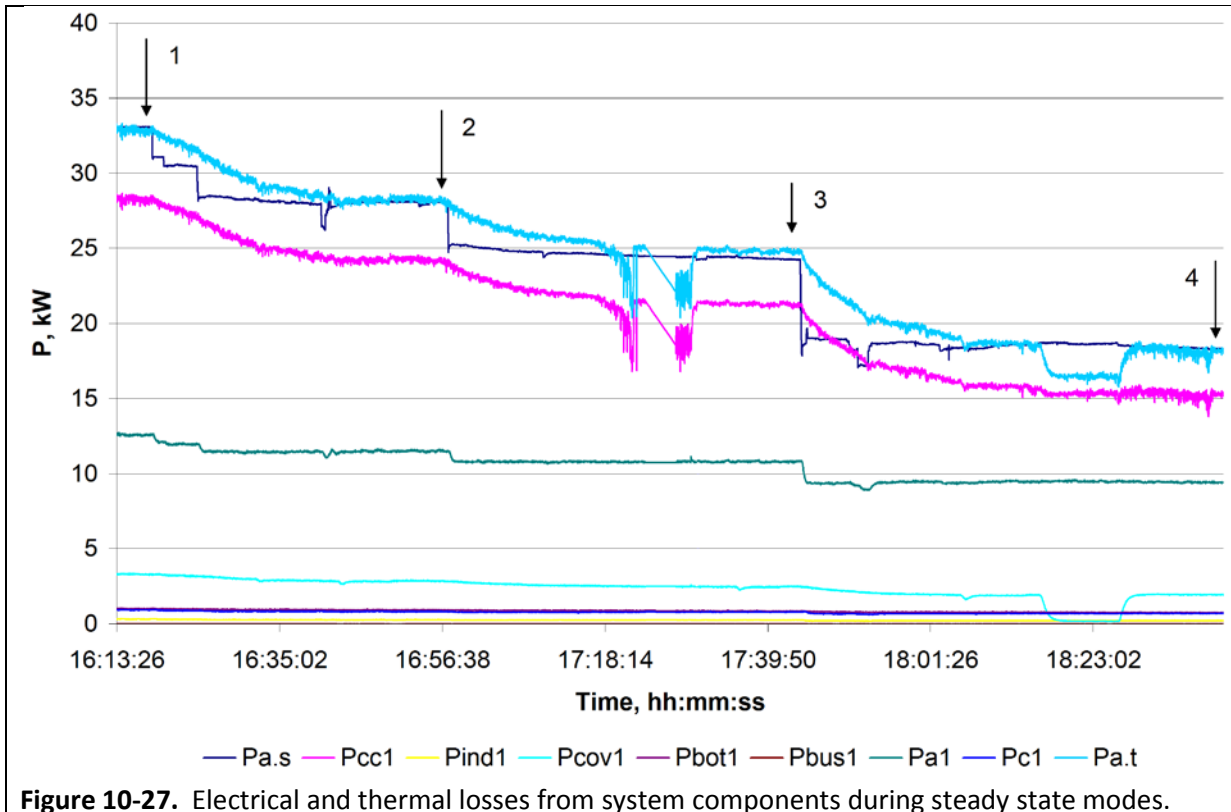
Figure 10-27. Electrical and thermal losses from system components during steady state modes.
(Pa.s is total active power in the melt from sensors, Pcc1 is electrical and heat losses in cold crucible, Pind1 is electrical losses in the inductor, Pcov1 is electric and heat losses in cover, Pbot1 is electrical and heat losses in bottom, Pbus1 is electrical losses in capacitor bank buses, Pa1 is heat losses in the generator lamp anode, Pc1 is electrical and heat losses in generator oscillatory circuits, Pa.t is total active power in the melt from calorimetry)

Table 10-4 provides a comparison of key operational and melt parameters for each steady state mode.

Table 10-4. Comparison of key parameters for steady state modes during Integrated Test #7b.

Mode	Ua, kV	Ia, A	Ig, A	Ucb, kV	T_{melt}, °C	$P_{a.t}$, kW	$P_{a.s}$, kW	U_{ind}, kV	I_{ind}, A
1	7.12	4.85	1.50	3.67	1,450	32.80	32.92	3.05	114
2	6.7	4.5	1.40	3.55	1,193	28.40	28.30	2.91	105
3	6.39	4.25	1.37	3.33	1,165	24.52	24.40	2.78	102
4	5.83	3.81	1.35	3.15	1,089	18.20	18.35	2.58	92

At each steady state mode, the immersion thermocouple was placed in the melt pool for a correlating temperature. The surface temperature taken by the optical pyrometer was located at a point that represented the hottest area on the melt pool. This is generally about 15 mm to 20 mm from the crucible wall and is characterized by the obvious bright color of the melt. The immersion thermocouple is located at the position that represents the hottest area within the melt volume, based on modeling and validated with measurements. Thus, the correlation is of the hottest surface

temperature with the hottest internal temperature of the melt pool. Table 10-5 provides comparative data for each steady state mode. T0.s is the pyrometer reading, Tr1 is the immersed thermocouple reading, ΔT0.s and ΔTr1 representative changes between modes for each.

Table 10-5. Comparison of maximum temperatures on surface and within melt volume.

Mode	T0.s, °C	Tr1, °C	ΔT=Tr1-T0.s, °C	ΔT0.s, °C	ΔTr1, °C
1	1,450	1,741	291		
2	1,193	1,605	412	-257	-136
3	1,165	1,583	418	-28	-22
4	1,089	1,376	287	-76	-207

The data taken for the four steady state modes shows that temperature differences between maximum surface and internal temperatures is in an approximate range of $300°C$ to $400°C$. These measurements are very consistent with the modeling results, providing another validation of its overall representativeness. Based on the model analyses, temperature ranges between $900°C$ and $1,600°C$ will be expected for a melt pool with a maximum surface temperature of $1,200°C$.

Figure 10-28 presents this information in graphical form through the duration of the test. This graph also includes temperature indications for the two thermocouples installed along the bottom surfaces of the crucible.

Figure 10-28. Comparison of maximum surface versus internal melt pool temperatures at various steady state modes.
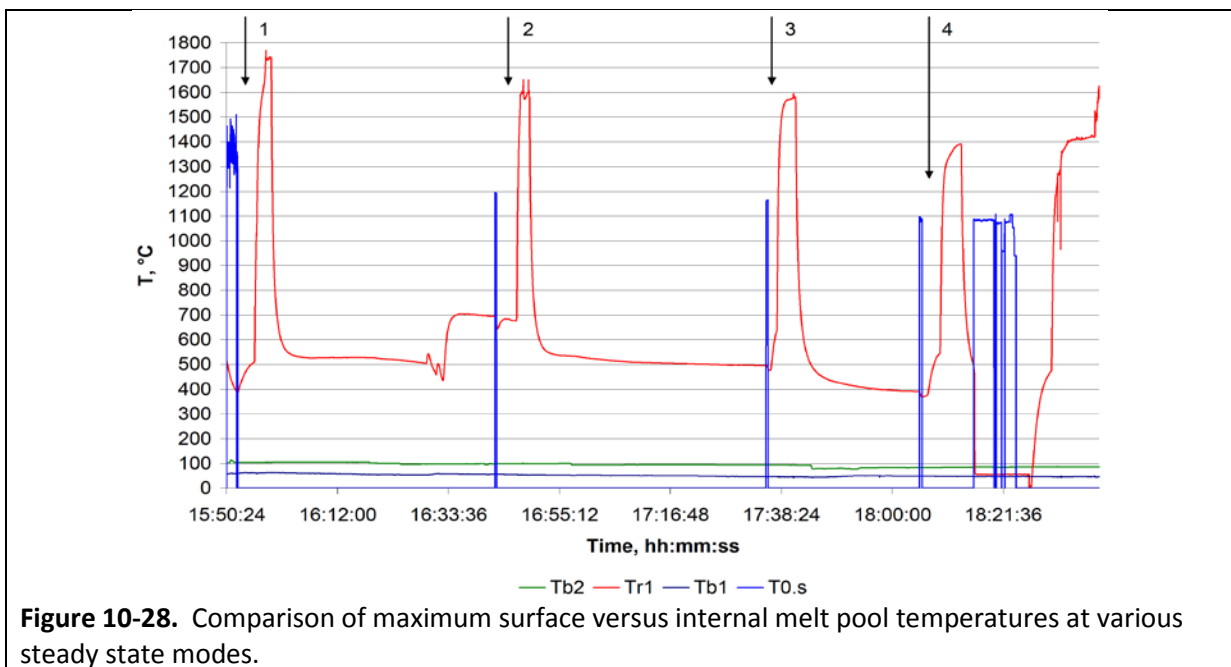
(Tb2 is internal bottom surface thermocouple, Tr1 is immersion thermocouple, Tb1 is external bottom surface thermocouple, T0.s is optical pyrometer reading on surface)

Crucible Translation Modes: During the last stage of Integrated Test #7b crucible translation modes were also investigated. Figure 10-29 shows the effect that upward and downward movements of the crucible (relative to the inductor) have on various power loss parameters. These effects will require additional analysis and further investigations to fully understand implications to this work. However, the overall results will be important in understanding the effects on the operational parameters, and thus boundary and/or initial conditions in the model when investigating optimum geometries for a CCIM system. In the prior test, the crucible was moved to create better conditions near the bottom to support the casting process. This was an expected effect; however, further investigations will provide a better understanding of the interrelations between the inductor position and optimal operational parameters, which will be particularly important for future scale-up efforts.

As part of this test effort, measurements were also taken to determine the power factor (cos φ) and the frequency. These measurements demonstrate that a strong correlation exists between these parameters and the inductor position relative to the crucible. While this is not directly related to the work reported herein, the data provides important information for advancing concepts for automated feedback control of CCIM systems.

On Figure 10-29, the location identified as "1" indicates the time at which the crucible started moving. The mechanism moves at approximately 20 mm per minute. All parameters are as previously defined.

Figure 10-29. Effects of crucible movement on power loss parameters of the system.
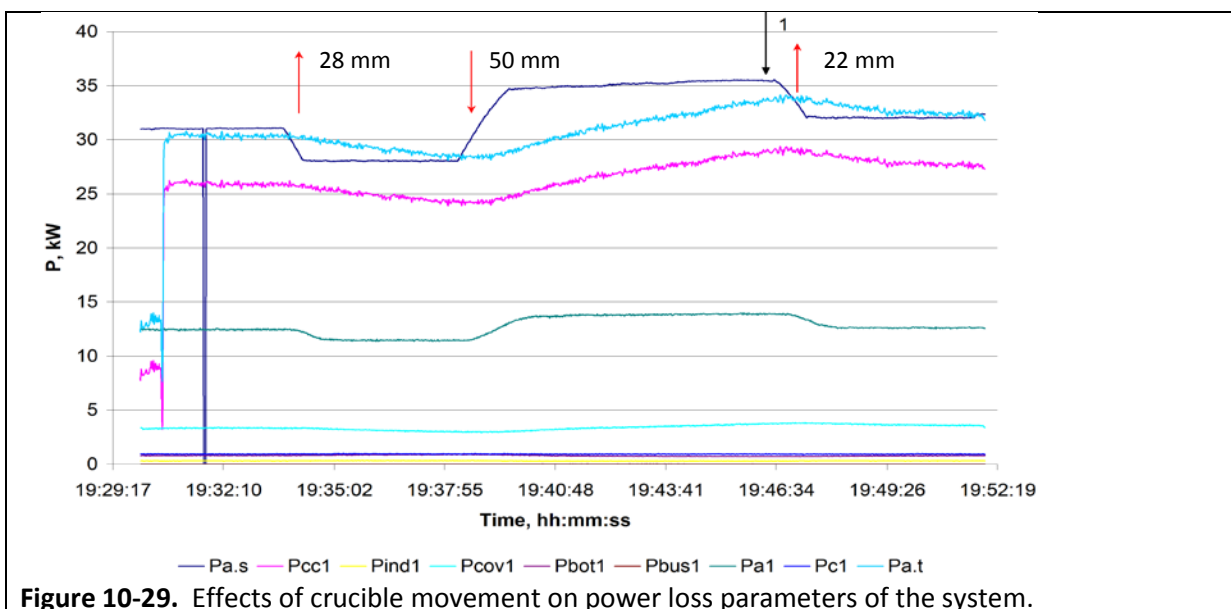
Table 10-6 provides summary information for the stages and conditions of Integrated Test #7b.

Table 10-6. Test stages and conditions during Integrated Test #7b.

Time, hr:min	Ia, A	Ig, A	Ucb, кV	Ua, кV	Note
10:25	-	-	2	-	The first calibration idling
10:45	-	-	3	-	The second calibration idling
10:55	-	-	4	-	The third calibration idling
11:07	1.68	1.8	5.1	7.2	The test beginning. Starting heating on a graphite ring
12:05	-	-	-	-	Because of excess of a voltage the voltage sensor was switched-off
12:50	2.63	2.09	7.3	9.9	The graphite ring has fused and the second graphite ring is entered
14:20	2.2	1.8	5.5	8.7	The voltage sensor is connected
14:21	-	-	-	-	Removal of the second ring
14:22	2.1	2.3	5.5	8.2	Charge filling
14:23	-	-	-	-	Removal of the first ring
14:24	-	-	-	-	Charge filling
15:52	4.85	1.5	3.67	7.12	The first mode. a_2 = 175 mm. T_{melt} =1,450^{o}C.
16:14	4.9	1.48	3.76	7.18	Calibration of inductor sensors
16:50	4.5	1.4	3.55	6.7	The second mode. T_{melt} = 1,193^{o}C.
17:40	4.25	1.37	3.33	6.39	The third mode. T_{melt} = 1,165^{o}C
18:04	3.81	1.35	3.15	5.83	The forth mode. T_{melt} = 1,089^{o}C
18:40	3.78	1.34	3.15	5.8	Temperature dependence study
19:05	-	-	-	-	First scanning of the melt surface
19:11	-	-	-	-	Second scanning of the melt surface
19:14	-	-	-	-	Charge added
19:21	-	-	-	-	Third scanning of the melt surface
19:23	-	-	-	-	Fourth scanning of the melt surface
19:34	-	-	-	-	Crucible raised 28 mm
19:38	-	-	-	-	Crucible lowered 50 mm
19:46	-	-	-	-	Crucible returned to initial position
20:00	-	-	-	-	Study of temperature dependencies of melt parameters

Key observations and conclusions: Integrated Test #7b observations and conclusions are as follows:

- For this specific glass and CCIM system, the transient time between modes is generally about 30 minutes. Additional measurements for different sizes and configurations may provide data that could be used to develop generalized correlations.

- As demonstrated in the model, temperature differences between the maximum surface temperature versus the maximum internal temperature for this glass and CCIM system can vary in the range of approximately 300°C to 400°C, with the internal temperature being higher.

- Modifications and improvements to the crucible design and configuration, as well as the drain device are required to produce conditions near the bottom of the crucible that will provide reliable and repeatable electromagnetic casting.

10.3.3. Improved Crucible Assembly Design

Based on the results of the previous investigations, an improved design for the crucible was developed. This was required for two primary purposes: 1) the current crucible configuration does not provide for installing a leak-tight cover lid, and 2) better electrical efficiency in the bottom of the crucible is needed to improve the heating conditions to support casting. In general, a larger diameter design was desired because it would provide a larger melt pool for longer duration casting processes. In practice, induction melting systems for processing radioactive waste are integrated with feed systems that provide for continuous, or semi-continuous. A larger diameter system that can process more volume in a given test will provide more opportunity to study various characteristics, parameters, and effects.

The maximum power supply available is rated at 60 kW continuous power. Accordingly, to be able to process larger volumes of glass with this generator, the crucible must be a very electrically efficient design. Scale-up studies were conducted using the ANSYS® model and the results from those investigations led to the design for the new crucible. The details are discussed below.

The crucible design envisioned is shown in Figure 10-30. The crucible is constructed completely from copper. The upper flange is designed to accommodate a cover lid that can be bolted on to provide a sufficient seal to provide the increased vacuum within the crucible for casting stoppage. The crucible will be constructed of 64 copper tubes of 20 mm outside diameter, the assembly diameter is approximately 407 mm inside diameter and the height is 400 mm. Clearance between each tube is 1 mm. The bottom is constructed of four 20 mm thick solid copper plates of 90° sectors, each with seven slits, resulting in eight fingers in each plate. The center opening is 135 mm

in diameter to accommodate the drain device. The drain device geometry is the same as the eight version, except that the slits were lengthened, constituting the *ninth version*.
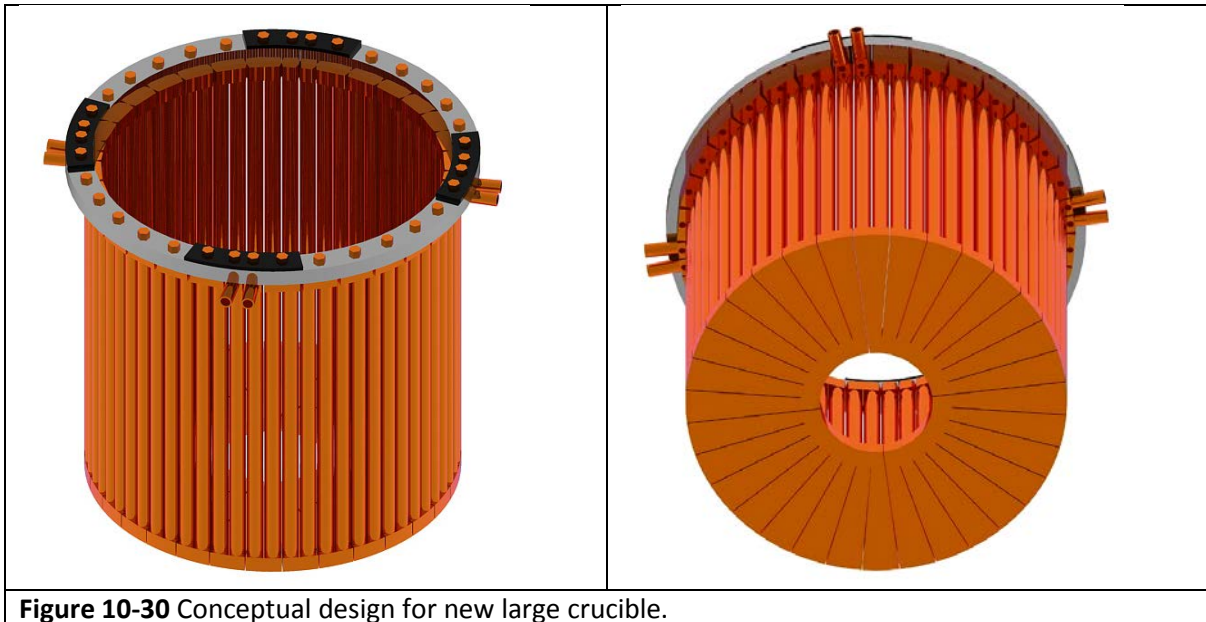
Figure 10-30 Conceptual design for new large crucible.

The inductor is a two-turn design of 200 mm total height. Each turn is made of an 85 mm wide copper sheet with a 30 mm gap between turns. The inductor has an inside diameter of 480 mm, providing a minimal clearance between the inductor and crucible of 16.5 mm. The inductor configuration was designed by ETU-LETI faculty to ensure compatibility with the operational parameters of the 1.76 MHz, 60 kW generator.

The cover lid is water-cooled with an outlet port that attaches to an induced draft fan to provide a vacuum within the crucible head space. The lid includes an access port for performing measurements, frit addition, and other activities during testing. Various views of the completed assembly are shown in Figure 10-31.

The system for providing the vacuum was designed to specifically operate with this crucible geometry. The inside diameter of the new crucible is 407 mm; however, the curves of the tubes result in an internal diameter that is approximately equal to 412 mm. The melt density at the lowest nominal test temperatures (conservative) is about 2.5 grams per cubic centimeter. Melt pool height will be in the range of 220 mm to 145 mm. This results in a hydrostatic pressure ranging between 3.6 kPa and 5.5 kPa (0.5 psig to 0.8 psig). Components were procured and assembled that would provide this range of vacuum. The actual system components are located in various places within

the laboratory, which makes providing a photograph not practical. However, a schematic of the system is provided in Figure 10-32.
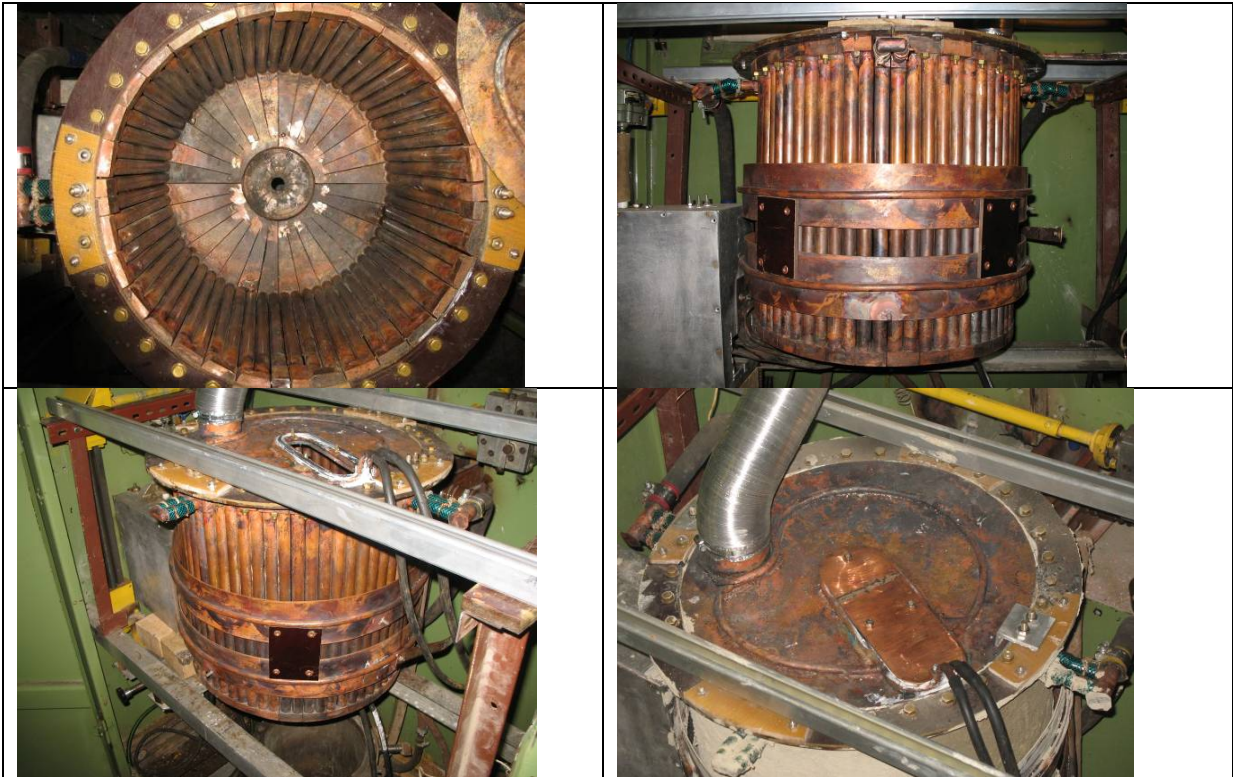
Figure 10-31. Views of the new crucible assembly design. Top left – looking into assembled crucible with ninth version of drain device installed. Top right – crucible with inductor installed. Bottom left – fully assembled system with access port on lid open. Bottom right – crucible with lid installed.
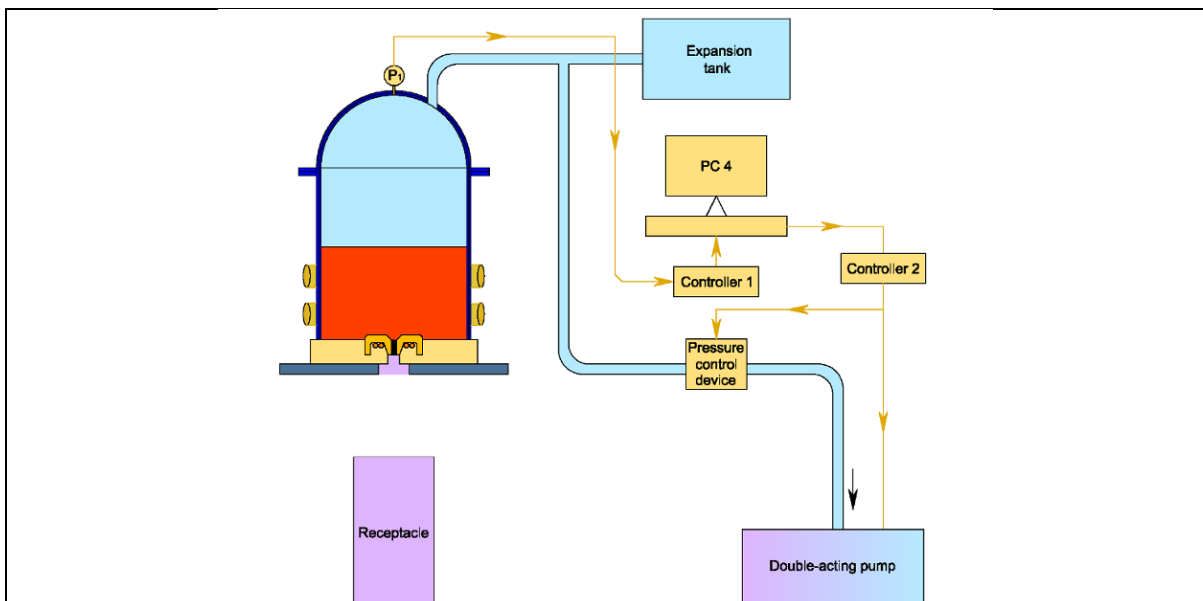
Figure 10-32. Schematic of vacuum assist casting control system.

10.4.   Feasibility Testing of New Crucible System– Integrated Test #8

The final test in this stage of the work was Integrated Test #8. This test had two key objectives: 1) to test the feasibility of the Option 2 Pressure Assist (vacuum) Casting Control concept, and 2) to gather some initial operational parameters and characteristics for the new 407 mm copper segmented crucible assembly.

Use of the new larger crucible required modifications to the 1.76 MHz generator. These changes were designed and implemented by ETU-LETI. Specifically, the existing voltage regulator circuit was not adequate to provide sufficient voltage during the melt initiation process. As a solution, an electrically moveable grounding point was added to the inductor. This capability allows starting the melt process with a mid-point ground, which effectively provides double the voltage during this stage as previously capable. Then, once the melt is initiated and a melt pool established, the ground point is changed back to the end of the coil.

The 27 MHz generator was also modified for this phase of testing, based on results of prior testing that indicated additional power was needed for various casting conditions. The existing air-cooled 4 kW generator tube was replaced with a water-cooled 10 kW generator tube. This will provide additional power and reliability, but also allows calorimetry data to be obtained on the 27 MHz generator. The ETU-LETI faculty designed and implemented this modification in support of the required testing. Finally, an automated voltage regulator was also added to the generator by ETU-LETI to provide interface with the data acquisition and control system, allowing remote operation of the 27 MHz generator.

The system used for Integrated Test #8 is shown in Figure 10-33. The outer and inner surfaces of the crucible are sealed with non-conductive ceramic putty to ensure a leak-tight system is achieved. A thermocouple was installed at the bottom surface, Tb1, to provide indications of the bottom conditions for casting with this new, larger crucible. This is also shown in Figure 10-31.

The melt was initiated using a graphite ring, as usual. However, due to the significant increase in melt volume (approximately twice as much as processed previously) a much longer time was required to achieve a full melt pool. Approximately 1.5 hours passed from start-up to removal of the ring, which was then followed by another hour before achieving a full melt pool. The system exhibited much different behavior upon removal of the ring, as shown in Figure 10-33.
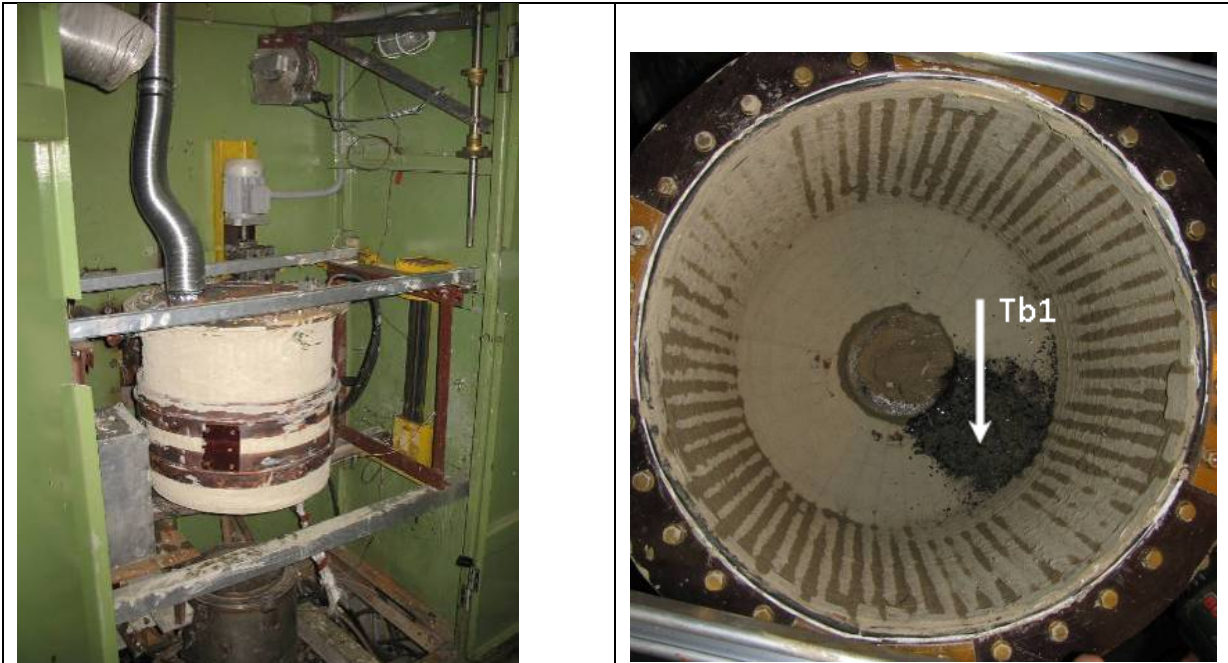
Figure 10-33. New crucible assembly at start of Integrated Test #8 (left), view inside crucible with ninth version of the drain device and thermocouple installed, prior to cover lid installation (right).

Figure 10-34. Power losses in system during melt initiation process for Integrated Test #8.
(Pcc1 is electrical and heat losses in cold crucible side wall, Pind1 is electrical losses in the 1.76 MHz inductor, Pcov1 is electrical and heat losses in cover lid, Pcc2 is electrical and heat losses in the drain, Pbus1 is electrical losses in capacitor bank buses, Pa1 is heat losses in the 1.76 MHz generator lamp anode, Pc1 is electrical and heat losses in 1.76 MHz generator oscillatory circuits, Pind2 is electrical losses in the 27 MHz inductor, Pa2 is heat losses in the 27 MHz generator lamp anode, Pa.t is active power in the melt determined by calorimetry)

10.4.1. Steady State Mode

A steady state mode was investigated during Integrated Test #8. For this test, one steady state mode of 1,200^{o}C was established. Then, the 1.76 MHz generator was powered off and back on for increasing durations of time. As seen in Figure 10-35, after about 20 minutes a steady state mode appears to be achieved. However, when other parameters are investigated, see Tb2 and Pcc2 behavior in Figure 10-36, this does not appear to be a steady state.
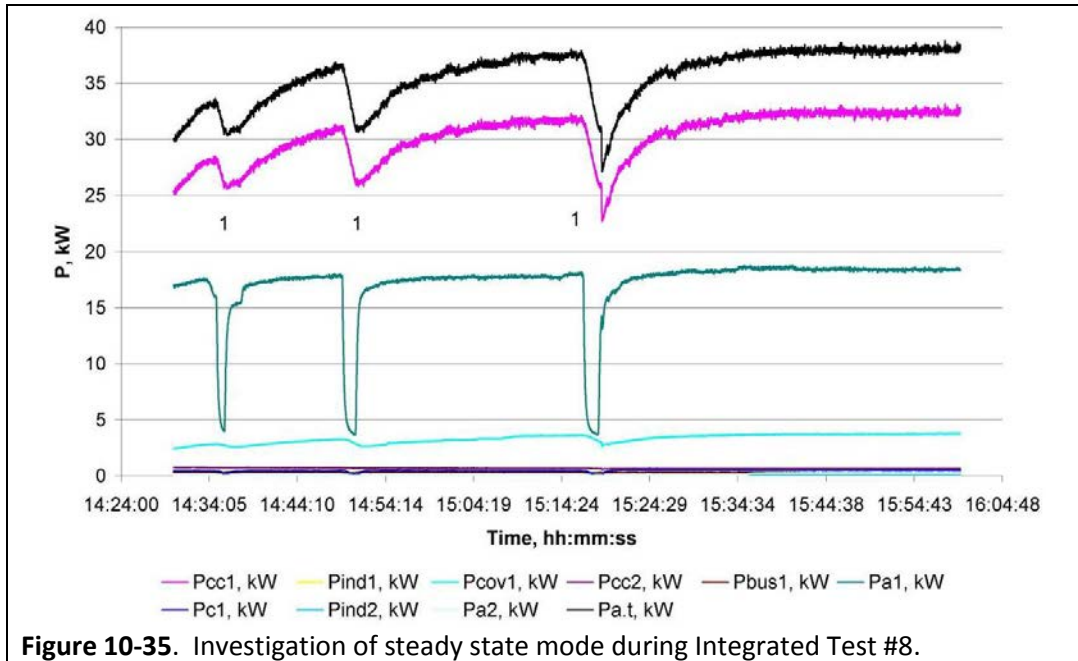
Figure 10-35. Investigation of steady state mode during Integrated Test #8.
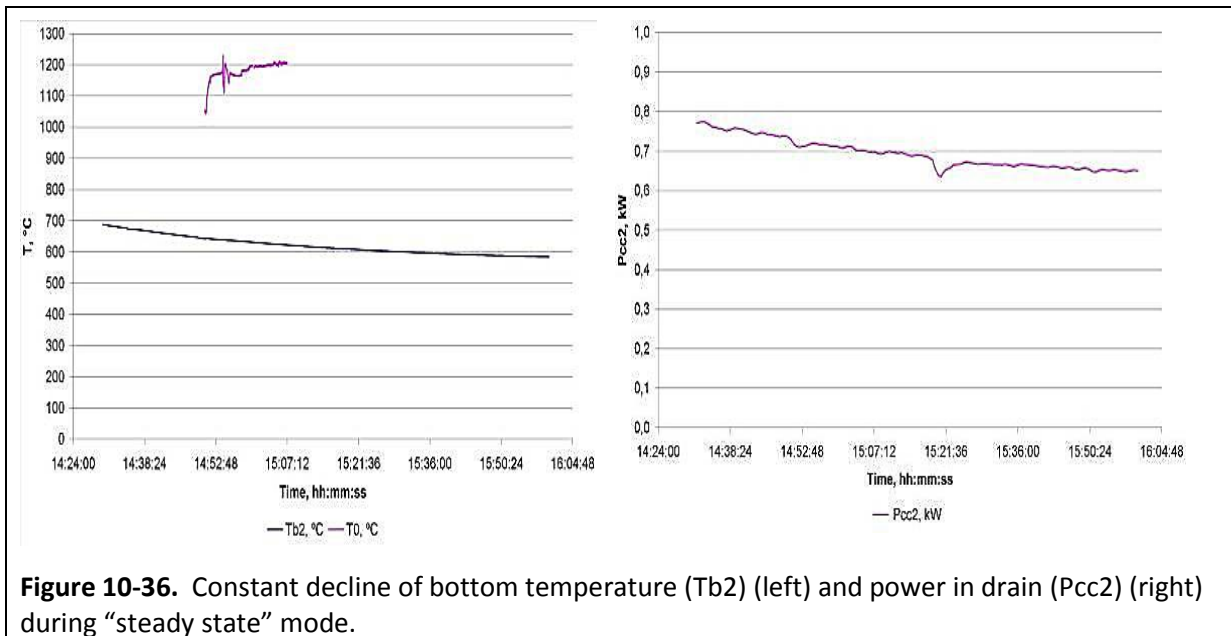
Figure 10-36. Constant decline of bottom temperature (Tb2) (left) and power in drain (Pcc2) (right) during "steady state" mode.

For example, the temperature along the bottom is decreasing, while the surface temperature is increasing. Similarly, the power in the drain was decreasing. It appears that a redistribution of power within the melt pool was occurring. Specifically, as time progressed, the bottom skull layer was growing thicker, reducing the volume that the induction field was coupling with, resulting in an increased specific power, and thus increased surface temperature.

Melt Casting could not be initiated electromagnetically as a result of the thick bottom skull layer formed. To investigate the Option 2 Pressure Assist system for casting stoppage, the casting was initiated externally using an oxy-hydrogen torch in the drain opening, followed by mechanical puncture with a metal rod.

10.4.2. Pressure Assist Casting Control – Option 2

The Option 2 Pressure Assist Casting Control system (i.e., vacuum) was evaluated once the casting process was initiated. The suction pump was powered on and a maximum of 3.6 kPa gage vacuum in the crucible was obtained. Areas of air in-leakage due to failure of seals restricted the system from achieving the level of 4 kPa gage needed for fully stopping the high melt pool (i.e., greater than 200 mm). Once, the level of the melt pool had dropped due to draining, the suction was gradually re-applied to the level required to effect a full stop of the glass flow. This was repeated several times. During this process, the ability of intermediate levels of suction were observed to effectively control the mass flow rate (i.e., diameter of pour stream was visibly reduced). Figure 10-37 provides a summary of the pressure assist casting control process completed during Integrated Test #8. The peak in the Pcc2 curve (indicated with a "2") is the time of max temperature when the final, long casting occurred.
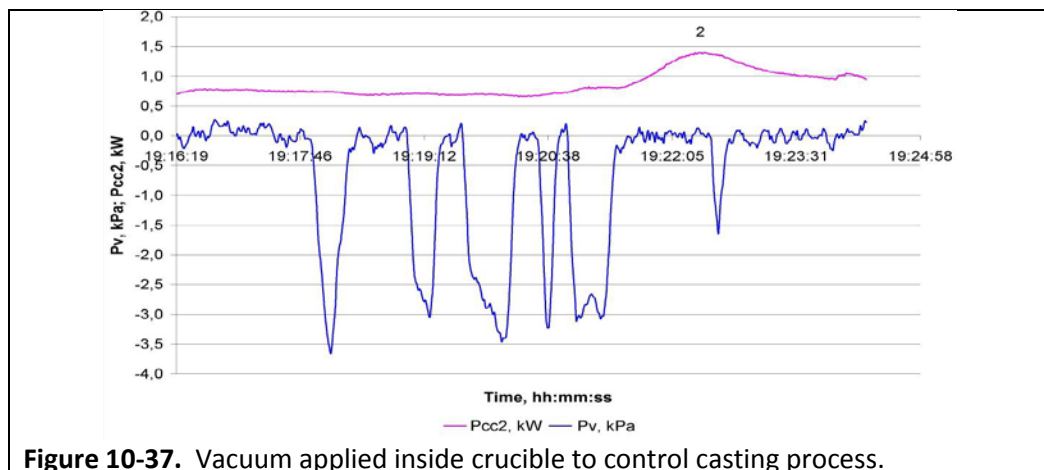
Figure 10-37. Vacuum applied inside crucible to control casting process.

Table 10-7 provides data for the test stages and conditions during Integrated Test #8.

Table 10-7. Test stages and conditions during Integrated Test #8.

Time, hr:min	Ia, A	Ig, A	Ucb, кV	Ua, кV	Note
11:20	4	1	2.2	4.5	Test start-up. Melt initiation using a new graphite ring.
12:54	-	-	-	-	Ring removal.
12:58	9.55	1.41	3.58	7.36	f=1.698 MHz.
13:57	-	-	-	-	Pool height is 160 mm.
14:19	7.7	1.53	2.7	5.5	The crucible cover was installed.
15:00	8.0	1.4	2.7	5.89	Access port opened. T_{melt}=1,160°C. a_2=145 mm. Distance between melt pool surface and cover lid is 285 mm. Depth over the drain was 125 mm. Skull thickness over the drain was 13 mm.
15:08	-	-	-	-	Access port closed.
15:46	-	-	-	-	Drain temperature determined by Raytek pyrometer was 150°C.
16:02	-	-	-	-	27 MHz generator powered on. Ig_{27} = 140 mA, Ia_{27} = 0.5 A.
16:55	-	-	-	-	Ig_{27} = 300 mA, Ia_{27} = 0.7 A
17:00	8.77	1.43	2.80	6.34	Drain temperature determined by a Raytek pyrometer was 200 °C.
18:20	-	-	-	-	Casting not initiated electromagnetically. Glass in drain heated with an oxy-hydrogen torch.
18:41	-	-	-	-	27 MHz generator was switched off.
18:46	-	-	-	-	Melt casting was stated by rod pressure on glass inside the drain below. Jet temperature was 1,200 °C.

Figure 10-38 shows key stages during Integrated Test #8.
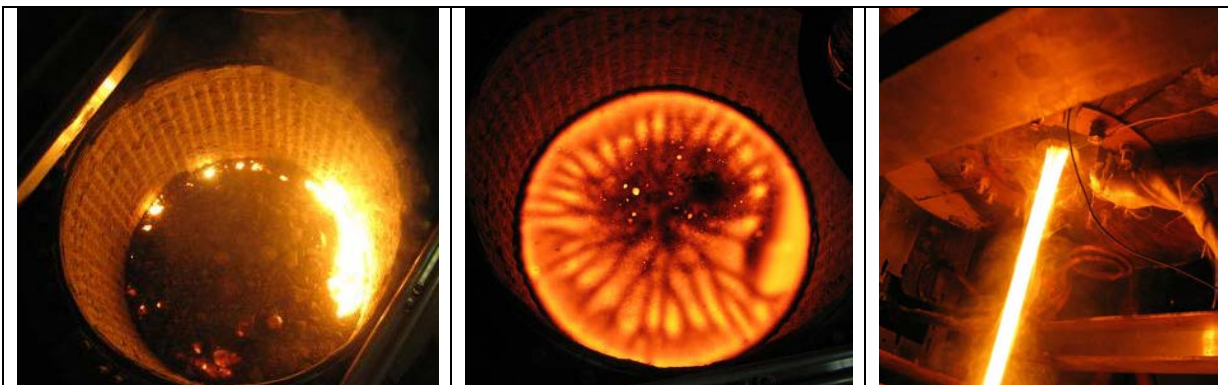
Figure 10-38. Key stages of Integrated Test #8. Left – melt initiation, Center – steady state of 1,200°C, Right - Casting

10.4.3. Key Observations and Conclusions

Observations from Integrated Test #8 are as follows:

- The melt pool height of 220 mm resulted in a very thick skull of approximately 30 mm due to insufficient sustained heating in the bottom zones. Both the crucible and drain device need to be modified to improve electrical efficiency for the large diameter integrated system.

- The optimal melt pool height for the 407 mm diameter crucible must be determined. The depth used in this test was not efficient and could not achieve steady state conditions.

- Reducing the melt pool depth generally causes the hottest zones in the melt pool to be eccentrically located from the central axis, which may require offsetting the drain device from the centerline.

- The pressure assist casting control concept was demonstrated to be feasible. The installation must be sealed better to minimize air in-leakage and insure that the required pressure can be maintained. Although, if the melt pool depth is decreased, the pressure requirements will also.

Additional tests were performed on the same test platform, with improvements to the 27 MHz generator implemented to increase the available power to 10 kW, as well as to improve the overall efficiency and reliability. Key data from these tests are included in Appendix C.

CHAPTER 11.   SYSTEM OPTIMIZATION TESTING

After the primary Integrated Tests were completed, supplemental testing was performed to further refine the drain design, as well as to improve the capacity and reliability of the equipment, particularly the 27 MHz generator. Several equipment improvements were incorporated as well as changes to the drain device, which constituted the *tenth version*. The new inductor design, which was based on modeling results, was a two-turn planar configuration, similar to the prior inductor, with a larger outside diameter (i.e., increased from 90 mm to 100 mm), a smaller inside diameter (i.e., from 60 mm to 50 mm) and a larger diameter tube. The increase in tube diameter was necessary to accommodate the higher current that is needed for reliable electromagnetic casting in the 407 mm diameter crucible. The other key change was implementation of a heated water supply for cooling the 27 MHz inductor coil. This system eliminates formation of condensation on the inductor coils and the resulting arcing and short circuits that were interfering with the casting process.

The final tests reported herein are the overall System Optimization Tests that were conducted to result in an optimized system design, which includes both the drain and crucible geometry.

11.1.   System Optimization Test Series #1

System Optimization Test #1 was conducted in two stages. The first stage, Test #1a, was focused on investigation of steady state modes for potential crucible optimization and validation of the new drain design, which is described below. Up to this point, electromagnetic casting initiation has not been successfully performed for larger diameter systems. The second stage, Test #1b, used the exact same test configuration, but was focused on testing the Option 2 Pressure Assist Casting Control system for functionality with the new drain design. This may lead to additional optimization of the drain device for the final integrated system. Note that the modified drain inductor was implemented in Test #1b only.

The tenth version of the drain device was designed based on prior testing and modeling. This design, which is shown in Figure 11-1, is constructed of a solid 8 mm thick copper plate. This is reduced from the 10 mm thick upper section in the previous version. Additionally, the drain body does not extend past the face of the lower surface, but rather the drain opening is flush. The number of sections was increased from 16 to 20. Finally, the electrical connections between sections were moved further out on the periphery with the use of U-shaped cooling tubes that

extend beyond the outer edge. While the overall diameter has increased due to the U-tubes, the central plate remained at 135 mm diameter to interface with the crucible bottom design. To maintain as much electrical isolation as possible between the crucible bottom and drain device, during installation, a layer of non-conductive ceramic putty is placed on the bottom surface of the crucible and the drain assembly is then located on top of this layer.
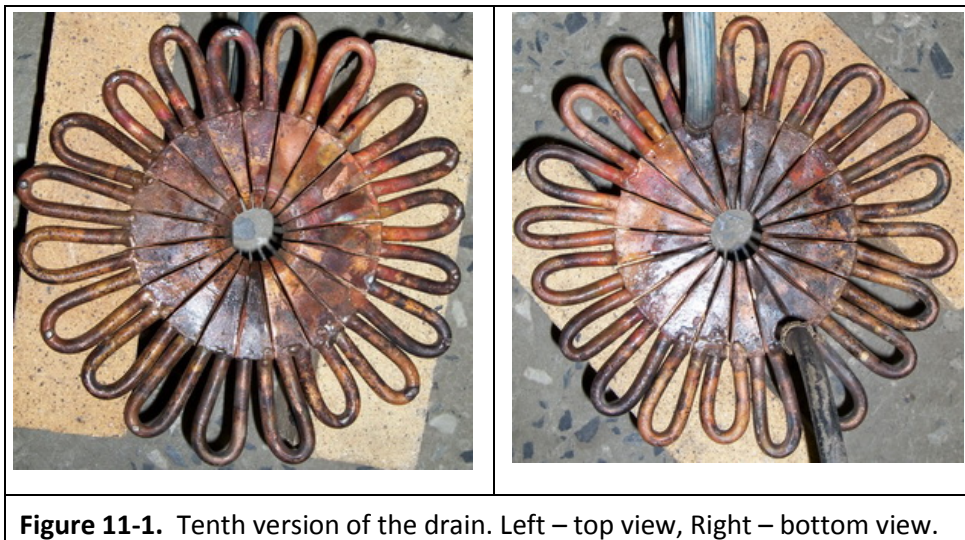
Figure 11-1. Tenth version of the drain. Left – top view, Right – bottom view.

11.1.1. System Optimization Test #1a

System Optimization Test #1a used the same crucible and inductor as the previous test. Namely, the 407 mm diameter copper crucible with the two-turn, 200 mm high inductor. The 1.76 MHz, 60-kW generator provided the primary power source. The 27 MHz had several iterations of improvements prior to this test, such that it is reliably providing 10 kW of power at higher current levels for the draining process. As previously mentioned, the drain inductor was modified to accommodate the increased power levels. Three thermocouples were used during the test. One was an immersed Tungsten/Rhenium (Type C) thermocouple that was positioned 40 mm deep, aligned with the hottest point on the surface (i.e., same position s pyrometer). The other two Type K thermocouples were installed 1) 20 mm above the drain opening, and 2) 10 mm above the crucible bottom between the drain edge and side wall. Selection of the type of thermocouple was determined by the temperatures observed in the area of installation from previous testing and modelling.

Melt Initiation Process: During the System Optimization Test #1a the melt initiation process was investigated to further evaluate the efficiency and performance of the new crucible. The start-up process required about 65 minutes, which was shorter than previous tests with the large crucible.

The behavior of key power parameters during the melt initiation process are shown in Figures 11-2 and 11-3.
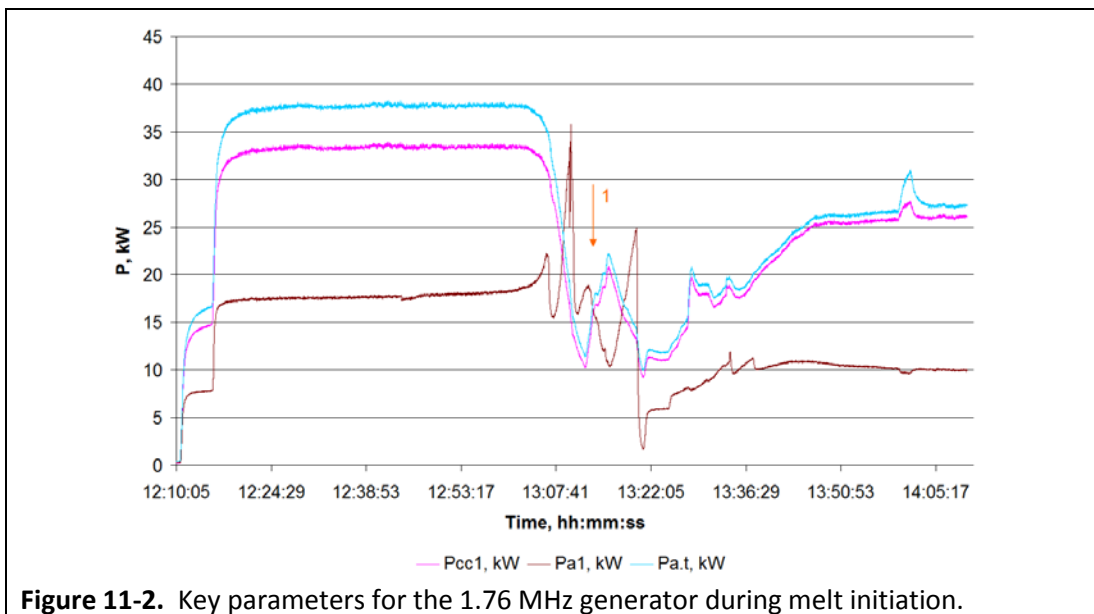
Figure 11-2. Key parameters for the 1.76 MHz generator during melt initiation.
(Pcc1 is electrical and heat losses in side walls of cold crucible; Pa1 is power loss on the 1.76 MHz generator anode, Pa.t is total active power to the inductor determined by calorimetry)
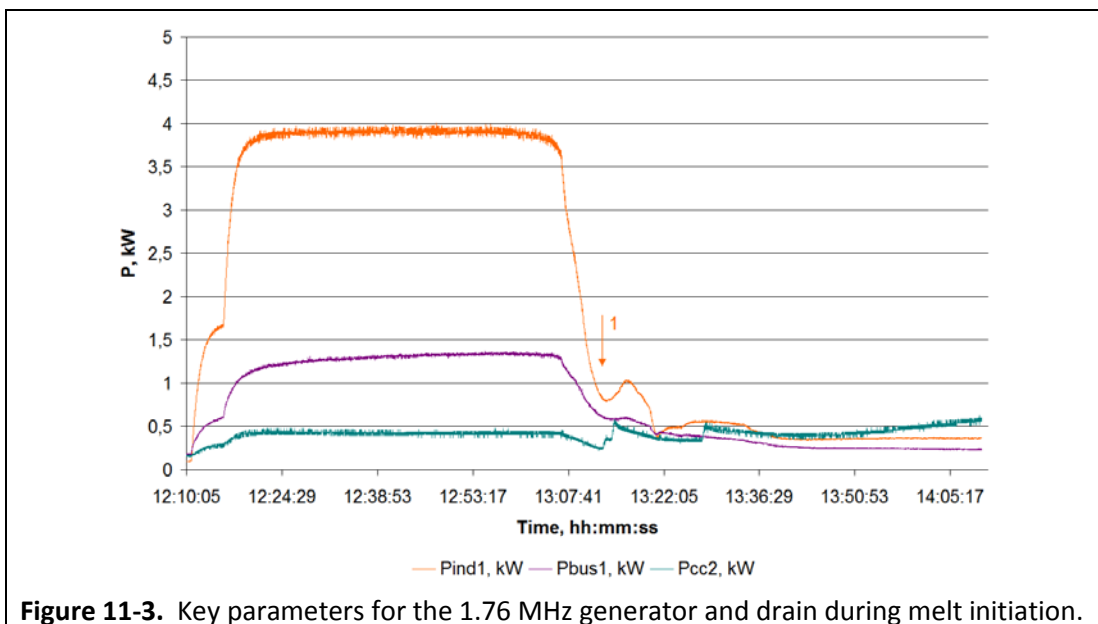
Figure 11-3. Key parameters for the 1.76 MHz generator and drain during melt initiation.
(Pind1 is electrical losses in the 1.76 MHz inductor, Pbus1 is electrical and heat losses in capacitor bank buses, Pcc2 is electrical and heat losses in the drain)

The time identified with "1" is the point at which the initiator ring was removed. At five minutes after that point, the ground location of the primary inductor was switched from the midpoint to the end. Both of these figures show that the melt pool is growing, with heating extending to the lower

layer within the crucible (i.e., Pcc1 and Pcc2 increasing). This improved start-up heating resulted from modifications to the 1.76 MHz generator implemented by ETU-LETI to better balance the oscillation circuit with the new crucible.

Steady State Modes: During the System Optimization Test #1a, three steady state modes with maximum surface temperatures of 1,030°C, 1,190°C, and 1,230°C were evaluated. These correlated to maximum internal melt temperatures of 1,352°C, 1,407°C, and 1,525°C, as measured by an immersed Type C thermocouple located near the hottest zone, as indicated from the modeling efforts. The melt pool surfaces for the three modes are shown in Figure 11-4.

Figure 11-4. Steady state modes evaluated during System Optimization Test #1a. Left - 1,030°C, Center - 1,190°C, Right - 1,230°C

Figure 11-5 shows the 1.76 MHz generator electrical parameters and calculated efficiencies for each of the steady state modes, indicated by corresponding numbers on the graph.
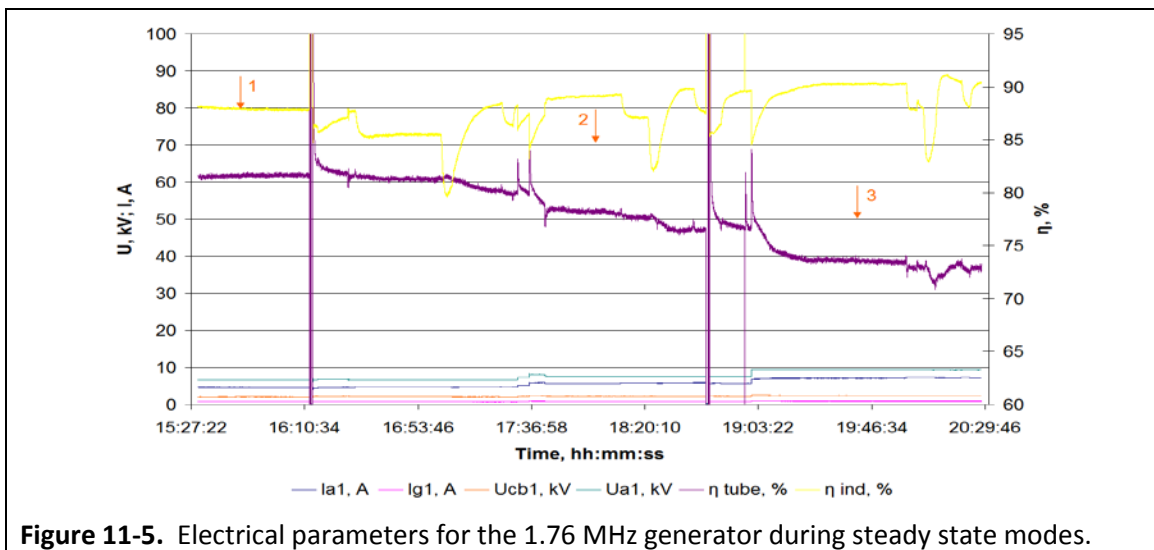
Figure 11-5. Electrical parameters for the 1.76 MHz generator during steady state modes.
(Ia1 is generator lamp anode current; Ig1 is generator lamp grid current; Ucb1 is voltage on the capacitor bank; Ua1 is voltage on generator lamp anode; ηind is inductor electric efficiency; η tube is generating lamp electric efficiency)

The power losses for various elements of the CCIM test platform are provided in Figures 11-6 and 11-7. In each, the identified points correspond to the steady state modes.
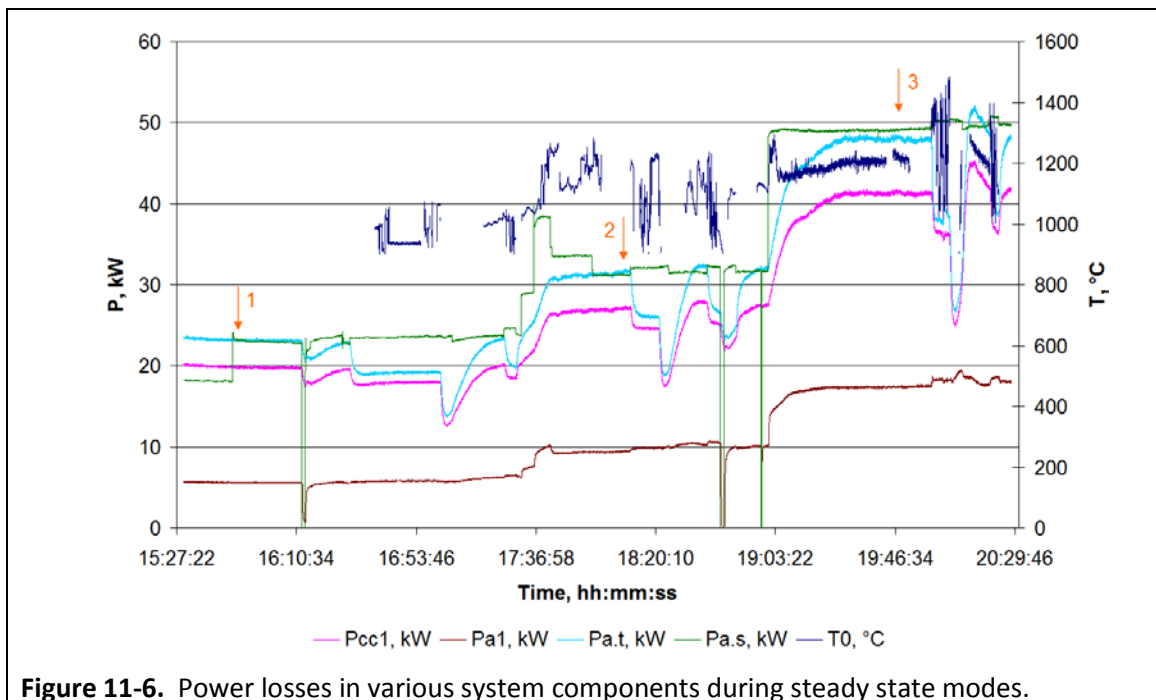
Figure 11-6. Power losses in various system components during steady state modes.
(Pcc1 is losses through side walls of crucible, Pa1 is electrical and het losses on 1.76 MHz generator anode, Pa.t is active power to the inductor determined by calorimetry, Pa.s is active power on the primary inductor determined by sensors, T0 is temperature on a glass melt surface)
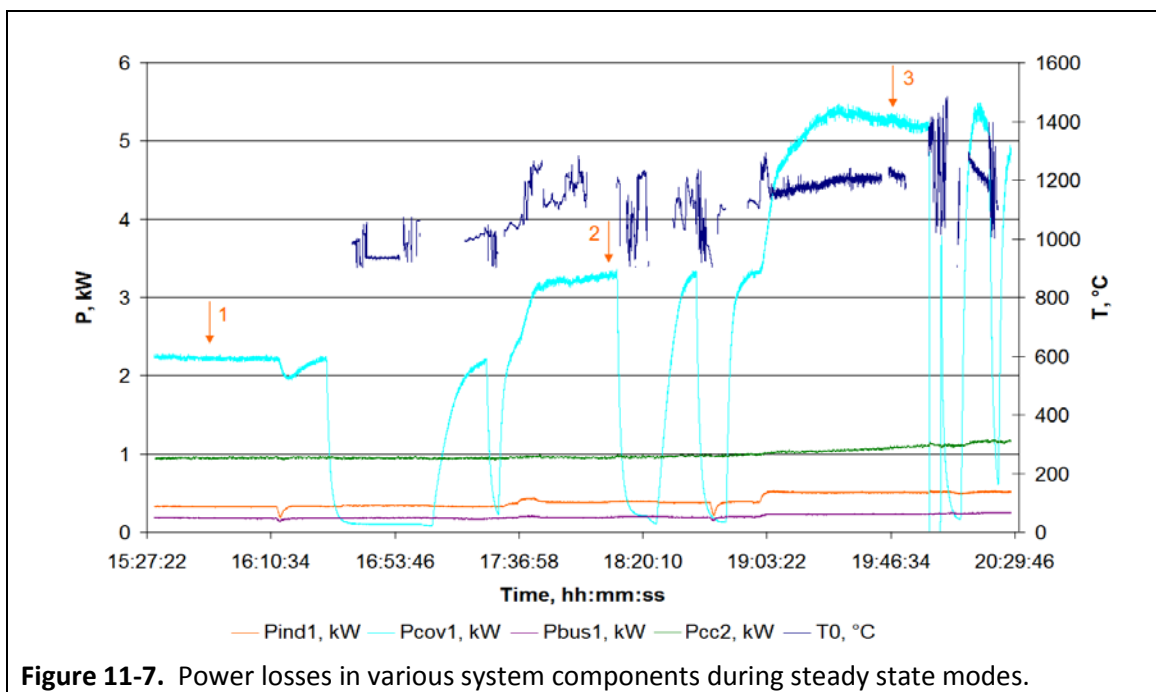
Figure 11-7. Power losses in various system components during steady state modes.
Pcov1 is total heat and electric losses in the cold crucible cover; Pcc2 is total heat and electric losses in the drain

A final correlation for the steady state modes observed was the maximum internal melt temperatures (i.e., immersed thermocouple) as compared to the bottom thermocouple readings. The bottom thermocouple was located 10 mm top surface of the drain device, approximately above the inductor coils. Figure 11-8 shows the maximum and bottom temperatures at these stages.
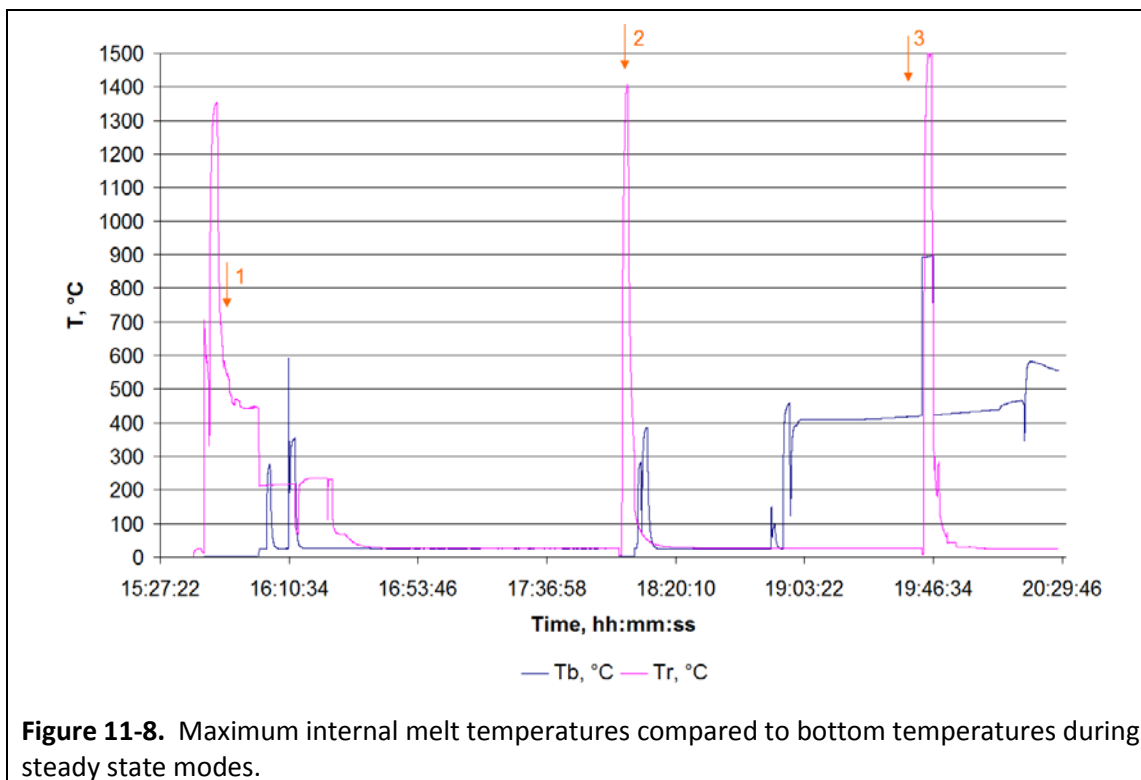
Figure 11-8. Maximum internal melt temperatures compared to bottom temperatures during steady state modes.
(Tb is indications of the bottom thermocouple, Tr is indications of the immersed thermocouple)

Melt Casting Process: During the System Optimization Test #1a, the melt casting process was investigated for the new tenth version of the drain device. The primary purpose was to test the operability of the new design to determine if casting could be initiated electromagnetically. Figure 11-9 shows stages of the process.
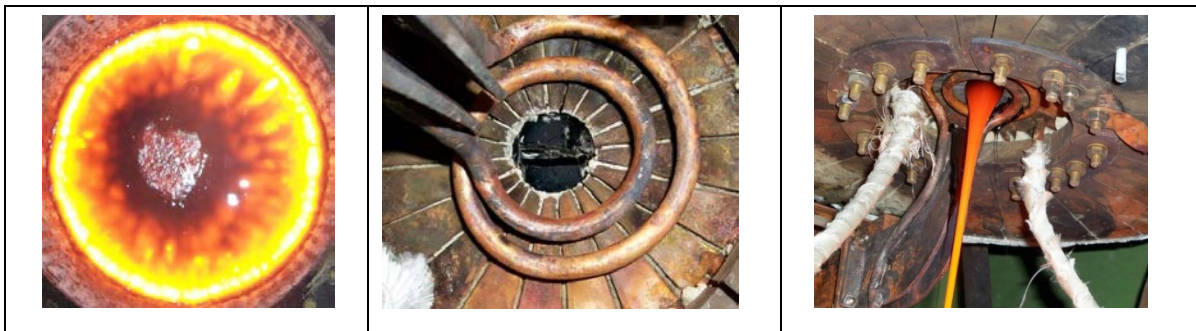
Figure 11-9. Melt initiation process. Left – melt surface prior to 27 MHz powered on, Center – tenth version of drain installed in crucible, Right – casting.

Figure 11-10 shows the key parameters of the 27 MHz generator throughout the melt initiation process. Point 1 indicates the time at which the generator was powered on and point 2 is the time at which electromagnetic casting occurred. The melt temperature prior to casting reached 1,419°C, and the glass temperature in the drain was 582°C, both measured by pyrometer.

Figure 11-10. Electric parameters of the 27 MHz generator and power losses in the drain during the casting process.
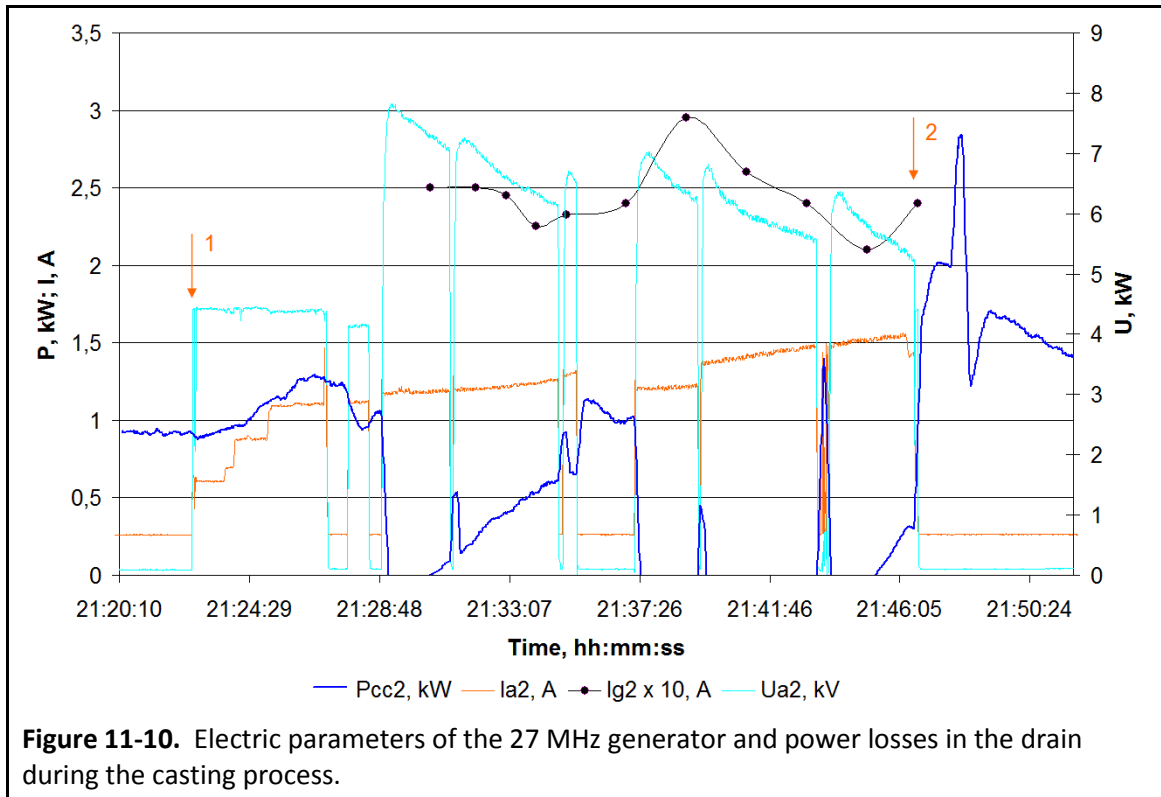
(Pcc2 is electrical and heat losses in drain, Ia2 is anode current in 27 MHz generator, Ig2 is grid current in 27 MHz generator, Ua2 is anode voltage in 27 MHz generator)

The 27 MHz generator had been operating less than 20 minutes when the casting was initiated. This was the first casting achieved from electromagnetic energy only I the large diameter system. The casting duration was approximately 5 minutes and 30 seconds, during which time 35.2 kg of glass were poured. This is a casting rate of about 6.4 kg/min or 380 kg/h. The maximum heat losses in the drain during casting reached 2.85 kW. During the casting, the melt jet deviated and contacted the inductor and buses. Modifications to the drain configuration, as well as the inductor will be implemented to mitigate this issue.

System Optimization Test #1a provided additional power loss data for a variety of different steady state modes. These are provided in Table 11-1. Efficiencies were also determined separately for the

generator tube and the inductor, the product of which provides the total efficiency for the system. This information will be used to further improve the model, as appropriate.

Table 11-1. Heat flux and efficiencies for various system components.

Mode #	Tr, °C	T_{melt}, °C	Td, °C	Tb, °C	P_{cc1}, kW	$P_{cc1.elec}$, kW	$P_{rad.cc1}$, kW	P_{cov1}, kW	$P_{cov1.elec}$, kW	P_{cc2}, kW	$P_{cc2.elec}$, kW
1	1,352	1,030	277	355	19.76	3.35	6.98	2.07	0.05	0.91	0.16
2	1,407	1,190	288	385	27.2	3.75	9.53	3.15	0.035	0.94	0.135
3	1,525	1,230	410	460	41.37	4.51	16.04	5.07	0.032	1.05	0.125

Table 11-1. Heat flux and efficiencies for various system components. (continuation)

Mode #	Tr, °C	$P_{ind1.elec}$, kW	$P_{a.t}$, kW	P_2t, kW	η_e, %	η_{tube}, %	η_{ins}, %	$P_{int.rad}$, kW	P_{side}, kW	$P_{0\,side}$, W/cm²	$P_{0\,rad}$, W/cm²
1	1,352	0.32	23.21	19.33	83.28	81.76	68.1	9.05	9.43	5.676	6.96
2	1,407	0.39	31.82	27.51	86.46	78.10	67.5	12.68	13.92	8.379	9.75
3	1,525	0.5	48.25	43.08	89.29	73.68	65.8	21.11	20.82	12.53	16.2

NOTES

1. Specific heat fluxes are determined using thermal losses only.

2. The melt temperature was determined by an immersed thermocouple in the same point that, on a vertical line, coincides with location of the pyrometer sight spot.

3. The area of the crucible bottom and cover, for a diameter of 407 mm, is 1,300.34 cm².

4. The area of heat flux through the crucible walls, based on an average depth of 130 mm for the fully melted portion (i.e., liquid) of the glass pool is 1,661.37 cm².

5. In this table: $P_{rad.cc1}$ is power of radiation heat transfer on crucible walls; $P_{rad.cov1}$ is power of radiation heat transfer on the crucible cover; $P_{int.rad}$ is power of radiation heat transfer from a melt surface (i.e., to crucible walls and cover); $P_{0\,rad}$ is specific heat flux from a melt surface; $P_{0\,side}$ is specific heat flux from melt to crucible walls; Tr, °C is melt temperature measured by the immersed thermocouple at depth of 40 mm below point of pyrometer (i.e., hottest location on surface); Tb, °C is temperature near the cold crucible bottom; Td, °C is temperature above the drain opening; T_{melt}, °C is melt surface temperature measured by a pyrometer; P_2t, kW is power released into the melt; η_{ins}, % is efficiency of the installation, which is the product of η_{tube} and η_e ; η_{tube}, % is efficiency of the generating lamp; η_e, % is electrical efficiency of the inductor.

New correlations were also derived from the operational data recorded during the test. Figures 11-11 and 11-12 show the dependence of total active power on the inductor and specific power in the

melt, respectively, on the melt temperature (maximum internal). These curves both demonstrate hysteresis depending on whether the melt is in a cooling or heating process. However, the total active power parameter appears to be a much better indicator of the melt condition for either process.
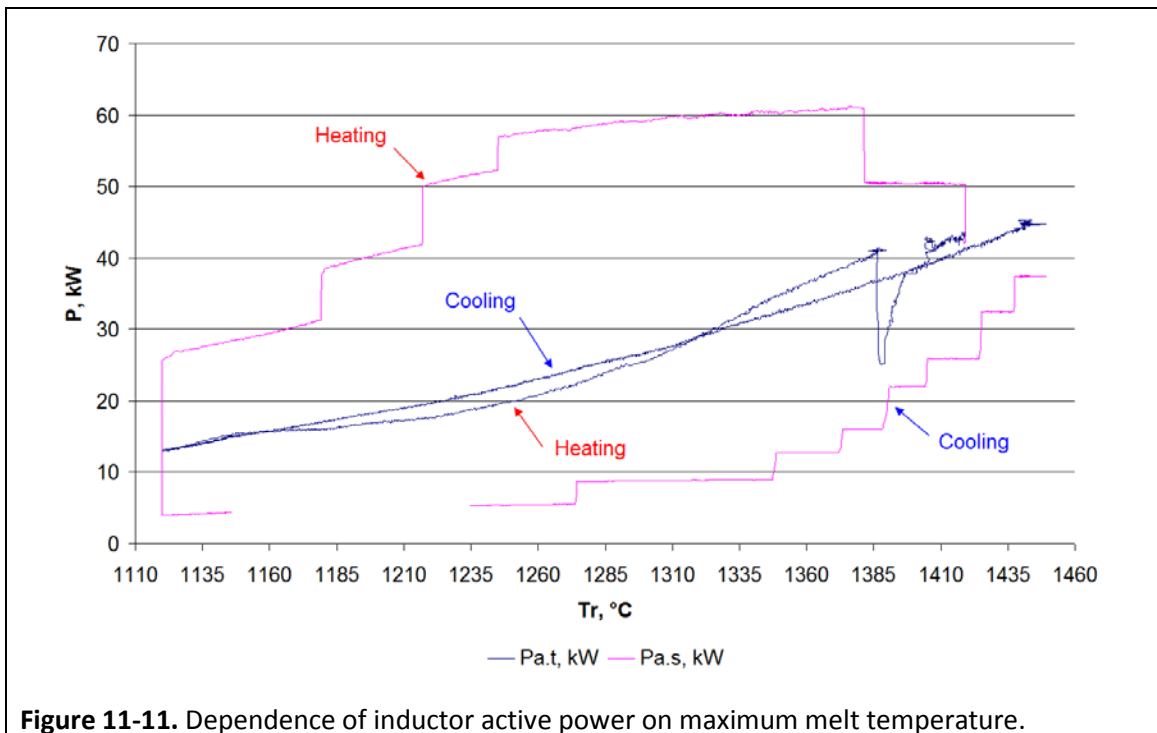
Figure 11-11. Dependence of inductor active power on maximum melt temperature.
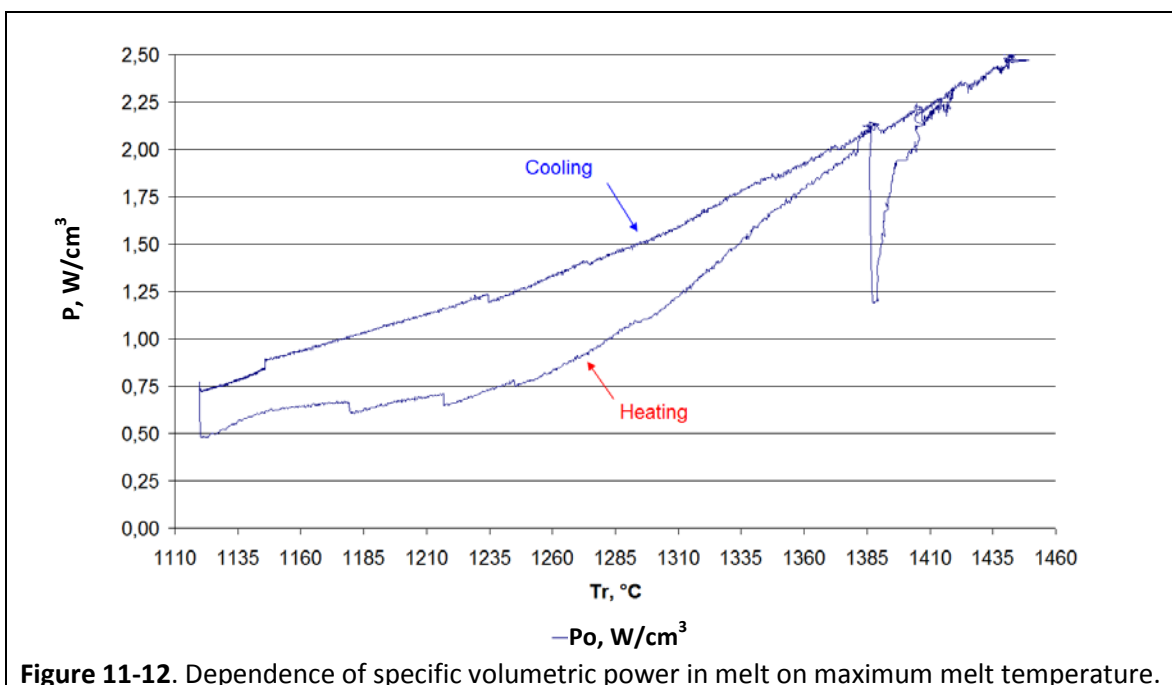
Figure 11-12. Dependence of specific volumetric power in melt on maximum melt temperature.

The stages and conditions for System Optimization Test #1a are provided in Table 11-2. As can be seen, this was a very comprehensive test with many stages and conditions that were evaluated, including determination of the glass emissivity value. This was discussed earlier.

Table 11-2. Stages and conditions of System Optimization Test #1a.

Time, hr:min	Ia, A	Ua, кV	Ig, A	Ucb, кV	F, MHz	Note
12:10	5	6.15	1.08	4.7	1.71	Starting heating on a graphite ring.
12:15	7.3	9	1.66	7.03	1.71	Generator mode increased.
13:06	7.7	7.47	1.25	5.39	1.71	Generator mode increased. Charge (frit and glass pieces) added.
13:10	7.9	5.7	0.7	3.64	1.74	Calibration of inductor sensors. Adjustment of generator circuits.
13:15	7.7	5.68	1	3.6	1.71	The graphite ring removed.
13:20	4.13	7.54	1.68	4.12	1.75	Inductor ground point switched.
13:24	5.5	8.56	1.75	4.5	1.76	Generator mode increased.
13:44	-	-	-	-	-	Phase shift calibration.
14:00	-	-	-	-	-	Crucible cover installed for a short time then removed.
14:57	5.5	6.3	0.88	2.5	-	Cover is re-installed.
15:05	4.5	6.29	0.7	1.1	-	The crucible is lifted.
15:06	4.6	6.28	0.7	1.9	-	The cover is removed.
15:16	4.7	6.64	0.79	2.02	1.83	Calibration of inductor sensors during generator idling. Generator mode increased back.
15:20	4.6	6.64	0.78	1.98	-	The cover is installed. Change of 2 kW in Pcc1 seen. Possible reflection from cover.
15:43	-	-	-	-	-	First stationary mode. Thermocouple immersed in melt pool 40 mm deep. Height from cover to melt pool surface is 303 mm. Tr=1,352^{o}C.
15:46	-	-	-	-	-	The thermocouple is removed.
16:03	-	-	-	-	-	Td=277°C.
16:10	-	-	-	-	-	a_2=100 mm, Tb=355°C.
16:29	4.6	6.6	0.8	2.05	-	The cover is removed.
16:41	-	-	-	-	-	Scanning of a melt surface before frit charging.
16:56	-	-	-	-	-	Infrared imaging of melt pool surface.
17:02	-	-	-	-	-	Melt pool surface covered with frit.
17:06	4.6	6.63	0.8	2	-	The cover is set.
17:25	-	-	-	-	-	The cover is removed.
17:27	-	-	-	-	-	Scanning of a melt surface after frit is melted.

Table 11-2. Stages and conditions of System Optimization Test #1a.

Time, hr:min	Ia, A	Ua, кV	Ig, A	Ucb, кV	F, MHz	Note
17:30	-	-	-	-	-	The cover is set., a_2=115 mm.
17:58	-	-	-	-	-	Calibration of inductor sensors.
18:01	-	-	-	-	-	Second stationary mode.
18:02	-	-	-	-	-	Tr=1,407 ºC.
18:07	-	-	-	-	-	Td=288 ºC. Tb=385 ºC.
18:10	5.76	7.6	0.83	2.16	-	The cover is removed.
18:15	-	-	-	-	-	Scanning of melt surface before.
18:20	-	-	-	-	-	Surface covered with frit
18:24	-	-	-	-	-	The cover is set.
18:38	5.9	7.6	0.7	2.1	-	The cover is removed.
18:40	-	-	-	-	-	Scanning of a melt surface after frit is melted.
18:49	5.65	7.6	0.8	2.25	-	The cover is set.
18:52	-	-	-	-	-	Temperature of a crucible bottom lower surface is 100^oC, Td=410^oC, Tb=460^oC.
19:00	6.8	9.3	1	2.6	-	Third stationary mode.
19:43	-	-	-	-	-	Tr=$1,525^oC$.
19:59	7.2	9.3	0.85	2.39	-	The cover is removed.
20:01	-	-	-	-	-	Scanning of a melt surface.
20:06	-	-	-	-	-	Surface is covered with frit.
20:10	7.14	9.3	0.85	2.39	-	The cover is set.
20:17	-	-	-	-	-	Td=582^oC.
20:20	-	-	-	-	-	The cover is removed.
20:21	-	-	-	-	-	Scanning of a melt surface after frit is melted.
20:23	7.12	9.3	0.8	2.42	-	Study of temperature dependencies for melting parameters. Cover is set. Measurement of temperature in the melt pool by the thermocouple during step reductions of the generator operation mode.
20:48	-	-	-	-	-	Emergency switching-off of the generator supply.
20:54	2.1	3.4	0.47	0.98	-	Generator operation is restored.
21:01	4.55	8.33	1.25	2.9	-	Measurement of temperature in the melt pool by the thermocouple at step increases of the generator operation mode.
21:18	-	-	-	-	-	The thermocouple is removed from melt.
21:19	-	-	-	-	-	Td=582^oC.

Table 11-2. Stages and conditions of System Optimization Test #1a.

Time, hr:min	Ia, A	Ua, кV	Ig, A	Ucb, кV	F, MHz	Note
21:22	-	-	-	-	-	Glass melt casting. The 27 MHz generator is powered on.
21:28	-	-	-	-	-	The inductor voltage sensor is switched-off.
21-46	-	-	-	-	-	Casting initiated. The maximum power in the drain at time of casting is 2.85 kW. Generators are switched-off. Total operating time of the 27 MHz generator is 19 min 50 sec.
21-52	-	-	-	-	-	Casting complete. Casting time is 330 sec. 35.23 kg of glass is cast. Casting velocity is 106 g/sec, or 6.4 kg/min., or 381.6 kg/h.

(I_a is 1.76 MHz generator lamp anode current, A; I_g is 1.76 MHz generator lamp grid current, A; U_{cb} is voltage on capacitor bank, kV; U_a is 1.76 MHz generator lamp anode voltage, kV; a_2 is melt pool height, measured by a immersed rod, mm; T_r is the melt internal temperature, measured by the immersed thermocouple, ^oC; Td is the glass temperature at height of 10 mm above the drain opening, ^oC; Tb is the glass temperature at height of 20 mm above crucible bottom between drain edge and wall, ^oC.

Key Conclusions and Recommendations: System Optimization Test #1a provided the following conclusions and recommendations:

- Additional data for thermal and electrical losses in various components of the system at several steady state modes was obtained. New monitoring and measurement in the platform and data acquisition provided additional information that allowed calculation of inductor, generator tube, and overall system efficiencies.

- The tenth version of the drain device has excellent electromagnetic transparency and was able to readily initiate melt casting without the use of any external means.

- During casting, the melt deviated due to the shape of the drain body and contacted the inductor and busses. Modifications are needed to further optimize the drain configuration and mitigate this issue.

- Melt initiation was faster in the new crucible with the modifications to the generator but still required over an hour. The potential for using other starting materials and configurations will be investigated to improve this process. Additionally, the crucible will be further optimized to improve its overall efficiency, for all process stages, including melt initiation, steady state, and casting.

- Good correlations were developed between the active power on the inductor, as determined from calorimetry, and the maximum temperature in the melt pool volume. The

correlation was demonstrated to be relatively representative for both heating and cooling processes, although some hysteresis was observed.

11.1.2. System Optimization Test #1b

System Optimization Test #1b used the same equipment and components as used in Test #1a except for the new drain inductor design, as previously described. Figure 11-13 shows a comparison between the inductor used in Test #1a and the new design used in this test.
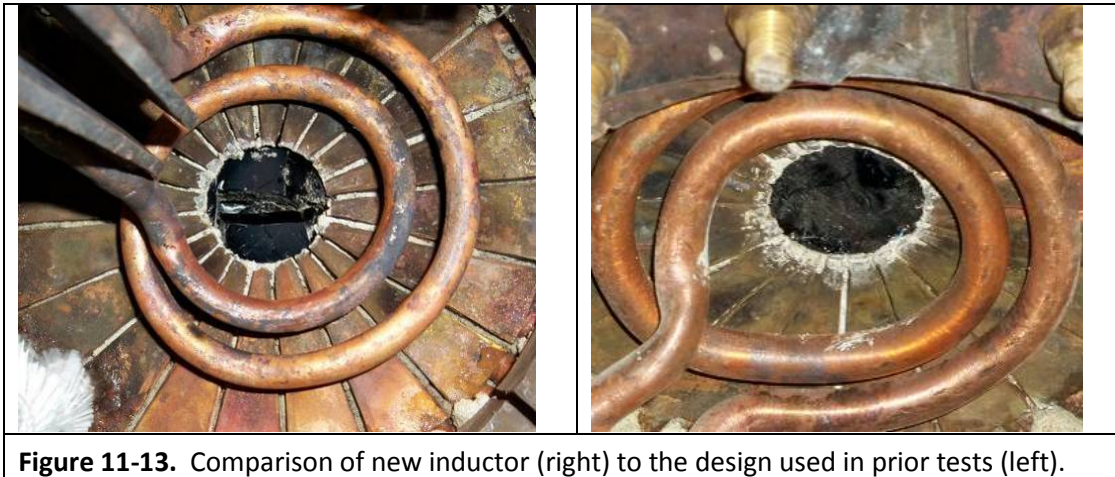
Figure 11-13. Comparison of new inductor (right) to the design used in prior tests (left).

One other key difference for System Optimization Test #1b was the material and configuration used for the melt initiation process. In all prior test, a graphite ring with a nominal 40 mm by 40 mm cross-section, and an outside diameter nominally about 75% of the inside diameter of the crucible. However, a mild steel wire was shaped into the form shown in Figure 11-14. The concept for this approach was based on the plasma arc formations in high voltage and frequency conditions that are near the conditions produced by the 1.76 MHz generator (i.e., inductor voltages are in

Figure 11-14. Steel initiator wire used for System Optimization Test #1b.

the 7 kV to 9 kV range during the melt initiation process). At these conditions, when the metal is melted at a point creating a small gap the high voltage will produce an arc that will provide extremely high localized temperatures adequate to produce plasma-like conductive paths. This can

occur at multiple locations along the length of the wire. The shape provides additional length, as well as contact with a larger volume of the glass. The results are discussed in the following section.

Melt Initiation Process: During this test a new melt initiation process was evaluated using the initiator wire, as described above. This approached reduced the melt initiation time by more than two thirds from the previous test, requiring only 20 minutes to establish the initial melt pool, as compared to 65 minutes. Figure 11-15 shows key generator electrical parameters during the melt initiation process. For the figure, and following ones as well, the locations identified represent the following conditions: 1) 1.76 MHz generator is powered on, 2) melt initiation completed, 3) inductor midpoint ground switched to end point, and 4) a steady state mode established.

After the generator is powered on, the anode current is observed to grow and the inductor current decreases, which are indicators of the melt pool growth and increased coupling of the electromagnetic field with the melt. At point 3 the inductor ground point is switched from the midpoint, and the electrical parameters sharply change absolute values. However, as the generator continues to operate the positive trends are continued, with the voltage on the capacitor bank and the grid current gradually reducing, which are also indicators of melt pool growth.
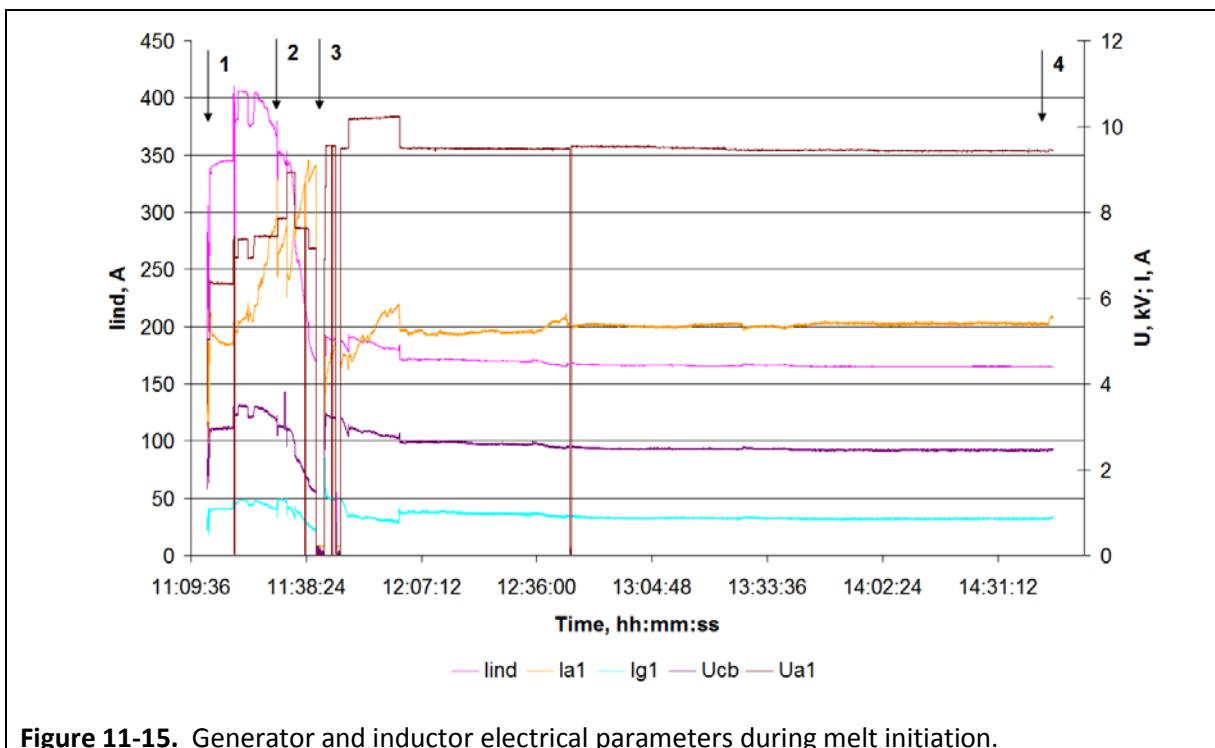
Figure 11-15. Generator and inductor electrical parameters during melt initiation.

(Iind is primary inductor current; Ia1 is generator lamp anode current; Ig1 is generator lamp grid current; Ucb1 is voltage on the capacitor bank; Ua1 is voltage on the generator lamp anode)

Figures 11-16 and 11-17 provide the power parameters of various system components. Similar trends as those seen with the electrical parameters are observed.
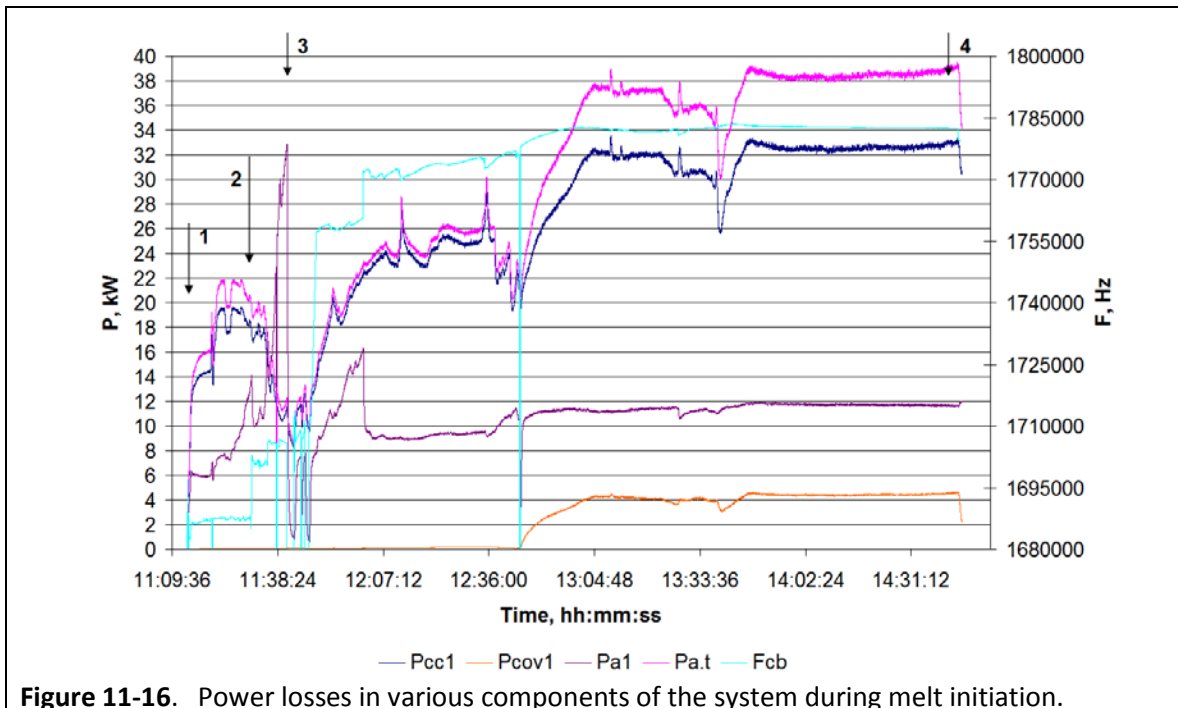
Figure 11-16. Power losses in various components of the system during melt initiation.
(Pcc1 is electrical and heat losses in side sections of the cold crucible; Pcov1 is power losses in the cold crucible cover; Pa1 is power losses on the generator lamp anode, Pa.t is active power to the inductor determined by calorimetry; Fcb is frequency of the capacitor bank current)
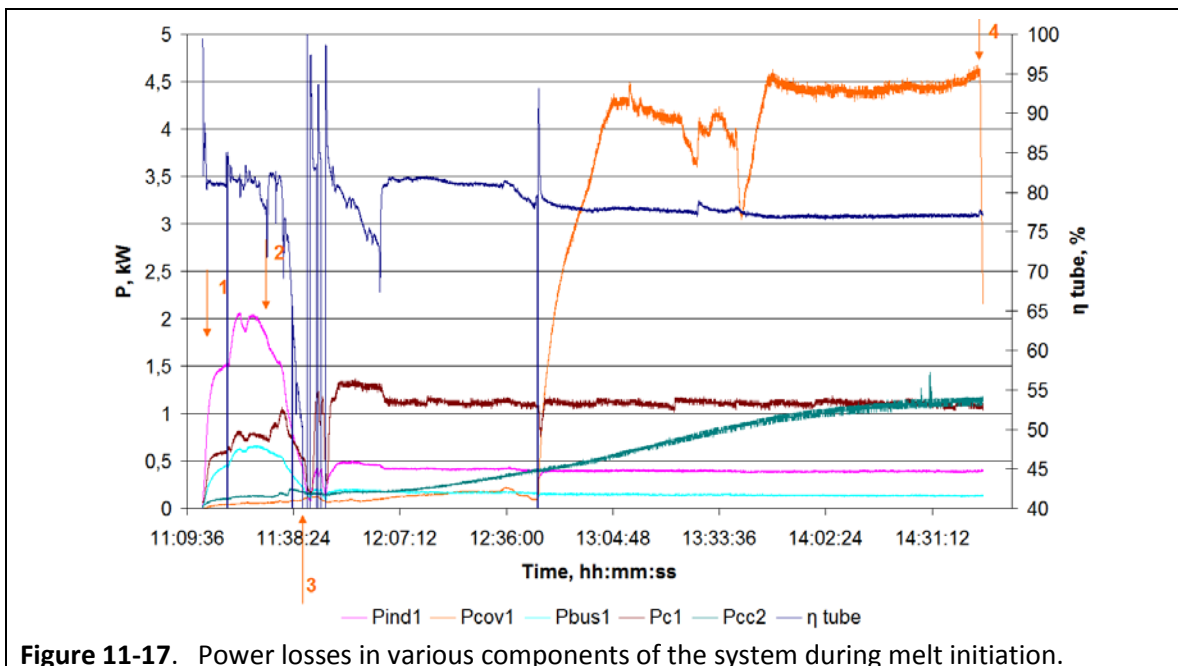
Figure 11-17. Power losses in various components of the system during melt initiation.
(Pind1 is electrical losses in the primary inductor, Pbus1 is losses in capacitor bank buses, Pcc2 is electrical and heat losses in the drain; η tube is generator lamp electrical efficiency)

Melt Casting Process: A primary focus for System Optimization Test #1b was the melt casting process, and specifically the Option 2 Pressure Assist Casting Control system. The melt pool was taken to a steady state mode of 1,480°C (maximum internal temperature from immersed thermocouple). At that time, the 27 MHz generator was powered on to induce the first casting. After 26 minutes of operation, the first casting was initiated electromagnetically. A second casting process was begun about two hours after the first casting. With only 20 minutes of operation of the 27 MHz generator, a second casting was initiated. However, after the second casting, the melt pool depth was only 55 mm. A third casting was unsuccessfully attempted. As much as 3 kW of power were deposited into the drain, which was more than any other casting process; however, it was not sufficient to initiate the casting.

It appears that the glass melt heated up by the 27 MHz inductor moved into the top part of the melt pool along the periphery of the drain, due to the buoyancy effects. This effectively resulted in heat and mass-transfer away from the drain. As a result, the frozen glass plug in the drain opening was only heated up to the softening temperature of about 600°C to 650°C, but no higher. During this attempt, the soft glass began bulging from the drain opening, but it was never able to actually pour out (see Figure 11-18).

During the second casting, the pour stream was deviated and, as in previous tests, contacted the drain inductor. This is shown in Figure 11-19. This effect will be mitigated with further drain optimizations.

Figure 11-18. View of softened bulging from drain opening after third casting attempt.

Figure 11-19. Pour stream during second casting contacting inductor.

Figures 11-20 and 11-21 provide power loss data for various components of the system. In each of the figures, points 1, 3, and 5 indicate times that the 27 MHz generator was powered on, and points 2 and 4 indicate times when casting was initiated and it was powered off.

Figure 11-20. Power losses in various components of the system during casting process.
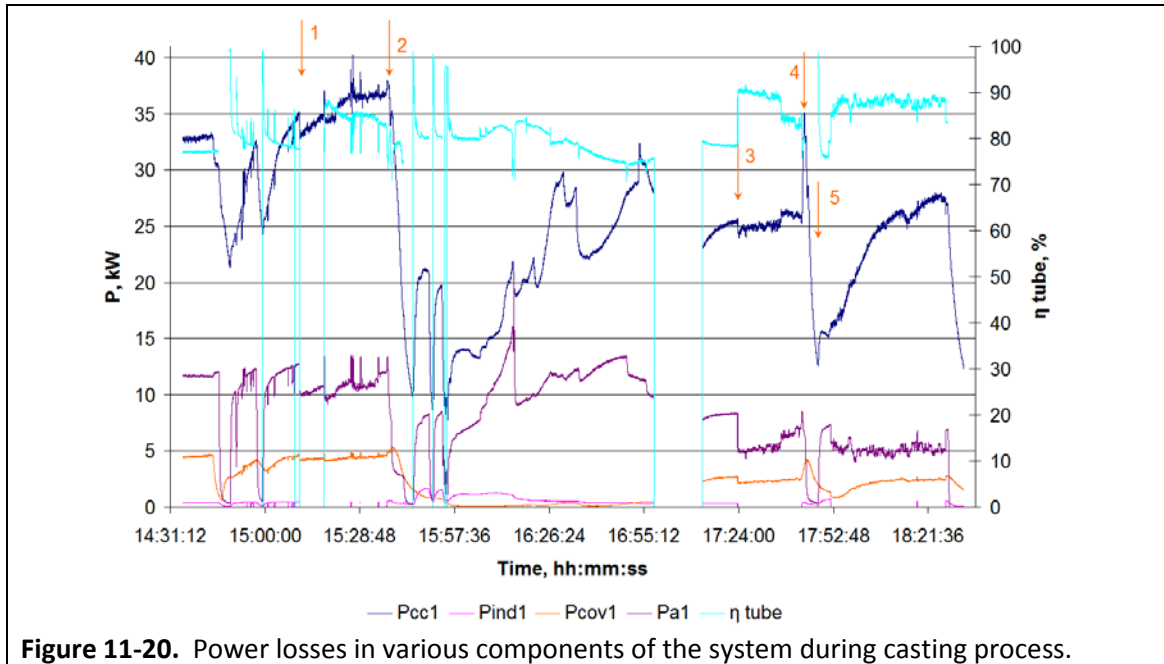
(Pcc1 is electrical and heat losses in crucible, Pind1 is electrical losses in the primary inductor, Pcov1 is heat losses in crucible cover, Pa1 is power losses on the generator lamp anode; η tube is generator lamp electrical efficiency)

Figure 11-21. Power losses in various components of the system during casting process.
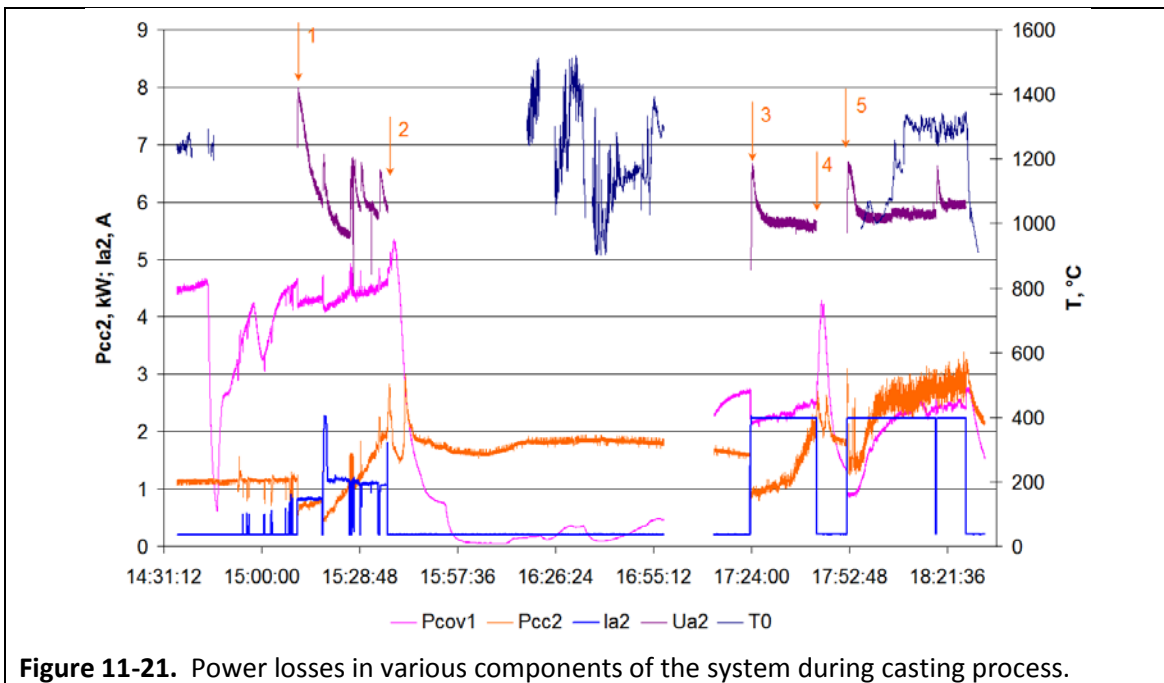
(Pcov1 is heat losses in crucible cover, Pcc2 is electrical and heat losses in drain, Ia2 is27 MHz generator lamp anode current, Ua2 is 27 MHz generator lamp anode voltage, T0 is thermocouple located near bottom [Tb]))

During the two successful castings, the pressure assist casting control system was deployed. Recall that this system is defined as Option 2, which applies a vacuum to the head space within the crucible. The feasibility of the approach was demonstrated in earlier tests; however, the drain device used (eighth version) did not have sufficient electromagnetic transparency and the casting process had to be initiated manually.

Unfortunately, the opposite effect was realized during these castings. The tenth version of the drain is very thin (i.e., 8 mm) and it does not include any drain spout. The total length of the melt flow path through the drain is thus only 8 mm. As a result, although the pour flow could be slowed down, the cooling effects above and within the drain were not sufficient to allow the melt to become cool enough such that it could be stopped. The process experienced during System Optimization Test #1b is depicted in the following series of negative exposure photographs (Figure 11-22), which help visualize the pour stream more clearly.

As the vacuum is applied the pour stream reduces in diameter, slowing the glass flow rate. This progression is in stages a through d. At this point, a large bubble would form and be pulled up from the drain, temporarily stopping the casting process, as seen in stage e. Movement of the bubble through the melt pool results in a momentum reaction that pushes a mass of glass through the drain, as in stages f and g. Then the melt pour stream is reformed and the process repeats, as seen in stages h through l. Specifically, the applied vacuum reduces the pour stream diameter, as seen in stages h through j. Again, a large bubble forms and the casting temporarily stops, a seen in stage k. Subsequently, the momentum of the glass bubble effectively pushes a mass of glass through the drain and casting restarts, as shown in stage l.

The characteristics of the pour streams in these photographs provide valuable information, and can be used to help determine the optimum geometry for achieving the desired characteristics of the pour stream. An optimal drain device design will combine the characteristics of the eighth/ninth versions of the drain that produced good control with the pressure assist system with the electromagnetic transparency of the tenth version of the drain, that provides reliable electromagnetically casting.

Table 11-3 provides a summary of the test stages and conditions recorded during System Optimization Test #1b. Analysis of these results, combined with those of System Optimization Test #1a, provides the information needed to design and implement the final refinements to the drain

device and the crucible design. These changes are expected to accomplish the goal of producing a system that will provide a means to perform ultra-high temperature processing of refractory oxides, including the ability to cast the resulting product from the crucible.
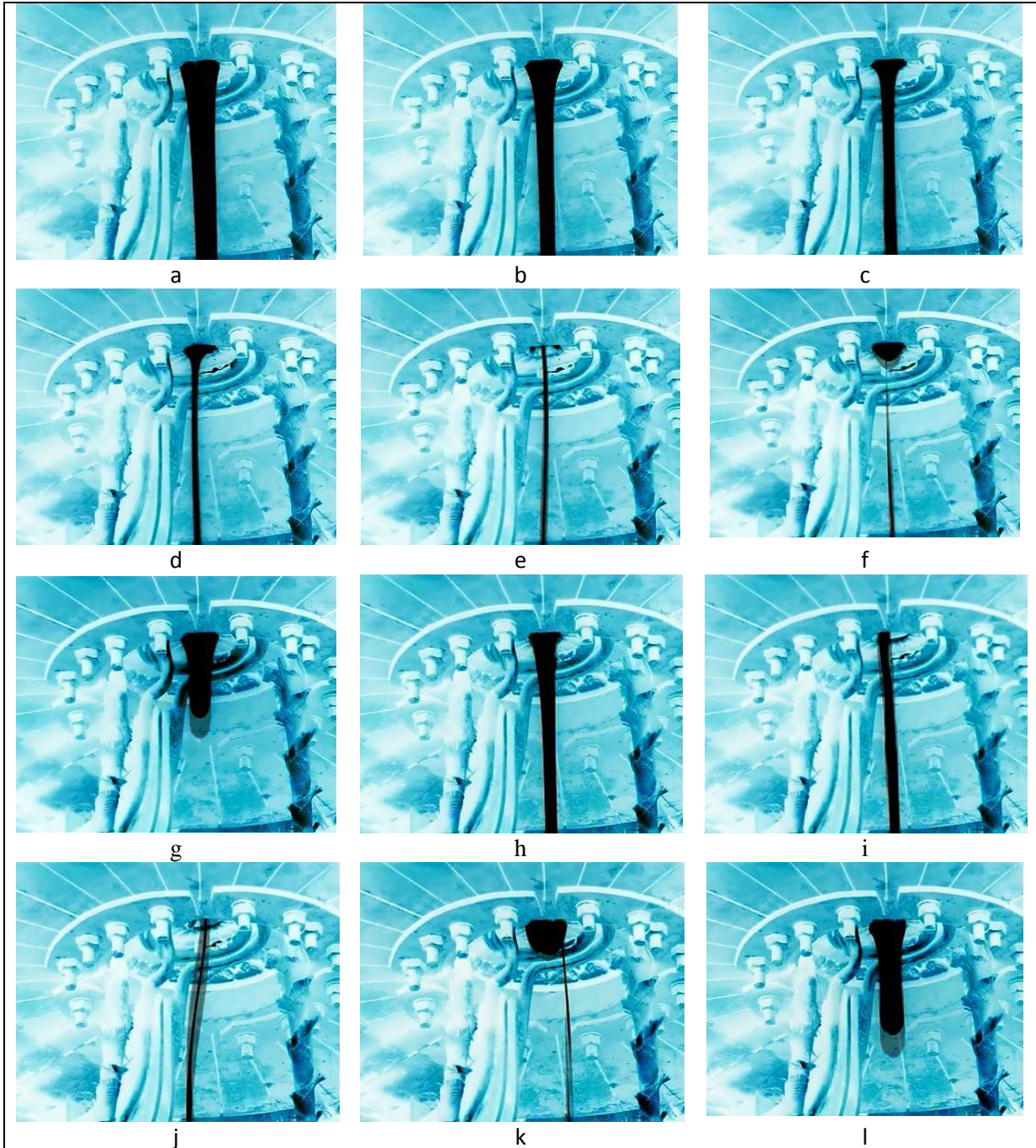
Figure 11-22. Characteristics of casting control system using vacuum with the tenth version of the drain device.

Table 11-3. Test stages and conditions for System Optimization Test #1b.

Time, hr:min	Ia, A	Ua, kV	Ig, A	Ucb, kV	F, MHz	Note
11:10	5.45	7.37	1.30	4.45	1.6864	Melt initiation using curved wire. Inductor at midpoint ground.
11:33	6.48	8.9	1.1	4.6	1.7002	Melt initiation successful; the wire oxidized and consumed/dissolved in melt.
11:42	4.67	9.5	1.3	2.8	1.7068	Inductor ground point switched to end.
11:47	4.53	9.49	1.17	3.08	1.7080	Cold crucible moving
13:17	5.37	9.49	0.86	2.45	1.7815	Immersion thermocouple at 40mm deep, T_{melt}=1,481°C, a_2=128 mm
14:20	5.40	9.42	0.86	2.44	1.7826	a_2=134 mm
14:23	5.40	9.42	0.86	2.44	1.7825	At height of 22 mm from crucible bottom T_b=495°C, T_d=16°C, thickness of skull is 35 mm
14:50	5.30	10.00	1.00	3.22	1.7819	Weight of receipt tank for melt with water is 38.8 kg
15:11	5.62	10.14	0.91	2.60	1.7831	The 27 MHz generator powered on for the first casting
15:26	-	-	-	-	1.7841	Power in the drain P_{cc2}=1.6 kW
15:35	-	-	-	-	1.7842	Power in the drain P_{cc2}=2.2 kW
15:37	-	-	-	-	1.7738	27 MHz generator is powered off. The first melt casting
15:40	2.36	5.9	0.77	1.82	1.7677	Unsuccessful pressure decline in the crucible due to insufficient seals and weak suction. Casting stopped mechanically.
15:44	-	-	-	-	-	The first casting is stopped. The 1.76 MHz generator is powered-on. Weight of receipt container after casting is 69.7 kg
15:50	5.17	10.50	1.9	3.95	1.7279	Crucible cover is removed
15:54	3.55	9	1.9	3.78	1.7269	The 1.76 MHz generator is powered-on. Charge is added. New melt pool forming.
16:53	5.10	8.92	0.75	2.33	1.7741	a_2=118 mm
17:23	4.50	8.56	0.77	2.34	1.7724	27 MHz generator powered on for the second casting.
17:43	-	-	-	-	1.7684	27 MHz generator powered-off. Second melt casting. The maximum power in the drain during casting P_{cc2}=2.58 kW
17:49	-	-	-	-	-	The second casting is stopped mechanically.
17:52	-	-	-	-	1.7628	27 MHz generator powered on for the third casting. 1.76 MHz generator is powered-on. Height of the pool above the drain is 55 mm.
18:27	-	-	-	-	1.7747	27 MHz generator powered-off. No casting initiated. The maximum power in the drain is P_{cc2}= 3 kW.
18:28	4.58	9.08	1.12	2.95	1.7747	Test ended. Generators powered off.

(I_a is generating lamp anode current, A; I_g is generating lamp grid current, A; U_{cb} is voltage on capacitor bank, kV; U_a is generating lamp anode voltage, kV; a_2 is melt pool height measured by a immersed rod, mm; T_{melt} is maximum internal melt temperature measured by the thermocouple, °C; T_b is glass temperature above cold crucible bottom, °C; T_d is glass temperature above the drain, °C)

Key Recommendations and Conclusions: The System Optimization Test #1 series provided the following conclusions and recommendations:

- The 407 mm diameter copper crucible performs reliably, although significant losses are still experienced in the interface area between the drain device and the bottom plate. This is where the bottom plate is electrically conductive (i.e., slits are from this point out to the periphery) and it is providing a path between the bottom and drain device. This is especially true when the 27 MHz generator is operating at very high levels for extended periods of time.
- An optimized bottom design will be finalized based on these performance characteristics and will be integrated with the drain device design.
- The tenth version of the drain provides excellent electromagnetic transparency, but does not allow any cooling of the pour stream during casting to allow reliable control and full stoppage using the pressure assist system (vacuum).
- An optimized drain design will be finalized based on these performance characteristics, as well as those of the previous versions. It will be integrated with the optimized inductor design.
- The drain device will include a defined exit aperture, similar to the eight/ninth versions, but incorporate the features of the tenth version that provide electromagnetic transparency, including 20 sections, translation of the conductive section farther away from the inductor and the drain opening, and a thinner main body section.

11.2.   System Optimization Test #2 – Final Optimized Design

The final test conducted as part of this research effort included the final optimized designs for the drain device and crucible (i.e., the bottom). The 27 MHz generator inductor and buss configuration used for this final system, which were determined by ETU-LETI, were also optimized for integration into and operation with the crucible and drain designs. The details of the final designs for the drain and crucible are described below, as well as the results of the System Optimization Test #2.

11.2.1. Drain Device Optimization

Based on the cumulative testing and modelling results, a final, optimized drain design was defined, in the context of the specific CCIM platforms and BSG composition used in this research. As

discussed throughout this dissertation, up to this point ten versions of the drain device had been tested. The design considered to be optimal, referred to as the *eleventh version*, is described in detail below. However, prior to that discussion, a summary of the evolution of the drain design is provided as a reminder.

Although there are eleven versions of the drain design, actually only four design basis variants exist. These are summarized in the following discussions

First Drain Design Basis

The initial drain design was based on a literal miniature version of a CCIM. It was constructed of copper tubes assembled into a cylinder. Two versions were tested, and the final configuration is shown in Figure 11-23. The earlier version did not include the water-cooled upper flange. This was added due to over-heating of the ceramic base that was observed. These versions were not implemented in CCIMs with water-cooled bases. Configurations with single and two-turn inductors were tested to develop performance data on the 27 MHz generator.

Figure 11-23. First Drain Design Basis.
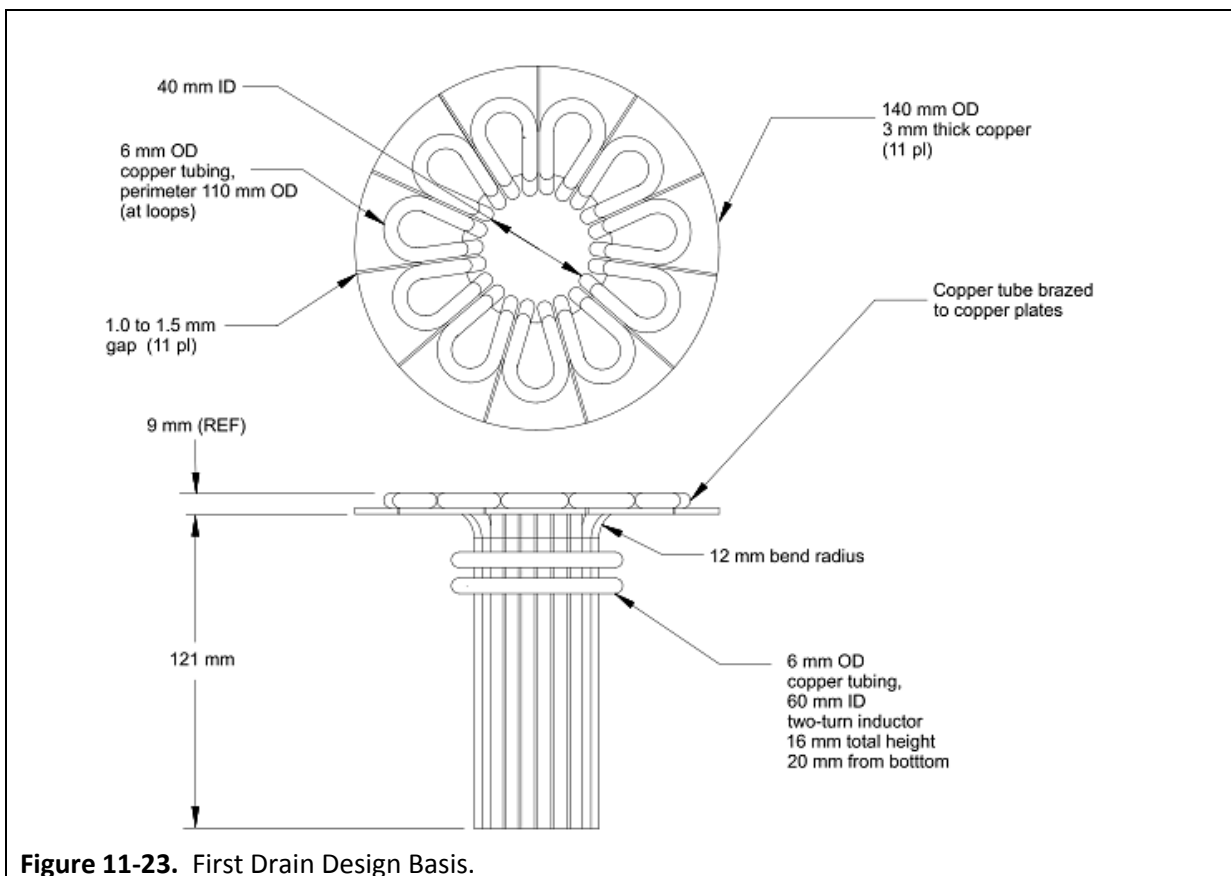
Second Drain Design Basis

The second drain design basis variant still employed copper tubes as the primary structure, but it was a markedly different approach than the first design basis. This design was approximately one quarter the height of the previous variant, because both experimental and modelling results demonstrated that a long cylinder design would not allow casting to proceed. The cooling tubes were bent to provide a basic drain shape, transitioning from a straight right circular cylinder geometry to a tapered aperture configuration. The final variant of the second drain design basis is shown in Figure 11-24.

This second drain design variant was used to investigate the ability to maintain a pool of molten glass after casting was completed, such that the CCIM could continue operation without requiring a complete restart process (i.e. replacing the initiator ring). Various heights of the drain assembly were evaluated, as well as different inductor geometries (i.e., one turn and two turn), including the ability to translate the inductor coil during different phases of the casting initiation process. For this variant, two versions were also fabricated and tested.

Figure 11-24. Second Drain Design Basis.
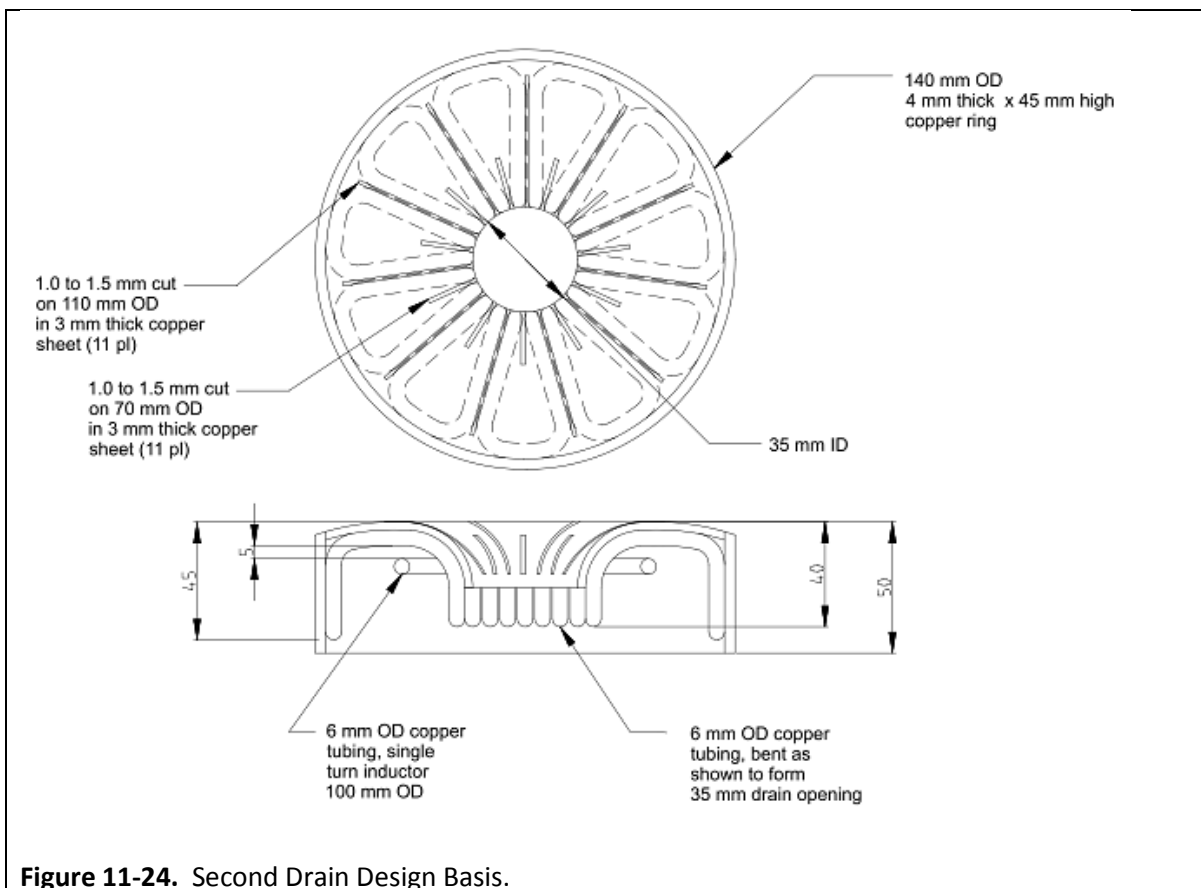
Once a more reliable drain design was developed, this capability was no longer necessary for processing the BSG composition used in the testing. However, testing of this concept continued during the stages of the evolution of the third variant of the drain device, and the experimental and modelling results provided operational and performance data for conditions in which this capability would be necessary.

Third Drain Design Basis

The two key differences between the second and third drain design basis variants were 1) the transition from copper tubes for the primary structure to an assembly that was fabricated from heavy copper sheet and plate components, and 2) dramatic reduction of the drain diameter. The prior testing had been conducted on drains with openings ranging between 35 mm and 40 mm. Once casting processes had been accomplished, the resulting data indicated that the glass flow rates were in excess of 700 kg/hr for the larger diameter drains. These rates are too high to achieve a controllable and reliable process for even the larger scale CCIM systems envisioned (e.g., a 1000 mm diameter CCIM would only contain around 500 kg when at the expected full processing depth). Modelling had indicated that casting was possible with smaller diameter drains, it would just require higher initial current loading on the 27 MHz generator.

The cooling water system of the third drain design basis was much simpler, and also maintained the drain at higher overall temperatures, which was also more conducive to electromagnetic bottom casting. In place of the complex arrangement of cooper tubes is a simple loop that is built directly into the design of the drain body. This approach was modelled for heat management and demonstrated to be acceptable. Subsequent testing in high temperature environments, including direct exposure to molten glass resulted in no damage to the drain device.

During the various phases of testing using this drain design basis variant, investigation of the ability to maintain a "bog" in the melt pool (i.e., a perimeter lip included on the drain base plate) was continued. In all, five versions of the drain device design used this basic platform. This design was approaching an optimal configuration, so the effects of minor changes were evaluated, including the number of slits, drain opening diameter changes (i.e., between 21.5 mm and 30 mm), and more variable inductor geometry. This configuration is very conducive to relatively easy modification, allowing investigation of these parameters. The final configuration of this variant is shown in Figure 11-25.

Figure 11-25. Third Drain Design Basis.
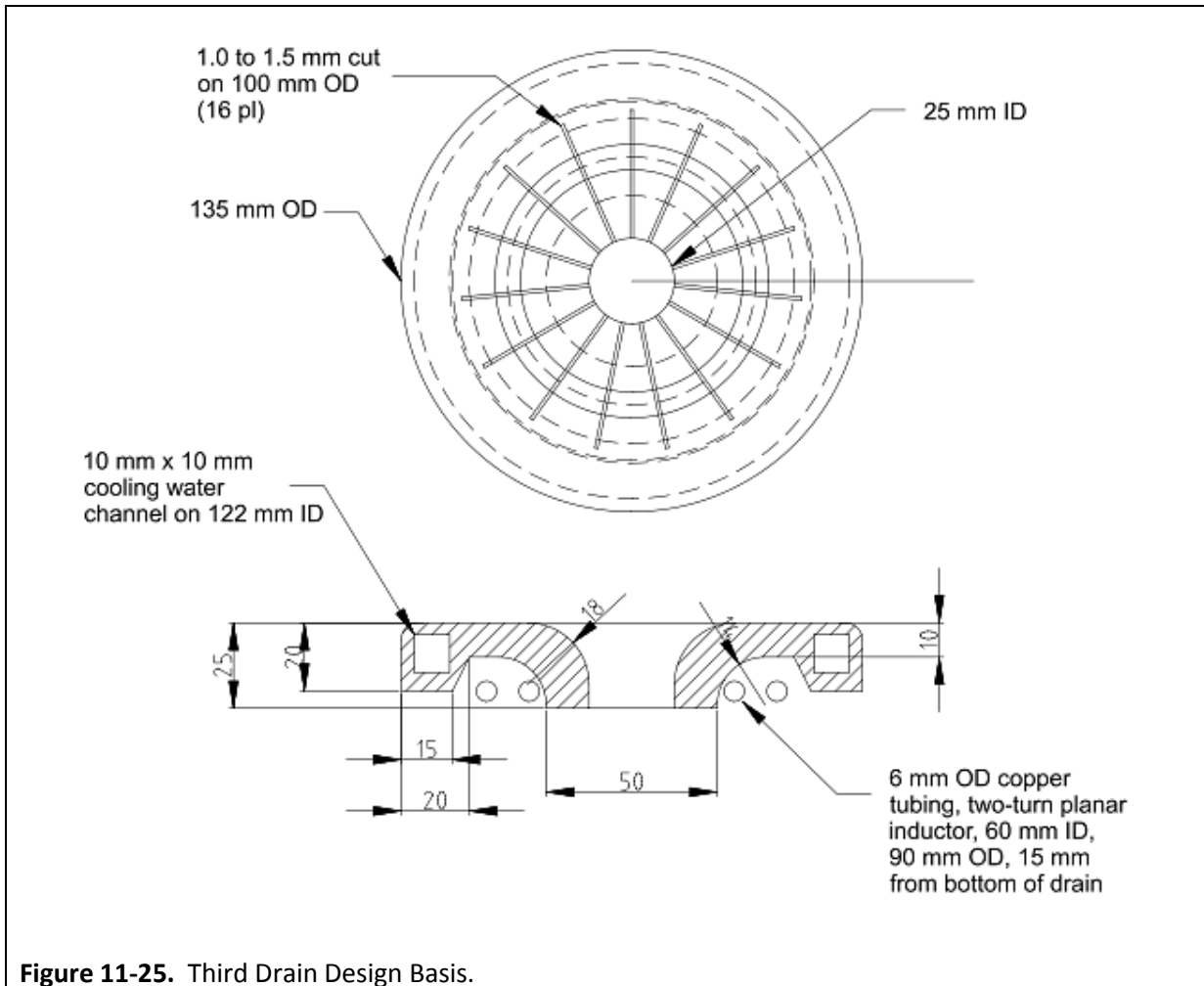
Fourth Drain Design Basis

The fourth, and final, drain design basis variant used the basic configuration developed during the previous variant, with one key change: the drain body was constructed of separate wedge shaped copper sections that significantly improved the overall electromagnetic transparency of the device. The design included 20 individual segments that are joined with external loops of copper tubing, which serve several key functions: 1) cool the drain device, 2) provide internal heating for the new design metal crucible bottom, 3) provide a stable mounting platform for the drain device, 4) eliminate the electrical path directly over the drain inductor coil, as in previous designs, by translating the electrical connection to the farthest perimeter of the drain. The final optimized configuration is shown in Figure 11-26. More details of how this design was established are discussed in the following section.
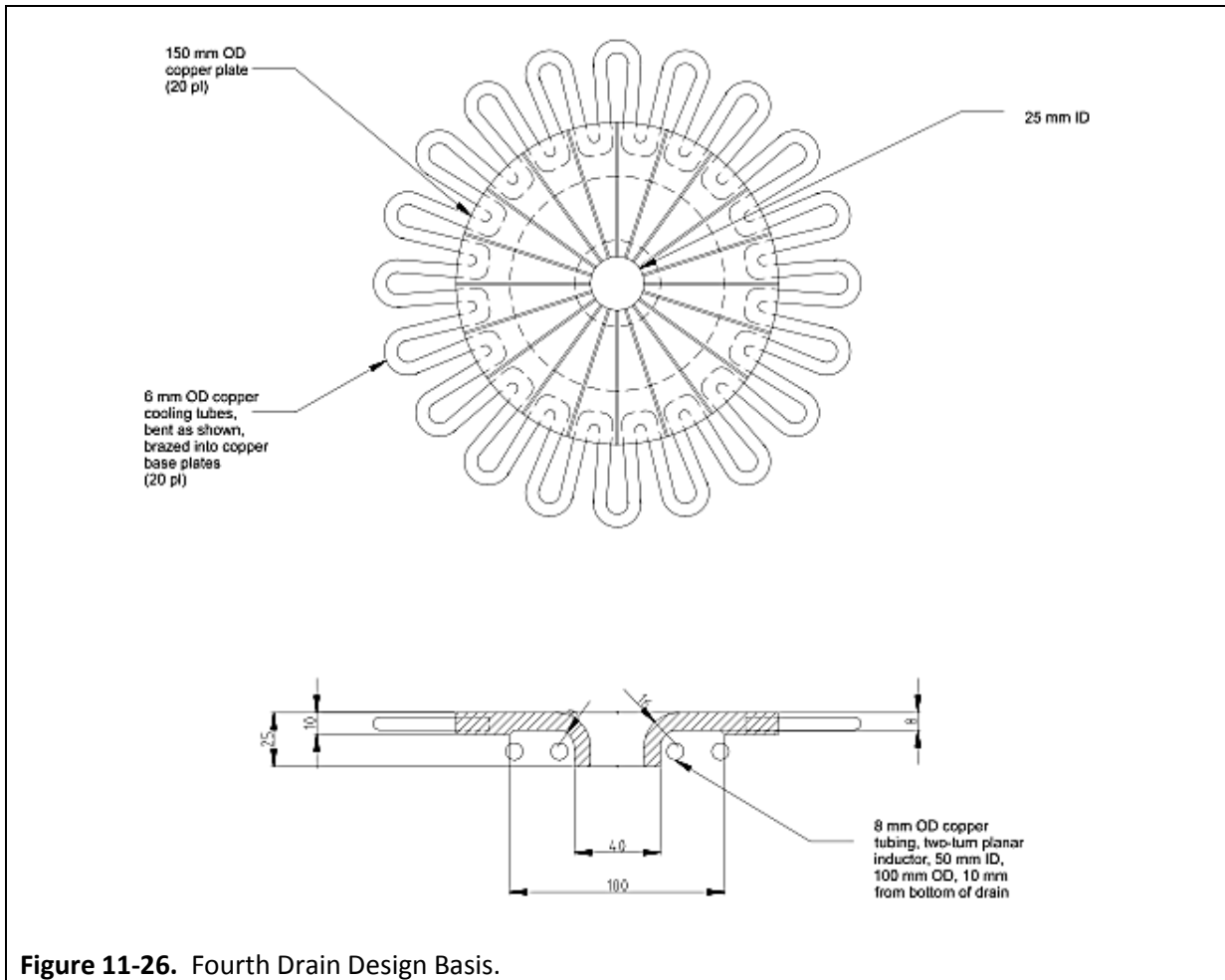
Figure 11-26. Fourth Drain Design Basis.

Details of Development of the Final Optimized Drain Configuration (Eleventh Version)

The prior test results demonstrated issues with operation and functionality of the tenth version of the drain device. Specifically, it demonstrated excellent electromagnetic transparency and castings were readily initiated using induction energy only. However, the total drain thickness was only 8 mm, which was too thin to provide any appreciable localized cooling during the casting process. As a result, the vacuum pressure assist system was not effective at stopping or controlling the casting process. Additionally, the exit temperature of the melt stream caused it to be less viscous and have less surface tension, which led to deviation of the pour stream and contact with the 27 MHz inductor and busses. While these were redesigned to help mitigate this issue, the primary factor contributing to this condition was the geometry of the drain aperture. Note that with the prior drain configurations (eighth and ninth versions) this was not an issue.

Thus, the following concept of the *eleventh version* of the drain device was determined based on experimental and modeling results:

1. The thickness of the upper drain plate should be 8 mm to 10 mm for structural; rigidity, while providing ability to cool sufficiently.

2. The quantity of drain sections should be between 16 and 20 to provide the necessary electromagnetic transparency.

3. The drain header (i.e., solid area that forms a conductive path around the drain body) should be at a minimum of 100 mm radius from the drain central axis.

4. The drain casting aperture should have a funneled portion with height of at least 20 mm.

Using these criteria, the eleventh version of the drain was designed and fabricated. Specific details are as follows: the outer diameter of the primary structure (i.e., not including the cooling tubes) is 150 mm, the minimum thickness on the drain plate is 8 mm, with a 25 mm wide, 10 mm thick shoulder at the perimeter for added structural rigidity and accommodating the cooling tubes. The drain aperture is 25 mm diameter. It is formed by a 25 mm thick section located on the central axis that has an outer diameter of 40 mm. The drain assembly includes 20 sections which are electrically isolated and sealed along the 19 slits using a high-temperature ceramic putty. U-shaped cooling tubes connect the adjacent sections at the perimeter of the 150 mm diameter plate. This provides both cooling and structural rigidity to the assembly. With these features, the eleventh version of the drain device combines the best features of the ninth and tenth versions, providing both good electromagnetic transparency, with the ability for pressure assisted casting control, and cleaner pouring characteristics.

Figure 11-27 shows the optimized, eleventh version of the drain device during installation into the crucible. Note the thermocouple installed for the final System Optimization Test #2. Figure 11-28 shows a comparison of the configurations for the eighth/ninth, tenth, and optimized eleventh versions. Drain design evolutions were driven by the experimental data. Once a design was agreed upon, ETU-LETI would arrange for its fabrication. The bottom right photograph in Figure 11-28 shows the drain device assembly placed on top of a non-conductive ceramic putty base. This provides electrical isolation between the bottom and drain during processing.
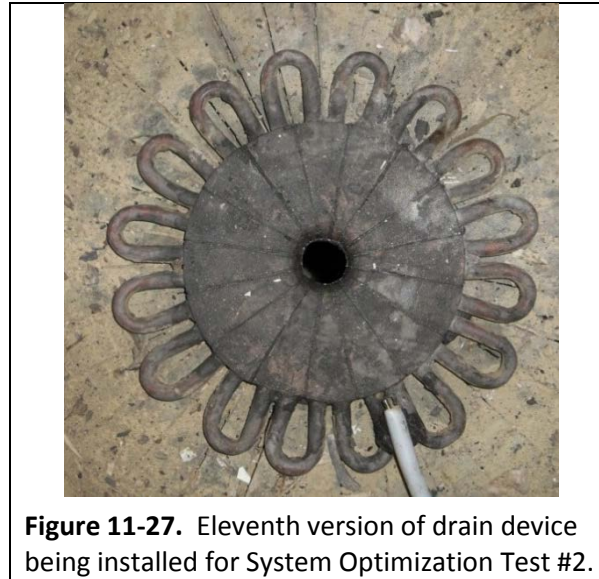
Figure 11-27. Eleventh version of drain device being installed for System Optimization Test #2.

| Ninth version bottom view | Tenth version bottom view | Eleventh version bottom view |
| Eighth version top view | Tenth version top view | Eleventh version top view |

Figure 11-28. Comparison of configurations for recent versions drain device.

(Note – The only difference between eighth and ninth versions is length of the slits.)
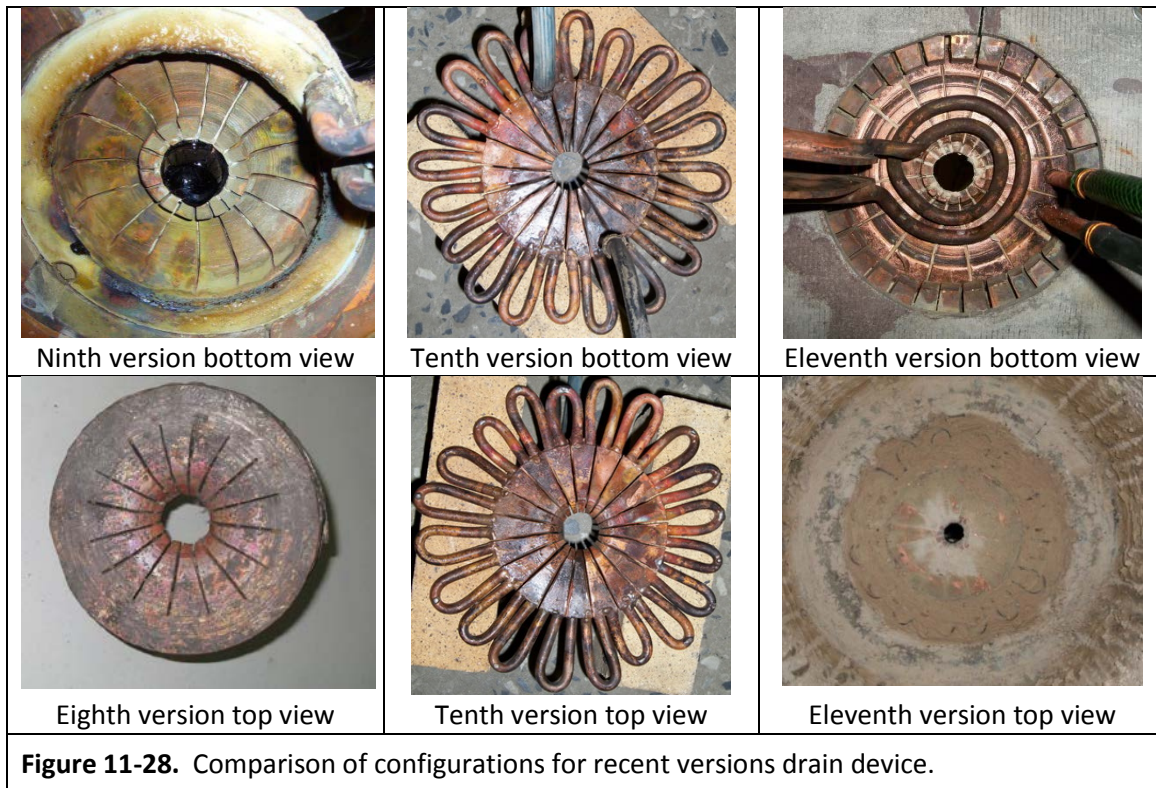
11.2.2. Crucible Bottom Optimization

Analysis of the results from prior tests using the new 407 mm diameter crucible indicated that significant eddy current losses occur in the bottom due to the structural ring located along its central axis. This provides a conductive path for the induction field, particularly that produced by

the 27 MHz generator during the casting process. In general, this promotes thicker bottom skull layers and makes bottom casting more challenging. Figure 11-29 shows the prior version of the crucible bottom with the area of electrical contact shown.

Figure 11-29. Conductive path near center on prior bottom design
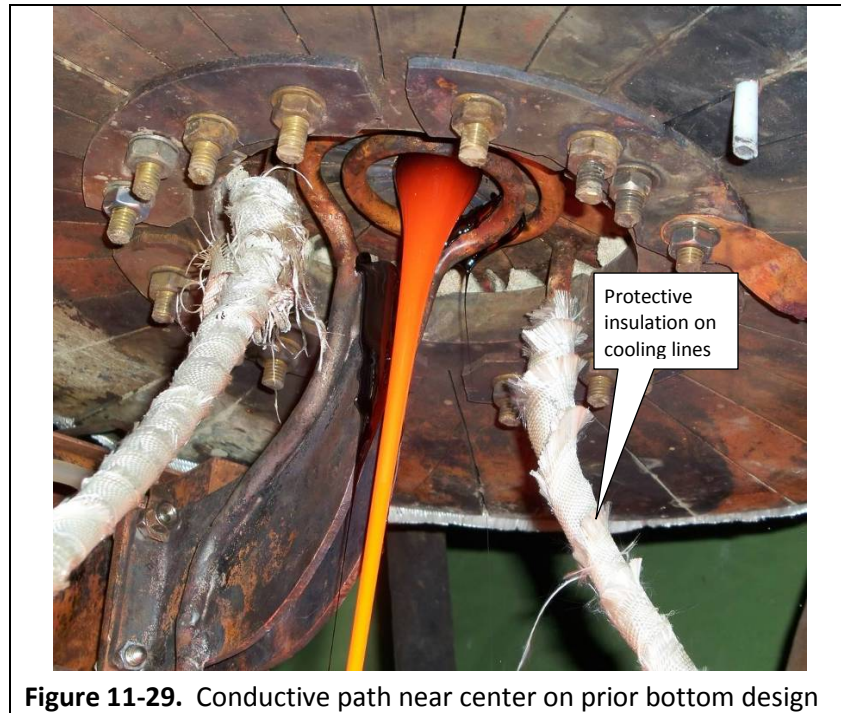
Additionally, in some instances in which very high power levels were required, the eddy currents led to high voltages on the bottom plate, resulting in arcing and shorting between adjacent corners of sections at the periphery.

A new bottom was designed to specifically mitigate these issues. The new bottom consists of 32 individual sectors that form a 407 mm inside diameter when the crucible side walls are installed, similar to the previous design. An insulating plate made of fiber-glass reinforced concrete is used to secure the components of the bottom plate. This material is non-conductive and acceptable for high temperature environments. This configuration completely eliminates the conductive path on the bottom near the drain device, and thus the power losses in the structure. This will improve the conditions of the melt in the lower zones near the bottom, supporting the casting process. The new bottom configuration is shown in Figure 11-30. Similar to the segmented drain device, during assembly, nonconductive putty is packed between the slits to provide electrical isolation, as well as sealing for the pressure assist casting control system.

Figure 11-30. Top and bottom views of the new bottom with 32 segments, during assembly.

Referring back to the two photographs on the far right side of Figure 11-22, these show the eleventh version of the drain device installed in the new crucible bottom in preparation for System Optimization Test #2.

11.2.3. System Optimization Test #2

The primary objective of System Optimization Test #2 was to demonstrate the operation of the eleventh version of the drain device for electromagnetic casting and pressure assist control. The designs of the drain and the bottom were optimized, as previously described, to ensure an optimized and reliable integrated system. Additionally, ETU-LETI implemented an improved design to the busses of the 27 MHz generator. The flat bar configuration was replaced with a coaxial design, which is much more electrically efficient, and will ensure that the maximum amount of power possible is available for the casting process. Other improvements were implemented in the circuit design of the 27 MHz to provide stable operation at power levels up to 10 kW.

With the exception of the redesigned components, System Optimization Test #2 used the same

equipment as the prior test. The 60 kW, 1.76 MHz generator was the primary generator. The inductor coil was a two-turn, 200 mm high configuration, with each coil being 85 mm high. A water-cooled cover lid with access port was installed to provide a leak tight environment. All of the gaps between drain segments, crucible bottom segments, and crucible side wall tubes were sealed with nonconductive putty. The outside was then wrapped with fiber glass cloth to help further seal the system. High temperature caulking was applied to leak-prone areas, such as the cover lid and its access port. The completed assembly for System Optimization Test #2 is shown in Figure 11-31.

Figure 11-32 shows the bottom of the assembly with the installed drain device, inductor, and new coaxial busses.

Figure 11-31. The complete assembled installation for System Optimization Test #2.

The optical pyrometer cannot be used to measure the surface melt temperature with the cover lid installed. For System Optimization Test #2, two thermocouples were installed. One Type K thermocouple was located 20 mm above the bottom surface coincident with the solid edge of the drain device. This configuration is shown in Figure 11-33. Also refer back to Figure 11-27.

Figure 11-32. Bottom test assembly used for System
Optimization Test #2.

130

20
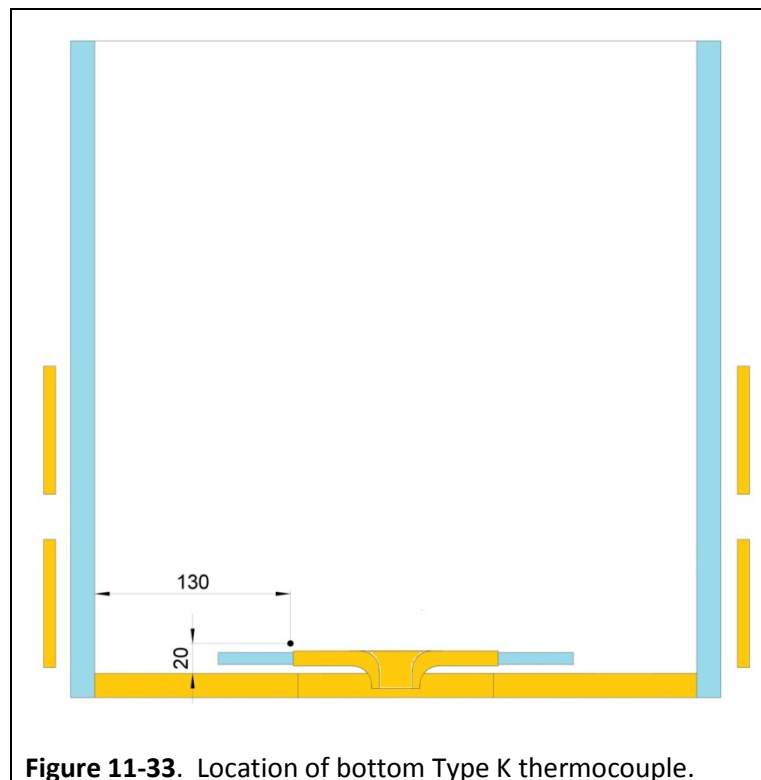
Figure 11-33. Location of bottom Type K thermocouple.

The second thermocouple, a Type C, was immersed in the melt pool just below the surface of the
melt, which provides a similar reading to the pyrometer when focused on a surface hot spot. The
thermocouple was fixed in one position to maintain a leak tight condition within the crucible
headspace. Accordingly, when the melt is cast, the reading is invalid until the melt pool is again built

up to the same level to the initial condition. However, with the cover lid installed, this was not possible for System Optimization Test #2.

Melt Initiation Process: For the improved crucible design, melt initiation was tested by beginning the test without switching the primary inductor ground location to the midpoint. Recall that this was done in the prior tests using the 407 mm diameter crucible to provide higher inductor voltage during melt initiation. After about one hour and ten minutes, the generator mode was reduced and the inductor ground was switched to the midpoint. Once this adjustment was made, the melt was initiated within about 33 minutes and the graphite initiator ring was removed. A steady state mode of approximately 1,300°C was obtained in preparation for the first casting. Key electrical and thermal parameters for the system during melt initiation up to the time of casting are shown in Figures 11-34 and 11-35, respectively.
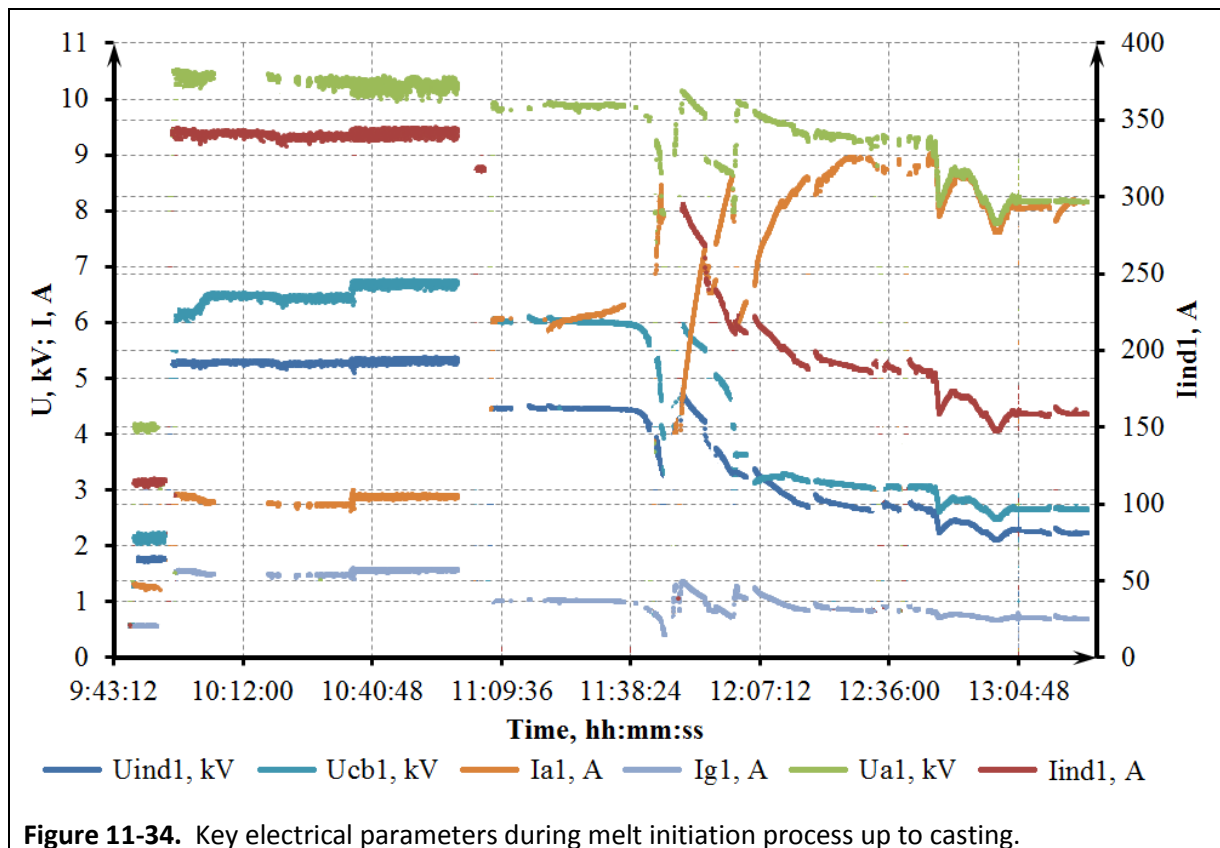
Figure 11-34. Key electrical parameters during melt initiation process up to casting.
(Uind1 is voltage on primary inductor, Ucb1 is voltage on the capacitor bank, Ia1 is generator lamp anode current, Ig1 is generator lamp grid current, Ua1 is voltage on the generator lamp anode, Iind1 is primary inductor current)

Figure 11-35. Thermal parameters during melt initiation process up to casting.
(T0 is immersion thermocouple °C, TC0 is bottom thermocouple °C, Pa.t.1 is total electrical and thermal losses on all water-cooled components [except drain inductor] kW)
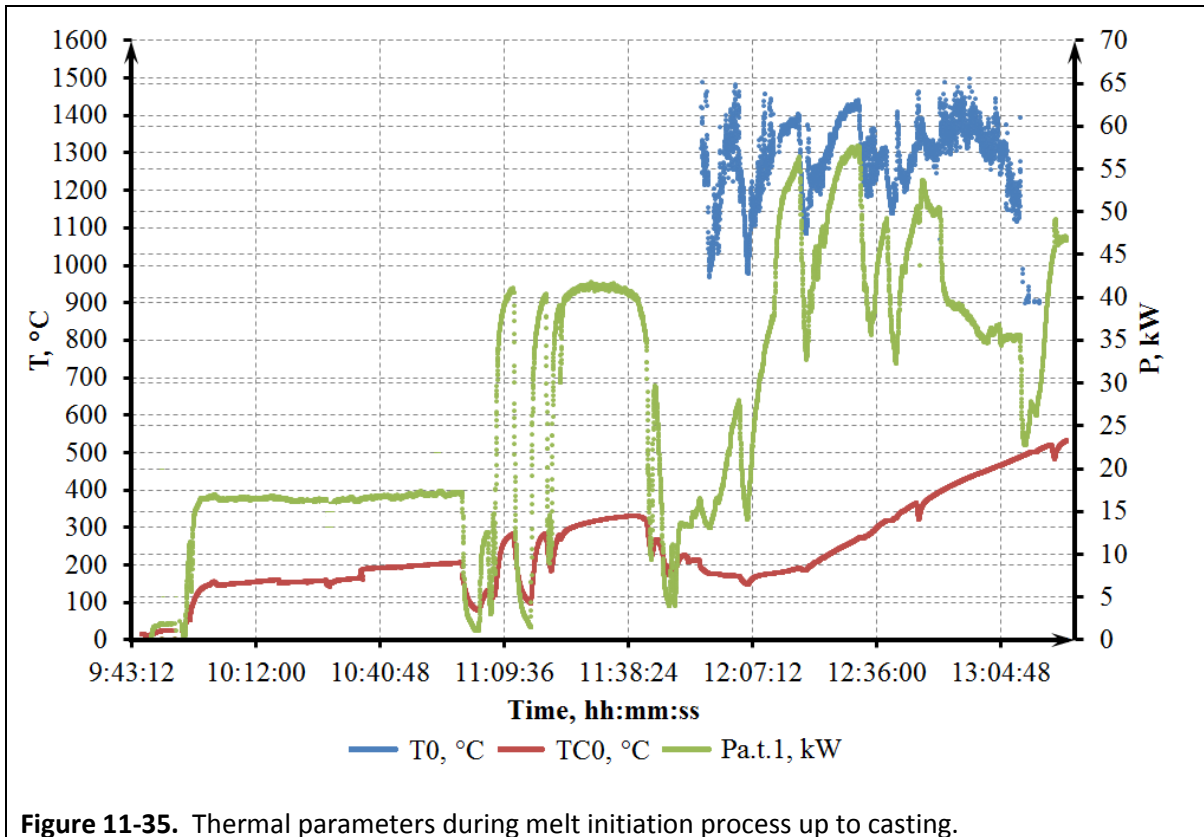
Melt Casting and Pressure Assist Control: During the System Optimization Test #2, both melt casting and pressure assist control were successfully demonstrated. Two castings occurred during the test. One was initiated manually with a metal probe and the other was initiated electromagnetically, with no external or mechanical assistance. Both castings were able to be completely stopped using solely the vacuum produced within the headspace of the cold crucible. Flow control was also demonstrated. The observed vacuum levels ranged from 3 kPa gage to 4 kPa gage for the first casting (i.e., greater hydrostatic pressure due to melt pool height) and approximately 2.4 kPa gage for the second casting.

During the first casting, several adjustments had to be made to the 27 MHz generator and this interfered with the melt pool growth process, allowing a thicker skull to form in the bottom. This is why the first casting had to be initiated manually. In all other tests, the second casting was always more prone to issues related to skull growth and/or glass plug melting. However, these problems did not recur and the second electromagnetic casting proceeded as expected, indicating that the issues with the first casting were due to the equipment problems rather than the system design.

After adjustments were made, the 27 MHz generator was powered on and the bottom melt began to heat up quickly, as indicated by the bottom thermocouple, TC0. However, the bottom skull was still thick and casting could not be initiated electromagnetically. For example, the temperature at the bottom during the first casting was only 775°C, while for the second casting it was at 900°C. Analysis of the large generator parameters and melt pool depth indicate that the melt pool should have been allowed to further increase to ensure a more stable steady state was established prior to attempting the casting (refer back to Figure 11-34). The key parameters appear to be trending downward and do not indicate that a steady state is achieved. Figure 11-36 shows some key electrical and thermal parameters of the 27 MHz generator and induction system during the first casting.

Figure 11-36. Key electrical and thermal parameters of the 27 MHz generator during first casting.
(Ua2 is voltage on the 27 MHz generator lamp anode V, Pcc2 is electrical and thermal losses in the drain kW, Ia2 is 27 MHz generator lamp anode current A, Ig2 is 27 MHz generator lamp grid current mA)
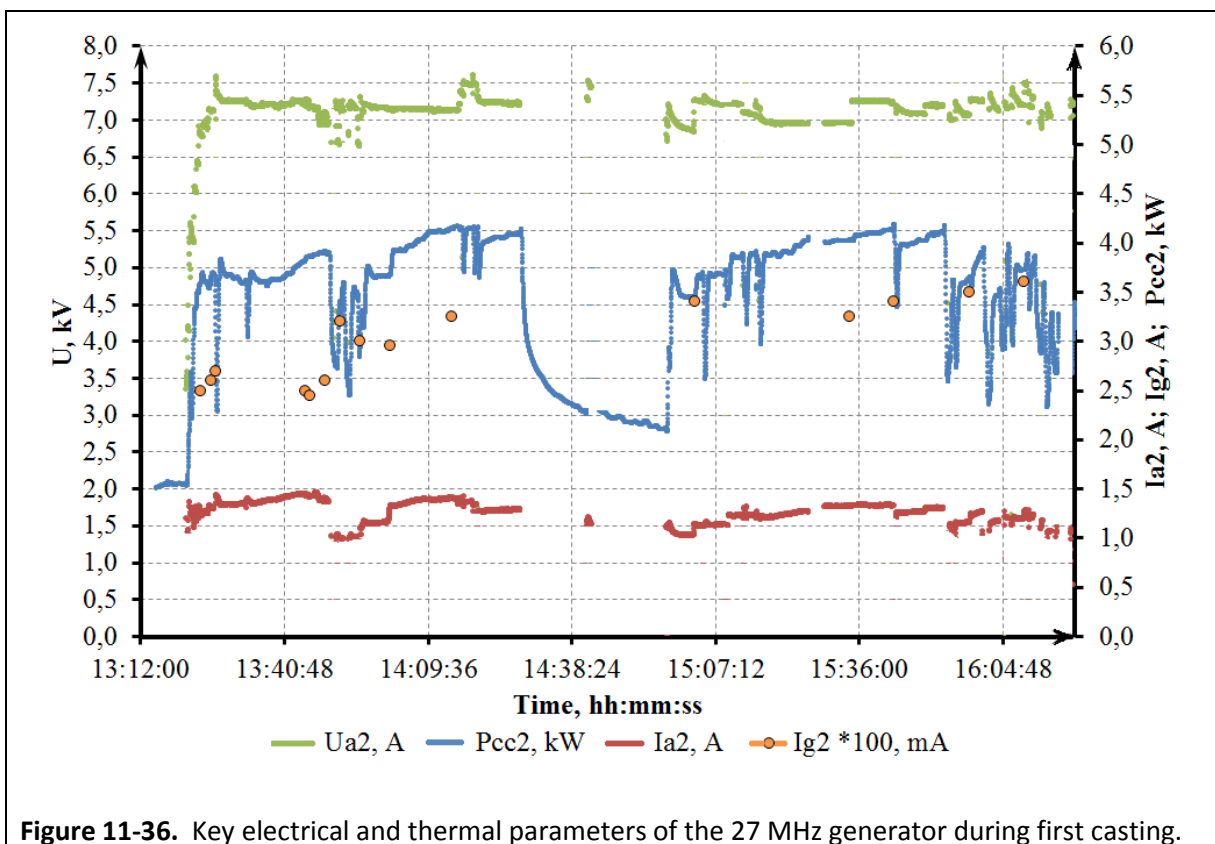
Figure 11-37 shows the temperature at the bottom during the two castings. The vacuum levels within the crucible are also shown on this figure. The initial pressure spikes of near 7.5 kPa gage and 6 kPa gage were recorded during testing of the vacuum system prior to the casting processes.

Figure 11-38 shows key electrical and thermal parameters during the second casting. These parameters are much more stable than those observed during the first casting, indicating a much better heated condition during this stage of the test.
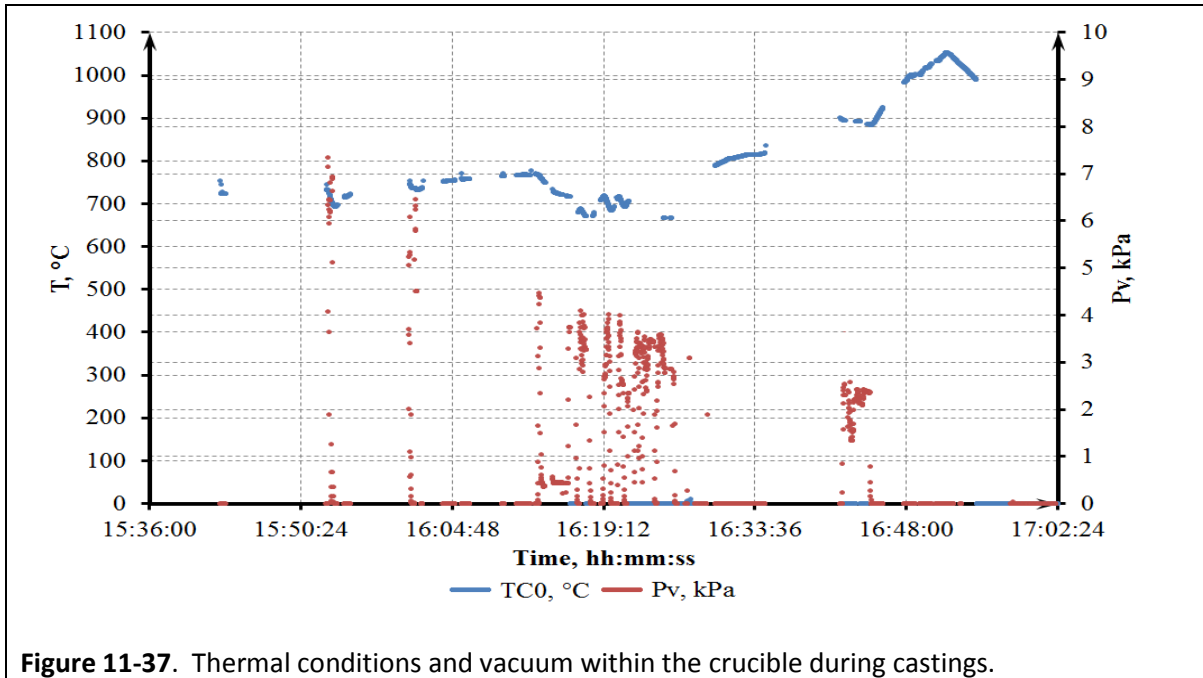
Figure 11-37. Thermal conditions and vacuum within the crucible during castings.

(TC0 is bottom temperature °C, Pv is vacuum in crucible kPa gage)
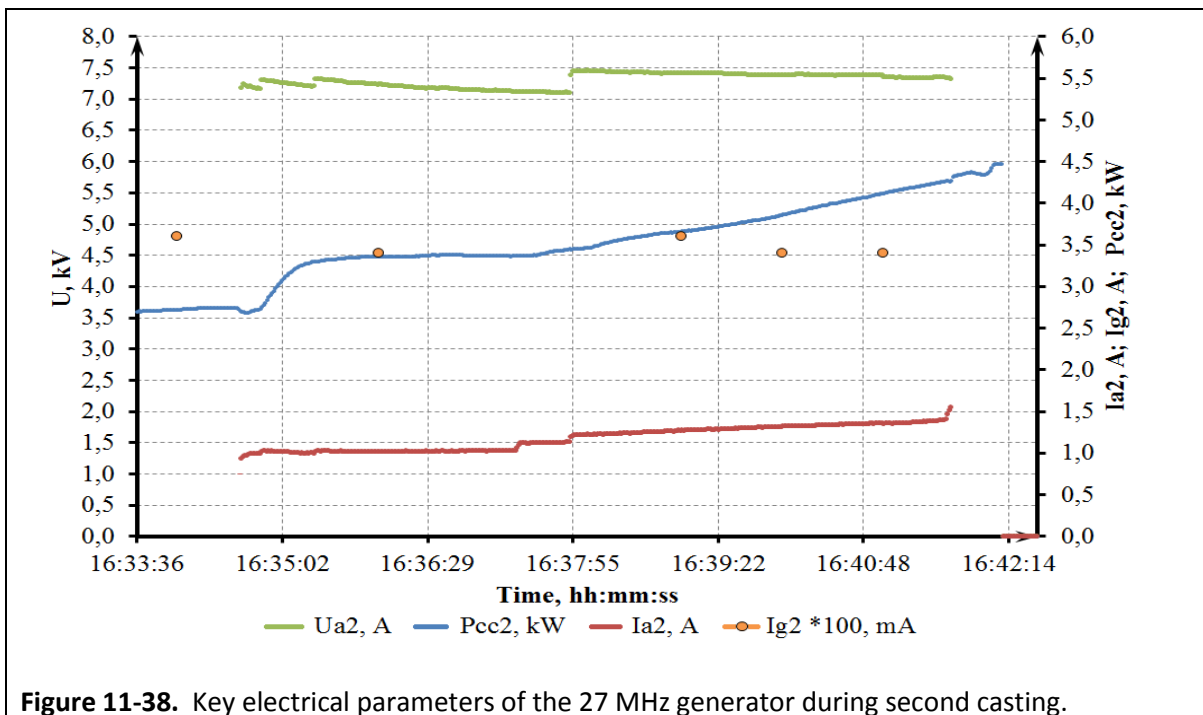
Figure 11-38. Key electrical parameters of the 27 MHz generator during second casting.

(Ua2 is voltage on the 27 MHz generator lamp anode V, Pcc2 is electrical and thermal losses in the drain kW, Ia2 is 27 MHz generator lamp anode current A, Ig2 is 27 MHz generator lamp grid current mA)

Table 11-4 provides a summary of the stages and conditions of the System Optimization Test #2.

Table 11-4. Stages and conditions for System Optimization Test #2.

Time hr:min	Ua1, kV	Ia1, A	Ig1, A	Ucb1, kV	Notes
09:50	10.40	2.90	1.54	6.20	Starting heating on a graphitic ring
10:29	10.30	2.74	1.48	6.40	Software setting
11:42	9.90	6.29	1.02	6.00	Removal of a starting ring
13:04	8.18	8.05	0.72	2.67	a_2=100 mm, thickness of a bottom skull is 48 mm
13:19	–	–	–	–	1-st switching-on of the small generator, TC0 = 535°C
13:49	–	–	–	–	Switching-off of the small generator for adjustment
13:52	–	–	–	–	Switching-on of the small generator, TC0=630°C
14:28	–	–	–	–	Switching-off of the small generator for adjustment, moving of the cold crucible upwards 15 mm, TC0=703°C
14:52	8.20	8.20	0.65	2.74	TC0=715°C
14:58	–	–	–	–	Switching-on of the small generator
15:43	–	–	–	–	TC0=724°C
15:54	–	–	–	–	Check of the vacuum system at 6 kPa gage
16:08	–	–	–	–	The mode of the big inductor power supply is increased
16:12	–	–	–	–	The beginning of the 1st casting by means of a probe
16:13	–	–	–	–	Casting is stopped by means of the vacuum system in the cold crucible at pressure of 3-4 kPa gage
16:34	–	–	–	–	Switching-on of the small generator
16:42	–	–	–	–	The beginning of 2nd melt casting
16:44	–	–	–	–	Casting is stopped at pressure of 2.4 kPa gage
16:52	–	–	–	–	End of test, TC0=1,050°C

(Ia1 is current on primary generator lamp anode; Ua1 is voltage on primary generator lamp anode; Ig1 is current of primary generator lamp grid; Ucb1 is voltage on the capacitor bank of primary generator; a_2 is depth of the melt pool; TC0 is indications of the bottom thermocouple)

Key Results and Conclusions: The System Optimization Test #2 provided the following results and conclusions:

- After appropriate conditions were established, the eleventh version of the drain device was able to reliably achieve electromagnetic casting in a large diameter crucible, with no external forces or assistance applied.

- Repeated, controllable melt casting including complete stoppages using an applied vacuum in the crucible headspace were successfully demonstrated. Minimal applied negative pressures ranging between 4 kPa gage and 2.4 kPa gage were adequate to control mass flow

of the glass during the casting process, to the point of complete stoppage. The required

vacuum is a function of the melt pool depth. For scale-up, a deeper melt pool will have a

higher hydrostatic pressure; however, this may be partially or completely offset by the

increase surface area. This should be further investigated to determine the optimum

balance between operational conditions, melt pool height to diameter ratio, and flow

control pressure.

- The final stage of optimization of the design for the drain device and crucible, for the work

  reported herein, appears to have resulted in an integrated system that functions as desired

  although further refinements are still necessary to provide a robust design for multiple

  applications.

CHAPTER 12.   ESTIMATED ACCURACY OF CALORIMETRY AND DATA ACQUISITION SYSTEMS – UNCERTAINTY ANALYSIS

Many of the components of the CCIM system are water cooled. This provides a direct method for determining an overall energy/power balance for the system. Early configurations of the melter system included an uncooled bottom and open top. Later a water-cooled lid was used to measure radiation heat losses from the melt surface, although initially no accurate method for differentiating radiation heat transfer to the crucible section above the melt from the conduction heat transfer from the melt was available. Eventually, however, improvements, enhancements, and modifications provided the capability to perform comprehensive, high accuracy calorimetry for virtually every aspect of the system, resulting in highly reliable results. These improvements are discussed in the context of the progressive experimental efforts, as appropriate. The following discussion provides a general description of the calorimetry system and components. The full system was shown in Figure 2-2, but is repeated here as Figure 12-1, for convenience.

Figure 12-1. Calorimetry and data acquisition system installed on CCIM test platform.
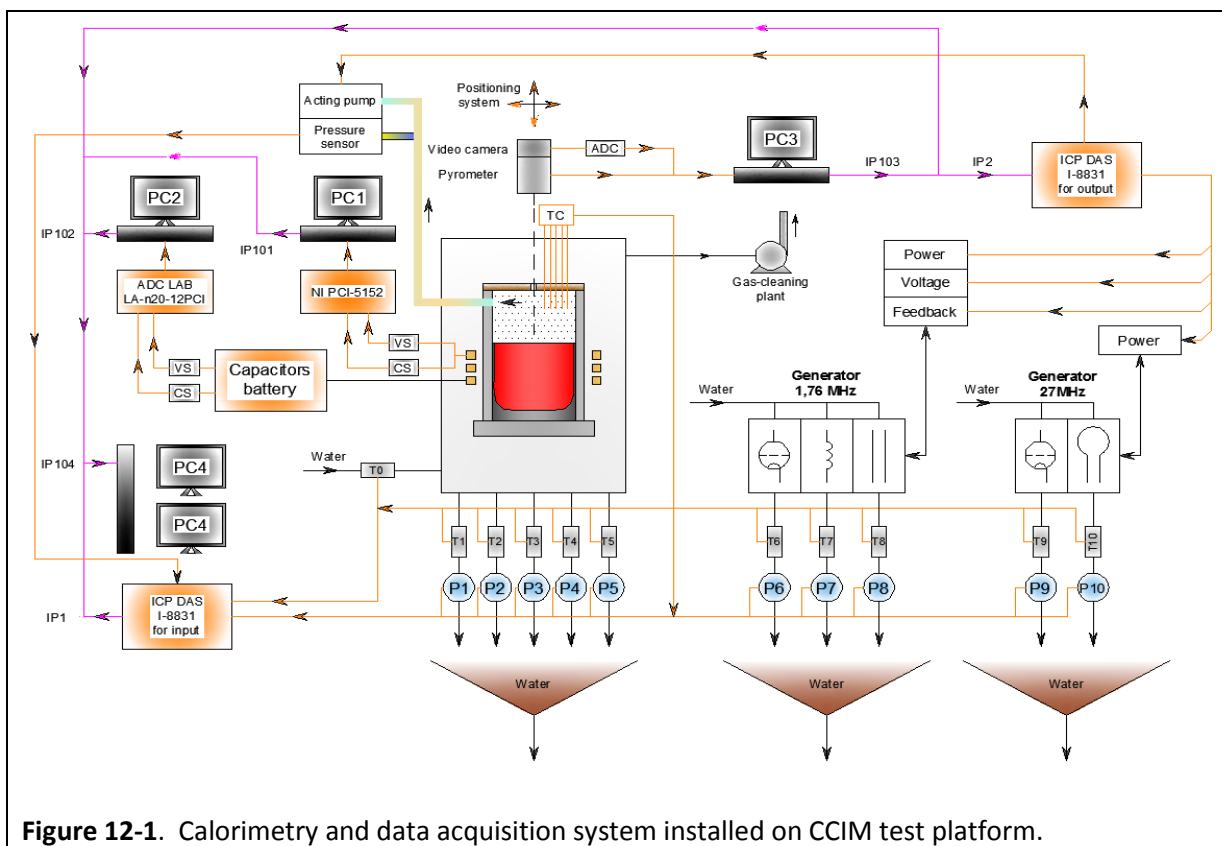
The cooling water flow to the various components is measured using high precision flow meters. This is an important feature because most of the material properties used for developing the ANSYS® model were extrapolated from 1,200^{o}C to 2,000^{o}C

Sensitivity studies were conducted on the model to determine the effect of potential inaccuracies for each of the properties. With high accuracy calorimetry, this provides the ability to input more exact boundary conditions, compare the results to experimental data, and, in an iterative process, the extrapolated properties can be modified such that the model provides more representative results. This provides an indirect method to more accurately define the material properties at high temperatures.

Two high capacity magnetic flow meters (Rosemount 8705 with Rosemount 8732E transmitter) are used in the system. One for the crucible and one for feed to the cooling water distribution manifold. The Rosemount flow meter assembly is shown in Figure 12-2. These are indicated as "Flowmeter" on Figure 12-1.

Figure 12-2. High flow, precision Rosemount flow meter.

The cooling water distribution manifold includes several single jet turbine flow meters of two different types for higher and lower flow rates (Siemens WFK2-D230 series for 2.5 m^{3}/hr and Siemens VLF-R-W for 1.5 m^{3}/hr). An example is shown in Figure 12-3. These flow meters provide only analog output; however, they were modified by ETU-LETI to include an infrared optical-pair digital counting system that allowed

Figure 12-3. Single jet, turbine type Siemens flow meter.

automated data acquisition and imaging. This system design is shown in Figure 12-4. These components are shown as "P1" through "P5" for low flow and "P6" through "P10" for high flow requirements.

The cooling water distribution system also includes several thermistors (i.e., for each cooling loop). The thermistors are high accuracy, platinum sensors (TRP-PT100). One is installed on the output side of the primary Rosemount flow meter, as well as one near the discharge point for each cooling

loop to measure temperature increase that occurs for each of the system elements being measured. These are shown as "T0" through "T10" on Figure 12-1.

Depending on the specifics of the experimental set-up, the components that are part of the calorimetry system vary. However, in general, they include the crucible wall, the crucible bottom, the cover lid, the drain, the 1.76 MHz generator, the 27 MHz generator, the primary inductor, and the drain inductor. The water flow distribution and temperature measurement system is shown in Figure 12-5.

Notes: 1. Wheel with precision apertures attached to counter axis
2. Infra-red optical pair

Figure 12-4. Modification to Siemens flow meters to allow automated digital data acquisition. (Designed by ETU-LETI)

Figure 12-5. Cooling water distribution, flow and temperature measurement.
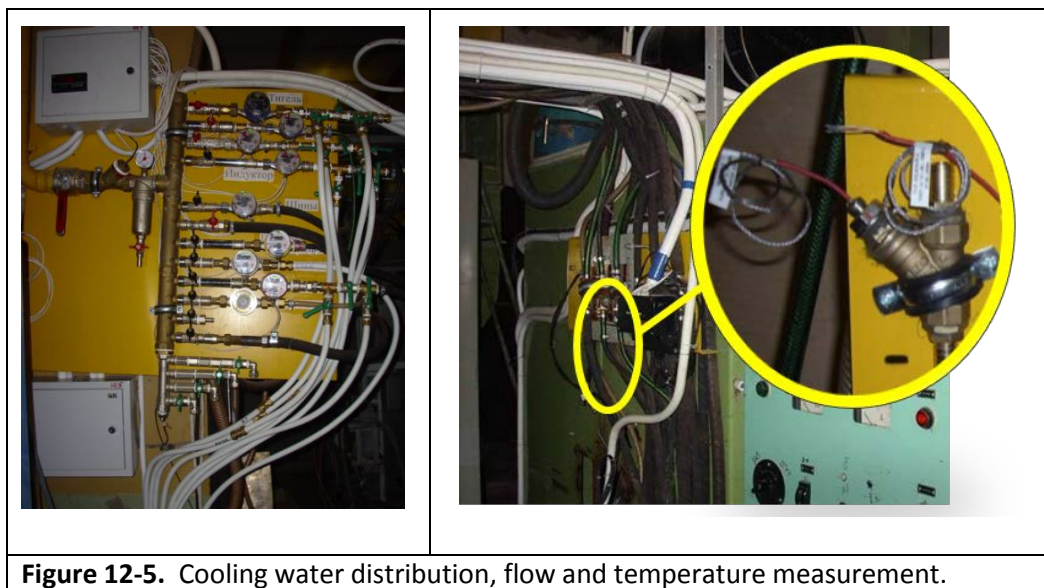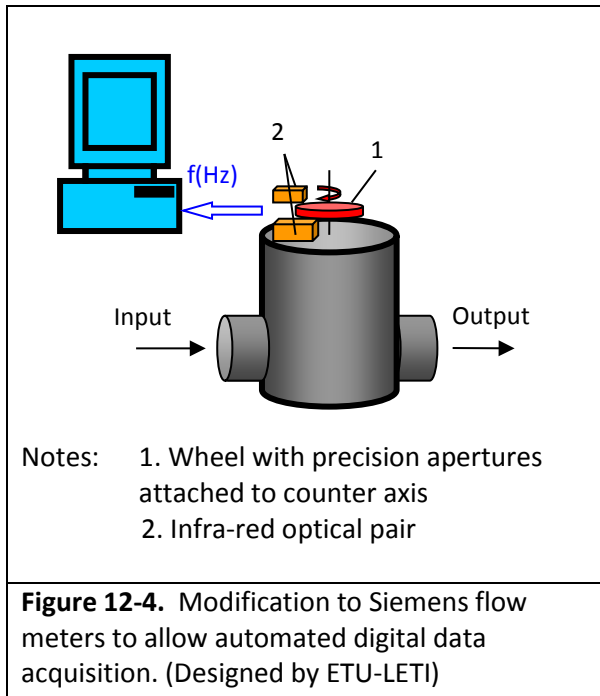
In addition to the thermistors for measuring the water temperature, several other temperature readings are taken during the testing, depending on the test objectives.

The thermocouple array for measuring the thermal profiles within the melt volume was previously described in Chapter 3. Its progression resulted in the eventual use of Type S thermocouple junctions with hafnium oxide insulation deployed within alumina (Al_2O_3) sheaths (Omega XTA-W5R26-U-125-30-H-Q-12). For lower temperature measurements that require better durability, a Type K thermocouple with a mineral insulation and specialty sheath (Omega Super OMEGACLAD XL TJ36-CAXL-18U-12 and TJ36-CAXL-116U-12. 1/8" and 1/16" diameter, respectively) were used. In addition, lower cost Type K thermocouples with mineral insulation in an Inconel sheath (Omega XC-14-K-12) are still used for spot temperature checks, as needed. Finally, Type C thermocouples with hafnium oxide insulation in a tantalum sheath (Omega XTX-W5R26-U-125-30-H-Q-20) were used for more accurate dip measurements within the melt pool volume for higher temperature conditions.

However, for this application, all of these thermocouples have been demonstrated to be consumable, and for long term deployment in a radioactive environment a more reliable thermocouple and/or deployment approach would be required.

For the thermocouples, the reliability of the readings is directly related to the accuracy of the data acquisition system since temperature differences are interpreted as fractions of millivolts. For example, for a Type S thermocouple, the induced voltage difference between 1,150^{o}C and 1,200^{o}C is only 0.600 millivolts (mV). This is of particular concern in a high frequency induction energy field that can couple with the conductive components of the thermocouple assembly itself, as well as develop coupled fields between adjacent thermocouples, such as in the measurement arrays used in the experimental work. This is even more problematic for metal sheathed thermocouples. While the effects of the 1.76 MHz signal were difficult to filter and shield, the 27 MHz signal was even a greater challenge. The best technique to resolve this is to replace the signal transmission lines with fiber-optic cables. Over time, as funding was available, this was done. However, prior to that, various techniques were investigated before a reliable approach was found. This included increasing the distance of the thermocouple connection block from the induction coils, shielding the transmission lines with aluminum foil, and filtering and capacitive grounding the thermocouple connectors.

To fully understand the effects of the induction field, as well as the effectiveness of the capacitive grounding, tests were conducted to measure the voltage on the thermocouple junction caused by the 1.76 MHz field. Table 12-1 shows the results for several conditions.

These results demonstrate that the capacitive grounding is very effective at filtering the induction field effects. The remaining background can be effectively removed through calibration. Nevertheless, during some initial experiments, coupling occurred between adjacent thermocouple signal wires at the connection terminal.

Table 12-1. Induced voltage effect on thermocouple junction.

No.	Voltage[*], mV	Note
1	350	Thermocouple in vertical position without capacitive grounding
2	510	Thermocouple at 30° to the axis without capacitive grounding
3	~15	Thermocouple in vertical position with capacitive grounding
4	~15	Thermocouple at 30° to the axis with capacitive grounding

Note: [*] Background noise effect on thermocouple is ~12 mV when inductor is de-energized.

Additional temperature measurements were made for the melt pool surface using a Siemens two-color optical pyrometer, spectral range of 0.95/1.05 microns. The model selected was an ARDOCELL PZ 40 AF 7, which operates between 1,000^{o}C and 3,000^{o}C. The manufacturer reports the uncertainty at 1% of the temperature. The Siemens pyrometer installed on the test platform is shown in Figure 12-6.

To ensure the highest accuracy possible, precision data acquisition products designed specifically for operation with the Omega thermocouples were installed. This includes the OMB-DAQ-56 Personal Daq, as well as the related software, for setup, data acquisition, and visualization. The OMB-DAQ-56 is basically a 32-bit analog to digital converter that also allows for digital calibration of the system. An example set-up similar to the one used for these experiments is shown in Figure 12-7.

Figure 12-6. Siemens Optical Pyrometer.
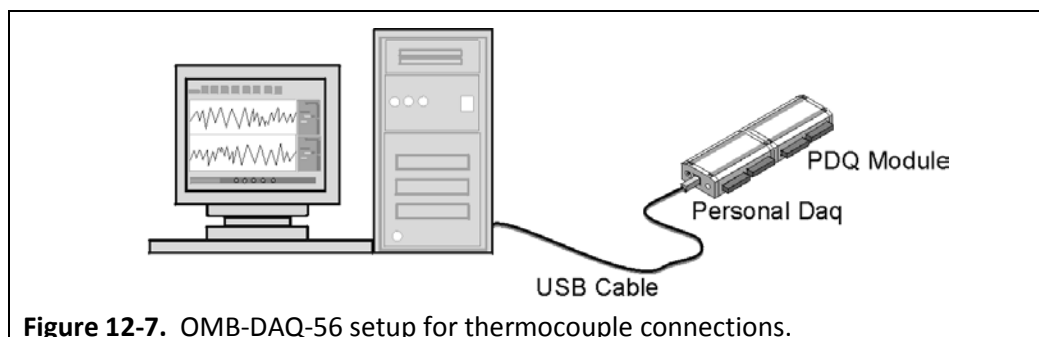
Figure 12-7. OMB-DAQ-56 setup for thermocouple connections.

The OMB-DAQ-56 is designed to operate a maximum of 16.4 feet from the thermocouple junction to maintain accuracy. Thus, when it became apparent that the Personal Daq needed to be located remotely, this limitation resulted in a decision to locate the unit such that the maximum wire length is 15 feet. This approach, coupled with shielding of the signal wires provided the protection necessary to successfully operate the thermocouple array, as well as other thermocouple measurements. The signal wires for other digital signals, such as those from the thermistors and flow meters, were also shielded and grounded. Most of these lines were eventually transitioned to fiber optic. The capacitive grounding technique used for the thermocouple signal wires, which was designed and implemented by ETU-LETI, is shown in Figure 12-8.
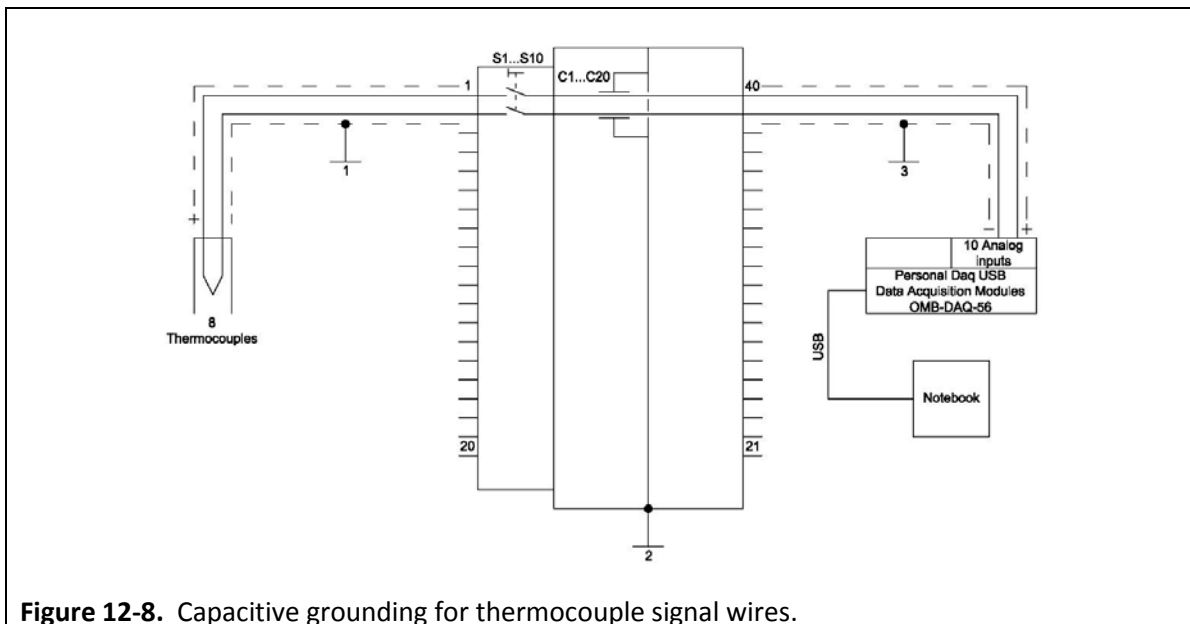
Figure 12-8. Capacitive grounding for thermocouple signal wires.

Taken together, the calorimetry system components and thermocouple connection and data acquisition systems resulted in a relatively high-accuracy measurement system. While the accuracies of the thermocouple and pyrometer measurements are very high, the most unreliable, and thus least accurate, parameter is the measurement of their physical locations. The positioning systems implemented were designed, built, and installed by ETU-LETI. Based on the tolerances of components used, as well as manufacturers' data on purchased components, ETU-LETI estimated these systems to be ±2.5% accurate. This was considered to be adequate for the purposes of the research conducted. Additionally, due to the extrapolation and estimation required to define the temperature dependent material properties through the entire temperature range needed, the resulting accuracies of the experimental systems are likely higher than those for the material

property data and boundary conditions used in the modeling effort. Nevertheless, the comparative modeling and experimental results were used to continually refine the data such that the model became very representative of the experimental results.

The accuracies of the individual system components and overall estimated system accuracies are summarized in Table 12-2.

Table 12-2. Estimated system accuracies.

Component	System	Accuracy	Factor	Total Component Accuracy	System Cumulative Accuracy
Rosemount 8705 Flow Meter to CCIM	Calorimetry	± 0.25%	1	± 0.25%	± 0.25%
Rosemount 8705 Flow Meter to Manifold	Calorimetry	± 0.25%	1	± 0.25%	± 0.50%
Siemens WFK2-D130 Flow Meter	Calorimetry	±0.50%	0.5	± 0.25%[*]	± 0.75%
Siemens VLF-R-W Flow Meter	Calorimetry	±0.50%	0.5	± 0.25%[*]	± 1.0%
TRP-PT100 Thermistors	Calorimetry	±0.12%	10	±1.2%	±2.2%
Electrical sensors for generator power	Calorimetry	±2.5%	1	±2.5%[**]	±4.7%
Cover Lid	Calorimetry	±5.0%	0.18[***]	±0.90%	**±5.6%**
Type K Thermocouples	Model, Melt Temperature	±0.75%	2	±1.5%	±1.5%
Type S/C Thermocouples	Model, Melt Temperature	±0.25%	1	±0.25%	±1.8%
Type K/Type S Interface at bottom	Model, Melt Temperature	±1.0%	2	±2.0%	±3.8%
Thermocouple Array Positioning System	Model, Melt Temperature	±2.5%	1	±2.5%[**]	±6.3%
Siemens ARDOCELL PZ-40 Pyrometer	Model, Melt Temperature	±0.50%	1	±0.50%	±6.8%
Pyrometer Positioning System	Model, Melt Temperature	±2.5%	0.18	±0.45%[**]	**±7.3%**

Notes: * Approximately half of the total flow passes through each of these two flow meters. The sum of the flows can be adjusted by total flow from the Rosemount 8705.
** ETU-LETI designs. Accuracy estimated based on data from ETU-LETI measurements/calculations.
*** From view factor geometry, approximately 82% of radiant heat loss goes to side wall when covered.

CHAPTER 13.   ONGOING EFFORTS AND FUTURE WORK

At the time that the work supporting this dissertation was completed, efforts continued in testing and optimization of the drain device, with focus on large scale (i.e., 0.5 m diameter) CCIM systems. The scale-up activities were still ongoing in 2012. The modelling efforts also continued through that time. This work was primarily in support of the U.S. Department of Energy Office of Environmental Management for evaluation of iron phosphate and high-crystalline alumino-silicate glasses for immobilization of target radioactive waste streams.

13.1.   Materials Property Estimation Using the ANSYS® Modeling

The US Department of Energy has interest in new glass compositions for some of the unique and more challenging waste chemistries that must be immobilized for long term safe storage. New compositions of alumino-silicate and iron phosphate glasses have been identified that offer significant improvements in waste loading over the baseline BSG. However, these compositions are not amenable to processing in conventional JHCMs and CCIMs are being investigated for these applications.

Because they are new glass formulations, limited material property data are available. In general, only viscosity and electrical conductivity data have been developed, and these are generally limited to $1,350^{o}C$ and below. Using compositional data and the limited known material properties, the ANSYS® model has been used as a tool to reverse engineer the material properties for both alumino-silicate and iron phosphate glass compositions.

Controlled testing was performed and extensive operational data were obtained, including relationships between melt temperature and generator parameters, full calorimetry, and other key data. Using this information, coupled with the known material property behaviors, the temperature-dependent material properties in the model were iteratively adjusted based on comparison of the model results to experimental results. The end product was a representative model that can now be used to conduct analyses of processing scenarios and system configurations with acceptable levels of representativeness, especially for the steady state modes. It is recognized that each material property model is not individually accurate. However, collectively, they have been demonstrated to provide representative results across a broad range of operating conditions and parameters.

13.2. Investigation and Testing of Large Scale CCIM Systems

Efforts have also continued related to modeling, optimization, and testing of large scale CCIM systems. Recent efforts have been focused on improving the conditions near the bottom zones in support of bottom casting. A 0.5m diameter crucible has been built based on these efforts and was most recently used to process a high temperature alumino-silicate glass composition, as well as an iron phosphate glass. The model was used to optimize the design and operational parameters (i.e., aspect ratio, operating temperature, etc.). See Figure 13-1. Based on these results, the coil and crucible were designed and built. See Figure 13-2.

Without bottom coil   With bottom coil
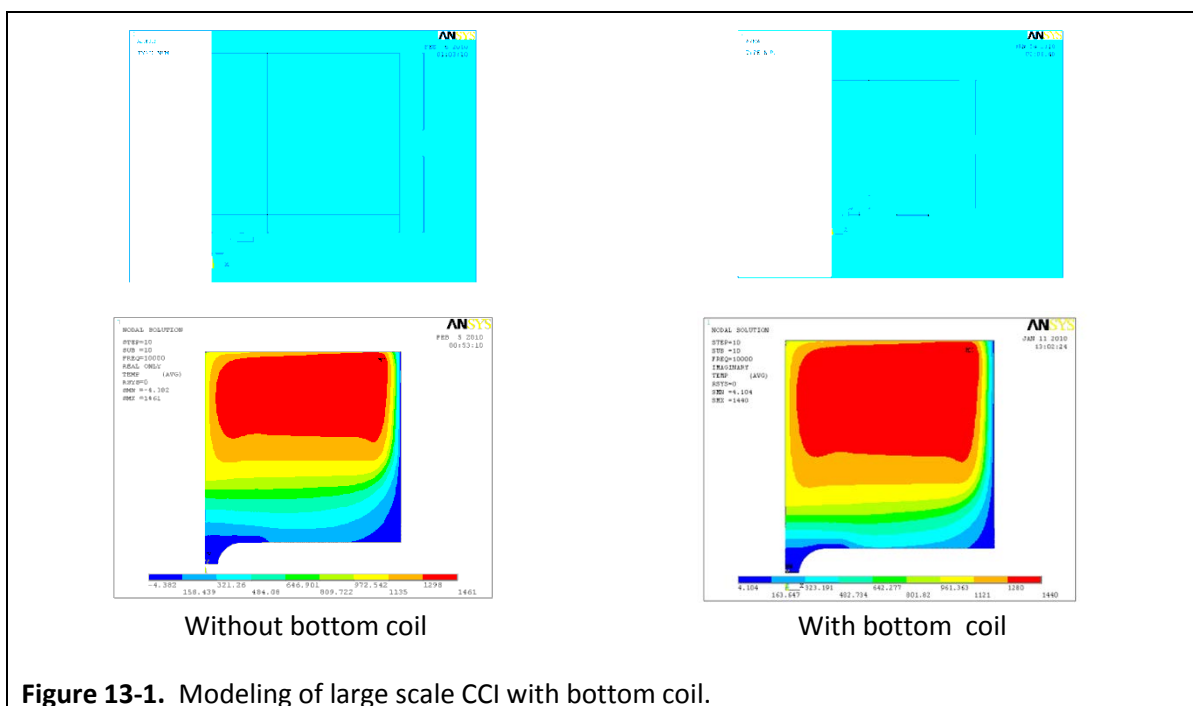
Figure 13-1. Modeling of large scale CCI with bottom coil.
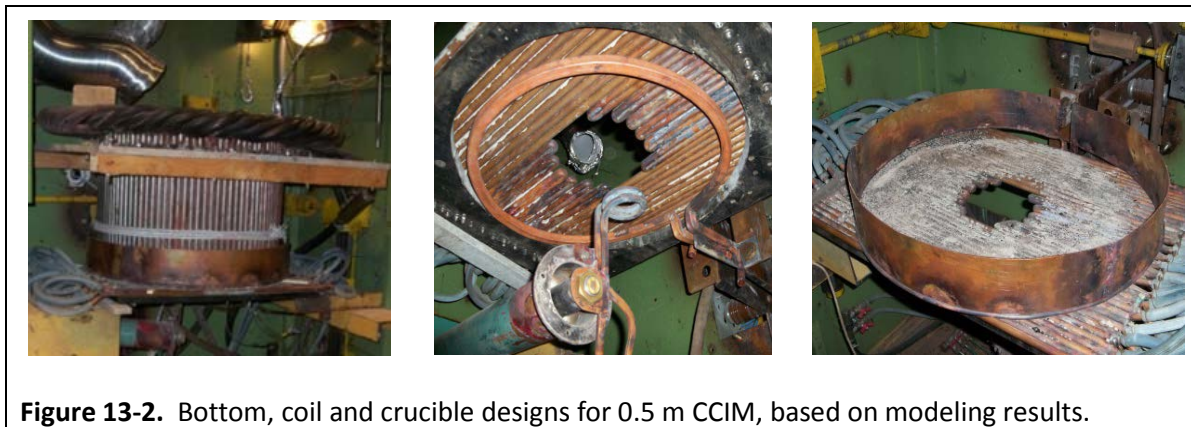
Figure 13-2. Bottom, coil and crucible designs for 0.5 m CCIM, based on modeling results.

Figure 13-3. Processing alumino-silicate (left) and iron phosphate (right) glasses in 0.5m CCIM.
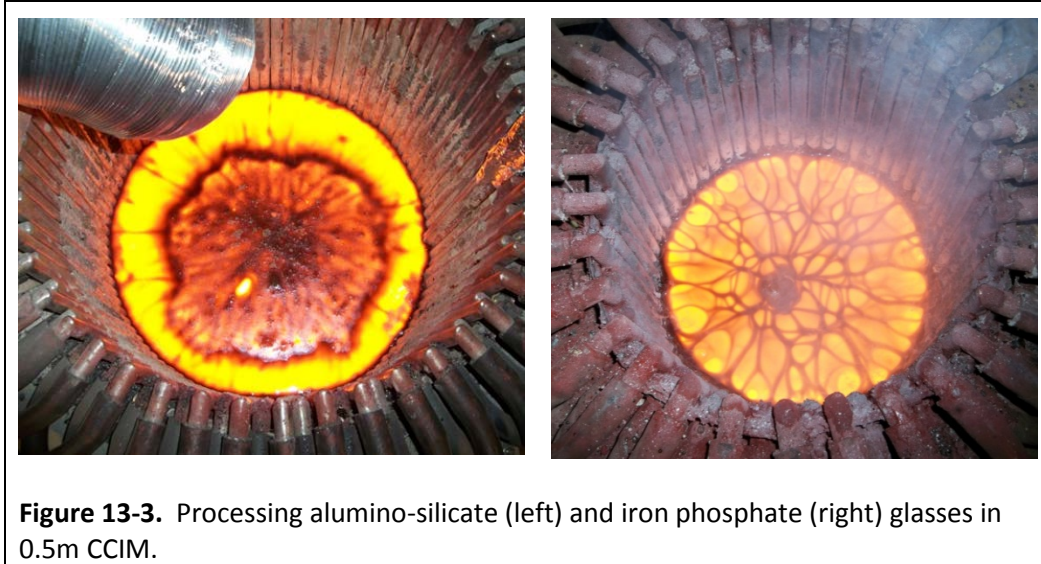
This melter has now been used to process the challenging alumino-silicate and iron phosphate glasses mentioned earlier. See Figure 13-3. One characteristic that is unique about this is that is powered with a 60 kW generator. As a point of reference, the system used by Areva to process radioactive waste is not much larger at 650 mm diameter, but requires a 300 kW power supply.

CHAPTER 14.   CONCLUSION

Over a period of approximately six years, extensive research and testing was conducted to evaluate the feasibility of developing an innovative technique for casting high temperature molten refractory oxides, with the primary focus on a known BSG composition. However, other alumino-silicate and iron phosphate glass compositions were also tested. The concept of this technique is based on application of an ultra-high frequency electromagnetic field to induce melting in a target zone such that conditions for casting the molten product are achieved. Based on the results reported herein, the objectives of this research were fully achieved.

In support of this work, a 2D axially symmetric model was developed using ANSYS® MultiPhysics software. This model served as an important analysis and design tool. Extensive efforts were made to develop representative temperature-dependent material property models, up to 2,000^{o}C, for density, specific heat, thermal conductivity, emissivity, electrical resistivity, and dynamic viscosity. Developing the emissivity model required data acquisition from several tests and application of several mathematical approaches to identify the relationship that was most representative of the experimental results. The model was developed in stages that increased in complexity beginning with fixed boundary conditions for all surfaces and average values for material properties, and eventually implementing temperature-driven boundary conditions (i.e., radiation and combined conduction/convection heat transfer modes).

The final model configuration was designed in three stages. The first stage included a significant enhancement that provided the ability to simulate the melt initiation process. This module allowed optimization studies for the melt initiation process, including materials and geometry of the initiator ring. In the final integrated model, this stage is coupled with a second stage that establishes a steady state for the melt pool using only the primary electromagnetic energy source (i.e., single frequency heating). The results of this stage are then coupled to a final stage in which a second, ultra-high frequency electromagnetic energy source is introduced (i.e., dual-frequency heating) such that conditions for initiating melt casting are produced in the melt. The "conditions for initiating melt casting" were defined primarily from the known material property and experimental data.

The model development and testing were conducted iteratively such that new information and improvements could be incorporated into system designs and the model algorithms. When significant differences between experimental and modelling results were observed, these could be

focused on to improve the representativeness of the model, and thus its ability to more accurately predict the performance of a particular system or component design. As an example, one interesting observation resulting from this development process is that the heat transfer characteristics along the bottom surface appear to be better described using a radiation heat transfer condition rather than a fixed heat flux or the combined conduction/convection approaches.

The experimental work was logically planned and scheduled to include:

1. Testing of CCIM systems, with no drain device installed, using continuously improved data acquisition and calorimetry systems to develop a comprehensive understanding of the characteristics near the bottom of the melt pool, such that they can be predicted and controlled. This test phase was also used to establish the initial heat transfer boundary conditions incorporated into the model.

2. Testing of prototype drain devices to demonstrate proof-of-principle for the concept and validating that the available specialized equipment (i.e, 27 MHz and 1.76 MHz high frequency generators) could be adapted to support the required experimentation. This test phase also provided initial boundary condition information relative to the drain device structure.

3. Testing of integrated CCIM systems with drain devices installed to optimize the designs for both the crucible and drain device.

4. Iteration between experimental efforts and modeling results to continually refine the design and enhance the representativeness of the model.

The conclusions from this comprehensive analysis and testing program are as follows:

1. The concept of an electromagnetic drain device for processing molten refractory oxides is feasible. However, the challenges and expense associated with operation of the ultra-high frequency generator (e.g., Faraday shielding, signal isolation for data acquisition, design sensitivity) lend its cost-effective use to specialty processing needs, such as very high temperature applications (i.e., above 1,600^{o}C) or highly corrosive/erosive melt chemistries.

2. Balancing the power demands for electromagnetic casting with protection (i.e., active cooling) of the surrounding system and components resulted in modification of the 27 MHz

generator to provide more than twice its original capacity (i.e., from 4.5 kW to 10 kW, with near 8 kW required for certain stages of the process), which initial calculations showed would be sufficient.

3. The 2D axially symmetric ANSYS® model appears to provide very representative results for the various stages of processing, including melt initiation, single-frequency heating steady state condition, and sual-frequency heating melt casting condition. In general, the melt initiation stage of the model provides qualitative results, although some aspects are quantitative (i.e., final temperature distributions) and design conclusions can be drawn when conducting comparative analysis. The other stages of the model, single-frequency and dual-frequency heating, provide quantitative end-state (i.e., steady state) conditions for temperature distribution, power requirements, and heat losses in the system.

4. The operability and effectiveness of the drain device and inductor are very sensitive to slight changes in geometry. The ability to translate the inductor coil during processing, by only a few millimeters, can determine if casting will be initiated or not.

5. For the BSG composition tested, casting could not be initiated using a drain device that was more than about 25 mm deep. As a result, the heat transfer from the glass into the drain body during casting was not sufficient to allow the glass to be cooled such that it would stop flowing (except when near empty). Due to the objective to develop a completely non-mechanical draining device, the concept of a vacuum-assisted casting control system was tested and demonstrated to be effective.

6. For the BSG composite tested, casting could not be controlled if the diameter of the drain opening was more than 25 mm diameter. Additionally, the casting could not be initiated if the diameter was much less than 25 mm, without the ability to provide excessive current loading on the inductor (i.e., in excess of 220 A for the 27 MHz generator used in the testing).

7. The eleventh, and final, version of the drain device design was demonstrated to be able to achieve reliable electromagnetic casting, provided that the melt pool was allowed to establish a legitimate steady state mode. It was also demonstrated to provide controllable casting with full stoppage using a very slight vacuum (i.e., 0.6 psig or less) in the crucible headspace for a 407 mm diameter system.

8. Pressure-assisted casting control was investigated using positive pressure below the drain exit point (i.e., through a sealed melt receipt container) and negative pressure (i.e., vacuum) above the drain entry point (i.e., through a sealed crucible lid using an induced draft fan in the offgas system). The positive pressure approach was not a manageable or controllable process due to the dynamics of changing volumes, head pressure, expanding gasses, etc.) The negative pressure approach was demonstrated to function reliably if the drain device was designed properly, and the sealing of the crucible lid and sides was effective and reliable. Using a combined approach was not investigated, but may provide the best balance of controllability and reliability.

9. An innovative method for melt initiation using a small diameter serpentine shaped wire ring provided a rapid start-up process. Near-plasma conditions are produced by the 1.76 MHz electromagnetic field that produces multiple spots at ultra-high temperature due to the plasma/arc path junctions that develop as the wire is melted and gaps are formed. This technique should be investigated further to better quantify the process.

10. For the system and BSG composition tested, the effective active power on the inductor, as determined by system calorimetry, appears to be almost linearly related to the maximum melt temperature, with very little hysteresis observed for heating versus cooling conditions. Sensors can be used to measure the instantaneous active power on the inductor; however, they do not account for the energy momentum within the glass volume and the associated system time constant, which is on the order of several minutes, depending on the melt pool volume.

11. The dynamic nature of induction melting and casting, coupled with the many interdependencies (i.e., material properties, electromagnetic coupling and feedback, heat transfer phenomenon, etc.) render this process extremely challenging to predict its behavior without extensive iteration between modeling and focused testing.

Further analysis, testing and development are needed to fully refine the integrated system design such that reliable and consistent melt initiation and processing can be achieved. Additionally, performance data are needed for larger diameter systems to understand design impacts related to scale-up.

REFERENCES

1. I. SOBOLEV, et al., "Vitrification of Intermediate Level Radioactive Waste by Induction Heating," ICEM'95, Berlin, Germany, September 3-9, 1995.

2. S**.** Stefanovsky, J. Marra, V. Lebedev, "Summary of Cold Crucible Vitrification Tests Results with Savannah River Site High Level Waste Surrogates", In Proc. Waste Management Symposium, Phoenix, AZ, March 2-6, 2014.

3. A. Kobelev, et al., "Cold Crucible Vitrification of Defense Waste Surrogate and Vitrified Product Characterization", In Proc. Materials Research Society (2006), 932, 88.1 doi:10.1557/PROC-932-88.1.

4. S. Naline, et al., "Vitrification 2010 – A Challenging French Vitrification Project to Retrofit a Cold Crucible Inductive Melter at the La Hague Plant", In Proc. Waste Management Symposium, Phoenix, AZ, March 7-1, 2010.

5. K. Yang, S. Shin, C. Moon, "Commissioning Tests of the Ulchin LLW Vitrification Facility in Korea", In Proc. Waste Management Symposium, Phoenix, AZ, March 1-5, 2009.

6. P. Sengupta, C. Kaushik, G. Dey, "Immobilization of High Level Nuclear Wastes: The Indian Scenario", in *On a Sustainable Future of the Earth's Natural Resources*, edited by M. Ramkumar, ISBN 978-3-642-32916-6, Springer Publsihing, 2013, Ch. 2.

7. G. Sugilal, P. Sengar, "Cold Crucible Induction Melting Technology for Vitrification of High Level Waste: Development and Status in India", In Proc. Waste Management Symposium, Phoenix, AZ, February 24-28, 2008.

8. J. Perez et al., "High-Level Waste Melter Study Report", PNNL-13582, July 2001.

9. J. Ahearne et al., "High-Level Waste Melter Review Report", TFA-0108, July 2001.

10. R. Treat et al., "Technical Evaluation of Hanford HLW Vitrification Process Alternatives: Report of the Independent Project Evaluation Team", July 2003.

11. D. Gombert III, et al., Global Nuclear Energy Partnership Integrated Waste Management Strategy Waste Treatment Baseline Study, GNEP-WAST-WAST-AI-RT-2007-000324, September 2007.

12. C. Girold, et al., "Cold Crucible Induction melter (CCIM) Demonstration Using a Representative Savannah River Site Simulant on the Large-Size Pilot Platform at the CEA-Marcoule," In Proc. Waste Management Symposium, Phoenix, AZ, February 24 –28, 2008.

13. O. Muck, German Patent No. 422,004. October 30, 1923 (No title available).

14. Siemens und Halske, "Verfahren zum Schmelzen schwerschmelzbarer Metalle. insbesondere von Tantal, Wolfram, Thorium oder Legierungen dieser Metalle in einem wassergekuhlten Behalter", German Patent No. 518,499, 1931.

15. J. Wenckus, et al., "Study, Design and Fabricate a Cold Crucible System", Air Force Cambridge Research Laboratories, March 31, 1975, AFCRL-TR-75-0213.

16. P. Clites, "The Inductoslag Melting Process", Bulletin 673, U.S. Department of the Interior, 1982.

17. D. Venable and T. Kinn, "Radio Frequency Heating Fundamentals and Applications", in *Industrial Electronics Reference Book*, Westinghouse Electric Corporation, John Wiley and Sons, Inc., 1948, Ch. 24.

18. D. Lopukh, "Process Research and Development of Equipment for Solidification of Radioactive Waste Simulators by Induction Cold Crucible Melting", Leningrad Electrotechnnical Institute, September 2003.

19. A. Sneyd and H. Moffatt, "Fluid Dynamical Aspects of the Levitation-Melting Process", *Journal of Fluid Mechanics*, 1982, Vol. 117, pp. 45-70.

20. K. Deng, et al., "The Electromagnetic Field Calculations and Analysis of Levitation Melting with Cold Crucible", *Acta Metallurgica Sinica, English Letters,* Vol. 13, No. 2, April 2000, pp. 702-707.

21. T. Tanaka, et al., "High Volume Reduction and Group Separation of Simulated Fission Products by Cold Crucible", *International Steel Institute of Japan,* Vol. 40, 2000, No. 2. pp. 105-113.

22. Z. Chen, et al., "Temperature Field Numerical Simulation of Induction Skull Melting Process", *Transactions of the Nonferrous Metals Society of China,* Vol. 13, Special 1, May 2003, pp. 115-118.

23. D. Kang, et al., "Electromagnetic Characteristics of Levitation Melting with Cold Crucible", *Transactions of Nonferrous Metals Society of China*, Vol. 9, No. 2, June 1999. pp. 387-392.

24. H. Ding, et al., "Electromagnetic Characteristics of Cold Crucible in an Induction Coil for Melting Purposes", *Journal of Harbin Institute of Technology (New Series)*, Vol. 13, No. 2, 2006, pp. 141-145.

25. W. Kim and J. Yoon, "Numerical Prediction of Electromagnetically Driven Flow in ASEA-SKF Ladle Refining by Straight Induction Stirrer", *Iron and Steel Making,* 1991, Vol. 18, No. 6, pp. 446-453.

26. P. Cha, et al., "Numerical Analysis on Cold Crucible Using 3D H-Φ Method and Finite Volume Method with Non-staggered BFC Grid System", *Iron and Steel Institute of Japan International*, Vol. 36, 1996, No. 9, pp. 1157-1165.

27. V. Clingoski and H. Yamashita, "Analysis of Induction Skull Melting Furnace by Edge Finite Element Method Excited from Voltage Source", *IEEE Transactions on Magnetics,* Vol. 30, No. 5, September 1994

28. S. Yanquing, et al., "Modeling of Temperature Field for Induction Skull Melting Process of Ti-47Ni-9Nb", *Metallurgical and Materials Transactions A,* Vol. 32A, November 2001, pp. 2895-2902.

29. Y. Su, et al., "Temperature Control of TiAl Melt during Induction Skull Melting", *Materials Science and Technology*, Nov 2001, Vol. 17 (ISSN 0267-0836), pp. 1434-1440.

30. J. Guo, et al., "Skull Variation during Induction Skull Melting Processing of Gamma-TiAl Alloy", *Materials Science and Technology,* Vols. 475-479 (2005), pp. 809-812.

31. V. Bejarevics, et al., "Induction Skull-Melting Dynamics for Different Materials: Numerical Modeling and Comparison with Experiments", *Modeling of Casting, Welding, and Advanced Solidification Processes,* Vol. X, 2003, pp. 591-598.

32. V. Bejarevics, et al., "The Development and Experimental Validation of an Induction Skull Melting Furnace", *Metallurgical and Material Transactions B,* Vol. 35B, August 2004, pp. 785-803.

33. V. Bejarevics, et al., "Experimental and Numerical Study of the Cold Crucible Melting Process", In Proc. Third International Conference on CFD in the Materials and Process Industry, CSIRO, December 2003, pp. 599-606.

34. V. Bojarevics and K. Pericieous, "Modelling Induction Skull Melting Design Modifications", In Proc. 2003 International Symposium on Liquid Metals, Journal of Materials Science*, #39 (2004), pp. 7245-7251.

35. R. Harding and M. Wickins, "Temperature Measurements During Induction Skull Melting of Titanium Aluminide", *Materials Science and Technology,* September 2003, Vol. 19, pp. 1235-1246.

36. R. Harding, et al., "Obtaining Data to Validate a Model of an Induction Skull Melting Furnace", *Modeling of Casting, Welding, and Advanced Solidification Processes X, The Minerals, Metals, and Materials Society*, 2003. pp. 741-748.

37. A. Umbrashko, et al., "Experimental Investigations and Numerical Modeling of the Melting Process in a Cold Crucible", *The International Journal for Computation and Mathematics in Electrical and Electronic Engineering,* Vol. 24, Issue 1, pp. 314-323.

38. E. Baake, et al., "Numerical Investigations of the Flow Dynamics in Systems with Several Recirculated Flow Eddies", In Proc. 2nd International Conference on Energy Transfer in Magnetohydrodynamics, Aussois, France, Vol. 1, pp. 349-358.

39. ANSYS® Multiphysics Academic Research Release 9.0, 10.0, 12.0, and 14.0, ANSYS Inc., Cecil Township, Pennsylvania.

40. G. Sugilal, "Experimental Analysis of the Performance of Cold Crucible Induction Glass Melter", *Applied Thermal Engineering,* No. 28, 2008, pp. 1952-1961.

41. C. Kim, et al., "Vitrification of Simulated LILW Using Induction Cold Crucible Melter Technology". In Proc. Waste Management Symposium, Tucson, AZ, February 26 – March 2, 2006.

42. J. Song, et al., "An Electromagnetic and Thermal Analysis of a Cold Crucible Melting", *International Communications in Heat and Mass Transfer,* No. 32, 2005, pp. 1325-1336.

43. B. Nacke, et al., "Induction Skull Melting of Oxides and Glasses in Cold Crucible", In Proc. International Scientific Colloquium – Modeling for Material Processing, Riga, June 8-9, 2006.

44. B. Nacke, et al., "Induction Skull Melting of Oxides and Glasses in a Cold Crucible", *Magnetohydrodynamic,* Vol. 43, No. 2, 2007, pp. 205-212.

45. B. Nacke, V. Frishfields and A. Jakovics, "Modeling of Inductive Melting of Oxides in Inductor Crucible Furnace", *Elektrowarme International Journal,* 2002, No. 3, pp. 105-109.

46. B. Nacke, et al., "Skull Melting Technology for Oxides and Glasses", In Proc. 15th Riga and 6th PAMIR Conference on Fundamental and Applied MHD, Electromagnetic Processing of Materials, June 27 – July 1, 2005, pp. 241-244.

47. V. Frishfields, B. Nacke and A. Jakovics, "Simulation of Inductive Melting Process of Oxides in Inductor-Crucible", In Proc. International Scientific Colloquium – Modeling for Electromagnetic Processing, Hannover, March 24-26. 2003, pp. 157-162.

48. M. Kudryash, T. Behrens and B. Nacke, "Induction Skull Melting of Oxides and Glasses", *Archives of Electrical Engineering,* Vol. LIV, No. 4, 2005, pp. 417-423.

49. V. Schiff, A. Zamyatin and A. Zhilin*, "*Numerical simulation of thermal convection of a glass melt in a cylindrical induction furnace*", Glass Science Technologies*, 1996, Vol. 69, No. 12, pp. 379-386.

50. FIDAP® Software Version 8.7.2, Fluent Inc., Lebanon, New Hampshire.

51. G. Hawkes, "*Modeling a Cold Crucible Induction Heated Melter*", Idaho National Engineering and Environmental Laboratory, INEEL/CON-03-00550, In Proc. HT-FED2004 2004 ASME Heat Transfer/Fluids Engineering Summer Conference, Charlotte, NC, July 2004.

52. G. Hawkes, "Modeling an RF Cold Crucible Induction Heated Melter with Subsidence", Idaho National Engineering and Environmental Laboratory, INEEL/CON-03-01375, In Proc. FIDAP/POLYFLOW User Group Meeting, Evanston, IL, June 2003.

53. L. Jacoutot, et al., "Numerical Modeling of Natural Convection in Molten Glass Heated by Induction", *Chemical Engineering and Processing,* No. 47, 2008, pp. 449-455.

54. L. Jacoutot, et al., "Numerical Modeling of Coupled Phenomena in a Mechanically Stirred Molten-Glass Bath Heated by Induction", *Chemical Engineering Science,* No. 63, 2008, pp. 2391-2401.

55. E. Sauvage, et al., "Thermoconvective Instabilities of Molten Glass Heated by Direct Induction in a Cold Crucible", In Proc. International Scientific Colloquium – Modeling for Electromagnetic Processing, Hannover, October 27-29. 2008, pp 151-156.

56. A. Bonnetier, "Nuclear Waste Immobilization by Vitrification in a Cold Crucible Melter: 3D Magnetic Model of a Melter", In Proc. Materials Research Society Conference, 1107, Scientific Basis for Nuclear Waste Management XXXI, Warrendale, PA, 2008.

57. P. Brun, E. Sauvage, and E. Chauvin, "3-D Thermal. Hydrodynamic & Magnetic Modeling of Elaboration of Glass by Induction in Cold Crucible", In Proc. Waste Management Symposium, Phoenix, AZ, March 1-5. 2009.

58. J. Platas, et al., "Coupling Electromagnetic and Thermo-Hydrodynamic Simulations to Optimize a Vitrification Furnace Heated by Direct Induction", In Proc. 11th Workshop on Optimization and Inverse Problems in Electromagnetism, Sofia, Bulgaria, 2010.

59. M. Roscini, "Fusion de verres par induction: étrude électromagnétique et thermo-hydraulique", Ph.D. Thesis, I. N. P. G., 1990.

60. FLUX2D® and FLUX3D® Software, Version unknown, Cedrat Inc., Meylan Cedex, France.

61. FLUENT® Software, Version unknown, acquired by ANSYS Inc. in 2006, Cecil Township, Pennsylvania.

62. V. Rudnev, et al., *Handbook of Induction Heating,* INDUCTOHEAT, Inc., ISBN 0-8247-0848-2, Madison Heights, MI, 2003.

63. R. Bird, W. Stewart and E. Lightfoot, *Transport Phenomenon,* Second Edition, John Wiley and Sons, ISBN 0-471-41077-2, New York, NY, 2002.

64. R. Wescott, S. Slate, "Vitrification of High-Level Wastes: A Review of the Computer Thermal Analyses for Storage Canisters", *Nuclear Engineering and Design,* No. 67, pp. 447 – 458, 1981R.

65. R. Farnsworth, et al. "Applications of TEMPEST Computer Code to Canister-Filling Heat Transfer Problems", PNL-6474, March 1988.

66. FERRO Corporation, Certificate of Analysis for AC18647H Frit Composition, July 19, 2000.

67. J. Vienna, et al., "Effect of Composition and Temperature on the Properties of High-Level Waste (HLW) Glass Melting Above 1200°C", PNNL-10987 UC-810, April 1996.

68. T. Edwards, et al. "DWPF Startup Frit Viscosity Measurement Round Robin Results", Unpublished. Provided by one of the authors via personal communication. Includes electrical resistivity measurement data for the same glass composition, Pacific Northwest National Laboratory and Savannah River Technology Center, July 2004.

69. S. Tarakanov, V. Leko, O. Mazurin, "Some problems of precise measurements of heat transfer coefficients in glass melts", *Glass Science Technology*, No. 68, No.10, 1995.

70. C. Veyer, et al., "Vitrification of a Representative Simulated SB4 Sludge in a CCIM Pilot Platform at Marcoule – Demonstration Report", Technical Report DTCD/2009/02

71. M. Smith, et al., "NETEC Cold Crucible Induction Melter Demonstration for SRNL with Simulated Sludge Batch 4 DWPF Waste", WSRC-STI-2008-003690, Washington Savannah River Company, Aiken, SC.

72. LabVIEW 2011, Build 11.0.0.4029, National Instruments, Inc., Austin, TX, June 2011.

APPENDIX A

Mathematical Development of Temperature-Dependent

Material Properties for SRL-411 Borosilicate Glass

(page images from MathCad calculation results)

Viscosity and Electrical
Resistivity Exponential

This model performs routine exponential regression for electrical resistivity and viscosity data for a DWPF start-up frit that is similar in composition to the frit being used in the research for CCIM automated feedback control and modualting drain valve research with ETU.

1. Electrical Resistivity Regression

  a. Input data

data :=

	0	1
0	617	525.78
1	622	464.82
2	651	250.95
3	652·	259.08
4	663	204.47
5	679	67.8
6	679	68.7
7	682	69
8	699	105.41
9	711	91.69

$T := data^{\langle 0 \rangle}$ $\varepsilon := data^{\langle 1 \rangle}$

  b. Exponential Regression based on the equation E = exp(A + B/(T-C))

$$F(n,a) := \begin{bmatrix} \exp\left(a_0 + \dfrac{a_1}{n - a_2}\right) \\[2em] \exp\left(a_0 + \dfrac{a_1}{n - a_2}\right) \\[2em] \dfrac{1}{n - a_2}\exp\left(a_0 + \dfrac{a_1}{n - a_2}\right) \\[2em] \dfrac{a_1}{(n - a_2)^2}\cdot\exp\left(a_0 + \dfrac{a_1}{n - a_2}\right) \end{bmatrix}$$

$$guess := \begin{pmatrix} -0.92 \\ 1740 \\ 500 \end{pmatrix}$$

$E := genfit(T, \varepsilon, guess, F)$

$$E = \begin{pmatrix} -0.91934 \\ 1.73946 \times 10^3 \\ 375.62301 \end{pmatrix}$$

Figure A-1. Electrical Resistivity curve fit (1).

$$E(x) := \exp\left(E_0 + \frac{E_1}{x - E_2}\right) \quad x := \min(T)\ ..\ \max(T) \qquad T_1 := T \qquad T_2(x) := x$$
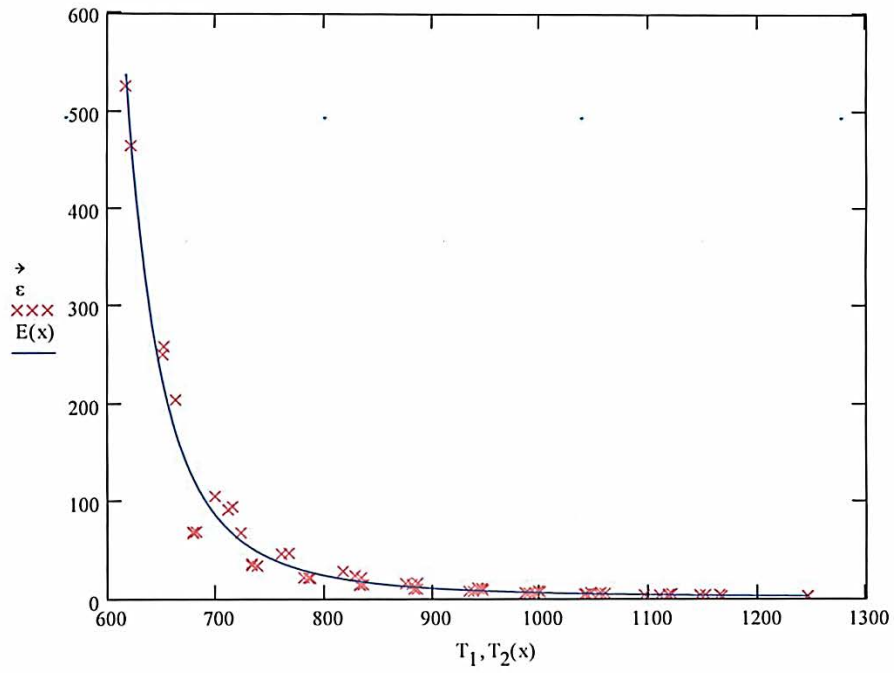
c. Data Correlation

$$E(x) := \exp\left(E_0 + \frac{E_1}{x - E_2}\right)$$

$$\text{corr}\left(\overrightarrow{E(T)}, \varepsilon\right) = 0.98713$$

Figure A-2. Electrical Resistivity curve fit (2).

2. Viscosity Regression

a. Data Input

data :=

	0	1
0	460.31	$4.7 \cdot 10^{11}$
1	461.16	$3.94 \cdot 10^{11}$
2	461.3	$4.38 \cdot 10^{11}$
3	462.11	$3.41 \cdot 10^{11}$
4	462.18	$4.23 \cdot 10^{11}$
5	462.23	$3.84 \cdot 10^{11}$
6	463.02	$2.87 \cdot 10^{11}$
7	463.1	$3.3 \cdot 10^{11}$
8	463.17	$3.57 \cdot 10^{11}$
9	463.92	$2.88 \cdot 10^{11}$

$T := data^{\langle 0 \rangle}$ $\eta := data^{\langle 1 \rangle}$

b. Exponential Regression based on equation E = exp (A + B/(T-C))

$$F(n,a) := \begin{bmatrix} \exp\left(a_0 + \dfrac{a_1}{n - a_2}\right) \\[2ex] \exp\left(a_0 + \dfrac{a_1}{n - a_2}\right) \\[2ex] \dfrac{1}{n - a_2} \exp\left(a_0 + \dfrac{a_1}{n - a_2}\right) \\[2ex] \dfrac{a_1}{\left(n - a_2\right)^2} \cdot \exp\left(a_0 + \dfrac{a_1}{n - a_2}\right) \end{bmatrix}$$

$$guess := \begin{pmatrix} -9 \\ 5831 \\ 280 \end{pmatrix}$$

$E := genfit(T, \eta, guess, F)$

$$E = \begin{pmatrix} -4.51459 \\ 6.14905 \times 10^3 \\ 264.741 \end{pmatrix}$$

$$H(x) := \exp\left(E_0 + \frac{E_1}{x - E_2}\right)$$ $x := min(T)..max(T)$ $T_1 := T$ $T_2(x) := x$

Figure A-3. Viscosity curve fit (1).
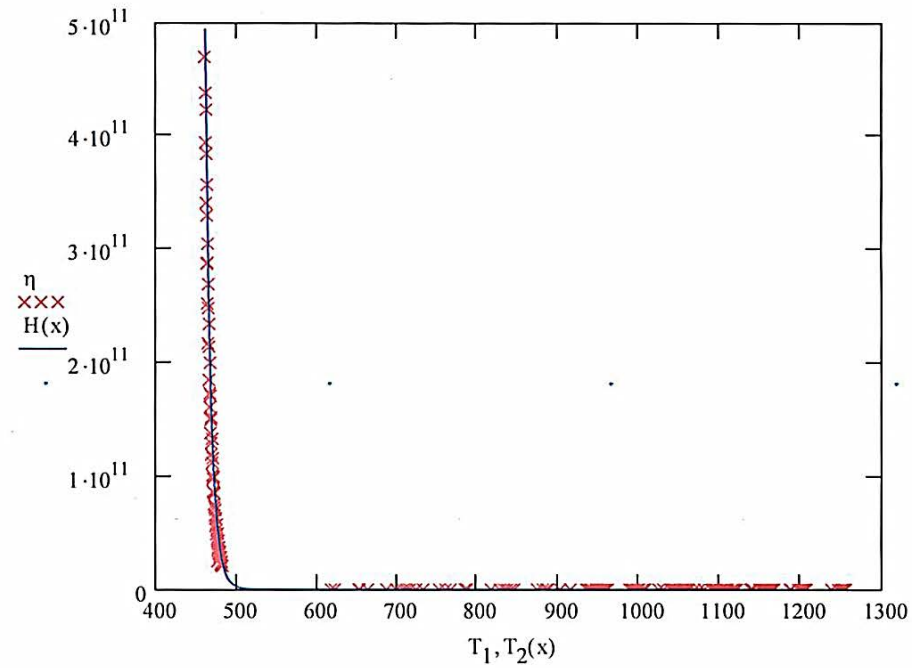
c. Data Correlation

$$H(x) := \exp\left(E_0 + \frac{E_1}{x - E_2}\right) \qquad \mathrm{corr}\left(\overrightarrow{H(T)}, \eta\right) = 0.99452$$

d. Comparison with Results from PNNL Viscosity Test Data

$$X(b) := \exp\left(-5.28918 + \frac{5831.1139}{b - 280.1372}\right) \qquad b := \min(T) .. \max(T)$$

$$\mathrm{corr}\left(\overrightarrow{X(T)}, \eta\right) = 0.99293$$

Figure A.4. Viscosity curve fit (2).

H(T) =			X(T) =			T =			η =	
	0			**0**			**0**			**0**
0	$4.94409 \cdot 10^{11}$		0	$5.72996 \cdot 10^{11}$		0	460.3138		0	$4.7 \cdot 10^{11}$
1	$4.31984 \cdot 10^{11}$		1	$4.92813 \cdot 10^{11}$		1	461.157		1	$3.94 \cdot 10^{11}$
2	$4.22102 \cdot 10^{11}$		2	$4.80244 \cdot 10^{11}$		2	461.3023		2	$4.38 \cdot 10^{11}$
3	$3.71404 \cdot 10^{11}$		3	$4.16339 \cdot 10^{11}$		3	462.1096		3	$3.41 \cdot 10^{11}$
4	$3.67301 \cdot 10^{11}$		4	$4.11212 \cdot 10^{11}$		4	462.18		4	$4.23 \cdot 10^{11}$
5	$3.64373 \cdot 10^{11}$		5	$4.07558 \cdot 10^{11}$		5	462.23074		5	$3.84 \cdot 10^{11}$
6	$3.21764 \cdot 10^{11}$		6	$3.54786 \cdot 10^{11}$		6	463.0227		6	$2.87 \cdot 10^{11}$
7	$3.17794 \cdot 10^{11}$		7	$3.4991 \cdot 10^{11}$		7	463.1021		7	$3.3 \cdot 10^{11}$
8	$3.14441 \cdot 10^{11}$		8	$3.45798 \cdot 10^{11}$		8	463.17		8	$3.57 \cdot 10^{11}$
9	$2.79676 \cdot 10^{11}$		9	$3.03478 \cdot 10^{11}$		9	463.9231		9	$2.88 \cdot 10^{11}$
10	$2.78896 \cdot 10^{11}$		10	$3.02536 \cdot 10^{11}$		10	463.9411		10	$2.52 \cdot 10^{11}$
11	$2.72118 \cdot 10^{11}$		11	$2.94359 \cdot 10^{11}$		11	464.1		11	$3.05 \cdot 10^{11}$
12	$2.46911 \cdot 10^{11}$		12	$2.64163 \cdot 10^{11}$		12	464.7303		12	$2.17 \cdot 10^{11}$
13	$2.4103 \cdot 10^{11}$		13	$2.57171 \cdot 10^{11}$		13	464.8872		13	$2.48 \cdot 10^{11}$
14	$2.34367 \cdot 10^{11}$		14	$2.49271 \cdot 10^{11}$		14	465.07		14	$2.69 \cdot 10^{11}$
15	$2.13915 \cdot 10^{11}$		15	$2.25194 \cdot 10^{11}$		15	465.6677		15	$1.85 \cdot 10^{11}$

X(T) is a better fit at important data points (i.e. operational temperature range) even though it does not have as good of an overall correlation factor. This equation will be used for ANSYS model properties data for viscosity.

Figure A-5. Viscosity curve fit (3)

This document establishes regression curve fits for extrapolating density, thermal conductivity, and specific heat of the SRL-411/AC18647H borosolicate glass composition.

1. Density

   a. Logistic Regression Curve Fit Attempt

density :=

	0	1
0	$2.2 \cdot 10^1$	$2.61 \cdot 10^3$
1	$1 \cdot 10^2$	$2.6 \cdot 10^3$
2	$2 \cdot 10^2$	$2.6 \cdot 10^3$
3	$3 \cdot 10^2$	$2.59 \cdot 10^3$
4	$4 \cdot 10^2$	$2.58 \cdot 10^3$
5	$5 \cdot 10^2$	$2.56 \cdot 10^3$

$\rho := density^{\langle 1 \rangle}$ $T := density^{\langle 0 \rangle}$

$a := intercept(T, \rho)$

$a = 2661.069007$

$b := \dfrac{mean(T)}{1000}$ $b = 0.601692$

$guess := \begin{pmatrix} a \\ b \\ -0.00001 \end{pmatrix}$ $x := 22, 42 .. 1222$

$L := lgsfit(T, \rho, guess)$

$L = \begin{pmatrix} 2697.922414 \\ 0.027845 \\ -0.001566 \end{pmatrix}$

This is not a good fit, as can be seen from the curve trace. The data is trending flat but the curve does not follow this trend.

$\rho T(x) := \dfrac{L_0}{1 + L_1 \cdot exp(-L_2 \cdot x)}$
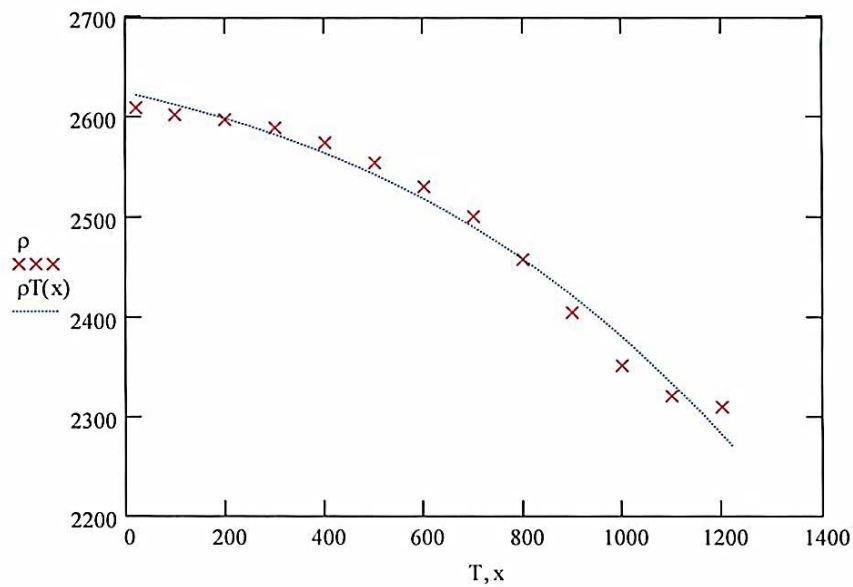
Figure A-6. Density curve fit (1).

b. Conduct Polynomial Regression on last four data points to get extrapolated data.

dentrunc :=

	0	1
0	900	2405
1	1000	2352
2	1100	2321
3	1200	2310

$T := dentrunc^{\langle 0 \rangle}$ $\rho := dentrunc^{\langle 1 \rangle}$

$g1 := exp\left(intercept\left(T, \overrightarrow{ln(\rho)}\right)\right)$ $g1 = 2701.748587$

$g2 := exp\left(slope\left(T, \overrightarrow{ln(\rho)}\right)\right)$ $g2 = 0.999866$

$Guess := \begin{pmatrix} g1 \\ \dfrac{g2}{1000} \\ 0 \end{pmatrix}$

$E := expfit(T, \rho, Guess)$ $E = \begin{pmatrix} 4.844363 \times 10^4 \\ -0.006758 \\ 2294.354471 \end{pmatrix}$

$x := min(T) .. max(T)$ $Rho(x) := E_0 \cdot exp\left(E_1 \cdot x\right) + E_2$
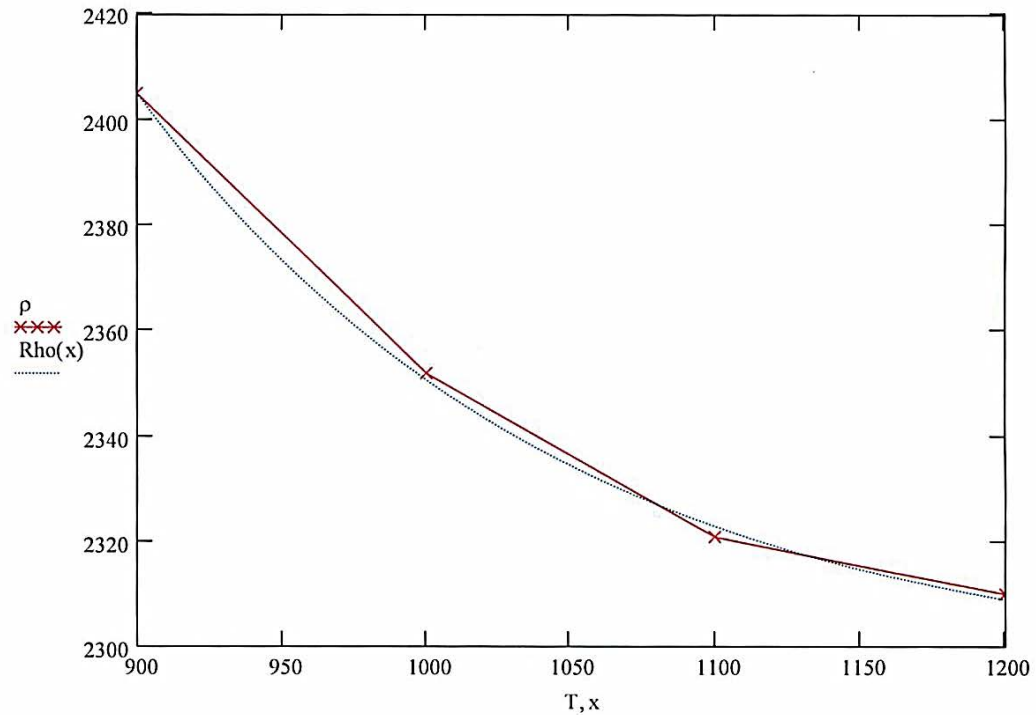
$corr\left(\overrightarrow{Rho(T)}, \rho\right) = 0.999366$

Figure A.7. Density curve fit (2).

Plot of extrapolated data for density

$xext := 900, 950 .. 2000$

The equation of the curve is:

$\rho(T) = (4.84436 \times 10^4) * e^{(-6.75765 \times 10^{-3}) * T} + 2294.35$
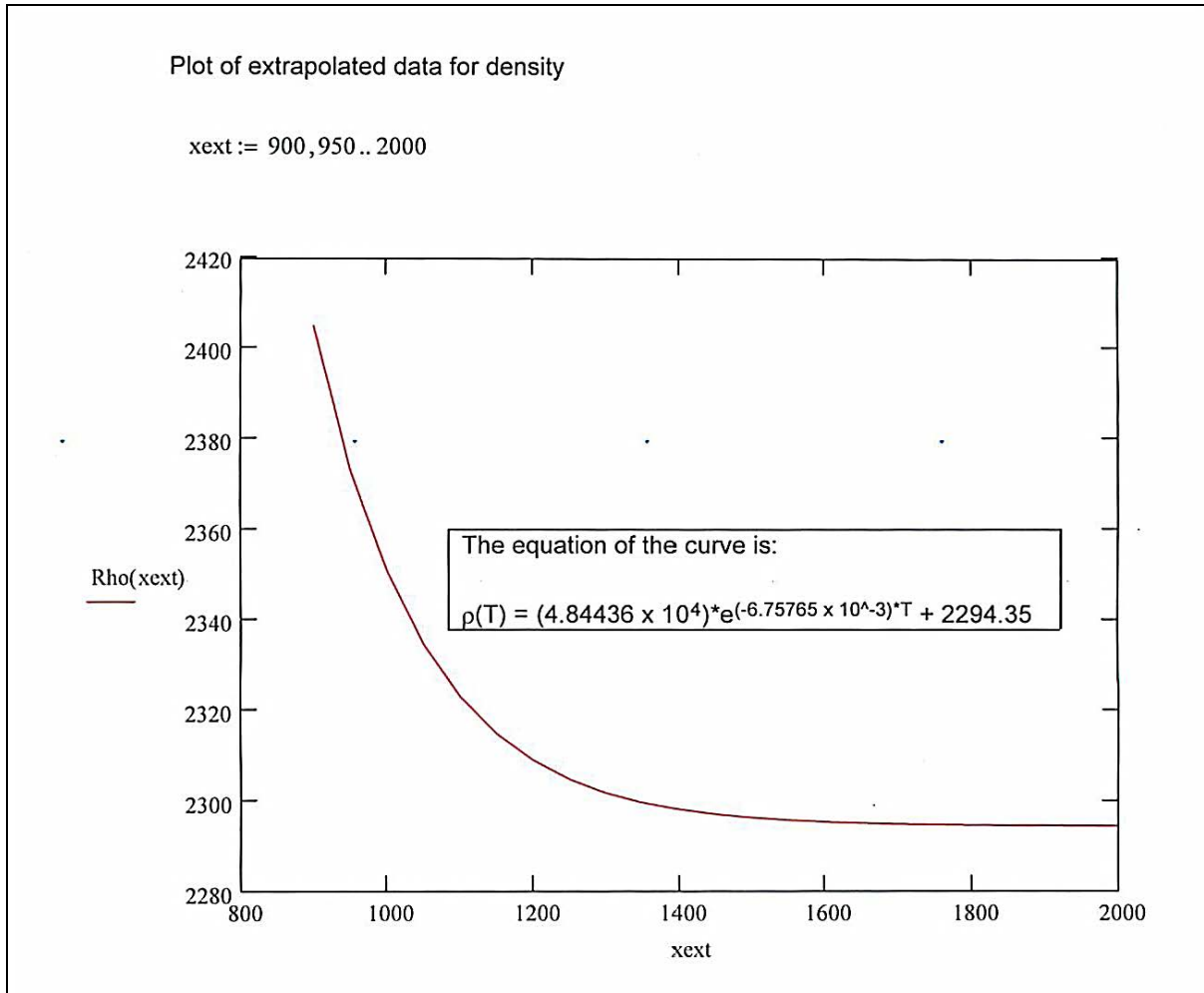
Figure A.8. Density curve fit (3).

2. Specific Heat

a. Plot of actual data with no curve fit

spheat :=

	0	1
0	22	920
1	100	1000
2	200	1100
3	300	1180
4	400	1270
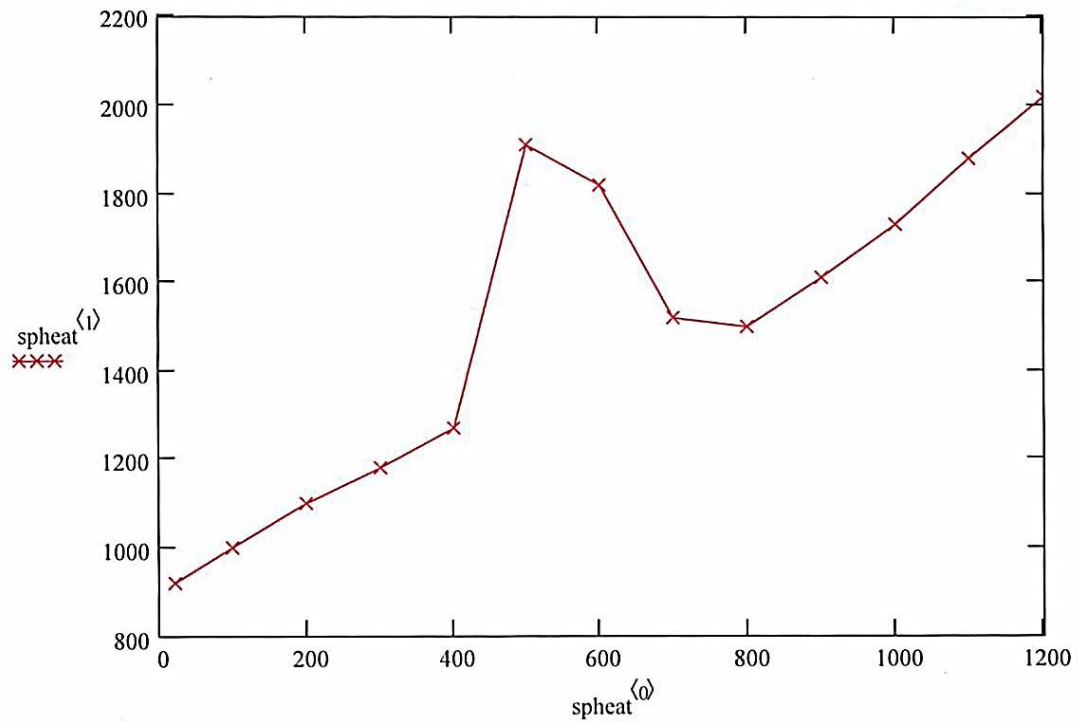
It is clear that no single curve, with exception of a cubic spline will fit this data. Therefore, the approach is to take the last three or four data points and extrapolate one data point, based on the measured trend and fit a second order polynomial to these data points.

Figure A-9. Specific Heat curve fit (1).

b. Extrapolation of the specific heat data using one extrapolated data point and a second order polynomial curve fit.

sphtrunc :=

	0	1
0	1000	1730
1	1100	1880
2	1200	2020
3	1300	2140

$T := \text{sphtrunc}^{\langle 0 \rangle}$ $C_p := \text{sphtrunc}^{\langle 1 \rangle}$

$x := \min(T) .. \max(T)$

$Z := \text{regress}(T, C_p, 2)$

$SpH(x) := \text{interp}(Z, T, C_p, x)$

$$Z = \begin{pmatrix} 3 \\ 3 \\ 2 \\ -615.5 \\ 3.095 \\ -7.5 \times 10^{-4} \end{pmatrix}$$
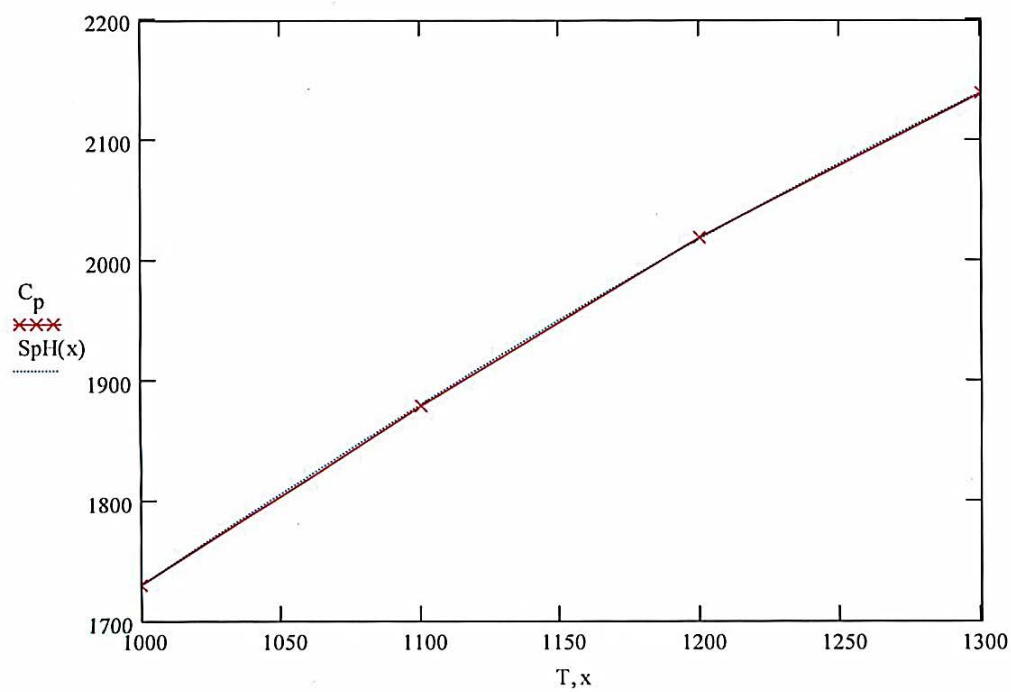
Figure A-10. Specific Heat curve fit (2).

Plot of extrapolated data curve for specific heat

$xext := 1000, 1050 .. 2000$

The equation of the curve is:

$C_p(T) = (-7.5 \times 10^{-4})*T^2 + 3.095*T - 615.5$

$corr\left(\overrightarrow{SpH(T)}, C_p \right) = 0.999973$
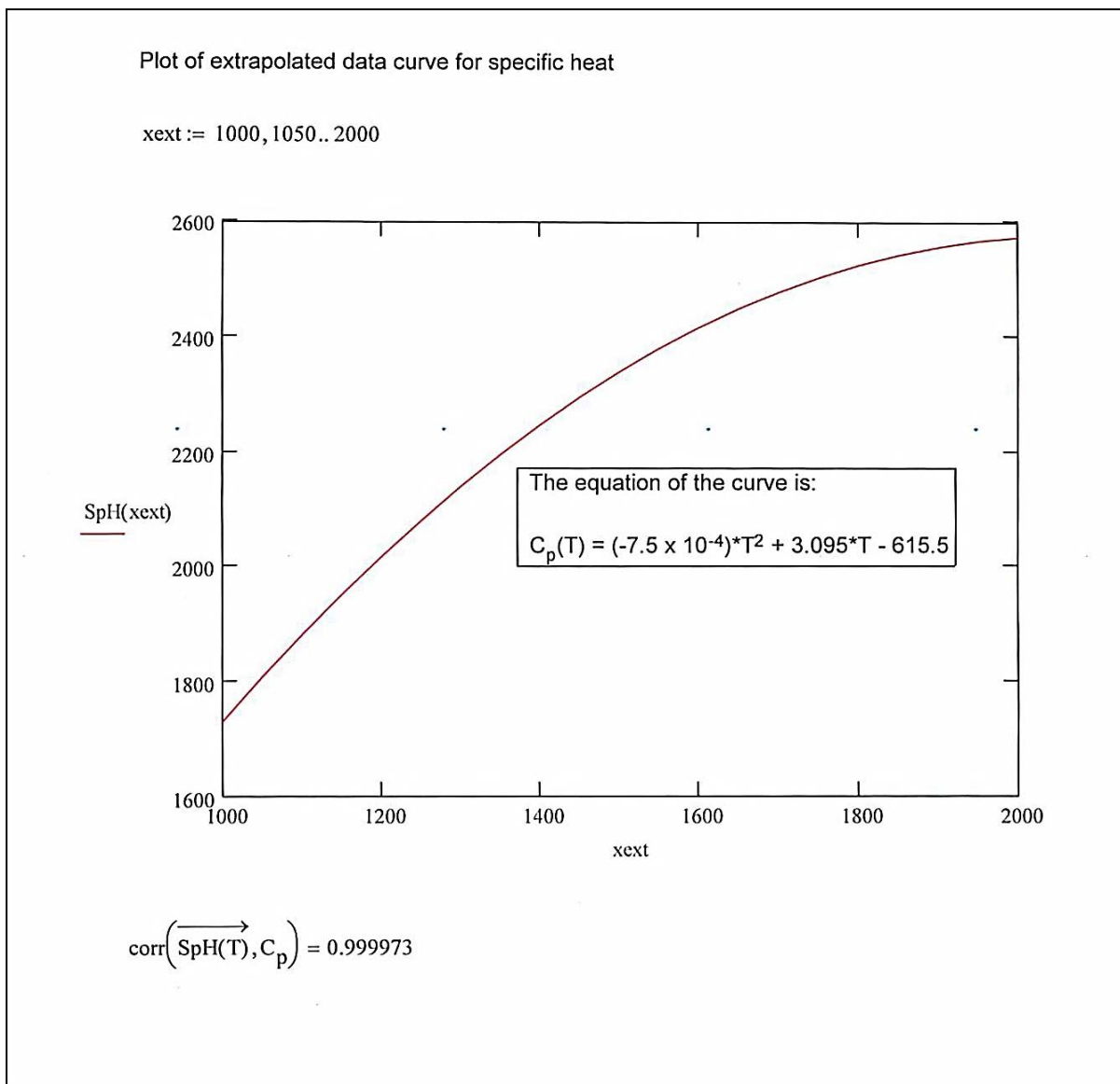
Figure A.11. Specific Heat curve fit (3).

3. Thermal Conductivity

a. Plot of actual thermal conductivity data

thcond :=

	0	1
0	22	1.05
1	100	1.11
2	200	1.16
3	300	1.16
4	400	1.22
5	500	1.63
6	600	1.17
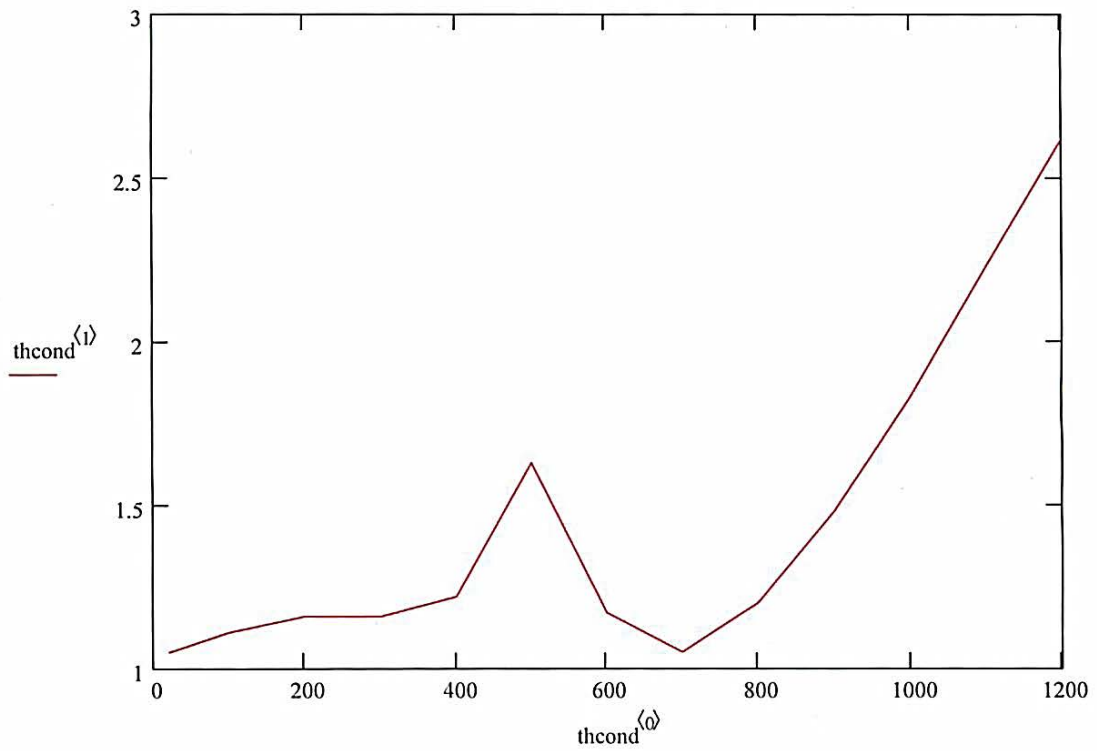
It is clear that no single curve, with exception of a cubic spline will fit this data. Therefore, the approach is to take the last three or four data points and extrapolate one data point, based on the measured trend and fit a second order polynomial to these data points.

Figure A.12. Thermal Conductivity curve fit (1).

b. Extrapolation of the thermal conductivity data using one extrapolated data point and a second orderpolynomial curve fit.

tcontrunc :=

	0	1
0	$1 \cdot 10^3$	$1.83 \cdot 10^0$
1	$1.1 \cdot 10^3$	$2.23 \cdot 10^0$
2	$1.2 \cdot 10^3$	$2.62 \cdot 10^0$
3	$1.3 \cdot 10^3$	$2.97 \cdot 10^0$

$T := \text{tcontrunc}^{\langle 0 \rangle}$

$k := \text{tcontrunc}^{\langle 1 \rangle}$

$x := \min(T) \, .. \, \max(T)$

$Z := \text{regress}(T, k, 2)$

$\text{ThC}(x) := \text{interp}(Z, T, k, x)$

$$Z = \begin{pmatrix} 3 \\ 3 \\ 2 \\ -3.6065 \\ 0.006685 \\ -1.25 \times 10^{-6} \end{pmatrix}$$
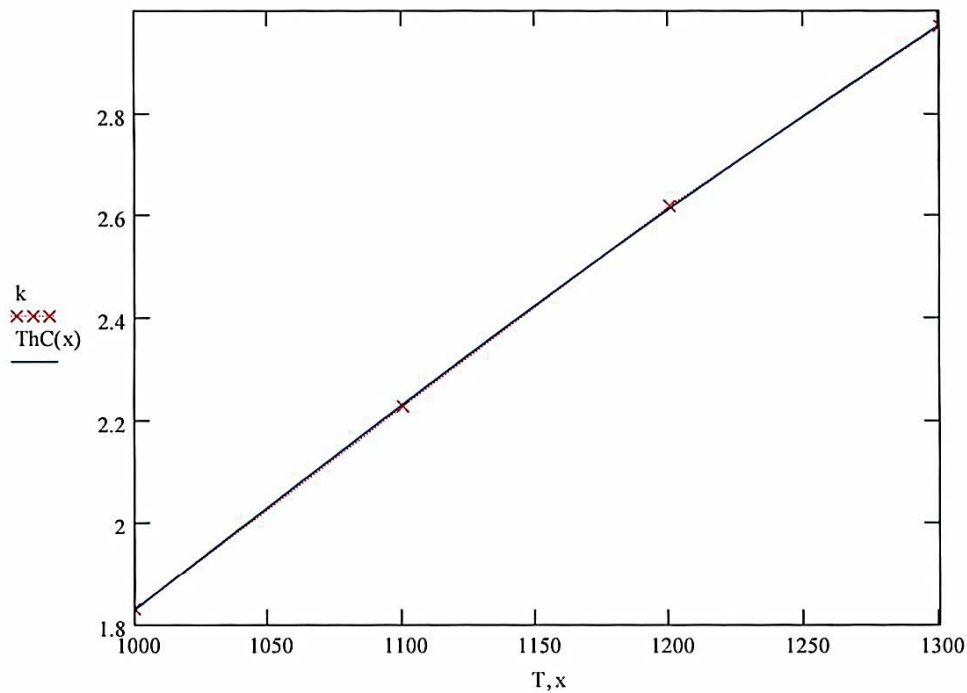
Figure A.13. Thermal Conductivity (2).

Plot of extrapolated data curve for thermal conductivity

ThC(xext)

The equation of the curve is:

$k(T) = (-1.25 \times 10^{-6})*T^2 + (6.685 \times 10^{-3})*T - 3.6065$

xext

$\mathrm{corr}\left(\overrightarrow{\mathrm{ThC(T)}}, k\right) = 0.999969$
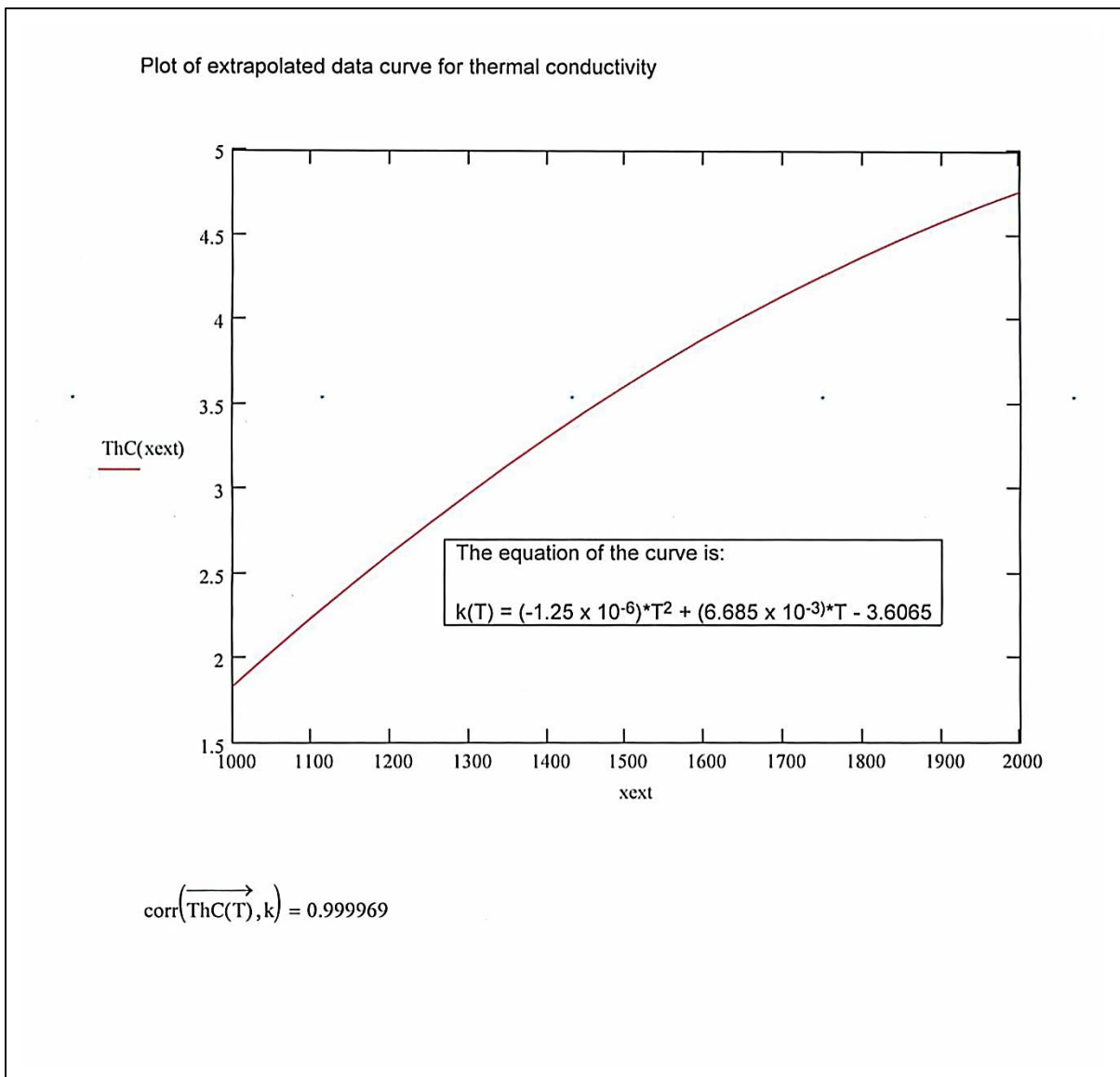
Figure A-14. Thermal Conductivity curve fit (3).

APPENDIX B

ANSYS MultiPhysics Code

Cold Crucible Induction Melter with Dual Frequency Heating Capability

and Melt Initiation Simulation

```
! STEP 1


finish     !! Var. U=const during all start

/clea

/FILENAME, !! beginning of melt start-up, with ring inside

/PREP7

/nerr,0

 mm=1          ! mesh step reduction factor

 freq1=1.76e6   ! frequency
 Uind=5000      ! voltage on inductor
 AMPL1=Uind
 PHAS1=0
 rho1=2e-8
 w_ind=2        ! number of turns on inductor
 g=0.6          ! metal-to-air ratio (inductor geometry)

 step1=20       ! time step
 tinc=100       ! time increment  for harmonic analysis

!***** beginning of the melt ******************

  ftime=500       ! final time of the process
  time=0          ! sets the time for initial load step
  timein=tinc     ! previous time of the process, lower-range value TINC



!***********************************************

 T_init=20.0
 al_side=2.0e4    ! heat transfer factors (alpha) on side
 al_bot=1e2
 T_env=20.0       ! environment temperature
 C_s=5.67e-8      ! Stefan-Boltzmann constant
 eps=0.5          ! emissivity factor for top surface
 delt=1e-9        !allowable error of the calculated temperature (convergence of process)

!************************************************

 emunit,mks
 pi=3.1416
```

```
R2=0.15      ! melt pool radius
Z2n=0.02     ! melt pool bottom coordinate
Z2km =0.18    ! melt pool top coordinate
R1n=0.16      ! large inductor  inner radius
R1k=0.162     ! large inductor external radius
Z1n=0.00      ! large inductor bottom coordinate
Z1k=0.18      ! large inductor top coordinate
R2sl=0.02     ! drain radius
Z2sl=0.023    ! drain height

R1sl_1n=0.034    !small inductor (turn 1) inner radius
R1sl_1k=0.040    !small inductor (turn 1) outer radius
Z1sl_1n=-0.022   !small inductor (turn 1) bottom location
Z1sl_1k=-0.016   !small inductor (turn 1) top location

Re=0.35      ! Shield radius (calculation space)
Zen=-.15     ! shield bottom
Zek=0.30     ! shield top

R2fl=0.08        ! flange radius
Zist=-0.02       ! Small inductor spacing factor
Z2ist=Z2n+Zist   !!on the bottom of the melt pool


Rarc1=R2sl     ! drain radius at top
Zarc1=-0.022
Rarc2=0.05     ! drain radius at bottom
Zarc2=Z2ist
Rint=0.030     ! drain radius at intermediate point
Zint=-0.010

R21n=0.09    ! starter ring outer radius
R21k=0.13    ! starter ring inner radius
Z21n=0.04    !starter ring upper surface
Z21k=0.08    !starter ring lower surface

  Abig=(R1k-R1n)*(Z1k-Z1n) ! large inductor face area

!****************** element emag ********************

  et,1,plane13,,,1     ! melt pool, drain
  et,2,plane13,,,1      ! ring
  et,3,plane13,,,1      ! airspace
  et,4,PLANE53,3,,1,     ! big inductor (3-STRANDED,1-without )
  et,5,plane13,6,,1      ! small inductor (for drain)
```

```
ET,6,CIRCU124,4,0     ! 4-power source,0-HARM ANALYS
ET,7,CIRCU124,5       ! 6-massive 5- stranded wire

R,1,AMPL1,PHAS1       ! REAL CONST voltage source
R,2,Abig,w_ind,,,g     ! REAL CONST external circuit
R,3,1
```

!****************** properties emag ***************

```
mp,murx,1,1   ! magnetic relative permeability for melt pool, drain
mp,murx,2,1   ! starter ring
mp,murx,3,1   ! airspace
mp,murx,4,1   ! large inductor
mp,murx,5,1   ! small inductor


mptemp
mptemp,1,0,100,500,600,700,800          ! electrical resistivity
mptemp,7,900,1000,1100,1200,1300,1400    !!for melt pool
mptemp,13,1500,1600,1700,1800,1900,2000

mpdata,rsvx,1,1,929,929,929,9.28,0.85,0.24
mpdata,rsvx,1,7,0.11,6.47E-2,4.4E-2,3.29E-2,2.62E-2,2.18E-2
mpdata,rsvx,1,13,1.873E-2,1.65E-2,1.48E-2,1.35E-2,1.25E-2,1.16E-2

mp,rsvx,2,1.0E-4      ! starter ring
mp,rsvx,3,1.0e+18     ! airspace
mp,rsvx,4,2.0E-8      ! large inductor
mp,rsvx,5,2.0E-8      ! small inductor
```

!*************** Geometry *****************************

```
  n,1
  n,2,Re+0.05,0.020
  n,3,Re+0.05,-0.020  !nodes for external circuit

k,1,0,-Z2sl
k,2,R2sl,-Z2sl
k,3,Rarc1,Zarc1
k,4,Rarc2,Zarc2
k,5,R2fl,Z2ist
k,6,R2,Z2ist
k,7,Rint,Zint          ! intermediate arc point
k,8,0,Z2n
k,9,0,Z2ist
k,10,R2fl,Z2n
k,11,r2,Z2n
```

```
k,12,R2fl,Z2km
k,13,0,Z2km
k,14,R2,Z2km

l,1,2,14*mm          !1
l,2,3,1*mm           !2
larc,3,4,7           !3  - drain
l,9,4,28*mm          !4
l,9,1,24*mm          !5
al,all
lsel,none

lsel,s,,,4
l,9,8,10*mm          !6
l,8,10,30*mm         !7
l,10,5,10*mm         !8  - melt area above the drain
l,5,4,30*mm          !9
al,all
lsel,none

lsel,s,,,8
l,5,6,30*mm          !10
l,6,11,10*mm         !11 - bottom melt layer
l,11,10,30*mm        !12
al,all
lsel,none

lsel,s,,,12
l,11,14,46*mm        !13
l,14,12,40*mm        !14 - right part of the melt
l,12,10,46*mm        !15
al,all
lsel,none

lsel,s,,,15
lsel,a,,,7
l,12,13,40*mm        !16
l,13,8,46*mm         !17 - left part of the melt
al,all

aglue,all

lsel,s,,,3
lesize,all,,,35*mm,
alls

ptxy,R1n,Z1n,R1k,Z1n,R1k,Z1k,R1n,Z1k         ! large inductor
```

```
poly

ptxy,0,Zen,0,Zek,Re,Zek,Re,Zen              ! airspace
poly

rectng,R1sl_1n,R1sl_1k,Z1sl_1n,Z1sl_1k       ! small inductor

rectng,R21n,R21k,Z21n,Z21k                   ! starter ring

lsel,s,,,29,32
lesize,all,,,20*mm

lsel,s,,,19
lsel,a,,,21
lesize,all,,,46*mm

aovlap,all
numcmp,all

alls

!/eof

!************** Associates element attributes with the selected areas ***

 asel,s,area,,1      ! for melt pool
 asel,a,area,,2       ! mat,,type elem
 asel,a,area,,3
 asel,a,area,,4
 asel,a,area,,8
 aatt,1,,1

 asel,s,area,,7       ! for ring
 aatt,2,,2            ! mat,real,type elem

 asel,s,area,,9       ! for airspace
 aatt,3,,3

 ASEL,S,AREA,,5        ! for large inductor
 AATT,4,2,4

 asel,s,area,,6    ! for small inductor
 aatt,5,,5

 ASUM

*GET,Abig,AREA,,AREA
```

```
allsel,all

!/eof

!****** Meshing ************************************************

  lsel,s,loc,y,Zen        ! Shield (bottom)
  lsel,r,loc,x,0,Re
  lesize,all,,,60*mm

  lsel,a,loc,y,Zek        ! Shield (top)
  lsel,r,loc,x,0,Re
  lesize,all,,,60*mm

  lsel,s,loc,x,Re         ! Shield (side)
  lsel,r,loc,y,Zen,Zek
  lesize,all,,,70*mm

  lsel,s,loc,x,0          ! melt pool radius at bottom
  lsel,r,loc,y,Zen,Z2n
  lesize,all,,,36*mm

  lsel,s,loc,x,0          ! melt pool radius at top
  lsel,r,loc,y,Z2k,Zek
  lesize,all,,,30*mm


  mshape,0,2d
  mshkey,2
  amesh,all
  allsel,all

!/eof

!***** electromagnetic task *****************************************
!***************** external circuit ***************************

  N1=NODE(R1n,0,0)

  TYPE,6   ! number of FE (ET124 - voltage source)
  REAL,1   ! 1 - number R
  E,2,1,3  ! nodes

  TYPE,7   ! ET124 - inductor
  real,3
  E,2,1,n1 ! node N1 is switched on
```

```
ESEL,S,MAT,,4
NSLE,S
CP,1,CURR,ALL
CP,2,EMF,ALL

finish

/solu

        lsel,s,loc,y,Zen     ! select boundary emag task
        lsel,a,loc,y,Zek
        lsel,a,loc,x,Re
 nsll,s,1
 d,all,az,0,0              ! boundary condition, Az=0

        lsel,s,loc,x,0
 nsll,s,1
 d,all,az,0,0              ! boundary condition, Az=0
 alls

 d,3,volt,0
 alls

!/eof

 antype,harmic            ! type of analysis
 harfrq,freq1             ! frequency
 OUTPR,ALL,ALL
 HROUT,On

  allsel,all

!   solve

 physics,write,emag1       ! write emag1 physics file

finish

!/eof

!/post1              ! review emag source, delete comment
!   set,last
!   esel,s,mat,,2
!   esel,a,mat,,1
!   plesol,jheat
!finish
```

```
!/eof

!***** flotran CFD ****************************
!**********************************************

/prep7

 lclear,all
 et,1,fluid141,,,1
 et,2,fluid141,,,1
 et,3,0
 et,4,0
 et,5,0
 et,6,0
 et,7,0

 cpdele,all

finish

/solu

 toffst,273
 fldata14,TEMP,NOMI,T_init  ! initial temperature

!********************** properties mat. 1 (glass) option ************
! ****************************************************************

 fldata12,PROP,DENS,16
 fldata13,VARY,DENS,1
 fldata12,PROP,VISC,16
 fldata13,VARY,VISC,1
 fldata12,PROP,COND,16
 fldata13,VARY,COND,1
 fldata12,PROP,SPHT,16
 fldata13,VARY,SPHT,1

!****************************************************************

 mptemp
 mptemp,1,0,100,200,300,400,500
 mptemp,7,600,700,800,900,1000,1100
 mptemp,13,1200,1300,1400,1500,1700,2000

 mpdata,dens,1,1,2610,2603,2598,2590,2575,2555   !Density
 mpdata,dens,1,7,2531,2501,2458,2405,2352,2321
```

mpdata,dens,1,13,2310,2301.76,2298.12,2296.26,2294.84,2294.41

fldata7,PROT,DENS,TABLE

!!**

mptemp   !Viscosity
mptemp,1,0,100,200,300,400,500
mptemp,7,600,700,800,900,1000,1100
mptemp,13,1200,1300,1400,1500,1700,2000

mpdata,visc,1,1,3.0e5,2.0e5,1.6e5,8.2e4,4.1e3,2.0e3
mpdata,visc,1,7,10.4e3,5.426e3,3.752e2,6.163e1,16.68,6.191
mpdata,visc,1,13,2.857,1.535,0.921,0.601,0.307,0.150

fldata7,PROT,VISC,TABLE

!**

mptemp
mptemp,1,0,100,200,300,400,500
mptemp,7,600,700,800,900,1000,1100
mptemp,13,1200,1300,1400,1500,1700,2000

mpdata,kxx,1,1,1.05,1.11,1.16,1.16,1.22,1.63,   !Thermal conductivity
mpdata,kxx,1,7,1.17,1.05,1.20,1.48,1.83,2.23
mpdata,kxx,1,13,2.615,2.972,3.30,3.61,4.145,4.76

fldata7,PROT,COND,TABLE

!**

mptemp
mptemp,1,0,100,200,300,400,500
mptemp,7,600,700,800,900,1000,1100
mptemp,13,1200,1300,1400,1500,1700,2000

mpdata,c,1,1,920,1000,1100,1180,1270,1910   !Specific heat
mpdata,c,1,7,1820,1520,1500,1610,1730,1881
mpdata,c,1,13,2018,2140,2247,2339,2478,2474

fldata7,PROT,SPHT,TABLE

!********************* properties mat. 2 (starter ring) **************
!**

```
  mp,dens,2,2200      !these properties are for graphite
  mp,visc,2,2.e5
  mp,kxx,2,35
  mp,c,2,1600
```

```
!****************************************************************
!*********************** convergence option **********************
```

```
  fldata1,solu,tran,1
  fldata1,solu,FLOW,1
  fldata1,solu,TEMP,1

  fldata4,time,step,step1     ! time step size
  fldata4,time,bc,0,          ! similarly KBC ,1-ramped,0-stepped (default)

  fldata4,time,NUMB,tinc/step1
  fldata4,time,TEND,ftime
  fldata4,time,GLOB,10,
  fldata4,time,VX,1e-4
  fldata4,time,VY,1e-4,
  fldata4,time,VZ,0.001,

  fldata4,TIME,OVER,0
  fldata4,TIME,APPE,1.0e6
  fldata4,TIME,SUMF,1.0e6

  fldata18,METH,TEMP,4
  fldata18,METH,PRESS,4

  fldata25,RELX,VX,0.5,        ! solution and property relaxation factors
  fldata25,RELX,VY,0.5,
  fldata25,RELX,PRES,0.8,
  fldata25,RELX,TEMP,0.8,

  fldata25,RELX,DENS,1,
  fldata25,RELX,SPHT,1,
  fldata25,RELX,VISC,1,
  fldata25,RELX,COND,1,

  fldata31,capp,VELO,1         ! Specifies dependent variable caps
  fldata31,capp,TEMP,1
  fldata31,capp,PRES,1

  fldata31,capp,UMIN,-1e+01
  fldata31,capp,UMAX,1e+01
  fldata31,capp,VMIN,-1e+01
  fldata31,capp,VMAX,1e+01
```

```
  fldata31,capp,TMIN,-3e+03
  fldata31,capp,TMAX,3e+03
  fldata31,capp,PMIN,-1e+020
  fldata31,capp,PMAX,1e+020


!*************************** Controls restart options ************

fldata32,REST,NSET,0
fldata32,REST,ITER,0
fldata32,REST,LSTP,0,
fldata32,REST,TIME,0
fldata32,REST,CLEAR,F
fldata32,REST,RFIL,0
fldata32,REST,WFIL,1
fldata32,REST,OVER,0


!**************** boundary condition (BC) ************************

  lsel,s,loc,x,0           ! melt pool axis
  lsel,r,loc,y,-Z2sl,Z2km
  nsll,s,1
    d,all,vx,0

  lsel,s,loc,x,R2          ! melt pool side
  lsel,r,loc,y,Z2ist,Z2km
  nsll,s,1
    sf,all,conv,al_side,T_env
    d,all,vx,0
    d,all,vy,0

  lsel,s,loc,y,Z2km         ! melt pool top
  lsel,r,loc,x,0,R2
    STEF,C_s
  nsll,s,1
    sf,all,rad,eps,T_env
    d,all,vy,0

  lsel,s,,,1              ! drain bottom
  lsel,a,,,9
  lsel,a,,,10
  nsll,s,1
    sf,all,conv,al_bot,T_env
    d,all,vx,0
    d,all,vy,0

  lsel,s,,,2
  nsll,s,1
```

```
   sf,all,conv,al_bot,T_env
    d,all,vx,0
    d,all,vy,0

 lsel,s,,,3
 nsll,s,1
    sf,all,conv,al_bot,T_env
    d,all,vx,0
    d,all,vy,0

 allsel,all
 acel,0,9.81,0,          ! gravity
 PHYSICS,WRITE,fluid, , ,

 save

finish

alls

!/eof

!***************** solution **************
!*****************************************
!*****************************************

  n_tinc= ftime/tinc
  *dim,P22,array,n_tinc    ! array of the POWER in melt
  *dim,P2Ri,array,n_tinc   ! array of the POWER in starter ring

*do,i,timein/tinc,ftime/tinc
        time=time+tinc

 physics,read,emag1

/solu

  *if,i,eq,1,then

    esel,s,mat,,1
    esel,a,mat,,2
    nsle,s,all
    fldada14,temp,nomi,T_init    !initial temperature

  *else

    ldread,temp,last,,,,,rfl
```

```
    *endif

   allsel,all

   solve

 fini

alls

!/eof

!**************power in the melt ****************

 /post1

   SET,LAST

      asel,s,mat,,1
      esla,s
      nsle,s

    *get,nmin,elem,0,num,min
    *get,nmax,elem,0,num,max
    *get,n_elem,elem,0,count

    *dim,vv1,array,n_elem     ! array of melt volume FEs
    *dim,w01,array,n_elem     ! array of volumetric sources

    p22big=0
    nn=0

    *do,i2,nmin,nmax,1

     *if,esel(i2),eq,1,then

       nn=nn+1

       *get,vv1(nn),elem,i2,volu
       *get,w01(nn),ELEM,i2,Jheat, ! Jheat sources written into array w01

      *endif                ! Jheat are volumetric heat sources from ANSYS

      p22big=p22big+w01(nn)*vv1(nn) ! power from voltage set on inductor U_ind

    *enddo
```

```
    p22(i)=p22big

!************** power in the starter ring ***********

! /post1

!    SET,LAST

     asel,s,mat,,2
     esla,s
     nsle,s

   *get,nmin,elem,0,num,min
   *get,nmax,elem,0,num,max
   *get,n_elem,elem,0,count

   *SET,vv1,
   *SET,w01,

   *dim,vv1,array,n_elem     ! array of melt volume FEs
   *dim,w01,array,n_elem     ! array of volumetric sources

   p22Ri=0
   nn=0

   *do,i2,nmin,nmax,1

     *if,esel(i2),eq,1,then

       nn=nn+1

       *get,vv1(nn),elem,i2,volu
       *get,w01(nn),ELEM,i2,Jheat, ! Jheat written into array w01

     *endif                ! Jheat are volumetric sources in ANSYS

     p22Ri=p22Ri+w01(nn)*vv1(nn)   ! power from voltage set on inductor U_ind

   *enddo

   p2Ri(i)=p22Ri

  finish

!**************************************************
```

```
physics,read,fluid

/assign,esav,fluid,esav
/assign,emat,fluid,emat

 /solu

    *if,i,gt,1,then

       fldata1,solu,tran,1

    *else

       esel,s,mat,,1
       esel,a,mat,,2

       nsle,s,all

       fldata14,temp,nomi,T_init    !initial temperature

    *endif

    time,time

    esel,s,mat,,1
    esel,a,mat,,2

    ldread,hgen,,,,2,,rst   !apply joule heating load from emag

    solve

  finish

 /assign,esav
 /assign,emat

    *SET,vv1,
    *SET,w01,

*enddo
save

!***************************************************
!**************** display temperatures ****************

/post1
```

```
    set,last

    plnsol,temp

*ASK,temperature,'  press OK to continue '

!******************* graph TEMP, path along melt pool top ******

    path,weg2t,2,30,20,     ! path between two points...
    ppath,1,,0,Z2k,0        ! point at the bottom melt pool by R=0
    ppath,2,,R2,Z2k,0       ! point at the bottom melt pool by R=R2
    path,stat

    pdef, ,TEMP            ! Interpolates TEMP onto a path

  /pbc,path, ,0           ! Show path on display

    plpath,TEMP            ! Display path TEMP along top

*ASK,TEMP_along_melt_pool_top,'   press OK to continue '

!******************* graph TEMP, path along melt pool bottom ****

    path,weg2dt,2,30,20,    ! path between two points...
    ppath,1,,0,Z2n,0        ! point at the top drain by R=0
    ppath,2,,R2,Z2n,0       ! point at the top drain by R=R2
    path,stat

    pdef, ,TEMP            ! Interpolates TEMP onto a path

  /pbc,path, ,0           ! Show path on display

    plpath,TEMP            ! Display path TEMP along bottom

*ASK,TEMP_along_bottom,'   press OK to continue '

!***************** graph heat flux path along melt pool side ******

    path,weg2,2          ! path between two points...
    ppath,1,,R2,Z2n,0      ! point at the bottom melt pool
    ppath,2,,R2,Z2k,0      ! point at the top melt pool

    pdef,  ,HFLU          ! Interpolates hflux onto a path

  /pbc,path, ,0           ! Show path on display

    plpath,HFLU            ! Display path hflux on a graph
```

```
*ASK,hflux_through_melt_pool_side,' press OK to continue '

!***************** graph heat flux path along melt pool bottom ***

    path,weg21,2        ! path between two points...
    ppath,1,,0,Z2n,0     ! point at the bottom melt pool R=0
    ppath,2,,R2,Z2n,0      ! point at the bottom melt pool R=R2

    pdef, ,HFLU          ! Interpolates hflux  onto a path

   /pbc,path, ,0         ! Show path on display

    plpath,HFLU           ! Display path TFY along bottom

*ASK,flux_through_melt_pool_bottom,' press OK to continue '

!******** heat losses from the melt pool side *********************
!******** calculate from mean TEMP and heat transfer factor (alpha) ***

    path,weg4al,2,30,20,   ! path along melt pool surface
    ppath,1,,R2,Z2n,0      ! point at the bottom melt pool
    ppath,2,,R2,Z2k,0      ! point at the top melt pool
    pdef,TEMP,TEMP

   /pbc,path, ,0         ! Show path on displays

    pcalc,intg,ploss2al,TEMP,s                ! integrates along path

    *get,ploss2al,path,,last,ploss2al

    m_Ts =ploss2al/(Z2k-Z2n)              ! mean temp
    Ps_ALP=al_side*(m_Ts-T_env)*2*pi*R2*(Z2k-Z2n)  ! summary losses from alpha
    m_Ps=Ps_ALP/(2*pi*R2*(Z2k-Z2n))

!******** heat losses from the melt pool bottom *******************
!******** calculate from mean TEMP and heat transfer factor (alpha) ***

    path,weg52alp,2,,20,   ! path along melt pool surface
    ppath,1,,0,Z2n,0       ! point  by R=0
    ppath,2,,R2,Z2n,0      ! point  R=R2
    pdef,TEMP,TEMP         ! Interpolates TEMP onto a path

   /pbc,path, ,0         ! Show path on displays

    pcalc,mult,prod11,TEMP,s
```

```
   pcalc,intg,ploss31al,prod11,s,2*pi     ! integrates along path
  *get,ploss31al,path,,last,ploss31al

  m_Tb  =ploss31al/(pi*R2**2)          ! mean temp
  Pb_ALP=al_bot*(m_Tb -T_env)*(pi*R2**2)  ! summary losses from alpha
  m_Pb=Pb_ALP/(pi*R2**2)
```

!**

```
  Ploss_C=Ps_ALP+Pb_ALP !convection loss from melt pool
```

!******** mean TEMP on the top ***************************
!******** by RADIATION **********************************

```
  path,weg53mT,2,,20,   ! path along melt pool top
  ppath,1,,0,Z2k,0     ! point at R=0
  ppath,2,,R2,Z2k,0    ! point at R=R2
  pdef,TEMP,TEMP       ! Interpolates TEMP onto a path

 /pbc,path, ,0        ! Show path on displays

  pcalc,intg,intT,TEMP,s,    ! integrates along path

 *get,intT,path,,last,intT
  m_Tt=intT/R2
```

!***
!***
!*************** Calculate heat source and power ***********************
!***

```
    physics,read,emag1

    /assign,esav
    /assign,emat

 /solu

    ldread,temp,last,,,,,rfl

   allsel,all

   solve

 finish
```

!**********visualization of heat sources ****************

```
/post1

  set,last

   esel,s,mat,,1
   esel,a,mat,,2

   plesol,jheat

*ASK,Small_ind_source,' press OK to continue '

!**************************************************

 asel,s,mat,,1  !power in glass (without area where ring  is located)

 esla,s
 nsle,s

   *get,nmin,elem,0,num,min
   *get,nmax,elem,0,num,max
   *get,n_elem,elem,0,count

   *SET,vv1,
   *SET,w01,
   *SET,w02,
   *SET,w0,

   *dim,vv1,array,n_elem
   *dim,w02,array,n_elem

 p2glar=0
 nn=0

  *do,i2,nmin,nmax,1

    *if,esel(i2),eq,1,then

     nn=nn+1

      *get,vv1(nn),elem,i2,volu
      *GET,w02(nn),ELEM,i2,Jheat

     *endif

    p2glar=p2glar+w02(nn)*vv1(nn)
```

```
   *enddo

!****************************************************

 asel,s,mat,,2  !power in ring area

 esla,s
 nsle,s

   *get,nmin,elem,0,num,min
   *get,nmax,elem,0,num,max
   *get,n_elem,elem,0,count

   *SET,vv1,
   *SET,w01,
   *SET,w02,
   *SET,w0,

   *dim,vv1,array,n_elem
   *dim,w02,array,n_elem

 p2riar=0
 nn=0

   *do,i2,nmin,nmax,1

     *if,esel(i2),eq,1,then

       nn=nn+1

       *get,vv1(nn),elem,i2,volu
       *GET,w02(nn),ELEM,i2,Jheat

     *endif

     p2riar=p2riar+w02(nn)*vv1(nn)

   *enddo

!/eof

!****************************************************

 /out,LOSS_POWER

   *vwrite,n_tinc
   (2x,'number of the last load step, tinc =',e10.4)
```

```
*vwrite,p22big
(2x,'power in glass area before fluid work, W =',e10.4)

*vwrite,p22Ri
(2x,'power in the ring area before fluid work, W =',e10.4)

*vwrite,p2glar
(2x,'power in the glass area after fluid work, W =',e10.4)

*vwrite,p2riar
(2x,'power in the ring area after fluid work, W =',e10.4)

*vwrite,Ps_ALP
(2x,'heat loss from melt pool side, W =',e10.4)

*vwrire,Pb_ALP
(2x,'heat loss from melt pool bottom, ,W =',e10.4)

*vwrite, Ploss_C
(2x,'summ. heat loss from melt pool bot+side ,W =',e10.4)

*vWrite
('mean TEMP')

*vwrite,m_Ts
(2x,'mean TEMP on the melt pool side,Deg_C =',e10.4)

*vwrite,m_Tb
(2x,'mean TEMP on the melt pool bottom,Deg_C =',e10.4)

*vwrite,m_Tt
(2x,'mean TEMP on the melt pool top,Deg_C =',e10.4)

*vWrite
('mean heat flux (HF)')

*vwrite,m_Ps
(2x,'mean HF from the melt pool side,W/m**2 =',e10.4)

*vwrite,m_Pb
(2x,'mean HF from the melt pool bottom,W/m**2 =',e10.4)

*vWrite
('see also file *.pfl for power from top')

allsel
```

```
 /out

! /go
!      physics,read,fluid
!   set,last
!   plnsol,temp

finish
```

```
! STEP 2

fini     !! Var. U=const during all start

/clea

/FILENAME, !! continue melt start-up process, with starter ring removed

/PREP7

/nerr,0

 mm=1        ! mesh step reduction factor

 freq1=1.76e6   ! frequency
 Uind=2500      ! voltage on inductor
 AMPL1=Uind
 PHAS1=0
 rho1=2e-8
 w_ind=2       ! number of turns on large inductor
 g=0.6         ! metal-to-air ratio (inductor geometry)

 step1=50      ! time step
 tinc=200       ! time increment  for harmonic analysis

!***** restart *********************************

   timein=500   ! previous time of the process
   ftime=6000   ! final time of the process
   time=timein

!*************************************************

 T_init=20.0
 al_side=2.0e4    ! heat transter factors (alpha) on side
 al_bot=1e2
 T_env=20.0      ! environment temperature
 C_s=5.67e-8      ! Stefan–Boltzmann constant
 eps=0.5         ! emissivity factor for top
 delt=1e-9        !error of the calc.T (convergence of process)

!*************************************************

 emunit,mks
 pi=3.1416
```

```
R2=0.15        ! melt pool radius
Z2n=0.02       ! melt pool bottom
Z2km=0.18      ! melt pool top maximum coordinate
R1n=0.16       ! big inductor  inner radius
R1k=0.162      ! big inductor external radius
Z1n=0.00       ! big inductor bottom
Z1k=0.18       ! big inductor top
R2sl=0.02      ! drain radius
Z2sl=0.023     ! drain height

R1sl_1n=0.034    !small induct (turn 1) inner radius
R1sl_1k=0.040    !small induct (turn 1) external radius
Z1sl_1n=-0.022   !small inductor (turn 1) bottom
Z1sl_1k=-0.016   !small inductor (turn 1) top

Re=0.35     !Shield radius
Zen=-.15    !shield bottom
Zek=0.30     !shield top

R2fl=0.08        !flange radius
Zist=-0.02       !Small inductor source zone
Z2ist=Z2n+Zist    !!on the bottom melt pool


Rarc1=R2sl     ! drain round first point (lower)
Zarc1=-0.022
Rarc2=0.05     ! drain round last point (upper)r
Zarc2=Z2ist
Rint=0.030     ! drain round intermediate point
Zint=-0.010

R21n=0.09    !starter ring outer radius
R21k=0.13    !starter ring inner radius
Z21n=0.04
Z21k=0.08

  Abig=(R1k-R1n)*(Z1k-Z1n) ! large inductor face area

!****************** element emag ********************

 et,1,plane13,,,1      ! melt pool, drain
 et,2,plane13,,,1      ! ring
 et,3,plane13,,,1      ! airspace
 et,4,PLANE53,3,,1,     ! large inductor (3-STRANDED,1-without)
 et,5,plane13,6,,1       ! small inductor (for drain)

 ET,6,CIRCU124,4,0
```

```
ET,7,CIRCU124,5

R,1,AMPL1,PHAS1      ! REAL CONST POWER SOURCE
R,2,Abig,w_ind,,,g    ! REAL CONST EXTERNAL CIRCUIT
R,3,1
```

!******************* properties emag ******************

```
mp,murx,1,1   ! magnetic relative permeability for melt pool, drain
mp,murx,2,1   ! starter ring
mp,murx,3,1   ! airspace
mp,murx,4,1   ! big inductor
mp,murx,5,1   ! small inductor

mptemp
mptemp,1,0,100,500,600,700,800          ! electrical resistivity
mptemp,7,900,1000,1100,1200,1300,1400    !! for melt pool
mptemp,13,1500,1600,1700,1800,1900,2000

mpdata,rsvx,1,1,929,929,929,9.28,0.85,0.24
mpdata,rsvx,1,7,0.11,6.47E-2,4.4E-2,3.29E-2,2.62E-2,2.18E-2
mpdata,rsvx,1,13,1.873E-2,1.65E-2,1.48E-2,1.35E-2,1.25E-2,1.16E-2

mptemp
mptemp,1,0,100,500,600,700,800          ! electrical resistivity
mptemp,7,900,1000,1100,1200,1300,1400    !! for ring area
mptemp,13,1500,1600,1700,1800,1900,2000

mpdata,rsvx,2,1,929,929,929,9.28,0.85,0.24
mpdata,rsvx,2,7,0.11,6.47E-2,4.4E-2,3.29E-2,2.62E-2,2.18E-2
mpdata,rsvx,2,13,1.873E-2,1.65E-2,1.48E-2,1.35E-2,1.25E-2,1.16E-2

mp,rsvx,3,1.0e+18     ! airspace
mp,rsvx,4,2.0E-8     ! big inductor
mp,rsvx,5,2.0E-8     ! small inductor
```

!*************** Geometry *****************************

```
n,1
n,2,Re+0.05,0.020
n,3,Re+0.05,-0.020   ! nodes for external circuit
```

```
k,1,0,-Z2sl
k,2,R2sl,-Z2sl
k,3,Rarc1,Zarc1
k,4,Rarc2,Zarc2
k,5,R2fl,Z2ist
```

```
k,6,R2,Z2ist
k,7,Rint,Zint        ! intermediate arc point
k,8,0,Z2n
k,9,0,Z2ist
k,10,R2fl,Z2n
k,11,r2,Z2n
k,12,R2fl,Z2km
k,13,0,Z2km
k,14,R2,Z2km


l,1,2,14*mm          !1
l,2,3,1*mm           !2
larc,3,4,7           !3  - drain
l,9,4,28*mm          !4
l,9,1,24*mm          !5
al,all
lsel,none


lsel,s,,,4
l,9,8,10*mm          !6
l,8,10,30*mm         !7
l,10,5,10*mm         !8  - melt area above the drain
l,5,4,30*mm          !9
al,all
lsel,none


lsel,s,,,8
l,5,6,30*mm          !10
l,6,11,10*mm         !11 - bottom melt layer
l,11,10,30*mm        !12
al,all
lsel,none


lsel,s,,,12
l,11,14,46*mm        !13
l,14,12,40*mm        !14 - right part of the melt
l,12,10,46*mm        !15
al,all
lsel,none


lsel,s,,,15
lsel,a,,,7
l,12,13,40*mm        !16
l,13,8,46*mm         !17 - left part of the melt
al,all


aglue,all
```

```
lsel,s,,,3
lesize,all,,,35*mm,
alls

ptxy,R1n,Z1n,R1k,Z1n,R1k,Z1k,R1n,Z1k          ! big inductor
poly

ptxy,0,Zen,0,Zek,Re,Zek,Re,Zen               ! airspace
poly

rectng,R1sl_1n,R1sl_1k,Z1sl_1n,Z1sl_1k        ! drain inductor

rectng,R21n,R21k,Z21n,Z21k                    ! starter ring

lsel,s,,,29,32
lesize,all,,,20*mm

lsel,s,,,19
lsel,a,,,21
lesize,all,,,46*mm

aovlap,all
numcmp,all

alls

!/eof

!************** Associates element attributes with the selected areas **

 asel,s,area,,1      ! for melt pool
 asel,a,area,,2       ! mat,,type elem
 asel,a,area,,3
 asel,a,area,,4
 asel,a,area,,8
 aatt,1,,1

 asel,s,area,,7       ! for ring
 aatt,2,,2            ! mat,real,type elem

 asel,s,area,,9       ! for airspace
 aatt,3,,3

 ASEL,S,AREA,,5        ! for large inductor
 AATT,4,2,4
```

```
  asel,s,area,,6    ! for small inductor
  aatt,5,,5

  ASUM

*GET,Abig,AREA,,AREA

allsel,all

!/eof

!****** Meshing *************************************************

  lsel,s,loc,y,Zen        !  Shield (bottom)
  lsel,r,loc,x,0,Re
  lesize,all,,,60*mm

  lsel,a,loc,y,Zek        !  Shield (top)
  lsel,r,loc,x,0,Re
  lesize,all,,,60*mm

  lsel,s,loc,x,Re        !  Shield (side)
  lsel,r,loc,y,Zen,Zek
  lesize,all,,,70*mm

  lsel,s,loc,x,0         ! melt pool upper surface
  lsel,r,loc,y,Zen,Z2n
  lesize,all,,,36*mm

  lsel,s,loc,x,0         ! axis melt pool lower surface)
  lsel,r,loc,y,Z2k,Zek
  lesize,all,,,30*mm


  mshape,0,2d
  mshkey,2
  amesh,all
  allsel,all

!/eof

!***** electromagnetic task ****************************************
!***************** EXTERNAL CIRCUIT ***************************

  N1=NODE(R1n,0,0)

  TYPE,6   ! number of FE (ET124 - voltage source)
```

```
  REAL,1   ! 1 - number R
  E,2,1,3  ! nodes

  TYPE,7   ! ET124 - inductor
  real,3
  E,2,1,n1 ! node N1 is switched on

 ESEL,S,MAT,,4
 NSLE,S

 CP,1,CURR,ALL
 CP,2,EMF,ALL

finish

/solu

        lsel,s,loc,y,Zen     ! select  boundary emag task
        lsel,a,loc,y,Zek
        lsel,a,loc,x,Re
 nsll,s,1
 d,all,az,0,0            ! boundary condition, Az=0

        lsel,s,loc,x,0
 nsll,s,1
 d,all,az,0,0            ! boundary condition, Az=0
 alls

 d,3,volt,0
 alls

!/eof

 antype,harmic           ! type of analysis
 harfrq,freq1            ! frequency
 OUTPR,ALL,ALL
 HROUT,On

  allsel,all

!   solve

 physics,write,emag1        ! write emag1 physics file

finish

!/eof
```

```
!/post1             ! review emag source, delete comment
!   set,last
!   esel,s,mat,,2
!   esel,a,mat,,1
!   plesol,jheat
!finish

!/eof

!***** flotran CFD ****************************
!*********************************************

/prep7

 lclear,all

 et,1,fluid141,,,1
 et,2,fluid141,,,1
 et,3,0
 et,4,0
 et,5,0
 et,6,0
 et,7,0

 cpdele,all

finish

/solu

 toffst,273
 fldata14,TEMP,NOMI,T_init  ! initial temperature

!*********************** properties mat. 1 (glass) option ************
! *****************************************************************

 fldata12,PROP,DENS,16
 fldata13,VARY,DENS,1
 fldata12,PROP,VISC,16
 fldata13,VARY,VISC,1
 fldata12,PROP,COND,16
 fldata13,VARY,COND,1
 fldata12,PROP,SPHT,16
 fldata13,VARY,SPHT,1

!****************************************************
```

```
mptemp
mptemp,1,0,100,200,300,400,500
mptemp,7,600,700,800,900,1000,1100
mptemp,13,1200,1300,1400,1500,1700,2000

mpdata,dens,1,1,2610,2603,2598,2590,2575,2555    !Density
mpdata,dens,1,7,2531,2501,2458,2405,2352,2321
mpdata,dens,1,13,2310,2301.76,2298.12,2296.26,2294.84,2294.41

fldata7,PROT,DENS,TABLE
```

!**

```
mptemp                             !viscosity
mptemp,1,0,100,200,300,400,500
mptemp,7,600,700,800,900,1000,1100
mptemp,13,1200,1300,1400,1500,1700,2000

mpdata,visc,1,1,3.0e5,2.0e5,1.6e5,8.2e4,4.1e3,2.0e3
mpdata,visc,1,7,10.4e3,5.426e3,3.752e2,6.163e1,16.68,6.191
mpdata,visc,1,13,2.857,1.535,0.921,0.601,0.307,0.150

fldata7,PROT,VISC,TABLE
```

!**

```
mptemp
mptemp,1,0,100,200,300,400,500
mptemp,7,600,700,800,900,1000,1100
mptemp,13,1200,1300,1400,1500,1700,2000

mpdata,kxx,1,1,1.05,1.11,1.16,1.16,1.22,1.63,    !Thermal conductivity
mpdata,kxx,1,7,1.17,1.05,1.20,1.48,1.83,2.23
mpdata,kxx,1,13,2.615,2.972,3.30,3.61,4.145,4.76


fldata7,PROT,COND,TABLE
```

!**

```
mptemp
mptemp,1,0,100,200,300,400,500
mptemp,7,600,700,800,900,1000,1100
mptemp,13,1200,1300,1400,1500,1700,2000

mpdata,c,1,1,920,1000,1100,1180,1270,1910        !Specific heat
```

```
mpdata,c,1,7,1820,1520,1500,1610,1730,1881
mpdata,c,1,13,2018,2140,2247,2339,2478,2474

fldata7,PROT,SPHT,TABLE
```

!************************ properties mat. 2 (graphite) *********
!**

```
mptemp
mptemp,1,0,100,200,300,400,500
mptemp,7,600,700,800,900,1000,1100
mptemp,13,1200,1300,1400,1500,1700,2000

mpdata,dens,2,1,2610,2603,2598,2590,2575,2555    !Density
mpdata,dens,2,7,2531,2501,2458,2405,2352,2321
mpdata,dens,2,13,2310,2301.76,2298.12,2296.26,2294.84,2294.41

fldata7,PROT,DENS,TABLE
```

!**

```
mptemp                          !viscosity
mptemp,1,0,100,200,300,400,500
mptemp,7,600,700,800,900,1000,1100
mptemp,13,1200,1300,1400,1500,1700,2000

mpdata,visc,2,1,3.0e5,2.0e5,1.6e5,8.2e4,4.1e3,2.0e3
mpdata,visc,2,7,10.4e3,5.426e3,3.752e2,6.163e1,16.68,6.191
mpdata,visc,2,13,2.857,1.535,0.921,0.601,0.307,0.150

fldata7,PROT,VISC,TABLE
```

!***

```
mptemp
mptemp,1,0,100,200,300,400,500
mptemp,7,600,700,800,900,1000,1100
mptemp,13,1200,1300,1400,1500,1700,2000

mpdata,kxx,2,1,1.05,1.11,1.16,1.16,1.22,1.63,    !Thermal conductivity
mpdata,kxx,2,7,1.17,1.05,1.20,1.48,1.83,2.23
mpdata,kxx,2,13,2.615,2.972,3.30,3.61,4.145,4.76


fldata7,PROT,COND,TABLE
```

!***

```
mptemp
mptemp,1,0,100,200,300,400,500
mptemp,7,600,700,800,900,1000,1100
mptemp,13,1200,1300,1400,1500,1700,2000

mpdata,c,2,1,920,1000,1100,1180,1270,1910          !Specific heat
mpdata,c,2,7,1820,1520,1500,1610,1730,1881
mpdata,c,2,13,2018,2140,2247,2339,2478,2474

fldata7,PROT,SPHT,TABLE

! ***********************************************************
!*********************** convergence option ****************

fldata1,solu,tran,1
fldata1,solu,FLOW,1
fldata1,solu,TEMP,1

fldata4,time,step,step1     ! time step size
fldata4,time,bc,0,        ! similarly KBC ,1-ramped,0-stepped (default)

fldata4,time,NUMB,tinc/step1
fldata4,time,TEND,ftime
fldata4,time,GLOB,10,
fldata4,time,VX,1e-4
fldata4,time,VY,1e-4,
fldata4,time,VZ,0.001,

fldata4,TIME,OVER,0
fldata4,TIME,APPE,1.0e6
fldata4,TIME,SUMF,1.0e6

fldata18,METH,TEMP,4
fldata18,METH,PRESS,4

fldata25,RELX,VX,0.5,        ! solution and property relaxation factors
fldata25,RELX,VY,0.5,
fldata25,RELX,PRES,0.8,
fldata25,RELX,TEMP,0.8,

fldata25,RELX,DENS,1,
fldata25,RELX,SPHT,1,
fldata25,RELX,VISC,1,
fldata25,RELX,COND,1,

fldata31,capp,VELO,1        ! Specifies dependent variable caps
```

```
fldata31,capp,TEMP,1
fldata31,capp,PRES,1

fldata31,capp,UMIN,-1e+01
fldata31,capp,UMAX,1e+01
fldata31,capp,VMIN,-1e+01
fldata31,capp,VMAX,1e+01
fldata31,capp,TMIN,-3e+03
fldata31,capp,TMAX,3e+03
fldata31,capp,PMIN,-1e+020
fldata31,capp,PMAX,1e+020

!*************************** Controls restart options ******

fldata32,REST,NSET,0
fldata32,REST,ITER,0
fldata32,REST,LSTP,0,
fldata32,REST,TIME,0
fldata32,REST,CLEAR,F
fldata32,REST,RFIL,0
fldata32,REST,WFIL,1
fldata32,REST,OVER,0

!*************** boundary condition (BC) ********************

 lsel,s,loc,x,0          ! melt pool axis
 lsel,r,loc,y,-Z2sl,Z2km
 nsll,s,1
   d,all,vx,0

 lsel,s,loc,x,R2         ! melt pool side
 lsel,r,loc,y,Z2ist,Z2km
 nsll,s,1
   sf,all,conv,al_side,T_env
   d,all,vx,0
   d,all,vy,0

 lsel,s,loc,y,Z2km       ! melt pool top
 lsel,r,loc,x,0,R2
   STEF,C_s
 nsll,s,1
   sf,all,rad,eps,T_env
   d,all,vy,0

 lsel,s,,,1              ! drain bottom
 lsel,a,,,9
 lsel,a,,,10
```

```
nsll,s,1
  sf,all,conv,al_bot,T_env
  d,all,vx,0
  d,all,vy,0

lsel,s,,,2
nsll,s,1
  sf,all,conv,al_bot,T_env
  d,all,vx,0
  d,all,vy,0

lsel,s,,,3
nsll,s,1
  sf,all,conv,al_bot,T_env
  d,all,vx,0
  d,all,vy,0

allsel,all
acel,0,9.81,0,          ! gravity

PHYSICS,WRITE,fluid, , ,

 save

finish

alls

!/eof

!***************** solution **************
!****************************************
!****************************************

 n_tinc= ftime/tinc

 *dim,P22,array,n_tinc     ! array of the POWER in melt
 *dim,P2Ri,array,n_tinc    ! array of the POWER in starter Ring

*do,i,timein/tinc,ftime/tinc
       time=time+tinc

physics,read,emag1

/solu

 *if,i,eq,1,then
```

```
   esel,s,mat,,1
   esel,a,mat,,2

   nsle,s,all

   fldada14,temp,nomi,T_init     !initial temperature

 *else

   ldread,temp,last,,,,,rfl

 *endif

 allsel,all

 solve

finish

alls

!/eof

!*************** power in the melt ************

 /post1

   SET,LAST

     asel,s,mat,,1
     asel,a,mat,,2
     esla,s
     nsle,s

   *get,nmin,elem,0,num,min
   *get,nmax,elem,0,num,max
   *get,n_elem,elem,0,count

   *dim,vv1,array,n_elem     ! array of volumes FE (glass)
   *dim,w01,array,n_elem     ! array of volumetric sources

   p22big=0
   nn=0

   *do,i2,nmin,nmax,1
```

```
  *if,esel(i2),eq,1,then

    nn=nn+1

    *get,vv1(nn),elem,i2,volu
    *get,w01(nn),ELEM,i2,Jheat,  ! Jheat values are written into array w01

   *endif                 ! Jheat is volumetric sources in ANSYS

   p22big=p22big+w01(nn)*vv1(nn) ! power from voltage set on inductor U_ind

 *enddo

  p22(i)=p22big

! finish

!***************  power in the starter ring ************

! /post1
!   SET,LAST
!     asel,s,mat,,1

     asel,s,mat,,2

     esla,s
     nsle,s

   *get,nmin,elem,0,num,min
   *get,nmax,elem,0,num,max
   *get,n_elem,elem,0,count

   *SET,vv1,
   *SET,w01,

   *dim,vv1,array,n_elem    ! array of melt volume FEs
   *dim,w01,array,n_elem    ! array of volumetric sources

   p22Ri=0
   nn=0

   *do,i2,nmin,nmax,1

    *if,esel(i2),eq,1,then

     nn=nn+1
```

```
   *get,vv1(nn),elem,i2,volu
   *get,w01(nn),ELEM,i2,Jheat, ! Jheat sources are written into array w01

  *endif              ! Jheat are volumetric heat sources in ANSYS

  p22Ri=p22Ri+w01(nn)*vv1(nn) ! power from voltage set on inductor. U_ind

 *enddo

 p2Ri(i)=p22Ri

finish
```

! **

```
physics,read,fluid

/assign,esav,fluid,esav
/assign,emat,fluid,emat

/solu

  *if,i,gt,1,then

    fldata1,solu,tran,1

  *else

    esel,s,mat,,1
    esel,a,mat,,2
    nsle,s,all

    fldata14,temp,nomi,T_init    !initial temperature

  *endif

  time,time
  esel,s,mat,,1
  esel,a,mat,,2

  ldread,hgen,,,,2,,rst   !apply joule heating load from emag

  solve

finish

/assign,esav
```

```
/assign,emat

    *SET,vv1,
    *SET,w01,

*enddo

save

!*****************************************************
!**************** display temperatures ****************

/post1

    set,last

    plnsol,temp

*ASK,temperature,'  press OK to continue '

!****************** graph TEMP, path along melt pool top *****

    path,weg2t,2,30,20,     ! path between two points...
    ppath,1,,0,Z2k,0        ! point at the bottom melt pool by R=0
    ppath,2,,R2,Z2k,0       ! point at the bottom melt pool by R=R2
    path,stat

    pdef, ,TEMP            ! Interpolates TEMP onto a path

   /pbc,path, ,0           ! Show path on display

    plpath,TEMP            ! Display path TEMP along top

*ASK,TEMP_along_melt_pool_top,'  press OK to continue '

!******* graph TEMP, path along melt pool bottom ***************

    path,weg2dt,2,30,20,    ! path between two points...
    ppath,1,,0,Z2n,0        ! point at the top drain at R=0
    ppath,2,,R2,Z2n,0       ! point at the top drain at R=R2
    path,stat

    pdef, ,TEMP            ! Interpolates TEMP onto a path

   /pbc,path, ,0           ! Show path on display

    plpath,TEMP            ! Display path TEMP along bottom
```

```
*ASK,TEMP_along_bottom,'  press OK to continue '

!***************** graph heat flux path along melt pool side *****

   path,weg2,2          ! path between two points...
   ppath,1,,R2,Z2n,0     ! point at the bottom melt pool
   ppath,2,,R2,Z2k,0     ! point at the top melt pool

   pdef,  ,HFLU          ! Interpolates hflux onto a path
  /pbc,path, ,0          ! Show path on display

   plpath,HFLU           ! Display path hflux on a graph

*ASK,hflux_through_melt_pool_side,'  press OK to continue '

!******************* graph heatflux path along melt pool bottom **

 path,weg21,2            ! path between two points...
   ppath,1,,0,Z2n,0      ! point at the bottom melt pool R=0
   ppath,2,,R2,Z2n,0     ! point at the bottom melt pool R=R2

   pdef, ,HFLU           ! Interpolates hfux  onto a path
  /pbc,path, ,0          ! Show path on display

   plpath,HFLU           ! Display path HFLU along bottom

*ASK,flux_through_melt_pool_bottom,'  press OK to continue '

!********* heat losses from the melt pool side ********************
!********* calculated from mean TEMP and heat transfer factor(alpha) *

   path,weg4al,2,30,20,   ! path along melt pool surface
   ppath,1,,R2,Z2n,0     ! point at the bottom melt pool
   ppath,2,,R2,Z2k,0     ! point at the top melt pool
   pdef,TEMP,TEMP

  /pbc,path, ,0          ! Show path on displays

   pcalc,intg,ploss2al,TEMP,s        ! integrates along path

   *get,ploss2al,path,,last,ploss2al

   m_Ts=ploss2al/(Z2k-Z2n)               ! mean temp
   Ps_ALP=al_side*(m_Ts-T_env)*2*pi*R2*(Z2k-Z2n)  ! summary losses from alpha
   m_Ps=Ps_ALP/(2*pi*R2*(Z2k-Z2n))
```

```
!******** heat loss from the melt pool bottom ********************
!******** calculated from mean TEMP and heat transfer factor(alpha) **

   path,weg52alp,2,,20,   ! path along melt pool surface
   ppath,1,,0,Z2n,0      ! point  by R=0
   ppath,2,,R2,Z2n,0     ! point  R=R2
   pdef,TEMP,TEMP        ! Interpolates TEMP onto a path

  /pbc,path, ,0          ! Show path on displays

   pcalc,mult,prod11,TEMP,s

   pcalc,intg,ploss31al,prod11,s,2*pi     ! integrates along path

   *get,ploss31al,path,,last,ploss31al

   m_Tb  =ploss31al/(pi*R2**2)          ! mean temp
   Pb_ALP=al_bot*(m_Tb -T_env)*(pi*R2**2)  ! summary losses from alpha
   m_Pb=Pb_ALP/(pi*R2**2)

!***********************************************************

   Ploss_C=Ps_ALP+Pb_ALP !convection loss from melt pool

!********** mean TEMP  on the top *************************
!********** by RADIATION ********************************

   path,weg53mT,2,,20,   ! path along melt pool top
   ppath,1,,0,Z2k,0     ! point at R=0
   ppath,2,,R2,Z2k,0    ! point at R=R2

   pdef,TEMP,TEMP       ! Interpolates TEMP onto a path

  /pbc,path, ,0         ! Show path on displays

   pcalc,intg,intT,TEMP,s,    ! integrates along path

   *get,intT,path,,last,intT

   m_Tt=intT/R2

!***********************************************************
!***********************************************************
!************** Calc. source and power *******************
!***********************************************************

      physics,read,emag1
```

```
        /assign,esav
        /assign,emat

  /solu

      ldread,temp,last,,,,,,rfl

      allsel,all

      solve

  finish

!*********** visualization of heat sources *****************************

 /post1

    set,last

    esel,s,mat,,1
    esel,a,mat,,2

    plesol,jheat

*ASK,Small_ind_source,' press OK to continue '

!***********************************************************

 asel,s,mat,,1  !power in glass(without area where ring place)

 esla,s
 nsle,s

    *get,nmin,elem,0,num,min
    *get,nmax,elem,0,num,max
    *get,n_elem,elem,0,count

    *SET,vv1,
    *SET,w01,
    *SET,w02,
    *SET,w0,

    *dim,vv1,array,n_elem
    *dim,w02,array,n_elem

 p2glar=0
```

```
nn=0

 *do,i2,nmin,nmax,1

   *if,esel(i2),eq,1,then

     nn=nn+1

      *get,vv1(nn),elem,i2,volu
      *GET,w02(nn),ELEM,i2,Jheat

     *endif

    p2glar=p2glar+w02(nn)*vv1(nn)

  *enddo

!****************************************************

 asel,s,mat,,2  !power  in ring  area

 esla,s
 nsle,s

   *get,nmin,elem,0,num,min
   *get,nmax,elem,0,num,max
   *get,n_elem,elem,0,count

   *SET,vv1,
   *SET,w01,
   *SET,w02,
   *SET,w0,

   *dim,vv1,array,n_elem
   *dim,w02,array,n_elem

 p2riar=0
 nn=0

  *do,i2,nmin,nmax,1

    *if,esel(i2),eq,1,then

      nn=nn+1

       *get,vv1(nn),elem,i2,volu
       *GET,w02(nn),ELEM,i2,Jheat
```

```
    *endif

   p2riar=p2riar+w02(nn)*vv1(nn)

  *enddo

!/eof

!*************************************************************

 /out,LOSS_POWER

  *vwrite,n_tinc
  (2x,'number of the last load step, tinc =',e10.4)

  *vwrite,p22big
  (2x,'power in glass area before fluid work, W =',e10.4)

  *vwrite,p22Ri
 (2x,'power in the ring area before fluid work, W =',e10.4)

  *vwrite,p2glar
  (2x,'power in the glass area after fluid work, W =',e10.4)

  *vwrite,p2riar
  (2x,'power in the ring area after fluid work, W =',e10.4)

  *vwrite,Ps_ALP
  (2x,'heat loss from melt pool side, W =',e10.4)

  *vwrire,Pb_ALP
  (2x,'heat loss from melt pool bottom, W =',e10.4)

  *vwrite, Ploss_C
  (2x,'sum of heat losses from melt pool bottom and side ,W =',e10.4)

   *vWrite
  ('mean TEMP')

   *vwrite,m_Ts
  (2x,'mean TEMP on melt pool side, deg_Cd =',e10.4)

   *vwrite,m_Tb
  (2x,'mean TEMP on melt pool bottom, deg_C =',e10.4)

   *vwrite,m_Tt
```

```
      (2x,'mean TEMP on the melt pool top, deg_C =',e10.4)

       *vWrite
      ('mean heat flux (HF)')

       *vwrite,m_Ps
      (2x,'mean HF from the melt pool side, W/m**2 =',e10.4)

       *vwrite,m_Pb
      (2x,'mean HF from the melt pool bottom, W/m**2 =',e10.4)

       *vWrite
      ('see also file *.pfl for power from top')

allsel

 /out
 ! /go
 !     physics,read,fluid
 !   set,last
 !   plnsol,temp
fini
```

```
! STEP 3

finish

!*****************************************************

/clea

/FILENAME,  !! finish melt process, 2nd frequency is on, ring is outside

/PREP7

/nerr,0

 mm=1           ! mesh step reduction factor

 freq1=1.76e6     ! frequency big inductor
 freq2=27.12e6    ! frequency small inductor

 I_sm_ind= 160    ! current small ind

 Uind=2500        ! voltage on inductor
 AMPL1=Uind
 PHAS1=0
 rho1=2e-8
 w_ind=2          ! turn number
 g=0.6     ! mark-to-space ratio

 p21=1.8e4        ! power of the  big inductor
 p21sm=4e3        ! max power of the  small inductor

 j_ind =1.90e6    ! initial current density of the big inductor

 T_init=20        ! initial temperature

 step1=100        ! time step
 tinc=500         ! time increment  for harmonic analysis

!***** restart ***********************************

   timein=6000    ! previous time of the process
   ftime=14000    ! final time of the process
   time=timein

!**************************************************

 al_side=2.0e4    ! heat transfer factors (alpha) on pool side and drain
```

```
al_bot=1e2      ! heat transfer factors (alpha) on pool bottom
T_env=20.0      ! environment temperature
C_s=5.67e-8     ! Stefan constant
eps=0.5         ! emissivity factor for top
delt=1e-9       ! error of the calc. T (convergence)
```

!***

```
emunit,mks

pi=3.1416

R2=0.15         ! melt pool radius
Z2n=0.02        ! melt pool bottom
Z2km=0.18       ! melt pool top maximum coordinate
R1n=0.16        ! big inductor  inner radius
R1k=0.162       ! big inductor external radius
Z1n=0.00        ! big inductor bottom
Z1k=0.18        ! big inductor top
R2sl=0.02       ! drain radius
z2sl=0.023      ! drain height

R1sl_1n=0.034   ! small induct (turn 1) inn radius
R1sl_1k=0.040   ! small induct (turn 1) ext radius
Z1sl_1n=-0.022  ! small inductor (turn 1) bottom
Z1sl_1k=-0.016  ! small inductor (turn 1) top

Re=0.35         ! Shield radius
Zen=-.15        ! shield bottom
Zek=0.30        ! shield top

R2fl=0.08       ! flange radius
Zist=-0.02      ! Small ind source sone
Z2ist=Z2n+Zist  !!on the bot melt pool


Rarc1=R2sl      ! drain radius at bottom
Zarc1=-0.022
Rarc2=0.05      ! drain radius at top
Zarc2=Z2ist
Rint=0.030      ! drain radius at intermediate point
Zint=-0.010

R21n=0.09       ! graphite ring outer radius
R21k=0.13       ! graphite ring inter radius
Z21n=0.04
Z21k=0.08
```

```
   Abig=(R1k-R1n)*(Z1k-Z1n)    ! inductor wire area

!****************** element emag1 ********************

   et,1,plane13,,,1       ! melt pool, drain
   et,2,plane13,,,1       ! ring
   et,3,plane13,,,1       ! airspace
   et,4,PLANE53,3,,1,     ! big inductor (3-STRANDED,1-without middle node)
   et,5,plane13,6,,1      ! small inductor (for drain)

   ET,6,CIRCU124,4,0     ! 4-power source,0-HARM ANALYS
   ET,7,CIRCU124,5       ! 6-massive, 5- stranded wire

   R,1,AMPL1,PHAS1       ! real const. power source
   R,2,Abig,w_ind,,,g     ! real const. external circuit
   R,3,1

!****************** properties emag ******************

mp,murx,1,1  ! magnetic relative permeability for melt pool ,drain
mp,murx,2,1  ! starter ring
mp,murx,3,1  ! airspace
mp,murx,4,1  ! big inductor
mp,murx,5,1  ! small inductor


mptemp
mptemp,1,0,100,500,600,700,800         ! electrical resistivity
mptemp,7,900,1000,1100,1200,1300,1400    !!for melt pool
mptemp,13,1500,1600,1700,1800,1900,2000

mpdata,rsvx,1,1,929,929,929,9.28,0.85,0.24
mpdata,rsvx,1,7,0.11,6.47E-2,4.4E-2,3.29E-2,2.62E-2,2.18E-2
mpdata,rsvx,1,13,1.873E-2,1.65E-2,1.48E-2,1.35E-2,1.25E-2,1.16E-2

mptemp
mptemp,1,0,100,500,600,700,800         ! electrical resistivity
mptemp,7,900,1000,1100,1200,1300,1400    !!for ring area
mptemp,13,1500,1600,1700,1800,1900,2000

mpdata,rsvx,2,1,929,929,929,9.28,0.85,0.24
mpdata,rsvx,2,7,0.11,6.47E-2,4.4E-2,3.29E-2,2.62E-2,2.18E-2
mpdata,rsvx,2,13,1.873E-2,1.65E-2,1.48E-2,1.35E-2,1.25E-2,1.16E-2

mp,rsvx,3,1.0E+18     ! airspace
mp,rsvx,4,2.0E-8      ! big inductor
```

```
mp,rsvx,5,2.0E-8      ! small inductor

!*************** Geometry *******************************

   n,1
   n,2,Re+0.05,0.020
   n,3,Re+0.05,-0.020   ! nodes for external circuit

k,1,0,-Z2sl
k,2,R2sl,-Z2sl
k,3,Rarc1,Zarc1
k,4,Rarc2,Zarc2
k,5,R2fl,Z2ist
k,6,R2,Z2ist
k,7,Rint,Zint          ! intermediate arc point
k,8,0,Z2n
k,9,0,Z2ist
k,10,R2fl,Z2n
k,11,r2,Z2n
k,12,R2fl,Z2km
k,13,0,Z2km
k,14,R2,Z2km


l,1,2,14*mm          !1
l,2,3,1*mm           !2
larc,3,4,7           !3  - drain
l,9,4,28*mm          !4
l,9,1,24*mm          !5
al,all
lsel,none

lsel,s,,,4
l,9,8,10*mm          !6
l,8,10,30*mm         !7
l,10,5,10*mm         !8  - melt area above the drain
l,5,4,30*mm          !9
al,all
lsel,none

lsel,s,,,8
l,5,6,30*mm          !10
l,6,11,10*mm         !11 - bottom melt layer
l,11,10,30*mm        !12
al,all
lsel,none
```

```
lsel,s,,,12
l,11,14,46*mm          !13
l,14,12,40*mm          !14  - right part of the melt
l,12,10,46*mm          !15
al,all
lsel,none

lsel,s,,,15
lsel,a,,,7
l,12,13,40*mm          !16
l,13,8,46*mm           !17  - left part of the melt
al,all

aglue,all

lsel,s,,,3
lesize,all,,,35*mm,
alls

ptxy,R1n,Z1n,R1k,Z1n,R1k,Z1k,R1n,Z1k          ! big inductor
poly

ptxy,0,Zen,0,Zek,Re,Zek,Re,Zen               ! airspace
poly

rectng,R1sl_1n,R1sl_1k,Z1sl_1n,Z1sl_1k        ! drain inductor

rectng,R21n,R21k,Z21n,Z21k                    ! graphite ring

lsel,s,,,29,32
lesize,all,,,20*mm

lsel,s,,,19
lsel,a,,,21
lesize,all,,,46*mm

aovlap,all
numcmp,all
alls

!/eof

!************** Associates element attributes with the selected areas ***

 asel,s,area,,1      ! for melt pool
 asel,a,area,,2       !!mat,,type element
 asel,a,area,,3
```

```
asel,a,area,,4
asel,a,area,,8
aatt,1,,1

asel,s,area,,7        ! for ring
aatt,2,,2              !!mat,real,type element

asel,s,area,,9        ! for airspace
aatt,3,,3

ASEL,S,AREA,,5        ! for big inductor
AATT,4,2,4

asel,s,area,,6    ! for drain inductor
aatt,5,,5

ASUM

*GET,Abig,AREA,,AREA

allsel,all

!/eof

!****** Meshing ********************************

lsel,s,loc,y,Zen        ! Shield (bottom)
lsel,r,loc,x,0,Re
lesize,all,,,60*mm

lsel,a,loc,y,Zek        ! Shield (top)
lsel,r,loc,x,0,Re
lesize,all,,,60*mm

lsel,s,loc,x,Re         ! Shield (side)
lsel,r,loc,y,Zen,Zek
lesize,all,,,70*mm

lsel,s,loc,x,0          ! melt pool radius at bottom
lsel,r,loc,y,Zen,Z2n
lesize,all,,,36*mm

lsel,s,loc,x,0          ! melt pool radius at bottom
lsel,r,loc,y,Z2k,Zek
lesize,all,,,30*mm
```

```
  mshape,0,2d
  mshkey,2
  amesh,all
  allsel,all

!/eof

!***** electromagnetic task1 (emag1) *************
!**************** external circuit *************

  N1=NODE(R1n,0,0)

  TYPE,6    ! number of FE (ET124 - voltage source)
  REAL,1    ! 1 - number R
  E,2,1,3   ! nodes

  TYPE,7    ! ET124 - inductor
  real,3
  E,2,1,n1   ! node N1 is switched on

 ESEL,S,MAT,,4
 NSLE,S

 CP,1,CURR,ALL ! union nodes
 CP,2,EMF,ALL  ! union nodes

finish

/solu

        lsel,s,loc,y,Zen    ! select  boundary emag task
        lsel,a,loc,y,Zek
        lsel,a,loc,x,Re
 nsll,s,1
 d,all,az,0,0            ! boundary condition, Az=0

        lsel,s,loc,x,0
 nsll,s,1
 d,all,az,0,0            ! boundary condition, Az=0
 alls

 d,3,volt,0             ! ground on point 3 of external circuit
 alls

!/eof

 antype,harmic          ! type of analysis
```

```
  harfrq,freq1            ! frequency
  OUTPR,ALL,ALL
  HROUT,On

  allsel,all

!   solve

  physics,write,emag1       ! write emag1 physics file

finish

!/eof

!/post1              ! review emag source, delete comment
!   set,last
!   esel,s,mat,,1
!   esel,a,mat,,2
!   plesol,jheat
!finish

!/eof


!*************************************************
!***** electromagnetic task2 (emag2) *************

/prep7

physics,clear
  lsclear,all

  et,1,plane13,,,1      ! melt pool,drain
  et,2,plane13,,,1      ! ring
  et,3,plane13,,,1      ! airspace
  et,4,PLANE53,3,,1      ! big inductor (3-STRANDED,1-without middle node)
  et,5,plane13,6,,1      ! small inductor (for drain)

  ET,6,CIRCU124,4,0     ! 4-power source,0-HARM ANALYS
  ET,7,CIRCU124,5       ! 6-massive, 5- stranded wire

  mp,murx,1,1              ! Magnetic relative permeability
  mp,murx,2,1
  mp,murx,3,1
  mp,murx,4,1
  mp,murx,5,1
```

```
mptemp
mptemp,1,0,100,500,600,700,800          ! electrical resistivity
mptemp,7,900,1000,1100,1200,1300,1400    !!for melt pool
mptemp,13,1500,1600,1700,1800,1900,2000

mpdata,rsvx,1,1,929,929,929,9.28,0.85,0.24
mpdata,rsvx,1,7,0.11,6.47E-2,4.4E-2,3.29E-2,2.62E-2,2.18E-2
mpdata,rsvx,1,13,1.873E-2,1.65E-2,1.48E-2,1.35E-2,1.25E-2,1.16E-2

mptemp
mptemp,1,0,100,500,600,700,800          ! electrical resistivity
mptemp,7,900,1000,1100,1200,1300,1400    !!for drain
mptemp,13,1500,1600,1700,1800,1900,2000

mpdata,rsvx,2,1,929,929,929,9.28,0.85,0.24
mpdata,rsvx,2,7,0.11,6.47E-2,4.4E-2,3.29E-2,2.62E-2,2.18E-2
mpdata,rsvx,2,13,1.873E-2,1.65E-2,1.48E-2,1.35E-2,1.25E-2,1.16E-2

  mp,rsvx,3,2.0E18
  mp,rsvx,4,1.0E18
  mp,rsvx,5,1.0E18

finish

alls

!/eof

/solu

  antype,harmic
  harfrq,freq2

         lsel,s,loc,y,Zen    ! select  boundary emag task
         lsel,a,loc,y,Zek
         lsel,a,loc,x,0
         lsel,a,loc,x,Re
 nsll,s,1
 d,all,az,0,0              ! boundary condition, Az=0

  allsel,all

!/eof

  asel,s,area,,6
  esla,s,1
  nsla,s,1
```

```
  cp,3,volt,all
  n2=node(R1sl_1n,Z1sl_1n,0)
  f,n2,amps,I_sm_ind

  allsel,all

! solve

  physics,write,emag2

finish

! /post1
! set,last
! esel,s,mat,,1
! esel,a,mat,,2
! plesol,jheat
! finish
!/eof

!***** flotran CFD ****************************
!*********************************************

/prep7

  lclear,all

  et,1,fluid141,,,1
  et,2,fluid141,,,1
  et,2,0
  et,3,0
  et,4,0
  et,5,0

CPDELE,ALL

finish

/solu

  toffst,273

!********************** properties options *************

  fldata12,PROP,DENS,16
  fldata13,VARY,DENS,1
  fldata12,PROP,VISC,16
```

```
 fldata13,VARY,VISC,1
 fldata12,PROP,COND,16
 fldata13,VARY,COND,1
 fldata12,PROP,SPHT,16
 fldata13,VARY,SPHT,1
```

!************* material 1 *****************************

```
 mptemp
 mptemp,1,0,100,200,300,400,500
 mptemp,7,600,700,800,900,1000,1100
 mptemp,13,1200,1300,1400,1500,1700,2000

 mpdata,dens,1,1,2610,2603,2598,2590,2575,2555   ! Density
 mpdata,dens,1,7,2531,2501,2458,2405,2352,2321
 mpdata,dens,1,13,2310,2300,2290,2280,2370,2360

 fldata7,PROT,DENS,TABLE
```

!***

```
 mptemp                              ! viscosity
 mptemp,1,0,100,200,300,400,500
 mptemp,7,600,700,800,900,1000,1100
 mptemp,13,1200,1300,1400,1500,1700,2000

 mpdata,visc,1,1,3.0e5,2.0e5,1.6e5,8.2e4,4.1e3,2.0e3
 mpdata,visc,1,7,10.4e3,5.426e3,3.752e2,6.163e1,16.68,6.191
 mpdata,visc,1,13,2.857,1.535,0.921,0.601,0.307,0.150

 fldata7,PROT,VISC,TABLE
```

!***

```
 mptemp
 mptemp,1,0,100,200,300,400,500
 mptemp,7,600,700,800,900,1000,1100
 mptemp,13,1200,1300,1400,1500,1700,2000

 mpdata,kxx,1,1,1.05,1.11,1.16,1.16,1.22,1.63,    ! Thermal conductivity
 mpdata,kxx,1,7,1.17,1.05,1.20,1.48,1.83,2.23
 mpdata,kxx,1,13,2.62,3.02,3.42,3.82,4.2,4.8

 fldata7,PROT,COND,TABLE
```

!***

```
mptemp
mptemp,1,0,100,200,300,400,500
mptemp,7,600,700,800,900,1000,1100
mptemp,13,1200,1300,1400,1500,1700,2000

mpdata,c,1,1,920,1000,1100,1180,1270,1910      ! Specific heat
mpdata,c,1,7,1820,1520,1500,1610,1730,1880
mpdata,c,1,13,2020,2160,2300,2440,2460,2480

fldata7,PROT,SPHT,TABLE
```

!*************** material 2 ***************************

```
mptemp
mptemp,1,0,100,200,300,400,500
mptemp,7,600,700,800,900,1000,1100
mptemp,13,1200,1300,1400,1500,1700,2000

mpdata,dens,2,1,2610,2603,2598,2590,2575,2555   ! Density
mpdata,dens,2,7,2531,2501,2458,2405,2352,2321
mpdata,dens,2,13,2310,2300,2290,2280,2370,2360

fldata7,PROT,DENS,TABLE
```

!***

```
mptemp                            ! viscosity
mptemp,1,0,100,200,300,400,500
mptemp,7,600,700,800,900,1000,1100
mptemp,13,1200,1300,1400,1500,1700,2000

mpdata,visc,2,1,3.0e5,2.0e5,1.6e5,8.2e4,4.1e3,2.0e3
mpdata,visc,2,7,10.4e3,5.426e3,3.752e2,6.163e1,16.68,6.191
mpdata,visc,2,13,2.857,1.535,0.921,0.601,0.307,0.150

fldata7,PROT,VISC,TABLE
```

!***

```
mptemp
mptemp,1,0,100,200,300,400,500
mptemp,7,600,700,800,900,1000,1100
mptemp,13,1200,1300,1400,1500,1700,2000

mpdata,kxx,2,1,1.05,1.11,1.16,1.16,1.22,1.63,   ! Thermal conductivity
mpdata,kxx,2,7,1.17,1.05,1.20,1.48,1.83,2.23
mpdata,kxx,2,13,2.62,3.02,3.42,3.82,4.2,4.8
```

```
fldata7,PROT,COND,TABLE

!**********************************************************

mptemp
mptemp,1,0,100,200,300,400,500
mptemp,7,600,700,800,900,1000,1100
mptemp,13,1200,1300,1400,1500,1700,2000

mpdata,c,2,1,920,1000,1100,1180,1270,1910        ! Specific heat
mpdata,c,2,7,1820,1520,1500,1610,1730,1880
mpdata,c,2,13,2020,2160,2300,2440,2460,2480

fldata7,PROT,SPHT,TABLE

!********************** convergence options *************

fldata1,solu,tran,1
fldata1,solu,FLOW,1
fldata1,solu,TEMP,1

fldata4,time,step,step1     ! time step size
fldata4,time,bc,0,          ! similarly KBC ,1-ramped,0-stepped (default)

fldata4,time,NUMB,tinc/step1 ! steps from time tinc
fldata4,time,TEND,ftime     ! finish time for boundary conditions
fldata4,time,GLOB,10,       ! number of iterations
fldata4,time,VX,1e-4
fldata4,time,VY,1e-4,
fldata4,time,VZ,0.001,

fldata4A,STEP,OVER,0,
fldata4,TIME,OVER,0
fldata4,TIME,APPE,1.0e6
fldata4,TIME,SUMF,1.0e6

fldata18,METH,TEMP,4
fldata18,METH,PRESS,4

fldata25,RELX,VX,0.5,       ! solution and property relaxation factors
fldata25,RELX,VY,0.5,
fldata25,RELX,PRES,0.8,
fldata25,RELX,TEMP,0.8,

fldata25,RELX,DENS,1,
fldata25,RELX,SPHT,1,
```

```
fldata25,RELX,VISC,1,
fldata25,RELX,COND,1,

FLDATA26,STAB,MOME,1e-1      ! Inertial relaxation factor
FLDATA26,STAB,PRES,1e-1,
FLDATA26,STAB,TEMP,1e+020,

fldata31,capp,VELO,1        ! Specifies dependent variable caps
fldata31,capp,TEMP,1
fldata31,capp,PRES,1

fldata31,capp,UMIN,-1e+01
fldata31,capp,UMAX,1e+01
fldata31,capp,VMIN,-1e+01
fldata31,capp,VMAX,1e+01
fldata31,capp,TMIN,0.0
fldata31,capp,TMAX,3e+03
fldata31,capp,PMIN,1e-010
fldata31,capp,PMAX,1e+010

!************************** Controls restart options ******

fldata32,REST,NSET,0
fldata32,REST,ITER,0
fldata32,REST,LSTP,0,
fldata32,REST,TIME,0          ! restart will be from the last results set
fldata32,REST,CLEAR,F
fldata32,REST,RFIL,0
fldata32,REST,WFIL,1
fldata32,REST,OVER,0

!*************** boundary condition (BC) *******************

lsel,s,loc,x,0          ! melt pool axis
lsel,r,loc,y,-Z2sl,Z2km
nsll,s,1
  d,all,vx,0

lsel,s,loc,x,R2          ! melt pool side
lsel,r,loc,y,Z2ist,Z2km
nsll,s,1
  sf,all,conv,al_side,T_env
  d,all,vx,0
  d,all,vy,0

lsel,s,loc,y,Z2km          ! melt pool top
lsel,r,loc,x,0,R2
```

```
  STEF,C_s
nsll,s,1
  sf,all,rad,eps,T_env
  d,all,vy,0

lsel,s,,,1              ! drain bottom
lsel,a,,,9
lsel,a,,,10
nsll,s,1
  sf,all,conv,al_bot,T_env
  d,all,vx,0
  d,all,vy,0

lsel,s,,,2
nsll,s,1
  sf,all,conv,al_bot,T_env
  d,all,vx,0
  d,all,vy,0

lsel,s,,,3
nsll,s,1
  sf,all,conv,al_bot,T_env
  d,all,vx,0
  d,all,vy,0

allsel,all

acel,0,9.81,0,           ! gravity
bfedele,ALL,JS,,,,j_ind      ! DELETE ALL applied current density to inductor

PHYSICS,WRITE,fluid, , ,

save

finish

alls

!/eof

!****************** solution *********************
!*************************************************

  /gst,on

imin= timein/tinc
imax=ftime/tinc
```

```
  deli=imax-imin+1

 *dim,psm_ind,array,deli

!***************************************************

*do,i,timein/tinc,ftime/tinc
        time=time+tinc

   physics,read,emag1

  /solu

  *if,i,eq,1,then
     esel,s,mat,,1
     esel,a,mat,,2
     nsle,s,all
     fldada14,temp,nomi,T_init     ! initial temperature

   *else

     ldread,temp,last,,,,,,rfl     ! last hydrodynamic results

   *endif

   allsel,all

   solve

  finish

   /post1

      SET,LAST

      asel,s,mat,,1
      asel,a,mat,,2

      esla,s
      nsle,s

    *get,nmin,elem,0,num,min
    *get,nmax,elem,0,num,max
    *get,n_elem,elem,0,count

    *dim,vv1,array,n_elem
    *dim,w01,array,n_elem
```

```
  *dim,w02,array,n_elem
  *dim,w0,array,n_elem

!*************************************************

  sw=0

*do,loop,1,10,1

  asel,s,mat,,1
  asel,a,mat,,2

  esla,s
  nsle,s

  p22big=0
  nn=0

  *do,i2,nmin,nmax,1

    *if,esel(i2),eq,1,then       ! if the element is selected
     nn=nn+1
     *get,vv1(nn),elem,i2,volu
     *get,w01(nn),ELEM,i2,Jheat, ! then write to the array

    *endif

    p22big=p22big+w01(nn)*vv1(nn)

  *enddo

  a=sqrt(p21/p22big)
  b=abs((p22big-p21)/P21)

  finish

  /solu

  *if,b,gt,0.05,then         ! power correction
    j_ind =j_ind*a
    ESEL,S,MAT,,4
    BFE,ALL,JS,,,,j_ind     ! current density from Z axis

    allsel,all

    solve
```

```
     sw=sw+1

   *else

      *exit

   *endif

 finish

*enddo

  /post1
        set,last

        asel,s,mat,,1
        asel,a,mat,,2

        esla,s
        nsle,s

        nn=0

       *do,j,nmin,nmax,1

          *if,esel(j),eq,1,then        ! if the element is selected

             nn=nn+1

             *GET,w01(nn),ELEM,j,Jheat, ! then write to the array

           *endif

         *enddo

 finish

!*************************************************************

        physics,read,emag2

        /assign,esav
        /assign,emat

    /solu

        *if,i,eq,1,then
```

```
        esel,s,mat,,1
        esel,a,mat,,2
        nsle,s,all

        fldada14,temp,nomi,T_init     ! initial temperature

      *else

        ldread,temp,last,,,,,rfl

      *endif

      allsel,all

      solve

    finish

!***************************************************************
!***** power limits to the small inductor ************************

   sw=0
   flag1=1
   flag2=1

 *do,iloop,1,10,1

   /post1

    set,last

    asel,s,mat,,1
    asel,a,mat,,2

    esla,s
    nsle,s

    p22sm=0
    nn=0

    *do,i2,nmin,nmax,1

     *if,esel(i2),eq,1,then        ! if the element is selected

       nn=nn+1
```

```
    *get,w02(nn),ELEM,i2,Jheat, ! then write to the array

  *endif

  p22sm=p22sm+w02(nn)*vv1(nn)

 *enddo

finish

/solu

  *if,p22sm,lt,p21sm,then

    Ism_ind1=I_sm_ind
    flag1=0

     *exit

   *endif

  a=sqrt(p21sm/p22sm)
  b=abs((p22sm-p21sm)/P21sm)

 *if,b,lt,0.05,then          ! power correction

    flag2=0

     *exit

  *endif

    Ism_ind1 =I_sm_ind*a

    asel,s,area,,6
    nsla,s,1
    cp,3,volt,all
    n2=node(R1sl_1n,Z1sl_1n,0)
    f,n2,amps,Ism_ind1

    allsel,all

    solve

finish

sw=sw+1
```

```
*enddo

/post1

 p22smk=0                 ! real power in small inductor
 nn=0

 *do,i2,nmin,nmax,1

  *if,esel(i2),eq,1,then        ! if the element is selected

    nn=nn+1

     *get,w02(nn),ELEM,i2,Jheat, ! then write to the array

   *endif

  p22smk=p22smk+w02(nn)*vv1(nn)

 *enddo

 psm_ind(i-imin+1)=p22smk

          set,last

          asel,s,mat,,1
                  asel,a,mat,,2

          esla,s
          nsle,s

           nn=0

          *do,j,nmin,nmax,1

             *if,esel(j),eq,1,then

                nn=nn+1

                *GET,w02(nn),ELEM,j,Jheat,

              *endif

          *enddo

          *do,j,1,n_elem
```

```
                w0(j)=w01(j)
            *enddo

   finish

!************************************************************

 physics,read,fluid           ! reading the hydrodynamic task

 /assign,esav,fluid,esav
 /assign,emat,fluid,emat

  /solu

   *if,i,gt,1,then

     fldata1,solu,tran,1

   *else

     esel,s,mat,,1
     esel,a,mat,,2
     nsle,s,all

     fldata14,temp,nomi,T_init    ! initial temperature

   *endif

    time,ftime

    esel,s,mat,,1
    esel,a,mat,,2

    *do,j,1,n_elem

        bfe,nmin,hgen,,w0(j)

        *GET,nmin,ELEM,nmin,NXTH

     *enddo

     allsel,all

     solve
```

```
/assign,esav
/assign,emat

   *SET,vv1,
   *SET,w01,
   *SET,w02,
   *SET,w0,

 finish

*enddo

 save

  /post1


!**************** display temperatures ************************

   set,last

   plnsol,temp

*ASK,temperature,'  press OK to continue

!******************graph TEMP, path along melt pool top *********

   path,weg2t,2,30,20,     ! path between two points...
   ppath,1,,0,Z2km,0       ! point at the bottom melt pool at R=0
   ppath,2,,R2,Z2km,0      ! point at the bottom melt pool at R=R2
   path,stat

   pdef, ,TEMP            ! Interpolates TEMP onto path
   /pbc,path, ,0          ! Show path on display

   plpath,TEMP            ! Display path TEMP along the bottom

*ASK,TEMP_along_melt_pool_top,'   press OK to continue '

!*******graph TEMP, path along melt pool bottom ******************

   path,weg2dt,2,30,20,    ! path between two points...
   ppath,1,,0,Z2n,0        ! point at the top drain by R=0
   ppath,2,,R2,Z2n,0       ! point at the top drain by R=R2
   path,stat

   pdef, ,TEMP            ! Interpolates TEMP onto a path
```

```
   /pbc,path, ,0          ! Show path on display

   plpath,TEMP            ! Display path TEMP along the bottom

*ASK,TEMP_along_melt_pool_bottom,'  press OK to continue '

! ****************** graph heat flux along melt pool side *******

   path,weg2,2            ! path between two points...
   ppath,1,,R2,Z2n,0      ! point at the bottom melt pool
   ppath,2,,R2,Z2km,0     ! point at the top melt pool

   pdef,  ,HFLU           ! Interpolates hflux onto a path
   /pbc,path, ,0          ! Show path on display

   plpath,HFLU            ! Display path hflux on a graph

*ASK,hflux_through_melt_pool_side,'  press OK to continue '

!******************* graph heatflux path along melt pool bottom *****

   path,weg21,2           ! path between two points...
   ppath,1,,0,Z2n,0       ! point at the bottom melt pool R=0
   ppath,2,,R2,Z2n,0      ! point at the bottom melt pool R=R2

   pdef, ,HFLU            ! Interpolates heat flux onto path
   /pbc,path, ,0          ! Show path on display

   plpath,HFLU            ! Display path HFLU along bottom

*ASK,flux_through_melt_pool_bottom,'  press OK to continue '

!******** heat losses from the melt pool side **********************
!******** calculated from alpha ***********************************

   path,weg4al,2,30,20,   ! path along melt pool surface
   ppath,1,,R2,Z2n,0      ! point at the bottom melt pool
   ppath,2,,R2,Z2km,0     ! point at the top melt pool

   pdef,TEMP,TEMP
   /pbc,path, ,0          ! Show path on displays.

   pcalc,intg,ploss2al,TEMP,s          ! integrates along path

   *get,ploss2al,path,,last,ploss2al

   m_Ts=ploss2al/(Z2km-Z2n)
```

```
    Ps_ALP=al_side*(m_Ts-T_env)*2*pi*R2*(Z2km-Z2n) ! summary losses from alpha
    m_PsALP=Ps_ALP/(2*pi*R2*(Z2km-Z2n))

!******** heat losses from the melt pool side **************************
!******** calculate from HFLU (for comparison with result calculated from alpha) *

    path,weg4fl,2,30,20,    ! path along melt pool surface
    ppath,1,,R2,Z2n,0       ! point at the bottom melt pool
    ppath,2,,R2,Z2km,0      ! point at the top melt pool

    pdef,HFLU,HFLU
   /pbc,path, ,0            ! Show path on displays

    pcalc,intg,Ps_HFL,HFLU,s,2*pi*R2          ! integrates along path

    *get,Ps_HFL,path,,last,Ps_HFL

    m_PsHFL=Ps_HFL/(2*pi*R2*(Z2km-Z2n))


!******** heat losses from the open surface of drain (0_R2sl) ****************
!******** calculate from HFLU ***********************************

    path,weg521alp,2,,20,   ! path along melt pool surface
    ppath,1,,0,Z2n,0        ! point  by R=R2sl
    ppath,2,,R2fl,Z2n,0     ! point  R=R2fl
    pdef,HFLU,HFLU          ! Interpolates TEMP onto a path

   /pbc,path, ,0            ! Show path on displays

    pcalc,mult,prod13,HFLU,s
    pcalc,intg,Pt_DR,prod13,s,2*pi     ! finds an integral

    *get,Pt_DR,path,,last,Pt_DR

    m_PtDR=Pt_DR/(pi*(R2fl**2-R2sl**2))

!******** heat losses from the melt pool bottom along flange (R2fl_R2) **
!******** calculated from HFLU ***************************************

    path,weg62alp,2,,20,    ! path along melt pool surface at flange
    ppath,1,,R2fl,Z2n,0     ! point  by R=0
    ppath,2,,R2,Z2n,0       ! point  R=R2
    pdef,HFLU,HFLU          ! Interpolates TEMP onto a path

   /pbc,path, ,0            ! Show path on displays
```

```
   pcalc,mult,prod12,HFLU,s
   pcalc,intg,Pbot,prod12,s,2*pi      ! integrates along path

  *get,Pbot,path,,last,Pbot

   m_Pbot=Pbot/(pi*(R2**2-R2fl**2))

!********* mean TEMP on the melt pool top ****************************

   path,weg53mT,2,,20,      ! path along melt pool top
   ppath,1,,0,Z2km,0        ! point at R=0
   ppath,2,,R2,Z2km,0       ! point at R=R2
   pdef,TEMP,TEMP           ! Interpolates TEMP onto a path

  /pbc,path, ,0            ! Show path on display

   pcalc,mult,prod,TEMP,s
   pcalc,intg,Tsum,prod,s,2*pi      ! integrates along a path

  *get,Tsum,path,,last,Tsum

   m_Tt  =Tsum/(pi*R2**2)          ! mean temp

finish

!************ calc. power from small inductor in drain and melt ***

      physics,read,emag2

      /assign,esav
      /assign,emat

 /solu

      ldread,temp,last,,,,,rfl

     asel,s,area,,6

     nsla,s,1
     esla,s,1

     f,n2,amps,Ism_ind1

     allsel,all

     solve
```

```
  finish

!**************************************************************

 /post1

   SET,LAST

 asel,s,mat,,1  !power from small inductor to melt
 asel,a,mat,,2

 esla,s
 nsle,s

   *get,nmin,elem,0,num,min
   *get,nmax,elem,0,num,max
   *get,n_elem,elem,0,count

   *SET,vv1,
   *SET,w01,
   *SET,w02,
   *SET,w0,

   *dim,vv1,array,n_elem
   *dim,w02,array,n_elem

 p22sm=0
 nn=0

  *do,i2,nmin,nmax,1

    *if,esel(i2),eq,1,then

     nn=nn+1

     *get,vv1(nn),elem,i2,volu
     *GET,w02(nn),ELEM,i2,Jheat,

    *endif

   p22sm=p22sm+w02(nn)*vv1(nn)

  *enddo

!****************************************************

 asel,s,area,,1  !power from small inductor to drain
```

```
   asel,a,area,,2

   esla,s
   nsle,s

     *get,nmin,elem,0,num,min
     *get,nmax,elem,0,num,max
     *get,n_elem,elem,0,count

     *SET,vv1,
     *SET,w01,
     *SET,w02,
     *SET,w0,

     *dim,vv1,array,n_elem
     *dim,w02,array,n_elem

   p22smDR=0
   nn=0

    *do,i2,nmin,nmax,1

      *if,esel(i2),eq,1,then
       nn=nn+1

        *get,vv1(nn),elem,i2,volu
        *GET,w02(nn),ELEM,i2,Jheat

      *endif

      p22smDR=p22smDR+w02(nn)*vv1(nn)

    *enddo

!********************************************************
!********************************************************

 /out,LOSS_POWER.dat

   *vWrite
  ('inductor power')

   *vwrite,P22big
  (2x,'heat_source power in big inductor, W =',e10.4)

   *vwrite,P22sm
  (2x,'heat_source power in small inductor, W =',e10.4)
```

```
   *vwrite,p22smDR
  (2x,'heat_source power from small inductor to drain, W =',e10.4)


!************************************************************

   *vWrite
  ('heat loss')

   *vwrite,Ps_ALP
  (2x,'heat loss from melt pool side, using alpha, W =',e10.4)

   *vwrite,Ps_HFL
  (2x,'heat loss from melt pool side, using HFLU, W =',e10.4)

   *vwrire,Pt_DR
  (2x,'heat loss from drain top, using HFLU, W =',e10.4)

   *vwrire,Pfl
  (2x,'heat loss from drain flange, using HFLU, W =',e10.4)

   *vwrire,Pbot
  (2x,'heat loss from melt pool bottom through flange, using HFLU, W =',e10.4)

!*************************************************************

   *vWrite
  ('mean TEMP')

   *vwrite,m_Tt
  (2x,'mean TEMP on the melt pool top surface, Deg_C =',e10.4)

!*************************************************************

   *vWrite
  ('mean heat flux')

   *vwrite,m_PsALP
  (2x,'mean heat flux from the melt pool side, using ALPHA,W/m**2 =',e10.4)

   *vwrite,m_PsHFL
  (2x,'mean heat flux from the melt pool side, using HFLU,W/m**2 =',e10.4)

   *vwrite,m_PtDR
  (2x,'mean heat flux from drain top ,W/m**2 =',e10.4)

   *vwrite,m_Pfl
```

```
(2x,'mean HF from flange ,W/m**2 =',e10.4)

 *vwrite,m_Pbot
(2x,'mean heat flux from the melt pool bottom through flange, W/m**2 =',e10.4)

/out

/go


   physics,read,fluid

  set,last

  plnsol,temp

finish
```

APPENDIX C

Selected Experimental Logs and Data

Table C-1. CCIM Test #1 300 mm Diameter CCIM Test Parameters – Three-Turn Coil.

Time hr:min	U_a, kV	I_a, A	I_g, A	U_{ind}, point	f, MHz	T_{melt}, ^{o}C	Note
13:40	10.5	-	-	1.0	-	-	Generator powered on
14:00	8.0	3.87	1.140	0.73	1.835	-	-
14:07	8.5	4.17	1.23	0.8	-	-	Melt initiated, graphite ring floats.
14:12	9.0	4.43	1.29	0.84	1.835	-	-
14:21	9.0	6.40	1.16	0.8	1.836	-	-
14:25	4.8	8.03	1.39	0.32	1.86	-	Removed graphite ring. Fine tuning of a generator mode.
14:36	4.8	8.2	1.35	0.31	-	1320-1440	-
14:40	4.9	8.23	1.38	0.32	-	-	a_2 on center axis - 65 mm, side ~30 mm.
14:52	4.9	8.24	1.27	0.30			-
15:00	5.8	9.0	1.40	0.35	1.897	1350	-
15:10	5.2	8.5	1.25	0.31		1400	-
15:20	5.2	8.2	1.19	0.3	1.897	1420	Melt surface even with bottom of top coil.
15:30	5.0	8.0	1.12	0.27	-	1340	-
15:31	4.6	7.5	1.05	0.26	-	1300	Temperature was measured in hot points
15:34	4.6	7.5	1.08	0.26	-	1300	-
15:37	4.25	7.0	1.00	0.25	-	1200	-
15:40	4.0	6.5	0.958	0.24	-	1180	Temperature was measured at hot zones. Under cold cap temperature was higher. From 14:52 to 15:40 frit was melted. a_2 - 110 mm.
15:50	4.0	6.65	1.011	0.25	1.866	1050	Temperature was measured on cold cap. Cover off. a_2 = 150 mm. Cover on. Calorimetry taken.
16:16	4.0	6.85	1.082	0.26	-	1200	Temperature checked with immersed thermocouple – 1190 ^{o}C. Taken at 70 mm depth at 75 mm radius.
16:30							Test ended.

(a_2 – melt pool depth; U_a – anode voltage, I_a – generator lamp anode current; I_g – generator lamp grid current on sensor; f – generator current frequency; U_{ind} – inductor voltage after inductor ground point, measured by voltmeter)

Table C-2. CCIM Test #2: 300 mm Diameter CCIM Test Parameters – Two-Turn Coil.

Time, min	U_a, A	I_a, A	P_{gen}, kW	I_g, A	f, MHz	U_{ind}, kV	T_{melt}, ºC	Notes
0	8.92	3.2	28.54	1.23	1.785	4.62	-	Generator powered on
3	9.38	3.5	32.83	1.32	1.785	4.81	-	Mode increased
10	10.25	3.9	39.97	1.44	1.785	5.18	-	Mode increased
27	10.18	4.6	46.82	1.33	1.889	5.14	-	Ring removed
33	6.98	6.1	42.57	1.03	1.889	2.96	-	Melt overheating
34	5.56	5	27.8	0.81	1.889	2.40	-	Mode decreased
39	5.52	4.9	27.04	0.84	1.889	2.40	1400*	a_2 = 50 cm
55	5.91	5.25	31.02	0.79	1.889	2.20	-	Frit melting e
67	5.4	6.1	32.94	1.23	1.93	2.59	1400*	a_2 = 95 mm
117	6	6	36	0.75	1.93	2.40	1350	The first mode*** a_2 = 105 mm
151	4.88	4.5	21.9	0.67	1.93	2.03	1150* 1280**	The second mode*** a_2 = 90 mm
186	4.5	3.95	17.77	0.67	1.862	1.94	1000* 1180**	Measurements by thermocouples
244	4.5	4	18	0.72	1.862	2.03	1000* 1180**	The third mode** a_2 = 90 mm

(P_{gen} – power consumed by the generator from the rectifier; *– Melt surface maximum temperature measurement; ** - Melt maximum temperature measurement under cold cap; *** – power measurement)
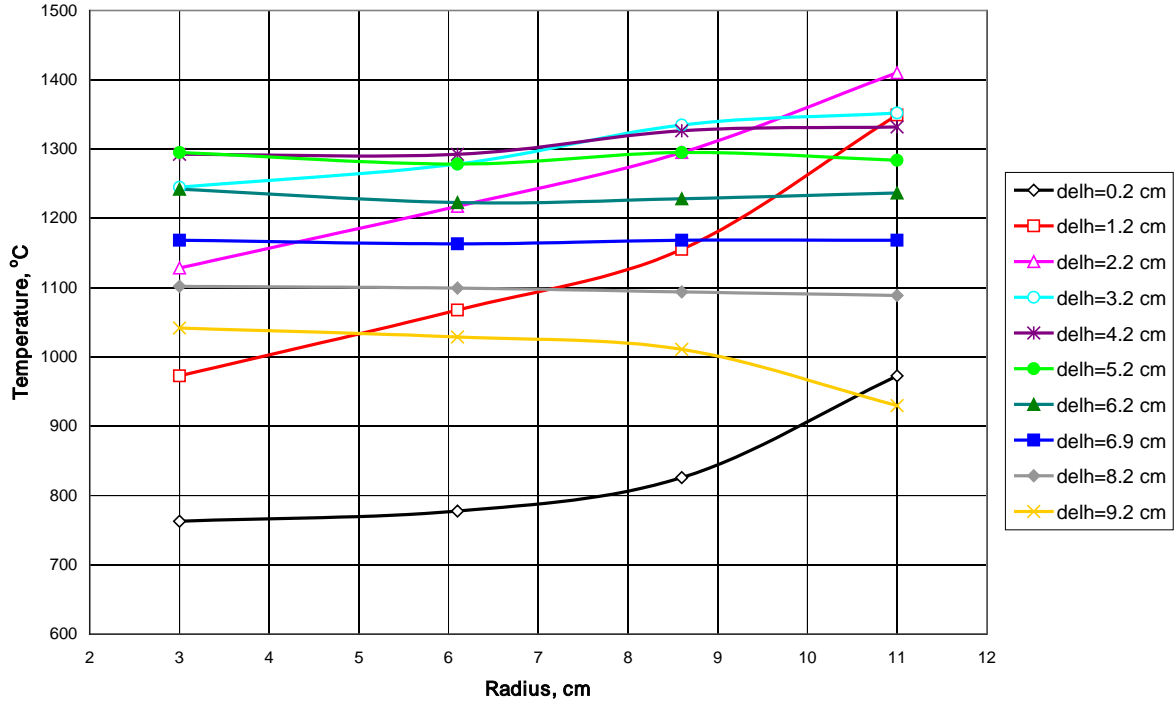
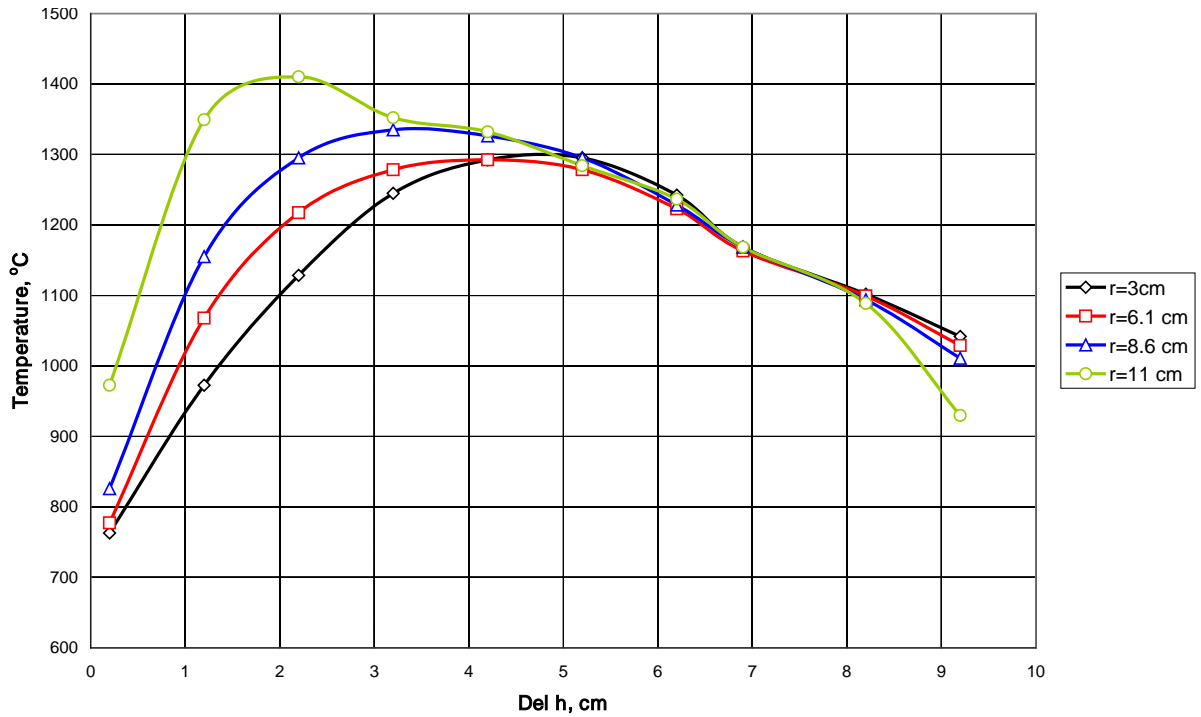**Figure C-1.** CCIM Test #2 horizontal temperature profiles at various depths of melt.

Figure C-2. CCIM Test #2 Temperature changes for various depths at various radii of melt pool.

Table C-3. CCIM Test #3 - 300 mm Diameter CCIM Test Parameters – Three-Turn Coil.

Time, hr:min	I_a, A	I_g, A	U_{ind}, kV	U_a, kV	f, MHz	U_c, kV	Note
13:10	3.2	1.3	6.45	8	1.87	-	Generator powered on
13:43	4.9	1.7	8.75	10.6	-	-	Mode increased
13:45	8	1.25	2.72	4.5	-	2.8	Graphite ring taken out
14:16	9	1.3	3.19	6.3	-	3.2	a_2 = 135 mm. Melt pool growth.
14:30	9	1.3	3.19	6.5	-	3.3	a_2 = 155 mm.
14:34	9	1.3	3.2	6.5	1.94	3.4	T_{melt} = 1400°C.
14:50	9	1.23	3.11	6.5	-	3.2	a_2 = 175 mm.
15:10	7.1	1.1	2.19	4.13	-	2.25	T_{melt} = 1100°C.
15:16	7.05	1.04	2.15	4.03	-	-	T_{melt} = 1050 – 1070°C.
15:20	7	1.07	2.13	3.92	-	2.2	T_{melt} = 1030°C.
15:25	6.9	1.07	2.11	3.71	-	2.2	T_{melt} = 1020°C.
16:07	6.9	1.12	2.77	3.69	-	2.8	Measurements by thermocouples were started
16:10	7.2	1.2	2.41	3.69	-	2.5	h_{tc} = 0.
16:12	7.3	1.2	2.41	3.69	-	2.5	h_{tc} = 12 mm.
16:42	7.15	1	2.38	3.69	-	-	h_{tc} = 62 mm.
17:33	-	-	-	-	-	-	Continuation of measurements by thermocouples
17:41	-	-	-	-	-	-	At h_{tc} = 150 mm, the outermost thermocouple contacted the skull. Thermocouple was taken out and measurements were continued.
17:50	7.3	1.2	2.28	3.71	1.95	2.3	h_{tc} = 152 mm. Thermocouples contacted the bottom skull
17:56	7.75	1.25	2.42	3.75	-	2.45	Mode was increased. T_{melt} = 1050°C. Thermocouple No 7 failed. Thermocouples were taken out in 20 mm steps.
19:08	-	-	-	-	-	-	Measurements by thermocouples were finished.
19:10	7.6	1.23	2.4	3.6	-	2.42	T_{melt} = 1010°C. a_2 = 155 mm.
19:30	7.7	1.28	2.5	3.7	-	2.65	T_{melt} = 1080°C. The generator was powered off.

(a_2 – melt pool height; U_a - anode voltage on sensor; I_a - generating lamp anode current on sensor; I_g - generating lamp grid current on sensor; f – generator current frequency; U_{ind} - voltage on the inductor; T_{melt} – maximum temperature on melt surface; h_{tc} – depth of the thermocouple junctions in the melt; U_c - voltage on a $C_{w\ cont}$ sensor on generator).

Table C-4. CCIM Test #3 Radial distribution of temperatures (descending).

Depth, cm	Steps	Radius, cm						
		1	2.95	5.7	7.65	10.3	12.3	13.65
0	1	508	437	437	508	817	906	864
1	2	834	793	876	929	1150	1260	1177
2	3	1057	1013	1169	1221	1346	1438	1376
3	4	1137	1097	1232	1326	1385	1438	1367
4	5	1246	1232	1288	1376	1367	1376	1288
5	6	1240	1288	1308	1376	1367	1376	1218
6	7	1288	1218	1317	1361	1346	1361	1191
7	8	1317	1196	1317	1346	1346	1346	1177
8	9	1280	1201	1265	1285	1280	1331	1097
9	10	1251	1204	1223	1232	1232	1317	1000
10	11	1177	1177	1169	1204	1204	1317	904
11	12	1110	1110	1097	1123	1131	1274	805
12	13	1039	1036	1031	1052	1057	1218	696
13	14	980	975	975	993	993	1163	642
14	15	929	929	924	929	891	1118	-
15	16	879	866	866	866	805	1031	-
16	17	837	829	817	817	756	967	-

Table C-5. CCIM Test #3 Radial distribution of temperatures (ascending).

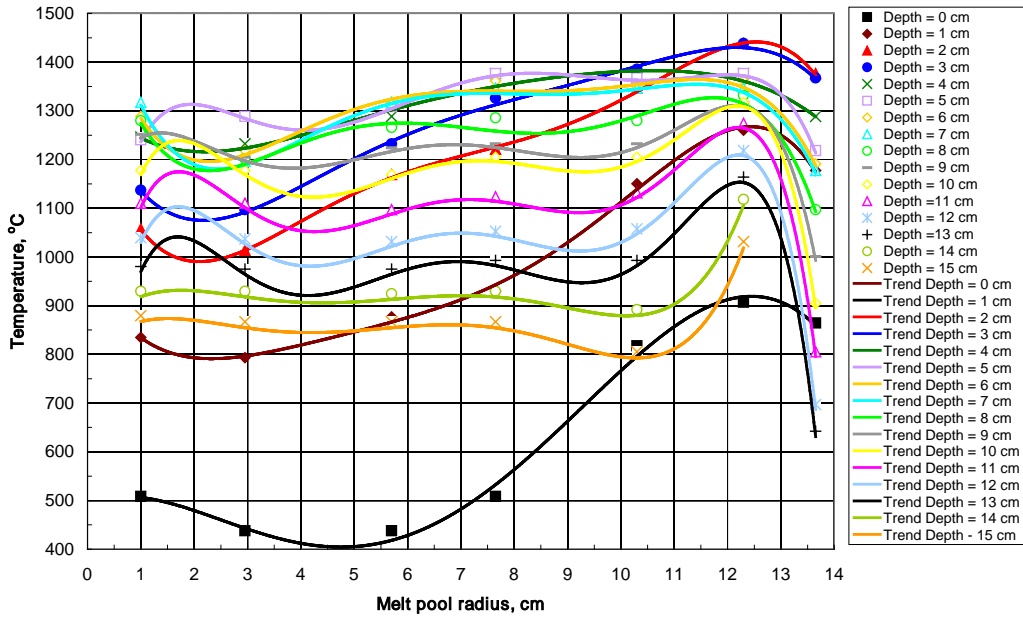|		Pool radius, cm				
Depth	Step	1	2.95	5.7	7.65	10.3
16	1	744	817	810	827	822
14	2	906	904	884	937	-
12	3	937	924	906	942	-
10	4	1052	1057	1049	1078	-
8	5	1223	1221	1215	1232	-
6	6	1215	-	-	-	-
4	7	1302	-	-	-	-
2	8	1317	-	-	-	-
0	9	1083	-	-	-	-

Figure C-3. CCIM Test #3 horizontal temperature profiles at various depths of melt (descending).
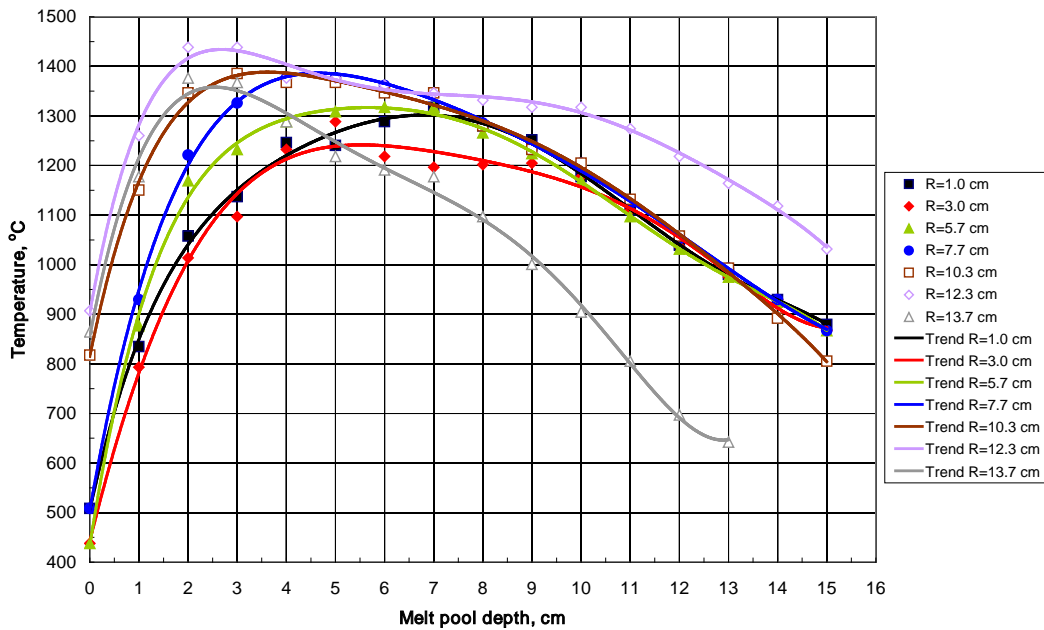

Figure C-4. CCIM Test #3 Temperature changes for various depths at various radii of melt pool (descending).

Table C-6. CCIM Test #4 - 300 mm Diameter CCIM Test Parameters – Three-Turn Coil.

τ, hr.min	I_a, A	I_g, A	U_{ind}, kV	U_a, kV	T_{CrAl}, mV	f, MHz	Note
14.00	2.55	0.9	4.97	6.93	20	1.69	Generator powered on.
14.17	2.71	1.0	5.38	7.5	35		
14.38	3.01	1.09	5.7	7.99	50		Mode increased
15.28	3.83	1.09	5.99	8.5	100	1.78	
15.36	5.17	0.9	3.42	5.1	110	1.74	Ring removed. Generator tuning.
15.59	7.28	1.2	3.04	5.66	140	1.76	Melt pool growth.
16.14	6.1	1.11	2.78	4.91	200		a_2 = 115 mm. T_{melt} = 1200°C.
16.20	5.98	1.21	2.99	4.91	230	1.747	Melt pool growth using glass pieces. Frequency tuning by capacity.
16.25	5.84	1.21	2.97	4.92	250		a_2 = 145 mm. T_{melt} = 1250°C.
16.56	6.44	1.15	2.83	5	320	1.75	T_{melt} = 1280°C. a_2 = 150 mm.
17.09	6.48	1.2	2.77	5.01	340		T_{melt} = 1300°C. a_2 = 150 mm.
17.17	6.43	1.1	2.78	5	355	1.75	Calorimetry taken.
17.23	5.78	1	2.48	4.5	360		T_{melt} = 1200°C. Mode reduction.
17.24	5.1	0.9	2.18	4	365		T_{melt} = 1120°C. Mode reduction.
17.30	5.08	0.9	2.24	4	370	1.74	T_{melt} = 1027°C. a_2 = 150 mm. Calorimetry taken.
17.41	4.63	0.89	2.14	3.7	380	1.74	T_{melt} = 980°C. Mode reduced.
17.48	4.55	0.9	2.18	3.7	385	1.74	a_2 = 164 mm on crucible axis. T_{melt} = 965°C. Calorimetry taken. Measurements by thermocouples.
18.56	5.69	1.09	2.61	4.5	390	1.745	T_{melt} = 1060°C. Measurements by thermocouples.
19.17						1.748	Generator powered off

(a_2 – melt pool height; U_a - anode voltage on sensor; I_a - generating lamp anode current on sensor; I_g - generating lamp grid current on sensor; f – generator current frequency; U_{ind} - voltage on the inductor; T_{melt} – maximum temperature on melt surface; h_{tc} – depth of the thermocouple junctions in the melt; U_c - voltage on a $C_{w\ cont}$ sensor on generator).

Figure C-5. CCIM Test #4 horizontal temperature profiles at various depths of melt (descending).

Figure C-6. CCIM Test #4 Temperature changes for various depths at various radii of melt pool (descending).
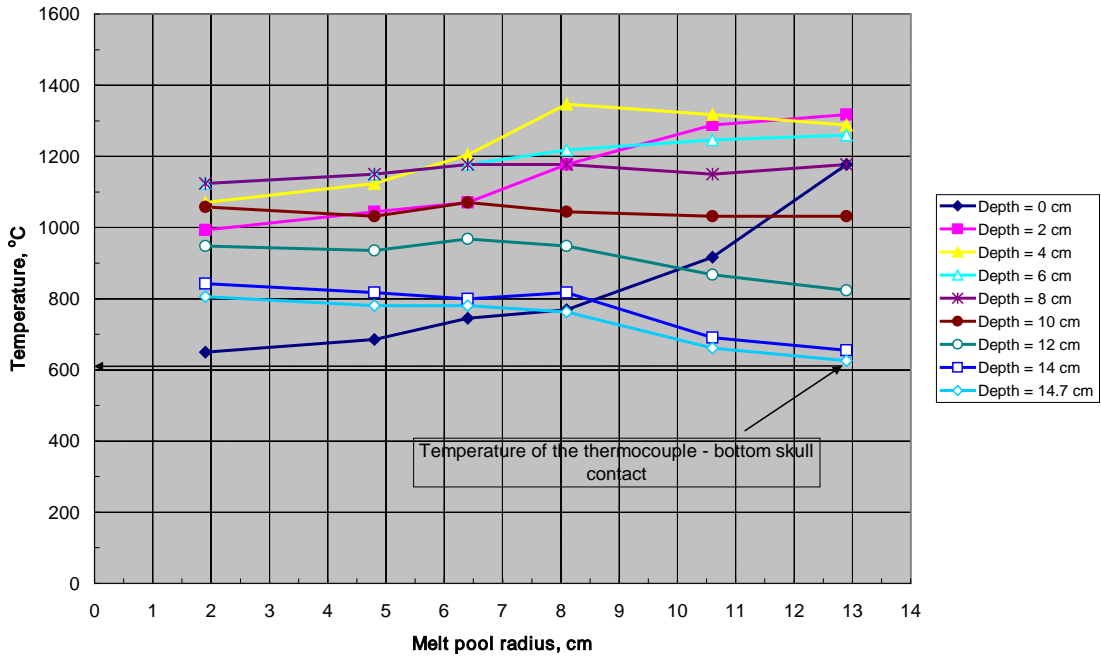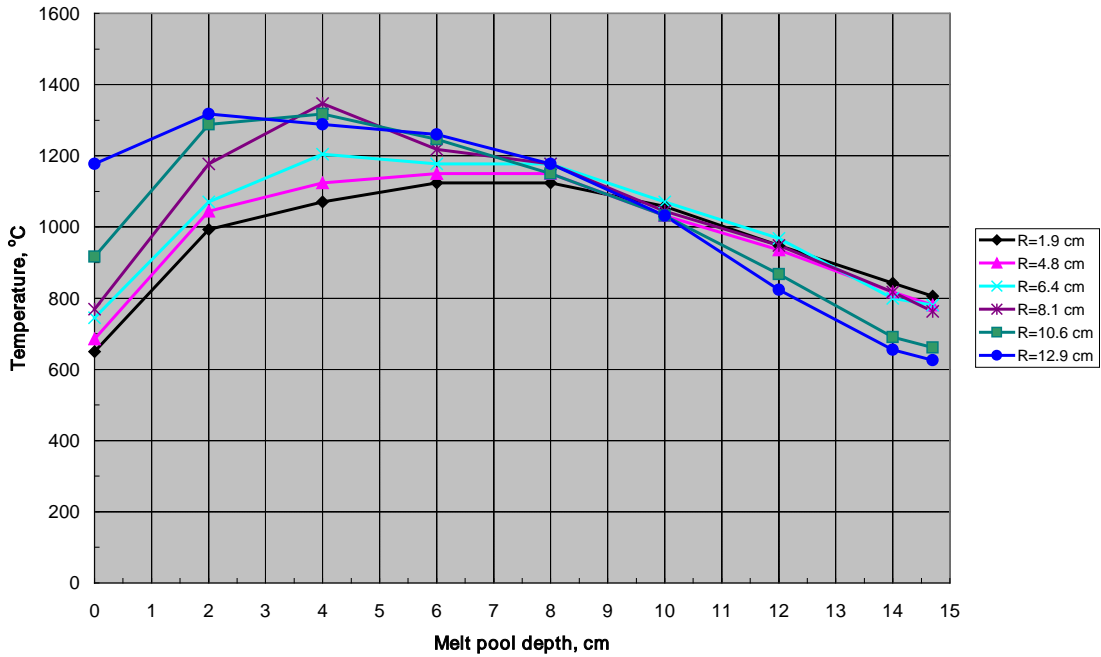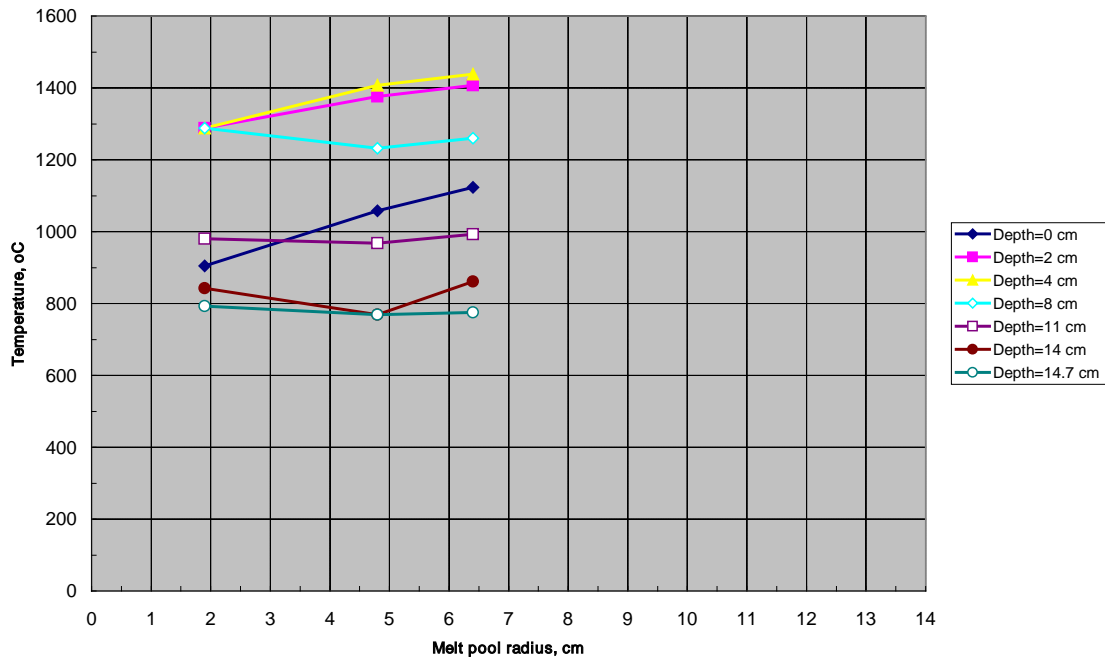
Figure C-7. CCIM Test #4 horizontal temperature profiles at various depths of melt (ascending).
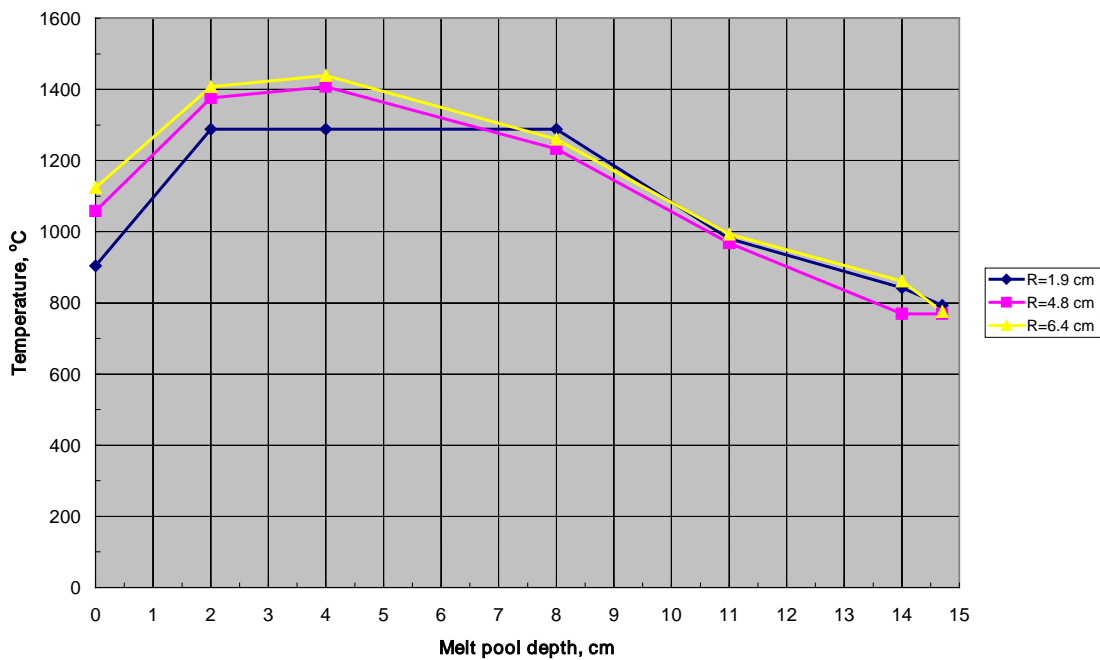

Figure C-8. CCIM Test #4 Temperature changes for various depths at various radii of melt pool (ascending).

Table C-7. CCIM Test #5 Data

Time, hr:min	I_a, A	I_g, A	U_{ind}, kV	U_a, kV	T_{tc1}, °C	T_{tc2}, °C	f, MHz	Notes
12:32	6.0	1.38	4.97	9.58	123	160	-	Generator powered on
13:07	4.21	1.03	5.38	7.73	242	273	1.826	Sensor signals recorded
13:24	3.87	0.97	2.3	7.08	-	-	-	The first mode. a_2 = 180 mm. T_{melt} = 1200°C.
14:30	3.61	0.97	2.4	7.02	352	529	1.822	Calorimetry
17:00	3.38	0,97	2.3	6.81	-	-	-	Sensor signals recorded
17:18	-	-	-	-	-	-	-	First temperature profile measurement. Thermocouples lowered
19:15	-	-	-	-	348	478	-	180 mm total depth.
19:25	3.61	1.07	2.43	7.33	348	472	1.822	The second mode was set. Signals recorded at 19:35. a_2 = 178 mm. T_{melt} = 1190°C.
19:40	-	-	-	-	-	-	-	Second temperature profile measurement. Thermocouples raised.
19:44	-	-	-	-	-	-	-	No. 8 thermocouple failed. It was replaced.
20:46	-	-	-	-	-	-	-	Thermocouples out of the melt
21:07	-	-	-	-	348	473	1.822	Calorimetry. Sensor signals recorded at 21:20. Thermocouples were changed. 6 thermocouples were set.
21:36	3.12	0.9	2.08	6.36	350	468	1.822	The mode was lowered. The third mode was set. T_{melt} = 1150°C. Calorimetry.
22:03	-	-	-	-	-	-	-	Sensor signals recorded
22:05	-	-	-	-	-	-	-	Third temperature profile measurement. Thermocouples were lowered.
22:19	-	-	-	-	-	-	-	No. 7 and 8 thermocouples contact skull at 150 mm depth.
22:29	-	-	-	-	355	541	-	180 mm total depth. No. Thermocouples at positions 3 through 6 were raised 2 mm.
22:37	-	-	-	-	354	547	-	Generator powered off

(T_{tc1} – indications of the ground thermocouple located in 100 mm from the pool axis, °C; T_{tc2} - indications of the ground thermocouple located on the pool axis, °C; I_a – lamp anode current, A; I_g – lamp grid current, A; U_{ind} – voltage on the inductor, kV; U_a – voltage on lamp anode, kV; f – current frequency, MHz)

Table C-8. Thermocouple indications inside melt pool for the first mode.

Depth, mm	Temperature, °C							
	Number of thermocouple							
	1	2	3	4	5	6	7	8
0	1137.9	1291.1	1270.6	1240.6	1286.1	1385.7	1447.6	-
10	1098.3	1233.6	1266.4	1306.4	1297.8	1386.9	1413.7	-
20	1065.4	1170.2	1092.3	1209.4	1295.4	1346.6	1428.3	-
30	1262.9	1286.6	1299.2	1330.3	1318.1	1363.3	1365.9	-
40	1344.3	1293.2	1265.6	1319.5	1318.4	1335.1	1343.9	-
50	1214.6	1296.4	1183.3	1283.4	1303.8	1299.0	1309.3	-
60	1226.4	1274.0	1200.1	1264.1	1278.3	1281.8	1301.4	-
70	1173.6	1202.6	1196.7	1237.7	1229.4	1258.1	1252.7	1271.3
80	1162.4	1166.3	1150.5	1161.4	1166.0	1134.9	1171.0	1141.6
90	1123.4	1123.0	1110.0	1126.2	1141.3	1080.4	1129.9	1073.6
100	1121.8	1127.0	1109.1	1128.3	1138.0	1085.9	1154.0	1058.4
110	1116.9	1123.2	1104.8	1122.1	1124.0	1098.8	1155.4	1058.5
120	1099.4	1108.0	1088.2	1105.0	1108.3	1085.7	1148.8	1015.0
130	1050.7	1064.9	1050.3	1064.8	1073.0	1045.6	1087.5	951.9
140	1023.3	1038.4	1024.1	1034.4	1045.1	1019.1	1023.5	921.5
150	971.8	959.7	965.9	978.5	987.6	968.1	1021.0	790.4
160	941.0	879.9	924.3	940.8	944.6	928.7	967.2	708.0
170	888.3	879.8	874.6	902.9	904.1	902.3	881.1	644.3
180	800.7	801.2	792.0	787.7	776.1	745.3	693.7	-

Table C-9. Thermocouple indications inside melt pool for the third mode.

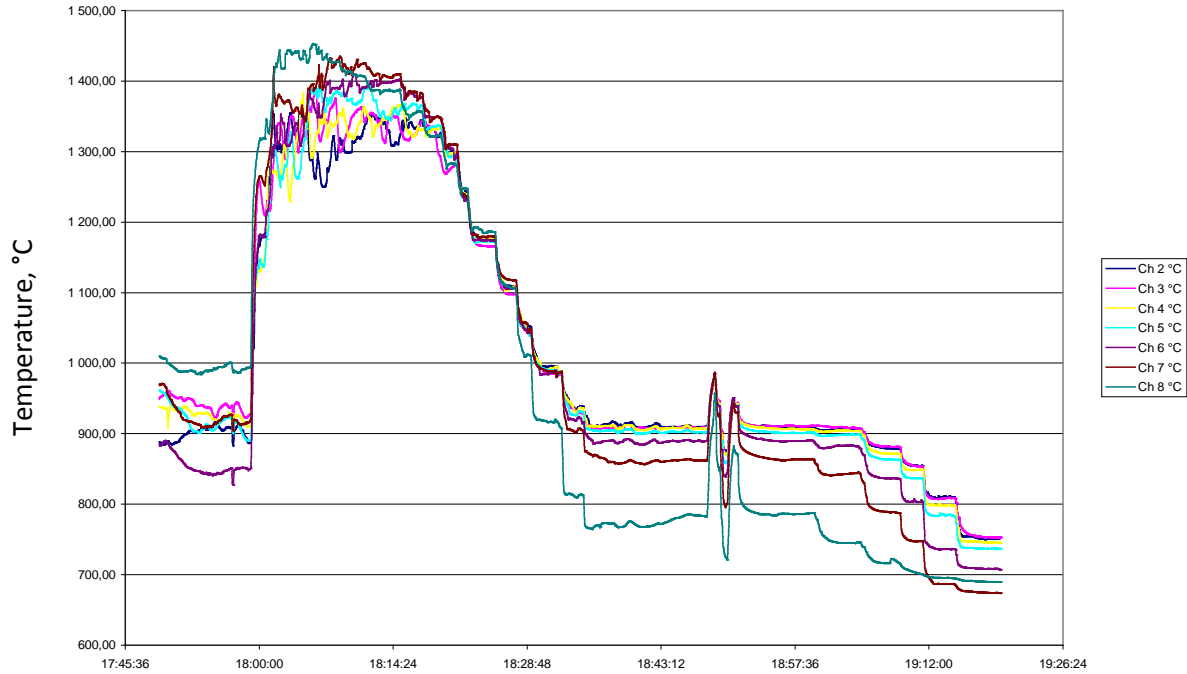| Depth, mm	Temperature, °C					
	Number of thermocouple					
	3	4	5	6	7	8
20	1251.4	1043.5	1277.5	1312.4	1319.5	1391.3
40	1254.0	1116.7	1274.7	1356.3	1372.8	1392.2
60	1267.2	1170.7	1239.8	1303.8	1306.7	1313.7
80	1244.8	1175.1	1218.9	1242.1	1295.8	1295.2
100	1158.5	1186.0	1138.8	1178.2	1174.3	1184.9
120	1057.9	1041.7	1061.0	1046.4	1090.4	1036.6
140	939.9	1016.7	948.5	978.9	1005.2	943.5
150	921.3	971.4	896.3	877.7	746.9	671.6
170	901.6	956.2	902.2	834.2	734.7	657.4
180	845.5	879.0	843.2	799.6	737.4	657.4

Figure C-9. CCIM Test #5 Temperature changes for various depths at various radii of melt pool during first mode (descending).
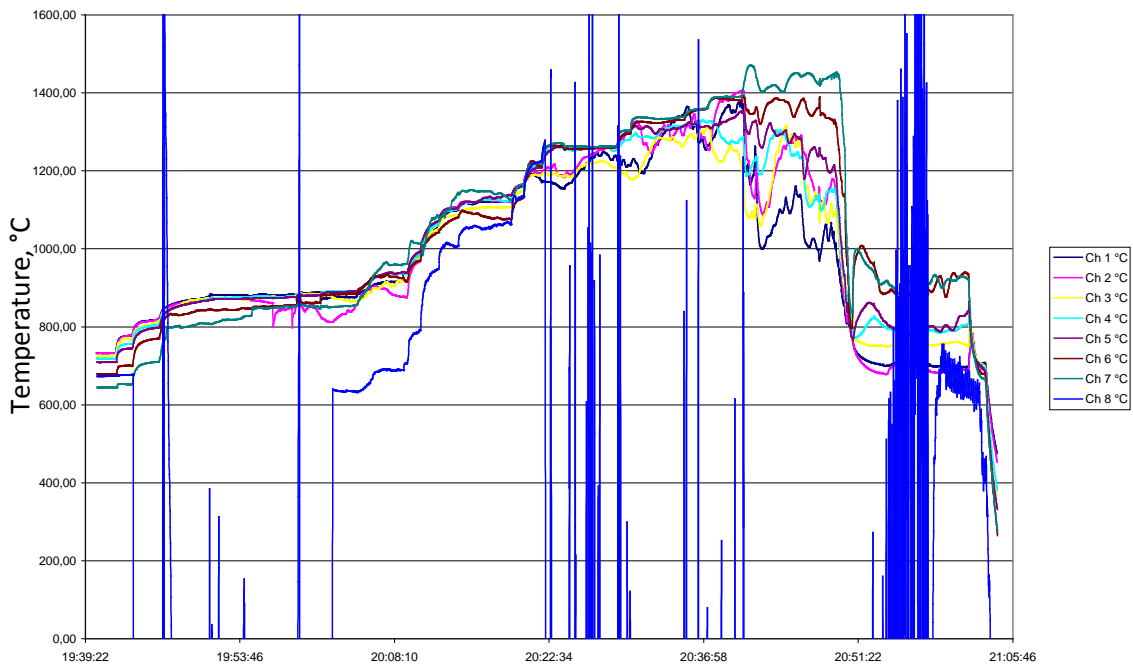

Figure C-10. CCIM Test #5 Temperature changes for various depths at various radii of melt pool during second mode (ascending).
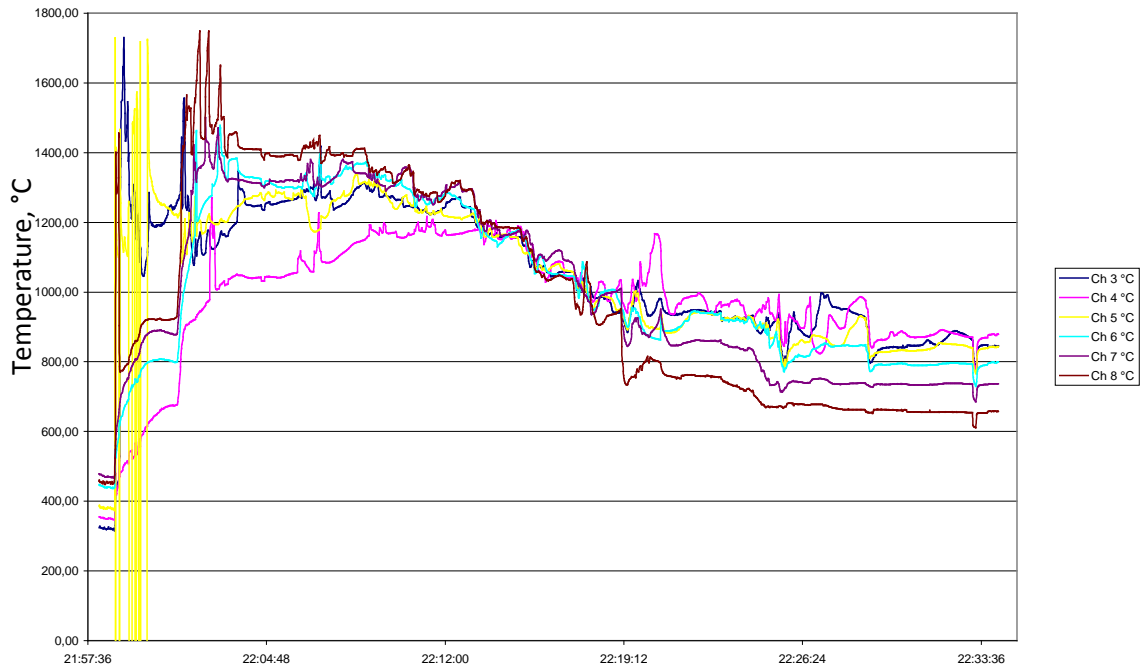
Figure C-11. CCIM Test #5 Temperature changes for various depths at various radii of melt pool during third mode (descending).
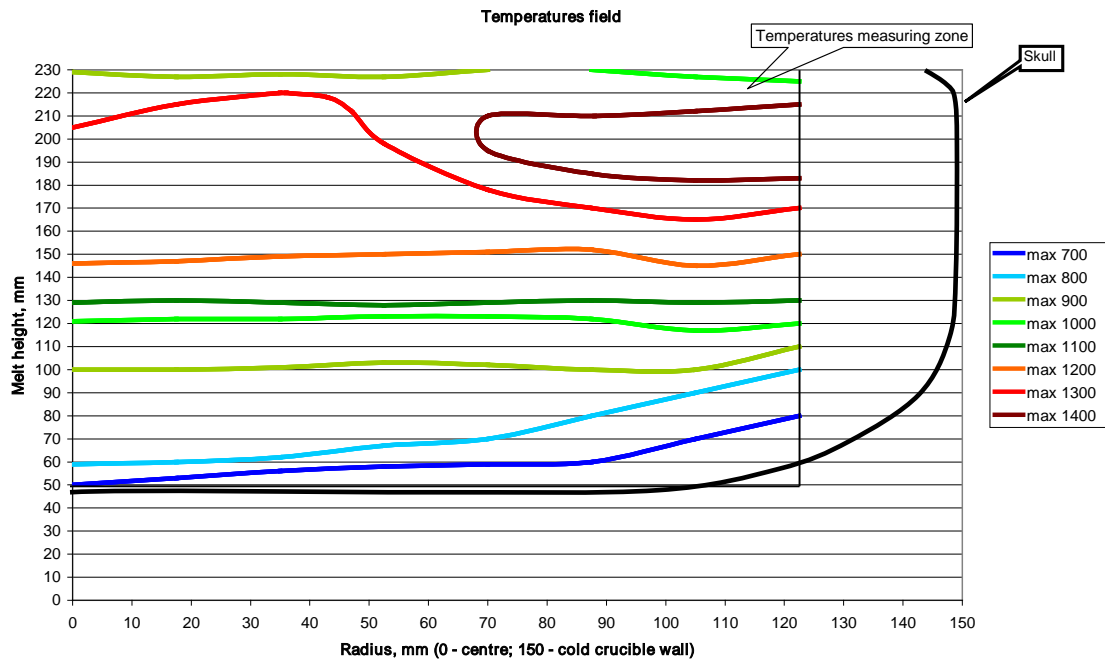

Figure C-12. CCIM Test #5 Temperature profile inside the melt during the first mode.
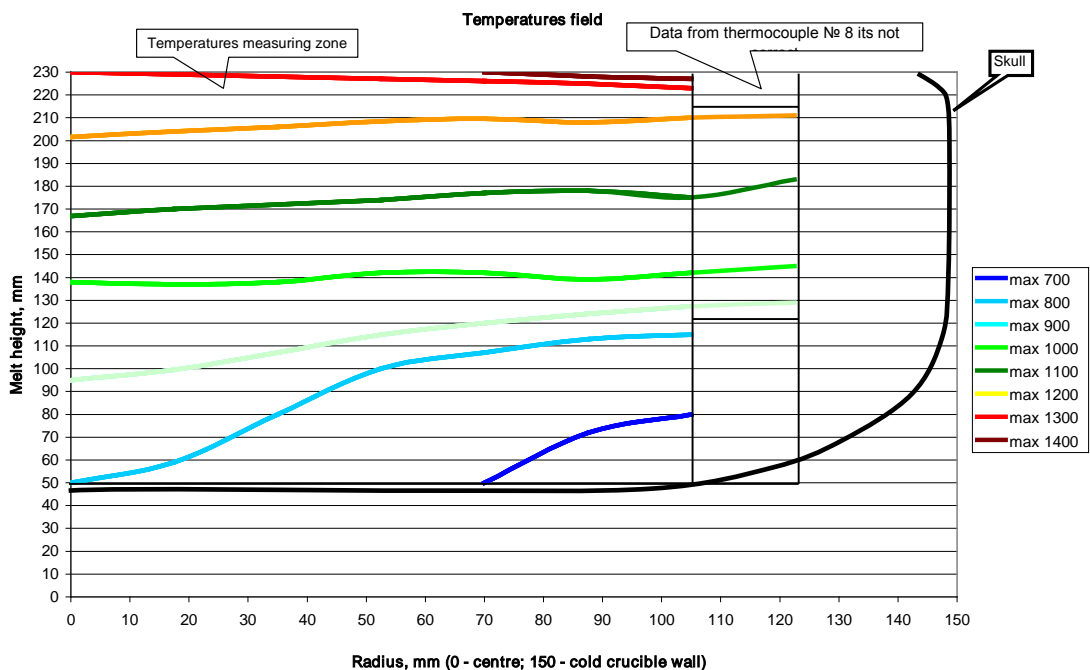
Figure C-13. CCIM Test #5 Temperature profile inside the melt during the second mode.
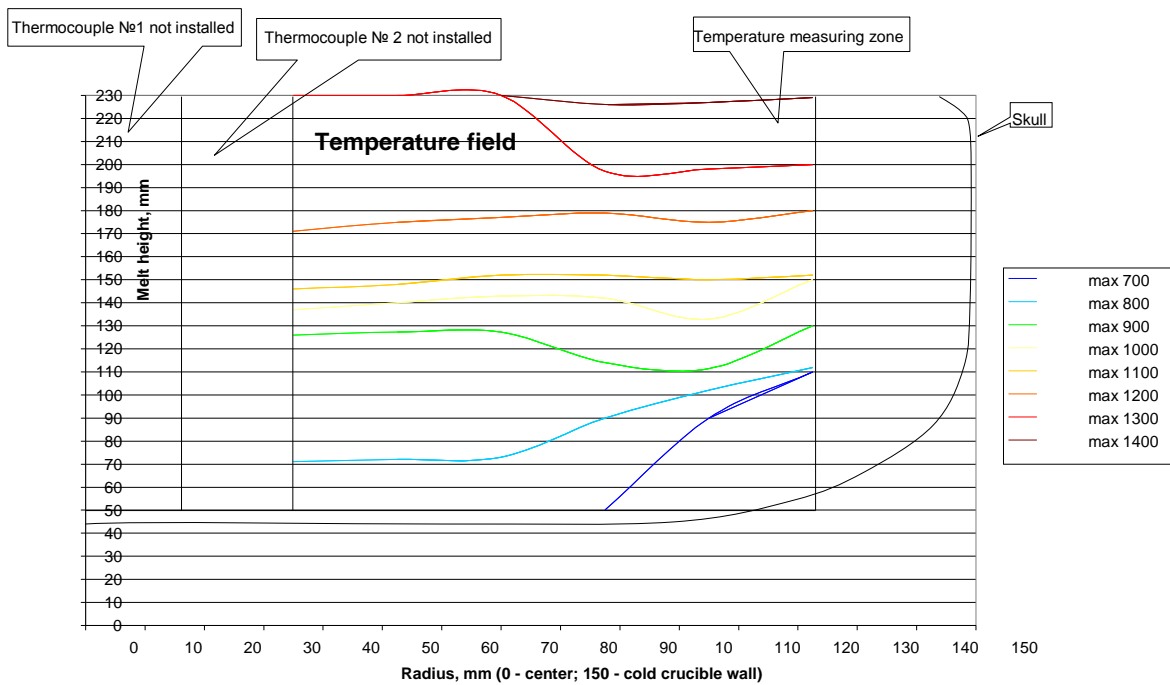

Figure C-14. CCIM Test #5 Temperature profile inside the melt during the third mode.

ADDITIONAL STUDIES ON GLASS EMISSIVITY FROM INTEGRATED TEST SERIES #7

To determine an integrated value for the emissivity of the glass melt, the following approach was used:

1. A melt pool was established and a stationary temperature mode obtained. Calorimetry is taken.
2. The melt pool surface was scanned across its diameter with the pyrometer.
3. The melt surface was then covered by a thin layer of frit to function as an insulator for eliminating the radiation heat transfer. Calorimetry is taken.
4. After the frit melted, a new stationary mode was established, and the process repeated.
5. Total power of losses due to radiation from the melt were determined by comparing the total calorimetry of the system, including the crucible and cover.
6. The melt pool surface was mathematically divided into rings with of a specific temperature based on the pyrometer measurements of temperature distribution for each radius measured.
7. The measured power of radiation from the melt pool $P_{int\,rad}$ is equal to the sum of the powers radiated from the melt "rings" with different temperatures, as determined by pyrometer scanning. Therefore, the melt emissivity value can be determined using the Stefan-Boltzmann law as follows

$$\varepsilon = \frac{P_{int\,rad} \cdot 10^8}{5.67 \cdot \sum ((T_i^4 - T_0^4) \cdot S_i)} \qquad \text{(C-1)}$$

$$S_i = (R_i^2 - R_{i-1}^2) \cdot \pi, \quad м^2 \qquad \text{(C-2)}$$

(T_i and S_i - melt temperature and area of the i ring; T_0 - ambient temperature equal to 300K; R_i - external radius of the i ring; R_{i-1} - external radius of the i-1 ring, equal to internal radius of the i ring)

Integrated Test #7a.

Based on the calorimetry and temperature data for the melt surface, the following observations can be made:

- The difference in total heat before and after charge filling is about 9 kW, see Figure C-15.
- Radiation heat transfer to the cover is 2.8 kW, see Figure C-16.
- Total power of radiation from melt surface is $P_{int\,rad}$ = 11.8 kW.

0 – time of frit addition

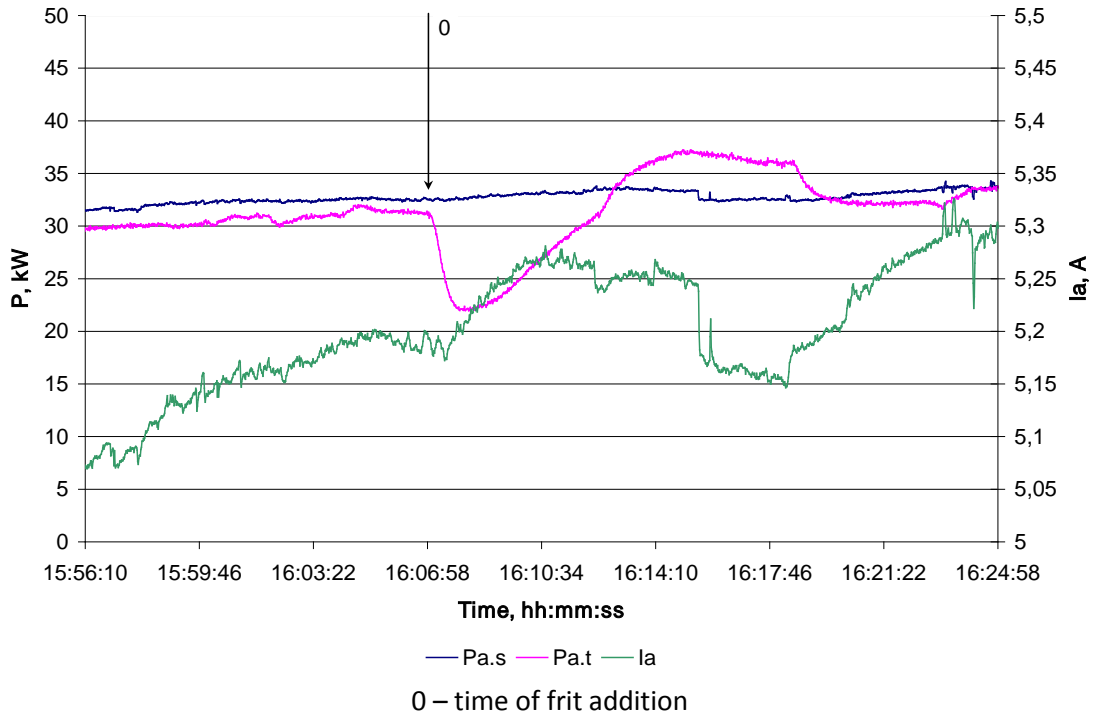**Figure C-15.** Key parameters and calorimetry data for determining emissivity of glass.

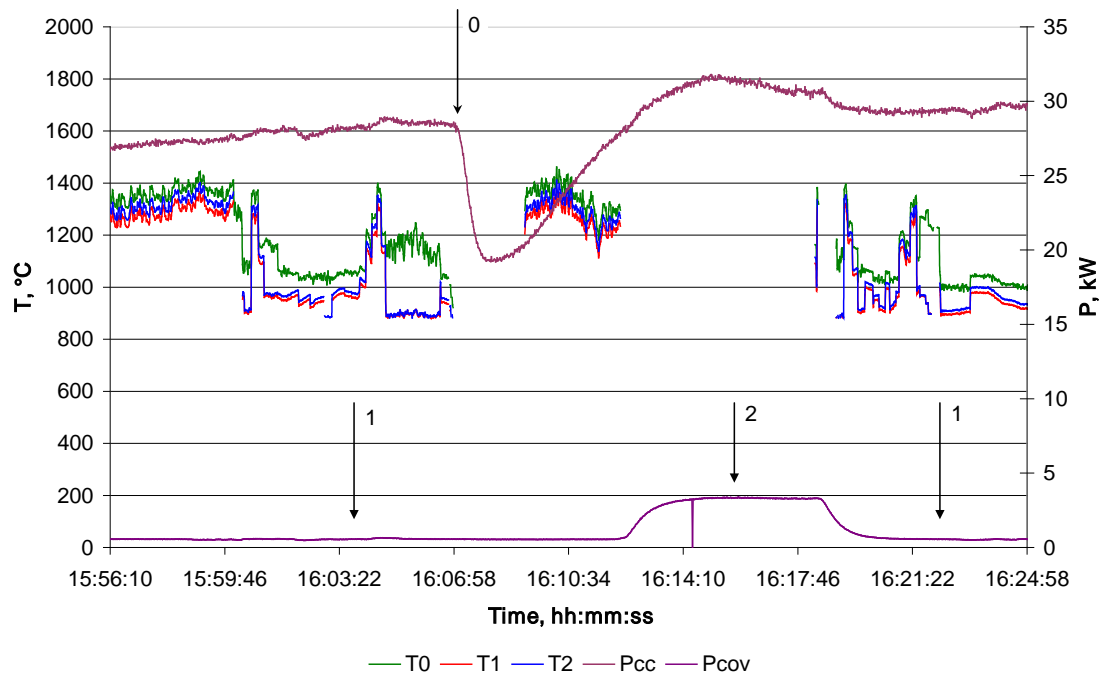0 – time of frit addition; 1 – cover lid off; 2 – cover in place.

Figure C-16. Key parameters and calorimetry data for determining emissivity of glass.

Figure C-17 and Figure C-18 show the temperature data taken during the surface scannings by the pyrometer. The data for each scan were curve fit using a sixth order polynomial. These were then combined to obtain an average. The first case is for the steady state modes, and the second case is for the modes immediately after the added frit had melted. Temperatures are reported in Kelvin.

$$y = -5E{+}08x^6 + 4E{+}06x^5 + 1E{+}07x^4 - 55527x^3 - 26388x^2 - 343{,}8x + 1050{,}4$$
$$R^2 = 0{,}9382$$

R – radius of the melt pool, mm
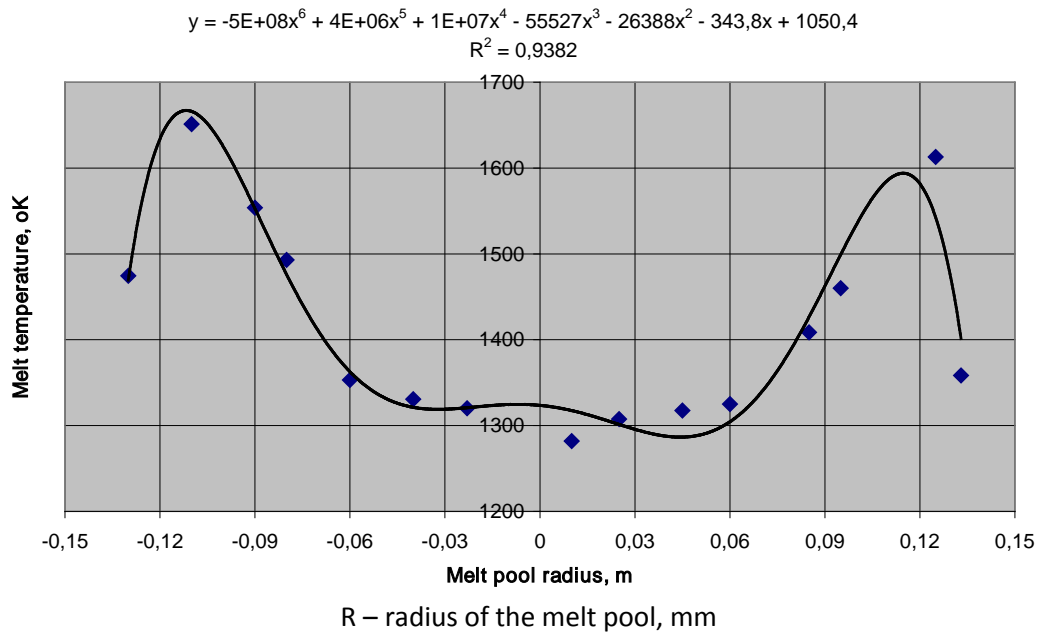
Figure C-17. Temperature data from scanning with polynomial curve fit at steady state.

$$y = -4E{+}08x^6 - 6E{+}06x^5 + 9E{+}06x^4 + 89854x^3 - 19753x^2 + 114{,}28x + 1327$$
$$R^2 = 0{,}9552$$

R – radius of the melt pool, mm

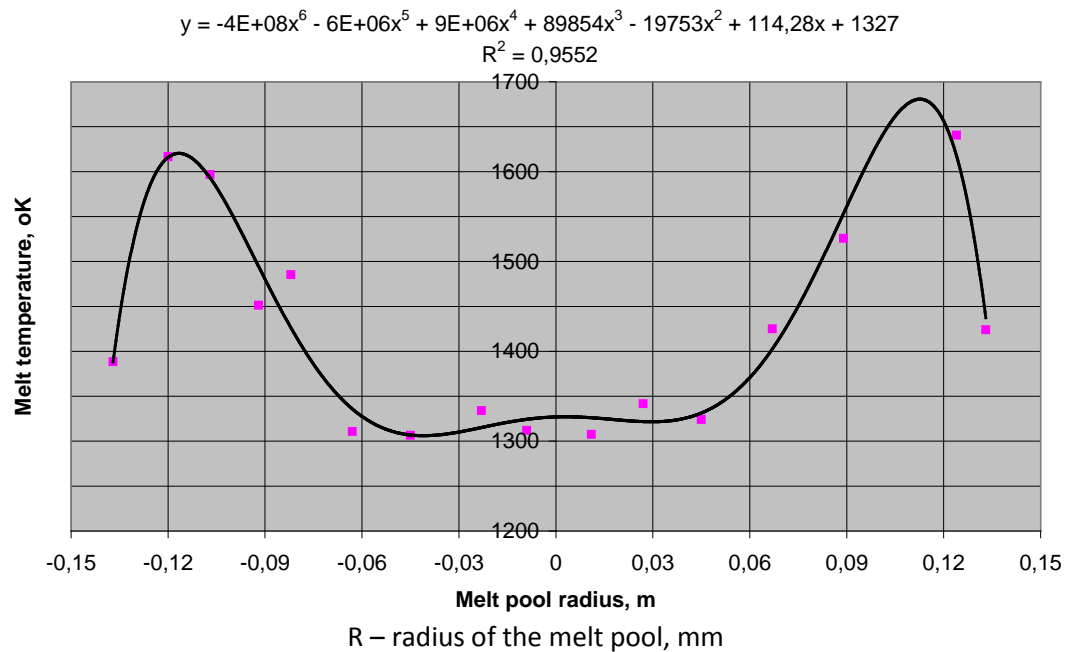**Figure C-18.** Temperature data from scanning with polynomial curve fit after frit melting.

Using Eq. C-1, with the polynomial distribution curve to determine values at specific radial locations, the surface was divided into rings and then the emissivity values were calculated. For the steady state mode the value was 0.414, and after the frit had melted, 0.382. As comparison, the value used in the model is 0.5, and this resulted in a radiation heat transfer value of 13.09 kW, or about 10.9 % more than in this test.

Integrated Test #7b.

During the next test, the emissivity value was measured again using the same method. Multiple data sets were needed to have representativeness because the surface that is being scanned is dynamic. To obtain better results scanning was performed on two diametrical paths, perpendicular to each other.

Based on the calorimetry and temperature data for the melt surface, the following observations can be made:

- The difference in total heat before and after frit addition is 7.8 kW, see Figure C-19.
- Radiation heat transfer to the cover is 4.5 kW, see Figure C-20.
- Total power of radiation from melt surface is $P_{int\ rad}$ = 12.3 kW, which corresponds to a heat flux of 17.4 W/cm^2.
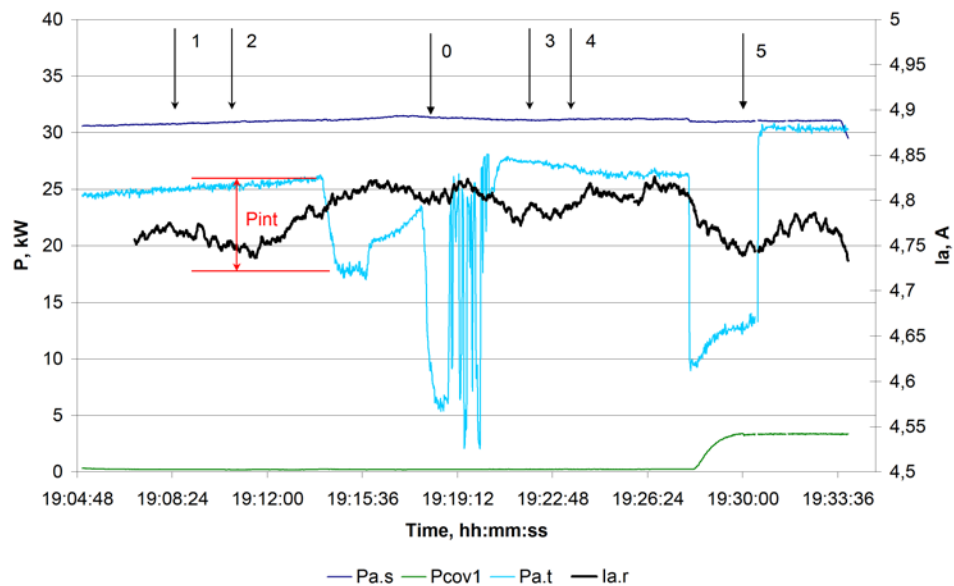
0 – charge filling starting moment, 1 and 2 – scanning moments before charge filling, 3 and 4 – scanning moments after charge filling, 5 – moment when a cover was mounted

Figure C-19. Key parameters and calorimetry data for determining emissivity of glass.

T0.s – temperature on a glass melt surface
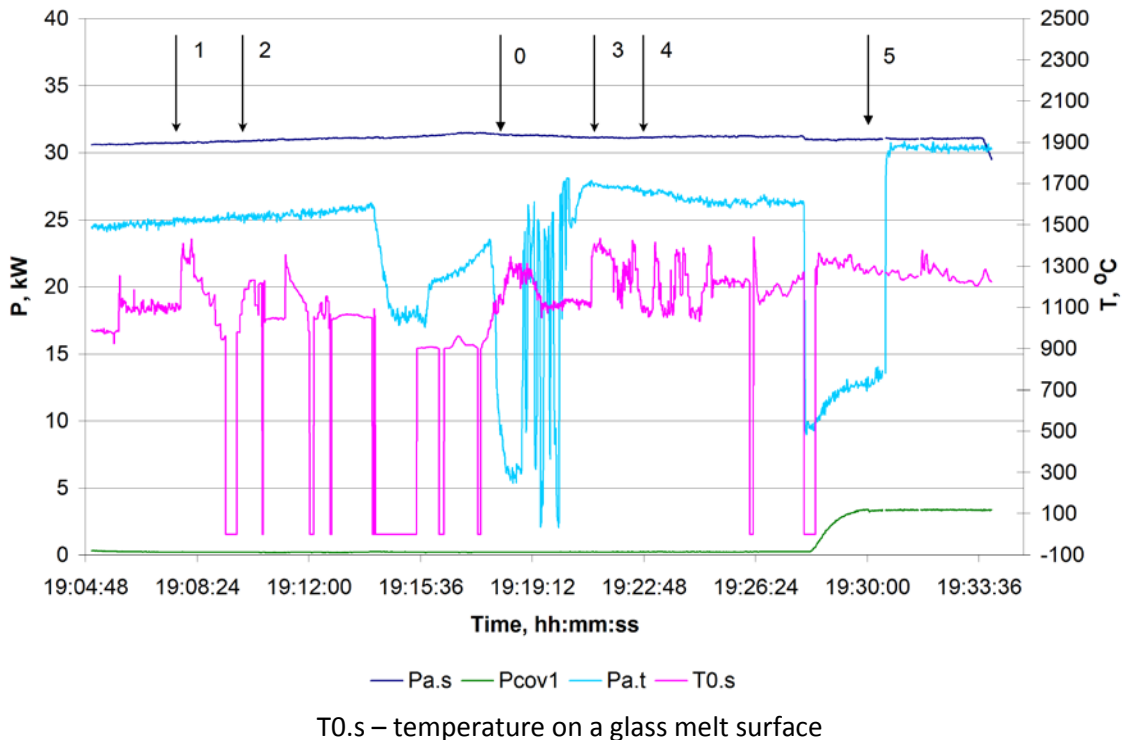
Figure C-20. Key parameters and calorimetry data for determining emissivity of glass.

Figure C-21 and Figure C-22 show the temperature distribution curves determined from the measurement data for the first steady state mode.

$$y = -3E+07x^6 - 854836x^5 - 800540x^4 + 26818x^3 + 39918x^2 - 165{,}91x + 1183{,}6$$

Rcc2 – melt pool radius, m

Figure C-21. Temperature data from scanning with polynomial curve fit at steady state**.**

Figure C-22. Temperature data from scanning with polynomial curve fit at steady state, 90° to previous diameter.

Figure C-23 and Figure C-24 show the temperature distributions for the melt pool surface after the added frit had melted.
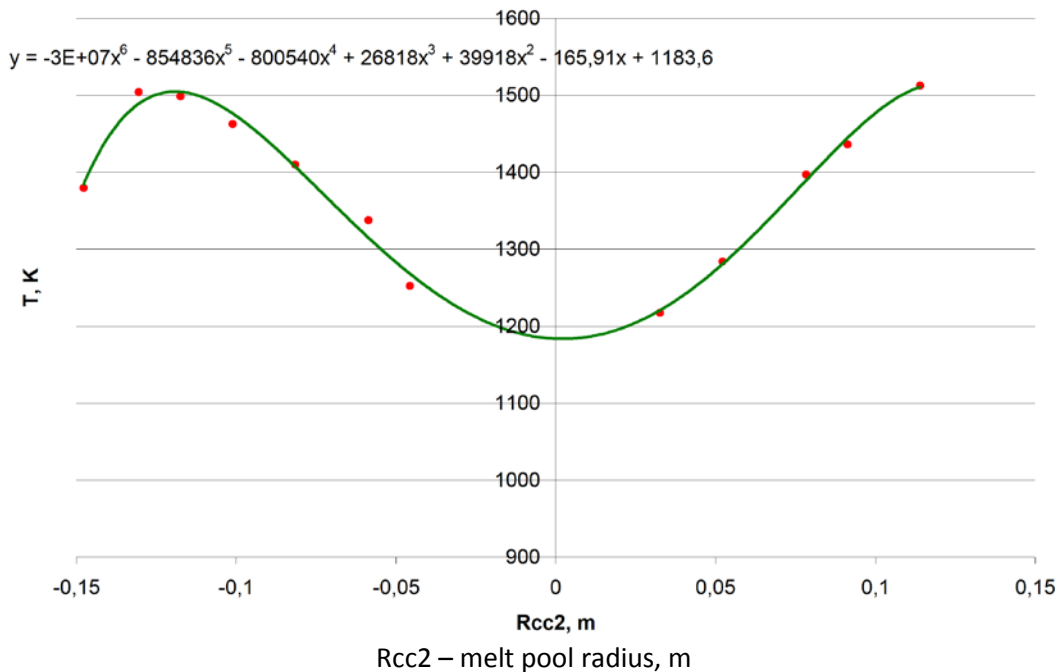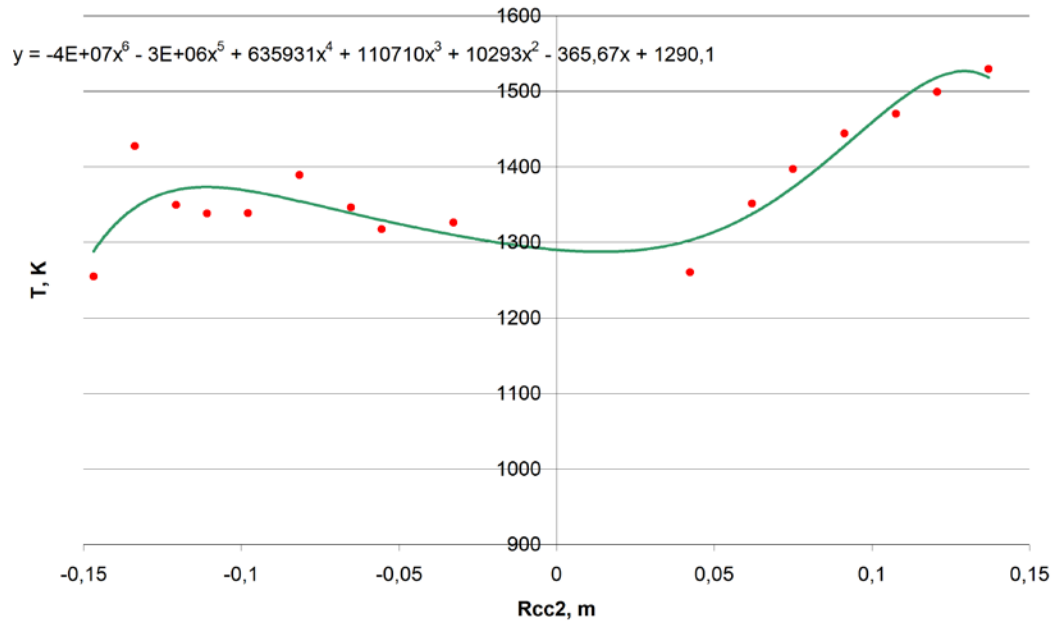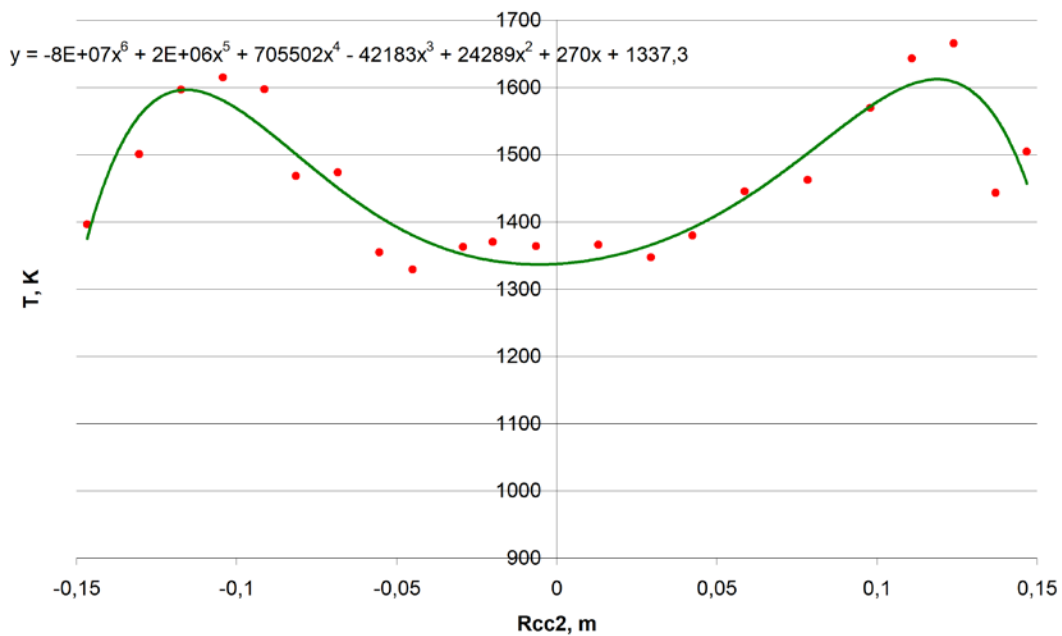

Figure C-23. Temperature data from scanning with polynomial curve fit after added frit was melted.
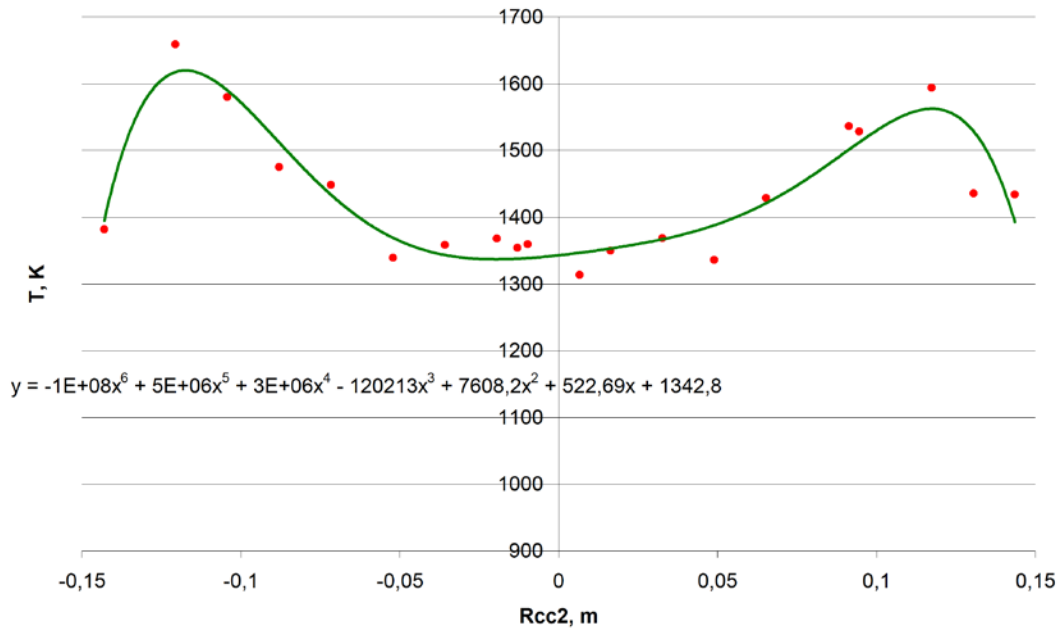
Figure C-24. Temperature data from scanning with polynomial curve fit after added frit was melted, 90° to previous measurement.

For these four scannings values of the integrated emissivity factor were calculated to bef 0.311 and 0.284 for the steady state mode, and 0.325 and 0.349 after the added frit was melted.

Comparison of the results from these two tests is provided in Table C-10. In general, while the methodology works, it is clear that additional data are needed. Values of emissivity are in an approximate range of 0.3 to 0.4, but this is not consistent with the temperatures seen in experiments and modeling results.

Table C-10. Comparison of emissivity values determined in Test #7a nd #7b.

	Scanning No.			
Test No.	Steady State		After frit melted	
	1	2	3	4
Test #7a	0.414	-	0.382	-
Test #7b	0.311	0.284	0.325	0.349

ADDITIONAL DATA FROM SUPPLEMENTAL INTEGRATED TEST SERIES

Prior to System Optimization Test Series, two supplemental tests were performed to implement and evaluate modifications to the 27 MHz generator to increase its power, as well as to the drain device to improve its performance. Results from the first test led to development and implementation of a heated water supply for the inductor cooling water loop. Additionally, a newly designed tenth version of the drain device resulted from these tests.

Supplemental Integrated Test #1

The modifications to the generator were primarily to increase the power available in support of casting in the larger diameter crucible melter, which prior testing had shown was required.

The ninth version of the drain device was similar to the eighth version in geometry, except that the slits were increased in length to provide better electromagnetic transparency. This would also allow use of a larger diameter drain inductor, which modeling had shown would provide better heating. Table C-11 provides the test conditions and stages.

Table C-11. Stages and conditions for Supplemental Test #1.

Time, hr:min	Ia, A	Ua, кV	Ig, A	Ucb, кV	Note
11:30	4.11	5.08	0.85	4	Test beginning. Starting heating on graphite rings.
11:46	6.33	7.64	1.36	5.9	Inductor sensors are switched-off.
13:00	7.73	8.5	1.43	6.12	The 1st ring (small) was removed, then the 2nd ring (big) was removed.
13:13	-	-	-	-	Switching of inductor ground point. Connection of sensors. Pool depth is 100 mm.
13:45	-	-	-	-	Crucible cover installed. Data acquisition for multiple stationary modes started.
14:51	-	-	-	-	The 1st stationary mode
15:50	-	-	-	-	The 2nd stationary mode. T_{melt}=1199°C.
16:17	-	-	-	-	The 3rd stationary mode. T_{melt}=1280°C, T_{tc}=1250°C.
16:33	6.8	7.8	1.45	3.1	The 4th stationary mode. T_{melt}=1180°C. The first calibration of inductor sensors is made.
16:47	7.7	8.5	1.52	3.25	The 5th stationary mode. T_{melt}=1215°C, T_{tc}=1500°C.
17:08	-	-	-	-	The 6th stationary mode. T_{melt}=1278°C.

Table C-11. Stages and conditions for Supplemental Test #1.

Time, hr:min	Ia, A	Ua, κV	Ig, A	Ucb, κV	Note
17:53	7.31	8.24	1.49	3.77	The 7th stationary mode. T_{melt}=1245°C. An agreeing resistor on the voltage sensor was repaired. The second calibration of inductor sensors was made.
18:08	-	-	-	-	The 8th stationary. T_{melt}=1270°C, T_{tc}=1457°C, a thermocouple is immersed to 68 mm depth.
18:10	-	-	-	-	1st casting has taken place at pressure decline in the cold crucible. Pool depth after casting was 66 mm. The maximum power in the drain was 3.1 kW.
18:36	-	-	-	-	Frit addition and melting.
19:04	-	-	-	-	Thermocouple was immersed into melt. T_{tc}=1576°C.
19:18	-	-	-	-	The 27 MHz generator was powered on.
19:23	-	-	-	-	Power supply of the pressure sensor and water flowmeters failed.
19:46	8.09	8.0	1.3	3.2	T_{dr}=400°C.
20:18	-	-	-	-	Casting was not achieved due to electrical arcing and shutdown of 27 MHz generator. Casting was started mechanically.
20:18	-	-	-	-	The 2nd casting
20:30	-	-	-	-	Casting finished
20:40	-	-	-	-	Generator powered off.

Electrical efficiency of the system was desired to help determine the maximum available power and the extent of scale-up that could be achieved using the available equipment for processing the specific glass composition being used in the testing. The electrical efficiency was determined using the following equation:

$$\eta = [Pa.t + Pbus1 + Pc1]/(Ia \cdot Ua) \tag{C-4}$$

where:

Pa.t – total active power supplied to inductor

Pbus1 – power losses on busses in capacitor bank

Pc1 – total electrical and thermal losses in generator circuits'

Ia – anode current of generator

Ua – anode voltage of generator

The electrical efficiency was calculated for various stages of the test including melt initiation, eight steady state modes, and casting. Additionally, generator parameters, calorimetry data, and temperature data were collected for these various stages. The following series of figures presents this information. Figure C-25 through Figure C-27 present the data for the melt initiation process. Figure C-28 through Figure C-29 provide the data for the eight steady state modes obtained. Finally, Figure C-30 through Figure C-32 present the data for the casting processes.

During the testing the 27 MHz generator did not demonstrate stable operation. Some of the components used in the modification were not compatible with the operational parameters of the generator during the melt casting initiation process. Additionally, condensation issues continued to cause shut-downs of the generator and interrupted heating, such that electromagnetic draining was not achieved. These issues were addressed for the follow-on test.
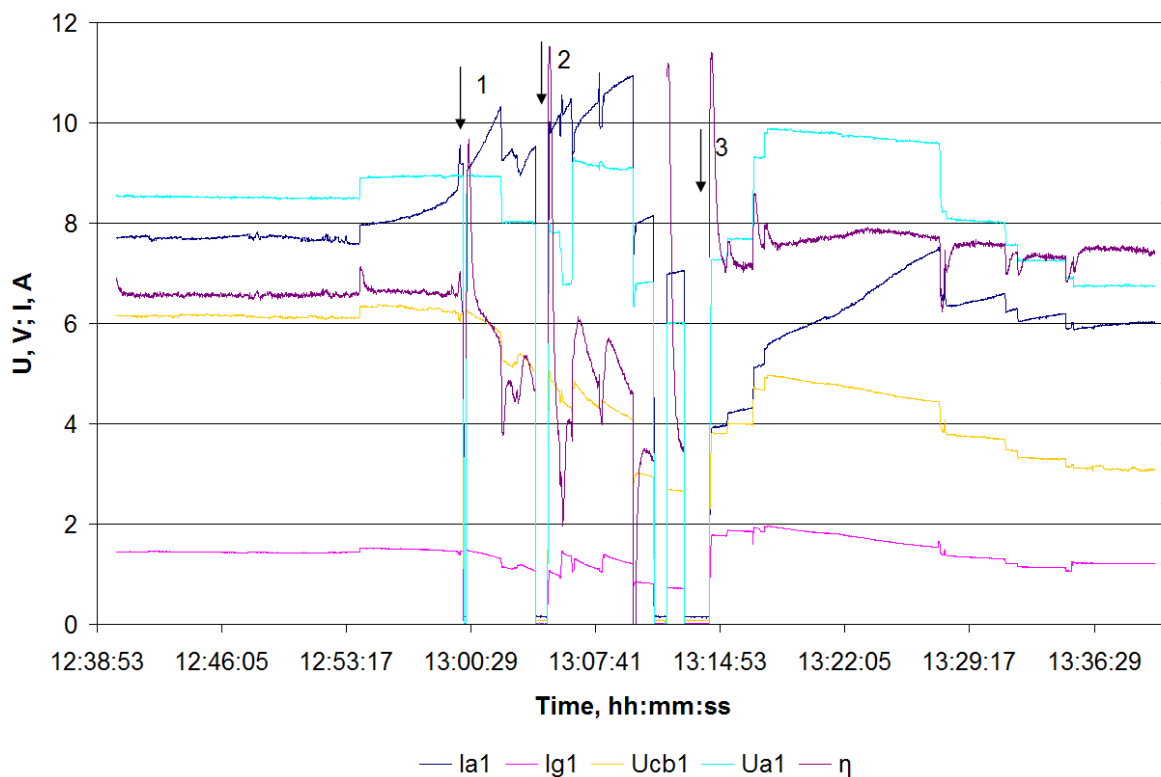
(Ia1 – generating lamp anode current; Ig1 – generating lamp grid current; Ucb1 – voltage on a capacitor bank; Ua1 – generating lamp anode voltage; η – efficiency of the generating lamp; 1 – the beginning of graphite rings removal; 2 – the beginning of average point switching; 3 – the beginning of melt pool melting)

Figure C-25. Generator electrical parameters during melt initiation.
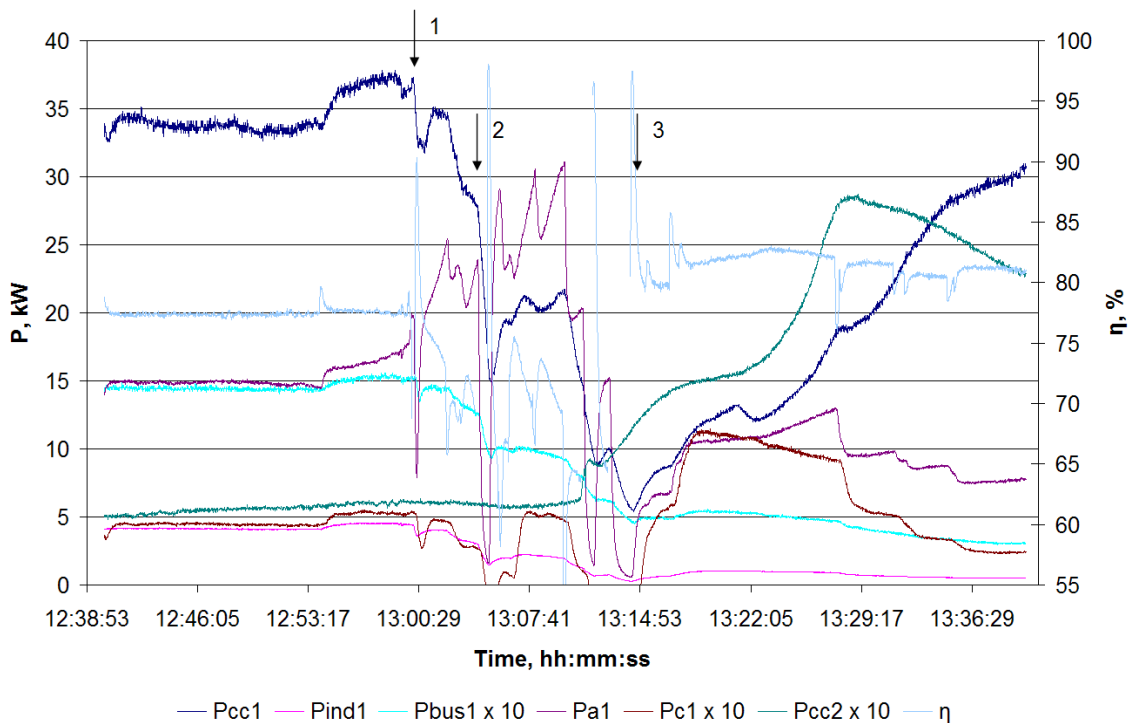
(Pcc1 – power of electric and heat losses in cold crucible lateral sections, Pind1 – electric losses power in the melter inductor, Pbus1 – power of electric losses in capacitor bank buses, Pa1 – power of calorimetry on the big generator lamp anode, Pc1 – power of electric and heat losses in generator oscillatory circuits, Pcc2 – power of heat and electric losses in the drain, Pind2 – power of electric losses in the inductor of the small generator, 1 – the moment of graphite rings removal)

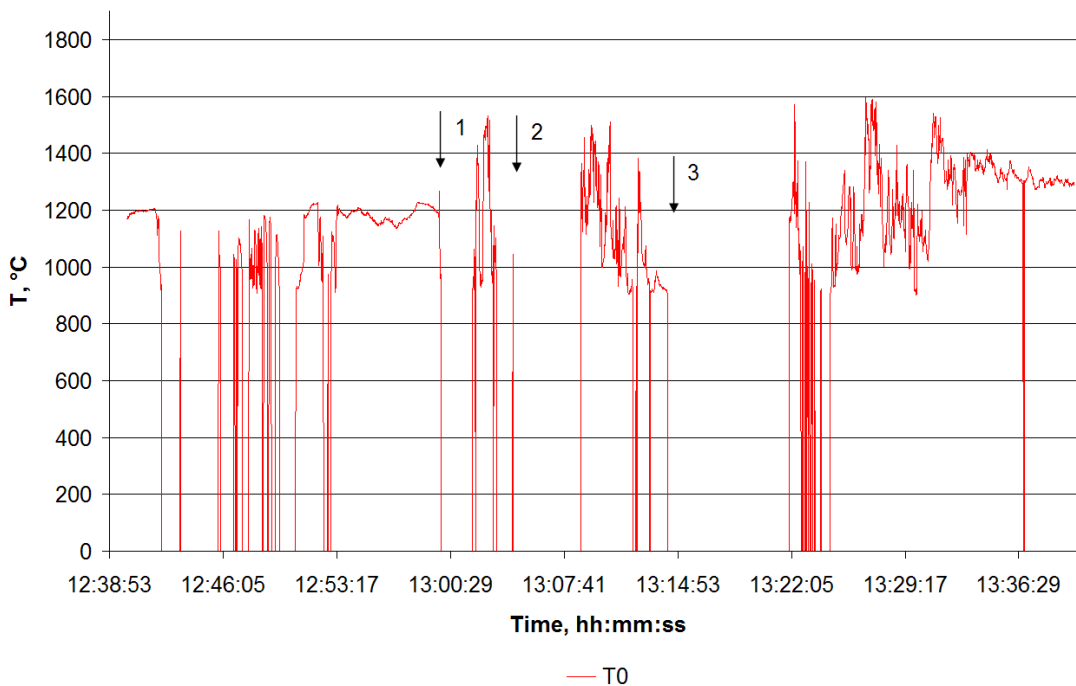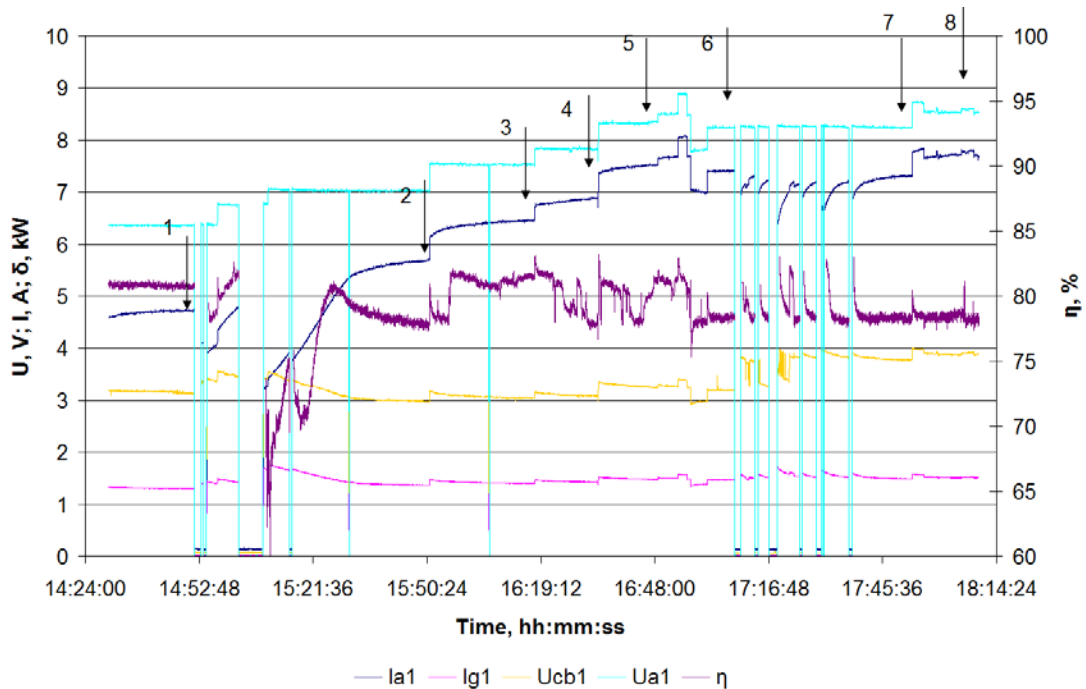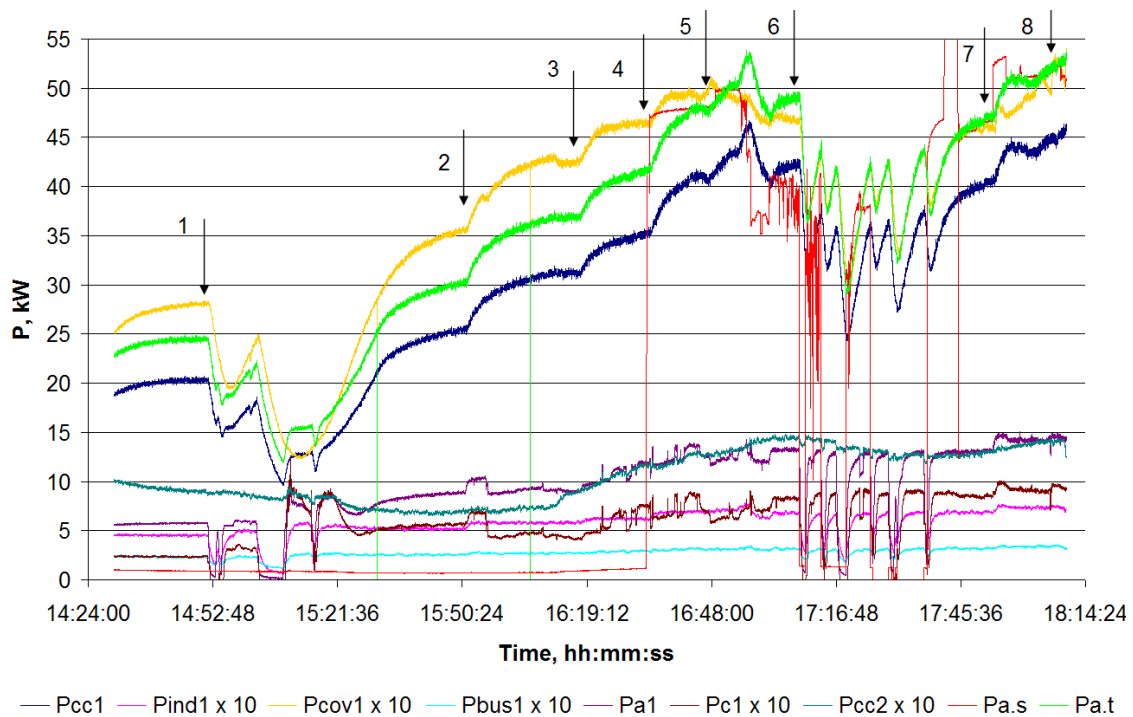**Figure C-26.** Power losses in various system elements during melt initiation.

Figure C-27. Surface maximum temperatures during melt initiation.

1through 8 – melting stationary modes

Figure C-28. Generator electrical parameters during steady state modes.

(1through 8 – melting steady state modes, Pa.s – active power, supplied to the inductor and determined on inductor current and voltage signals, Pa.t – active power, supplied to the inductor and determined by means of calorimetric measurements)

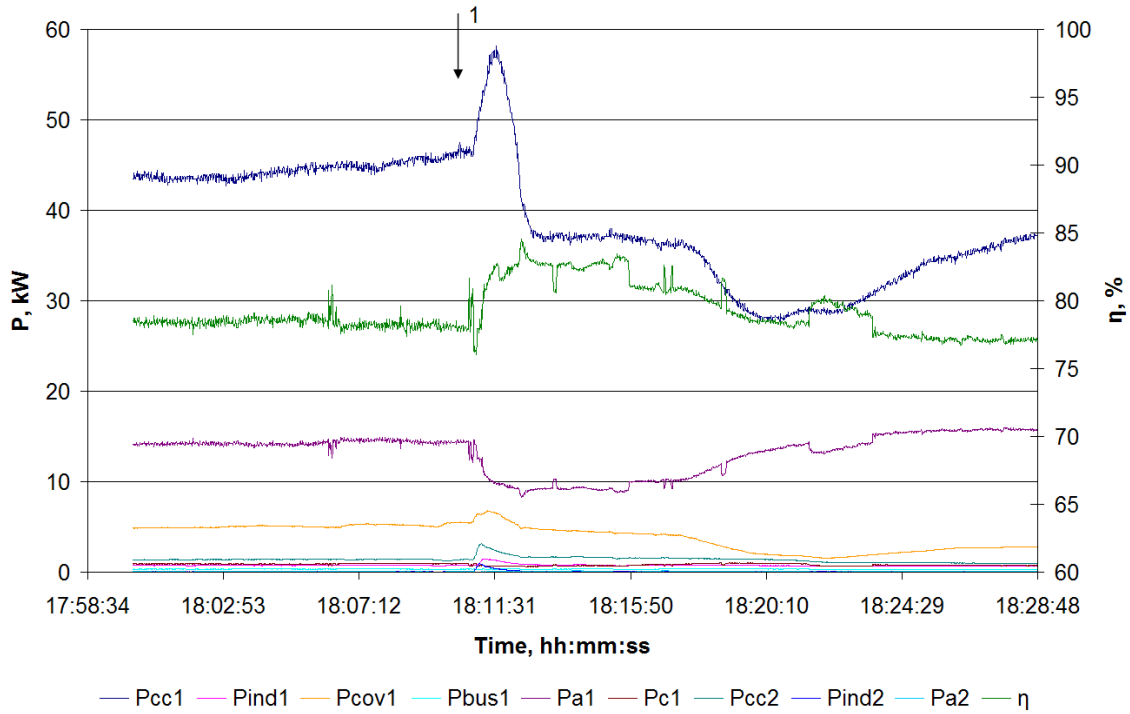**Figure C-29.** Electrical and heat losses in system elements during steady state modes**.**

Figure C-30. Electrical and heat losses in system elements during the first casting.
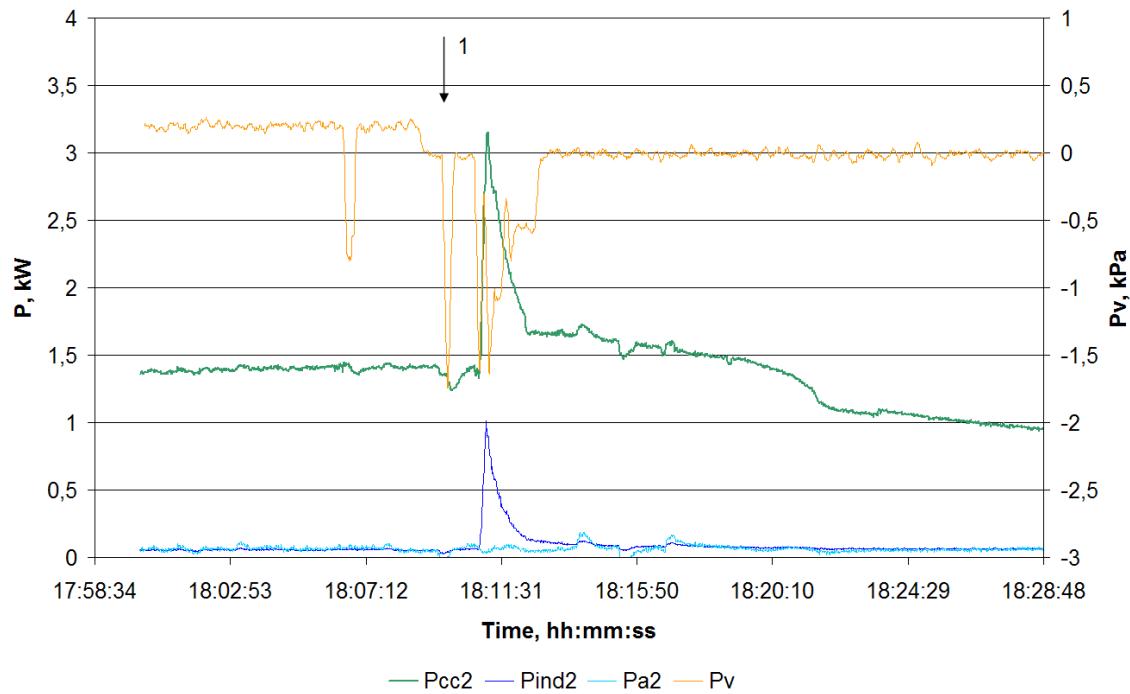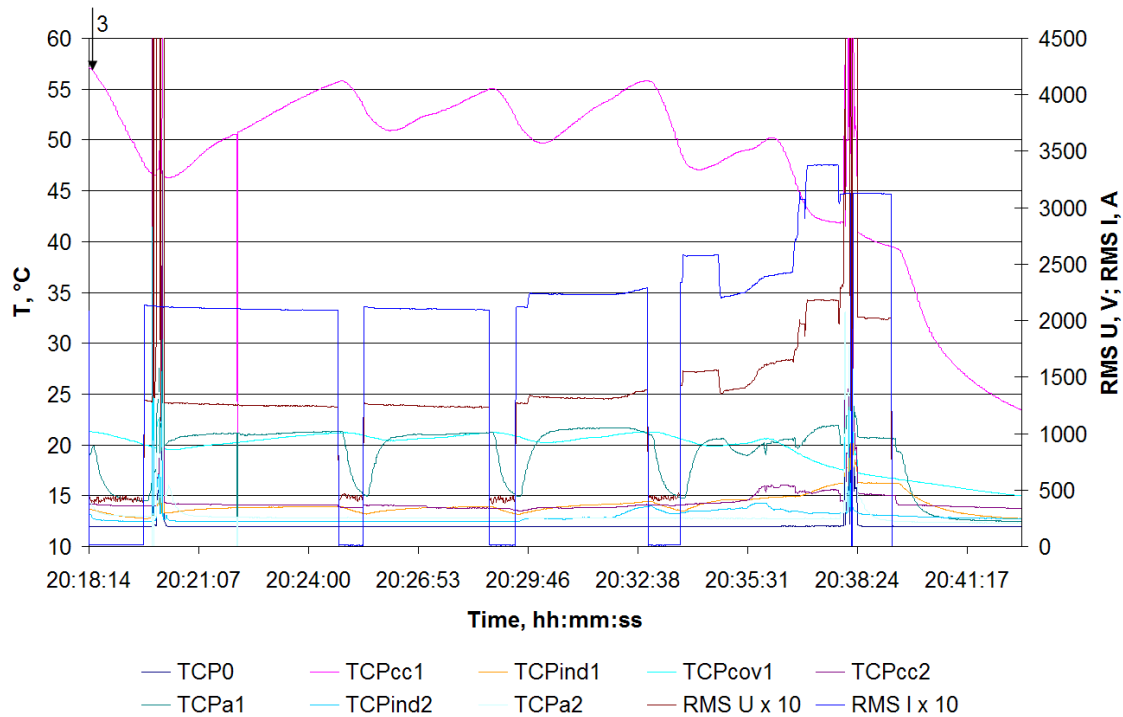

Figure C-31. Electrical and heat losses in system elements during the first casting.

TCP0 – feed water temperature, TCPcc1 – output temperature of cold crucible water, TCPind1 – output temperature of primary inductor water, TCPcov1 – output temperature of cold crucible cover water, TCPbus1 – output temperature of capacitor bank buses water, TCPa1 – output temperature of primary generator lamp anode water, TCPc1 – output temperature of primary generator oscillatory circuits water, TCPcc2 – output temperature of drain water, TCPind2 – output temperature of drain generator inductor water, TCPa2 – output temperature of drain generator lamp anode water, 3 – time of the second casting

Figure C-32 Output cooling water temperature for various elements during second casting.

Supplemental Integrated Test #2

This test had three primary objectives:

1. Evaluate the new drain device concept, the tenth version, especially in conjunction of the modified 27 MHz generator.

2. To test the new design of the 27 MHz generator with an improved high-frequency generating tube, with the following new devices:
   - The power supply of 10 kW.
   - The capacitor bank.
   - The inductor and feed busses.

The capacitor bank was redesigned to be physically smaller such that it could be positioned better under the crucible bottom. The new design also reduces the length of the busses significantly,

reducing the electrical losses. Additionally, the case of the capacitor bank is made from copper, which also reduces losses. This new configuration allowed the busses to the inductor to be re-oriented such that they aligned vertically, rather than horizontally.

A new inductor two-turn planar coil, with larger diameter, was also designed and manufactured. The inductor was designed to be capable of operating at the higher current with lower electric losses. Modeling showed that this configuration would provide the best coupling between the drain inductor and the melt pool. The spacing between the inductor and the drain were minimized at 3-4 mm.

Finally, a water heating system for the drain inductor cooling loop was designed and implemented. The controller and heating tank are shown in Figure C-33.

Figure C-33. Primary components of the water heating system for drain inductor cooling loop. Upper – controller, lower – heating tank.

Table C-12 shows the test stage and conditions for this supplemental test.

Table C-12. Stages and conditions for Supplemental Test #2.

Time, hr:min	Ia, A	Ua, кV	Ig, A	Ucb, кV	Note
13:06	2.5	9	1.6	5.3	Generator powered on. Melt initiation with a graphite ring.
13:17	3	10.5	2	8	Inductor voltage sensor is switched-off.
15:17	7.5	9.5	1.2	5	
15:32	-	-	-	-	Graphite ring is removed.
15:44	-	-	-	-	Inductor voltage sensor is connected.
16:45	6.07	5.88	0.77	2.29	a_{melt} = 130 mm.
16:55	-	-	-	-	Calibration of calorimetry system.
17:05	-	-	-	-	Arcing on cold crucible.
17:52	-	-	-	-	a_{melt} above the drain is 120 mm. Distance from melt to top of the cold crucible assembly ring is 29 cm.
18:02	6.14	5.90	0.77	2.40	The small generator is powered on. Ia2=0.6 A, Ig2=300 mA. T_{dr} = 250°C. Power in the drain is .,6 kW.
18:02	-	-	-	-	IIS fails when 27 MHz generator is powered on.
18:17	-	-	-	-	Ia2=1.1 A, Ig2=300 mA.
18:20	-	-	-	-	Ia2=1.5 A, Ig2=235 mA.
18:23	-	-	-	-	Ia2=1.7 A, Ig2=296 mA.
18:28	-	-	-	-	Ia2=1.6 A, Ig2=275 mA.
18:32	-	-	-	-	Ia2=1.8 A, Ig2=335 mA.
18:38	-	-	-	-	Ia2=1.8 A, Ig2=320 mA.
18:52	-	-	-	-	T_{dr} = 360°C.
19:03	7.2	7.5	1.25	3.3	Ia2=1.81 A, Ig2=315 mA.
19:08	-	-	-	-	The crucible is raised. Distance from the primary inductor end face up to cold crucible bottom is 1 cm.
19:12	-	-	-	-	Ia2=1.2 A, Ig2=390 mA.
19:18	-	-	-	-	Ia2=1.4 A, Ig2=390 mA. Current outflow on cooling hoses of the cold crucible is found out and liquidated, that has resulted in increase of losses in the drain up to 2 kW
19:22	-	-	-	-	Ia2=1.45 A, Ig2=380 mA.
19:27	-	-	-	-	Ia2=1.5 A, Ig2=361 mA. T_{dr} = 402 °C.
19:45	-	-	-	-	Ia2=1.6 A, Ig2=340 mA. T_{dr} = 440 °C.
19:50	-	-	-	-	Ia2=1.61 A, Ig2=340 mA. T_{dr} = 534 °C.
19:55	-	-	-	-	The 1st casting. Both generators are switched-off for a casting stoppage.
20:00	-	-	-	-	The big generator is switched-on.

Table C-12. Stages and conditions for Supplemental Test #2.

Time, hr:min	Ia, A	Ua, кV	Ig, A	Ucb, кV	Note
20:03	-	-	-	-	The small generator is switched-on.
20:10	-	-	-	-	The small generator is switched-off because of breakdowns.
20:12	-	-	-	-	Ia2=0.6 A, Ig2=200 mA. The crucible is grounded. Breakdowns have stopped.
20:26	-	-	-	-	Ia2=0.7 A, Ig2=340 mA.
20:32	-	-	-	-	Ia2=1.3 A, Ig2=310 mA. Breakdowns have renewed. The small generator is switched-off.
20:40	-	-	-	-	Melt casting by mechanical means.
20:50	-	-	-	-	Generator powered off.

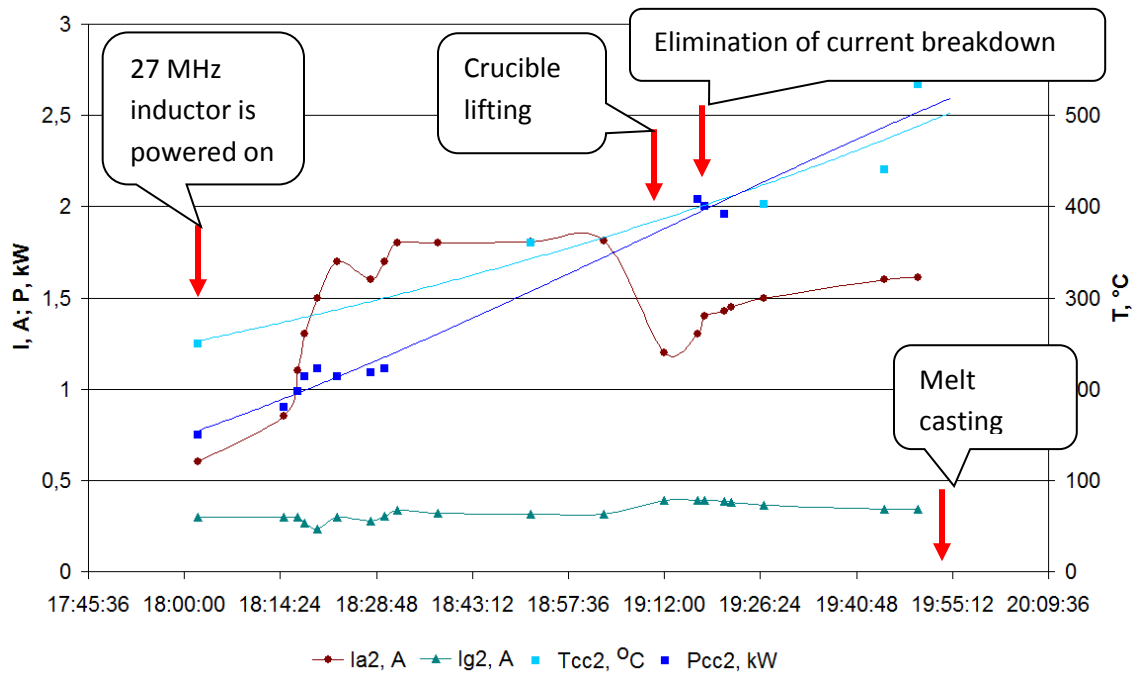Figure C-34 shows some key electrical and thermal parameters during the various test stages.

Figure C-34. Key electrical and thermal parameters during test stages. (Tcc2 is the temperature of the glass in the drain measured with a pyrometer.)

At 19:18 a current leak from the capacitor bank was discovered. A hose from the crucible cooling water supply was contacting the case of the chamber of the 27 MHz generator. Once eliminated, growth of the anode current and decreasing of the lamp grid current of the 27 MHz generator were observed. It testified to positive dynamics of glass heating above the drain.

Electromagnetic melt casting occurred at 19:55. This was the first time that a successful draining using only electromagnetic energy had been achieved in the 407 mm diameter crucible. However, it is necessary to enhance the drain design further for improved electromagnetic transparency.